supporting partners

48th INTERNATIONAL CONGRESS ON SCIENCE TECHNOLOGY AND TECHNOLOGY-BASED INNOVATION

"SCIENCE AND TECHNOLOGY FOR ADVANCING TOWARDS SDGs"

~PROCEEDING BOOK~

Table of Contents (Proceeding Book)

Oral Session

Session A: PHYSICS / APPLIED PHYSICS

AN ATTENUATION OF SOLAR RADIATION BY DIFFERENT CLOUD TYPES AT NAKHON PATHOM

Udomphan Nacksriphod*, Wilawan Thainlueang, Korntip Tohsing Sahussa Peengam

Department of Physics, Faculty of Science, Silpakorn University, Nakhon Pathom 73000, Thailand

*e-mail: nacksriphod_u@silpakorn.edu

Abstract:

Clouds can attenuate the solar radiation by scattering, reflecting, and absorbing processes. During a direct obstacle of the sun by clouds, an amount of the solar radiation intensity changes in both direct and indirect ways. Clouds normally change in types, heights, or shapes, which are complicated to measure, especially in a tropical area. Therefore, in this study, an attenuation of broadband solar radiation or global solar radiation by clouds, which are divided into three levels: low clouds, middle clouds, and high clouds was investigated. All measured data were conducted in Nakhon Pathom Province using a ceilometer, pyranometer and sky view. Then, these data were used to determine a cloud modification factor (CMF) with in one minute of interval during the year of 2019 - 2020. From the analyzed results, the most amounts of clouds occupied in the sky were mid – level clouds and the highest value of CMF was found to be 0 – 25%. For this case study, the stratus clouds delivered the highest CMF compared to other clouds found on the selected date. The results obtained in this work can be used to estimate solar radiation for generating an electricity from solar cells.

Introduction:

The solar radiation reaching to the Earth's surface is a spectrum emitted by the sun with a wavelength of 300 -3000 nm. At present, the solar radiation is increasingly applied for the benefit of the clean energy. But solar radiation is absorbed and scattered by various components in the atmosphere. Cloud is one of component in the atmosphere affecting the attenuation of solar radiation. Clouds change their type, height, and shape over time, which vary by different climate zones. A height of the cloud or cloud base height (CBH) is categorized into three levels as shown Table 1 [1]. Low-level clouds have a cloud base not higher than 2,000 meters and most of the particles inside the cloud are water droplets. For mid-level clouds, they are observed at an altitude between 2,000 and 7,000 meters. These clouds form at the temperature between $0^{\circ}$and 40° depending on altitude and season. Therefore, they may consist of water droplets and ice crystals. High-level clouds locate at altitudes above 7,000 meters. At this altitude, the air is relatively cold and dry leading to the composition on of high-level clouds being ice crystals. In the past, researchers have measured and analyzed the solar radiation attenuation by clouds in different areas. Monteith and Unsworth (1988) have found that a thickness of low-level clouds may reduce solar radiation intensity by 80 – 90%. In certain conditions, tall convective clouds may raise its value by 10 – 15% when compared with a cloudless weather. Schafer (1996) studied a dependence of CMF with cloud amount and the solar zenith angle. Foyo-Moreno (2001) studied the information of clouds obtained from two radiometric stations. The first one was located at University of Almeria, a seashore location (36.83°N, 2.41°W, 20 m above sea level) during 1993 -1994 and solar global irradiance was measured using a Kipp & Zonen (model CM-11). The second one was located in a border of Granada (37.18°N, 3.58°W, 660 m above sea level) during 1994 – 1995. In this study, they focused on Ultraviolet (UV) radiation and the

cloud influence over it. The CMF in the UV part was defined for two different cloud types according to their altitude into low-medium and high-level clouds. The results of this indicated that an empirical model under cloudless condition combined with the cloud modification factor can estimate the global ultraviolet radiation with a high confidence level. Josep Calbo (2005) proposed the CMF of UV (280 – 400 nm) as expressed in Equation 1

$$CMF = UV_{cloudy}/UV_{clear} \quad (1)$$

where UV_{cloudy} is the UV irradiance measured under cloudy sky, and UV_{clear} is the UV irradiance simulated or estimated for the same atmospheric conditions such as ozone column, aerosol, pressure, temperature, and solar zenith angle under clear sky condition. This calculation was similar to the study of UVB radiation characteristics at Cordoba, Argentina proposed by Mara Laura Lopez (2009) and it was found that the CMF of UVB for the wavelength of 320 – 420 nm can be defined in Equation 2 expressed below

$$CMF = UVB_{cloudy}/UVB_{clear} \quad (2).$$

Adam (2011) studied the effect of different cloud levels on solar radiation. The data used were collected and analyzed at the South Valley University (SVU) (26.2°N, 32.7°E, 96 m above sea level) during 2004 – 2007. The cloud information was obtained from the Precision Spectral Pyranometer (PSP) with a spectral range of 295 – 2800 nm. It was found that clouds can significantly reduce the amount of solar radiation. The attenuation of solar and terrestrial radiation due to different cloud amounts and cloud types was also proposed by El-Nouby (2010). A 10 – yeas period of data at Hamburg Meteorological Observatory was investigated. The change in radiation flux largely depends on the density and frequency of occurrence of the different cloud types. Considering to the tropical region, clouds are rapidly change in shapes, types and heights. Moreover, there are only few researches on clouds in the tropics, especially the attenuation of broadband solar radiation by clouds observed in Thailand. Therefore, the aims of this work are to investigate the cloud height of the measured data using a ceilometer and to study the attenuation of global solar radiation by different cloud types and heights in Nakhon Pathom, Thailand, which located in the tropical region near the equator representing the hot and humid climate.

Table 1.
Classification of cloud levels by cloud base height [1]

Cloud base height (meters)	Cloud level
surface – 2,000	low
2,000 – 7,000	medium
7,000 – 12,000	high

Methodology

3.1 Instruments and data

The data used in this work was collected at Nakhon Pathom Province (13.82°N, 100.4°E), Thailand during the year of 2019 – 2020. The cloud base height was observed by the ceilometer (Model: CS- 135, Campbell Scientific Company). The device sends a red laser pulse (905 nm) into the sky and measures the backscattered signal from the clouds above the instrument. Simultaneously, a timer is used to measure the signal transmission and estimate the CBH according to the Equation 3 expressed below [8].

$$CBH = \frac{ct}{2} \quad (3)$$

where CBH is the distance between the ceilometer and the cloud [m]
c is the speed of light which is equal to 3×10^8 m /s
t is the transmission time [s].

To investigate the attenuation of global solar radiation, a pyranometer from Kipp&Zonen (model: CMP11) was installed and collected the data. An output of the pyranometer is a voltage signal. This voltage is then converted into the global solar radiation by divided by a sensitivity obtained from a manufacturer of the pyranometer. The solar radiation incident on the pyranometer depends also on the cosine of incident angle. Ideally, the precise pyranometer responses to the incident sunlight the same as ideal cosine of angle of incidence. However, the pyranometer used in this work has a cosine response error about 5-10% for the solar zenith angle greater than 80 degrees. This error is acceptable for the accurate measurement of solar radiation [1]. In order to classify the cloud type occurred on the sky, sky images were obtained using a sky view from Prede (model: PSV – 100). These instruments are shown in Figure 1 and the images obtained from the sky view on different dates also shown in Figure 2 for cloudy and clear sky conditions in Figure 2(a) and 2(b), respectively. The overview of all instruments used in this work located in the same area is shown in Figure 3.

a **b** **c**

Figure 1.
The instruments used for the data acquisition in this work a) ceilometer b) pyranometer and c) sky view.

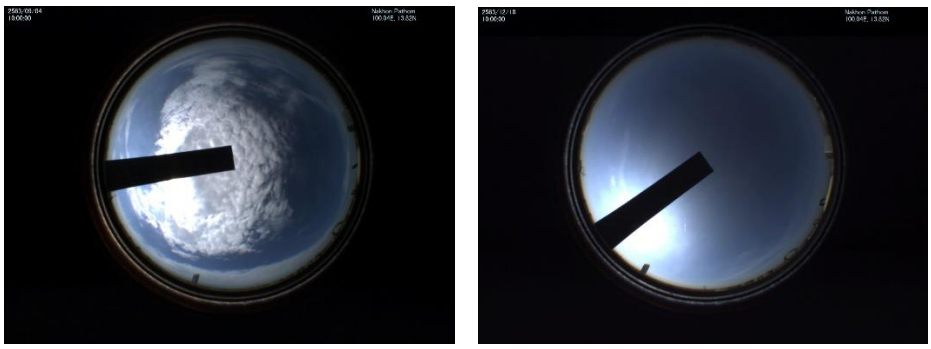

a. **b.**

Figure 2.
Examples of photographs in this works a) Image in 4 September 2020 at 10:00 a.m. b) Image in 18 December 2020 at 10:00 a.m.

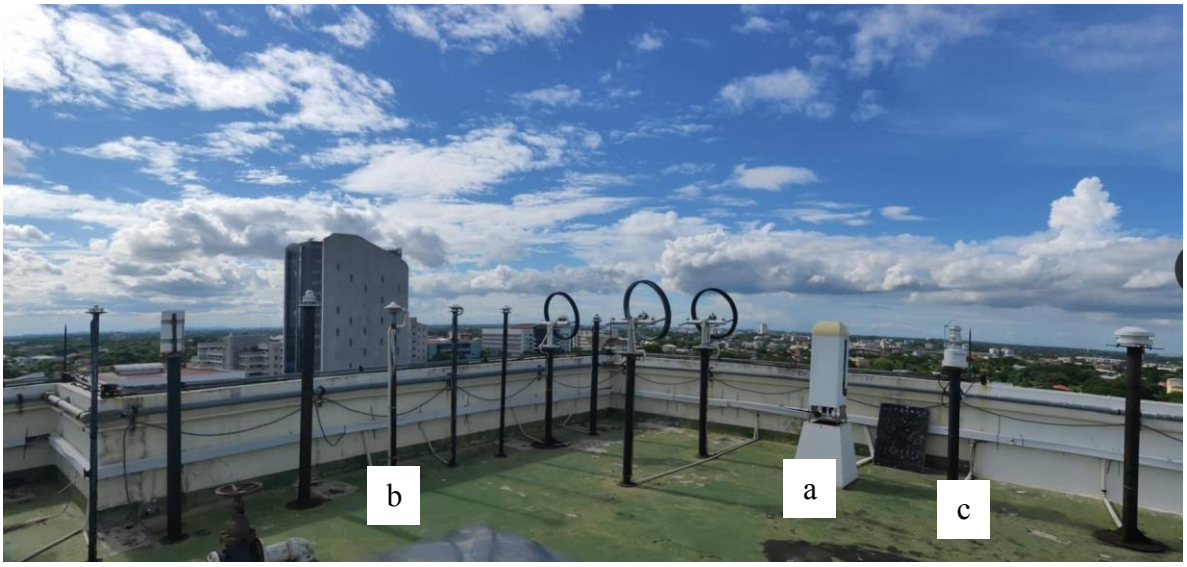

Figure 3.
Overview of instruments installed on the roof of Science Building 1, Silpakorn University a) ceilometer b) pyranometer and c) sky view

3.2 Data analysis

To obtain a statistical characteristic of the clouds and the attenuation of solar radiation at Nakhon Pathom, two analytical processers were presented as the details below.

3.2.1 Cloud base height analysis

The CBH from the ceilometer for every minute during 2019 – 2020 was collected for investigating the occurrence of clouds at different heights in terms of hourly, monthly and yearly data.

A histogram of the accumulative cloud amount was also presented. Moreover, the histograms of diurnal cloud amount according to three base heights on 1 July 2019was analyzed.

3.2.2 Cloud modification factor (CMF)

An incident solar radiation at the Earth's surface is attenuated by clouds and other atmosphere components. In order to investigate the effect of clouds on global solar radiation, a cloud modification factor (CMF) is proposed. The CMF is a percentage value that represents the attenuation of clouds on solar radiation and it can be calculated by using the amount of global solar radiation under clear sky and all-sky conditions (see Figure 4) expressed in Equation 4.

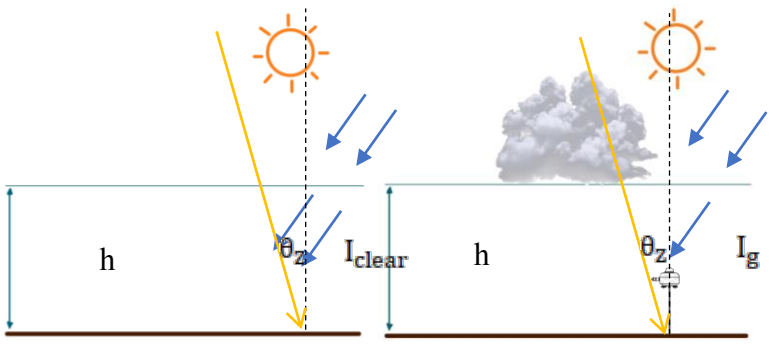

a b

Figure 4.
a) The global solar radiation under clear sky condition calculated from an empirical model and b) The global solar radiation measured by pyranometer.

$$\%CMF = \left(1 - \frac{I_g}{I_{clear}}\right) \times 100 \quad (4)$$

where I_g is the global solar radiation measured by pyranometer [W/m^2]

I_{clear} is the global solar radiation under clear sky condition calculated from an empirical model in as [W/m^2] expressed in Equation 5 [2].

$$I_{clear} = 1098 \cos\theta_z \exp(-0.057/\cos\theta_z) \quad (5)$$

where θ_z is a solar zenith angle [degree].

The constant values of 1098 and -0.057 are the model coefficients obtained by the relationship [9] between the solar radiation and the solar zenith angle proposed by Serm Janjai (2011) and the model performance was validated by comparing the solar radiation under clear sky condition calculated from the model with that obtained from measurements at Chiang Mai Station, Ubon Ratchathani, Nakhon Pathom and Songkhla. It was found that the model delivered a good agreement between both data.

The CMF data of 1 - minute interval during the year of 2019 and 5 - minute interval of 2020 was calculated. The different time steps of each year depend on the sky images from the sky view, which were applied for classifying the type of clouds. The CMF for each cloud type was also determined using the data on 4 July, 2019 and 4 September, 2020 from 7 A.M. to 5 P.M.

Results and Discussion:

4.1 Cloud base height and cloud amount analysis

The hourly cloud cumulative frequency of three cloud height levels during July 2019 to September 2020 was analyzed and the exampling result on 1 July 2019 is presented in Figure 5. The distribution showed that mid – level cloud was mostly found in the morning and low – level clouds frequently occupied the sky during a daytime. Whereas, the high – level clouds were mostly observed at night. The occurrence of different cloud heights at different time might be from the difference in air temperature and water droplets or ice crystals in the clouds. Considering the cumulative frequency of the whole period during this study, the result is shown in Figure 6.

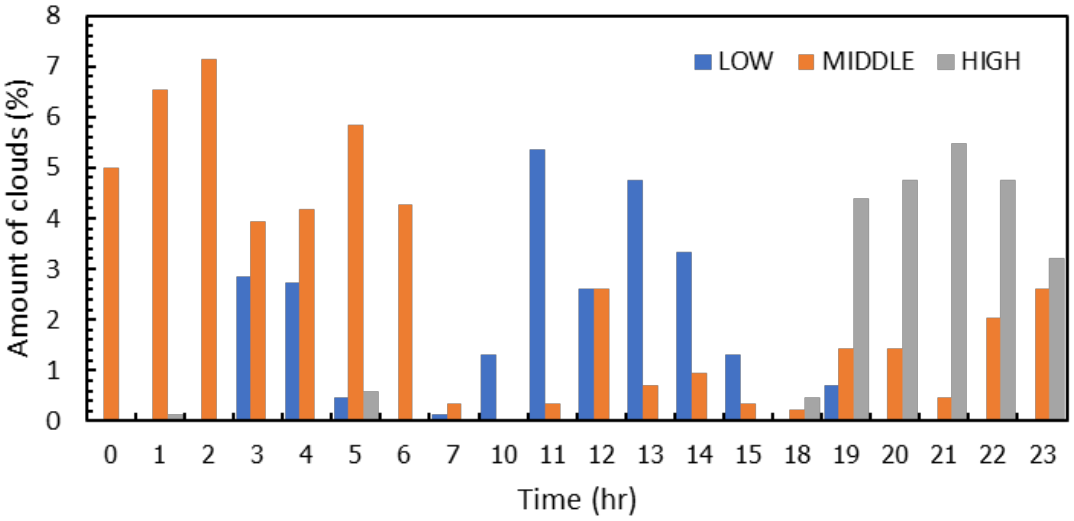

Figure 5.
Histogram of cloud occurrence on 1 July 2019 at Nakhon Pathom

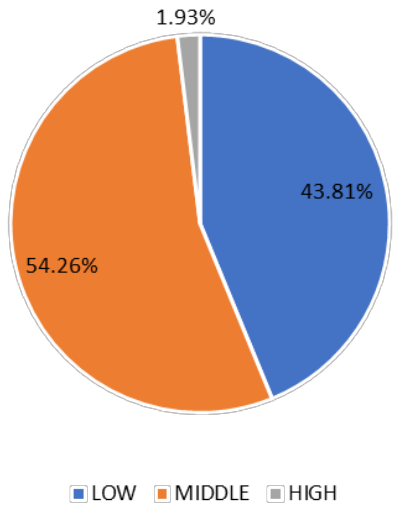

Figure 6.
Cumulative frequency for the whole period of the study of 2019 – 2020

Most clouds occurred in the sky during the year 2019 – 2020 were mid – level cloud with the frequency of 54.26% following with 48.81% of low – level cloud and the small amount of high – level cloud of 1.98%. This characteristic of the cloud can be affected by two seasonal monsoons in Nakhon Pathom. A northeast monsoon during winter time (November – February) brings a cold and dry airmass from China to Thailand causing small amount of cloud appeared in the sky. During a southwest monsoon (May – October), moist air from the sea and ocean were carried to the country getting more clouds on the sky as shown in Figure 7 and 8. However, the low cloud amount between October and December were different for both years, which might cause from seasonal change in Thailand. In the year of 2019, the Positive Indian Ocean Dipole (Positive IOD) phenomenon resulting in the southwest

monsoon blowing from the Indian Ocean to Thailand and the northeast monsoon blowing through the western North Pacific Ocean and the South China Sea to Thailand was weaker than usual. This led to less rain than usual (Meteorological Department of Thailand). Whereas in 2020, La Niña was occurred with wet conditions across large parts of South East Asia, Australia and the latest seasonal outlook was consistent with historical La Nina conditions.

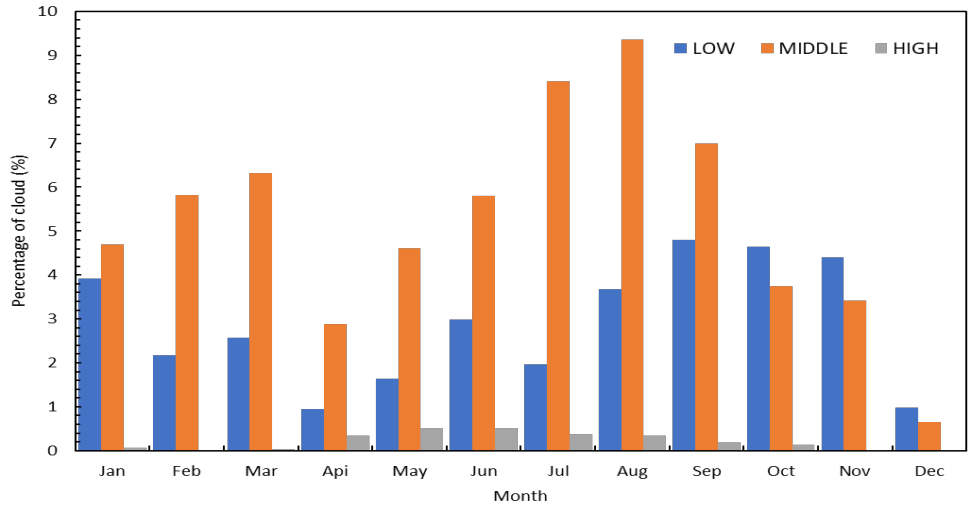

Figure 7.
The amount of different cloud heights from the ceilometer in 2019 at Nakhon Pathom

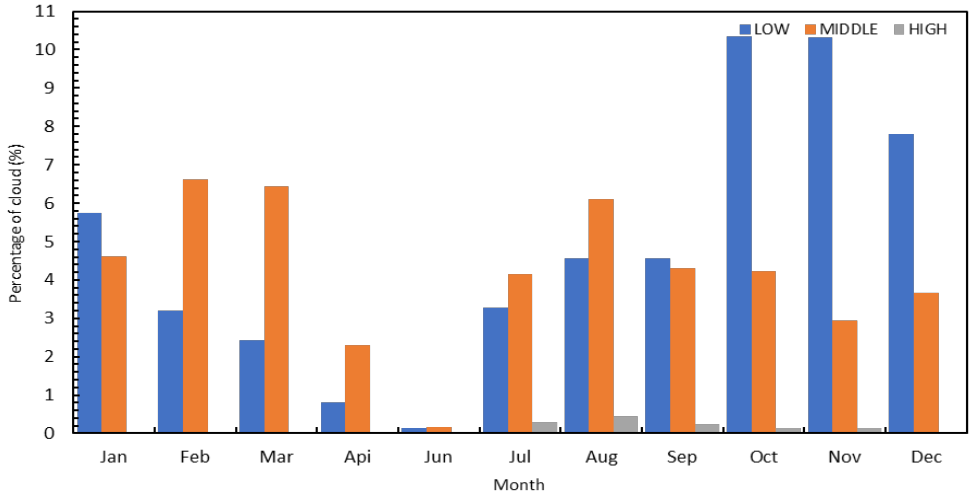

Figure 8.
The amount of different cloud heights from the ceilometer in 2020 at Nakhon Pathom

4.2 Cloud modification factor at Nakhon Pathom

The global solar radiation from the pyranometer and the global solar radiation under clear sky condition calculated from the empirical model of the same time were applied for determining the CMF of 2019 and 2020. Then, the histogram of the CMF, which was separated into 4 ranges of a percentage of solar radiation attenuation such as 0 – 25%, 26 – 50%, 51 – 75% and 76 – 100% and the result is demonstrated in Figure 9.

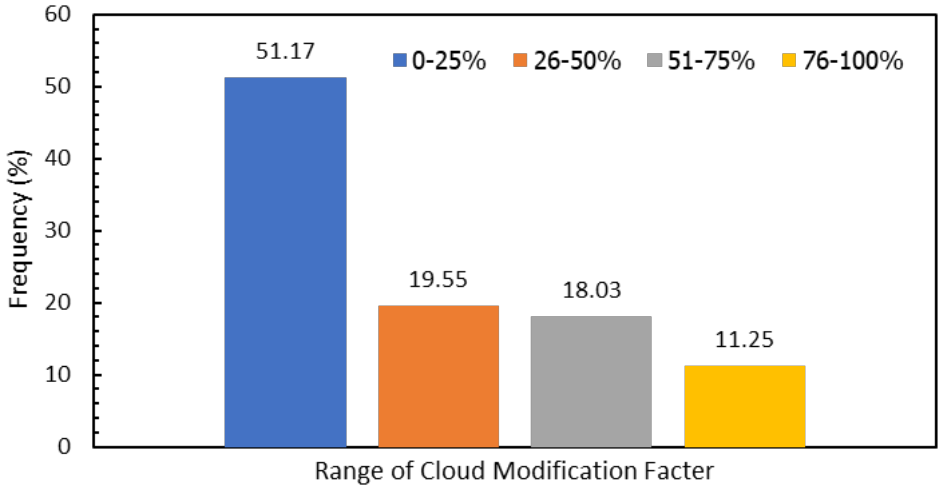

Figure 9.
The amount of the cloud modification factor of 2019 – 2020

From Figure 9, most clouds with the frequency of 51.17% can reduce the global solar radiation at the Earth's surface up to 25%. Each month has also different CMF depending on the season, which was occupied by clouds as already shown in Figure 10 and 11. To investigate the CMF of each cloud type, the sky image was used to classify the type of clouds and the CMF of each cloud was calculated. The preliminary results of CMF by cloud types observed for the date selected in the case study, namely stratus, nimbostratus, altostratus, altocumulus, stratocumulus and cumulonimbus that were observed on 4 July, 2019 and 4 September, 2020, were presented in Figure 10 and 11, respectively.

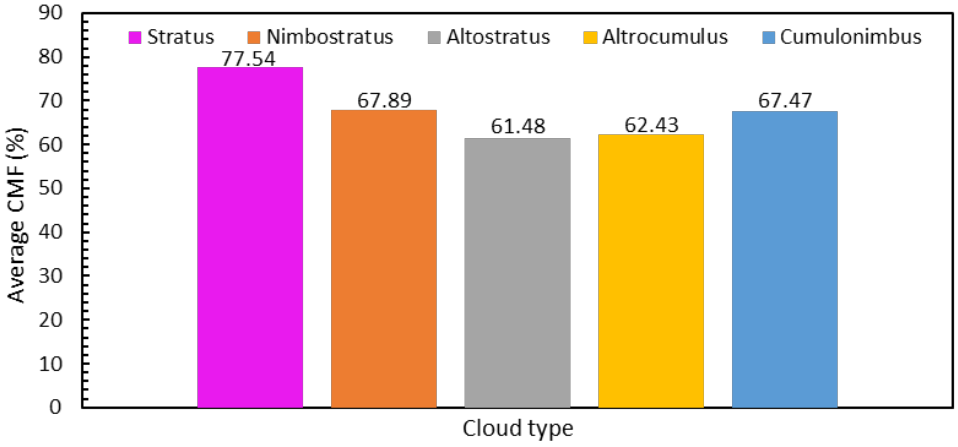

Figure 10.
Percentage of the cloud modification factor by different clouds on July 4 2019

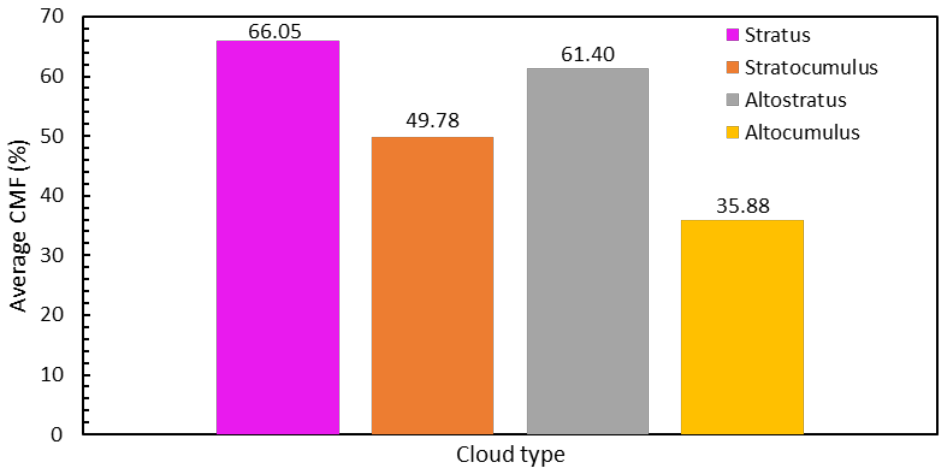

Figure 11.
Percentage of the cloud modification factor by different clouds on 4 September 2020

The results showed that the cloud modification factor varied depending on the cloud types. From the investigation, stratus clouds can reduce more solar radiation than other cloud types for both selected days.

Conclusion:

In this work, a cloud base height (CBH) measured by a ceilometer at Nakhon Pathom, Thailand, which is located in the tropical area leading the rapid change in cloud features (shape, type, height and size) encompassing the year of 2019 and 2020 was collected and analyzed. The results showed that most clouds in Nakhon Pathom were mid – level clouds at the height between 2,000 and 7,000 meters. The cloud modification factor, which is a number for describing the attenuation of global solar radiation by clouds was analyzed. From the investigation, most clouds in the sky of Nakhon Pathom can decrease the global solar radiation up to 25%. It was also found that stratus clouds delivered the highest values for cloud types observed in the case study. The difference in CMF values might cause from the local situations or atmospheric constituents at the station. From these results, it can be concluded that clouds play a very important role in the attenuation of global solar radiation. The information obtained from this research is very important for clean energy applications, especially the prediction of solar radiation under all-sky conditions for planning the efficient generation of electricity in the solar powerplant.

References:

1. Janjai S., Solar Radiation. 2 nd ed.Nakorn Pathom, Phetkasem Printing Group. 2017;144-323.
2. Monteitb JL., Unsworth MH. (1988). Principles of Environmental Physics. Edward Arnold: London.
3. Estpinan. J.G., Raman, S., Crescenti, G.H., Streicher, J.J., Barnard, W.F. Effects of
4. clouds and haze On UV-B radiation. Journal of Geophysical Research 101 (D11).1996;16807-16816.

5. Mereno F., I., J. Vida, and L. Alados – Arboledas, On the use of a cloud modification factor for Solar UV (290 - 385) spectral range, Theor. Appl. Meteor. 2001;68:41-50.181-185.
6. Calbo J., Pages, D., Gonzalez, J.A. Empirical studies of cloud effects on UV radiation: a review Rev. Geophys. 43, RG2002. Doi: 2005;1029/204RG00155.
7. Laura Lopez M. Effect of different types of clouds on surface UV-B and total solar irradiance at southern mid-latitudes: CMF determination at Cordoba, Argentina, Atmospheric Environment.2009;43:3130-3136.
8. El-Nouby M.A. Effect of Macrophysical Parameters of Clouds on Broadband Solar Radiation (295-2800 nm) at a Subtropical Location, Atmosphere and oceanic science letters. 2011;4(3):181-185.
9. Peengam S. (2017), A study of cloud base height and cloud cover at a tropical site in northern Thailand, Thesis. (Physics Department), Nakhon Pathom. Silpakorn University. Retrieved October 1. 2021, Copy.
10. Haurwitz, B. Insolation in relation to cloudiness and cloud density. Journal of Meteorology 1945;2:154-166.
11. Janjai S., Sricharoen, K., and Pattarapanitchai S. Semi-empirical models for the estimation Of clear sky solar global and direct normal irradiances in the tropics. Applied Energy 2011;88:4749-4755.

THE ELECTRIC POTENTIAL AND ELECTRIC FIELD ON CONDUCTING MATERIALS

Sirapat Lookrak, Anol Paisal*

EmOne (Thailand) Co., Ltd., Bangkok, Thailand
*e-mail: Anol.p@emone.co.th

Abstract:
This research work is a part of the space technology startup project. The company is interested in many material removals by the new company's invention. The main idea of this alternative method is the attractive force from an electric induction. Assuming that the conducting materials which are supposed to be space debris are lying between the positive and negative circular electrodes. These circular electrodes are connected to the electrical generators. The electric charges in the conducting materials are induced by an external electric field generated from these electrodes. The electric potential and electric field on a conducting surface are calculated by an image charge method. The value and the position of an image charge are specified by the Dirichlet condition. For simplicity, the image charge position is lying on a line between the center of a circular electrode and the center of a conducting sphere. However, this approximation method can be used well when the conducting sphere is moving near the central axis of an electrode or far away from an electrode due to the symmetry of the circular electrode. The result of the electric potential for near-field and far-field approximation up to the second order is shown in this article. Referring to the result, the electric field and electric potential will gradually be stronger if the conducting sphere is moving away from the central axis for near-field approximation while the far-field approximation gives the result in the opposite direction.

Introduction:

The article will present the invention of the company to solve a problem of space technology and activity by preventing the damage to the spacecraft or space station. The main idea is using an attractive force from an electrostatic induction to remove all of the conducting materials at the same time. The idea comes from the attraction between pieces of paper and a plastic comb. While the comb is being rubbed with a flannel, some electric charges are transferred to the flannel and the comb consequently becomes charged. Then, the charged plastic comb is able to attract all pieces of paper. This phenomena inspires us to use the electrostatic induction of the materials. If an external electric field is fully filled in the space, it will be able to induce electric charge even in insulating materials or composite materials. Then, the electrode acts an electric force on the conducting sphere via an electric field but the electric force calculation will not be written in this article. However, the only conducting materials is studied in this article. The thought experiment includes two circular electrodes which are connected to an external electric generator and the conducting space debris is assumed to be a sphere. Then, the electric field is applied to the system due to the accumulated electric charge on the circular electrode.

The concept is that the electric field on a surface of a conductor comes from the external electric field and induces charges such that the total electric field inside the conductor is zero. The well known physical method to solve this problem is an image charge method. For a single charge outside a conducting sphere as a source of an electric field, the image charge will be

simply located somewhere on a line between an outside electric source to the center of the conducting sphere.

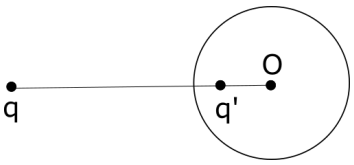

Figure 1. An image charge q' on a line between the center of the conducting sphere and the electric charge q

If the electric potential all over a conducting surface is zero, so will the potential inside a conducting material refer to the uniqueness theorem. The theorem stated that an electric field derived from an electric potential function satisfying Poisson's equation under the boundary conditions is unique.

$$\nabla^2 V = \frac{\rho}{\epsilon_0} \tag{1}$$

The Dirichlet boundary conditions are applied to the system in which the system meets the following requirements

1. The electric potential is zero in the whole region enclosed by this boundary.

2. The gradient of the electric potential or electric field is zero in the whole region enclosed by this boundary.

The electric potential from a distributed electric charge on a circular electrode is written as

$$V = \int \frac{k\sigma dA'}{r} \tag{2}$$

When σ is a surface electric charge density and dA' is an area element of a circular electrode. For simplicity in the calculation, the image charge is approximately located on a diameter line from the center of a circular electrode. However, the crucial restriction for this method is that the conducting sphere has to be near the central axis of an electrode or be very far away from an electrode. Otherwise, the error is large so this method is not appropriate.

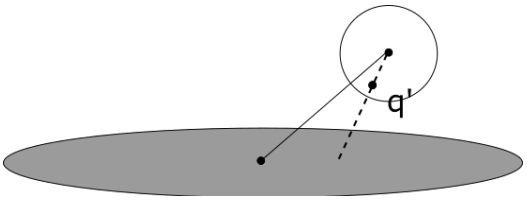

Figure 2. An image charge q' on a dashed line

The total electric potential is straightforward to be calculated from the position of an image charge. Then, the electric field is the gradient of the total potential.

$$\vec{E} = -\vec{\nabla} V_{total} \tag{3}$$

When the gradient will be written in a cylindrical coordinate. This article will devide the calculation into two parts, near-field and far-field approximation. The binomial theorem is applied to this approximation but the coefficient is written in terms of a gamma function.

THE MULTIPOLE EXPANSION OF AN ELECTRIC POTENTIAL

A. Near-Field Approximation

Since the total electric potential is zero at the surface of the conducting sphere, the general term of total electric potential is shown in the equation 4

$$V_{total} = \int \frac{k\sigma dA'}{\sqrt{\rho^2+\rho'^2-2\rho\rho' cos\alpha'+z^2}} + \frac{kq'}{r'} \tag{4}$$

The first term comes from the electrode with a uniform electric charge distribution and the second term comes from an image charge. When $r' = \sqrt{\left(\rho^2 + \rho_q^2 - 2\rho\rho' cos\theta_{cm}\right) + \left(z - z_q\right)^2}$ is the relative distance from an image charge to an observed position, θ_{cm} is the angle between the radial component of the center of mass and the radial component of an arbitrary observed position ρ. The multipole expansion of the electric potential up to the second order is

$$V_{total} \approx \int \frac{k\sigma\rho' d\rho' d\alpha'}{\sqrt{\rho'^2+z^2}} \times \left[1 - \frac{1}{2}\frac{\rho^2-2\rho\rho' cos\alpha'}{\rho'^2+z^2} + \frac{3}{8}\left(\frac{4\rho^2\rho'^2 \cos^2\alpha'}{(\rho'^2+z^2)^2}\right)\right] + \frac{kq'}{r'} \tag{5}$$

When ρ_q is a radial component of an image charge position. After the integration, the electric potential is obtained

$$V_{total} = k\sigma\left[2\pi\left(\sqrt{z^2+a^2} - z\right) - \frac{\pi\rho^2 a^2}{2(a^2+z^2)^{\frac{3}{2}}}\right] + \frac{kq'}{r'} \tag{6}$$

When a is a radius of a circular electrode.

B. Far-Field Approximation

The electric potential for the far-field approximation is written as

$$V_{total} \approx \int \frac{k\sigma\rho' d\rho' d\alpha'}{\sqrt{\rho^2+z^2}} \times \left[1 + \frac{1}{2}\frac{\rho'^2-2\rho\rho' cos\alpha'}{\rho^2+z^2} - \frac{3}{16}\left(\frac{4\rho^2\rho'^2 \cos^2\alpha'}{(\rho^2+z^2)^2}\right)\right] + \frac{kq'}{r'} \tag{7}$$

The approximation is done only up to the second order of the position of electric charge.

$$V_{total} \approx \frac{k\sigma\pi a^2}{\sqrt{\rho^2+z^2}} + \frac{kq'}{r'} \tag{8}$$

Only one term is obtained because the rest of them are the higher order terms which can be ignored.

THE POSITION AND VALUE OF AN IMAGE CHAGRE

The position of an image charge is supposed to be on the line between the center of the conducting sphere and the center of a circular electrode. The calculation will give a high precision if the conducting sphere is nearly around the central axis of the circular electrode and is far away from an electrode as shown in figure 3.

Figure 3 An image charge q' on a line between the centre of the conducting sphere and the centre of a circular electrode. The left figure shows the conducting sphere is moving nearly around the center of a circular electrode and the right figure shows the conducting sphere is far away from a circular electrode.

The position labelled by A and B can be written in terms of center of mass and the radius of the conducting sphere which is written in the equation [9]-[12]

$$z_A = z_{cm} - r \times \frac{z_{cm}}{\sqrt{z_{cm}^2+\rho_{cm}^2}} \tag{9}$$

$$z_B = z_{cm} + r \times \frac{z_{cm}}{\sqrt{z_{cm}^2+\rho_{cm}^2}} \tag{10}$$

$$\rho_A = \rho_{cm} - r \times \frac{\rho_{cm}}{\sqrt{z_{cm}^2+\rho_{cm}^2}} \tag{11}$$

$$\rho_B = \rho_{cm} + r \times \frac{\rho_{cm}}{\sqrt{z_{cm}^2+\rho_{cm}^2}} \tag{12}$$

The Dirichlet condition is used to be a boundary condition of a conducting sphere. The electric potential on the surface of the conducting sphere is only zero. The two points A and B are intersections between the diameter of the conducting sphere and the surface. Those intersections are applied to find the location of an image charge.

A. Near-Field Approximation

For near-field approximation, the boundary condition equations are

$$k\sigma\left[2\pi\left(\sqrt{z_A^2+a^2}-z_A\right)-\frac{\pi\rho_A^2a^2}{2(a^2+z_A^2)^{\frac{3}{2}}}\right]+\frac{kq'}{r_A'}=0 \tag{13}$$

$$k\sigma\left[2\pi\left(\sqrt{z_B^2+a^2}-z_B\right)-\frac{\pi\rho_B^2a^2}{2(a^2+z_B^2)^{\frac{3}{2}}}\right]+\frac{kq'}{r_B'}=0 \tag{14}$$

From (13) and (14), we can find an electric charge q'. The value of an image of an electric charge is defined as

$$q'=\frac{(C_1+C_2)\left(2r-\sqrt{(\rho_A-\rho_q)^2+(z_A-z_q)^2}\right)\sqrt{(\rho_A-\rho_q)^2+(z_A-z_q)^2}}{2\left(r-\sqrt{(\rho_A-\rho_q)^2+(z_A-z_q)^2}\right)} \tag{15}$$

After the substitution of all parameters, q' is a negative charge as it should be. The position z_q and ρ_q are able to write in terms of the center of mass since all points are on the same line passing through the center of mass. They can be written as

$$\rho_q=\frac{\rho_{cm}}{z_{cm}}\times z_q \tag{16}$$

$$z_q=\frac{\left(\frac{\rho_A\rho_{cm}}{z_{cm}}+z_A\right)+\sqrt{\left(\frac{\rho_A\rho_{cm}}{z_{cm}}+z_A\right)^2-\left(\frac{\rho_{cm}^2}{z_{cm}^2}+1\right)\left(\rho_A^2+z_A^2-4r^2(2C_1+C_2)^2\right)}}{\left(\frac{\rho_{cm}^2}{z_{cm}^2}+1\right)} \tag{17}$$

When the constant C_1 and C_2 are defined as in the equations [18], [19] repectively.

$$C_1=-\sigma\left[2\pi\left(\sqrt{z_A^2+a^2}-z_A\right)-\frac{\pi\rho_A^2a^2}{2(a^2+z_A^2)^{\frac{3}{2}}}\right] \tag{18}$$

$$C_2=\sigma\left[2\pi\left(\sqrt{z_B^2+a^2}-z_B\right)-\frac{\pi\rho_B^2a^2}{2(a^2+z_B^2)^{\frac{3}{2}}}\right] \tag{19}$$

and r is a radius of the conducting sphere.

B. Far-Field Approximation

For far-field approximation, the equations are

$$0=\frac{k\sigma\pi a^2}{\sqrt{\rho_A^2+z_A^2}}+\frac{kq'}{r'} \tag{20}$$

$$0=\frac{k\sigma\pi a^2}{\sqrt{\rho_B^2+z_B^2}}+\frac{kq'}{r'} \tag{21}$$

Solving the equations, we find that the position and the value of an image charge are written in

the form as

$$\rho_q = \frac{\rho_{cm}}{z_{cm}} \times z_q \tag{22}$$

$$z_q = \frac{\frac{\rho_A \rho_{cm}}{z_{cm}} + z_A + \sqrt{\left(\frac{\rho_A \rho_{cm}}{z_{cm}} + z_A\right)^2 - \left(\frac{\rho_{cm}^2}{z_{cm}^2} + 1\right)\left(\rho_A^2 + z_A^2 - \frac{4r^2(2C_3 + C_4)^2}{(3C_3 + C_4)^2}\right)}}{\frac{\rho_{cm}^2}{z_{cm}^2} + 1} \tag{23}$$

When the constant C_3 and C_4 are defined as in the equations [24], [25] respectively.

$$C_3 = -\frac{\sigma \pi a^2}{\sqrt{\rho_A^2 + z_A^2}} \tag{24}$$

$$C_4 = \frac{\sigma \pi a^2}{\sqrt{\rho_B^2 + z_B^2}} \tag{25}$$

The image charge is written as

$$q' = \left(\frac{\sigma \pi a^2}{\sqrt{\rho_B^2 + z_B^2}} - \frac{\sigma \pi a^2}{\sqrt{\rho_A^2 + z_A^2}}\right) \frac{2r - \sqrt{(\rho_A - \rho_q)^2 + (z_A - z_q)^2}}{2\left(r - \sqrt{(\rho_A - \rho_q)^2 + (z_A - z_q)^2}\right)} \tag{26}$$

THE ELECTRIC FIELD

The electric field can be calculated in near-field and far-field approximation defined from the negative of the gradient of the total electric potential.

$$\vec{E} = -\vec{\nabla} V_{total} \tag{27}$$

The electric field in the cylindrical coordinate is written as

$$\vec{E}_{near} = k\left[\frac{\pi \sigma \rho a^2}{(a^2 + z^2)^{\frac{3}{2}}} + \frac{q'(\rho - \rho_q)}{\left((\rho - \rho_q)^2 + (z - z_q)^2\right)^{\frac{3}{2}}}\right]\hat{\rho}$$

$$+k\left[\sigma\left(1 - \frac{z}{\sqrt{a^2 + z^2}} + \frac{3\pi \rho^2 a^2 z}{2(a^2 + z^2)^{\frac{3}{2}}}\right) + \frac{q'(z - z_q)}{\left((\rho - \rho_q)^2 + (z - z_q)^2\right)^{\frac{3}{2}}}\right]\hat{k} \tag{28}$$

$$\vec{E}_{far} = k\left[\frac{\pi \sigma \rho a^2}{(\rho^2 + z^2)^{\frac{3}{2}}} + \frac{q'(\rho - \rho_q)}{\left((\rho - \rho_q)^2 + (z - z_q)^2\right)^{\frac{3}{2}}}\right]\hat{\rho} + k\left[\frac{\pi \sigma z a^2}{(\rho^2 + z^2)^{\frac{3}{2}}} + \frac{q'(z - z_q)}{\left((\rho - \rho_q)^2 + (z - z_q)^2\right)^{\frac{3}{2}}}\right]\hat{k} \tag{29}$$

The electric field is written as a function of a position when the center of the electrode is a reference. However, this is the electric field on a conducting surface so the position is on a conducting sphere.

Conclusion:

The electric potential and electric field under the Dirichlet boundary condition is obtained as well as the approximated image charge. The electric field strrength and electric potential will gradually increase when the conducting sphere is moving away from the central axis for near-field approximation while the far-field approximation gives the result in the opposite direction. The result is limited to be used because of the near-field and far-field condition.

Acknowledgements:

The author thanks the EmOne company for supporting all budgets for the conference, transportation and accommodation. Moreover, Anol Paisal, CEO and project manager of the company, provides all the required facilities so it is more convenient to accomplish this research project.

References:

1. Poursina M, Butcher EA. AAS. 2019.
2. Bennett T, Schaub H. CAPITALIZING ON RELATIVE MOTION IN ELECTROSTATIC DETUMBLING OF AXI-SYMMETRIC GEO OBJECTS, In: 6th ICATT.2016
3. Sprugnoli R. Negation of binomial coefficients, Discrete Math. 2008;308:5070-5077
4. Cheng AHD, Cheng DT. Eng Anal Bound Elem.2005;29:268-302
5. Santos FC, Tort AC. Eur. J. Phys. 2004 **25** 859

Session B:
BIOLOGICAL SCIENCES

DEVELOPMENT OF MICROSATELLITE MARKERS AND SCREENING IN TWO-SPOTTED CRICKETS (*Gryllus bimaculatus* De Geer, 1773)

Kittiya Inchoetchai, Somjit Homchan, Yash Munnalal Gupta*

Department of Biology Faculty of Science, Naresuan University, Thailand
*e-mail: yashmunnalalg@nu.ac.th

Abstract:
Molecular markers are utilized to study the genetic variation of any population. Specially, simple sequence repeats (SSRs), also known as microsatellites. However, traditional SSR marker development approaches are laborious and time consuming. Therefore, the current study proposes using the Basic Sequence Alignment Tool (BLAST) to find polymorphic SSRs in *Gryllus bimaculatus* genomes. 25 polymorphic SSRs were found from 400 randomly selected sequences from the whole genome using an *in silico* method. The *in silico* method is also validated using DNA amplification, in which, 6 out of 12 primer pairs were able to amplify DNA fragments with expected size. The developed polymorphic SSR markers can be used to study the genetic variation of *G. Bimaculatus* and other related species. The alternative approach proposed in this study will be valuable for developing SSR markers from genomic and transcriptomic sequence data in other species.

Introduction:
Edible insects comprise one such category of under-utilized foods that offer significant potential to contribute to future global food demands. In approximately 100 countries around the world, insects have long been a key element of human diets, particularly in Asia and the Pacific, Africa, and Latin America [1]. Crickets are becoming increasingly popular as a result of their ease of rearing and low space requirement for farming. In general, insects can provide protein and fat, as well as vitamins and minerals that are beneficial to human health [2]. The two-spotted cricket, Gryllus bimaculatus, is a species of insect that was once kept as a pet and used to combat other crickets. However, it is now fried, roasted, or fed to a variety of pets as animal feed. As a result, while cricket farming is a profitable business, growing them in captivity might reduce genetic variation. Without genetic variation as a reaction to environmental stressors or other genetic factors, it would be difficult to adapt to the environment. As a result, it may result in death. An important precaution for long-term production sustainability was to maintain genetic variation in the captive population [3]. As a result, the development of microsatellite markers could be useful in the screening of genetic variation in breeding systems.

A microsatellite marker would be used to determine the SSR within the genome of the two-spotted cricket in this study. SSR (Simple Sequence Repeat) DNA, also known as microsatellite DNA, is found in the chromosomes of eukaryotes and distributed throughout the genome. Most of them were found in the intergenic region rather than in the gene. SSR markers are co-dominant DNA markers that can detect difference between homozygotes and heterozygotes and can also be used to check for genetic variation. SSRs are distributed throughout the genome and also have a high variation compared to other DNA regions. The high mutation rate in microsatellites leads to variation in particular locus. Microsatellite markers are considered to be highly polymorphic markers. A polymorphic microsatellite locus means that there are several possible alleles at a single locus. As a result, they are ideal for genetic studies on species populations. Therefore, SSR marker can be used as a molecular marker for the differentiation of each organism. However, the SSR marker has a limitation.

The SSR development process is complicated, consuming and costly [4]. To improve the efficiency of SSR development, a bioinformatic algorithm and advanced BLAST must be explored. This benefits SSR research by enhancing accuracy and reproducibility while decreasing labor and costs.

The traditional method for isolating microsatellite loci is generating a limited DNA library and screening it using microsatellite-specific probes [5]. Therefore, microsatellite isolation is usually laborious, time-consuming, and costly. A number of alternative techniques have already been created to save time, cost, and labor by avoiding the construction of a genomic library [6, 7]. Most of these processes are either costly or time-consuming. Furthermore, microsatellite isolation requires the development of genetically engineered bacteria, which increases marker development costs and time [8]. These developments, however, might not even be sufficient and the use of microsatellites is quite limited [5].

In the present study, we used bioinformatics, which is *in silico* method based on BLAST (megablast). Phobos software can be used to find microsatellites [9], and NCBI BLAST can be used to find polymorphic SSRs. The Basic Sequence Alignment Tool (BLAST) can search polymorphic SSRs and construct alignments with gaps, which is important for finding SSR sequence insertions and deletions. Currently, the accessibility of genomic sequences, bioinformatic tools are assisting as a resource for the development of SSR [10]. As a result, microsatellite isolation and cloning processes can be avoided in this study, which can save cost, labor, and time for developing a microsatellite marker.

Methodology:

The two-spotted cricket were used for the development of microsatellite markers in this study. *G. bimaculatus* DNA, scaffold, whole genome shotgun sequence was taken from the NCBI. Afterwards, microsatellites were searched by Phobos software and took the sequences containing SSR to NCBI BLAST for search polymorphic SSR. Then designed the primer by Primer3 from sequences containing polymorphic SSRs. The SSR primers were selected for use to amplify microsatellite sequence from *G. bimaculatus* DNA by PCR amplification. The two-spotted cricket from Phitsanulok farm were taken to use to extract the DNA to test the primer pair.

SSR sequence detection from genome datasets

Search genome of *G. bimaculatus* from NCBI, GenBank: BOPP00000000.1 for SSR sequence detection. Genome wide search for SSRs would be done using Phobos software version 3.3.12. After searching would get the sequences that containing SSRs. Next, took the 400 sequences containing SSRs that were chosen randomly to NCBI BLAST by megablast. The sequences containing SSRs would be extracted from the genome advanced BLAST. Total 25 polymorphic SSRs were found from 400 randomly selected sequences from the whole genome of *G. bimaculatus*. Afterwards, took 25 sequences containing polymorphic SSRs to design the primer by Primer3 tool. Complete design the sequences and get 12 primers. PCR products were separated on 1.5% agarose gel using gel electrophoresis to check the results. Increase the amount of MgCl2, if the result shows a faint band. After the master mix and DNA were prepared, the PCR machine was used to amplify the amount of target DNA for 40 cycles.

Results and Discussion:

In silico polymorphism screening in G. bimaculatus genomes

The whole genome shotgun sequence of *G. bimaculatus* DNA, which has the length of the sequences is 29,751,334 bases. BLAST 400 sequences randomly of *G. bimaculatus* genome for SSR variation analysis, only 25 sequences out of them were found to be polymorphism. Bioinformatics tools, the BLAST algorithm could be utilized to search for polymorphic SSRs using *in silico* method. The advantage of SRA datasets was whether they contained unassembled raw sequence data. GenBank sequences were assembled sequences that might have assembly due to misinterpretation of repeats in the assembling process. As a result, this study used the BLAST method to identify polymorphic SSR by comparing sequences containing SSR to unassembled sequences from different individuals. BLAST might examine the conservativeness of primer binding sites of sequences containing SSR by comparing them to raw sequences before designing the primer for DNA amplification. As a result, aligning raw reads provides data on the decrease of DNA amplification errors.

Polymerase chain reaction for SSR primer pairs validation

Checking primer binding site first *in silico* method may help to reduce the number of primer pairs required for laboratory testing. Moreover, when trying to generate a large number of markers for applications such as genetic linkage analysis, a minor increase in efficiency could save time and cost [11]. Microsatellites had reported being efficient in insect population genetic studies because they have a high polymorphic rate and were easily scored [12]. From the results of the experiment, a total of 6 primers had a positive result but only 4 out of 12 of gel electrophoresis were consistent with *in silico* method that could amplified sequences containing polymorphic SSR with expected size. Some primers pair found many bands which might be consistent with *in silico* method because multiple gaps were found in microsatellite sequences. As a result, the various sizes of DNA bands were found. Some primer contains insertion mutation in subject sequence. Therefore, this primer could not be amplified the expected size. Negative results, long and multiple gaps were found, as a result, PCR product were not found. The results are displayed in **Figure 1 and Figure 2 G-L**. Sequences containing polymorphic SSRs taken by researcher were quite long in repeat length. The longer repeat lengths were associated with increased mutation rates [12]. Microsatellites from *C. avellana*, the large percentage of which were from genomic sequences, amplified >80% across *Corylus* species, according to [13], meanwhile, a few more microsatellites isolated from *C. avellana* transcriptome sequences found a lower average value (57%) [14]. Microsatellites from transcriptome sequences showed a high rate of transferability [15].

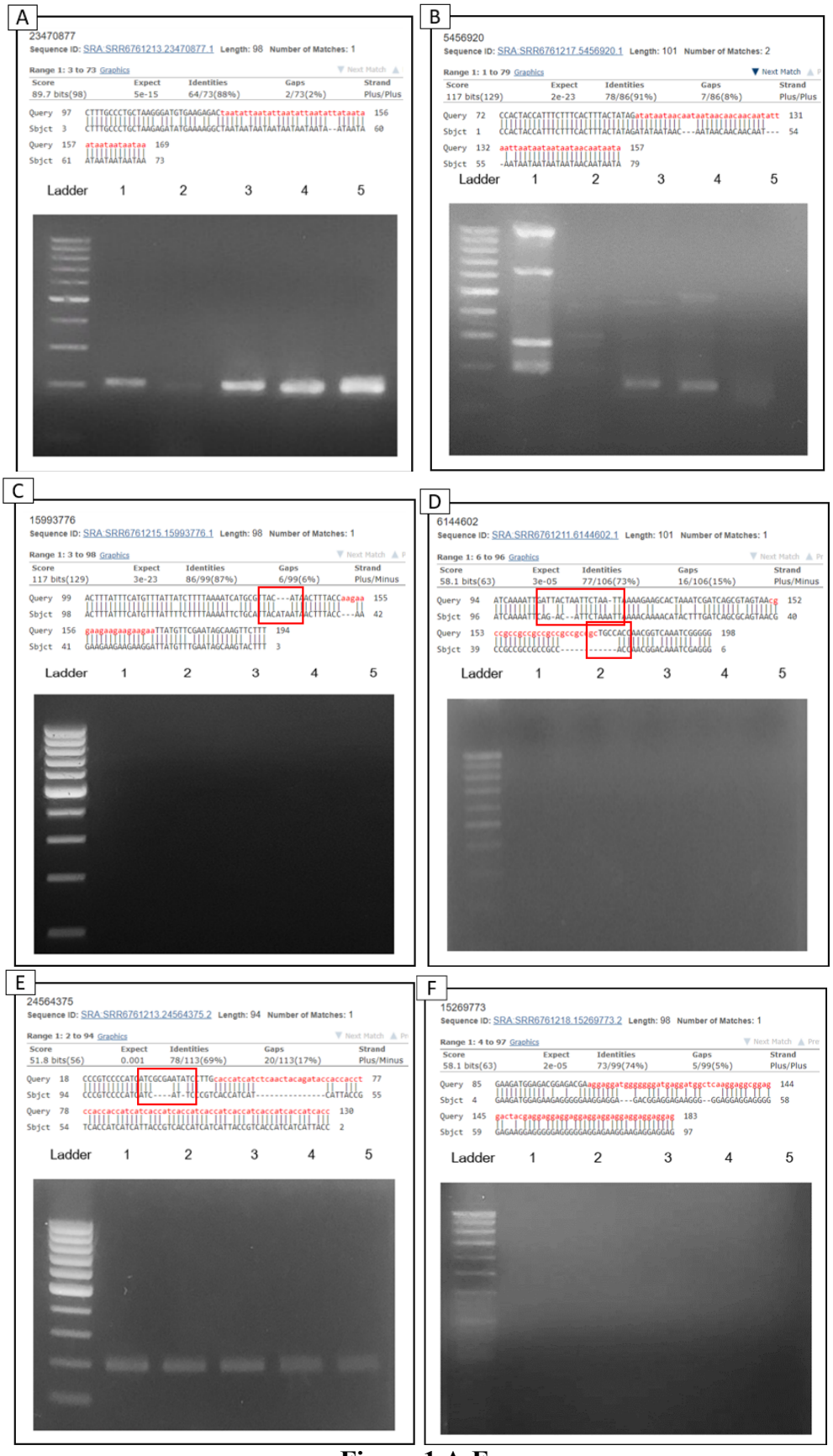

Figure 1 A-F

Visualization of comparison of *in silico* and *in vitro*.

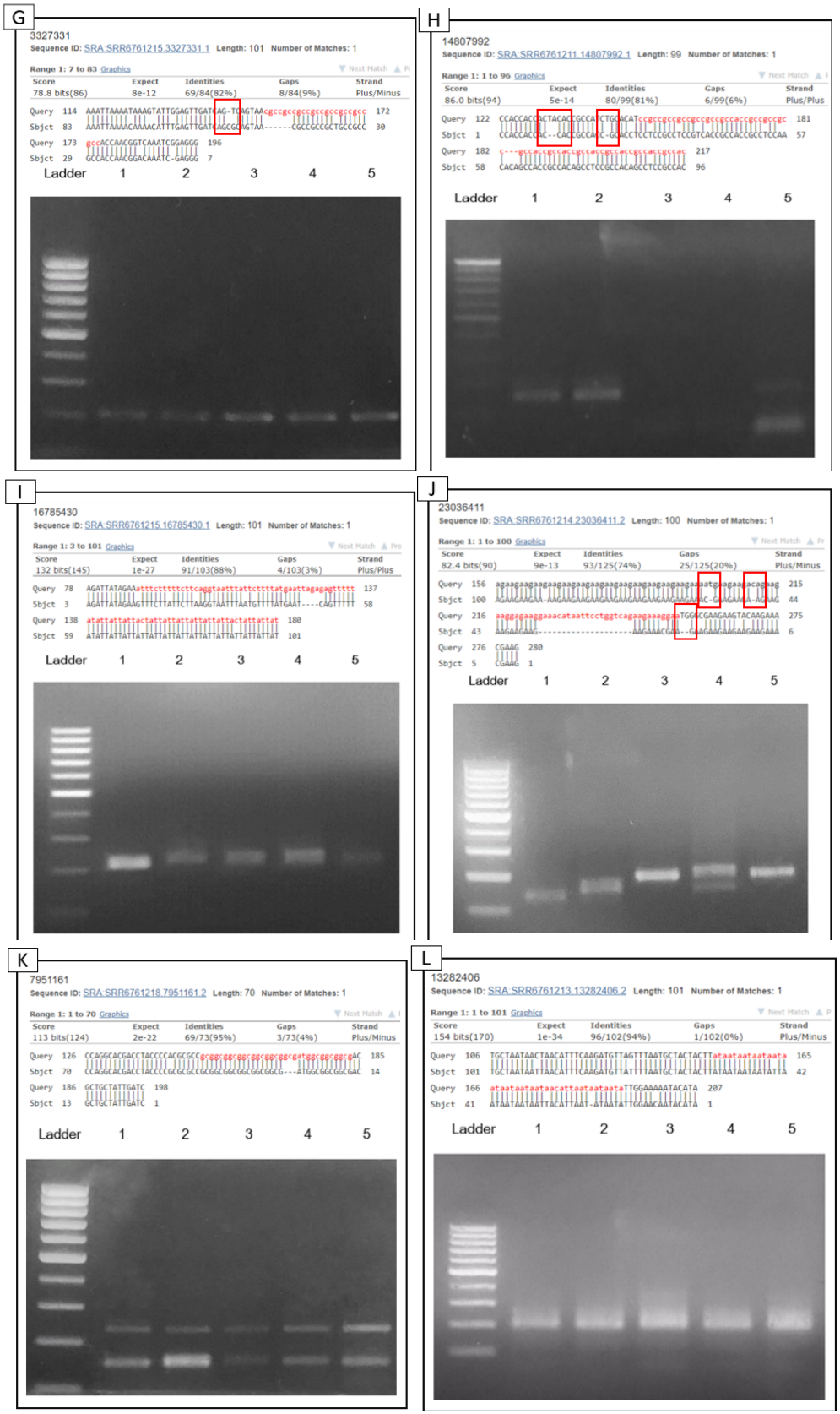

Figure 2 G-L
Visualization of comparison of *in silico* and *in vitro*.

Development of SSR markers from genomes

In comparison, genomic microsatellites had high polymorphism and were found numerous than transcriptome microsatellites[16]. Because SSRs can cause gene function gain or loss through frameshift mutations, microsatellites found in protein coding regions have low allele polymorphism and short repeat lengths [17]. If microsatellites are found in gene promoters and intergenic regions, they have been shown the affect expression. SSRs within promotor make gene expression vulnerable to changes caused by repeat sequence expansion or contraction [18]. Alteration in transcription factor linkage sites produces an increase or decrease in gene expression, which can lead to silent genes. Tandem repetitions in intergenic regions can change the secondary structure of DNA by forming loops and changing chromatin, which can lead to changes in the expression of neighboring genes and eventually phenotypic changes [18, 19]. Although, transcriptome microsatellites showed a high rate of transferability [15]. However, if you want to study about the polymorphic SSR, genomic microsatellites might be a good choice because they had high polymorphism and abundant.

SSRs are the markers of choice in genetic studies, genetic variation analysis, parental identification, and genetic linkage map construction. Because of their co-dominant nature, high repeatability, and genome coverage [11]. Moreover, SSR marker development will probably facilitate the creation of strategies to address some of the problems encountered by farmed populations suffering from inbreeding depression [3, 20, 21]. Therefore, many genetic studies currently require microsatellite markers, even though there are still significant issues regarding how to isolate them [22].

Conclusion:

The study shows the search polymorphic microsatellite from *G. bimaculatus* genomes using BLAST could be examined and visualized as gaps in the sequence alignment. In considering the development of multiple SSRs *in silico* for *in vitro* testing. The method *in silico* saves a lot of time compared to conventional methods and enables the development of microsatellite markers effectively. The method is applicable to any research that requires the development of microsatellite markers for the study of genetics. In addition, *in vitro*, 6 primers were able to check the accuracy of the sequences that contain the expected size. The remaining 6 primers could not be used, 3 primers are negative results, they disappear any band. Another 3 primers are non-specified, they appear unexpected size. Although, one of them appears expected size. The results of this study were quite satisfactory. Therefore, the researchers hope that this study guide will serve as a model for studying genetic variation in crickets and other species, and it is a promising alternative for SSR marker development from the genomes and transcriptomes of cricket.

References:

1. Durst, P. and Y. Hanboonsong, *Small-scale production of edible insects for enhanced food security and rural livelihoods: experience from Thailand and Lao People's Democratic Republic.* Journal of Insects as Food and Feed, 2015. **1**(1): p. 25-31.
2. Hanboonsong, Y., T. Jamjanya, and P.B. Durst, *Six-legged livestock: edible insect farming, collection and marketing in Thailand.* RAP publication, 2013. **3**: p. 8-21.
3. Gupta, Y.M., et al., *Development of microsatellite markers for the house cricket, Acheta domesticus (Orthoptera: Gryllidae).* Biodiversitas Journal of Biological Diversity, 2020. **21**(9).
4. Powell, W., G.C. Machray, and J. Provan, *Polymorphism revealed by simple sequence repeats.* Trends in plant science, 1996. **1**(7): p. 215-222.

5. Lian, C., Z. Zhou, and T. Hogetsu, *A simple method for developing microsatellite markers using amplified fragments of inter-simple sequence repeat (ISSR).* Journal of plant research, 2001. **114**(3): p. 381-385.
6. Browne, D. and M. Litt, *Characterization of (CA) n microsatellites with degenerate sequencing primers.* Nucleic acids research, 1992. **20**(1): p. 141.
7. Ender, A., et al., *RAPD identification of microsatellites in Daphnia.* Molecular Ecology, 1996. **5**(3): p. 437-441.
8. Abdelkrim, J., et al., *Fast, cost-effective development of species-specific microsatellite markers by genomic sequencing.* BioTechniques, 2009. **46**(3): p. 185-192.
9. Hodel, R.G., et al., *The report of my death was an exaggeration: a review for researchers using microsatellites in the 21st century.* Applications in plant sciences, 2016. **4**(6): p. 1600025.
10. Sablok, G. and N. Shekhawat, *Bioinformatics analysis of distribution of microsatellite markers (SSRs)/single nucleotide polymorphism (SNPs) in expressed transcripts of Prosopis Juliflora: frequency and distribution.* J. Comput. Sci. Syst. Biol, 2008. **1**: p. 87-91.
11. Khodaeiaminjan, M., et al., *In silico polymorphic novel SSR marker development and the first SSR-based genetic linkage map in pistachio.* Tree Genetics & Genomes, 2018. **14**(4): p. 1-14.
12. Tinkrathok, S., *Population Genetic Study of the Melon Fly Parasitoid, Psyttalia Fletcheri Silvestri (Hymenoptera: Braconidae) Using Microsatellite Markers*. 2007, Mahidol University.
13. Gürcan, K. and S.A. Mehlenbacher, *Transferability of microsatellite markers in the Betulaceae.* Journal of the American Society for Horticultural Science, 2010. **135**(2): p. 159-173.
14. Boccacci, P., et al., *In silico mining, characterization and cross-species transferability of EST-SSR markers for European hazelnut (Corylus avellana L.).* Molecular breeding, 2015. **35**(1): p. 1-14.
15. Colburn, B.C., S.A. Mehlenbacher, and V.R. Sathuvalli, *Development and mapping of microsatellite markers from transcriptome sequences of European hazelnut (Corylus avellana L.) and use for germplasm characterization.* Molecular breeding, 2017. **37**(2): p. 1-14.
16. Xia, Y., et al., *Microsatellite development from genome skimming and transcriptome sequencing: comparison of strategies and lessons from frog species.* BMC genomics, 2018. **19**(1): p. 1-13.
17. Li, Y.-C., et al., *Microsatellites within genes: structure, function, and evolution.* Molecular biology and evolution, 2004. **21**(6): p. 991-1007.
18. Vieira, M.L.C., et al., *Microsatellite markers: what they mean and why they are so useful.* Genetics and molecular biology, 2016. **39**: p. 312-328.
19. Gao, C., et al., *Revisiting an important component of plant genomes: microsatellites.* Functional Plant Biology, 2013. **40**(7): p. 645-661.
20. Gao, B., et al., *Effect of inbreeding on growth and genetic diversity of Portunus trituberculatus based on the full-sibling inbreeding families.* Aquaculture international, 2015. **23**(6): p. 1401-1410.
21. Santos, C., et al., *Loss of genetic diversity in farmed populations of Colossoma macropomum estimated by microsatellites.* Animal Genetics, 2016. **47**(3): p. 373-376.

22. Zane, L., L. Bargelloni, and T. Patarnello, *Strategies for microsatellite isolation: a review.* Molecular ecology, 2002. **11**(1): p. 1-16.

INHIBITORY EFFECT OF *Carissa carandas* LINN. EXTRACT ON ADIPOGENESIS AND LIPID ACCUMULATION OF 3T3-L1 ADIPOCYTE

Ararat Jaiaree,[1,2] Jirarat Karinchai,[2] Pornsiri Pitchakarn,[2] Ariyaphong Wongnoppavich,[2] Arisa Imsumran[2,*]

[1]Graduate/M.Sc. Program in Biochemistry, Faculty of Medicine, Chiang Mai University

[2]Department of Biochemistry, Faculty of Medicine, Chiang Mai University, Chiang Mai

*Corresponding author E-mail: arisa.bonness@cmu.ac.th

Abstract:

In this study, we aimed to investigate the anti-obesity activity of *Carissa carandas* Linn. (CC) extract and its possible mechanism on 3T3-L1 adipocytes. CCA and CCE were obtained from ripe fruit by aqueous and ethanol extraction, respectively. CCE contained higher amounts of phenolic, flavonoid, and anthocyanin compounds than CCA. CC extracts treatment up to a concentration of 400 µg/mL had no cytotoxicity in 3T3-L1 cells. CCE (200-400 µg/mL) treatment during 12 days of adipocytes differentiation exhibited a dose-dependent reduction of lipid accumulation compared to the control ($p<0.05$) whereas CCA at 400 µg/mL significantly possessed this inhibitory activity. Interestingly, CCE treatment (100-400 µg/mL) of 3T3-L1 cells for 72 hours during initiation of adipocytes differentiation significantly suppressed lipid accumulation in a dose dependent manner. Thus, CCE was selected to further analyze expression of adipogenic genes. Notably, CCE treatment of 3T3-L1 cells at 400 µg/mL significantly suppressed the expression of major adipogenic transcription factors, including CCAT/enhancer-binding proteinα (C/EBPα) and peroxisome proliferator-activated receptorγ (PPARγ). Therefore, the inhibition of adipogenesis by regulating the expression of C/EBPα and PPARγ by CCE occurred primarily in the early stages of differentiation. Overall, *C. carandas* extract demonstrated anti-adipogenic activity, which has a potential effect in anti-obesity in 3T3-L1 adipocytes.

Introduction:

Obesity is an important public health problem worldwide, including in Thailand. Obesity is a high risk factor of several major non-communicable diseases, including diabetes mellitus, coronary artery disease, stroke and cancer (1). Long-term greater energy intake than energy expenditure results in excessive accumulation of lipids in adipose tissue, which ultimately leads to obesity (2). Enlargement of adipose tissue mass in obesity is closely related to increasing the size (hyperthrophy) and number (hyperplasia) of mature adipocytes through adipogenesis (3). Adipogenesis is a multi-step process of cell differentiation which convert undifferentiated preadipocytes into mature, lipid-containing adipocytes. It is regulated by the precisely ordered of expression of transcription factors. CCAAT-enhancer-binding protein α (C/EBPα) and peroxisome proliferator-activated receptor γ (PPARγ) are the major transcription factors that regulate adipocyte differentiation by stimulating gene expression to promote triglycerides synthesis and accumulation within the cell (4).

In addition to lifestyle changes, medications are often used to treat obesity. There are two groups of approved drugs for obesity treatment based on different mechanisms, first reduction of food intake via effects on the central nervous system and second, interference with fat absorption via the gastrointestinal tract. Both have undesirable side effects; the first, drowsiness; the second, diarrhea and nausea (6). Thus, a novel strategy that targets adipose tissue directly is of significant interest.

Recently, numerous bioactive compounds have been reported for their anti-obesity activity in adipose tissue, including capsaicin (7), curcumin (8), cyanidin-3-glucoside (9, 10, 11), and anthocyanin (9,12,13). In 2020 Lee *et al*. reported that anthocyanin-rich black soybean containing cyanidin-3-glucoside and delphinidin-3-glucoside has an anti-obesity activity by reducing PPARγ protein expression and triglyceride accumulation in 3T3-L1 adipocytes (9). *Carissa carandas* Linn has been reported in Thailand for its high amounts of anthocyanin and cyanidin-3-glucoside and its biological activity for cancer, type 1 and type 2 diabetes treatments (14, 15). It is also reported to have antioxidant activity that helps aging and wrinkles (16). At present, *C. carandas* Linn. in the form of herbal juice or herbal capsules has been claimed to have pharmacological properties for treating various diseases such as diabetes mellitus, emphysema, kidney disease, liver disease, cancer, paralysis, and weight control. However, there have been limited studies on the anti-obesity potential of *C. carandas* fruit in adipocytes.

Therefore, in this study, we investigated the anti-obesity activity of *C. carandas* fruit extracts through measuring lipid accumulation as well as the mRNA expression levels of adipogenic genes involved in adipocyte differentiation in 3T3-L1cells.

Methodology

Plant extracts

The ripe fruits of *C. carandas* were obtained from Nakhon Chaisri, Nakhon Pathom, Thailand. A voucher of specimen and a preparation of plant extracts have previously been described by our research group (15). Briefly, *C. carandas* powder 30 g was extracted at room temperature for 24 hours with 300 mL deionized water or 0.5% acetic acid in 70% ethanol to obtain aqueous extract (CCA) or ethanolic extract (CCE), respectively. The CC extracts were filtered using Whatman No. 2. After that, the ethanol solvent was then removed from the CCE filtrate using a vacuum rotary evaporator. Finally, CCA and CCE were obtained using a lyophilizer and stored at -20 ºC.

Determination of total phenolic contents

Total phenolic content of the CCA and CCE were determined using the Folin-Ciocalteu reagent (17). A sample was mixed with Folin-Ciocalteu reagent and incubated at room temperature for 6 minutes. Then, 7.5% sodium carbonate solution were added to the mixture, mixed and incubated for 1 hours at room temperature. The absorbance was measured using a 765 nm microplate reader. The total phenolic content was calculated as milligrams of gallic acid equivalent (GAE) per one hundred grams dry wight using gallic acid calibration curve.

Determination of total flavonoid contents

Total flavonoid content was determined using an aluminum chloride colorimetric assay with slight modification (18). A sample was mixed with 5% sodium nitrite for 5 minutes and incubated at room temperature. Then 10% aluminum chloride and 1M sodium hydroxide was added to the mixture. The mixture was mixed. The absorbance was measured using a microplate reader at 510 nm. Total flavonoid content was calculated as milligrams of rutin equivalent (RUE) per one hundred grams dry wight using the rutin calibration curve.

Determination of total anthocyanin content

Total anthocyanin content was determined using a pH-differential method (19). A sample was mixed with 0.025 M potassium chloride buffer (pH 1.0) or 0.4 M sodium acetate

buffer (pH 4.5). The absorbance was measured using a UV-VIS spectrophotometer at 520 and 700 nm. Total anthocyanin content was calculated using the following equation (20).

$$\text{Total anthocyanin content (mg of C3G/g extract)} = \frac{A \times MW \times DF \times V \times 1000}{\varepsilon \times l \times Wt}$$

Where A is the absorbance $(A_{520} - A_{700})_{pH\ 1.0}$ - $(A_{520} - A_{700})_{pH\ 4.5}$, MW is the molecular weight of cyanidin-3-glucoside, DF is the dilution factor, V is the final volume (mL), Ɛ is the molar absorptivity (26,900 L.mol− 1.cm− 1), l is the cell path length (1 cm) and Wt is the extract weight (mg). The final anthocyanin content was expressed as milligrams of cyanidin-3-glucoside equivalents per one hundred grams dry wight.

Cell culture

Mouse 3T3-L1 preadipocyte cells (ATCC, USA) were maintained in Dulbecco's Modified Eagle Medium (DMEM) (Gibco, USA) containing 10% calf serum (Thermo Fisher Scientific, USA) and 1% antibiotics (Invitrogen, USA), and incubated at 37 °C in a humidified air atmosphere of 5% CO_2. For adipocyte differentiation, the confluent 3T3-L1 cells were induced in DMEM supplemented with 0.5 µg/mL dexamethasone, 0.5 mM 3-isobutyl-1-metylxanthine (IBMX), 0.5 µg/mL insulin (Sigma Aldrich) and 10% FBS for 72 hours (Day 0 to day 3). Then, the cells were differentiated for a further 72 hours in the same medium without IBMX and dexamethasone (Day 4 to day 6). Differentiation was completed within 6 days by replacing with DMEM with 10% FBS every 3 days (Day 7 to day 12).

Cytotoxicity assay

The 3T3-L1 adipocytes (3×10^3 cells/well) were seeded in 96-well plate for 24 hours. The cells were then treated with CCA or CCE at various concentration (50-400 µg/mL). After 72 hours of treatment, the test solutions were then removed. The cells were fixed with 10% (w/v) trichloroacetic acid solution at 4°C for 1 hour, washed with deionized water for 3 times and dried overnight. Next, the cells were stained with 0.057% sulforhodamine B (SRB) solution at room temperature for 30 minutes. The cells were washed with 1% acetic acid and dried overnight. Finally, cells were dissolved with 10 mM Tris-base pH 7.4. The absorbance was measured using a microplate reader at 510 nm, and the cell viability was calculated as a percentage of the untreated control cells.

Effect of CC extracts on lipid accumulation using Oil Red O staining

3T3-L1 adipocytes (3×10^3 cells/well) were seeded in 96-well plates and differentiated as described above. The treatment was performed into two conditions. First, cells were treated with various concentrations of CCA or CCE (100-400 µg/mL) in a series of differentiation medium from Day 0 to day 12. Second, cells were treated with various concentrations of CCA or CCE (100-400 µg/mL) in a differentiation medium for 72 hours (Days 0 to day 3) and then further differentiated until day 12. Cells were washed with cold PBS, fixed in 4% formaldehyde at room temperature for 1 hour and stained with Oil Red O solution for 5 minutes. After washing with deionized water, lipid-bound Oil red O was dissolved using 100% isopropanol and measured absorbance at 520 nm using a microplate reader.

Effect of CC extracts on adipogenic gene expression using RT-qPCR

3T3-L1 adipocytes (8×10^4 cells/well) were seeded in 6-well plates and differentiated as described above. Cells were treated with various concentrations of CCE (100-400 µg/mL)

in a differentiation medium for 72 hours (Days 0 to day 3). Then, total RNA was extracted from the 3T3-L1 cells with TRIzol® reagent (Invitrogen, USA). The cDNA synthesis from total RNA was performed by RevertAid RT Reverse Transcription Kit (Thermo Fisher Scientific, USA) according to the manufacturer's protocol. Expression of adipogenic genes, C/EBPα and PPARγ, were quantified by real-time PCR using a 7500 Real-Time PCR System (Thermo Fisher Scientific, USA) with SensiFAST™ SYBR Lo-ROX Kit (Bioline, UK). The PCR primer was synthesized from Bio Basic (USA). The nucleotide sequences for PCR primers were listed in Table 1. Gene expression analysis was calculated by the $2^{-\Delta\Delta CT}$ method (21) after normalization to β-actin.

Table 1
Nucleotide sequences of the forward primer and reverse primer.

Gene	Forward primer	Reverse primer
C/EBPα	GCAAAGCCAAGAAGTCGGTG	TCACTGGTCAACTCCAGCAC
PPARγ	TCCGCTGATGCACTGCCTAT	GGAATGCGAGTGGTCTTCCA
β-actin	TGGTGGGAATGGGTCAGAAG	TGTAGAAGGTGTGGTGCCAG

Statistical analysis

Data from triplicate samples of three independent experiments were expressed as means ± SD. Statistical evaluation was performed using one-way analysis of variance (ANOVA) with post-hoc Tukey's tests or post-hoc Dunnett's test using GraphPad Prism software (GraphPad Software Inc., USA). Values of $P < 0.05$ were considered significant.

Results and Discussion

Extraction yield

Aqueous extraction (CCA) gave the red crude extract with the extraction yield of 37.43% while 0.5% acetic acid in 70% ethanolic extraction (CCE) gave the dark purple crude extract with the extraction yield of 50.20%. The yield of *C. carandas* fruit extraction in this study is comparable to a previous study. Their results revealed that the 70% ethanolic extract and the aqueous extract of the *C. carandas* fruit gave an extraction yield of 46.0% and 32.0%, respectively (22). The extraction yield of 70% ethanolic extract was higher than that of aqueous extract. This might be due to extraction of both polar and nonpolar substances with aqueous organic solvents.

Total phenolic, flavonoids, and anthocyanin content of CC extracts

As shown in Table 2, the content of total phenolic, flavonoid and anthocyanin in CCE were 881 ± 2 mg of GAE/100 g DW, 1112 ± 9 mg of RUE/100 g DW and 83 ± 9 mg of C3G/100 g DW, respectively which is higher than those of CCA (468 ± 1 mg of GAE/100 g DW, 411 ± 1 mg of RUE/100 g DW and 24 ± 2 mg of C3G/100 g DW). A similar result was reported in the previous study by Dhar *et al.* in 2017 on the effect of extraction solvents on the phenolic and flavonoid contents of the *Carissa carandas* fruit. They reported that the ethanolic extract had the phenolic and flavonoid contents with the concentration of 1082 ± 106 mg of GAE/100 g DW and 874 ± 40 mg of CE/100 g DW, respectively while aqueous extract had the phenolic and flavonoid contents with the concentration of 529 ± 38 mg of GAE/100 g DW and 273 ± 15 mg of CE/100 g DW, respectively (22). However, the amount of total phenolic contents in our extracts were lower than that in the Dhar *et al.* study while

the flavonoid contents were higher than that in the Dhar *et al*. study (22). Variation may be a result from the difference of ripening stage or geographical location (23).

Table 2
Total phenolic, flavonoids and anthocyanin content of *Carissa carandas* extracts.

CC extracts	Phenolic contents (mg GAE/100 g DW)	Flavonoid contents (mg RUE/100 g DW)	Anthocyanin contents (mg C3G/100 g DW)
CCA	468 ± 1	411 ± 1	24 ± 2
CCE	881 ± 2	1112 ± 9	83 ± 9

Values are mean ± SD.

Cytotoxicity of CC extracts on 3T3-L1 adipocytes

To determine whether the *Carissa carandas* extracts affect the cell viability of 3T3-L1 adipocytes, cells were treated with various concentrations of CCA or CCE (100-400 µg/mL) for 72 hours. Cell viability less than 80% was considered to be toxic. As shown in Figure 1, CCA and CCE at up to 400 µg/mL did not present a cytotoxic effect to the cells. Moreover, CCA and CCE were able stimulate the cell growth in 3T3-L1 adipocytes and these effects may be due to phytochemicals in the CCA and CCE.

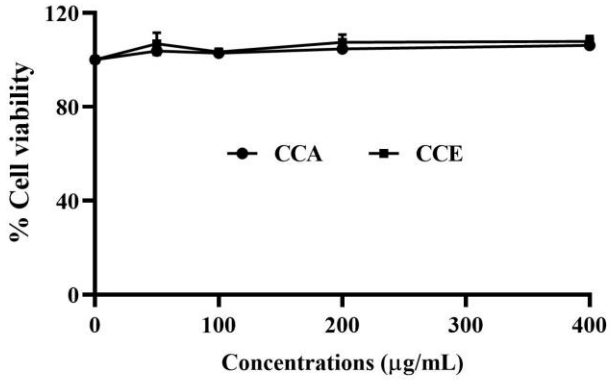

Figure 1
Effect of CCA and CCE on cell viability of 3T3-L1 adipocyte. Cells were treated with various doses of CCA or CCE (50-400 µg/mL). And then the cell viability was determined using SRB assay. Values are expressed as means ± SD.

Effect of CC extracts on lipid accumulation using Oil Red O staining

To determine the effects of CCA and CCE treatment on lipid accumulation in 3T3-L1 adipocytes. First, cells were treated with various concentrations of CCA or CCE (100-400 µg/mL) in a series of differentiation medium from Day 0 to day 12. Then, the lipid content in aidipocytes were stained using Oil Red O. The results in figure 2A and 2B indicated that CCA only at concentration 400 µg/mL significantly reduced lipid accumulation in 3T3-L1 whereas CCE at concentration 200 and 400 µg/mL significantly decreased lipid accumulation in a dose dependent manner, respectively. To investigate the effects of CCA and CCE treatment during initiation of adipocytes differentiation, 3T3-L1 cells were treated with

various concentrations of CCA or CCE (100-400 µg/mL) in a differentiation medium for 72 hours (Days 0 to day 3) and then further differentiated until day 12. CCE treatment (100-400 µg/mL) of 3T3-L1 cells for 72 hours significantly suppressed the lipid accumulation in a dose dependent manner. Therefore, the inhibition of adipogenesis by regulating the expression of PPARγ and C/EBPα by CCE occurred primarily in the early stages of differentiation. CCA only at concentration 400 µg/mL significantly reduced lipid accumulation in 3T3-L1. Interestingly (Figure 2C). CCE at concentration 100, 200 and 400 µg/mL significantly decreased lipid accumulation in a dose dependent manner (Figure 2D). According to result, the treatment with ethanolic extract of *C. carandas* fruit for 72 hours is therefore selected for further investigation to verify their anti-adipogenesis activity in 3T3-L1 adipocytes.

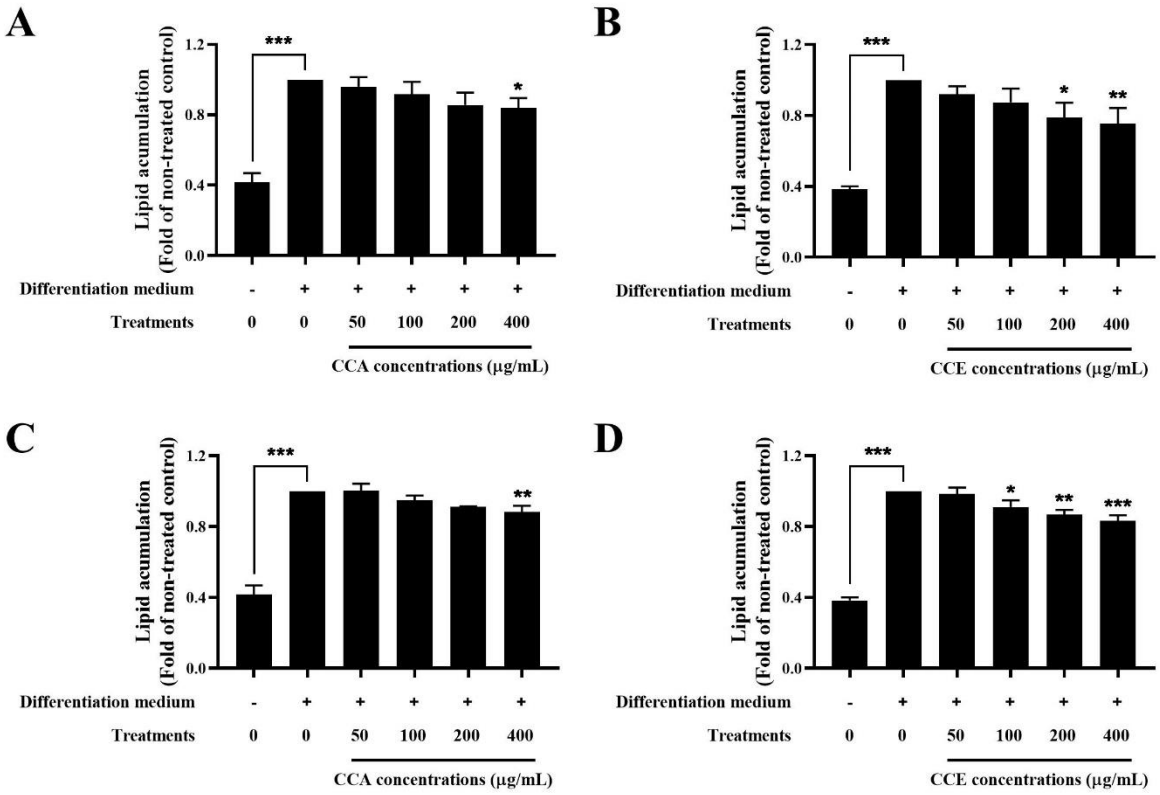

Figure 2

Effect of CCA and CCE on lipid accumulation in 3T3-L1 adipocyte for 12 days (A,B) and 72 hours (C,D). Cells were treated with various doses of CCA or CCE (0-400 µg/mL). And then the lipid accumulation was determined using Oil Red O staining. Values are expressed as means ± SD.

Effect of CC extracts on adipogenic gene expression using RT-qPCR

To determine the effects of CCE on gene expression include C/EBPα and PPARγ of 3T3-L1 adipocytes. Cells were treated with various concentrations of CCE (100-400 µg/mL) for 72 hours. As shown in Figure 3A, CCE treatment at 400 µg/mL significantly decreased C/EBPα gene expression as well as PPARγ gene expression (Figure 3B) in 3T3-L1 adipocytes These effects may be due to the anthocyanin in CCE that have anti-adipogenesis activity. Previous studies have also revealed that several anthocyanins such as cyanindin-3-glucoside and delphinidin-3-glucoside inhibit lipid accumulation and also gene expression of major transcription factor in adipogenesis (9,10). Further investigation should be performed to confirm the effects of CCE on protein expression of these transcription factors.

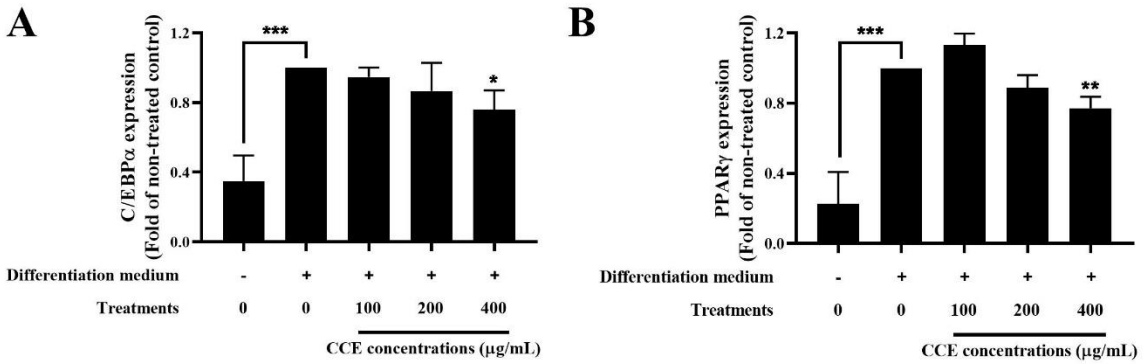

Figure 3

Effect of CCE on gene expression, including (A) C/EBPα and (B) PPARγ in 3T3-L1 adipocyte for 72 hours. Cells were treated with various doses of CCE (0-400 µg/mL). And then the gene expression was determined using RT-qPCR. Values are expressed as means ± SD.

Conclusion

The current study showed the inhibitory effects of *C. carandas* fruit extract on adipogenesis and lipid accumulation. CCE treatment during the early stages of differentiation significantly caused a reduction in the expression of the key transcriptional regulators, C/EBPα and PPARγ, in 3T3-L1 adipocytes. We also demonstrated that CCE inhibited lipid accumulation of 3T3-L1 adipocytes in a dose-dependent manner. These results suggest that the anti-obesity effects of *C. carandas* fruit CCE result from a decrease in adipogenesis.

Acknowledgements

This work was supported by Faculty of Medicine Research Fund, Chiang Mai University, (Grant No. 090-2565)

References

1. Hossain P, Kawar B, El Nahas M. Obesity and diabetes in the developing world — A growing challenge. N Engl J Med. 2007;356(3):213-5.
2. Karelis AD, Faraj M, Bastard JP, St-Pierre DH, Brochu M, Prud'homme D, et al. The metabolically healthy but obese individual presents a favorable inflammation profile. J Clin Endocrinol Metab. 2005;90(7):4145-50.
3. Arner P, Spalding KL. Fat cell turnover in humans. Biochem Biophys Res Commun. 2010;396(1):101-4.
4. Cornelius P, MacDougald OA, Lane MD. Regulation of adipocyte development. Annu Rev Nutr. 1994; 14:99-129.
5. Rosen ED, Walkey CJ, Puigserver P, Spiegelman BM. Transcriptional regulation of adipogenesis. Genes Dev. 2000; 14(11):1293-307.
6. Khera R, Murad MH, Chandar AK, et al. Association of Pharmacological Treatments for Obesity With Weight Loss and Adverse Events. A Systematic Review and Meta-analysis. JAMA. 2016;315(22):2424–2434. Accessed July 26, 2019 at doi:10.1001/jama.2016.7602.

7. Fan L, Xu H, Yang R, Zang Y, Chen J, Qin H. Combination of capsaicin and capsiate induces browning in 3T3-L1 white adipocytes via activation of the peroxisome proliferator-activated receptor γ/β(3)-adrenergic receptor signaling pathways. J Agric Food Chem. 2019;67(22):6232-40.
8. Lone J, Choi JH, Kim SW, Yun JW. Curcumin induces brown fat-like phenotype in 3T3-L1 and primary white adipocytes. J Nutr Biochem. 2016;27:193-202.
9. Lee M, Lee M. The effects of C3G and D3G anthocyanin-rich black soybean on energy metabolism in beige-like adipocytes. J Agric Food Chem. 2020;68(43):12011-8.
10. Molonia MS, Occhiuto C, Muscara C, Speciale A, Bashllari R, Villarroya F, Saija A, Cimino F, Cristani M, 2020. Cyanidin-3-O-glucoside restores insulin signaling and reduces inflammation in hypertrophic adipocytes. Arch. Biochem. Biophys. 691,. https://doi.org/10.1016/j.abb.2020.108488 108488
11. Matsukawa T, Villareal MO, Motojima H, Isoda H. Increasing cAMP levels of preadipocytes by cyanidin-3-glucoside treatment induces the formation of beige phenotypes in 3T3-L1 adipocytes. The Journal of Nutritional Biochemistry. 2017;40:77-85.
12. Lee YM, Yoon Y, Yoon H, Park HM, Song S, Yeum KJ. Dietary Anthocyanins against Obesity and Inflammation. Nutrients. 2017 Oct 1;9(10):1089. doi: 10.3390/nu9101089. PMID: 28974032; PMCID: PMC5691706.
13. Yildiz E, Guldas M, Ellergezen P, Acar A G, & Gurbuz O. (2021). Obesity-associated pathways of anthocyanins. Food Science and Technology, 41(Suppl. 1), 1-13. http://dx.doi.org/10.1590/fst.39119.
14. Dua D, Srivastav NS. Anti-cancerous and antioxidant potential of aqueous extracts of Annona reticulata, Podophyllum peltatum, Psidium guajava, Ananas comosus, Carissa carandas on MCF-7 cancer cell line. Int J Integr Sci Innov Technol Sec. 2013;2:15-9.
15. Lailerd M, Lailerd N, Amornlerdpison D, Pitchakarn P, Wongnoppavich A, Imsumran A. Anti-inflammation and anti-insulin resistance activities of Carissa carandas Linn. Fruit extract. The 46th International Congress on Science, Technology and Technology-based Innovation (STT46), Ramkhamhaeng University, Bangkok, Thailand, Oct 5-7, 2020, pp 986-91.
16. Devmurari V, Shivanand P, Goyani M, Vaghani S, Jivani N. A review: Carissa Congesta: Phytochemical constituents, traditional use and pharmacological properties. Pharmacogn Rev. 2009;3:375-7.
17. Gorinstein S, Zachwieja Z, Katrich E, Pawelzik E, Haruenkit R, Trakhtenberg S, et al. Comparison of the contents of the main antioxidant compounds and the antioxidant activity of white grapefruit and his new hybrid. LWT-FOOD SCI TECHNOL. 2004;37(3):337-43.
18. Zhishen J, Mengcheng T, Jianming W. The determination of flavonoid contents in mulberry and their scavenging effects on superoxide radicals. Food Chem. 1999;64(4):555-9.
19. Le XT, Huynh MT, Pham TN, Than VT, Toan TQ, Bach LG, et al. Optimization of total anthocyanin content, stability and antioxidant evaluation of the anthocyanin extract from Vietnamese Carissa Carandas L. fruits. Processes. 2019;7(7).
20. Yang L, Rong-Rong C, Ji-Li F, Ke Y. Total anthocyanins and cyanidin-3-O-glucoside contents and antioxidant activities of purified extracts from eight different pigmented plants. Phcog Mag 2019;15:124-9
21. Overbergh L, Giulietti A, Valckx D, Decallonne R, Bouillon R, Mathieu C. The use of real-time reverse transcriptase PCR for the quantification of cytokine gene expression. J Biomol Tech. 2003;14(1):33-43.

22. Dhar G, Akther S, Sultana A, May U, Islam MM, Dhali M, Sikdar D. Effect of extraction solvents on phenolic contents and antioxidant capacities of A. chaplasha and C. carandas fruits from Bangladesh. J App Biol Biotech. 2017; 5 (03): 039-044.
23. Gul J, Sultana B, Anwar F, Naseer R, Ashraf M, Ashrafuzzaman M. Variation in antioxidant attributes at three ripening stages of guava (Psidium guajava L.) fruit from different regions of Pakistan. Molecules. 2012;17:3165-3180.

THE EXISTENCE OF *Platerodrilus* BEETLES IN NAKHON SI THAMMARAT PROVINCE, SOUTHERN THAILAND

Kanitta Keeratipattarakarn*, Fahmida Wazed Tina
Faculty of Science and Technology, Nakhon Si Thammarat Rajabhat University, Tha Ngio, Nakhon Si Thammarat 80280, Thailand
*e-mail: kanitta_kee@nstru.ac.th

Abstract:
This study reports the existence of neotenic net-winged beetles (*Platerodrilus sinuatus* group) for the first time from Nakhon Si Thammarat province, southern Thailand. These insects are terrestrial and mostly found in rainforest habitats. They prefer to live on dead wood, forest litter, and soil with a higher organic matter content. In these beetles, the males and females are morphologically different. Though the males undergo complete metamorphosis and become fully winged adults, the females do not pupate and stay in larval morphology even when they are sexually matured. Females are longer than males. Due to the winglessness of the females they are not able to disperse so far. Whereas, the males look like other typical lycid beetles and they can fly for a short distance. In this study, three females were observed in 'Khao Mahachai' mountain located in Nakhon Si Thammarat Rajabhat University area, Nakhon Si Thammarat province, and their photographs were taken. This mountain has tropical moist evergreen forest. The first female was observed in July 2020 which was 3.84 cm long, the 2nd one was observed in November 2020 which was 2.92 cm long, and the 3rd female was observed in May 2021 which was 4.78 cm long. Unfortunately, no male was obtained through using light traps since *Platerodrilus* males do not respond to light traps. To our knowledge, this is the first photographic record and published report on the existence of *P. sinuatus* group beetles in southern Thailand. Reporting these *P. sinuatus* group beetles is important for their conservation in Thailand. For doing this, protection and preservation of mountainous rainforests in Thailand are necessary.
Keywords: Animal conservation, mountainous rainforest, Nakhon Si Thammarat Rajabhat University, *Platerodrilus* beetles

Introduction:

The net-winged beetles (Lycidae) are diverse and abundant in humid tropics [1]. They are terrestrial animals and mostly found in forest habitats. They occur mostly on dead wood, in forest litter, and on soil with a higher organic matter content [1]. These beetles are interesting since the adult males and females are morphologically very different [2, 3]. The males undergo complete metamorphosis and become fully winged adults [4]. The males look like other typical lycid beetles and their body length varies from 1.3-10 mm [5]. On the other hand, the females are neotenous; they do not pupate and stay in larval morphology even when they are sexually matured [4, 6]. Females are longer than males and they can reach up to 70 mm [7]. Due to the winglessness of the larviform females, their dispersal is very limited. However, though males have wings, they fly in a short distance only when they need to search for the females [7]. When a male finds a female, he tightly attaches to the gonopore of the female and inserts his long and curved genitalia into the female's gonopore. They stay in this condition for about 5 hours. After releasing the female, the male dies within 3-4 hours [4]. The female lays low number of large-sized eggs the next day. In these beetles, the females may live for several years whereas males live shorter than females [4].

The diet of lycid larvae is highly controversial. They feed on fermenting juices exuded from rotting logs and branches of trees, fungi, slime moulds, molluscs, Diptera larvae, *Bostrichus* larvae, and *Clytus* larvae. For example, *Lygistopterus sanguineus* larvae are carnivorous and they prey upon the larvae of *Bostrichus* and *Clytus* [8]. Similarly, larvae of *Lycostomus* sp. and *Calopteron reticulatum* are also carnivorous and they consume molluscs and Diptera larvae [9, 10]. The larvae of *Calopteron fasciatum, Xylobanellus erythropterus* and *Lopheros lineatus* feed on fermenting juices exuded from rotting logs of trees [11-13]. It was observed that *Duliticola hoiseni* (= *Platerodrilus ruficollis*) fed on juices of rotting woods, and examined a drop of liquid squeezed from that piece of wood under microscope [4]. It was found that collected wood juice contained a wide variety of microorganisms including protozoa, rotifers, nematodes, copepods, nauplii larvae and mites. The gut contents of several *D. hoiseni* specimens were examined by the scientists (4) and found the same microorganisms in there. According to those scientists, *D. hoiseni* larvae actually fed on microorganisms within the juices of the rotting wood [4].

The feeding behavior of *D. hoiseni* was investigated by [4] and found that the larvae were moving on the surface of fallen logs with their heads and antennae. From time to time, they were observed to lower their heads and examine the surface with their antennae. Their antennae might serve a sensory function to assess the dampness of the wood. During feeding, they attach their heads and mouthparts into the crevices.

The taxonomy of net-winged beetles is based on the males, especially on the morphology of their genitalia. Although a large number of net-winged beetles are observed in southeast Asia, very few of them have been described, and most of them are female larvae. The reason is that females are encountered frequently whereas obtaining males of the same species is challenging since lycid males do not respond to light traps. The only way to obtain males is to capture them when they mate with the females [4].

There are 97 genera and 4000 described species belong to the family Lycidae [1] and *Platerodrilus* is one of them. They are found in three major biodiversity hotspots- Indo-Burma, Sundaland and the Philippines including Palawan [5]. They prefer to live in humid tropical rainforests, especially in mountain region [7]. The males of this genus can easily be identified by looking at their antennae; there are 11 segments in their antennae [14]. On the other hand, the female larvae can be recognized by their apical antennomere with peg-like processes [15].

In this study, three *Platerodrilus* females were observed for the first time in Nakhon Si Thammarat province, southern Thailand. Afterwards their species group was confirmed.

Methodology:

In this study, three *Platerodrilus* females were observed in/nearby 'Khao Mahachai' mountain which is located in the area of Nakhon Si Thammarat Rajabhat University (8°27'50"N 99°51'37"E). Khao Mahachai mountain is a tropical moist evergreen forest. There are two seasons in this forest. Rainy season from May to January with the heaviest rainfall from October to December, and the hot season is between February to April. Many types of trees are seen in this forest such as wood fern or buckler ferns, palm trees, malacca teak, and white backed palm. Several wild orchid species and hundreds of animal species are also found in this forest. Some of the forest areas are now used for rubber, durian, banana, and mangosteen plantation.

The first *Platerodrilus* female was observed at around 7.00 am on 21st July, 2020. It was walking on a concrete walkway nearby 'Khao Mahachai' mountain which is located in the Nakhon Si Thammarat Rajabhat University area (Coordinates: 8°27'50"N 99°51'37"E) (Figure 1). The temperature was 26°C, humidity was 80%, and the weather was cloudy on that time. The length of that female was 3.84 cm. The second one was observed at around

7.30 am on 29th November, 2020 when the temperature was 23°C, and the humidity was 88%. The weather of that time was also cloudy. That *Platerodrilus* female was walking inside the forest of the mountain (Figure 1 and 2). The length of that female was 2.92 cm. Finally, the third female was also observed on the same concrete walkway nearby 'Khao Mahachai' mountain at 6.42 am on 26th May, 2021. On that time, temperature was 25°C, humidity was 82%, and the weather was cloudy. The length of that female was 4.78 cm. Several necessary photographs were taken of all these females for identification.

Figure 1. The concrete walkway nearby 'Khao Mahachai' mountain in Nakhon Si Thammarat Rajabhat University area (Source: 8°27'50.0"N 99°51'37.0"E - Google Maps).

Figure 2. The mountainous forest where *Platerodrilus sinuatus* group female was observed.

Results and Discussion:
After analyzing all these photographs based on [5], several characteristics like flat and wide bodies, triangular pronotum without prominent glabrous tubercles on the disc (except two tubercles in the middle of posterior margin), similar-shaped mesothorax and metathorax, presence of four tubercles (upper is rounded and lower is slightly transverse in shape) on both mesothorax and metathorax, and the abdominal segments with slender and long lateral processes confirm that these females are belong to *Platerodrilus sinuatus* group (Figure 3). This group contains species from continental Asia, Sumatra, Java and Malay Peninsula. The larvae from continental Asia do not have any tubercles in the thoracic terga (i.e., smooth thorax) but in Sumatra, Java and Malay, larvae have tubercles in the discs of the thoracic terga [5], like our specimens. However, more specimens, specially males are needed to examine in detail to confirm the species of *P. sinuatus* group beetles found in Nakhon Si Thammarat. Unfortunately, in this study, no male was obtained through using light traps since *Platerodrilus* males do not respond to light traps [4].

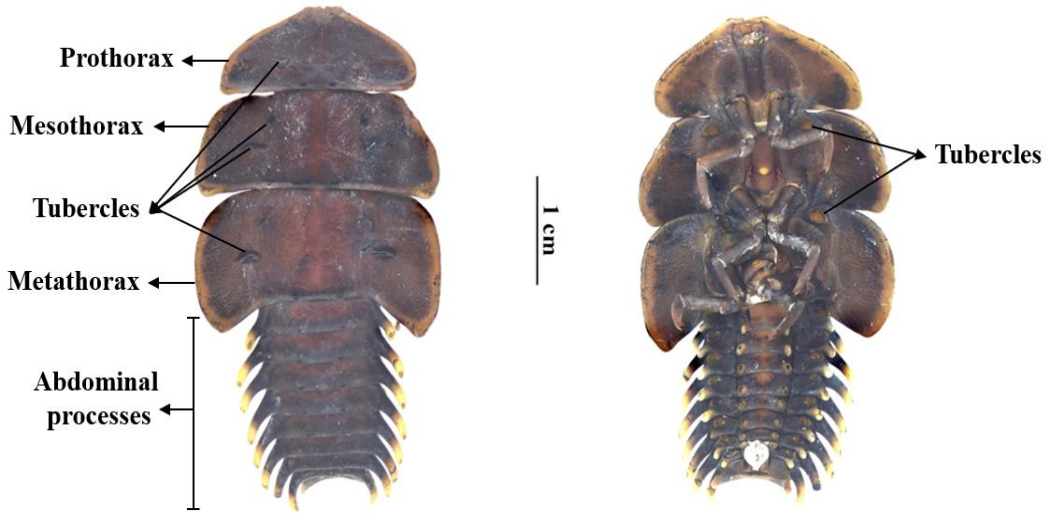

Figure 3. Dorsal (a) and ventral (b) views of *Platerodrilus sinuatus* group female specimen.

Previously *Platerodrilus* beetles have been reported from many countries (e.g., Malaysia, India, the Philippines, Indonesia, Singapore, Laos, and Thailand) [5]. In Thailand, only one species (*Platerodrilus grootaerti*) was reported from Na Haeo district in Loei province, Northeastern Thailand [16]. However, there is no published record on the existence of *Platerodrilus* beetles from southern Thailand. To our knowledge, this is the first photographic record and published report on the existence of *P. sinuatus* group beetles from Nakhon Si Thammarat province, southern Thailand.

Conclusion:
The dispersal ability of *Platerodrilus* females is very low and even the winged males do not fly effectively and cannot disperse more. They entirely depend on moist rainforest since their larvae require constant access to liquid food in the rainforest. Their extremely low dispersal ability favors in situ diversification but it limits their exchange between major geographical regions. Therefore, it is essential to conserve these net-winged beetles in their habitats in Thailand. For doing this, protection and preservation of mountainous rainforests are necessary. Besides, an extensive networking system is required to protect most of the tropical rainforests and mountain ranges in South East Asia where net-winged beetles are found. Finally, further research is required to know the species diversity, distribution, population structure and behavior of *P. sinuatus* group beetles in Thailand.

Acknowledgements:
The authors are thankful to Nakhon Si Thammarat Rajabhat University, Thailand.

References:
1. Bocak L, Bocakova M. Ann Zool. 2008;58:695-720.
2. Bocak L, Bocakova M, Hunt T, Vogler AP. P Roy Soc B. 2008;275:2015-2023.
3. Masek M, Ivie MA, Palata V, Bocak L. Raffles Bull Zool. 2014;62:136-145.
4. Wong ATC. Raffles Bull Zool. 1996;44:173-187.
5. Masek M, Bocak L. ZooKeys 2014;426:29-63.
6. Mjöberg E. Psyche 1925;32:119-156.
7. Masek M, Palata V, Bray TC, Bocak L. PLoS One 2015;10:p.e0123855.
8. Perris É. Latr Ann Soc Entomol Fr. 1846;4:343-346.
9. Miller RS. Ohio J Sci. 1988;88:119-120.
10. Shelford R. Oxford University Press 1916;1-331.
11. Withycombe CL. In Proc Entomol Soc London 1926;1:32-33.
12. Burakowski B. Pol Pis Entomol. 1988;58:575-585.
13. Burakowski B. Pol Pis Entomol. 1990;59:719-72.
14. Li Y, Pang H, Bocak L. Ann Zool. 2017;67:679-687.
15. Bocak L, Matsuda K. J Nat Hist. 2003;37:1463-1507.
16. Kazantsev SV. Russ Entomol J. 2009;18:55-62.

CORDYCEPS EXTRACT-LOADED NANOPARTICLES PROMOTES COLLAGEN SYNTHESIS AND ENHANCES WOUND HEALING

Nawapol Upatcha, Palakorn Kaokaen, Parinya Noisa*

Laboratory of Cell-Based Assays and Innovations, School of Biotechnology, Institute of Agricultural Technology, Suranaree University of Technology, 111 University Avenue, Nakhon Ratchasima, 30000, Thailand
*e-mail: p.noisa@sut.ac.th

Abstract:

The most common cause of slow-healing wounds is a loss of fibroblast function and a decreased response to tissue injury. Cordycepin, a bioactive compound of *Cordyceps militaris*, is the potential herbal bioactive compound, which has various activities, including antioxidant, anti-inflammatory, and tissue remodeling process. The aim of the present study was to improve the effective of cordycepin, and evaluate the synthesis of collagen and elastin by dermal fibroblasts to support wound healing activity. Human dermal fibroblasts were cultured and treated with cordycepin, cordycepin medium (CM), and CM-loaded cassava starch nanoparticles (CMP). The treated cells were evaluated, including cell proliferation, gene expression of collagen and elastin, protein expression of type 1 collagen (Col1A1), and wound healing activity. The result showed that CMP could significantly increase cell proliferation up to 10-fold, gene expression of Col1A1, KRT18, and Elastin up to 2.44 to 5.53-folds, when compared with the untreated control cells. In addition, CMP could promote Col1A1 up to 27-, 21- and 3-folds, comparing to the untreated control, cordycepin, and CM, respectively. Noteworthy, CMP improved the potential of wound healing activity 12-, 4.46- and 3.12-folds, when compared to the untreated group, cordycepin and CM, respectively. Thus, this evidence supported that the encapsulated nanoparticle of CMP could enhance the efficiency of wound healing process in human dermal fibroblasts and might be applicable for cosmetic product development.

Introduction:

Generally, in normal healthy people, when an injury occurs (injuries to the dermis), the skin layer has a natural healing mechanism known as the wound healing process [1]. The most frequent of slow-healing wounds is the loss of skin fibroblast function. Since the dermis consists of two main proteins, collagen and elastin, these proteins are essential for the repair and regeneration of human skin after injury or deterioration [2]. Dermal fibroblasts are the main cell type present in skin connective tissue (dermis) that interacts with epidermal cells and plays a critical role during wound healing and in bioengineering of skin, for example helping to repair wounds, wounds caused by heat destruction and treatment of burns. If there is no fibroblast at the wound site, it will not be able to form the extracellular matrix and the epidermal cells will not be able to propagate above the wound site. [3]. In addition, fibroblast cells play a role in the production of fibroblast growth factors (FGF) involved in stimulating the synthesis of type I collagen and elastin, which are responsible for skin resistance and elasticity, characteristics that are diminished with skin aging.

Cordyceps is a genus of entomopathogenic fungus that includes about 600 species. The genus Cordyceps is classified under the order Hypocreales; family Ophiocordycipitaceae and phylum; Ascomycota [4]. Cordyceps is a genus of entomopathogenic fungus that includes about 600 species. *Cordyceps militaris* is a species of medicinal mushroom capable of producing the bioactive compound Cordycepin (3'-deoxyadenosine), which has pharmaceutical

effects for antioxidant, anti-inflammatory, and tissue remodeling process effects [6]. Cordycepin can be produced from cordyceps in both submerge culture and solid-state fermentation, resulting in a range of biologically active compounds such as. polysaccharides, cordycepin, adenosine, amino acid, organic selenium, ergosterol, sterols, cordycepic acid, superoxide dismutase, and vitamins (A, E, B2, B3, and C) [7].

In addition, decreased levels of growth factors, reduced amount of collagen, abnormal accumulation of elastin, and reduction in the epidermal and dermal thickness are often indicative of clinical signs such as xerosis, wrinkles, sagging, blemishes, and all signs of skin aging. In previous studies, we found that cordycepin increases the rate of cell migration of intracellular fibroblasts, helping the skin stimulate the production of Collagen and accelerating tissue regeneration through Adenosine Receptor-Mediated Wnt/β-Catenin Pathway Stimulation by regulating GSK3b activity [8]. However, we may be able to enhance the effectiveness of cordyceps extract or cordycepin extract in rejuvenating skin, stimulating cell growth, and improving wound healing. Therefore, in this study, it was interesting to develop cordyceps extracts using extract encapsulation and nanotechnology and to study the potential of CMP in wound healing compared to cells treated with cordycepin and CM *in vitro*.

Methodology:

Reagents and chemicals

Cordycepin standard and cordycepin medium derived from Laboratory of Cell-Based Assays and Innovations (CBAI), School of Biotechnology, Institute of Agricultural Technology, Suranaree University of Technology. 3-(4,5-dimethyl-2-thiazolyl)-2,5-diphenyl-2H-tetrazolium bromide (MTT), dimethyl sulfoxide (DMSO), was purchased from Sigma-Aldrich Chemical Co. (St. Louis, MO). Dulbecco's Modified Eagle Medium (DMEM), and fetal bovine serum (FBS) was purchased from HyClone (HyClone, Logan, UT).

Fabrication of cordycepin medium-loaded nanoparticles

The preparation method of cassava starch nanoparticles was modified from physical treatment. These methods are comprised of three steps in which (1) starch was extracted, (2) CM was encapsulated, and (3) aqueous nanosuspensions of CM-loaded cassava starch nanoparticles (CMP). First, 4% cassava starch powder was dissolved in 1,000 ml of DI water under a magnetic stirrer for 30 min and added to ethanol (dropwise) ratio of 1:1.5 into a slurry of hot starch and stirred for 30 min. Then, the hydrolyzed starch was collected by centrifugation at 10,000 rpm for 5 min. The hydrolyzed starch was transferred to a hot air oven (60 °C) for 1-2 days. Second, 6% of hydrolyzed starch powder from physical treatment was mixed with 2.5 mM of cordyceps medium while continuously stirring for 30 min. The solution was added dropwise with ethanol at a ratio of 1:1.5 into a starch solution and stirred at room temperature for 24 hrs. After incubation, the encapsulated nanoparticles were collected by centrifugation at 10,000 rpm for 5 min. Finally, 0.1% of CMP was dissolved by 10 ml of DI water and sonicated by Ultrasonicator at 40% amplitude for 10 min (pulse on 5 minutes and pulse off 10 minutes) to disperse and reduce the size of nanoparticles. The aqueous suspension of CMP was collected at room temperature for future use.

Cytotoxicity Assays

MTT cell survival assay was used to determine the effect of cordycepin (C), cordyceps medium extract (CM), and CMP on cell viability. The human dermal fibroblast cell line was maintained in DMEM, supplemented with 10% FBS and 1% penicillin-streptomycin, and 1% L-glutamine. The fibroblast cells were seeded in 96-well plates at a density of 1.5×10^4 cells/well and incubated at 37°C in a humidified atmosphere containing 5% CO_2 for 24 hrs. These cells were treated with a varied concentration of C, CM, and CMP for 24 hrs. The MTT solution was added to each well at the final concentration of 0.25 mg/ml before further incubation for 4 hours at 37°C in the darkroom. The formazan crystal was solubilized in

DMSO. The absorbance was measured at 570 nm by using a microplate reader (BMG Labtech, Ortenberg, Germany). The 50% inhibitory concentration (IC50) was obtained from the dose-response curve of percent viability (Y) versus concentration tested (X) and calculated with a linear regression performed using Microsoft Excel.

RNA Isolation and Reverse Transcription (RT-PCR)

Gene expression was examined by RT-PCR. Human dermal fibroblast cells were cultured and transferred into the 6-well plates at 80% confluence. In normal condition, these cells were treated with C, CM and CMP (1 µM, 1 µM and 0.1 µM, respectively) for 24 hrs After incubation, total RNA was extracted with Macherey-Nagel Kit (Macherey- Nagel, Düeren Germany). Total RNA was then converted into cDNA by ReverTra Ace® qPCR RT Master Mix with gDNA Remover (TOYOBO CO., LTD., Japan). The PCR was carried out in a Biorad/T100 Thermal cycler (Biorad, CA, USA) with specific primers, and amplified cDNA products were identified by electrophoresis using a 1.5% agarose gel. The gel was visualized using Red safe staining and gel documentation. Normalization of the relative expression level of a target gene with the *GAPDH* gene as an internal control was used to determine the relative expression level of a target gene. The expression of the type I collagen genes will be performed by PCR (BioRad, USA) will be used the primer shown in **Table 1**.

Immunofluorescence

Human dermal fibroblast was cultured and in 24-well plates upper sterilized cover slip at 80% confluence. After cell treatment, the treated cells were fixed with 4% paraformaldehyde for 30 minutes at room temperature. Then, the cells were washed with PBS twice and permeabilized with 3% bovine serum albumin (BSA) in 0.1% triton-X 100 of PBS for 20 minutes at 4°C. After 20 minutes, the cells were incubated with primary antibody (1:500 of Anti-collagen type 1 Rabbit pAb, EMD Millipore Corp., USA). All incubations will be performed for overnight, and then the samples were incubated with the secondary antibody (Alexa Flouor™ 488 goat, Life technologies corporation, USA) (1:1,000) for 30 minutes. Nuclei were stained with DAPI and observed under the fluorescence microscope (ZOE™ fluorescence cell imager, BioRad, USA).

Wound healing assay

To assess wound healing, a 10 µl pipette tip was applied to the cell surface in a straight line and the loose cells are washed. Cells were then treated for 24 h at 37 °C in 95% atmosphere, air and 5% CO_2. Cells were determined under a light microscope and the wound healing site was measured at incubation time (0, 12, 24 and 48 hours).

Statistical analysis of data

Each experiment was observed in Triplicate. The data were presented as mean ± S.E.M. and Statistical analysis was performed using SPSS (version 26.0, SPSS Inc., USA). Significant differences between the treatment and control were determined by one-way ANOVA analysis, followed by student T-tests, and $*p < 0.05$, $**p < 0.01$ and $***p < 0.001$ was considered as statistically significant.

Results and Discussion:

Cytotoxicity and cell viability of C, CM, and CMP in HDF cells.

The toxicity effects of C, CM, and CMP on HDF cells. The HDF cells were treated with these bioactive compounds for 24h, and cell viability was determined by using MTT assay. Results showed that C and CM can stimulate the proliferation of HDF cells at concentrations of 1 µM, while CMP can stimulate the proliferation of HDF cells at a concentration 0.1 µM. The half-maximal inhibitory concentration on HDF cells treated with C, CM and CMP was

1,439, 519, and 106 µM, respectively **Figure1**. Many studies have demonstrated the cytotoxic effects of *cordyceps militaris* extract concentration of 10-100 µg/mL was no significant change in the cell viability [11]. Overall, the results showed that the developed CMP was able to increase cell proliferation by up to 10 times.

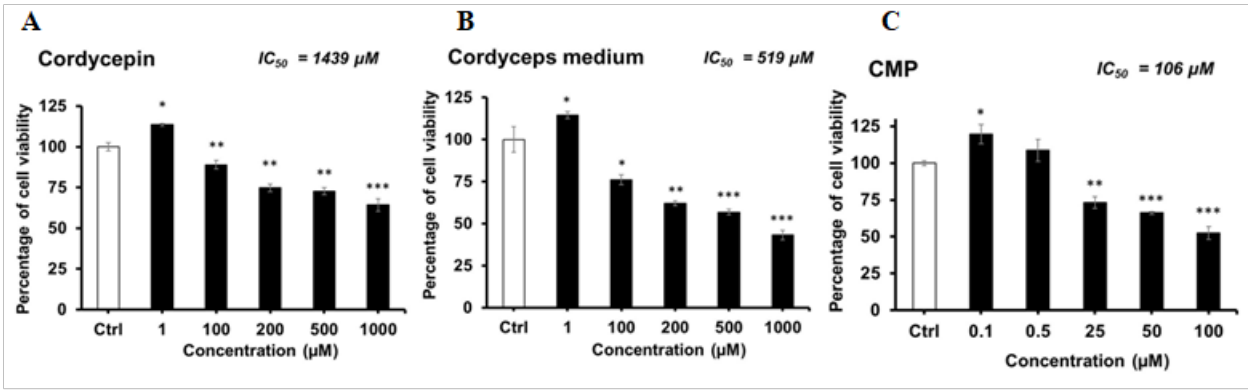

Figure 1. Cell viability and cytotoxic testing. The HDF cells were treated with Cordycepin (A), CM (B), and CMP (C) for 24 hours. The treated cells were determined by MTT assay. Data were presented as mean ± SD (n = 3) *$p < 0.05$, **$p < 0.01$, and ***$p < 0.001$ vs. control cells.

CMP can increase the gene expression of Collagen- and Elastin-rich synthesis on HDF cells.

To determine and compare the gene expression of collagen-related genes on HDF treatment with C, CM, and CMP treatment. The HDF cells were determined the expression of collagen- and elastin-rich synthesis including *Collagen type 1 (Col1A1), Elastin, Keratin 18 (KTR18),* and *Vimentin* after treatment for 24 hours. As shown in Figures.2, the expression level of *Collagen type 1 (Col1A1)* of C, CM, and CMP was increased higher than that of the control group (untreated) at 1.85, 2.10, and 2.44-fold, respectively. The expression level of *Elastin* was increased 2.10, 2.20, and 6.67-fold, respectively. The level of *Keratin 18 (KTR18)* expression was 1.95, 4.37, and 5.53-fold, respectively. While *Vimentin* expression was 0.88, 0.96, and 0.94-fold, respectively. Therefore, the CMP can increase the gene expression of *Col1A1, KRT18* and *Elastin* up to 2.44-5.53-fold when compared to untreated group, cordycepin, and CM, respectively. The CMP can increase the gene expression of Collagen- and Elastin-rich synthesis on HDF cells. That accorded with Yu-Kan Liu [12], they succeed in using cordycepin to increase the expression of Tissue Inhibitor of Metalloproteinase (TIMP), which inhibits the action of Matrix Metalloproteinase, it can stimulate HSC to produce collagen I and III and simultaneously prevent their breakdown (MMP). This study found that nanoparticle encapsulation by CM extract induce collagen- and elastin-group.

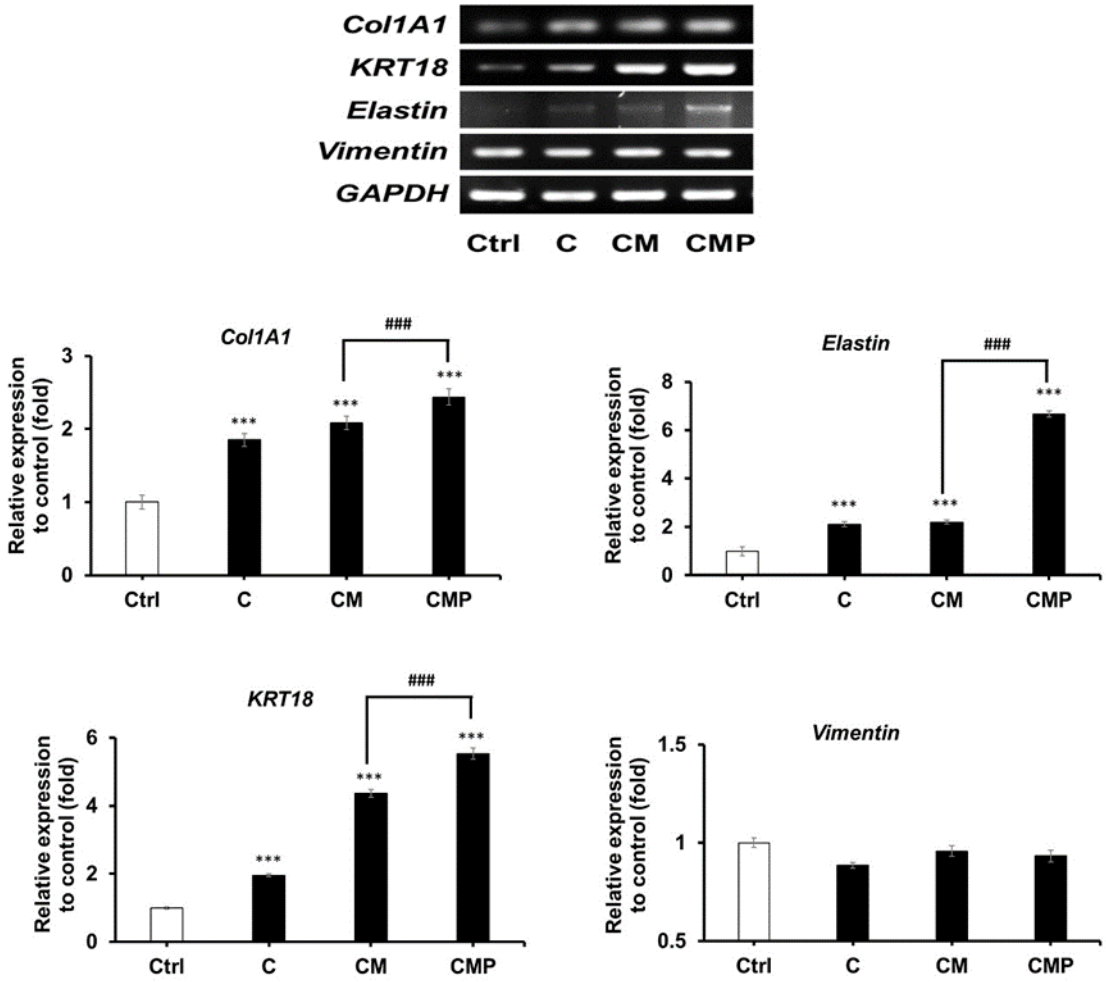

Figure 2. Gene expression of Collagen- and Elastin-rich synthesis on HDF cells. Expression of *Col1A1, KRT18, Elastin and Vimentin* of HDF cells. The mRNA expression levels of genes relative to controls (fold) after HDF cells were treated with a concentration (1 µM, 1 µM and 0.1 µM) of C, CM and CMP, respectively. Significance vs. control cells was indicated as follows: *$p < 0.05$, **$p < 0.01$, and ***$p < 0.001$.

CMP can promote the expression of Collagen Type 1 on HDF cells.

To determine the production of Collagen Type 1 in treatment cells. The HDF cells were treated with C, CM and CMP and evaluated by Immunofluorescence staining (Figures 3). The results showed that the expression of collagen in C, CM, and CMP groups was 1.45, 9.34, and 27.58-fold, respectively. These results demonstrated the CMP can promote the Col1A1 up to 27, 21, and 3-fold when compared to untreated group, cordycepin, and CM, respectively. Collagen's functions in skin and wounds are described in a number of recent reviews. According to recent mapping research of collagen structure and function, collagen fibrils in healthy, injured tissue are in a closed conformation that, when exposed to blood post-injury, exposes cell- and ligand-binding sites that may aid in the healing process [13].

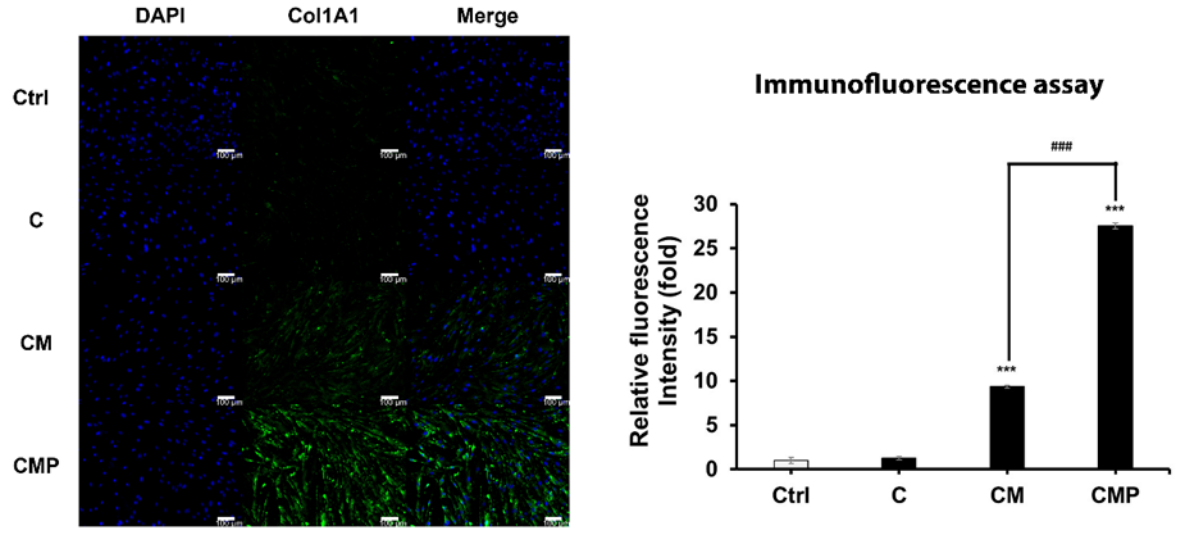

Figure 3. Protein expression of Collagen Type 1 on HDF cells. The treated cells were staining using Anti-collagen type 1. The staining cells were observed under fluorescence microscope. The relative fluorescence intensity was compared to the control. Values were expressed as mean ± SD (n = 3). Significance vs. control cells was indicated as follows: $*p < 0.05$, $**p < 0.01$, and $***p < 0.001$.

CMP can improve the potential of wound healing activity on HDF cells.

To study the efficiency of wound healing in HDF cells treated with cordycepin, CM and CMP *in vitro*. The wound area after HDF treatment were evaluated and calculated the gap area by ImageJ program (Figures 4). The results showed that the gap area (μm^2) at times (0, 12, 24, and 48 hrs.) of control were 320,351, 240,528, 206,194, and 91,902(μm^2), respectively. The C were 313,491, 197,454, 120,964, and 55,581 (μm^2), respectively. The CM was 313,452, 141,678, 107,598, and 57,784 (μm^2), respectively. The CMP was 303,149, 110,197, 77,116, and 24,662 (μm^2), respectively. Moreover, these results showed that CMP was able to significantly reduce the gap area after scattering when compare CM. Therefore, the nanoparticles of CMP can improve the potential of wound healing activity 12, 4.46 and 3.12-fold when compared to untreated group, cordycepin, and CM, respectively. Cell therapies with CM and CMP have shown that it can induce collagen more than cordycepin. The collagen serves as a natural substrate for cellular attachment, proliferation, and differentiation in addition to contributing to the mechanical strength and elasticity of tissues [13]. Collagen applied as an adjunct therapy in wound healing could promote healing potentially by acting as a substrate aiding in the migration of key cellular components of wound healing or the promoter of intracellular matrix, anti-inflammatory environment to resolve the injury toward healing [14].

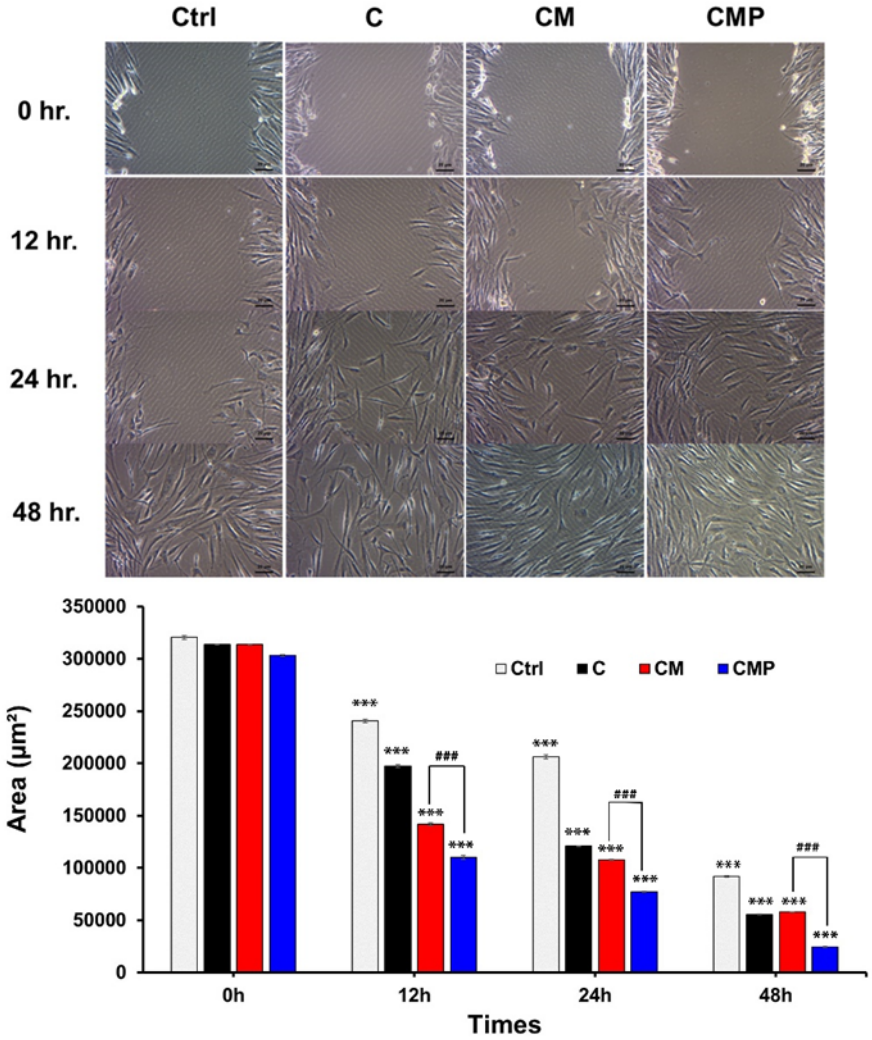

Figure 4. The efficiency of wound healing on HDF cells. HDF cells were pre-scattering before treated with C, CM and CMP for 12, 24 and 48 hours. The gap area was determined by ImageJ program. Values were expressed as mean ± SD (n = 3). Significance vs. control cells was indicated as follows: *$p < 0.05$, **$p < 0.01$, and ***$p < 0.001$.

Table 1. Primer used in the experiment.

Primer	Sequence (5'-3')
Collagen1A1 (Forward)	CTGGATGGATTGAAGGGACA
Collagen1A1 (Reverse)	CAACACGTCCTCTCTCACC
KTR18 (Forward)	CAGCAGCAGCTTCAGTACCAGTGTCTA
KTR18 (Reverse)	GGTGTAGGTATCATAACTCCGCCCATT
Elastin (Forward)	CCGCTAAGGCAGCCAAGTATGGA
Elastin (Reverse)	AGCTCCAACCCGTAAGTAGGAAT
Vimentin (Forward)	CCAGATGCGTGAAATGGAAG
Vimentin (Reverse)	TGAGTGGGTATCAACCAGAG
GAPDH (Forward)	ACCTGACCTGCCGTCTAGAA
GAPDH (Reverse)	GCTCAGGGGCCTTTGGACATCTCTT

Conclusion:

Many collagen peptides have been identified from many different collagen types and have been shown to regulate processes such as cell proliferation, migration, apoptosis, and reduce angiogenesis of fibroblast cells via the secretion of collagen precursors. The nanoparticle of CMP promoted collagen synthesis in fibroblast cells. Since the cells are located in the dermis, it is critical for wound healing during the damage of the skin layer. CMP activated wound healing via the stimulation of HDF proliferation and collagen synthesis. The result showed that CMP was more effective than CM in all observed parameters. CMP upregulated collagen synthesis genes and wound healing activity, in which the effective concentration was less than C, and CM over 10 times. Thus, CMP could increase the efficiency of the wound healing process *in vitro*. Based on these experiments, CMP might be applicable for further developing into cosmetics, dietary supplements, or medicines in the future.

Acknowledgements:

This work was supported by One Research One Grant (OROG) Scholarship, and Suranaree University of Technology (SUT) Research, and Development Fund.

References:

1. Rinnerthaler, M., et al., Biomolecules, 2015. **5**(2): p. 545-89.
2. Tracy, L.E., R.A. Minasian, and E.J. Caterson, Adv Wound Care (New Rochelle), 2016. 5(3): p. 119-136.
3. Hu, M.S., et al., Organogenesis, 2018. **14**(1): p. 46-63.
4. Tuli, H.S., et al., World Journal of Pharmacy and Pharmaceutical Sciences, 2014. 3(4): p. 1525-1535.
5. Meena, H., et al., Electronic Journal of Environmental, Agricultural & Food Chemistry, 2010. 9(10).
6. Tuli, H.S., S.S. Sandhu, and A.K. Sharma, 3 Biotech, 2014. **4**(1): p. 1-12.
7. Shih, L., K.-L. Tsai, and C. Hsieh, Biochemical engineering journal, 2007. **33**(3): p. 193-201.
8. Kim, J., et al., International journal of molecular sciences, 2021. **22**(11): p. 5571.
9. Pardeike J, Hommoss A, Muller RH. Int J Pharm. 2009; 366:170-84.
10. Pardeike J, Muller RH. Pharmaceut Tech Eur. 2007;19(7):46-9.
11. Park, J.M., et al., Nutrients, 2014. 6(9): p. 3711-26.
12. Liu, Y.K. and W. Shen, World J Gastroenterol, 2003. 9(3): p. 529-33.
13. San Antonio, J.D., et al., Bioengineering (Basel), 2020. 8(1): p. 3.
14. Elgharably, H., et al., Wound Repair Regen, 2013. 21(3): p. 473-81.

CHARACTERIZATION OF BACTERIAL CYTOLOGICAL PROFILE OF ANTIBIOTIC RESISTANT *Acinetobacter baumannii*

Rubsadej Suwansaeng, Thanadon Samernate, Htut Htut Htoo, Poochit Nonejuie*
Institute of Molecular Biosciences, Mahidol University, Salaya, Nakhon Pathom, Thailand
*e-mail: poochit.non@mahidol.ac.th

Abstract:

The rapid increase of antimicrobial resistance caused by drug misuse and overuse is currently a serious global public health. One of the causes arises from prescribing broad-spectrum antibiotics prior to diagnosing the pathogen, mainly because the current antibiotic susceptibility testing methods are time consuming. To reduce the turnaround time, this study aims to develop and apply a bacterial cytological profiling (BCP) method that can differentiate antibiotic-sensitive and resistant strains of *Acinetobacter baumannii*, based on the degree of morphological changes after antibiotic treatment. The results showed that the minimal inhibitory concentration (MIC) of ciprofloxacin in *A. baumannii* was 0.5 μg/mL. Five strains of ciprofloxacin-resistant *A. baumannii* with various degree of resistance were isolated by serial passage method and these were used as the test models. Next, fluorescent microscopy was employed to observe the morphological changes of both ciprofloxacin-sensitive and resistant strains of *A. baumannii* following exposure to 1x MIC of ciprofloxacin. From the BCP analysis based on 34 morphological parameters of the bacteria, the result showed that all resistant strains exhibit less morphological changes when compared to their sensitive counterparts upon antibiotic treatment as indicated by the degree of cluster separation via Uniform Manifold Approximation and Projection. Collectively, these results suggest that degree of morphological changes of the bacteria upon antibiotic treatment could be useful for the development of a single-cell and rapid antibiotic susceptibility test in the future.

Introduction:

Nowadays, the antimicrobial resistance (AMR) situation is a major global public threat to human health. According to the report in 2019, around 1.27 million people die annually from AMR infection (1). If appropriate action is not taken, the death toll from AMR will rise to 50 million in 2050 (2). In 2020, the World Health Organization, revealed that only a few antibiotics have been approved in recent years, 82% of which are adaptations of existing antibiotic classes (3). It indicated that the research, development, manufacture, and effective distribution of antibiotics is currently unable to keep up with the rate of emergence of AMR. Conversely, bacteria have evolved several mechanisms to resist against antibiotics, i.e., antibacterial molecule inactivation, modification at the binding site of the target, reduced antibiotic penetration and accumulation (efflux pump), and biofilm formation. In particular, a group of pathogens, abbreviated as ESKAPE, encompassing *Enterococcus faecium, Staphylococcus aureus, Klebsiella pneumoniae, Acinetobacter baumannii, Pseudomonas aeruginosa, and Enterobacter* species were designated as priority status (4), especially *A. baumannii*.

A. baumannii is gram-negative, rod-shaped (coccobacilli) bacterium that is normally found in soil and natural water but also found in hospitals. Thus, it is one of the major organisms causing nosocomial infections such as bloodstream infections, pneumonia, and meningitis (5). Moreover, it is intrinsically resistant to multiple classes of antibiotics (6). At

present, various antibiotics are being used against *A. baumannii* in the clinic including amikacin, cefepime, ciprofloxacin, piperacillin/tazobactam, ampicillin/sulbactam, and imipenem (7). Although several factors can induce resistance, there are two main reasons why *A. baumannii* can become resistant to antibiotics: drug misuse and overuse (8). Drug misuse can occur when the patient has not completed the course of antibiotics. Thus, the concentration of the drug is not sufficient to kill the bacteria causing infection. On the other hand, drug overuse may occur if the doctors prescribe a broad-spectrum antibiotic, i.e., any antibiotic that acts against a wide range of disease-causing bacteria (9) to save the patient's life without waiting for confirmation from the laboratory result. This just-in-case prescription is the result of the long turnaround time of the conventional antibiotic susceptibility testing (AST) methods used in the clinical laboratories; thereby, broad-spectrum antibiotics prescription is preferable.

The general AST methods includes disc diffusion, agar dilution, and the broth microdilution methods (8). These methods are reliable and have been highly standardized. However, the common limitation of these AST methods at present is that they are very time-consuming. For example, in the disc diffusion method, the total turnaround time is around 48 hours at least (10). Many methods have been developed to cut down the turnaround time of the AST by focusing on molecular detection of the known antibiotic resistant genes which can reduce the turnaround time to a few-hour scale. However, the molecular detection method is heavily dependent on prior knowledge of resistant genes responsible for each antibiotic and, hence, limiting its use to only a well-known set of resistant genes. To overcome a forementioned obstacles, various rapid AST methods have been carried out based on the single cell phenotypic-based assays such as Microfluidic system (11), Single Cell Morphological Analysis (SCMA), Magnetic bead biosensor (12), and Bacterial Cytological Profiling (BCP) (13). Among others, BCP, which is a tool that relies on the analysis of bacterial morphological changes upon antibiotic treatment and uses morphological alteration pattern to predict the mechanism of action (MOA) of the antibiotics, is particularly interesting. The advantages of BCP are its simplicity, rapidly identifying targets, thereby overcoming the longstanding time consumption problem, and its ability to be adapted to single-cell phenotypic profiling. Furthermore, BCP can distinguish between antibacterial molecules that affect different cellular pathways as well as different targets within the same pathway, and it does not require growth data such as viable cell counts before screening (13). Moreover, BCP has been used previously in resistance detection in *S. aureus*, where they developed a rapid antimicrobial susceptibility assay of *S. aureus*. They used 71 cytological profiles from treating *S. aureus* with beta-lactam antibiotics such as oxacillin and cephalexin. After that, they used linear discriminant analysis (LDA) to generate a linear classifier. Therefore, they were able to discriminate between methicillin-susceptible and -resistant strains obtained from clinical isolates within 1-2 hours (14).

The aim of this project is to advocate BCP as a next generation AST method, and to demonstrate that morphological differences can be used to discriminate between sensitive and resistant strains of *A. baumannii*, when treating bacteria with antibiotics. We hypothesize that if the bacteria are susceptible to antibiotics, upon treatment, the treated cell will have a different morphology from untreated cells. On the contrary, resistant strains should show no morphological changes based on the assumption that antibiotics do not affect the resistant strains. Here we isolated five ciprofloxacin-resistant *A. baumannii* and showed that resistant strains exhibited less morphological changes when compared to a wild-type strain upon antibiotic treatment as indicated by the degree of cluster separation via Uniform Manifold

Approximation and Projection (UMAP) (15) analysis suggesting its potential in further development of a rapid AST in the future.

Methodology:

MIC determination

The MIC of ciprofloxacin was determined by the microdilution method. First, *A. baumannii* ATCC17978 from frozen stocks was streaked on LB agar plates and incubated overnight until single colonies were obtained. The following day, a single colony was picked and inoculated into 5 mL of LB broth and incubated overnight at 30°C on a roller incubator. The next morning, the overnight culture was diluted in fresh LB media to attain OD_{600} of 0.2-0.4. Meanwhile, a 96-well plate was prepared by aspirating 100 µL of LB broth into each well. Appropriate concentrations of ciprofloxacin were added into the first column of wells, and then 2-fold serial dilution was performed along the rows. After that, the bacteria culture was diluted 1,000-fold into 96-well plate that contained LB media with a suitable concentration of antibiotics. A negative control containing only bacteria culture and a positive control containing only LB broth were prepared for every condition of drug tested. The plate was incubated at 30°C for 24 hours. The MIC was determined by visually observing the lowest concentration of the drug able to inhibit the growth of the bacteria. Moreover, this observation was further confirmed by a microplate reader, by using OD_{600} to measure the density of media in each well and compare with control.

Resistant mutant isolation by serial passage

The overnight culture was diluted 1,000-fold and transferred to a 96-well plate containing one-quarter of the MIC of ciprofloxacin in LB, which was incubated at 30°C until the bacteria grew in the medium. Once the bacteria were growing well, it was sub-cultured in LB media containing higher concentrations of ciprofloxacin and incubated further. The method was repeated until the bacterial grew in media containing up to four times the MIC, and resistance was achieved. Each passage was accompanied by a media-adaption (positive) control containing no antibiotics and a negative control containing only LB to examine the possibility of spontaneous mutations and also to detect any contamination in the process.

Confirmation of resistant strains

After obtaining the resistant strains, the bacteria were first grown on LB agar plates containing four times the MIC of the antibiotic to verify the drug-resistance ability. The colonies from that plate were transferred to Leeds agar plates (16) to confirming that they were *Acinetobacter* species. After confirming both the drug resistance and the species, the MIC of these strains were once again determined as mentioned previously. Furthermore, 16S rRNA sequencing was also carried out to confirm *A. baumannii*. For 16S rRNA sequencing, the bacteria were first grown on LB plates and the DNA was extracted from the bacteria by using the colony PCR. Next, the DNA was amplified by PCR using bacterial universal primers, forward (F) primer BSF8/20 (5'-AGAGTTTGATCCTGGCTCAG-3') and reverse (R) primer REVB (5'-GGTTACCTTGTTACGACTT-3'). The PCR products were purified by a commercial kit following the manufacturer's instructions and lastly, sent for sequencing.

Fluorescence microscope and image analysis

Both the sensitive and the resistant strains of *A. baumannii* were first grown to the early log phase. Ciprofloxacin at the MIC concentration was added and incubated for one hour at 30°C on a roller incubator. After that, the cells were collected by centrifugation at 10,000 rpm and resuspended back in 1/10 of the original volume. *A. baumannii* cells were stained with fluorescence dye, i.e., FM 4-64 (1 µg/mL), DAPI (2 µg/mL), and SYTOX green (0.5 µM). The stained bacteria were loaded to agarose pads (1.2% agarose in 20% LB broth) on concave glass slides. Fluorescence microscopy was performed with consistent imaging parameters throughout all experiments. Targeted number of cells from each condition will be at least 1,000 cells from 3 independent experiment for downstream image analysis. Image analysis was carried out by first subjecting the images to FIJI software followed by CellProfiler 4.0 software and from this, 34 cell morphological parameters were collected based on previous studies (17). These parameters were then used to analyze and plot in a 2-dimensional graph by using UMAP (15).

Results and Discussion:

We first determined MIC of ciprofloxacin against *A. baumannii* ATCC17978 by microdilution method. The result showed that the MIC value of ciprofloxacin is 0.5 µg/mL (Table 1). Once the MIC was obtained, the ciprofloxacin-resistant strains were isolated from *A. baumannii* ATCC17978 by serial passage method, as detailed in the methodology section, using 25% of the MIC as the starting concentration. This resulted in five strains that showed resistant towards ciprofloxacin, with strains RS1056 and RS1058 showing 8 times higher and strains RS1060, RS1061, and RS1064 exhibiting 16 times higher MICs than wildtype strain (Table 1). According to the CLSI standard (18), based on the MIC level, sensitive (≤ 1 µg/mL), intermediate (2 µg/mL), and resistant (≥ 4 µg/mL) (18). All five resistant strains isolate in this study could be categorized as the resistant strain. To prevent any contamination possibility during resistant strain isolation, the identities of the strains were periodically confirmed by Leeds agar plates, which are selective media for *Acinetobacter* species, and followed by the final confirmation via 16S rRNA sequencing that showed 98.8-99.6% identity to *A. baumannii.*

Table 1.

Table showing the MIC of all strains of *A. baumannii* together with CLSI susceptibility indicators.

Strains	MIC (µg/mL)	CLSI standards [a]
ATCC17978	0.5	S
RS1056	4	R
RS1058	4	R
RS1060	8	R
RS1061	8	R
RS1064	8	R

[a] CLSI standards, S = Sensitive, I = Intermediate, and R = Resistant (18)

Since previous studies of BCP used high concentration of antibiotics such as 2 to 5 times the MIC in order to detect the morphological changes of the bacteria (17), we first

tested if the morphological changes of the *A. baumannii* could be detected at 1X MIC concentration of ciprofloxacin or not. Interestingly, we also found that, upon ciprofloxacin treatment at 1X MIC, the cells also elongate, and the DNA condensed in the middle of the cell similar to what was reported at higher concentration in a previous study (Figure 1A-B) suggesting that, at lower concentration, ciprofloxacin also induces morphological changes of the bacteria. Next, to confirm that morphological changes between untreated and treated-cells are distinguishable, we performed single-cell profiling analysis using a previously reported morphological parameters (34 parameters) via UMAP analysis to see the single cell data pattern on a 2-dimentional scatter plot. As expected, the resulting graph (Figure 1C) showed two separated clusters corresponding to the untreated (gray) and ciprofloxacin-treated (red) cells, indicating a clear difference between the two groups. It is worth noting that, the distance between the two clusters is proximal which is possibly due to the use of a previously reported 34 cytological parameters that were not particularly tailored to differentiate untreated from ciprofloxacin-treated cells in this study. Therefore, it is interesting to explore the pipeline development that is specific to each antibiotic in the future. A previous study (19) employed a machine learning algorithm called Support Vector Machine-Recursive Feature Elimination (SVM-RFE) to select the most discriminative features from a high dimensional dataset to increase data interpretation accuracy. Similarly, since BCP dataset is also high dimensional, an appropriate machine learning algorithm could also be applied in the process of feature selection instead of using handpicked features; thus, providing a more descriptive and unbiased morphological features for the analysis of bacterial morphological changes.

Since 1X MIC concentration of ciprofloxacin could induce detectable morphological changes of the sensitive strain of the bacteria, we were next intrigued to see if this pipeline can be applied to the analysis of resistant strains, similar to a previous study done in *S. aureus* (14). We hypothesized that upon treatment with ciprofloxacin, sensitive strains will display a change in morphology while resistant strains would remain unchanged, presenting similar morphologies to those of the untreated cells. The results from fluorescent microscopy showed that the resistant strains RS1056, RS1058 and RS1060 (Figure 2A-C) displayed similar morphologies between untreated and ciprofloxacin-treated cells (Figure 2A-C). In accordance with the observed morphology, image analysis and UMAP plot revealed that the untreated cells (grey dots) and treated cells (red dots) from those of resistant strains formed overlapping clusters (Figure 2A(iii)-C(iii)), further indicating that the morphologies of the ciprofloxacin-treated cells of the resistant strains are indistinguishable from the untreated group.

Slightly difference from the first 3 strains, resistant strains RS1061 and RS1064 exhibited heterogenous morphological changes upon ciprofloxacin treatment. We found that some of the ciprofloxacin-treated cells of these two resistant strains exhibit marginally changes of the morphology that are similar to those of sensitive strains (Figure 2D and E, arrows). These slight changes in observed morphology were also reflected in the UMAP analysis revealing that the clusters between untreated and treated cells are in very close proximity (Figure 2D and E) but do not completely overlap. Even though the two clusters from resistant strains were not completely separated, this finding is slightly contradicting with our hypothesis. We speculate that the 1X MIC concentration of ciprofloxacin used in this study is probably too high, thus still having morphological effect even with resistant strains. Also, a previous study showed that the antibiotic concentration as low as one fourth the MIC of the antibiotic could induce changes of bacterial phenotypic fingerprint (similar to BCP) (20). Therefore, it is important, in the future, to examine the lowest effective dose of

antibiotic that could induce morphological changes of the sensitive bacteria rather than using a constant 1X MIC from a CLSI standard as a cut-off. Having a clear cut-off will benefit the process of defining the decision boundary for classification of sensitive and resistant strains in the future.

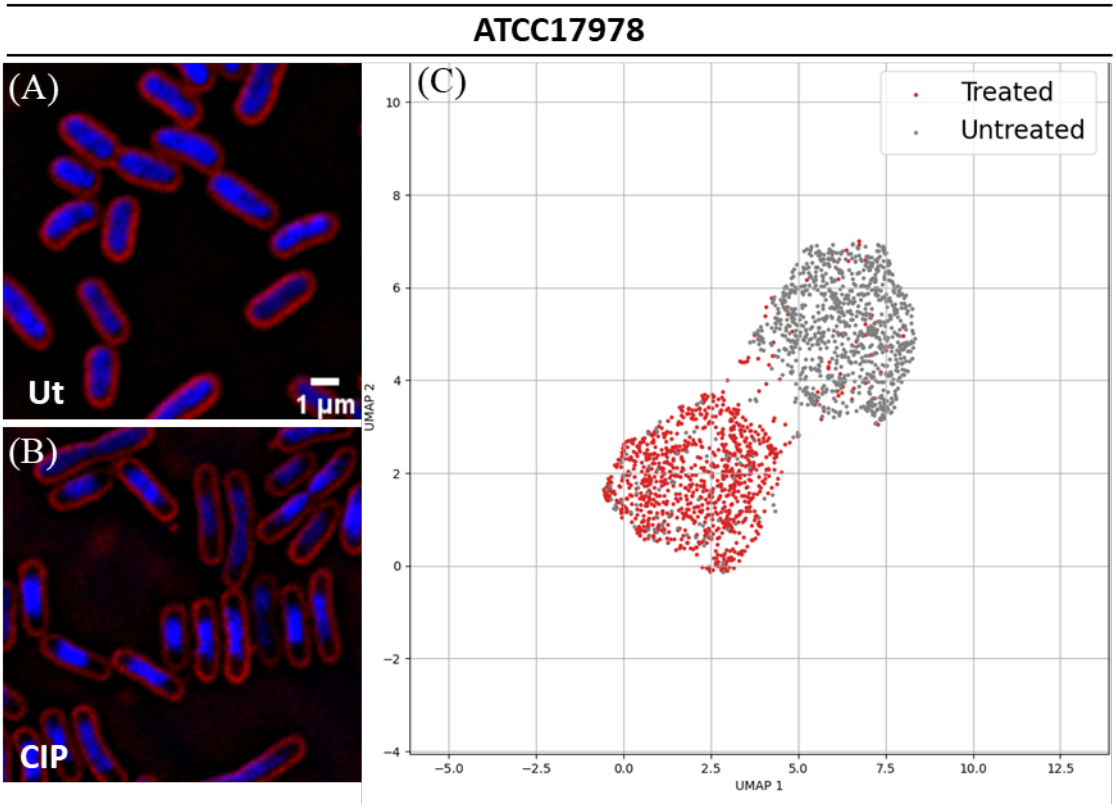

Figure 1.
The morphology observation of *A. baumannii* ATCC17978 untreated, Ut (A) and treated cells with ciprofloxacin, CIP at MIC concentration (B). The cell membranes were stained with FM4-64 (red) while DNA was stained with DAPI (blue) and SYTOX Green (green). SYTOX Green indicates membrane permeability. Scatter plot graph from UMAP analysis (C) between untreated (gray) and treated (red) with ciprofloxacin at MIC concentration (n=1,000).

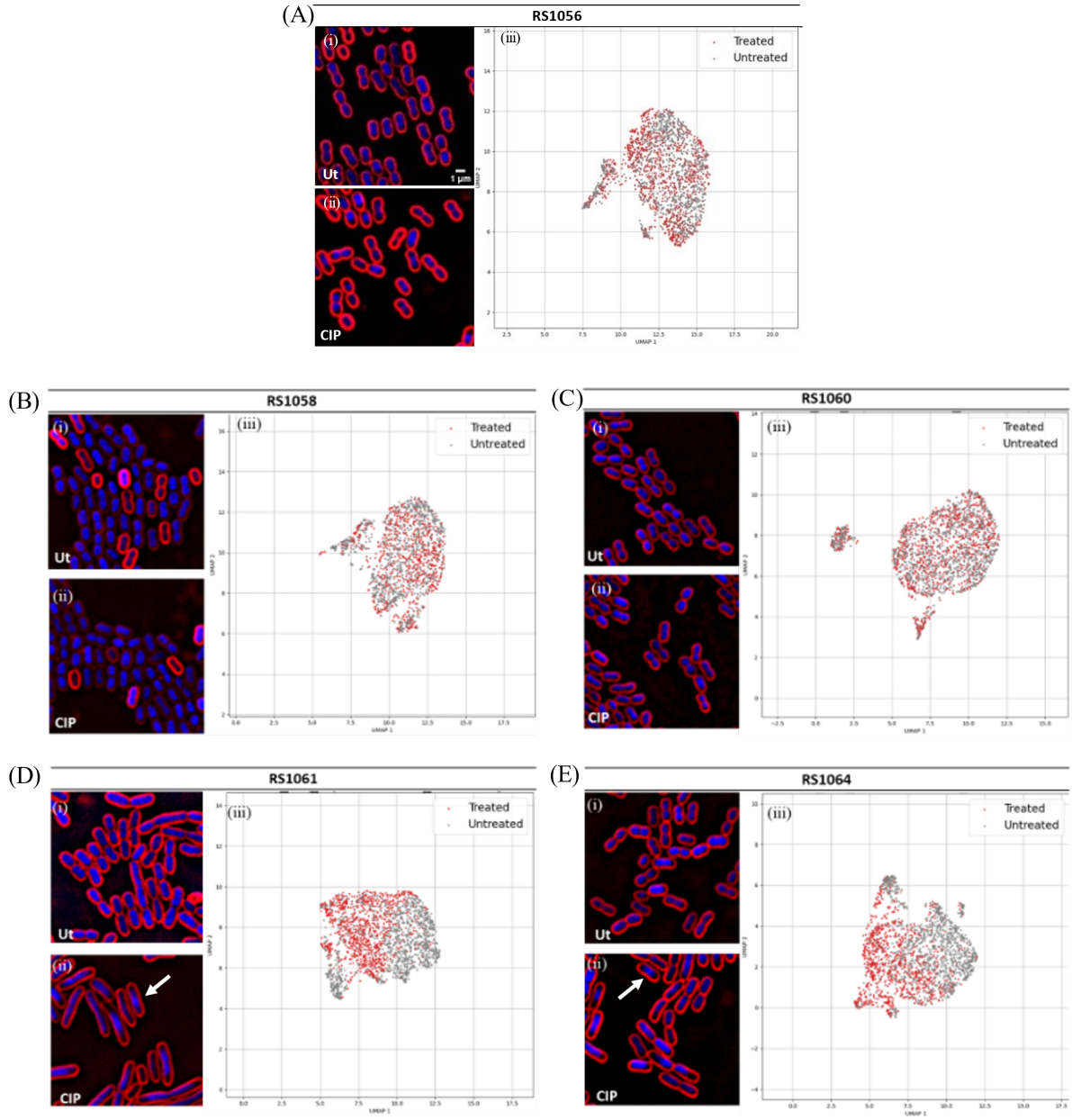

Figure 2.

The morphology observation of *A. baumannii* resistant strains encompassing; RS1056 (A), RS1058 (B), RS1060 (C), RS1061 (D), and RS1064 (E) between untreated, Ut (i) and treated cells with ciprofloxacin, CIP (ii) at MIC concentration. The cell membranes were stained with FM4-64 (red) while DNA was stained with DAPI (blue) and SYTOX Green (green). SYTOX Green indicates membrane permeability. Scatter plot graph from UMAP analysis (iii) between untreated (gray) and treated (red) with ciprofloxacin at MIC concentration (n=1,000).

Conclusion:

In this study, we successfully isolated 5 strains of ciprofloxacin-resistant *A. baumannii* with 8 to 16 times more resistant than the parent strain via serial passage method. We then performed single-cell image analysis showing that, at 1x MIC concentration, ciprofloxacin could induce morphological changes in the sensitive strain, thus separating into two different clusters of profiles (untreated and treated) on 2-dimensional plot of UMAP. Lastly, we showed that ciprofloxacin-resistant strains exhibit no or low degree of morphological changes upon the antibiotic treatment, suggesting that single-cell BCP could differentiate resistant from sensitive strains based on the degree of morphological changes. This finding will be useful in developing a rapid AST based on BCP in the future to reduce the turnaround time of the conventional AST which generally relying upon a time-consuming bacterial population growth analysis. However, to eliminate the limitations mentioned in this study, future work should focus on 1) exploring pipelines that use machine learning to select best-fit morphological parameters for a better analysis and 2) investigating the lowest effective dose of the drug that can induce morphological changes of the bacteria prior to select the concentration cut-off for the analysis.

Acknowledgements:

This research was supported by the Coordinating Center for Thai Government Science and Technology Scholarship Students (CSTS) – the National Science and Technology Development Agency (NSTDA) grant no. JRA-CO-2563-13729-TH. We would like to thank Mahidol University Frontier Research Facility (MU-FRF) for instrumentation support for DeltaVisionTM Ultra and the Advanced Cell Imaging Center, Institute of Molecular Biosciences, Mahidol University for the fluorescent microscopy imaging, operated by Ms Patporn Chankong. RS was partially supported by the scholarship from Molecular Genetics and Genetic Engineering program at Institute of Molecular Biosciences, Mahidol university. RS also thanks Miss Ammararat Makaewkulaseth for relevant laboratory supports.

References:

1. C. J. L. Murray, et al. THE LANCET. 2022;399:629-655.
2. O'neill J. Review on Antimicrobial Resistance;2014.
3. Giuseppee M, Angelina M, et al. Pathogens. 2021;10:1310
4. Oliveira DMPD, Forde BM, et al. Clincal microbiology Reviews. 2020;33:e00181-19.
5. Alrahmany D, Omar AF, et al. Antibiotics. 2021;10:630.
6. Howard A, Donoghue MO. Landes Bioscience. 2012;3:243-250.
7. Budh S, Ilhem B. Antibiotics (Basel). 2021;10:137
8. Chen C, Hong W. antibiotics. 2021;10:311.
9. Fair R J , Tor Y. Perspectives in Medicinal Chemistry. 2014;6:25-64
10. Behera B, G. K. Anil Vishnu et al. Biosensors and Bioelectronics. 2019;142:111552
11. Li H, Torab P, et al. Proceedings of the National Academy of Sciences of the United States of America (PNAS). 2019;116:10270-10279.
12. Choi J, Yoo J, et al. Science Translational Medicine. 2014;6:267ra174.
13. Nonejuie P, Burkart M. Proceedings of the National Academy of Sciences of the United States of America. 2013;110:16169-16174.
14. Quach DT, Sakoulas G. EBioMedicine. 2016;4:95-103.
15. Becht E, Mclnnes L, et al. Nature Biotechnology. 2019;37:38-44.

16. Jawad A, Hawkey PM. Journal of clinical microbiology. 1994;32:2353-2358.
17. Htoo HH, Brumage L et al. Antimicrobial agents and chemotherapy. 2019;63:e02310-18.
18. CLSI. Clinical and laboratory standards institute. 2020;19:46-49.
19. Lin X, Yang F, et al. Journal of Chromatography B. 2012;910:149-155.
20. Zoffmann S, Vercruysse M, et al. Scientific Reports. 2019;9:1:5013.

LEPTIN ENHANCES INFLAMMATORY EFFECT OF INTERLEUKIN-1-BETA IN HUMAN SYNOVIOCYTES VIA NF-KB AND STAT SIGNALING

Atitaya Wayupat,[1,2] Prachaya Kongtawelert, [1,2] Peraphan Pothacharoen,[1,2] Thanyaluck Phitak[1,2,*]
[1]Graduate/M.Sc. Program in Biochemistry, Faculty of Medicine, Chiang Mai University, Chiang Mai
[2]Thailand Excellence Center for Tissue Engineering and Stem Cell. Department of Biochemistry, Faculty of Medicine, Chiang Mai University, Chiang Mai
*e-mail: thanyaluck.phitak@cmu.ac.th

Abstract:
Osteoarthritis (OA) is the inflammation of a whole joint, which is commonly found in elderly and obese patients. While OA is mostly found in load-bearing joints like knee joint, non-load bearing joints such as hand and wrist joints were also affected, especially in obese population. Thus, some factors other than the weight-bearing might be accounting for OA in these joints. Leptin, a cytokine secreted from the adipose tissue and found to be increased in the synovial fluid of obese patients, was reported to link with OA. However, the combined effect of leptin and other inflammatory cytokines on fibroblast-like synoviocytes (FLSs) has not yet studied. The objective of this study is to investigate the effect of leptin alone and combined leptin and the pro-inflammatory cytokine, IL-1β, on inflammation of FLSs. Our study found that leptin induced the expressions of pro-inflammatory cytokines IL-6 and IL-8, both gene and secretory protein levels, in FLSs significantly. Moreover, leptin enhanced the inductive effect of IL-1β on expressions of these cytokines via NF-κB and STAT signaling pathways. From these results, leptin, via enhancing the inflammatory effect of IL-1β, might be participated in the progression of OA in non-loading joints of obese patients.

Introduction:

Osteoarthritis (OA) is one of the most common types of arthritis which involves inflammation of the whole joint resulting in pain, stiffness, and loss of physiological movement. It is a disease with high incidence in elderly and obese people. Major characteristics of OA are articular cartilage breakdown and synovial inflammation, synovitis (1).

Joint is a part of body where two bones are joined and the cavity between two bones is filled with synovial fluid to lubricate the movement without friction. Joint is sealed with synovial membrane or synovium which is composed of several cell types such as fibroblast-like synoviocytes (FLSs), macrophages and white blood cells which are embedded in extracellular matrix (ECM). The synovium maintains the sterile condition of the joint and controls the cellular and molecular transport into the joint (2). Osteoarthritis is mostly found in load-bearing joints such as knee and ankle since excessive weight increases mechanical loading to joint resulting in production of pro-inflammatory cytokines such as IL-1β, IL-6, and IL-8. These cytokines induce FLSs and chondrocytes, the cell type found at the surface of articular cartilage, resulting in inflammation of these cells which promotes further production of pro-inflammatory cytokines. Moreover, these cytokines were reported to induce the expression of degradative enzymes such as a disintegrin and metalloproteinase with thrombospondin motif (ADAMTS) and matrix metalloproteinase (MMP). These enzymes degrade collagen and proteoglycan in ECM leading to OA progression. However, OA has also been found in non-load bearing joints such as hand and wrist of obese people (3, 4). Therefore, excessive joint-loading may not be the sole factor for OA in obese people

Obesity is defined as excessive fat accumulation in white adipose tissue across the body. Adipose tissue is an endocrine organ and is comprised of many cell types but mainly adipocytes which can produce many adipokines (Leptin, adiponectin), cytokines (IL-1β, IL-6, IL-8) and metabolites (4, 5). These molecules can circulate in the blood resulting in low-grade inflammation even under physiological condition (3). Leptin, an adipokine-like hormone, is a small polypeptide (16 kDa) which interacts with its receptor called obese receptor (Ob-Rb) (6). This receptor is highly expressed in hypothalamus, the part of brain which regulates food intake and energy expenditure. Moreover, it has been found in many tissues including joint cartilage and synovium. Previous studies reported that leptin was positively correlated with body mass index (BMI) of obese OA patients (7); and leptin level in synovial fluid and blood of OA patients was higher than that of healthy people and is proportionate with severity of OA (8, 9). Moreover, leptin was reported to activate NF-κB and MAPK pathway resulting in MMP-1, 3, 13 production and enhance the effect of IL-1β that increased the production of catabolic factors, MMP-3, 13 and ADAMTS-4, 5, 9, in human articular cartilage (10-12). However, the effect of combined leptin with IL-1β in synoviocytes has not yet reported. So, this study aimed to investigate and compare the effect of leptin alone and combined leptin with IL-1β in SW982, human synovial cell line.

Methodology:

Cell culture

SW982 cell line was obtained from ATCC (HTB-93) and authenticated by the European Collection of Authenticated Cell Cultures in May 2017. Cells were grown in Leibovitz's L-15 medium (Gibco) containing 10% fetal calf serum (FBS) at 37°C and 5% CO_2.

Cytotoxicity test

MTT, 3-(4,5-Dimethylthiazol-2-yl)-2,5-diphenyltetrazolium bromide, was purchased from invitrogen™ and used to determine cell viability. Cells were grown in 96-well plate overnight before treated with various concentrations of leptin (1-1000 ng/mL) and leptin with IL-1β for 24 h. Conditional media were discarded and MTT at 0.5 mg/mL was added (100 μL/well) and incubated for 4 h. Then, media were removed and DMSO was added (200 μL/well) to dissolve formazan crystal. The absorbance at 540 nm were measured by micro-plate reader and percent of cell viability was calculated using (absorbance of sample/absorbance of control)×100.

mRNA analysis by real time PCR

Cells were cultured in 6-well plate overnight and starved in serum-free media before treated with conditional media for 24 h. Total RNA was extracted using Illustra™ Mini RNA Isolation Kits (GE Healthcare) and converted to cDNA using Tetro cDNA Synthesis kit (Bioline). cDNA was mixed with specific primer of each gene as follows;

GAPDH,	F: 5′-GAA GGT GAA GGT CGG AGT C-3’ and
	R: 5′-GAA GAT GGT GAT GGG ATT TC -3’
IL-6,	F: 5’-GGT ACA TCC TCG ACG GCA TCT-3’ and
	R: 5’-GTG CCT CTT TGC TTT CAC-3’
IL-8,	F: 5’-CTC TCT TGG CAG CCT TCC-3’ and
	R: 5’-CTC AAT CAC TCT CAG TTC TTT G-3’
TNF-α	F: 5’CCCCAGGGACCTCTCTCTAATC3’ and
	R: 5’GGTTTGCTACAACATGGGCTACA3’

Then, master mix was amplified for 45 cycles with 7500 Fast Real time PCR system (Applied Biosystems). Each reaction cycle included denaturation at 95°C, annealing at 60°C and extension at 72°C. The data of each interested gene was normalized with that of housekeeping gene, GAPDH and calculated using $2^{-\Delta\Delta Ct}$ method (13).

Western blot analysis

After cells were cultured in 6-well plate for overnight and starved, various conditional media were added and incubated for 30 minutes. Then, cells were washed with cold-PBS on ice and proteins were extracted by 200 µL of RIPA buffer. Lysate were centrifuged and then supernatant was collected. Protein concentration of each sample was measured using Bradford's assay before loading into 12% SDS-PAGE. After electrophoresis at constant 90 volt for 2 h, protein on gel were transferred to nitrocellulose membrane by semi-dry blotting (BioRad) at constant 200 mA for 1.15 h. Non-specific proteins on membrane were blocked with 5% skim milk for 1 h on a shaker. After that, membrane was washed 4 times using 0.1% Tween-20 in 1XPBS (0.1%T-PBS) and incubated with primary antibody against interested proteins (p65, akt, p38, erk, stat1, stat3 and β-actin) in 1:1000 dilution at 4-8°C overnight. Then, membrane was washed and incubated with secondary antibody (1:1000) (horseradish peroxidase-conjugated goat anti-rabbit IgG) for 1 h at room temperature. Protein bands were detected using SuperSignal ECL Chemiluminescent kit (Thermo Scientific) and exposed in ChemiDoc™ Imagine System (BioRad). Band intensity was measured by ImageJ program.

Measurement of secretory protein of IL-6 and IL-8 by Enzyme-linked immunosorbent assay (14)

Fresh conditional media were collected and centrifuged at 12,000 rpm at 4°C. IL-6 and IL-8 protein levels in supernatant were detected using ELISA MAX™ Deluxe Set Human (BioLegend®), according to the manufacturer's procedure.

Statistical analysis

The results from three independent experiments were analyzed by one-way analysis of variance (15), followed by Dunnett's using GraphPad Prism 9 program. Values are displayed as mean ± standard deviation (SD). $P<0.05$ was accepted as statistically significant.

Results and Discussion:

Effect of leptin and leptin with IL-1β on gene expression of pro-inflammatory cytokines in SW982

Obesity is a major risk factor of OA which is mainly accounted by overloading of weight bearing joints (knee, hip), however, it cannot explain OA in non-weight bearing joint (16). As obesity is regarded as a kind of inflammatory condition, many inflammatory cytokines such as IL-6, IL-1β or TNF-α and adipokines were reported to be increased and cause low-grade inflammation in obese people (17). Leptin, an adipokine-like hormone, is one of them and its level is found to be even higher in synovial fluid than in circulation due to synovium may loss permeability (6, 16, 18, 19). A study using human chondrocytes reported that leptin is positively related to degradation of cartilage and can enhance the carbolic effect of IL-1β, a well-known cytokine that induces OA progression in both *in vivo* and *in vitro* (20). However, information about the effect of leptin and its influence on IL-1β-induced inflammation in synovial cells is still lacking.

In this study, leptin concentrations were chosen from leptin levels found in synovial fluid: physiological concentration (1-10 ng/ml), pathological concentration (10-100 ng/ml) (8, 9) and supra-pathological concentration (500-1000 ng/ml). Human synoviocytes, SW982, was induced with IL-1β at 0.1 ng/mL (20). The effect of various concentrations of leptin and IL-1β, either individual or combined treatment, on cell viability of SW982 was first tested to

ensure the tolerability of the cells. The result showed that leptin up to 1000 ng/mL had no significant cytotoxic effect. Similarly, neither of 0.1 ng/mL IL-1β or leptin combined with IL-1β was toxic to SW982 cells (**Figure 1.**). All these concentrations were used to evaluate the gene expression of pro-inflammatory cytokines.

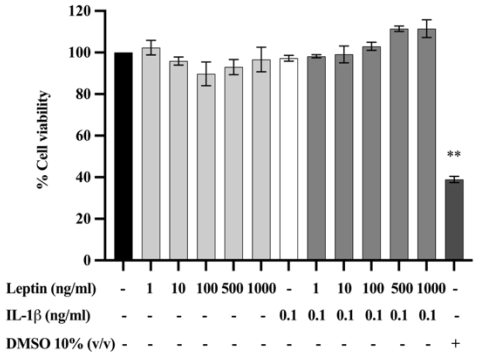

Figure 1. Cell viability measured by MTT assay. SW982 were treated with various concentrations of leptin, IL-1β 0.1 ng/ml or leptin with IL-1β 0.1 ng/ml for 24 h. DMSO (10% v/v) was used as a positive control. n=3. ** $p<0.01$ significant compared with control.

IL-6, IL-8, and TNF-α are pro-inflammatory cytokines commonly used as inflammatory markers and high level of these pro-inflammatory cytokines, especially IL-6 and IL-8, was found in synovial fluid of OA patients (21, 22). IL-1β was shown to upregulate the expression and secretion of these pro-inflammatory cytokines in synoviocytes (23-26). It was reported that leptin increases phosphorylation of c-Jun which binds to AP-1 element within IL-6 promotor thereby increasing IL-6 production (27). Furthermore, leptin can also enhance IL-8 production via increasing phosphorylation of STAT-3 that binds with GAS element which is located within IL-8 promotor (28, 29). Combination effect of leptin and IL-1β on production of these cytokines in FLSs has not been reported yet. Hence, in this study, gene expression levels of IL-6 and IL-8 in SW982 cells were measured by real time PCR and compared between individual cytokine, either leptin or IL-1β, and combined treatment of leptin with IL-1β. The result showed that leptin at physiological, pathological, and supra-pathological (500 ng/ml) concentrations induced IL-6 and IL-8 up-regulation but not statistically significant, whereas leptin at supra-pathological concentration (1000 ng/ml) significantly upregulated the expression of these genes (**Figure 2. A and B**). TNF-α expression was also induced by leptin treatment. however, any statistically significant increase was not found in all three concentrations when compared with control (**Figure 2. C**). These results agreed with previous studies although the significant level was not the same (30).

On the other hand, IL-1β treatment significantly enhanced the expression of all 3 investigated genes, *IL-6*, *IL-8,* and *TNF-α*, in accordance with the results of previous studies (**Figure 2)**.

Regarding to the combined treatment of leptin and IL-1β, leptin in all concentrations, even low concentration like 1 ng/mL, significantly enhanced the inductive effect of IL-1β on IL-6 and IL-8, resulting in much higher IL-6 and IL-8 genes expression than IL-1β treatment (**Figure 2. A and B**). However, this enhanced effect was not seen in case of TNF-α gene expression (**Figure 2. C**).

From this experiment it was suggested that while leptin alone can cause inflammation of FLSs at low level, it enormously enhanced the inflammatory effect of IL-1β, specifically IL-6 and IL-8 up-regulation, once it has IL-1β in system. However, the activation of leptin combined with IL-1β has been not reported and largely unknown in FLSs.

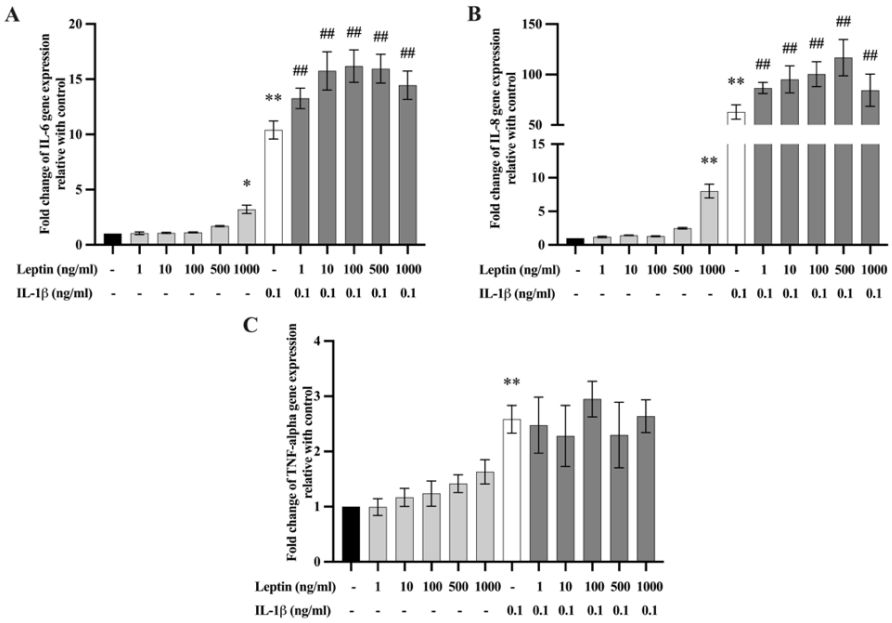

Figure 2. mRNA expression level of (A) *IL-6*, (B) *IL-8* and (C) *TNF-α* measured by real time PCR technique. SW982 were treated with various concentrations of leptin, IL-1β 0.1 ng/ml or leptin with IL-1β 0.1 ng/ml for 24 h. *GAPDH* was used as a control house-keeping gene. Results are displayed as mean±SD. n=3. * $p<0.05$, ** $p<0.01$ significant compared with control. ## $p<0.01$ significant compared with IL-1β treatment.

Effect of leptin and leptin with IL-1β on production of secretory IL-6 and IL-8 proteins in SW982

There are many reports that leptin bind with their receptor (Ob-Rb) on cell membrane and auto-phosphorylate to JAK2 at receptor tail of leptin then, phosphorylation and activation of STAT3 protein. STAT3 protein dimerized and translocated into nucleus to bind with IL-8 promoter, leading to IL-8 production (28, 31, 32).

In the next experiment, level of IL-6 and IL-8 protein secretion in SW982 cells induced by various treatments was detected using ELISA assay to confirm the result of real time PCR.

The result showed that no significant induction of IL-6 and IL-8 by leptin was seen at secretory protein level **(Figure 3.)**

Interestingly, leptin, starting from low or physiological concentration (10 ng/ml), significantly enhanced the IL-1β-mediated upregulation of IL-6 and IL-8 protein secretions, agreeing to the result of gene expression analysis by real time PCR. From these experiments, it can be speculated that leptin, even at physiological concentration, can potentiate the inflammatory effect of IL-1β in synovial cells, thereby, involving in rapid progression of OA in obese people.

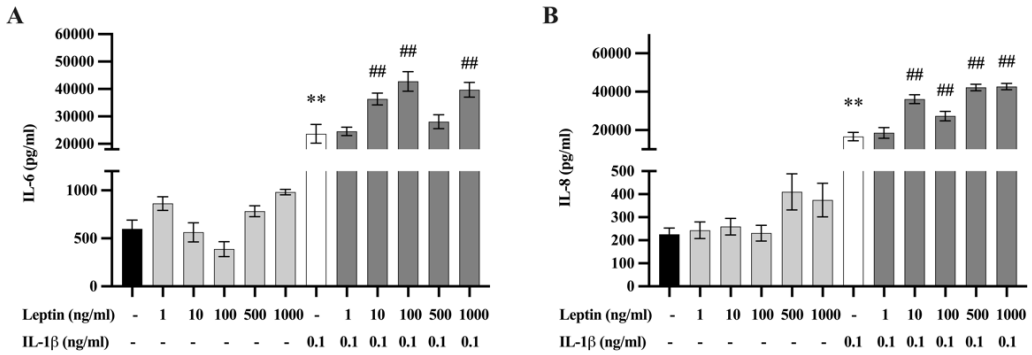

Figure 3. Levels of IL-6 and IL-8 proteins secreted into culture media measured by ELISA assay. After SW982 were treated with various concentrations of leptin, IL-1β 0.1 ng/ml or leptin with IL-1β 0.1 ng/ml for 24 h, culture media was collected and centrifuged. Supernatant was used to detect IL-6 and IL-8 in media by ELISA. Results are displayed as mean±SD. n=2. ** $p<0.01$ significant compared with control. ## $p<0.01$ significant compare with IL-1β treatment.

Effect of leptin and leptin with IL-1β on intracellular-signaling pathways activation in SW982

Leptin receptor (Ob-R) is found in many cell types such as chondrocytes, synovial fibroblasts, and osteoblasts. Binding of leptin with their receptors on cell membrane led to autophosphorylation of JAK2 at receptor tail which was followed by phosphorylation and activation of STAT3 protein. STAT3 proteins were then dimerized and translocated into nucleus influencing the expression of target proteins like inflammatory cytokines. In addition, more pathways were reported to be involved in leptin signaling, such as NF-κB and MAPK pathways (12, 28, 31-33). Therefore, members of NF-κB, MAPK and STAT signaling pathways, p65, p38, ERK, JNK, STAT1 and STAT3, were measured in SW982 cells induced with individual treatments, leptin, IL-1β, or combined leptin and IL-1β. The result of NF-κB pathway showed that while leptin at physiological concentration (1 ng/ml) significantly stimulated p65 phosphorylation compared with control, leptin at pathological (100 ng/ml) and supra-pathological (1000 ng/ml) can significantly enhance the p65 activation mediated by 0.1 ng/mL IL-1β proposing the role of NF-κB pathway in increased production of inflammatory cytokines by combined leptin and IL-1β treatment in previous experiments (**Figure 4 A**).

Among p38, ERK and JNK, intracellular signaling proteins in MAPK pathway, leptin significantly stimulated p38 and JNK compared with control, however, a significant enhancement by the treatment with combination of leptin at physiological (1 ng/ml) and pathological (1000 ng/ml) and IL-1β compared with individual cytokines treatments was seen only in ERK activation (**Figure 4 B-D**).

STAT1 and STAT3 are sub-family of the STAT pathway. The result showed that leptin significantly stimulated STAT1 but did not stimulate STAT3. Interestingly, while combination of leptin and IL-1β significantly stimulated both of STAT1 and STAT3. STAT3 activation only was significantly enhanced by combination treatment when compared with individual treatments on the other hand. These results highlighted the importance of STAT signaling, especially STAT3, for the leptin activity in SW982 synovial cells (**Figure 4 E and 4F**).

According to this whole experiment, it was suggested that p65 of NF-κB and STAT3 of STAT signaling may be responsible for the additive effect shown by leptin on the inflammatory effect of IL-1β in synovial cells, thereby proposing the role of these signaling proteins as a potential therapeutic target to prevent progression of OA in obese population.

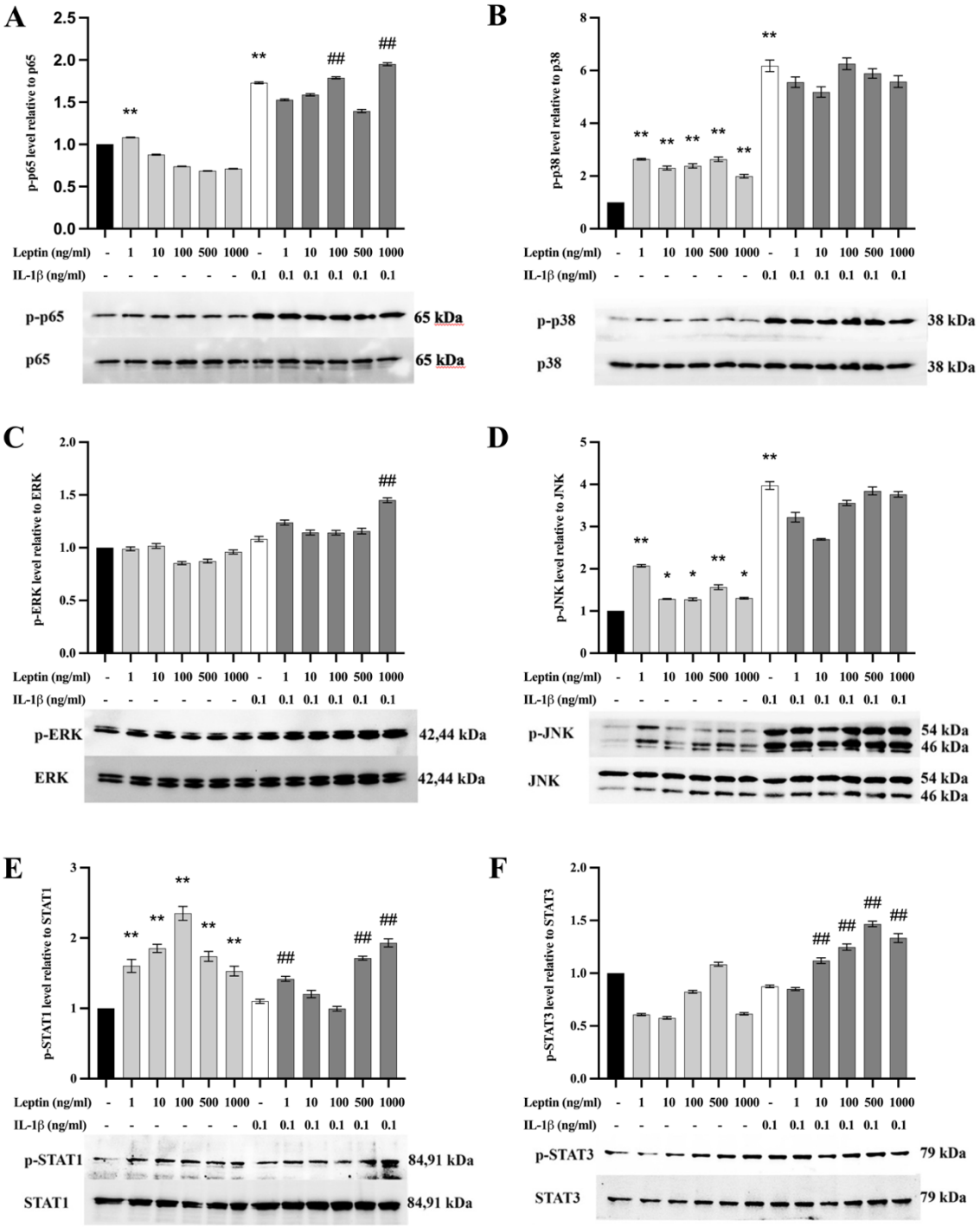

Figure 4. Representative graphs for activation status of intracellular signaling pathways measured by western blotting: (A) p65 (B) p38 (C) ERK (D) JNK (E) STAT1 (F) STAT3. After SW982 were treated with various concentrations of leptin, IL-1β 0.1 ng/ml or leptin with IL-1β 0.1 ng/ml for 15 minutes, cells were collected and target signaling proteins were then detected. Band density of phosphorylated forms were normalized with that of total forms. Results are displayed as mean±SD. n=3. * $p<0.05$, ** $p<0.01$ significant compared with control. ## $p<0.01$ significant compared with IL-1β treatment.

Effect of NF-κB *and JAK inhibitors on expression of pro-inflammatory cytokines: IL-6 and IL-8 induced by leptin and leptin with IL-1β in SW982*

To confirm the main signaling pathway responsible for induction of *IL-6 and IL-8* BAY117062, NF-κB inhibitor, and ruxolitinib, JAK1 and JAK2 inhibitor, were used and their inhibitory effects on gene expression of inflammatory cytokines, *IL-6, and IL-8,* were investigated.

The result showed that BAY117062 significantly inhibited both of IL-1β-induced *IL-6 and IL-8* gene expressions. Moreover, it can significantly reduce the expressions of *IL-6 and IL-8* upregulated by combination treatment as well, whereas JAK inhibitor, Ruxolitinib did not show any reduction in expression of these genes. Hence, it is indicated that p65 might be the main signaling pathway responsible.

Furthermore, combined inhibition with BAY117062 and ruxolitinib significantly inhibited the enhanced effect of leptin and IL-1β on IL-6 and IL-8 expression similarly, however, the level of reduction was not significant compared with single inhibition with BAY117062 (**Figure 5 A, B**). Results from this experiment indicated that p65 might be the main pathway and blocking of NF-κB pathway alone is comparable to inhibition of both NF-κB and STAT pathways, suggesting the potential treatment options for OA in obese people.

For further study, effect of inhibitors on production secretory proteins, *IL-6, and IL-8*, will be determined by ELISA in SW982 induced with leptin and leptin with IL-1β to confirm the current results.

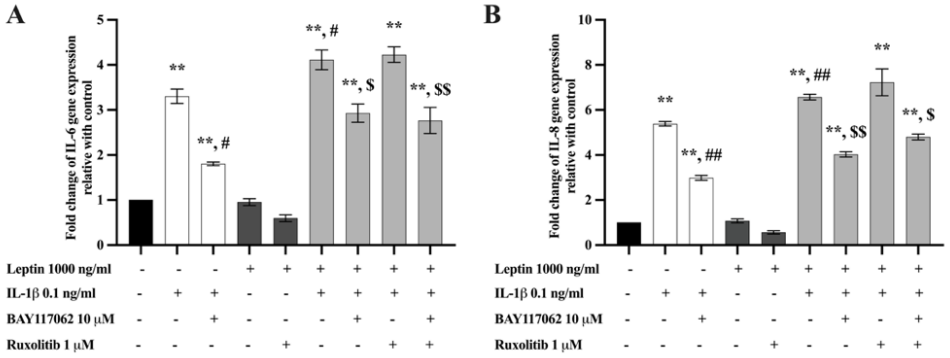

Figure 5. Effect of inhibitors on mRNA expression level of (A) *IL-6* and (B) *IL-8* in SW982. Cells were pre-treated with BAY117062 at 10 μM and ruxolitinib at 1 μM for 2 h before induction with individual cytokines (leptin 1000 ng/ml or IL-1β 0.1 ng/ml) or combined leptin with IL-1β 0.1 ng/ml for 24h. *GAPDH* was used as a control house-keeping gene. Results are displayed as mean±SD. n=3. * $p<0.05$, ** $p<0.01$ significant compared with control. # $p<0.05$, ## $p<0.01$ significant compared with IL-1β treatment. \$<0.05, \$\$<0.01 significant compared with combination of leptin and IL-1β treatment.

Conclusion:

Leptin, an adipokine-like hormone, is high in synovial fluid of obese patients with OA suggesting its potential involvement in pathogenesis of OA, especially in non-weigh bearing joints. This study focused the combination effect of leptin with IL-1β on pro-inflammatory cytokines expression in SW982 human synoviocytes. It was found that leptin even at low physiological concentration can potentiate the inflammatory effect of pro-inflammatory cytokine, IL-1β, significantly and this effect was mediated through NF-κB and STAT pathways while NF-κB might be the major responsible pathway.

Acknowledgements:
This study has been supported by Faculty of Medicine Research Fund, Chiang Mai University, Thailand and Thailand Excellence Center for Tissue Engineering and Stem Cells, Faculty of Medicine, Chiang Mai University.

References:

1. Sacitharan PK. Ageing and Osteoarthritis. Biochemistry and Cell Biology of Ageing. 2019;91:123-59.
2. Kapoor M. Pathogenesis of Osteoarthritis. Osteoarthritis2015. p. 1-28.
3. Thijssen E, van Caam A, van der Kraan PM. Obesity and osteoarthritis, more than just wear and tear: pivotal roles for inflamed adipose tissue and dyslipidaemia in obesity-induced osteoarthritis. Rheumatology. 2015;54(4):588-600.
4. Wang T, He C. Pro-inflammatory cytokines: The link between obesity and osteoarthritis. Cytokine and Growth Factor Reviews. 2018;44:38-50.
5. Aguilar-Valles A, Inoue W, Rummel C, Luheshi GN. Obesity, adipokines and neuroinflammation. Neuropharmacology. 2015;96:124-34.
6. Dumond H, Presle N, Terlain B, Mainard D, Loeuille D, Netter P, et al. Evidence for a key role of leptin in osteoarthritis. Arthritis and Rheumatism. 2003;48(11):3118-29.
7. Vuolteenaho K, Koskinen A, Moilanen T, Moilanen E. Leptin levels are increased and its negative regulators, SOCS-3 and sOb-R are decreased in obese patients with osteoarthritis: a link between obesity and osteoarthritis. Annals of the Rheumatic Diseases. 2012;71(11):1912-3.
8. Yan M, Zhang J, Yang H, Sun Y. The role of leptin in osteoarthritis. Medicine. 2018;97(14(e0257)):1-5.
9. Ku JH, Lee CK, Joo BS, An BM, Choi SH, Wang TH, et al. Correlation of synovial fluid leptin concentrations with the severity of osteoarthritis. Clin Rheumatol. 2009;28(12):1431-5.
10. Phitak T, Boonmaleerat K, Pothacharoen P, Pruksakorn D, Kongtawelert P. Leptin alone and in combination with interleukin-1-beta induced cartilage degradation potentially inhibited by EPA and DHA. Connective Tissue Research. 2018;59(4):316-31.
11. Koskinen A, Vuolteenaho K, Nieminen R, Moilanen T, Moilanen E. Leptin enhances MMP-1, MMP-3 and MMP-13 production in human osteoarthritic cartilage and correlates with MMP-1 and MMP-3 in synovial fluid from OA patients. Clinical and Experimental Rheumatology. 2011;29:57-64.
12. Yaykasli KO, Hatipoglu OF, Yaykasli E, Yildirim K, Kaya E, Ozsahin M, et al. Leptin induces ADAMTS-4, ADAMTS-5, and ADAMTS-9 genes expression by mitogen-activated protein kinases and NF-kB signaling pathways in human chondrocytes. Cell Biology International. 2015;39(1):104-12.
13. Livak KJ, Schmittgen TD. Analysis of relative gene expression data using real-time quantitative PCR and the 2(-Delta Delta C(T)) Method. Methods. 2001;25(4):402-8.
14. Pereira D, Ramos E, Branco a. Osteoarthritis. Acta Medica Port. 2015;28(1):99-106.
15. Swain S, Sarmanova A, Mallen C, Kuo CF, Coupland C, Doherty M, et al. Trends in incidence and prevalence of osteoarthritis in the United Kingdom: findings from the Clinical Practice Research Datalink (CPRD). Osteoarthritis and Cartilage. 2020;28(6):792-801.
16. Presle N, Pottie P, Dumond H, Guillaume C, Lapicque F, Pallu S, et al. Differential distribution of adipokines between serum and synovial fluid in patients with osteoarthritis. Contribution of joint tissues to their articular production. Osteoarthritis Cartilage. 2006;14(7):690-5.

17. Hotamisligil GS. Inflammation and metabolic disorders. Nature. 2006;444(7121):860-7.
18. Yiying Zhang RP, Margherita Maffei, Marisa Barone, Lori Leopold & Jeffrey M. Friedman Positional cloning of the mouse obese gene and its human homologue. Nature. 1994;372:425-32.
19. Tsuchiya H, Fujio K. Emerging role of leptin in joint inflammation and destruction. Immunol Med. 2022;45(1):27-34.
20. Kapoor M, Martel-Pelletier J, Lajeunesse D, Pelletier JP, Fahmi H. Role of proinflammatory cytokines in the pathophysiology of osteoarthritis. Nature Reviews Rheumatology. 2011;7(1):33-42.
21. Tsuchida AI, Beekhuizen M, Hart MCt, Radstake TR, Dhert WJ, Saris DB, et al. Cytokine profiles in the joint depend on pathology, but are different between synovial fluid, cartilage tissue and cultured chondrocytes. Arthritis Research and Therapy. 2014;16(441):1-15.
22. Scanzello CR, Umoh E, Pessler F, Diaz-Torne C, Miles T, Dicarlo E, et al. Local cytokine profiles in knee osteoarthritis: elevated synovial fluid interleukin-15 differentiates early from end-stage disease. Osteoarthritis Cartilage. 2009;17(8):1040-8.
23. Miyazawa K, Mori A, Miyata H, Akahane M, Ajisawa Y, Okudaira H. Regulation of interleukin-1beta-induced interleukin-6 gene expression in human fibroblast-like synoviocytes by p38 mitogen-activated protein kinase. J Biol Chem. 1998;273(38):24832-8.
24. Brescia AC, Simonds MM, Sullivan KE, Rose CD. Secretion of pro-inflammatory cytokines and chemokines and loss of regulatory signals by fibroblast-like synoviocytes in juvenile idiopathic arthritis. Proteomics Clin Appl. 2017;11(5-6).
25. Wang JH, Shih KS, Liou JP, Wu YW, Chang AS, Wang KL, et al. Anti-arthritic effects of magnolol in human interleukin 1beta-stimulated fibroblast-like synoviocytes and in a rat arthritis model. PLoS One. 2012;7(2):e31368.
26. Garcia-Arnandis I, Guillen MI, Gomar F, Pelletier JP, Martel-Pelletier J, Alcaraz MJ. High mobility group box 1 potentiates the pro-inflammatory effects of interleukin-1beta in osteoarthritic synoviocytes. Arthritis Res Ther. 2010;12(4):R165.
27. Yang WH, Liu SC, Tsai CH, Fong YC, Wang SJ, Chang YS, et al. Leptin induces IL-6 expression through OBRl receptor signaling pathway in human synovial fibroblasts. PLoS One. 2013;8(9):e75551.
28. Tong KM, Shieh DC, Chen CP, Tzeng CY, Wang SP, Huang KC, et al. Leptin induces IL-8 expression via leptin receptor, IRS-1, PI3K, Akt cascade and promotion of NF-kappaB/p300 binding in human synovial fibroblasts. Cellular Signalling. 2008;20(8):1478-88.
29. Gharavi NM, Alva JA, Mouillesseaux KP, Lai C, Yeh M, Yeung W, et al. Role of the Jak/STAT pathway in the regulation of interleukin-8 transcription by oxidized phospholipids in vitro and in atherosclerosis in vivo. J Biol Chem. 2007;282(43):31460-8.
30. Khansai M, Phitak T, Klangjorhor J, Udomrak S, Fanhchaksai K, Pothacharoen P, et al. Effects of sesamin on primary human synovial fibroblasts and SW982 cell line induced by tumor necrosis factor-alpha as a synovitis-like model. BMC Complementary and Alternative Medicine. 2017;17(1):532.
31. Sahu A. Intracellular leptin-signaling pathways in hypothalamic neurons: the emerging role of phosphatidylinositol-3 kinase-phosphodiesterase-3B-cAMP pathway. Neuroendocrinology. 2011;93(4):201-10.
32. Kloek C, Haq AK, Dunn SL, Lavery HJ, Banks AS, Myers MG, Jr. Regulation of Jak kinases by intracellular leptin receptor sequences. J Biol Chem. 2002;277(44):41547-55.
33. Xiong H, Li W, Li J, Fang W, Ke J, Li B, et al. Elevated leptin levels in temporomandibular joint osteoarthritis promote proinflammatory cytokine IL-6 expression in synovial fibroblasts. J Oral Pathol Med. 2019;48(3):251-9.

EXTRACTION AND CHARACTERIZATION OF HYDROPHOBINS CLASS I AND CLASS II FROM MUSHROOMS AND MACROFUNGI IN THAILAND

Sirapong Papan, Yaovapa Aramsirirujiwet, Chetsada Pothiratana*

Department of Microbiology, Faculty of Science, Kasetsart University, Bangkok,10900
* e-mail: fscicsd@ku.ac.th

Abstract:
Hydrophobins are small amphipathic proteins found only in mushrooms and filamentous fungi. They are classified into 2 groups: class I and class II based on their hydropathy patterns and solubility. Hydrophobins can reduce water surface tension and reverse the wettability of the coated surface. They play important biological roles throughout fungal life cycle, such as aerial hyphae, fruiting body formation and distribution of hydrophobic spores. Hydrophobins can be applied in current biotechnology such as food innovation and medical technology. The objectives of this study are to extract hydrophobins from *Cookeina sulcipes*, *Xylaria cf. polymorpha*, *Ganoderma lucidum* and *Schizophllum commune* in Thailand and study their emulsifying property. The highest concentration of extracted hydrophobin (class I) was up to 1 mg/ml from mycelia of *S. commune*. Their yields were in the range of 1-9 mg protein/g dried mycelia which were higher than basidiomycete fungi. Putative hydrophobins (class I and class II) were approximately ranging from 10-40 kDa. Extracted hydrophobins acted as potential emulsifiers in 60% ethanol solvent.
Keyword: Hydrophobins, Fungi, Protein extraction

Introduction:

Mushrooms and macrofungi are belonging to Kingdom Fungi, which are mostly found in Phylum Basidiomycota and Ascomycota (Ball et al., 2020). They are common in nature with distinctive characteristics playing a major role as decomposers. Hydrophobins are proteins strictly produced by fungal mycelia. They are amphipathic proteins harboring both hydrophobic and hydrophobic parts. Hydrophobins are a small protein with molecular weights below 20 kDa, and capable of exhibiting a wide range of surface activity due to their amphipathic property. (Ball et al., 2020; Khalesi et al., 2020). Hydrophobin protein contains 8 cysteine residues in conserved positions, which form 4 disulfide bonds to stabilize the whole protein structure. They can be divided into two groups, class I and class II, based on their different properties. Hydrophobin class I has high stability and hardness, which is found in both basidiomycetes and ascomycetes. For hydrophobin class II, it has less robust, single-plane boundary molecular structure, which is restricted only in ascomycetes. Although amino acid sequences of hydrophobins are highly diverse, class II contains more conserved regions than class I (Linder et al., 2005, Ball et al., 2020). For extraction, class I hydrophobin can be extracted using 100% TFA (Trifluoroacetic acid), while class II hydrophobin can be extracted using 60-70% TCA (Trichloroacetic acid). Interestingly, hydrophobin class I exhibits amphipathic property, which is able to assemble into an amphipathic monolayer called “rodlet layer”. They can converse a surface property from hydrophilic to hydrophobic and vice versa (Bary et al., 2012). Hydrophobins were able to stabilize emulsions as effective protein biosurfactants and emulsifiers. The formation of hydrophobins as novel functional ingredients are the key role players within industrially relevant molecules are the low molecular weight emulsifiers and foaming agents, such as mono- and di-glycerides, proteins, especially milk-derived proteins (Pitocchi et al., 2020). Hydrophobins used emulsifiers with other particles such as tri-glyceride for a mechanism for emulsion and foam stabilization. Hydrophobins can interact with different interfaces to reduce the surface tension of water and to modify the hydropathic properties on solid surfaces. These properties make hydrophobins attractive for medical and biotechnological applications (Rocha-Pino et al., 2018). For instance, hydrophobins can be used to disperse hydrophobic materials; to stabilize foam in food products; and to immobilize enzymes, peptides, antibodies, cells, organic molecules on surfaces and to stabilize emulsions as well as CO_2

droplets in liquid–gas systems (Ren et al., 2013). There are several potential biotechnological applications using hydrophobins such as modification of surface wettability, protein immobilization, medical and pharmaceutical uses, and emulsifier in food industry. Microbial biodiversity in Thailand is relatively high and considered as valuable sources for screening of novel peptides or active compounds. The discovery of novel hydrophobinsthat are able to self-assemble from a soluble form into an insoluble and amphipathic monolayer at hydrophilic: hydrophobic interfaces. hydrophobins are very stable against external stress, like thermal heating. these unique structural features hydrophobins can be considered as rigid bio-surfactants. (Ren et al., 2913; Bary et al., 2012; Lugones et al, 2004). Hydrophobins are able to stabilize emulsions by forming a time-dependent, after adsorbing at the oil-water interface. This is also a strong confirmation of hydrophobin property between the hydrophobin-covered oil droplets in an emulsion. Hydrophobins were a huge interest in using natural emulsifiers and surfactants considered with amphipathic properties (Reger et al. 2011) that distinctive properties are expected. Therefore, this study aims to extract hydrophobin class I and II from diverse mushrooms and macrofungi in Thailand were examined for their properties in regard to emulsification.

Methodology:

1. Fungal strains and culture medium

Fungal strains used were *Cookeina sulcipes*, *Xylaria cf. polymorpha*, *Ganoderma lucidum* and *Schizophllum commune.* Potato dextrose broth (PDB) was used as a culture medium.

2. Hydrophobins extraction

Hydrophobins were extracted using modified methods as previously described (Lugones et al., 1996). Fungal mycelia were cultivated in PDB and incubated statically at room temperature (25 ± 2^{o}C). The mycelial mats were harvested using Whatman No.1 filter paper. The mycelia were frozen with liquid nitrogen and grounded with mortar. The samples were collected in 50 mL centrifuge tubes and stored at -80 °C for 24 h. For class I hydrophobin, mycelia were treated with hot sodium dodecyl sulfate buffer (SDS buffer) and further performed lyophilization. Class I hydrophobin was extracted using trifluoroacetic acid (TFA). After TFA evaporation using stream of nitrogen gas, the remaining hydrophobin pellet was then dissolved in 60% (v/v) ethanol. Crude class I hydrophobin was stored at 4^{o}C. Class II hydrophobin was extracted by lyophilization prior to extraction with 20% trichloroacetic acid (TCA). After sonication at 5.5 Hz. for 2 h, the extraction was centrifuged at 9100 g and filtrated. Crude Class II hydrophobin solution was stored at 4^{o}C.

3. Qualitative and quantitative analysis of crude hydrophobin extracts

The protein concentration of hydrophobin extracts were determined using Bradford Assay (Bradford, 1976). Extracted proteins were separated using 16.5% Tricine-Soduim Dodecyl Sulfate-Polyacrylamide gel electrophoresis (Tricine-SDS-PAGE). Proteins were loaded at concentrations of 30 µg/lane. Gel was then stained with Coomassie Brilliant Blue R250 for 20 min and destained until obtaining a clear background.

4. Determination of stability of oil in water emulsion

Hydrophobin extracts in 60 % ethanol at a concentration of 50 and 100 µg/ml with a volume of 500 µl were mixed with 1500 µl of olive oil. After mix for 2 minutes, samples were stood for 24 h Mixture of 1% SDS with deionized water and 60% ethanol were used as positive controls. Deionized water and 60% ethanol were used as negative controls. The extent of emulsion after 24 h (%E24) was calculated in accordance with the following equation (Masakorala et al., 2013);

$$\%E24 = \frac{\text{Height of emulsion layer (cm}}{\text{Height of whole solution (cm)}} \times 100$$

Results and Discussion:

Qualitative and quantitative analysis of crude hydrophobin extracts

Protein concentration of hydrophobin extracted from *C. sulcipes* (Class I), *C. sulcipes* (Class II), *X. cf. polymorpha* (Class I), *X. cf. polymorpha* (Class II), *G. lucidum* and *S. commune* were 85.6±6.2, 79.2±9.0, 115.5±13.2, 102.5±11.1, 600.0±7.5, and 1052.7±12.1µg/ml, respectively. Yield of extracted hydrophobin from *G. lucidum* and *S. commune* were 9 µg protein/g dried mycelia. A lower yield at 1.4-1.5 µg protein/g dried mycelia weight was obtained from hydrophobin extracted from *X. cf. polymorpha* and *C. sulcipes* (Table1).

From Tricine-SDS PAGE, it was observed that hydrophobin extracts (Class I) from *G. lucidum* showed 2 main protein bands (Figure 1, Lane2) at 19.3 and 20.0 kDa. *X.cf. polymorpha* (Figure 1, Lane 3) and *C. sulcipes* (Figure 1, Lane 4) showed unclear putative hydrophobin band possibly that class I hydrophobin extraction used in this study was based on Basidiomycota, which may not be suitable for Ascomycota. *S. commune* hydrophobin extract showed multiple bands (Figure 1, Lane5) ranging from 12.0-20.2 kDa. Hydrophobin extracts (Class II) from *X. cf. polymorpha* (Figure 1, Lane 6,7) showed 2 main bands approximately at 14.5 and 19 kDa while that from *C. sulcipes* (Figure 1, Lane8,9) showed a dominant protein band approximately at 7.8 kDa (Figure 1). *C. sulcipes* and *X. cf. polymorpha* were belonging to Ascomycota and *G. lucidum*, and *S. commune* was belonging to Basidiomycota. This result suggested that we extracted putative class I hydrophobin from all 2 species: *G. lucidum* and *S. commune* and class II hydrophobins was extracted from *C. sulcipes* and *X. cf. polymorpha* but the extraction of putative class I hydrophobin of *C. sulcipes* and *X. cf. polymorph* were unclear result. However, hydrophobin class I from *C. sulcipes* and *X. cf. polymorpha* should be extracted using specific methods for Ascomycota fungi. According to the results of the *S. commune* experiment, consistent with the report of Lugones et al, 1999, the SDS-PAGE was able to demonstrate the multiple hydrophobin bands of *S. commune.* Hydrophobin in *S. commune* SC4 was found in four iso-forms, having sizes of 8.32, 8.39, 8.4, and 8.7 kDa. The reporting by Lugones et al, 2004 studying the expression of SC3 and SC15 of *S. commune* showed multiple bands of hydrophobin sizes at 15-24 kDa. These reports are consistent with our results for multiple bands of hydrophobin sizes.

Table 1 Protein concentration and yield of hydrophobin extracts

Mushrooms	Hydrophobin class	Protein concentration (μg/ml) (Mean ± SD)	Yield (mg protein/ g dried mycelia)
Schizophllum commune	Class I	1052.7±12.1	9.35
Ganoderma lucidum	Class I	600.0±7.5	9.60
Xylaria cf. polymorpha	Class I	115.5±13.2	1.54
	Class II	102.5±11.1	1.54
Cookeina sulcipes	Class I	85.5±6.2	1.44
	Class II	79.2±9.0	1.44

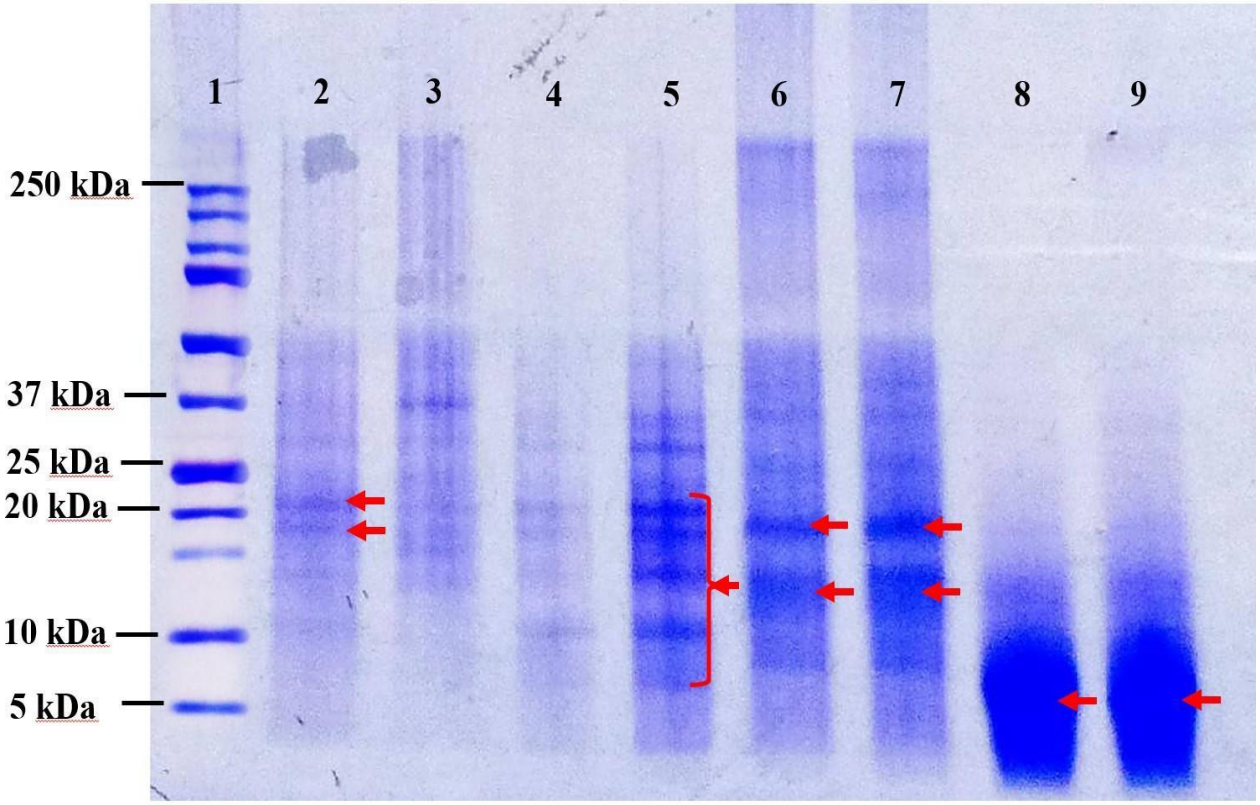

Figure 1. Tricine-SDS-PAGE of extracted hydrophobin from different fungal strains. Lane 1: Protein ladder (2 -250 kDa); Lane2: Crude hydrophobin class I extracts from *G. lucidum* arrow indicated 2 main protein bands at 19.3 and 20.0 kDa; Lane3: Crude hydrophobin class I extracts from *Xylaria cf. polymorpha* ; Lane4: Crude hydrophobin class I extracts from *C. sulcipes*; Lane5: Crude hydrophobin class I extracts from *S. commune* arrow indicated multiple bands ranging from 12.0-20.2 kDa; Lane 6-7: Crude hydrophobin class II extracts from *Xylaria cf. polymorpha* arrow indicated 2 main protein bands approximately at 14.5 and 19 kDa; Lane 8-9: Crude hydrophobin class II extracts from *C. sulcipes* arrow indicated main protein bands approximately at 7.8 kDa.

Determination of stability of oil in water emulsion

Putative hydrophobin class I and class II extracts at the concentrations of 50 and 100µg/ml dissolved in 60% ethanol showed emulsifying property when tested with olive oil. The results revealed that all class I and II hydrophobin extracts exhibited %E24 values ranging from 70-90%. For class II hydrophobin, the extracted protein only at 50 µg/ml was tested due to low amounts of samples. Interestingly, hydrophobin extracts from the *S. commune* exhibited the highest %E24 values at 90%. For control, mixture of 1% SDS with deionized water showed %E24 values of 100%. The %E24 value of hydrophobin extracts was compared between negative control and positive control. These results indicated %E24 value of hydrophobin extracts exhibited the values higher than those of negative control and positive control (Table 2). However, there was no difference between %E24 values (about 50%) of 1% SDS in 60% ethanol and 60% ethanol alone, suggesting that 1%SDS could not well function as emulsifier in 60% ethanol. (Figure 2, (B,D)). The results revealed that all class I and II hydrophobin extracts exhibited %E24 values, not different between concentrations 50 and 100µg/ml. Therefore, hydrophobins could be potential emulsifiers in 60% ethanol solvent. The %E24 values of hydrophobin extracts were displayed in Table 2. As reported by Pothiratana et al., 2020, the emulsifier capabilities of hydrophobin between aerial mycelia and culture media concentrations of approximately 120 µg/mL from *Agrocybe cylindracea* were determined based on %E24, showing %E24 values at 6.6% and 25% respectively. The previous study by Rocha-Pino et al., 2018 showed %E24 values of the class I hydrophobin from *Lecanicillium lecanii* was at 95%. The study of Alamprese et al., 2022 showed %E24 values of Class II hydrophobin based food ingredient from *Trichoderma reesei* at concentrations of 0.1, 0.25, and 0.5 g/100 mL were 70%, 80%, and 81%, respectively. These results supported that hydrophobins can be used as a protein emulsifier, which can be applied in many biotechnological fields.

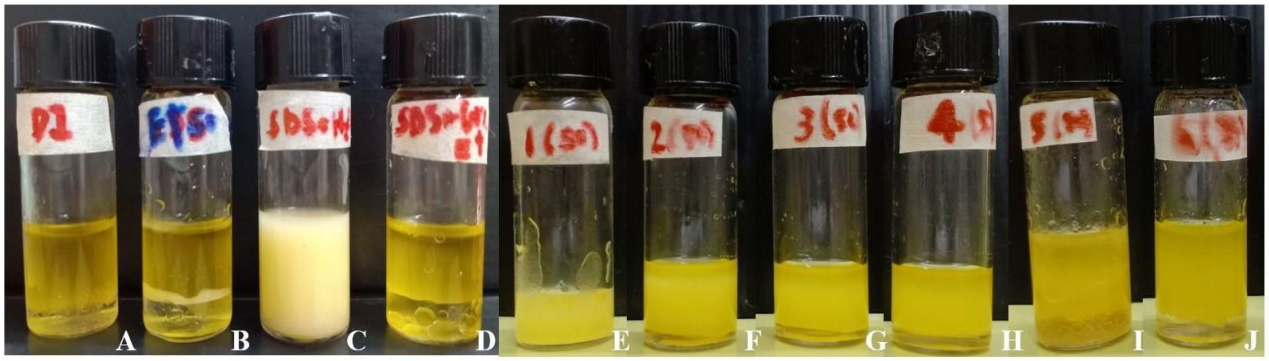

Figure 2. Emulsion layer from a mixture of olive oil with (A) distillation water (DI), (B) 60% ethanol, (C) 1%(w/v) SDS with DI, (D) 1%SDS (w/v) with 60% ethanol. Crude hydrophobin extracts (50 µg/ml) from (E) *G. lucidum* (class I), (F) *X. cf. polymorpha* (class I), (G) *C. sulcipes* (class I), (H) *S. commune* (class I), (I) *X. cf. polymorpha* (class II) and (J) *C. sulcipes* (class II) after 24 h of incubation at room temperature.

Conclusion:

Class I hydrophobins can extract from *G. lucidum* and *S. commune* and class II hydrophobins from *G. lucidum*, and *S. commune* were extracted in this study. Class I hydrophobins extracts from *G. lucidum* and *S. commune* had higher concentration and yield than those of *X. cf. polymorpha,C. sulcipes.* Multiple proteins bands of putative hydrophobin ranging from 10-20 kDa were observed. In *C. sulcipes*, there was one dominant band at 7.8 kDa of class II hydrophobin. All hydrophobin extracts showed promising emulsifying properties in 60% ethanol solvent. Potentially, hydrophobin could be applied as an emulsifier in biotechnology. In the next study, the protein purification and application of the extracted hydrophobins such as surface coating will be performed.

Table 2 Emulsification index (%E24) of hydrophobin extract

Test	Sample	Hydrophobin concentration (μg/ml)	%E24
Negative control	Deionized water (DI)	-	0.0
	60% ethanol	-	48.7
Positive control	1% SDS in DI	-	100.0
	1% SDS in 60% ethanol	-	52.8
Hydrophobin class I	*G. lucidum*	50	87.5
		100	90.0
	X. cf. polymorpha	50	75.0
		100	80.0
	C. sulcipes	50	72.7
		100	72.7
	S. commune	50	90.9
		100	91.7
Hydrophobin class II	*X. cf. polymorpha*	50	79.5
	C. sulcipes	50	78.2

Acknowledgements:

We would like to thank Development and Promotion of Science and Technology Talents Project, Thai government scholarship (DPST scholarship) for research opportunity and financial support.

References:

Alamprese, C., Rollini, M., Musatti, A., Ferranti, P., & Barbiroli, A. (2022). Emulsifying and foaming properties of a hydrophobin-based food ingredient from Trichoderma reesei: A phenomenological comparative study. *LWT, 157*, 113060. doi:https://doi.org/10.1016/j.lwt.2021.113060

Bayry, J., Aimanianda, V., Guijarro, J. I., Sunde, M., & Latgé, J.-P. (2012). Hydrophobins—Unique Fungal Proteins. *PLOS Pathogens, 8*(5), e1002700. doi:10.1371/journal.ppat.1002700

Blesic, M., Dichiarante, V., Milani, R., Linder, M., & Metrangolo, P. (2018). Evaluating the potential of natural surfactants in the petroleum industry: the case of hydrophobins. *Pure and Applied Chemistry, 90*(2), 305-314. doi:doi:10.1515/pac-2017-0703

Bradford, M. M. (1976). A rapid and sensitive method for the quantitation of microgram quantities of protein utilizing the principle of protein-dye binding. *Analytical Biochemistry, 72*(1), 248-254. doi:https://doi.org/10.1016/0003-2697(76)90527-3

De Vries, O. M., Moore, S., Arntz, C., Wessels, J. G., & Tudzynski, P. (1999). Identification and characterization of a tri-partite hydrophobin from Claviceps fusiformis. A novel type of class II hydrophobin. *Eur J Biochem, 262*(2), 377-385. doi:10.1046/j.1432-1327.1999.00387.x

Khalesi, M., Mamashli, F., Goliaei, B., Moosavi-Movahedi, A. A., & Derdelinckx, G. (2020). Class II Hydrophobin HFBII: A Potential Carrier for Antitumor Agents. *Current Bioactive Compounds, 16*(1), 80-84. doi:10.2174/1573407214666180420092631

Linder, M. B., Szilvay, G. R., Nakari-Setala, T., & Penttila, M. E. (2005). Hydrophobins: the protein-amphiphiles of filamentous fungi. *FEMS Microbiol Rev, 29*(5), 877-896. doi:10.1016/j.femsre.2005.01.004

Lugones, L. G., Bosscher, J. S., Scholtmeyer, K., de Vries, O. M. H., & Wessels, J. G. H. (1996). An abundant hydrophobin (ABH1) forms hydrophobic rodlet layers in Agaricus bisporus fruiting bodies. *Microbiology (Reading), 142 (Pt 5)*, 1321-1329. doi:10.1099/13500872-142-5-1321

Lugones, L. G., de Jong, J. F., de Vries, O. M., Jalving, R., Dijksterhuis, J., & Wösten, H. A. (2004). The SC15 protein of Schizophyllum commune mediates formation of aerial hyphae and attachment in the absence of the SC3 hydrophobin. *Mol Microbiol, 53*(2), 707-716. doi:10.1111/j.1365-2958.2004.04187.x

Lugones, L. G., Wös, H. A. B., & Wessels, J. G. H. (1998). A hydrophobin (ABH3) specifically secreted by vegetatively growing hyphae of Agaricus bisporus (common white button mushroom). *144*(8), 2345-2353. doi:https://doi.org/10.1099/00221287-144-8-2345

Pitocchi, R., Cicatiello, P., Birolo, L., Piscitelli, A., Bovio, E., Varese, G. C., & Giardina, P. (2020). Cerato-Platanins from Marine Fungi as Effective Protein Biosurfactants and Bioemulsifiers. *Int J Mol Sci, 21*(8). doi:10.3390/ijms21082913

Pothiratana, C., Fuangsawat, W., Jintapattanakit, A., Teerapatsakul, C., & Thachepan, S. (2020). Putative hydrophobins of black poplar mushroom (Agrocybe cylindracea). *Mycology, 12*(1), 58-67. doi:10.1080/21501203.2020.1804474

Reger, M., Sekine, T., Okamoto, T., Watanabe, K., & Hoffmann, H. (2011). Pickering emulsions stabilized by novel clay–hydrophobin synergism. *Soft Matter, 7*, 11021-11030. doi:10.1039/C1SM06525D

Ren, Q., Kwan, A. H., & Sunde, M. (2013). Two forms and two faces, multiple states and multiple uses: Properties and applications of the self-assembling fungal hydrophobins. *Peptide Science, 100*(6), 601-612. doi:https://doi.org/10.1002/bip.22259

Rocha-Pino, Z., Ramos-López, J. I., Gimeno, M., Barragán-Aroche, F., Durán-Valencia, C., López-Ramírez, S., & Shirai, K. (2018). Enhanced oil recovery by hydrophobins from Lecanicillium lecanii. *Fuel, 224*, 10-16. doi:10.1016/j.fuel.2018.03.058

Schägger, H., & von Jagow, G. (1987). Tricine-sodium dodecyl sulfate-polyacrylamide gel electrophoresis for the separation of proteins in the range from 1 to 100 kDa. *Anal Biochem, 166*(2), 368-379. doi:10.1016/0003-2697(87)90587-2

Wösten, H. A. B. (2001). Hydrophobins: Multipurpose Proteins. *Annual Review of Microbiology, 55*(1), 625-646. doi:10.1146/annurev.micro.55.1.625

EXPRESSION, PURIFICATION AND CHARACTERIZATION OF QUINONE REDUCTASE FROM *Leishmania orientalis*

Theerapat Tangsupatawat,[1] Panu Pimviriyakul,[1] Yuvarun Kapaothong[1]
Affiliation of Theerapat Tangsupatawat
Department of Biochemistry, Faculty of Science,Kasetsart university in Thailand
Affiliation of Panu Pimviriyakul
Department of Biochemistry, Faculty of Science,Kasetsart university in Thailand
Affiliation of Yuvarun Kapaothong
Department of Biochemistry, Faculty of Science,Kasetsart university in Thailand
e-mail: Theerapat.ta@ku.th

Abstract:

Leishmaniasis disease is caused by the infection of *Leishmania* parasites that are transmitted through the bites of infected sandflies, especially in tropical and subtropical landscapes. Quinone reductase which is an oxidoreductase that functions as free radicals scavenger in the cell via quinone substrate reduction is one attractive target for Leishmaniasis treatment. In the research project, the overexpression, purification and characterization of quinone reductase from *Leishmania orientalis* (QR) were investigated. QR was overexpressed from QR-pET-28a plasmid that was co-transformed pG-KJE8 chaperone plasmid into *E. coli* BL21 (DE3) under auto-induction approach at 16ºC. QR was purified by DEAE-Sepharose anion-exchange column chromatography yields pure QR with subunit molecular weight 34.72 kDa in size. The kinetic experiment of QR was monitored by measuring the reduction of NAD(P)H at a wavelength of 340 nm over time. The experimental results showed the QR is flavin-dependent enzyme which can use both flavin mononucleotide (FMN) and flavin adenine dinucleotide (FAD) as cofactors where FMN give the higher enzyme activity. Consider to the kinetic variables such as K_m, k_{cat} and k_{cat}/K_m, NADH is better electron donor than NADPH, while menadione is the best electron acceptor comparing to nitrofurazone and 1,4-benzoquinone. The information obtained from this research, could be further studied in-depth to develop the QR as a drug target for the treatment of Leishmaniasis in the future.

Introduction:

Leishmania, phylum Sarcomastigophora, is a haemoflagellate blood protozoan that causes Leishmaniasis through infected by sandflies. There are two types of symptoms that people experience when infected skin and visceral leishmaniasis. By the occurrence of the skin lesions will look like pitted wounds. The blister is smooth or hard plated. And leishmaniasis can cause a disease of the mucous membrane of the skin with redness and lesions in the nasopharynx. Later, inflammation of the nasal septum appears, in some cases obstruction of the pharynx and larynx may occur. and in the part of the internal organs There will be symptoms that are common, including a fever that goes up and down. Over a long period of time, weight loss, decreased appetite, anemia, and an enlarged stomach from an enlarged spleen and liver. thrombocytopenia and low white blood cell At present, *Leishmania* spp. has been discovered in Thailand, namely *Leishmania orientalis*, formerly known as *Leishmania siamensis*. *Leishmania* is classified as an emerging disease in Thailand

because its genetic material is different from Leishmania. In other countries that have been reported before In this experiment, the quinone reductase of *Leishmania orientalis* (QR)was used to characterize the enzyme. QR is a member of the dehydrogenase/reductase family and it is used in kinetics studies because quinone reductase acts in the elimination of free radicals in cells. It catalyzes the reduction reaction of quinone to a stable hydroquinone compound replacing semiquinone, which can produce reactive oxygen species (ROS), which are cytotoxic.

Methodology:

Expression–Initially, the coding regions of quinone reductase gene from *Leishmania orientalis* was cloned into pET-28a expression vector (QR-pET-28a), then mixed with Competent Cell (*E. coli* BL21 (DE3)) and frozen in ice 30 min. and heat shock at 42ºC for 90 s., then rest in ice for 5 min for plasmid to enter the cells and then cultured in LB Broth, incubated at 37ºC for 1 hr., after that, The organisms were dispersed in a petri dish containing LB Agar medium to which a final concentration of 25 µg/ml of the antibiotic Kanamycin was added to every plate to screen for plasmid-containing cells and then incubated at 37ºC overnight. One colony from overnight incubation at 37ºC was selected and cultured in LB broth (IPTG induction) and ZY media (Auto-induction) with the addition of kanamycin (25 µg/ml) antibiotic. Incubated at 37ºC overnight as a starter of both LB media and ZYM Starter media. After IPTG induction, 1% v/v inoculum pipette was added to LB broth with the addition of 25 µg/ml of Kanamycin. 3 vials were incubated at 37ºC for 2.5 hr. The absorbance was measured at a wavelength of 600 nm to equal 1. IPTG 1 mM was added to all 3 vials and incubated at different temperatures. The difference is at 16ºC, 25ºC and 37ºC overnight for Auto-induction. The 1% v/v inoculum pipette was added to 3 vials of ZYP-5052 rich media and incubated at 37ºC for 2.5 h. The absorbance was measured at a wavelength of 600 nm to be 1. Incubated at different temperatures of 16ºC, 25ºC and 37ºC overnight. All 6 vials (LB&ZY media) were centrifuged at 5,000 rpm for 15 min at 4ºC and discarded the top water for storage. Cell sludge, then 50 mM Tris-HCl pH7 was added and the cell was dissociated by ultrasonic vibration at 30% amplitude for 2 min, by turn on 7 s. and turn off 10 s., from Pipette 1 ml in each of the 6 vials was centrifuged at 15,000 rpm at 4ºC for 1 hr., then clear and sludge were separated. Both parts were then taken for a Bradford assay using BSA as the standard protein. To calculate the amount of protein used in gel electrophoresis. To analyze the quinone reductase enzyme from molecular weight, the optimal condition for the expression of quinone reductase was carried out. After that, plasmids for five Chaperone species were added to see if each Chaperone was tested. Enhanced expression of quinone reductase and incubated in appropriate condition.

Purification–Subsequently, the supernatant obtained from ultrasonic vibration was precipitated by added polyethyleneimine (PEI) 0.1% W/V with ice around the beaker to prevent enzymatic deterioration, then magnetized swirls to disperse the PEI across the beaker for 15 min and centrifuged at 15,000 rpm for 30 min at 4ºC and then store the supernatant for enzymatic purification. The enzyme was purified by Nickel Affinity Column Chromatography, since the N terminal end of the quinone reductase contained PolyHis-tag.

The obtained supernatant was placed in columns and washed with wash buffer (50 mM Tris + 300 mM NaCl + 20 mM Imidazole) pH7.5, 1 column volume, followed by Elution Buffer (50 mM Tris + 300 mM NaCl + volume). Imidazole concentration 50-350 mM). We will collect the extracted substance from wash buffer to Elution Buffer with 350 mM Imidazole concentration. Then select the substance in each part to dilute 5 times and run the gel to We looked at the quinone reductase enzyme in which the concentration of Imidazole was released, and the result was that the quinone reductase was released during the wash buffer, thus changing the method of purifying the enzyme. Quinone reductase with

DEAE-Sepharose Chromatography due to the overall charge of quinone reductase was negatively charged at pH7.5. Transparency obtained from nucleic precipitation with PEI was dialysis by placing the transparencies in cellophane bags and then immersing them in 50 mM Tris pH7.5. overnight refrigerator It was then centrifuged at 15,000 rpm for 30 min at 4ºC and the clear fraction was used for enzymatic purification. where 1 ml of the transparent part was sucked and the transparent part was loaded into the column Then wash with Wash Buffer 50 mM Tris pH7.5 2 column volume, followed by Elution Buffer (50 mM Tris + NaCl concentration 50-350 mM) pH7.5 2 column volume each. Wash buffer to last elution buffer (50 mM Tris + 350 mM NaCl) absorbance was measured at 280 nm to measure protein content to select the interval of rinsing to run gel to determine the purity of the enzyme. Quinone Reductase and then select the extraction interval for the quinone reductase enzyme to be stored by The selected cleaning intervals are poured together and poured into Centrifugal Filter units with a filter hole size of 10 kDa and centrifuged at 5,000 rpm for 20 minutes at 4ºC, then sucked together for further spinning. at 5,000 rpm for 20 min at 4ºC, 50 mM Tris pH7.5 was added and centrifuged at 5000 rpm for 20 min at 4ºC to remove NaCl and centrifuge at 15,000 rpm for 10 min. at 4ºC and suck the clear. The enzyme (quinone reductase) was stored at -18ºC for the measurement of enzyme activity.

Enzyme Characterization–An experiment to determine the cofactor between Flavin mononucleotide (FMN) or Flavin adenine dinucleotide (FAD) as flavin-dependent enzyme by mixing 0.5 μM enzymes, NAD(P)H 100 μM, Menadione 50 μM and FMN or FAD 0-200 μM. were mixed and Then, absorbance was measured at a wavelength of 340 nm every 5 minutes for 2 hours.

An experiment to analyze the reducing substrates between NADH and NADPH by mixing enzyme concentrations 0.5 μM, FMN 2 μM, Menadione 50 μM and NADH or NADPH 0-200 μM were mixed and Then, absorbance was measured at a wavelength of 340 nm every 5 minutes for 2 hours.

Oxidizing substrates analysis trials included Menadione, Nitrofurazone and 1,4-Benzoquinone by mixing enzyme concentrations of 0.5 μM, FMN 2 μM NADH 200 μM and Menadione/ Nitrofurazone/ 1,4-Benzoquinone 0-200 μM were mixed and Then, absorbance was measured at a wavelength of 340 nm every 5 minutes for 2 hours.

Results and Discussion:

1. Expression of the enzyme quinone reductase.

1.1*Optimum temperature determination of quinone reductase expression in LB media*

The quinone reductase enzyme expression of both IPTG induction and auto-induction in both supernatant and pellet at 16ºC, 25 ºC, and 37ºC was shown in Fig.1. It was concluded that cultured *E.coli* BL21 (DE3) containing plasmid QR-pET-28a grown in IPTG induction media, the expressed enzymes were mostly in unfolded form. However, when cultured in ZY media, enzymes expressed in unfolded form were found to have approximately the same quantity as the properly correct folded enzymes present in the supernatant. In 16ºC of both IPTG induction and Auto-induction, it was found that the correct folded enzymes were more expressed at 25ºC and 37ºC, so 16ºC was chosen for protein expression.

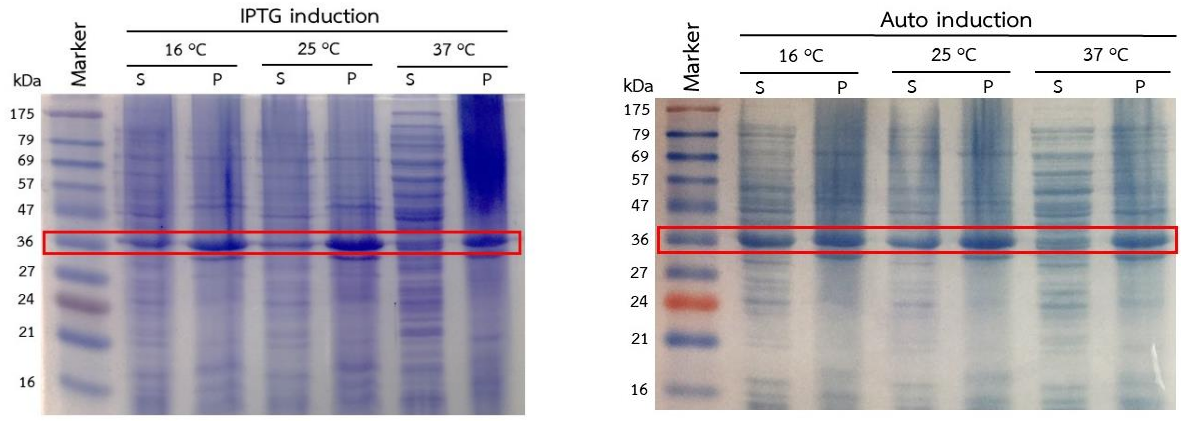

Figure 1.
SDS-PAGE gel of the expression of quinone reductase by IPTG induction (left) and Auto-induction (right) of both Supernatant and Pellet at 16ºC, 25 ºC and 37ºC.

1.2 *Optimal conditions for quinone reductase expression When Chaperone Plasmid is inserted in LB media.*

The quinone reductase enzyme was expressed by IPTG induction, and Chaperone-expressed Plasmid (pG-KJE8, pGro7, pKJE7, pG-Tf2, pTf16) was added to both the transparent sections. Supernatant and pellet at 16ºC, 25ºC and 37ºC are shown in Fig.2 It can be concluded that Plasmid with Chaperone expression cannot assist in the curling of quinone reductase enzyme. when cultured in LB media from the size of the protein band on the gel of the transparencies. The size of the protein band on the gel of the non-Plasmid containing Chaperone expression.

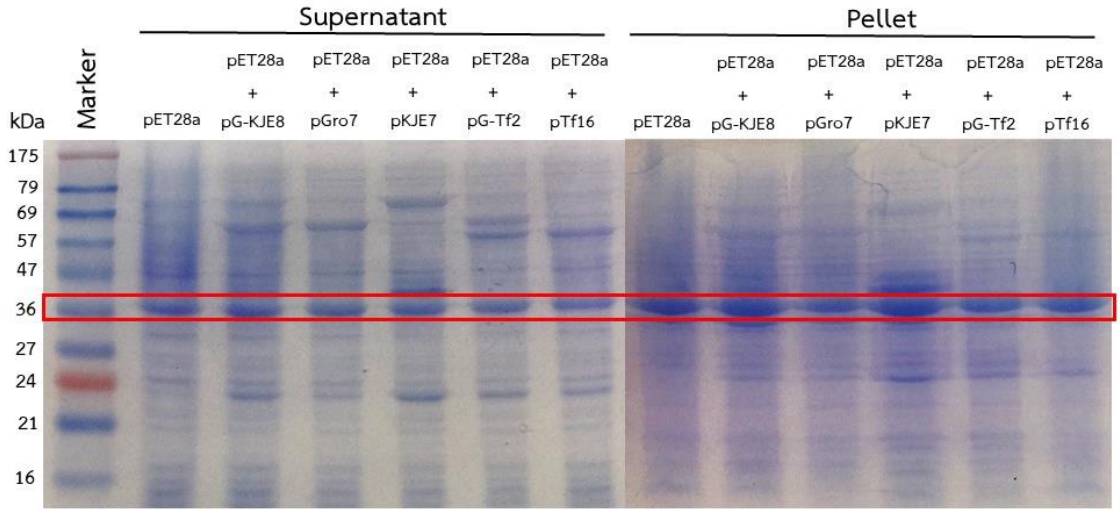

Figure 2.
SDS-PAGE gel of the quinone reductase expression by IPTG induction and Plasmid with Chaperone expression of both supernatant and pellet at 16ºC.

1.3 *Optimal conditions for quinone reductase expression When Chaperone Plasmid is added in ZY media*.

The expression of quinone reductase by Auto-induction and Plasmid (pG-KJE8, pGro7, pKJE7, pG-Tf2, pTf16) with Chaperone expression of both supernatant and pellet at 16ºC were shown in Fig.3. It was concluded that by culture *E.coli* BL21 (DE3) containing QR-pET-28a and pG-KJE8 plasmid in ZY media, protein bands of quinone reductase were found to be in the correct folded form supernatant are thicker than the protein. bands in the plasmid-expressed or non-expressed plasmid state of other chaperone species. Show that the raising conditions *E.coli* BL21 (DE3) containing the plasmid QR-pET-28a and pG-KJE8 plasmid in ZY media at 16ºC are optimal conditions.

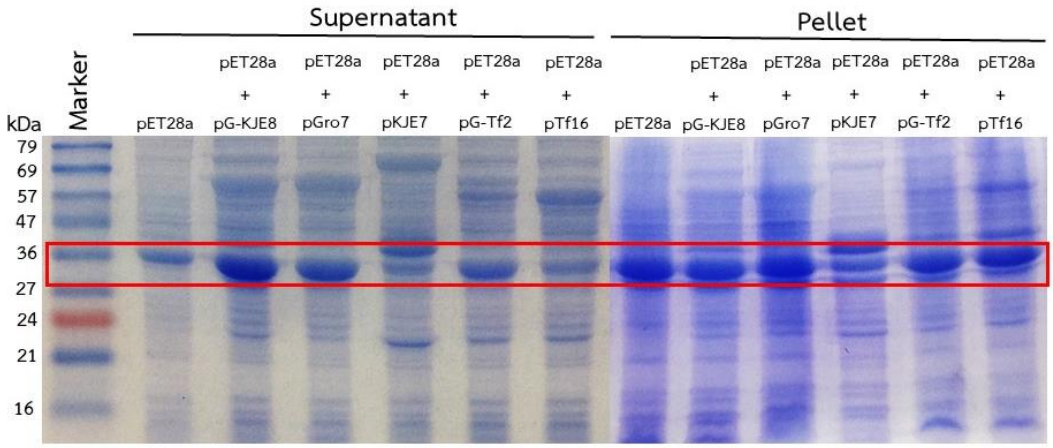

Figure 3.
SDS-PAGE gel of quinone reductase expression by Auto-induction and Plasmid with Chaperone expression of both supernatant and pellet at 16ºC.

2. Purification

2.1 *Results of trial enzyme purification conditions (based on E. coli BL21 (DE3) containing plasmid QR-pET-28a and pG-KJE8 plasmid) by Nickel Affinity Column Chromatography.*

The enzyme purification by immobilized metal affinity chromatography (IMAC) by nickel column chromatography was effective when run gel was shown in Fig. 4, which shows that the quinone reductase enzyme was It was initially observed from the protein bar of the body that was leached with wash buffer, and it was concluded that nickel column chromatography could not be used to purify the quinone reductase enzyme.

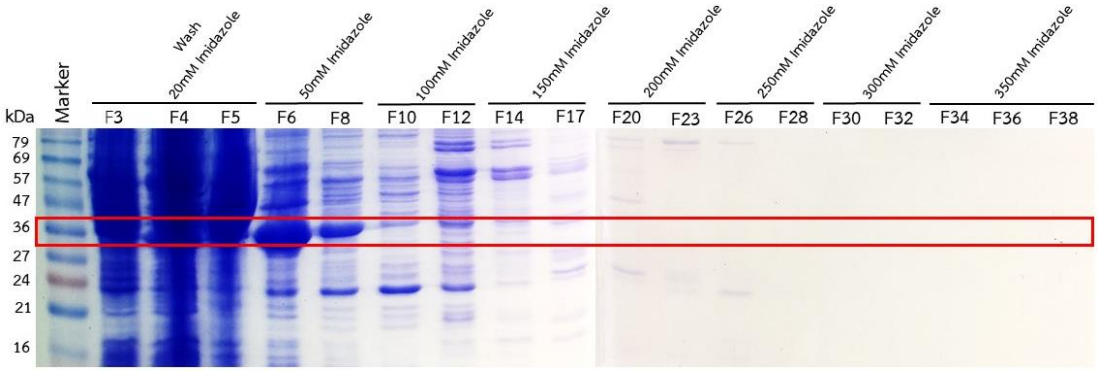

Figure 4.
SDS-PAGE gel of immobilized metal affinity chromatography (IMAC) enzyme purification by nickel column chromatography.

2.2 *Results of trial enzyme purification conditions (based on E. coli BL21 (DE3) containing plasmid QR-pET-28a and pG-KJE8 plasmid) by DEAE-Sepharose anion-exchange column chromatography.*

Enzyme purification by DEAE Column Chromatography The results shown in Fig. 5 showed that the quinone reductase subunit had a subunit size of approximately 35 kDa. The enzyme was eluted in the concentration range of 100-150 mM NaCl of the Elution Buffer.

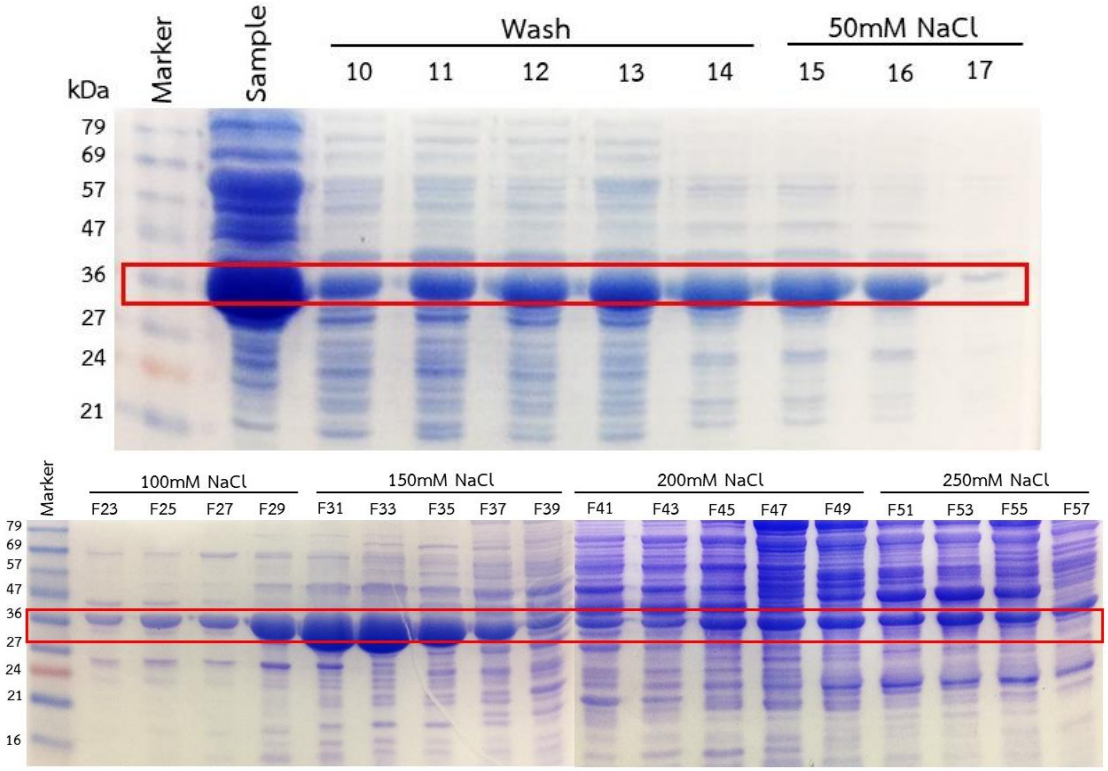

Figure 5.

SDS-PAGE gel of enzymatic purification by DEAE Column Chromatography Of the wash buffer, Sample will be the part before purification and the concentration range of 50-250 mM NaCl of the Elution Buffer.

2.3 *The results of enzymatic purification with DEAE-Sepharose anion-exchange column chromatography with gradient elution buffer from the 0-400 mM NaCl concentration range of the Elution Buffer.*

The absorbance measurement results at a wavelength of 280 nm of Fraction 2-96 are shown in Fig. 6, it can be seen that Fraction 26-60 is the period with the highest absorbance.

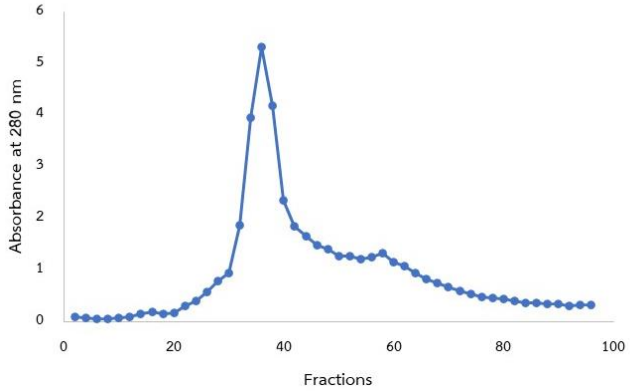

Figure 6.
The chromatogram shows the absorbance at a wavelength of 280 nm from Fraction 2-96 and the run gel result of Fraction 36, which has the highest absorbance.

Fraction 26-60 was then purified by DEAE Column Chromatography. The result is shown in Figure. 7, causing the researcher to choose Fraction 28-42 to collect the enzyme because the protein band size range is larger and purer than other fractions. The absorbance at a wavelength of 280 nm was then calculated for the enzyme concentration which was 2.83 mM, volume 4 ml, and the enzyme was tested for further properties.

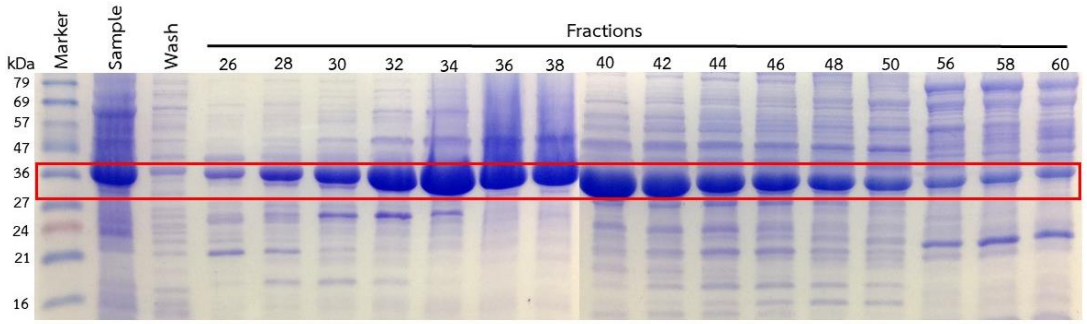

Figure 7.
SDS-PAGE gel of DEAE Column Chromatography enzymatic purification with gradient diffusion Fraction 26-60 which is in the highest absorbance range.

3. Measurement of enzyme kinetics

3.1 *Experimental results to show whether the quinone reductase enzyme needs flavin as a cofactor.*

The concentrations of quinone reductase, menadione and NAD(P)H were fixed and the concentration range of FMN and FAD was set at 0-12 µM. Measure the absorbance at wavelength of 340 nm every 5 min for 2 hr. can be calculated for the degradation velocity of NAD(P)H at various FMN and FAD concentrations as shown in Fig. 8, which shows that both NADH and NADPH have a reduction was rapid in the presence of FMN and FAD in the reaction, and at various FMN concentrations there was a faster reduction rate of NAD(P)H than FAD.

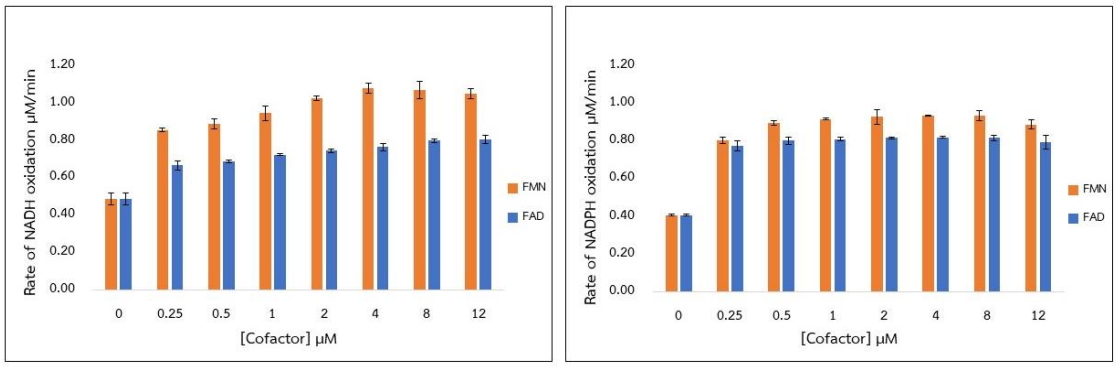

Figure 8.

The graphs show the decreasing velocity of NAD(P)H at various FMN and FAD concentrations.

3.2 *Results of an experiment to test the effectiveness of reducing substrate between NADH and NADPH.*

When the quinone reductase, FMN and Oxidizing Substrate concentrations were fixed and the concentration range of NADH and NADPH was set at 0-200 µM, the absorbance was measured at wavelength of 340 nm every 5 min for 2 hr. can be calculated to create the Michaelis-Menten equation and Lineweaver-Burk equation as shown in Fig. 9. From the graph, it can be concluded that NADH is a better electron donor to the quinone reductase than NADPH, based on the V_{max} of NADH of approximately 2.5 µM/min and the V_{max} of NADPH of approximately 1.5 µM/min.

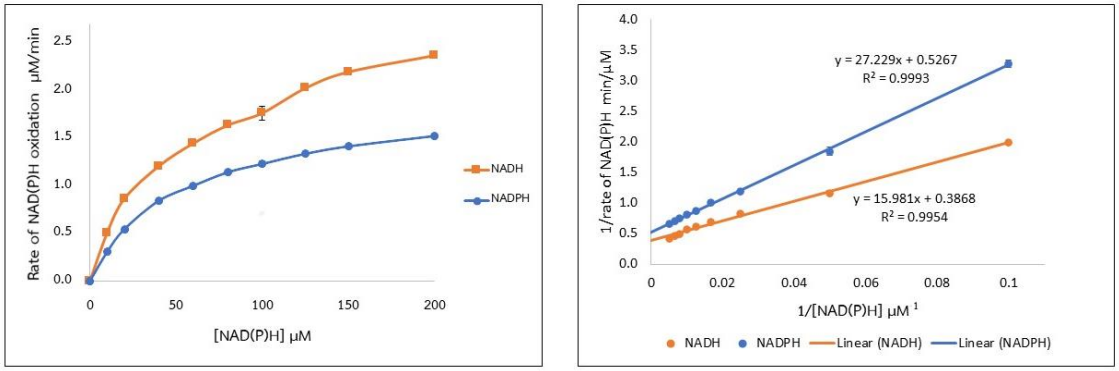

Figure 9.

Comparative curves of the intensity intervals of NADH and NADPH in the kinetics of quinone reductase by the Michaelis-Menten equation (left) and the Lineweaver-Burk equation (right).

From the graph line Weaver-Berg. The k_{cat}, K_m and k_{cat}/K_m values could be obtained, the concentration range of NADH and NADPH was 0-200 µM, and the concentrations of quinone reductase, Menadione and FMN were fixed, as shown in the table. 1. In conclusion, NADH was moreeffective in reducing substrate of quinone reductase than NADPH, the k_{cat}/K_m of NADH was greater than NADPH.

Table 1.
The table shows k_{cat}, K_m and k_{cat}/K_m when Vary NAD(P)H and the concentrations of quinone reductase, Menadione and FMN are fixed.

Vary Substrate	$K_{cat}(min^{-1})$	$K_m(\mu M)$	$K_{cat}/K_m(mM^{-1}\cdot min^{-1})$
NADH	5.17	41.32	125
NADPH	3.80	51.70	73

3.3 *The results of the trials to test the efficacy of Oxidizing Substrates included Menadione, Nitrofurazone and 1,4-Benzoquinone.*

When quinone reductase, FMN and NADH concentrations were fixed and the Menadione concentration range of 0-200 µM was determined, the absorbance was measured at a wavelength of 340 nm every 5 min. for 2 hours, it can be calculated to generate Michaelis-Menten equation and Lineweaver-Burk equation as shown in Figure 10.

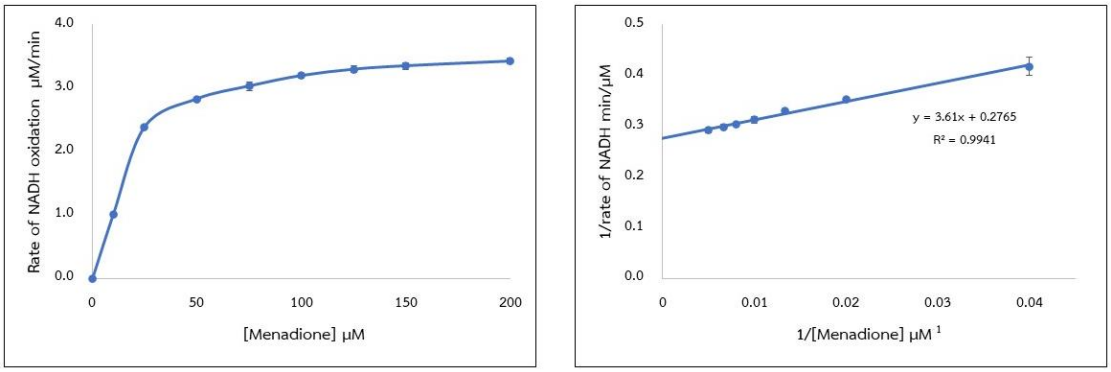

Figure 10.
Reaction curve when using Menadione as an oxidizing substrate by Michaelis-Menten equation (left) and the Lineweaver-Burk equation (right).

When quinone reductase, FMN and NADH concentrations were fixed and the Nitrofurazone concentration range of 0-200 µM was determined, the absorbance was measured at a wavelength of 340 nm every 5 min. for 2 hours, it can be calculated to generate Michaelis-Menten equation and Lineweaver-Burk equation as shown in Figure 11.

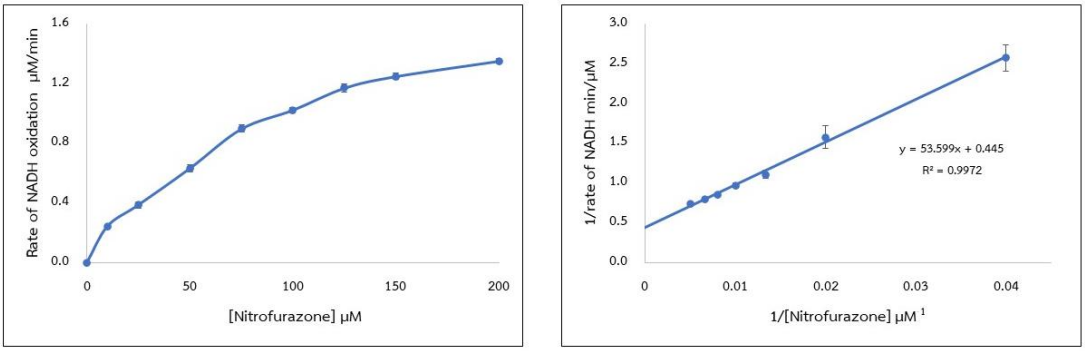

Figure 11.
Reaction curve when using Nitrofurazone as an oxidizing substrate by Michaelis-Menten equation (left) and the Lineweaver-Burk equation (right).

When quinone reductase, FMN and NADH concentrations were fixed and the 1,4-Benzoquinone concentration range of 0-120 μM was determined, the absorbance was measured at a wavelength of 340 nm every 5 min. for 2 hours, it can be calculated to generate Michaelis-Menten equation and Lineweaver-Burk equation as shown in Figure 12.

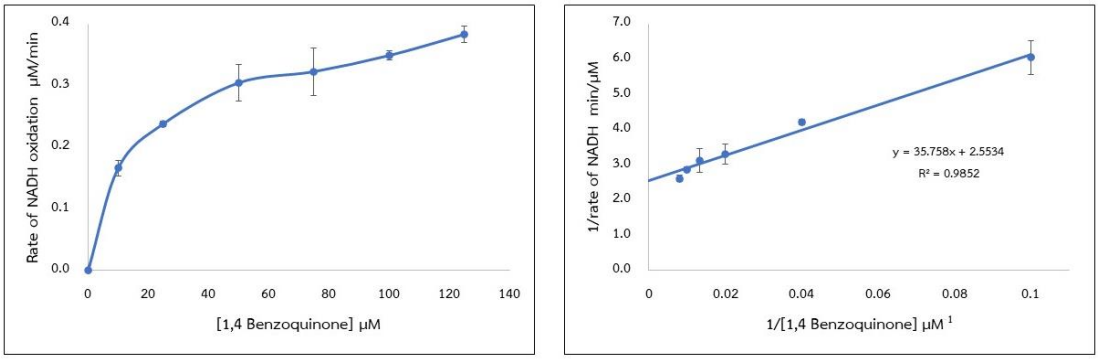

Figure 12.
Reaction curve when using 1,4-Benzoquinone as an oxidizing substrate by Michaelis-Menten equation (left) and the Lineweaver-Burk equation (right).

From the Lineweaver-Burk equation obtained under the conditions of the Oxidizing Substrate interval and the concentrations of quinone reductase, NADH and FMN were fixed. The values of k_{cat}, K_m and k_{cat}/K_m were obtained as shown in Table 2. It was concluded that Menadione was more effective as an Oxidizing Substrate than Nitrofurazone and 1,4-Benzoquinone because Menadione had higher k_{cat}/K_m values from the experiment.

Table 2.
The table shows k_{cat}, K_m and k_{cat}/K_m when Vary Oxidizing substrates and determines the constant quinone reductase, NADH and FMN concentrations.

Vary substrate	$k_{cat}(min^{-1})$	$K_m(\mu M)$	$k_{cat}/K_m(mM^{-1}\cdot min^{-1})$
Menadione	7.23	13.06	554
Nitrofurazone	4.49	120.45	37
1,4-Benzoquinone	0.78	14.00	56

Conclusion:

The quinone reductase expression was more pronounced in ZY media than in LB media since ZY media contained a carbon source. derived from glucose, lactose and Peptone, whereas LB media is carbon sourced from peptone, *E. coli* BL21 (DE3) was able to grow better. In addition, ZY media contained MPS as an aid in acidity control. When the Chaperone plasmid, especially plasmid pG-KJE8, was added, it was found that the amount of enzyme in the correct folded form was increased due to plasmid pG-KJE8. Dnak, DnaJ, GrpE, GroES and GroEL are expressed, where DnaJ binds to incomplete or non-folded proteins in the hydrophobic region and to DnaK. The DnaK-binding ATP is then Hydrolysis by activation of DnaJ causes DnaK-ADP to bind tightly to incompletely coiled proteins. GrpE then accelerates ADP release from DnaK, releases DnaK from incomplete or non-folded proteins and The protein will then fold itself until it is completely folded. Partially folded, it is sent to the GroEL/GroES system. Incompletely folded proteins bind to GroEL pockets that are not suppressed by GroES, then seven ATP molecules are attached to each GroEL subunit. Then ATP will be hydrolyzed, ADP will be released, 14 molecules of ADP will be released (7 molecules from GroEL and 7 molecules from GroES) and GroES will be released and 7 molecules of GroES and ATP will bind to GroEL, GroES will Filled with GroEL, proteins can't be released. causing the protein to fold inside A complete or partially folded protein is then released. And proteins that do not curl when released are quickly recaptured by GroEL. For this reason, more accurate folded enzyme content is obtained.

In the enzymatic purification section using Nickel Affinity Column Chromatography, where the buffer pH greater than the polyHis-tag amino histidine was uncharged, the nitrogen of the Imidazole group of the Histidine was uncharged. Histidine is deprotonated and coordinate with Ni2+ gives the octahedral shape of the molecule. but from the experiment Nitrogen of the Imidazole group in PolyHis-tag does not chelation with Ni2+ because the N terminal with PolyHis-tag precedes the amino acid M G S S, causing the N- end amino acid bonds to form. terminal to make PolyHis-tag not wire out and go to chelation with Ni2+ and using DEAE-Sepharose anion-exchange column chromatography in enzyme purification Since the total enzyme charge was negative at pH7.5, a QR concentration of 2.83 mM was obtained with a volume of 4 ml. Since the enzyme had a theoretical pI of 6.23, we used DEAE-Sepharose. The positively charged enzyme binds to the negatively charged enzyme and is leached with buffers of various ionic strengths to compete with the ion exchanger. Our enzymes are leached in the 100-150 mM concentration range of NaCl in the Elution Buffer.

Acknowledgements:

Research project on expression, purification The characterization of quinone reductase from Leishmania orientalis was successful. from diligent research efforts including receiving assistance and courtesy from the following people:

Thank you Dr. Panu Pimwiriyakul A research project advisor who supports and advises throughout the research period. It also teaches equipment preparation and use of research tools. It also provides knowledge and information about research in various fields.

Thank you Jane for helping me in research work throughout the research work. without any involvement or avoidance to help

References:

1. Al Massri, S. (2017). Characterizing the cofactor specificity of NQO2.
2. Esch, K. J., & Petersen, C. A. (2013). Transmission and epidemiology of zoonotic protozoal diseases of companion animals. *Clin Microbiol Rev*, *26*(1), 58-85.
3. Flores, E., & Gadda, G. (2018). Kinetic Characterization of PA1225 from Pseudomonas aeruginosa PAO1 Reveals a New NADPH:Quinone Reductase. *Biochemistry*, *57*(21), 3050-3058.
4. Pimviriyakul, P., & Chaiyen, P. (2018). A complete bioconversion cascade for dehalogenation and denitration by bacterial flavin-dependent enzymes. *J Biol Chem*, *293*(48), 18525-18539.
5. Reddy, K. (2019). Current Perspectives on Leishmaniasis. *Journal of Gandaki Medical College-Nepal*, *12*(1).
6. ภาควิชาปรสิตวิทยา คณะสัตวแพทยศาสตร์ มหาวิทยาลัยเกษตรศาสตร์. 2565. Leishmania. แหล่งที่มา: http: //ku-vim.vet.ku.ac.th/?page_id=35, 7 มีนาคม 2565.
7. หน่วยปฏิบัติการ วิจัย โรคอุบัติใหม่ และ อุบัติซ้ำในสัตว์ คณะสัตวแพทยศาสตร์ จุฬาลงกรณ์มหาวิทยาลัย. 2552. Leishmaniasis (cutaneous and visceral). แหล่งที่มา: https://www.cfsph.iastate.edu/Factsheets/th/leishmaniasis.pdf, 7 มีนาคม 2565.

PHYLOGENETIC ANALYSIS AND ORTHOLOG PREDICTION OF THE LEGUME NAC TRANSCRIPTION FACTORS

Oratai Thakom,[1] Piyada Juntawong[2]
[1] Department of Genetics, Faculty of Science, Kasetsart University, Thailand
e-mail: Oratai.tha@ku.th
[2] Department of Genetics, Faculty of Science, Kasetsart University, Thailand
e-mail: fscipdj@ku.ac.th

Abstract:

The NAC (NAM, ATAF, and CUC) transcription factor is one of the most prominent plant-specific transcription factor families. Members of this family play an essential role in regulating plant growth and development as well as abiotic and biotic stress responses. Among the legume family, most studies have focused on the genome-wide identification and evolution of NAC transcription factors in a given plant. However, little is known about the overview of *NAC* gene evolution and specific functions in the legume family. We obtained NAC transcription factor sequence data of the ten legumes and *Arabidopsis thaliana* from the PlantTFDB database. The phylogeny of NAC proteins in ten legumes demonstrated that they could be classified into 16 subgroups. Most legume *NAC* genes belong to the *ATAF* subgroup, which plays a role in photosynthesis and stress signaling. We also analyzed the orthologous relationship and found that legume NAC might have some specific response functions. These results will be helpful for insight into understanding the evolution and functional characteristics of legume *NAC* genes in the future.

Introduction:

NAC proteins constitute one of the largest and most widespread plant-specific transcription factors family, with more than 100 representatives in most plants, including model plants like *Arabidopsis thaliana* (Nakashima et al., 2012). The NAC acronym is from three reported proteins that were discovered to contain a particular conserved *NAC* domain at the N-terminal region: *NAM* (No Apical Meristem), *ATAF1/2* (*Arabidopsis thaliana* Transcription Activator Factor 1/2), and *CUC2* (Cup-shaped Cotyledon 2). The N-terminal DNA binding domain contains approximately 160 amino acids, which can be divided into five subdomains (A–E). Subdomain A is related to the stabilization of proteins. Subdomains B and C are involved in the functional diversity of the NAC gene. Furthermore, subdomains D and E act as parts of the DNA binding domain (Hao et al., 2010). The C-terminal region of the NAC transcription factor (TF) is diverse, functions as a transcriptional regulatory domain, and is involved in protein-protein interactions (Jensen et al., 2007). NAC TF plays imperative roles in various biological processes, such as development (Ko et al., 2007), senescence, and morphogenesis (Li et al., 2018). Additionally, they are involved in signaling pathways in response to different phytohormones and multiple abiotic and biotic stress (Marques et al., 2017).

Although NAC TF has been studied in many plants concerning developmental and other processes but lacks certain functions that are important to agriculture, such as the ability regarding nitrogen-fixing symbioses with root rhizobia and soil nutrient-scavenging symbioses with fungi. In other directions, legumes can produce such advantageous symbioses and have been the mainstay of sustainable agriculture for many years (Libault et al., 2009). The legume family includes important food crops that have good sources of protein and contain higher folate and iron levels, such as soybean (*Glycine max*), mungbean (*Vigna radiata*), common bean (*Phaseolus vulgaris*), alfalfa (*Medicago* spp.), and clover (*Trifolium* spp.). Interestingly, legumes can also be used as a source of biomass for biofuel production (Biswas et al., 2011). These advantages make legumes unique and interesting to be studied in the field of development, breeding, and evolution.

Genome-wide identification has been reported for legume species, and their phylogenetic relationships have been revealed based on genomic data. However, studies on the phylogenetic relationships of the *NAC* gene family are limited in these legume species. In this study, we obtained NAC TF data of the ten legumes and *A. thaliana* from the PlantTFDB database for phylogenetic relationship analysis. Furthermore, we identified orthologous clusters to predict the specific function of legumes. These results provide a greater understanding of evolution and follow-up studies on the functional features of the *NAC* gene in legumes.

Methodology:

1. Phylogenetic Analysis and Classification of the *NAC* Gene Family in legumes

TimeTree, the time scale of life web database (Kumar et al., 2017), was used to calculate the divergence time between the ten legume species and *A. thaliana*. The multiple sequence alignment of all *NAC* domains was executed using ClustalW (http://www.clustal.org). The best-fitting model of sequence evolution was determined by ProtTest (Darriba et al., 2011). The circle-shaped phylogenetic tree was constructed with Maximum likelihood (ML) analyses using IQ-TREE (Nguyen et al., 2015). It was estimated using an SH-aLRT test with 1000 random addition replicates and ultrafast bootstrap approximation set to 10,000 replicates. MEGA11 (http://www.megasoftware.net/) was used to display the summarized and classified *NAC* gene family.

2. Orthologous *NAC* gene clusters identification

The comparison and annotation of orthologous gene clusters of the *NAC* genes among the ten legumes and *A. thaliana* were analyzed using the online software OrthoVenn2 (https://orthovenn2.bioinfotoolkits.net) under default parameters (Xu et al., 2019).

Results and Discussion:

Most of the knowledge of plant TF was obtained from studies of the *Arabidopsis thaliana,* which is a plant genetic model. Thus far, most of the NAC TF characterized belong to *Arabidopsis*. Therefore, an attractive strategy is to compare and apply the knowledge established in *Arabidopsis* to legume NAC TF (Libault et al., 2009). Table 1 contains the information on the *NAC* genes from the ten legume species and the *Arabidopsis thaliana* obtained from the PlantTFDB. The numbers of *NAC* genes found in each species are shown in Table 1. The time tree scale panels from the TimeTree display the time scale divergence (Figure

1). The results obtained from the time tree scale demonstrated that *Arabidopsis* and legumes have different divergence times. But there have also been reports of microsynteny in some regions between Arabidopsis and legumes. For instance, analysis of allergen genes showed microsynteny between *Arachis hypogaea* and *Arabidopsis* (Ratnaparkhe et al., 2014). The legumes began to differ at an estimated time of 58.5 MYA and are divided into three monophyletic groups Papilionoid legumes, Dalbergioid, Phaseoloids, and Galegoids (Bertioli et al., 2009). Most agriculturally important species fall within the Phaseoloids group. The Phaseoloids are an essentially tropical group, including mungbean (*Vigna radiata*), cowpea (*V. unguiculata*), soybean (*Glycine max*), and pigeon pea (*Cajanus cajan*). The Galegoids are essentially temperate and include clover and forage plants. The notable exception is peanut (*Arachis hypogaea*) within the Dalbergioid clade, which has divergence with the Phaseoloids and Galegoids. This divergence may involve rapid expansions and reductions in transposon numbers within legume species (Ma et al., 2004).

Table 1

The number of NAC proteins in *Arabidopsis thaliana* and ten legume species.

Species	Number of NAC genes
Arabidopsis thaliana	138
Arachis hypogaea	32
Cajanus cajan	96
Cicer arietinum	96
Glycine max	152
Medicago truncatula	123
Phaseolus vulgaris	106
Vigna angularis	115
V. radiata	82
V. unguiculata	20
Trifolium pratense	97
Total	1057

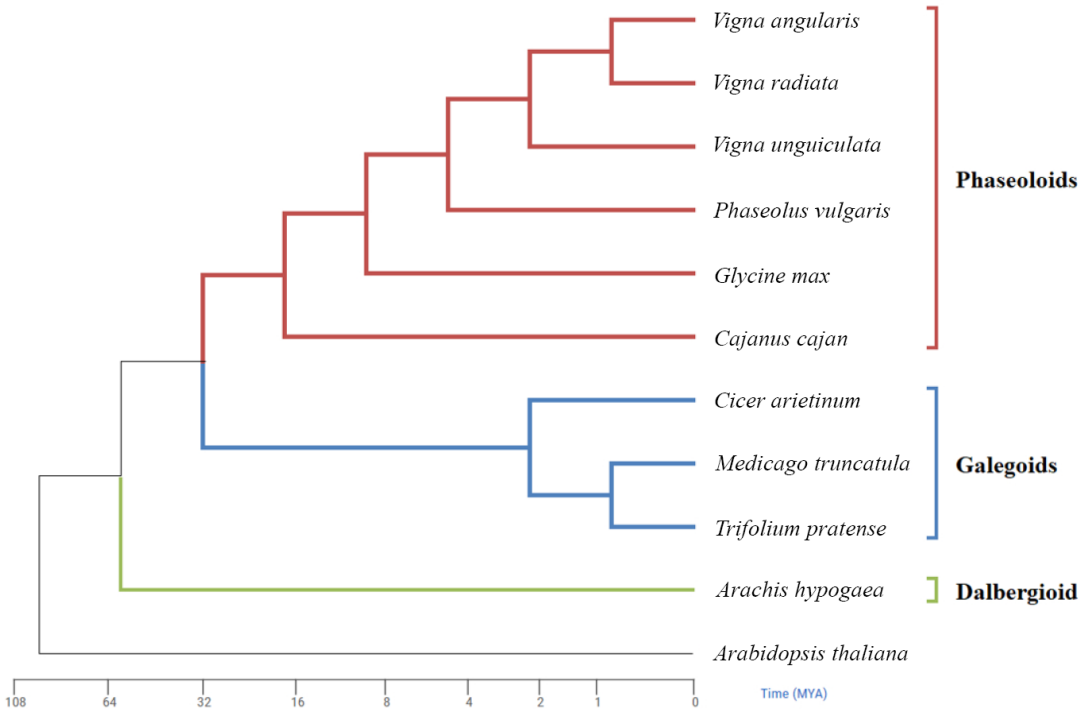

Figure 1
A tree representation of the phylogeny of the *Arabidopsis* and legumes

To investigate the evolutionary relationship of *NAC* genes between *Arabidopsis* and legumes, we constructed a phylogenetic tree with the maximum likelihood method. The ML tree showed that the NAC proteins could be classified into 16 subgroups: *NAM*, *ATAF*, *NAP*, *NAC1*, *NAC2*, *NAC3*, *ANAC001*, *ANAC011*, *ANAC063*, *ONAC003*, *ONAC022*, *OsNAC7*, *SEUN5*, *TERN*, *TIP*, and *NTL9* (Figure 2) based on the homology of NAC proteins in *Arabidopsis*. Among the 16 subgroups, *ATAF* contains the most significant number of NACs (135). Previous studies reported that the *ATAF* subgroup participates in photosynthesis and stress signaling processes (Christianson et al., 2010). NACs in most legumes may play a role in the light response and stress signaling. The *ONAC003* and *NTL9* had the lowest number of NAC members. Interestingly, *ONAC003*, which relates to drought and heat tolerance (Fang et al., 2015), is the only subgroup without NAC members of *Arabidopsis*. *ONAC003* contains only members of *P. vulgaris*, *V. angularis*, *V. radiata*, and *V. unguiculata* that are within the Phaseoloids group of agricultural importance. This observation indicates that these genes differentiated long ago and undergone many changes during their adaptation.

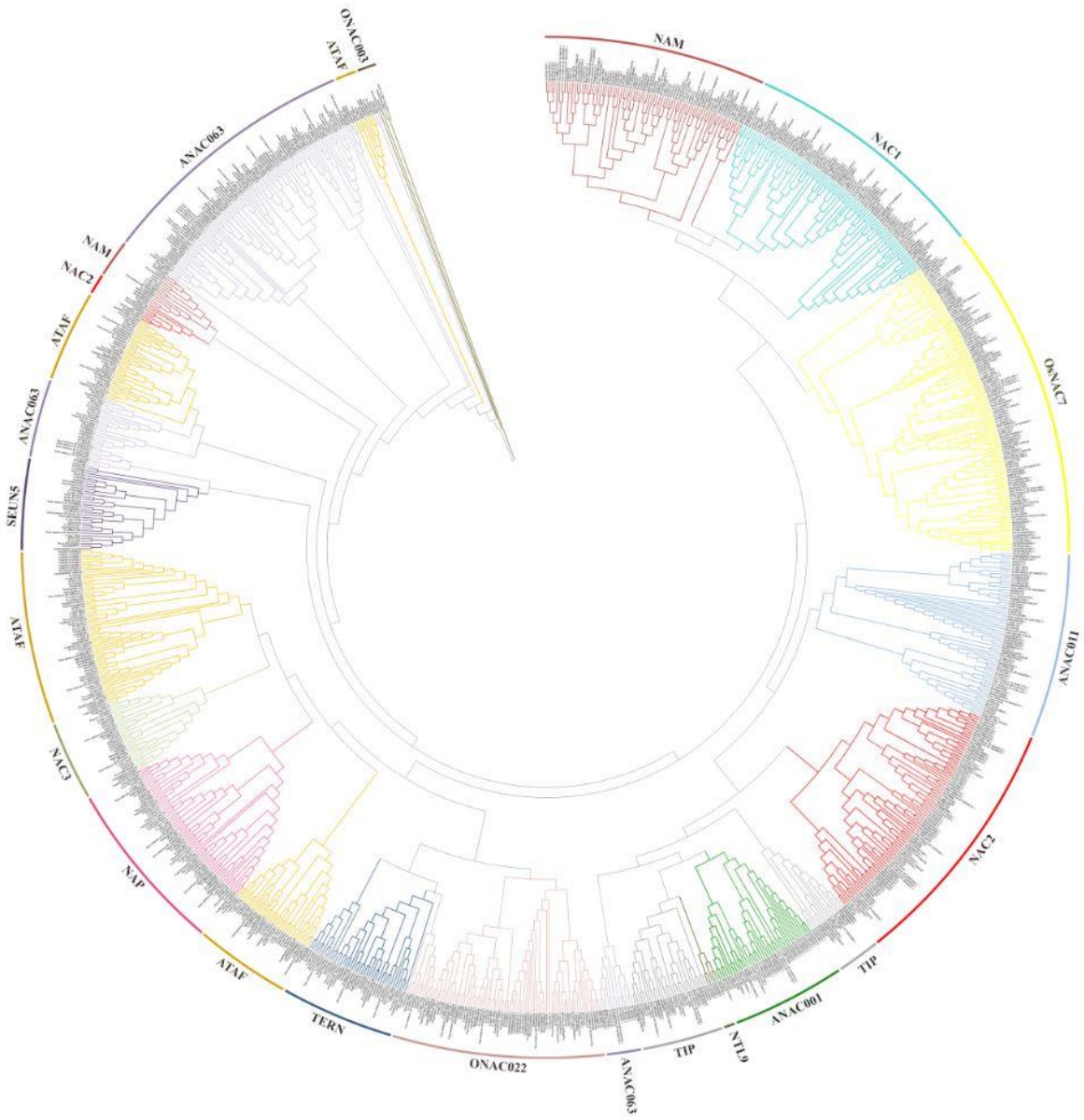

Figure 2

Phylogenetic tree of *NAC* gene family from the ten legumes and *Arabidopsis thaliana*

The ortholog functional prediction constitutes the basis of functional annotation of genomes that is important for experimental biology (Gabaldón & Koonin, 2013). We predicted an orthologous relationship analysis to study NAC-specific functions in legumes. We observed five overlapped clusters (Figure 3). Gene ontology (GO) annotation of these clusters revealed their roles in development and stress responses (Table 2). The results suggest that *NAC* genes of *Arabidopsis* and legumes within the same groups are evolutionarily correlated and may play a common role.

On the other hand, there are two clusters containing only legumes (clusters 33 and 34) regarding positive regulation of transcription and response to an absence of light (Table 2). Previous studies demonstrated that some plants, including legumes, have photoreceptors that

can sense changes in light intensity. Their leaves may close up as night approaches, and their stems may droop, known as Nyctinasty. It is the rhythmic nastic movement of plants in response to the onset of darkness (Chang-Ming et al., 2015). Furthermore, the dark condition prevented the legume decrease in dry matter due to the lighting. It aims at preserving the nutrient content (Mastropasqua et al., 2020). Altogether, these data suggested the roles of the specific legume NACs in the species adaptation.

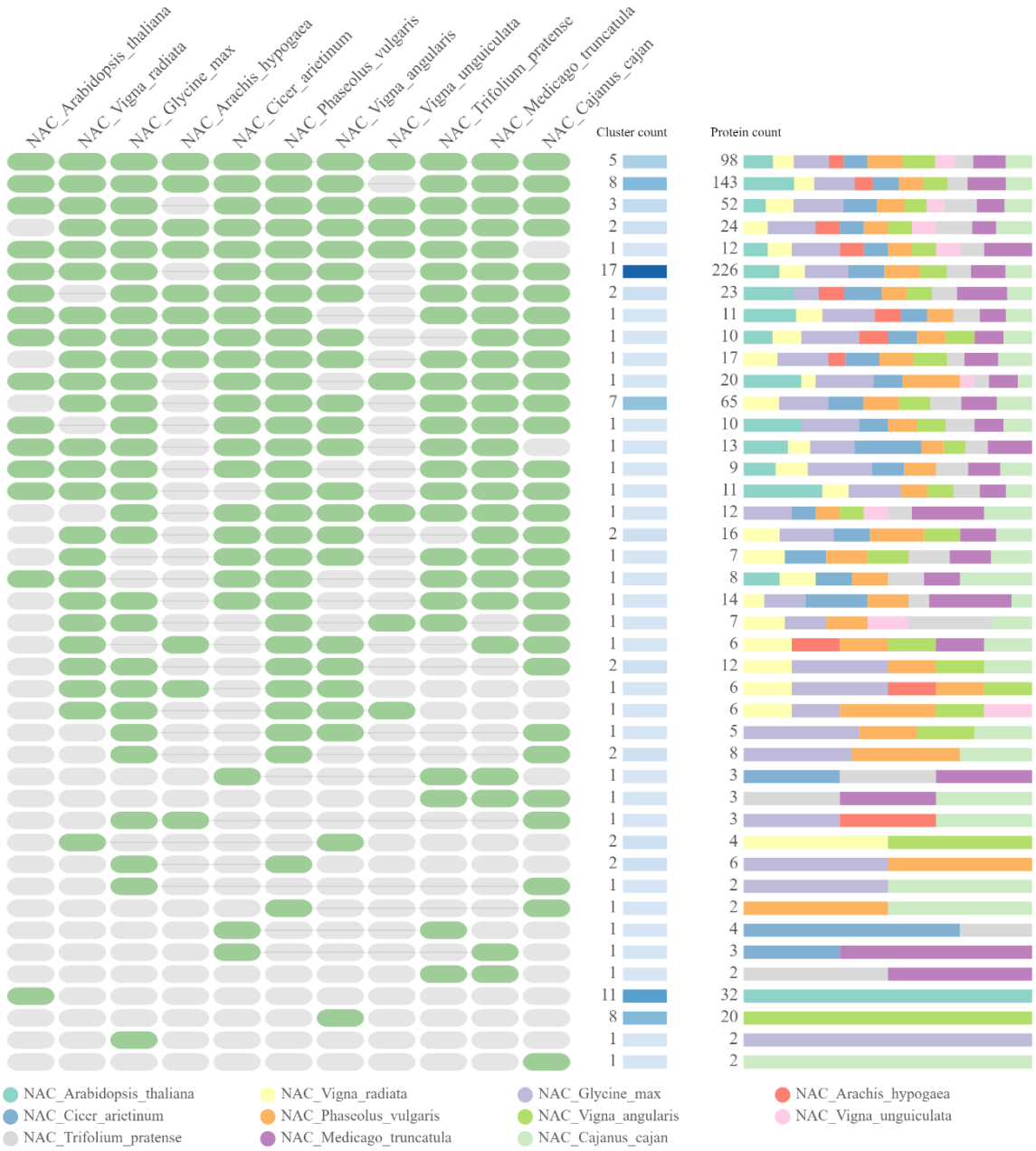

Figure 3

The orthologous relationship between *Arabidopsis thaliana* and ten legumes

Table 2

Orthologous *NAC* gene clusters between *Arabidopsis thaliana* and ten legumes

Cluster	Protein number	Swiss-Prot ID	GO annotation	Protein list
cluster3	24	Q8H115	GO: 0001666; P: response to hypoxia; IMP:TAIR	Phvul.009G152800.1 Phvul.009G152900.1 Medtr3g096920.1 Medtr3g096920.2 AT5G08790.1 AT5G63790.1 Vun002116 Vradi07g31420 C.cajan_38151 Cicer_arietinum_XP_004503901.1 Tp57577_mRNA38625 Phvul.002G275000.1 Vang10g03960.1 Medtr8g094580.1 GmNAC030 Vun008488 C.cajan_15921; GmNAC018 Vun009142 Ahy004174 Cicer_arietinum_XP_004502989.1 Vradi0051s00540 Vang0087s00030.1 Tp57577_mRNA8126

cluster5	23	Q9FY93	GO: 0010089; P: xylem development; IMP:TAIR	Phvul.008G001000.1 Phvul.008G001000.2 GmNAC054 GmNAC033 Vun009374 Ahy012574 C.cajan_19098 Cicer_arietinum_NP_001266090.1 Tp57577_mRNA22313 Vang10g04870.1 Medtr7g005280.1 AT5G13180.1 GmNAC065 Vradi07g30030 C.cajan_30687 Cicer_arietinum_XP_004503781.1 Phvul.002G283600.1 Medtr8g099750.1 C.cajan_28603 Phvul.009G163200.1 Medtr3g098810.1 GmNAC040 Cicer_arietinum_XP_004501729.1
cluster9	19	Q6NQK2	GO: 0010332; P: response to gamma radiation; IMP:TAIR	Vang0190s00010.2 Vang0190s00010.1 AT5G14490.1 AT3G01600.1 Vun007533 Ahy007630 Vradi0007s01760 C.cajan_46953 Cicer_arietinum_XP_004499395.1 Tp57577_mRNA1150 Phvul.008G159200.1 Medtr7g033320.1 GmNAC142 Vradi01g00290 GmNAC025 C.cajan_31437 Phvul.004G004900.1 Vang02g14320.1 Phvul.008G159200.2

cluster16	16	Q7F2L3	GO: 0048364; P: root development; IMP:UniProtKB	Vang0041ss00850.3 Vang0041ss00850.4 Vang0041ss00850.2 Vang0041ss00850.1 Medtr3g088110.2 Medtr3g088110.1 GmNAC035 GmNAC022 Vun004457 Ahy003428 Vradi05g06640 C.cajan_01304 Cicer_arietinum_XP_004502479.1 Tp57577_mRNA21786 Phvul.009G125900.1 AT1G01720.1
cluster17	16	Q9LDY8	GO: 0009414; P: response to water deprivation; IMP:TAIR	Medtr2g079990.1 Medtr2g079990.2 AT3G15500.1 AT1G52890.1 AT4G27410.2 AT4G27410.3 GmNAC101 GmNAC092 Vun010348 Ahy022629 C.cajan_43030 Cicer_arietinum_XP_004487679.1 Tp57577_mRNA40277 Phvul.005G084500.1 Vradi06g09740 Vang0029ss00050.1
cluster33	12	Q93VY3	GO: 0045893; P: positive regulation of transcription, DNA-templated; IBA:GO_Central	GmNAC043 GmNAC085 Vun004525 Ahy021850 Vradi02g09860 C.cajan_43785 Cicer_arietinum_XP_004514350.1 Tp57577_mRNA37157 Phvul.011G147800.1 Vang02g07100.1 Medtr8g059170.1 C.cajan_43786

cluster34	12	K4BNG7	GO: 0009646; P: response to absence of light; IMP:UniProtKB	GmNAC052 GmNAC148 Vun003442 Ahy008545 Vradi07g06320 C.cajan_20225 Cicer_arietinum_XP_012572610.1 Tp57577_mRNA35877 Phvul.002G170200.1 Vang0126s00070.1 Medtr4g081870.1 Tp57577_mRNA35201

Conclusion:

Our results demonstrated that the *NAC* genes of the ten legumes could be classified into 16 subgroups based on the homology of NAC proteins. Most legume *NAC* genes belong to the *ATAF* subgroup, which plays a role in photosynthesis and stress signaling. We identified the legume-specific NAC subgroups, indicating that the evolutionary relationship between *Arabidopsis* and legumes differentiated long ago. In addition, we also analyzed the orthologous relationship and found that legumes might have a specific response function to an absence of light. This study provides an overview of the *NAC* gene's evolution and particular role in legumes.

References:

1. Bertioli DJ, Moretzsohn MC, Madsen LH, Sandal N, Leal-Bertioli SC, Guimarães PM, et al. BMC Genomics. 2009;10:45.
2. Biswas B, Scott P, Gresshoff P. J Plant Physiol. 2011;168:1877-1884.
3. Chang-Ming Z, Yun-Qing W, Ying L, Xiao-Hong Z, Shan T. Chin J Plan Ecolo. 2015;39:909-916.
4. Christianson JA, Dennis ES, Llewellyn DJ, Wilson IW. Plant Signal Behav. 2010;5:428-432.
5. Darriba D, Taboada GL, Doallo R, Posada D. Bioinformatics. 2011;27:1164-1165.
6. Fang Y, Liao K, Du H, Xu Y, Song H, Li X, et al. J Exp Bot. 2015;66:6803-6817.
7. Gabaldón T, Koonin EV. Nat Rev Genet. 2013;14:360–366.
8. Hao YJ, Song QX, Chen HW, Zou HF, Wei W, Kang XS, et al. Planta. 2010;232:1033-1043.
9. Jensen MK, Rung JH, Gregersen PL, Gjetting T, Fuglsang AT, Hansen M, et al. Plant Mol Biol. 2007;65:137-150.
10. Ko JH, Yang SH, Park AH, Lerouxel O, Han K-H. Plant J. 2007;50:1035-1048.
11. Kumar S, Stecher G, Suleski M, Hedges SB. Mol Biol Evol. 2017;34:1812-1819.
12. Li W, Li X, Chao J, Zhang Z, Wang W, Guo Y. Front Plant Sci. 2018;9:1900.
13. Libault M, Joshi T, Benedito VA, Xu D, Udvardi MK, Stacey G. Plant Physiol. 2009;151:991–1001.
14. Ma J, Devos KM, Bennetzen JL. Genome Res. 2004;14:860-869.

15. Mastropasqua L, Dipierro N, Paciolla C. Antioxidants. 2020;9:558.
16. Mohanta TK, Yadav D, Khan A, Hashem A, Tabassum B, Khan AL, et al. PLoS One. 2020;15:e0231425.
17. Marques D, Savio SP, Souza CRB. Plant Gene. 2017;11:170-179.
18. Nakashima K, Takasaki H, Mizoi J, Shinozaki K, Yamaguchi K. Biochim Biophys Acta. 2012;1819:97-103.
19. Nguyen LT, Schmidt HA, Haeseler Av, Minh BQ. Mol Biol Evol. 2015;32:268-274.
20. Ratnaparkhe MB, Lee TH, Tan X, Wang X, Li J, Kim C, et al. Genome Biol Evol. 2014;6:2468-2488.
21. Xu L, Dong Z, Fang L, Luo Y, Wei Z, Guo H, et al. Nucleic Acids Res. 2019;47:52-58.

ROLE OF DNA METHYLTRANSFERASES ON TSHR EXPRESSION AND ORBITAL FIBROBLASTS ACTIVATION

Pimchanok Phankeaw[1], Sopita Visamol[1], Tanapat Palaga[2], Preamjit Saonanon[3], Vannakorn Pruksakorn[3], Willem A. Dik[4] and Sita Virakul[2,*]
[1]Medical Microbiology, Interdisciplinary Program, Graduate School, Chulalongkorn University, Bangkok, Thailand
[2]Department of Microbiology, Faculty of Science, Chulalongkorn University, Bangkok, Thailand
[3]Department of Ophthalmology, Faculty of Medicine, Chulalongkorn University, Bangkok, Thailand
[4]Department of Immunology, Laboratory Medical Immunology, Erasmus MC, Rotterdam, Netherlands
*e-mail: Sita.V@chula.ac.th

Abstract:

Graves' ophthalmopathy (GO) is the extra-thyroidal complication of Graves' disease (GD), an autoimmune disease induced by TSHR autoantibody. The characteristics of GO are erythema of periorbital tissue, upper eyelid retraction, conjunctivitis, proptosis, and fibrosis. Severe symptoms of GO could lead to sight-threatening symptoms from keratitis and optic nerve compression. Current treatments of GO including glucocorticoid treatment and decompression surgery are not effective and could induce side effects. Therefore, a new therapy for GO requires further investigation. Previous studies demonstrated that platelet-derived growth factor (PDGF)-BB plays an important role in GO pathogenesis by inducing orbital fibroblast activities such as proliferation, cytokine and hyaluronan production, adipogenesis, and *TSHR* expression. Novel GO pathogenesis during orbital fibroblast activation induced by Epigenetics modification has recently been reported which play important roles in regulating gene expression level by several mechanisms. One of the mechanisms is DNA methylation which could reduce gene expression level. The previous studies suggested that global DNA methylation level in GO orbital fibroblasts is significantly higher than in healthy control orbital fibroblasts. However, the role of DNA methyltransferases (DNMT) in orbital fibroblasts activation is unknown. Consequently, this study aims to investigate the role of DNA methylation by using decitabine, a DNMT inhibitor, on PDGF-BB-induced *TSHR* mRNA expression and orbital fibroblasts activation. Inhibition of DNMT significantly decreases PDGF-BB-induced orbital fibroblasts proliferation ($p<0.01$) and *TSHR* mRNA expression ($p<0.05$). On the other hand, decitabine did not affect PDGF-BB-induced IL-6 and hyaluronan production by orbital fibroblasts. These results support the important role of DNA methylation on *TSHR* mRNA regulation. However, the effects of decitabine in orbital tissue required further investigation which might lead to the development of a new approach for GO therapy.

Keywords: Graves' ophthalmopathy, orbital fibroblasts, PDGF-BB, DNA methylation, TSHR

Introduction:

Graves' ophthalmopathy (GO) develops in about 30-50% of Graves' disease (GD) patients [1]. This disease is also known as thyroid-associated ophthalmopathy or thyroid eye disease [2]. The clinical features of GO patients are conjunctival chemosis (edema), bilateral erythema,

excess proptosis, and severe symptoms such as corneal ulcers and optic neuritis leading to loss of vision [2]. GO progression is divided into two clinical stages. In the early stage or active stage, the patients develop inflammation and eye edema which result in eye swelling, redness, and pain [3]. Then, GO develops into inactive stage with tissue remodeling and fibrosis leading to orbital tissue expansion and accumulation of extracellular matrix [4].

Orbital fibroblasts play an important role in GO pathogenesis. Autoantigen, thyroid stimulating hormone receptor (TSHR) and insulin-like growth factor 1 receptor (IGF-1R), are expressed on orbital fibroblasts, and can be stimulated by circulating autoantibodies. [2, 5]. Activated orbital fibroblasts by autoantibodies induce orbital fibroblasts differentiation into myofibroblasts [2] and increase inflammatory mediators production such as IL-6 and IL-8 [2]. Moreover, the extracellular matrix is also produced by orbital fibroblasts, especially hyaluronan and causes orbital tissue expansion and fibrosis in GO [6]. Furthermore, *TSHR* expressions increased when orbital fibroblasts differentiate into adipocytes [7]. Thus, TSHR is an important key factor in GO progression.

Previous studies found that gene expression of platelet-derived growth factor B (*PDGF-B*) upregulated in GO orbital tissue during both inactive and active stages [8]. Moreover, PDGF-BB increased cell proliferation, *TSHR* expression, IL-6, IL-8, and hyaluronan production by orbital fibroblasts [4]. In addition, PDGF-BB also enhanced adipogenesis in orbital fibroblasts [9]. Therefore, PDGF-BB is the key factor in GO progression.

GO treatment is based on the severity and activity of the disease [10]. The first line of treatment for patients with active disease is an immunosuppressive or anti-inflammatory treatment, glucocorticoid [10]. On the other hand, surgery should be considered in active GO to alleviate severe symptoms and in inactive GO patients for rehabilitation purposes [11]. However, prolonged glucocorticoid use may increase the risks of infection and induce diabetes [12]. Currently, targeted therapy, for example, Teprotumumab (IGF-1R antagonist), has been revealed to be effective as a treatment for inactive GO patients [13]. However, according to pharmacy medical necessity guidelines approved by Food and drug administration (FDA), teprotumumab should be used for moderate to severe GO patients or active GO patients [14]. To provide an effective treatment for both inactive and active GO, further targeted therapy studies are required.

Novel pathogenesis on the role of epigenetics has been reported in GO. Epigenetics modifications, DNA methylation and histone modification, control gene expression in a manner independent of DNA sequence [15]. DNA methylation strongly regulates gene expression, X-chromosome inactivation, parental imprinting, and cell differentiation in health and diseases [16]. DNA methyltransferases (DNMTs) act as methylating agents at CpG regions located mainly on the promoters. Therefore, methylated promoters act as the epigenetics silencers preventing the binding of transcription factors during transcription [16]. DNMTs are characterized into two types [17]. Firstly, DNMT1 maintains specific methylation patterns during cell division [17, 18]. Secondly, DNMT3A and DNMT3B perform *de novo* methylation.

Previous studies demonstrated DNA methylation plays an important role in fibroblasts activation in lung fibrosis [19] , hepatic fibrosis [20], and renal fibrosis [21]. Recently, global DNA methylation of GO orbital fibroblasts showed that DNA methylation level in GO orbital fibroblasts is significantly higher than control orbital fibroblasts [22, 23]. Moreover, the TSHR network and PDGF signaling have been reported with the highest score linking to the organismal injury and abnormalities, cellular growth and proliferation, and cellular development network of hypermethylated genes [22]. Thus, this study suggested that DNA

methylation might play role in *TSHR* mRNA expression and orbital fibroblast activation. Therefore, this study aims to investigate the role of DNA methyltransferases on *TSHR* expression and orbital fibroblast activation which could potentially be an attractive therapeutic target for the treatment of GO.

Methodology:

Material and reagents

DNMT inhibitor (5-AZA-2'-deoxycytidine; decitabine) was purchased from Selleck Chemicals, Inc. (TX). Recombinant human PDGF-BB was obtained from BioLegend, Inc. (CA).

Sample collection and orbital fibroblasts isolation

GO and normal healthy orbital tissues who underwent plastic surgery were collected from King Chulalongkorn Memorial Hospital. Ethical approval was obtained from the institutional review board of the faculty of medicine, Chulalongkorn University (Bangkok, Thailand) committee with the protocol number 401/61. Orbital fibroblasts were isolated from fresh tissues by cutting tissue and placing them on 6-well plates. Dulbecco's modified Eagle's medium (DMEM; GE Lifesciences, MA) with 20% fetal bovine serum (FBS; Life Technologies, Inc., Germany) and 100 µg/mL Gentamicin (Life Technologies, Inc., Germany) as described previously [24] were used for culturing the orbital tissue for orbital fibroblast isolation.

Cell cytotoxicity and proliferation from DNMT inhibitor

1) Lactate dehydrogenase (LDH) cytotoxicity assay

Orbital fibroblasts were seeded at 6 x 10^3 cells/well with 1% FBS/DMEM in presence of gentamicin in 96-well plates overnight. Then, cells were treated with decitabine (5, 10, 15 µM) for 24 hours. The supernatants were collected to determine cytotoxicity by LDH assay according to the manufacturer's protocol (Biovision, Inc., CA). After that, the percentage of cytotoxicity was calculated and compared with negative control (supernatant from unstimulated condition) and positive control (supernatant from cell lysis treatment).

$$\%\text{Cytotoxicity} = \frac{(\text{OD of test sample} - \text{negative control}) \times 100}{(\text{OD of positive control} - \text{negative control})}$$

2) MTT assay

Orbital fibroblasts were seeded at 6 x 10^3 cells/well in 96-well plates with 1% FBS/DMEM in presence of gentamicin overnight. Then, cells were pretreated with decitabine (5, 10, 15 µM) for 24 hours. After that, the cells were further stimulated with 50 ng/ml PDGF-BB in presence of decitabine for 24 hours. Next, the cells were treated with 5 mg/ml of Thiazolyl Blue tetrazolium bromide (Alfa Aesar, part of Thermo Fisher Scientific Inc., NY) for 4 hours at 37°C. Subsequently, DMSO was used to elude formazan from the cells and absorbance was measured with microplate reader at 540 nm. %Cell proliferation was calculated using 1%FBS/DMEM as blank and supernatant from the unstimulated condition as the negative control.

$$\%\text{Cell Proliferation} = \frac{(\text{OD of test sample} - \text{blank}) \times 100}{(\text{OD of negative control}) - \text{blank}}$$

DNMTs mRNA expression in orbital fibroblasts

Orbital fibroblasts were seeded at 2.5 x 10^5 cells/well in six-well plates (Thermo Fisher Scientific, Inc., NY) with DMEM containing 1% FBS and gentamicin overnight. Orbital fibroblasts were stimulated with PDGF-BB (50 ng/mL) for 0, 6, and 24 hours. Total RNA was extracted using RNeasy Mini Kit according to the manufacturer's protocol (QIAGEN, Austin, Texas, USA) and cDNA was converted using the iScript™ cDNA synthesis Kit according to the manufacturer's protocol (Bio-Rad, Inc., CA)

Expression level of *DNMT1, 3A* and *3B* mRNA were determined by TaqMan® Gene Expression Assays (Thermo Fisher Scientific, Inc.: Hs00154749_m1, Hs01027166_m1, and Hs00171876_m1, respectively) [Table 1] with SsoAdvanced™ Universal Probes Supermix (Bio-Rad, Inc.) by real-time PCR (CFX96 Touch™ Real-Time PCR Detection System; Bio-Rad, Inc.). *DNMTs* expression levels were normalized to *ABL*.

Effects of decitabine treatment on TSHR mRNA expression

Orbital fibroblasts were seeded at 2.5 x 10^5 cells/well into six-well plates in DMEM with 1% FBS and gentamicin overnight. Then, cells were pretreated with 2.5 μM decitabine for 24 hours. Subsequently, cells were stimulated with 50 ng/mL PDGF-BB in the presence of decitabine for 24 hours. Then, total RNA was extracted to measure mRNA expression of *TSHR* as described above.

Table 1. Primer and Probe lists for real-time PCR analysis

Gene	Primer sequence		Taqman probe
ABL	F	5'-TGGAGATAACATCTAAGCATAACTAA AGGT- 3'	FAM-CCATTTTTGGTTTGGGCTTCACACCATT - TAMRA
	R	5'-GATGTAGTTGCTTGGGACCA-3'	
DNMT1	Hs00154749_m1 (Applied biosystems Inc., USA)		
DNMT3A	Hs01027166_m1 (Applied biosystems Inc., USA)		
DNMT3B	Hs00171876_m1 (Applied biosystems Inc., USA)		
TSHR	Hs01053846_m1 (Applied biosystems Inc., USA)		

Effects of decitabine treatment on IL-6 and hyaluronan production

Orbital fibroblasts were seeded at 1 x 10^5 cells/well into twelve-well plates in DMEM with 1% FBS and gentamicin overnight. Then, cells were treated with 15 μM decitabine for 24 hours. Subsequently, cells were stimulated with 50 ng/mL PDGF-BB in the presence of decitabine for 24 hours. Then, the supernatants were collected for IL-6 (BioLegend Inc., CA, USA) and hyaluronan (R&D systems, Inc.) and measured by ELISA kits according to the manufacturer's protocol.

Statistical analysis

All experiments used at least three orbital fibroblasts which were harvested from different individuals. Each symbols represent individual orbital fibroblasts form each individual and the horizontal bar represents mean. Differences between groups were assessed by One way ANOVA. Statistical significance was indicated by * as $p<0.05$, ** as $p<0.01$ and *** as $p<0.001$ compared to unstimulated condition or PDGF-BB-stimulated condition.

Results and Discussion:

DNA methyltransferases (DNMTs) expression in healthy control, inactive GO, and active GO orbital fibroblasts

To investigate DNMTs expression levels in orbital fibroblasts isolated from Thai healthy control, inactive GO, and active GO orbital tissue (n= 3-6). mRNA expressions were determined by RT-qPCR. *DNMT1, DNMT3A*, and *DNMT3B* mRNA expression significantly upregulated in orbital fibroblasts of active GO patient compared to control with p-value < 0.05, 0.01, and 0.05, respectively. *DNMT1* and *DNMT3A* were significantly upregulated in active GO orbital fibroblasts compared to inactive GO with p-value <0.05 and 0.01, respectively (Figure 1). This data suggested that DNMTs may play role in GO.

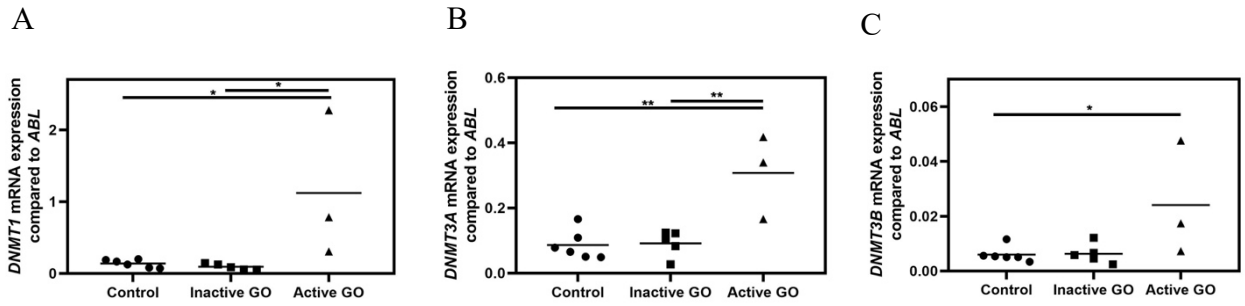

Figure 1. (A) *DNMT1* mRNA expression, (B) *DNMT3A* mRNA expression, and (C) *DNMT3B* mRNA expression in Thai healthy control, inactive GO, and active GO orbital fibroblasts were determined by RT-qPCR and normalized to the control gene *ABL*. Individual symbols represent orbital fibroblasts cultured from individual patients and horizontal bar represents mean.

DNA methylatransferases (DNMTs) expression in PDGF-BB-induced orbital fibroblasts

As previous studies demonstrated the role of PDGF-BB in GO progression [8, 9, 24], the effects of PDGF-BB on DNMTs expression of orbital fibroblasts were investigated in healthy control and inactive GO orbital fibroblasts (n = 5-6). Orbital fibroblasts were stimulated with 50 ng/ml PDGF-BB for 6 and 24 hours. *DNMT1* and *DNMT3B* mRNA expression of healthy control orbital fibroblasts were time-dependently upregulated at 24 hours compared to unstimulation ($p<0.01$) and 6 hours of stimulation ($p<0.05$) (Figure 2A and 2C). *DNMT1* mRNA expression of inactive GO was upregulated at 24 hours compared to unstimulation ($p<0.05$). However, PDGF-BB did not regulate *DNMT3A* mRNA expression in both control and inactive orbital fibroblast (Figure 2B). This data suggested that PDGF-BB induces *DNMT1* in both healthy control inactive GO, and *DNMT3B* mRNA expression of healthy control.

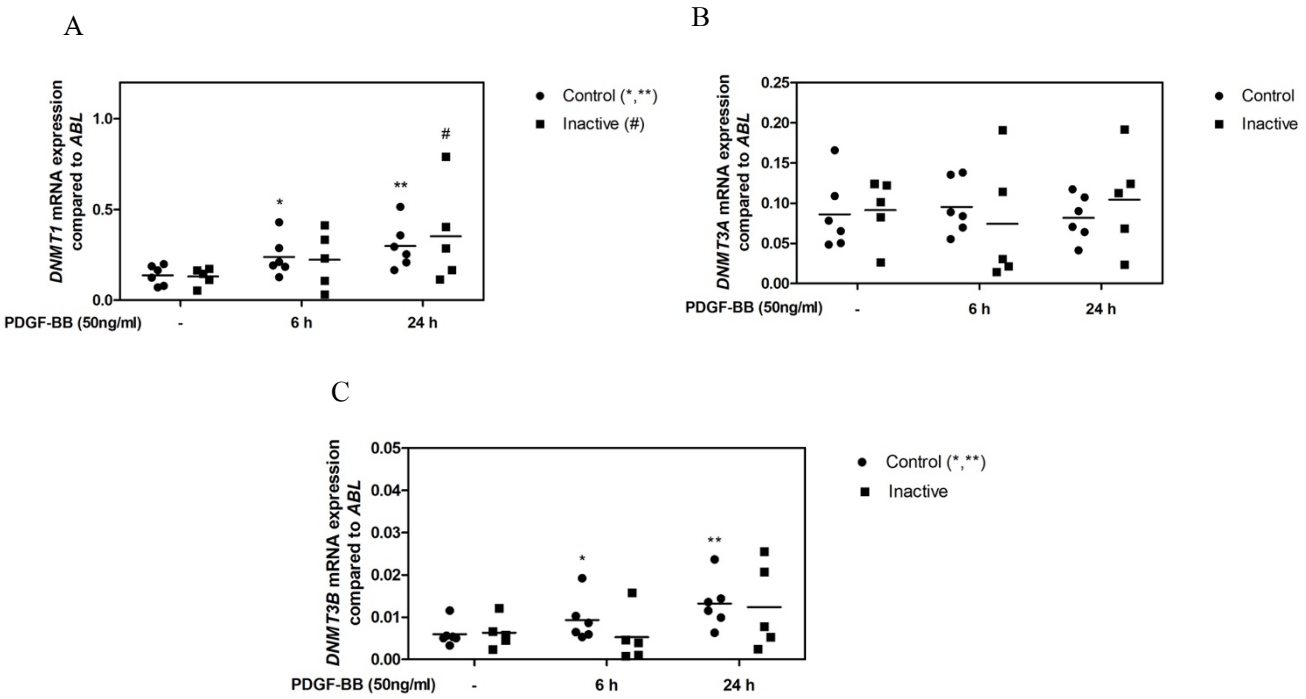

Figure 2. (A) *DNMT1* mRNA expression. (B) *DNMT3A* mRNA expression. (C) *DNMT3B* mRNA expression expression in healthy control and inactive GO orbital fibroblasts in the presence of PDGF-BB (50 ng/ml) for 6 and 24 hours. Each symbol represents individual orbital fibroblast from each patients and bar graph showed mean value. * as $p<0.05$ and ** as $p<0.01$ compared to unstimulated condition in control group, while # as $p<0.05$ compared to unstimulated condition in inactive GO group.

The effects of decitabine (DNMT inhibitor) on cell cytotoxicity and cell proliferation

To investigate the role of DNMTs on orbital fibroblasts activation, decitabine was used in the experiments. Firstly, orbital fibroblasts from inactive GO (n = 3-5) were treated with various concentration of decitabine (2.5, 5, 10, and 15 μM). %Cell cytotoxicity was accessed by LDH assay, and no cytotoxicity were observed (Figure 3A). Next, %proliferation was investigated by MTT assay. Decitabine at 10 μM and 15 μM significantly decreased basal proliferation, while 2.5 μM and 5 μM did not affect basal proliferation (Figure 3B). As PDGF-BB can increase cell proliferation [25], the effects of decitabine to decrease cell proliferation in presence of PDGF-BB (50 ng/ml) were investigated by MTT assay. 2.5 μM and 5 μM of decitabine significantly decrease %cell proliferation ($p<0.01$ and $p<0.001$, respectively) to the basal level (Figure 3C). These data suggested that 2.5 μM and 5 μM of decitabine was not toxic and significantly decreased cell proliferation. Therefore, decitabine at 2.5 μM was used in further experiments.

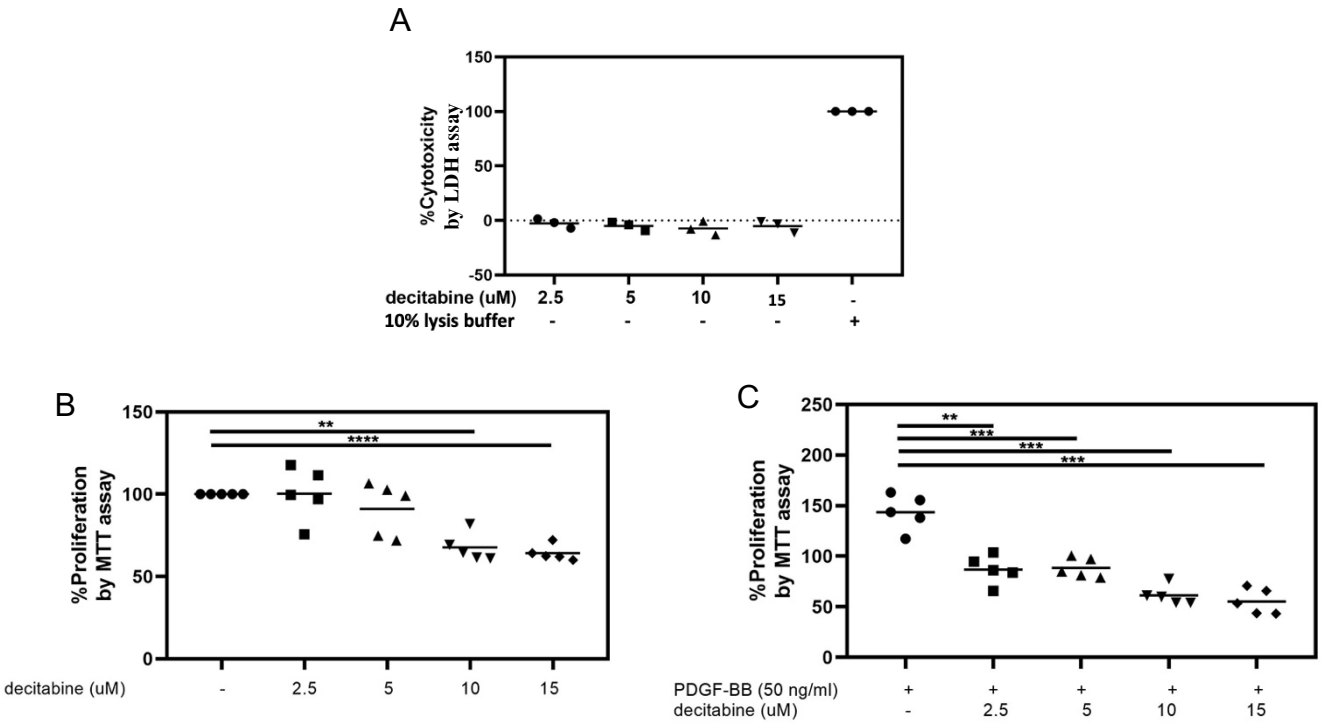

Figure 3. The effects of decitabine on cell cytotoxicity and cell proliferation. (A) %Cell cytotoxicity of orbital fibroblasts treated with various concentration of decitabine (2.5, 5, 10, and 15 μM) measured by LDH assay. 100% indicates the highest cytotoxicity. (B) %Cell proliferation of orbital fibroblasts treated with decitabine measured by MTT assay. (C) %Cell proliferation of orbital fibroblasts treated with decitabine in presence of PDGF-BB (50 ng/ml) measured by MTT assay. 100% indicates basal cell numbers from unstimulated condition. Each symbol represents individual orbital fibroblast from each inactive GO patients and horizontal bar represents mean.

The effects of decitabine (DNMTs inhibitor) on *TSHR* mRNA expression

To obtain the role of DNA methyltransferases on *TSHR* expression, inactive GO orbital fibroblasts (n = 5) were used to treat with 2.5 μM decitabine for 24 hours and cells were subsequently stimulated with 50 ng/ml PDGF-BB for another 24 hours in the presence of decitabine. PDGF-BB significantly increased *TSHR* mRNA expression ($p<0.05$) and decitabine in presence of PDGF-BB significantly decreased *TSHR* mRNA expression ($p<0.05$) (Figure 4). This data suggested that DNA methyltransferases regulate *TSHR* expression in orbital fibroblasts.

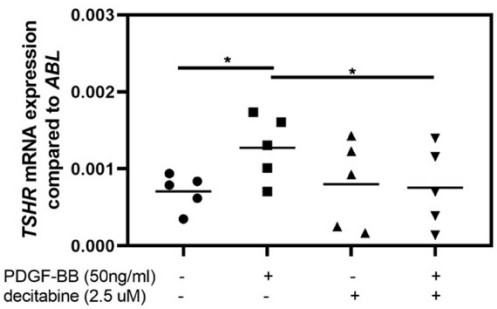

Figure 4. The effect of decitabine on *TSHR* mRNA expression. Each symbol represents individual orbital fibroblast from each inactive GO patients and horizontal bar represents mean.

The effects of decitabine (DNMTs inhibitor) on IL-6 and hyaluronan production

Next, the effect of decitabine on PDGF-BB-induced IL-6 and hyaluronan production by orbital fibroblasts were investigated by ELISA. To examine the maximum inhibitory effect of decitabine on IL-6 and hyaluronan production, 15 μM decitabine was used to pretreated orbital fibroblasts (n = 5) for 24 hours and subsequently stimulated with PDGF-BB (50 ng/ml) in the presence of decitabine. Decitabine did not affect IL-6 and hyaluronan production by orbital fibroblast (Figure 5).

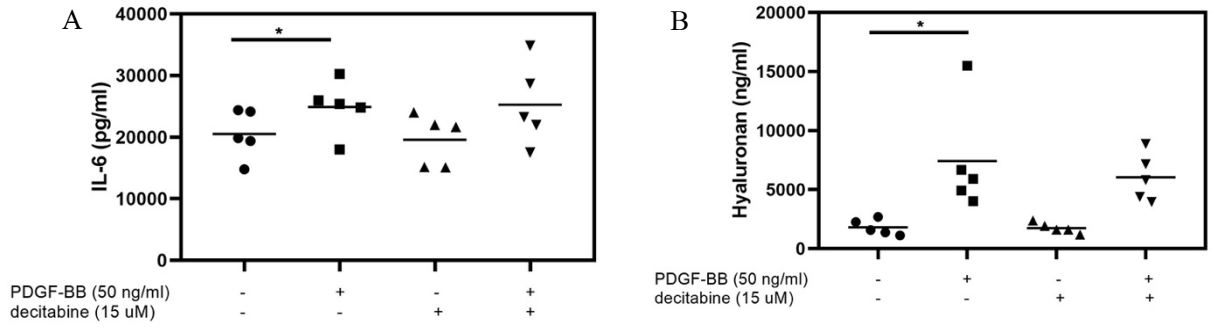

Figure 5. The effects of decitabine on (A) IL-6 and (B) hyaluronan production by orbital fibroblasts. Each symbol represents individual orbital fibroblasts from each inactive GO patient. The horizontal bar represents mean.

Conclusion:

Our current data suggest the involvement of DNMTs in regulating PDGF-BB-induced cell proliferation and autoantigen *(TSHR*) mRNA expression, but not IL-6 and hyaluronan production in orbital fibroblasts from GO patients. Gene depletion experiments of DNMTs are required to confirm the mechanism of DNMTs in orbital fibroblasts activation. Moreover, *ex vivo* experiments of decitabine treatment in orbital tissues also require which might lead to the new approach of GO therapy.

Acknowledgements:

This work (Grant No. RGNS 64-019) was supported by Office of the Permanent Secretary, Ministry of Higher Education, Science, Research and Innovation (OPS MHESI), Thailand Science Research and Innovation (TSRI), The 72nd anniversary of his Majesty King Bhumibol Adulyadej, and Research assistance scholarship, Chulalongkorn university, Thailand

References:

1. Smith, T.J. and J. Janssen, *Insulin-like Growth Factor-I Receptor and Thyroid-Associated Ophthalmopathy.* Endocr Rev, 2019. **40**(1): p. 236-267.
2. Bahn, R.S., *Graves' ophthalmopathy.* N Engl J Med, 2010. **362**(8): p. 726-38.
3. Taylor, P.N., et al., *New insights into the pathogenesis and nonsurgical management of Graves orbitopathy.* Nat Rev Endocrinol, 2020. **16**(2): p. 104-116.
4. van Steensel, L., et al., *PDGF enhances orbital fibroblast responses to TSHR stimulating autoantibodies in Graves' ophthalmopathy patients.* J Clin Endocrinol Metab, 2012. **97**(6): p. E944-53.
5. Smith, T.J., L. Hegedus, and R.S. Douglas, *Role of insulin-like growth factor-1 (IGF-1) pathway in the pathogenesis of Graves' orbitopathy.* Best Pract Res Clin Endocrinol Metab, 2012. **26**(3): p. 291-302.
6. Dik, W.A., S. Virakul, and L. van Steensel, *Current perspectives on the role of orbital fibroblasts in the pathogenesis of Graves' ophthalmopathy.* Exp Eye Res, 2016. **142**: p. 83-91.
7. Valyasevi, R.W., et al., *Differentiation of human orbital preadipocyte fibroblasts induces expression of functional thyrotropin receptor.* J Clin Endocrinol Metab, 1999. **84**(7): p. 2557-62.
8. Virakul, S., et al., *Platelet-derived growth factor: a key factor in the pathogenesis of graves' ophthalmopathy and potential target for treatment.* Eur Thyroid J, 2014. **3**(4): p. 217-26.
9. Virakul, S., et al., *Platelet-Derived Growth Factor-BB Enhances Adipogenesis in Orbital Fibroblasts.* Invest Ophthalmol Vis Sci, 2015. **56**(9): p. 5457-64.
10. Weiler, D.L., *Thyroid eye disease: a review.* Clin Exp Optom, 2017. **100**(1): p. 20-25.
11. Bartalena, L., et al., *Management of Graves' hyperthyroidism: present and future.* Expert Rev Endocrinol Metab, 2022. **17**(2): p. 153-166.
12. Hwang, J.L. and R.E. Weiss, *Steroid-induced diabetes: a clinical and molecular approach to understanding and treatment.* Diabetes Metab Res Rev, 2014. **30**(2): p. 96-102.
13. Elia, G., et al., *Precision Medicine in Graves' Disease and Ophthalmopathy.* Front Pharmacol, 2021. **12**: p. 754386.
14. Douglas, R.S., et al., *Teprotumumab for the Treatment of Active Thyroid Eye Disease.* N Engl J Med, 2020. **382**(4): p. 341-352.

15. Wang, B., et al., *The Emerging Role of Epigenetics in Autoimmune Thyroid Diseases.* Front Immunol, 2017. **8**: p. 396.
16. Meng, H., et al., *DNA methylation, its mediators and genome integrity.* Int J Biol Sci, 2015. **11**(5): p. 604-17.
17. Jurkowska, R.Z., T.P. Jurkowski, and A. Jeltsch, *Structure and function of mammalian DNA methyltransferases.* Chembiochem, 2011. **12**(2): p. 206-22.
18. Illum, L.R.H., et al., *DNA methylation in epigenetic inheritance of metabolic diseases through the male germ line.* J Mol Endocrinol, 2018. **60**(2): p. R39-R56.
19. Rajasekar, P., J. Patel, and R.L. Clifford, *DNA Methylation of Fibroblast Phenotypes and Contributions to Lung Fibrosis.* Cells, 2021. **10**(8): p.1977.
20. Bian, E.B., et al., *DNA methylation: new therapeutic implications for hepatic fibrosis.* Cell Signal, 2013. **25**(1): p. 355-8.
21. Yang, Q., et al., *Alcohol promotes renal fibrosis by activating Nox2/4-mediated DNA methylation of Smad7.* Clin Sci (Lond), 2020. **134**(2): p. 103-122.
22. Virakul, S., et al., *Integrative Analysis of Proteomics and DNA Methylation in Orbital Fibroblasts From Graves' Ophthalmopathy.* Front Endocrinol (Lausanne), 2020. **11**: p. 619989.
23. Rotondo Dottore, G., et al., *Genetic Profiling of Orbital Fibroblasts from Patients with Graves' Orbitopathy.* J Clin Endocrinol Metab, 2021. **106**(5): p. e2176-e2190.
24. Virakul, S., et al., *Basic FGF and PDGF-BB synergistically stimulate hyaluronan and IL-6 production by orbital fibroblasts.* Mol Cell Endocrinol, 2016. **433**: p. 94-104.
25. Ekronarongchai, S., et al., *Histone Deacetylase 4 Controls Extracellular Matrix Production in Orbital Fibroblasts from Graves' Ophthalmopathy Patients.* Thyroid, 2021. **31**(10): p. 1566-1576.

ANTIBACTERIAL ACTIVITY OF ALLICIN AGAINST PATHOGENS CAUSING BACTERIAL MENINGITIS

Kankawi Satsantitham, Nawarat Nantapong, Nuannoi Chudapongse, Oratai Weeranantanapan*
School of Preclinical Sciences, Institute of Science, Suranaree University of Technology, Nakhon Ratchasima 30000, Thailand
*e-mail: oratai@g.sut.ac.th

Abstract:

Bacterial meningitis is a life-threatening disease that occurs when the pathogens can penetrate the blood-brain barrier (BBB) and cause inflammation of the meninges. Allicin, a major active compound derived from garlic (*Allium sativum*), exhibits antibacterial activity against a wide range of bacteria, including some of the meningitis pathogens. There are studies suggesting that allicin may be able to pass the BBB. The objective of this study is to investigate the antibacterial activity against pathogens causing bacterial meningitis. The broth microdilution method was used to investigate the antibacterial activity of allicin against tested bacterial pathogens. The results revealed that the minimum inhibitory concentration (MIC) values of allicin against *Neisseria meningitidis* ATCC13090 DMST7950, *Listeria monocytogenes* DMST20093, *Escherichia coli* TISTR780, *E. coli* O157:H7 DMST12743, and methicillin-resistant *Staphylococcus aureus* (MRSA) DMST20654 were 3, 30, 25, 25, and 15 µg/ml, respectively. According to the range of tested allicin concentrations, the results demonstrated that the minimum bactericidal concentration (MBC) value of allicin against *N. meningitidis* was 4 µg/ml. Our findings demonstrated for the first time that allicin exhibited antibacterial activity against the most common meningitis bacterium, *N. meningitidis,* with low MIC and MBC values, suggesting that allicin could be beneficial for the treatment of meningitis caused by *N. meningitidis*.

Introduction:

Bacterial meningitis is one of the serious, life-threatening brain infections, which occurs when there is an inflammation of the membrane (meninges) surrounding the brain and spinal cord caused by bacterial infection[1]. Generally, the common pathogens causing meningitis could be bacteria (bacterial meningitis) or viruses (viral meningitis). In most cases, viral meningitis is considered to be the least deadly meningitis form compared to bacterial meningitis due to its mild symptoms and no significant long-term sequelae after recovery[2]. On the other hand, bacterial meningitis is a significant cause of infection-related deaths. Over 1.2 million cases of bacterial meningitis are estimated to occur worldwide each year[3]. The incidence and mortality rates vary by age group, pathogen, region, country, immune status, and vaccination programs. The mortality rates can reach 70% if the patients have been left without treatment[4]. Moreover, long-term sequelae such as neuron degeneration and permanent damage of the visual and hearing systems were found in 10-20% of the bacterial meningitis survivors[5]. The most common pathogens of bacterial meningitis are *N. meningitidis*, *L. monocytogenes*, *Streptococcus pneumoniae*, and *Haemophilus influenzae*[6]. Other bacteria that occasionally cause bacterial meningitis could be *E. coli*, *Streptococcus agalactiae* (Group B streptococcus; GSB), *Pseudomonas aeruginosa*, *Klebsiella pneumoniae*, and MRSA[4,7]. The pathogenesis of bacterial meningitis begins with the colonization of the pathogens within the host nasopharynx or other less common routes (e.g., the spreading from sinusitis and mastoiditis area, skull fracture, or ventricular shunts). Then, the bacterial

pathogens invade the bloodstream and replicate themselves within the blood to a high level, resulting in bacteremia[1,8]. The central nervous system (CNS) has the BBB to strictly control the passage of substances from the blood into the brain and shield the CNS from toxins and pathogens circulating within the blood[9]. The penetration of some bacterial pathogens across the BBB induces inflammation, BBB disruption, and recruitment of blood-borne neutrophils into the CNS (pleocytosis), which leads to meningitis progression[8].

Allicin is a principal active compound of freshly crushed garlic (*Allium sativum*). Previous studies have revealed that allicin possesses a wide range of biological properties, which are anti-inflammatory[10], antihypertensive[11], anticancer[12], and antimicrobial activities[13]. Due to the multiple inhibitory effects of allicin on the various thiol-dependent enzymatic system, allicin exhibits a broad spectrum of antibacterial activity against Gram-negative and Gram-positive bacteria including species of *Escherichia*, *Salmonella*, *Klebsiella*, *Proteus*, *Bacillus*, *Streptococcus*, *Staphylococcus,* and some of the meningitis bacteria, such as *L. monocytogenes*, MDR (multi-drug resistant) and non-MDR *S. pneumoniae*, and *N. meningitidis*[13-16]. Recently, Itepu et al. have constructed the 2D structure of allicin and its modified molecule to examine their ability to penetrate BBB by using the SwissADME server. The study showed that allicin is predicted to possess the ability for BBB penetration[17]. Moreover, the neuroprotective effects of allicin on ischemia-reperfusion brain injury (IRBI) in mice has been reported, leading to the presumption that allicin may be able to pass BBB[18]. According to the broad-spectrum antibacterial activity of allicin and the possibility that allicin might be able to pass the BBB, this study aims to investigate the antibacterial activity against pathogens causing bacterial meningitis.

Methodology:

Bacterial strains

The MRSA DMST20654, *E. coli* TISTR780, *E. coli* O157:H7 DMST12743, and the most common meningitis pathogens, including *L. monocytogenes* DMST20093 and *N. meningitidis* ATCC13090 DMST7950 were purchased from the culture collection of the Department of Medical Sciences Thailand (DMST) and Thailand Institute of Scientific and Technological Research (TISTR). The most common meningitis pathogens were cultured on Tryptic soy agar (TSA) plates, and other strains were cultured on Mueller Hinton agar (MHA) plates at 37°C for 24 h for daily use and stored in the broth along with 40% glycerol at -80°C for subsequent uses. Tryptic soy broth (TSB) and Mueller Hinton broth (MHB) were purchased from Himedia (India). The media were sterilized by autoclaving at 121°C for 20 min before being used in the experiments.

Allicin

Allicin (purity >98%) was purchased from Abcam (USA). The stock solution of allicin (1 mg/ml) was prepared by dissolving in absolute ethanol (RCI Labscan, Thailand). Then, the stock allicin was aliquot and stored at -20°C until used. The new aliquot of stock allicin was used in the individual experiment.

Minimum inhibitory concentration (MIC) assay

The antibacterial activity of allicin against bacterial pathogens was examined to determine the minimum inhibitory concentration (MIC) using the broth microdilution method following the Clinical Laboratory Standards Institute (CLSI, 2012) guidelines and Wiegand et al.[19] The broth microdilution test was performed in sterile 96-well microtiter plates (Corning, China). Briefly, bacterium was streaked onto an appropriate culture medium agar and incubated at 37°C for 24 h. The colonies were selected and transferred to an appropriate culture medium broth. The bacterial cell turbidity was measured spectrophotometrically. The

absorbance was adjusted into the same range as 0.5 McFarland standard (OD_{625} nm approximately at 0.08–0.13) by diluting with broth. Then, diluted the inoculum 1:100 in broth and transferred 50 µl of the bacterial suspension into a 96-well microplate containing 50 µl of allicin at concentration ranging from 0.5 to 50 µg/ml. The final inoculum density was approximately 5 x 10^5 CFU/ml. Positive growth control was filled with 50 µl of broth and 50 µl of the bacterial suspension. Negative growth control was filled with 100 µl of broth. The experiments were repeated in triplicate. Afterward, the plates were incubated at 37°C for 20-24 h. After incubation, the lowest concentration of allicin that inhibits the visible growth of the bacterial pathogens was determined as MIC value.

Minimum bactericidal concentration (MBC) assay

Determination of minimum bactericidal concentration (MBC) was performed following Reiter et al.[15] Ten microliters of culture from wells with no visible growth in the MIC plate were pipetted onto either MHA or TSA plate and incubated at 37°C overnight. The lowest concentration without bacterial growth on the agar medium was determined as the MBC value.

Results and Discussion:

MIC values of allicin against bacterial pathogens

The results showed that MIC values of allicin ranged from 3 to 30 µg/ml. Allicin exhibited the strongest antibacterial activity against *N. meningitidis* ATCC13090 DMST7950 with the MIC value of 3 µg/ml. The weakest antibacterial activity of allicin was observed against *L. monocytogenes* DMST20093 with the MIC value of 30 µg/ml (Table 1). These results revealed that *N. meningitidis* was the most sensitive pathogen to allicin.

Table 1. The MIC values of allicin against bacterial pathogens.

Bacterial pathogens	MICs (µg/ml)[a]
N. meningitidis ATCC13090 DMST7950	3
L. monocytogenes DMST20093	30
E. coli TISTR780	25
E. coli O157:H7 DMST12743	25
MRSA DMST20654	15

[a] Each value was obtained from n=3 experiments

According to the evidence that allicin exhibited a broad spectrum of antibacterial activity against Gram-positive and Gram-negative bacteria including some of the meningitis pathogens[13-16]. In this study, the antibacterial activity of allicin was investigated against two of the most common meningitis bacteria, which are *N. meningitidis* and *L. monocytogenes*, and other bacteria occasionally being as causative pathogens for bacterial meningitis. *E. coli* is regularly found as a cause of meningitis among neonates, infants, the elderly, and immunocompromised people[4]. MRSA rarely causes bacterial meningitis, but the symptoms could be severe and lead to death. MRSA meningitis occurred in patients who received recent neurosurgery or acquired cerebrospinal fluid (CSF) devices[7]. The previous study has been reported that MIC values of allicin against *E. coli* and *L. monocytogenes* were 32 and 64 µg/ml, respectively[14], whereas our obtained results showed the lower MICs in *E. coli* (25 µg/ml), *E. coli* O157:H7 (25 µg/ml) and *L. monocytogenes* (30 µg/ml). According to this finding, our study could define the MIC value more precisely because the tested concentration of allicin was in a range of 0.5-50 µg/ml, while their study used 2-fold serial dilutions of allicin in a range of 2-1,024 µg/ml. Cutler and Wilson have investigated the effect of allicin against 30 clinical isolates of MRSA and revealed that 88% of strains had

MICs at 16 µg/ml, and all strains were inhibited at 32 µg/ml[20]. In comparison to our study, the obtained result showed the correlated MICs of allicin against MRSA at 15 µg/ml in most tested strains. The previous study revealed that allicin has enormous inhibitory activity against *N. meningitidis*[16]. However, there is no available report of MIC value of allicin against *N. meningitidis*. Therefore, our study provided the first evidence that the MIC value of allicin against *N. meningitidis* was 3 µg/ml.

MBC values of allicin against bacterial pathogens

MBC value of allicin against *N. meningitidis* was 4 µg/ml. Our results also showed that the MBC values of allicin against *L. monocytogenes* and MRSA were >50 and >25 µg/ml, respectively due to the highest concentrations of allicin that were used to test with *L. monocytogenes* and MRSA were 50 and 25 µg/ml (Table 2). Compared with previous studies which reported that the MBC values of allicin against *L. monocytogenes* and MRSA were 1,024 and 128-256 µg/ml, respectively, our results showed a similar trend to these previous studies[14,20]. Although our study did not determine the MBC values of allicin against *E. coli* and *E. coli* O157:H7, the previous study reported that the MBC value of allicin against *E. coli* was 64 µg/ml[14]. According to the effect of allicin on the cell viability of human cerebral microvascular endothelial cell line hCMEC/D3, which is the brain endothelial cells of BBB, our results from the MTT assay revealed that the MBC values of allicin against *L. monocytogenes*, MRSA, and *E. coli* were much higher than the non-toxicity concentrations of allicin on hCMEC/D3 cells (data not shown). These findings suggested that allicin might have a low potential for the treatment of meningitis caused by *L. monocytogenes*, MRSA, and *E. coli*. However, the MBC value of allicin against *N. meningitidis*, which is the leading cause of bacterial meningitis, was in a range of non-toxicity concentrations of allicin on hCMEC/D3 cells. Therefore, allicin might be beneficial for the treatment of meningitis caused by *N. meningitidis*.

Table 2. The MBC values of allicin against bacterial pathogens.

Bacterial pathogens	MBCs (µg/ml)[a]
N. meningitidis ATCC13090 DMST7950	4
L. monocytogenes DMST20093	>50
E. coli TISTR780	n.d.
E. coli O157:H7 DMST12743	n.d.
MRSA DMST20654	>25

[a] Each value was obtained from n=3 experiments
n.d.: not determined

The Gram-negative *N. meningitidis* is a significant cause of bacterial meningitis worldwide with high morbidity and mortality[21]. There are several antibiotics used for the treatment of meningitis caused by *N. meningitidis*, such as cephalosporins: cefotaxime or ceftriaxone, penicillin G, ampicillin, and chloramphenicol[22]. According to the results from this study, allicin inhibited growth and killed *N. meningitidis* with low MIC and MBC values compared to other tested pathogens. Moreover, there was a previous study revealed that allicin has a synergistic effect with chloramphenicol against *Mycobacterium tuberculosis*[23]. Thus, allicin might have the potential to synergize with chloramphenicol for the treatment of *N. meningitidis*-caused meningitis. Therefore, in case allicin is proved to be able to cross the BBB, it will be beneficial for the treatment of meningitis caused by *N. meningitidis*.

Conclusion:

The results of our study demonstrated that *N. meningitidis* was the most sensitive pathogen to allicin among the tested pathogens. Moreover, our study is the first to report MIC and MBC values of allicin against the most common meningitis bacteria, *N. meningitidis*. For further study, the direct prove of the ability of allicin to cross BBB should be studied in order to propose allicin as a therapeutic candidate for the treatment of *N. meningitidis*-causing meningitis.

Acknowledgements:

This research was financially supported by the One Research One Grant (OROG) scholarship. We also gratefully acknowledge to School of Preclinical Sciences, Institute of Science, Suranaree University of Technology, Thailand, for the facility supporting in this work.

References:

1. Kim KS. Nat Rev Neurosci. 2003;4(5):376-385.
2. Hoffman O, Weber RJ. Ther Adv Neurol Disord. 2009;2(6):1-7.
3. Borchorst S, Moller K. Acta Anaesthesiol Scand. 2012;56(10):1210-1221.
4. Ekizoğlu M. Nanotechnol Methods Neurol Dis Brain Tumors. 2017;291-315.
5. Edmond K, Clark A, Korczak VS, Sanderson C, Griffiths UK, Rudan I. Lancet Infect Dis. 2010;10(5):317-328.
6. Van de Beek D, de Gans J, Tunkel AR, Wijdicks EF. N Engl J Med. 2006;354(1):44-53.
7. Pintado V, Pazos R, Jime´nez-Mejı´as ME, Rodrı´guez-Guardado A, Gil A, Garcı´a-Lechuz JM, Cabellos C, Chaves F, Domingo P, Ramos A, Pe´rez-Cecilia E, Domingo D. Medicine (Baltimore). 2012;91:10-17.
8. Agyeman P, Grandgirard D, Leib SL. Springer Nature. 2017;213–252.
9. Abbott NJ, Patabendige AA, Dolman DE, Yusof SR, Begley DJ. Neurobiol Dis. 2010;37(1):13-25.
10. Alam RTM, Fawzi EM, Alkhalf MI, Alansari WS, Aleya L, Abdel-Daim MM. Oxid Med Cell Longev. 2018;1780956.
11. Borlinghaus J, Albrecht F, Gruhlke MC, Nwachukwu ID, Slusarenko AJ. Molecules. 2014;19(8):12591-12618.
12. Oommen S, Anto RJ, Srinivas G, Karunagaran D. Eur J Pharmacol. 2004;485(1-3):97-103.
13. Ankri S, Mirelman D. Microbes Infect. 1999;1(2):125-129.
14. Imani Rad H, Arzanlou M, Ranjbar Omid M, Ravaji S, Peeri Doghaheh H. J. Funct. Foods. 2017;28:321-325.
15. Reiter J, Levina N, Linden MV, Gruhlke M, Martin C, Slusarenko AJ. Molecules. 2017;22(10):1711.
16. Shrivastava A, Garg HK. World J Pharm Res. 2015;4(12):1052-1056.
17. Itepu VE, Umezinwa OJ, Ilukho FA, Collins DA, Cosmas S. AJRB. 2019;5(3):1-7.
18. Kong X, Gong S, Su L, Li C, Kong Y. Oncotarget. 2017;8(61):104492-104507.
19. Wiegand I, Hilpert K, Hancock REW. Nat Protoc. 2008;3(2):163-175.
20. Cutler RR, Wilson P. J Biomed Sci. 2004;61(2):71-74.
21. Rouphael NG, Stephens DS. Methods Mol Biol. 2012;799:1-20.
22. Tunkel AR, Hartman BJ, Kaplan SL, Kaufman BA, Roos KL, Scheld WM, Whitley RJ. Clin Infect Dis. 2004;39(9):1267-1284.
23. Gupta KC, Viswanathan R. Antibiot Chemother (Northfield). 1955;5(1):24-27.

EFFECT OF BIOACTIVE COMPOUNDS FROM *Eurycoma longifolia* Jack. ON ANTI-INVASIVE ACTIVITY IN HUMAN NON-SMALL CELL LUNG CANCER CELLS

Pratchayanon Soddaen,[1, 2] Jirarat Karinchai,[2] Arisa Imsumran,[2] Pornsiri Pichakarn,[2] Ariyaphong Wongnoppavich[2,*]

[1]Graduate/M.Sc. Program in Biochemistry, Faculty of Medicine, Chiang Mai University
[2]Department of Biochemistry, Faculty of Medicine, Chiang Mai University, Chiang Mai, Thailand
*e-mail: ariyaphong.w@cmu.ac.th

Abstract

Non-small cell lung cancer (NSCLC) is the predominant form of lung cancer. About 40% of diagnosed NSCLC cases are metastatic cancers. Migration and invasion are essential steps for cancer progression. Inhibition of these processes effectively attenuates the metastasis of cancer. Eurycomalactone (ECL) and Eurycomanone (ECN) are major compounds found in the root extract of *Eurycoma longifolia* Jack. Both have potent cytotoxic activity against various carcinoma cell lines including human NSCLC cells and they can inactivate the NF κB signaling pathway. Yet, whether ECL and ECN inhibit cancer cell migration and/or invasion in NSCLC cells remains unknown. Therefore, this study aims to investigate the anti-invasive effect of ECL and ECN. In this study, TGF-β1 was used to promote cell migration and invasion of human NSCLC cells, Calu-1. ECL showed higher cytotoxicity to Calu-1 than ECN. Using the wound-healing assay, TGF-β1 enhanced cancer cell migration, but only ECN could significantly reduce this effect. In addition, the non-toxic doses of ECN could suppress TGF-β1-induced cell invasion through Matrigel by significantly decreasing the secretion of matrix metalloproteases-2 (MMP-2). Therefore, this study has provided evidence on the application of ECN as an alternative therapy for metastatic NSCLC.

Introduction

Lung cancer is still the most diagnosed cancer and is often detected in the late stage whereby cancer cells spread and form the secondary tumor in distant organs, leading to the cause of cancer death[1]. Non-small cell lung cancer (NSCLC) is the most predominant form of lung cancer. About 40% of diagnosed NSCLC cases acquire metastatic cancers[2]. The metastatic process is the dissemination of cancer cells which require invasive capacities allowing them to migrate and invade to leave their primary tumor. Induction of cellular motility and enzymatic degradation of the extracellular matrix (ECM) using protease enzymes such as matrix metalloproteinases (MMPs) are necessary for cancer cell migration and invasion through degraded ECM before they entry into the circulatory system and/or spread (metastasize) to areas outside the local tissue through the bloodstream or the lymph system[3]. The development of chemopreventive agents is needed to prevent or reduce the migration and invasion of cancer cells to inhibit the initiating process of cancer metastasis. Recently, effective medicinal plant compounds and their extract have been actively investigated to target these processes as potential adjuvant therapy in the treatment of metastatic cancer.

Eurycoma longifolia Jack. is a popular medicinal plant used in traditional medicine in Southeast Asia. Mostly, the root of *E. longifolia* is used as a folk medicine for sexual dysfunction, malaria, diabetes, anxiety and also used as an appetite stimulant and health supplement[4, 5]. *E. longifolia* has been reported that rich in many bioactive compounds such as quassinoids, alkaloids, triterpene tirucallane type, squalene derivatives, and bioactive steroids.

Among these phytochemicals, quassinoids (C-18, C-19, C-20) are account for a major compound of the *E. longifolia* root phytochemicals, including various types of Eurycomanone (pasakbumin-A), Eurycomanols and Eurycomalactones types. Several studies have reported many bioactivities of quassinoid compounds such as antimalarial, antimicrobial, anti-inflammation, antidiabetic, and strong anticancer activities[5, 6]. Eurycomalactone (ECL) and Eurycomanone (ECN) are C-19 and C-20 quassinoids, respectively are found as major constituents in the root of this plant. ECN showed lower cytotoxic effect against tested cancer cell lines compared to ECL[6, 7]. However, both ECL and ECN are potent cytotoxic against various carcinoma cell lines such as human lung cancer cell line (A549), human breast cancer cells (MCF-7), B16-BL6 melanoma and human hepatocarcinoma cells (HepG2)[6-8]. ECL inactivates the AKT/NF-κB signaling pathway, leading to the induction of cancer cell apoptosis, and it can improve the chemosensitivity to cisplatin in the human NSCLC cells, A-549 and Calu-1[9]. ECL also exhibited a potent alternative radiosensitizer for increasing the radiation therapy efficiency against the human NSCLC[10]. Similarly, ECN has the potential to be developed as a co-chemotherapeutic agent for Doxorubicin by synergically increasing the cytotoxic effect through cell death induction on both MCF-7 and T47D human breast cancer cells[11]. However, it is unknown the anti-invasive effect of ECL and ECN in human cancer. Thus, this study aims to investigate whether ECL and ECN inhibit cell migration and invasion in human NSCLC cells.

Methodology

Chemicals and reagents

ECL and ECN were commercially obtained from Chengdu Biopurify Phytochemicals Ltd. and was dissolved in dimethyl sulfoxide (DMSO) for using in all experiments. Culture media Roswell Park Memorial Institute (RPMI)-1640 were purchased from Thermo Fisher Scientific, Inc. Fetal bovine serum (FBS) was purchased from GE Healthcare Life Sciences. MTT (3-[4,5-dimethylthiazol-2-yl]-2,5 diphenyl tetrazolium bromide) was obtained from AppliChem GmbH.

Cell line and cell culture

The human NSCLC cell line, Calu-1 was obtained from the Cell Lines Service (CLS), Germany. They were cultured in RPMI-1640 medium supplemented with 10% FBS, 1% glutamine, and 1% penicillin-streptomycin at 37°C in a humidified atmosphere containing 5% CO_2.

MTT assay

Cells were cultured in 96-well plates and tested with various concentrations of ECL or ECN for 24 h. After that, MTT dye solution was added to each well at 0.5 mg/mL, and incubated at 37ºC for 4 h. Finally, all solutions were removed and DMSO was added to dissolve the formazan crystal. The optical density (OD) of the violet solution was spectrophotometrically measured at 540 and 630 nm using a microplate reader. A percentage of cell viability was calculated. The non-toxic concentrations ($\leq IC_{20}$) on NSCLC cells were selected for further experiments.

Wound healing assay

Cells were cultured in 6-well plates until they reached about 90-100% confluence. Next, one linear wound was scraped in each well with a 200 µl sterile pipette tip, and cells were washed with PBS to remove the unattached cells. Then, cells were co-treated with or without TGF-β1-ECL or TGF-β1-ECN in serum-free media for 24 h. Images of the wound area were

captured at 0 and 24 h under an inverted microscope. The gap area was determined using the Image J program and the migration percentage was calculated.

Gelatin zymography assay

Conditional media was collected after the treatment of Calu-1 cells co-treated with or without TGF-β1-ECL or TGF-β1-ECN. An equal amount of protein was separated on an 8% SDS-PAGE gel containing 0.1% (w/v) gelatin under nonreducing conditions for 2 h. Then, the gel was washed in a solution containing 2.5% (v/v) Triton X-100 for 30 min with a constant shaking condition. After that, gels were incubated in activation buffer for the enzymatic reaction for 24 h. Next, gels were stained with Coomassie blue solution for 30 min and further incubated in a de-staining buffer. Zones of gelatinolytic activity were detected as clear bands against a blue background.

Matrigel transwell invasion assay

Cell invasion was evaluated using an 8-µm pore size transwell chamber coated with matrigel. Briefly, 50 µl matrigel was coated on the membrane at the base of the transwell chamber and air-dried. Then, Calu-1 cells suspended in serum-free media with or without TGF-β1-ECN were placed into the upper layer of the transwell chamber at a concentration of 2×10^4 cells/well and cultured for 24 h. The medium of 5% FBS was added to the lower layer of the transwell chamber. The invading cells were fixed with 100% EtOH for 5 min whereas the non-invading cells were gently removed. Then, cells were stained with 0.5% crystal violet in 20% MeOH for 30 min and rinsed with PBS buffer to remove excess dye. Finally, five random fields in each treatment were selected. The number of invading cells were counted and the invasion percentage was calculated.

Statistical Analysis

All values are given as mean ± standard derivation (X ± SD) from triplicate samples of three independent experiments. Overall differences among the treatment groups were determined using one-way analysis of variance (ANOVA), followed by Tukey test by Prism 3.0 software.
P values < 0.05 are regarded as significant.

Results and Discussion

Cytotoxicity of ECL and ECN on NSCLC cells

To determine the cytotoxicity of ECL and ECN on NSCLC cells using an MTT assay, the cell viability of Calu-1 was tested with various concentrations of ECL (0-20 µM) or ECN (0-30 µM) for 24 h. As shown in Fig.1A and 1B, the inhibitory concentration of 20% of cell viability (IC_{20}) of ECL and ECN were approximately 2.5 and 15 µM, respectively, suggesting that the cytotoxic effect of ECL is more potent than that of ECN in Calu-1 cells. In line with a previous study, among isolated quassinoids from the *E. longifolia* roots, ECL showed the most potent anticancer activity against all tested cancer cell lines[6, 7]. Nonetheless, ECN also showed potent cytotoxic activity against various carcinoma cell lines including human lung cancer cell line (A549)[7]. These prompted us to investigate the other anticancer effect such as anti-metastatic activity. Then, the non-toxic concentrations ($\leq IC_{20}$) of ECL and ECN were selected for further experiment.

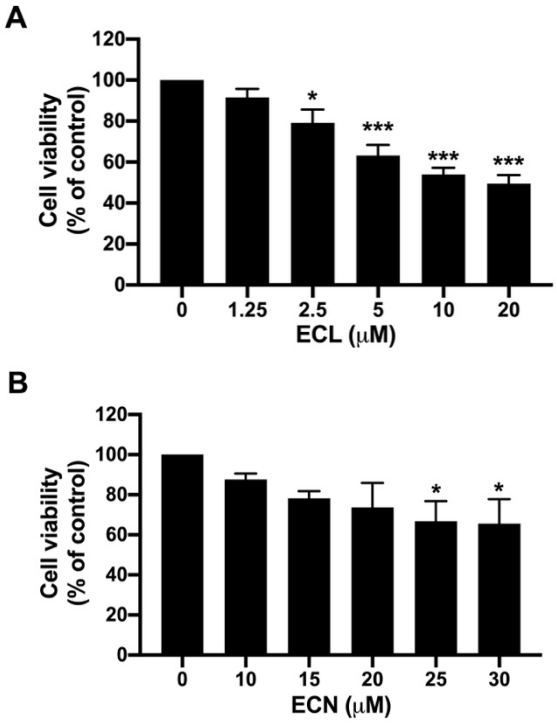

Figure 1.
The cytotoxicity of ECL and ECN on NSCLC. Calu-1 cells were treated with various doses of (A) ECL or (B) ECN for 24 h and the cell viability was determined using an MTT assay. *$p<0.05$, **$p<0.01$, ***$p<0.001$ vs. the non-treated control.

The effects of ECL and ECN on TGF-β1-induced NSCLC cell migration and MMP-2 secretion.

Transforming growth factor-beta 1 (TGF-β1) is one of important cytokines that plays a role in both normal physiological condition as well as in cancer progression. Cancer cells respond to TGF-β1 to undergo epithelial-mesenchymal transition (EMT) process and later achieve the increasing in ability of migration, production and secretion of protease enzymes such as MMP-2 and MMP-9 which participate in the degradation of ECM components, including the basement membrane and cell surface during cancer metastasis, resulting in cancer cells invade and migrate through extracellular matrix into the near tissue[12,13, 14].

We next pre-evaluated the effect of ECL and ECN on TGF-β1-induced cell migration and the secretion of MMP-2, one of the protease enzymes secreted by cancer cell itself to degrade the gelatin substrate in ECM. The wound-healing assay displayed that TGF-β1 can promote cell migration. Interestingly, ECL did not inhibit TGF-β1-induced migration (Fig.2A) while ECN visibly reduced this effect of TGF-β1 (Fig.2B). As shown by gelatin zymography assay, TGF-β1 increased the secretion of MMP-2 from Calu-1 cells. Like the above result, the secretion of MMP-2 was noticeably decreased by ECN (Fig.2D) while ECL had little or no effect (Fig.2C). Thus, ECN was further investigated anti-invasive activity in the next experiment.

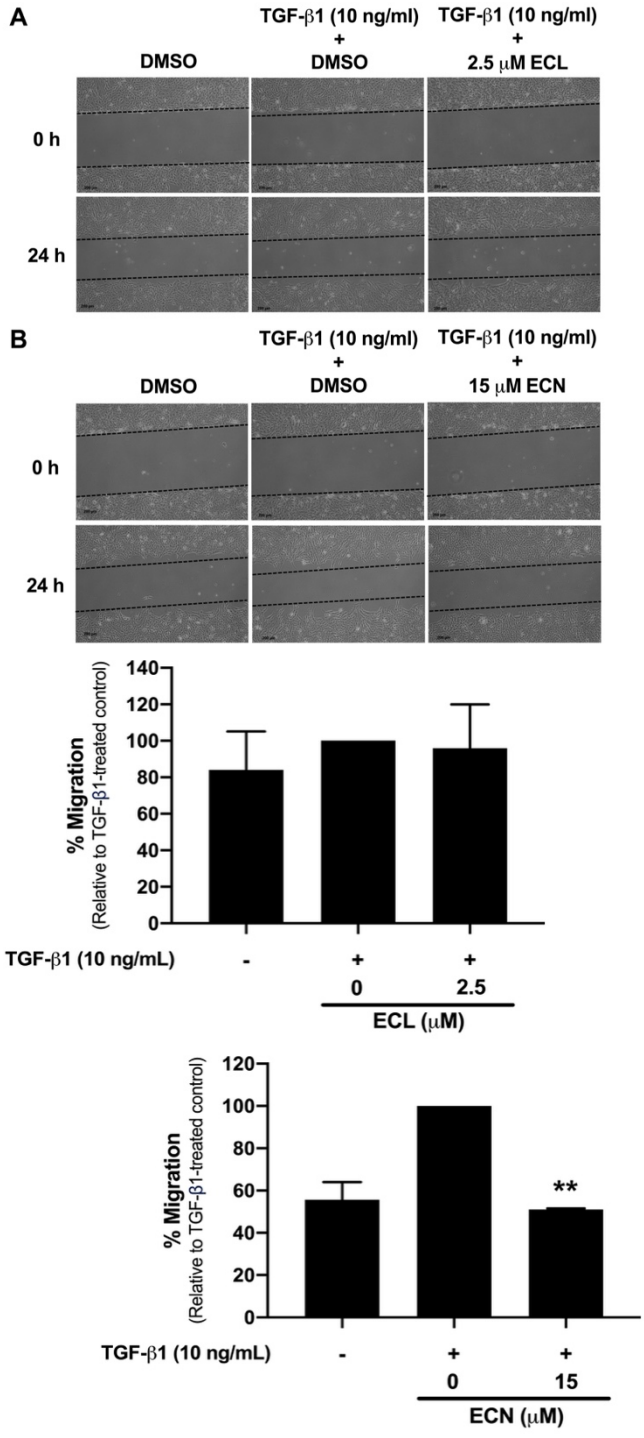
A
TGF-β1 (10 ng/ml) + DMSO
TGF-β1 (10 ng/ml) + 2.5 μM ECL
DMSO
0 h
24 h
B
TGF-β1 (10 ng/ml) + DMSO
TGF-β1 (10 ng/ml) + 15 μM ECN
DMSO
0 h
24 h
% Migration
(Relative to TGF-β1-treated control)
140
120
100
80
60
40
20
0
TGF-β1 (10 ng/mL) - + +
0 2.5
ECL (μM)
% Migration
(Relative to TGF-β1-treated control)
120
100
80
60
40
20
0
**
TGF-β1 (10 ng/mL) - + +
0 15
ECN (μM)

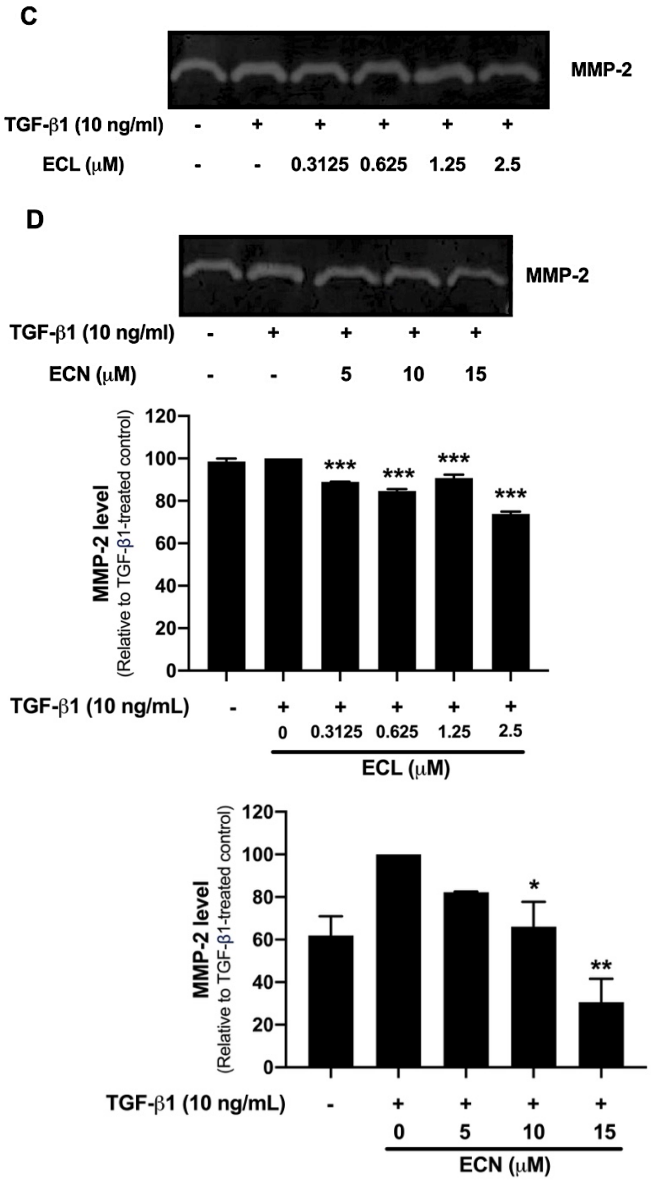

Figure 2.

The effect of ECL and ECN on TGF-β1-induced Calu-1 cell migration was determined by a wound-healing assay (A and B) and TGF-β1-induced MMP-2 secretion was determined by a gelatin zymography assay (C and D). **p<0.05, **p<0.01, ***p<0.001* vs. the TGF-β1-treated control.

The effect of ECN on TGF-β1-induced Calu-1 cell invasion

The induction of cellular motility and the ability of cancer cells that can degrade the ECM using proteases lead to the invasion of cancer cells through degraded ECM[15]. We last examine whether ECN reduces TGF-β1-induced invasion of Calu-1 cells. Our findings using the Matrigel transwell invasion assay showed that TGF-β1 highly promoted Calu-1 cell invasion, but this effect was visibly suppressed by ECN as shown in Fig.3.

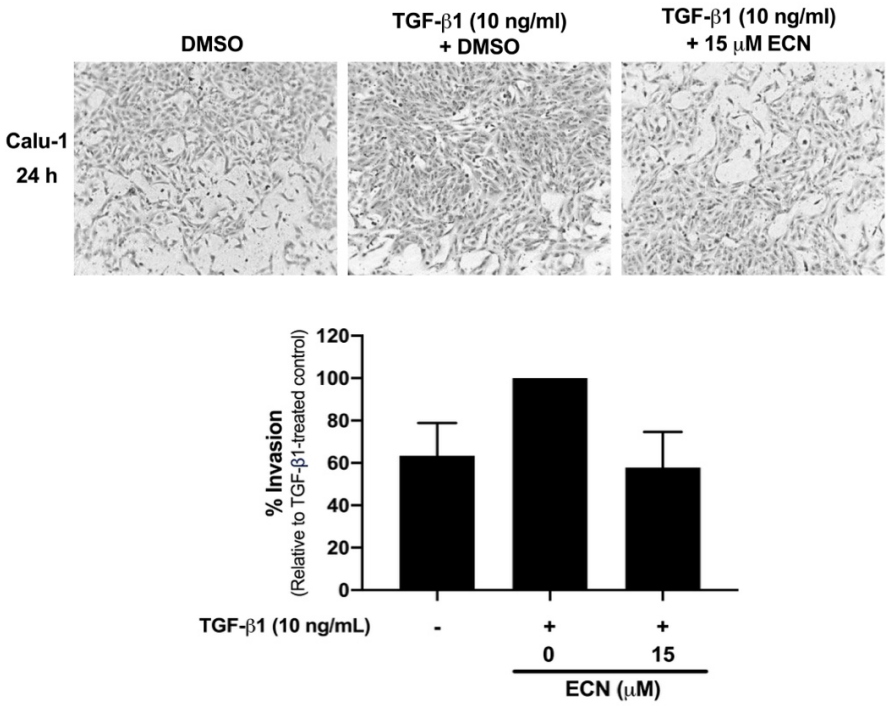

Figure 3.
The effect of ECN on TGF-β1-induced Calu-1 cell invasion was determined by the Matrigel transwell invasion assay.

The TGF-β signaling pathway has a central role in promoting cell growth and proliferation as well as cell invasion and motility in various cancer including NSCLC[16]. The downstream signal transduction of TGF-β can be divided into smad pathway (TGF-β/smad) and non-smad pathway (such as PI3K/Akt and NF-κB signaling) which cooperate to induce the epithelial-mesenchymal transition (EMT) program in cancer cell[17]. NF-kB signaling especially mediates the induction of EMT and then promotes an invasive phenotype of cancer. Many previous studies showed some effective medicinal plant compounds that inhibit NF-κB signaling can reduce the invasiveness of cancer cells via blocking the EMT process[18, 19]. ECN has been demonstrated that it can inactivate the NF-κB signaling pathway[20]. Hence, one of the mechanisms by which ECN suppressed the invasive properties of NSCLC cells might be through inhibition of the NF-κB signaling pathway. Furthermore, ECN may further inhibit the EMT program leading to the reduction in TGF-β1-induced migration and invasion of NSCLC cells. Nonetheless, the effect of ECN through the directly TGF-β/smad pathway remains unknown. Therefore, the molecular mechanism for suppression of the invasive properties of NSCLC cells by ECN will be investigated in future studies.

Conclusion

In summary, ECN suppressed the TGF-β1-induced NSCLC cell invasion by decreasing the matrix metalloproteases-2 (MMP-2) secretion and migration of cancer cells. This study has provided evidence on the anti-invasive activity of ECN for inhibiting NSCLC cancer metastasis or the use as potential adjuvant therapy for metastatic cancer.

Acknowledgement

This work was supported by Faculty of Medicine Research Fund, Chiang Mai University, (Grant No. 068-2565)

References

1. Walters S, Maringe C, Coleman MP, Peake MD, Butler J, Young N, et al. Thorax. 2013;68(6):551-64.
2. Ramalingam S, Belani C. Oncologist. 2008;13 Suppl 1:5-13.
3. Hecht I, Bar-El Y, Balmer F, Natan S, Tsarfaty I, Schweitzer F, et al. Sci Rep. 2015;5:10622.
4. Rehman SU, Choe K, Yoo HH. Molecules. 2016;21(3):331.
5. Bhat R, Karim AA. Fitoterapia. 2010;81(7):669-79.
6. Miyake K, Li F, Tezuka Y, Awale S, Kadota S. Nat Prod Commun. 2010;5(7):1009-12.
7. Kuo PC, Damu AG, Lee KH, Wu TS. Bioorg Med Chem. 2004;12(3):537-44.
8. Zakaria Y, Rahmat A, Pihie AHL, Abdullah NR, Houghton PJ. Cancer Cell. 2009;9(1):16.
9. Dukaew N, Chairatvit K, Pitchakarn P, Imsumran A, Karinchai J, Tuntiwechapikul W,
et al. Oncol Rep. 2020;44(4):1441-54.
10. Dukaew N, Konishi T, Chairatvit K, Autsavapromporn N, Soonthornchareonnon N, Wongnoppavich A. Oncol Res. 2020;28(2):161-75.
11. Yusuf H, Satria D, Suryawati S, Fahriani M. Syst Rev Pharm. 2020;11:335-41.
12. Syed V. J Cell Biochem. 2016;117(6):1279-87.
13. Itoh Y, Nagase H. Essays Biochem. 2002;38:21-36.
14. Gialeli C, Theocharis AD, Karamanos NK. Febs j. 2011;278(1):16-27.
15. Kirfel G, Rigort A, Borm B, Herzog V. Eur J Cell Biol. 2004;83(11-12):717-24.
16. Chen T, Zhu J, Cai T, Du W, Zhang Y, Zhu Q, et al. J Cancer. 2019;10(24):6014-24.
17. Dongre A, Weinberg RA. Nat Rev Mol Cell Biol. 2019;20(2):69-84.
18. Li W, Jiang Z, Xiao X, Wang Z, Wu Z, Ma Q, et al. Int J Oncol. 2018;52(5):1593-602.
19. Zhang L, Chen WX, Li LL, Cao YZ, Geng YD, Feng XJ, et al. Front Pharmacol. 2020;11:572616.
20. Hajjouli S, Chateauvieux S, Teiten MH, Orlikova B, Schumacher M, Dicato M, et al. Molecules. 2014;19(9):14649-66.

Session C:
CHEMISTRY (Analytical Chemistry)

NON-ENZYMATIC ELECTROCHEMICAL SENSOR FOR CREATININE DETECTION BASED ON POROUS COPPER FOAM AND GRAPHENE OXIDE MODIFIED ELECTRODE

Natcha Rasitanon, Natha Nontipichet, Apon Numnuam, Panote Thavarungkul, Proespichaya Kanatharana, Suntisak Khumngern*
Center of Excellence for Trace Analysis and Biosensor and Division of Physical Science, Faculty of Science, Prince of Songkla University, Hat Yai, Songkhla 90110, Thailand
*e-mail: flukesuntisak@hotmail.com

Abstract:

A glassy carbon electrode (GCE) was modified with graphene oxide (GO) to support the electrodeposition of porous copper (Cu) foam. The modified electrode was used to create a non-enzymatic electrochemical sensor to detect creatinine (Cr), which is a byproduct of phosphocreatine metabolism in muscles. Cr is eliminated by the kidneys via urine, therefore certain levels of Cr in urine can indicate chronic renal disease. The detection of Cr by the proposed sensor is enabled by the formation of a soluble Cu-Cr complex. The porosity of Cu foam enhanced the accessibility of active sites and the passage of ions, and the large surface area of GO allowed a large amount of Cu foam to be electrodeposited. The surface morphology of the modified electrode was studied with scanning electron microscopy (SEM). Cyclic voltammetry (CV) and linear sweep voltammetry (LSV) were used to study the electrocatalytic activity of Cr on the sensor and analytical performances. Under optimum conditions, the developed sensor showed a linear range of 5.0–600 µM with a detection limit of 3.12 µM. The method exhibited good reproducibility (RSD < 6%) and was devoid of interferences from uric acid, glucose, ascorbic acid, and dopamine. The developed sensor determined Cr in real human serum and urine samples with good recoveries.

Introduction:

Creatinine (2-Amino-1-methyl-2-imidazolin-4-one; Cr) is a byproduct of the metabolism of creatine, which is a molecule of major importance for energy production in muscles. Cr is filtered from the bloodstream by the kidneys in relatively constant amounts every day.[1] The normal physiological levels of Cr are 40−150 µM in blood serum and 1–27 mM in urine.[2] However, increased Cr levels can lead to kidney, thyroid, and muscular disorders. Therefore, the measurement of Cr levels is essential for clinical diagnosis and monitoring of patients who need peritoneal dialysis.[3]

In general, the conventional method applied for Cr detection is a spectrophotometric technique which involves the conversion of Cr by the Jaffe reaction into an orange-colored product.[3] Unfortunately, the reaction can be disrupted by various interferences normally found in blood, including uric acid (UA), dopamine (DA), glucose (Glu), and ascorbic acid (AA). In clinical analysis, biomedical analyzers are used to detect the urinary albumin to creatinine ratio (ACR). In this method, Cr is quantified by an enzymatic colorimetric technique using multiple enzymes to produce colored products. This technique is costly, time-consuming, and requires operational expertise.[4]

Cr has also been detected by electroanalytical methods, which are typically, but not always, highly sensitive, simple and rapid, and reduce costs.[5] For example, a Cr sensor based on direct electro-oxidation requires a complicated procedure to selectively determine Cr.[6] A simpler and more effective sensor could be developed but electrocatalytic performances have to be maximized. Electrode modification is a critical consideration and analytical performances can be enhanced by graphene oxide (GO). GO has a large surface area with good conductivity that promotes electron transfer. It can also be used as a supporting material for a catalyst. The electrode would present more electrocatalytic sites and by enabling a uniform dispersion of catalyst, GO can effectively improve catalytic efficiency.[7]

Electroanalytical performances have also been improved by micro/nanostructures such as nanorods, nanoflowers, and dendritic and porous structures.[8-10] Porous structures facilitate and increase catalytic efficiency toward analytes and metal-based porous structures have been successfully employed in various applications. In electrochemical sensing, their large specific surface area and good electrical conductivity are especially useful.[10, 11] Porous Cu foam is a three-dimensional metal structure that can be easily synthesized by electrodeposition. It has good electrocatalytic properties, high porosity, and large specific surface area, all of which can play important roles in the electrocatalytic oxidation of Cr. Transition metals are interesting materials in electrochemical applications and the transition metal ion Cu(II) can form complexes with Cr in its main tautomeric form by creating bioligands with donor groups of Cr.[12]

In the present work, an electrochemical sensor based on a Cu foam/GO-modified electrode was developed to detect Cr. The highly porous Cu foam enhanced the surface area available for catalysis. Sensor sensitivity was improved by the excellent conductivity and large surface area of GO. Affecting parameters were studied to achieve the highest sensitivity. The analytical performances of the sensor were then evaluated by analyzing Cr in real urine and serum samples.

Methodology:

Materials and Reagents

All chemical reagents were used without any further purification. Copper (II) sulfate pentahydrate ($CuSO_4 \cdot 5H_2O$) was purchased from Scharlau Chemie S.A. (Sentmenat, Spain). Sulfuric acid (H_2SO_4) was provided by RCI Labscan (Bangkok, Thailand). Dopamine hydrochloride (DA), potassium ferrocyanide, L-ascorbic acid (AA), D-(+)-glucose, urea, graphene oxide (GO) and creatinine (Cr) were purchased from Sigma-Aldrich (St. Louis, USA). Potassium dihydrogen phosphate (≥98%), di-potassium hydrogen phosphate anhydrous (≥98%) were from Ajax Finechem (Sydney, Australia). All aqueous solutions were prepared with deionized water.

Apparatus

Electrochemical experiments were carried out using the Autolab PGSTAT302N (Metrohm Autolab B.V., the Netherlands) controlled with NOVA 2.1 software. The electrochemical cell consisted of a three-electrode system with a glassy carbon electrode (GCE) as the working electrode, a platinum rod counter electrode, and a silver/silver chloride reference electrode (in 3M KCl). Surface morphology was studied with a scanning electron microscope (SEM, Quanta 400, FEI, Japan).

Electrode fabrication

Prior to modification, the GCE was polished with 1.0 and 0.3 µm alumina powders and ultrasonically washed with DI water and ethanol. After that, 3.0 µL of a 1.0 mg mL^{-1} GO dispersion was dropped onto the GCE and dried at room temperature. The modification of the GO/GCE with Cu foam was achieved by the electrodeposition of 0.30 M $CuSO_4$ in 0.50 M H_2SO_4 solution for 5 seconds at a constant potential of −0.30 V. The electrodeposition of Cu generated hydrogen bubbles, which created the foam. Then, the modified electrode was carefully rinsed with DI water and dried. A simple illustration of the fabrication process is shown in Figure 1.

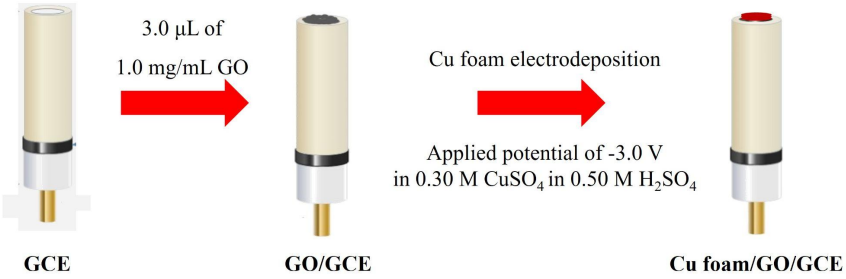

Figure 1. The fabrication of the Cu foam/GO modified GCE.

Electrochemical detection of Cr

Cyclic voltammetry (CV) was conducted to characterize the electrodes at each step of modification. CV was performed at a scan rate of 100 mV s^{-1}. The electrochemical detection of Cr was carried out by linear sweep voltammetry (LSV) at a scan rate of 100 mV s^{-1} in a potential range of -0.50 to 0.75 V. All electrochemical measurements were performed in 0.10 M phosphate buffer solution at pH 7.00

Results and discussion:

Surface morphology of the modified electrode

An SEM image of the surface of the bare GCE (Figure 2A) shows the smooth surface of the electrode. After deposition of GO, a planar sheet-like structure of GO flakes was formed which greatly increased the surface area of the modified electrode (Figure 2B). A three-dimensional porous foam-like structure can be seen on the Cu foam/GO/GCE (Figure 2C). The structure was formed by the hydrogen evolution reaction that occurred during the electrodeposition of Cu. The hydrogen bubbles acted as a porous template for Cu^{2+} reduction. As a result, the Cu foam developed a porosity that greatly increased the surface area of the electrochemical interface. The expanded interface allows more Cu-Cr complex to be formed and thus helps to amplify the detection signal.

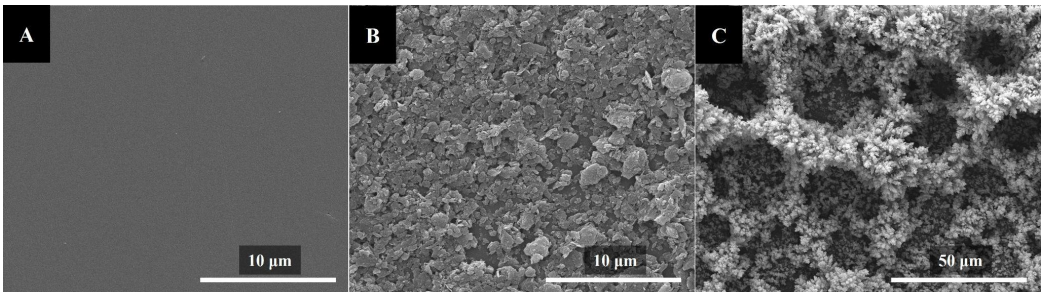

Figure 2. SEM images are of (A) bare GCE at 5000× magnification, (B) GO/GCE at 5000× magnification, and (C) Cu foam/GO/GCE at 1000× magnification.

Electrochemical characteristics of the modified electrode

The CV responses of the bare GCE and various modified electrodes were recorded in 0.10 M phosphate buffer solution (pH 7.0) (Figure 3A). No redox peaks were produced at the bare GCE **(curve a)** and GO/GCE **(curve b)**. At the Cu foam/GCE, a pair of redox peaks of porous Cu foam were produced **(curve c)** and these peaks were significantly increased at the Cu foam/GO/GCE **(curve d)**. The increase was due to the excellent conductivity and large surface area of GO.

The electrochemical behavior of the Cu foam/GO/GCE towards Cr detection was also evaluated using CV in 0.10 M phosphate buffer solution (pH 7.0). The oxidation peak current increased in the presence of 100 µM Cr (Figure 3B) due to the increased conversion of Cu to Cu-Cr. Porous Cu foam is a copper ion source, and when the electrode was oxidized, the generated Cu^{2+} chelated with the Cr, facilitating the formation of the soluble Cu-Cr complex. The Cu-Cr complex enabled the electrocatalytic oxidation of Cr, producing a signal. The behavior of the Cu foam/GCE towards Cr detection was also evaluated for comparison (Figure 3C). The higher response of the Cu foam/GO/GCE towards Cr was a result of the higher loading of Cu foam supported by the GO substrate compared to the GCE substrate. The higher loading of Cu foam enhanced the electrocatalytic oxidation of Cr. No responses toward Cr were observed at the bare GCE and GO/GCE (data not shown).

The kinetics governing the electrochemical behavior of Cr on the modified electrode were investigated by exploring the relationship between scan rate and peak current during the electrocatalytic oxidation of Cr. CV was performed at different scan rates from 10 to 300 mV s^{-1} in 0.10 M PBS containing 100 µM Cr (Figure 3D). The increments in anodic and cathodic peak currents were linearly proportional to the square root of the scan rate (Figure 3D, inset). This indicated that the electrochemical kinetics were controlled by the diffusion of Cr onto the electrode surface.

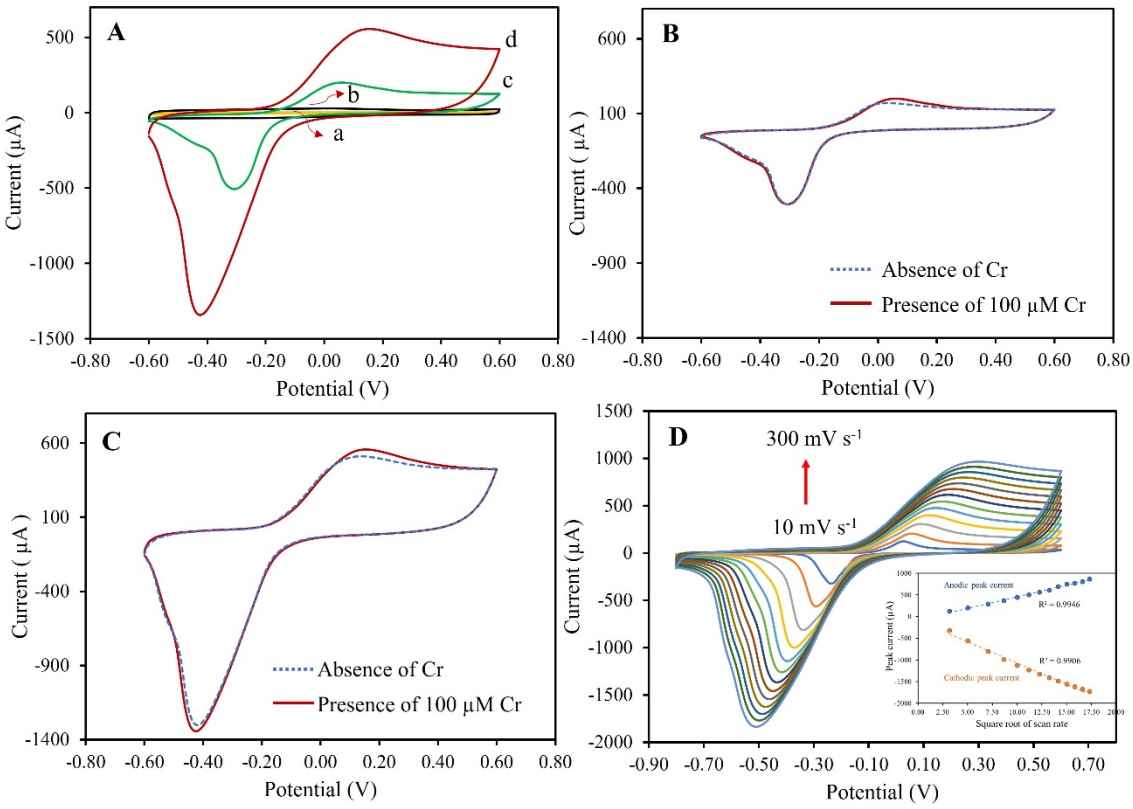

Figure 3. CVs were produced at the (a) bare GCE, (b) GO/GCE, (c) Cu foam/GCE and (d) Cu foam/GO/GCE in 0.10 M phosphate buffer solution (PBS) at pH 7.0 containing 100 µM Cr (A). The inset shows the relationship between peak current and the square root of the scan rate. CVs of the Cu foam/GCE (B) and the Cu foam/GO/GCE (C) were produced in the absence (dash line) and the presence (solid line) of 100 µM Cr. CVs of the sensor were produced at scan rates of 10, 25, 50, 75, 100, 125, 150, 200, 225, 250, 275 and 300 mV s^{-1} in 0.10 M PBS (pH 7.00) containing 100 µM Cr (D).

Optimizations

In order to improve the electrocatalytic properties of the Cu foam/GO/GCE towards Cr oxidation, certain experimental parameters were optimized. The thickness of the porous Cu foam on the GO/GCE was affected by the electrodeposition time, therefore electrodeposition time was optimized. Also, the pH of the supporting electrolyte has an important effect on the determination of an analyte due to its influence on the charge on the electrode surface and dissociation of the analyte.[13] Therefore, pH was also optimized.

The electrodeposition of 0.30 M $CuSO_4$ in 0.50 M H_2SO_4 solution was optimized for 3, 5, 7 and 10 s to fabricate a series of Cu foam/GO/GCEs. LSV was used to record the responses of the fabricated electrodes toward Cr concentrations of 25, 50, 75, 100, and 125 µM in 0.10 M phosphate buffer solution (PBS) at pH 7.0. The sensitivity of the response of

each electrode, determined from calibration curves, was then compared. The results showed that sensitivity increased with increased deposition time from 0 to 5 s, and then remained constant at deposition times longer than 5 s (Figure 4A). This behavior can be explained by considering the time-dependent development of the layer of Cu foam deposited on the electrode. The quantity of porous Cu foam on the electrode increased with time, resulting in improved electrocatalytic activity towards Cr oxidation. However, when the electrodeposition time was > 5 s, the Cu foam deposited could not integrate with the porous structure, which prevented further improvement. Thus, an electrodeposition of 5 s was selected as the optimal condition.

To investigate the effect of pH on the oxidation of the Cu-Cr complex, 100 µM Cr was detected by CV in 0.10 M of phosphate buffer solution at pH 6.0, 6.5, 7.0, 7.5 and 8.0 (Figure 4B). The oxidation of the Cu-Cr complex was best at pH 7.0 (Figure 4C). Hence, pH 7.0 was chosen as the optimal condition. The results obtained reflect the acid dissociation behavior of the Cr molecule, which has two dissociation constants (pKa_1 = 4.8 and pKa_2 = 9.2). The result implies that neutral-form Cr primarily exists in aqueous solutions at pH 7.0 [14] and is advantageous for Cr detection, since pH 7.0 is close to the pH of urine. Therefore, no pH adjustment will be required in real sample analysis.

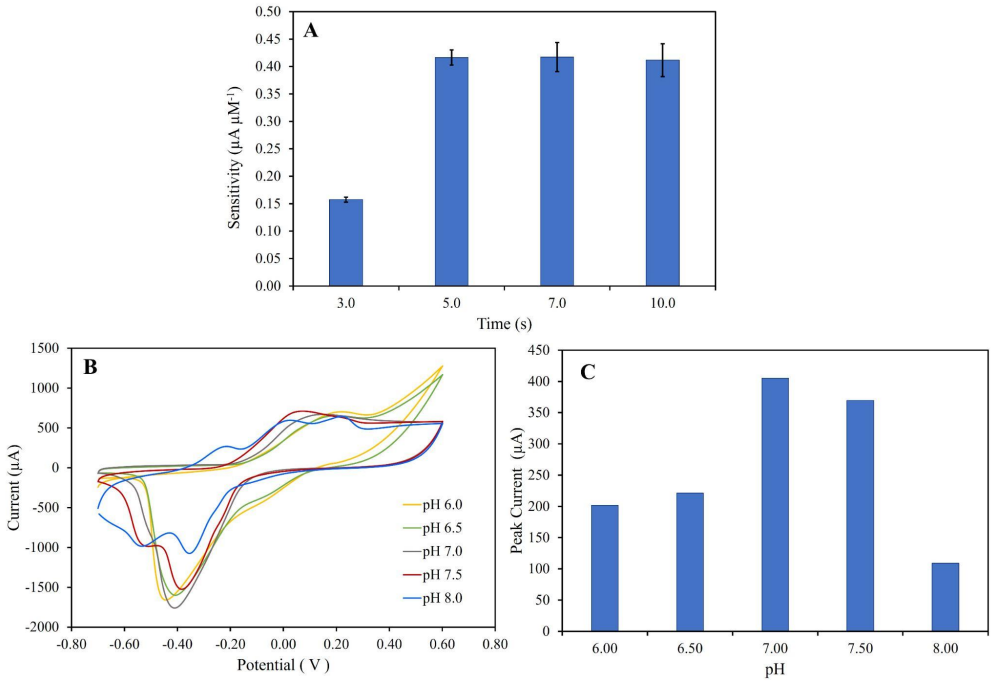

Figure 4. (A) Effect of electrodeposition time of Cu foam. (B) CV responses of Cu foam/GO/GCE on different pH of phosphate buffer solution. (C) Charts of pH versus peak current obtained from CVs.

Analytical performances

Linear range and detection limit

To investigate the analytical performances of the proposed sensor, Cr was detected by LSV under optimum conditions. The LSV responses of the Cu foam/GO/GCE increased with increments of Cr concentration (Figure 5A). The relationship between anodic peak current

change and Cr concentration was linear in the ranges of 5.0–600 µM (R^2 = 0.998) with a detection limit of 3.12 µM (3SD/m) (Figure 5B).

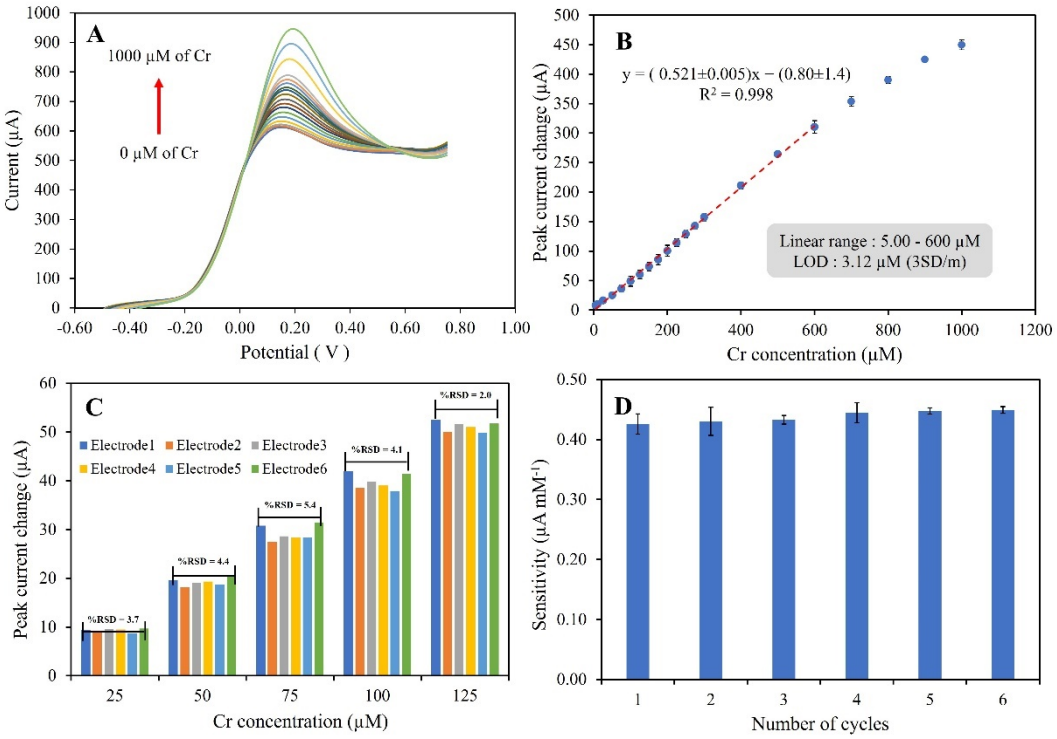

Figure 5. (A) LSV responses at the Cu foam/GO/GCE in the presence of Cr concentrations from 0 to 1000 µM. (B) The calibration curve of peak current changes against Cr concentration. Chart (C) shows the signal obtained from six fabricated electrodes and chart (D) shows the sensitivities obtained from continuous detection of Cr at 25, 50, 75, 100, and 125 µM.

Reproducibility and repeatability

The reproducibility of the electrode fabrication was examined by preparing six electrodes in the same condition to detect Cr concentrations of 25, 50, 75, 100, and 125 µM. The responses of the six electrodes toward the different concentrations were then compared. The relative standard deviations (RSDs) were 3.7, 4.4, 5.4, 4.1, and 2.0 % for 25, 50, 75, 100, and 125 µM, respectively (Figure 5C). Since RSDs were less than 6 %, the proposed method demonstrated good reproducibility.

Repeatability can be considered an important indicator of electrode stability. Repeatability was evaluated here by repeatedly detecting a series of Cr concentrations of 25, 50, 75, 100, and 125 µM with one prepared electrode. The change in sensitivity of detection was used to evaluate the electrode performance. The sensitivities obtained were not

significantly different over 6 cycles of detection (Figure 5D), which indicated that the stability of the prepared electrode was excellent for 6 cycles, or 30 individual detections.

Selectivity

The selectivity of the Cu foam/GO/GCE was investigated using common blood serum and urine interfering species, including 6.0 mM glucose (Glu), 125 µM ascorbic acid (AA), 125 µM uric acid (UA), and 65 µM dopamine (DA). The response of the proposed electrode was not significantly different toward Cr in the presence of interfering species than toward Cr alone (Figure 6). This result demonstrated that the proposed sensor could selectively measure Cr in blood serum and urine samples.

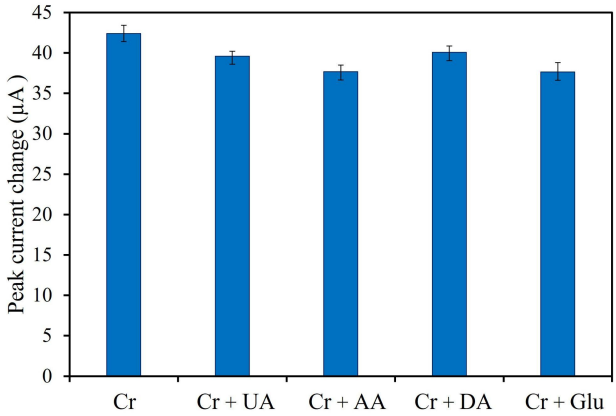

Figure 6. The chart shows the results of a selectivity study using the Cu foam/ GO/GCE in the presence of four interferences commonly found in blood serum or urine.

Recovery and clinical application of the proposed Cr sensor

The proposed sensor was applied to determine different concentrations of Cr added in human serum (diluted 10-fold) and urine (diluted 100-fold). The samples were obtained from Songklanagarin Hospital, Hat Yai, Thailand (approved by the Human Research Ethics Committee of the Faculty of Medicine, Prince of Songkla University, REC 64–591–19–9). The experimental results are shown in **Table 1**. Recoveries from urine and serum samples ranged from 98.0 to 107.8 % and from 95.7 to 108.7 %, respectively. The results indicate that the proposed Cr sensor can effectively determine Cr in real samples.

Table 1 Recovery of Cr in spiked human urine and serum samples by the proposed sensor.

Sample	Added Cr (µM)	Found (µM)	Recovery (%)
Urine	25	24.5	98.0
	100	107.8	107.8
	125	131.5	105.2
Serum	25	24.0	98.0
	100	95.7	95.7
	125	135.8	108.7

Conclusion:

A novel creatinine sensor was successfully developed based on a copper foam/graphene oxide modified electrode. The high surface area of copper foam effectively improved the catalytic oxidation of creatinine, eliminating effects from interferences present in real samples. The good conductivity and large surface area of graphene oxide helped to enhance sensitivity. The designed sensor performed well in the optimized condition, showing excellent analytical performances that included a low limit of detection, a wide linear range, and good reproducibility, repeatability, and selectivity. The developed sensor was successfully applied to measure creatinine levels in human urine and serum samples. This porous copper foam/graphene oxide modified electrode shows the potential to be developed for use in a clinical setting.

Acknowledgments:

We would like to thank the Talent Management Project of Prince of Songkla University, the Ministry of Higher Education, Science, Research and Innovation. The authors acknowledge assistance from the Development and Promotion of Science and Technology Talents (DPST) Project, Center of Excellence for Trace Analysis and Biosensor (TAB-CoE), Division of Physical Science, and Faculty of Science, Prince of Songkla University, Hat Yai, Songkhla, Thailand.

References:

1. Fekry AM, Abdel-Gawad SA, Tammam RH, Zayed MA. Measurement. 2020;163:107958.
2. Rifai N. Tietz textbook of clinical chemistry and molecular diagnostics: Elsevier Health Sciences; 2017.
3. Mohabbati-Kalejahi E, Azimirad V, Bahrami M, Ganbari A. Talanta. 2012;97:1-8.
4. Kvam C, Dworsky E, Campbell AT, Karlson JR, Jernberg E, Swensen MH, Holtlund J, Tøn H, Faaren AL, Nordhei AK, Frantzen F. Point of Care: The Journal of Near-Patient Testing & Technology. 2009;8(1):16-20.
5. Hooshmand S, Es'haghi Z. Analytica Chimica Acta. 2017;972:28-37.
6. Chen JC, Kumar AS, Chung HH, Chien SH, Kuo MC, Zen JM. Sens Actuators B. 2006;115(1):473-80.
7. Beitollai H, Safaei M, Tajik S. Int J Nano Dimens. 2019;10:125-40.
8. Tee SY, Teng CP, Ye E. Mater Sci Eng C. 2017;70:1018-30.
9. Justice Babu K, Sheet S, Lee YS, Gnana kumar G. ACS Sustain Chem Eng 2018;6(2):1909-18.
10. Huang A, He Y, Zhou Y, Zhou Y, Yang Y, Zhang J, Luo L, Mao Q, Hou D, Yang J. J Mater Sci. 2019;54(2):949-73.
11. Jin J, Zheng G, Ge Y, Deng S, Liu W, Hui G. Electrochim Acta. 2015;153:594-601.
12. Mitewa M. Coord Chem Rev. 1995;140:1-25.
13. Bukkitgar SD, Shetti NP, Kulkarni RM, Reddy KR, Shukla SS, Saji VS, Aminabhavi TM. J Electrochem Soc. 2019;166(9):B3072.

14. Khasanah M, Handajana U, Widati AA, Abdulloh A, Rindarti RR. Anal Bioanal Electrochem. 2018;10(4):429-38.

METHANOL DETECTION BY DIGITAL-IMAGE COLORIMETRY USING OPTICAL NANOPARTICLES WITH N-METHYLPOLYPYRROLE

Sophanat Khenthaphak,[1] Waranya Benhasan,[2] Orawon Chailapakul,[1] Eakkasit Punrat [2,*]
[1]Electrochemistry and Optical Spectroscopy Center of Excellence, Department of Chemistry, Faculty of Science, Chulalongkorn University, Pathumwan, Bangkok, 10330, Thailand
[2]Department of Chemistry, Faculty of Science, Ramkhamhaeng University, Bangkapi, Bangkok, 10240, Thailand
*e-mail: eakkasit.p@rumail.ru.ac.th

Abstract:
Almost of nanoparticles such as metal nanoparticles and quantum dots (QDs) has optical properties like a specific color or fluorescence. In this work, gold nanoparticles (AuNPs) and manganese-doped zinc sulfide quantum dots (Mn/ZnS-QDs) were synthesized and studied their optical properties by spectroscopy and digital-image colorimetry (DIC). AuNPs were studied their color intensity by DIC under a white light, while Mn/ZnS-QDs were studied their fluorescence intensity by DIC under a black light. The minimum concentration limits of AuNPs and Mn/ZnS-QDs which can be detected by DIC were found to be 25 and 50 mg L^{-1}, respectively. N-methypolypyrrole (NMPPy) with sodium dodecyl benzene sulfonate was added into the optical nanoparticles. It was found that NMPPy did not significantly affect the optical response of AuNPs, but Mn/ZnS-QDs with NMPPy has a lower fluorescent response under the black light than a without one. Finally, an addition of methanol into Mn/ZnS-QDs with NMPPy can slightly increase the fluorescent response. This result shows a potential of Mn/ZnS-QDs with NMPPy that can be used as an optical nanoparticle for the methanol detection by DIC, besides a naked eye.

Introduction:
Methanol is an organic chemical found in nature that accounts for about 45% of the global volume used in the energy sector for vehicles, boats, and airplanes. Moreover, methanol is used in the production of biodiesel, a fuel made from plant and animal fats, as well as in the blending of future alternative fuel sources and renewable energy sources [1]. The advantages of methanol include its usage as an antifreeze, a solvent, and a precursor for synthesis. It is also inexpensive and available in huge quantities. Therefore, methanol is required for the manufacture of industrial drugs, electronics, pesticides, fuel cells, science, and so on [2]. Due to its volatile organic compound, which can be absorbed through the skin [3] and induce nausea, headaches, abdominal pain, and severe neurological conditions that can result in blindness or death [4], methanol has drawbacks that are hazardous to humans and the environment. World Health Organization (WHO) restricts methanol concentrations in alcohol drinking to 0.2 - 1.5% (v/v).

Gas chromatography (GC) [5], high-performance liquid chromatography (HPLC) [6], spectrophotometry [7], electrochemical [8] and enzymatic technique [9] are currently popular techniques for detecting methanol. However, the disadvantages of these techniques are high operating costs and complicated procedures in a laboratory with a long analysis time. Thus, in this study, the method for methanol detection using DIC was developed to analyze color intensity of solutions. The benefits of this method are that it is simple, inexpensive, quick, and easy to analyze.

Due to their small particle size and unique properties, nanoparticles are widely employed to construct sensors. The advantage of the small size at nanoscale is that it has a large

active area and is easy to modify on the surface for reaction. It also has optical and color properties that can be observed with the naked eye. Applications of nanoparticles considering color properties such as a sensor were developed by combining lead ions with gold nanoparticles modified with gallic acid to improve the surface area of gold nanoparticles. When adding lead ions into the solution and adjusting the conditions to a pH of 4.5, it can enhance the sensitivity and selectivity for lead ions, because they can form aggregations of gold nanoparticles, which affects surface plasmon resonance properties with the limit of detection (LOD) of 10 nM lead ions [10]. Moreover, the optical properties of nanomaterials were also investigated. Ferric ion with semiconductor tin disulfide quantum dots (f-SnS_2 QDs), which have an energy band gap, can improve the optical properties by modifying the surface area with L-cysteine for quenching the optical properties of f-SnS_2 QDs (switch off). When adding ferric ions into the solution, the optical properties returned (switch on) with the LOD of 0.84 μM [11]. As a result of their high sensitivity and selectivity, nanoparticles are excellent for use as sensors.

Nowadays, polymer-nanomaterials or hybrid materials are becoming popular for modifying the surface area of nanoparticles to improve properties such as soluble polar or functional groups [12]. For example, gold nanoparticles modified with hyperbranched polyethyleneimine were researched for Cr(VI) detection in water. It was found that Cr(VI) can make the emission fluorescent of the modified gold nanoparticles quenching with high sensitivity and selectivity in the concentrations ranges of 2.8-5.9 μM and 5.9-29 μM [13]. Additionally, a lead-ion sensor using CuInS/ZnS QDs was developed, and it was reported that the sensor has higher selectivity and sensitivity to lead-ion detection by quenching the emission fluorescence of the CuInS/ZnS QDs. It can detect the lead ion in concentration range of 5-50 ppb with the LOD of 4.48 ppb [14]. Furthermore, N-methypolypyrrole (NMPPy) with nanoparticles is commonly used for methanol detection, as seen in many applications for sensors of organic chemicals such as methanol [15], picric acid [16], and 2,4,6-trinitrotoluene [17].

In this research, AuNPs and Mn/ZnS-QDs were studied and improved by the addition of NMPPy, and their optical and color properties were tested using DIC for methanol detection.

Methodology:

Chemicals and apparatus

Chloroauric acid ($HAuCl_4$) in analytical grade was purchased from Fujifilm Wako Pure Chemical Corporation (Japan). Manganese chloride ($MnCl_2$), zinc chloride ($ZnCl_2$), ammonium persulfate ($(NH_4)_2S_2O_8$), N-methylpyrrole and tris-HCl were purchased from Sigma-Aldrich (analytical grade, Germany). Sodium sulfide (Na_2S) was purchased from PanReac AppliChem ITW Reagent (technical grade, Spain). Acetonitrile (CH_3CN) and chloroform (CH_3Cl) were purchased from Merck Millipore (analytical grade, Germany). Sodium chloride (NaCl) was purchased from Ajex Chemical (analytical grade, Australia). $Na_3C_6H_5O_7$ was purchased from Fluka Guarantee (Germany) analytical grade. All working solutions were prepared and diluted by deionized water.

UV-visible spectra and fluorescence spectra were performed by a UV-visible spectrophotometer (UV-1800 spectrophotometer, Shimadzu, Japan) and fluorometer (Cary Eclipse, Agilent, USA), respectively.

Synthesis of AuNPs

Gold nanoparticles were synthesized by Turkevich method. Briefly, a 50 mL of 1 mM $HAuCl_4$ was stirred and boiled in a flask. A 3.5 mL of 1% w/v sodium citrate was added into the boiled solution. After heating for 15 min, the color of the solution changed from colorless to red-wine due to the formation of AuNPs with 2–50 nm particle size. The synthesized AuNPs solution was used in further steps.

Synthesis of Mn/ZnS-QDs

Mn/ZnS-QDs were synthesized by a chemical precipitation method. Briefly, a 10 mL of 0.5 M tri-sodium citrate, a 10 mL of 0.01 M $MnCl_2$ and a 10 mL of $ZnCl_2$ were mixed and then stirred for 10 min. After that, a 10 mL of 1.0 M Na_2S was added drop-by-drop into the mixture at 80°C for 3 hours, and then the mixture was continuously stirred for 3 hours. The solution will be a colloidal suspension of Mn/ZnS QDs. The colloidal suspension was centrifuged. The precipitates were separated and then redispersed into 40 mL of distilled water at a considered concentration.

Polymerization of NMPPy

One-hundred and three milligrams of N-methylpyrrole monomer and 53 mg of sodium dodecyl benzene sulfonate were added to 8.75 mL in a solvent containing acetonitrile and deionized water (60:40). After the solution was heated up to 60 °C, 1.25 mL of 165 mg of ammonium persulphate in acetonitrile and deionized water (60:40) was added into the solution under continuous stir at 60 °C for 7 hours; the polymerization reaction occurred. The NMPPy polymer was extracted by adding 5 mL chloroform and some NaCl. The NMPPy with dark-brown color in water phase was separated and then evaporated. The NMPPy polymer was obtained as a solid product.

Results and Discussion:

Spectroscopic properties of AuNPs and Mn/ZnS-QDs

The absorbance spectra of a solution containing 350 mg L^{-1} synthesized AuNPs was investigated using a UV-visible spectrophotometer in the range of 400 – 800 nm wavelength. It was discovered that the absorbance was higher than 1.0 au., which was an excessive value for analytical acceptance. Therefore, the AuNPs solution was diluted to clearly define it, and the results demonstrated that a concentration of 35 mg L^{-1} AuNPs was sufficient for giving the spectra with a maximum wavelength of 520 nm as shown in **Figure 1**.

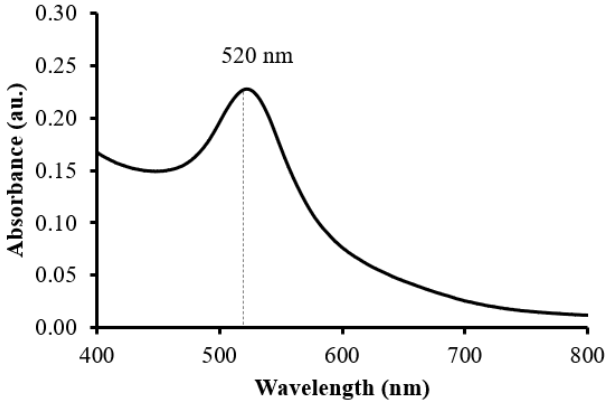

Figure 1. The absorbance spectra of a solution containing 35 mg L^{-1} AuNPs

The optical properties of Mn/ZnS-QDs were examined using a fluorometer for both an excitation wavelength and an emission wavelength. The synthesized Mn/ZnS-QDs was weighted and dissolved to be 0.1 g L^{-1} of Mn/ZnS-QDs in deionized water (DI water) using an ultrasonic bath. The excitation wavelength of the Mn/ZnS-QDs suspension was found at 312 nm. And then, the fixed excitation wavelength of 312 nm provided the emission wavelengths were 413 and 569 nm, as shown in **Figure 2**.

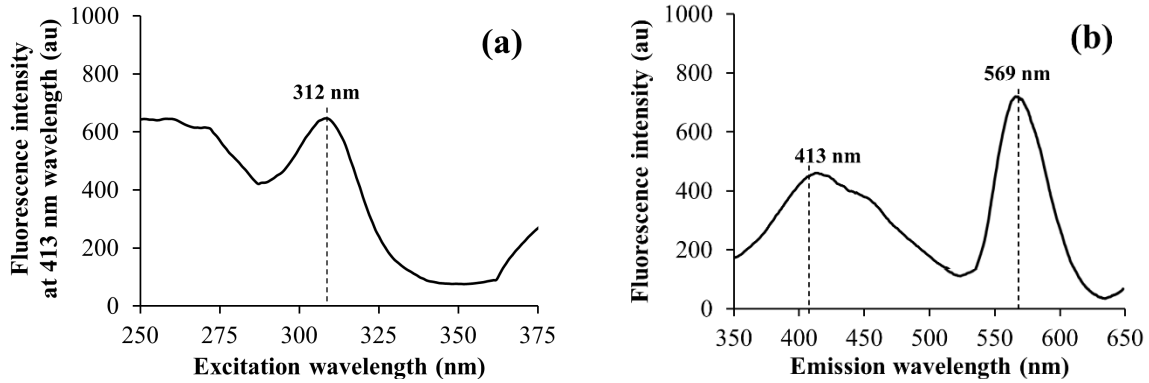

Figure 2. The optical properties of 0.1 g/L Mn/ZnS-QDs suspension in DI water: (a) The excitation spectra using a fixed emission wavelength of 413 nm, (b) The fluorescence spectra using a fixed excitation wavelength of 312 nm

DIC of AuNPs under white light

The AuNPs solutions, which is red solutions under the nature light, were diluted to concentrations of 1, 5, 10, 25, 50, 75, 100, 200, 300, and 350 mg L^{-1}. A smartphone (iPhone5, Apple, USA) was used to photograph of the AuNPs solutions for four replicates in a light box (a photographer tool). These digital photos in the smartphone were exported to a computer, and then analyzed the color intensity in gray-scale mode by the ImageJ software. The results from DIC are shown in **Table 1**.

Table 1. The color intensity in gray-scale mode of the AuNPs solutions at various concentrations analyzed by DIC using ImageJ software

Concentration of AuNPs (mg L^{-1})	Color intensity
1	120.87 ± 2.22
5	121.45 ± 6.02
10	126.34 ± 1.56
25	133.51 ± 3.60
50	143.61 ± 4.07
75	153.70 ± 1.44
100	158.36 ± 2.48
200	169.57 ± 1.68
300	177.84 ± 1.03
350	185.47 ± 0.64

The minimum concentration limit of AuNPs detected by DIC was investigated by the limit of detection method. A blank solution was analyzed for 20 replicates to find the average color intensity ($\bar{y}_{blank}$) and the standard deviation (sd). The minimum color intensity, which is significantly different from the blank (calculated by $\bar{y}_{blank}$ + 3sd), was found to be 133.5 According to **Table 1**, the minimum concentration limit of AuNPs detected by DIC that gave the color intensity more than 133.5 was found to be 25 mg L^{-1}.

DIC of Mn/ZnS-QDs under black light

The suspensions of 10, 25, 50, 75, 100, 250, 500, 750, 1000, 2000, and 3000 mg L^{-1} Mn/ZnS-QDs were studied their fluorescence intensity under black light. The suspensions presented red fluorescence under black light. The photo of each suspension was taken using the smartphone for four replicates in a black light box. After that, these photos were analyzed the fluorescence intensity in gray-scale mode and of red channel in RGB mode by the ImageJ software. The results from DIC are shown in **Table 2**.

Table 2. The fluorescence intensity in gray-scale mode and of red-channel in RGB mode of Mn/ZnS-QDs suspension at various concentrations analyzed by the ImageJ software

Concentration of Mn/ZnS-QDs (mg L^{-1})	Fluorescence intensity	
	Gray-scale mode	Red channel in RGB mode
10	34.43 ± 1.12	5.59 ± 0.70
25	36.08 ± 0.98	6.42 ± 0.63
50	38.22 ± 1.05	8.23 ± 0.58
75	40.94 ± 1.30	10.49 ± 0.56
100	40.05 ± 1.50	12.47 ± 0.84
250	48.09 ± 1.42	24.26 ± 1.07
500	57.60 ± 1.30	37.05 ± 0.60
750	67.89 ± 1.50	49.42 ± 0.83
1000	75.44 ± 2.47	61.15 ± 2.25
2000	100.02 ± 2.02	95.43 ± 1.76
3000	119.84 ± 2.38	127.28 ± 2.64

The minimum concentration limit of Mn/ZnS-QDs detected by DIC was investigated by the limit of detection method as same as the AuNPs results mentioned above. The minimum fluorescence intensities required for gray-scale mode and red-channel in RGB mode were found to be 37.92 and 6.45, respectively. According to **Table 2**, the minimum concentration limits of Mn/ZnS-QDs detected by DIC were equally found at 50 mg L^{-1}.

Effect of NMPPy to the color intensity of AuNPs solution

The concentration of 350 mg L^{-1} AuNPs was selected to be investigated in this section due to its high response. A 50 µL of 1000 mg L^{-1} NMPPy with sodium dodecyl benzene sulfonate was added to the 3 mL of AuNPs solution. Then the solution was photographed by a smartphone in a light box until finished adding 1000 µL of NMPPy. The digital photos were analyzed the color intensity in gray-scale mode by the ImageJ software with four replicates as shown in **Figure 3**. It was discovered that NMPPy did not significantly affect the color intensity of AuNPs solution.

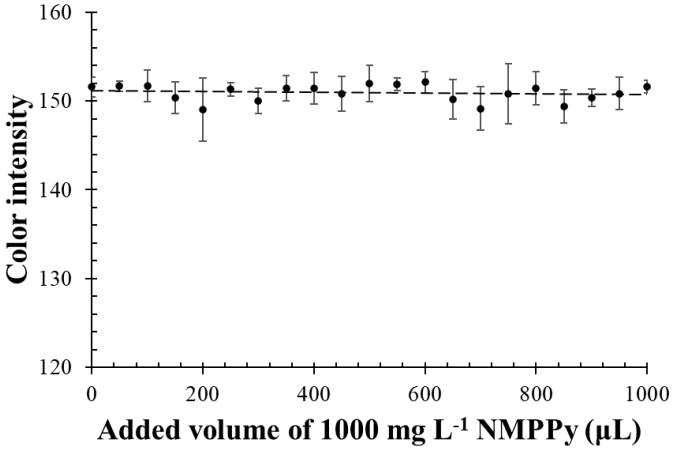

Figure 3. The effect of adding the 1000 mg L^{-1} NMPPy with various volumes into a 3 mL of 350 mg L^{-1} AuNPs solution to its color intensity in gray-scale mode.

Effect of NMPPy to the fluorescence intensity of Mn/ZnS-QDs suspension

For this investigation, a concentration of 3000 mg L^{-1} Mn/ZnS-QDs was selected since it would yield a higher response. A 50 µL of 1000 mg L^{-1} NMPPy with sodium dodecyl benzene

sulfonate was added to the 3 mL of Mn/ZnS-QDs suspension. Then the solution was taken the photo by a smartphone under black light until finished adding 1000 µL of NMPPy. The digital photos were analyzed the fluorescence intensity of red channel in RGB mode by the ImageJ software with four replicates as shown in **Figure 4**.

However, it was evident that the color of the Mn/ZnS-QDs suspension with NMPPy under black light had changed from red to white via naked eye observation. The change of color of the Mn/ZnS-QDs suspension with NMPPy was related to the increase of green color in the RGB color system, so green value in green channel of RGB mode was considered in this research. Therefore, the R/G fluorescence intensity would be chosen for analysis in subsequent experiments. It was clear that R/G value gives more sensitivity for the change of fluorescence intensity in this case as shown in **Figure 5**.

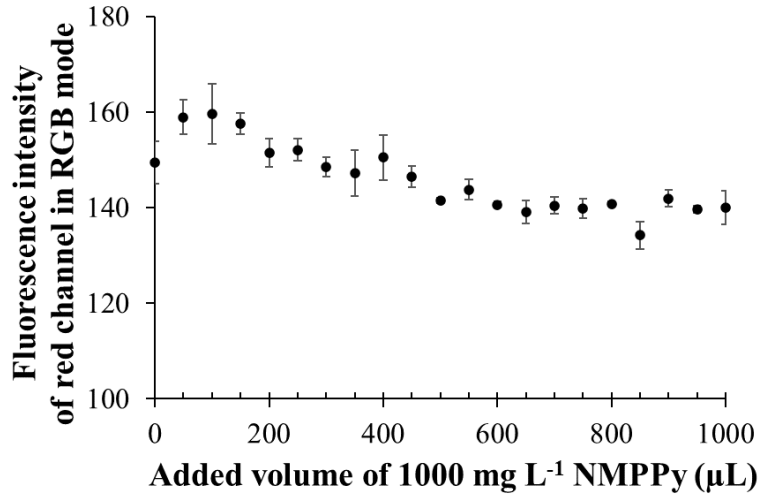

Figure 4. The effect of adding the 1000 mg L^{-1} NMPPy with various volumes into a 3 mL of 3000 mg L^{-1} Mn/ZnS-QDs suspension to its fluorescence intensity of red channel in RGB mode

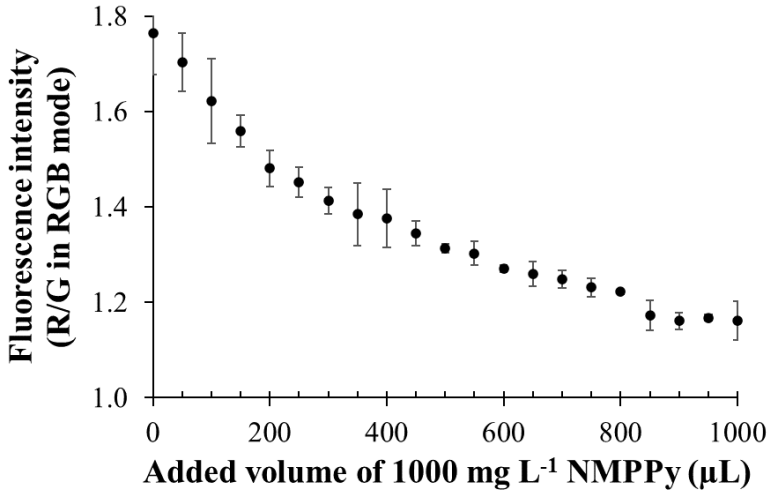

Figure 5. The effect of adding the 1000 mg L^{-1} NMPPy with various volumes into a 3 mL of 3000 mg L^{-1} Mn/ZnS-QDs suspension to its fluorescence intensity using R/G value in RGB mode

Mn/ZnS-QDs with NMPPy for methanol detection

Three milliliters of 3000 mg L^{-1} Mn/ZnS-QDs suspension and 800 µL of 1000 mg L^{-1} NMPPy were mixed, and then 200 µL 50 mM tris-HCl buffer solution (pH 8.5) was added to control pH of the solution. A sample solution of 1 mL was added to receive the DIC result. The solution was taken the photo by a smartphone under black light. The digital photos were analyzed the fluorescence intensity of R/G value in RGB mode by the ImageJ software with four replicates.

Methanol and ethanol at the concentration of 70 %v/v were tested; the typical resulting photos are shown in **Figure 6** comparing to a blank solution (DI water). The R/G values in RGB mode from the resulting solution of ethanol and methanol were found to be 1.039 ± 0.013 and 1.125 ± 0.021, respectively, though the R/G value from a blank was 0.997 ± 0.003. According to Student's t-test with 95% confidence level, the responses of ethanol and blank was not significantly different, while the response of ethanol and methanol was significantly different. Therefore, the results as shown in **Figure 7** are promising that the optical nanoparticles of Mn/ZnS-QDs with NMPPy can be used for the selective methanol detection.

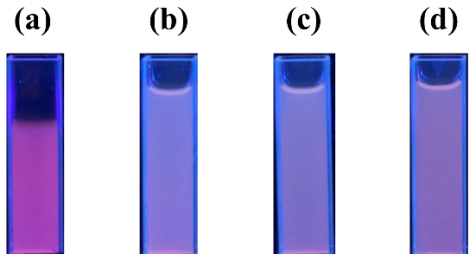

Figure 6. The photographs under the black light of (a) 3000 mg L^{-1} Mn/ZnS-QDs suspension without NMPPy, (b) 3000 mg L^{-1} Mn/ZnS-QDs suspension with 1000 mg L^{-1} NMPPy, (c) 3000 mg L^{-1} Mn/ZnS-QDs suspension with 1000 mg L^{-1} NMPPy and 70 %v/v ethanol, and (d) 3000 mg L^{-1} Mn/ZnS-QDs suspension with 1000 mg L^{-1} NMPPy and 70 %v/v methanol.

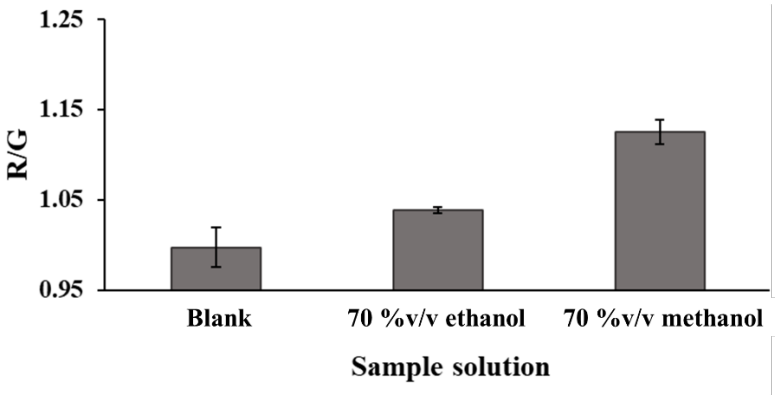

Figure 7. The R/G values in RGB mode from the resulting solutions using Mn/ZnS-QDs with NMPPy by DIC

Conclusion:

AuNPs and Mn/ZnS-QDs were synthesized and compared for their selectivity for methanol detection. Their spectroscopic properties were investigated, and the color intensities were analyzed using digital-image colorimetry (DIC). The minimum concentration limits of AuNPs and Mn/ZnS-QDs were discovered to be 25 and 50 mg L^{-1}, respectively. Moreover, N-methypolypyrrole (NMPPy) was added to those nanoparticles and the color intensity was investigated by DIC. It was found that the addition of NMPPy did not affect the color intensity of AuNPs solution, but it did change the fluorescence intensity of Mn/ZnS-QDs in term of red to green color intensity (R/G value). The R/G value of Mn/ZnS-QDs with NMPPy was clearly

reduced, resulting in a lower fluorescent response. Finally, Mn/ZnS-QDs with NMPPy were investigated further for methanol detection. Methanol was discovered to slightly increase the fluorescent response. This is the first step toward developing a future methanol detection method.

Acknowledgement:
This work was supported by the Research and Development Institute, Ramkhamhaeng University. The authors are grateful to Department of Chemistry, Faculty of Science, Ramkhamhaeng University and Electrochemistry and Optical Spectroscopy Center of Excellence, Department of Chemistry, Faculty of Science, Chulalongkorn University for instrument supports.

References:

1. Argo A, Bongiorno D, Bonifacio A, et al. Am J Forensic Med Pathol. 2010;31(2):186-91.
2. Renó MLG, Lora EES, Palacio JCE, et al. Energy. 2011;36(6):3716-26.
3. Osterloh JD, D´Alessandro A, Chuwers P, et al. J Occup Environ Med. 1996;38(6):571-6.
4. Yang M, Lu J, Miao J, et al. J Alzheimers Dis. 2014;41(4):1117-29.
5. Winkel DR, Hendrick SA. J Pharm Sci. 1984;73(1):115-7.
6. Aloke C, Emelike CU, Obasi NA, et al. Arab J Chem. 2021;14(12):103428.
7. Chen X, Zhu L, Ma Z, et al. Appl Surf Sci. 2022;604:154442.
8. Rahman MM, Alam MM, Asiri AM, et al. J Ind Eng Chem. 2022;106:503-11.
9. Sekine Y, Suzuki M, Takeuchi T, et al. Anal Chim Acta. 1998;280(2):179-84.
10. Huang KW, Yu CJ, Tseng WL. Biosens Bioelectron. 2010;25(5):984-9.
11. Srivastava RR, Singh VK, Srivastava A. Opt Mater. 2020;109:110337.
12. Hezinger AFE, Teßmar J, Göpferich A. Eur J Pharm Biopharm. 2008;68(1):138-52.
13. Wang N, Wang L, Yang H, et al. Int J Anal Chem. 2019;2019:1756014.
14. Elkony Y, Ali M. Ebrahim A, Adel R. J Insorg Organomet Polym Mater. 2022;32(8):3106-16.
15. Abbasi F, Alizadeh N. Food Chem. 2020;328:127091.
16. Abbasi F, Akbarinejad A, Alizadeh N. Spectrochim Acta A Mol Biomol Spectrosc. 2019;216:230-5.
17. Alizadeh N, Akbarinejad A, Ghoorchian A. ACS Appl Mater Interfaces. 2016;8(37):24901-8.

LIGANDLESS SOLIDIFIED FLOATING ORGANIC DROP MICROEXTRACTION (SFODME) FOR LEAD DETERMINATION IN WATER SAMPLES BY ELECTROTHERMAL ATOMIC ABSORPTION SPECTROMETRY (ETAAS)

Naruesorn Samanpong, Yutthapong Udnan, and Wipharat Chuachuad Chaiyasith*

Department of Chemistry, Faculty of Science, Naresuan University, Phitsanulok, Thailand
*e-mail: wipharatc@nu.ac.th

Abstract:

In the present work, a method for the determination of lead in water samples was developed by solidified floating organic drop microextraction (SFODME) without chelating agent. The method was based on ion pair formation between anion compound of lead in form of $[PbI_4]^{2-}$ complexes and cation compound of surfactant of *N*-Cetyl-*N*, *N*, *N*-trimethyl ammonium bromide (CTAB) forming hydrophobic complexes and detected by electrothermal atomic absorption spectrometry (ETAAS). The optimization of important parameters for extraction procedure *i.e.* pH, concentration of potassium iodide, concentration of CTAB, extraction temperature, extraction time, type and volume of organic solvent were investigated. Under the optimized condition, the calibration graph of the proposed method was linear in the range of 4.12 – 20.0 µg/L with the limit of detection (LOD) corresponding to three times of standard deviation (3 x SD, n = 5) of 1.24 µg/L. The percentage recoveries for lead in tap water samples were found in the ranges of 98.6 – 111.2. The precision defined as percentage relative standard deviation (%RSD) for lead determination was in the range of 1.41 – 3.35 at the concentration of 5.0 – 20.0 µg/L. The method was applied to tap water samples. The accuracy of the method by spiked recovery gave satisfactorily results. The results showed that lead concentration in tap water samples did not exceed the guideline level.

Introduction:

Lead is a one of heavy metals because it is related high densities compared with water for 5 times. It has the density of 11.29 g/ml and highly toxic and potentially dangerous to human health.[1] Furthermore, accumulation of lead was usually in soil, leaf, animal and surface water *e.g.* river, ground water. Utilization of surface water for manufacture drinking water cause lead contamination in human.[2] However, lead is the most useful metal in daily life such as battery, cable sheathing, weigh belts for driving, and radiation protection for irradiation in hospital. World health organization (WHO) has set the maximum concentration of lead in drinking water and it is 10 µg/L.[3]

Contamination of lead in the environment is generally in trace level which requires sensitive analytical technique and preconcentration method. Atomic absorption spectrometry (AAS) is the normally used for elemental analysis because its high sensitivity, and selectivity.[4] Traditionally, electrothermal atomic absorption spectrometry (ETAAS) has been applied in such cause[5] because it combines a fast analysis time, relative simplicity, lower cost, low sample volume requirement and lower detection limit compared with other AAS technique. All of these features have been responsible for its broad utilization in the determination of trace and ultra-trace elements in difference samples.[5]

Most widely used technique for separation and preconcentration of heavy metals in trace concentration is microextraction due to the use of low volume of organic solvent, high enrichment factor, environmental friendly, and low cost. There are several techniques in microextraction such as single drop microextraction (SDME), solid phase microextraction

(SPME), dispersive liquid-liquid microextraction (DLLME), and solidified floating organic microextraction (SFODME).

Solidified floating organic microextraction (SFODME) based on solidification the drop of organic solvent in an ice bath after extraction process and it was melted before analytical process. In the extraction process, the drop of organic solvent floated on the surface of an aqueous solution. Properties of organic solvent drop are the melting point near the room temperature (in the range of 10 – 30 °C), density lower than water for floating on the surface of an aqueous solution, immiscible with water.[6] Advantages of SFODME are simplicity, low cost, minimum organic solvent, environmental friendly, and high enrichment factor.[7]

Since 2001, complex formation without ligand or ligand-less process was applied for determination of heavy metals by AAS based on ion-pair formation of anion complexes containing metal ion and counter cations .[8] Complex formation without ligand have been developed in several ways *i.e.* surfactant-metal complex,[9] metal-hydroxide/chloride complex,[10]

In the present work, the novel combination of ligand-less and SFODME technique for determination of lead in water samples detected by ETAAS was firstly developed. It was used the ion pair formed between PbI_4^- by KI as anion forming agent and CTAB as counter with the use of microliter volume of 1-dodecanol as organic solvent. Important parameters were optimized such as pH of solution, concentration of potassium iodide, concentration of CTAB, extraction temperature, extraction time, types of extraction solvent, and extraction volume.

Methodology:

Instrumentation

A Varian Model SpectrAA 220Z Atomic Absorption Spectrometer equipped with Zeeman background correction was used. A lead hollow cathode lamp was used as the light source. The most sensitive wavelength was 283.3 nm, spectra bandwidth (0.5 nm), argon gas flow rate (3.0 L/min), and lamp current (10.0 mA) were used as recommended by manufacturer. The temperature program was presented in Table 1. The portable pH meter was measured of pH (Hanna Instrument, USA). The solutions and samples were stirred and heated by magnetic stirrer, magnetic bar and hotplate (Fisherbrand, Thermo Fisher Scientific, China). Longitudinal graphite tube atomizer was employed for lead determination.

Reagents and solutions

All reagent used in this study were of analytical reagent grade. All solutions were prepared with deionized water. Stock solution of Pb (II) was obtained from PanReac Quimica (Applichem GmbH, Germany) as 1000 mg/L and diluted daily for preparing working standard solution prior to use. Solutions for calibration graph were freshly prepared by appropriate dilution from the stock solution with deionized water and adjusted of pH by buffer solution (pH 9) using ammonium chloride (Ajax Finechem Pty Ltd, New Zealand) mixed with ammonia solution (LOBA Chemie PVT.LTD, India) before extraction process. Anion forming agent, potassium iodide (KI) in 1 M was purchased from Ajax Finechem (Ajax Finechem Pty Ltd, New Zealand). Counter ion or cationic surfactant of *N*-Cetyl-*N*, *N*, *N*-trimethyl ammonium bromide (CTAB) in 0.022 %w/v was supplied by LOBA Chemie (LOBA Chemie PVT.LTD, India). 1-dodecanol of Merck (Germany) was used as extraction solvent. After the extraction process, 1-dodecanol was dissolved in ethanol (RCL Labsacan Limited, Thailand) and 10±0.2 g/ L of Pd $(NO_3)_2$/HNO_3 15% was dilluted to 500 mg/L and used as matrix modifier (Merck, Germany). The laboratory glasswares were soaked overnight in a 10% HNO_3 solution. It was washed with deionized water and dried in air prior to use.

Table 1. Temperature program of ETAAS for determination of Pb

Step	Temperature program	Temperature (°C)	Time (s)	Argon gas flowrate (L/min)
1	Drying	85	5.0	3.0
2	Drying	95	40.0	3.0
3	Drying	120	10.0	3.0
4	Ashing	400	5.0	3.0
5	Ashing	400	1.0	3.0
6	Ashing	400	2.0	0.0
7	Atomization	2100	0.9	0.0
8	Atomization	2100	2.0	0.0
9	Cleaning	2100	2.0	3.0

Ligandless-SFODME procedure

Aliquot of 15 mL of sample or standard solution was added into the 25 mL glass vial for extraction containing magnetic bar. 1 mL of NH_3/NH_4Cl buffer solution (pH 9) to adjust pH value was then added. 300 µL of 1 M potassium iodide was added for anion complex formation. 40 µL of 0.022%w/v CTAB was used as counter ion and thoroughly, mixed 90 µL of 1-dodecanol was dropped into the solution and extracted for 40 min (50 °C, at 630 rpm). After that, the vial was placed in an ice bath in order to solidify the organic solvent. The solidified organic drop of 1-dodecanol was transferred in another small glass vial and dissolved 410 µL of ethanol. Therefore, final volume of organic drop has 500 µL and 10 µL was introduced into ETAAS for lead absorbance measurement.

Sample preparation

Three difference tap water samples were collected by PET bottles (Dormitory, Naresuan university, Phitsanulok, Thailand). These samples were filtered to remove sediment and suspended particles by filter paper (Whatman, No.1), stored at 4 °C in the refrigerator and the optimized extraction procedure was applied for the determination of lead content.

Results and Discussion:

Effect of type of the extraction solvent

In LL-SFODME, the extraction solvent is important factor which influences the extraction efficiency. It was chosen based on appropriate properties *i.e.* having density lower than water, immiscible with water, low volatility, good extraction efficiency, a melting point near room temperature (in the range of 10-30 °C), and low toxicity level.[11] 1-dodecanol and 1-undecanol were selected as the extraction solvent. Effect of the extraction solvent was shown in Figure 2. The relative absorbance of 1-dodecanol was more than 1-undecanol because 1-dodecanol structural (Figure 1.) give high extraction efficiency of ion-pair complexes based on like dissolve like principle. So, 1-dodecanol was chosen as appropiate extraction solvent in this study.

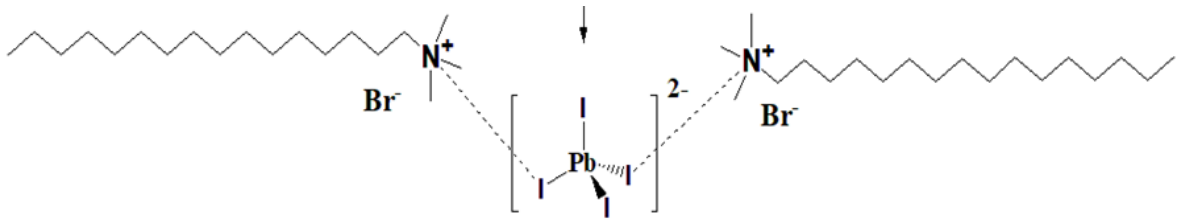

Figure 1. Ion-pair complex structure.

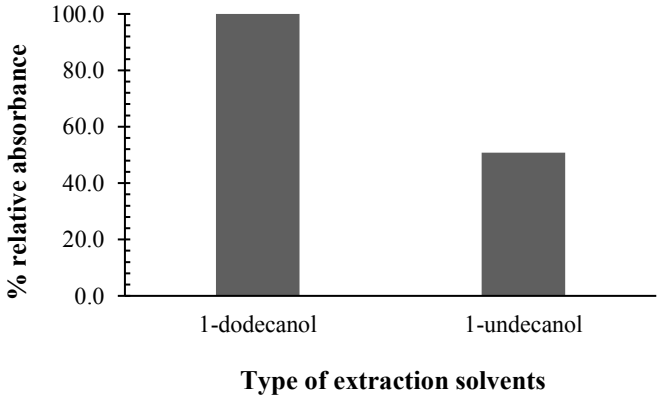

Figure 2. Effect of extraction solvent type. Conditions: 15 mL of 5 µg/L Pb^{2+} ,1000 µL of Buffer solution (pH 9), 300 µL of 1M KI, 40 µL of 0.022 %w/v CTAB, 90 µL various extraction solvent, 40 min extraction time, 630 rpm, and 50 °C extraction temperature.

Effect of extraction solvent volume

Extraction solvent volume of 1-dodecanol was investigated in the range of 30-180 µL as shown in Figure 3. It is indicated that %relative absorbance value increased continuously to 120 µL and decreased after 120 µL but %relative absorbance between 90 µL and 120 µL are nearly constants. Finally, 90 µL was chosen as proper extraction solvent volume for further because standard deviation (SD) of 90 µL was lower than that of 120 µL.

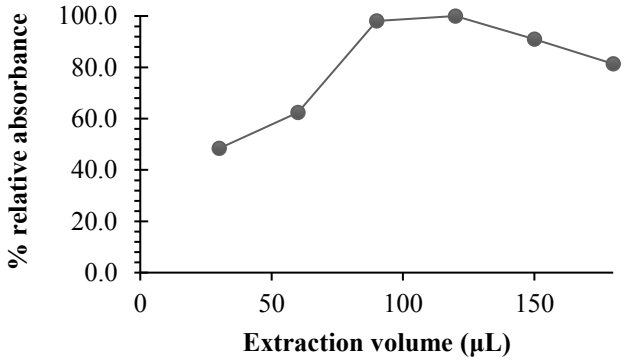

Figure 3. Effect of extraction solvent volume. Conditions: 15 mL of 5 µg/L Pb^{2+} ,1000 µL of Buffer solution (pH 9), 300 µL of 1M KI, 40 µL of 0.022 %w/v CTAB, various volume of 1- dodecanol , 40 min extraction time, 630 rpm, and 50 °C extraction temperature.

Effect of pH

Stability of ion-pair complex between PbI_4^- and CTAB including PbI_4^- formation depends on specific pH value. In addition, pH of solution influences toward the extraction

efficiency of Pb (II). For this reason, Pb (II) standard solutions (5 µg/L) were adjusted by adding 1 mL proper buffer solution in the range of 6-10. Influence of pH on absorbance signal was presented in Figure 4. %Relative absorbance value was maximized at pH 9 and gradually decreased. Decreasing %relative absorbance at high pH value were probably due to $Pb(OH)_2$ formation affecting lead ions in the solution decreased. At high pH value, competition of hydrogen ions and lead ions interact with iodide ions and anion complex was decreased. Therefore, the pH of solution was adjusted to pH 9 for further experiment.

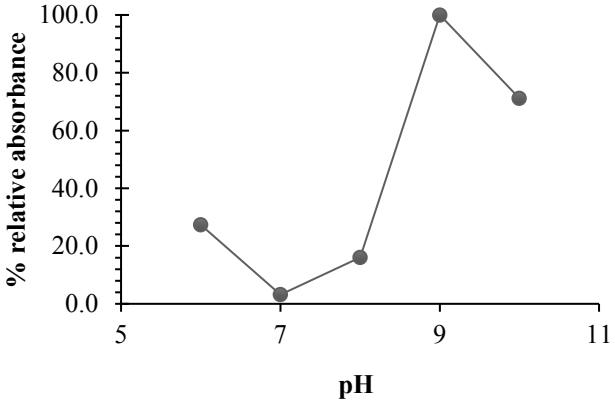

Figure 4. Effect of pH. Conditions: 15 mL of 5 µg/L Pb^{2+} ,1000 µL of various buffer solution, 300 µL of 1M KI, 60 µL of 0.022 %w/v CTAB, 90 µL 1-dodecanol, 20 min extraction time, 630 rpm, and room extraction temperature.

Effect of KI concentration

Anion complexes formation of PbI_4^- was succeed completely occurred. In appropriate ratio of 1:4. Potassium iodide (KI) was used as iodide source. In this study, KI concentration was investigated in the range of 5-50 mM by adding 1 M KI in various volume. The results given in Figure 5 showed that %relative absorbance value increased in KI concentration up to 20 mM and then decreased. Thus, final KI concentration of 20 mM when using 300 µL of 1M KI was selected for further experiment.

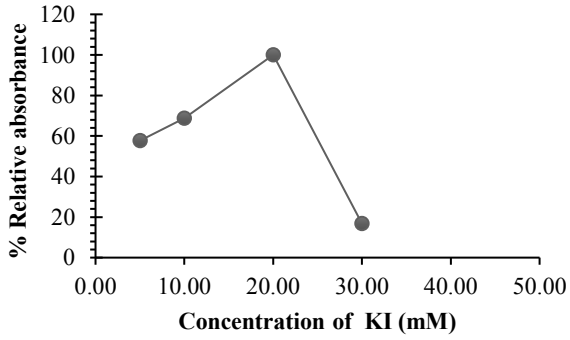

Figure 5. Effect of potassium iodide concentration. Conditions: 15 mL of 5 µg/L Pb^{2+} ,1000 µL of buffer solution (pH 9), various volume of 1M KI, 60 µL of 0.022 %w/v CTAB, 90 µL 1-dodecanol, 20 min extraction time, 630 rpm, and room extraction temperature.

Effect of CTAB concentration

For ion-pair formation, CTAB concentration was important factor which influenced extraction to drop of organic solvent. The effect of CTAB concentration was studied ranging from 0.87-4.33 µM by using difference of 0.022 %w/v CTAB. As seen in this Figure 6, %relative absorbance value increased up to 1.73 µM and decreased. Therefore, 1.73 µM of CTAB was chosen as proper CTAB concentration for further experiment.

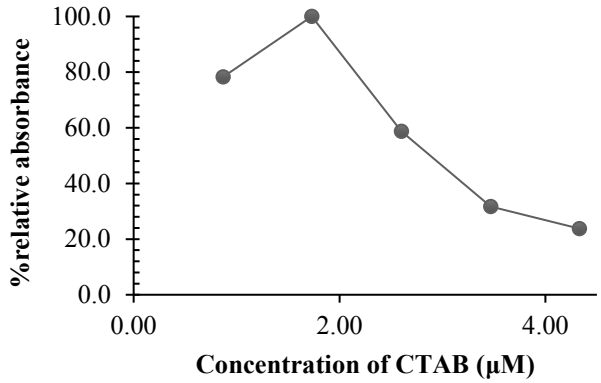

Figure 6. Effect of concentration of CTAB. Conditions: 15 mL of 5 µg/L Pb^{2+} ,1000 µL of buffer solution (pH 9), 300 µL of 1M KI, various volume of 0.022 %w/v CTAB, 90 µL 1-dodecanol, 20 min extraction time, 630 rpm, and room extraction temperature.

Effect of extraction temperature

In extraction process, ion-pair complexes were transferred from aqueous solution to organic solvent based on temperature. Moreover, the emulsification and solubility of organic solvent in water were occurred during extraction process. Appropriate temperature was optimized in the range of 25-90 °C and maximized up to 50 °C as showed in Figure 7. However, further increase in temperature caused a decrease in %relative absorbance value due to dissolve of organic phase at higher temperature. Therefore, 50 °C was chosen as extraction temperature for further experiment.

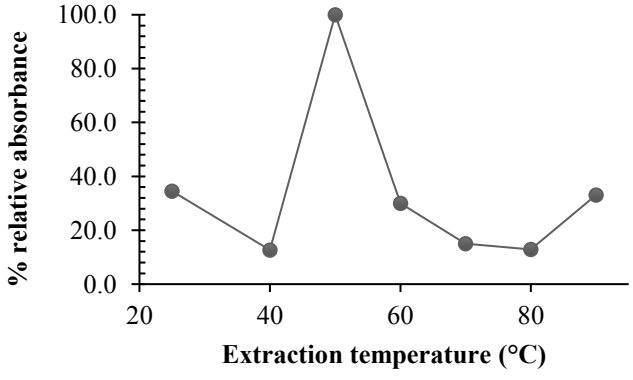

Figure 7. Effect of extraction temperature. Conditions: 15 mL of 5 µg/L $Pb^{2+,}$1000 µL of buffer solution (pH 9), 300 µL of 1M KI, 40 µL of 0.022 %w/v CTAB, 90 µL 1-dodecanol, 20 min extraction time, 630 rpm, and various extraction temperature.

Effect of extraction time

Extraction of ion-pair complexes from aqueous solution to the organic solvent is dependent on mass transfer. Therefore, the extraction time is an important factor that may have

significant effects on extraction efficiency. The extraction time was studied within a range of 10-50 min under the constant experimental conditions. The results given in Figure 8. Denonstrated that %relative absorbance values remained constant in the range of 10 -30 min and increased up to 40 min. Thus, the extraction of 40 min was chosen for further experiment.

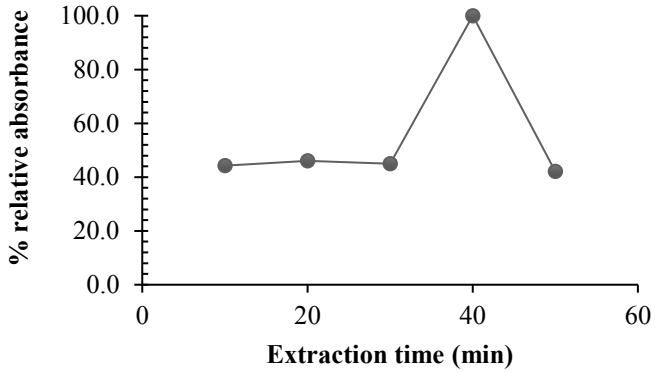

Figure 8. Effect of extraction time. Conditions: 15 mL of 5 µg/L Pb^{2+} ,1000 µL of buffer solution (pH 9), 300 µL of 1M KI, 40 µL of 0.022 %w/v CTAB, 90 µL 1-dodecanol, various extraction time, 630 rpm, and 50 ˚ C extraction temperature.

Analytical figure of merit

The calibration graphs obtained under the optimized condition for LL-SFODME process were linear in the range of 5.00-20.00 µg/L lead. The linear equation for lead determination by LL-SFODME was y = 0.0017x + 0.0004, where y is the absorbance value and x is concentration of lead ions in the solution (µg/L) and correlation coefficient of calibration curve was 0.9931. The linear equation for direct lead analysis without preconcentration was y = 0.0010x – 0.0014 and correlation coefficient of this calibration curve was 0.9969; linear range between 20-100 µg/L. The enrichment factor (EF) calculated by using ratio of the slope of calibration curve with preconcentration to that prior preconcentration was found as 1.7.

Preconcentration factor (PF) was found as 30 by using ratio the initial volume to final volume. The characteristic mass (m_0) to check of sensitivity in AAS technique was 50.6 pg. The limit of detection (LOD), defined as the concentration equivalent to three times the standard deviation of blank solution ($3SD_{blank}$) in 5 measurements divided by slope of calibration with preconcentration was 1.24 µg/L and limit of quantification (LOQ) is the lowest concentration can be measured accurately and precisely, defined as ten times the standard deviation of blank solution in 5 measurements divided by slope of calibration with preconcentration was 4.12 µg/L. The precision in %RSD was found as 1.41 % (n=5) for 5 µg/L lead. Table 2 presented the summary of analytical features of the method.

Table 2 Comparison of characteristic performance obtained by other liquid-liquid microextraction technique for lead determination

Analytical technique	Detection technique	Ligand	Sample	Linear range (μgL^{-1})	LOD (μgL^{-1})	PF	EF	Refeer ence
SFODME	ETAAS	APDC	Water and infant formula base powder samples	0.2-10	0.058	100	113	[12]
SFODME	ETAAS	PAN	biscuit and water samples	0.05-40	0.042	17	300	[13]
SFODME	ETAAS	DZ	tap water, well water, river water and sea water,	0.004-0.03	0.009	19	500	[14]
LL-DES	FAAS	-	soil, hair and several water samples	2-250	0.4	100	99	[15]
SFODME	ETAAS	-	Tap water	ETAAS	1.24	30	1.7	This work

Analysis of real samples

Evaluation of the accuracy of the proposed method by recovery value were obtained by spiking different concentration Pb (II) of water samples in order to validate the method. For this purpose, different concentrations were added into 15 mL of tap water samples (Thailand). The results were presented in Table 5. The recovery values were higher than 98%, and these results confirm the validity of the method.

Table 3. Result for the determination of lead in various samples (*n*=3).

Samples	Linear equations and R^2	Lead added (µg/L)	Lead detected (µg/L ± SD)	%Recovery (% ± SD)
Tap water 1	y = 0.0016x + 0.0050 R^2 = 0.9972	0.0	3.13 ± 0.09	-
		5.0	8.62 ± 0.41	109.9 ± 8.11
		15.0	18.02 ± 0.25	98.61 ± 1.64
Tap water 2	y = 0.0016x + 0.0110 R^2 = 0.9972	0.0	6.88 ± 0.15	-
		5.0	12.31 ± 0.16	108.5 ± 3.19
		15.0	21.88 ± 0.25	98.61 ± 1.65
Tap water 3	y = 0.0014x + 0.0097 R^2 = 0.9946	0.0	6.93 ± 0.33	-
		5.0	12.49 ± 0.99	111.2 ± 19.83
		15.0	21.46 ± 0.46	98.61 ± 3.08

Conclusions:

The developed method was based on ion-pair formation of PbI_4^- and CTAB for lead determination in tap water samples by ETAAS. In the solidification process, the solidified drop of organic solvent was in yellow color because ion-pairs were formed. For this study, the use of low volume of anion forming agent and CTAB also contributes to the principle of green chemistry. This is the first study which ion-pair formation was used in the preconcentration of lead in tap water samples. Advantages of the developed method are low cost, environmental friendly, simplicity, high precision, and extraction efficiency. Additional studies are progress to evaluate the parameters of the LL-SFODME method for preconcentration and determination of other metals using various anion forming agents and counter ions in different matrices.

Acknowledgements:

This work was supported by Department of Chemistry, Faculty of science, Naresuan University. Authors would like to thank the Promotion of Science and Technology Talents Project (DPST) for financial support.

References:

1. Çig˘dem A and Itır A. Anal. Chem. 2018; 102: 1-7
2. Ali Mazloomifara ,Nafiseh Khatibi. Adv.Mater. 2014; 829: 825-830.
3. Mohammad Taghi Naseri, Mohammad Reza Milani Hosseini [a,b], Yaghoub Assadi [a,b,*], and Armin Kiani. Talanta. 2008; 75: 56-62.
3. Heloisa R. Cadorim, Mauana Schneider, Julia Hinz, Fabiana Luvizona ,Adrian N. Diasb, Eduardo Carasek, and Bernhard Welz. Anal. Lett, 2019; 52: 1-16
4. Carmen Cabrera. Anal. Chem. 1994; 9: 1423-1426
5. Mahmonud Chamsaz, Jeiran Akhoundzadeh, Mahammad Hossein Arbab-zavar. Adv. Res. 2013; 4: 361-366.
6. Abbas Afkhami, Masoumeh Pirdadeh-beiranvand and Tayyebeh Madrakian. Anal. Bioanal. Chem. Res. 2017; 4: 1-10.
7. Hong Sun, Liping Zhao, Binwu Yang, and Qiao Liu. At. Spectrosc. 2014; 35(6): 265-269.
8. Young-Sang Kim, Yoon-Seok Choi, Won Lee, and Yong-Ill Lee. Bull. Korean Chem. Soc. 2001; 22(6): 821-826.
9. Cigdem Arpa Sahin, ˙Ilknur Durukan, Talanta, 2011; 85: 657-661.
10. Sayed Zia MOHAMMADI, Tayebeh SHAMSPUR, Daryoush AFZALI, Mohammad Ali TAHER[2], Laleh KARIMZADEH[1]. GU J Sci. 2013; 26(1): 11-19.
11. Gholamreza Khayatian, and Shahed Hassanpoor. J IRAN CHEM SOC. 2013; 10: 113-121.
12. Mahmoud Chamsaz, Jeiran Akhoundzadeh, Mohammad Hossein, and Arbab-zavar. Adv. Res. 2013: 4: 361-366.
13. Oya AydJn Urucu, Feyda Dönmez, and Ece Kök YetimoLlu. Anal. Chem. 2017; 68: 1-7.
14. Shayessteh Dadfarnia, Ali Mohammad Salmanzadeh, Ali Mohammad Haji Shabani. Anal. Chim. Acta. 2008; 623: 163-167.
15. Mehdi Karimi, Ali Mohammad Haji Shabani, and Shayessteh Dadfarni. Microchim. Acta. 2016; 183: 563-571.

DETERMINATION OF MAGNESIUM USING PAPER-BASED ANALYTICAL DEVICE

Wipaporn Thananchai
Department of chemistry, Faculty of science, Chulalongkorn University, Bangkok 10330, Thailand
*e-mail: Thananchai.wipaporm@gmail.com

Abstract:
This research aimed to develop a paper-based analytical device coupled with colorimetric detection for determination of magnesium in urine samples because magnesium is one of components in urine that can inhibit calcium oxalate stones formation. Normally, the magnesium concentration in urine samples should not be lower than 50 mg L^{-1} because the low magnesium concentration in urine sample has a potential to cause calcium oxalate stones. In this work, the determination of magnesium was performed using the reaction between magnesium and xylidyl blue in an alkaline condition to form a red complex. The change of color intensity is related to the amount of magnesium in sample solutions. The optimized conditions for the analysis of magnesium were 1 mol L^{-1} NaOH, 2 mmol L^{-1} xylidyl blue, and 10 minutes for the reaction time. The intensity of red color was measured from the picture of the reaction using ImageJ program. The linearity was in the magnesium concentration range of 5–50 mg L^{-1}. The limits of detection and quantitation were found to be 1.6 mg L^{-1} and 5.2 mg L^{-1}, respectively. The developed method was successfully used to determine urinary magnesium with high accuracy and precision. The recovery percentage of standard magnesium spiked in artificial and real urine samples, which was in the range of 87.8 – 1 0 7.0%. The intra-day and inter-day precisions of the analysis were determined from percentage of relative standard deviation (%RSD) of the color intensity obtained from artificial urine spiked with known amounts of magnesium, which were found to be lower than 7%. Accordingly, the paper-based analytical device coupled with colorimetric detection was successfully developed to be a reliable method for determination of magnesium in urine samples. The developed method will hold a great promise to be a simple, rapid, portable, and convenient tool for determination of magnesium, especially in for on-site measurement.

Introduction:
Urinary tract stones and kidney stones are common and found all over the world. The most common stones are calcium-containing stones. This problem of gallstones is found in about 20 percent in tropical countries. It is found in tropical countries more than western countries[1]. Urinary tract problems are more common in the northeastern region of Thailand. Most of the problems with this disease occur in people in the wilderness. This makes it difficult to access treatment[2]. Gallstones in Thai people have a high risk of recurrence of stones. This causes both patients and the public sector to lose high treatment costs and prevent recurrence of gallstones. The main cause of gallstone formation is dysfunction of metabolic processes in the body and the functioning of ionic and transport proteins in the gastrointestinal tract and kidneys. In the urinary system, there are gallstones such as calcium, oxalate, phosphate, and smaller gallstone inhibitors, citrate, potassium, magnesium. These gallstone inhibitors have the ability to Scrambling for gallstones and forming compounds that are highly soluble in water. The concentration of these ions in the urine can be used to analyze the risk of gallstones. Ion determinations can be performed in a number of ways, including chromatography, spectrophotometry and inductively coupled plasma (ICP). These methods

are complex, time-consuming, and costly. In this research, he is interested in developing a paper-based analytical device. This is a technique that can analyze the concentration of ions and various substances easily, cheaply, and quickly. The device is small and convenient for use outside the laboratory[3]. In the past, there have been researches that have developed paper-based analytical devices for calcium determination. and magnesium in water[4], using ion-specific reagents to study. Ion content analysis was performed by measuring the color of the reagent before and after reacting with the analyte ions present in the sample water. The measured color intensity was related to the concentration of ions to be analyzed. Therefore, in this project the aim of this project was to determine the concentration of magnesium, an ion that acts as an inhibitor of calcium oxalate gallstone formation. Because it can bind to oxalates, magnesium oxalate compounds are highly soluble in water. If the amount of magnesium in urine is known, it can be used to diagnose the risk of developing gallstones. Magnesium ion determination is based on the same principle as the research study of the determination of ions in water using paper-based analyzers. and select reagents that are specific to magnesium ions. The color of the reagent was measured before and after the reaction with the magnesium ions in the urine sample. A standard curve between the color and magnesium concentrations was used by analyzing the magnesium standard solution on a paper base analyzer for the determination of magnesium ion concentration in urine samples. It is hoped that this project will be able to analyze the magnesium concentration accurately, quickly and efficiently.

Methodology:

All standard solution of chemical was purchased from Sigma-Aldrich and prepare in milli-Q water. Urine sample from Faculty of Medicine, Chulalongkorn University.

Fabrication of the paper-based

The paper base analyzer was designed using Corel draw X7 program and printed on Whatman Grade No.1 filter paper with a wax printer. Then the printed paper base analyzer was heated with a hotplate at 150 °C for 10 min and then mounted. Tape on the back of the paper to prevent the solution from flowing out.

Magnesium analysis using paper-based analytical device

Start by dropping a 1 mol/L NaOH solution with a volume of 0.65 µL into the measurement area. Then let it dry for 3 minutes. Then, a 0.65 µL solution of 2 mmol/L of xylidyl blue was added to the measurement area. Then let it dry for 3 minutes and then drop a 10 mg/L solution of magnesium or 20 µL of the sample to be measured into the sample loading area. The reaction was then left for 10 minutes and the results were photographed in the light control box. Finally, bring the results of the experiment into the computer. Then analyze the color intensity in the measurement area with ImageJ program.

This research developed a method for analyzing magnesium in urine using a paper-base analytical device in combination with color determination. In this research, there were 3 parts of experiments, namely, the study of suitable conditions for the experiment. Verification of the validity of analytical methods and analysis of magnesium content in urine samples.

Results and Discussion:

Study of Magnesium Content Analysis with Paper-Based Analytical Devices It was found that the reagent volume fit to the measurement area was 0.65 µL. The suitable concentrations of the various solutions for the magnesium content analysis were 1 mol/L NaOH solution, 2 mmol/L xylidyl blue solution. Color intensity values in the measurement area with ImageJ program using the red channel. and the reaction time between magnesium and xylidyl blue was 10 min.

From the validation of the developed magnesium content analysis method, it was found that the standard curve (Figure 1.) has a linearity in the range of 5 – 50 mg/L, an R2 value of 0.9986, and the interference of substances that may interfere with the measurements are within acceptable limits. This analytical method has a measurement limit of 1.6 mg/L and a quantitative limit of 5.2 mg/L. In addition, the magnesium content analysis method has an analytical accuracy which can be seen in %recovery from the analysis. Magnesium was added to the artificial urine and urine samples at three concentrations: low (8 mg/L), medium (25 mg/L), and high (40 mg/L). The values were in the range of 87.8 - 107.0%, 91.6 - 106.9%, 90.4 - 106.7%, respectively. For the method reliability of magnesium content from the same day analysis at low, medium and high concentrations, there was %RSD of the values. Intensities were 4.2, 4.2, and 4.3, respectively, and in the different day analyses, average %RSD of chromaticity values were 5.6, 3.2 and 3.2, respectively, where %recovery and %RSD were within acceptable limits.

Analysis of magnesium content in urine samples using the developed paper-based analytical device, the urine magnesium content can be analyzed. As shown in Table 1, the measured magnesium content was less than the normal value, less than 50 mg/L[3], but this data cannot be used to analyze the risk of gallstones. This is because the analysis relies on the amount of other ions in the urine that affect the formation of stones.

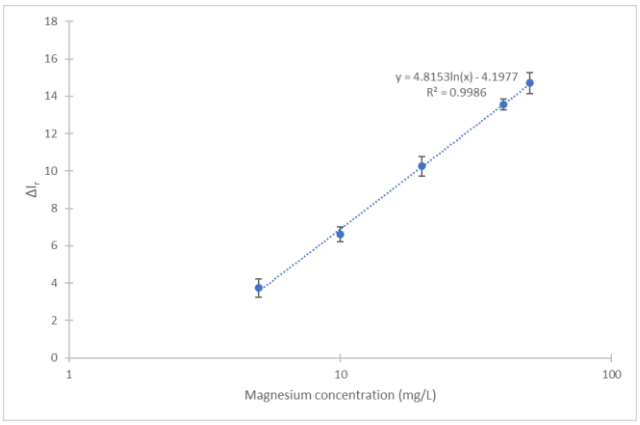

Figure 1. linear relationship was in range of 5 to 50 ppm (log scale plot).

Table 1. Mg Concentration in urine sample

Sample	Mg Concentration (mg/L)
Sample86	6.0
Sample91	13.5
MAN08	31.8
MAN09	5.7
MAN10	12.1

Conclusion:

A determination of magnesium using a paper-base analyzer revealed that the standard curve was linear in the range of 5 – 50 mg/L, and the interference of substances that may interfere with the measurements were within acceptable limits. This analytical method has a measurement limit of 1.6 mg/L and a quantitative limit of 5.2 mg/L. In addition, the

magnesium content analysis method has an analytical accuracy which can be seen in %recovery of the analysis. The amount of magnesium added to the artificial urine and urine samples was found to be %recovery in the range of 87.8 – 107.0%, and for the same day analysis method's reliability of magnesium content, %RSD of the color intensity. was 4.3, and in the different day analyses, the mean %RSD of color intensity was 5.6, where %recovery and %RSD were within the acceptable range. Therefore, paper-based analytical devices are reliable for analyzing magnesium concentrations in urine samples.

References:

1. Ramello A, Vitale C, Marangella M. J Nephrol. 2000;13;45-50.
2. Yanagawa M, Kawamura J, Onishi T. Int J Urol. 1997;4;537–540.
3. Martinez AW, Phillips ST. Angew Chem Int Ed Engl. 2007;46;1318–1320.
4. Karita S, Kaneta T. Anal Chim Acta. 2016;924-960.

Session C:
CHEMISTRY (Inorganic Chemistry)

SYNTHESIS, CHARACTERIZATION AND DNA BINDING STUDY OF NICKEL(II) AND ZINC(II) COMPLEXES USING BENZOTHIAZOLE SCHIFF BASE LIGANDS

Naritsara Kornkanlaya, Bussaba Pinchaipat, Ratanon Chotima*
Department of Chemistry, Faculty of Science, Naresuan University, Phitsanulok, Thailand
*e-mail: ratanonc@nu.ac.th

Abstract:

Ni(II) and Zn(II) complexes were synthesized using benzothiazole Schiff base ligands obtained by the condensation reaction between 2-aminobenzothiazole and R-salicylaldehyde (R = 3,5-Cl (**HL^1**), 5-Cl (**HL^2**), 3,5-Br (**HL^3**), 5-Br (**HL^4**)). The ligands and complexes were characterized by spectroscopic techniques. Study of the metal to ligand ratio and the stability constants of the complexes were determined and calculated by Job's method. The formation of Ni(II) complexes (**cpx 1-cpx 4**) show 1:2 metal to ligand ratio and the stability constants of complexes suggest the strong interaction between the metal(II) ion and ligands. The binding interactions of the complex with calf thymus DNA (CT-DNA) were determined by UV-Visible and fluorescence spectroscopic techniques. The binding constants and Gibb's free energy values of complexes confirm the binding ability of the complex with CT-DNA.

Introduction:

Schiff base is a compound containing an imine or an azomethine (–C=N–) functional group. It can be easily prepared through a one-step synthetic procedure by the condensation reaction between an aldehyde or a ketone and a primary amine.[1] Schiff base ligand has the capability of forming extraordinarily stable transition metal complexes.[2] 2-aminobenzothiazole has been interesting in the biological field due to its potent pharmacological activities. Moreover, the transition metal complexes with benzothiazole Schiff base ligands have shown antibacterial, antifungal, antioxidant, anti-tumour, and anticancer properties.[3] Transition metal complexes play a significant role in organisms *via* non-covalent bond with nucleic acid by intercalation, groove binding or electrostatic binding. Intercalation and groove binding are the two most important binding modes to DNA damage that can lead to anticancer and anti-bacterial properties of molecules.[4] The intercalation process has great therapeutic implications and intercalators are often used as drugs in cancer treatments.[5]

Metal ions in complexes are one of the factors that affect drug action and the efficiency of biological activities. Therefore, the design of novel transition metal complexes capable of binding with DNA and structural selectivity has been increased continuously. Ni(II) and Zn(II) are essential for many biological processes in organisms. Ni(II) has been used as enzyme cofactors and these essential enzymes catalyze a variety of remarkable chemical reactions. Zn(II) is vital for the stabilization of DNA and for gene expression. The properties of Zn(II) have been exhibited as an antioxidant and have played a major role in cancer prevention.[6]

In this work, Ni(II) and Zn(II) complexes will be synthesized using benzothiazole Schiff base ligands which are derived from the condensation reaction between 2-aminobenzothiazole and R-salicylaldehyde (R = -Cl, -Br). The ligands and complexes will be characterized by spectroscopic techniques. Furthermore, the stoichiometric ratio and stability constants of the complexes will be determined by Job's method. The binding interaction of complexes with CT-DNA will also be confirmed by spectroscopic techniques.

Methodology:

Materials and physical measurements

All solvents and chemicals were purchased from commercial sources and used without any further purification. 2-aminobenzothiazole, 3,5-dibromosalicylaldehyde, 3,5-dichlorosalicylaldehyde, 5-bromosalicylaldehyde, 5-chlorosalicylaldehyde and nickel(II) acetate tetrahydrate ($Ni(C_2H_3O_2)_2{\cdot}4H_2O$) were purchased from Sigma Aldrich. Zinc(II) nitrate hexahydrate ($Zn(NO_3)_2{\cdot}6H_2O$) was purchased from Ajax Finechem Pty Limited. Ethidium bromide (EB) and calf thymus DNA (CT-DNA) were obtained from Loba Chemie and Invitrogen, respectively.

FT-IR spectra were recorded on a Perkin Elmer FT-IR spectrophotometer Model Spectrum GX (4000-400 cm^{-1}). The ^{1}H-NMR spectra were recorded on a 400 MHz spectrometer (Bruker). Mass spectrometric analysis was performed using ESI technique (Agilent 6540 LC/MS system). Absorption spectra were measured using a UV-Vis Spectrophotometer (specord 200 plus) and Emission spectra were recorded on PerkinElmer LS 55 Luminescence spectrometer.

Synthesis of benzothiazole Schiff base ligands

R-salicylaldehyde (4.0 mmol) was dissolved in hot ethanol and then was added into a stirring solution of 2-aminobenzothiazole (4.0 mmol) in hot ethanol. The mixture was stirred at 60 ºC for 6-11 hours. The solution mixture was slowly evaporated at room temperature. After 7 hours, the solid was precipitated. The solid was filtered and washed with cool ethanol (3×3 mL) and diethyl ether (3×3 mL).

Synthesis of complexes

The metal salt (0.2 mmol) was dissolved in methanol and then was added dropwise into the stirring ligand (0.4 mmol) and triethylamine (0.4 mmol) in dichloromethane. The solution mixture was stirred at room temperature and the reaction time depends on the appropriate condition of each complex. The product was filtered and washed with cool ethanol (3×3 mL) and diethyl ether (3×3 mL).

Job's method

1 mM of metal salt (0.0, 0.1, 0.2, 0.3, 0.4, 0.5, 0.6 mL) in methanol was pipetted out and transferred into seven of 10 mL volumetric flasks and 1 mM of ligand (0.6, 0.5, 0.4, 0.3, 0.2, 0.1, 0.0 mL) in tetrahydrofuran was added in such a way that the mole fraction of solution remained constant. The absorbance of each complex was recorded at the maximum wavelength as shown in Table 1.

Table 1. The maximum wavelength of the absorption spectrum of complexes

cpx	1	2	3	4	5	6	7	8
λ_{max}(nm)	450	460	460	460	480	460	480	490

A stability constant is an equilibrium constant for the formation of a complex in solution. It suggests the strength of the interaction between metal ions and ligands which come together to form the complexes. The stability constant was calculated using the following equations: [7]

$$K = \frac{[ML]}{[M] \times [L]} \quad (1)$$

$$K = \frac{[A_2/A_1]}{[1 - A_2/A_1] \times [(C_L - C_M) \times A_2/A_1]} \quad (2)$$

Where, A_1= absorbance at break point, A_2= actual absorbance, C_M = concentration of metal(II) ion and C_L= concentration of ligand

DNA binding experiments

The stock solution of CT-DNA was prepared according to the standard procedure.[8] 1 mg/mL of deoxyribonucleic acid sodium salt from calf thymus (CT-DNA) was dissolved in Tris–HCl buffer solution (pH 7.0). The buffer was prepared with a mixture of 5 mM Tris-HCl and 50 mM sodium chloride in distilled water. The pH of the buffer solution was monitored by universal indicator paper. The ratio of UV absorbance at 260 nm and 280 nm of the solution is ca. 1.8, which indicates that the stock solution of CT-DNA does not have any protein contamination. The concentration of the stock solution was measured by considering the molar extinction coefficient of the CT-DNA at 260 nm to be 6600 $M^{-1}cm^{-1}$. The stock solution of CT-DNA was stored at -20 °C and was used within two weeks.

UV-Visible absorption titrations, the binding between complexes (cpx **1**, cpx **2**, cpx **6** and cpx **8**) and CT-DNA were recorded on UV-Vis spectrometer using cuvettes of 1 cm path length and the spectral scan range set at 200 - 800 nm. The solution of 50 µM complexes were prepared in DMSO-buffer mixture pH 7.0 (0.5 %v/v). Absorption spectra were recorded at room temperature. Each complex was titrated with increasing concentration of the CT-DNA solution (0-100 µM) by successive additions.

Fluorescence emission titrations, emission intensity measurements were recorded on fluorescence spectrometer using cuvettes of 1 cm path length and all the solution of complexes (cpx **1**, cpx **2**, cpx **6** and cpx **8**) were detected at room temperature (slit widths = 5 nm). Excitation wavelength (λ_{ex}) and emission wavelength (λ_{em}) range were set at 525 nm and 545 - 700 nm, respectively. Successive addition in fluorescence experiment was performed on 10 µM of CT-DNA and 4 µM of ethidium bromide (EB) in the buffer solution by addition of complexes (0-24 µM).

Results and Discussion:

Synthesis and spectroscopic characterization

All ligands and complexes were prepared by standard procedure as shown in Figure 1 and Figure 2, respectively. They were obtained in different color. The percentage yield of some complexes appears to be more than 100. These results suggest that the formation of complexes might not be as the expected structure or contain some remaining reactants. However, the product is unable to be separated due to similar solubility and polarity of reactants and product.

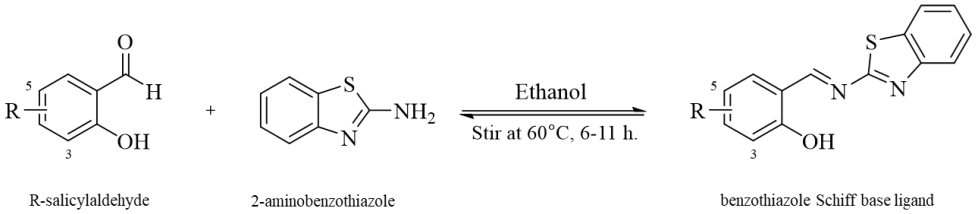

Figure 1. Synthesis of benzothiazole Schiff base ligands (R = 3,5-Cl (**HL^1**), 5-Cl (**HL^2**), 3,5-Br (**HL^3**), 5-Br (**HL^4**))

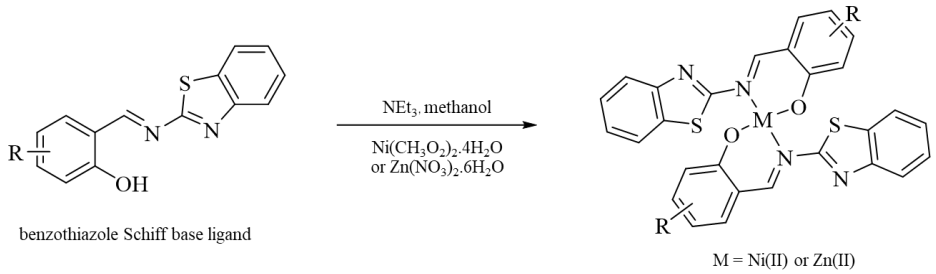

Figure 2. Synthesis of complexes (**cpx 1-8**)
(R = 3,5-Cl (**HL^1**), 5-Cl (**HL^2**), 3,5-Br (**HL^3**), 5-Br (**HL^4**))

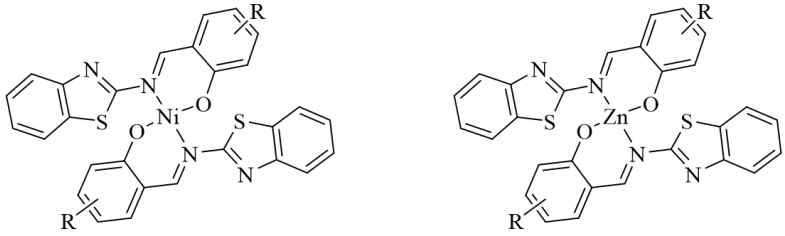

[Ni(L$_1$)$_2$], **cpx 1**
[Ni(L$_2$)$_2$], **cpx 2**
[Ni(L$_3$)$_2$], **cpx 3**
[Ni(L$_4$)$_2$], **cpx 4**

[Zn(L$_1$)$_2$], **cpx 5**
[Zn(L$_2$)$_2$], **cpx 6**
[Zn(L$_3$)$_2$], **cpx 7**
[Zn(L$_4$)$_2$], **cpx 8**

Figure 2. Structure of complexes (**cpx 1-8**)

The molecular ion peaks of all ligands are in good agreement with suggested empirical formula. However, the molecular ion peaks of the complex which correspond to the empirical formula are found only for **cpx 1**, **cpx 2**, **cpx 6** and **cpx 8**.

The FT-IR spectra of the ligands and complexes (**cpx 1**, **cpx 2**, **cpx 6** and **cpx 8**) show the band around 1584-1633 cm^{-1}, which is assigned to C=N stretching frequency. The band around 1132-1156 cm^{-1} is assigned to C-O stretching frequency. To consider C=N stretching and C-O stretching frequency of ligands as compared to their complexes, the results indicate the coordination of the ligand to the metal(II) center by the nitrogen of imine group and oxygen of hydroxyl group.

The ^{1}H-NMR spectra of all ligands are in good agreement with the expected structure. According to the results of **cpx 1**, **cpx 2**, **cpx 6** and **cpx 8**, the spectra of **cpx 1** and **cpx 2** show broad and negligible signals because these complexes are paramagnetic compounds. The suggested structures of **cpx 1** and **cpx 2** would be rationally octahedral coordination with d^8 electron configuration of Ni(II) complex. The clear spectra of the complexes occur only **cpx 6** and **cpx 8** due to d^{10} electron configuration of Zn(II) complex as diamagnetic compounds. The disappearance of the signal belonging to the hydroxyl group in these conplexes (**cpx 6** and **cpx 8)** and the shifting to high frequency reveals that the ligand is coordinated to the metal (II) center the nitrogen of imine group and oxygen of hydroxyl group.

Job's method

The maximum wavelength of each complex was selected according to the absorption of mixing solution between metal ion and ligands. Therefore, the wavelengths in Table 1 were considered to determine the metal to ligand ratio and the stability constant of the complex. Ni(II) complexes (**cpx 1**-**cpx 4**) show maximum absorption at the mole fraction around X_{Ni} = 0.33, which correspond to the 1:2 metal to ligand ratio of the complex. The

absorbance intensity of Zn(II) complexes (**cpx 5- cpx 8**) is relatively much lower so there is difficulty in the indication of Zn(II) ion to ligands ratio.

The stability constants were determined by the data collected from Job's plot. The stability constant values of all synthesized complexes were relatively similar except **cpx 5** and **cpx 6** that were unable to calculate their stability constants. These results suggest the strong interaction between the metal(II) ion and ligands.

DNA-binding studies

The spectra show two absorption bands of **cpx 1**, **cpx 2**, **cpx 6** and **cpx 8** around 260 nm and 340-395 nm. The absorption band at 395 nm of **cpx 1** shows hypochromism and bathochromism around 5 nm upon the addition of CT-DNA (0-100 μM) and the absorption bands at 340 nm of **cpx 2**, **cpx 6** and **cpx 8** show hypochromism. This observation suggests that **cpx 1** can bind to CT-DNA through intercalation whereas **cpx 2**, **cpx 6** and **cpx 8** are assigned to be groove binding. K_b values of complexes were found in the range of 1.00×10^5 to 2.00×10^5 M^{-1}, which is close to the binding constant of Ni(II) complex and Zn(II) complex in references (10^5 M^{-1}).[9-13] These values confirm the binding ability of the complex with CT-DNA. The negative free energy values were found to be -28.91 to -30.65 kJ mol^{-1}, which confirm spontaneous binding ability of the complex with DNA.

The fluorescence intensity was gradually decreased after the addition of each complex (0-24.0 μM). The result suggests either the replacement of the EB from DNA or the deformation of the secondary DNA structure.[13] K_{sv} values of complexes were found in the range of 1.56×10^4 to 9.67×10^4 M^{-1}, these values confirm the ability of complexes to replace EB from DNA. K_{app} values were calculated to be 2.67×10^6 M^{-1} which is close to the binding constant of classical intercalators and metallointercalators (10^7 M^{-1}).[14] The process of quenching can be divided into two broad types that were dynamic and static quenching. The suggested process of the EB-DNA fluorescence quenching would be static quenching instead of dynamic quenching because the calculated k_q values were more than the maximum dynamic quenching constant for various quenchers with biopolymers (10^{10} $M^{-1}s^{-1}$).[15]

Conclusion:

The complexes between benzothiazole Schiff base ligands and Ni(II) ion or Zn(II) ion were synthesized and characterized by mass spectrometry. The **cpx 1**, **cpx 2**, **cpx 6** and **cpx 8** show the results corresponding empirical formula. Therefore, the **cpx 1**, **cpx 2**, **cpx 6** and **cpx 8** were further characterized by FT-IR and ^{1}H-NMR.

The ratio between metal and ligand including stability constant of complexes were determined by Job's method. The data show the formation of Ni(II) complexes (**cpx 1**-cpx **4**) having 1:2 metal to ligand ratio and the stability constants of complexes suggest the strength of the interaction between the metal(II) ion and ligands.

Furthermore, the binding interaction between CT-DNA and **cpx 1**, **cpx 2**, **cpx 6** and **cpx 8** have been studied by UV-Vis spectroscopy and fluorescence emission spectroscopy. The binding constants and Gibb's free energy values of **cpx 1**, **cpx 2**, **cpx 6** and **cpx 8** confirm the binding ability of the complex with CT-DNA.

In future work, the complexes will be studied to confirm the structure by single crystal x-ray diffraction and further biological studies such as antimicrobial activity or antiproliferative activity.

Acknowledgements:

This work was supported by Department of Chemistry, Faculty of Science, Naresuan University. I also thanks Development and Promotion of Science and Technology Talents Project (DPST) for financial support.

References:

1. Schiff H. Justus Liebigs Ann Chem. 1864;131:118–119.
2. Anacona, J R, Rincones M. Spectrochim Acta A Mol Biomol Spectrosc. 2015;141:169–175.
3. Ekennia A C, Osowole A A, Olasunkanmi L O, Onwudiwe D C, Ebenso E E. Res Chem Intermed. 2017;43:3787–3811.
4. Li H H, Aubrecht J, Fornace A J. Mutat Res. 2007;623:98–108.
5. Mukherjee A, Sasikala W D. Adv Protein Chem Struct Biol. 2013;92:1–62.
6. Stefania F, Giorgio B, Leonardo C, Marco C, Clara D C. J Environ Pathol Toxicol Oncol. 2006;25:597–610.
7. Tirmizi S A, Feroza H W, Muhammad H S W, Saadia S, Allah N M, Allah B G. Arab J Chem. 2012;5:309–314.
8. Husain M A, Ishqi H M, Sarwar T, Rehman S U, Tabish M. MedChemComm. 2017;8: 1283–1296.
9. Krishnamoorthy P, Sathyadevi P, Cowley A H, Butorac R R, Dharmaraj N. Eur J Med Chem. 2011;46:3376–3387.
10. Kumar R R, Mohamed Subarkhan M K, Ramesh R. RSC Adv. 2015;5:46760–46773.
11. Revathi N, Sankarganesh M, Rajesh J, Raja J D. J Fluoresc. 2017;27:1801–1814.
12. Krishnamoorthy P, Sathyadevi P, Cowley A H, Butorac R R, Dharmaraj N. Eur J Med Chem. 2011;46:3376–3387.
13. Ghorai P, Saha R, Bhuiya S, Das S, Brandão P, Ghosh D, Bhaumik T, Bandyopadhyay P, Chattopadhyay D, Saha A. Polyhedron. 2018;141:153–163.
14. Hussain A, AlAjmi M, Rehman M, Khan A, Shaikh P, Khan R. Molecules. 2018;23:1232–1249.
15. Wongsuwan S, Chatwichien J, Pinchaipat B, Kumphune S, Harding D J, Harding P, Boonmak J, Youngme S, Chotima R. J Biol Inorg Chem. 2021;26:327–339.

DRUG DELIVERY SYSTEM USING POROUS SILICA-MANNAN NANOCOMPOSITES

Purinat Trisirimongkol, Numpon Insin*
Department of Chemistry, Faculty of Science, Chulalongkorn University, Bangkok, 10330, Thailand
*e-mail: numpon.i@chula.ac.th

Abstract:

Developing a drug delivery system is crucial for ensuring that the drug molecules are transported to the correct target in the body efficiently. In this work, a drug delivery system consisting of nanocomposites of porous silica and mannan is developed with the purpose of transporting the drugs to one interesting target: dendritic cells. Firstly, the porous silica nanoparticles were successfully synthesized via a mechanism involving a microemulsion system. Morphology and size of the particles were characterized using SEM, TEM, and XRD, and it was found that the particles had a spherical shape with the size of 356 ± 15 nm. A study about effects of calcination on methylene blue adsorption was performed, and it was found that calcination at 550°C for 6 hours helped in getting rid of the template and letting the nanoparticles adsorb more molecules into their pores. Amino functionalization followed by the EDC/NHS coupling reaction was performed to synthesize the mannan polysaccharide-coated porous silica nanoparticles. A test for sugar using phenol-sulfuric acid method confirmed the presence of mannan and success of attachment of mannan on the surface of the porous silica nanoparticles. The nanocomposites based on porous silica and mannan show a great potential as a drug delivery system for targeted-drug delivery to dendritic cells.

Introduction:

Medication is a vital part of symptom alleviation and disease treatment for patients; however, misuse of drugs can lead to harming patients instead of treating them. If drug molecules were transported to parts of the body that are not of their target, they could have a toxic effect to the body. Also, even though the drug molecules can be delivered to the correct target site, there are still many concerns about their bioavailability, efficacy, and potency. While these properties of a drug depend on a number of intrinsic factors such as its solubility[1] and size,[2] environmental factors such as pH of the medium also play a major role in dictating the effectiveness of a drug to a target.[3] Some molecules have potential for treatment but unfortunately cannot be used as a medication due to lack of stability in the human body or low solubility in water, resulting in low bioavailability and pharmacological effect.[4] Therefore, improving drug delivery systems are necessary.

There are many challenges to be faced in developing a drug delivery system as it needs to overcome all of the limitations preventing the drug molecules from producing therapeutic effects to the body. The drug molecules must be delivered at a controlled and appropriate rate to a specific target in a reproducible manner to achieve maximum efficiency. If the drugs were delivered at a rate which is too fast, the therapeutic effects might not be properly established as the concentration of the drug at the target at any given time would be too low, resulting in the requirement for unnecessarily large amounts of drugs.

Several types of materials are currently being used as drug delivery systems, including biopolymers,[5,6] liposomes,[7,8] functionalized graphene oxides,[9] metal nanoparticles,[10] and magnetic nanoparticles.[11] Among all these types of materials, one emerges as one of the most promising materials to be used as drug delivery systems: porous

silica nanoparticles. Their advantageous features include low cytotoxicity,[12] thermal stability,[13] size tunability,[14] and ease for mass production.[15] The drugs can be loaded into the porous structure of the material, making it suitable as a drug delivery system.[16] Porous silica nanoparticles can be modified to further enhance favorable properties. Modifications to the bare porous silica nanoparticles include changing the sizes of the particles[17] and varying sizes of the pores in the particles.[18] Other ways to modify the particles are to functionalize the surface with groups such as amino group, thiol group, and hydroxyl group[19–21] or to attach the surface of the particles with other substances to increase specificity to the target.

The drug target of our interest is dendritic cells, a type of antigen-presenting cells (APCs), which are cells that display antigens on their surfaces for recognition by the immune system. They would attack a pathogen, degrade it, and present parts of it on their membrane, giving signals to stimulate other defensive mechanisms of our bodies. Due to their properties, dendritic cells have been used as drug targets for various treatments. For example, dendritic cell-targeted drugs have been used for antitumor immunity and tumor immunotherapy.[22] On the other hand, since dendritic cells are responsible for sending messages to the immune systems, tackling them would result in interference with the immune responses of the body, which can be beneficial for treatment of autoimmune diseases as immunosuppressive drugs can target dendritic cells, causing the body to produce less immune response and prevent it from attacking itself.[23]

Expressed by these antigen-presenting cells, including dendritic cells, are mannose receptors. Mannan is a polysaccharide which can be isolated from the cell wall of the yeast Saccharomyces cerevisiae, consisting of the sugar mannose, to which the mannose receptors of dendritic cells have a strong affinity.[24] This makes mannan a strong candidate as a material to be attached on the surface of the porous silica nanoparticles as they are recognized by the mannose receptors, helping enhance cellular uptake of the nanoparticles used as the drug delivery system and increase the efficacy of the drug.

Therefore, this work aims at synthesis of nanocomposites of porous silica and mannan to be used as a drug delivery system.

Methodology:

Synthesis of porous silica nanoparticles (PSN)

The nanoparticles were synthesized using a modified version of a previously reported method.[25] Firstly, 2.0 mL of TEOS was added into a mixture of cyclohexane (15.0 mL) and hexan-1-ol (0.8 mL) under magnetic stirring. Then, a solution consisting of CTAB (1.4 g), urea (0.3 g), and milliQ water (15.0 mL) was added, and the reaction mixture was stirred for 30 minutes. Then, the reaction mixture was heated at 130°C for 4.5 hours. The synthesized product was later washed via centrifugation using milliQ water three times and ethanol once, and dried at 50°C. The synthesized particles were denoted as PSN-1. To achieve the author's preferred size, which is around 350 nm, several batches of porous silica nanoparticles (PSNs) were synthesized with various reaction conditions. The amounts of the reagents and the duration in the oven are listed in Table 1. PSN-4 was selected for further study.

Table 1. Reaction conditions for synthesis of each PSN batch

Batch	TEOS (mL)	CTAB (g)	Other reagents	Duration in oven
PSN-1	2.0	1.4	0.8 mL 1-hexanol	4.5 hours
PSN-2	2.0	1.4	15.0 mL cyclohexane	Overnight
PSN-3	2.0	0.7	0.3 g urea	4.5 hours
PSN-4	2.0	0.7	15.0 mL milliQ water	Overnight

Study of effects of calcination on methylene blue adsorption of PSN-4

To assess the effects of calcination on porosity of the nanoparticles, methylene blue adsorption experiment was performed. Roughly 60 mg of the previously synthesized PSN-4 was calcined at 550°C for 6 hours. 10 mg of calcined and uncalcined PSN-4 were soaked in a 10-mL solution of methylene blue in separate bottles and were let to adsorb the dye for 1 hour. Because methylene blue can also degrade under ultraviolet radiation, the procedure was also performed on the methylene blue solution without adding any PSN as negative control. The solutions were then centrifuged to separate the particles from the mixture, and the methylene blue content in the remaining solutions were determined using UV-visible spectroscopy by measuring the absorbance at 663 nm.

Synthesis of nanocomposites of porous silica and mannan (PSN-MN)

Firstly, amino functionalization on the surface of the particles was performed. 150 mg of PSN-4 were sonicated in 10 mL of hexane for 10 minutes. Then, 200 µL of APTES was added to the mixture, and the mixture was then further sonicated for an hour, a step in which PSN-NH_2 was obtained. EDC/NHS coupling was utilized for attachment of mannan. PSN-NH_2 was dispersed in water and then added to a mixture containing mannan (30 mg), 1-ethyl-3-(3-dimethylaminopropyl)carbodiimide (EDC) (50 mg), and *N*-hydroxysuccinimide. (NHS) (40 mg) The mixture was then stirred at room temperature for 24 hours. The solid product was then washed with water, and the final product, denoted as PSN-MN, was freeze dried and kept at 4°C.

Characterization

The size and morphology of the synthesized PSNs were observed using a transmission electron microscope (TEM) and a scanning electron microscopy (SEM). The phase structure of the materials was determined via X-ray diffractometry. (XRD) To evaluate the success of mannan attachment on PSN, colorimetric assay involving the sulfuric acid-phenol method was used. First, concentrated H_2SO_4 was added to PSN-MN. H_2SO_4 can digest the mannan on the particles into its monosaccharide compartments. Then, 5% phenol solution was added, with which the monosaccharides react to form a furfural compound, providing a yellowish solution. The mixture was then heated to 90 °C for five minutes to develop the color. The color of the solution was compared with the control solution.

Results and Discussion:

The morphology of PSN-1 was characterized using SEM (**Figure 1**) and TEM (**Figure 3a**). The particles were uniform and had a spherical shape. The size of the particles was determined from the TEM image and was calculated to be 288 ± 12 nm. In addition, structural analysis of PSN-1 was performed using XRD. (**Figure 2**) The diffraction pattern of PSN-1 showed a broad peak at around 22°, agreeing with the standard diffraction pattern of amorphous silica. (JCPDS 29-0085) The morphology and size of PSN-2, PSN-3, and PSN-4 were observed using TEM. (**Figure 3b**, **3c**, **3d**) All of the batches are spherical in shape but with different sizes. The average size of the particles from each batch was determined from the TEM images and is displayed in **Table 1**. It is evident that the particles synthesized with reduced amount of CTAB, PSN-3 and PSN-4, were larger than the particles synthesized with original amount of CTAB, PSN-1 and PSN-2. This was because by reducing the amount of CTAB in the process, the amount of hemimicelles formed also decreased, resulting in formation of less amount of CTA^+/silicate oligomers and consequently led to larger particles formed. The duration in the oven, however, did not significantly affect the size of the product.

The effects of calcination on porosity of the particles were tested by observing the adsorption of methylene blue on the particles from batch PSN-4. The absorption spectra were illustrated in **Figure 4**. A drop in absorbance of the solution can be observed in the methylene blue solution with added porous silica nanoparticles, with the solution with added calcined nanoparticles showing a higher degree of decrease in absorbance than that with added uncalcined nanoparticles. The percent adsorption was calculated to be 56.5% for the solution with uncalcined nanoparticles and 93.9% for the solution with calcined nanoparticles. The phenomenon might be because some amount of CTAB still persisted even after the washings during the synthesis process and blocked the pores in the nanoparticles, and the calcination process helped get rid of the CTAB, freeing those pores and consequently let more amount of methylene blue get adsorbed into those pores.

Nanocomposites of porous silica and mannan was successfully synthesized. In order to attach mannan on the surface of the porous silica nanoparticles, amino groups had to be attached onto the nanoparticles first to form PSN-NH_2. Presence of PSN-NH_2 was confirmed using ninhydrin test. A small amount of PSN-NH_2 was dispersed in water, and the mixture dropped into a filter and let dry. Then, ninhydrin reagent is sprayed onto the filter paper, and the filter paper is heated at 90°C for five minutes. Ninhydrin can react with amino group to form a purple compound. The result is depicted in **Figure 5**, which showed a purple compound throughout the paper, indicating that PSN-NH_2 was indeed generated in the amino functionalization process.

Mannan attachment was then performed on PSN-NH_2, producing PSN-MN. Investigation of the attachment was done using sulfuric acid-phenol method. When the synthesized PSN-MN was tested, it was found that the colour of the mixture turned into dark yellowish brown which differed drastically compared to the control solution, as illustrated in **Figure 6**. This phenomenon helped confirm that mannan has been successfully attached on the surface of the synthesized porous silica nanoparticles.

The author then attempted to quantitatively identify the mannan content attached onto the porous silica nanoparticles by measuring the absorbance of the solution at 490 nm using UV-visible spectrophotometer. However, the absorbance of the mixture could not be correctly identified. This may be because some amount of silica nanoparticles remained in the mixture after centrifugation and filtration of the mixture, interfering with the absorbance of the solution. The author suggests that the quantitative analysis to determine the amount of mannan attached on the silica particles in this case could have been done on supernatant instead of the particles itself, and the amount of mannan content attached on the particles could be calculated by subtracting the amount of mannan found in the supernatant from the original amount of mannan added in the reaction process of synthesizing PSN-MN.

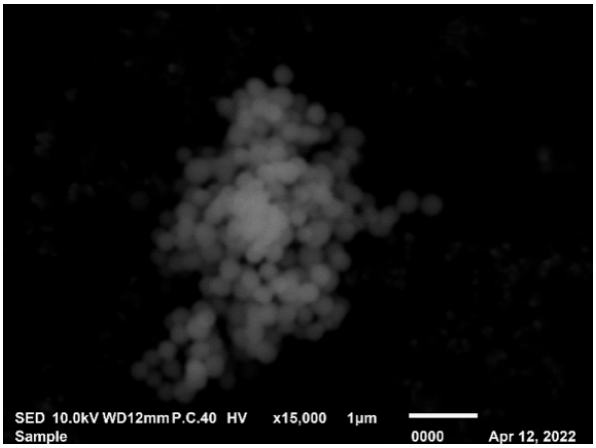

Figure 1. SEM image of PSN-1

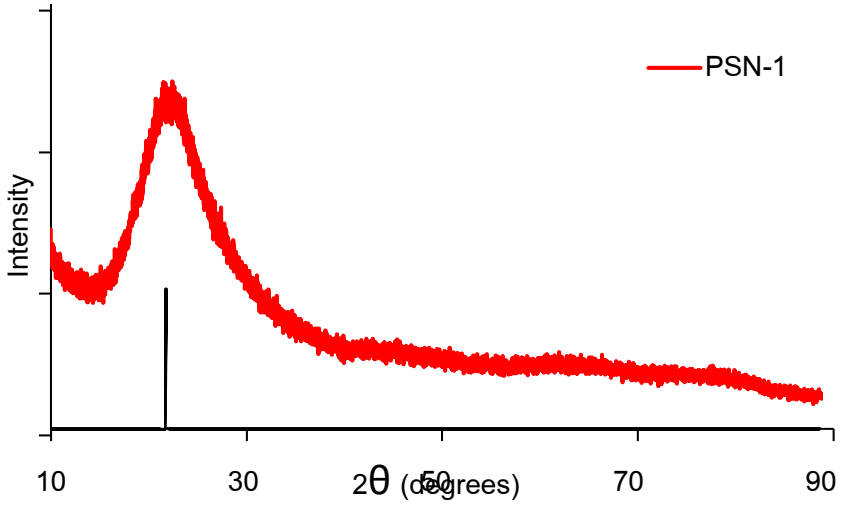

Figure 2. XRD pattern of PSN-1 and reference pattern of amorphous silica oxide

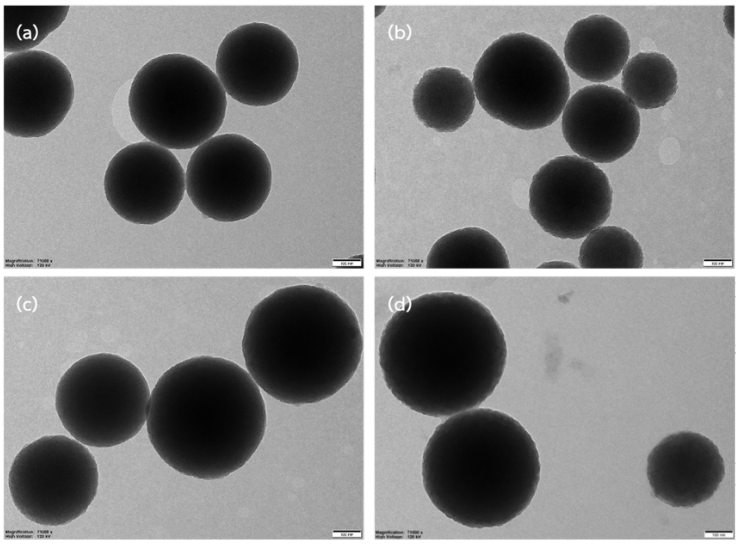

Figure 3. TEM images of (a) PSN-1 (b) PSN-2 (c) PSN-3 (d) PSN-4

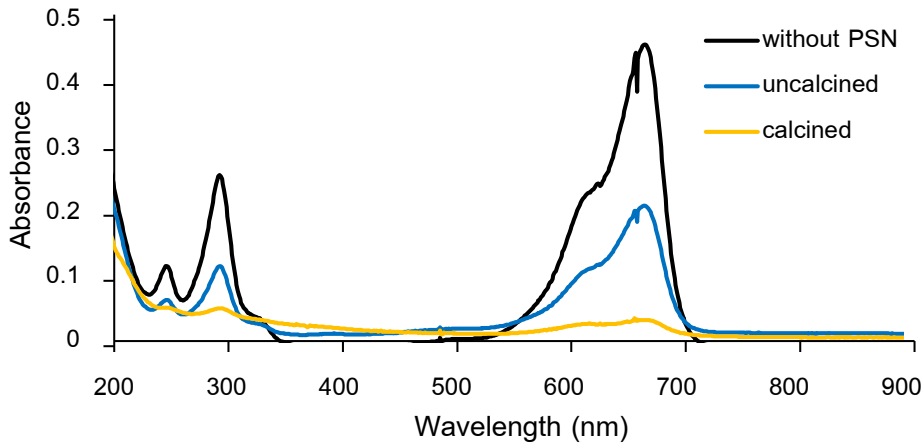

Figure 4. UV-visible spectra of methylene blue solution with different conditions

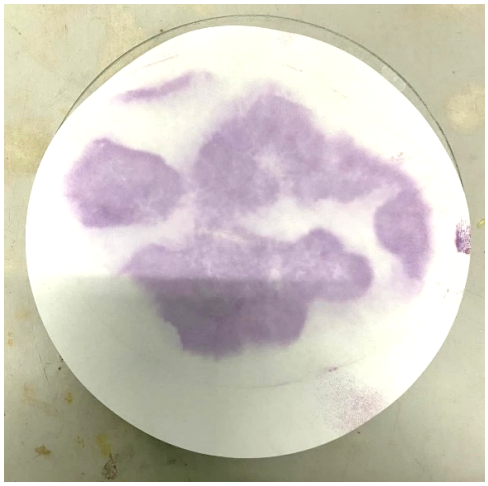

Figure 5. Filter paper after performing ninhydrin test to comfirm the presence of PSN-NH_2

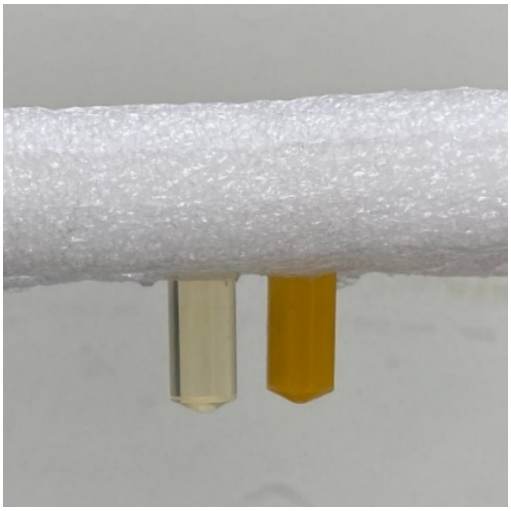

Figure 6. The solutions after testing control solution (left) and mixture of dispersed PSN-MN in water (right) for carbohydrate using the sulfuric acid-phenol method

Table 2. Calculated size of PSN-1, PSN-2, PSN-3, and PSN-4 from TEM images

Batch	Calculated size (nm)
PSN-1	288 ± 12
PSN-2	298 ± 14
PSN-3	432 ± 18
PSN-4	356 ± 15

Conclusion:

Drug delivery system consisting of nanocomposites of porous silica and mannan has been successfully developed. Porous silica nanoparticles are successfully synthesized via a method involving generating a microemulsion system. The morphology and size of the porous silica nanoparticles were characterized using TEM, SEM, and XRD, and the particles were seen to be spherical in shape and 356 ± 15 nm in size. It was found that the amount of template affected the size of the particles, with lower amounts giving rise to larger particles. It was also found that calcination at 550°C for 6 hours helped with getting rid of the template still left in the pores. Amino functionalization followed by EDC/NHS coupling was used for attaching mannan on the surface of the silica nanoparticles. A characterization method using

the reaction between sugar and sulfuric acid and phenol confirmed the presence of mannan on the surface of the particles. The synthesized nanocomposites showed a great promise as a new drug delivery system and will be further studied about their ability to deliver drugs to dendritic cells in the future works.

Acknowledgements:

This research was supported by the Development and Promotion of Science and Technology Talents Project. (DPST)

References:

1. Faller B, Desrayaud S, Berghausen J, Laisney M, Dodd S. Solubility in Pharmaceutical Chemistry. 2019;113–132.
2. Caster JM, Yu SK, Patel AN, Newman NJ, Lee ZJ, Warner SB, Wagner KT, Roche KC, Tian X, Min Y, Wang AZ. Nanomedicine. 2017;13:1673–1683.
3. Blum RA, D'andrea DT, Florentino BM, Wilton JH, Hilligoss DM, Gardner MJ, Henry EB, Goldstein H, Schentag JJ. Increased Gastric pH and the Bioavailability of Fluconazole and Ketoconazole. 1991.
4. Han, D-G, Cha E, Joo J, Hwang JS, Kim S, Park T, Jeong Y-S, Maeng H-J, Kim S-B, Yoon I-S, Bansal AK. Pharmaceutics. 2021;13:175.
5. Nitta SK, Numata K. Int J Mol Sci. 2013;14:1629–1654.
6. Müller A, Ni Z, Hessler N, Wesarg F, Müller FA, Kralisch D, Fischer D. J Pharm Sci. 2013;102:579–592.
7. Maia ALC, e Silva ATM, César ALA, Giuberti CS, Evangelista FCG, Lemos J de A, Sabino AP, Malachias Â, Fernandes C, de Barros ALB, Soares DCF, Ramaldes, GA. J Drug Deliv Sci Technol. 2021;65:102686.
8. Yu J, Wang S, Qi J, Yu Z, Xian Y, Liu W, Wang X, Liu C, Wei M. Int Immunopharmacol. 2021;101:108148.
9. Yousuf S, Siddique HR, Arjmand F, Tabassum S. J Drug Deliv Sci Technol. 2022;71,103281.
10. Ramachandran R, Krishnaraj C, Sivakumar AS, Prasannakumar P, Abhay Kumar VK, Shim KS, Song CG, Yun S. Mater Sci Eng C Mater Biol Appl. 2017;73,674–683.
11. Xie X, Zhang L, Zhang W, Tayebee R, Hoseininasr A, Vatanpour HH, Behjati Z, Li S, Nasrabadi M, Liu L. J Mol Liq. 2020;309,113024.
12. Chauhan S, Manivasagam G, Kumar P, Ambasta RK. Pharm Nanotechnol. 2018;6,245–252.
13. Wu Y, Chen S, Liu Y, Lu Z, Song S, Zhang Y, Xiong C, Dong L. J Mater Sci Technol. 2020;50,139–146.
14. Bouchoucha M, Côté MF, C-Gaudreault R, Fortin MA, Kleitz F. Chem Mater. 2016;28.4243–4258.
15. Zhang K, Xu LL, Jiang JG, Calin N, Lam KF, Zhang SJ, Wu HH, Wu GD, Albela B, Bonneviot L, Wu P. J Am Chem Soc. 2013;135,2427–2430.
16. Lehto VP, Riikonen J. Porous Silicon for Biomedical Applications. 2014;337–355.
17. Dogra P, Adolphi NL, Wang Z, Lin YS, Butler KS, Durfee PN, Croissant JG, Noureddine A, Coker EN, Bearer EL, Cristini V, Brinker CJ. Nat Commun. 2018;9,4551.
18. Li J, Shen S, Kong F, Jiang T, Tang C, Yin C. RSC Adv. 2018;8,24633–24640.
19. Zhang Q, Neoh KG, Xu L, Lu S, Kang ET, Mahendran R, Chiong E. Langmuir. 2014;30,6151–6161.

20. Martínez-Carmona M, Ho QP, Morand J, García A, Ortega E, Erthal LCS, Ruiz-Hernandez E, Santana MD, Ruiz J, Vallet-Regí M, Gun'Ko YK. Inorg Chem. 2020;59,10275–10284.
21. Que DE, Hou WC, Ang MBMY, Lin CC. Aerosol Air Qual Res. 2020;20,1987–2020.
22. van Broekhoven CL, Parish CR, Demangel C, Britton WJ, Altin JG. Cancer Res. 2004;64,4357–4365
23. Hackstein H, Thomson AW. Nat Rev Immunol. 2004;4,24–34.
24. Milone MC, Fitzgerald-Bocarsly P. J Immunol. 1998;161,2391–2399
25. Chen H, Liu H, Wang R, Jiang X, Zhu M. Dent Mater J. 2021;37,961–971.

DEVELOPMENT OF ENZYME RESPONSIVE TRIS-CYCLOMETALATED IRIDIUM COMPLEXES

Sureemas Meksawangwong,[1] Filip Kielar[1,2,]*
[1]Department of Chemistry, Faculty of Science, Naresuan University, Phitsanulok, Thailand
[2]Centre of Excellence in Biomaterials, Faculty of Science, Naresuan University, Phitsanulok, Thailand
*e-mail: filipkielar@nu.ac.th

Abstract:
Two tris-cyclometalated iridium complexes derived from the archetypal structure [Ir(ppy)$_3$] (ppy = 2-phenyl pyridine), each containing a substituent on a single ppy ligand, have been synthesized. The first complex [Ir(ppy)$_2$ppy-OH] (**1**) contains a hydroxy methyl group while the second complex [I(ppy)$_2$ppy-Oct] (**2**) is an octanoate ester derivative of the first one. The complexes have been synthesized with the aim of developing a method for ratiometric method for the determination of activity of ester hydrolyzing enzymes. The investigation of the photophysical properties of the two complexes in aqueous solution has shown that they posses emission spectra with emission maxima at 520 nm and 580 nm for complex **1** and complex **2**, respectively. The ester containing complex **2** has been incubated with several ester hydrolyzing enzymes. Incubation with porcine liver esterase led to changes in the emission spectra consistent with the hydrolysis of the ester group. The results indicate the possibility to further develop these complexes as responsive probes for enzymatic activity.

Introduction:
Enzymes perform a wide range of chemical transformations and fulfill a host of biologically important functions.[1] Spatiotemporal control over enzymatic activity is needed for proper functioning of a biological system. Abnormal enzymatic activity, on the other hand, can be an indication of an issue or disease.[2,3,4] Serine hydrolyses are enzymes involved in hydrolysis of various chemical bonds and include enzyme classes such as lipases, esterases, thioesterases, amidases, peptidases, and proteases.[5,6] In mammals, these enzymes represent ~ 1% of all proteins. Furthermore, serine hydrolases are involved in important processes such as blood clotting, digestion, nervous system signaling, inflammation, and cancer development.[5,6] The importance of these enzymes therefore necessitates the monitoring of their activity.

Various methods of monitoring enzymatic activity of serine hydolases have been designed and developed.[7] Most commonly, spectrophotometric methods are used, where the enzymatic activity is detected by changes in UV-vis absorption spectra of the substrate after its conversion to the product. This is typified by usual commercial colorimetric tests for lipase activity.[8] Higher sensitivity can be achieved using fluorescent sensors, which can exhibit turn on, turn off, or ratiometric responses.[9-12] Luminescent metal complexes, including cyclometalated iridium complexes, are one class of the potential luminophores that could be used in such probes, which exhibit various interesting properties such as large Stokes' shifts or long luminescence lifetimes.[13,14]

We have previously published reports on tris-cyclometalted iridium complexes, which were derived from the archetypal structure [Ir(ppy)$_3$] and contain various aminoalkyl substitutents on one of the ppy ligands.[15,16] This work has indicated that the emission properties of these complexes in aqueous solutions are affected by the nature of the alkyl substituent on the amino group. In general, longer chains increasing the lipophilicity of the complexes, and their propensity to aggregate, resulted in emission spectra with an additional

feature at 580 nm, in addition to the peak at 520 nm observed in organic solvents. In fact, this second peak at 580 nm in became dominant in several cases. We have therefore hypothesized, that a pair of iridium complexes, which would be differentiated by their lipophilicity and, which could be chemically interconverted, could constitute a basis of a ratiometric luminescent sensor, as the conversion of one of these to the other would change the lipophilicity and thus the emission spectrum. To demonstrate this concept, we report here on the properties of a hydroxymethyl iridium complex and its octanoate ester analogue. We propose that the latter of these two could act as ratiometric sensor for ester hydrolyzing enezymes and report the initial investigation of these properties.

Methodology:

Unless otherwise stated, all commercial reagents were used as received. Silver trifluoromethanesulfonate, octanoic acid, methyl octanoate, sodium borohydride, lipase B from *Candida antarctica*, lipase B from *Candida antarctica* immobilized on acrylic resin, and porcine liver esterase were purchased from Sigma Aldrich. 2-phenylpyridine (ppy), 2-ethoxyethanol, and silicagel were purchased from Merck. Iridium(III)chloride trihydrate were purchased from Fisher. Dichlromethane, methanol, hexane and triethyl amine were purchased from Carlo Erba. Sodium bicarbonate, anhydrous sodium sulphate, and trisodium phosphate were purchased from Univar. Acetonitrile and dimethyl sulfoxide were purchased from RCI. Lipozyme® TL and Novozyme® were purchased from Strem. The precursor complex [Ir(ppy)$_2$(fppy)] and complex **1** [Ir(ppy)$_2$ppy-OH] were synthesized as previously reported.[15] ^{1}H spectra were recorded on a Bruker Avance 400 MHz instrument operating at 400 MHz for. Mass spectra were recorded with an Agilent technologies UHD Accurate-Mass Q-TOF LC-MS instrument model 6540. UV-Visible spectra were recorded using Analytik Jena 210 plus diode array spectrophotometer. Steady state emission spectra were recorded using Fluoromax-4 spectrofluorometer from Yvon Horiba.

Synthesis of complex (**2**) [Ir(ppy)$_2$ppy-Oct]

[Ir(ppy)$_2$ppy-OH] (**1**) (50 mg, 0.073 mmol), methyl octanoate (66 µL, 0.365 mmol), and lipase B from *Candida antarctica* immobilized on acrylic resin were suspended in hexane. The reaction mixture was stirred at 45°C for 48 h. The reaction mixture was allowed to cool down to room temperature, filtered, and the solvent was removed using reduced pressure. The residue was purified by column chromatography on silica using dichloromethane and methanol as eluent. The product was obtained as a yellow solid (15 mg, 0.018 mmol, 25%). ^{1}H NMR (400 MHz, $CDCl_3$, δ) 0.88 (t, J = 7.2 Hz, 3 H), 1.28 (m, 6 H), 1.57 (m, 4H), 2.25 (t, J = 7.6 Hz, 2 H), 4.91 (m, 2H), 6.71-6.90 (m, 11 H), 7.45-7.55 (m, 6H), 7.62 (t, J = 6.0 Hz, 3H), 7.83 (d, J = 8.4 Hz, 3H). HRMS (ES$^+$) calcd. for $C_{42}H_{40}IrN_3NaO_2$ (834.2645); found 834.2617 [M+Na]$^+$.

Enzymatic Hydrolysis

A solution of complex [Ir(ppy)$_2$ppy-Oct] (10 µM) in phosphate buffered saline (5 mL, pH 7.4) was incubated at 45°C for 48 h in the presence of the selected enzymes. The emission spectra of the reaction mixture were acquired with excitation at 390 nm.

Results and Discussion:

The first of the two complexes ([Ir(ppy)$_2$ppy-OH)]) (**1**) utilized in this work was synthesized using procedures established in the literature in three steps.[17] First, a chloride bridged iridium dimer was formed in a reaction of iridium chloride and 2-phenylpyridine. The iridium dimer was then converted into a monomeric iridium complex containing a single formyl group on one of the ppy ligands in a reaction with 4-(pyridine-2-yl)benzaldehyde. Finally, the formyl

group was converted into a hydroxymethyl group in a reaction with sodium borohydride. The octanoyl ester complex **2** was then synthesized in and enzymatic esterification between the hydroxy complex and methyl octanoate catalyzed by lipase B from *Candida antarctica* immobilized on acrylic resin (Scheme 1). The reaction was carried out at 45°C in hexane for 48h. The product was isolated after column chromatography and characterized by ^{1}H NMR and MS spectroscopies.

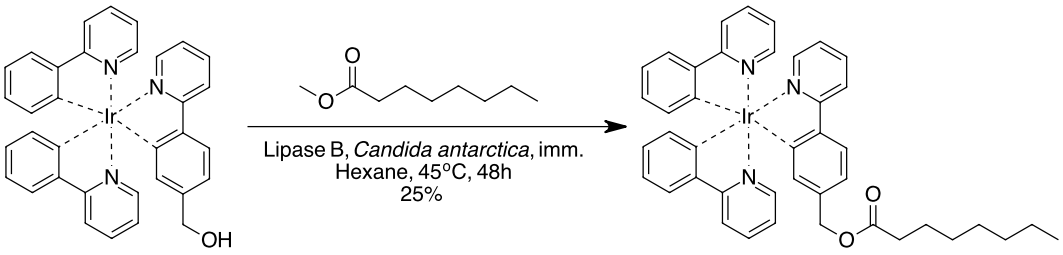

Scheme 1. Synthesis of iridium complex **2**

The complexes investigated in this work were synthesized based on our previous observations, which indicated that more lipophilic iridium complexes in a group of monosubstituted derivatives of [Ir(ppy)$_3$] would show an increased propensity to aggregate in aqueous solutions, which would affect their emission spectra. Specifically, less lipophilic and well dispersed complexes are expected to exhibit broad profiles with single emission maximum between 520 and 530 nm, more lipophilic complexes are expected to exhibit dual emission with maximum at 580 nm and a shoulder at 520 to 530 nm.[14,15] Iridium complexes **1** and **2** were made as representatives of these two classes of complexes with complex **1** being the less lipophilic and complex **2** being the more lipophilic. We therefore investigated the emission spectra of solutions of complexes **1** and **2** (10 μM) in phosphate buffer (0.5 M, pH 7.4) to determine if this expectation would be validated in their emission profiles. The results are shown in **Figure 1**, which validates the expectations. Complex **1** exhibits a broad emission profile with a single maximum at 524 nm, while complex **2** shows a more complex emission profile with a maximum at 578 nm and a shoulder around 520 nm. Furthermore, the ratio of the emission intensity at 580 nm and 520 nm for complexes **1** and **2** is 0.6 and 1.9, respectively.

In addition, complexes **1** and **2** were prepared with the expectation that they can be interconverted by esterification or ester hydrolysis. Based on the results shown in **Figure 1** it can be expected that such a conversion would result in a ratiometric change in the emission profile. To test this hypothesis, complex **2** was incubated with lipase B from *Candida antarctica*, Lipozyme® TL, Novozyme®, and porcine liver esterase at 45°C in phosphate buffer (pH 7.4) for 48 h. Control incubation of complex **2** in the same system in the absence of any enzyme was carried out as well. The results of the experiment can be seen in **Figure 2**. The emission spectrum of complex **2** incubated in the model system in the absence of enzyme maintains the characteristics observed for complex **2** in **Figure 1**. This result indicates that no or only very limited amount of background hydrolysis of complex **2** is taking place. Varying degree of change in the emission profile can be seen in the case of the solutions of complex **2** incubated in the presence of various enzymes.

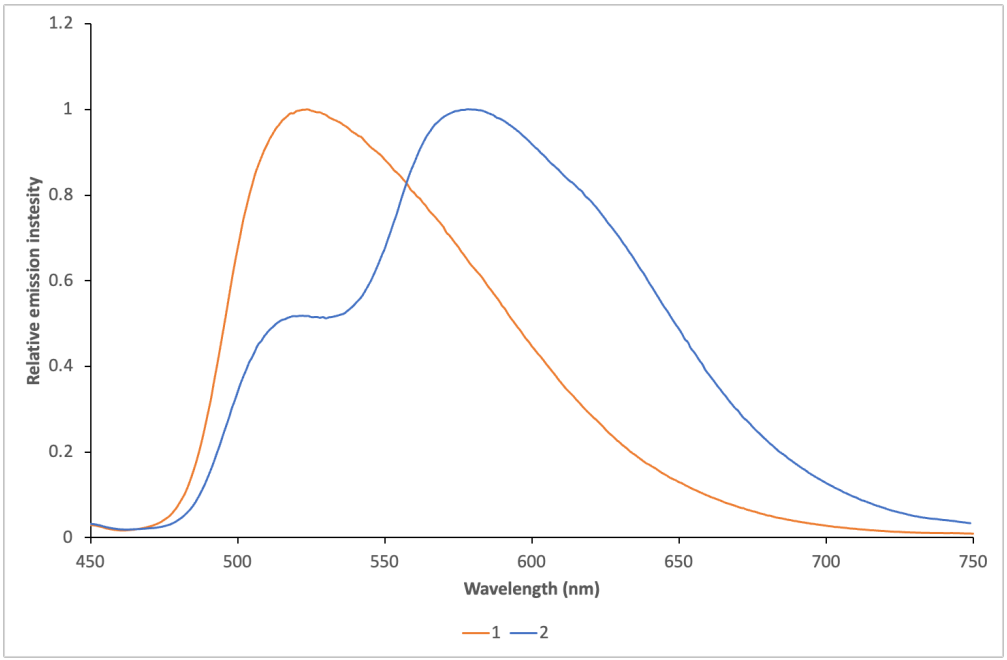

Figure 1. Emission profiles of complexes **1** and **2** (10 μM) in phosphate buffer (pH 7.4) obtained after excitation at 390 nm

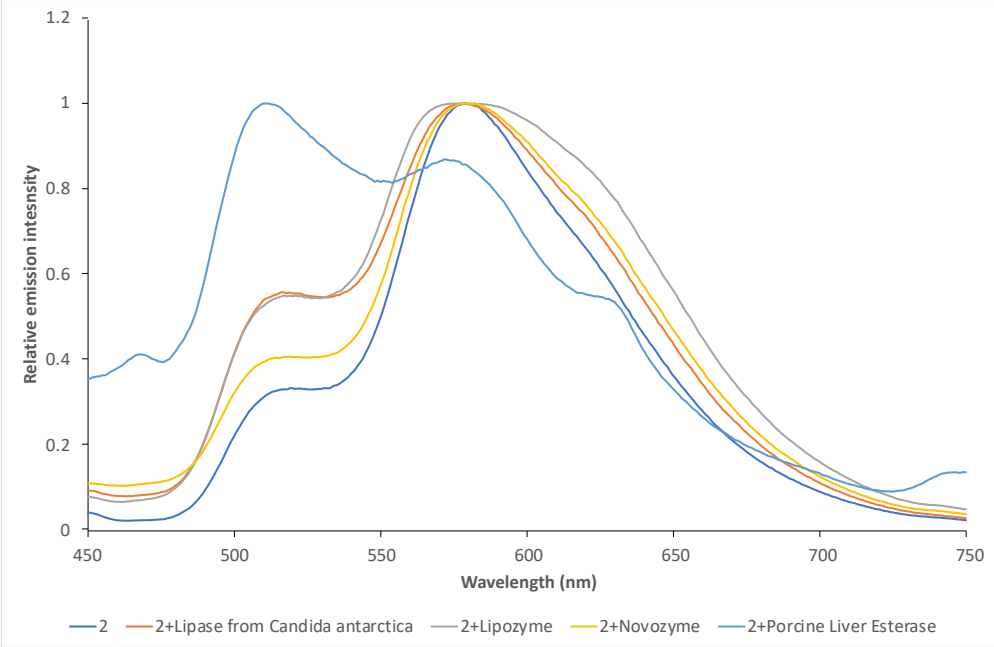

Figure 2. Emission spectra of complex **2** incubated in phosphate buffer (pH 7.4) in the absence and presence of various ester hydrolyzing enzymes at 45°C for 48 h (λ_{ex} = 390 nm)

The smallest change in the emission profile was observed for the incubation carried out in the presence of Novozyme®. A larger change in the emission profile was observed for incubations carried out in the presence of lipase B from *Candida antarctica* and Lipozyme. In all these cases, the feature at 580 nm remains the emission maximum. However, an increase in the relative intensity of the shoulder between 520 nm and 530 nm is observed. The largest

change in the emission profile was observed for the incubation carried out in the presence of porcine liver esterase, where the emission maximum again appears at 520 nm. However, even in this case the emission spectrum does not completely correspond to the emission spectrum of complex **1**, which suggests that the conversion is not complete. In summary, these results support our hypothesis of the possibility of using similar interconvertible iridium complexes with different lipophilicities as potential ratiometric luminescent probes. This will be explored further in the future.

Conclusion:

Two iridium complexes [Ir(ppy)$_2$ppy-OH] (**1**) and [Ir(ppy)$_2$ppy-Oct] (**2**) have been synthesized. The complexes exhibit different emission profiles in phosphate buffer at pH 7.4. Complex **1** has a simple broad emission peak with a maximum at 524 nm while complex **2** shows a more complex emission profile with a peak at 580 nm and a shoulder between 520 and 530 nm. These results have been rationalized, based on previous results, with the higher lipophilicity of complex **2**, which gives it a higher propensity to aggregate. Complex **2** has been incubated in the presence of four ester hydrolyzing enzymes. The emission spectra obtained after these incubations, especially in the case of incubation of complex **2** in the presence of porcine liver esterase, exhibit changes, which are consistent with the expected hydrolysis of the ester group of complex **2** and formation of complex **1**. These results suggest the possibility of developing of ratiometric luminescent sensors based on these types of triscyclometalated iridium complexes utilizing the change in their emission profile in response to change in their structure and propensity to aggregate.

Acknowledgements:

The authors acknowledge financial support from Fundamental Fund grant No. R2565B073. S.M. also acknowledges the support from the Science Achievement Scholarship of Thailand (SAST).

References:

1. Zubay GL, Parson WW, Vance DE. Principles of Biochemistry. Wm. C. Brown. Publishers. 1995.
2. da Rosa Witeck C, Schimtz AC, de Oliveira JMD, Porporatti AL, Canto GDL, de Souza Pires MM. J. de Ped. 2022;98:4-14.
3. Liu T-T, Liu X-T, Chen Q-X, Shi Y. Biomed & Pharmacotherapy. 2020;128:110314.
4. Fukami T, Yokoi T. Drug Metab Parmacokinet. 2012;27:466-477
5. Long JZ, Cravatt BF. Chem Rev. 2011;111:6022-6063.
6. Bachovchin DA, Cravatt, BF. Nat Rev Drug Disc. 2012;11:52-68.
7. Jin Q, Song L-L, Ding L-L, Zhang J, Wang D-D, Song Y-Q, Zou L-W, Ge G-B. TrAC Trends in Analytical Chemistry. 2022; 152:116620.
8. Martinez-Gurin K, Hubert N, Frazier K, Urlass S, Musch MW, Ojeda P, Pierre JF, Miyoshi J, Sontag TJ, Cham CM, Readon, CA, Leone V, Chang EB. Cell Host Microbe. 2018;23:458-469.
9. Liu Z-M, Feng L, Ge G-B, Lv X, Hou J, Cao Y-F, Cui J-N, Yang L. Biosens & Bioelect. 2014; 57: 30-35.
10. Li X, Gao X, Shi W, Ma H. Chem. Rev. 2014; 114: 590-659.
11. Zhu B, Guo B, Zhao Y, Zhang B, Du B. Biosens. Bioelectron. 2014; 55: 72-75.
12. Qiao Z, Zhang H, Zhang Y, Wang K. iScience. 2020;23:1-10.

13. Ma D-L, Ma VP-Y, Chan DS-H, Leung K-H, He H-Z, Leung, C-H. Coord. Chem. Rev. 2012;256:3087-3113.
14. Xu G-X, Mak EC-L, Lo KK-W. Inorg. Chem. Front. 2021;8:4553-4579.
15. Sansee A, Meksawangwong S, Chainok K, Franz KJ, Gál M, Pålsson L-O, Punyain W, Traiphol R, Pal R, Kielar F. Dalton Trans. 2016;45:17420-17430.
16. Meksawangwong S, Gohil B, Punyain W, Pal R, Kielar F. Inorg. Chim. Act. 2020;508, 119609.
17. Wan X-Y, Kimyonok A, Weck M. Chem. Comm. 2006;37:3933-3935.

WATER-SOLUBLE POLYMER DOTS FOR POTENTIAL AEROBIC OXIDATION IN AQUEOUS MEDIA

Phurinat Lorwongkamol, Ratanakorn Teerasaranyanon, Junjuda Unruangsri*
Department of Chemistry, Faculty of Science, Chulalongkorn University, Thailand
*e-mail: junjuda.u@chula.ac.th

Abstract:

A series of conjugated polymers containing a varying ratio of tetraphenylporphyrin cobalt(II) (CoTPP) were synthesized by the Suzuki-cross coupling reaction. By co-precipitating with amphiphilic species, poly(styrene-*co*-maleic anhydride), the water-soluble polymeric nanoparticles (Pdots) were obtained, with average sizes of less than 50 nm to larger than 100 nm in diameters depending on the amount of the incorporated metalloporphyrin units. The optical properties of both conjugated polymers and Pdots were studied and compared using UV-visible and fluorescence spectroscopy. Incorporating more CoTPP resulted in a larger blueshift of the absorption wavelengths and a considerable decline in luminescence intensity, both of which can be explained by the interruption of π-conjugation chain length by CoTPP units. The fluorescence intensity of conjugated polymers was completely quenched in Pdots, implying the efficient energy transfer caused by the compact polymer chains in the nanoparticles. The representative of Pdots has demonstrated its potential as a catalyst for sulfide-to-sulfoxide conversion in water, reaching up to 43% yield under 5-h-blue light irradiation and 31% yield in the dark, in which the reaction was assumed to proceed *via* different mechanisms under both conditions. Given the initial results, Pdots could potentially be candidates for efficient catalysis in a green solvent – water.

Introduction:

Regarding the incoming energy crisis and climate change, storing and utilization of infinite solar energy as renewable clean energy has become the main target for a future society. Taking the example from the photosynthesis in plants, the solar energy also benefits resource production a great deal as a mean of input energy for chemical synthesis and alternative fuel production.[1-3] To harvest light energy efficiently, a photocatalyst or a photosensitizer is essential. These species can absorb a broad wavelength range of photon energy, preferably in the visible light region. The collected energy will be passed on to the target molecule and start the chemical reaction.

Recently, a material known as conjugated polymer has received a lot of attention in photocatalysis study. The chemical structure of a conjugated polymer is based on the alternation of single and double bonds, making electron delocalization a prominent character throughout the structure, and this π-conjugation system is what creates the foundation of its electrical and optical properties. Importantly, the selection and modification of monomeric components allow the material to be fine-tuned to the molecular level.[4]

Nevertheless, the insolubility of organic polymers in water has limited their uses only in organic solvents. By putting together the hydrophobic conjugated polymer chain with an amphiphilic polymer into the aqueous phase, one can obtain the polymeric nanoparticles (Pdots) through self-assembly of both components. Pdots have gained tremendous attention in the development of imaging agents and fluorescence probes used in biological systems owing to their intense emission, high stability, and low toxicity.[5, 6] Recently, Pdots have been used in the visible-light driven hydrogen production, demonstrating the potential to be a promising photocatalyst.[7, 8]

In this work, we aim to demonstrate the potential of Pdots on the oxidation of sulfide into sulfoxide in water. Sulfoxides have been regarded as crucial intermediates in organic synthesis, especially in the preparation of many pharmaceuticals and biologically active compounds.[9] To replace the conventional way of sulfoxide production, which is to oxidize sulfide using a stoichiometric amount of toxic inorganic salts or peroxy acids, the current interests have been shifted towards photocatalytic aerobic oxidation – a process in which the reaction is driven by light energy, and molecular oxygen is used as the oxidant. The key to success lies in the catalyst which harvests the photon energy, enhances the reaction rate, and controls the product selectivity.[10, 11]

In addition to the conjugated polymer entity, porphyrin has been chosen to be incorporated into the polymer chain as a co-catalyst. Since the potential of porphyrins in generating reactive oxygen species is well-studied,[12, 13] we expected that integration of both porphyrin and conjugated polymer would lead to an improvement of in-chain interaction and facilitate the energy transfer, which eventually boosts the generation of reactive oxygen species. Many examples of conjugated polymers in photocatalytic aerobic oxidation of sulfides have been reported including heterogeneous triazine-based conjugated microporous polymers,[14, 15] and porphyrin-incorporated polymers.[16] The oxidation reaction occurs via the photo-generated singlet oxygen, or superoxide anion, producing the sulfoxide product in excellent conversion/yield with only a small amount of over-oxidized sulfone. In addition, the formation of Pdots has been reported to enhance the interchain interaction stemming from the close distance between polymer chains in a nanoparticle.[17, 18]

In this work, we prepared series of CoTPP-Pdots dispersed in water by co-precipitating the metalloporphyrin-incorporated conjugated polymer together with poly(styrene-*co*-maleic anhydride). Three types of conjugated polymers were selected: PF (poly(9,9'-dioctylfluorene)), PFBT (poly[(9,9'-dioctylfluorene)-*co*-(2,1,3-benzothiadiazole)]), and PFEDOT (poly([(9,9'-dioctylfluorene)-*co*-(3,4-ethylenedioxythiophene)]). The porphyrin of choice is tetraphenylporphyrin cobalt(II) (CoTPP) as its catalytic activity in the aerobic oxidation reaction of sulfides has rarely been studied. Effects of the varying amounts of CoTPP units in the conjugated polymer backbone and the formation of Pdots were investigated and discussed using UV-visible and fluorescence spectroscopy techniques. In a preliminary study, the selected CoTPP-containing Pdots showed promising catalytic activity in the aerobic oxidation of thioanisole into its corresponding sulfoxide without detecting sulfone as the over-oxidized product.

Methodology:

Chemicals and Reagents

All solvents (analytical grade) were purchased from commercial sources and were dried on molecular sieves and stored under nitrogen atmosphere before use. All chemicals and reagents are analytical grade and were used without further purification. 9,9'-dioctylfluorene-2,7-diboronic acid (F-BOH) was purchased from Chemenu. tetrakis(triphenylphosphine)palladium(0), and poly(styrene-*co*-maleic anhydride) (avg. M_n ~ 1,900) were purchased from Sigma Aldrich. 9,9'-dioctyl-2,7-dibromofluorene (F-Br_2), 4,7-dibromo-2,1,3-benzothiadiazole (BT-Br_2), 2,5-Dibromo-3,4-ethylenedioxythiophene (EDOT-Br_2), and thioanisole were purchased from TCI Chemical.

Synthesis of 5,15-bis(4-bromophenyl)-10,20-diphenylporphyrin cobalt(II) (CoTPP-Br_2)

Synthesis procedure of Br_2-CoTPP was brought from the previous literature.[19] First, benzaldehyde and excess amount of pyrrole underwent condensation reaction to create 5-phenyldipyrromethane. Next, one equivalent of 4-bromobenzaldehyde was added to form the porphyrin ring with two bromophenyl groups opposite to each other. The last step is the coordination of cobalt(II) ion, which can be achieved by reacting the as-synthesized

porphyrin and Co(II) acetate in a solution at elevated temperature, resulting in an intense red powder.

General Procedure for Polymerization via Suzuki Cross-coupling

In a reaction flask was added F-BOH, CoTPP-Br_2, dibromo monomer, $Pd(PPh_3)_4$, 2 M solution of K_2CO_3, and THF, then the mixture was refluxed under N_2 atmosphere for 48 h. Bromobenzene was added at the end of the reaction time and the reflux was kept on for another 12 h. The reaction was stopped by adding DI water, and the product was extracted by $CHCl_3$. Purification was achieved by precipitating a concentrated polymer solution in $CHCl_3$ to methanol, followed by washing the solid product with DMF, and methanol, sequentially. Finally, the polymer was dried in a vacuum oven at 60 ˚C overnight. The corresponding polymer structure and the ratio of the components are illustrated in the following **Scheme 1**. Each conjugated polymer was called according to its component (PF, PFBT, or PFEDOT) followed by the number signifying the mole percentage fraction of CoTPP (5%Co, 15%Co, or 30%Co).

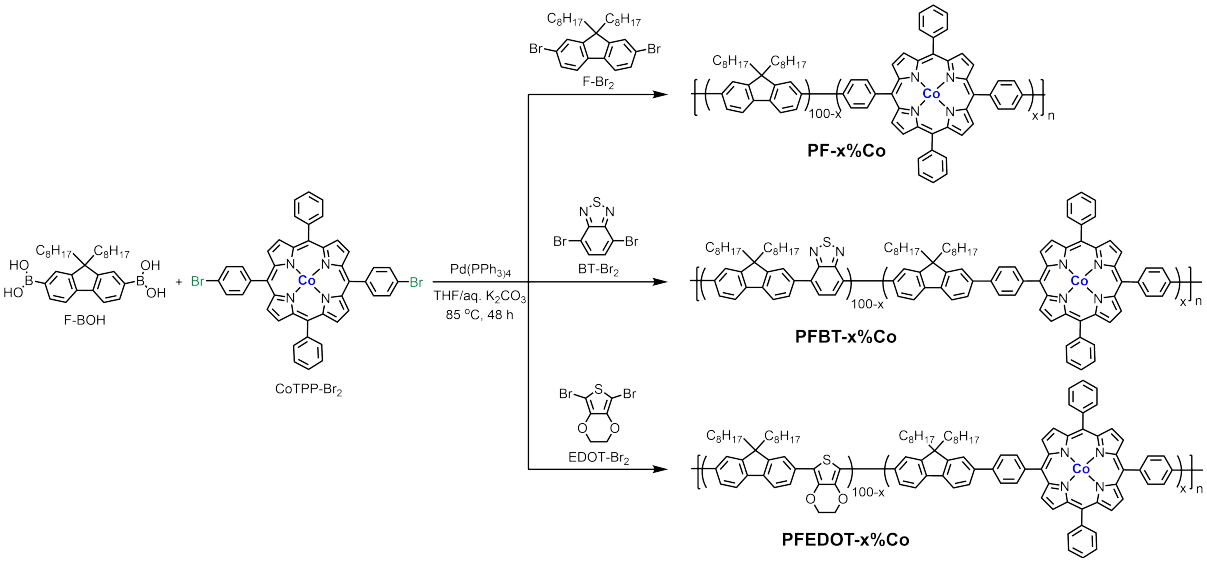

Scheme 1. The syntheses of CoTPP-containing conjugated polymers.

Preparation of Pdots

The following **Scheme 2** illustrates the preparation of Pdots. Firstly, the stock solutions of conjugated polymer, and poly(styrene-*co*-maleic anhydride) (PSMA), each with the concentration of 1 mg/mL in THF, were prepared separately. Then, 250 µL of polymer solution and 187.5 µL of PSMA solution were pipetted into 5 mL of THF, and the mixture was briefly sonicated until homogeneous. After that, the mixture was quickly injected into 10 mL of sonicated Milli-Q water. The THF was removed by purging the solution with a stream of N_2 while keeping the sonication on for 30 min. At the end, the solution was filtered through a 0.45 µm nylon filter, giving the clear solution with the color corresponding to the conjugated polymer used.

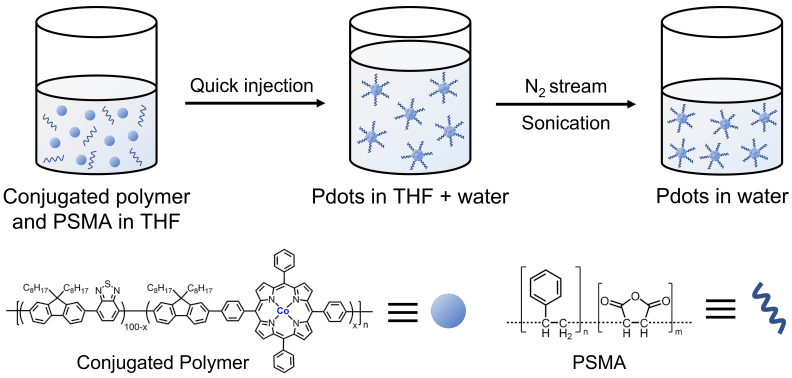

Scheme 2. Preparation of Pdots

Catalysis study

In a 10-mL test tube equipped with a stir bar was added 2 mL of Pdots solution and 0.2 mmol of thioanisole. The mixture was sparged with a stream of O_2 for 10 min and the tube was equipped an oxygen balloon to supply the gas throughout the reaction. The mixture was then irradiated by a commercial blue LED strip (15 W) for 5 h under constant stirring while heat from the light source was minimized by strong air flow. Product was collected by extracting the mixture with $CDCl_3$ and the yield was evaluated by comparing the integration of ^{1}H-NMR methyl signals of the reactant (δ = 2.48 ppm, C$\underline{H}_3$) and the product (δ = 2.73 ppm, C$\underline{H}_3$) to a known amount of anisole (δ = 3.81 ppm, C$\underline{H}_3$) as the internal standard. For the experiment without light, the same condition was applied while the test tube was wrapped in aluminium foil and the experiment was carried in a black box.

Results and Discussion:

Optical Properties of the Conjugated Polymers

The optical properties of each conjugated polymer were investigated by both UV-Visible spectroscopy and fluorescence spectroscopy. Absorption spectra of the polymers with different ratios of CoTPP for each series are shown in **Figure 1**. Two characteristic absorption bands of porphyrins, the narrow Soret band at around 440 nm and the broad Q bands appearing between 500–650 nm, are presented in every spectrum. Compared to those of the monomer CoTPP-Br_2, these characteristic CoTPP bands shifted to longer wavelengths and became broader as expected from the conjugation in the polymer chain. In contrast, the absorption band of the polymer chain gradually blue-shifted with higher content of CoTPP because of the naturally twisted phenyl rings on each porphyrin, which, in turn, interrupted the π-conjugation and conductivity of the entire polymer chain.

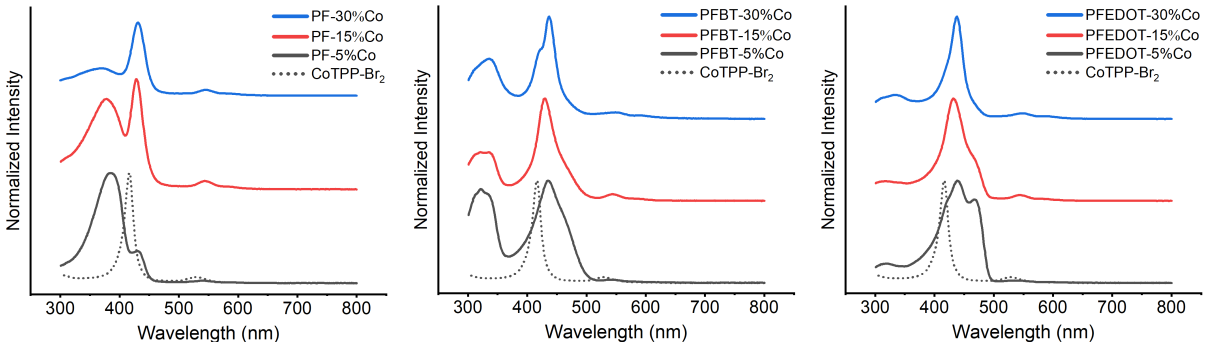

Figure 1. UV-Visible spectrum of each conjugated polymer with different CoTPP ratio (solid line). Metalloporphyrin monomer, Br_2-CoTPP, was included for comparison (dashed line).

Strong fluorescence emission is also the main feature of conjugated polymers. The incorporation of higher cobalt porphyrin contents resulted in a drastic decrease in fluorescence intensity as observed in the emission-excitation spectra shown in **Figure 2**. This consequence can be explained by the interruption of the electron delocalization system, which shortens the conjugate chain length and reduces the emission-excitation activity. Moreover, while CoTPP does not emit fluorescence, its absorption is comparatively strong which can act as the quencher in the solution. This implies that energy transfer could occur between the conjugated polymeric parts and the metalloporphyrin units efficiently. This effect is however weighed out with the lower photo-harvesting ability of shortened conjugated chain length in the polymers. The amount of CoTPP in the structure therefore directly affects the electronic property of the polymers, and ultimately the catalytic activity.

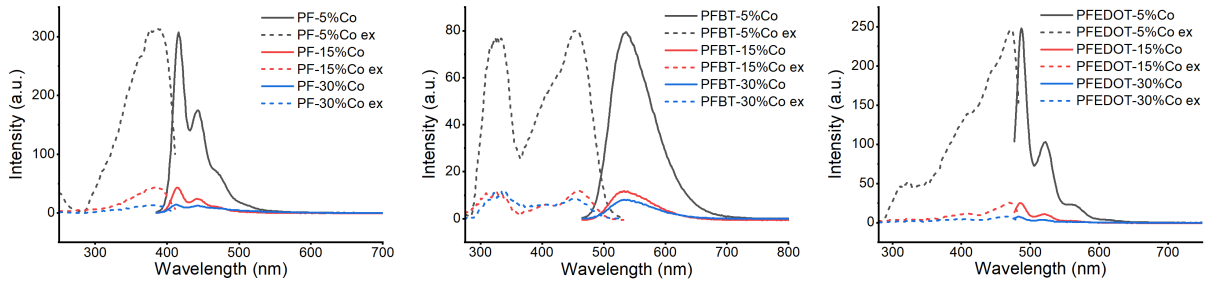

Figure 2. Emission (solid lines) and excitation (dashed lines) spectra of each conjugated polymer with different ratio of CoTPP. All measurement were conducted with 5 μg/mL solution, 2.5 nm slit width, and detector voltage set to 590 V.

Formation of Polymeric Nanoparticles

The size distribution of Pdots (**Figure 3**) was evaluated by the dynamic light scattering technique. With CoTPP amounts smaller than 15 mol%, it is possible to form nanoparticles having an average diameter of less than 50 nm. On the other hand, the inclusion of metalloporphyrin at 30 mol% into the polymers led to nanoparticles with diameters larger than 100 nm. As the formation of Pdots relies on the hydrophobic interaction between polymer chains, which results in the densely packed structure,[20] the twisted and bulky structure of the porphyrin might intervene in this interaction and loosen the nanoparticle core. More attempts to form Pdots from conjugated polymers with such high CoTPP content sometimes resulted in non-uniform size distribution including varying average sizes. Given the poor repeatability, this series of Pdots will be excluded from further study in this work.

UV-Visible and fluorescence spectroscopic measurements were used to observe the optical properties of the Pdots and compare them with the bare polymer chains in the organic solvent. Blue-shifted signals were observed in the absorption spectra of Pdots (**Figure 4a**) as a result of lower π-conjugation caused by chain bending in a hydrophobically confined space. The formation of Pdots has completely quenched the fluorescence of the conjugated polymers as can be seen from the emission spectra of those polymers with 5mol% CoTPP (**Figure 4b**). This could signify the superior energy transfer due to the proximity of polymer chains in a nanoparticle.[21]

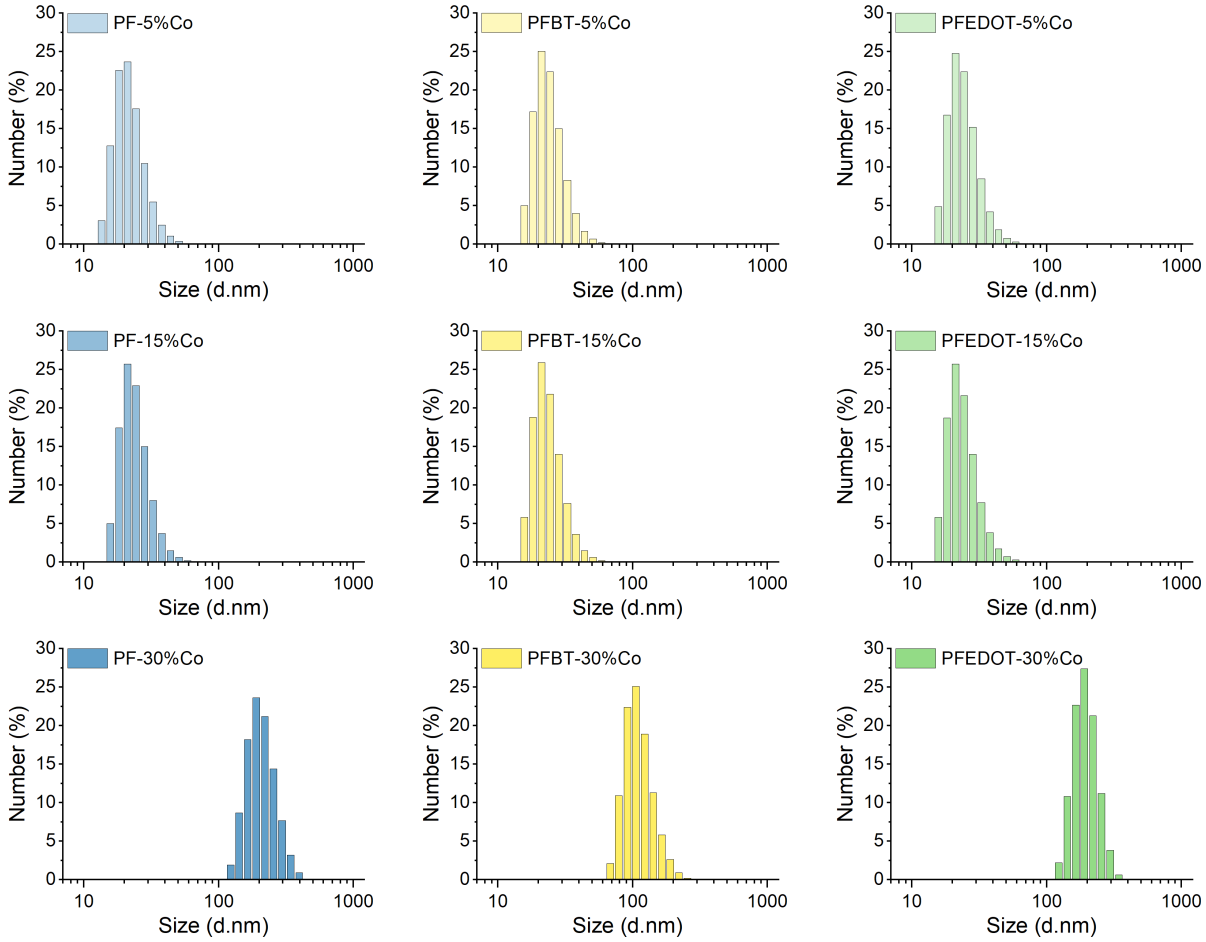

Figure 3. Dynamic light scattering spectrum of Pdots from different conjugated polymer.

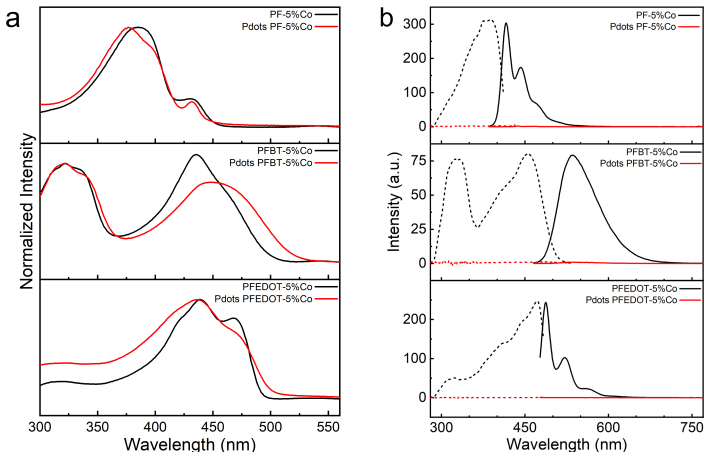

Figure 4. Comparison of UV-visible spectra (a), and excitation-emission spectra (b) between bare polymers dissolved in THF and their corresponding Pdots in water.

Catalysis Study

A preliminary test using the Pdots of PF-5%Co and PF-15%Co (Pdots-PF-5%Co and Pdots-PF-15%Co) was conducted to examine the potential of Pdots in catalyzing the oxidation of thioanisole into methyl phenyl sulfoxide under an O_2 atmosphere at room temperature, both with and without light irradiation.

Under 5 h blue-light irradiation, Pdots-PF-5%Co was able to convert thioanisole into methyl phenyl sulfoxide at 43% yield. When Pdots-PF-15%Co was used as a catalyst, the

oxidized product was formed in a smaller yield (ca. 30%). These experiments have pointed out the lower catalytic activity was a consequence of shorter conjugated chain length and worsen the light-harvesting ability of the polymer chain. Without the catalyst, no sulfoxide was detected, confirming that the thioanisole was not oxidized only under an oxygen atmosphere. Concurrently, the significance of the catalyst was affirmed in this reaction.

When the irradiation was off, the conversion of thioanisole to the corresponding sulfoxide was also obtained with closer to 30% yielding, in the presence of Pdots-PF-5%Co as a catalyst. The detected product was formed in slightly smaller quantities compared to those obtained under the irradiation condition. The previous studies denoted that cobalt porphyrins could catalyze the oxidation reaction through a radical pathway or high-valent oxo complex intermediate.[22-25] Given the present condition, the polymer chains and the environment inside the Pdots could help stabilize the active intermediate, and the reaction proceeded even in dark.

At this point, it could be postulated that both conjugated polymer backbone and CoTPP unit contribute to the oxidation of thioanisole in this study both in the presence of light irradiation or in dark. The materials could catalyze the oxidation in two separate pathways: (i) the backbone works as a photosensitizer, absorbing photon energy and then passing it to CoTPP to generate reactive oxygen species, and (ii) the CoTPP units in polymers could catalyze the oxidation through the oxo-complex formation or radical intermediate. The insight investigation is underway.

Conclusion:

In conclusion, a series of conjugated polymer nanoparticles containing CoTPP in the polymer backbone were synthesized, and their optical properties were investigated by spectroscopic techniques. Tailoring CoTPP into the polymer chain resulted in a decrease in the degree of π-conjugation as evidenced by the blueshift of the absorption wavelength and a drastic decrease in fluorescence intensity. This creates a balance between the energy transfer between the conjugated chain length and CoTPP units, and the photo-harvesting ability of the polymeric chains. With an appropriate amount of CoTPP, the polymer chains were able to be assembled into nanoparticles with small diameters (< 50 nm). Fluorescence quenching was observed for all Pdots as a result of interchain interaction, leading to efficient energy transfer. In the catalysis study, Pdots-PF-5%Co was able to convert thioanisole into methyl phenyl sulfoxide, reaching up to 43% yield within 5 h under irradiation. The current work has shown the potential of the metalloporphyrin-incorporated Pdots to be an efficient catalyst for the aerobic oxidation reaction of sulfide. Nevertheless, there are still wide opportunities to improve the catalytic activity of this material. The ongoing works include finding the optimized ratio of metalloporphyrin, extending substrate scope, and studying catalyst recyclability. In the end, we believe that the advantage of the catalyst being able to work in a fully aqueous media could contribute to the sustainable development of environmentally benign chemical processes.

Acknowledgements:
We acknowledge the Thailand Toray Science Foundation (TTSF) for the financial support.

References:

1. Shaw M H, Twilton J, MacMillan D W C. J. Org. Chem. 2016;81:6898-6926.

2. Ni M, Leung M K H, Leung D Y C, Sumathy K. Renewable Sustainable Energy Rev. 2007;11:401-425.
3. Yamazaki Y, Takeda H, Ishitani O. J. Photochem. Photobiol., C 2015;25:106-137.
4. Dai C, Liu B. Energy Environ. Sci. 2020;13:24-52.
5. Wu C, Chiu D T. Angew. Chem. Int. Ed. Engl. 2013;52:3086-3109.
6. Wu C, Schneider T, Zeigler M, Yu J, Schiro P G, Burnham D R, McNeill J D, Chiu D T. J. Am. Chem. Soc. 2010;132:15410-15417.
7. Jayakumar J, Chou H H. ChemCatChem 2020;12:689-704.
8. Lin W-C, Elsayed M H, Jayakumar J, Ting L-Y, Chang C-L, Elewa A M, Wang W-S, Chung C-C, Lu C-Y, Chou H-H. Int. J. Hydrogen Energy 2020;45:32072-32081.
9. Fernández I, Khiar N. Chem. Rev. 2003;103:3651-3706.
10. Skolia E, Gkizis P L, Kokotos C G. ChemPlusChem 2022;87:e202200008.
11. Shi Z, Zhang C, Tang C, Jiao N. Chem. Soc. Rev. 2012;41:3381-3430.
12. Macdonald I J, Dougherty T J. J. Porphyrins Phthalocyanines 2001;05:105-129.
13. DeRosa M C, Crutchley R J. Coord. Chem. Rev. 2002;233-234:351-371.
14. Luo J, Lu J, Zhang J. J. Mater. Chem. A 2018;6:15154-15161.
15. Lan X, Wang J, Li Q, Wang A, Zhang Y, Yang X, Bai G. ChemSusChem 2022;15:e202102455.
16. Jiang J, Liang Z, Xiong X, Zhou X, Ji H. ChemCatChem 2020;12:3523-3529.
17. Pati P B, Damas G, Tian L, Fernandes D L A, Zhang L, Pehlivan I B, Edvinsson T, Araujo C M, Tian H. Energy Environ. Sci. 2017;10:1372-1376.
18. Dmitriev R I, Borisov S M, Düssmann H, Sun S, Müller B J, Prehn J, Baklaushev V P, Klimant I, Papkovsky D B. ACS Nano 2015;9:5275-5288.
19. Yujia X, Fengyong Z, Pingle L, Fang H, He'an L. Can. J. Chem. 2014;92:49-53.
20. Wu C, Hansen S J, Hou Q, Yu J, Zeigler M, Jin Y, Burnham D R, McNeill J D, Olson J M, Chiu D T. Angew. Chem. Int. Ed. 2011;50:3430-3434.
21. Wu C, Zheng Y, Szymanski C, McNeill J. J. Phys. Chem. C 2008;112:1772-1781.
22. Jiang Q, Xiao Y, Tan Z, Li Q-H, Guo C-C. J. Mol. Catal. A: Chem. 2008;285:162-168.
23. Nakazono T, Parent A R, Sakai K. Chem. Commun. 2013;49:6325-6327.
24. Wang D, Groves J T. Proc. Natl. Acad. Sci. U.S.A. 2013;110:15579-15584.
25. Huang G, Mo L Q, Wei Y X, Zhou H, Guo Y A, Wei S J. Catalysts 2018;8:199.

Session C:
CHEMISTRY
(Organic & Medicinal Chemistry)

REVELATION OF PARAMETERS INFLUENCING THE SYNTHESIS OF THE 7-AZAINDOLES VIA THE LAROCK HETEROANNULATION REACTION

Thanawit Thippong, Poomsith Thangsan, Pitak Chuawong*
Department of Chemistry and Center of Excellence for Innovation in Chemistry, Faculty of Science, Special Research Unit for Advanced Magnetic Resonance (AMR), Kasetsart University, Bangkok 10900, Thailand
*e-mail: Pitak.C@ku.th

Abstract:

A synthetic methodology for 2,3-diphenyl-7-azaindole via the Larock heteroannulation is described. Our model reaction utilizes diphenyl acetylene and 2-amino-3-bromopyridine as reactants. Different additives and bases were screened to achieve the desired product. The optimized reaction conditions require 140 °C with $Pd(OAc)_2/PPh_3$ as a catalyst, Na_2CO_3 as a base, and *n*-Bu_4NCl as an additive, providing 2,3-diphenyl-7-azaindole in 56% yield. The presence of an acetyl or trifluoroacetyl substituent on the amino group of 2-amino-3-bromopyridine reactant does not enhance the reaction efficiency. The DFT calculations were employed to investigate the reaction energetics in the oxidative addition step, the rate-determining step in the Larock reaction. The results indicated similar energy barriers in the presence or absence of the electron-withdrawing substituent on the 2-amino-3-bromopyridine, agreeing with the experimental observations.

Introduction:

Azaindoles are aromatic heterocyclic compounds consisting of a pyrrole ring fused to a pyridine ring (**Figure 1**). Azaindoles are considered bioisosteres of indole with a variation of the position of the nitrogen atom on the benzene ring.[1] There are four possible positional isomers: 4-, 5-, 6-, and 7-azaindoles. In particular, 7-azaindoles have attracted much attention because of their remarkable physicochemical and pharmacological properties.[2] The presence of the nitrogen atom at the 7-position of the indole enhances hydrogen bond formation between the 7-azaindole and its biological targets. Marketed drugs with a 7-azaindole core structure include Vemurafenib for treating late-stage melanoma and Venetoclax for treating chronic lymphocytic leukemia (**Figure 1**).[3,4] Several methods for the preparation of 7-azaindole derivatives have been developed, including the Fisher, Madelung, and Reissert procedures. However, poor yields and limited reaction scope are some disadvantages of the methods mentioned above.[5] Therefore, developing a more effective synthetic methodology to afford 7-azaindole is of great interest.

Larock heteroannulation is an effective method to synthesize indole derivatives in a single step.[6] The first 7-azaindole synthesis via the Larock reaction was achieved using 2-amino-3-iodopyridine and internal alkyne reactants to afford 2,3-disubstituted-7-azaindole.[7,8] Moreover, the Larock conditions using the less reactive 2-amino-3-bromopyridine have also been reported by Ontoria and co-workers.[9] The Larock reaction between methyl ester substituted 2-amino-3-bromopyridine and sterically hindered internal alkynes provided 7-azaindole derivatives in good yields. In 2016, Reisman and co-workers reported the unnatural tryptophan synthesis using substituted 2-amino-3-bromopyridine and alkynyl substrates containing peptide functionality.[10] Notably, reactive palladium catalysts, such as $Pd(dppf)Cl_2$

or Pd[P(^{t}Bu)$_3$]$_2$, were utilized in the Larock heteroannulation reaction with bromopyridine, while Pd(OAc)$_2$ was ineffective.[8,10]

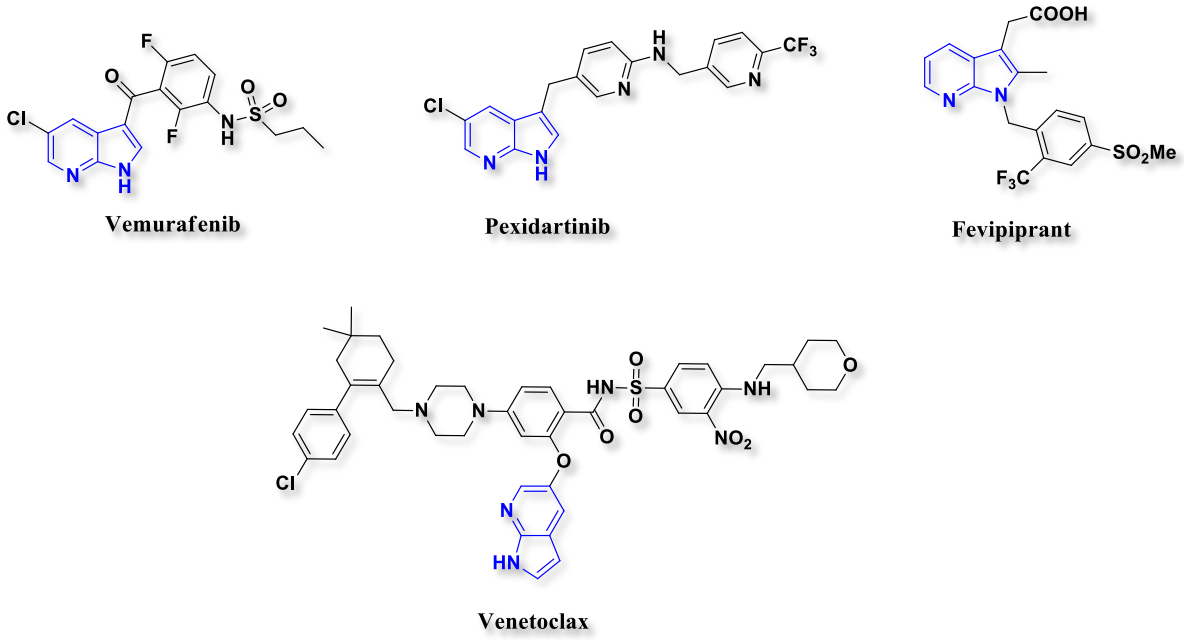

Figure 1. Examples of marketed drugs containing 7-azaindole scaffolds.[3,4]

This work aimed to optimize the Larock reaction protocol to synthesize 2,3-disubstituted 7-azaindoles from 2-amino-3-bromopyridine and diarylacetylenes. The initially reported Larock reaction conditions with Pd(OAc)$_2$, PPh$_3$, Na$_2$CO$_3$, and *n*-Bu$_4$NCl were utilized. The reaction efficiency was temperature-dependent, allowing the starting material to be consumed entirely at a higher temperature. The electronic perturbation at the amino group was created to expedite the oxidative addition step. However, incomplete conversion of the reactant was observed under the same reaction conditions. Density functional theory (DFT) calculations revealed similar activation energies of the oxidative addition with different bromopyridine reactants.

Methodology:

1. General Procedure

Starting material, 2-amino-3-bromopyridine **1**, was purchased from Combi-Blocks and used without further purification. Chemical structures of the synthesized compounds were identified based on nuclear magnetic resonance spectroscopy (NMR) and high-resolution mass spectrometry (HRMS). The ^{1}H and ^{13}C{^{1}H} NMR spectra were recorded at 400 and 100 MHz, respectively, on a Bruker 400 MHz AVANCE III HD spectrometer. Residual peaks of CHCl$_3$ (7.26 ppm for ^{1}H and 77.16 ppm for ^{13}C{^{1}H} NMR), (CH$_3$)$_2$SO (2.50 ppm for ^{1}H and 39.52 ppm for ^{13}C{^{1}H} NMR) were used as internal references. TMS was added to CDCl$_3$ and used as an internal reference when signals superimposed the residual peak from samples. Chemical shifts (δ) were reported in parts per million (ppm) and coupling constants (J) were in Hertz (Hz). High-resolution mass spectra (HRMS) were recorded on Bruker, microTOF (Bruker Daltonics, Bremen, Germany) in the positive mode with electrospray ionization (ESI). Thin-layer chromatography (TLC) was conducted on Merck® aluminum-backed 0.2 mm thick silica gel 60 F254 plates, Germany. The plates were visualized under a 254 nm and 365 nm UV lamp, followed by spraying with visualizing reagents, including vanillin, ninhydrin, or

phosphomolybdic acid solutions. Flash column chromatography was performed on SiliCycle® silica gel 60 (70-230 mesh), Canada.

*2. Synthesis of N-(3-bromopyridin-2-yl)-2,2,2-trifluoroacetamide (**2**)*

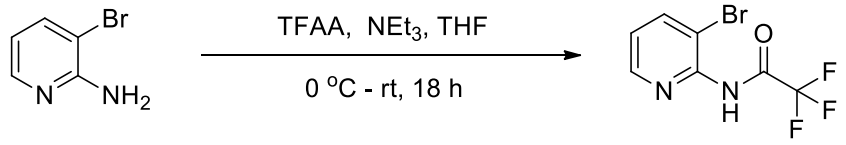

1 **2**

Scheme 1. Synthesis of *N*-(3-bromopyridin-2-yl)-2,2,2-trifluoroacetamide (**2**)

To a solution of 2-amino-3-bromopyridine (**1**) (0.26 g, 1.5 mmol) in THF (4 mL) was added NEt_3 (0.25 mL, 1.8 mmol) and trifluoroacetic anhydride (TFAA, 0.25 mL, 1.5 mmol) dropwise at 0℃. The reaction mixture was stirred for 10 min before cooling to room temperature and continued stirring for 18 h. Subsequently, the reaction was quenched with water, extracted with EtOAc (3×50 mL), washed with brine, and dried over anhydrous Na_2SO_4. Then, the crude mixture was concentrated *in vacuo* to give compound **2** as an off-white solid (363.5 mg, 90%); ^{1}H NMR (400 MHz, $CDCl_3$) δ 11.03 (s, 1H), 8.07 (dd, J = 7.7, 1.5 Hz, 1H), 7.89 (dd, J = 6.2, 1.5 Hz, 1H), 6.75 (dd, J = 7.7, 6.2 Hz, 1H); ^{13}C{^{1}H} NMR (100 MHz, $CDCl_3$) δ 162.8, 162.4, 153.2, 145.9, 135.9, 113.2, 107.8.

*3. Synthesis of N-(3-bromopyridin-2-yl)acetamide (**3**)*

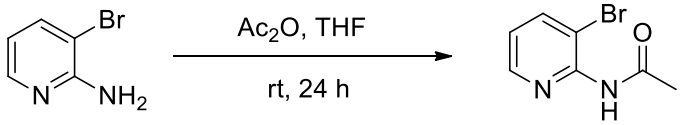

1 **3**

Scheme 2. Synthesis of *N*-(3-bromopyridin-2-yl)acetamide (**3**)

To a solution of 2-amino-3-bromopyridine (**1**) (0.52 g, 3.0 mmol) in THF (3 mL) was added Ac_2O (0.57 mL, 6.0 mmol). The reaction mixture was stirred at room temperature for 24 h. Subsequently, the reaction was quenched with water, extracted with EtOAc (3×50 mL), and dried over anhydrous Na_2SO_4. Then, the mixture was filtered and concentrated *in vacuo* to obtain a crude mixture. The crude mixture was purified by flash column chromatography using EtOAc to give compound **3** as a yellow solid (367.7 mg, 57%); ^{1}H NMR (400 MHz, $CDCl_3$) δ 8.34 (dd, J = 4.7, 1.6 Hz, 1H), 7.87 (dd, J = 7.9, 1.6 Hz, 2H), 6.95 (dd, J = 7.9, 4.7 Hz, 1H), 2.45 (s, 3H); ^{13}C{^{1}H} NMR (100 MHz, $CDCl_3$) δ 171.8, 151.6, 148.7, 142.6, 125.7, 121.2, 26.4. The spectroscopic data are in agreement with those previously reported.[11]

*4. Synthesis of diphenylacetylene (**6**) via the Sonogashira coupling reaction*

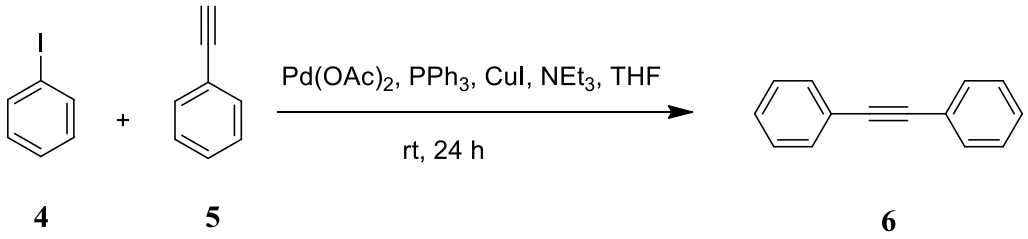

Scheme 3. Synthesis of diarylacetylene (**6**)

To a 20 mL Schlenk tube charged with a stirring bar was added 1 mol% $Pd(OAc)_2$ (11.2 mg, 0.05 mmol), 2 mol% PPh_3 (52.4 mg, 0.2 mmol), and 1 mol% CuI (9.52 mg, 0.05 mmol). After evacuation and flush with argon thrice, iodobenzene (**4**) (0.56 mL, 5.0 mmol), phenylacetylene (**5**) (0.65 mL, 6.0 mmol), THF (5 mL), and NEt_3 (3.5 mL, 25 mmol) were added subsequently. The mixture was stirred at room temperature for 24 h. After the aryl iodide was completely consumed, the reaction was quenched with saturated NH_4Cl (50 mL) and extracted with EtOAc (3×50 mL). The organic layers were combined and washed with water and brine, dried over anhydrous Na_2SO_4, and concentrated *in vacuo*. The crude reaction mixture was purified by flash column chromatography using hexane to give compound **6** as an off-white solid (828.8 mg, 93%); ^{1}H NMR (400 MHz, $CDCl_3$) δ 7.57 – 7.52 (m, 4H), 7.39 – 7.33 (m, 6H); $^{13}C\{^1H\}$ NMR (100 MHz, $CDCl_3$) δ 131.8, 128.5, 128.4, 123.4, 89.5. The spectroscopic data are in agreement with those previously reported.[12]

5. Synthesis of 2,3-diphenyl-1H-pyrrolo[2,3-b]pyridine (7) via the Larock heteroannulation reaction

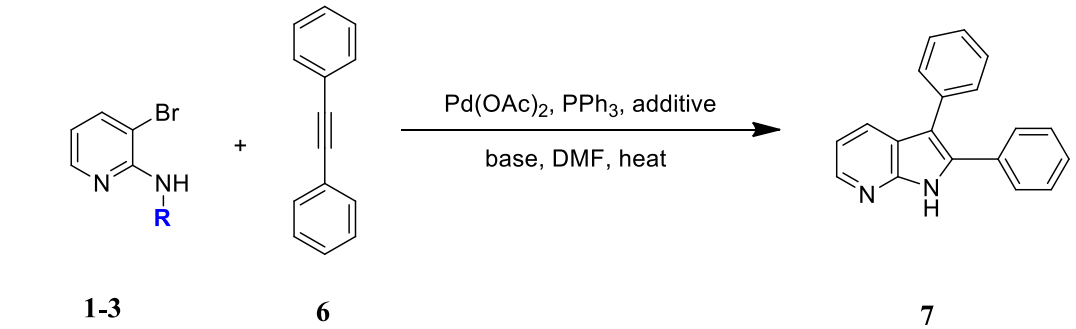

R = H, $COCH_3$, $COCF_3$

Scheme 4. Synthesis of 7-azaindole compounds (**7**)

To a Schlenk tube equipped with a magnetic stirrer was added 10 mol% $Pd(OAc)_2$ (11.2 mg 0.05 mmol), 20 mol% PPh_3 (26.22 mg, 0.1 mmol), an additive (0.5 mmol), a base (2.50 mmol), 2-amino-3-bromopyridine **1** (0.5 mmol), diphenylacetylene (0.7 mmol), and anhydrous DMF (5 mL). The mixture was heated under an argon atmosphere for 24 h. Subsequently, the reaction mixture was quenched with saturated NH_4Cl (50 mL) and extracted with EtOAc (3 × 50 mL). The organic layers were washed with water and brine, dried over anhydrous Na_2SO_4,

and concentrated *in vacuo*. The crude reaction mixture was purified by flash column chromatography using 20% EtOAc/hexane to give compound **7** as a yellow solid (75.7 mg, 56%); ^{1}H NMR (400 MHz, DMSO-d_6) δ 12.14 (s, 1H), 8.28 (dd, J = 4.6, 1.6 Hz, 1H), 7.87 (dd, J = 7.9, 1.6 Hz, 1H), 7.51 – 7.46 (m, 2H), 7.43 – 7.27 (m, 8H), 7.12 (dd, J = 7.9, 4.7 Hz, 1H); ^{13}C{^{1}H} NMR (100 MHz, DMSO-d_6) δ 148.6, 143.4, 134.6, 134.4, 131.7, 129.6, 128.8, 128.6, 128.5, 128.0, 126.7, 126.4, 120.3, 116.4, 111.8. HRMS (ESI-TOF) *m/z*: $[M + H]^+$ calcd for $C_{19}H_{15}N_2$, 271.1230; found, 271.1231. The spectroscopic data are in agreement with those previously reported.[13]

6. Computational Details

All structures involved in the oxidative addition step of the Larock reaction were optimized using the hybrid density functional B3LYP method in the Gaussian 09.[14] The basis set for palladium was LANL2DZ effective core potential (ECP). All other atoms were treated with the 6-31G(d,p) basis set. The polarizable continuum model was applied to all calculations to model the effect of solvent (DMF) on the energy profile. The free energies of all optimized geometries at 373.15 K and 1 atm were obtained via single-point calculations at the same level of theory.

Results and Discussion:

The aim of this work is to optimize the reaction conditions for the 7-azaindole synthesis using the Larock heteroannulation reaction. We started with the preparation of diphenylacetylene **6** via the Sonogashira coupling. Reactant consumptions were investigated using ^{1}H-NMR of the crude reaction mixture dissolved in DMSO-d_6. As a result, compound **6** was obtained in 93%. With the internal alkyne **6** in hand, the reaction optimization was conducted, and the results were summarized in Table 1.

Initially, the Larock conditions previously utilized by us were utilized.[15] The reaction was performed at 80 ℃ for 24 h, but the reaction did not proceed, and the reactant was recovered (entry 1). Subsequently, the additive was changed because it was reported as an essential component in the reaction.[16,17] Lithium chloride, a commonly used additive in the Larock reaction, was added to the reaction, but the reaction did not proceed (entry 2). Next, the reaction temperature was increased to 100 ℃ and 120 ℃, respectively. At this point, the reaction was still incomplete, providing modest yields of compound **7** (entries 3 and 4). Besides, the reaction using LiCl conducted at 120 ℃ gave a similar reaction outcome (entry 5). Prolonged reaction time (48 h) did not improve the reaction efficiency, as illustrated in entry 6. Furthermore, changing the inorganic base to Cs_2CO_3 or CH_3COOK did not provide a complete consumption of the reactant with similar product yields as the previously attempted conditions (entries 7 and 8). Gratifyingly, the complete conversion was observed when the reaction temperature was increased to 140 ℃ with the isolated yield of the desired 7-azaindole product of 56% (entry 9). Therefore, the high-temperature conditions were chosen to be optimum to achieve the desired product. The ^{1}H NMR spectroscopic analysis of the crude reaction mixture revealed that no reactant remained in the reaction at 140 ℃, as illustrated in **Figure 2**.

Table 1. The optimization of reaction condition for synthesis of 7-azaindole compounds via the Larock heteroannulation reaction

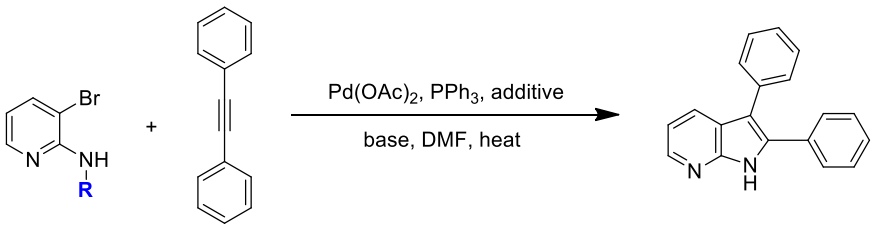

1-3 **6** **7**

R = H, $COCH_3$, $COCF_3$

Entry	R	Additive	Base	Temperature (°C)	Substrate consumption[a]	Isolated yield (%)
1	H	*n*-Bu_4NCl	Na_2CO_3	80	No reaction	-
2	H	LiCl	Na_2CO_3	80	No reaction	-
3	H	*n*-Bu_4NCl	Na_2CO_3	100	incomplete	20
4	H	*n*-Bu_4NCl	Na_2CO_3	120	incomplete	15
5	H	LiCl	Na_2CO_3	120	incomplete	21
6[b]	H	LiCl	Na_2CO_3	120	incomplete	28
7	H	LiCl	Cs_2CO_3	120	incomplete	26
8	H	LiCl	CH_3COOK	120	incomplete	25
9	H	*n*-Bu_4NCl	Na_2CO_3	140	complete	56
10	$COCF_3$	*n*-Bu_4NCl	Na_2CO_3	80	incomplete	17
11	$COCF_3$	*n*-Bu_4NCl	Na_2CO_3	100	incomplete	21
12	$COCH_3$	*n*-Bu_4NCl	Na_2CO_3	100	incomplete	20
13	$COCH_3$	*n*-Bu_4NCl	Na_2CO_3	120	incomplete	15

[a]The substrate consumption was monitored by ^{1}H-NMR of the crude reaction mixtures in DMSO-d_6.
[b]Reaction time was 48 h.

Recently, our group demonstrated that the electronic properties of the starting material influenced the overall rate of the Larock reaction.[17] The oxidative addition, proposed as the rate-determining step of the reaction, could be facilitated by an electron-withdrawing substituent. We envisioned that the acylation of the amino group of the reactant might improve the reaction effectiveness. Accordingly, compound **1** was acylated to provide *N*-(3-bromopyridin-2-yl)-2,2,2-trifluoroacetamide **2** and *N*-(3-bromopyridin-2-yl)acetamide **3** in excellent and moderate yields, respectively. Compounds **2** and **3** were subsequentially utilized in the Larock reaction using *n*-Bu_4NCl, and Na_2CO_3 at different temperatures (entries 10-13). Nonetheless, the reactants remained in the reactions, and compound **7** was isolated in low yields. It is worth noting that the reactions with *N*-protected reactants gave the same indole product with no substituent on the indolic nitrogen. Introducing an electron-withdrawing group to reduce the electron density of the reactant did not apparently improve the reaction outcome. Further optimization with different phosphine ligands is ongoing in our laboratory.

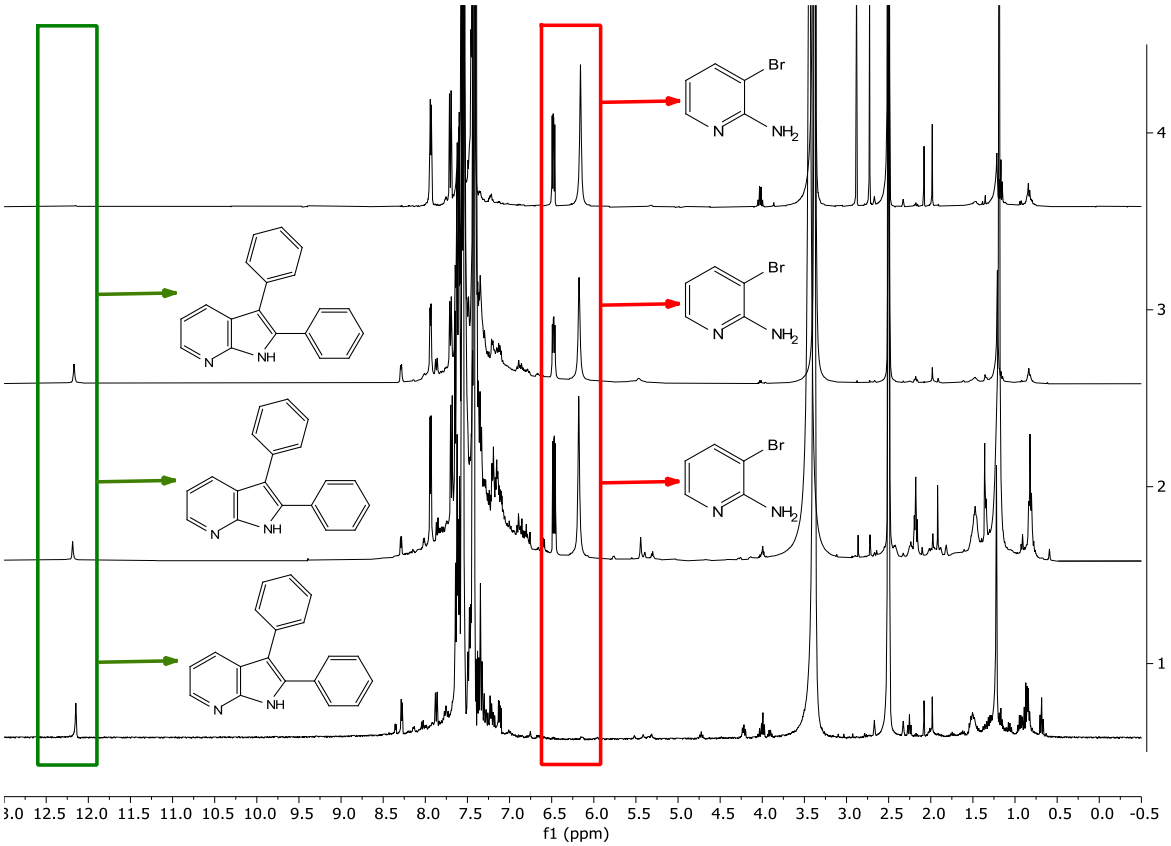

Figure 2. Substrate consumption of the Larock reactions conducted at 80 ℃, 100 ℃, 120 ℃, and 140 ℃. The indolic signal of the product was in the green box, while the aromatic signals of the reactant were in the red box.

To better understand the experimental results, DFT calculations for the oxidative addition step were carried out using the hybrid density functional B3LYP method, similar to our previous report.[17] All three reactants with different electronic modulators on the amino group of the 2-amino-3-bromopyridine reactant were chosen for analysis. Since the adsorption complex between the 2-amino-3-bromopyridine derivatives and bis(triphenylphosphine)palladium(0) could not be located in this study, the energies of both substrates were used as the reference points, and the energy profiles are illustrated in **Figure 3**. The activation free energies of different *N*-substituted 2-amino-3-bromopyridines range from 229.07 to 231.58 kcal/mol. These artificially high energy barriers are presumably due to the use of the two isolated structures of the reactants as the reference point for the activation energy assessment. It is worth noting that the same strategy was successfully utilized in our previous report, resulting in reasonable activation energy for the oxidative addition step of the Larock reaction.[17] Nevertheless, the energy barrier differences among the three reactants are small. These data are in agreement with our experimental observations, where reactions of 2-amino-3-bromopyridine and its derivatives at 100 °C proceed with similar efficiency (Table 1, entries 3, 11, and 12). The intrinsic reaction coordinate (IRC) calculations in the forward direction are in progress to help locate a stable adduct that could be utilized as initial geometries to locate the adsorption complex, which will then be utilized in the activation energy calculations to provide more reasonable barrier values.

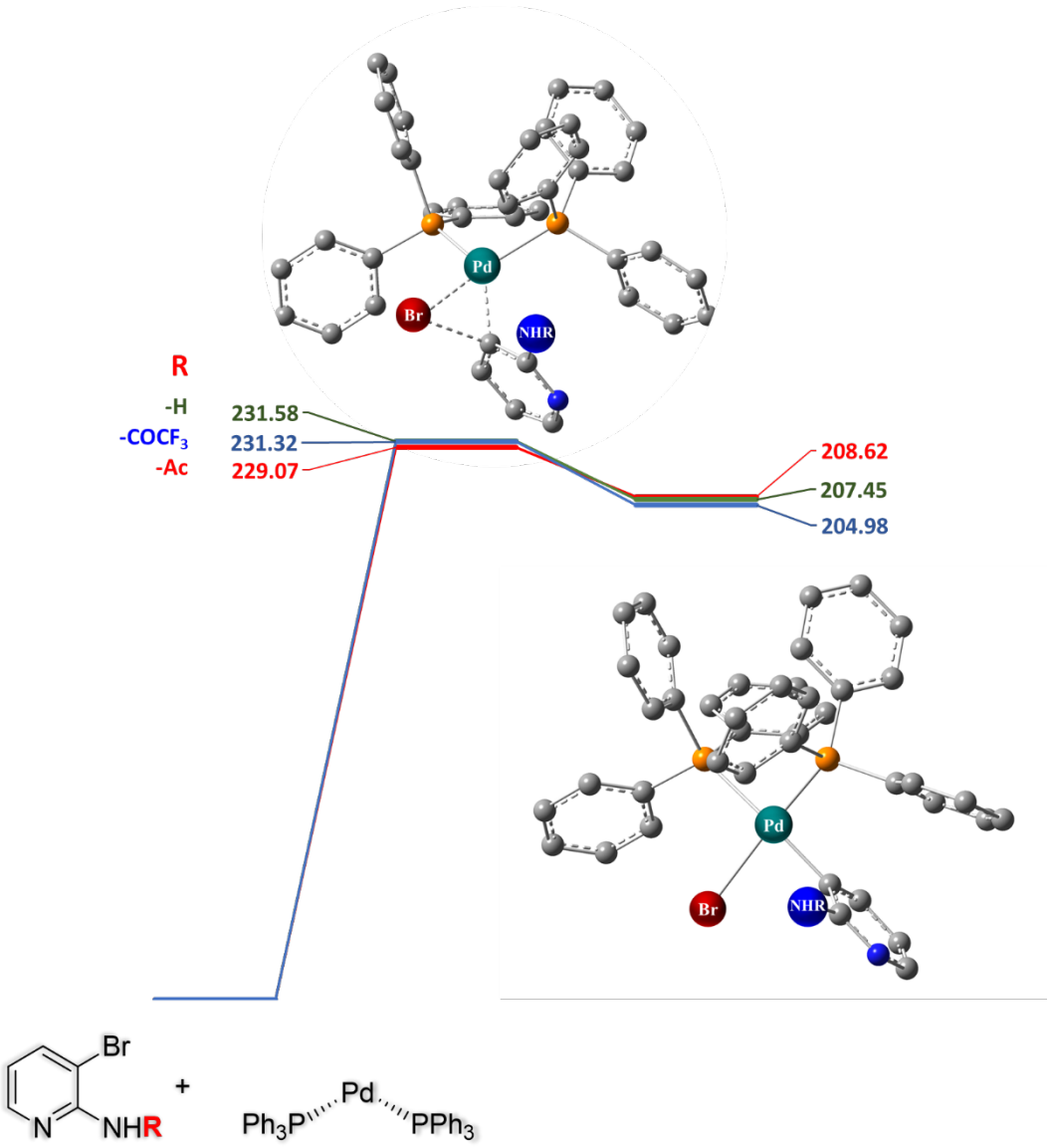

Figure 3. Relative free energy for the oxidative addition of 2-amino-3-bromopyridine and its derivatives to bis(triphenylphosphine)palladium(0).

Conclusion:

In summary, we have demonstrated the optimal condition of the Larock heteroannulation reaction to synthesize 2,3-diphenyl-7-azaindole. The reaction temperature was critical to expediting the overall reaction rate, resulting in the reaction completion, and the desired product was accomplished in moderate yield. The electron-withdrawing substituents on the amino group of the 2-amino-3-bromopyridine reactant exerted no significant effect on the reaction efficiency, and the DFT calculations also affirm these experimental observations. Further investigation to expand the substrate scope of this reaction is in progress and will be reported in due course.

Acknowledgements:

This work was supported by the Center of Excellence for Innovation in Chemistry (PERCH-CIC) and Department of Chemistry, Faculty of Science, Kasetsart University.

References:

1. Mérour JY, Buron F, Plé K, Bonnet P, Routier S. Molecules. 2014;19:19935–19979.
2. Han Y, Dong W, Guo Q, Li X, Huang L. Eur J Med Chem. 2020;203:112506.
3. Motati DR, Amaradhi R, Ganesh T. Bioorg Med Chem. 2020;28:115830.
4. Roberts A, Ma S, Kipps T, Coutre S, Davids M, Eichhorst E, Hallek M, Byrd J, Humphrey K, Zhou L, Chyla B, Nielsen J, Potluri J, Kim S, Verdugo M, Stilgenbauer S, Wierda W, Seymour J. Blood. 2019;134:111–122.
5. Popowycz F, Routier S, Josepha B, Mérour JY. Tetrahedron. 2007;63:1031–1064.
6. Larock RC, Yum EK. J Am Chem Soc. 1991;113:6689−6690.
7. Park SS, Choi JK, Yum EK, Ha DC. Tetrahedron Lett. 1998;39:627–630.
8. Ujjainwalla F, Warner D. Tetrahedron Lett. 1998;39:5355–5358.
9. Ontoria JM, Hernando JM, Malancona S, Attenni B, Stansfield I, Conte I, Ercolani C, Habermann J, Ponzi S, Filippo MD, Koch U, Rowley M, Narjes F. Bioorg Med Chem Lett. 2006;16:4026–4030.
10. Chuang KV, Kieffer ME, Reisman SE. Org Lett. 2016;18:4750−4753.
11. Malm J, Rehn B, Hörnfeldt AB, Gronowitz S. J Heterocyclic Chem. 1994;31:11–15.
12. Wang M, Li P, Wang L. Synth Commun. 2004;34:2803–2812.
13. Roy S, Das SK, Khatua H, Das S, Singh KN, Chattopadhyay B. Angew Chem Int Ed. 2021;60:8772–8780.
14. Frisch MJ, Trucks GW, Schlegel HB, Scuseria GE, Robb MA, Cheeseman JR, Scalmani G, Barone V, Petersson GA, Nakatsuji H et al. 2009. Gaussian, Inc, Wallingford CT, USA.
15. Phetrak N, Rukkijakan T, Sirijaraensre J, Prabpai S, Kongsaeree P, Klinchan C, Chuawong P. J Org Chem. 2013;78:12703−12709.
16. Larock RC, Yum EK, Refvik MD. J Org Chem. 1998;63:7652−7662.
17. Yiamsawat K, Gable KP, Chuawong P. J Org Chem. 2022;87:1218−1229.

SYNTHESIS OF COUMARIN DERIVATIVES AND THEIR ANTI-INFLUENZA ACTIVITY

Daychaton Siravarang,[1] Jaraspim Narkpuk,[2] Peera Jaru-Ampornpan,[2] Torsak Luanphaisarnnont[1,3,*]
[1]Department of Chemistry, Faculty of Science, Mahidol University, Bangkok 10400, Thailand
[2]Virology and Cell Technology Research Team, National Center for Genetic Engineering and Biotechnology (BIOTEC), Pathum Thani 12120, Thailand
[3]Center of Excellence for Innovation in Chemistry (PERCH-CIC), Faculty of Science, Mahidol University, Bangkok 10400, Thailand
*e-mail: torsak.lua@mahidol.ac.th

Abstract:

Coumarin derivatives are an important class of bioactive natural products with useful applications in various fields. Although many coumarin derivatives have been tested for different bioactivity, investigation of their anti-influenza activity has been limited. This work reported a synthesis of coumarin derivatives using Brønsted acid catalysis, giving the products in moderate to good yields. Investigation of the anti-influenza activity of the synthesized derivatives was also reported.

Introduction:

Development of efficient synthetic methods for syntheses of structurally complex molecules has remained an important challenge in organic chemistry. Green chemistry has been a focus of recent development because it helps reduce the environmental impact of chemical syntheses. Catalysis is among different approaches that lead to more environmentally friendly syntheses. In catalytic reactions, only a substoichiometric amount of catalysts is required, therefore making syntheses of structurally complex molecules more efficient.

Coumarin (2*H*-1-benzopyran-2-one) is an important motif found in many natural products and synthetic compounds, which can be used in many applications such as dyes,[1-3] rodenticides,[4-5] and fluorescent probes (Figure 1).[6-7] Many coumarin derivatives have also been reported as effective drugs such as anti-coagulant,[8] anti-cancer,[9] anti-HIV,[10] anti-bacterial,[11] anti-tumor,[12-13] and anti-viral (Figure 1).[14-15]

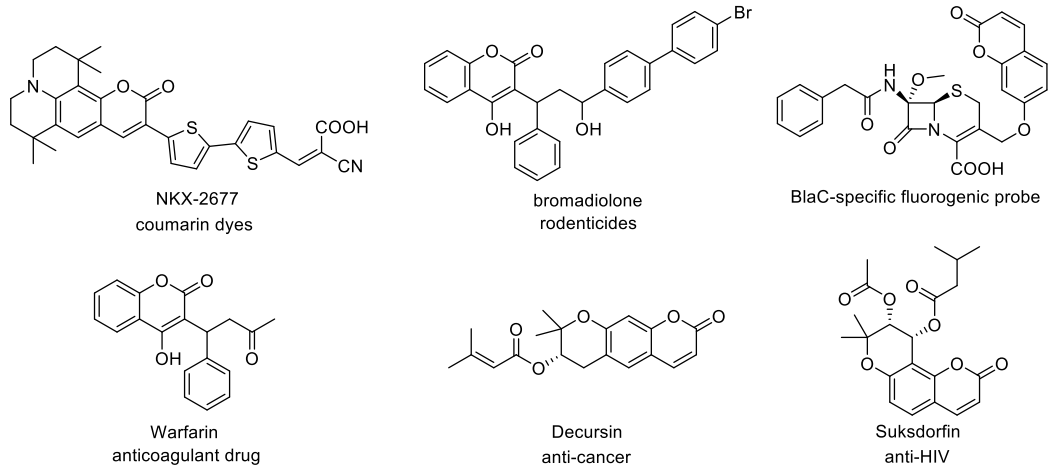

Figure 1 Coumarin derivatives

Previous syntheses of coumarin derivatives have been reported using different strategies such as Brønsted acid catalysis,[16] Lewis acid catalysis,[17] silicon-based catalysis,[18] flow chemistry,[19] microwave reaction,[20] and ring-closing metathesis.[21] Classic reactions such as Perkin reactions,[22-23] Pechmann reactions,[16-18] Wittig reactions,[24] and Knoevenagel reactions[20] have been reported for syntheses of coumarin derivatives. A variety of substrates such as *β*-ketoester and alkynoic ester were effective in the reactions; however, the use of allenic esters as a starting material for a synthesis of coumarins derivatives is limited despite their high reactivity compared with alkenic and alkynoic esters.[25-26] Only one example that used allenic ester has been reported for coumarin syntheses; however, the rection required the use of a stoichiometric amount of triflic acid, a very strong acid.[27] Development of a catalytic variant of the reaction can lead to a more environmentally friendly synthesis. Herein, we reported a synthesis of coumarin derivatives from allenic esters and resorcinol derivatives using *p*-toluenesulfonic acid monohydrate as a catalyst.

Methodology:

General procedure: ^{1}H- and ^{13}C-NMR spectra were obtained from Bruker Advance 400 MHz and JEOL JNM-ECZS 400 MHz NMR spectrometers. Chemical shifts are reported in ppm from tetramethylsilane (TMS) with the residual solvent resonance as an internal standard (DMSO-d_6 at δ_H 2.50 and δ_C 39.5; and $CDCl_3$ at δ_H 7.26 and δ_C 77.2). Data are reported as follows: s = singlet, d = doublet, t = triplet, m = multiplet; coupling constant(s) in Hz, integration. Thin layer chromatography was performed on aluminum sheet with Merck silica gel 60 (0.063–0.200 nm) as a stationary phase.

Material: Commercial reagents, organic solvents, and antibody were purchased from TCI, Merck, Sigma-Aldrich, Daejung, SouthernBiotech, and BioLegend. They were used without further purification unless otherwise noted.

General procedure for synthesis of coumarins: To a solution of resorcinol derivatives (0.125 mmol, 1 equiv.) and *p*-toluenesulfonic acid monohydrate (PTSA·H_2O, 0.05 mmol, 0.2 equiv.) in toluene (0.125 mL), ethyl 2,3-butadienoate (0.1375 mmol, 1.1 equiv.) was added. The reaction was heated to reflux for 2 hours. The reaction mixture was cooled to room temperature, extracted with ethyl acetate (3 x 30 mL), washed with saturated NaCl solution (50 mL), and dried with anhydrous Na_2SO_4. The solvent was removed under *vacuo*. The crude product was purified by column chromatography to give the desired product.

Synthesis of 7-hydroxy-4-methyl-2*H*-chromen-2-one (3a): The compound was synthesized according to the general procedure. Resorcinol (27.5 mg, 0.25 mmol) was used as the resorcinol derivative. The crude product was purified by column chromatography (silica gel: EtOAc/Hexanes, 1/2, v/v). The product was obtained as a white solid (39.6 mg, 90%). The NMR spectra of compound **3a** were identical to those reported in the literature.[27] ^{1}H NMR (400 MHz, DMSO-d_6) δ 10.50 (s, 1H), 7.56 (d, J = 8.6 Hz, 1H), 6.77 (dd, J = 8.6, 2.4 Hz, 1H), 6.67 (d, J = 2.4 Hz, 1H), 6.10 (s, 1H), 2.33 (s, 3H). ^{13}C NMR (100 MHz, DMSO-d_6) δ 161.7, 160.8, 155.4, 154.1, 127.2, 113.4, 112.6, 110.8, 102.7, 18.5.

Synthesis of 5,7-dihydroxy-4-methyl-2*H*-chromen-2-one (3b): The compound was synthesized according to the general procedure. Phloroglucinol (31.5 mg, 0.25 mmol) was used as the resorcinol derivative. The crude product was purified by column chromatography (silica gel: Acetone/Hexanes, 1/2, v/v). The product was obtained as a white solid (32.0 mg, 67%). The NMR spectra of compound **3b** were identical to those reported in the literature.[28] ^{1}H NMR (400 MHz, DMSO-d_6) δ 10.54 (s, 1H), 10.32 (s, 1H), 6.26 (d, J = 2.4 Hz, 1H), 6.17 (d, J = 2.3 Hz, 1H), 5.86 (s, 1H), 2.49 (s, 3H). ^{13}C NMR (100 MHz, DMSO-d_6) δ 161.5, 160.5, 158.4, 156.9, 155.4, 109.3, 102.5, 99.5, 94.9, 23.9.

Synthesis of 7,8-dihydroxy-4-methyl-2*H*-chromen-2-one (3c): The compound was synthesized according to the general procedure. Pyrogallol (31.5 mg, 0.25 mmol) was used as the resorcinol derivative. The crude product was purified by column chromatography (silica gel: Acetone/Hexanes, 1/2, v/v). The product was obtained as a light-yellow solid (22.7 mg, 48%). The NMR spectra of compound **3c** were identical to those reported in the literature.[28] ^{1}H NMR (400 MHz, DMSO-d_6) δ 10.07 (s, 1H), 9.30 (s, 1H), 7.09 (d, J = 8.7 Hz, 1H), 6.81 (d, J = 8.7 Hz, 1H), 6.12 (s, 1H), 2.35 (s, 3H). ^{13}C NMR (100 MHz, DMSO-d_6) δ 160.6, 154.4, 149.8, 143.7, 132.6, 115.9, 113.2, 112.5, 110.6, 18.7.

Synthesis of 6-chloro-7-hydroxy-4-methyl-2*H*-chromen-2-one (3d): The compound was synthesized according to the general procedure. 4-Chlororesorcinol (36.1 mg, 0.25 mmol) was used as the resorcinol derivative. The crude product was purified by column chromatography (silica gel: Acetone/Hexanes, 1/2, v/v). The product was obtained as a white solid (5.3 mg, 10%). The NMR spectra of compound **3d** were identical to those reported in the literature.[29] ^{1}H NMR (400 MHz, DMSO-d_6) δ 7.69 (s, 1H), 6.86 (s, 1H), 6.16 (s, 1H), 2.34 (s, 3H). ^{13}C NMR (100 MHz, DMSO-d_6) δ 160.3, 156.7, 153.4, 153.3, 126.5, 117.3, 113.2, 111.7, 103.7, 18.5.

Synthesis of 7-methoxy-4-methyl-2*H*-chromen-2-one (3e): The compound was synthesized according to the general procedure. 3-Methoxy phenol (27.4 µL, 0.25 mmol) was used as the resorcinol derivative. The crude product was purified by column chromatography (silica gel: EtOAc/Hexanes, 1/4, v/v). The product was obtained as a white solid (27.5 mg, 58%). The NMR spectra of compound **3e** were identical to those reported in the literature.[30] ^{1}H NMR (400 MHz, $CDCl_3$) δ 7.45 (d, J = 8.8 Hz, 1H), 6.81 (dd, J = 8.8, 2.5 Hz, 1H), 6.74 (d, J = 2.5 Hz, 1H), 6.08 (s, 1H), 3.83 (s, 3H), 2.35 (s, 3H). ^{13}C NMR (100 MHz, $CDCl_3$) δ 162.6, 161.3, 155.2, 152.7, 125.5, 113.5, 112.2, 111.9, 100.8, 55.7, 18.7.

General procedure for anti-influenza screening: Tested compounds were dissolved in dimethyl sulfoxide (DMSO) as a 10 mM stock solution and stored at -20 °C. Madin Darby Canine Kidney (MDCK) cells were seeded in Opti-MEM supplemented with 10% fetal bovine serum in flat-bottomed 96-well plates to form a confluent monolayer overnight. Cell media was removed from cells and rinsed with 300 µL PBS. Serial 2-fold dilutions of coumarins were made starting with a 100 µM to 0.78 µM in Opti-MEM with 2 µg/mL TPCK and mixed with 100 plaque-forming units (PFU) of influenza A virus (PR8). The mixture was incubated with cells for 24 hours at 37 °C in 5% CO_2 incubator, and supernatants were removed and rinsed with 300 µL PBS. Cells were fixed with ice cold 80% acetone (100 µL per well) for 15 minutes at room temperature. Cells were washed once with 300 µL PBS, then 200 µL blocking buffer (2% bovine serum albumin [BSA] in PBS) was added and incubated at room temperature for 30 minutes. Blocking buffer was then removed, and primary antibody (Mouse Anti-Influenza A, Nucleoprotein-UNLB 1:2,000 in 1% BSA) 50 µL/well was added and incubated at room temperature for 60 minutes. The primary antibody was removed, and the cells were washed 4 times with 300 µL PBS with Tween. Secondary antibody (HRP Goat anti-mouse IgG 1:10,000 in 1% BSA) 50 µL/well was added and incubated at room temperature for 60 minutes. The secondary antibody was then removed, and cells were washed 4 times with 300 µL PBS with Tween. TMB substrate was added 50 µL/well and incubated for 15 minutes. The reaction was quenched by 0.5 M H_2SO_4. Absorption was measured by microplate reader at 450 nm. The IC_{50} values of the compounds were determined from dose-response curves with 8 concentrations of each compound in duplicate in 2-3 independent experiments. Curves were fitted to data points using nonlinear

regression analysis, and IC_{50} values were calculated from GraphPad prism 9.0.0 software. The IC_{50} values shown are average ± standard deviation.

Results and Discussion:

To investigate the feasibility of a condensation reaction between allenic esters and resorcinol derivatives, resorcinol (**1a**) and ethyl 2,3-butadienoate (**2a**) were selected as model substrates for reaction optimization (Table 1). In the absence of an acid (entry 1), no desired product was obtained. When PTSA·H_2O was used as a catalyst in the reaction (entry 2), 7-hydroxy-4-methylcoumarin was obtained in 62% yield. $MeSO_3H$ gave the product in 56% yield (entry 3). Other Brønsted acids such as CF_3COOH, HCOOH, and PhCOOH did not afford any product (entries 4–6). These results suggested that the acidity of organic Brønsted acids played an important role in the reaction. Stronger sulfonic acids were effective catalysts, giving the product in good yields; whereas, weaker carboxylic acids were ineffective in the reaction. $FeCl_3$ and HCl gave the desired product in 51% and 0% yields, respectively (entries 7 and 8). Therefore, PTSA·H_2O was the optimal catalyst.

Next, the solvent effect in the reaction was investigated. Polar protic solvents (EtOH and H_2O, entries 9–10) and polar aprotic solvents (MeCN, DMSO, and EtOAc, entries 11, 12, and 13) were not effective for the reaction, giving the product in less than 10% yield. When DCE was used as a solvent, the product was obtained in 50% yield. Accordingly, the optimal solvent was toluene.

Subsequently, the effect of the reaction temperature was studied. When the reaction temperature was lowered (room temperature and 50 °C, entries 15 and 16), the yield of the product decreased to 11% and 33% yields, respectively. Increasing the reaction temperature to reflux afforded the product in 90% yield. Thus, refluxing condition was chosen as the optimal reaction temperature.

Table 1 Reaction optimization

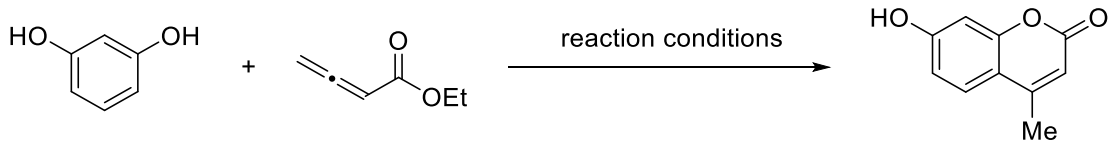

1a **2a** **3a**

Entry	Acid	Solvent	Temperature (° C)	Yield[a] (%)
1	-	Toluene	70	0
2	PTSA·H_2O	Toluene	70	62
3	$MeSO_3H$	Toluene	70	56
4	CF_3COOH	Toluene	70	0
5	HCOOH	Toluene	70	0
6	PhCOOH	Toluene	70	0
7	$FeCl_3$	Toluene	70	51
8	HCl	Toluene	70	0
9	PTSA·H_2O	EtOH	70	4
10	PTSA·H_2O	H_2O	70	0
11	PTSA·H_2O	MeCN	70	6
12	PTSA·H_2O	DMSO	70	1
13	PTSA·H_2O	EtOAc	70	5
14	PTSA·H_2O	DCE	70	50
15	PTSA·H_2O	Toluene	RT	11
16	PTSA·H_2O	Toluene	50	33
17	PTSA·H_2O	Toluene	reflux	87 (90)

Reaction conditions: resorcinol (**1a**) (13.7 mg, 0.125 mmol, 1 equiv.), ethyl 2,3-butadienoate (**2a**) (16.0 µL, 0.1375 mmol, 1.1 equiv.), PTSA·H_2O (4.7 mg, 0.025 mmol, 20 mol%), and toluene (125 µL), 70 °C, 2 hours.
[a]NMR yields. The value in parenthesis indicated isolated yields.

With the optimized reaction conditions in hand, the substrate scope of the reaction was investigated (Table 2). Resorcinol derivatives with various substituents were studied. When 1,3,5-trihydroxybenzene (**1b**) was used as a substrate, the corresponding product (**3b**) was obtained in 67% yield (entry 2), which was lower than the yield of resorcinol (**1a**). Although **1b** was more electron-rich than **1a** because the number of electron-donating substituents in **1b** was higher, the lower yield of **1b** could be explained by its higher steric demand at the reacting site. 1,2,3-Trihydroxybenzene (**1c**) gave the corresponding product (**3c**) in 48% yield (entry 3). The presence of the hydroxy group at the meta-position relative to the reacting site lowered the electron density of the compound as suggested by the Hammett value of m-OH (+0.12).[31] When 1,3-dihydroxy-4-chlorobenzene (**1d**) was used, the product **3d** was obtained in 10% yield (entry 4), consistent with the lower electron density of **1d** due to the presence of an electron-withdrawing chlorine substituent.

To further investigate the requirement of the substrate, monomethylated resorcinol (**1e**) gave the product **3e** in 58% yield (entry 5). This result suggested that only one hydroxy group was necessary for the reaction to occur albeit with lower yield. When phenol (**1f**) was used as a substrate, no desired product **3f** was obtained (entry 6), suggesting that the electron density of the substrate played an important role in the reaction.

Table 2 Substrate scope

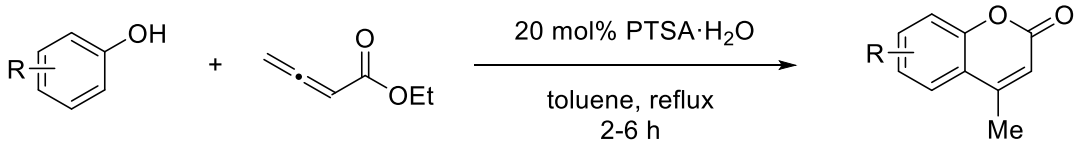

1a-f **2** **3a-f**

Entry	Resorcinol derivatives	Allenic ester	Product	Yield (%)
1	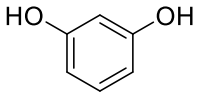 **1a**	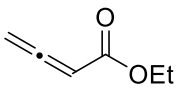	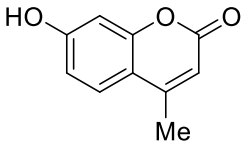 **3a**	90
2	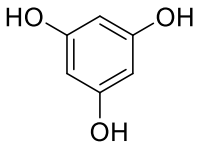 **1b**	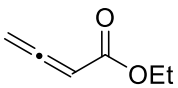	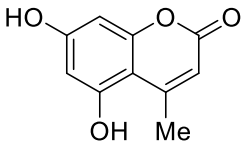 **3b**	67

3	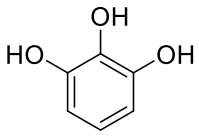 **1c**	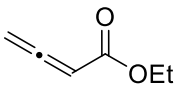	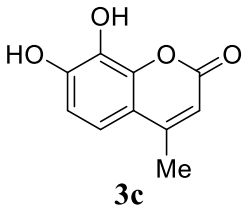 **3c**	48
4	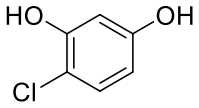 **1d**	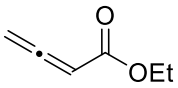	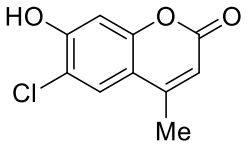 **3d**	10
5	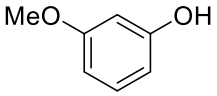 **1e**	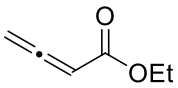	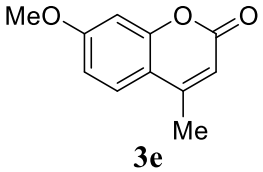 **3e**	58
6	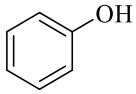 **1f**	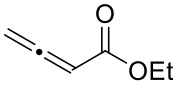	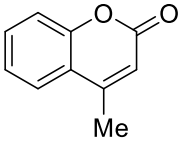 **3f**	0

Reaction conditions: resorcinol (**1**) (0.25 mmol, 1 equiv.), ethyl 2,3-butadienoate (**2a**) (31.9 µL, 0.275 mmol, 1.1 equiv.), PTSA·H_2O (9.5 mg, 0.05 mmol, 20 mol%), and toluene (250 µL), reflux. Isolated yields.

After coumarin derivatives (**3a**–**3e**) were synthesized, their anti-influenza activity was studied (Table 3). The IC_{50} values were calculated from an NP ELISA assay. Compounds **3a** and **3b** (entries 1 and 2) did not exhibit anti-influenza activity in the concentration range of the study (100–0.78 µM). Coumarin derivatives **3c** and **3d** showed anti-influenza activity, with the IC_{50} values of 42.62 ± 4.12 and 74.10 ± 27.20 µM, respectively (entries 3 and 4). The IC_{50} value of **3e** was calculated to be 101.91 ± 22.34 µM (entry 5). Among the synthesized coumarin derivatives, **3c** showed the strongest anti-influenza activity. But it was approximately 2.4-fold less active than favipiravir (entries 3 and 6).

Table 3 Half-maximal inhibitory concentration of anti-influenza activity of coumarins.

Entry	Compounds	IC_{50} values (µM)
1	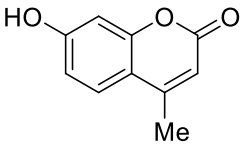 **3a**	>100
2	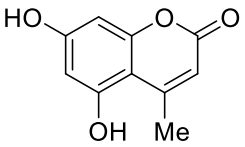 **3b**	>100

3	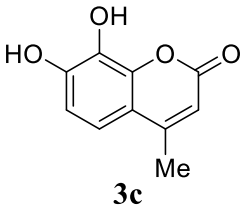 **3c**	42.62 ± 4.12
4	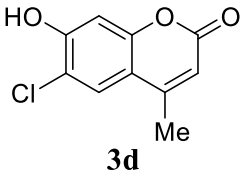 **3d**	74.10 ± 27.20
5	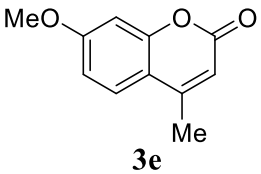 **3e**	101.91 ± 22.34
6	favipiravir	17.86 ± 6.78

Conclusion:

PTSA·H_2O-catalyzed condensation between allenic esters and resorcinol derivatives was developed to synthesize coumarin derivatives. The reaction conditions were simple to operate and required no use of transition metals. From the anti-influenza activity study, coumarin derivative **3c** showed the strongest activity with the IC_{50} value of 42.62 ± 4.12 μM.

Acknowledgements:

This research was supported by the Thailand Graduate Institute of Science and Technology (TGIST); Virology and Cell Technology Research Team, National Center for Genetic Engineering and Biotechnology (BIOTEC); NSTDA, Ministry of Higher Education, Science, Research and Innovation, Thailand; Center of Excellence for Innovation in Chemistry (PERCH-CIC), Ministry of Higher Education, Science, Research and Innovation; and the Department of Chemistry, Faculty of Science, Mahidol University. We also thank the Central Instrumental Facility (CIF) at the Faculty of Science, Mahidol University for research facilities.

References:

1. Hara K, Wang Z-S, Sato T, Furube A, Katoh R, Sugihara H, Dan-oh Y, Kasada C, Shinpo A, Suga S. J Phys Chem B. 2005;109:15476–15482.
2. Seo KD, Song HM, Lee MJ, Pastore M, Anselmi C, De Angelis F, Nazeeruddin MK, Gräetzel M, Kim HK. Dyes Pigm. 2011;90:304–310.
3. Wong BM, Cordaro JG. J Chem Phys. 2008;129:214703.
4. Chalermchaikit T, Felice LJ, Murphy MJ. J Anal Toxicol. 1993;17:56–61.
5. Rowe FP, Plant CJ, Bradfield A. J Hyg. 1981;87:171–177.
6. Xie H, Mire J, Kong Y, Chang M, Hassounah HA, Thornton CN, Sacchettini JC, Cirillo JD, Rao J. Nat. 2012;4:802–809.
7. Zhang Y-R, Chen X-P, Shao J, Zhang J-Y, Yuan Q, Miao J-Y, Zhao B-X. Chem Commun. 2014;50:14241–14244.
8. Venugopala KN, Rashmi V, Odhav B. BioMed Res Int. 2013;2013:1–14.

9. Yim D, Singh RP, Agarwal C, Lee S, Chi H, Agarwal R. Cancer Res. 2005;65:1035–1044.
10. Yu D, Suzuki M, Xie L, Morris-Natschke SL, Lee K-H. Med Res Rev. 2003;23:322–345.
11. Lee S, Shin D-S, Kim JS, Oh K-B, Kang SS. Arch Pharm Res. 2003;26:449–452.
12. Lee S, Lee YS, Jung SH, Shin KH, Kim B-K, Kang SS. Arch Pharm Res. 2003;26:727–730.
13. Chimichi S, Boccalini M, Cosimelli B, Viola G, Vedaldi D, Dall'Acqua F. Tetrahedron Lett. 2002;43:7473–7476.
14. Hassan MZ, Osman H, Ali MA, Ahsan MJ. Eur J Med Chem. 2016;123:236–255.
15. Mishra S, Pandey A, Manvati S. Heliyon. 2020;6:e03217.
16. Sugino T, Tanaka K. Chem Lett. 2001;30:110–111.
17. Corrie JET. J Chem Soc, Perkin Trans 1. 1990;2151.
18. Khder AERS, Ahmed SA, Khairou KS, Altass HM. J Porous Mater. 2017;25:1–13.
19. Zak J, Ron D, Riva E, Harding HP, Cross BCS, Baxendale IR. Chem Eur J. 2012;18:9901–9910.
20. Bogdał D. J Chem Res. 1998;468–469.
21. Chatterjee AK, Toste FD, Goldberg SD, Grubbs RH. Pure Appl Chem. 2003;75:421–425.
22. Crawford M, Shaw JAM. J Chem Soc. 1953;3435.
23. Holme I. Color Technol. 2006;122:235–251.
24. Harayama T, Nakatsuka, K, Noshioka, H, Murakami, K, Hayashida, N, Ishii, H. Chem Pharm Bull. 1994;42:2170–2173.
25. Kiattisewee C, Kaidad A, Jiarpinitnun C, Luanphaisarnnont T. Monatsh Chem. 2018;149:1059–1068.
26. Saejong P, Somprasong S, Rujirasereesakul C, Luanphaisarnnont T. Synlett. 2022;33: 1399–1404.
27. Kim S, Kang D, Lee C-H, Lee PH. J Org Chem. 2012;77:6530–6537.
28. Sahu PK, Sahu PK, Agarwal DD. J Mol Catal A Chem. 2014;395:251–260.
29. Jadhav NH, Sakate SS, Rasal NK, Shinde DR, Pawar RA. ACS Omega. 2019;4:8522–8527.
30. Abbasi Z, Rezayati S, Bagheri M, Hajinasiri R. Chin Chem Lett. 2017;28:75–82.
31. Hammett LP. J Am Chem Soc. 1937;59:96–103.

MOLECULAR DOCKING AND MOLECULAR DYNAMICS SIMULATION STUDY OF THE INTERACTIONS OF *Holothuria scabra* TRITERPENE GLYCOSIDES AND THEIR METABOLITES ON ANDROGEN RECEPTOR ALLOSTERIC SITES

Kanta Pranweerapaiboon,[1,2,*] Bhak Nitithum,[1] Arthur Garon,[2] Thomas Seidel,[2] Thierry Langer[2]

[1]Chulabhorn International College of Medicine, Thammasat University, Pathumthani, Thailand

[2]Department of Pharmaceutical Chemistry, Faculty of Life Sciences, University of Vienna, Austria

*e-mail: kantapra@tu.ac.th

Abstract:

Prostate cancer is the second most common male malignancy and is the fourth most common cancer overall. However, prostate cancer can undergo an adaptive mechanism to eventually become castration-resistant, being able to proliferate even with castrate-level of androgen and posing a limitation for current treatment. This study focuses on the interactions of the sea cucumber's triterpene glycosides, especially holothurin A, holothurin A2, and metabolites from the deglycosylation reaction pathway, on AR by using molecular docking and molecular dynamics (MD) simulations. The docking results showed that HAM2, which is the metabolite of holothurin A comprising only D-xylose and D-quinovose, exhibited the best binding affinity of -17.50 kcal/mol with the Binding Function 3 (BF3) surface groove of AR. The MD simulation data confirmed and demonstrated that HAM2 can form a stable complex with BF3 via hydrophobic and hydrogen bond acceptor interactions. All computational studies indicated that HAM2 can act as an allosteric inhibitor at the BF3 site and might be a promising candidate for further prostate cancer treatment.

Introduction:

Prostate cancer is the second most common cancer among men[1]. Even precious screening tools have been developed for early detection, but the main strategy targeting the androgen receptor (AR) is limited. Prostate cancer turns to drug resistance among patients as a consequence of AR mutation.[2] AR is the steroid hormone receptor. It comprises three main domains which are the N-terminal domain, DNA-binding domain, and the C-terminal ligand-binding domain (LBD). LBD is a place where androgen binds to. It also harbours the other two coactivator binding surfaces which are activation function 2 (AF2) and binding function 3 (BF3).[3] AF2 acts as a docking site for coactivator proteins such as steroid receptor coactivator (SRC) and androgen receptor-associated protein (ARA).[4] BF3 plays a vital role in allosteric regulation and affects the function of AF2.[5] Several studies suggested that blocking AF2 or BF3 sites by ligands or small molecules binding can alter AR function and tend to be a novel target for prostate cancer treatment.[4]

Sea cucumbers, *Holothuria scabra,* are the echinoderm marine invertebrates that distribute throughout the Pacific Ocean. The sea cucumbers are a nutraceutical and have long been utilized in Asian traditional foods and folk medicines.[6] Triterpene glycosides are the vital secondary metabolites produced by sea cucumbers.[7] They are composed of lanostane aglycones with an 18(20)-lactone. The glycone moieties of sea cucumber triterpene glycosides usually include D-xylose, D-quinovose, D-glucose, and D-3-O-methylglucose.[8] Holothurin A (HA) and holothurin A2 (HA2) have been reported as the most abundant triterpene glycosides in *H.*

scabra.[9] Accumulated evidence has been studied and revealed the significant role of these compounds for a wide spectrum of bioactivities, including neuroprotective, anti-inflammatory, cytotoxicity, and anti-cancer effects.[10,11,12] A previous study showed the effects of HA on the androgen receptor by interfering with AR activities and resulting in decrease the viability of prostate cancer cell line.[13] Nevertheless, using a cell culture technique to in studying the effect of HA and HA2 has some limitations. In oral administration, these compounds are digested by intestinal microbiota subsequence to be absorbed into the bloodstream.[14] As shown in Figure 1, the deglycosylation reaction pathway is the major metabolic pathway that reduces each group of glycosides and makes the different forms of the metabolites HA as HAM1, HAM2, HAM3, and the metabolites of HA2 as HA2M1, HA2M2, HA2M3, respectively.[14] Therefore, studying the interaction of metabolite forms is also important to understand the exact bioactivity mechanism of HA and HA2. This study aims to investigate and compare the possible potential interaction of HA, HA2, and their metabolites with the binding pocket and binding grooves (AF2 and BF3) of androgen receptors by means of in silico approaches like molecular docking and molecular dynamics simulations. This would be a complementary drug for prostate cancer therapeutics.

Methodology:

Molecular docking

The X-ray crystallographic structure of the ligand-binding domain of the androgen receptor was taken from the Protein Data Bank (PDB ID: 2PIV).[15] The 2PIV structure presents LBP, AF2, and BF3. The structures of the macromolecule, ligands, and binding sites were prepared and optimized by LigandScout 4.4 Expert (Intel:Ligand GmbH, Vienna, Austria). Protein-ligand docking and docking result analysis performed and visualized using the built-in AutoDock Vina 1.1 module of LigandScout 4.4 Expert. The parameters of the docking runs were: 8 for exhaustiveness, 9 for the maximum number of binding modes to generate, and 3 for the maximum energy difference between the best binding mode and the worst one.

Molecular dynamics simulation

The crystal structure of AR (chain A of 2PKL) was used as a starting point for running the MD simulations. The conformation of all ligands was generated by LigandScout 4.4 Expert. The ligand and protein topologies were optimized in Maestro (Schrödinger, New York, USA). Ligand parameters were generated in SwissParam.[16] All systems were simulated using a CHARMM36 all atom force field in Gromacs (Version 5.0.5). The AR was placed in a decahedral box of 1 Å marginal radius. The box was filled with water molecules using the TIP3P model. The system was neutralized by adding NaCl using the genion tool of the Gromacs package. All generated systems were subjected to a force field of 10.0 kJ/mol for 50,000 steps. The system temperature was held at 300 K by the Berendsen temperature coupling method. The systems were energy minimized for 100 ps. Subsequently, the systems were subjected to a molecular dynamics simulation for 100 ns. Frames were saved every 2 ps. The results were analysed and visualized in LigandScout 4.4 Expert and VMD (University of Illinois, IL, USA). The graphs were plotted using Grace (Oregon Graduate School of Science and Technology, OR, USA).

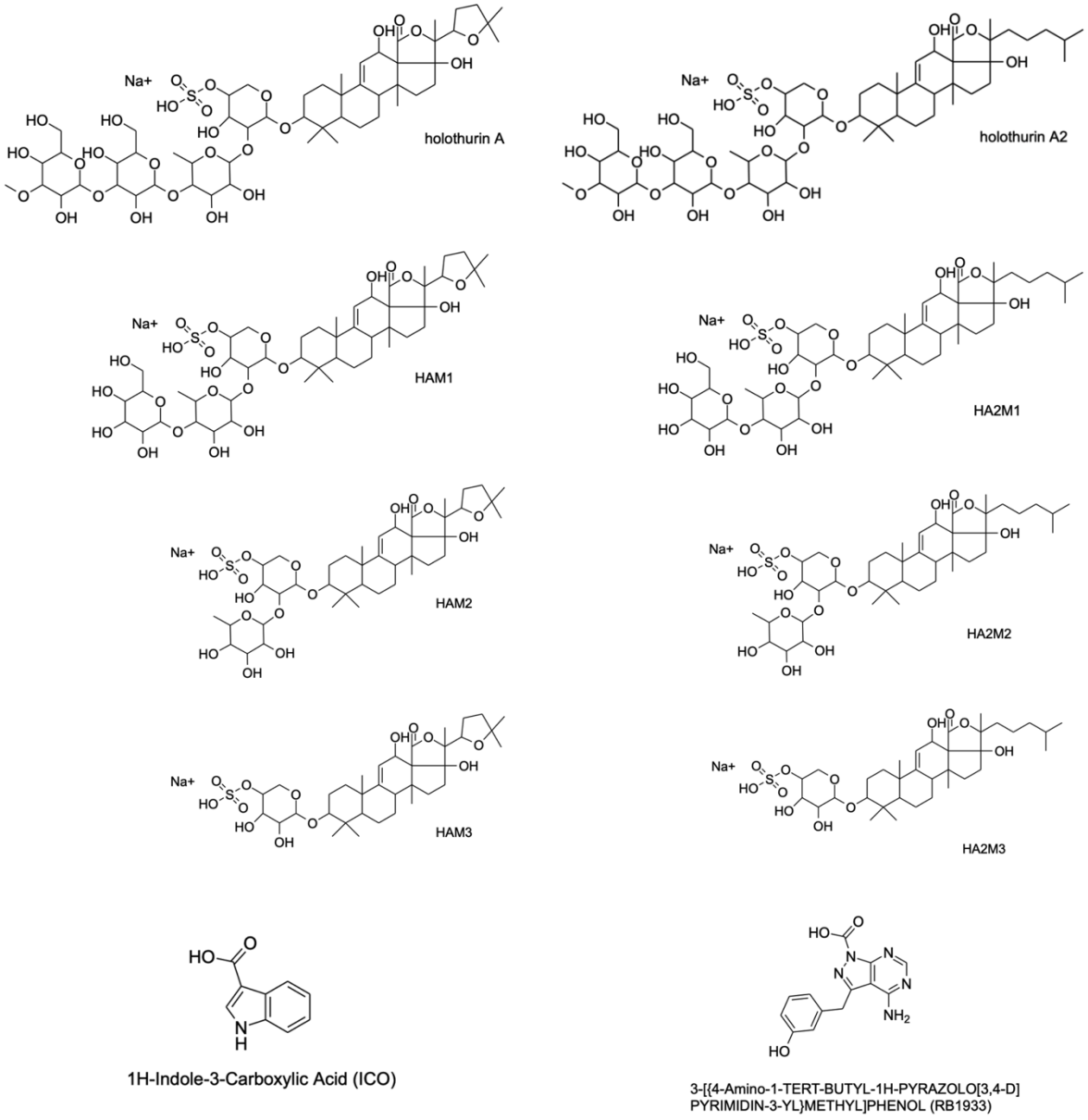

Figure1.
The chemical structures of holothurin A (HA), HAM1, HAM2, HAM3, holothurin A2 (HA2), HA2M1, HA2M2, HA2M3, ICO, and RB1933

Results and Discussion:

The crystallized structure of AR LBD (PDB ID: 2PKL) was selected as a model for investigating the binding poses, affinities, and potential interactions of all compounds of interest. As expected, the dihydrotestosterone (DHT) bound strongly to the ligand biding pocket (LBP) by -23.50 kcal/mole. Co-crystalized compounds, RB1933 and ICO, were redocked into its binding site. The binding affinities of RB1933-AF2 and ICO-BF3 were -11.30 and -9.30 kcal/mol, respectively. In addition, a molecular docking study exhibited the potential

of HA, HA2, and their metabolites, including HAM1, HAM2, HAM3, HA2M1, HA2M2, and HA2M3, for a binding to the AF2 and BF3 sites, but not LBD (Table 1). This might be a result of the larger molecules and longer side chain which limits binding by the enclosed nature of the LBP. HAM2 was the best binding molecule which had a binding affinity of -13.60 and -17.50 kcal/mol to the AF2 and BF3 site, respectively (Figure 2 and 3). The previous study found that HAM2 is also the most abundant form of metabolite that was found in rat's serum.[14] This may suggest that HAM2 has a high potential for prostate cancer treatment by binding to the surface grooves of the androgen receptor.

Table 1.

Binding affinity of compounds from the sea cucumber, *Holothuria scabra,* towards binding pocket, AF2, and BF3 of androgen receptors (2PKL)

	Binding sites (kcal/mol)		
	LBP	**AF2**	**BF3**
HA	**-**	-10.20	-10.20
HAM1	**-**	-12.20	-15.20
HAM2	**-**	**-13.60**	**-17.50**
HAM3	**-**	-10.30	-15.10
HA2	**-**	-10.30	-13.40
HA2M1	**-**	-10.60	-12.80
HA2M2	**-**	-10.70	-13.70
HA2M3	**-**	-9.60	-14.70
DHT	**-23.50**		
RB1933		**-11.30**	
ICO			**-9.30**

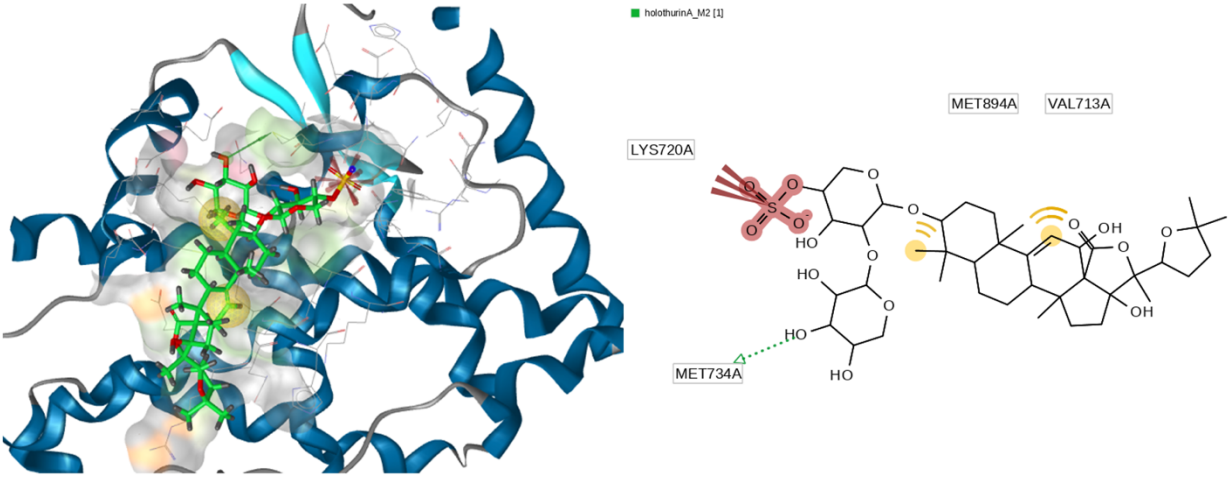

Figure 2.

Molecular docking results of HAM2 to AF2 AR in 3D and 2D analysed by LigandScout

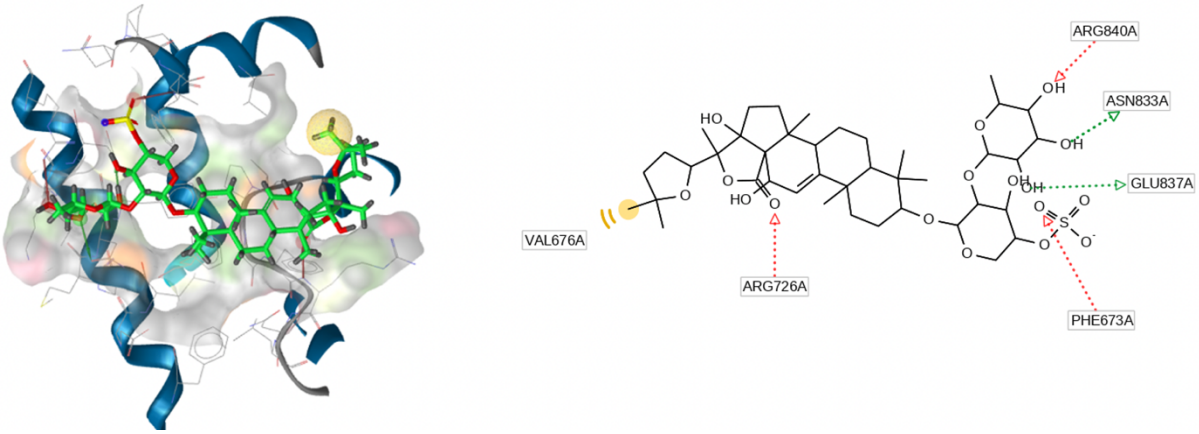

Figure 3.
Molecular docking results of HAM2 to BF3 AR in 3D and 2D analysed by LigandScout

The 20 ns MD simulation was performed to explore the stability and behaviour of HAM2 in the AF2 and BF3 sites. The RMSD of backbone atoms of 2PKL showed the stability of the system at around 5000 ps and remained within 0.11 nm. The RMSD fluctuation of all complex systems revealed a similar trend throughout the simulations (Figure 4). This data revealed that the system is stable and can be used for further analyses. A slightly drift of RMSD value of AF2-2PKL in complex with HAM2 (0.10 nm) indicated HAM2 could stabilize the AR-LBD conformation (Figure 4A). In contrary to BF3-2PKL in complex with HAM2, the average RMSD value was increased up to 0.14 nm which reflected the significant distortion of LBD AR (Figure 4B).

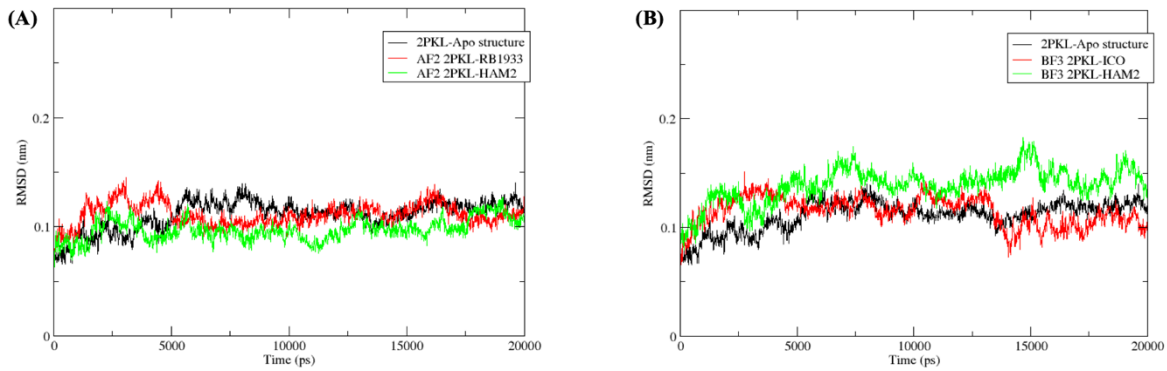

Figure 4.
The RMSD plots of all ligands-2PKL trajectories after 20 ns MD simulation (A) The RMSD of the backbone atoms of AF2 2PKL in complex with RB1933 and HAM2 (B) The RMSD of the backbone atoms of BF3 2PKL in complex with ICO and HAM2

In order to analyse whether ligand binding induces conformational changes at the residue level, the root mean square fluctuation (RMSF) and the protein backbone atoms was

computed based on the 20 ns simulation data. The RMSF graph of the 2PKL-unliganded (2PKL-Apo structure) revealed a fluctuation of residues in the loop and flexible regions of LBD AR (Figure 5). After 20 ns MD simulation, the RMSF of HAM2 in complex with AF2 and BF3 clearly indicates that the binding of the ligand to the sites interrupts the original conformation of the residues. AF2 2PKL-HAM2 showed the fluctuation of residues in the loop between H3-H4/5 loop (residues ARG726 and VAL730), H5 (residues ASN758), beta-strand between H8 and H9 (residue GLY820 and LYS822), H11 (residue MET886), and H12 (residue ILE898) (Figure 5A). Interrupted the key residues in AF2 such as VAL730 and ILE898 interfered the formation of AF2 binding pocket and induced conformational changes.[3] Interestingly, BF3 2PKL-HAM2 complex exhibited large fluctuations of residues in the linker region (residue ASN692), H3-H4/5 loop (residue VAL730), H7 (residue SER778), beta-strand between H8 and H9 (residue GLN824 and LYS847), H10 (residue PRO868), H11 (residue MET886), and H 12 (residue VAL903 and LEU907) (Figure 5B). Either HAM2 in complex with AF2 or BF3, it interacted with H3-H4/5 loop and H9 which are the key sites in allosteric communication of AF2 and BF3.[3]

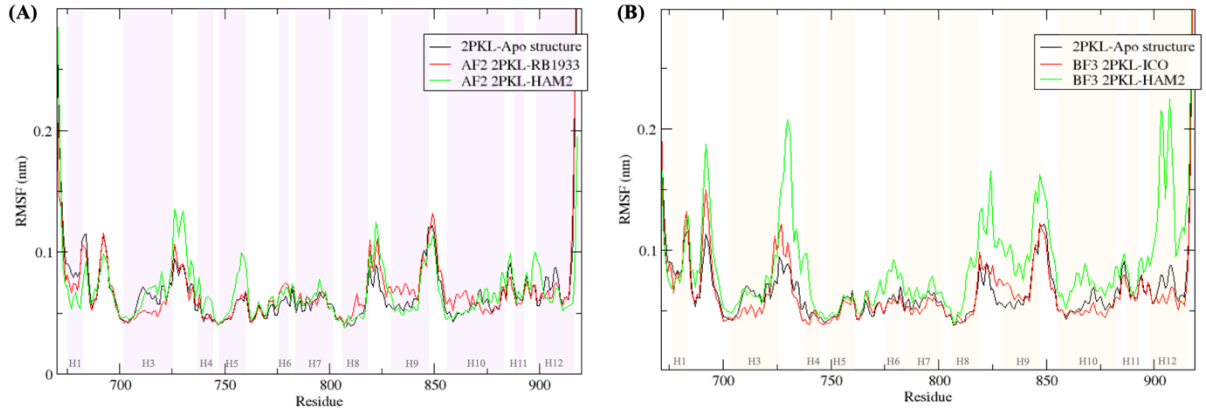

Figure 5

The RMSF of all ligands in complex with 2PKL after 20 ns MD simulation. (A) RMSF of AF2-2PKL in complex with RB1933 and HAM2 (B) RMSF of BF3-2PKL in complex with ICO and HAM2

For further confirmation, HAM2 in complex with AF2 and BF3 of 2PKL were extracted from the 20 ns MD simulation and redocked. The binding affinities of HAM2 to AF2 and BF3 were greater than before the MD simulation at -20.80 and -19.70 kJ/mol, respectively. This indicated that HAM2 favours binding to AF2 and BF3. The pharmacophore interaction map after 20 ns MD simulation of AF2 2PKL-HAM2 complex showed that ARG726, LYS717, VAL713, and VAL716 were the most active residues by forming H-bonding, hydrophobic, and ionic interactions (Figure 6). However, the overall percentage of appearance was at the mid-level. The superimposition of HAM2 in complex with AF2 2PKL after 20 ns furthermore showed the instability of ligand due to movement toward to the BF3 groove when compared with the starting position (Figure 6B). In contrary to the 20 ns MD simulation of HAM2-BF3 2PKL, the pharmacophore interaction map showed the stronger hydrophobic interaction of HAM2 to residues in the BF3 groove (Figure 7C). The most active residues in response to HAM2 interaction in BF3 groove were ALA721, ARG726, ILE672, ILE680, PHE673, and VAL676 (Figure 7A and 7C). The superimposition of start frame and end frame after 20 ns MD simulation of HAM2 in a complex of BF3 showed that the ligand remained within the BF3 groove and is similar to the starting pose. These findings suggest that HAM2 could form a more stable complex in the BF3 groove and might be a potent BF3 inhibitor compound.

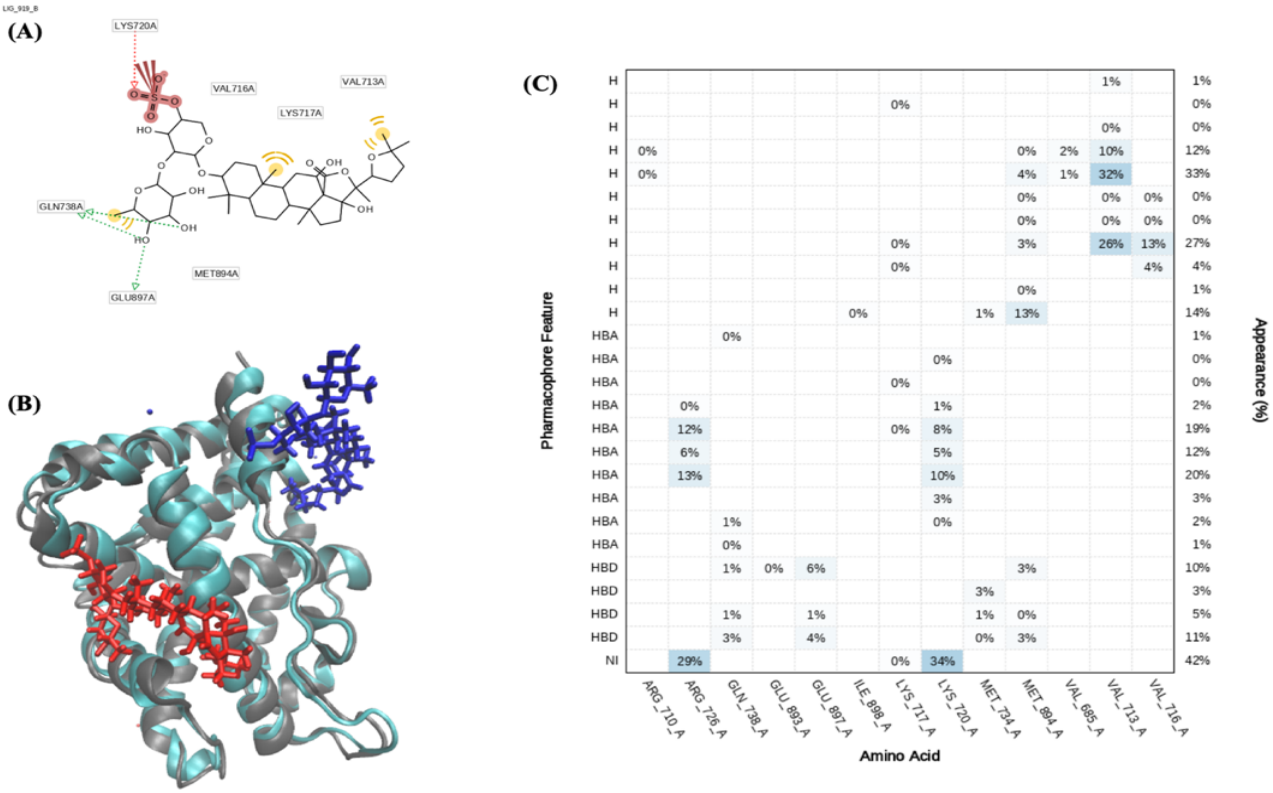

Figure 6

The interaction of HAM2 with the AF2 site during a 20 ns MD simulation. (A) The interactions of the redocked HAM2 with the AF2 site of 2PKL. (B) HAM2 in complex with AF2 2PKL; starting pose of 2PKL and HAM2 are crayon and red, respectively, while grey and blue are the 2PKL and HAM2 after the 20 ns simulation. (C) MD interaction plot of the 20 ns simulation of HAM2 in complex with AF2-2PKL as analysed by LigandScout

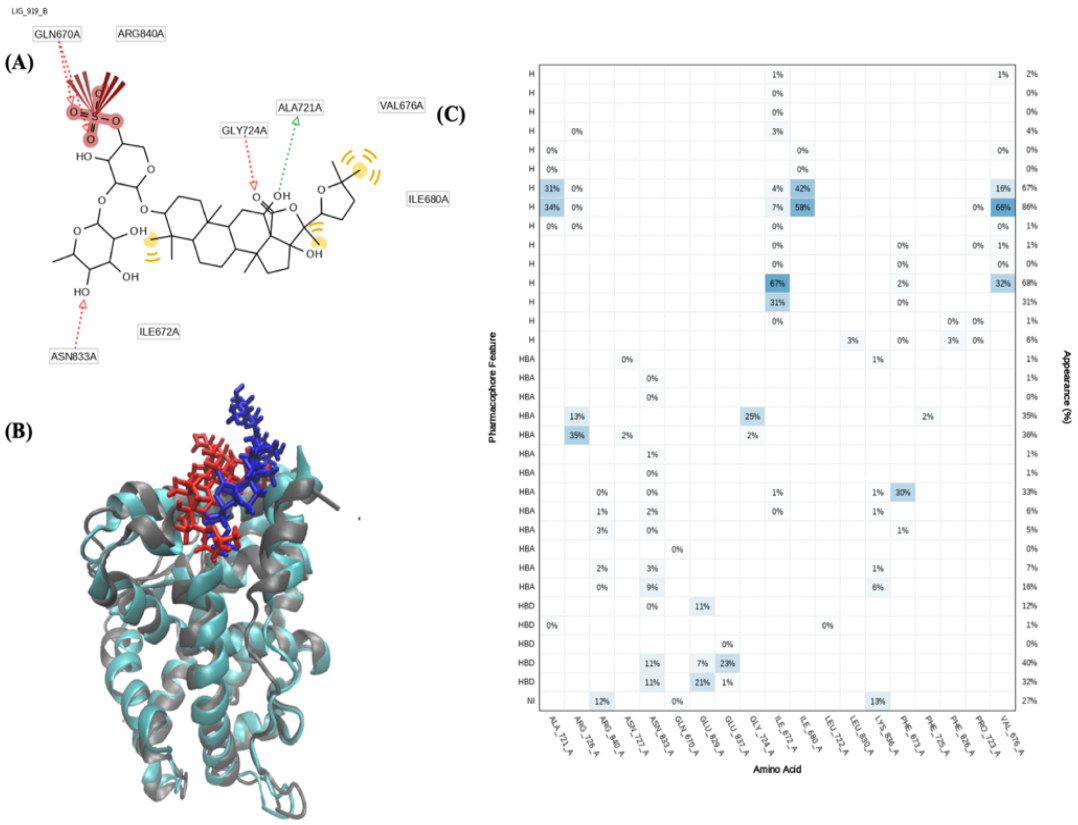

Figure 7

The interaction of HAM2 with BF3 site after 20 ns MD simulation. (A) The interaction of redocked HAM2 with the BF3 site of 2PKL. (B) HAM2 in complex with BF3 2PKL; starting pose of 2PKL and HAM2 are in crayon and red, respectively, while grey and blue show 2PKL and HAM2 after 20 ns of simulation. (C) MD interaction plot of the 20 ns simulation of HAM2 in complex with BF3-2PKL as analysed by LigandScout

Conclusion: Holothurin A and holothurin A2 exhibited a cytotoxic potential on the prostate cancer cell line. The molecular docking analysis indicated that HAM2, which is the most abundant metabolite form after digestion and absorption, exhibited stronger interactions with binding surface sites (AF2 and BF3) of AR. During MD simulation, HAM2 is binding more stable to BF3 than to AF2 via hydrophobic and hydrogen bond acceptor interactions. This study concludes that HAM2 could be effectively used for prostate cancer drug development by alteration AR activities via binding at the allosteric site of the receptor.

Acknowledgements: This research was supported by Austrian Agency for International Cooperation in Education Research (Östereichischer Austauschdienst (OeAD); grant number: ICM-2018-10228) to Kanta Pranweerapaiboon.

References: Please make sure that all references comply with the conference format.

1. Siegel RL, Miller KD, Jemal A. CA Cancer J Clin. 2018;68:7-30.
2. Javidan J, Deitch AD, Shi XB, White RW. Cancer Invest. 2015;23:520-28.
3. Grosdidier S, Carbo LR, Buzon V, Brooke G, Nguyen P, Baxter JD, Bevan C, Webb P, Estebanez-Perpina E, and Fernandez-Recio J. Mol Endocrinol. 2012;26:1078-90.
4. Lallous N, Dalal K, Cherkasov A, Rennie PS. Int J Mol Sci. 2013;14:12496-519.
5. Munuganti RS, Leblanc E, Axerio-Cilies P, Labriere C, Frewin K, Singh K, Hassona MD, Lack NA, Li H, Ban F, Guns ET, Young R, Rennie PS, and Cherkasov A. J Med Chem. 2013;56:1136-48.

6. Wargasetia TL, Widodo. Invest New Drugs. 2017;35:820-26.
7. Han H, Li L, Yi Y, Wang X, Pan M. Chin Herb Med. 2012;4:183-88.
8. Mondol MAM, Shin HJ, Rahman MA, Islam MT. Mar Drugs. 2017;15:1-35.
9. Song S, Zhang L, Cao J, Xiang G, Cong P, Dong P, Li Z, Xue C, Xue Y, Wang Y. J Food Sci. 2017;82:1961-67.
10. Zhang SY, Yi Y, Tang H. J Nat Prod. 2006;69:1492-95.
11. Wang J, Han H, Chen X, Yi Y, Sun H. Mar Drugs. 2014;12:4274-90.
12. Yu S, Ye X, Huang H, Peng R, Su A, Lian XY, Zhang Z. Planta Med. 2015;81:152-59.
13. Pranweerapaiboon K, Garon A, Seidel T, Janta S, Plubrukarn A, Chaithirayanon K, Langer T. J Biomol Struct Dyn. 2021;13:1-9.
14. Song S, Cong P, Xu J, Li G, Liu X, Li Z, Xue C, Xue Y, Wang Y. J Funct Foods. 2016;25:62-69.
15. Estebanez-Perpina E, Arnold LA, Nguyen P, Rodrigues ED, Mar E, Bateman R, Pallai P, Shokat MK, Baxter JD, Guy RK, Webb P, Fletterick RJ. Proc Natl Acad Sci USA. 2007;104:16074-79.
16. Zoete V, Cuendet MA, Grosdidier A, Michielin O. J Comput Chem. 2011;32:2359-68.

DEUTERATION OF ORGANIC COMPOUNDS BY HYDROTHERMAL PROCESS

Nattasiri Phaisarn,[1] Tirayut Vilaivan[2,*]
[1]Program in Petrochemistry and Polymer Science, Faculty of Science,
Chulalongkorn University, Pathumwan, Bangkok 10330, Thailand
[2]Organic Synthesis Research Unit, Department of Chemistry, Faculty of Science,
Chulalongkorn University, Pathumwan, Bangkok 10330, Thailand
*e-mail: vtirayut@chula.ac.th

Abstract:

Deuterium-labelled compounds are widely used in many applications including standard in various analytical techniques, improving drug metabolism, and as NMR solvents. Herein, the objective of this study is to develop a method for the deuteration of organic compounds with deuterium oxide (D_2O) as the deuterium source under hydrothermal conditions. The deuteration experiments performed with various substrates showed that the hydrogen-deuterium exchange (HDx) at the *ortho*-, *para*- positions of phenols and α-position of amino acids occurred efficiently under hydrothermal reaction without the need for any catalyst or additive. The HDx of amino acids occurred with complete racemization at the α-position. The HDx reaction also occurs at the α-position of esters and on the indole ring. Accordingly, the developed hydrothermal HDx provides a green approach for synthesizing deuterated organic compounds that are useful in pharmaceutical, analytical, and many other fields.

Introduction:

Isotopic labelling involves the replacement of one or more atoms in an organic molecule such as H, C, and N with their isotopes. Mostly, stable isotopes such as $^{2}H(D)$, ^{13}C, and ^{15}N are preferred due to their high stability and less toxicity. In most cases, physical and chemical characteristics are little affected by isotopic replacements, but the molecular masses are changed. This make isotopic-labeled compounds useful as standards for quantitative mass spectrometry (MS) and high-performance liquid chromatography (HPLC).[1] In nuclear magnetic resonance spectroscopy (NMR), deuterated solvents such as DMSO-d_6 or chloroform-*d* are routinely used due to the absence of an interfering signal in the proton frequency range. Also, the deuterium provided a lock frequency signal which is necessary for measuring the NMR signal. Furthermore, the C–D bond (341.4 kJ/mol) is stronger than the C–H bond (338.4 kJ/mol) as shown by the bond dissociation energy,[2] thus it is more difficult to break. This can tremendously affect the pharmacokinetic properties of drugs. Deuterated drugs are eliminated from the human body more slowly than non-deuterated drugs at the same dosage level.[3] In addition, the longer half-life of deuterated drugs reduces the dose and thus side effects of the drugs. Consequently, deuterated substances play a crucial role in improving medicinal efficiency.

Deuterium-labelled compounds can be prepared by conventional chemical synthesis starting from simple deuterated starting materials such as methanol-d_4. However, the substrates or reagents must be pre-labeled with deuterium, which is normally expensive, especially when considering that the final yield for synthesis can be low. Another commonly used method is the exchange of hydrogen by deuterium (HDx). The HDx reaction occurs efficiently when the hydrogen atom is attached to an atom with high electronegativities such as oxygen or nitrogen. Moreover, the HDx reactions of hydrogen atoms attached on carbon

are possible when there is one or more electron withdrawing groups (EWG) attaching to the carbon atom.

Typically, the HDx reaction involves the transfer of one or more deuterium atoms between the substrate and the deuterating agents such as deuterium oxide (D_2O),[4, 5] dimethyl sulfoxide (DMSO-d_6),[6] methanol-d_4 (CD_3OD),[7] formic acid-d_2,[8] and D_2 gas which produced by photocatalytic D_2O splitting.[8, 9] The HDx reaction is usually performed in the presence of acid, base or metal catalysts,[10] especially palladium and platinum.[11] The reaction may occur at ambient temperature, under conventional heating, microwave,[12] and hydrothermal processes.[4, 5] However, the previously reported HDx reaction under hydrothermal conditions were typically performed in extreme conditions (reaction temperatures >300 °C), and required an additive such as a strong base or acid.

The hydrothermal condition involves the reactions that are performed in a closed system, under high temperature and pressure. If the temperature is higher than the critical point of the medium, it became supercritical. Thus, the medium becomes more acidic and less polar which can dissolve the organic compounds that are normally insoluble in water. The advantages of hydrothermal conditions are less time-consuming, small-scale synthesis, reduction of hazardous chemicals usage and can occur with no requirement of catalyst or additives.[13]

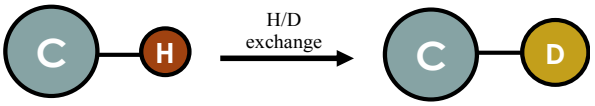

Figure 1. HDx of organic compounds

In this study, we aim to investigate the suitable conditions for the hydrogen-deuterium exchange reaction under the hydrothermal process for a range of organic substrates with various functional groups. Also, the selectivity and limitation of HDx were studied. We expect that the study would provide a green, efficient, and inexpensive method for the synthesis of deuterium-labelled compounds that are useful in many applications.

Methodology:

Materials

Stainless steel tubes with screw caps were purchased from Swagelok. All starting materials were purchased from standard suppliers and were used as received without further purification. Vanillin, 4-bromophenol, *trans*-4-hydroxy-L-proline, and α-methylbenzylamine were purchased from Fluka. L-leucine, L-lysine, L-tryptophan, L-tyrosine, L-threonine, and γ-decalactone were purchased from Sigma-Aldrich. L-aspartic acid and anisole were purchased from BDH. *N*-Acetyl-*trans*-4-hydroxy-L-proline was purchased from Fluorochem. Phenol and sodium bicarbonate ($NaHCO_3$) were purchased from Suksapan Panit. Salicylic acid and acetic acid (CH_3COOH) were purchased from Merck. Deuterium oxide (D_2O, 99.8 atom% D) was purchased from Cambridge Isotope Laboratories. ^1H NMR spectra were recorded in a suitable deuterated solvent on a JEOL JNM-ECZ500R/S1 operating at 500 MHz (^1H).

Methods

All reactions were carried out in a screw-capped reactor made from stainless steel 316 tube with 3/8 in. OD, 0.049 in. wall thickness, and 6.0 cm length (total cell volume ~2.0 mL). In all reactions, 10 mg of the substrate and 500 μL of D_2O (100-200 mM concentration, depending on the substrate) were placed in the reactor and heated at the specified temperature for the specified period of time in a pre-heated electrical metal melting furnace from ToAuto (model SG-RRL-V.1.2-9KG-220V). After cooling to ambient temperature, the reactor was carefully opened and the obtained products as a D_2O solution were transferred to the NMR

tube. The solution was then adjusted by D_2O to make a final volume solution of 560 μL and followed by characterization using ^1H NMR spectroscopy. When the obtained products are non-polar and insoluble in water, extraction with organic solvents (diethyl ether or ethyl acetate) was performed required prior to the characterization by the ^1H NMR technique. For the reactions under acid or base-catalyzed conditions, CH_3COOH or $NaHCO_3$ (0.076 mmol, 1 equiv.) were added to the reaction before heating.

Assuming no other competing reactions, the percent hydrogen-deuterium exchange (%HDx) was calculated from ^1H NMR spectrum using equation (1).

$$\%HDx = \frac{mol_{product}}{mol_{product} + mol_{substrate}} \times 100 \quad (1)$$

Where $mol_{product}$ and $mol_{substrate}$ can be calculated from the peak areas of the signal of interest in the product and substrate, respectively.

Results and Discussion:

We proposed that hydrogen-deuterium exchange reaction (HDx) could occur under hydrothermal conditions, which involves heating the substrate in D_2O at a high temperature and pressure in a closed system. Under such conditions, the water (or D_2O in this case) became more acidic and less polar. This makes it possible to dissolve organic compounds that are normally insoluble in water.[5] In this work, various substrates were screened to find suitable CH moieties that can undergo efficient HDx under hydrothermal conditions. Two potential candidates are the α-CH protons of amino acids and *ortho*/*para*-CH protons of aromatic rings.

We initially used 4-bromophenol as a representative aromatic substrate and *trans*-4-hydroxy-L-proline as a representative amino acid substrate. Both compounds were heated with D_2O in the absence of any catalysts. The reaction temperature range of 150-250 °C was investigated with the same 1 h heating period. For 4-bromophenol, the HDx was observed exclusively at the *ortho*-position as confirmed by the disappearance of the *ortho*-proton signal at 6.72 ppm and the collapse of the *meta*-proton signal at 7.33 ppm into a singlet peak due to the loss of coupling with the adjacent *ortho*-protons (**Figure 2**). The %HDx could be estimated based on the ratio of the *meta*-protons from the starting material and the *ortho*-protons of the starting material and product. The results showed that the HDx became more efficient at higher temperatures, but the reaction was not yet complete after heating at 250 °C for 1 h (67% exchange yield). However, at the same temperature with an extended reaction time from 1 to 2 h, the %HDx was increased to more than 97% indicating practically complete labeling.

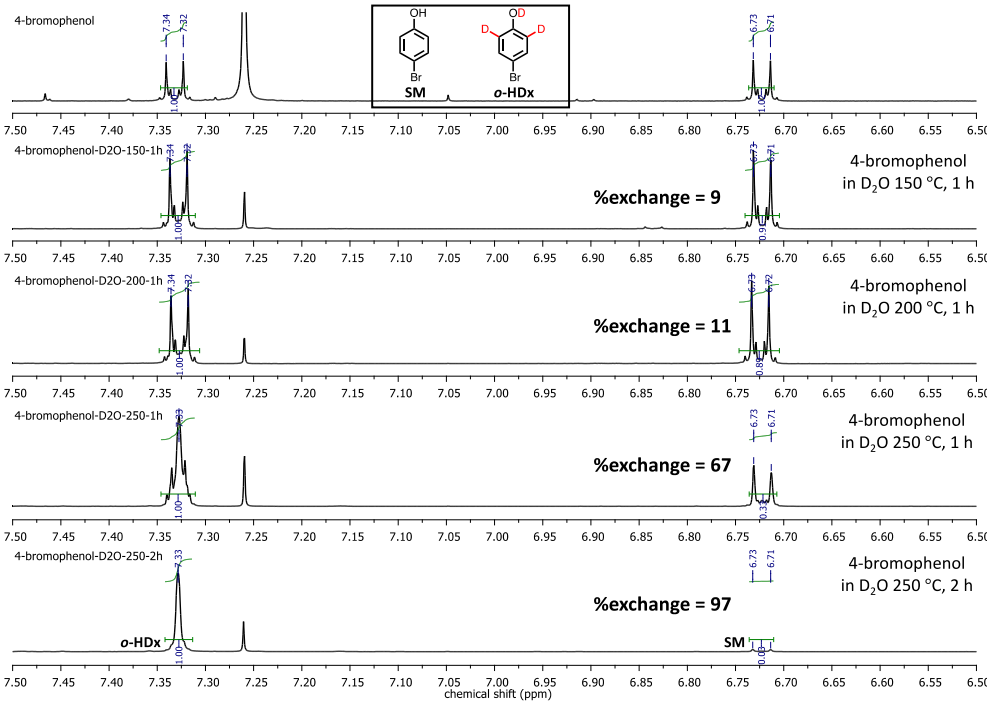

Figure 2. ^{1}H NMR spectra of the HDx reaction of 4-bromophenol at different temperatures

In the case of *trans*-4-hydroxy-L-proline, the deuteration started to occur at 200 °C and it occurred exclusively at the α-position as shown by the diminished intensity of the α-CH signal at 4.12 ppm (**Figure 3**). For this substrate, the HDx was accompanied by epimerization as shown by the presence of two sets of signals, one corresponded to the *trans*-4-hydroxy-L-proline without the α-CH, which showed a somewhat simplified signal due to the absence of coupling with the α-proton. Another set of signals with a similar pattern, but slightly different chemical shifts were also observed. This was confirmed, by comparison with the authentic sample, to be the *cis*-4-hydroxy-D-proline which was the product of epimerization of *trans*-4-hydroxy-L-proline at the α-position. The ratio of *cis:trans* isomer increased with temperature and the value of 41:59 was obtained at 250 °C. No further change was observed upon heating beyond this temperature or time suggesting that the epimerization reached its equilibrium, which was in agreement with the complete disappearance of the α-CH signal.

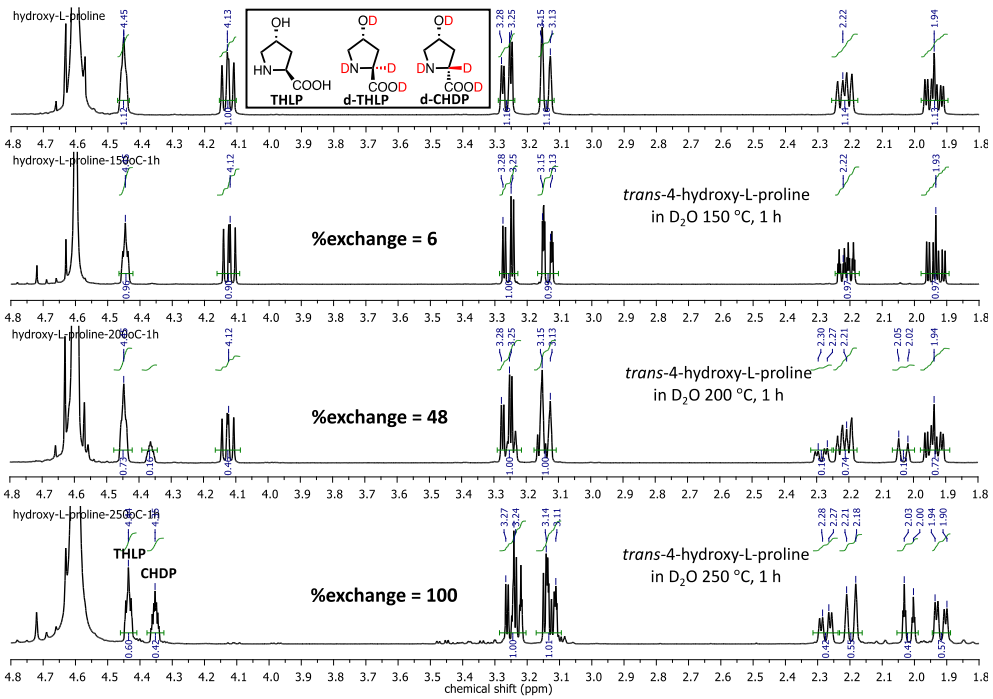

Figure 3. ^{1}H NMR spectra of the HDx reaction of *trans*-4-hydroxy-L-proline at different temperatures

Next, the pH effects on the HDx of 4-bromophenol and *trans*-4-hydroxy-L-proline were evaluated. Acetic acid (CH_3COOH) and sodium bicarbonate ($NaHCO_3$) (1 equiv. each) were added as model acid and base catalyst, respectively. The results indicated that the base can promote the HDx in both cases. 4-Bromophenol underwent efficient HDx (98% exchange) at the *ortho*- position and *trans*-4-hydroxy-L-proline was also deuterated at α-position (100% exchange, *cis:trans* = 50:50). In contrast, lower %exchange was observed under acidic conditions and the %HDx of 4-bromophenol and *trans*-4-hydroxy-L-proline were reduced to only 69 and 42, respectively.

Encouraged by the above results that the HDx could occur for both *ortho*-aromatic protons and α-protons of amino acids at a temperature in the range of 200 to 250 °C, additional substrates were further studied. An example includes vanillin, in which the deuterated derivative would be useful as a standard for quantitation of vanillin by LC-MS.[14] The ^{1}H NMR spectra of vanillin before and after heating with D_2O for 1 hour at 230 °C are shown in **Figure 4**. This temperature was chosen based on practical consideration since this is the highest temperature that is still safe for a Teflon-lined reactor typically used for the scaled-up synthesis. To our delight, the NMR spectra indicated a complete HDx (~100%) exclusively at the proton *ortho*- to the phenolic -OH group as shown by the complete disappearance of the proton signal at 6.92 ppm (d J = 8.1 Hz, 1H). In addition, the *ortho*-coupling with this proton (J = 8.1 Hz) was lost in the HDx product, while the *meta*-coupling (J = 1.8 Hz) between the other two protons remained. Other signals remained the same indicating the compatibility of the present hydrothermal HDx with substrates carrying complex functional groups (in this case: ether, aldehyde, and phenol).

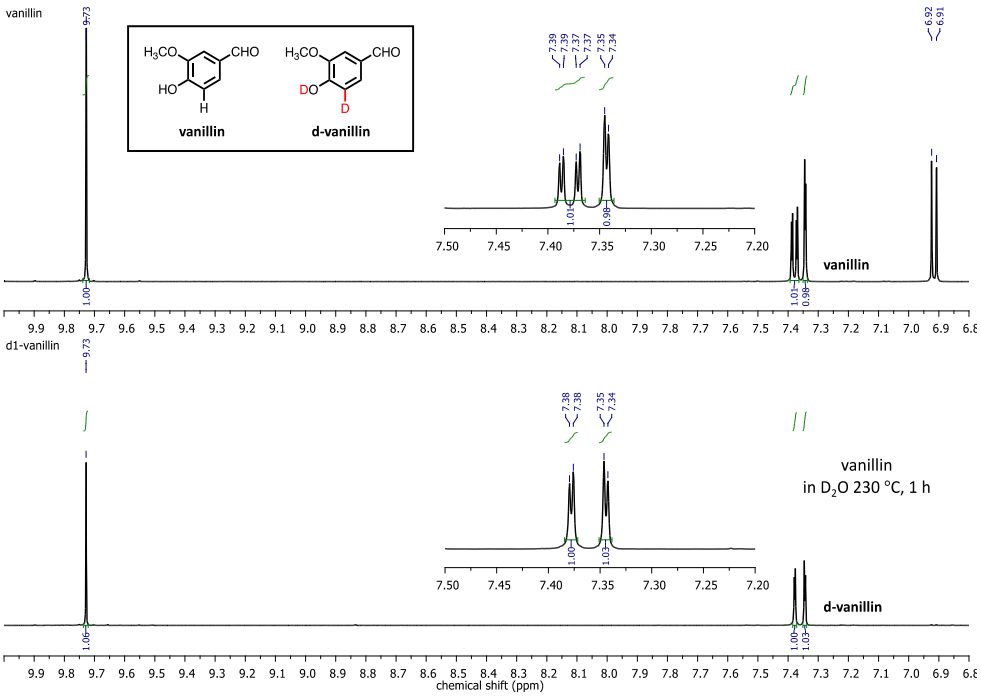

Figure 4. ^{1}H NMR spectra of vanillin before and after hydrothermal HDx

The hydrothermal HDx was further applied to additional substrates including aliphatic, alicyclic, aromatic, and heterocyclic compounds (mostly amino acid and simple aromatic compounds) as shown in **Figure 5**. The HDx of L-tryptophan and L-tyrosine also occurred efficiently at 230 °C. In addition to the complete HDx at the α-positions, the HDx also occurred quantitatively at the indole C_2H of L-tryptophan and the phenolic *ortho*-CHs of L-tyrosine. The HDx of other amino acids including L-leucine and L-lysine occurred exclusively at the α-position. In all α-amino acids, the α-HDx presumably occurred with complete racemization, but this would not be observable by NMR as in the case of hydroxyproline since the racemized product would have an identical ^{1}H NMR spectrum to the starting compound. However, when a simple cyclic ester γ-decalactone was tested, the α-CH_2 linked to the ester group was found to be inert. Therefore, the generality of HDx for α-CH_2 linked to only one electron-withdrawing group should be investigated further. *N*-acetyl-*trans*-4-hydroxy-L-proline underwent a clean HDx with concomitant hydrolysis to form acetic acid as a by-product. Further investigation should be performed to confirm the necessity of the free amino group in assisting the HDx.

For aromatic compounds, in contrast to 4-bromophenol and vanillin which underwent almost quantitative HDx, no reaction was observed with anisole and benzoic acid. This suggests that only phenolic protons are effectively exchanged under this condition. For the parent phenol, the results showed that the HDx occurred faster at the *ortho*- than the *para*-positions. The extent of HDx for the *ortho*-H was 68% and 91%, and for the *para*-H was 44% and 72% following heating with D_2O at 230 °C for 1 and 2 h, respectively. The mechanism of the exchange in phenols may involve keto-enol tautomerism between phenols and cyclohexadienones. Few other compounds, including salicylic acid, α-methylbenzylamine, L-threonine, and L-aspartic acid when subjected to the same hydrothermal HDx condition yielded complex mixtures possibly due to different rates of HDx at different positions or decomposition of the substrates/products. In the case of salicylic acid, it is likely that the *para*-proton exchange as well as partial decarboxylation might also occur in addition to the expected *ortho*-HDx.[15]

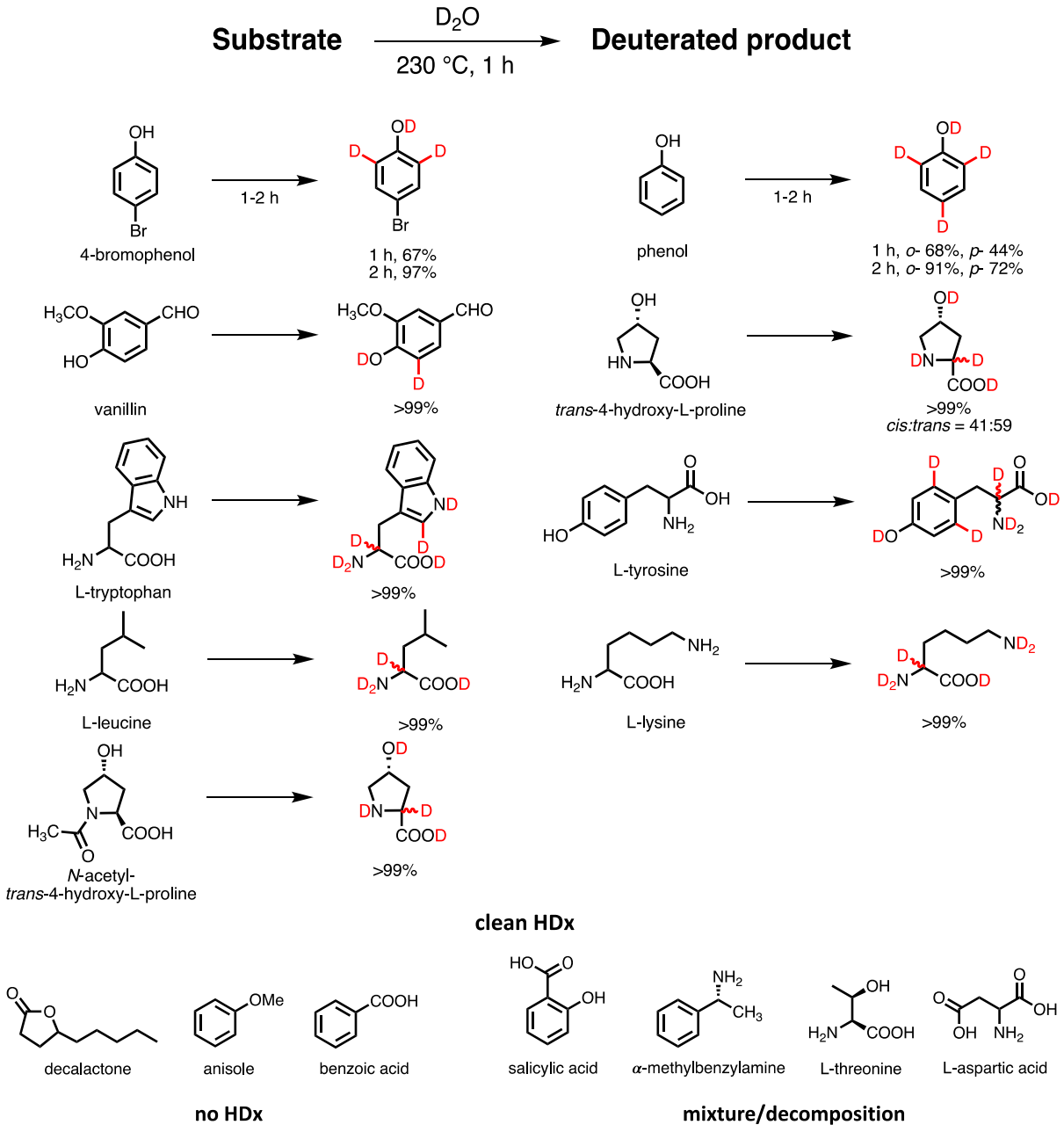

Figure 5. Deuterated substrates and HDx percentage in this work.

Conclusion:

In summary, a hydrothermal proton-deuterium exchange (HDx) reaction of selected organic compounds with various functional groups has been investigated. Overall, the HDx occurred cleanly and in high yield without requiring additional catalyst. α-Amino acids and phenols are good substrates for the hydrothermal HDx, which selectively occurred at the α-CH and *ortho*-positions, respectively. This method could provide a green approach for preparing deuterated compounds. The reaction should be further investigated to determine the generality/limitation of the reaction and to expand the substrate scope.

Acknowledgements:

The authors acknowledge financial supports from Petrochemistry and Polymer Science Fund, Faculty of Science, Chulalongkorn University, and the financial support from the National Science, Research and Innovation Fund (NSRF) via the Program Management Unit for Human Resources & Institutional Development, Research and Innovation (B16F640101) is gratefully acknowledged.

References:

1. Grocholska P, Bąchor R. Molecules. 2021;26:2989.
2. Luo YR. Handbook of Bond Dissociation Energies in Organic Compounds: CRC Press; 2002. 66.
3. Schneider F, Bradbury M, Baillie TA, Stamler D, Hellriegel E, Cox DS, et al. Clin Transl Sci. 2020;13:707-717.
4. Yao J, Evilia RF. J Am Chem Soc. 1994;116:11229-11233.
5. Junk T, Catallo WJ. Tetrahedron Lett. 1996;37:3445-3448.
6. Patel M, Saunthwal RK, Verma AK. ACS Omega. 2018;3:10612-10623.
7. Darshana D, Sureram S, Mahidol C, Ruchirawat S, Kittakoop P. Org Biomol Chem. 2021;19:7390-7402.
8. Wang W-H, Hull JF, Muckerman JT, Fujita E, Hirose T, Himeda Y. Chem - Eur J. 2012;18:9397-9404.
9. Liu C, Chen Z, Su C, Zhao X, Gao Q, Ning G-H, et al. Nat Commun. 2018;9:80.
10. Garreau AL, Zhou H, Young MC. Org Lett. 2019;21:7044-7048.
11. Krause-Heuer AM, Yepuri NR, Darwish TA, Holden PJ. Molecules. 2014;19:18604-18617.
12. Martins A, Lautens M. Org Lett. 2008;10:4351-4353.
13. Kubo M, Takizawa T, Wakai C, Matubayasi N, Nakahara M. J Chem Phys. 2004;121:960-969.
14. de Jager LS, Perfetti GA, Diachenko GW. J Chromatogr A. 2007;1145:83-88.
15. Willi AV. Trans Faraday Soc. 1959;55:433-441.

Session C:
CHEMISTRY
(Physical & Theoretical Chemistry)

MOLECULAR DOCKING STUDIES OF THE 2,5-DIKETOPIPERAZINE DERIVATIVES AS POTENTIAL ANTI-SARS-CoV2 ACTIVITY

Poomipat Tamdee, Chanakan Winyakul, Waya S. Phutdhawong, Jitnapa Sirirak *

Department of Chemistry, Faculty of Science, Silpakorn University, Nakhon Pathom 73000, Thailand

*e-mail: sirirak_j@silpakorn.edu, +66-34255797

Abstract:

Drugs for the treatment of COVID-19 are continuously developed by scientists and physicians worldwide due to the severe acute respiratory syndrome caused by COVID-19. 2,5-Diketopiperazine derivatives consisting of benzylidene and alkylidene substituents at 3 and 6 positions have been known as the core structure for their antiviral activities. Our group previously reported the novel 2,5-Diketopiperazine derivatives as anti-influenza virus (H5N2). Herein, the potential of our natural 2,5-Diketopiperazine derivatives: Lansai C (LS-C) and synthetic 2,5-Diketopiperazine derivatives (**13a-d**) as COVID-19 inhibitors were investigated with molecular docking approach, using SARS-CoV-2 3CL main protease and SARS-CoV-2 spike receptor-binding domain bound with ACE2 as the receptors, and the results were compared with that of Favipiravir. It was found that LS-C and compound **13d** bound in the active sites of both protein targets and their binding energies were also either similar or lower than those of Favipiravir. Moreover, the piperazine and carbonyl groups on 2,5-DKP scaffold of LS-C and **13d** effectively interacted with amino acids in the active site of both receptors. This indicated that the 2,5-DKP scaffold of our compounds could be the key to bind and inhibit the enzyme involved in anti-SARS-CoV-2 activities leading to the potential COVID-19 drugs.

Introduction:

Coronavirus disease (Covid-19) was the novel severe acute respiratory syndrome coronavirus 2 (SARS-CoV-2) which began in Wuhan, China. In 11 March 2020, WHO announced the COVID-19 outbreak a global pandemic. Currently, there are highly infectious, this virus poses a grave threat to the global populations associated with a high rate of mortality [1-3]. The symptoms linked with this disease include fever, myalgia, cough, dyspnea and fatigue [4].

Coronavirus disease caused by the SARS-CoV-2, belonging to beta-coronavirus that originated from bats has an envelope and sense single-stranded RNA. There are four important enzymes that are essential for the pathogenesis: Spike protein that facilitates virus entry through the angiotensin converting enzyme 2 (ACE2) to the host cell surface receptor, 3 chymotrypsin like protease (3CLpro), the papain-like protease (PLpro) involved in the assembly of new viruses, and RNA-dependent RNA polymerase (RdRp) that facilitates CoV RNA genome replication [5]. Accordingly, drugs are often developed to inhibit structure-active mechanisms that are important in the pathogenesis of human disease [6].

3 chymotrypsin like protease (3CLpro) has been validated as a potential target for the development of drugs since it plays an important role in transcription and replication of viruses. 3CLpro has conserved catalytic dyad residue Cysteine-Histidine involved the replication function of virus [7]. Moreover, SARS-CoV-2 spike receptor-binding domain bound with ACE2, (SARS-CoV-2 RBD with ACE2) is another potential target for drug therapies because it involves the binding to the host cell receptor angiotensin converting enzyme 2 (ACE2) and releases the viral RNA genome to host cell for replication and increase

the number of vial genomes in host cell [8]. Therefore, in this work, 3CLpro and SARS-CoV-2 RBD with ACE2 were selected as the receptors for our potential drugs for the treatment of COVID-19.

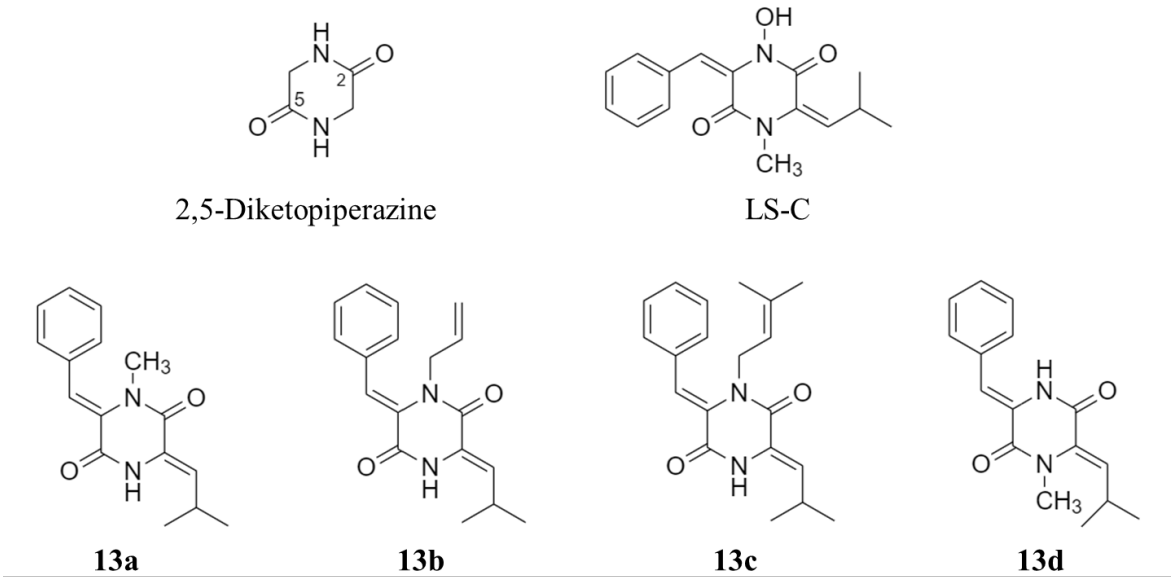

Figure 1. The structure of 2,5-Diketopiperazine, Lansai C (LS-C) and 2,5-DKP derivatives **13a-13d**

2,5-Diketopiperazine (2,5-DKP) is a six-membered cyclic dipeptide, often found in a variety of natural products from microorganisms, animals and plants including Lansai C (LS-C). LS-C contains benzylidene and alkylidene substituents at 3 and 6 positions of the 2,5-DKP core structure. LS-C is produced by *Streptomyces* sp. SUC1 isolated from the aerial roots of Ficus benjamina in our campus [9]. Since LS-C has substituents on α-carbon in the opposite direction to N-substituents which could orient the functionalized chain in the appropriate direction to receptors [10], it is interested compounds for drug development. Moreover, in previously study of our group, we designed and synthesized the novel 2,5-DKP derivatives (**13a-d**) as shown in Figure 1. **13a-d** exhibited the antiviral activity against influenza virus (H5N2). Therefore, it would be interested to explore the potential anti-SAR-CoV2 activity of **13a-d** and LS-C.

Herein, molecular docking was employed to explore the possible binding of LS-C and our 2,5-DKP derivatives (**13a-d**) in the binding pocket of two following receptors: SARS-CoV-2 3CL main protease (SARS-CoV-2 3CLpro, PDB ID: 6LU7) and SARS-CoV-2 spike receptor-binding domain bound with ACE2, (SARS-CoV-2 RBD with ACE2, PDB ID: 6M0J) and compared with that of Favipiravir. Our results would give valuable guidance at a molecular level for the development of new 2,5-DKP derivatives as the anti-SAR-CoV2 drugs.

Methodology:

The 3D structures of 2,5-DKP derivatives and LS-C were prepared using GAUSSIAN09 and their optimized structures were obtained at the B3LYP/6-311g* level. The protein structures of SARS-CoV-2 3CL main protease (SARS-CoV-2 3CLpro, PDB ID: 6LU7), and SARS-CoV-2 spike receptor-binding domain bound with ACE2, (SARS-CoV-2 RBD with ACE2, PDB ID: 6M0J) were downloaded from Protein Data Bank. The iGEMDOCK v.2.1. [11] was utilized to conduct molecular docking studies using the accurate

docking (very slow) with population size (N=800), 80 generation and 10 solutions. For each ligand-protein complex, the docking pose with lowest binding energy value was analyzed and imaged using BIOVIA Discovery Studio Visualizer.

Results and Discussion:

The comparison of binding positions of our selected compounds with virus propagation inhibitor potential: LS-C and compounds **13a**–**d** in the active site of two interested receptors were displayed in Figure 2. The binding energies, amino acid interaction along with hydrogen bond length of our compounds bound in the active site of receptors were demonstrated in Table 1. It was found that three of our compounds (**13a**, **13d** and LS-C) fit in the binding site of SARS-CoV-2 3CLpro while all of our compounds bound in the cavity of SARS-CoV-2 RBD with ACE2, located between the spike receptor-binding domain and the host cell receptor angiotensin converting enzyme 2 (ACE2).

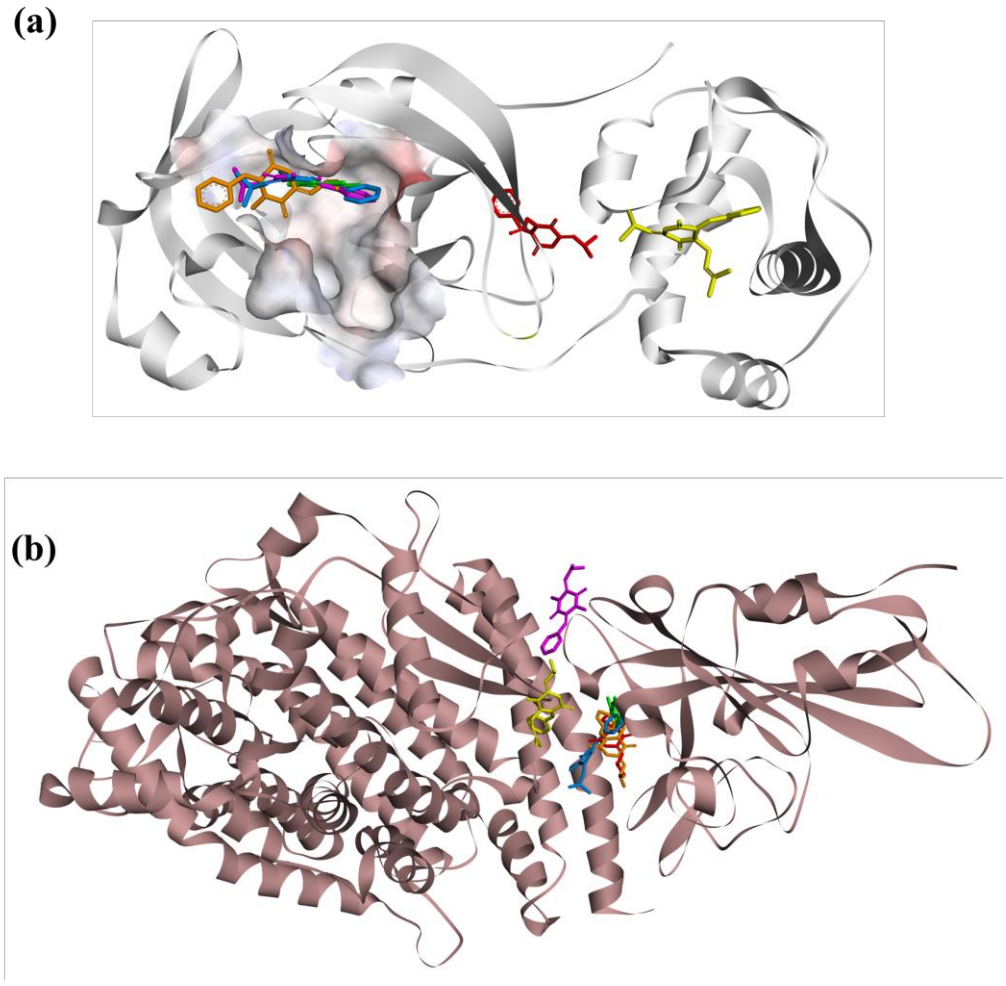

Figure 2. Comparison of the binding positions of Favipiravir (green), LS-C (pink), **13a** (orange), **13b** (red), **13c** (yellow) and **13d** (sky blue) in the cavity of (a) SARS-CoV-2 3CL main protease, and (b) SARS-CoV-2 spike receptor-binding domain bound with ACE2.

For SARS-CoV-2 3CLpro, the binding energy of compound **13d** and LS-C (−92.90 and −98.31 kcal/mol, respectively) were lower than that of Favipiravir (−81.43 kcal/mol),

while **13a** (−74.81 kcal/mol) had a much higher binding energy than Favipiravir. This may be because **13a** bound in the cavity of 3CLpro with a different orientation to **13a** and LS-C (Figure 2a). Moreover, in SARS-CoV-2 RBD with ACE2, **13a-d** and LS-C had either similar or lower binding energy (−79.30 to −84.84 kcal/mol) than Favipiravir (−80.92 kcal/mol). However, only **13a**, **13b** and **13d** bound in active site at the same position as Favipiravir.

It could be noticed that, for both SARS-CoV-2 3CLpro and SARS-CoV-2 RBD with ACE2, only LS-C and **13d** were able to bind and interact with amino acids in both active sites. The hydrogen bonds and 2D interactions of LS-C and **13d** in SARS-CoV-2 3CLpro and SARS-CoV-2 RBD with ACE2 were shown in Figure 3 and Figure 4, respectively.

Table 1. Summary of binding energies, amino acid interaction, and hydrogen bond length of 2,5-diketopiperazine derivatives and Favipiravir in molecular docking studies.

Proteins	Compounds	Binding energy (kcal/mol)	Amino acid residues	H-bond length (Å)
COVID-19 3CL main protease	**13a**	−74.81	-	-
	13d	−92.90	SER144, CYS145	2.89,1.63
	LS-C	−98.31	SER144, CYS145	2.61,1.99
	Favipiravir	−81.43	HIS163	2.23
SARS-CoV-2 spike receptor-binding domain bound with ACE2	**13a**	−84.40	-	-
	13b	−80.47	-	-
	13c	−86.15	GLY504	2.67
	13d	−79.30	ARG403, ARG303, TYR505	1.55, 2.38, 2.63
	LS-C	−84.84	ASN330, ASN439, GLN506	1.97, 2.70, 1.96
	Favipiravir	−80.92	HIS34, LYS353, TYR453, GLN493	3.09, 2.24, 2.45, 1.95

As can be seen in Figure 3, the carbonyl groups on the 2,5-DKP scaffold of **13d** and LS-C formed hydrogen bonds with amino acid residues in the binding pocket of SARS-CoV-2 3CLpro and SARS-CoV-2 spike receptor-binding domain bound with ACE2. Interestingly, for SARS-CoV-2 3CLpro, **13d** and LS-C formed hydrogen bond with CYS145 which was one of catalytic dyad residues involved in the replication function of virus. Additionally, piperazine and benzyl moiety of **13d** and LS-C effectively interacted with amino acid residues in both SARS-CoV-2 3CLpro and SARS-CoV-2 RBD with ACE2 as shown in Figure 4. This indicated that 2,5-DKP scaffold of 13d and LS-C played the important role in SARS-CoV-2 inhibition. According to our results, LS-C and **13d** could be potential anti-SARS-CoV-2 inhibitors and 2,5-Diketopiperazine (2,5-DKP) could be utilized for the development of potential COVID-19 drugs.

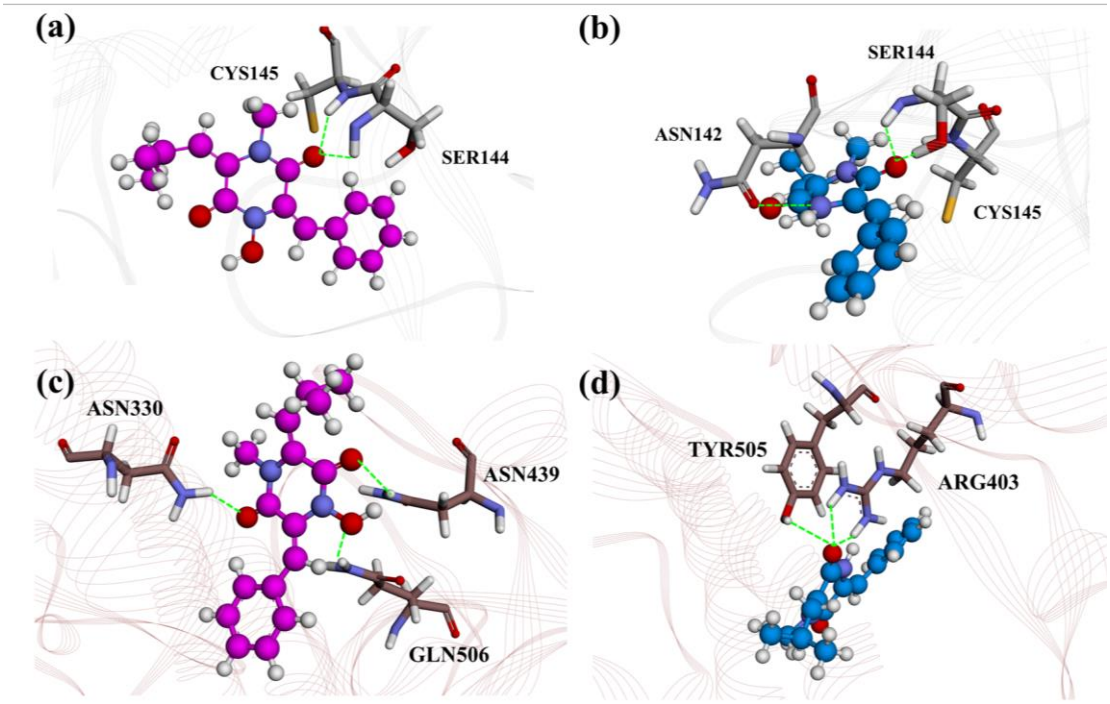

Figure 3. Hydrogen bond interactions of **13d** (sky blue) and LS-C (pink) in the cavity of (a, b) SARS-CoV-2 3CL main protease, and (b) SARS-CoV-2 spike receptor-binding domain bound with ACE2.

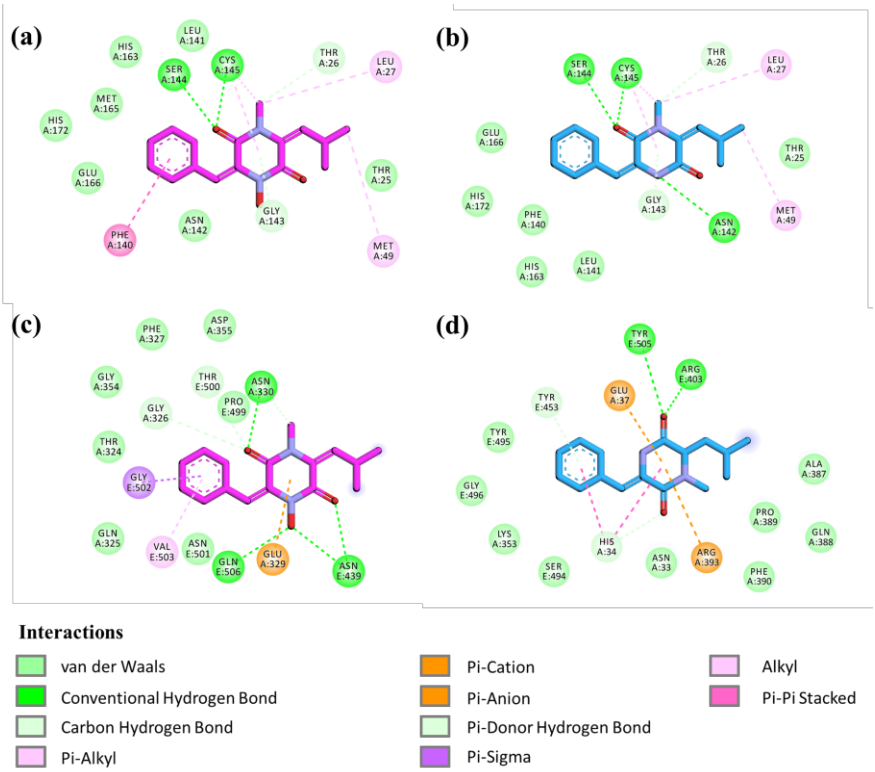

Figure 4. 2D interactions of **13d** (sky blue) and LS-C (pink) in the cavity of COVID-19 3CL main protease (a,b), and SARS-CoV-2 spike receptor-binding domain bound with ACE2 (c,d)

Conclusion:

The molecular docking study of the 2,5-DKP derivatives showed that LS-C and **13d** fit in the binding pocket of both SARS-CoV-2 3CLpro and SARS-CoV-2 RBD with ACE2 with similar binding energy to Favipiravir, indicating their anti-SARS-CoV-2 potential. Additionally, it was found that the 2,5-DKP scaffold of our compounds could be the key to bind and inhibit the enzyme involved in anti-SARS-CoV-2 activities. Our results, hence, would be useful for the design and development of new promising anti SARS-CoV-2 drugs.

Acknowledgements:

This research was supported by the DPST scholarship and Department of Chemistry, Silpakorn University, Thailand.

References:

1. Granlinski LE, Menachery VD. Viruses. 2020; 12:135.
2. Wu F, Zhao S, Yu B, Chen Y, Wang W, Song Z, et al. Nature. 2020; 579,265–269.
3. Zhao S, Lin Q, Ran J, Musa SS, Yang G, Wang W, et al. Int. J. Infect. Dis. 2020; 92, 214–217.
4. Huang C, Wang Y, Li X, Ren L, Zhao J, Hu Y, et al. China. Lancet. 2020;395,497–506.
5. Hussaina A, Hasan A, Babadaei MMN, Bloukh SH, Chowdhury MEH, Sharifig M, et al. Biomedicine & Pharmacotherapy. 2020;130,1-10
6. Mercorelli B, Palù G, Loregian A. Trends Microbiol. 2018;26, 865–876
7. He J, Hu L, Huang X, Wang C, Zhang Z, et al. International Journal of Antimicrobial Agents. 2020;56, 1-10
8. Huang Y, Yang C, Xu X, Xu W, Lui S. Acta Pharmacologica Sinica. 2020;41,1141-1149
9. Tuntiwachwuttikul P, Taechowisan T, Wanbanjob A, Thadaniti S, Taylor WC. Tetrahedron. 2008, 64, 7583-7586.
10. Saavedra CJ, Cuevas F, Romero-Estudillo I, Boto A. Adv. Synth. Catal. 2020, 362, 3158-3169.
11. Hsu KC, Chen YF, Lin SR, Yang JM. BMC bioinformatics. 2011, 12, 1-11.

Session D:
MATHEMATICS / STATISTICS / COMPUTER SCIENCE / DATA SCIENCE / AI

APPLICATION OF THE CORRELATIVE EQUATIONS TO "FILL UP" A MONITORING WATER QUALITY DATA TO SUPPORT THE ASSESSMENT OF WATER QUALITY AND SELF-CLEANING CAPACITY.

Bui Viet Hung[1]*, Nguyen Ngoc Diep[2]
[1] Faculty of Environment, VNUHCM - University of Science
[2] University of Labors and Society of Ho Chi Minh City
*e-mail: bvhung@hcmus.edu.vn

Abstract:
The monitoring of water quality is one of the annual important tasks of environmental management of administrative agencies. However, due to various reasons, the monitoring work does not take place continuously, causing discontinuity/lack of data sets. The lack of data and the discontinuity of the monitoring data set causes the heterogeneity or weak representativeness of the analysis/assessment results about the level quality or self-cleaning capacity of water. The Highest order polynomial fitting Cure Equation (HopCEq) and Multivariable Regression Correlative Equation (MrCEq) are the commonly methods used interpolation/simulation and gives suitable results. In the study, the assessment of water quality and self-cleaning capacity of Nhieu Loc Thi Nghe canal (NLTN) in Ho Chi Minh City (HCMC), the HopCEq and MrCEq are applied to "fill up"/"make continuous" the monitoring data sets by the space and time. This helps to increase efficiency in the analysis/assessment and increases the representativeness of research results with an appropriate correlation coefficient (R) and the corresponding degree of close correlation.

Introduction:
General environmental pollution and especial water pollution is a prominent problem of mankind. In many places, environmental pollution has become a disaster causing many adverse impacts on life, production as well as ecological diversity. Environmental monitoring is considered an important work in environmental management. This work accurately gives the current status of environmental quality with specific quality criteria. The set of quality environmental data and information, including the water quality, is an important input database for most assessment studies, planning or solutions to respond, overcome and improve the environmental quality status. However, the environmental quality monitoring is an extremely difficult problem, often intermittently or "broken" due to various practical reasons such as limited implementation finance, maintenance, not enough human resources and often running after the economic and social development of the region (Le, 2019).

The consequences of above problems cause the environmental quality monitoring, especially the water, are a lack of water quality data and missing monitoring locations... (Le, 2019). For example, the water quality monitoring data set in period 2012-2015 at Cau Dien Bien Phu position on the NLTN canal (see table below). In 2012, the monitoring months of January, March, May, August, October and December not implement. In the remaining months of 2012, some water quality components are lacking (due to non-implementation) such as turbidity, oxygen concentration, etc. While in 2015, all months implement the monitoring with full water quality components.

With the "intermittence" of monitoring data between years and between monitoring locations, it will cause difficult to evaluate and analyze related to the variant processes on the quality and ability by time and space. If the number of observations in a year is a little, the representativeness of the research results will be reduced.

Table 1.
The monitoring data of water quality at Dien Bien Phu Bridge position on NLTN canal

Year	Duration		T°C	pH	Turb.	NH4	DO	COD	BOD5	Cd	Pb	Cr	Cu	Coliform
	Month	Tide	()	()	NTU	mg/l	mg/l	mg/l	mg/l	mg/l	mg/l	mg/l	mg/l	MPN/100ml
2012	02	low	26.8	6.94		13.1		193	100	0.001	0.007	0.003	0.004	4600000
	04	low	29.9	7.03		8.91		91.6	15.1	0.002	0.003	0.006	0.01	4600000
	09	low	28.6	6.76		10.9		73.4	37	0.001		0.004	0.01	930000
	11	low	29.1	7.04		9.07		60.4	29.9	0.004	0.006		0.008	430000
2015	01	low	26.4	6.94	3.28	3.65	5.33	9.97	4.8	0.002	0.01	0.001	0.003	900
	02	low	26.8	7.02	17.3	3.45	3.1	14.7	5.81	0.004	0.007	0.003	0.015	43000
	03	low	29	7	3.5	0.52	3.35	9.81	5.6	0.001	0.002	0.002	0.002	240000
	04	low	29.9	6.98	9.05	1.60	3.8	6.3	2.9	0.001	0.005	0.002	0.009	23000
	05	low	30.7	7.02	8.95	1.03	4.92	7.6	2.5		0.002			46000
	06	low	29.2	7.37	8.11	0.89	3.19	13.2	4.24			0.001	0.001	43000
	07	low	28.9	6.84	10.1	0.56	3.1	8.75	6.04		0.002	0.001	0.001	460000
	08	low	29	6.57	7.53	0.78	3.68	23	15	0.002	0.005	0.03	0.05	150000
	09	low	28.6	6.12	12.3	0.04	1.81	37.7	24.95	0.002	0.005	0.03	0.05	93000
	10	low	28.7	6.79	14.2	3.64	3.97	19	12	0.002	0.005	0.03	0.05	460000
	11	low	29.1	5.83	9.31	2.12	3.79	22	15	0.002	0.005	0.03	0.05	43000
	12	low	28.6	6.75	8.21	0.08	4.41	25	17	0.002	0.005	0.03	0.05	110000

(Source: HCMC DONRE, 2022)

At present, many studies offered different methods for simulation to supplement an information and data, including the water quality. The simulation of water quality components is mainly based on mathematical models and these models can be divided into two groups (Le, 2019):

- *The process-based model*. The type of model unites the mathematic – physical – chemical – biochemical fields to simulate the variant processes by time and space. In other words, this type of model simulates the laws of hydrology, hydraulics, substance propagation, and chemical and biochemical reactions by the groups of relevant mathematical equations (the models are the mathematical models). The advantage of groups of mathematical models is very high accuracy in the representing trends and the progression on rules. However, this group often requires large, continuous background data (measured data) with a sufficiently large time period. Therefore, the number of inputs (marginal and adjusted) determines the degree of accuracy (Ross, 2019; Lin, 2019).
- *The artificial intelligence model or the correlative interpolation model*. This type of model uses different interpolation learning algorithms to find/establish a suitable correlation between information/data fields, for example K - Nearest Neighbors, nonlinear multivariable correlation, Multivariable regression, Decision Tree, Random Forest, Support Vector Machine, Artificial Neural Network, and Long Short - Term Memory (LSTM). This type of models has the advantages of being easy to apply, having high accuracy, and require big and continuous amounts of data. In addition, this group of models often standardizes a variety of information, including information related to the economy, society and perception of the regional community. In other words, the interpolation model group can accept many types of information and data which could impact/effect on the simulated object. However, because these models belong to the "black-box" group, it is sometimes difficult to interpret the results as well as the analysis process (Ross, 2019; Palani, 2008; Hunter, 2018), even though the nature of the models bases on the choosing one or more correlative functions or distribution equations of one or more variables with different correlations.

Within the framework of our research project to assess the water quality and self-cleaning capacity of the urban inner canals in Ho Chi Minh City in the period 2012 - 2021, the

research has applied two types of interpolative functions/equations including the Highest order polynomials fitting Curve Equation (HopCEq) and the Multivariable Regression Correlations Equation (MrCEq). The data and information including the water quality components, key influencing factors such as tidal regime, season, local eco-social information is used for these equations to "fill up" the missing monitoring data at observation positions in the period 2012-2021.

Methodology:

The study area is the urban inner canal Nhu Loc Thi Nghe (NLTN) in Ho Chi Minh City with monitoring points on the main stream namely Cau So 1, Cau Le Van Si, Chua Hai Duc, Cau Dien Bien Phu and Cau Thi Nghe 2. The remaining positions belong to the branches of the canal such as: Cau Bui Huu Nghia, Cau Van Thanh; Cau Van Thanh 2, Cau Do and Cau Bui Dinh Tuy (implement from 2022). Location of NLTN canal and monitoring positions see **Figure 1**.

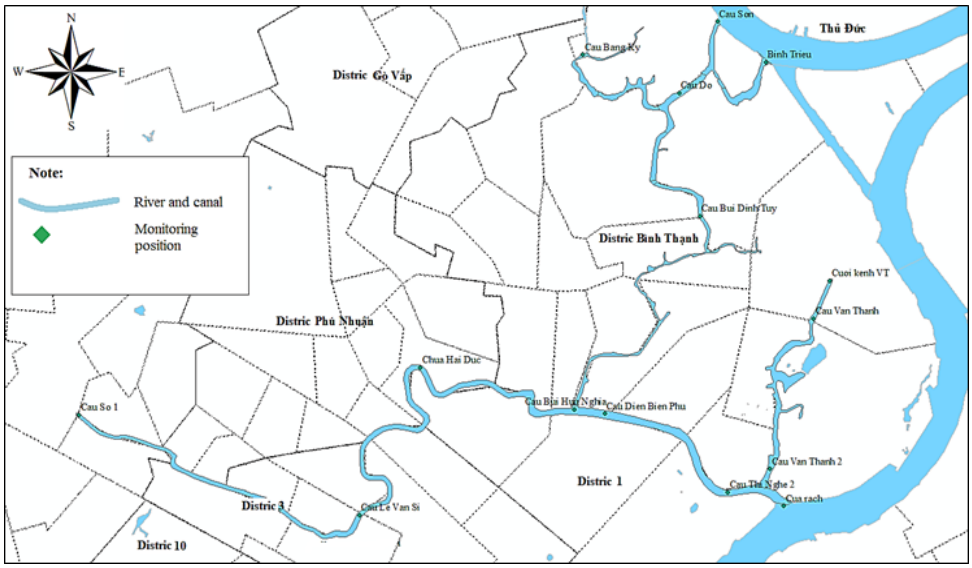

Figure 1.
The locations of monitoring positions of water quality on NLTN canal

The research approach "fills up" the monitoring water quality data set of inner canal which has the missing or non-existent values in the period 2012 – 2021, as shown below in **Figure 2**.

Selection of the base-years and base-positions.

Determining the base-positions and *filling-positions* needing to fill up the water quality components at NLTN canal. The results are summarized in the below tables of the water quality data set in the period 2012-2021.

Based on the above **Table 2**, the positions implementing the most continuously monitoring in the period 2012-2021 include Cau So 1, Cau Le Van Si, Chua Hai Duc, Cau Dien Bien Phu and Cau Thi Nghe 2 with the continuous period from 2014 to 2019 and 2021.

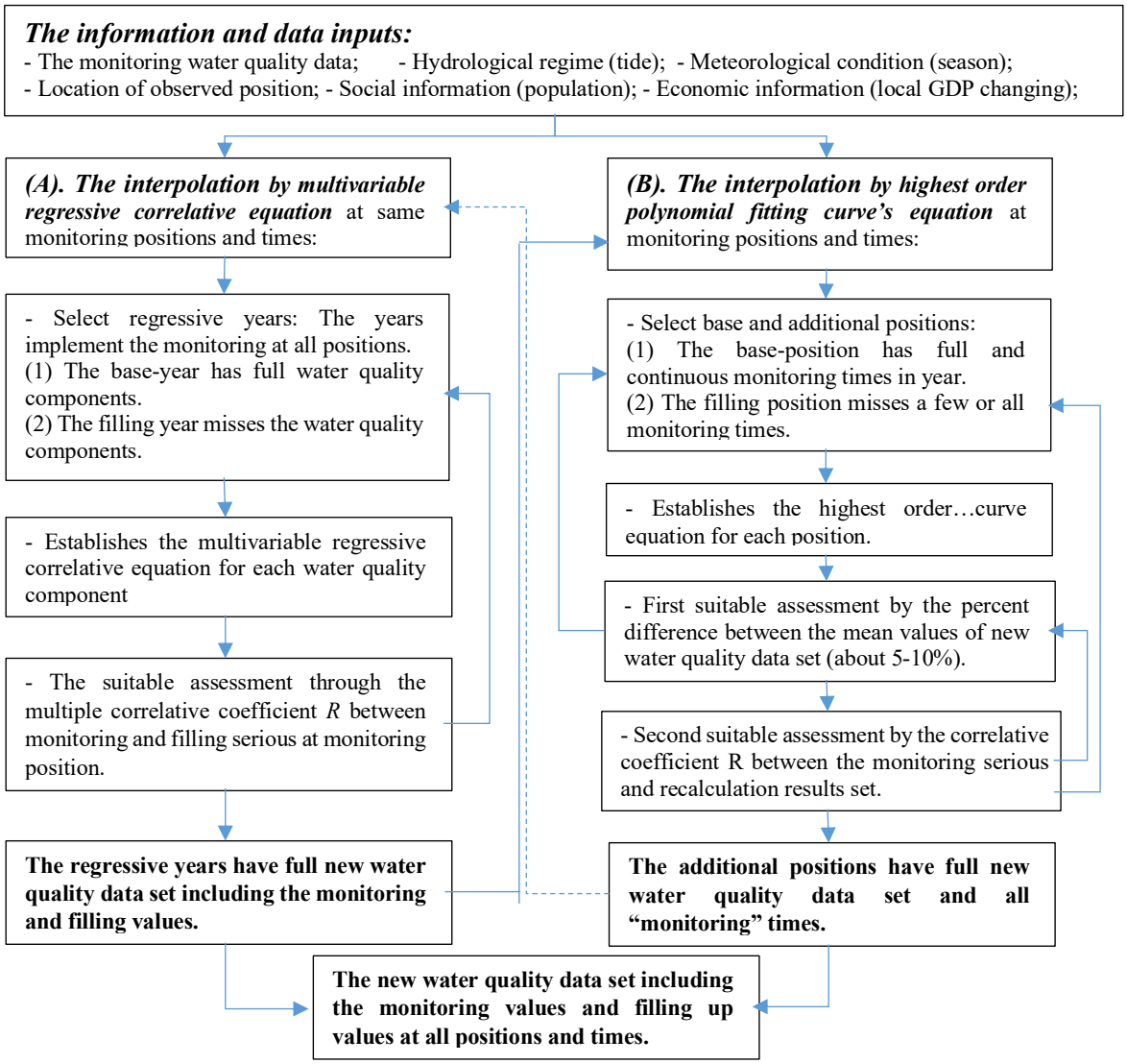

Figure 2.
Approach diagram in the study "filling up" the water quality monitoring data set

Table 2.
The monitoring positions have the implementing observation in the period 2012-2021

Position / Year	Cau So 1	Cau Le Van Si	Chua Hai Duc	Cau Dien Bien Phu	Cau Thi Nghe 2
2012		x		x	
2013		x		x	
2014	x	x	x	x	x
2015	x	x	x	x	x
2016	x	x	x	x	x
2017	x	x	x	x	x
2018	x	x	x	x	x
2019	x	x	x	x	x
2020				x	
2021		x	x	x	x

Determination of the monitoring years that needs to fit up the value of water quality according to the monitoring times. For example, at the Cau Dien Bien Phu position, the monitoring times implement the monitoring in years as follows:

Table 3.
The months have the observation at Cau Dien Bien Phu in the period 2012-2021

Years \ Months	January	February	March	April	May	June	July	Aug.	Sept.	Oct.	Nov.	Dec.
2012		x		x					x		x	
2013		x		x					x		x	
2014	x	x	x		x		x		x		x	
2015	x	x	x	x	x	x	x	x	x	x	x	x
2016				x	x	x	x	x	x	x	x	x
2017	x	x	x	x	x	x	x	x	x	x	x	x
2018	x	x	x	x	x				x	x	x	x
2019						x	x	x	x	x	x	x
2020	x	x	x	x	x							
2021	x	x	x	x	x							

Thus, in order to determine the monitoring base-years and base-positions for the interpolating water quality components at other monitoring positions and in monitoring years, it should be necessary to combine and compare the contents of **Table 2** and similar tables to **Table 3**. Through the comparison, the research has selected the monitoring base-positions and base-year for NLTN canal as follows:

- The monitoring base-positions: Cau Le Van Si; Cau Dien Bien Phu;
- The monitoring filling-positions filled up the water quality components by the interpolation of multivariable regression correlation equation: (1) Main stream: Cau So 1, Chua Hai Duc, Cau Thi Nghe 2; (2) branch lines: Cau Bui Huu Nghia, Cau Van Thanh, Cau Van Thanh 2, Cau Son and canal outlets;
- The monitoring base-years and the filling-years that need to be filled up through the interpolation of multivariable regression correlation equation: 2014-2019 (base-years) and the remaining monitoring years in the period 2012-2021 (filling-years).
- The monitoring basic-years and filling-years that need to be filled up through the interpolation of the higher-order polynomial fitting curve equation include 2015, 2017 (base-years) and the remaining monitoring years in the period 2012-2021 (filling-years).

The two interpolating methods are normally applied in the research (See **Figure 2**) in order steps by the first being MrCEq and the second being HopCEq.

The Multivariable Regression Correlative Equation (MrCEq) is applied in the research as:

$$Y_j = f\left(\sum_{i=1}^{n} y_i, Season, tide, q_{xa\ thai}, GDP_{changing}\right) \quad (1)$$

Where are:

Y_j is the calculating water quality at the monitoring position and in the monitoring time of the monitoring year (j);

y_i is the monitoring water quality implemented in year (i) at the same monitoring position and in the same monitoring time of year (j);

Season is the seasonal information (1-dry, 2-rain);

Tide is the tidal information (1-highest; 2-lowest);

$q_{waste\ discharge}$ is the waste discharge near the monitoring position;

$GDP_{changing.}$ is the local economical information;

The information (season, tide, $q_{wast\ discharge}$, and $GDP_{changing}$) corresponds to the natural (flow regime) and eco-social conditions in Ho Chi Minh City.

To assess the suitability, the study uses a part of the monitoring data series with full water quality components to analyze the correlative regression with the "re-calculation" results through the above multivariable regression correlative equation (MrCEq).

The Highest order polynomial fitting Curve Equation (HopCEq) is applied in the study as:

$$Y_{i,j} = A_{i,o} + \sum_{k=1}^{9} A_{i,k} T^k \quad (2)$$

Where are:

$Y_{i,j}$ is the water quality component needs to fill up at monitoring position and time (j) in year (i);

T is the monitoring time in year.

$A_{i,o}$, $A_{i,k}$ is the HopCEq's coefficients in year (i). These coefficients are interpolated by IDW method from the corresponding coefficients at same positions, in base-years and years filled up (i-1, i+1,...).

Evaluation on the suitable levels of the results of the HopCEq, it is by step (1) the degree of difference between the meaning values of the new data series and the value calculated according to the monitoring series at the base-positions. Usually, this difference fluctuates in the range of 5% - 10%; Step (2) through the correlation coefficient (R) between the real observed data and the resulting series is determined by the HopCEq at a base-position.

The assessment of self-cleaning capacity (SCC) of NLTN water in the period 2012-2021 is a task of our research. Based on the water quality data set of NLTN canal observed in the period 2012-2021, the research analyzed and filled up the missing values and components to make the suitable data set by time and space. The water quality data sets being original and filled up which are used to assess the quality and self-cleaning capacity.

Assessment of self-cleaning capacity of water body is usually based on the assessment of variations of the pollutants' concentrations (Nuruzzaman, 2018). There are many approaches to assess the self-cleaning capacity of water corresponding to each water quality parameters such as BOD_5 (the organic oxidation process), DO – dissolced oxy (the degradating process of dissolved oxy). The research applied the degradating process of dissolved oxy and the corresponding simulating equation is the Streeter-Phelpse equation.

The Streeter-Phelpse equation applied to our research is:

$$D_t = \frac{k_1.L_0}{k_2 - k_1}\left(e^{-k_1.t} - e^{-k_2.t}\right) + \frac{k_3.N_0}{k_2 - k_3}\left(e^{-k_3.t} - e^{-k_2.t}\right) + \frac{SOD}{k_2 H}\left(1 - e^{-k_2.t}\right) + D_0\, e^{-k_2.t} \quad (3)$$

Where are:

k_1 is the coefficient of oxygen decomposition due to BOD_5 and calculated

$$k_1 = k_{1,T(20)}\, x\, f(T) \quad (4)$$

k_2 is the coefficient of oxygen permeation into water and calculated

$$k_2 = k_{2,T(20)}\, x\, f(T) \quad (5)$$

k_3 is the coefficient of oxygen decomposition due to NH_4 and calculated

$$k_3 = k_{3,T(20)}\, x\, f(T) \quad (6)$$

$k_{1,T(20)}$, $k_{2,T(20)}$ and $k_{3,T(20)}$ the experiment numbers/functions on the decomposition and permeation processes are determined in the laboratory at 20°C. Our research inherited some experiment function from the national and abroad relevant researches such as Hydroscience (1971), Langbein (1967) and Thomann (1987).

U and *H* is flow velocity and depth. They are simulated by the MIKE11 for the inner canal system.

D_t – the level of oxygen declination in flow;

L_o, N_o, D_o, SOD the initial values of components BOD_5; NH_4; Oxy and sediment oxygen demand (Wei-Bo Chen, 2012).

The formula applied to assess the self-cleaning capacity for NLTN canal on the period 2012-2021 (Trinh, 2004):

$$f = k_2 / k_1 \quad (7)$$

Where are:

f – the rate between the coefficients of oxygen decomposition and permeation processes. The classification of water SCC is (i) Weak ($f<2$), (ii) Normal ($2<f<4$), (iii) Good ($4<f<10$) and (iv) Very good ($f>10$) (Trinh, 2004).

Results and Discussion:

According to the approach in the "filling up" water quality monitoring data of the NLTN canal in the period 2012-2021, the calculation of interpolation in the method (A) or (B) has also the checking suitability by the correlation level between calculated results and observed data over the years. Through the analysis of regressive correlation in period 2014 - 2019, the multivariable regressive correlation coefficients (R) of water quality component observed at all monitoring positions on NLTN canal are summarized in the below **Table 4**.

Table 4.
The multivariable correlative coefficients (R) at the monitoring positions

Position / Parameter	Cau So 1	Chua Hai Duc	Cau Thi Nghe 2	Cau Le Van Si	Cau Dien Bien Phu
pH	0.60	0.94	0.87	0.91	0.94
TSS	0.66	0.87	0.75	0.86	0.82
Turbidity	0.80	0.85	0.74	0.87	0.85
NH4	0.58	0.75	0.73	0.72	0.78
PO4	0.55	*0.27*	*0.46*	*0.40*	*0.48*
DO	0.64	0.93	0.85	0.89	0.91
COD	0.55	0.83	0.56	0.80	0.72
BOD5	*0.49*	0.76	0.58	0.72	0.68
Coliform	0.87	*0.34*	0.73	*0.29*	0.73
E. Coli	0.94	0.71	0.96	0.70	0.97

(Note: the red values correspond to the medium close)

Table 4 shows that the multivariate correlation coefficient mostly has a value greater than 0.5. So, the relationship is corresponding to the good close. Particularly, the positions of Cau Le Van Si and Cau Dien Bien Phu have the high values of correlation coefficient between the recalculated water quality results (according to the adjacent positions) with the observed data corresponding to quite good close degree.

The checking suitability of application HopCEq to interpolate the water quality values lacked, the research used the observed and recalculated water quality values (example BOD_5) at Cau Dien Bien Phu position. The correlative coefficient R between two above sets is very high and can see in the below in **Figure 3**.

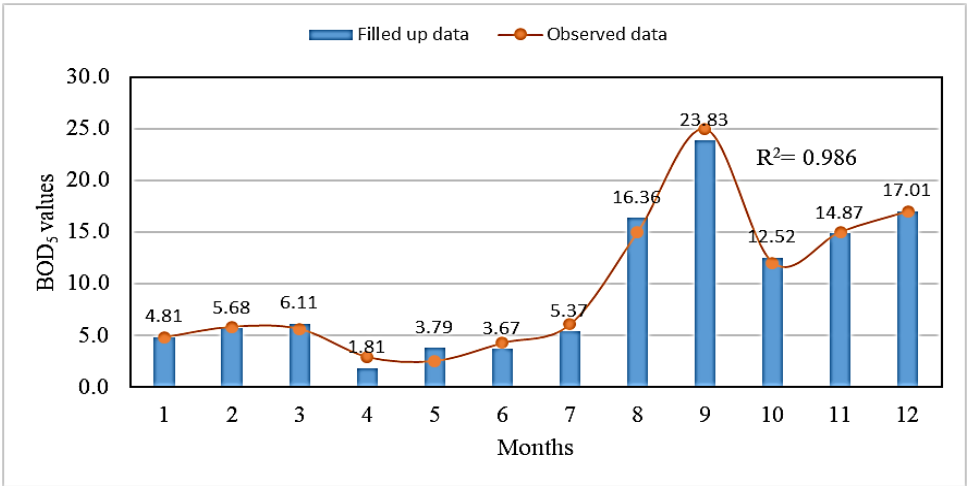

Figure 3.
The observed and filled up data sets of BOD_5 at Cau Dien Bien Phu position

The interpolation by multivariable regressive correlative equation (MrCEq)**.** Through the multivariable regression correlative analysis, the multivariable regression correlative equation (1) has significant variables (coefficients of variables greater than 0.01) including the water quality components at the base-positions (Cau Le Van Si and Cau Dien Bien Phu), information on tidal regime (high tides, low tides) and seasons (rainy, dry).

The MrCEq using to interpolate the water quality components on the period 2014-2019, 2021 is formula as:

$$Y_j = A_{tide}\, Tr. + A_{season}\, Season + A_{LeVanSi}\, y_{LeVanSi} + A_{DienBienPhu}\, y_{DienBienPhu} + A_o \qquad (8)$$

Based on the water quality data set observed on the period 2014-2019, 2021, the MrCEq's coefficients are determined by the regressive analysis method for each water quality component and each filling-position. The MrCEq' coefficient set is summarized in the below **Table 5** (Example for the Chua Hai Duc position).

Table 5.
The MrCEq's coefficient set of each water quality component at Chua Hai Duc position.

Coeff. / Water quality	A_{tide}	A_{season}	$A_{LeVanSi}$	$A_{DienBienPhu}$	A_o
pH	-0.01	0.06	0.56	0.42	0.04
TSS	-0.87	-4.86	0.38	0.58	9.01
Turbidity	2.18	2.94	0.60	0.38	-6.98
NH4	-0.59	-0.99	0.61	0.39	2.58
PO4	-0.01	0.06	0.56	-0.03	-0.02
DO	0.00	0.06	0.51	0.42	0.10
COD	0.41	-0.71	0.53	0.58	-2.74
BOD5	0.44	-0.92	0.54	0.55	-0.79
Coliform	-7095.39	55824.10	0.14	0.12	-7058.90
E. Coli	7364.43	-3922.20	0.18	0.47	-4378.61

Interpolation through high-order polynomial fitting curve equation (HopCEq). The HopCEq with 9th order applied to determine/interpolate the water quality component at a monitoring position and in a monitoring year has the following formula:

$$Y_{i,j} = A_{o,j}+A_{1,j}\,T+A_{2,j}\,T^2+A_{3,j}\,T^3+A_{4,j}\,T^4+A_{5,j}\,T^5+A_{6,j}\,T^6+A_{7,j}\,T^7+A_{8,j}\,T^8+A_{9,j}\,T^9 \qquad (9)$$

Where are: T is the monitoring time in year (month/time); The HopCEq's coefficient sets for the water quality components in two base-years 2015 and 2017 determined by the observed data set at the base-positions are summarized in the below Table 6 (Example for BOD_5 and COD at the Cau Dien Bien Phu position).

Table 6.
The HopCEq's coefficients for BOD_5, COD at Cau Dien Bien Phu position in 2015

WQ	COD				BOD_5			
Tide	Lowest		Highest		Lowest		Highest	
Year	2015	2017	2015	2017	2015	2017	2015	2017
A_9	-4.7E-04	-3.7E-04	-4.57E-04	-2.70E-04	-2.7E-04	-2.2E-04	-4.42E-04	-1.45E-04
A_8	2.7E-02	2.1E-02	2.60E-02	1.54E-02	1.6E-02	1.3E-02	2.54E-02	8.35E-03
A_7	-6.6E-01	-5.0E-01	-6.26E-01	-3.70E-01	-3.8E-01	-3.1E-01	-6.23E-01	-2.04E-01
A_6	8.8E+00	6.6E+00	8.37E+00	4.91E+00	5.0E+00	4.2E+00	8.49E+00	2.75E+00
A_5	-7.2E+01	-5.2E+01	-6.80E+01	-3.93E+01	-4.1E+01	-3.5E+01	-7.04E+01	-2.24E+01
A_4	3.6E+02	2.5E+02	3.45E+02	1.94E+02	2.1E+02	1.8E+02	3.66E+02	1.13E+02
A_3	-1.1E+03	-7.4E+02	-1.08E+03	-5.85E+02	-6.6E+02	-5.6E+02	-1.18E+03	-3.47E+02
A_2	2.1E+03	1.2E+03	1.99E+03	1.02E+03	1.2E+03	1.0E+03	2.24E+03	6.20E+02
A_1	-2.0E+03	-1.0E+03	-1.93E+03	-9.07E+02	-1.2E+03	-9.6E+02	-2.24E+03	-5.69E+02
A_0	7.5E+02	3.4E+02	7.45E+02	3.21E+02	4.6E+02	3.5E+02	8.78E+02	2.06E+02

The HopCEq's coefficients set of the remaining years in the period 2012-2021 are determined through IDW interpolation. Using the HopCEq with coefficient sets to calculate the missing water quality components of the monitoring data set in the period 2012-2021. For example, the data of water quality compositions is filled up at Cau Dien Bien Phu position in 2012 summarized on below table:

Table 7.
The water quality data filled up at Cau Dien Bien Phu in 2012

Year	Condition		T°C	pH	TSS	NH4	PO4	DO	COD	BOD5	Coliform	E.Coli
	Month	Tide	()	()	mg/l	mg/l	mg/l	mg/l	mg/l	MPN/100ml	mg/l	MPN/100ml
2012	01	Low	*26.4*	*7.71*	*137.3*	*4.05*	*0.02*	*3.36*	*13.4*	*8.5*	*13003*	*1483*
	02	Low	26.8	6.94	106	13.14	0.189	*1.49*	193.3	100.0	4600000	430000
	03	Low	*29.0*	*7.56*	*104.3*	*0.23*	*0.05*	*3.31*	*23.7*	*35.4*	*66801*	*63276*
	04	Low	29.9	7.03	86	8.91	0.832	*3.20*	91.6	15.1	4600000	930000
	05	Low	*30.7*	*8.30*	*112.5*	*2.25*	*0.06*	*2.73*	*26.2*	*29.7*	*12863*	*0*
	06	Low	*29.2*	*8.42*	*102.3*	*3.74*	*0.05*	*3.01*	*23.1*	*28.1*	*98177*	*205230*
	07	Low	*28.9*	*6.84*	*28.00*	*6.14*	*0.06*	*4.95*	*14.6*	*16.3*	*187187*	*449018*
	08	Low	*29.0*	*3.89*	*2.65*	*13.27*	*0.00*	*5.52*	*27.7*	*10.5*	*168194*	*272217*
	09	Low	28.6	6.76	55	10.95	1.168	*1.44*	73.4	37.0	930000	40000
	10	Low	*28.7*	*6.80*	*16.25*	*0.64*	*0.18*	*3.96*	*19.5*	*3.8*	*100395*	*452077*
	11	Low	29.1	7.04	48	9.07	0.899	*5.84*	60.4	29.9	430000	90000
	12	Low	*28.6*	*6.25*	*26.12*	*20.92*	*0.20*	*5.29*	*36.3*	*15.9*	*68980*	*26560*

(Note: the inclining values are filled up)

After the filling up values of water quality components at all missing positions on the period 2012-2021, the analysis and assessment of water quality according to VN-WQI index and self-cleaning capacity of water canal are advantage and show the trends of fluctuations in time and space.

When calculating the water quality of the NLTN canal according to VN-WQI index (according to Decision No. 1460 of the Ministry of Natural Resources and Environment), the results show that the VN-WQI value increases gradually from the end to outlet of the canal (the estuary of the NLTN canal) (See **Figure 4**).

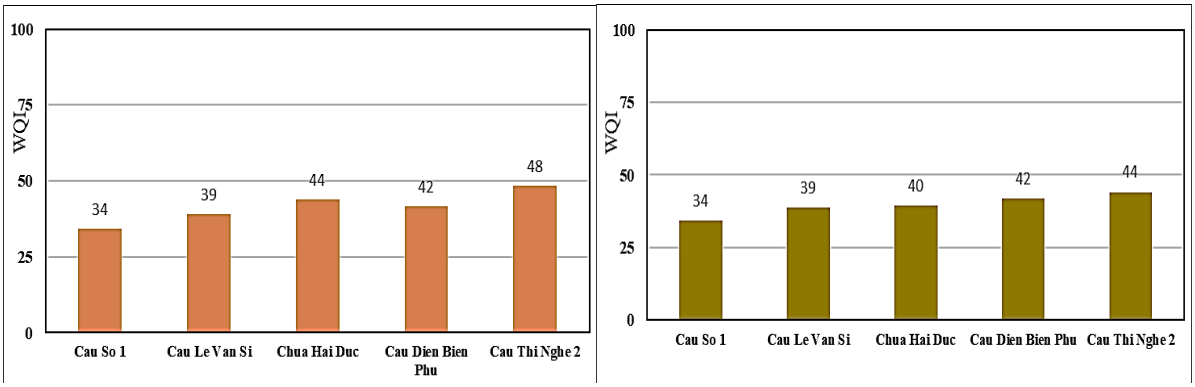

Figure 4.
The distribution of VN-WQI values along NLTN canal when use the original (left side) and filling up (right side) data sets.

Similar to the assessment of VN-WQI, the assessment of self-cleaning capacity also shows the appropriateness of the data set after "filling up".

Figure 5 shows that, in 2021, at the Cau Dien Bien Phu position only observed in 3 months/12 months, the year-average value (f) reached (3.2). When the water quality data set used to assess is original. There are only three months having the observations in 2021. So, the values of self-cleaning capacity are only three numbers. The representativeness of the self-cleaning calculation results for the NLTN canal is quite weak for 2021.

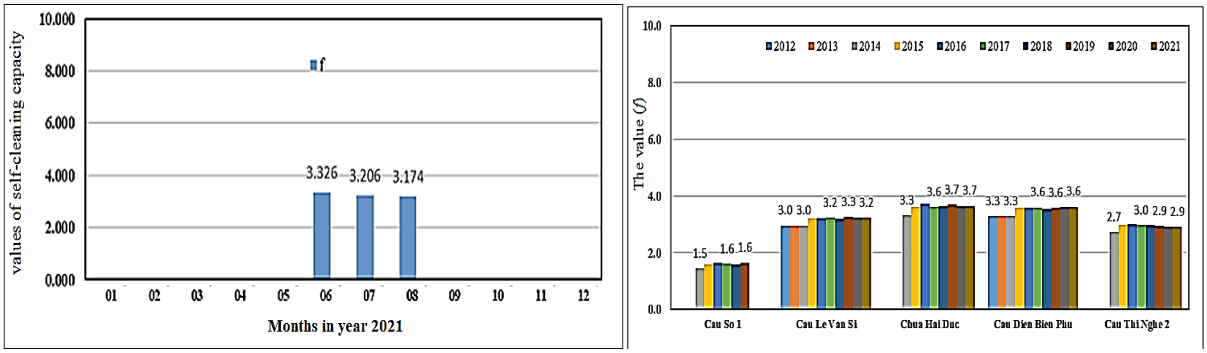

Figure 5.
The rate (f) values are at Cau Dien Bien Phu in 2021 and for all canal (the original data set)

Figure 6 shows that, in 2021, at the Cau Dien Bien Phu position, the *f*-value is distributed over all months and represents the variation in water quality of the canal (the self-cleaning capacity's value low is usually the beginning of the dry and rainy seasons) and the year-average value (*f*) is high (3.3). When the water quality data set used to assess is filled up.

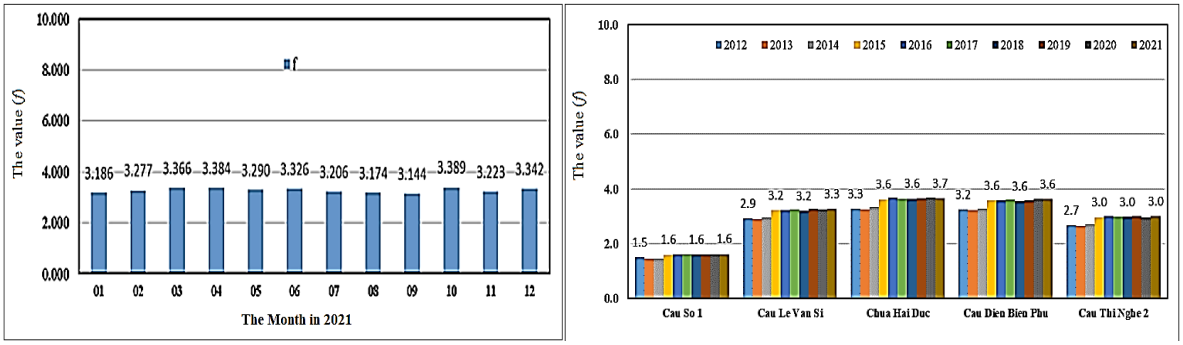

Figure 6.

The rate (*f*) values are at Cau Dien Bien Phu in 2021 and for all canal (the data set filled up)

Based on the results of analysis and assessment of the self-cleaning capacity of NLTN canal in the period 2012-2021, using the ARGIS software tool to map the zoning of the canal's water self-cleaning capacity level (See the map below).

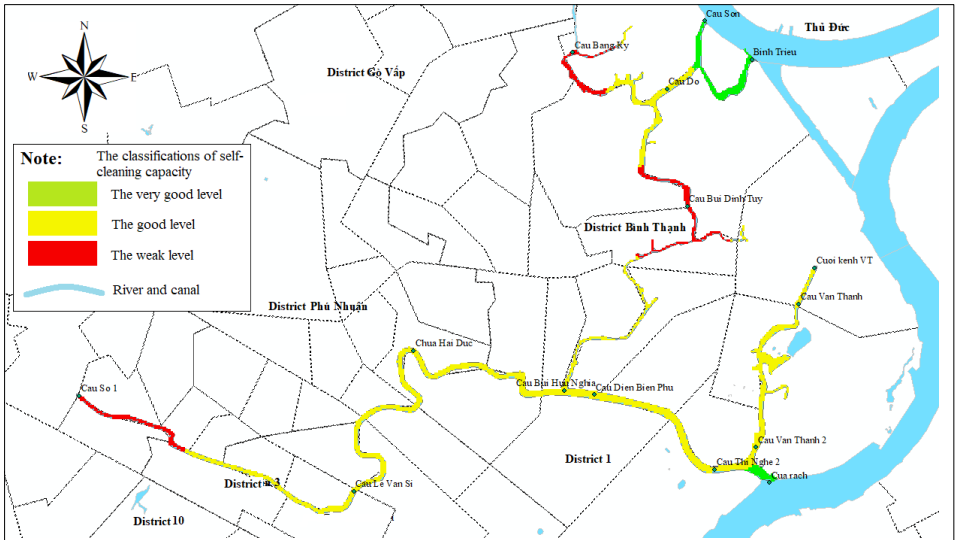

Figure 7.

The zoning map of self-cleaning capacity of NLTN canal in the period 2012-2021

Conclusion:

With the application of multivariable regression correlative equation (MrCEq) and high-order polynomial fitting curve equation (HopCEq) in alternately interpolating water quality components of Nhieu Loc Thi Nghe canal for all monitoring positions missing data in the period 2012-2021 shows that, the correlation coefficients (R) are quite high (above 0.5) corresponding to good close relationship. Besides, the application of the above two functions/equations is quite easy and convenient in the calculation process because there is no "black box" as in many AI models being applied in many researches.

After the monitoring data set of water quality components was added and filled up all the gaps of values, it showed the continuity, the representativeness and showed the trend of quality "variation" in space and time over the monitoring year and phase. This leads to more information for researchers and managers in making judgments and decisions. Through the calculation of water quality according to VN-WQI index and self-cleaning capacity of Nhieu

Loc Thi Nghe canal water in the period 2012-2021, the application of interpolation method on fitting up values for the water quality data to assess and analyze is workable and easily disseminated.

However, the calculation shows that some water quality components have low correlation coefficient (R), so further research and adjustment is needed.

Acknowledgements.
The article is implemented with results from the research "Survey, assessment of water quality and self-cleaning capability, built an automatic water quality forecast system and proposed solutions for control of water quality management".

References:

1. Hunter JM, Maier HR, Gibbs MS, Foale ER, Grosvenor NA, Harders NP and Kikuchi-Miller T. C. (2018). Framework for developing hybrid process-driven, artificial neural network and regression models for salinity prediction in river systems. Hydrology and Earth System Sciences. 2018;22(5):2987-3006. https://doi.org/10.5194/hess-22-2987-2018.
2. Hydroscience, Inc., (1971). Simplified Mathematical Modeling of Water Quality, EPA-Water Programs.
3. Langbein, W.B., and W.H. Durum. (1967). The Aeration Capacity of Streams. U. S. Geological Survey Circular S42.
4. Le XH, Ho HV, Lee G and Jung S., (2019). Application of long short-term memory (LSTM) neural network for flood forecasting. Water. 2019;11(7):1387. https://doi.org/10.3390/w11071387.
5. Lin K, Lu P, Xu CY, Yu X, Lan T and Chen X. (2019). Modeling saltwater intrusion using an integrated Bayesian model averaging method in the Pearl River Delta. Journal of Hydro informatics. 2019; 21(6):1147-1162. https://doi.org/10.2166/hydro.2019.073.
6. Nuruzzaman Md., Al-Mamun A. and Salleh N. B., (2018). Experimenting biochemical oxygen demand decay rates of Malaysian river water in a laboratory flume. Environ. Eng. Res. 2018; 23(1). P.99-106.
7. Palani S, Liong SY and Tkalich P., (2008). An ANN application for water quality forecasting. Marine Pollution Bulletin. 2008;56(9):1586-1597. https://doi.org/10.1016/j.marpolbul.2008.05.021.
8. Ross AC and Stock CA., (2019). An assessment of the predictability of column minimum dissolved oxygen concentrations in Chesapeake Bay using a machine learning model. Estuarine, Coastal and Shelf Science. 2019;221:53-65. https://doi.org/10.1016/j.ecss.2019.03.007.
9. Thomann R. V. and Mueller J. A., (1987), Principles of Surface Water Quality Modeling and Control, Harper International Edition, New York.
10. Trinh L. and Hung N. Q., (2004). Environment in Dong Nai - Sai Gon River Basin, Science and technology Publisher, 2004.
11. Wei-Bo Chen, Wen-Cheng Liu and Li-Ting Huang, (2012). Measurement of sediment oxygen demand for modeling the dissolved oxygen distribution in a Subalpine lake, International Journal of Physical Sciences, 2012, 7 (27), 5036-5048.

THE EQUITABLE CHROMATIC NUMBERS OF CARTESIAN PRODUCTS OF SOME GRAPHS

Annob Jobpan,* Kittikorn Nakprasit

Department of Mathematics, Faculty of Science, Khon Kaen University, Khon Kaen, Thailand

*e−mail: annobjo@kkumail.com

Abstract :

A graph G is *equitably k-colorable* if its vertex set can be partitioned into independent sets $V_1, V_2, \ldots, V_k$ such that for any $i \neq j$, $||V_i| - |V_j|| \leq 1$. The *equitable chromatic number* of G, denoted by $\chi_=(G)$, is the smallest positive integer k such that G is equitably k-colorable. The *Cartesian product* of graphs $G_1(V_1, E_1)$ and $G_2(V_2, E_2)$ denoted by $G_1 \square G_2$, has the vertex set $\{(u,v) \mid u \in V_1 \text{ and } v \in V_2\}$ and $\{(u,x),(v,y)\}$ is an edge if and only if $u = v$ and $xy \in E_2$ or $x = y$ and $uv \in E_1$. In this paper, we obtain the equitable chromatic numbers of Cartesian products of the graphs as follows:

$\chi_=(K_{1,1,1,1} \square K_{1,3}) = 4$, $\chi_=(K_{\underbrace{1,1,\ldots,1}_{m}} \square K_{1,n}) = m$, $\chi_=(K_{m,m,m} \square K_{1,n}) = 3$,

$\chi_=(K_{\underbrace{m,m,\ldots,m}_{r}} \square K_{1,n}) = r$, $\chi_=(K_{\underbrace{1,1,\ldots,1}_{m}} \square K_{s,t}) = m$, $\chi_=(K_{\underbrace{m,m,\ldots,m}_{r}} \square K_{s,t}) = r$,

$\chi_=(K_{\underbrace{m,m,\ldots,m}_{n}} \square K_{r,s,t}) = n$ and $\chi_=(K_{\underbrace{m,m,\ldots,m}_{r}} \square K_{n_1,n_2,\ldots,n_k}) = r$.

Introduction :

Throughout this paper, graphs are finite undirected graphs without loops and without multiple edges. If $G = (V(G), E(G))$ or $G = (V, E)$ is a graph, $V(G)$ and $E(G)$ are denoted as its vertex set and edge set, respectively.

A graph G is *k-colorable* if its vertex set can be partitioned into independent sets $V_1, V_2, \ldots, V_k$. The *chromatic number* of G, denoted by $\chi(G)$, is the smallest positive integer k such that G is k-colorable.

A graph G is *equitably k-colorable* if its vertex set can be partitioned into independent sets $V_1, V_2, \ldots, V_k$ such that for any $i \neq j$, $||V_i| - |V_j|| \leq 1$. The *equitable chromatic number* of G, denoted by $\chi_=(G)$, is the smallest positive integer k such that G is equitably k-colorable. The *Cartesian product* of graphs $G_1(V_1, E_1)$ and $G_2(V_2, E_2)$ denoted by $G_1 \square G_2$, has the vertex set $\{(u,v) \mid u \in V_1 \text{ and } v \in V_2\}$ and $\{(u,x),(v,y)\}$ is an edge if and only if $u = v$ and $xy \in E_2$ or $x = y$ and $uv \in E_1$.

In 1998, Chen et al. [1] studied the equitable chromatic numbers of Cartesian products of paths, cycles, hypercubes and complete graphs. In 2006, Furmańczyk [2] studied in Cartesian products of bipartite graphs and r-partite graphs. And in 2012, Lin and Chang [3] studied the equitable chromatic numbers of Cartesian products of complete bipartite graphs.

In this paper, we obtain the equitable chromatic numbers of Cartesian products of the graphs as follows:

$\chi_=(K_{1,1,1,1} \square K_{1,3}) = 4$, $\chi_=(K_{\underbrace{1,1,\ldots,1}_{m}} \square K_{1,n}) = m$, $\chi_=(K_{m,m,m} \square K_{1,n}) = 3$,

$\chi_=(K_{\underbrace{m,m,\ldots,m}_{r}} \square K_{1,n}) = r$, $\chi_=(K_{\underbrace{1,1,\ldots,1}_{m}} \square K_{s,t}) = m$, $\chi_=(K_{\underbrace{m,m,\ldots,m}_{r}} \square K_{s,t}) = r$,

$\chi_=(K_{\underbrace{m,m,\ldots,m}_{n}}\Box K_{r,s,t}) = n$ and $\chi_=(K_{\underbrace{m,m,\ldots,m}_{r}}\Box K_{n_1,n_2,\ldots,n_k}) = r$.

Results :

Theorem 1. $\chi_=(K_{1,1,1,1}\Box K_{1,3}) = 4$.

Proof Let $G_1(V_1,E_1) = K_{1,1,1,1}$ and $G_2(V_2,E_2) = K_{1,3}$,
$V(G_1) = \{u_i : 1 \le i \le 4\}$,
$E(G_1) = \{u_iu_k : 1 \le i < k \le 4\}$,
$V(G_2) = \{v_j : 1 \le j \le 4\}$,
$E(G_2) = \{v_1v_l : 2 \le l \le 4\}$.
Let $V(G_1\Box G_2) = \{(u_iv_j) : u_i \in V(G_1), v_j \in V(G_2)\}$ and
$E(G_1\Box G_2) = \{(u_iv_j)(u_sv_t) : i = s$ and $v_jv_t \in E(G_2)$ or $j = t$ and $u_iu_s \in E(G_1)\}$.
Let $c(u_iv_1) = i+1 \pmod 4$, where $1 \le i \le 4$ and $c(u_iv_j) = i$, where $1 \le i \le 4, 2 \le j \le 4$.
For $1 \le i \le 4$, let V_i be denoted as the set of vertices with a color i.
Then

$$V_1 = \{(u_4v_1),(u_1v_2),(u_1v_3),(u_1v_4)\},$$
$$V_2 = \{(u_1v_1),(u_2v_2),(u_2v_3),(u_2v_4)\},$$
$$V_3 = \{(u_2v_1),(u_3v_2),(u_3v_3),(u_3v_4)\},$$
$$V_4 = \{(u_3v_1),(u_4v_2),(u_4v_3),(u_4v_4)\}.$$

It follows that $|V_1| = |V_2| = |V_3| = |V_4| = 4$.

Consider each edge $\{(u_iv_j)(u_sv_t)\}$ as follows:
Case 1 : $u_i = u_s$. It follows that v_j or $v_t = v_1$.
Without loss of generality, let $v_t = v_1$.
Then $c(u_iv_j) = i$ and $c(u_sv_t) = c(u_iv_1) = i+1$.
Hence u_iv_j and u_sv_t have different colors.
Case 2 : $v_j = v_t$. It follows that $u_i \ne u_s$ for some $i,s \in \{1,2,3,4\}$, $i \ne s$.
Case 2.1 : $j \ne 1$. Then $c(u_iv_j) = i$ and $c(u_sv_t) = c(u_sv_j) = s$ for some $i,s \in \{1,2,3,4\}$ such that $i \ne s$.
Hence u_iv_j and u_sv_t have different colors.
Case 2.2 : $j = 1$. Then $c(u_iv_j) = c(u_iv_1) = i+1$ and $c(u_sv_t) = c(u_sv_j) = c(u_sv_1) = s+1$ for some $i,s \in \{1,2,3,4\}$ such that $i \ne s$.
Hence u_iv_j and u_sv_t have different colors.
Therefore, $K_{1,1,1,1}\Box K_{1,3}$ is equitably 4-colorable.
Since $K_{1,1,1,1}$ is a complete graph of order 4, the equitable chromatic number of $K_{1,1,1,1}\Box K_{1,3}$ equals 4.
Hence $\chi_=(K_{1,1,1,1}\Box K_{1,3}) = 4$. □

Theorem 2. Let m,n be positive integers and $m \ge 2$. Then $\chi_=(K_{\underbrace{1,1,\ldots,1}_{m}}\Box K_{1,n}) = m$.

Proof Let $G_1(V_1,E_1) = K_{\underbrace{1,1,\ldots,1}_{m}}$ and $G_2(V_2,E_2) = K_{1,n}$,

$V(G_1) = \{u_i : 1 \le i \le m\}$,

$E(G_1) = \{u_iu_k : 1 \le i < k \le m\}$,
$V(G_2) = \{v_j : 1 \le j \le n+1\}$,
$E(G_2) = \{v_1v_l : 2 \le l \le n+1\}$.
Let $V(G_1 \square G_2) = \{(u_iv_j) : u_i \in V(G_1), v_j \in V(G_2)\}$ and
$E(G_1 \square G_2) = \{(u_iv_j)(u_sv_t) : i = s \text{ and } v_jv_t \in E(G_2) \text{ or } j = t \text{ and } u_iu_s \in E(G_1)\}$.
Let $c(u_iv_1) = i+1 \pmod m$, where $1 \le i \le m$ and $c(u_iv_j) = i$,
where $1 \le i \le m, 2 \le j \le n+1$.
For $1 \le i \le m$, let V_i be denoted as the set of vertices with a color i.
Then

$$\begin{aligned} V_1 &= \{(u_mv_1), (u_1v_j) : 2 \le j \le n+1\}, \\ V_2 &= \{(u_1v_1), (u_2v_j) : 2 \le j \le n+1\}, \\ V_3 &= \{(u_2v_1), (u_3v_j) : 2 \le j \le n+1\}, \\ &\vdots \\ V_{m-1} &= \{(u_{m-2}v_1), (u_{m-1}v_j) : 2 \le j \le n+1\}, \\ V_m &= \{(u_{m-1}v_1), (u_mv_j) : 2 \le j \le n+1\}. \end{aligned}$$

It follows that $|V_1| = |V_2| = |V_3| = \cdots = |V_{m-1}| = |V_m| = n+1$.

Consider each edge $\{(u_iv_j)(u_sv_t)\}$ as follows:
Case 1 : $u_i = u_s$. It follows that v_j or $v_t = v_1$.
Without loss of generality, let $v_t = v_1$.
Then $c(u_iv_j) = i$ and $c(u_sv_t) = c(u_iv_1) = i+1$.
Hence u_iv_j and u_sv_t have different colors.
Case 2 : $v_j = v_t$. It follows that $u_i \ne u_s$ for some $i, s \in \{1, 2, \ldots, m\}$, $i \ne s$.
Case 2.1 : $j \ne 1$. Then $c(u_iv_j) = i$ and $c(u_sv_t) = c(u_sv_j) = s$
for some $i, s \in \{1, 2, \ldots, m\}$ such that $i \ne s$.
Hence u_iv_j and u_sv_t have different colors.
Case 2.2 : $j = 1$. Then $c(u_iv_j) = c(u_iv_1) = i+1$ and $c(u_sv_t) = c(u_sv_j) = c(u_sv_1) = s+1$.
for some $i, s \in \{1, 2, \ldots, m\}$ such that $i \ne s$.
Hence u_iv_j and u_sv_t have different colors.
Therefore, $K_{\underbrace{1,1,\ldots,1}_{m}} \square K_{1,n}$ is equitably m-colorable.
Since $K_{\underbrace{1,1,\ldots,1}_{m}}$ is a complete graph of order m, the equitable chromatic number
of $K_{\underbrace{1,1,\ldots,1}_{m}} \square K_{1,n}$ equals m. Hence $\chi_=(K_{\underbrace{1,1,\ldots,1}_{m}} \square K_{1,n}) = m$. □

Theorem 3. Let m, n be positive integers. Then $\chi_=(K_{m,m,m} \square K_{1,n}) = 3$.

Proof Let $G_1(V_1, E_1) = K_{m,m,m}$ and $G_2(V_2, E_2) = K_{1,n}$,
$V(G_1) = X_1 \cup X_2 \cup X_3$, where $X_1 = \{u_1, u_2, \ldots, u_m\}$, $X_2 = \{u_{m+1}, u_{m+2}, \ldots, u_{2m}\}$ and
$X_3 = \{u_{2m+1}, u_{2m+2}, \ldots, u_{3m}\}$,
$E(G_1) = \{ab : a \in X_i, b \in X_j, 1 \le i < j \le 3\}$,
$V(G_2) = \{v_j : 1 \le j \le n+1\}$,
$E(G_2) = \{v_1v_l : 2 \le l \le n+1\}$.
Let $V(G_1 \square G_2) = \{(u_iv_j) : u_i \in V(G_1), v_j \in V(G_2)\}$ and

$E(G_1 \square G_2) = \{(u_i v_j)(u_s v_t) : i = s \text{ and } v_j v_t \in E(G_2) \text{ or } j = t \text{ and } u_i u_s \in E(G_1)\}$.
Let $c(u_i v_1) = r$, where $u_i \in X_r, 1 \leq r \leq 3$ and
$c(u_i v_j) = r+1 \pmod 3$, where $u_i \in X_r, 1 \leq r \leq 3, 2 \leq j \leq n+1$.
For $1 \leq r \leq 3$, let V_r be denoted as the set of vertices with a color r.
Then

$$V_1 = \{(u_i v_1) : u_i \in X_1\} \cup \{(u_i v_j) : u_i \in X_3, 2 \leq j \leq n+1\},$$
$$V_2 = \{(u_i v_1) : u_i \in X_2\} \cup \{(u_i v_j) : u_i \in X_1, 2 \leq j \leq n+1\},$$
$$V_3 = \{(u_i v_1) : u_i \in X_3\} \cup \{(u_i v_j) : u_i \in X_2, 2 \leq j \leq n+1\}.$$

It follows that $|V_1| = |V_2| = |V_3| = m(n+1)$.

Consider each edge $\{(u_i v_j)(u_s v_t)\}$ as follows:
Case 1 : $u_i = u_s$. It follows that v_j or $v_t = v_1$.
Without loss of generality, let $v_t = v_1$.
Then $c(u_i v_j) = r+1$ and $c(u_s v_t) = c(u_i v_1) = r$.
Hence $u_i v_j$ and $u_s v_t$ have different colors.
Case 2 : $v_j = v_t$. It follows that $u_i \in X_{r_1}, u_s \in X_{r_2}$ for some $r_1, r_2 \in \{1,2,3\}$, $r_1 \neq r_2$.
Case 2.1 : $j \neq 1$. Then $c(u_i v_j) = r_1 + 1$ and $c(u_s v_t) = c(u_s v_j) = r_2 + 1$
for some $r_1, r_2 \in \{1,2,3\}$ such that $r_1 \neq r_2$.
Hence $u_i v_j$ and $u_s v_t$ have different colors.
Case 2.2 : $j = 1$. Then $c(u_i v_j) = c(u_i v_1) = r_1$ and $c(u_s v_t) = c(u_s v_j) = c(u_s v_1) = r_2$
for some $r_1, r_2 \in \{1,2,3\}$ such that $r_1 \neq r_2$.
Hence $u_i v_j$ and $u_s v_t$ have different colors.
Therefore, $K_{m,m,m} \square K_{1,n}$ is equitably 3-colorable.
Since $K_{m,m,m}$ is a complete tripartite graph, the equitable chromatic number of $K_{m,m,m} \square K_{1,n}$ equals 3.
Hence $\chi_=(K_{m,m,m} \square K_{1,n}) = 3$. □

Theorem 4. Let m, n and r be positive integers and $r \geq 2$.
Then $\chi_=(\underbrace{K_{m,m,\ldots,m}}_{r} \square K_{1,n}) = r$.

Proof Let $G_1(V_1, E_1) = \underbrace{K_{m,m,\ldots,m}}_{r}$ and $G_2(V_2, E_2) = K_{1,n}$,
$V(G_1) = X_1 \cup X_2 \cup \cdots \cup X_r$, where $X_1 = \{u_1, u_2, \ldots, u_m\}$, $X_2 = \{u_{m+1}, u_{m+2}, \ldots, u_{2m}\}, \ldots,$
$X_r = \{u_{(r-1)m+1}, u_{(r-1)m+2}, \ldots, u_{rm}\}$,
$E(G_1) = \{ab : a \in X_i, b \in X_j, 1 \leq i < j \leq r\}$,
$V(G_2) = \{v_j : 1 \leq j \leq n+1\}$,
$E(G_2) = \{v_1 v_l : 2 \leq l \leq n+1\}$.
Let $V(G_1 \square G_2) = \{(u_i v_j) : u_i \in V(G_1), v_j \in V(G_2)\}$ and
$E(G_1 \square G_2) = \{(u_i v_j)(u_s v_t) : i = s \text{ and } v_j v_t \in E(G_2) \text{ or } j = t \text{ and } u_i u_s \in E(G_1)\}$.
Let $c(u_i v_1) = k$, where $u_i \in X_k, 1 \leq k \leq r$ and
$c(u_i v_j) = k+1 \pmod r$, where $u_i \in X_k, 1 \leq k \leq r, 2 \leq j \leq n+1$.
For $1 \leq k \leq r$, let V_k be denoted as the set of vertices with a color k.

Then

$$\begin{aligned}
V_1 &= \{(u_iv_1) : u_i \in X_1\} \cup \{(u_iv_j) : u_i \in X_r, 2 \le j \le n+1\},\\
V_2 &= \{(u_iv_1) : u_i \in X_2\} \cup \{(u_iv_j) : u_i \in X_1, 2 \le j \le n+1\},\\
V_3 &= \{(u_iv_1) : u_i \in X_3\} \cup \{(u_iv_j) : u_i \in X_2, 2 \le j \le n+1\},\\
&\vdots\\
V_{r-1} &= \{(u_iv_1) : u_i \in X_{r-1}\} \cup \{(u_iv_j) : u_i \in X_{r-2}, 2 \le j \le n+1\},\\
V_r &= \{(u_iv_1) : u_i \in X_r\} \cup \{(u_iv_j) : u_i \in X_{r-1}, 2 \le j \le n+1\}.
\end{aligned}$$

It follows that $|V_1| = |V_2| = |V_3| = \cdots = |V_{r-1}| = |V_r| = m(n+1)$.

Consider each edge $\{(u_iv_j)(u_sv_t)\}$ as follows:
Case 1 : $u_i = u_s$. It follows that v_j or $v_t = v_1$.
Without loss of generality, let $v_t = v_1$.
Then $c(u_iv_j) = k+1$ and $c(u_sv_t) = c(u_iv_1) = k$.
Hence u_iv_j and u_sv_t have different colors.
Case 2 : $v_j = v_t$. It follows that $u_i \in X_{k_1}, u_s \in X_{k_2}$ for some $k_1, k_2 \in \{1,2,\ldots,r\}$, $k_1 \ne k_2$.
Case 2.1 : $j \ne 1$. Then $c(u_iv_j) = k_1 + 1$ and $c(u_sv_t) = c(u_sv_j) = k_2 + 1$
for some $k_1, k_2 \in \{1,2,\ldots,r\}$ such that $k_1 \ne k_2$.
Hence u_iv_j and u_sv_t have different colors.
Case 2.2 : $j = 1$. Then $c(u_iv_j) = c(u_iv_1) = k_1$ and $c(u_sv_t) = c(u_sv_j) = c(u_sv_1) = k_2$
for some $k_1, k_2 \in \{1,2,\ldots,r\}$ such that $k_1 \ne k_2$.
Hence u_iv_j and u_sv_t have different colors.
Therefore, $K_{\underbrace{m,m,\ldots,m}_{r}}\Box K_{1,n}$ is equitably r-colorable.

Since $K_{\underbrace{m,m,\ldots,m}_{r}}$ is a complete r-partite graph, the equitable chromatic number of $K_{\underbrace{m,m,\ldots,m}_{r}}\Box K_{1,n}$ equals r.

Hence $\chi_=(K_{\underbrace{m,m,\ldots,m}_{r}}\Box K_{1,n}) = r$. □

Theorem 5. Let m, s and t be positive integers, $m \ge 2$ and $t \ge s$.
Then $\chi_=(K_{\underbrace{1,1,\ldots,1}_{m}}\Box K_{s,t}) = m$.

Proof Let $G_1(V_1,E_1) = K_{\underbrace{1,1,\ldots,1}_{m}}$ and $G_2(V_2,E_2) = K_{s,t}$,

$V(G_1) = \{u_i : 1 \le i \le m\}$,
$E(G_1) = \{u_iu_k : 1 \le i < k \le m\}$,
$V(G_2) = Y_1 \cup Y_2$, where $Y_1 = \{v_1, v_2, \ldots, v_s\}$ and $Y_2 = \{v_{s+1}, v_{s+2}, \ldots, v_{s+t}\}$,
$E(G_2) = \{ab : a \in Y_i, b \in Y_j, 1 \le i < j \le 2\}$,
Let $V(G_1\Box G_2) = \{(u_iv_j) : u_i \in V(G_1), v_j \in V(G_2)\}$ and
$E(G_1\Box G_2) = \{(u_iv_j)(u_xv_y) : i = x$ and $v_jv_y \in E(G_2)$ or $j = y$ and $u_iu_x \in E(G_1)\}$.
Let $c(u_iv_j) = i + r \pmod m$, where $v_j \in Y_r, 1 \le i \le m, 1 \le r \le 2$.
For $1 \le i \le m$, let V_i be denoted as the set of vertices with a color i.

Then

$$\begin{aligned}
V_1 &= \{(u_m v_j) : v_j \in Y_1\} \cup \{(u_{m-1} v_j) : v_j \in Y_2\},\\
V_2 &= \{(u_1 v_j) : v_j \in Y_1\} \cup \{(u_m v_j) : v_j \in Y_2\},\\
V_3 &= \{(u_2 v_j) : v_j \in Y_1\} \cup \{(u_1 v_j) : v_j \in Y_2\},\\
&\vdots\\
V_{m-1} &= \{(u_{m-2} v_j) : v_j \in Y_1\} \cup \{(u_{m-3} v_j) : v_j \in Y_2\},\\
V_m &= \{(u_{m-1} v_j) : v_j \in Y_1\} \cup \{(u_{m-2} v_j) : v_j \in Y_2\}.
\end{aligned}$$

It follows that $|V_1| = |V_2| = |V_3| = \cdots = |V_{m-1}| = |V_m| = s+t$.

Consider each edge $\{(u_i v_j)(u_x v_y)\}$ as follows:
Case 1 : $u_i = u_x$. It follows that $v_j \in Y_{r_1}, v_y \in Y_{r_2}$ for some $r_1, r_2 \in \{1,2\}$, $r_1 \neq r_2$.
Without loss of generality, let $v_j \in Y_1$. Then $v_y \in Y_2$.
Then $c(u_i v_j) = i+1$ and $c(u_x v_y) = c(u_i v_y) = i+2$.
Hence $u_i v_j$ and $u_x v_y$ have different colors.
Case 2 : $v_j = v_y$. It follows that $u_i \neq u_x$ for some $i, x \in \{1,2,\ldots,m\}$, $i \neq x$.
Then $c(u_i v_j) = i+r$ and $c(u_x v_y) = c(u_x v_j) = x+r$ for some $i, x \in \{1,2,\ldots,m\}$ such that $i \neq x$.
Hence $u_i v_j$ and $u_x v_y$ have different colors.
Therefore, $K_{\underbrace{1,1,\ldots,1}_{m}} \square K_{s,t}$ is equitably m-colorable.

Since $K_{\underbrace{1,1,\ldots,1}_{m}}$ is a complete graph of order m, the equitable chromatic number of
$K_{\underbrace{1,1,\ldots,1}_{m}} \square K_{s,t}$ equals m. Hence $\chi_=(K_{\underbrace{1,1,\ldots,1}_{m}} \square K_{s,t}) = m$. □

Theorem 6. Let m, r, s and t be positive integers, $r \geq 2$ and $t \geq s$. Then $\chi_=(K_{\underbrace{m,m,\ldots,m}_{r}} \square K_{s,t}) = r$.

Proof Let $G_1(V_1, E_1) = K_{\underbrace{m,m,\ldots,m}_{r}}$ and $G_2(V_2, E_2) = K_{s,t}$,
$V(G_1) = X_1 \cup X_2 \cup \cdots \cup X_r$, where $X_1 = \{u_1, u_2, \ldots, u_m\}$, $X_2 = \{u_{m+1}, u_{m+2}, \ldots, u_{2m}\}, \ldots,$
$X_r = \{u_{(r-1)m+1}, u_{(r-1)m+2}, \ldots, u_{rm}\}$,
$E(G_1) = \{ab : a \in X_i, b \in X_j, 1 \leq i < j \leq r\}$,
$V(G_2) = Y_1 \cup Y_2$, where $Y_1 = \{v_1, v_2, \ldots, v_s\}$ and $Y_2 = \{v_{s+1}, v_{s+2}, \ldots, v_{s+t}\}$,
$E(G_2) = \{cd : c \in Y_i, d \in Y_j, 1 \leq i < j \leq 2\}$.
Let $V(G_1 \square G_2) = \{(u_i v_j) : u_i \in V(G_1), v_j \in V(G_2)\}$ and
$E(G_1 \square G_2) = \{(u_i v_j)(u_x v_y) : i = x$ and $v_j v_y \in E(G_2)$ or $j = y$ and $u_i u_x \in E(G_1)\}$.
Let $c(u_i v_j) = k+n \pmod r$, where $u_i \in X_k, 1 \leq k \leq r$ and $v_j \in Y_n, 1 \leq n \leq 2$.
For $1 \leq k \leq r$, let V_k be denoted as the set of vertices with a color k.

Then

$$\begin{aligned}
V_1 &= \{(u_iv_j) : u_i \in X_r, v_j \in Y_1\} \cup \{(u_iv_j) : u_i \in X_{r-1}, v_j \in Y_2\},\\
V_2 &= \{(u_iv_j) : u_i \in X_1, v_j \in Y_1\} \cup \{(u_iv_j) : u_i \in X_r, v_j \in Y_2\},\\
V_3 &= \{(u_iv_j) : u_i \in X_2, v_j \in Y_1\} \cup \{(u_iv_j) : u_i \in X_1, v_j \in Y_2\},\\
&\vdots\\
V_{r-1} &= \{(u_iv_j) : u_i \in X_{r-2}, v_j \in Y_1\} \cup \{(u_iv_j) : u_i \in X_{r-3}, v_j \in Y_2\},\\
V_r &= \{(u_iv_j) : u_i \in X_{r-1}, v_j \in Y_1\} \cup \{(u_iv_j) : u_i \in X_{r-2}, v_j \in Y_2\}.
\end{aligned}$$

It follows that $|V_1| = |V_2| = |V_3| = \cdots = |V_{r-1}| = |V_r| = m(s+t)$.

Consider each edge $\{(u_iv_j)(u_xv_y)\}$ as follows:
Case 1 : $u_i = u_x$. It follows that $v_j \in Y_{n_1}, v_y \in Y_{n_2}$ for some $n_1, n_2 \in \{1,2\}$, $n_1 \neq n_2$.
Without loss of generality, let $v_j \in Y_1$. Then $v_y \in Y_2$.
Then $c(u_iv_j) = k+1$ and $c(u_xv_y) = c(u_iv_y) = k+2$.
Hence u_iv_j and u_xv_y have different colors.
Case 2 : $v_j = v_y$. It follows that $u_i \in X_{k_1}, u_x \in X_{k_2}$ for some $k_1, k_2 \in \{1,2,\ldots,r\}$, $k_1 \neq k_2$.
Then $c(u_iv_j) = k_1 + n$ and $c(u_xv_y) = c(u_xv_j) = k_2 + n$ for some $k_1, k_2 \in \{1,2,\ldots,r\}$ such that $k_1 \neq k_2$.
Hence u_iv_j and u_xv_y have different colors.
Therefore, $\underbrace{K_{m,m,\ldots,m}}_{r}\Box K_{s,t}$ is equitably r-colorable.

Since $\underbrace{K_{m,m,\ldots,m}}_{r}$ is a complete r-partite graph, the equitable chromatic number of
$\underbrace{K_{m,m,\ldots,m}}_{r}\Box K_{s,t}$ equals r. Hence $\chi_=(\underbrace{K_{m,m,\ldots,m}}_{r}\Box K_{s,t}) = r$. □

Theorem 7. Let m, n, r, s and t be positive integers, $n \geq 3$ and $r \leq s \leq t$. Then $\chi_=(\underbrace{K_{m,m,\ldots,m}}_{n}\Box K_{r,s,t}) = n$.

Proof Let $G_1(V_1, E_1) = \underbrace{K_{m,m,\ldots,m}}_{n}$ and $G_2(V_2, E_2) = K_{r,s,t}$,
$V(G_1) = X_1 \cup X_2 \cup \cdots \cup X_n$, where $X_1 = \{u_1, u_2, \ldots, u_m\}$, $X_2 = \{u_{m+1}, u_{m+2}, \ldots, u_{2m}\}, \ldots,$
$X_n = \{u_{(n-1)m+1}, u_{(n-1)m+2}, \ldots, u_{nm}\}$,
$E(G_1) = \{ab : a \in X_i, b \in X_j, 1 \leq i < j \leq n\}$,
$V(G_2) = Y_1 \cup Y_2 \cup Y_3$, where $Y_1 = \{v_1, v_2, \ldots, v_r\}, Y_2 = \{v_{r+1}, v_{r+2}, \ldots, v_{r+s}\}$ and
$Y_3 = \{v_{(r+s)+1}, v_{(r+s)+2}, \ldots, v_{r+s+t}\}$,
$E(G_2) = \{cd : c \in Y_i, d \in Y_j, 1 \leq i < j \leq 3\}$.
Let $V(G_1 \Box G_2) = \{(u_iv_j) : u_i \in V(G_1), v_j \in V(G_2)\}$ and
$E(G_1 \Box G_2) = \{(u_iv_j)(u_xv_y) : i = x$ and $v_jv_y \in E(G_2)$ or $j = y$ and $u_iu_x \in E(G_1)\}$.
Let $c(u_iv_j) = k + l \pmod n$, where $u_i \in X_k, 1 \leq k \leq n$ and $v_j \in Y_l, 1 \leq l \leq 3$.
For $1 \leq k \leq n$, let V_k be denoted as the set of vertices with a color k.

Then

$$V_1 = \{(u_iv_j) : u_i \in X_n, v_j \in Y_1\} \cup \{(u_iv_j) : u_i \in X_{n-1}, v_j \in Y_2\} \cup \{(u_iv_j) : u_i \in X_{n-2}, v_j \in Y_3\},$$
$$V_2 = \{(u_iv_j) : u_i \in X_1, v_j \in Y_1\} \cup \{(u_iv_j) : u_i \in X_n, v_j \in Y_2\} \cup \{(u_iv_j) : u_i \in X_{n-1}, v_j \in Y_3\},$$
$$V_3 = \{(u_iv_j) : u_i \in X_2, v_j \in Y_1\} \cup \{(u_iv_j) : u_i \in X_1, v_j \in Y_2\} \cup \{(u_iv_j) : u_i \in X_n, v_j \in Y_3\},$$
$$\vdots$$
$$V_{n-1} = \{(u_iv_j) : u_i \in X_{n-2}, v_j \in Y_1\} \cup \{(u_iv_j) : u_i \in X_{n-3}, v_j \in Y_2\} \cup \{(u_iv_j) : u_i \in X_{n-4}, v_j \in Y_3\},$$
$$V_n = \{(u_iv_j) : u_i \in X_{n-1}, v_j \in Y_1\} \cup \{(u_iv_j) : u_i \in X_{n-2}, v_j \in Y_2\} \cup \{(u_iv_j) : u_i \in X_{n-3}, v_j \in Y_3\}.$$

It follows that $|V_1| = |V_2| = |V_3| = \cdots = |V_{n-1}| = |V_n| = m(r+s+t)$.

Consider each edge $\{(u_iv_j)(u_xv_y)\}$ as follows:
Case 1 : $u_i = u_x$. It follows that $v_j \in Y_{l_1}, v_y \in Y_{l_2}$ for some $l_1, l_2 \in \{1,2,3\}$, $l_1 \neq l_2$.
Without loss of generality, let $v_j \in Y_1$. Then $v_y \in Y_2$ or $v_y \in Y_3$.
Case 1.1 : $v_y \in Y_2$. Then $c(u_iv_j) = k+1$ and $c(u_xv_y) = c(u_iv_y) = k+2$.
Hence u_iv_j and u_xv_y have different colors.
Case 1.2 : $v_y \in Y_3$. Then $c(u_iv_j) = k+1$ and $c(u_xv_y) = c(u_iv_y) = k+3$.
Hence u_iv_j and u_xv_y have different colors.
Case 2 : $v_j = v_y$. It follows that $u_i \in X_{k_1}, u_x \in X_{k_2}$ for some $k_1, k_2 \in \{1,2,\ldots,n\}$, $k_1 \neq k_2$.
Then $c(u_iv_j) = k_1 + l$ and $c(u_xv_y) = c(u_xv_j) = k_2 + l$ for some $k_1, k_2 \in \{1,2,\ldots,n\}$ such that $k_1 \neq k_2$.
Hence u_iv_j and u_xv_y have different colors.
Therefore, $\underbrace{K_{m,m,\ldots,m}}_{n} \square K_{r,s,t}$ is equitably n-colorable.

Since $\underbrace{K_{m,m,\ldots,m}}_{n}$ is a complete n-partite graph, the equitable chromatic number of $\underbrace{K_{m,m,\ldots,m}}_{n} \square K_{r,s,t}$ equals n.

Hence $\chi_=(\underbrace{K_{m,m,\ldots,m}}_{n} \square K_{r,s,t}) = n$. □

Theorem 8. Let $k, m, n,$ and r be positive integers, $n_1 \leq n_2 \leq \cdots \leq n_k$ and $r \geq k$. Then $\chi_=(\underbrace{K_{m,m,\ldots,m}}_{r} \square K_{n_1,n_2,\ldots,n_k}) = r$.

Proof Let $G_1(V_1,E_1) = \underbrace{K_{m,m,\ldots,m}}_{r}$ and $G_2(V_2,E_2) = K_{n_1,n_2,\ldots,n_k}$,
$V(G_1) = X_1 \cup X_2 \cup \cdots \cup X_r$, where $X_1 = \{u_1, u_2, \ldots, u_m\}$, $X_2 = \{u_{m+1}, u_{m+2}, \ldots, u_{2m}\}, \ldots,$
$X_r = \{u_{(r-1)m+1}, u_{(r-1)m+2}, \ldots, u_{rm}\}$,
$E(G_1) = \{ab : a \in X_i, b \in X_j, 1 \leq i < j \leq r\}$,
$V(G_2) = Y_1 \cup Y_2 \cup \cdots \cup Y_k$, where $Y_1 = \{v_1, v_2, \ldots, v_{n_1}\}$, $Y_2 = \{v_{n_1+1}, v_{n_1+2}, \ldots, v_{n_1+n_2}\}, \ldots,$
$Y_k = \{v_{(n_1+n_2+\cdots+n_{k-1})+1}, v_{(n_1+n_2+\cdots+n_{k-1})+2}, \ldots, v_{n_1+n_2+\cdots+n_k}\}$,
$E(G_2) = \{cd : c \in Y_i, d \in Y_j, 1 \leq i < j \leq k\}$.
Let $V(G_1 \square G_2) = \{(u_iv_j) : u_i \in V(G_1), v_j \in V(G_2)\}$ and
$E(G_1 \square G_2) = \{(u_iv_j)(u_xv_y) : i = x$ and $v_jv_y \in E(G_2)$ or $j = y$ and $u_iu_x \in E(G_1)\}$.
Let $c(u_iv_j) = s + t \pmod r$, where $u_i \in X_s, 1 \leq s \leq r$ and $v_j \in Y_t, 1 \leq t \leq k$.
For $1 \leq s \leq r$, let V_s be denoted as the set of vertices with a color s.

Then

$$V_1 = \{(u_i v_j) : u_i \in X_r, v_j \in Y_1\} \cup \{(u_i v_j) : u_i \in X_{r-1}, v_j \in Y_2\} \cup \cdots \cup \{(u_i v_j) : u_i \in X_1, v_j \in Y_k\},$$
$$V_2 = \{(u_i v_j) : u_i \in X_1, v_j \in Y_1\} \cup \{(u_i v_j) : u_i \in X_r, v_j \in Y_2\} \cup \cdots \cup \{(u_i v_j) : u_i \in X_2, v_j \in Y_k\},$$
$$V_3 = \{(u_i v_j) : u_i \in X_2, v_j \in Y_1\} \cup \{(u_i v_j) : u_i \in X_1, v_j \in Y_2\} \cup \cdots \cup \{(u_i v_j) : u_i \in X_3, v_j \in Y_k\},$$
$$\vdots$$
$$V_{r-1} = \{(u_i v_j) : u_i \in X_{r-2}, v_j \in Y_1\} \cup \{(u_i v_j) : u_i \in X_{r-3}, v_j \in Y_2\} \cup \cdots \cup \{(u_i v_j) : u_i \in X_{r-1}, v_j \in Y_k\},$$
$$V_r = \{(u_i v_j) : u_i \in X_{r-1}, v_j \in Y_1\} \cup \{(u_i v_j) : u_i \in X_{r-2}, v_j \in Y_2\} \cup \cdots \cup \{(u_i v_j) : u_i \in X_r, v_j \in Y_k\}.$$

It follows that $|V_1| = |V_2| = |V_3| = \cdots = |V_{r-1}| = |V_r| = m(n_1 + n_2 + \cdots + n_k)$.

Consider each edge $\{(u_i v_j)(u_x v_y)\}$ as follows:
Case 1 : $u_i = u_x$. It follows that $v_j \in Y_{t_1}, v_y \in Y_{t_2}$ for some $t_1, t_2 \in \{1, 2, \ldots, k\}$, $t_1 \neq t_2$.
Then $c(u_i v_j) = s + t_1$ and $c(u_x v_y) = c(u_i v_y) = s + t_2$ for some $t_1, t_2 \in \{1, 2, \ldots, k\}$ such that $t_1 \neq t_2$.
Hence $u_i v_j$ and $u_x v_y$ have different colors.
Case 2 : $v_j = v_y$. It follows that $u_i \in X_{s_1}, u_x \in X_{s_2}$ for some $s_1, s_2 \in \{1, 2, \ldots, r\}$, $s_1 \neq s_2$.
Then $c(u_i v_j) = s_1 + t$ and $c(u_x v_y) = c(u_x v_j) = s_2 + t$ for some $s_1, s_2 \in \{1, 2, \ldots, r\}$ such that $s_1 \neq s_2$.
Hence $u_i v_j$ and $u_x v_y$ have different colors.
Therefore, $\underbrace{K_{m,m,\ldots,m}}_{r} \square K_{n_1,n_2,\ldots,n_k}$ is equitably r-colorable.

Since $\underbrace{K_{m,m,\ldots,m}}_{r}$ is a complete r-partite graph, the equitable chromatic number of $\underbrace{K_{m,m,\ldots,m}}_{r} \square K_{n_1,n_2,\ldots,n_k}$ equals r.

Hence $\chi_{=}(\underbrace{K_{m,m,\ldots,m}}_{r} \square K_{n_1,n_2,\ldots,n_k}) = r$. □

Conclusion :

In summary, in this paper, we obtain the equitable chromatic numbers of Cartesian products of graphs as in table 1:

$G_1 \square G_2$	$\chi_{=}(G_1 \square G_2)$
$K_{1,1,1,1} \square K_{1,3}$	4
$\underbrace{K_{1,1,\ldots,1}}_{m} \square K_{1,n}$	m
$K_{m,m,m} \square K_{1,n}$	3
$\underbrace{K_{m,m,\ldots,m}}_{r} \square K_{1,n}$	r
$\underbrace{K_{1,1,\ldots,1}}_{m} \square K_{s,t}$	m
$\underbrace{K_{m,m,\ldots,m}}_{r} \square K_{s,t}$	r
$\underbrace{K_{m,m,\ldots,m}}_{n} \square K_{r,s,t}$	n
$\underbrace{K_{m,m,\ldots,m}}_{r} \square K_{n_1,n_2,\ldots,n_k}$	r

Table 1: The equitable chromatic numbers of Cartesian products of graphs G_1 and G_2

References :

[1] Chen B.-L, Lih K.-W, Yan J.-H, manuscript. 1998.
[2] Furmańczyk H, Opuscula Mathematica. 2006;26(1):31–44.
[3] Lin W.-H, Chang G. J, Discrete Applied Mathematics. 2012;160:239–247.

THE MAXWELL – BURR III DISTRIBUTION: ITS PROPERTIES AND APPLICATION TO THE NEW COPD PATIENT RATE IN KHON KAEN, THAILAND

Kamonrut Koobubpha[1, *], Aliyu Ismail Ishaq[2], Theeraphat Thanwiset[1], Uthumporn Panitanarak[3, *]
[1]Department of Statistics, Faculty of Science, Khon Kaen University, Khon Kaen 40002 Thailand
[2] Department of Statistics, Ahmadu Bello University, Zaria, 810107, Nigeria
[3] Department of Biostatistics, Faculty of Public Health, Mahidol University, Bangkok 10400 Thailand
[1,]*e-mail: k.kamonrat@kkumail.com, [3,]*e-mail: uthumporn.pan@mahidol.ac.th

Abstract:

This research aimed to propose the newly developed Burr III distribution named The Maxwell–Burr III distribution. We applied the Maxwell generalized family of distributions to construct the proposed distribution by adding the scale parameter. This new expansion has enhanced the flexibility of the basic distribution with the potential to model various types of lifetime data since the hazard curve of the proposed distribution can be increasing and decreasing. The standard statistical functions of Maxwell–Burr III distribution were defined including cumulative distribution function, probability density function, survival function, hazard function, and quantile function. The parameter estimation was constructed by using maximum likelihood method. A simulation study was conducted to access the performance of maximum likelihood estimators. Maxwell–Burr III distribution was also applied to model real lifetime data set relating to the new COPD patient rates in Khon Kaen, Thailand to demonstrate the ability of the distribution against other competing distributions. The results showed that it performed the best among others in terms of information criteria, AIC, CAIC.

Introduction:

In these decades, people are becoming increasingly interested in data analytics. Moreover, with efficient data storage technology, there is a greater variety of information available than in the past but some datasets still cannot be well explained by classical distribution. Therefore, Generating the new distribution is one of the most filed that many researchers pay attention. The new distribution resulting from the expansion of the original distribution by means of adding extra parameters plays an important role in exploring the altered properties. and it is the way to increase flexibility to the original distribution.
The new distribution resulting from the expansion of the original distribution by means of adding extra parameters plays an important role in exploring the altered properties. and it is the way to increase flexibility to the original distribution.

Burr system distribution was proposed by Burr in 1942 and consists of 12 different forms of continuous distribution to model the positive data. Among all types of Burr system, the Burr type III distribution with two parameters is widely studied and discussed for application in various areas such as the spread of income, actuarial science, and environmental science. The cumulative distribution function Burr III distribution (for $x > 0$), is given below:

$$G(x;c,k) = (1+x^{-c})^{-k} \quad (1)$$

The corresponding probability density function to (1) is

$$g(x;c,k) = ckx^{-(c+1)}(1+x^{-c})^{-(k+1)}, \tag{2}$$

where $c > 0$ and $k > 0$ are the shape parameters. Because Burr III distribution has a simple form and its ability to apply to a variety of real phenomena data, Burr III distribution was extended by many generalized family of distributions to receive a new distribution with different properties and applications from the original Burr III distribution. For instance, Marshall Olkin modified Burr-III (Ali et al., 2015), Kumaraswamy Burr-III (Behairy et al., 2016), extended Burr-III distribution (Cordeiro et al., 2017), generalized Marshall-Olkin BurrIII (Chakraborty et al. 2020), odd Log-Logistic Burr III (Handique et al., 2020), extended Marshall-Olkin Burr III (Haq et al., 2021) and so on.

The goal of this research is to study the Maxwell-Burr III distribution developed from the Burr III distribution by adding the scale parameter from the Maxwell Generalized family of distributions. This structure of this article is designed as follows. In Section 2, the Methodology describes the methods to propose the Maxwell-Burr III distribution. In Section 3, some mathematical and statistical properties of the proposed distribution are presented. In Section 4, the parameters estimation by using maximum likelihood methods was derived and the performance of maximum likelihood estimators were shown by simulation study. In Section 5, the application to real datasets is presented. Finally, section 6 is the conclusion.

Methodology:

This research presents new continuous distribution named the Maxwell-Burr III distribution. The method used to derive the cumulative distribution function and the probability density function of the proposed distribution is provided in this section.

The Maxwell Generalized (M-G) family of distributions introduced by Ishaq and Abiodun in 2020. the cumulative distribution function (cdf) and the probability density function (pdf) of the M-G family of distributions, respectively, are given as:

$$F\left(x;\beta,r\right) = \frac{2}{\sqrt{\pi}}\gamma\left(\frac{3}{2}, \frac{1}{2\beta^2}\left(\frac{G\left(x;\varepsilon\right)}{1-G\left(x;\varepsilon\right)}\right)^2\right);\ x \in \sim \tag{3}$$

and

$$f\left(x;\beta,\omega\right) = \frac{2g\left(x;\omega\right)}{\beta^3\sqrt{2\pi}\left\{1-G\left(x;\omega\right)\right\}^2}\left(\frac{G\left(x;\omega\right)}{1-G\left(x;\omega\right)}\right)^2 \exp\left\{-\frac{1}{2\beta^2}\left(\frac{G\left(x;\omega\right)}{1-G\left(x;\omega\right)}\right)^2\right\}, \tag{4}$$

where $\beta > 0$ is a scale parameter, $\gamma\left(a,b\right) = \int_a^b t^{a-1}e^{-t}dt$ is an incomplete gamma function, $G\left(x;\omega\right)$ and $g\left(x;\omega\right)$ are the cdf and pdf of the baseline distribution with parameter ω, respectively. we define and study the Maxwell-Burr III (M-BIII) distribution by inserting (1) in (3) The cdf of M-BIII distribution becomes,

$$F\left(x;\beta,c,k\right) = \frac{2}{\sqrt{\pi}}\gamma\left(\frac{3}{2}, \frac{1}{2\beta^2}\left(\frac{(1+x^{-c})^{-k}}{1-(1+x^{-c})^{-k}}\right)^2\right);\quad x > 0. \tag{5}$$

The corresponding pdf of (5) is given by

$$f(x;c,k)=\frac{2ckx^{-(c+1)}(1+x^{-c})^{-(3k+1)}}{\beta^3\sqrt{2\pi}\left[1-(1+x^{-c})^{-k}\right]^4}\exp\left\{-\frac{1}{2\beta^2}\left[\frac{(1+x^{-c})^{-k}}{1-(1+x^{-c})^{-k}}\right]^2\right\};\ x>0, \tag{6}$$

where $\beta>0$ is the scale and $c,k>0$ are shape parameters, respectively.

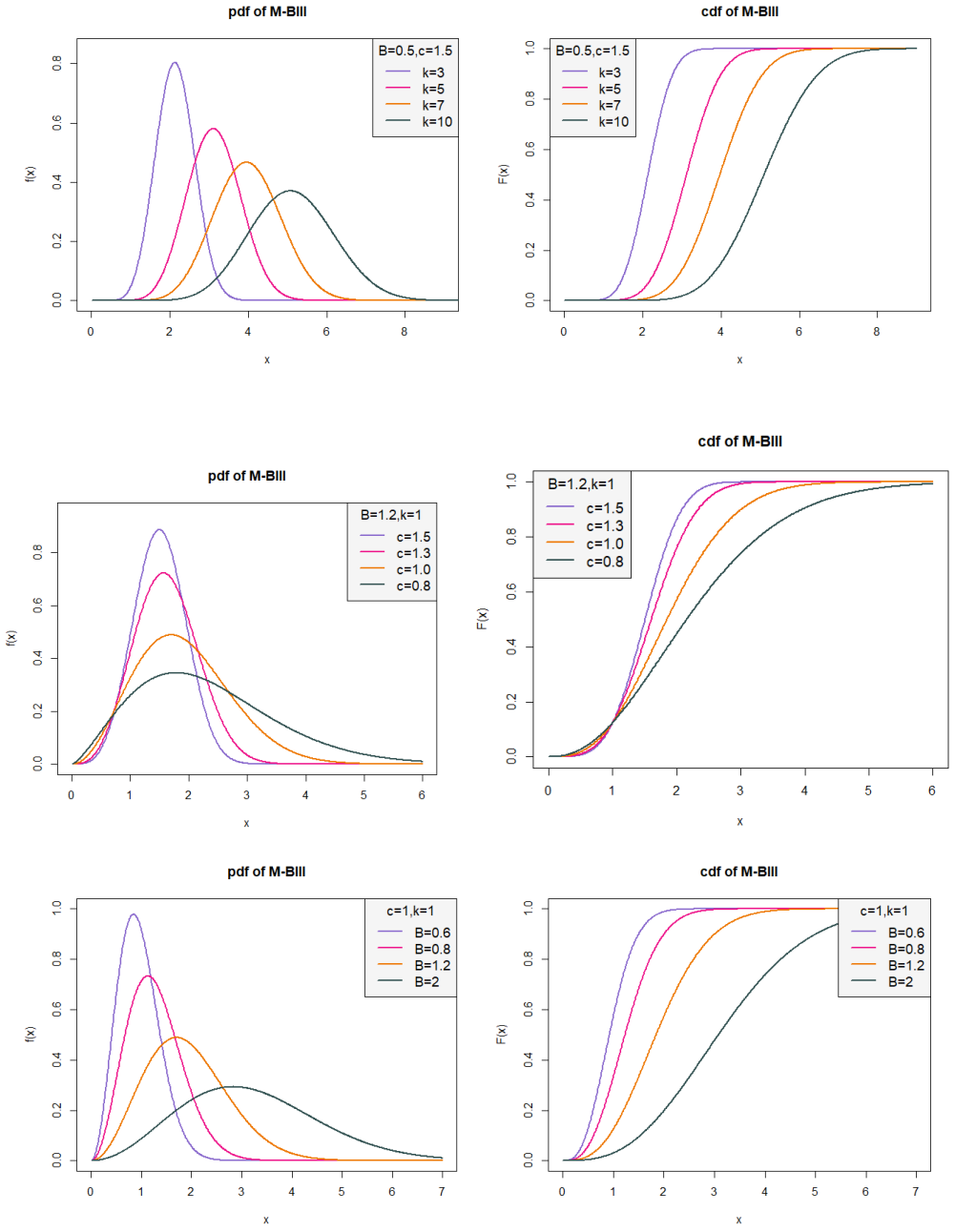

Figure 1.
The pdf and cdf plots of the M-BIII distribution with different values of β, c and k

Properties of the Maxwell-Burr III distribution:
The survival function of the M-BIII distribution is obtained from (5) as

$$s(x;\beta,c,k)=1-\frac{2}{\sqrt{\pi}}\gamma\left(\frac{3}{2},\frac{1}{2\beta^2}\left(\frac{(1+x^{-c})^{-k}}{1-(1+x^{-c})^{-k}}\right)^2\right);\quad x>0. \tag{7}$$

The hazard function of the M-BIII distribution is obtained from (6) and (7) as

$$h(x;\beta,c,k)=\frac{\dfrac{2ckx^{-(c+1)}(1+x^{-c})^{-(3k+1)}}{\beta^3\sqrt{2\pi}\left[1-(1+x^{-c})^{-k}\right]^4}\exp\left\{-\dfrac{1}{2\beta^2}\left[\dfrac{(1+x^{-c})^{-k}}{1-(1+x^{-c})^{-k}}\right]^2\right\}}{1-\dfrac{2}{\sqrt{\pi}}\gamma\left(\dfrac{3}{2},\dfrac{1}{2\beta^2}\left(\dfrac{(1+x^{-c})^{-k}}{1-(1+x^{-c})^{-k}}\right)^2\right)};\quad x>0, \tag{8}$$

where $\beta>0$ is the scale and $c,k>0$ are shape parameters, respectively. The hazard curve of the M-BIII distribution can be increasing and decreasing as shown in Figure 2.

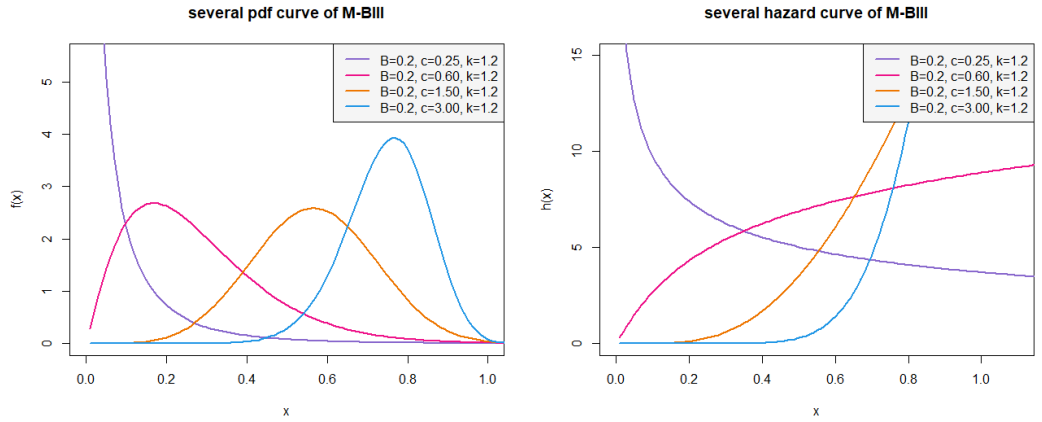

Figure 2.
The several curves of the M-BIII distribution with different values of β, c and k

The quantile function of M-BIII distribution can be derived from an inverse function of the cdf defined in (3) as

$$x_q=\left\{\left(\frac{1+\left[2\beta^2\gamma^{-1}\left(\frac{3}{2},u\Gamma\left(\frac{3}{2}\right)\right)\right]^{\frac{1}{2}}}{\left[2\beta^2\gamma^{-1}\left(\frac{3}{2},u\Gamma\left(\frac{3}{2}\right)\right)\right]^{\frac{1}{2}}}\right)^{\frac{1}{k}}-1\right\}^{-\frac{1}{c}}, \tag{9}$$

where u has a uniform distribution on interval 0 to 1.

The moment function of the M-BIII distribution can be derived from the definition of moment function as

$$E(X^r) = \int_{-\infty}^{\infty} x^r f(x) dx. \tag{10}$$

Consider the expansion of pdf of M-BIII distribution. We know that

$$e^{-t} = \sum_{m=0}^{\infty} \frac{(-1)^m t^m}{m!} \tag{11}$$

$$(1-z)^{-p} = \sum_{j=0}^{\infty} \frac{\Gamma(j+p)}{j!\Gamma(p)} z^j \text{ for } |m| < 1 \text{and } c > 0 \tag{12}$$

By using (11) and (12) the pdf of M-BIII can be written as

$$f(x;c,k) = \frac{ck}{\beta^3} \sum_{m,j=0}^{\infty} A_{m,j} x^{-(c+1)} (1+x^{-c})^{-(2km+3k+jk+1)}; \; x > 0, \tag{13}$$

where $A_{m,j} = \frac{(-1)^m \Gamma(2m+4+j)}{\sqrt{\pi} 2^{m-3/2} m! \beta^{2m} \Gamma(2m+4)}$ and where $\beta > 0$ is the scale and $c, k > 0$ are shape parameters, respectively. By inserting (13) in (10), we obtain

$$E(X^r) = \frac{ck}{\beta^3} \sum_{m,j=0}^{\infty} A_{m,j} \int_0^{\infty} x^{r-(c+1)} (1+x^{-c})^{-s} dx. \tag{14}$$

Let $y = x^{-c}$ it implies that $dx = -\frac{1}{c} y^{-\left(\frac{1}{c}+1\right)} dy$, that is

$$E(X^r) = \sum_{m,j=0}^{\infty} \Omega_{m,j} \int_0^{\infty} y^{-\frac{r}{c}} (1+y)^{-s} dy \tag{15}$$

And let $y = \frac{t}{1-t}$, we get $dy = \frac{t}{(1-t)^2} dt$, that is

$$E(X^r) = \sum_{m,j=0}^{\infty} \Omega_{m,j} \int_0^1 t^{-\frac{r}{c}} (1-t)^{\frac{r}{c}+s-2} dt. \tag{16}$$

Finally, we obtain $E(X^r) = \sum_{m,j=0}^{\infty} \Omega_{m,j} \mathrm{B}\left(1-\frac{r}{c}, \frac{r}{c}+s-1\right)$ for $c > r$, where $\Omega_{m,j} = -\frac{k}{\beta^3} A_{m,j}$, $\mathrm{B}(a,b); \; a > 0, b > 0$ is the beta function, and $s = 2km + 3k + jk + 1$ which is the moment of the M-BIII distribution.

Parameter Estimation

In this section, the estimates of parameters of the M-BIII distribution using the maximum likelihood method were provided.

Let $X_1, X_2, X_3, ..., X_n$ be a random variable of sample size n from the M-BIII distribution with parameters β, c and k then the likelihood function of the M-BIII distribution is obtained from (6) as

$$L=\prod_{i=1}^{n} f(x_i)=\left(\frac{2ck}{\beta^3\sqrt{2\pi}}\right)^n \prod_{i=1}^{n}\left[\frac{x_i^{-(c+1)}(1+x_i^{-c})^{-(3k+1)}}{\left[1-(1+x_i^{-c})^{-k}\right]^4}\right]\prod_{i=1}^{n}\exp\left\{-\frac{1}{2\beta^2}\left[\frac{(1+x_i^{-c})^{-k}}{1-(1+x_i^{-c})^{-k}}\right]^2\right\} \tag{17}$$

The log-likelihood function of (30) denoted by l is

$$\begin{aligned} l=\log l &= n\log 2+n\log c+n\log k-3n\log\beta-\frac{n}{2}\log 2\pi-(c+1)\sum_{i=1}^{n}\log x_i-(3k+1)\sum_{i=1}^{n}\log(1+x_i^{-c}) \\ &-4\sum_{i=1}^{n}\log[1-(1+x_i^{-c})^{-k}]-\frac{1}{2\beta^2}\sum_{i=1}^{n}\left[\frac{(1+x_i^{-c})^{-k}}{1-(1+x_i^{-c})^{-k}}\right]^2. \end{aligned} \tag{18}$$

The first partial derivative of (18) with respect to parameters β, c and k are

$$\frac{\partial L}{\partial\beta}=-\frac{3n}{\beta}+\frac{1}{\beta^3}\sum_{i=1}^{n}\left[\frac{(1+x_i^{-c})^{-k}}{1-(1+x_i^{-c})^{-k}}\right]^2 \tag{19}$$

$$\frac{\partial L}{\partial c}=\frac{n}{c}-\sum_{i=1}^{n}\log x_i+(3k+1)\sum_{i=1}^{n}\left[\frac{x_i^{-c}\log x_i}{1+x_i^{-c}}\right]-4k\sum_{i=1}^{n}\left(\frac{x_i^{-c}(\log x_i)(1+x_i^{-c})^{-(k+1)}}{1-(1+x_i^{-c})^{-k}}\right)-\frac{k}{\beta^2}\sum_{i=1}^{n}\left[\frac{x_i^{-c}(\log x_i)(1+x_i^{-c})^{-(2k+1)}}{\left[1-(1+x_i^{-c})^{-k}\right]^3}\right] \tag{20}$$

$$\frac{\partial L}{\partial k}=\frac{n}{k}-3\sum_{i=1}^{n}\log(1+x_i^{-c})-4k\sum_{i=1}^{n}\left[\frac{(1+x_i^{-c})^{-k}\log(1+x_i^{-c})}{1-(1+x_i^{-c})^{-k}}\right]+\frac{1}{\beta^2}\sum_{i=1}^{n}\left[\frac{(1+x_i^{-c})^{-2k}\log(1+x_i^{-c})}{\left[1-(1+x_i^{-c})^{-k}\right]^3}\right]. \tag{21}$$

Set (19), (20) and (21) to zero and solve these equations to get the maximum likelihood estimator $\hat{\beta}$, $\hat{c}$ and $\hat{k}$ but it is impossible to get the closed forms of these estimators. However, the Newton-Raphson method was used as numerical technique to receive value of estimators. In this research we used the R program which is the statistical software to access the maximum likelihood estimators.

We appraised the performance of the maximum likelihood estimators of parameters of the M-BIII distribution through a simulation study. Data was generated from a quantile function defined in (9). Data was generated for three different sample sizes (n), 20, 50 and 100, which are referred to small, medium and large sample sizes of data, respectively. The simulation was considered 4 cases $(1,1.2,0.6)$, $(1,1.2,1.5)$, $(0.7,0.3,0.6)$ and $(0.7,0.3,1.5)$, respectively. The repetition of the simulation is 1,000 times for each sample size to obtain the mean, bias and variance. The results of simulation provided in Tables 1-4.

Table 1.
The mean, bias and variance of the M-BIII distribution $\beta = 1, c = 1.2$ and $k = 0.6$

$(\beta, c, k) = (1, 1.2, 0.6)$				
Sample size	**ML estimates**		**Bias**	**Variance**
20	$\hat{\beta}$ =	1.01104	0.01104	0.00000
	$\hat{c}$ =	1.21762	0.01762	0.00007
	$\hat{k}$ =	0.02817	-0.57183	0.00027
50	$\hat{\beta}$ =	1.01444	0.01443	0.00000
	$\hat{c}$ =	1.22292	0.02292	0.00005
	$\hat{k}$ =	0.03722	-0.56278	0.00044
100	$\hat{\beta}$ =	1.01128	0.01128	0.00001
	$\hat{c}$ =	1.21698	0.01698	0.00001
	$\hat{k}$ =	0.03087	-0.56913	0.00061

Table 2.
The mean, bias and variance of the M-BIII distribution $\beta = 1, c = 1.2$ and $k = 1.5$

$(\beta, c, k) = (1, 1.2, 1.5)$				
Sample size	**ML estimates**		**Bias**	**Variance**
20	$\hat{\beta}$ =	0.40457	-0.59543	0.03721
	$\hat{c}$ =	1.32162	0.12162	0.00435
	$\hat{k}$ =	0.02920	-1.47080	0.00028
50	$\hat{\beta}$ =	0.22156	-0.77844	0.00005
	$\hat{c}$ =	1.47882	0.27882	0.00059
	$\hat{k}$ =	0.03950	-1.46050	0.00053
100	$\hat{\beta}$ =	0.21735	-0.78265	0.00008
	$\hat{c}$ =	1.54349	0.34349	0.00248
	$\hat{k}$ =	0.04298	-1.45702	0.00076

Table 3.
The mean, bias and variance of the M-BIII distribution $\beta = 0.7, c = 0.3$ and $k = 0.6$

$(\beta, c, k) = (0.7, 0.3, 0.6)$				
Sample size	**ML estimates**		**Bias**	**Variance**
20	$\hat{\beta}$ =	0.75328	0.05328	0.00015
	$\hat{c}$ =	0.39339	0.09339	0.00122
	$\hat{k}$ =	0.01921	-0.58079	0.00018
50	$\hat{\beta}$ =	0.74374	0.04374	0.00007
	$\hat{c}$ =	0.37956	0.07956	0.00083
	$\hat{k}$ =	0.01696	-0.58304	0.00012
100	$\hat{\beta}$ =	0.74042	0.04042	0.00001
	$\hat{c}$ =	0.37274	0.07274	0.00019
	$\hat{k}$ =	0.01642	-0.58358	0.00009

Table 4.
The mean, bias and variance of the M-BIII distribution $\beta = 0.7, c = 0.3$ and $k = 1.5$

$(\beta, c, k) = (0.7, 0.3, 1.5)$				
Sample size	**ML estimates**		**Bias**	**Variance**
20	$\hat{\beta}$ =	0.30413	-0.39587	0.00269
	$\hat{c}$ =	0.42302	0.12302	0.06276
	$\hat{k}$ =	0.01222	-1.48778	0.00007
50	$\hat{\beta}$ =	0.56981	-0.13019	0.07503
	$\hat{c}$ =	0.37379	0.07379	0.00314
	$\hat{k}$ =	0.01526	-1.48475	0.00016
100	$\hat{\beta}$ =	0.62868	-0.07132	0.00013
	$\hat{c}$ =	0.38540	0.08540	0.00016
	$\hat{k}$ =	0.01652	-1.48348	0.00008

As observed the simulation results from Tables 1, 2, 3, and 4, based on the bias, we noticed that, $\hat{\beta}$ and $\hat{c}$ are good estimators, but $\hat{k}$ could not estimate close to the exact values of the parameter k. By focusing on the sample size, in most cases, the larger the sample size provided estimates close to the exact values of parameters.

Application to real datasets:

In this section, we illustrated the potentiality of the M-BIII distribution dealing with real data sets. We worked with the data set consisted of 94 observations of the new COPD patient rates in Khon Kaen, Thailand between October 2014 to 25 July 2022. The data set was obtained from the Ministry of Public Health of Khon Kaen, Thailand website. See the link [HDC - Report (moph.go.th)] for mor details.

We compared the results of M-BIII distribution with the Weibull classical distribution and the odd log-logistic Burr III (Handique et al., 2020) distribution extended the same

baseline of proposed distribution. The evaluation measures used in this research included Akaike Information Criterion (AIC) and Consistent Akaike Information Criterion (CAIC) According to these criteria, the less the score indicated the better model.

Table 5.
The maximum likelihood estimators and information criterion values of the real data set

Comparative models	ML estimators	AIC	CAIC
M-BIII	$\hat{\beta}$ = 0.27061 $\hat{c}$ = 0.74664 $\hat{k}$ 1.02338	-59.14132	-58.87465
OLL-BIII	$\hat{\alpha}$ = 5.452263 $\hat{\beta}$ = 0.330201 $\hat{\delta}$ = 1.622083	-46.75674	-46.49007
W	$\hat{\lambda}$ = 1.80599 $\hat{k}$ = 0.40122	-54.81777	-54.68590

Maxwell-Burr III (M-BIII), odd log-logistic Burr III (OLL-BIII) and Weibull (W) distributions.

Tables 5 showed that the M-BIII distribution provided the minimum value of all information criteria. Thus, it gave the best fit for data sets relating to the new COPD patient rates in Khon Kaen, Thailand compared to other distributions. Moreover, Figure 3 also shows that the M-BIII distribution was the best model for fitting this dataset.

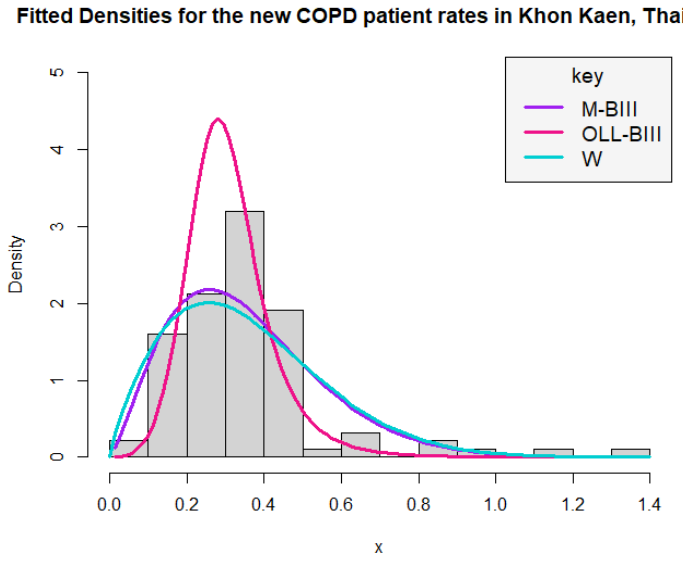

Figure 3.
The density plots for the M-BIII distribution and other comparative distributions for the new COPD patient rates in Khon Kaen, Thailand

Conclusion:

We proposed a novel distribution, the Maxwell–Burr III (M-BIII) distribution. The probability density function of proposed distribution could be right-skewed, right-skewed with a long right tail and almost symmetric. The basic properties of this distribution such as, survival, hazard, quantile and moment functions were explored. The hazard curve of the proposed distribution could be increasing and decreasing. The simulation study based on a quantile function was conducted to evaluate the performance of the proposed distribution with the maximum likelihood estimators. The results show that, for parameter β and c the larger the sample size, the closer the estimators' value to the exact parameters' value but the estimator $\hat{k}$ is not as efficient at estimating as it could be for parameter k. Finally, application of the propose distribution are displayed through model real data relating to the new COPD patient rates in Khon Kaen, Thailand between October 2014 to 25 July 2022. The result based on AIC and CAIC indicated that the M-BIII performed the best among OLL-BIII and W distributions.

Acknowledgements:

The Development and Promotion of Science and Technology Talents Project (DPST) is acknowledged.

References:

1. Ali A, Hasnain S A, Ahmad M. Pak J Stat. 2015; 31: 697-708.
2. Burr I W. Ann Math Stat. 1942; 13: 215-232.
3. Chakraborty S, Handique L, Usman R M. Ann Data Sci. 2020; 7: 17-31.
4. Cordeiro G M, Gomes A M, da-Silva C Q, Ortega E M. J Stat Dist Appl. 2017; 4-24.
5. Handique L,Muhammad U R, Chakraborty S. Thail Stat. 2020; 18(3): 267-280.
6. Haq M A,Afify A Z, Mofleh H A, Usman R M, Alqawba M, Sarg A M. Pak J Stat. 2021; 17(1): 1-14.
7. Ishaq A I, Abiodun A A. Ann Data Sci. 2020; 7(4): 639-662.

TIME REDUCTION METHOD FOR HEURISTIC ALGORITHMS USING LOCAL TEMPORAL MEMORY

Yuno Otsuka, Wasakorn Laesanklang *
*wasakorn.lae@mahidol.ac.th
Department of Mathematics, Faculty of Science, Mahidol University, Bangkok, Thailand

Abstract:

Vehicle routing problem in an urban area is challenging mainly because travel times vary by traffic during the day. Therefore, using a single time frame to create the whole routing plan would deviate from the result and result in fewer efficiency plans. In addition, the Bangkok travel time approximation is currently available as road traffic data are constantly collected by the intelligent traffic information center foundation using traffic CCTV cameras, traffic probes on public transport, and probe applications on mobile phones. The real-time traffic data can be acquired through a traffic data provider, where the data package can be requested online by the map application interface. However, acquiring ad-hoc traffic data is time-consuming, especially when using heuristic algorithms for the vehicle routing problem. Therefore, this project implements a temporal cache of traffic data on-premise to reduce the communication time used by the map application interface. The result showed that applying the cache allowed the heuristic algorithm to search for more solutions and get better solutions.

Introduction:

Several algorithms were developed for designing vehicle routing to deliver customer parcels to their places. But some people may overlook one problem, the accuracy of the time. To see this, suppose the algorithm is solved at 6 AM. which means the data for computing is based on 10 AM., and assume that the vehicle delivers some package at 2 PM, a different timeframe, so the number of cars on the road with different timeframe may not be the same. If that road has a clear street and 10 AM but traffic jams at 2 PM, delivering other packages on the other road may lead to a better way. That is, computing the algorithms in a single timeframe can lead to a huge error. And fetching the data within an accurate timeframe is a time-consuming process. That is the problem is there a lot of time-consuming for fetching the different timeframe traffic data and those data are important because they can provide more efficiency for algorithms that are used since the algorithms will know more accurate detail which may lead to better routing management or the better solution. So, when the algorithms construct the vehicle routing, if the algorithms use different timeframe traffic data it will then use a long computation time.

Due to the number of vehicles and stops, the exact algorithms for finding the optimal solution are not decent. To see this, the number of solutions due to this particular problem can have at most $P(s\text{-}v\text{-}1,v\text{-}1)$ solutions where s is the number of stops and v is the number of vehicles, and $P(n,k) = \frac{n!}{k!}$ is the number of permutation of k object in n objects since we can arrange s stops in the straight line and put in-distinguish $v\text{-}1$ pegs into this straight line for partition those stops into the subsets of stops which mean those subsets are the set of customer stops that have been allocated to the vehicles. Since the number of different permutations of $s+v\text{-}1$ objects with $v\text{-}1$ in-distinguish objects equals $P(s+v\text{-}1,v\text{-}1)$ so do the number of different solutions to the CVRP problem. Since this project uses 10 vehicles and 100 stops, if all possible solutions valid the constraints, there are at most $P(100+10\text{-}1,10\text{-}1)$ =

P(109,10-1) = 3.978889944892233 × 10^{170} different solutions, which exact algorithms can be doomed, due to the prominent big number of the possible solution.

One way to fix the time-consuming process can be divided into two parts. First, fetch the data within a different timeframe and save them to the cache, the data containers. Then executing the program with cache, and those data in cache will be held in a temporal memory or the high-speed data storage, which the algorithms can receive those data directly. That is the algorithms can run per se without fetching the different timeframe traffic data because the cache is already provided.

Unfortunately, filling all of the data in the matrix form in any timeframe is time-consuming. It takes several minutes for filling just one single timeframe. But the total timeframe on that day is 1440 timeframes which came from slowly increasing 1 minute from midnight to 11.59 PM. To collect all of the timeframes, it should take a time at least 14400 minutes or 4 hours to compute the single solution. So maybe the approximation will do the trick which means selecting some of the timeframes, not all of them to reduce the time consumption.

Notice that two kinds of APIs are used for fetching the distance data between two locations and the APIs that respond in the matrix form are going to be used to store the timeframe traffic data. Also, the initial and destination location limits are 8 and 400 locations, respectively.

So, to fill the matrix in a single time frame, there needs to be the matrix that keeps the distance and duration data between places and places, vehicles (from the start location at the depot) and places, and places to the vehicles because the distance and duration between outward and returning can be different. So, if there are n stops and v vehicles, the matrix APIs must call $\lceil \frac{n}{8} \rceil \lceil \frac{n}{400} \rceil$ times, $\lceil \frac{v}{8} \rceil \lceil \frac{n}{400} \rceil$ times, and $\lceil \frac{n}{8} \rceil \lceil \frac{v}{400} \rceil$ times respectively. Notice that for the real number x, $\lceil x \rceil$ is the integer such that $x \leq \lceil x \rceil < x + 1$

This project will construct the cache in 2 different ways. The first way to construct is using some of the timeframe traffic data but not all of them since the process of constructing the cache is a time-consuming process, then using them to approximate the real data. If there are lots of errors or not worthy then do the second way. The second way is to construct by using all of the necessary timeframes. Then after constructing the cache, compare the algorithms that use and do not use the cache, to see the efficiency. After those experiments will be a conclusion and suggestion.

Methodology:

This project uses heuristic algorithms instead, using the saving algorithms motley with VNS algorithms to improve the solution. When adding any stop to each vehicle route must not violate the constraint. In the VNS algorithm, the local search process will select the random two random routes and select a random stop in one of those routes then try to add the random stop into the other random route until the end of the local search iteration. There are three stages in the perturbing phase of **VNS** algorithms, the first stage is to destroy one of the solutions and try to add each stop in this solution to another route. If there is any remaining stop, then do the second stage which will select the random route and try to add the remaining stop by removing each stop in that random route, if adding a remaining stop by removing the other stop in any random route validate the constraint, then add it into that route and update the route, also put the removed stop to the remaining list of stops, the first stage will be terminated when access limit of the iteration of this stage which is 100 iterations. The final stage is similar to the previous stage, instead of removing two stops of the random route and the iterations limit at 150 iterations. Finally, the remaining stops will be designated to the vehicle whose route has been destroyed at the first stage. That is the algorithms are

guaranteed to be terminated when run of the iterations and for each iteration, each task can be done fast since each process of any task is done iteratively.
From the APIs *https://maps-api.rtic-thai.info/v0.1/distancematrix,* the results of the response are already in the matrix form. So, using a 2-dimensional array is decent for those. Notice that Python is the programing language used in this project. The built-in data structure is a list, a dynamic array instead of an array.

To be able to use the array in Python, there needs to include one of the famous libraries called NumPy which relies on C++, a very fast run time programing language. So, the simple process is creating the NumPy array for keeping the list of the different request timeframe traffic data that have already transformed from **JSON** format to Python code and then moving those response data into the 2-dimensional array. Notice that the idea of a procedure or pseudo-code can be expressed below.

```
import JSON library;
import NumPy library;

function building_cache (n×n matrix [1…n][1…n]: response_data)
       NumPy array: d = new array with length n
              from i = 1 to i = n
              d[i] = new array with length n;
       from j = 1 to j = n
       d[i][j] = response_data[i][j]
       return d;

array: a = new array with a length of the total timeframe traffic data;
for each t in different timeframe traffic data with ascending order
       JSON data: response = send the request data to the APIs with
                                          departure time t;
       2-dimensional array t = turn JSON data to the Python code with JSON
                               library.
       Send t to the function building_cache and then append those 2-dimensional
       array from into the array a;
```

The next task is to save the array "***a"*** from the above procedure, list of the 2-dimensional arrays, into a single file. That is the data in a cache is the data in array "***a".***

First will examine the approximation data on some different timeframes, if it cannot use for the approximate full of timeframe, then do another experiment that will fetch all of the timeframes to the cache. Then after the timeframe problem has been solved, so apply it to the saving algorithms and ***VNS*** algorithm to determine the efficiency after applying. Remark that for fetching the timeframe traffic data to fill the matrix, with APIs *https://maps-api.rtic-thai.info/v0.1/distancematrix.* **APIs** provide the result in matrix form.

Since the cache has a gap between the contiguous timeframe as close as possible since the fineness of time from APIs is in the unit of a minute. then apply cache to the algorithms and compare the iterations between those who use the cache and those who do not. Notice that when the algorithm runs out of iteration, it will be finished for finding a better solution. So, comparing the iteration can identify the efficiency between them.

Results and Discussion:

When fetching the data in one timeframe, gathering the data ideally should not consume lots of time since the heuristic algorithm has been applied. First, start with large gaps in the timeframe of data, which each gap takes 15 minutes. Adding each time frame to the list starts with index 0, so the following list will have 95 indices, because 1 day has 24

hours, and each hour fetches 4 different data timeframes. By running automated python scripts.

Now let's see whether this cache can use to approximate all of the timeframe traffic data. So, let's take the experiment by selecting the depot and other 100 stops to determine the distance between real and approximation distance. Several kinds of approximations are used, which are spline function, linear regression, and interpolation determined at one timeframe, chaotic one, which is 6:15 AM.

Let's use the spline function which is the method in numerical analysis for creating the function from the given data, and python language has a convenient way to use it by appl ying a Python library called **SciPy.**

Given ***rd*** refers to the real distance from depot to any stop from the given timeframe , ***ad*** refers to the approximation data which applies the previous condition. Let's examine the experiment in **figure 1**, **figure 2**, and **figure 3**

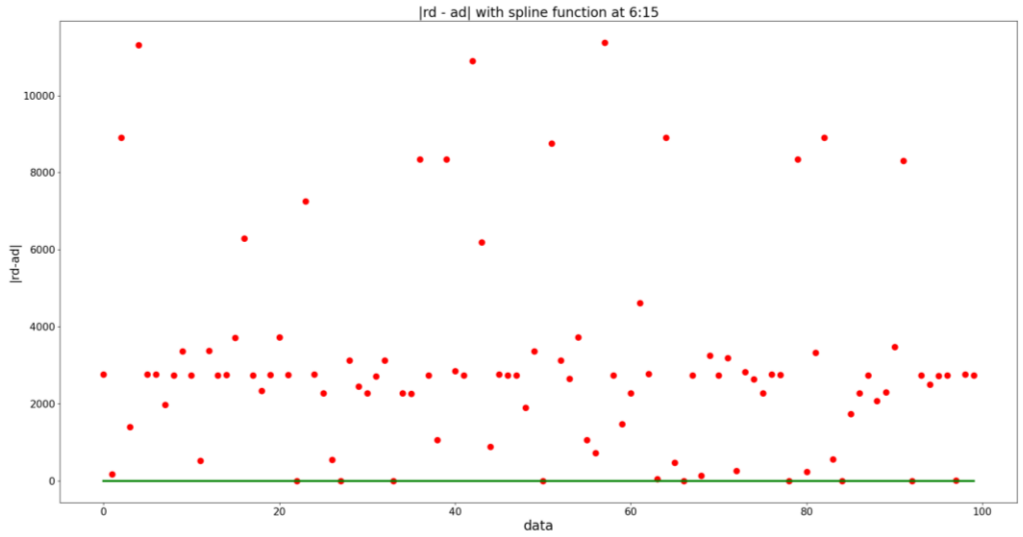

Figure 1.
|rd-ad| of spline function deviation plot.

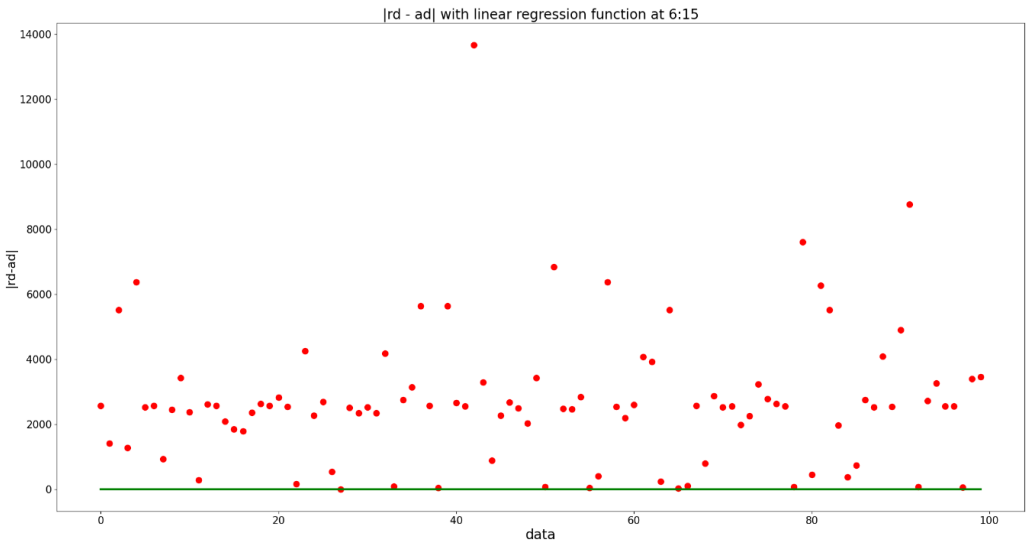

Figure 2.
|rd-ad| of linear regression function deviation plot.

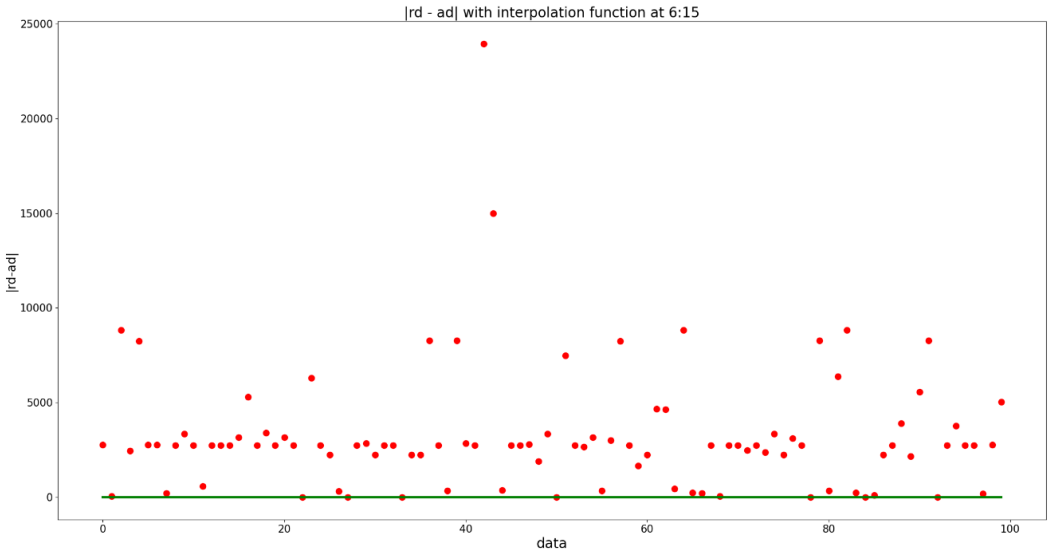

Figure 3.
|rd-ad| of interpolation function deviation plot.

As you can see through all of the figures. Most of the approximation data deviate at least 2 kilometers which is a huge error for all kinds of approximation methods that are used. Notice that we use a single timeframe which is 6.15 AM. and determine just one condition that the depot is the initial place. That is if there are different timeframes and different initial places such as some other particular stops in the CVRP problem, the problem should be more ardent. The one reason that occult behind the scene is the cache data use 6.67% of all timeframe traffic data because there are 96 timeframe traffic data out of 1,440 timeframe traffic data. So, if the gap between the contiguous timeframe is getting lower than 15, the cache must be more accurate at approximation.

So, if we want to use 50% of all data for the cache. There must be 720 data. And since each timeframe traffic data consumes around 10.8463 seconds. So, if we want to get 720 timeframe traffic data, there must be around 2 hours and 10 minutes to consume. So, I decide to adjust the strategy by using one day for gathering the timeframe traffic data. And use that data to solve the ***CVRP*** problem on the other days which can be solved in just a few minutes, due to the heuristic algorithms and the data already being fetched. Since the time for gathering data is not going to be a concern, this project will fetch all 1,440-timeframe traffic data. It should use around 4 hours and 20 minutes, and the next experiment will take on constructing the cache with all of the timeframe traffic data by using 1 minute on the gap between any two contiguous timeframes.

The results from **figure 4** show that fetching distance data between the depot and other stops at 12.15 PM. from 1,440 timeframe traffic data has no error from fetching directly from the APIs. First, the average time for solving the ***CVRP*** problem is 49.3813 seconds when using the cache, but it consumes 4 hours and 5 minutes. So, if we fix the time at 4 hours and 6 minutes plus one more minute due to the time-consuming heuristic algorithm, then apply the algorithms with no cache but will terminate when it hit 4 hours and 6 minutes and compare the iterations. The result is shown below in **figure 5**

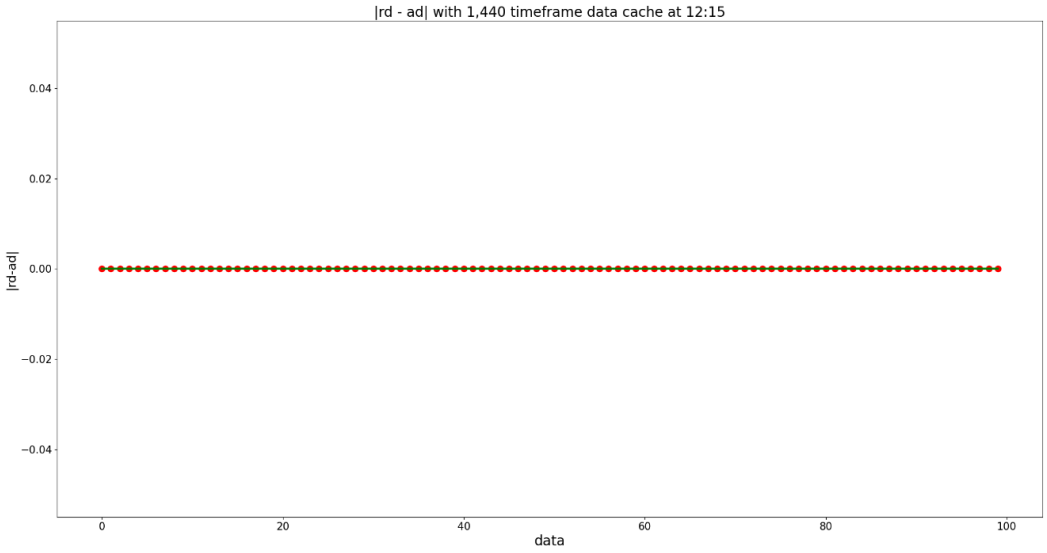

Figure 4.
|rd-ad| of 1,440 timeframe cache data.

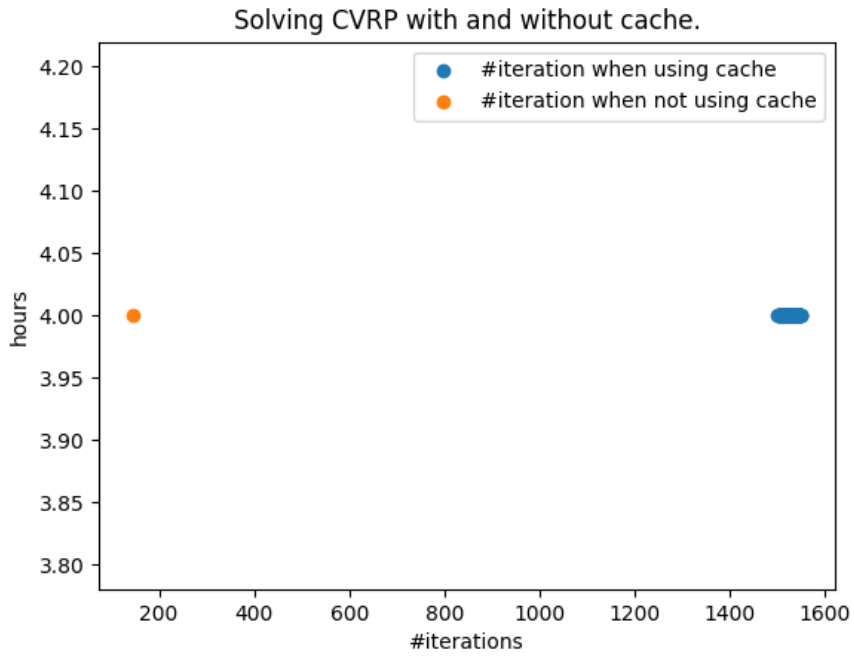

Figure 5.
Comparison of iterations between VNS algorithm with and without cache

So, the iterations when not using cache take 144 iterations while using cache take about 1,500 to 1,550 iterations. That is when using the cache, the iterations are approximately at least 10.7 times better than not using the cache. Through, the cache consumes 4785.5 MB of local temporal memory space, and that provides for 17,280,000 data since one timeframe traffic data contains the matrix between stops with 100×100 dimension, the matrix from the vehicle to the stops with 10×100 dimension, and the matrix from the stops to the vehicle with 100×10 dimension and there are 1,440 timeframe traffic data which use local temporal memory space of 276.9387 bytes per data.

Additionally, the trends of the consuming time with non-using cache when increasing stops from one stop to ten stops are growing exponentially in **figure 7 (left).** When increasing

the local search iteration from one to twenty iterations is also growing linearly in **figure 7 (right)**. Notice that both of them use a fixed number of vehicles which is 4, use fixed VNS iteration at 2, and fixed perturb iteration process at 5. **Figure 7 (left)** uses 15 iterations of local search.

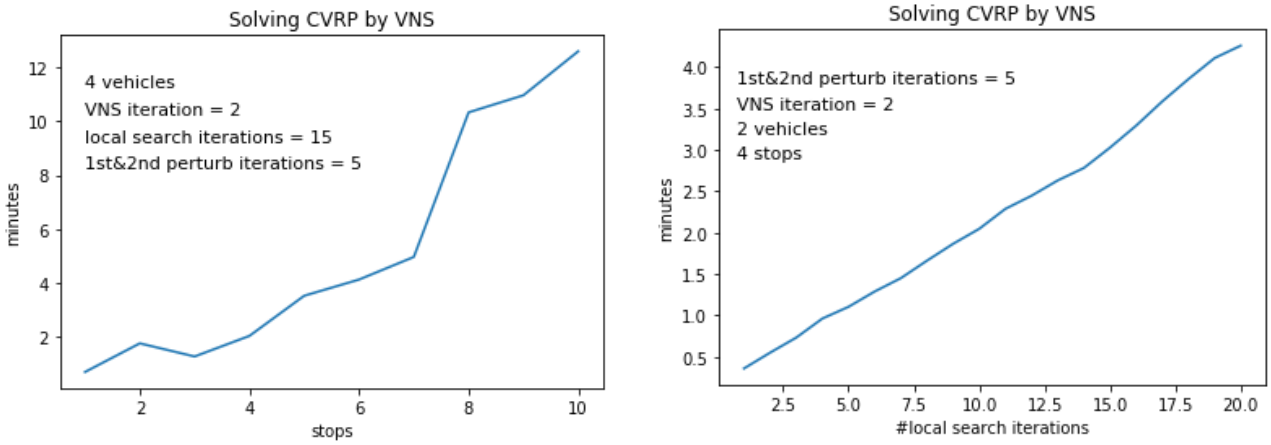

Figure 7.
The left figure shows the trend when increasing the stops, and the right figure shows the trend when increasing the local search iterations which both of them run without the cache.

Conversely, the trends of the consuming time when using cache when increasing stops from 50 stops to 100 stops are growing linearly with a small amount of slope shown in **figure 8 (left).** When increase the local search iteration from 1,500 iterations to 1,550 iterations is also growing linearly with a slight value of slope in **figure 8 (right)**. Notice that both of them use a fixed number of vehicles which is 10, use fixed VNS iteration at 2 and fixed perturb iteration process at 100 and 150. **Figure 8 (left)** uses 1,500 iterations of local search.

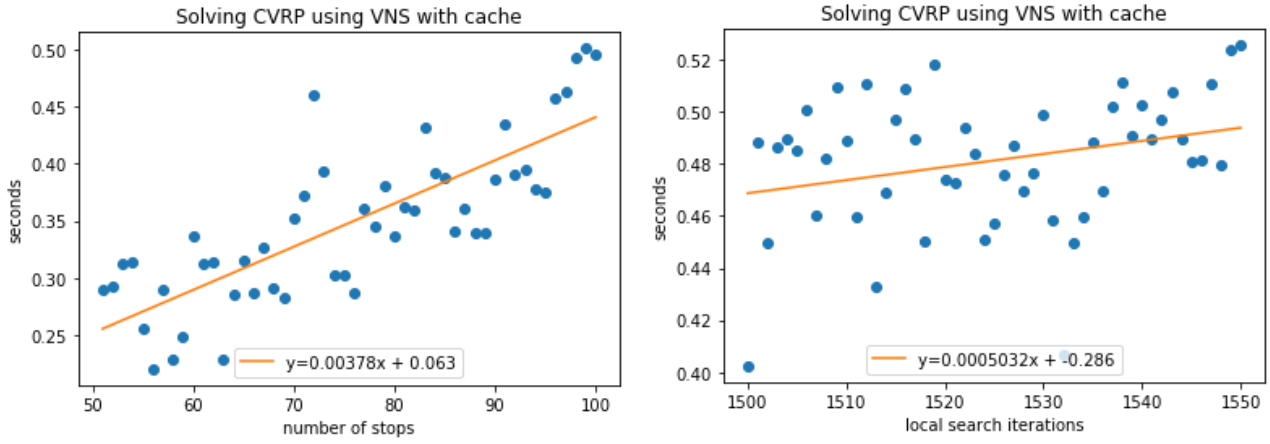

Figure 8:
The left figure shows the trend when increasing the stops, and the right figure shows the trend when increasing the local search iterations which both of them run with the cache.

Conclusion:

The vehicle routing problem can be solved with many algorithms. When the input is considered to be large, the heuristic algorithms will become august. This project use heuristic algorithms called saving algorithms and improve the solution by using VNS algorithms. The very important thing that algorithms rely on is the data between places such as the distance between 2 places which can be different when moving outward and returning, since it may use a different route. The accurate data can be received by fetching from the APIs but there are a lot of data to the gathering, and the problem turns out to be a lot of time-consuming while gathering the timeframe traffic data from the APIs. If the strategy is to use one day for gathering the data, then compute the CVRP problem on the other days, then build the cache with a minimum gap between each contiguous timeframe can resolve the problem of inaccurate data. The cache construction consumes a time of about 4 hours and 5 minutes and computes the CVRP problem in around 49 seconds, with 1500 to 1550 iterations, conversely in 4 hours and 6 minutes, when computing the CVRP problem without a cache, the maximum iteration is 144 iterations. The iterations can identify a better solution from the algorithms. Although there are about 10.7 times better iterations when using the cache, the local temporal memory moves up to 4785.5 MB.

Although the heuristic algorithm can compute the solution in polynomial time, without cache, the trend grows up exponentially when increasing the vehicle.

Nowadays, the world has cloud technology that uses another resource to compute the task, and the customer can rent those resources to compute some tasks. So, if the space complexity is a serious concern, I suggest using cloud technologies by running the algorithms with cache on the other resources. The cache is also flexible from the other algorithms which are different from this project since the cache is just some structure that stores lots of data.

Notice that the time and memory depend on the machines that are used for the experiment, This project focus on the trends of time complexity.

References:

1. G. Clarke, J. W. Wright: *Scheduling vehicles from a central delivery depot to several delivery points.* In: *Operations Research Quarterly.* Band 12, 1964, S. 568–581.
2. Nenad Mladenović; Pierre Hansen (1997). "Variable neighborhood search". *Computers and Operations Research*. **24** (11): 1097–1100.

WEIBULL–EXPONENTIAL DISTRIBUTION AND ITS PROPERTIES

Kusuman Pongpaew, Nawarat Ekkarntrong
School of Mathematics, Khon Kaen University, Khon Kaen 40002, Thailand
*E-mail: Kusuman_po@kkumail.com

Abstract:

This project proposes a new distribution resulting from a finite mixture of weibull distribution and exponential distribution and discuss theoretical properties such as survival functions, hazard rate, kth moment, the generating function, order statistics and parameter estimation.

Introduction:

When mentioned to the model used to describe the damage data. We will think of exponential gamma pareto weibull, which is a distribution involving continuous random variables. The damage data may come from many data sources, which may behave differently as the exponential distribution is a continuous probability distribution that often concerns the amount of time until some specific event happens, and the weibull distribution is used to analyse life data, model failure times and access product reliability. Both distributions belong to the same family and are used to describe similar information. The researcher was therefore interested in creating a new distribution from these two distributions. Assuming to use the parameter some of the same. In statistical research, new distributions are created in several ways. Many researchers have been interested in the new distribution that has exponential distribution. In 1988, M. M. Nassar [7] proposed Exponential-Exponential distribution from finite mixture distribution. The properties include cumulative distribution function, probability density function and hazard rate function. And In 1998, Jiang and Murthy [5] proposed Weibull-Weibull distribution from finite mixture distribution. The properties include Cumulative Distribution Function, Probability Density Function, and hazard rate function. There are also other distributions resulting from finite mixture distribution, such as gamma-exponential distribution, exponentiated exponential – exponential distribution, beta-exponential distribution, etc.

In this project, we will create a new distribution from a finite mixture of weibull distribution and exponential distribution. We also investigate the theoretical properties of the new distribution, including the survival functions, hazard rate, kth moment, the generating function, order statistics and parameter estimation.

Results and Discussion:

Let X be a random variable from weibull - exponential distribution with parameters α, θ, τ and usually denoted $X \sim WE(\alpha, \theta, \tau)$, then the cumulative density function of the proposed distribution of random variable X are respectively of the form:

$$F_{WE}(x) = \alpha\, F_W(x) + (1-\alpha)F_E(x) \text{ when } x > 0, 0 < \alpha < 1$$

where $F_W(x) = 1 - e^{-(x/\theta)^\tau}$ and $F_E(x) = 1 - e^{-(x/\theta)}$ when $x > 0, \theta > 0.$

That is,

$$\begin{aligned} F_{WE}(x) &= \alpha\left(1 - e^{-(x/\theta)^{\tau}}\right) + (1-\alpha)\left(1 - e^{-(x/\theta)}\right) \\ &= \alpha - \alpha\, e^{-(x/\theta)^{\tau}} + 1 - e^{-(x/\theta)} - \alpha + \alpha\, e^{-(x/\theta)} \\ &= 1 - \alpha\, e^{-(x/\theta)^{\tau}} - (1-\alpha)e^{-(x/\theta)} \end{aligned} \quad (1)$$

where $x > 0, 0 < \alpha < 1, \theta > 0$ and $\tau > 0$.

The graph of the cumulative density function is shown in Figure 1.

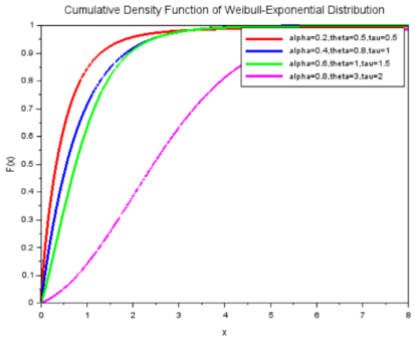

Figure 1.
Graph of cumulative density function of weibull - exponential distribution.

Define the probability density function as follows:

$$f_{WE}(x) = \frac{\alpha\tau(x/\theta)^{\tau-1}e^{-(x/\theta)^{\tau}} + (1-\alpha)e^{-(x/\theta)}}{\theta} \quad (2)$$

The graph of the probability density function is shown in Figure 2.

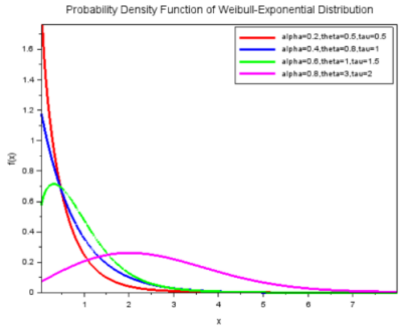

Figure 2.
Graph of probability density function of weibull - exponential distribution.

The survival function is

$$S_{WE}(x) = \alpha\, e^{-(x/\theta)^{\tau}} + (1-\alpha)e^{-(x/\theta)} \quad (3)$$

The hazard rate is

$$h_{WE}(x) = \frac{\alpha\tau(x/\theta)^{\tau-1}e^{-(x/\theta)^{\tau}} + (1-\alpha)e^{-(x/\theta)}}{\theta}\left(1 - \left[1 - \alpha\, e^{-(x/\theta)^{\tau}} - (1-\alpha)e^{-(x/\theta)}\right]\right)^{-1} \quad (4)$$

1. Moments

THEOREM1 The kth raw moment of a random variable X, where $X \sim WE(\alpha, \theta, \tau)$ and $0 < \alpha < 1, \theta > 0, \tau > 0$ is given by

$$\mu'_k = E[X^k] = \theta^k\left[\alpha\Gamma\left(\frac{k}{\tau} + 1\right) + (1-\alpha)\Gamma(k+1)\right]$$

Proof Let $X \sim WE(\alpha, \theta, \tau)$

$$\begin{aligned}\mu'_k &= E[X^k] \\ &= \int_0^\infty x^k f_{WE}(x)dx \\ &= \int_0^\infty x^k \left[\frac{\alpha\tau(x/\theta)^{\tau-1}e^{-(x/\theta)^\tau}}{\theta} + \frac{(1-\alpha)e^{-(x/\theta)}}{\theta}\right]dx \\ &= \left(\frac{\alpha\tau}{\theta}\right)\int_0^\infty x^k(x/\theta)^{\tau-1}e^{-(x/\theta)^\tau}\,dx + \left(\frac{1-\alpha}{\theta}\right)\int_0^\infty x^k e^{-(x/\theta)}\,dx. \qquad (5)\end{aligned}$$

Let $I_1 = \left(\frac{\alpha\tau}{\theta}\right)\int_0^\infty x^k(x/\theta)^{\tau-1}e^{-(x/\theta)^\tau}\,dx$ and $I_2 = \left(\frac{1-\alpha}{\theta}\right)\int_0^\infty x^k e^{-(x/\theta)}\,dx$.

Consider, I_1 ; set $y = (x/\theta)^\tau$, $x = \theta y^{\frac{1}{\tau}}$ and $dx = \frac{\theta}{\tau}y^{(1-\tau)/\tau}dy$,

$$\begin{aligned}I_1 &= \left(\frac{\alpha\tau}{\theta}\right)\int_0^\infty \left(\theta y^{\frac{1}{\tau}}\right)^k (\theta y^{\frac{1}{\tau}}/\theta)^{\tau-1}\frac{\theta}{\tau}y^{(1-\tau)/\tau}dy \\ &= \alpha\theta^k\int_0^\infty y^{\frac{k}{\tau}}e^{-y}dy \\ &= \alpha\theta^k\int_0^\infty y^{\left(\frac{k}{\tau}+1\right)-1}e^{-y}dy \\ &= \alpha\theta^k\Gamma\left(\frac{k}{\tau}+1\right). \qquad (6)\end{aligned}$$

Consider, $I_2 = \left(\frac{1-\alpha}{\theta}\right)\int_0^\infty x^k e^{-(x/\theta)}\,dx$; set $u = x/\theta$, $x = u\theta$ and $dx = \theta du$,

$$\begin{aligned}I_2 &= \left(\frac{1-\alpha}{\theta}\right)\int_0^\infty (u\theta)^k e^{-u}\theta du \\ &= (1-\alpha)\theta^k\int_0^\infty u^k e^{-u}du \\ &= (1-\alpha)\theta^k\int_0^\infty u^{(k+1)-1}e^{-u}du \\ &= (1-\alpha)\theta^k\Gamma(k+1). \qquad (7)\end{aligned}$$

Upon substituting $I_1$and I_2into (5) The kth raw moment of X is giving by

$$\mu'_k = \theta^k\left[\alpha\Gamma\left(\frac{k}{\tau}+1\right) + (1-\alpha)\Gamma(k+1)\right]$$

and expected value of X is

$$E[X] = \theta\left[\alpha\Gamma\left(\frac{1}{\tau}+1\right) + (1-\alpha)\Gamma(2)\right].$$

THEOREM2 The kth central moment of X, where $X \sim WE(\alpha, \theta, \tau)$ and $0 < \alpha < 1, \theta > 0$, $\tau > 0$ is given by

$$\mu_k = E[(x-\mu)^k] = \sum_{r=0}^{k}\binom{k}{r}(-1)^r\mu^r\theta^{(k-r)}\left[\alpha\Gamma\left(\frac{k-r}{\tau}+1\right) + (1-\alpha)\Gamma(k-r+1)\right]$$

Proof Let $X \sim WE(\alpha, \theta, \tau)$

$$\begin{aligned}\mu'_k &= E[(x-\mu)^k] \\ &= \int_0^\infty (x-\mu)^k f_{WE}(x)dx \\ &= \int_0^\infty (x-\mu)^k \left[\frac{\alpha\tau(x/\theta)^{\tau-1}e^{-(x/\theta)^\tau}}{\theta} + \frac{(1-\alpha)e^{(x/\theta)}}{\theta}\right]dx \\ &= \left(\frac{\alpha\tau}{\theta}\right)\int_0^\infty (x-\mu)^k(x/\theta)^{\tau-1}e^{-(x/\theta)^\tau}\,dx + \left(\frac{1-\alpha}{\theta}\right)\int_0^\infty (x-\mu)^k e^{-(x/\theta)}\,dx\end{aligned}$$

$$= \left(\frac{\alpha\tau}{\theta}\right)\int_0^{\infty}\sum_{r=0}^{k}\binom{k}{r}(-1)^r x^{k-r}\mu^r\left(\frac{x}{\theta}\right)^{\tau-1}e^{-\left(\frac{x}{\theta}\right)^{\tau}}dx$$
$$+ \left(\frac{1-\alpha}{\theta}\right)\int_0^{\infty}\sum_{r=0}^{k}\binom{k}{r}(-1)^r x^{k-r}\mu^r e^{-(x/\theta)}dx$$
$$= \left(\frac{\alpha\tau}{\theta}\right)\sum_{r=0}^{k}\binom{k}{r}(-1)^r\mu^r\int_0^{\infty}x^{k-r}\left(\frac{x}{\theta}\right)^{\tau-1}e^{-\left(\frac{x}{\theta}\right)^{\tau}}dx$$
$$+ \left(\frac{1-\alpha}{\theta}\right)\sum_{r=0}^{k}\binom{k}{r}(-1)^r\mu^r\int_0^{\infty}x^{k-r}e^{-(x/\theta)}dx \quad (8)$$

Let $I_1 = \left(\frac{\alpha\tau}{\theta}\right)\sum_{r=0}^{k}\binom{k}{r}(-1)^r\mu^r\int_0^{\infty}x^{k-r}\left(\frac{x}{\theta}\right)^{\tau-1}e^{-\left(\frac{x}{\theta}\right)^{\tau}}dx$
and $I_2 = \left(\frac{1-\alpha}{\theta}\right)\sum_{r=0}^{k}\binom{k}{r}(-1)^r\mu^r\int_0^{\infty}x^{k-r}e^{-(x/\theta)}dx$.

Consider, I_1 ; set $y = (x/\theta)^{\tau}$, $x = \theta y^{\frac{1}{\tau}}$ and $dx = \frac{\theta}{\tau}y^{(1-\tau)/\tau}dy$,

$$I_1 = \left(\frac{\alpha\tau}{\theta}\right)\sum_{r=0}^{k}\binom{k}{r}(-1)^r\mu^r\int_0^{\infty}\left(\theta y^{\frac{1}{\tau}}\right)^{k-r}(\theta y^{\frac{1}{\tau}}/\theta)^{\tau-1}\frac{\theta}{\tau}y^{(1-\tau)/\tau}dy$$
$$= \alpha\sum_{r=0}^{k}\binom{k}{r}(-1)^r\mu^r\theta^{k-r}\int_0^{\infty}y^{\frac{k-r}{\tau}}e^{-y}dy$$
$$= \alpha\sum_{r=0}^{k}\binom{k}{r}(-1)^r\mu^r\theta^{k-r}\int_0^{\infty}y^{\left(\frac{k-r}{\tau}+1\right)-1}e^{-y}dy$$
$$= \alpha\sum_{r=0}^{k}\binom{k}{r}(-1)^r\mu^r\theta^{k-r}\Gamma\left(\frac{k-r}{\tau}+1\right). \quad (9)$$

Consider, $I_2 = \left(\frac{1-\alpha}{\theta}\right)\sum_{r=0}^{k}\binom{k}{r}(-1)^r\mu^r\int_0^{\infty}x^{k-r}e^{-\left(\frac{x}{\theta}\right)}dx$; set $u = \frac{x}{\theta}$, $x = u\theta$ and $dx = \theta du$.

$$I_2 = \left(\frac{1-\alpha}{\theta}\right)\sum_{r=0}^{k}\binom{k}{r}(-1)^r\mu^r\int_0^{\infty}(u\theta)^{k-r}e^{-u}\theta du$$
$$= (1-\alpha)\sum_{r=0}^{k}\binom{k}{r}(-1)^r\mu^r\theta^{k-r}\int_0^{\infty}u^{k-r}e^{-u}du$$
$$= (1-\alpha)\sum_{r=0}^{k}\binom{k}{r}(-1)^r\mu^r\theta^{k-r}\int_0^{\infty}u^{(k-r+1)-1}e^{-u}du$$
$$= (1-\alpha)\sum_{r=0}^{k}\binom{k}{r}(-1)^r\mu^r\theta^{k-r}\Gamma(k-r+1). \quad (10)$$

Upon substituting $I_1$and I_2into (8) The kth central moment of X is giving by

$$\sum_{r=0}^{k}\binom{k}{r}(-1)^r\mu^r\theta^{(k-r)}\left[\alpha\Gamma\left(\frac{k-r}{\tau}+1\right)+(1-\alpha)\Gamma(k-r+1)\right]$$

2. Tail Distribution

THEOREM3 Let $X \sim WE(\alpha,\theta,\tau)$.
Consider, tail of X by moment is giving by X has the kth raw moment for all k.
Thus, X is a light tail.

3. The Generating Function

THEOREM4 Let $X \sim WE(\alpha,\theta,\tau)$ and $x > 0, 0 < \alpha < 1, \theta > 0, \tau > 0$. The moment-generating function of X is given by

$$M_X(z) = E[e^{zX}] = \alpha\sum_{n=0}^{\infty}\frac{(z\theta)^n}{n!}\Gamma\left(\frac{n}{\tau}+1\right)+\frac{1-\alpha}{1-z\theta} \quad \text{when } z < 1/\theta.$$

Proof Let $X \sim WE(\alpha,\theta,\tau)$.

$$E[e^{zX}] = \int_0^{\infty}e^{zx}f_{WE}(x)dx$$
$$= \int_0^{\infty}e^{zx}\left[\frac{\alpha\tau(x/\theta)^{\tau-1}e^{-(x/\theta)^{\tau}}}{\theta}+\frac{(1-\alpha)e^{(x/\theta)}}{\theta}\right]dx$$
$$= \left(\frac{\alpha\tau}{\theta}\right)\int_0^{\infty}(x/\theta)^{\tau-1}e^{zx-(x/\theta)^{\tau}}dx + \left(\frac{1-\alpha}{\theta}\right)\int_0^{\infty}e^{zx}e^{-(x/\theta)}dx \quad (11)$$

Let $I_1 = \left(\frac{\alpha\tau}{\theta}\right)\int_0^\infty (x/\theta)^{\tau-1} e^{zx-(x/\theta)^\tau}\,dx$ and $I_2 = \left(\frac{1-\alpha}{\theta}\right)\int_0^\infty e^{zx}e^{-(x/\theta)}\,dx$.

Consider, I_1 ; set $u = (x/\theta)$, $du = \frac{1}{\theta}dx$ and $x = \theta u$,

$$\begin{aligned} I_1 &= \left(\frac{\alpha\tau}{\theta}\right)\int_0^\infty u^{\tau-1} e^{z\theta u-u^\tau}\theta du \qquad (\because u = x/\theta) \\ &= \alpha\tau\int_0^\infty x^{\frac{1}{\tau}(\tau-1)} e^{z\theta x^{\frac{1}{\tau}}}e^{-x}\frac{1}{\tau x^{\frac{1}{\tau}(\tau-1)}}dx \quad (\because x = u^\tau, u = x^{\frac{1}{\tau}}, du = \frac{1}{\tau x^{\frac{1}{\tau}(\tau-1)}}dx) \\ &= \alpha\tau\int_0^\infty e^{z\theta x^{\frac{1}{\tau}}} e^{-x}dx \\ &= \alpha\tau\int_0^\infty \sum_{n=0}^\infty \frac{(z\theta)^n}{n!} x^{\frac{n}{\tau}} e^{-x}dx \\ &= \alpha\tau\sum_{n=0}^\infty \frac{(z\theta)^n}{n!}\int_0^\infty x^{\left(\frac{n}{\tau}+1\right)-1} e^{-x}dx \\ &= \alpha\tau\sum_{n=0}^\infty \frac{(z\theta)^n}{n!}\Gamma\left(\frac{n}{\tau}+1\right) \end{aligned} \tag{12}$$

Consider, $I_2 = \left(\frac{1-\alpha}{\theta}\right)\int_0^\infty e^{zx}e^{-(x/\theta)}\,dx$,

$$\begin{aligned} I_2 &= \left(\frac{1-\alpha}{\theta}\right)\int_0^\infty e^{x(z-1/\theta)}dx \\ &= \left(\frac{1-\alpha}{\theta}\right)\int_0^\infty e^{x\left(z-\frac{1}{\theta}\right)}\frac{1}{z-\frac{1}{\theta}}d(x(z-\tfrac{1}{\theta})) \\ &= \left(\frac{1-\alpha}{\theta}\right)\left(\frac{1}{z-\frac{1}{\theta}}\right)\lim_{b\to\infty}\left[e^{x(z-1/\theta)}\right]_0^b \\ &= \left(\frac{1-\alpha}{\theta}\right)\left(\frac{1}{z-\frac{1}{\theta}}\right)\lim_{b\to\infty}\left[e^{b(z-1/\theta)}-1\right] \\ &= \left(\frac{1-\alpha}{\theta}\right)\left(\frac{1}{z-\frac{1}{\theta}}[0-1]\right) \qquad \text{when } z < 1/\theta \\ &= \left(\frac{1-\alpha}{\theta}\right)\left(\frac{\theta}{1-z\theta}\right) \qquad \text{when } z < 1/\theta \\ &= \frac{1-\alpha}{1-z\theta} \qquad \text{when } z < 1/\theta \end{aligned} \tag{13}$$

Upon substituting $I_1$and I_2into (13) The moment-generating function of X is giving by

$$M_X(z) = \alpha\sum_{n=0}^\infty \frac{(z\theta)^n}{n!}\Gamma\left(\frac{n}{\tau}+1\right) + \frac{1-\alpha}{1-z\theta} \quad \text{when } z < 1/\theta.$$

THEOREM5 Let $X \sim WE(\alpha,\theta,\tau)$ and $x > 0, 0 < \alpha < 1,\ \theta > 0, \tau > 0$. The probability generating function of X is given by

$$P_X(z) = M_X(\ln z) = \alpha\sum_{n=0}^\infty \frac{(\ln z\theta)^n}{n!}\Gamma\left(\frac{n}{\tau}+1\right) + \frac{1-\alpha}{1-\ln z\theta} \quad \text{when } z < e^{1/\theta} \tag{14}$$

where $0 < \alpha < 1,\ \theta > 0, \tau > 0$.

4. Characteristic function

THEOREM6 The characteristic function of X, where $X \sim WE(\alpha,\theta,\tau)$ and $x > 0, 0 < \alpha < 1,\ \theta > 0, \tau > 0$. The characteristic function of X is given by

$$\varphi_X(z) = E\left[e^{izX}\right] = \alpha\sum_{n=0}^\infty \frac{(iz\theta)^n}{n!}\Gamma\left(\frac{n}{\tau}+1\right) + \frac{1-\alpha}{1-iz\theta} \quad \text{when } z < i/\theta.$$

Proof Let $X \sim WE(\alpha, \theta, \tau)$.

$$E\left[e^{izX}\right] = \int_0^\infty e^{izx} f_{WE}(x)dx$$
$$= \int_0^\infty e^{izx}\left[\frac{\alpha\tau(x/\theta)^{\tau-1}e^{-(x/\theta)^\tau}}{\theta} + \frac{(1-\alpha)e^{(x/\theta)}}{\theta}\right]dx$$
$$= \left(\frac{\alpha\tau}{\theta}\right)\int_0^\infty (x/\theta)^{\tau-1}e^{izx-(x/\theta)^\tau}\,dx + \left(\frac{1-\alpha}{\theta}\right)\int_0^\infty e^{izx}e^{-(x/\theta)}\,dx \quad (15)$$

Let $I_1 = \left(\frac{\alpha\tau}{\theta}\right)\int_0^\infty (x/\theta)^{\tau-1}e^{izx-(x/\theta)^\tau}\,dx$ and $I_2 = \left(\frac{1-\alpha}{\theta}\right)\int_0^\infty e^{izx}e^{-(x/\theta)}\,dx$.

Consider, I_1 ; set $u = (x/\theta)$, $du = \frac{1}{\theta}dx$ and $x = \theta u$,

$$I_1 = \left(\frac{\alpha\tau}{\theta}\right)\int_0^\infty u^{\tau-1}\,e^{iz\theta u-u^\tau}\theta du \qquad (\because u = x/\theta)$$
$$= \alpha\tau\int_0^\infty x^{\frac{1}{\tau}(\tau-1)}\,e^{iz\theta x^{\frac{1}{\tau}}}e^{-x}\frac{1}{\tau x^{\frac{1}{\tau}(\tau-1)}}dx \quad (\because x = u^\tau, u = x^{\frac{1}{\tau}}, du = \frac{1}{\tau x^{\frac{1}{\tau}(\tau-1)}}dx)$$
$$= \alpha\tau\int_0^\infty e^{iz\theta x^{\frac{1}{\tau}}}\,e^{-x}dx$$
$$= \alpha\tau\int_0^\infty \sum_{n=0}^\infty \frac{(iz\theta)^n}{n!}x^{\frac{n}{\tau}}\,e^{-x}dx$$
$$= \alpha\tau\sum_{n=0}^\infty \frac{(iz\theta)^n}{n!}\int_0^\infty x^{\left(\frac{n}{\tau}+1\right)-1}\,e^{-x}dx$$
$$= \alpha\tau\sum_{n=0}^\infty \frac{(iz\theta)^n}{n!}\Gamma\left(\frac{n}{\tau}+1\right) \quad (16)$$

Consider, $I_2 = \left(\frac{1-\alpha}{\theta}\right)\int_0^\infty e^{izx}e^{-(x/\theta)}\,dx$,

$$I_2 = \left(\frac{1-\alpha}{\theta}\right)\int_0^\infty e^{x(iz-1/\theta)}dx$$
$$= \left(\frac{1-\alpha}{\theta}\right)\int_0^\infty e^{x\left(iz-\frac{1}{\theta}\right)}\frac{1}{iz-\frac{1}{\theta}}d(x(iz-\tfrac{1}{\theta}))$$
$$= \left(\frac{1-\alpha}{\theta}\right)\left(\frac{1}{iz-\frac{1}{\theta}}\right)\lim_{b\to\infty}\left[e^{x(iz-1/\theta)}\right]_0^b$$
$$= \left(\frac{1-\alpha}{\theta}\right)\left(\frac{1}{iz-\frac{1}{\theta}}\right)\lim_{b\to\infty}\left[e^{b(iz-1/\theta)}-1\right]$$
$$= \left(\frac{1-\alpha}{\theta}\right)\left(\frac{1}{iz-\frac{1}{\theta}}[0-1]\right) \qquad \text{when } z < i/\theta$$
$$= \left(\frac{1-\alpha}{\theta}\right)\left(\frac{\theta}{1-iz\theta}\right) \qquad \text{when } z < i/\theta$$
$$= \frac{1-\alpha}{1-iz\theta} \qquad \text{when } z < i/\theta \quad (17)$$

Upon substituting $I_1$and I_2into (15) The characteristic function of X is giving by

$$\alpha\sum_{n=0}^\infty \frac{(iz\theta)^n}{n!}\Gamma\left(\frac{n}{\tau}+1\right) + \frac{1-\alpha}{1-iz\theta} \qquad \text{when } z < i/\theta.$$

5. Order Statistics

THEOREM7 Let $X_1, X_2, \ldots, X_n$ are independent random variables and for $j = 1,2,3\ldots, n$. Let $X \sim WE(\alpha, \theta, \tau)$ where $x > 0, 0 < \alpha < 1, \theta > 0, \tau > 0$. The kth order statistics when $k = 1,2,3\ldots, n$ by

$$f_{k:n}(x) = \frac{n!}{(k-1)!(n-k)!}\left[1-\alpha\, e^{-(x/\theta)^\tau} - (1-\alpha)e^{-(x/\theta)}\right]^{k-1}$$
$$\left[1-(1-\alpha\, e^{-(x/\theta)^\tau} - (1-\alpha)e^{-(x/\theta)})\right]^{n-k}\left(\frac{\alpha\tau(x/\theta)^{\tau-1}e^{-(x/\theta)^\tau}+(1-\alpha)e^{-(x/\theta)}}{\theta}\right)$$

For $k = 1$

$$f_{1:n}(x) = \frac{n!}{(1-1)!(n-1)!}\left[1 - \alpha\, e^{-(x/\theta)^{\tau}} - (1-\alpha)e^{-(x/\theta)}\right]^{1-1}$$
$$[1 - (1 - \alpha\, e^{-(x/\theta)^{\tau}} - (1-\alpha)e^{-(x/\theta)})]^{n-1}\left(\frac{\alpha\tau(x/\theta)^{\tau-1}e^{-(x/\theta)^{\tau}} + (1-\alpha)e^{-(x/\theta)}}{\theta}\right)$$
$$= n[1 - (1 - \alpha\, e^{-(x/\theta)^{\tau}} - (1-\alpha)e^{-(x/\theta)})]^{n-1}\left(\frac{\alpha\tau(x/\theta)^{\tau-1}e^{-(x/\theta)^{\tau}} + (1-\alpha)e^{-(x/\theta)}}{\theta}\right)$$

and $k = n$

$$f_{n:n}(x) = \frac{n!}{(n-1)!(n-n)!}\left[1 - \alpha\, e^{-(x/\theta)^{\tau}} - (1-\alpha)e^{-(x/\theta)}\right]^{n-1}$$
$$[1 - (1 - \alpha\, e^{-(x/\theta)^{\tau}} - (1-\alpha)e^{-(x/\theta)})]^{n-n}\left(\frac{\alpha\tau(x/\theta)^{\tau-1}e^{-(x/\theta)^{\tau}} + (1-\alpha)e^{-(x/\theta)}}{\theta}\right)$$
$$= n\left[1 - \alpha\, e^{-(x/\theta)^{\tau}} - (1-\alpha)e^{-(x/\theta)}\right]^{n-1}\left(\frac{\alpha\tau(x/\theta)^{\tau-1}e^{-(x/\theta)^{\tau}} + (1-\alpha)e^{-(x/\theta)}}{\theta}\right)$$

6. Parameter Estimation

6.1. Method of moment estimation

THEOREM8 Let $X_1, X_2 \ldots, X_n \sim WE(\alpha, \theta, \tau)$ be a random sample and let $\widehat{\mu_k'} = \frac{1}{n}\sum_{j=1}^{n} x_j^k$.
For the first moment estimation, consider $\widehat{\mu_1'} = \mu_1'(\theta)$.
That is,

$$\frac{1}{n}\sum_{j=1}^{n} x_j^1 = \alpha\theta\Gamma\left(\frac{1}{\tau} + 1\right) + (1-\alpha)\theta\Gamma(2) \quad (18)$$

Thus, $\bar{X} = \theta\left[\alpha\Gamma\left(\frac{1}{\tau} + 1\right) + (1-\alpha)\Gamma(2)\right]$ where $\bar{X} = \frac{1}{n}\sum_{j=1}^{n} x_j^1$.
For the second moment estimation, consider $\widehat{\mu_2'} = \mu_2'(\theta)$.
That is,

$$\frac{1}{n}\sum_{j=1}^{n} x_j^2 = \alpha\theta^2\Gamma\left(\frac{2}{\tau} + 1\right) + (1-\alpha)\theta^2\Gamma(3) \quad (19)$$

For the third moment estimation, consider $\widehat{\mu_3'} = \mu_3'(\theta)$.
That is,

$$\frac{1}{n}\sum_{j=1}^{n} x_j^3 = \alpha\theta^3\Gamma\left(\frac{3}{\tau} + 1\right) + (1-\alpha)\theta^3\Gamma(4) \quad (20)$$

It is clear that equations (18) - (20) has no explicit analytical solution, hence, it can be solved numerically using Bisector Method, Newton-Raphson method, Secant method which are powerful techniques for solving nonlinear system of equations.

6.2. Maximum Likelihood (MLE)

Let $X_1, X_2 \ldots, X_n \sim WE(\alpha, \theta, \tau)$ be a random sample of size n, then the likelihood function denoted by L or $L(\alpha, \theta, \tau; x)$ is defined by

$$L(\alpha, \theta, \tau; x) = L(\alpha, \theta, \tau; x_1, x_2, \ldots, x_n)$$
$$= f_{WE}(x_1, x_2, \ldots, x_n; \alpha, \theta, \tau)$$
$$= f_{WE}(x_1; \alpha, \theta, \tau) f_{WE}(x_2; \alpha, \theta, \tau) \cdots f_{WE}(x_n; \alpha, \theta, \tau)$$
$$= \prod_{i=1}^{n} f_{WE}(x_i; \alpha, \theta, \tau)$$

and

$$l = \ln\ L(\alpha,\theta,\tau;x) = \ln\prod_{i=1}^{n} f_{WE}(x_i;\alpha,\theta,\tau)$$
$$= \ln\prod_{i=1}^{n}\left[\frac{\alpha\tau(x/\theta)^{\tau-1}e^{-(x/\theta)^{\tau}}+(1-\alpha)e^{-(x/\theta)}}{\theta}\right]$$
$$= \sum_{i=1}^{n}\ln\left[\frac{\alpha\tau(x/\theta)^{\tau-1}e^{-(x/\theta)^{\tau}}+(1-\alpha)e^{-(x/\theta)}}{\theta}\right]$$

For a parameter α,

$$\frac{\partial l}{\partial\alpha} = \sum_{i=1}^{n}\frac{\partial l}{\partial\alpha}\ln\left[\frac{\alpha\tau(x/\theta)^{\tau-1}e^{-(x/\theta)^{\tau}}+(1-\alpha)e^{-(x/\theta)}}{\theta}\right]$$
$$= \sum_{i=1}^{n}\frac{\theta}{\alpha\tau(x/\theta)^{\tau-1}e^{-(x/\theta)^{\tau}}+(1-\alpha)e^{-(x/\theta)}}\left[\frac{\partial}{\partial\alpha}\left(\frac{\alpha\tau(x/\theta)^{\tau-1}e^{-(x/\theta)^{\tau}}}{\theta}\right)+\frac{\partial}{\partial\alpha}\left(\frac{(1-\alpha)e^{-(x/\theta)}}{\theta}\right)\right]$$
$$= \sum_{i=1}^{n}\frac{\theta}{\alpha\tau(x/\theta)^{\tau-1}e^{-(x/\theta)^{\tau}}+(1-\alpha)e^{-(x/\theta)}}\left[\frac{\tau(x/\theta)^{\tau-1}e^{-(x/\theta)^{\tau}}}{\theta}-\frac{e^{-(x/\theta)}}{\theta}\right]. \quad (21)$$

For a parameter θ,

$$\frac{\partial l}{\partial\theta} = \sum_{i=1}^{n}\frac{\partial l}{\partial\theta}\ln\left[\frac{\alpha\tau(x/\theta)^{\tau-1}e^{-(x/\theta)^{\tau}}+(1-\alpha)e^{-(x/\theta)}}{\theta}\right]$$
$$= \sum_{i=1}^{n}\frac{\theta}{\alpha\tau(x/\theta)^{\tau-1}e^{-(x/\theta)^{\tau}}+(1-\alpha)e^{-(x/\theta)}}\left[\frac{\partial}{\partial\theta}\left(\frac{\alpha\tau(x/\theta)^{\tau-1}e^{-(x/\theta)^{\tau}}}{\theta}\right)+\frac{\partial}{\partial\theta}\left(\frac{(1-\alpha)e^{-(x/\theta)}}{\theta}\right)\right]$$
$$= \sum_{i=1}^{n}\frac{\theta}{\alpha\tau(x/\theta)^{\tau-1}e^{-(x/\theta)^{\tau}}+(1-\alpha)e^{-(x/\theta)}}\left[\frac{\alpha\tau^{2}(x/\theta)^{\tau}((x/\theta)^{\tau}-1)e^{-(x/\theta)^{\tau}}}{x\theta}+\frac{(1-\alpha)(x-\theta)e^{-(x/\theta)}}{\theta^{3}}\right] \quad (22)$$

For a parameter τ,

$$\frac{\partial l}{\partial\tau} = \sum_{i=1}^{n}\frac{\partial l}{\partial\tau}\ln\left[\frac{\alpha\tau(x/\theta)^{\tau-1}e^{-(x/\theta)^{\tau}}+(1-\alpha)e^{-(x/\theta)}}{\theta}\right]$$
$$= \sum_{i=1}^{n}\frac{\theta}{\alpha\tau(x/\theta)^{\tau-1}e^{-(x/\theta)^{\tau}}+(1-\alpha)e^{-(x/\theta)}}\left[\frac{\partial}{\partial\tau}\left(\frac{\alpha\tau(x/\theta)^{\tau-1}e^{-(x/\theta)^{\tau}}}{\theta}\right)+\frac{\partial}{\partial\tau}\left(\frac{(1-\alpha)e^{-(x/\theta)}}{\theta}\right)\right]$$
$$= \sum_{i=1}^{n}\frac{\theta}{\alpha\tau(x/\theta)^{\tau-1}e^{-(x/\theta)^{\tau}}+(1-\alpha)e^{-(x/\theta)}}$$
$$\left[\frac{\alpha}{\theta}(x/\theta)^{\tau-1}e^{-(x/\theta)^{\tau}}\left(-\tau\ln\frac{x}{\theta}(x/\theta)^{\tau}+\tau\ln\frac{x}{\theta}+1\right)\right]. \quad (23)$$

The MLEs can be obtained by solving $\frac{\partial l}{\partial\alpha}=0$, $\frac{\partial l}{\partial\theta}=0$ and $\frac{\partial l}{\partial\tau}=0$ simultaneously.
It is clear that equations (21) - (23) has no explicit analytical solution, hence, it can be solved numerically using Newton-Raphson iterative method, Fixed-point iterating method, Secant method which are powerful techniques for solving nonlinear system of equations.

References:

[1] Kritsana Neammanee. Probability Theory. Department of Mathematics and Computer Science, Faculty of Science, Chulalongkorn University, 1999.
[2] Jirat Sukaket. Probability and Basic Statistics. Kasetsart University Press, 2005.
[3] Saichon Sinsomboon. Basic Statistics. Chamchuree Products, 2010.
[4] Dusit Chaiprasithikul. Parameters Estimation Of The Weibull Distribution Under Random Censored Samples. Mathematics and Statistics, Faculty of Science and Technology, Thammasat University, 2017.
[5] R. Jiang and D. N. P. Murthy. Mixture of weibull distributions – parametric characterization of failure rate function. Weily Online Library, 14(0):47–65, 1998.
[6] MQ Shahbaz MS Rana, SH Shahbaz and MM Rahman. ParetoWeibull Distribution with Properties and Applications. PhD thesis, Islamic University, Department of Statistics, Islamic University, Kushtia, Bangladesh, January 2021. Available at www.researchgate.net.

[7] M. M. Nassar. Two properties of mixtures of exponential distributions. Ieee transactions on reliability, 37(4):383–385, 1988.
[8] Ketsuda Buranaphansak. Calculus 2, 2015.
[9] S. Ross. A First Course in Probability. Pearson Education, Incorporated 2014.
[10] Prasanna Sahoo. Probability and Mathematical Statistics. USA : Louisville, 2015.
[11] Harry H. Panjer Stuart A. Klugman and Gordor E. Willmot. Loss Models. Society of actuaries, 2019.

SOCIAL DISTANCING DETECTOR IN LECTURE CLASSROOM FROM REAL TIME VIDEO

Sathit Prasomphan[1]*, Arnon Jitrathai[2], Primlata Ngeinngokngam [3]

Department of Computer and Information Science,
King Mongkut's University of Technology North Bangkok, Bangkok, 10800 THAILAND
*e-mail: sathit.p@sci.kmutnb.ac.th

Abstract:
The development of a social distancing detection in the classroom from real time video, which can be displayed the result of video detection via web application, is originated from the problem of the current situation of the epidemic of the COVID-19 virus. The goal of this project is to made social distancing detector in the lecturer classroom by incorporating machine learning technologies and the policy of university about the decreasing of spreading of COVID-19 virus. This project was created and developed real-time classroom social distance detection technology. The system can be detected the distance between each person in classroom. There are three status that can indicate the distance between individual in lecturer classroom: red indicates a status with a distance of less than one meter, yellow indicates a status that is within range, and blue indicates a status with a distance greater than one kilometer. The experimental results indicate that adopting a convolutional neural network for training to detect a person in realtime video can be successfully used to detect the distancing between people. The proposed algorithms can be utilized to classify the type of activity of people with an accuracy rate of 88.24 percent.

Introduction:
Due to the increasing of cases recorded globally, the World Health Organization (WHO) has classified Covid-19 as a pandemic [1]. Many nations have established a lockdown strategy where the government has made it mandatory for residents to stay indoors during this crucial time in order to the pandemic. The easiest way to prevent the spreading of Covid-19 is to avoid close contact with other people, according to the Centers for Disease Control and Prevention (CDC) and other public health organizations [2]. Physical activity in social distance policy is being performed by people all over the world to prevent the Covid-19 pandemic [3].

Travel, meetings, gatherings, workshops, and prayer were all prohibited during the quarantine period in order to enforce social segregation. To decrease the amount of face-to-face interaction, participants are urged to use mobile phone and email as much as possible to manage and conduct activities. Persons are also urged to use good hygiene practices, such as often washing their hands, wearing masks, and avoiding close contact with sick people, in order to further stop the virus's spreading. However, there is a difference between knowing what to do and actually doing to stop the spread of the infection [3].

The COVID-19 virus can be transferred by human secretions such as saliva, snot, and other body fluids. To limit the risk of infection, the primary preventative is to use hand sanitizer and wear a face mask. Polls indicate that most of people won't wear face masks in small areas. As a result, we came to the conclusion that an assistant system would be useful for controlling the distance between people. It may help minimize the spread of the virus or tracking people who were at risk at this place.

Classroom social distancing detection system based on real-time video is originated from the problem of the current situation which has the epidemic of the COVID-19 virus that can cause contagious diseases from people who are close to each other or in a closed place without wearing a protective mask.

This project can detect the distance of people in the classroom from the surveillance camera in real time and take the image in the video for detection process to detect the distance of the person in the video and identify the person in the picture using face recognition technique. The project include collecting density coordinates in the area to be compiled into statistics and extract the data to analyze the risk points that may result in the spread of virus, which the data will be presented in the form of spatial analytics dash board to allow users to be aware of the location of the various risk points. All of the above methods enabled real-time video surveillance of social distancing in the classroom. To help reduce the spread and identify the density in the area to effectively reduce the risk of spreading the COVID-19 virus or other pathogens that can cause infectious diseases.

Related Theory:

A. Social Distancing

Distance between individuals is created through social distancing policy. In addition to avoiding unnecessary outings and engaging in group activities, spend more time at home on a daily basis, all of them is social distancing, in order to avoid the transmission of disease.

The COVID-19 pandemic is a serious issue for the healthcare sector. In addition to protect it at all times, the "social distancing" practice till the end of covid-19 pandemic is required. Maintaining a distance of 1 to 2 meters between each participant and reducing the room's density are essential for interacting with people. Focus on getting a workout by walking the stairs instead of using the elevator. It is possible to limit the spread of COVID-19 by engaging in activities in the community. Since the Spanish flu pandemic, it's had been employed in a number of global epidemics. This demonstrates that pandemic prevention efforts that are spaced out are beneficial and can help with this situation. In many countries, the government has enacted social distancing policies that is stricter and more inclusive. The number of sick and deceased people is highest in Italy. The Italian government has introduced social distancing as a result of the substantial increase in recent weeks. Travel can be intensified, such as prohibiting more than 60 million individuals from leaving their homes. Only if police approval is granted, including the closure of schools, museums, theatres, and shops. Except for grocery stores and pharmacies, which are permitted by the government. Many countries, in addition to Italy, similar policies have been implemented. It depends on the intensity of the outbreak and how quickly the administration makes decisions. In Thailand, Ministry of Public Health has started to make social distancing policy such as temporary shutdown of entertainment places, to keep the virus from spreading throughout Thai people.

B. Machine Learning

Machine Learning (ML) is the use of mathematics and computer science to teach computers to learn and make judgments without having to follow strict rules. Machine learning can read and interpret the information offered by humans so that they can make the judgments that human desire. There are numerous versions, including the following tasks.

a. Predict new types of data that machine learning has never seen before, what is the value, and what category does it belong to?

b. Group data by using information in the same group that has similar qualities.

c. Separate particular types of data from the rest of the data, such as speech from voice and environment.

d. Learning from the original interests to introduce new pieces of information that humans are predicted to be interested. The advantages of machine learning are numerous. Anyone or any organization that wants to employ machine learning in their job.

Machine learning can be divide into two categories: the first category is supervised learning which provide a class label in the dataset. For instance, regression which can find numerical responses, such as nutritional information for child, what is the expected height of this child? Classification which come up with a categorical answer, such as a prophecy for the Thoracic X-ray image. Whether or not the patient has lung cancer (the answer is yes/no, hence the name is binary). Alternatively, supply information about a child's relatives in order to anticipate the child. This one is in the good development/normal development/slow development category (the answer will have many groups which called multiclass classifications). The second category is unsupervised learning which the fact that no one knows the correct answer is. For example, clustering which build communication strategies with diverse categories of customers, group information, such as donor information, into three groups. Other non-clustering difficulties, such as detecting part data, are addressed in section. Other example of unsupervised learning are anomaly detection, recommendation system which provides material that users are likely to be interested in.

C. Convolution Neural Network

Developing machines that can learn, anticipate, or create knowledge is an important issue in artificial intelligence development. Deep learning, artificial neural networks, support vector machines, and other techniques can be used to teach machines how to learn and build information. The artificial neural network concept is based on the neural network system of the human nervous system. The input layer, output layer, and hidden layer are the three layers that make up the architecture of an artificial neural network. ANNs have the ability to make decisions on difficult problems that humans are unable to solve. Currently, deep learning is one of the most widely used techniques [8] [9][10]. Deep learning is a more advanced form of artificial neural network used in machine learning. Deep learning and artificial neuron networks have various hidden layers, as shown in **Fig. 1** [8][9][10], with deep learning having more hidden layers than artificial neuron networks. Deep learning can be used to address the challenges in facial recognition. A large dataset can be learned from diverse faces in the dataset using this technique. It can be used to recognize individual faces, tag photos on Facebook, or extract non-human objects. This approach can also be utilized as a part of an unmanned vehicle system [8]. In this study, CNNs, also known as deep learning, are related theories. Deep learning [8][9][10] is a sort of machine learning that mimics the neural system of the human brain. As a result, it is possible that future abilities will be supernatural. It can increase the processing power, allowing an artificial neural network to simulate nerves and neurons. Deep learning is a subfield of machine-learning research that attempts to obtain machine learning closer to one of its original goals. Deep learning is a type of artificial neural network with a large number of hidden layers. The ability to process a greater amount of data than usual However, this is challenging because there are many hidden layers. The architecture of deep learning is depicted in **Fig. 2** [8][9][10].

.

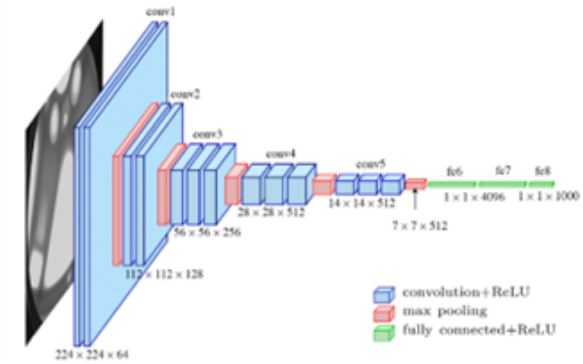

Figure 1.
Convolution neural network.

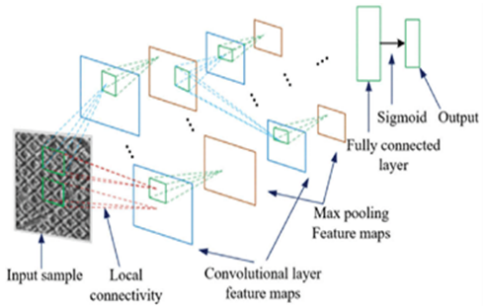

Figure 2.
Deep learning neural network [8] [9][10]

D. OpenCV and utilization

The default programming function library which used in this research is OpenCV (Open Source Computer Vision). Computer Vision in real-time was firstly created from Intel. OpenCV was a cross-library created by Willow Garage and Itseez (which was eventually acquired by Intel) under the opensource BSD license, it is cross-platform and free to use. OpenCV also supports deep learning frameworks. These include TensorFlow, Torch/PyTorch and Caffe. Examples of OpenCV applications are as follows: 2D and 3D feature toolkits, estimation of egomotion, facial recognition, gesture secognition, human-computer interaction.

F. Related work.

In [3], in order to lessen the effects of this coronavirus pandemic, the paper offers a deep learning-based methodology for social distance detection. By analyzing a video feed, the detection tool was created to warn individuals to keep a safe distance from one another. The open-source object detection pre-trained model based on the YOLOv3 method was utilized for pedestrian detection using the video frame from the camera as input.

In [4], based on a thermal camera, this study suggests a real-time AI platform for people detection and social distance classification of persons. In this study, YOLOv4-tiny is recommended for object detection. Its straightforward neural network architecture makes it appropriate for embedded devices that are reasonably priced. Comparing the suggested model to other real-time detection methods, it is a better choice.

In [5], this study suggests an artificial intelligence method for categorizing people's social distance using thermal pictures. An innovative deep learning detection technique for seeing and following people in both indoor and outdoor settings is developed by utilizing the YOLOv2 (you look at once) approach. Additionally, a distance measurement and classification technique is used, along with a system to automatically determine whether or not social distance standards are being followed.

In [6], in order to lessen the impact of the epidemic, this system makes use of video frame input to determine the distance between persons. In order to achieve this, a video feed from a security camera is examined. The video is adjusted for a bird's eye view before being provided as an input to the YOLOv3 model, an object detection model that has already been trained. Utilizing the Common Object in Context, the YOLOv3 model is trained.

In [7], a real-time crowd monitoring and management system is proposed for providing better healthcare through social distance detection and classification in public locations utilizing deep learning-based YOLO v4 object detection and deepsort algorithms. The circle of influence approach is used to determine how close a group is to another by using the bounding box formed around the individuals. Additionally, the technology creates a heatmap of the physical environment that is color-coded to show where and how severely social distance is being breached.

Methodology:

In this section, we describe procedures and methods of developing application as follows.

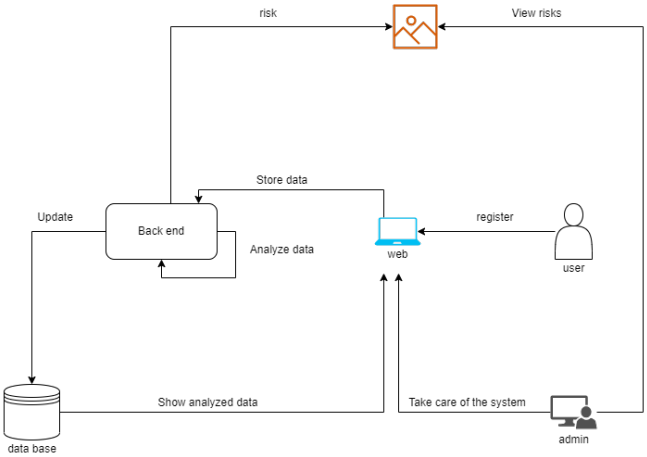

Figure 3.
System Architecture overview.

Figure 3 shows a system architecture overview. The user registers and logs in to the system, which can be used to view information about classroom access. To see the risk in that classroom from the beginning of the system's processing until it is stored in the database, for which the admin is liable. In order for the system to be used and processed, it must be shown to users in the form of an updated dashboard. Admins may also see the threats posed by CCTV, as well as the identities and details of all users. The framework of social distance system was described below.

In this section, we'll go over the crucial procedures needed to construct a sequence design in order to ascertain and verify if the people in the videos adhere to the social distance norms or not.

1. Streaming videos with people inside the video.
2. Extract video frames and save to images
3. Using YOLOv4 architecture to exclusively find people in frame.
4. Count the number of people in the videos.
5. Determine the separation between the center points of the bounding boxes that the people in the videos are included within.

In this project, we use the Google open picture dataset to train the YOLOv4 network on the class "Person" and test the recognition on a real video that was recorded by a classroom camera.

You Only Look Once is referred to as YOLO. One-Stage Detectors and Two-Stage Detectors are the two primary families of this object detection model, which is employed in deep learning use cases.

The category of One-Stage Detectors includes YOLO. A sliding window strategy combined with classification entails looking at the image and classifying it for each window. In terms of accuracy (average precision) and speed (FPS), the two metrics often use to evaluate an object identification algorithm, YOLOv4 has improved over YOLOv3. The YOLOv4 model's greatest strength is its ability to train models on a single GPU. The architecture of the model is shown below:

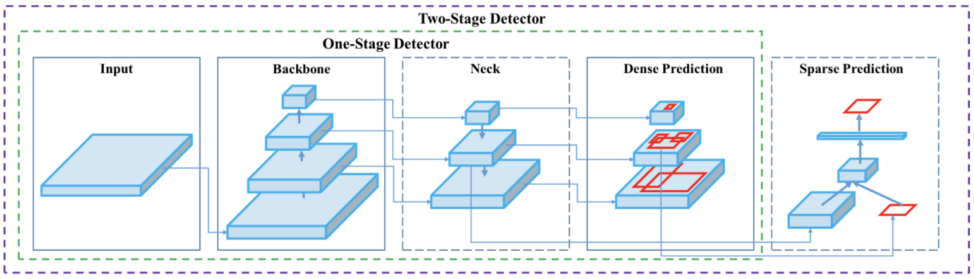

Figure 4:
Object detector with YOLOv4 architecture [11].

Detect person: Once the streaming videos from CCTV was upload to the system, it was sent to the processing in model 1. The outputs are images, which have many bounding boxes of predicted person that have a probability score. The outputs from model 1 are not returned to the user, rather they are sent for processing in model 2, to determine the separation between the center points of the bounding boxes that the people in the videos are included within.

Users can input any size and resolution images as the program will convert the image size to 416x416 pixels (using YOLO format). Our algorithm was divided into 2 models: object detection, determine the separation between the center points of the bounding boxes. Details of these two models are described as follows:

Model 1 was for object detection. In this step, the person were detected. The cropped images were then put into a bounding box size and sent to model 2.

Model 2 was to determine the separation between the center points of the bounding boxes that the people in the videos are included within. All outputs were then returned to the User. After the datasets were collected, each image was labelled using YOLO annotation tools. The pattern of the Annotation format was: <object-class> <x> <y> <width> <height>

Results and Discussion:
A real-time video-based classroom distancing detection system can determine the distance between each person. It can recognize the user's face and detect persons who aren't wearing mask. The system will mark as a risk and putting it on the webpage that will be displayed from the system. Inside the dashboard, users can quickly see the warning while image is in risk status in the classroom. The data will be deleted from the system after 14-day period. So, the person who is administrator of the system can be view the history in the database.

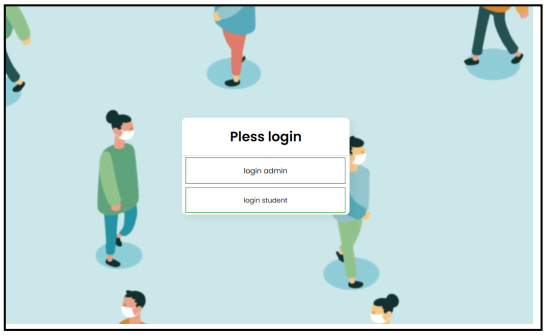

Figure 4.
Administrator login page.

When a user signs into the website, there are two option for authorization as show in figure 4. Firstly, user can login with student option. Secondly, user can login with administrator option.

Figure 5.
Administrator home page

When the administrator logs in successfully, the administrator is redirected to the Home page. The system's media source is displayed on this page. It will allow administrator access to the system’s manual.

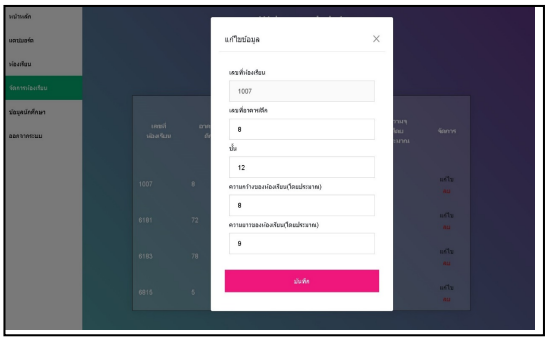

Figure 6.
Page for adding and editing classrooms information.

In Figure 6, the page for adding and editing classroom information was shown. This page is used for adding and editing classroom details. Administrator can fill the classroom data. If administrator enters incorrect information, the edit button was clicked for editing new information. Data can be deleted by clicking delete button.

Administrator can monitor classrooms using CCTV cameras to ensure that all students are present in the classroom. Administrator can check how many students are there in total, and how much risk level in this classroom as shown in Figure 7.

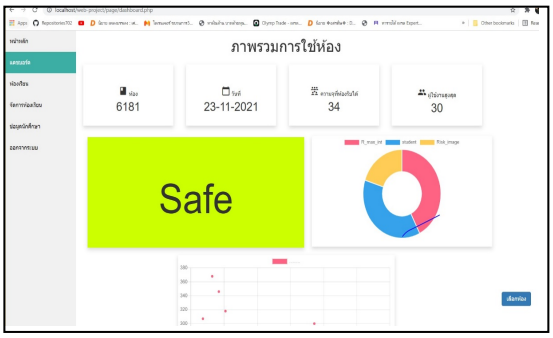

Figure 7.
Dashboard display page.

The risks level inside classroom are presented as a dashboard. The dashboard will show the list of students, room details and dates, the total number of student in the classroom, the classroom's capacity and ability to determine whether the room is safe or harmful for users and finally the risk level of classroom.

Performance Indexed

One of the most powerful techniques for reflecting the performance of classification results is the use of a confusion matrix. In this technique, each row shows the predicted class and each column shows the original class. This technique can be used to visualize classification errors. We calculated the precision, recall, f-1 score and accuracy using the following equation:

$$\boldsymbol{Precision} = \frac{TP}{TP+FP} \tag{1}$$

where TP is the true positive value and FP is the false positive value. Precision is the value that measures the number of correct predicting answers by dividing by the total number of images in the dataset.

$$\boldsymbol{Recall} = \frac{TP}{TP+FN} \tag{2}$$

where TP is the true positive value and FN is the false negative value. Recall is the value that measures the number of correct predicting answers for each class and is divided by the total number of that class which is the ground truth.

$$F1-Score=2\frac{Precision x Recall}{Precision+Recall} \quad (3)$$

where Precision is the precision value calculated from (1) andRecall is the recall value calculated from (2).

$$Accuracy=\frac{TP+TN}{N} \quad (4)$$

where TP is the true positive value, TN is the true negative value, and N is total number of images.

The classification results obtained by applying the proposed algorithms to detect the people inside video were used to demonstrate the experimental findings. Consequently, the classification accuracy ensures the efficiency of our image classification algorithms. **Table. 1** illustrates the categorization accuracy. The experimental results indicate that adopting a convolutional neural network for training to detect a person in realtime video can be successfully used to detect the distancing between people. The proposed algorithms can be utilized to classify the type of activity of people with an accuracy rate of 88.24 percent.

Table 1: Comparison of average precision of classification between traditional deep learning and proposed classification technique

Classification technique	Precision
AlexNet	86.58%
YOLO	84.52%
Simple CNN	87.52%
proposed classification	88.24%

Conclusion:

This research was create a real-time social distancing systems in the lecture classroom by using openCV library and python. The social distance mechanism in the classroom has been developed for decreasing the spread of COVID-19 by using a real-time video. The output of system are to detect people not wearing face masks and the distance between each people. The detection is then sent to the dashboard for display information of the risk area. The system can consider the number of individuals in the room versus the classroom's maximum capacity. When the number of students attending the class exceeds the room's capacity, a notice will be issued via the dashboard page with non-safe flag, also collects the coordinates of the red state's risk points.

References:

1. Implementation of Mitigation Strategies for Communities with Local COVID-19, [online] Available: https://www.who.int/emergencies/diseases/novel-coronavirus-2019.
2. Implementation of Mitigation Strategies for Communities with Local COVID-19 Transmission, [online] Available: https://www.cdc.gov/coronavirus/2019-ncov/downloads/community-mitigation-strategy.pdf.
3. Y. C. Hou, M. Z. Baharuddin, S. Yussof and S. Dzulkifly, "Social Distancing Detection with Deep Learning Model," 2020 8th International Conference on Information Technology and Multimedia (ICIMU), 2020, pp. 334-338, doi: 10.1109/ICIMU49871.2020.9243478.
4. Saponara, S., Elhanashi, A. & Zheng, Q. Developing a real-time social distancing detection system based on YOLOv4-tiny and bird-eye view for COVID-19. J Real-Time Image Proc 19, 551–563 (2022). https://doi.org/10.1007/s11554-022-01203-5
5. Saponara, Sergio & Elhanashi, Abdussalam & Gagliardi, Alessio. (2021). Implementing a real-time, AI-based, people detection and social distancing measuring system for Covid-19. Journal of Real-Time Image Processing. 18. 10.1007/s11554-021-01070-6.
6 Shalini, G & Margret, M & Niraimathi, M & Subashree, S. (2021). Social Distancing Analyzer Using Computer Vision and Deep Learning. Journal of Physics: Conference Series. 1916. 012039. 10.1088/1742-6596/1916/1/012039.
7. Sangeeta Yadav, Preeti Gulia, Nasib Singh Gill, Jyotir Moy Chatterjee, "A Real-Time Crowd Monitoring and Management System for Social Distance Classification and Healthcare Using Deep Learning", Journal of Healthcare Engineering, vol. 2022, Article ID 2130172, 11 pages, 2022. https://doi.org/10.1155/2022/2130172
8. L. Deng and D. Yu, "Deep learning: methods and applications foundations and trends," Signal Processing, vol. 7, no. 3–4, pp. 197–387, 2014.
9. Y. Bengio, A. Courville and P. Vincent, "Representation learning: a review and new perspectives," IEEE Transactions on Pattern Analysis and Machine Intelligence vol. 35, no. 8, pp. 1798–1828, 2013.
10. S. Prasomphan and J. E. Jung, "Mobile application for archaeological site image content retrieval and automated generating image descriptions with neural network," Mobile Networks and Applications, vol. 22, pp. 642–649, 2017.
11. Bochkovskiy A, Wang CY, Liao HY. Yolov4: Optimal speed and accuracy of object detection. arXiv preprint arXiv:2004.10934. 2020 Apr 23.

ON FIXED POINT THEOREMS FOR KANNAN AND CHATTERJEA TYPE MAPPINGS

Nattapol Rachpira,* Pongsakorn Yotkaew

Department of Mathematics, Faculty of Science, Khon Kaen University, Khon Kaen, Thailand
*e−mail: Nattapol_ra@kkumail.com

Abstract :

In this paper, we prove some fixed point theorems for generalized Kannan and Chatterjea type mappings in compact metric spaces or complete metric spaces. Moreover, we characterize the completeness of the underlying space in terms of a unique fixed point of such mapping.

Introduction :

One of the most important theorems in mathematical analysis is the Banach fixed point theorem with many important mathematical applications such as applying it to show the existence and uniqueness of the solutions of ordinary differential equations, and it can be used to prove existence and uniqueness of solutions of integral equations.

Theorem 1 (The Banach Fixed Point Theorem)**.** Let (X,d) be a metric space and $T:X\to X$ be a mapping such that

$$d(Tx,Ty)\leq \alpha d(x,y) \text{ for all } x,y\in X \text{ where } \alpha\in[0,1).$$

If (X,d) is a complete metric space then, T has a unique fixed point $v\in X$ and for any $x\in X$, an iterative sequence $\{T^n x\}$ converges to v.

In 1968, Kannan [6] proved a fixed point and convergence theorem for Kannan type mappings in a complete metric space.

Theorem 2 ([6])**.** Let (X,d) be a complete metric space and $T:X\to X$ be a mapping. Assume that T is a **Kannan type mapping**, that is, there exists $K\in[0,\frac{1}{2})$ satisfying

$$d(Tx,Ty)\leq K\left(d(x,Tx)+d(y,Ty)\right) \text{ for all } x,y\in X.$$

Then T has a unique fixed point $v\in X$ and for any $x\in X$, an iterative sequence $\{T^n x\}$ converges to v.

In 1972, Chatterjea [1] proved a fixed point theorem for Chatterjea type mappings in a complete metric space.

Theorem 3 ([6])**.** Let (X,d) be a complete metric space and $T:X\to X$ be a mapping. Assume that T is a **Chatterjea type mapping**, that is, there exists $K\in[0,\frac{1}{2})$ satisfying

$$d(Tx,Ty)\leq K\left(d(x,Ty)+d(y,Tx)\right) \text{ for all } x,y\in X.$$

Then, T has a unique fixed point $v \in X$ and for any $x \in X$, an iterative sequence $\{T^n x\}$ converges to v.

In 1974, Ciric [2] proved a fixed point and convergence theorem for quasi-contraction mappings in a T-orbitally complete metric space.

Theorem 4 ([2])**.** Let T is a **quasi-contraction mapping** on a metric space X, that is, there exists $q \in [0,1)$ satisfying

$$d(Tx,Ty) \leq q\max\{d(x,Tx),d(y,Ty),d(x,Ty),d(y,Tx),d(x,y)\} \text{ for all } x,y \in X.$$

If X is T-orbitally complete, then T has a unique fixed point $v \in X$ and for any $x \in X$, an iterative sequence $\{T^n x\}$ converges to v.

In 2017, Górnicki [5] proved some fixed point and convergence theorems for generalized Kannan type mappings in complete metric spaces or compact metric spaces.

Theorem 5 ([5])**.** Let (X,d) be a complete metric space and $T : X \to X$ be a mapping such that

$$d(Tx,Ty) \leq Ad(x,Tx) + Bd(y,Ty) + Cd(x,y) \text{ for all } x,y \in X$$

where A,B,C are nonnegative and $A+B+C<1$. Then T has a unique fixed point $v \in X$ and for any $x \in X$, an iterative sequence $\{T^n x\}$ converges to v.

Theorem 6 ([5])**.** Let (X,d) be a compact metric space and $T : X \to X$ be a continuous function such that

$$d(Tx,Ty) < \frac{1}{2}(d(x,Tx) + d(y,Ty)) \quad \text{for all} \quad x,y \in X \quad \text{with} \quad x \neq y.$$

Then T has a unique fixed point $v \in X$ and for any $x \in X$, an iterative sequence $\{T^n x\}$ converges to v.

Theorem 7 ([5])**.** Let (X,d) be a compact metric space and $T : X \to X$ be a continuous function such that

$$d(Tx,Ty) < Ad(x,Tx) + Bd(y,Ty) + Cd(x,y) \text{ for all } x,y \in X \text{ with } x \neq y$$

where A,B,C are positive and $A+B+C=1$. Then T has a unique fixed point $v \in X$ and for any $x \in X$, an iterative sequence $\{T^n x\}$ converges to v.

In 2018, Garai, Dey and Senapati [4] introduced the result which provides a sufficient condition of completeness of the underlying space via fixed point property.

Theorem 8 ([4])**.** Let every self-mapping T on a metric space (X,d) satisfying

$$d(Tx,Ty) < \frac{1}{2}(d(x,Tx) + d(y,Ty)) \tag{1}$$

for all $x,y \in X$ with $x \neq y$, has a unique fixed point. Then (X,d) must be a complete metric space.

In this project, we prove fixed point theorems for generalized Kannan and Chatterjea type mappings in complete metric spaces or compact metric spaces. We also show convergence theorems of iterative sequences for such mappings. Moreover, we characterize the completeness of the underlying spaces in terms of a unique fixed point of these mappings.

Results :

Let (X,d) be a metric space. A mapping $T:X\to X$ is said to be:

- **generalized Kannan and Chatterjea type (1)** if there exists $K\in[0,\frac{1}{2})$ satisfying

$$d(Tx,Ty)\leq K\max\{d(x,Tx)+d(y,Ty),d(x,Ty)+d(y,Tx)\} \text{ for all } x,y\in X.$$

- **generalized Kannan and Chatterjea type (2)** if

$$d(Tx,Ty)\leq Ad(x,Tx)+Bd(y,Ty)+Cd(x,Ty)+Dd(y,Tx)+Ed(x,y) \text{ for all } x,y\in X$$

where A,B,C,D,E are nonnegative and $A+B+C+D+E<1$.

- **generalized Kannan and Chatterjea type ($1'$)** if

$$\begin{aligned}&d(Tx,Ty)\\&<\max\{A_1d(x,Tx)+B_1d(y,Ty)+C_1d(x,y),A_2d(x,Ty)+B_2d(y,Tx)+C_2d(x,y)\}\end{aligned}$$

for all $x,y\in X$ with $x\neq y$ where A_1,B_1,C_1,A_2,B_2,C_2 are nonnegative, $A_1,B_1,A_2,B_2<1$ and $A_1+B_1+C_1=1=A_2+B_2+C_2$.

- **generalized Kannan and Chatterjea type ($2'$)** if

$$d(Tx,Ty)<Ad(x,Tx)+Bd(y,Ty)+Cd(x,Ty)+Dd(y,Tx)+Ed(x,y)$$

for all $x,y\in X$ with $x\neq y$ where A,B,C,D,E are nonnegative and $A+B+C+D+E=1$.

Remark 1. Let (X,d) be a metric space and $T:X\to X$ be a generalized Kannan and Chatterjea type (1) mapping. Then T is a quasi-contraction mapping.

Example 1 ([2])**.** Let

$$\begin{aligned}M_1&=\left\{\frac{m}{n}:m=0,1,3,9,\cdots;n=1,4,\cdots,3k+1,\cdots\right\},\\M_2&=\left\{\frac{m}{n}:m=1,3,9,27,\cdots;n=2,5,\cdots,3k+2,\cdots\right\},\end{aligned}$$

and let $M=M_1\cup M_2$ with the usual metric. Define $T:M\to M$ by

$$Tx=\begin{cases}\frac{3x}{5} & ;\ x\in M_1\\ \frac{x}{8} & ;\ x\in M_2.\end{cases}$$

Then T is a quasi-contraction mapping but not a generalized Kannan and Chatterjea type (1) mapping.

Remark 2. Let (X,d) be a metric space and $T:X\to X$ be a generalized Kannan and Chatterjea type (2) mapping. Then T is a quasi-contraction mapping.

Example 2. Let $X=[-1,2]$ and $T:X\to X$ be defined by

$$Tx=\begin{cases}-1 & ;\ x=2\\ \dfrac{x}{3} & ;\ -0.8<x<2\\ e^{x} & ;\ -1\le x\le -0.8.\end{cases}$$

Then T is a generalized Kannan and Chatterjea type (1) mapping but not Kannan type and Chatterjea type.

Lemma 1. Let (X,d) be a metric space, $T:X\to X$ be a continuous function and $f:X\to\mathbb{R}$ be defined by $f(x)=d(x,Tx)$ for all $x\in X$. Then f is a continuous function.

Lemma 2. Let (X,d) be a metric space, $\{x_n\}$ be a Cauchy sequence but not convergent in X and $A:=\{x_n:n\in\mathbb{N}\}$. Then $d(x,A)>0$ for all $x\in X\setminus A$.

Lemma 3. Let (X,d) be a metric space, r be a positive number and $\{x_n\}$ be a Cauchy sequence but not convergent in X such that all terms of the sequence $\{x_n\}$ are distinct. Then for each $n_0\in\mathbb{N}$ there exists $n_0'\in\mathbb{N}$ such that if $m\in\mathbb{N}$ and $m\ge n_0'>n_0$, then $d(x_m,x_{n_0'})<rd(x_{n_0'},x_{n_0})$.

By Theorem 4, we have the following Corollaries.

Corollary 1. Let (X,d) be a T-orbitally complete metric space and $T:X\to X$ be a generalized Kannan and Chatterjea type (1) mapping. Then T has a unique fixed point $v\in X$ and for any $x\in X$, an iterative sequence $\{T^nx\}$ converges to v.

Corollary 2. Let (X,d) be a T-orbitally complete metric space and $T:X\to X$ be a generalized Kannan and Chatterjea type (2) mapping. Then T has a unique fixed point $v\in X$ and for any $x\in X$, an iterative sequence $\{T^nx\}$ converges to v.

Theorem 9. Let (X,d) be a compact metric space and $T:X\to X$ be a continuous function and generalized Kannan and Chatterjea type ($1'$) mapping. Then T has a unique fixed point $v\in X$ and for any $x\in X$, an iterative sequence $\{T^nx\}$ converges to v.

Proof Let $f:X\to\mathbb{R}$ be defined by $f(x)=d(x,Tx)$ for all $x\in X$. By Lemma 1, we get that f is continuous. Since X is a compact, there exists $v\in X$ such that

$$f(v)=\min_{x\in X}f(x).$$

First, we will show that v is a fixed point of T. Suppose that $v \neq Tv$.
Case 1 : $A_2 \leq B_2$. Consider

$$d(Tv,T^2v) < \max\{A_1d(v,Tv)+B_1d(Tv,T^2v)+C_1d(v,Tv),A_2d(v,T^2v)+B_2d(Tv,Tv)+C_2d(v,Tv)\}.$$

If $A_1d(v,Tv)+B_1d(Tv,T^2v)+C_1d(v,Tv) \geq A_2d(v,T^2v)+B_2d(Tv,Tv)+C_2d(v,Tv)$, then

$$d(Tv,T^2v) < A_1d(v,Tv)+B_1d(Tv,T^2v)+C_1d(v,Tv).$$

This implies that

$$d(Tv,T^2v) < \left(\frac{A_1+C_1}{1-B_1}\right)d(v,Tv) = d(v,Tv).$$

On the other hand, if $A_1d(v,Tv)+B_1d(Tv,T^2v)+C_1d(v,Tv) < A_2d(v,T^2v)+B_2d(Tv,Tv)+C_2d(v,Tv)$, then

$$\begin{aligned} d(Tv,T^2v) &< A_2d(v,T^2v)+B_2d(Tv,Tv)+C_2d(v,Tv) \\ &\leq A_2\left(d(v,Tv)+d(Tv,T^2v)\right)+C_2d(v,Tv). \end{aligned}$$

It follows that

$$d(Tv,T^2v) < \left(\frac{A_2+C_2}{1-A_2}\right)d(v,Tv) \leq d(v,Tv).$$

Case 2 : $B_2 < A_2$. Consider

$$d(T^2v,Tv) < \max\{A_1d(Tv,T^2v)+B_1d(v,Tv)+C_1d(Tv,v),A_2d(Tv,Tv)+B_2d(v,T^2v)+C_2d(Tv,v)\}.$$

If $A_1d(Tv,T^2v)+B_1d(v,Tv)+C_1d(Tv,v) \geq A_2d(Tv,Tv)+B_2d(v,T^2v)+C_2d(Tv,v)$, then

$$d(Tv,T^2v) < A_1d(Tv,T^2v)+B_1d(v,Tv)+C_1d(Tv,v).$$

This implies that

$$d(Tv,T^2v) < \left(\frac{B_1+C_1}{1-A_1}\right)d(v,Tv) = d(v,Tv).$$

On the other hand, if $A_1d(Tv,T^2v)+B_1d(v,Tv)+C_1d(Tv,v) < A_2d(Tv,Tv)+B_2d(v,T^2v)+C_2d(Tv,v)$, then

$$\begin{aligned} d(Tv,T^2v) &< A_2d(Tv,Tv)+B_2d(v,T^2v)+C_2d(Tv,v) \\ &\leq B_2\left(d(v,Tv)+d(Tv,T^2v)\right)+C_2d(v,Tv). \end{aligned}$$

As a result, we obtain

$$d(Tv,T^2v) < \left(\frac{B_2+C_2}{1-B_2}\right)d(v,Tv) < d(v,Tv).$$

Therefore, $d(Tv,T^2v) < d(v,Tv)$, which is contradiction. Hence $Tv = v$.

Second, we will show that T has a unique fixed point.

Let $w \in \text{Fix}(T)$ with $w \neq v$.

$$\begin{aligned} d(w,v) &= d(Tw,Tv) \\ &< \max\{A_1 d(w,Tw) + B_1 d(v,Tv) + C_1 d(w,v), A_2 d(w,Tv) + B_2 d(v,Tw) + C_2 d(w,v)\} \\ &= \max\{C_1 d(w,v), d(w,v)\} \\ &= d(w,v), \end{aligned}$$

which is a contradiction. Thus, T has a unique fixed point.

Let $x_0 \in X$ and $\{x_n\}$ be a sequence in X defined by

$$x_n = Tx_{n-1} \text{ for all } n \in \mathbb{N}.$$

Finally, we will show that $\{x_n\}$ converges to v.

Case 1 : $T^N x_0 = T^{N+1} x_0$ for some $N \in \mathbb{N}$. Then $x_n = v$ for all $n \geq N$. Thus, $x_n \to v$.

Case 2 : $T^n x_0 \neq T^{n+1} x_0$ for all $n \in \mathbb{N}$.

Case 2.1 : $A_1 \leq B_1$. Consider

$$\begin{aligned} d(T^{n+1}x_0, v) &= d(T^{n+1}x_0, Tv) \\ &< \max\{A_1 d(T^n x_0, T^{n+1}x_0) + B_1 d(v,Tv) + C_1 d(T^n x_0, v), A_2 d(T^n x_0, Tv) \\ &\quad + B_2 d(v, T^{n+1}x_0) + C_2 d(T^n x_0, v)\}. \end{aligned}$$

If $A_1 d(T^n x_0, T^{n+1}x_0) + B_1 d(v,Tv) + C_1 d(T^n x_0, v) \geq A_2 d(T^n x_0, Tv) + B_2 d(v, T^{n+1}x_0) + C_2 d(T^n x_0, v)$, then

$$\begin{aligned} d(T^{n+1}x_0, v) &< A_1 d(T^n x_0, T^{n+1}x_0) + B_1 d(v,Tv) + C_1 d(T^n x_0, v) \\ &= A_1 d(T^n x_0, T^{n+1}x_0) + C_1 d(T^n x_0, v) \\ &\leq A_1 \left(d(T^n x_0, v) + d(v, T^{n+1}x_0) \right) + C_1 d(T^n x_0, v). \end{aligned}$$

This implies that

$$d(T^{n+1}x_0, v) < \left(\frac{A_1 + C_1}{1 - A_1} \right) d(T^n x_0, v) \leq d(T^n x_0, v).$$

On the other hand, if $A_1 d(T^n x_0, T^{n+1}x_0) + B_1 d(v,Tv) + C_1 d(T^n x_0, v) < A_2 d(T^n x_0, Tv)$ $+ B_2 d(v, T^{n+1}x_0) + C_2 d(T^n x_0, v)$, then

$$d(T^{n+1}x_0, v) < A_2 d(T^n x_0, v) + B_2 d(v, T^{n+1}x_0) + C_2 d(T^n x_0, v).$$

It follows that

$$d(T^{n+1}x_0, v) < \left(\frac{A_2 + C_2}{1 - B_2} \right) d(T^n x_0, v) = d(T^n x_0, v).$$

Case 2.2 : $B_1 < A_1$. Consider

$$\begin{aligned} d(T^{n+1}x_0, Tv) &= d(Tv, T^{n+1}x_0) \\ &< \max\{A_1 d(v,Tv) + B_1 d(T^n x_0, T^{n+1}x_0) + C_1 d(v, T^n x_0), A_2 d(v, T^{n+1}x_0) \\ &\quad + B_2 d(T^n x_0, Tv) + C_2 d(v, T^n x_0)\}. \end{aligned}$$

If $A_1d(v,Tv)+B_1d(T^nx_0,T^{n+1}x_0)+C_1d(v,T^nx_0)\geq A_2d(v,T^{n+1}x_0)+B_2d(T^nx_0,Tv)+C_2d(v,T^nx_0)$, then

$$\begin{aligned} d(T^{n+1}x_0,v) &< A_1d(v,Tv)+B_1d(T^nx_0,T^{n+1}x_0)+C_1d(v,T^nx_0) \\ &= B_1d(T^nx_0,T^{n+1}x_0)+C_1d(v,T^nx_0) \\ &\leq B_1\left(d(T^nx_0,v)+d(v,T^{n+1}x_0)\right)+C_1d(v,T^nx_0). \end{aligned}$$

This implies that

$$d(T^{n+1}x_0,v) < \left(\frac{B_1+C_1}{1-B_1}\right)d(T^nx_0,v) < d(T^nx_0,v).$$

On the other hand, if $A_1d(v,Tv)+B_1d(T^nx_0,T^{n+1}x_0)+C_1d(v,T^nx_0) < A_2d(v,T^{n+1}x_0)$ $+B_2d(T^nx_0,Tv)+C_2d(v,T^nx_0)$, then

$$d(T^{n+1}x_0,v) < A_2d(v,T^{n+1}x_0)+B_2d(T^nx_0,v)+C_2d(v,T^nx_0).$$

As a result, we have

$$d(T^{n+1}x_0,v) < \left(\frac{B_2+C_2}{1-A_2}\right)d(T^nx_0,v) = d(T^nx_0,v).$$

Thus, $d(T^{n+1}x_0,v) < d(T^nx_0,v)$ for all $n\in\mathbb{N}$. Let $a_n = d(T^nx_0,v)$. Then $\{a_n\}$ is nonincreasing and convergent. Let $0\leq a = \lim_{n\to\infty}a_n$. Suppose that $a>0$.
Since X is compact, there exists $\{T^{n_i}x_0\}\subseteq\{T^nx_0\}$ such that $T^{n_i}x_0\to z$ where $z\in X$ as $i\to\infty$.
We get that

$$0 < a = \lim_{i\to\infty} d(T^{n_i+1}x_0,v) = d(Tz,v).$$

It follows that

$$a = \lim_{i\to\infty} d(T^{n_i+2}x_0,v) = d(T^2z,v) = d(T^2z,Tv) < d(Tz,v) = a,$$

which is a contradiction. Thus, $a=0$. Hence $T^nx_0\to v$. □

Theorem 10. Let (X,d) be a compact metric space and $T:X\to X$ be a continuous function and generalized Kannan and Chatterjea type $(2')$ mapping. Then T has a unique fixed point $v\in X$ and for any $x\in X$, an iterative sequence $\{T^nx\}$ converges to v.

Proof Let $f:X\to\mathbb{R}$ be defined by $f(x)=d(x,Tx)$ for all $x\in X$. By Lemma 1, we get that f is continuous. Since X is a compact, there exists $v\in X$ such that

$$f(v) = \min_{x\in X} f(x).$$

First, we will show that v is a fixed point of X. Suppose that $v\neq Tv$.
Case 1 : $A+C+E=0$ or $B+D+E=0$. Without loss of generality, suppose that

$A+C+E=0$.
Then $B+D=1$. It follows that

$$\begin{aligned} d(Tv,T^2v) &< Ad(v,Tv)+Bd(Tv,T^2v)+Cd(v,T^2v)+Dd(Tv,Tv)+Ed(v,Tv) \\ &= Bd(Tv,T^2v) \\ &\leq d(Tv,T^2v), \end{aligned}$$

which is a contradiction. Thus, $v=Tv$. Note that $X=\{v\}$. To see this, let $x\in X$ with $x\neq v$. Then

$$\begin{aligned} d(Tx,Tv) &< Ad(x,Tx)+Bd(v,Tv)+Cd(x,Tv)+Dd(v,Tx)+Ed(x,v) \\ &= Dd(Tv,Tx) \\ &\leq d(Tv,Tx), \end{aligned}$$

which is a contradiction. Hence $X=\{v\}$.
Case 2 : $A+C+E\neq 0$ and $B+D+E\neq 0$.
Case 2.1 : $D\leq C$. Then

$$\begin{aligned} d(T^2v,Tv) &< Ad(Tv,T^2v)+Bd(v,Tv)+Cd(Tv,Tv)+Dd(v,T^2v)+Ed(Tv,v) \\ &\leq Ad(Tv,T^2v)+Bd(v,Tv)+D\left(d(v,Tv)+d(Tv,T^2v)\right)+Ed(Tv,v). \end{aligned}$$

This implies that

$$d(T^2v,Tv)<\left(\frac{B+D+E}{1-A-D}\right)d(v,Tv)\leq d(v,Tv).$$

Case 2.2 : $C<D$. Then

$$\begin{aligned} d(T^2v,Tv) &= d(Tv,T^2v) \\ &< Ad(v,Tv)+Bd(Tv,T^2v)+Cd(v,T^2v)+Dd(Tv,Tv)+Ed(v,Tv) \\ &\leq Ad(v,Tv)+Bd(Tv,T^2v)+C\left(d(v,Tv)+d(Tv,T^2v)\right)+Ed(v,Tv). \end{aligned}$$

It follows that

$$d(T^2v,Tv)<\left(\frac{A+C+E}{1-B-C}\right)d(v,Tv)<d(v,Tv).$$

Therefore, $d(T^2v,Tv)<d(v,Tv)$, which is a contradiction. Hence $Tv=v$.

Next, we will show that X has a unique fixed point. Let $w\in \mathrm{Fix}(T)$ with $w\neq v$. Then

$$\begin{aligned} d(v,w) &= d(Tv,Tw) \\ &< Ad(v,Tv)+Bd(w,Tw)+Cd(v,Tw)+Dd(w,Tv)+Ed(v,w) \\ &= (C+D+E)d(v,w) \\ &\leq d(v,w), \end{aligned}$$

which is a contradiction. Hence T has a unique fixed point.
Let $x_0\in X$ and $\{x_n\}$ be a sequence in X defined by

$$x_n=Tx_{n-1} \text{ for all } n\in\mathbb{N}.$$

Finally, we will show that $\{x_n\}$ converges to v.
Case 2.1 : $T^N x_0 = T^{N+1} x_0$ for some $N \in \mathbb{N}$. Then $x_n = v$ for all $n \geq N$. Thus, $x_n \to v$.
Case 2.2 : $T^n x_0 \neq T^{n+1} x_0$ for all $n \in \mathbb{N}$. If $A \leq B$, then

$$\begin{aligned} d(T^{n+1}x_0, v) &= d(T^{n+1}x_0, Tv) \\ &< Ad(T^n x_0, T^{n+1}x_0) + Bd(v, Tv) + Cd(T^n x_0, Tv) + Dd(v, T^{n+1}x_0) + Ed(T^n x_0, v) \\ &\leq A\left(d(T^n x_0, v) + d(v, T^{n+1}x_0)\right) + (C+E)d(T^n x_0, v) + Dd(T^{n+1}x_0, v). \end{aligned}$$

This implies that

$$d(T^{n+1}x_0, v) < \left(\frac{A+C+E}{1-A-D}\right) d(T^n x_0, v) \leq d(T^n x_0, v).$$

On the other hand, if $B < A$, then

$$\begin{aligned} d(T^{n+1}x_0, v) &= d(T^{n+1}x_0, Tv) \\ &= d(Tv, T^{n+1}x_0) \\ &< Ad(v, Tv) + Bd(T^n x_0, T^{n+1}x_0) + Cd(v, T^{n+1}x_0) + Dd(T^n x_0, Tv) + Ed(v, T^n x_0) \\ &\leq B\left(d(T^n x_0, v) + d(v, T^{n+1}x_0)\right) + Cd(T^{n+1}x_0, v) + (D+E)d(T^n x_0, v). \end{aligned}$$

As a result, we have

$$d(T^{n+1}x_0, v) < \left(\frac{B+D+E}{1-B-C}\right) d(T^n x_0, v) < d(T^n x_0, v).$$

Thus, $d(T^{n+1}x_0, v) < d(T^n x_0, v)$ for all $n \in \mathbb{N}$. Let $a_n = d(T^n x_0, v)$. Then $\{a_n\}$ is nonincreasing and convergent. Let $0 \leq a = \lim_{n\to\infty} a_n$. Suppose that $a > 0$.
Since X is compact, there exists $\{T^{n_i}x_0\} \subseteq \{T^n x_0\}$ such that $T^{n_i}x_0 \to z$ where $z \in X$ as $i \to \infty$.
We get that

$$0 < a = \lim_{i\to\infty} d(T^{n_i+1}x, v) = d(Tz, v).$$

It follows that

$$a = \lim_{i\to\infty} d(T^{n_i+2}x_0, v) = d(T^2 z, v) = d(T^2 z, Tv) < d(Tz, v) = a,$$

which is a contradiction. Thus, $a = 0$. Hence $T^n x_0 \to v$. □

Theorem 11. Assume that every self-mapping T on metric space (X, d) satisfying

$$d(Tx, Ty) < \frac{1}{3}\left(d(x, Ty) + d(y, Tx) + d(x, y)\right) \text{ for all } x, y \in X \tag{2}$$

with $x \neq y$, has a unique fixed point. Then (X, d) must be a complete metric space.

Proof Suppose that (X,d) is not a complete metric space, then there must be a Cauchy sequence $\{x_n\}$ in X, which is not convergent in X. Without loss of generality, suppose that all terms of sequence $\{x_n\}$ are distinct. Let $A := \{x_n : n \in \mathbb{N}\}$. By Lemma 2, we have $d(x,A) > 0$ for all $x \in X \setminus A$. Let $x \in X$.
Case 1 : $x \in X \setminus A$. Then there exists $n_x \in \mathbb{N}$ such that

$$\begin{aligned} d(x_m, x_{n_x}) &< \frac{1}{3} d(x,A) \text{ for all } m \geq n_x \\ &\leq \frac{1}{3} d(x, x_n) \text{ for all } n \in \mathbb{N}. \end{aligned}$$

Case 2 : $x \in A$. Then $x = x_{n_0}$ for some $n_0 \in \mathbb{N}$. By Lemma 3 there exists $n_0^{'} \in \mathbb{N}$ such that

$$d(x_m, x_{n_0'}) < \frac{1}{4} d(x_{n_0}, x_{n_0'}) \text{ for all } m \geq n_0^{'} > n_0.$$

Let $T : X \to X$ be defined by

$$Tx = \begin{cases} x_{n_x} & ; \ x \in X \setminus A \\ x_{n_0'} & ; \ x \in A \text{ and } x = x_{n_0}. \end{cases}$$

Note that T has no a fixed point. Let $x, y \in X$ with $x \neq y$.
First, we will show that T satisfy

$$d(Tx, Ty) < \frac{1}{3} (d(x, Ty) + d(y, Tx) + d(x, y)).$$

Case 1 : $x, y \in X \setminus A$. Then $Tx = x_{n_x}$ and $Ty = y_{n_y}$ for some $n_x, n_y \in \mathbb{N}$. Without loss of generality, suppose that $n_y \geq n_x$. Then

$$\begin{aligned} d(Ty, Tx) &= d(y_{n_y}, x_{n_x}) \\ &< \frac{1}{3} d(x, y_{n_y}) \\ &= \frac{1}{3} d(x, Ty). \end{aligned}$$

This implies that

$$d(Tx, Ty) < \frac{1}{3} (d(x, Ty) + d(y, Tx) + d(x, y)).$$

Case 2 : $x, y \in A$. Then $x = x_{n_0}$ and $y = x_{m_0}$ for some $n_0, m_0 \in \mathbb{N}$. Then $Tx = x_{n_0'}$ and $Ty = x_{m_0'}$ for some $n_0^{'}, m_0^{'} \in \mathbb{N}$. Without loss of generality, suppose that $m_0^{'} \geq n_0^{'}$. Then we have

$$\begin{aligned} d(Ty, Tx) &= d(x_{m_0'}, x_{n_0'}) \\ &< \frac{1}{4} d(x_{n_0}, x_{n_0'}) \\ &\leq \frac{1}{4} \left(d(x_{n_0}, x_{m_0'}) + d(x_{m_0'}, x_{n_0'}) \right) \\ &= \frac{1}{4} (d(x, Ty) + d(Ty, Tx)). \end{aligned}$$

It follows that

$$\begin{aligned} d(Tx,Ty) &< \frac{1}{3}d(x,Ty) \\ &\leq \frac{1}{3}\left(d(x,Ty)+d(y,Tx)+d(x,y)\right). \end{aligned}$$

Case 3 : $x \in X \setminus A$ and $y \in A$. Then $y = x_{m_0}$ for some $m_0 \in \mathbb{N}$. Hence $Tx = x_{n_x}$ and $Ty = x_{m_0'}$ for some $n_x, m_0' \in \mathbb{N}$. If $m_0' \geq n_x$, then

$$\begin{aligned} d(Ty,Tx) &= d(x_{m_0'},x_{n_x}) \\ &< \frac{1}{3}d(x,x_{m_0'}) \\ &= \frac{1}{3}d(x,Ty). \end{aligned}$$

This implies that

$$d(Tx,Ty) < \frac{1}{3}\left(d(x,Ty)+d(y,Tx)+d(x,y)\right).$$

On the other hand, if $m_0' < n_x$, then

$$\begin{aligned} d(Tx,Ty) &= d(x_{n_x},x_{m_0'}) \\ &< \frac{1}{4}d(x_{m_0'},x_{m_0}) \\ &\leq \frac{1}{4}\left(d(x_{m_0'},x_{n_x})+d(x_{n_x},x_{m_0})\right) \\ &= \frac{1}{4}\left(d(Ty,Tx)+d(Tx,y)\right). \end{aligned}$$

As a result, we have

$$\begin{aligned} d(Tx,Ty) &< \frac{1}{3}d(y,Tx) \\ &\leq \frac{1}{3}\left(d(x,Ty)+d(y,Tx)+d(x,y)\right). \end{aligned}$$

Therefore, for all $x,y \in X$ with $x \neq y$, we have

$$d(Tx,Ty) < \frac{1}{3}\left(d(x,Ty)+d(y,Tx)+d(x,y)\right).$$

This leads us to a contradiction. Hence (X,d) must be a complete metric space. □

By Theorem 11, we get the following Corollary.

Corollary 3. Assume that every self-mapping T on metric space (X,d) satisfying

$$d(Tx,Ty) < \frac{1}{3}\max\{d(x,Tx)+d(y,Ty)+d(x,y), d(x,Ty)+d(y,Tx)+d(x,y)\}$$

for all $x,y \in X$ with $x \neq y$, has a unique fixed point. Then (X,d) must be a complete metric space.

Theorem 12. Let every self-mapping T on metric space (X,d) satisfying

$$d(Tx,Ty) < \frac{1}{5}(d(x,Tx)+d(y,Ty)+d(x,Ty)+d(y,Tx)+d(x,y)) \text{ for all } x,y \in X \qquad (3)$$

with $x \neq y$, has a unique fixed point. Then (X,d) must be a complete metric space.

Proof Suppose that (X,d) is not a complete metric space, then there must be a Cauchy sequence $\{x_n\}$ in X, which is not convergent in X. Without loss of generality, suppose that all terms of sequence $\{x_n\}$ are distinct. Let $A := \{x_n : n \in \mathbb{N}\}$. By Lemma 2, we have $d(x,A) > 0$ for all $x \in X \setminus A$. Let $x \in X$.
Case 1 : $x \in X \setminus A$. Then there exists $n_x \in \mathbb{N}$ such that

$$\begin{aligned} d(x_m,x_{n_x}) &< \frac{1}{5}d(x,A) \text{ for all } m \geq n_x \\ &\leq \frac{1}{5}d(x,x_n) \text{ for all } n \in \mathbb{N}. \end{aligned}$$

Case 2 : $x \in A$. Then $x = x_{n_0}$ for some $n_0 \in \mathbb{N}$. By Lemma 3, there exists $n_0' \in \mathbb{N}$ such that

$$d(x_m,x_{n_0'}) < \frac{1}{5}d(x_{n_0},x_{n_0'}) \text{ for all } m \geq n_0' > n_0.$$

Let $T : X \to X$ be defined by

$$Tx = \begin{cases} x_{n_x} & ; \ x \in X \setminus A \\ x_{n_0'} & ; \ x \in A \text{ and } x = x_{n_0}. \end{cases}$$

Note that T has no a fixed point. Let $x,y \in X$ with $x \neq y$.
First, we will show that T satisfy

$$d(Tx,Ty) < \frac{1}{5}(d(x,Tx)+d(y,Ty)+d(x,Ty)+d(y,Tx)+d(x,y)).$$

Case 1 : $x,y \in X \setminus A$. Then $Tx = x_{n_x}$ and $Ty = y_{n_y}$ for some $n_x, n_y \in \mathbb{N}$. Without loss of generality, suppose that $n_y \geq n_x$. Then

$$\begin{aligned} d(Ty,Tx) &= d(y_{n_y},x_{n_x}) \\ &< \frac{1}{5}d(x,x_{n_x}) \\ &= \frac{1}{5}d(x,Tx). \end{aligned}$$

This implies that

$$d(Tx,Ty) < \frac{1}{5}(d(x,Tx)+d(y,Ty)+d(x,Ty)+d(y,Tx)+d(x,y)).$$

Case 2 : $x, y \in A$. Then $x = x_{n_0}$ and $y = x_{m_0}$ for some $n_0, m_0 \in \mathbb{N}$. Then $Tx = x_{n_0'}$ and $Ty = x_{m_0'}$ for some $n_0', m_0' \in \mathbb{N}$. Without loss of generality, suppose that $m_0' \geq n_0'$. Then

$$\begin{aligned} d(Ty, Tx) &= d(x_{m_0'}, x_{n_0'}) \\ &< \frac{1}{5} d(x_{n_0}, x_{n_0'}) \\ &= \frac{1}{5} d(x, Tx). \end{aligned}$$

It follows that

$$d(Tx, Ty) < \frac{1}{5} \left(d(x, Tx) + d(y, Ty) + d(x, Ty) + d(y, Tx) + d(x, y) \right).$$

Case 3 : $x \in X \setminus A$ and $y \in A$. Then $y = x_{m_0}$ for some $m_0 \in \mathbb{N}$.
Hence $Tx = x_{n_x}$ and $Ty = x_{m_0'}$ for some $n_x, m_0' \in \mathbb{N}$. If $m_0' \geq n_x$, then

$$\begin{aligned} d(Ty, Tx) &= d(x_{m_0'}, x_{n_x}) \\ &< \frac{1}{5} d(x, x_{n_x}) \\ &= \frac{1}{5} d(x, Tx). \end{aligned}$$

This implies that

$$d(Tx, Ty) < \frac{1}{5} \left(d(x, Tx) + d(y, Ty) + d(x, Ty) + d(y, Tx) + d(x, y) \right).$$

On the other hand, if $m_0' < n_x$, then

$$\begin{aligned} d(Ty, Tx) &= d(x_{n_x}, x_{m_0'}) \\ &< \frac{1}{5} d(x_{m_0'}, x_{m_0}) \\ &= \frac{1}{5} d(Ty, y). \end{aligned}$$

As a result, we have

$$d(Tx, Ty) < \frac{1}{5} \left(d(x, Tx) + d(y, Ty) + d(x, Ty) + d(y, Tx) + d(x, y) \right).$$

Therefore, for all $x, y \in X$ with $x \neq y$, we have

$$d(Tx, Ty) < \frac{1}{5} \left(d(x, Tx) + d(y, Ty) + d(x, Ty) + d(y, Tx) + d(x, y) \right).$$

This leads us to a contradiction. Hence (X, d) must be a complete metric space. □

Example 3. Let $X=[-2,1]$ and $T:X\to X$ defined by

$$Tx=\begin{cases}-1 & ;\ x=1\\ \dfrac{x-1}{4} & ;\ x\in(-1.1,1)\\ e^{x} & ;\ x\in[-2,-1.1].\end{cases}$$

Then T satisfies (1) but not satisfy (2) and (3).

Example 4. Let $X=[0,1]$ and $T:X\to X$ defined by $T=\dfrac{x}{3}$. Then T satisfies (2) and (3) but not satisfy (1).

Example 5. Let $X=[-1,-0.6]\cup[0,2]$ and $T:X\to X$ defined by

$$Tx=\begin{cases}-1 & ;\ x=2\\ \dfrac{x}{3} & ;\ x\in[0,2)\\ e^{x} & ;\ x\in[-1,-0.6].\end{cases}$$

Then T satisfies (3) but not satisfy (2).

Example 6. Let $X=(-2,-1.5)\cup\{1\}$ and $T:X\to X$ defined by

$$Tx=\begin{cases}1 & ;\ x=1\\ \dfrac{x-3}{3} & ;\ x\in(-1.8,-1.5)\\ \dfrac{3}{x} & ;\ x\in(-2,-1.8].\end{cases}$$

Then T satisfies (2) but not satisfy (3).

Conclusion :

We prove fixed point theorems for generalized Kannan and Chatterjea types in compact metric spaces. We also show convergence theorems of iterative sequences for such mappings. Moreover, we characterize the completeness of the underlying space in terms of a unique fixed point of some mappings satisfy (2) and (3).

References :

[1] Chatterjea S. K, C. R. Acad. Bulgare. Sci. 1972;25:727 –730.
[2] Ciric L. B, Proceeding Am. Math. Soc. 1974;45:267 –273.
[3] Edelstein M, J. Lond. Math. Soc. 1972;37:74 –79.
[4] Garai, H, Dey, L. K, Senapati, T, Numerical Functional Analysis and Optimization. 2018.
[5] Górnicki, J, J. Fixed Point Theory Appl. 2017;19:2145 –2152.
[6] Kannan, R, Bull. Calcutta Math. Soc. 1968;60:71 –76.
[7] Powar P. L, Sahu G. R. K, Pathak A, INTERNATIONAL JOURNAL OF COMPUTER SCIENCES AND ENGINEERING. 2017;5:140 –143.

THE INFLUENCED DESTINATION CULTURAL ATTRACTION USING DECISION TREE METHOD

Amarita Ritthipakdee1,[1] Somkid Soottitantawat,[2] Prombuncha Prommala [3]
[1]Department of Information technology, Phranakhon Rajabhat University, Thailand
[2] Department of Computer science, Phranakhon Rajabhat University, Thailand
[3] Department of Computer animation and multimedia, Phranakhon Rajabhat University, Thailand
* e-mail: amarita@pnru.ac.th, somkid@pnru.ac.th, prombuncha.p@pnru.ac.th

Abstract:

The objective of this research is to search the influenced destination cultural attraction places by collecting the attraction place along the green line train, Bangkok, Thailand with total instance of 400, number of cultural attractions is 30, considered from the distance around all 16 green line train stations and classify 3 classes forms of tourism, comprising with Buddhism, Museum and Natural. This research method uses decision trees to establish rules for introducing influenced destination cultural attractions, the results reveal the accuracy is 62.36%, Buddhism class precision value is 57.69%, Museum class precision value is 64.29%, Natural class precision value is 68.97%, Buddhism class recall value is 63.83%, Museum class recall value is 51.43%, Natural class recall value is 74.07%, and the Influencer Destination places are MOCA Bangkok, St. Michael's Church, Songyae and Jib Sing Sang Tung respectively.

Introduction:

Nowadays, tourism is one of the most popular activities among all groups of people. Both government and business sectors have promoted tourism in many areas including increasing of more tourists. Cultural tourism means tourism to study the way of life of human beings in their society or any ethnic group where are consisted of knowledge, beliefs, arts, culture, laws, traditions, ceremonies, science, and everything that is thought up and done in that society. Bangkok is one of tourist destinations, many tourists would like to come and study art, culture including food which are very popular. However, one of the issues with tourism is that tourists do not have access to the information they need. If there are facilities or system available for tourists, they can use internet or mobile devices with convenient access to information. Tourists can easily plan their trips and will be able to forecast and control budget in order to make travel decision. This research has adopted the decision tree method, to analyze the relationship to tourist attractions and classify important tourist attractions in order to introduce interesting cultural attractions.

Data classification is a technique or method of data mining, it is a type of supervised learning, where supervised learning is machine learning that requires labeling as the goal of data training. The data mining consists with two steps, the first step is learning. Classification algorithms are made to analyze training data which is expressed in the form of rules or classification rules. The second step is a classification process, using test data to assess the validity of established normative classifications such as member classification, grouping of customers.

Decision tree is a well-known method. It is a tool that helps in analyzing events, situation for systematic decision making, it displays form which is similar to a tree with roots and branches, branching out of the tree in one direction until leading to a final conclusion for decision making. There is various research use decision tree, by classification data into classes

using attributes in the classification. The decision tree gained from learning indicates that what attributes determine the classification and how important does each feature differ from each other. [1] Summarized various algorithms recommended by the Internet of Things for this tourist route and works out the experimental data methods of these algorithms for cross-modal tourism route recommendation. The researchers analyze and summarize the simulation results. At present, there is no comparative analysis of the performance of ant colony algorithm, genetic algorithm, and its optimization algorithm in tourism route recommendation. On the basis of crawling the tourism data on the Internet, the research applies ant colony algorithm, genetic algorithm, max–min optimization ant colony algorithm, and hybrid ant colony algorithm based on greedy solution to tourism route recommendation and evaluates and compares the algorithms from three aspects: average evaluation score, optimal evaluation score, and algorithm time. Experimental results show that the max–min optimization ant colony algorithm and the hybrid ant colony algorithm based on greedy solution can be effectively applied to automated tourist route recommendation. [2] Investigating transportation decision-making indicates that key factors affecting mode selection are cost, transit time, complexity of shipper behavior and preferences, as well as the variety of supply chain configurations. Identification of factors affecting mode selection decisions by shippers based on information obtained from qualitative methods with decision tree methods. The results revealed that the major attributes in selecting transport modes by cargo shippers, taking into account access to three modes of transport to the seaports hinterland, are consignment size and time pressure, then owning or having access to barge terminals by cargo shippers, and the annual volume of cargoes generated by them. The analysis may be helpful for supply chain managers in making decisions regarding choosing a transport route. [3] Solving the dense transportation problem using the decision tree method, to create a route that is suitable for transportation based on behavioral factors and determine the relationship of the route. The experiment is divided into two dynamic modes, searching, and switching. The results where compare decision tree methods with logit models revealed that decision tree methods are able to find better paths. [4] Developed Travel Recommendation Systems (TRSs) to recommend destinations with a focus on finding destinations from users. The system takes into account the properties of the C4.5 Decision Tree. Results revealed that TRS is able to provide personalized recommendations on attractions that cater to the targeted tourist.

Methodology:

Decision Tree

It is popular and widely used method of decision-making. It has tree structural pattern comprises with root node and branches, branching from root for an answer. The positioning of the root node represents the tree hierarchy. Tree nodes can be categorized into three types:

1. Root Node, is the top node, at this node there is no input and has no output or has more than one output
2. Internal Node, is a branching node, at this node there is only one input and has at least two outputs
3. Leaf Node or Terminal Node, it is the final node, at this node there is only one input and has no output.

Algorithm C4.5

The C4.5 algorithm is a group of Decision Tree algorithms. It has input in the form of training samples and samples. Training samples are sample data used to build a tree that has been tested for truth. The C4.5 algorithm to calculate the entropy value, the value of information gain, the split info value, and the value of the gain ratio.

Entropy of each attribute can be calculated using the formula

$$\text{Entropy(x)} = \sum_{i=1}^{n} -p \log_2 p \quad (1)$$

Information Gain of each attribute can be calculated using the formula

$$\text{Gain(x, a)} = Entropy(x) - \sum_{i-1}^{n} \frac{|xi|}{|x|} Entropy(x_i) \quad (2)$$

When;
a represents a specific attribute or class label
$Entropy(x)$is the entropy of dataset, x
$|xi|$ represents the proportion of the values in x_i to the number of values in dataset, x
Entropy (x_i) is the entropy of dataset, x_i

Split info value of each attribute can be calculated using the formula

$$\text{Split Info (x,a)} = \sum_{i-1}^{n} \frac{|x_i|}{|x|} \log_2 \frac{|x_i|}{|x|} \quad (3)$$

Gain ratio value of each attribute can be calculated using the formula

$$\text{Gain Ratio (x,a)} = \frac{Information\ Gain\ \text{Gain(x,a)}}{\text{Split Info (x,a)}} \quad (4)$$

When;

x is sample data use for training
a is attribute
i is number attribute
|x| is the number of cases in x
Entropy (x_i) is the entropy of dataset, x_i

Destination Information Preparation

Data from 30 cultural attractions from a total of 16 Green Line train stations in Bangkok are collected in this research, as shown on the Table 1,

Table 1.
Cultural Attractions

No.	Station	Destination Picture	Destination Name
1	Ha Yaek Lat Phrao Station		Vachirabenjatas Park
2	Wat Phra Sri Mahathat Station		Wat Phra Si Mahathat
. . .			
30	Yaek Kor Por Aor Station		National Memorial

This research is conducted using decision trees. There are a total number of 400 instances of the data set with a total of 31 columns. The data are classified from the decision tree making recommendations of 30 tourist attractions from 16 stations as follows:

Vachirabenjatas Park, Children's Discovery Museum Bangkok 1, SCB Market, Elephant Tower, Major Cineplex Ratchayothin, Soil Museum MOCA BANGKOK, Bangkok Aquarium, Bangkok Herbarium, Forest Department Museum, Nutural Resources & Environment, Wat Bangbua, Bangbua Restaurant, Baan Bang Khen Museum, Kaw Tom Ka Kai, Wat Phra Si Mahathat, BMA LOCAL MUSEUM, BANG KHEN, Buddhavijjalaya College, Wat Ratniyomtum, Tirqiyatul Ihihan Mosque, St. Michael's Church Songyae, Jib Sing Sang Tung, Chaopho Sombun Shrine, Royai Thai Air Force Heal. RTAF Library, National Aviation Museum Of The Royal Thai Air Force, National Memorial, Chaloem Phra Kiat, Wat Sai Mai And Wat Phosopphoncharoen.

The initial step in this research is to study and collecting databases of cultural attractions. The data are obtained from interviews and a survey questionnaire. The purpose is to recommend landmarks visible for users from the platform. The use of decision tree has therefore generated a suitable tourist attraction pattern. Researchers have classified 3 types of targeted tourism as 1) Buddhism, which is a route that consists mainly of Buddhist sites. Those who have guidelines for making merit and participating in religious activities can consider choosing a tour plan. 2) Museum is a recommendation tour for those who are interested in the history that is displayed in the museum in a structured way, and 3) Natural shows natural and relaxing attractions, as illustrated in Table 2.

Table 2.
Data set

No.	Destination 1	Destination 2	…	Destination30	Recommend
X1	1	1		0	Buddhism
X2	0	1		1	Museum
.					
.					
.					
X400	1	1		0	Natural

Definition of performance measures

This research is to calculate efficiency by three approaches, Precision, Recall and Accuracy with the following equations,

Precision can be calculated by Equation 5,

$$\text{Precision} = \frac{\text{TP}}{\text{TP+FP}} \tag{5}$$

Recall can be calculated by Equation 6,

$$\text{Recall} = \frac{\text{TP}}{\text{TP +FN}} \tag{6}$$

Accuracy can be calculated by Equation 7,

$$Accuracy = \frac{\text{TP +TN}}{\text{TP+TN+FP +FN}} \tag{7}$$

Where,
TP = True Positive, TN = True Negative, FP = False Positive, FN = False Negative

Results and Discussion:

This research is conducted using RapidMiner Studio 9.1 program for data analysis of decision tree diagram, results are shown in Figure 1.

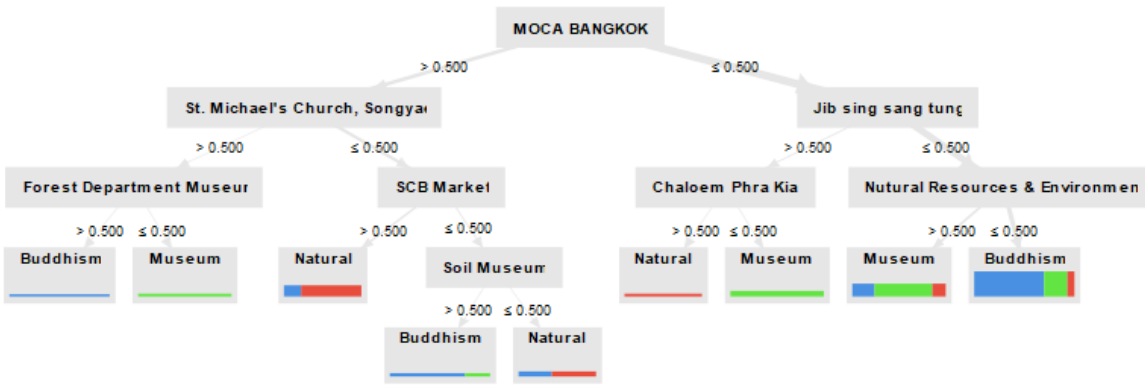

Figure 1.
Decision Tree Diagram

Conclusion:
This research is conducted using Decision tree recommendation cultural attractions to lead the influenced destination attractions for other tourist and the experimental is classified class into 3 classes, Buddhism, Museum and Neutral respectively. The experimental revealed that the accuracy is 62.36%, Buddhism class precision value is 57.69%, Museum class precision value is 64.29%, Natural class precision value is 68.97%, Buddhism class recall value is 63.83%, Museum class recall value is 51.43%, Natural class recall value is 74.07%, and the Influencer Destination places are MOCA Bangkok, St. Michael's Church, Songyae and Jib Sing Sang Tung respectively.

Table 3.
Accuracy: 62.36% +/- 10.91% (micro average: 62.39%)

	true Buddhism	true Museum	true Natural	class precision
Buddhism	30	17	5	57.69%
Museum	8	18	2	64.29%
Natural	9	2	20	68.97%
Class recall	63.83%	51.43%	74.07%	

Acknowledgement:
Researchers would like to thank to Phranakhon Rajabhat University for Fundamental Found 65 from Thailand Science Research and Innovation (TSRI), Owner of Fund.

References:

1. Yuran Zhang, and Ziyan Tang. 2021, Cross-Modal Travel Route Recommendation Algorithm Based on Internet of Things Awareness, Hindawi Journal of Sensors, Volume 2021, 2-11. doi.org/10.1155/2021/5981385
2. Izabela Kotowska, Marta Mańkowska,Michał Pluciński. 2020, The Decision Tree. Approach for the Choice of Freight Transport Mode: The Shippers' Perspective in Terms of Seaport Hinterland Connections, European Research Studies Journal, Issue3:446-459.DOI:10.35808/ersj/1649
3. Liang Tang, Chenfeng Xiong, Lei Zhang. 2015, Decision tree method for modeling travel mode switching in a dynamic behavioral process. Transportation Planning and Technology, 38:8, 833-850, DOI: 10.1080/03081060.2015.1079385
4. Pree Thiengburanathum, Shuang Cang, Hongnian Yu. 2015. A decision tree based recommendation system for tourists, Proceedings of the 21th International Conference onAutomation & Computing, University of Stratchclyde, Glasgow, G1 1XJ, UK, 11-12 September 2015. pp.1-8

AN ALTERNATIVE METHOD TO DETECT OUTLIERS IN MULTIVARIATE DATA

Theeraphat Thanwiset, Wuttichai Srisodaphol*, Kamonrut Koobubpha
Department of Statistics, Faculty of Science, Khon Kaen University, Khon Kaen 40002 Thailand
*e-mail: wuttsr@kku.ac.th

Abstract:

This study proposes techniques for finding outliers in multivariate data. It is based on the Mahalanobis distance and multiple linear regression. The Mahalanobis distance is used to filter the data across all variables to break the data set into two groups, i.e., normal data and data that might be outliers. After that, a multiple linear regression model is built using the normal data to provide a reliable estimate for the cut-off point. For figuring out how well the proposed method works, a simulation study is done with multivariate normal data with and without contaminated data at different levels: 0, 0.01, 0.05, and 0.10. The performance of the proposed method is compared with the earlier methods; Mahalanobis distance and Mahalanobis distance with the robust estimators using the minimum volume ellipsoid method, the minimum covariance determinant method, and the minimum vector variance method. The findings demonstrated that the proposed method effectively identifies the highest accuracy of outliers detected at all levels of contamination regardless of sample size or the number of variables. When the proposed method is used on real data, it also shows that it can find outlier values that are consistent with the real data.

Introduction:

Data points that stand out from the rest in statistics are known as outliers. The analysis of data is affected by outliers in datasets. The outliers will make the study's conclusions statistically significant even if they were not previously, and vice versa. Outliers are divided into several categories, but this research focuses on outliers caused by inherent variance only (Anscombe, 1960). Troubleshooting outliers generally eliminates the above-mentioned outliers from the dataset before statistically analyzing the data. If we verify that some data values are very different from others by nature, we will investigate those outliers. In terms of the level of analysis, there are three primary statistical analyses, i.e., univariate, bivariate, and multivariate. The most basic statistical data analysis method is univariate analysis, which is used when there is only one variable in the data. Bivariate analysis is a little more analytical when there are two variables in the data set than univariate analysis is. When a data set has more than two variables, a more complex statistical analysis method is used, called multivariate analysis.

Currently, a number of techniques exist to identify outliers; the most well-known is the boxplot (McGill et al., 1978). This method is employed to detect outliers in univariate data. There are several methods for detecting outliers. However, a dependent variable may or may not be present in bivariate or multivariate data. Many publications have presented the detection of outlier methods if the data includes a dependent variable, such as Cook's distances (Cook, 1977), the hat matrix (Hoaglin and Welsch, 1978), DFFITS (Nurunnabi et al., 2008), studentized residuals (Ranganai, 2016), and R-student (Ranganai, 2016).

The Mahalanobis distance (Mahalanobis, 1936), which effectively measures the distance of the vector from the mean using the covariance matrix, is the most frequently utilized when the data does not include a dependent variable. Samples based on maximum

likelihood estimators (MLEs) of the mean vector and covariance matrix exhibit a Mahalanobis distance that follows a chi-square distribution with p degrees of freedom, where p is the number of variables. In general, the cut-off point for Mahalanobis distance follows the square root of the chi-square distribution with the degrees of freedom equal to the dimension of data used to identify outliers. In addition, the Mahalanobis distance was employed to identify outliers using robust estimators of the mean vector and covariance matrix. The minimum volume ellipsoid (MVE) (Aelst and Rousseeuw, 2009), minimum covariance determinant (MCD) (Hubert and Debruyne, 2010), and minimum vector variance (MVV) were used to create robust estimators (Herdiani et al., 2019). The MVV is based on the minimum vector variance covering a subset of data, whereas the MVE and MCD are based on the minimum volume ellipsoid and minimum covariance determinant, respectively.

Only datasets without a dependent variable are taken into account in this research since they are often found in the companies that collect them and have high dimensionality and large sample sizes. The commonly used Mahalanobis distance method for these datasets detects outliers in a chi-square distribution, where the quantile value is a necessary descriptor. As a result, the dataset may contain outliers, but some datasets do not necessarily have outliers. Consequently, this research suggests a method for identifying outliers in multivariate data by combining Mahalanobis distance with multiple linear regression. The Mahalanobis distance is used to filter data across all variables first, with the square root of the chi-square distribution with the degrees of freedom equal to 1, and data for all variables that did not exceed the square root of the chi-square distribution with the degrees of freedom equal to 1 are labeled as normal data. The remaining data is then examined for outliers using multiple linear regression.

The paper is organized as follows. The Methodology section describes the proposed method. The results and discussion show an experiment on simulated data with and without contaminated multivariate normal data to compare the proposed method with the previous methods and show the behavior on a real dataset example. Finally, the conclusions are provided.

Methodology:

This research proposes outlier detection methods as follows: multiple linear regression using data split with the Mahalanobis distance method (MLRSMD). The proposed method is shown in the following steps.

Step 1: A dataset $\mathbf{X}$ with n observations and p variables, we use a Mahalanobis distance (MD) to filter the data in each variable, splitting the data into 2 sets where $n = n_1 + n_2$.

Set 1 (n_1 observations and p variables) is an observation with at least one variable whose MD value exceeds the square root of the chi-square distribution with the degrees of freedom equal to 1. It contains observations that may be outliers.

Set 2 (n_2 observations and p variables) is an observation where all variables whose MD value does not exceed the square root of the chi-square distribution with the degrees of freedom equal to 1. It contains observations that are not outliers.

Step 2: After getting 2 sets of data in step 1, we construct multiple linear regression equations (p equations) and compute $R_l^2; l = 1, 2, \ldots, p$ from data set 2. All the variables are thought of as a single dependent variable (Y), while the other variables are called independent variables. For example, let X_1 be a dependent variable (Y_1) and other variables $X_2, X_3, \ldots, X_p$ are independent variables and so on,

$$\hat{Y}_1 = b_0 + b_2 x_2 + b_3 x_3 + \ldots + b_p x_p$$
$$\hat{Y}_2 = b_0 + b_1 x_1 + b_3 x_3 + \ldots + b_p x_p$$
$$\hat{Y}_3 = b_0 + b_1 x_1 + b_2 x_2 + \ldots + b_p x_p$$
$$\vdots$$
$$\hat{Y}_p = b_0 + b_1 x_1 + b_2 x_2 + \ldots + b_{p-1} x_{p-1}.$$

Step 3: For the $R_l^2; l = 1, 2, \ldots, p$ of multiple linear regression equations in step 2, we select the multiple linear regression equation with the maximum R_l^2 to denote the cut-off point. The cut-off point is $\bar{e} + 3 * sd(e)$; e is an error in this equation.

Step 4: For the multiple linear regression equation with the maximum R^2 that we found in step 3, we make a prediction with the data from set 1 and get the absolute errors for that prediction.

Step 5: If any observation in the data set 1 has an absolute error in step 4 greater than the cut-off point obtained from step 3, it is labeled an outlier.

This proposed outlier detection method is illustrated in Figure 1.

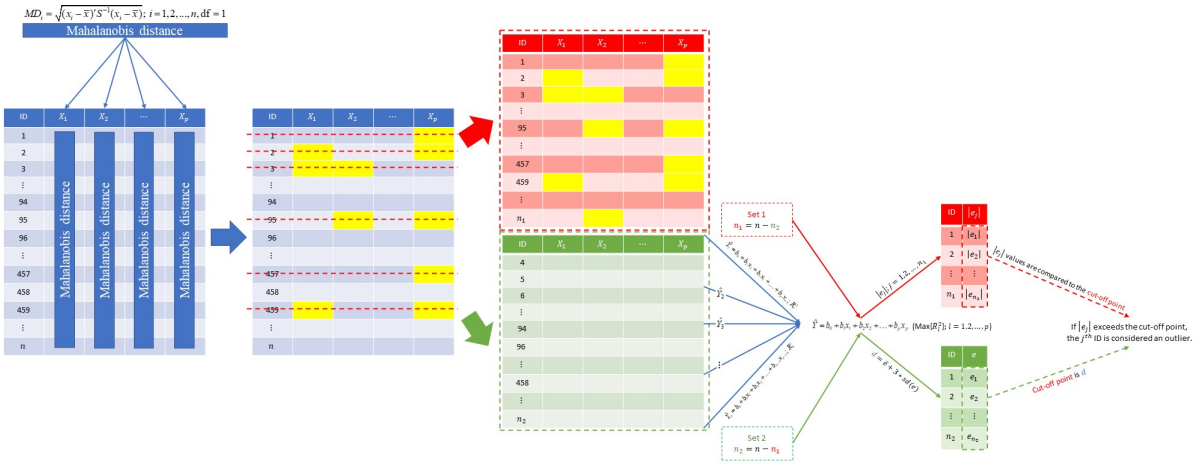

Figure 1. The proposed outlier detection method: MLRSMD

Results and Discussion:

In order to evaluate the performance of the proposed method with the existing methods, in this section, we simulate the data using a multivariate normal distribution with and without contaminated data.

Step 1: We generate the p-variate normal data with sample sizes n = 100, 300, 500, 800, 1000 and variables p = 3, 5, 7, 11 with and without contaminated data for the multivariate normal distribution using the R program. A contaminated multivariate normal distribution is given as the following form,

$$(1-\alpha)N(\mathbf{0}, I) + \alpha N(\delta\boldsymbol{\mu}, \lambda I),$$

where $\boldsymbol{\mu}$ denotes the p-dimensional vector of ones and covariance matrix I, the distance of the outliers $\delta = 5$ and the concentration of the contamination $\lambda = 0.1$. The contamination levels were α. (Cabana et al., 2019)

The simulated data with and without contaminated data can be considered under the denoting value of α. If α = 0, the simulated data is without contaminated data, and vice versa. The contaminated data that is inserted into the generated data are called outliers with α = 0.01, 0.05, 0.10.

Step 2: We use the proposed method (MLRSMD) to find outliers in each situation.

Step 3: We repeat Steps 1 to 2 for 1,000 iterations.

Step 4: We calculate the accuracy of the detected outliers, which is the criterion to evaluate the performance of the proposed methods.

The performance of the proposed method and the previous methods (MD, MVE, MCD, MVV) for p = 5, 11 and n = 100, 300, 500, 800, 1000 are showed in Tables 1-10. The same results for p = 3, 7 and n = 100, 300, 500, 800, 1000 were obtained (also available from the corresponding author).

Table 1. The accuracy of the detected outliers for p = 5 and n = 100

Method	**Contaminated levels α**			
	0.00	**0.01**	**0.05**	**0.10**
MLRSMD	0.98287	0.98765	0.99379	0.99189
MD	0.95686	0.97228	0.97202	0.86779
MVE	0.93167	0.93443	0.94579	0.96236
MCD	0.93790	0.94111	0.95164	0.96501
MVV	0.59937	0.60431	0.64033	0.68295

Table 2. The accuracy of the detected outliers for p = 5 and n = 300

Method	**Contaminated levels α**			
	0.00	**0.01**	**0.05**	**0.10**
MLRSMD	0.98820	0.99205	0.99664	0.99853
MD	0.95213	0.96824	0.96905	0.86441
MVE	0.94943	0.95253	0.96298	0.97447
MCD	0.94992	0.95328	0.96460	0.97527
MVV	0.63078	0.63817	0.66853	0.70769

Table 3. The accuracy of the detected outliers for $p = 5$ and $n = 500$

Method	Contaminated levels α			
	0.00	**0.01**	**0.05**	**0.10**
MLRSMD	0.98952	0.99283	0.99726	0.99871
MD	0.95114	0.96791	0.96825	0.86312
MVE	0.95051	0.95473	0.96527	0.97576
MCD	0.95056	0.95474	0.96585	0.97630
MVV	0.64413	0.65236	0.68146	0.71927

Table 4. The accuracy of the detected outliers for $p = 5$ and $n = 800$

Method	Contaminated levels α			
	0.00	**0.01**	**0.05**	**0.10**
MLRSMD	0.99003	0.99336	0.99728	0.99879
MD	0.95084	0.96687	0.96768	0.86290
MVE	0.95114	0.95444	0.96549	0.97669
MCD	0.95057	0.95423	0.96570	0.97709
MVV	0.65291	0.66022	0.69042	0.72635

Table 5. The accuracy of the detected outliers for $p = 5$ and $n = 1000$

Method	Contaminated levels α			
	0.00	**0.01**	**0.05**	**0.10**
MLRSMD	0.99039	0.99347	0.99731	0.99877
MD	0.95099	0.96702	0.96778	0.86284
MVE	0.95163	0.95490	0.96614	0.97674
MCD	0.95092	0.95453	0.96641	0.97702
MVV	0.65677	0.66443	0.69342	0.72978

Table 6. The accuracy of the detected outliers for p = 11 and n = 100

Method	Contaminated levels α			
	0.00	**0.01**	**0.05**	**0.10**
MLRSMD	0.95367	0.97504	0.98746	0.98227
MD	0.96298	0.97281	0.92368	0.85975
MVE	0.88545	0.89134	0.91029	0.92897
MCD	0.89979	0.90213	0.91848	0.93528
MVV	0.59659	0.60551	0.63382	0.51999

Table 7. The accuracy of the detected outliers for p = 11 and n = 300

Method	Contaminated levels α			
	0.00	**0.01**	**0.05**	**0.10**
MLRSMD	0.98162	0.98794	0.99356	0.99225
MD	0.95402	0.96575	0.91782	0.85075
MVE	0.94370	0.94677	0.95805	0.96820
MCD	0.94809	0.95011	0.96072	0.96990
MVV	0.62631	0.63306	0.66279	0.49744

Table 8. The accuracy of the detected outliers for p = 11 and n = 500

Method	Contaminated levels α			
	0.00	**0.01**	**0.05**	**0.10**
MLRSMD	0.98552	0.99028	0.99565	0.99668
MD	0.95201	0.96450	0.91657	0.84944
MVE	0.94841	0.95177	0.96220	0.97207
MCD	0.95009	0.95346	0.96365	0.97288
MVV	0.65622	0.66253	0.69163	0.50110

Table 9. The accuracy of the detected outliers for $p = 11$ and $n = 800$

Method	Contaminated levels α			
	0.00	**0.01**	**0.05**	**0.10**
MLRSMD	0.98790	0.99205	0.99688	0.99812
MD	0.95160	0.96387	0.91575	0.84841
MVE	0.95073	0.95328	0.96362	0.97340
MCD	0.95116	0.95402	0.96460	0.97406
MVV	0.67512	0.68196	0.70963	0.50397

Table 10. The accuracy of the detected outliers for $p = 11$ and $n = 1000$

Method	Contaminated levels α			
	0.00	**0.01**	**0.05**	**0.10**
MLRSMD	0.98866	0.99247	0.99695	0.99846
MD	0.95146	0.96398	0.91537	0.84829
MVE	0.95128	0.95413	0.96401	0.97396
MCD	0.95137	0.95448	0.96463	0.97449
MVV	0.68379	0.68945	0.71655	0.50668

Tables 1–10 illustrate each simulation scenario using multivariate normal data. The results showed that the proposed method, MLRSMD, had the highest accuracy of outliers detected at all levels of contamination that were chosen. Therefore, the proposed method performed excellently in all scenarios.

A real dataset is utilized in this section to demonstrate the efficiency of the proposed method. Hepatitis C virus (HCV) data, which contains laboratory values of blood donors and Hepatitis C patients, contains 589 records and 11 variables (Lichtinghagen et al., 2013).

We use the effective MLRSMD method for detecting outliers that was studied during the simulation research. In this dataset, hepatitis C patients and blood donors were first separated into five groups according to severity, from least to greatest: 0 (526 blood donors), 0s (7 suspicious blood donors), 1 (20 hepatitis), 2 (12 fibrosis), and 3. (24 cirrhosis). We'll divide it into the following categories to make studying easier: non-morbid (0) in green points, moderate (0s, 1, 2) in grey points, and severe (3) in red points.

Of the total data, there were 589 patients. Using the MLRSMD method for detecting outliers (patients with disease), two groups of patients were identified, the first group being normal patients (466 patients), and the next group being the group that may have patients with the disease (123 patients). Only those groups that may have the disease (123 cases) were

considered with the cut-off point. Figure 2 shows that the MLRSMD method can find outlier values, which are abnormal people. Individuals are classified as abnormal when their absolute error points are more extreme than the cut-off point value (blue line). The method was able to detect 23 red points, 13 gray points, and 11 green points. This means that, based on real data, the proposed method might be able to find almost all patients with serious diseases.

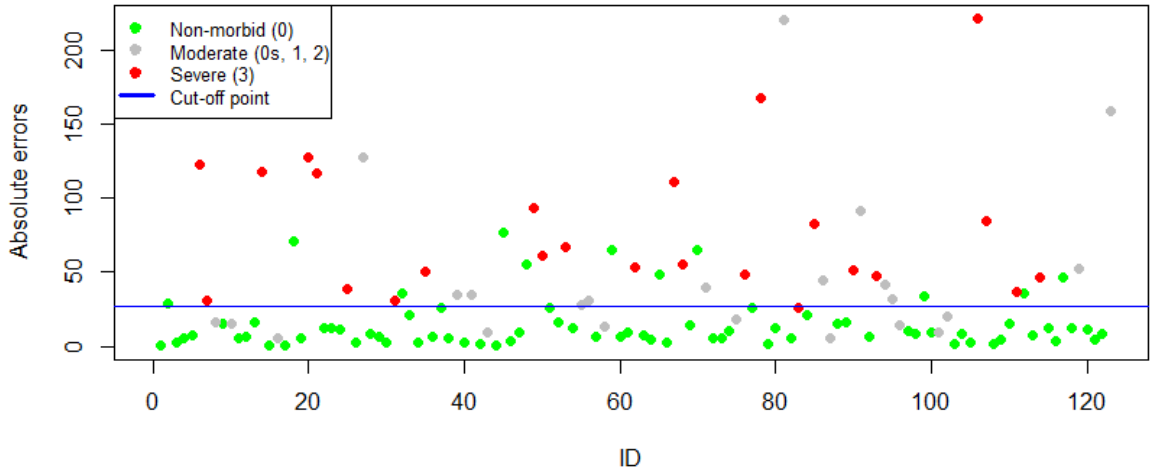

Figure 2. The MLRSMD detected outliers for Hepatitis C virus (HCV) data

Conclusion:

We focused on datasets that frequently emerge in organizations and have both high dimensionality and large sample sizes. The Mahalanobis distance and the Mahalanobis distance with the robust methods, i.e., MVE, MCD, and MVV are the most widely utilized. In the proposed method (MLRSMD), the Mahalanobis distance is used to filter data across all variables first with the square root of the chi-square distribution with the degrees of freedom equal to 1, and data for all variables that did not exceed the square root of the chi-square distribution with the degrees of freedom equal to 1 were labeled as normal data. After that, we used multiple linear regression to detect outliers in the rest of the data and found that this way could solve a problem like the Mahalanobis distance method since some datasets don't have to have outliers if there is no contamination. We also found the highest accuracy of our method for outlier detection across all levels of contamination compared to other methods. The outcomes show that using an initially filtered Mahalanobis distance in the suggested methods is a sensible idea. We also used the proposed method to find outliers in real datasets of blood donors and people with hepatitis C. The proposed method detects almost all severe cases.

Acknowledgements:

The Development and Promotion of Science and Technology Talents Project (DPST) is acknowledged.

References:

1. Aelst S V, Rousseeuw P. WIREs Computational Statistics. 2009; 1: 71-82.
2. Anscombe F J, Guttman I. Technometrics. 1960; 2(2): 123-147.
3. Cabana E, Lillo R E, Laniado H. Springer. 2019; 1:1-27.
4. Cook R D. Technometrics. 1977; 19: 15-18.
5. Herdiani E T, Sari P P, Sunusi N. Journal of Physics: Conference Series. 2019; 1341: 1-5.
6. Hoaglin D C, Welsch R E. Am. Stat. 1978; 32: 17-22.

7. Hubert M, Debruyne M. WIREs Computational Statistics. 2010; 2: 36-43.
8. Lichtinghagen R, Pietsch D, Bantel H, Manns M P, Brand K, Bahr M J. J Hepatol 2013; 59: 236-242
9. Mahalanobis P C. Proceedings of the National Institute of Sciences of India. 1936; 2(1): 49-55.
10. McGill R, Tukey J W, Larsen W A. The American Statistician. 1978; 32(1): 12-16.
11. Nurunnabi A, Imon A, Nasser M. Proceedings of International Conference on Statistical Science. 2008; 165-173.
12. Ranganai E. SpringerPlus. 2016; 5(1): 1-11.

A METHOD FOR OUTLIER DETECTION IN UNIVARIATE CIRCULAR DATA USING PARTITIONING DATA

Thawatchai Thianthong, Wuttichai Srisodaphol*
Department of Statistics, Faculty of Science, Khon Kaen University, Khon Kaen 40002 Thailand
*e-mail: wuttsr@kku.ac.th

Abstract:

Circular data is the value of the direction data and is recorded in the form of an angle. Many fields, such as geology, biology, meteorology, physics, psychology, image analysis, and medicine, correspond to this data. Circular data in the data analysis is still concerned about the outliers because the dataset can be obtained the outliers. The outliers can indicate some properties or anomalies of the sample unit. This research aims to propose a method for detecting outliers for univariate circular data that can detect outliers appropriately and should be easy to implement. The concept of the proposed method is based on the summation of the distance between any point and any other point, and then the partitioning of the data. The performance of the proposed method is evaluated in the simulation study. The results show that the proposed method has a preference over the other methods. Also, the outliers using this method for one real dataset are illustrated.

Introduction:

Circular data is a type of cyclic data that is the value of the direction data and is recorded in the form of an angle. This can occur in various forms in many fields, such as geology, biology, meteorology, physics, psychology, image analysis, and medicine. In circular data measurements, for example, in geology, researchers may be interested in the direction of the Earth's magnetic poles. While in biology, researchers may measure the direction of migration of birds or the direction of travel of animals. This data is defined as circular data. Circular data can be divided into two types: 1) data displayed on the two-dimensional circumference of a unit circle and measured in degrees with values in the range $\left[0^{\circ},360^{\circ}\right]$ or measured in radians with values in the range $\left[0,2\pi\right]$; and 2) data represented in three dimensions with two angles as points on the surface of a sphere or as points on the surface of the earth measured by longitude and latitude (Jammalamadaka & SenGupta, 2001).

Circular data cannot be represented on a straight line, and it is not appropriate to analyze like conventional linear data due to the geometric properties of circular data. The arithmetic mean of the linear data and the mean of the circular data are different. For example, we consider the following data: 100°, 300°. Considering the data as linear, the arithmetic mean is 200° but the circular mean is 20°. The geometric mean of the linear data and the circular mean are different (Mahmood et al, 2017). In outlier detection, there is a difference as well. Outliers are data points that are significantly different from other data. Data can be either very low or very high within the same dataset. In linear data, outliers are data points that are very different from other data, known as extremes. But circular data may not have extreme values (Collett, 1980). Consider the following datasets: 10°, 18°, 33°, 48°, 67°, 350°, if this dataset is considered linear data, 350°is the extreme value and outlier (Figure 1. (a)). When considering this data set as circular data in the [0°, 360°], 350° is clearly not an extreme value and is consistent with the outlier (Figure 1. (b)).

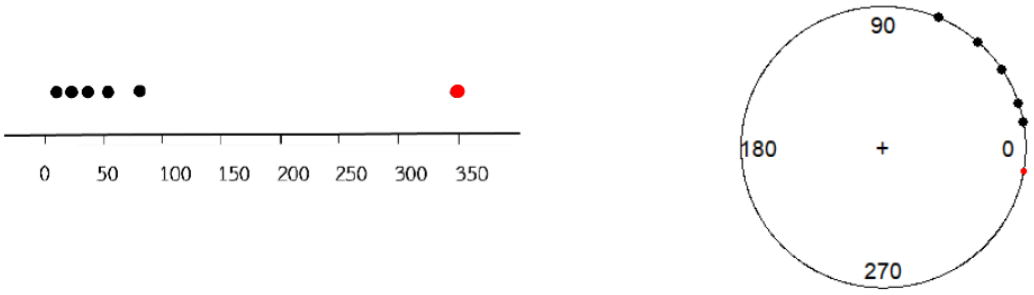

(a) Linear data (b) Circular data

Figure 1. Type of data

Therefore, as a result, the method for finding outliers in circular data is different from the method for finding them in linear data.

In statistical analysis, the causes of outliers are generally classified into three categories: (1) Natural variation: which is a variation that occurs within the population, (2) Measurement error: which is the variation arising from the difference between the measured value and the actual value. This variation is caused by poor quality measuring instruments, and (3) Operational errors: which is a variation caused by errors in recording data including the selection of a sample that is inconsistent with the population (Anscombe, 1960). In linear data with a single variable, there are numerous methods to find outliers. A box plot is the most commonly used for finding outliers in linear data. It does not directly apply to circular data. As a result, it is necessary to find a method to identify outliers in circular data. Mardia (1975) proposed statistics to detect outliers for univariate circular data. The method is to calculate the sum of circular data, which is a unit vector called the resultant length. Observations that significantly affect the resultant length are considered outliers. Collett (1980) presented the C-statistical and M-statistical outlier detection statistics to identify outliers for univariate circular data. The C-statistical outlier detection method is the method that uses the mean resultant length calculated from the ratio between the resultant length and the total number of observations. The M-statistical approach was created from Mardia's method and is based on resultant length. An outlier is the maximum resultant length that can be determined by removing one data observation. A-statistics are suggested by Abuzaid et al. (2009) to identify outliers in univariate circular data by calculating the sum of the circle distances from a point of interest to all other points on the circumference of one unit circle. The data with the highest distance total in comparison to the other data is the outlier. Abuzaid (2010) advised utilizing Chord statistics. It is a method that utilizes the sum of the distances of a chord between any point and any other point, like A-statistics. The outliers are the data that has the largest sum of the distances of the chord compared to the other data as well. Both the A-statistic and the Chord-statistic performed equally well. Moreover, Mahmood et al. (2017) presented RCDu-statistics to detect outliers in univariate circular data, which uses the distance between the observations and the median. The outliers are observations with the largest sum of the distance between them and the median compared to other observations. This method is more effective for detecting outliers than the previous methods. But this method, it is difficult to compare the statistical value to the cutoff points. This was obtained by simulating the von Mises distribution when the sample size and concentration parameters were different at various values.

Therefore, this research aims to propose a method for detecting outliers for univariate circular data that can detect outliers appropriately. That is, if the data set does not contain any outliers, they should not be detected. Or, if there should be outliers, more than one can be found, and it's easy to find outliers.

Methodology:

This research proposes an outlier detection method, which is called the Partition Distance method (PD). We use the summation of the distance between any point and any other point, and then partition the data into two sets. Dataset A has the small of the summation of the distance and Dataset B has the large of the summation of the distance (the outliers can appear in this dataset). Then we use dataset A to make a cutoff point for checking the outliers, which are contained in dataset B. The steps of our proposed method are as follows.

Step 1: Calculate the distance between the i observation and all other observations when $\theta_1, \theta_2, ..., \theta_n$ is given as n observations from univariate circular data. Data should be in radians. If the data is in degrees, it must be converted to radians by converting from $\theta_i^* \pi / 180$ where θ_i^* is the data in degrees. Rao (1969) defined the circular distance between θ_i and θ_j as

$$d_{ij} = 1\text{-}\cos(\theta_i - \theta_j),\ i, j = 1, 2, \ldots n$$

where d_{ij} is a function of $\left(\theta_i - \theta_j\right)$ that monotonically increases, and $d_{ij} \in [0, 2]$. The summation of all circular distances from point θ_j to all other points is represented by

$$D_j = \sum_{i=1}^{n} \left(1\text{-}\cos(\theta_i - \theta_j)\right),\ j = 1, 2, \ldots n.$$

Step 2: Let D_j be observations of dataset D, we find $\max(\text{dataset D})$ and $\min(\text{dataset D})$.

Step 3: Let m and M be $\left|D_j - \min(\text{dataset D})\right|$ and $\left|D_j - \max(\text{dataset D})\right|$, respectively.

Step 4: We divide the data into 2 sets where Dataset A: D_j observation j has m value less than or equal to M value and Dataset B: D_j observation j has m value more than M value.

Step 5: Following obtaining 2 sets of data in step 4, we create a cutoff point using the Dataset A by

$$\text{cutoff point} = \max(D_j \text{dataset A}) - 1.5(\max(D_j \text{dataset A}) - \min(D_j \text{dataset A})).$$

Step 6: We identify the outliers in Dataset B with the cutoff point obtained in step 5. For D_j in dataset B is greater than the cutoff point, then θ_j will be labeled as the outliers.

Results and Discussion:

In this section, we simulate the data using a von Mises distribution with and without contaminated levels of 0 and 0.05 to compare the performance of the proposed PD method with the performance of the RCDu method.

Step 1: We generate the circular data with sample sizes n = 20, 40, 60, 100 with mean direction μ = 0 and concentration parameter k = 2, 3, 5, 6, 8, 10 , with and without contaminated for the von Mises distribution $\left[\text{vM}(0, k)\right]$ using the R program. The data are contaminated with the outlier θ_c defined by

$$\theta_c = \theta + \lambda\pi \bmod(2\pi)$$

where λ is the degree of contamination, ($0 \le \lambda \le 1$).
There is no contamination if $\lambda = 0$. If λ is equal to 1, the circular data is found at its anti-mode.

Step 2: We apply the proposed PD method to identify outliers in each situation.

Step 3: We perform Steps 1 and 2 for 1,000 times for all situation s of the sample size and concentration parameter with $\lambda = 0.8$.

Step 4: We calculate an average proportion of the detected outliers and the rates of masking and swamping for the proposed PD method and the 5% and 10% of cutoff points of $RCDu$ method, which is the criterion to evaluate the performance of the proposed methods. It has the highest proportion of detection of outliers and low rate of masking and swamping for all contaminated levels and for all combinations.

Note that: The masking rate is a ratio indicating outlier values is normal.

The swamping rate is a ratio indicating normal values is outliers.

Performance of the proposed PD method and the $RCDu$ method with the 5% and 10% of cutoff points for $k = 2, 3, 5, 6, 8, 10$ and sample sizes $n = 20, 40, 60, 100$ with levels of contaminated 0 for no contamination and 0.05 contamination are showed in Tables 1-8, respectively.

Table 1. The average proportion of the detected outliers for no contamination and $n = 20$

k	**PD**	**RCDu 5%**	**RCDu 10%**
2	0.1300	0.0050	0.0127
3	0.1315	0.0122	0.0260
5	0.1400	0.0015	0.0042
6	0.1330	0.0222	0.0415
8	0.1380	0.1280	0.1920
10	0.1407	0.0882	0.1472

Table 2. The average proportion of the detected outliers for no contamination and $n = 40$

k	**PD**	**RCDu 5%**	**RCDu 10%**
2	0.0119	0.0030	0.0053
3	0.0116	0.0029	0.0062
5	0.0101	0.0040	0.0083
6	0.0107	0.0057	0.0113
8	0.0105	0.0098	0.0181
10	0.0096	0.0039	0.0073

Table 3. The average proportion of the detected outliers for no contamination and $n = 60$

k	**PD**	**RCDu 5%**	**RCDu 10%**
2	0.0016	0.0053	0.0103
3	0.0015	0.0018	0.0041
5	0.0010	0.0018	0.0032
6	0.0020	0.0025	0.0053
8	0.0015	0.0017	0.0035
10	0.0015	0.0040	0.0068

Table 4. The average proportion of the detected outliers for no contamination and $n = 100$

k	PD	RCDu 5%	RCDu 10%
2	0.0000	0.0003	0.0006
3	0.0000	0.0006	0.0014
5	0.0001	0.0004	0.0007
6	0.0001	0.0002	0.0005
8	0.0001	0.0019	0.0035
10	0.0002	0.0010	0.0019

From Tables 1-4, in case of no contaminated data, we found that the average proportion of the detected outliers using the PD, RCDu 5% and 10% methods close to the 0 contamination level for all concentration parameter. Moreover, the PD method is more effective for detecting outliers than the RCDu 5% and 10% methods when large sample sizes.

Table 5. The proportion of outliers detected, and rates of masking and swamping for levels of contaminated 0.05 and $n = 20$

k	proportion of outliers detected			Masking rate			Swamping rate		
	PD	RCDu 5%	RCDu 10%	PD	RCDu 5%	RCDu 10%	PD	RCDu 5%	RCDu 10%
2	0.3690	0.0010	0.0030	0.6310	0.9990	0.9970	0.0084	0.0017	0.0037
3	0.4930	0.0040	0.1160	0.5070	0.9960	0.8840	0.0058	0.0014	0.0026
5	0.6850	0.9220	0.9270	0.3150	0.0780	0.0730	0.0018	0.0002	0.0003
6	0.7750	0.9100	0.9100	0.2250	0.0900	0.0900	0.0012	0.0001	0.0003
8	0.8910	0.9150	0.9190	0.1090	0.0850	0.0810	0.0007	0.0000	0.0000
10	0.9320	0.9080	0.9080	0.0680	0.0920	0.0920	0.0003	0.0000	0.0000

Table 6. The proportion of outliers detected, and rates of masking and swamping for levels of contaminated 0.05 and $n = 40$

k	proportion of outliers detected			Masking rate			Swamping rate		
	PD	RCDu 5%	RCDu 10%	PD	RCDu 5%	RCDu 10%	PD	RCDu 5%	RCDu 10%
2	0.1115	0.0000	0.0000	0.8885	1.0000	1.0000	0.0029	0.0005	0.0009
3	0.2220	0.0000	0.0000	0.7780	1.0000	1.0000	0.0018	0.0001	0.0000
5	0.4325	0.0000	0.0005	0.5675	1.0000	0.9995	0.0003	0.0000	0.0000
6	0.5720	0.0000	0.0475	0.4280	1.0000	0.9525	0.0002	0.0000	0.0000
8	0.7170	0.7005	0.8395	0.2830	0.2995	0.1605	0.0002	0.0000	0.0000
10	0.8545	0.8205	0.8205	0.1455	0.1795	0.1795	0.0001	0.0000	0.0000

Table 7. The proportion of outliers detected, and rates of masking and swamping for levels of contaminated 0.05 and $n = 60$

k	proportion of outliers detected			Masking rate			Swamping rate		
	PD	RCDu 5%	RCDu 10%	PD	RCDu 5%	RCDu 10%	PD	RCDu 5%	RCDu 10%
2	0.0343	0.0000	0.0000	0.9656	1.0000	1.0000	0.0011	0.0007	0.0014
3	0.0980	0.0000	0.0000	0.9020	1.0000	1.0000	0.0006	0.0002	0.0008
5	0.2550	0.0000	0.0000	0.7450	1.0000	1.0000	0.0001	0.0000	0.0001
6	0.4050	0.0000	0.0000	0.5950	1.0000	1.0000	0.0001	0.0000	0.0000
8	0.6313	0.7953	0.8416	0.3686	0.2046	0.1583	0.0000	0.0000	0.0000
10	0.7893	0.8276	0.8276	0.2106	0.1723	0.1723	0.0000	0.0000	0.0000

Table 8. The proportion of outliers detected, and rates of masking and swamping for levels of contaminated 0.05 and $n = 100$

k	proportion of outliers detected			Masking rate			Swamping rate		
	PD	RCDu 5%	RCDu 10%	PD	RCDu 5%	RCDu 10%	PD	RCDu 5%	RCDu 10%
2	0.0020	0.0000	0.0000	0.9980	1.0000	1.0000	0.0000	0.0001	0.0003
3	0.0132	0.0000	0.0000	0.9868	1.0000	1.0000	0.0000	0.0001	0.0001
5	0.1056	0.0000	0.0000	0.8944	1.0000	1.0000	0.0000	0.0000	0.0000
6	0.2022	0.0000	0.0000	0.7978	1.0000	1.0000	0.0000	0.0000	0.0000
8	0.4538	0.0000	0.5546	0.5462	1.0000	0.4454	0.0000	0.0000	0.0000
10	0.6836	0.5980	0.7350	0.3164	0.4020	0.2650	0.0000	0.0000	0.0000

From Tables 5-8, in the case of levels of contaminated 0.05, we found that the proportion of outliers detected is more than the RCDu 5% and 10% for all concentration parameters and all sample sizes. Moreover, we found that the PD method can indicate normal values as outliers at a lower rate (swamping rate). But it indicates outlier values as normal (masking rate) at a higher rate while being less than the RCDu 5% and 10% for small concentration parameters and all sample sizes.

When we must consider the method to use for detecting outliers, we can use the PD method, but we may concern in the case of indicating normal values as outliers.

The effectiveness of the PD method is illustrated in this section using a real dataset. 14 frogs 104°, 110°, 117°, 121°, 127°, 130°, 136°, 145°, 152°, 178°, 184°, 192°, 200°, 316° were taken as a sample from the mud flats close to Indianola, Mississippi (Collett, 1980). The frogs were released, and their cues were followed after 30 hours. The PD method can identify one outlier in this dataset. The results can be shown in Figure 2. (a) using the PD method. Moreover, Figure 2. (b) shows the location of the outlier on the circle.

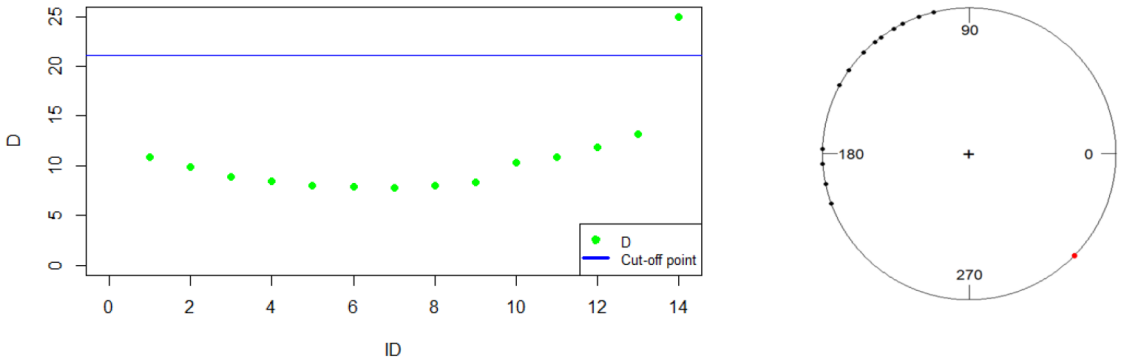

(a) The outlier is indicated with the PD method

(b) The outlier is plotted on the circle

Figure 2. The outlier is indicated in the frog data

Conclusion:

We propose a method for detecting outliers for univariate circular data that can detect outliers appropriately and is easy to find outliers. The summation of the distance between any point and any other point, and then partitioning the data into two sets (normal dataset and dataset that may have outliers) is the concept of this proposed method. The performance of the proposed method is considered in the simulation study using a von Mises distribution. We simulate data with and without contamination and consider the criterion for evaluating the method, i.e., the proportion of detection of outliers, masking rate, and swamping rate. We can conclude that the proposed method has good performance, but we may concern in the case of indicating normal values as outliers. Moreover, when we use the proposed method for detecting outliers in a real dataset, we illustrate the outlier in a circle.

Acknowledgements:

We would like to thank Department of Statistics, Faculty of Science, Khon Kaen University for financial support.

References:

1. Abuzaid AH. Ph.D. thesis, University of Malaya, Kuala Lumpur, Malaysia. 2010.
2. Abuzaid AH, Mohamed IB, Hussin AG. Communications in Statistics – Simulation and Computation. 2009; 38(4), 682-691.
3. Anscombe F. Technometrics. 1960; 2(2), 123-147.
4. Collett D. Appl Stat 1980; 29(1):50–57.
5. Jammalamadaka SR, SenGupta A. World Scientific Press, Singapore. 2001.
6. Mahmood EA, Rana S, Midi H, Hussin AG. Journal of Modern Applied Statistical Methods. 2017; 16(2), 418-438.
7. Mardia KV. Journal of the Royal Statistical Society. Series B (Methodological). 1975; 37(3), 349-393.
8. Rao JS. Ph.D. thesis, Indian Statistical Institute, Calcutta, India. 1969.

COMPARISION OF PERFORMANCE OF DATA CLASSIFICATION USING DECISION TREE AND RANDOM FOREST TECHNIQUES

Patitta Suksomboon, Orraya Suwanno
Faculty of management science, Prince of Songkla University, Thailand
*e-mail: patitta.s@psu.ac.th, orraya.s@psu.ac.th

Abstract:

The objective of this research is to determine the efficiency of two popular models of data classification, Decision Tree model and Random Forest model. Nowadays, a problem of classification is a concern for researchers to optimize the efficiency of classification accurately. Researcher therefore conducted experiments with four different data sets from UCI data set test, including with: a) Breast Cancer Wisconsin (Diagnostic) data set, which was divided into two classes, Malignant and Benign. b) Heart Disease data set c) Lymphography data set and d) Statlog (Heart) data set.

Results from the Decision Tree method reveal that when considering accuracy, the Heart Disease data set has the highest value at 82.49%, followed by the Lymphography Data set is 81.19%, Statlog (Heart) data set is 79.26% and Breast Cancer Wisconsin (Diagnostic) data set is 73.54%.

Considering Recall values, they reveal that the Breast Cancer Wisconsin (Diagnostic) data set is 65.78% for True Malignant and 79.40% for True Benign. The Heart Disease data set is 75.57% for True Positive and 87.79% for True Negative, the Lymphography data set is 80.33% for True Malign lymph, 85.91% for True Metastases and 50.00% for True Fibrosis. The Statlog (Heart) data set is 80.00% for True Presence and 78.67% for True Absence.

Considering Precision values, they reveal that the Breast Cancer Wisconsin (Diagnostic) data set is 70.71% of Malignant and 75.42% for Benign. The Heart Disease data set is 82.50% for Positive and 82.51% for Negative, the Lymphography data set is 77.78% for Malign lymph, 85.91% for Metastases and 66.67% for Fibrosis. The Statlog (Heart) data set is 75.00% for Presence and 83.10% for Absence.

Results from the Random forest method reveal that when considering accuracy, the Lymphography data set has the highest value at 87.19% followed by, Statlog (Heart) data set is 85.19%, the Heart Disease data set is 80.22% and Breast Cancer Wisconsin (Diagnostic) data set is 74.96%.

The recall values of the random forest experiments, the Breast Cancer Wisconsin (Diagnostic) data set is 63.46% for True Malignant and 83.67% for True Benign. The Heart Disease data set is 63.46% for True Positive and 83.67% for True Negative, the Lymphography data set is 86.89% for True Malign lymph, 91.36% for True Metastases and 50.99% for True Fibrosis. The Statlog (Heart) data set is 77.50% for True Presence and 91.33% for True Absence.

Considering Precision values, they reveal that the Breast Cancer Wisconsin (Diagnostic) data set is 74.61% of Malignant and 75.17% for Benign. The Heart Disease data set is 74.61% for Positive and 75.17% for Negative, the Lymphography data set is 84.13% for Malign lymph, 89.16% for Metastases and 100.00% for Fibrosis. The Statlog (Heart) data set is 87.74% for Presence and 83.54% for Absence.

If we compare accuracy values of 4 data sets, the Random forest model gives higher value in 3 of 4 data sets which are Breast Cancer Wisconsin (Diagnostic) data set,

Lymphography data set and Statlog (Heart) data set. For Heart Disease data set, accuracy value of Random forest method is 2.27% less than Decision Tree method. The precision values of Random forest method are performed better than Decision Tree method with all of fours data sets.

Introduction:

Ali et al. [1] presented the comparison of the classification results obtained from two methods, Random Forest and Decision Tree. They took 20 data sets available from UCI repository containing instances varying from 148 to 20000. The classification results show that Random Forest gives better results for the same number of attributes and large data sets. Savargiv et al. [5] presented a method based on learning automata which the adaptive capabilities of the problem space are added to the random forest to increase its efficiency. The evaluation results of the research confirm the improvement of random forest efficiency.

To accelerate research in the field of Machine Learning, in-depth study of existing work related to Random Forest can help. There is scope for improvement in accuracy by using different split measures and combining functions; and in performance by dynamically pruning a forest and estimating optimal subset of the forest. Herrera et al. [2] described how initial Random Forest implementation has been optimized and has become an efficient distributed machine learning implementation for Big Data. They took full advantage of the HPCC (the High Performance Computing Cluster) Systems Platform's Big Data processing and analytics capabilities.

The Decision Tree approach got the highest accuracy which is 99.93% comparing to other techniques such as k-Nearest Neighbors, Logistic Regression, Support Vector Machine, and Naïve Bayes which are less performing than the Decision Tree approach. [3]. Based on the study [5], Decision Tree -based methods are introduced to the field of content marketing, and Decision Tree -based methods intrinsically follow the process of human decision making. The results of the study show that the Decision Tree -based method can provide reasonable and accurate suggestions for content marketing.

Methodology:

Decision Trees have been widely used in data mining and machine learning. This method is the most powerful and popular tool for classification and prediction. Therefore, classification is useful in helping user analyze data and make more accurate decisions. The tree is formed by successively dividing data according to one of the predictor variables. A decision tree consists of three types of nodes: root node, internal nodes, and leaf nodes. It has tree structural pattern comprises with internal node, branch/link and leaf node as in figure 1.

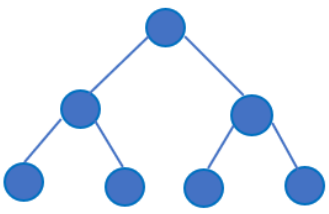

Figure 1.
Decision Tree

1) An internal node represents the features of a data set. The internal node that is the starting point of the tree is called the root node. 2) Branch or link is the value of the attribute

in the internal node that branches out. Branch represents the decision rules. An internal node will branch an amount equal to the number of attribute values in that internal node. 3) Leaf node is a group which is the result of data classification.

The computation of the branch is a structure used to express the rules derived from the classification technique. Important issue to consider when creating a Decision Tree is which attribute should be the root node in each branch of the tree and each subtree. The criterion used in the selection of attributes is to calculate the Gain Criterion. This is a value that indicates how well the attribute can classify the data. The value of the data axis can be calculated as in Equation 1.

$$I(s_{1,}s_{2,}s_n) = \sum_{i=1}^{n} \frac{s_1}{s} \log_2 \frac{s_1}{s} \quad (1)$$

s is the set of data which consists of s records.
n is the total number of different groups of that data set.
i represents the group in class i, where i is between 1 and n
s_i represents the number of members of s and belongs to the group C_i
s_{ij} represents the number of data that is a member of s in group i by dividing the data by possible values of the A attribute.

The entropy of the A attribute can be calculated from Equation 2.

$$E(A) = \sum_{i=1}^{n} \frac{s_1+s_2+s_n}{s} I(s_1, s_2, s_n) \quad (2)$$

Random forest is a machine learning algorithm that is used widely in classification and regression problems. It generates many classification trees by selecting subsets of the given dataset and selecting subsets of predictor variables randomly, finally aggregating the results of all models to obtain a random forest. It combines the output of multiple Decision Trees to reach a single result as in figure 2. The algorithm establishes the outcome based on the predictions of the Decision Trees. It predicts by taking the average or mean of the output from various trees. Increasing the number of trees increases the precision of the outcome. Random forest workflow is;

1. Randomly select k attributes from total mm attributes where $k < m$, the default value of k is generally $\sqrt{m}$.
2. Among the k attributes, calculate the node dd using the best split point
3. Split the node into a number of nodes using the best split method. by default R random Forest, uses Gini impurity values
4. Repeat the previous steps build an individual Decision Tree
5. Build a forest by repeating all steps for n number times to create n number of trees

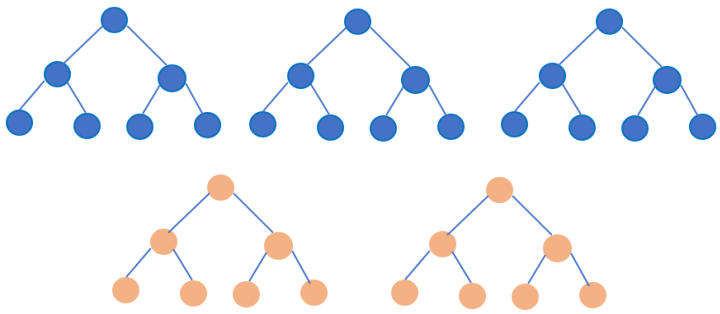

Figure 2.
Random Forest

This research compares the operation of the Decision Tree and random forest with test data from the well-known UCI Data set database. The researcher selected four complex data set s as shown in table 1.

Table 1.
UCI Data set test

Data set	Attribute Characteristics	Number of Instances	Number of Attributes
Breast Cancer Wisconsin (Diagnostic)	Real Number	569	32
Heart Disease	Categorical Integer Real Number	303	75
Lymphography	Categorical Number	148	18
Statlog (Heart)	Categorical Real Number	270	13

1. Breast Cancer Wisconsin (Diagnostic) data set Attribute Characteristics is Real Number of Instances: 569 Number of Attributes: 32
2. Heart Disease data set Attribute Characteristics: Categorical, Integer, Real Number of Instances: 303 Number of Attributes:75
3. Lymphography data set Attribute Characteristics: Categorical Number of Instances: 148 Number of Attributes:18
4. Statlog (Heart) data set Attribute Characteristics: Categorical, Real Number of Instances: 270 Number of Attributes:13

In this research, we evaluated the model with datasets test and report the performance of a model via accuracy, Precision, Recall.

Precision is the ratio of correctly predicted positive observations to the total predicted positive observations. The precision is calculated between the number of *Positive* samples correctly classified to the total number of samples classified as *Positive* (either correctly or incorrectly).

Recall is the ratio of correctly predicted positive observations to the all observations in actual class. The recall is calculated between the numbers of *Positive* samples correctly

classified as *Positive* to the total number of *Positive* samples. The recall measures the model's ability to detect *Positive* samples. The higher the recall, the more positive samples detected.

Accuracy is the most intuitive performance measure and it is simply a ratio of correctly predicted observation to the total observations. Accuracy is a metric that generally describes how the model performs across all classes. It is useful when all classes are of equal importance. It is calculated between the numbers of correct predictions to the total number of predictions.

Results and Discussion:

The results were compared between the Decision Tree and the random forest from the Breast Cancer Wisconsin (Diagnostic) data set. This data set was divided into two classes, Malignant and Benign. The results of the Decision Tree were used with an accuracy of 73.54% Precision Malignant is equal to 70.71% Benign is equal to 75.42% Recall True Malignant is equal to 65.78% True Benign is equal to 79.40% as shown in Table 2-3

Table 2.
Decision Tree Breast Cancer Wisconsin (Diagnostic) data set

Accuracy 73.54%

	True Malignant	**True Benign**	**Precision**
Malignant	198	82	70.71%
Benign	103	316	75.42%
Recall	65.78%	79.40%	

Table 3.
Random forest Breast Cancer Wisconsin (Diagnostic) data set

Accuracy 74.96%

	True Malignant	**True Benign**	**Precision**
Malignant	191	65	74.61%
Benign	110	333	75.17%
Recall	63.46%	83.67%	

The results of the comparison between Decision Tree and the random forest from the Heart Disease data set are shown in Table 4-5.

Table 4.
Decision Tree Heart Disease data set

Accuracy 82.49%

	True Positive	**True** Negative	**Precision**
Positive	99	21	82.50%
Negative	32	151	82.51%
Recall	75.57%	87.79%	

Table 5.
Random forest Heart Disease data set

Accuracy 80.22%

	True Positive	**True** Negative	**Precision**
Positive	191	65	74.61%
Negative	110	333	75.17%
Recall	63.46%	83.67%	

The results of the comparison between Decision Tree and the random forest from the Lymphography data set are shown in Tables 6-7.

Table 6.
Decision Tree Lymphography data set

Accuracy 81.19%

	True Malign lymph	**True** Metastases	**True** Fibrosis	Normal find	**Precision**
Malign lymph	49	11	2	1	77.78%
Metastases	11	69	0	1	85.91%
Fibrosis	1	0	2	0	66.67%
Normal find	0	1	0	0	0
Recall	80.33%	85.91%	50.00%	0.00%	

Table 7.
Random forest Lymphography data set

Accuracy 87.19%

	True Malign lymph	**True** Metastases	**True** Fibrosis	Normal find	**Precision**
Malign lymph	53	7	2	1	84.13%
Metastases	8	78	0	1	89.16
Fibrosis	0	0	2	0	100.00%
Normal find	0	0	0	0	0
Recall	86.89%	91.36%	50.99%	0.00%	

The results of the comparison between Decision Tree s and random forest from Statlog (Heart) data set 8-9.

Table 8.
Decision Tree Statlog (Heart) data set

Accuracy 79.26%

	True Presence	**True** Absence	**Precision**
Presence	96	32	75.00%
Absence	24	118	83.10%
Recall	80.00%	78.67%	

Table 9.
Random forest Statlog (Heart) data set

Accuracy 85.19%

	True Presence	**True** Absence	**Precision**
Presence	93	13	87.74%
Absence	27	137	83.54%
Recall	77.50%	91.33%	

Conclusion:

This research is conducted experiments with four different data sets from UCI data set test, including with: a) Breast Cancer Wisconsin (Diagnostic) data set b) Heart Disease data set c) Lymphography data set and d) Statlog (Heart) data set which is a data set containing instances and classes with challenging class attributes. The precision values of Random forest method are performed better than Decision Tree method with all of fours data sets while the Random forest model gives higher value in 3 of 4 data set. The efficiency evaluation of Decision Tree model versus Random Forest model, the experiments reveal that Random Forest model returns better result values compared to Decision Tree model for the same data set.

References:

1. Ali J, Khan R, Ahmad N and Maqsood I. Random Forests and Decision Trees. I International Journal of Computer Science Issues. 2012;9:272-278.
2. Herrera VM, Khoshgoftaar TM, Villanustr F and Furht B. Random forest implementation and optimization for Big Data analytics on LexisNexis's high performance computing cluster platform. Journal of Big Data. 2019;6:1-36.
3. Jijo BT, Abdulazeez AM. Classification based on decision tree algorithm for machine learning. Journal of Applied Science and Technology Trends. 2021;02:20-28.
4. Liu Y and Shuo Y. Application of Decision Tree-Based Classification Algorithm on Content Marketing. Journal of Mathematics. 2022:1-10
5. Savargiv M, Masoumi B and Keyvanpour MR. A New Random Forest Algorithm Based on Learning Automata. Computational Intelligence and Neuroscience. 2021:1-19.

INDIFFERENCE PRICING OF EXOTIC OPTIONS UNDER MEAN-VARIANCE UTILITY WITH FINITE LIQUIDITY

Pornnapat Yamphram, Udomsak Rakwongwan*

Department of Mathematics, Kasetsart University, Bangkok 10900, Thailand
*e-mail: udomsak.ra@ku.th

Abstract:

We empirically study the portfolio selection problem where tradable assets are a bank account, and standard put and call options written on S&P 500 index. The problem is mathematically formulated as an optimization problem where the variance of the portfolio is perceived as risk. The task is to find the portfolio which has a satisfactory return but has the minimum variance. The underlying is modeled by a variance gamma process which can explain the extreme price movement of the asset. We also study how the optimized portfolio changes subject to a user's view on the future asset price. Moreover, the optimization model is extended for asset pricing. To illustrate the pricing technique, we compute indifference prices for buying and selling six options namely a European call option, a quadratic option, a sine option, a butterfly spread option, a digital option, and a log option and propose the hedging portfolios, which are the portfolios one needs to hold to minimize risk from selling or buying such options, for all the options. The sensitivity of the price from modeling parameters is also investigated. Our hedging strategies are decent. The payouts of the hedging portfolios are very close to those of the bought or sold options. The results shown in this study are just the illustrations of the techniques. The approach can also be used for other assets such as stocks, bonds, or derivatives in any financial markets with just some small adjustments.

Introduction:

Financial risk and liability can be mitigated through appropriately trading in financial markets. In other words, having a liability, which is normally stochastic, a user would want to reduce his or her risk by buying or selling some other financial instruments available in the markets. In complete markets, where all assets are perfectly liquid and there is no transaction cost, it has been shown by Black and Scholes [2] that financial derivatives can be uniquely priced and perfectly hedged by dynamically trading their underlying and cash. However, this is not true in incomplete markets, in which liquidity is limited. Moreover, the pricing and hedging problems, in practice, are highly subjective. Different agents may have different current financial positions, view risk differently, and have different views on the future values of the assets, see e.g. [13] and [14].

Most works in pricing and hedging financial derivatives assume market completeness. Following the ground-breaking work by Black and Scholes [2], there has been extensive literature on derivative pricing based on a risk-neutral measure. The fair price of a derivative

is determined by the expectation of the discounted terminal payoff of the derivative under a risk-neutral measure. The price, in terms of the expectation, can be easily and analytically derived if its density is known, see [19]. For those where the density is unknown, the no-arbitrage price can be computed by solving the corresponding partial differential equation derived from the Feynman–Kac theory. For example, Sepp [20] derived analytical pricing formulas for options on realized variance under Heston stochastic volatility model, whereas the pricing formula for an interest rate swap under the extended Cox–Ingersoll–Ross (ECIR) process was proposed by Boonklurb et al [3].

In incomplete markets, the classic risk-neutral approach cannot be applied. Most works derive formulas for indifference prices by using convex duality theory, see e.g. [11], [12], and [15]. However, the scheme is complex and hard to apply in practice. A more practical approach for option pricing was proposed by Breeden and Litzenberger [4]. The option payoff is replicated by the collection of other options with different strikes finitely available in the markets. The price of the payoff is thus the cost of replication. Although the approach works reasonably well in practice when there are enough options available in the markets, the combination replicating the payoff might not be most suitable. Moreover, the subjective factors, which are different for each individual, are not taken into account. Thus, a more efficient scheme of pricing called "indifference pricing" was proposed. An indifference price is a price a seller (buyer) needs to take (can pay) so that the risk after selling or buying is not worsened, see [8] and [14]. In contrast to the approaches mentioned above, indifference pricing takes subjectivity into account. The selling and buying prices of financial derivatives for different agents can be different. Moreover, the approach ensures that the combination for derivatives hedging is the best available in the markets. The indifference pricing approach is built on an optimal investment model. Armstrong et al. [1] illustrated the use of the indifference pricing technique to price and hedge index options written on S&P 500 index under the exponential loss utility by numerically directly solving the primal problem. Another recent work that focused on indifference pricing and hedging by solving the primal problem was by Pennanen and Bonatto [16]. They computed hedging portfolios in oil markets under the exponential loss utility. As opposed to the exponential loss utility, there are various risk measures such as the mean-variance criteria, the value-at-risk (VaR), and the conditional value-at-risk (CVaR). Although the portfolio optimization models of such risk measures have been extensively studied, see [10] [17] [5] [18] [7], the study of the indifference prices and hedging, in practice, is still limited.

In this paper, we consider indifference pricing and hedging where risk is measured by a portfolio's return variance, and the quotes come with bid-ask prices as well as the sizes, and the maximum quantities one can buy or sell. In other words, our portfolio optimization model in which the indifference pricing and hedging are built upon is an extension of the mean-variance portfolio optimization, first proposed by Markowitz [10], where we have bid-ask prices and illiquidity. As an example, the technique is illustrated in the mini S&P 500 index options market. The trading assets are a bank account with zero interest rate, and the mini put and call options written on S&P 500 index. The case where the interest rate is not zero can be done in the same manner. The underlying is modeled by a variance-gamma process (see [8] and [6]), which is similar to the Geometric Brownian motion except that the time change is

gamma distributed. This lets the process have control over skewness and kurtosis which is more realistic as it is known that a return in stock markets usually has fat tails.

Given a required average return, we first determine the optimal portfolio and plot its payout as a function of the index value at maturity. We also numerically illustrate the effects of various parameters including modeling parameters and the required return and plot the efficient frontier of the portfolio. Next, we compute indifference prices for buying and selling six different options namely a call option, a quadratic option, a log option, a digital option, a butterfly spread option, and a sine option. The hedging portfolio, the portfolio one needs to hold after selling or buying in order to mitigate risk, for each option is also computed. We showed that all options are hedged reasonably well given the quantity constraints and spreads. The technique can be applied to any other markets for any European options whose payouts are functions of the underlying at maturity.

Methodology:

1. The Market

The tradable assets are a bank account with zero interest rate, and 199 mini S&P 500 put and call options with different strikes. Table 1 shows an example of mini S&P 500 option prices taken on 19 May 2020 at 12:00:01 New York time. The spot is 295.42. The investment horizon is one month which is exactly the time when all of the options expire. One can see that the options come with finite liquidities. For example, if a trader wants to buy a call option with strike 262 (the first row), there are only 10 contracts available. Although we have 199 options, it is worth noting that there is only one random factor which is the value of the index at maturity as all of the options are written on the same index.

Table 1.

Taken from Bloomberg terminal on the 19th of May 2020 at 12:00:01 Bangkok time.

Bloomberg Ticker	Bid Price	Ask Price	Bid Size	Ask Size
S&P 19/05/2020 C262 Equity	34.54	35.09	10	10
S&P 19/05/2020 P262 Equity	1.93	2.01	7	26
S&P 19/05/2020 C263 Equity	33.63	34.18	10	10
S&P 19/05/2020 P263 Equity	2.02	2.1	12	5

2. Portfolio Optimization

The variance of a portfolio return can be perceived as a risk. Given the same average return, a portfolio whose return has a higher chance of deviating from the mean is considered riskier. The mean-variance optimization was introduced by Markowitz (1952). Let J denotes a set of all tradable assets. Given a portfolio vector x, the units invested in each tradable asset, and the covariance matrix of the assets' payouts Σ, the variance of payout of the portfolio x, denoted by $Var(s_1 \cdot x)$, can be written as,

$$Var(R_x) = x^T \Sigma x \,. \tag{1}$$

The derivation of (1) can be found in [9].

For a required return r, the portfolio optimization model where variance is perceived as risk can be written as,

$$\begin{aligned} Min \quad & Var(s_1 \cdot x) && \text{over} \quad x \in \mathbb{R}^n \\ \text{s.t.} \quad & s_0 \cdot x \leq w, \\ & m \cdot x \geq r, \\ & x \geq 0 \end{aligned} \tag{2}$$

where s_0 is a vector of the current prices of the assets, m is a vector of the average returns of the assets, and $w \in \mathbb{R}$ is an initial wealth.

However, as the quotes come with bid and ask prices, which means the cost of buying and selling are not the same, the model (2) need to be modified. This can be done by splitting the decision variable x into three parts which are (i) the quantities invested in the assets with no bid-ask spreads, (ii) the quantities invested in the assets when one can only buy, and (iii) the quantities invested in the assets when one can only sell. Rigorously, let $\hat{x}$ denote the new decision variable, we have that $\hat{x} = [x^0 \; x^a \; x^b]$ where x^0 is the quantity held in cash, and x^a and x^b are vectors of quantities invested in the assets if one wants to buy and sell, respectively. Note that x^a and x^b are nonnegative, and the quantity invested in option i is equal to $x_i^a - x_i{}^b$. Similarly, we also need to introduce the new covariance matrix $\hat{\Sigma}$, the cost vector $\widehat{s_0} = [s_0^0 \; s_0^a \; s_0^b]$, the future payout vector of the assets $\widehat{s_1} = [s_1^0 \; s_1^a \; s_1^b]$, the and the new average return vector $\widehat{m} = [m^0 \; m^a \; m^b]$ in the same manner. It is worth noting that $s_1^a = s_1^b$. In addition, as we do have quantity constraints, the quantity one wants to buy (sell) a particular asset should not exceed its ask size (bid size).

The portfolio optimization model in which the bid-ask spreads and the illiquidity are taken into account can be written as,

$$\begin{aligned} & Min \quad Var(s_1^0 \cdot x^0 + s_1^a \cdot x^a - s_1^b \cdot x^b) \quad \text{over} \quad \hat{x} \in \mathbb{R}^n \\ \text{s.t.} \quad & s_0^0 \cdot x^0 + s_0^a \cdot x^a - s_0^b \cdot x^b \leq w, \\ & m_0^0 \cdot x^0 + m_0^a \cdot x^a - m_0^b \cdot x^b \geq r, \\ & x^a \geq 0 \\ & x^b \geq 0. \end{aligned} \tag{3}$$

In this work, we assume that the return of the index follows the Variance Gamma Model. Variance gamma process, introduced in Finance by Madan and Seneta [8], is obtained by evaluating Brownian motion (with constant drift and volatility) at a random time change given by a gamma process, which can be expressed as

$$X(t;\, \sigma_J;\, v;\, \theta) = \theta\gamma(t) + \sigma_J W[\gamma(t)], \tag{4}$$

where v is the rate of variance of the gamma process $\gamma(t)$, σ_J is the instant volatility, and W is a standard Brownian motion. The value of the index in equation (4), $S(t)$, is given by

$$S(t) = s_0 exp[(\mu + \omega)t + X(t; \sigma_J; v; \theta)], \tag{5}$$

where μ is the instant expected rate and ω is the negative of the logarithm of the Variance-Gamma characteristic function.

We use the Variance gamma process to model the index return as opposed to the Geometric Brownian motion due to the jumps exhibited in historical data. Unless otherwise stated, the parameters used in the variance gamma model are as Table 2.

Table 2.
The statistical density parameters on variance gamma models.

Parameter estimated	Variance gamma
m	0.000001
T	0.83333
s	295.42
ν	0.01
θ	0

α is the mean rate of return, T is time to maturity, s is the strike price, ν captures the excess kurtosis, and θ is the control for the skewness.

3. Indifference Pricing and Hedging

In this section, we describe the scheme of finding indifference prices, which are the prices which do not worsen the risk of a user if he or she agrees to commit to the transaction, for financial derivatives. As the indifference pricing is built on an optimal investment model. We first need to define the optimal value function $\varphi(w, c)$ as a function of an initial wealth w and the future liability $c \in L^0(\Omega, F, P)$. Let D denotes the optimization constraints stated in (3), the optimal value function can be defined by

$$\varphi(w, c) := inf\{Var(c - [s_1^0 \cdot x^0 + s_1^a \cdot x^a - s_1^b \cdot x^b]) \mid x \in D\}. \quad (6)$$

We can see that $\varphi(w, c)$ is the minimal variance possible once the liability c is taken. This formulation makes sense terms of pricing as normally, after taking the liability c, one would want to find the suitable collection of assets, usually are correlated with the liability, to trade to reduce the risk. The optimal value function is non-increasing in w and is non-decreasing in c, that means the unhappiness of traders will not increase if they have more initial wealth.

The remaining question is how much a seller charge should charge if he or she decides to sell a particular financial derivative creating a liability c. Considering a trader with initial wealth $\bar{w}$ and initial liability $\bar{c}$, the indifference price for selling a financial derivative creating a claim c is given by

$$\pi_s(\bar{w}, \bar{c}, c) := inf\{w \mid \varphi(\bar{w} + w, \bar{c} + c) \leq \varphi(\bar{w}, \bar{c})\}. \quad (7)$$

This is the minimal amount of money a seller needs to charge so that the risk after selling, $\varphi(\bar{w} + w, \bar{c} + c)$, is not higher than that before selling, $\varphi(\bar{w}, \bar{c})$.

Similarly, the indifference price for buying a financial derivative in order to receive the claim c in the future is given by

$$\pi_b(\bar{w}, \bar{c}, c) := sup\{w \mid \varphi(\bar{w} - w, \bar{c} - c) \leq \varphi(\bar{w}, \bar{c})\}. \quad (8)$$

This is the minimal amount of money a buyer can pay so that the risk after buying, $\varphi(\bar{w} - w, \bar{c} - c)$, is not higher than that before buying, $\varphi(\bar{w}, \bar{c})$. It is worth noting that after the purchase, the buyer has lower initial wealth, but will has low liability as well.

We can see that in order to find indifference prices for selling and buying, one needs to solve the infimum and the supremum problems. This can be done by a line search algorithm such as the bisection method. In other words, to compute the indifference prices, a user need to guess w and solve the optimization problem (3) iteratively and determine its infimum or supremum.

Once the prices are computed, the hedging portfolio, which is a portfolio one need to hold after selling or buying can be determined by $x - \bar{x}$ where x and $\bar{x}$ are optimal portfolio after and before taking the claim, respectively. This hedging portfolio should have a payout close to that of the claim, especially at the points with high probability of occurring.

Results and Discussion:

1. Results: Portfolio Optimization

Our current available information is the S&P's stock price and the European options' prices written on the stock on the 19th of May 2020.

Let's assume that we are holding 100,000 units of the option with the spot 295.42. By assuming that the stock price follows the Variance Gamma Model with $\mu = 0.01$ and $\sigma = 0.2$ and we need 0.05 return per 1 month. We will consider the results of the bid and ask spread. For this project, we have 200 assets: one cash and 199 options. We split the asset by bid and ask price effect into two. Thus, we have a total of 399 assets. Of all 199 assets, we will be able to both buy and sell. By doing so, we will be able to consider different returns for buying and selling, which are affected by bid and ask spread. This is an algorithm,

1. Find the matrix of asset return.
   (a) Calculate the value of the cash after 30 days.
   (b) Simulate stock price scenarios after 30 days.
   (c) Compute the options' payoffs of all options using the simulation stock prices.
   (d) defines the matrix of return Each column of the matrix identifies the type of content, while each row refers to a different situation.
2. Calculate means and covariances of returns.
3. Use the built-in quadprog function to solve problems.

From Table 3, we can see that the minimum standard deviation is 1756.98 and the expectation of the payoff is 105000.00.

Table 3.

The expectation and the standard deviation of the standard deviation minimization portfolio with bid and ask spread using numberOfScenarios = 10,000.

Expectation	Standard deviation
105000.00	1756.98

The Figure 1 shows the optimized portfolios. The bottom panel shows the optimal portfolio with bars corresponding to the optimal position in the asset, that is, it illustrates a quantity of put option will notice that the nature of the option's is negative, or it can be said that put option

is interpreted as a negative sentiment about the future value of the underlying stock. On the other hand, the call option will have a positive value. The top panel, it can be noticed that the left tail is thinner and then gradually increased, thus avoiding higher risk, resulting in a spread of returns.

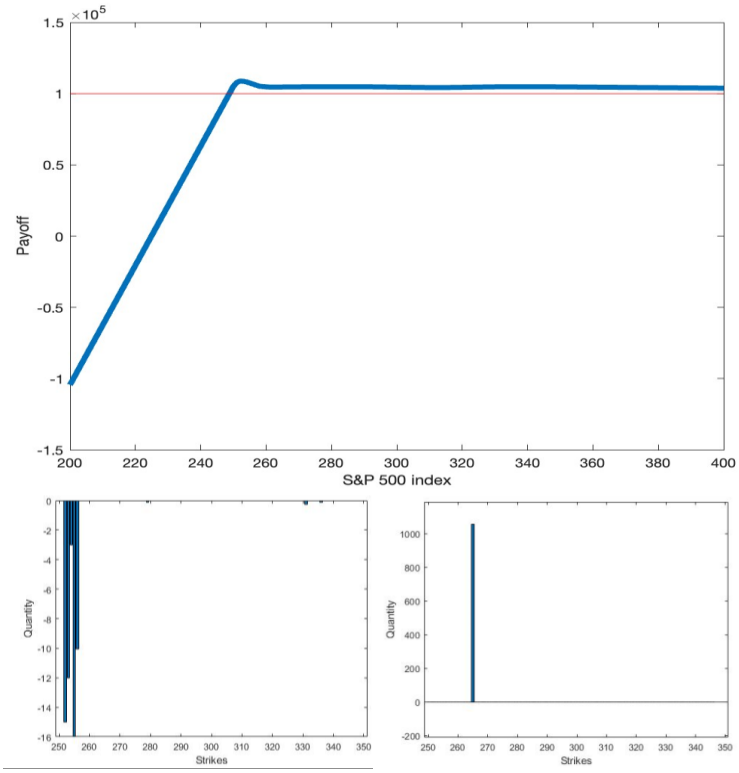

Put Option *Call Option*

Figure 1.

The optimal portfolios obtained (bottom), the payoffs of the optimal portfolios as functions of the S&P 500 index (top).

The Figure 2 shows the efficient frontier of the standard deviation minimization given bid and ask spread. The x-axis indicates the standard derivation, whereas the y-axis indicates the level of the expected return. We can see that as the expected return moves further away from 0, the value of Var increases, that is, the higher the risk, the higher the return.

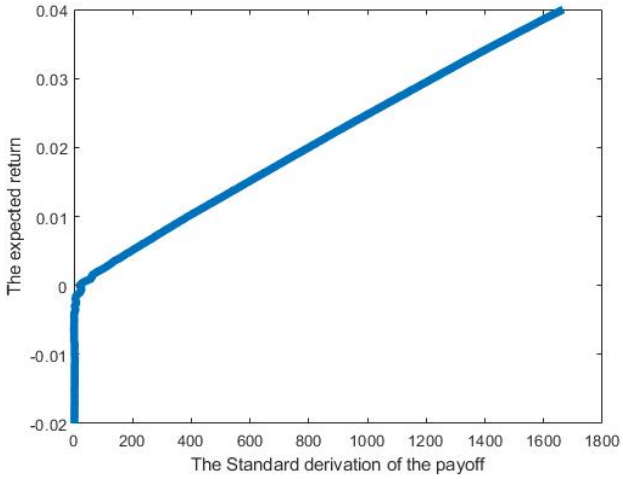

Figure 2.

The coefficient frontier of the standard deviation minimization with bid and ask prices.

The Figure 3 shows the minimum standard deviation of the portfolio payout distribution. When the bid and request spreads between $\sigma = 0.2$ (blue line), and $\sigma = 0.3$ (yellow line) where the required return is 5%. It is evident that at $\sigma = 0.3$, there will be a distribution of returns greater than $\sigma = 0.2$. In combination with Figure 4, it is clear that $\sigma = 0.3$ has a wider tail than $\sigma = 0.2$.

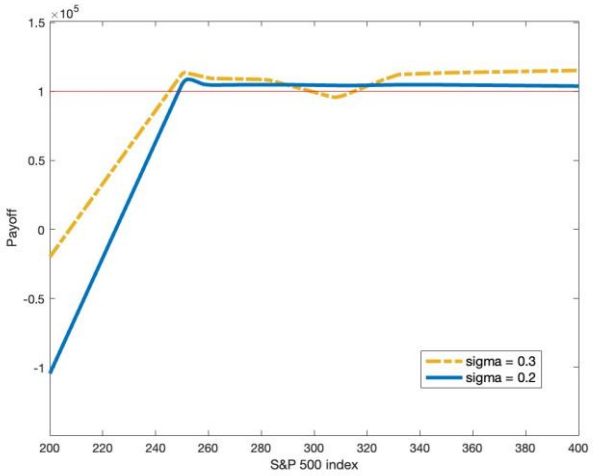

Figure 3.

The minimum standard deviation of the portfolio payout distribution between $\sigma = 0.2$ and $\sigma = 0.3$.

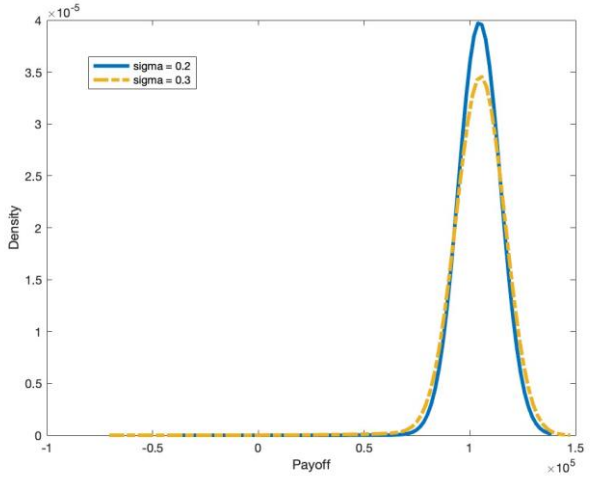

Figure 4.
The kernel density estimation of the portfolio payout between $\sigma = 0.2$ and $\sigma = 0.3$.

The Figure 5 shows the minimum standard deviation of the portfolio payout distribution. When the bid and ask spread with r =0.2 (green line), r = 0.1 (orange line), and r = 0.05 (blue line) where $\sigma = 0.2$ $, at the required return r = 0.2, notice that the green line is above the blue and orange line means that the more required return, the more payoff. We can see the distribution from Figure 6, it shows the kernel density estimation of the portfolio payout with r =0.2, r = 0.1, and r = 0.05.

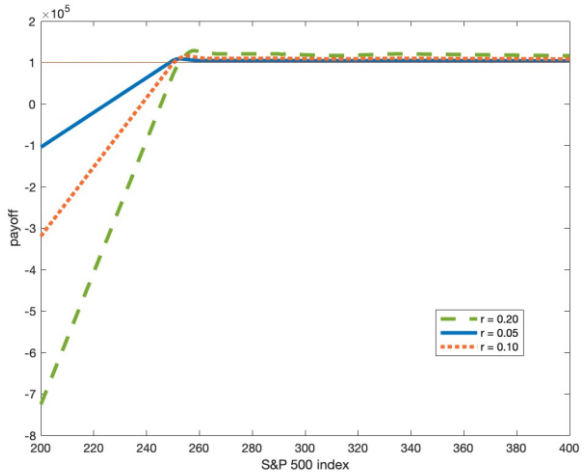

Figure 5.
The minimum standard deviation of the portfolio payout distribution with r = 0.2, r = 0.1, and r = 0.05.

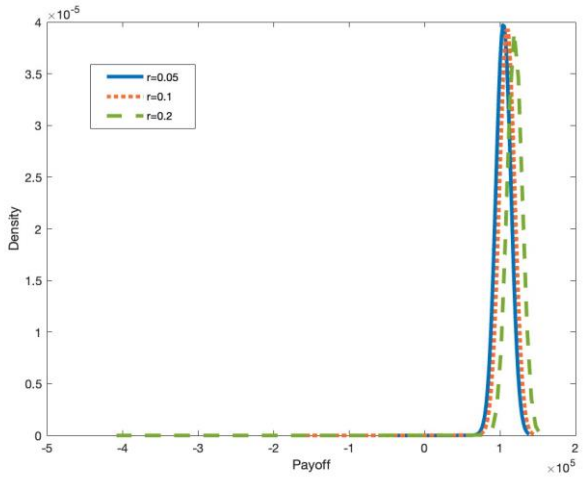

Figure 6.

The kernel density estimation of the portfolio payout with r = 0.2, r = 0.1, and r = 0.05.

The Figure 7 shows the transaction cost of the portfolio payout. We increase the bid-ask spread by adding a 5% and 10% transaction costs for all trades. We can see that the graph with transaction cost added has a more negative payoff than non-added transaction cost (where r= 0.05 and σ = 0.2).

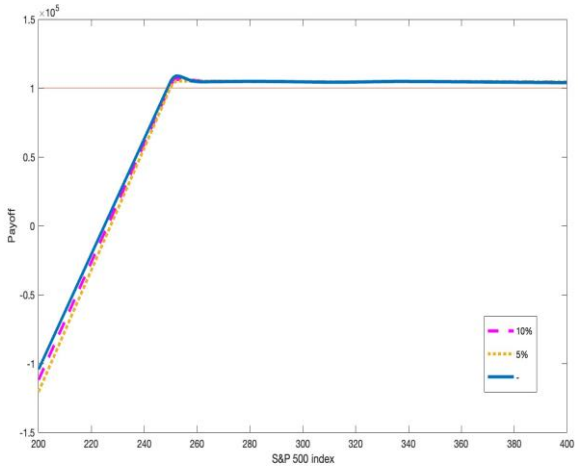

Figure 7.

The transaction cost of the portfolio payout.

Table 4 and Figure 8 show that when we change ν (the parameter in variance gamma models), the kurtosis changes. The higher the kurtosis, ν = 0.1, the greater the value of the risk and when we lower the kurtosis, ν = 0.00001, the value of the risk also decreases. In other words, the fatter the tip. The price of the simulation will also jump.

Table 4.

The ν change in variance gamma models and the standard deviation of the standard deviation minimization portfolio.

ν	**Standard deviation**
0.1	5214.13
0.00001	1018.50

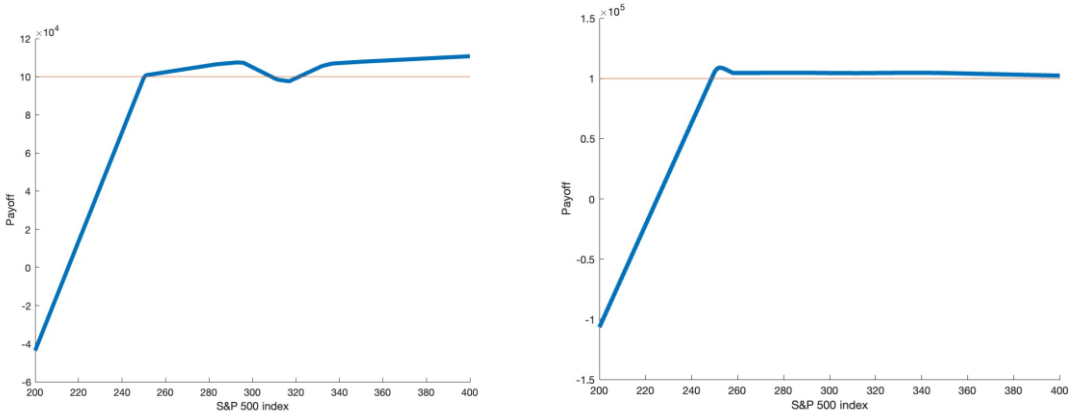

Figure 8.

The payoffs of the optimal portfolios at ν = 0.1 (left) and ν = 0.00001 (right).

2. Results: Static Hedging

In this section, we price 6 difference "exotic" options namely, a European call option, a "quadratic option" with $c(ST) = |ST - K|^2$, a "log-option" with $c(ST) = 1000\ ln(K/ST)$, a "digital option" with $c(ST) = ST \geq K$, a "butterfly spread option" with $c(ST) = (ST - 295) - 2(ST - K) + (ST - 305)$, and a "sine option" with $c(ST) = sin(ST \times 2\pi/10)$,all with strike $K = 300$.

We compute the indifference prices assuming that $\bar{w}$ = 100,000 and $\bar{c}$ = 0, that is, assuming the agent has an initial position consisting only of 100,000 units of cash. The indifference prices for buying and selling are given in Table 5.

Table 5.

Indifference prices.

Claim	**selling price**	**buying price**
call	5.6	5.6
quadratic option	544.5	541
log-option	38.8	38.5
digital option	513.4	462.5
butterfly spread option	68.7	54.8
sine option	351.9	0.1

Figures 9–13 illustrates the hedging portfolios, defined by $x - \bar{x}$ where x and $\bar{x}$ are optimal portfolio after and before selling, for the sale of all exotic options mentioned above and compare the payouts of the hedging portfolios as functions of the index value at the maturity with the payouts of the exotic options. One can see that the hedging portfolio replicates the payout of the sold option reasonably well under the incompleteness of the market. Note that if the payout of the hedging portfolio is above that of the sold option, the seller will end up with some profit. This is because the seller enters this hedging portfolio after receiving the selling price from the buyer. If the payout of the hedging portfolio is higher than that of the sold option, the seller will have some money left after paying the buyer.

Compared with the work by Armstrong et al. where the risk is measured by the exponential loss function, the hedging portfolio under mean-variance criteria focuses more on reducing the deviation of the hedging portfolio payout from that of the exotic option than to make profit. Unlike the exponential loss utility, which is more sensitive to the loss, for mean-variance criteria, the discrepancy on both profit and loss sides are equally minimized. Whether or not this hedging scheme is better is subjective. Some users may focus more on the perfect hedging where the hedging payoff is as close as possible to that of the exotic option. However, some may be willing to sacrifice the low discrepancy for the opportunity for making more profit.

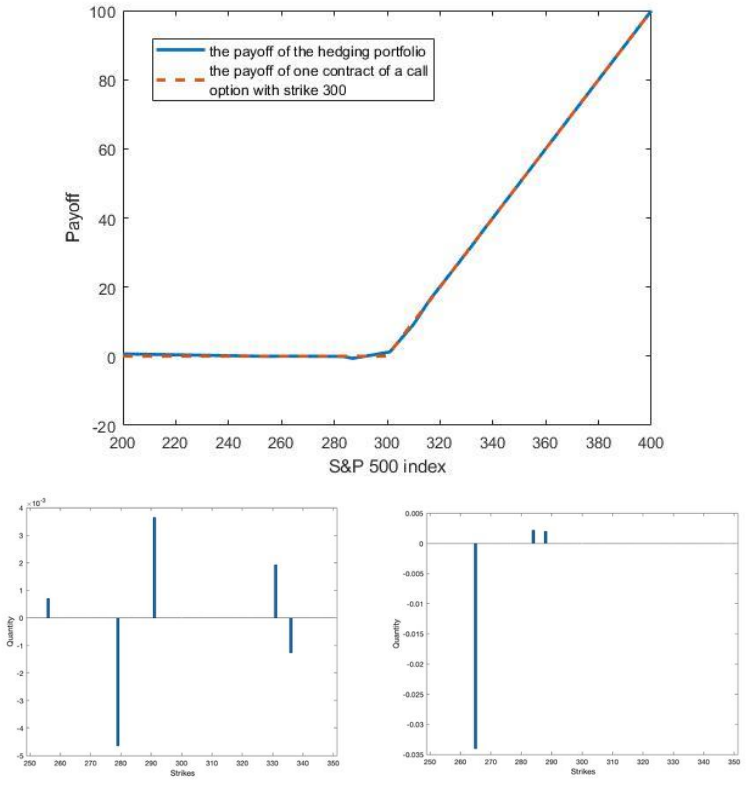

Put Option *Call Option*

Figure 9.

The hedging portfolios (bottom), the payoff of the hedging portfolio (solid line) together with the payoff of the claim being priced of a call option (top).

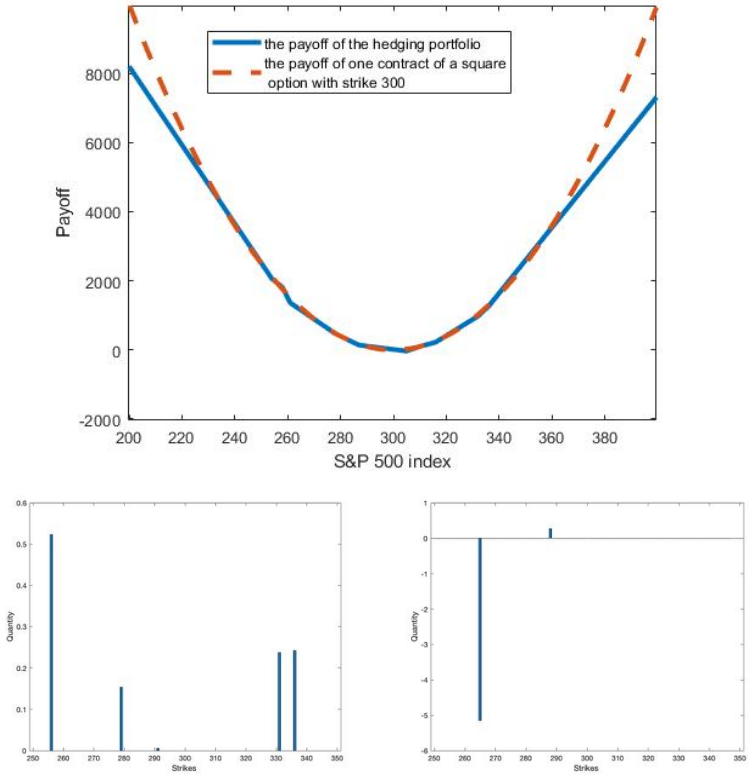

Put Option *Call Option*

Figure 10.

The hedging portfolios (bottom), the payoff of the hedging portfolio (solid line) together with the payoff of the claim being priced of a quadratic option (top).

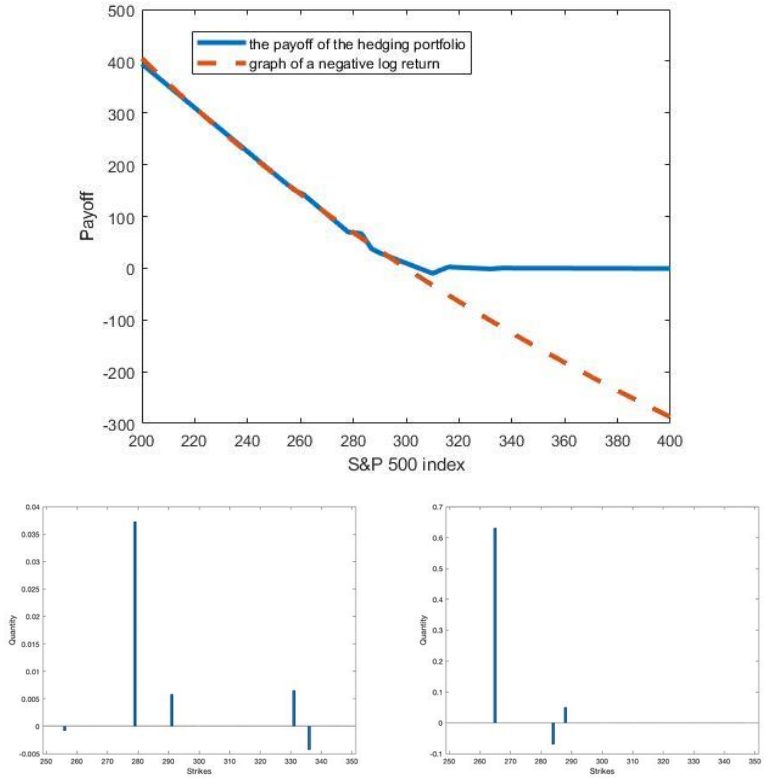

Put Option *Call Option*

Figure 11.

The hedging portfolios (bottom), the payoff of the hedging portfolio (solid line) together with the payoff of the claim being priced of a log-option (top).

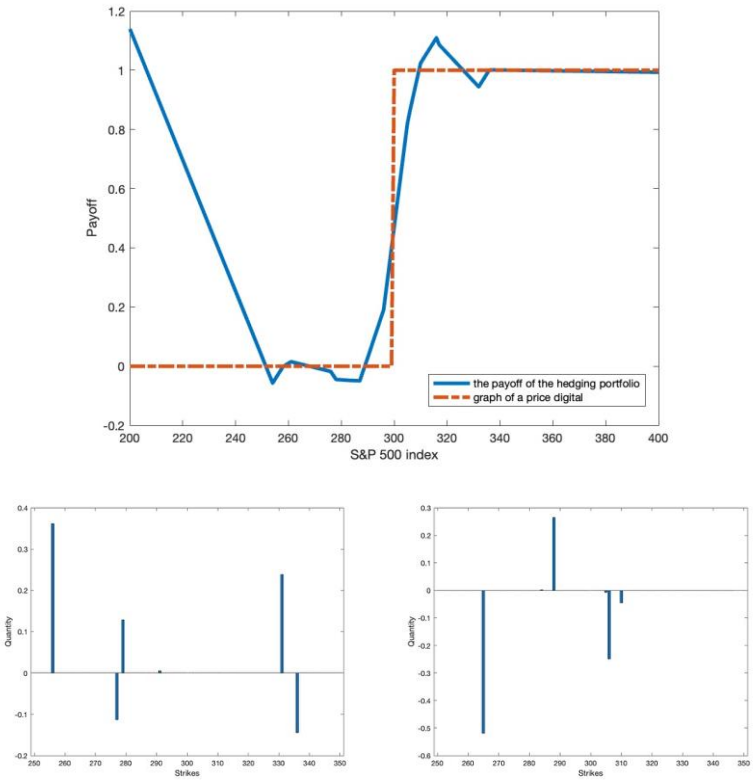

Put Option *Call Option*

Figure 12.

The hedging portfolios (bottom), the payoff of the hedging portfolio (solid line) together with the payoff of the claim being priced of a price digital (top).

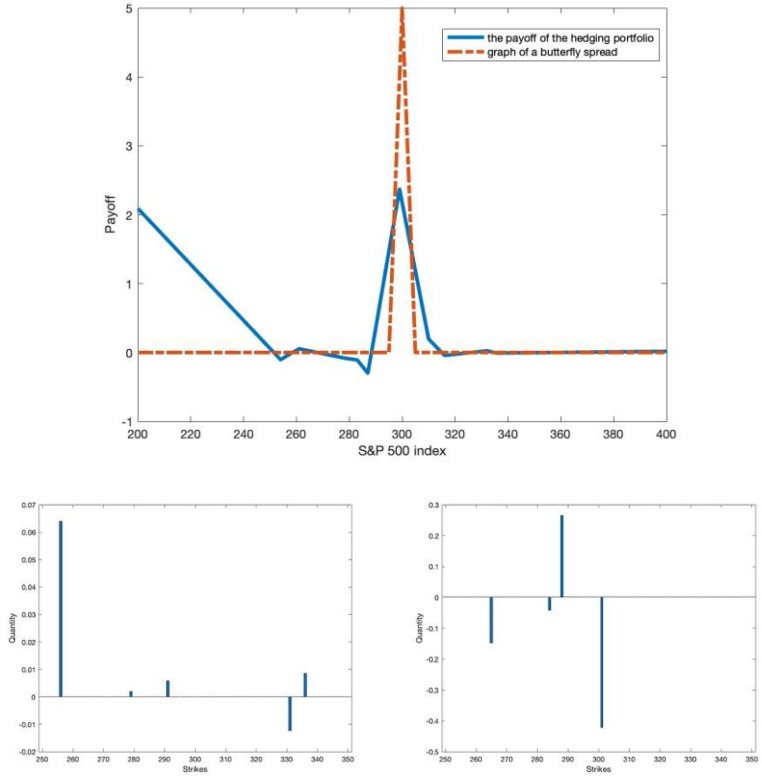

Put Option *Call Option*

Figure 13.

The hedging portfolios (bottom), the payoff of the hedging portfolio (solid line) together with the payoff of the claim being priced of a butterfly spread option (top).

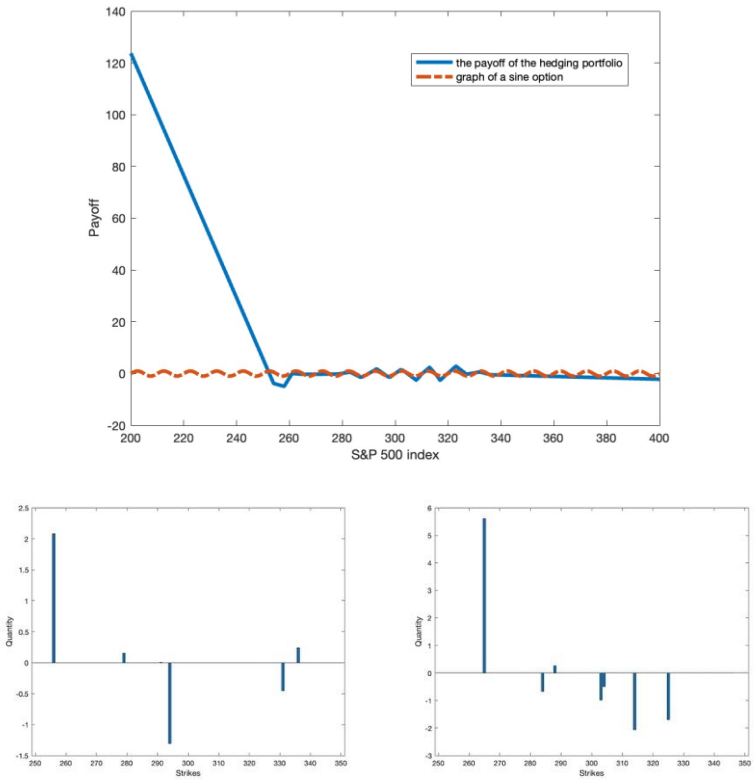

Put Option *Call Option*

Figure 14.

The hedging portfolios (bottom), the payoff of the hedging portfolio (solid line) together with the payoff of the claim being priced of a sine option (top).

Conclusion:

In this paper, we propose a scheme to compute indifference prices and the hedging portfolios for financial derivatives in incomplete markets where the quotes come with finite liquidity and bid-ask spreads. The scheme is built upon the modified mean-variance portfolio optimization model as computing the indifference prices is the same as iteratively solving the optimal investment problems. We illustrate the application of the scheme in the S&P 500 mini options market where the tradable assets are cash, and mini put and call mini options written on the S&P 500 index. The index return is modeled by the variance gamma process which gives the user control over the skewness and kurtosis.

We first solve the portfolio optimization problem and demonstrate the effects of various parameters such as modeling parameters and the required average return on the optimal portfolio and its payoff. After that, we compute the indifference prices for 6 exotic options which are a European call option, a “quadratic option”, a “log-option”, a “digital option”, a “butterfly spread option”, and a “sine option”. We show that the hedging portfolios obtained under this scheme provide decent approximations of the payoffs of the exotic options.

References:

1. Armstrong J, Pennanen T, Rakwongwan U. Pricing index options by static hedging under finite liquidity. 2018;21(06), 1850044.
2. Black F, Sholes M. The pricing of options and corporate liability. 1973;81(3): 637–654.
3. Boonklurb R, Duangpan A, Rakwongwan U, Sutthimat P. A Novel Analytical Formula for the Discounted Moments of the ECIR Process and Interest Rate Swaps Pricing. 2022;6(2):58.
4. Breeden DT, Litzenberger RH. Prices of state-contingent claims implicit in option prices. 1978:621–651.
5. Gaivoronski AA, Pflug G. Value-at-risk in portfolio optimization: properties and computational approach. Journal of risk, 2005;281 7(2):1-31.
6. Madan DB, Carr PP, Chang EC. The Variance Gamma Process and Option Pricing. 1998;2: 79–105.
7. Maasar MA, Roman D, Date P. Portfolio Optimization Using Risky Assets with Options as Derivative Insurance. 2016; 9:1–17.
8. Madan DB, Seneta E. The Variance Gamma (V.G.) Model for Share Markets. Journal of Business. 1990;63:511–524.
9. Marakbi Z. Mean-Variance Portfolio Optimization: Challenging the role of traditional covariance estimation. 2016;63:19-20.
10. Markowitz H. Portfolio Selection Efficient Diversification of Investments. 1959.
11. Monoyios M. Utility indifference pricing with market incompletness. 2008.
12. Musiela M, Zariphopoulou T. An example of indifference prices under exponential preferences. 2004; 8:229–239.
13. Pennanen T. Introduction to convex optimization in financial markets. 2012;134:157–186.
14. Pennanen T. Optimal investment and contingent claim valuation in illiquid markets. 2014;18:733–754.
15. Pennanen T, Perkkiö AP. Convex duality in optimal investment and contingent claim valuation in illiquid markets. 2018;*22*(4):733–771.
16. Pennanen T, Sbaraini Bonatto, L. A stochastic oil price model for optimal hedging and risk management. 2022.
17. Puelz AV. Value-at-risk based portfolio optimization. In Stochastic optimization: Algorithms and applications. Springer, Boston, 293 MA. 2001;54:279–302.
18. Rockafellar RT, Uryasev S. Optimization of conditional value-at-risk. Journal of risk. 2000;2(3),21-42.
19. Rujivan S, Rakwongwan U. Analytically pricing volatility swaps and volatility options with discrete sampling. 2021;100.
20. Sepp A. Pricing Options on Realized Variance in Heston Model with Jumps in Returns and Volatility. (2008);11(4):37–70.

Session E:
ENERGY / ENVIRONMENTAL & EARTH SCIENCE / MATERIALS SCIENCE / SPIN CROSSOVER

EXPRESSION OF MHETase ENZYME BY RECOMBINANT BACTERIA FOR POLYETHYLENE TEREPHTHALATE (PET) PLASTIC DEGRADATION

Mona Abdelkarim,[1] Kitipong Angsujinda,[2] Wanchai Assavalapsakul[3,4,*]

[1]Master student at Hazardous substance and environmental management program (IP-HSM) Chulalongkorn university, Thailand 10330
[2]Aquatic Resources Research Institute, Chulalongkorn University, Thailand 10330
[3]Department of Microbiology, Faculty of Science, Chulalongkorn University, Thailand 10330
[4]Center of Excellent of Microbial Technology for Marine Pollution Treatment, Department of Microbiology, Faculty of Science, Chulalongkorn University, Bangkok, Thailand 10330
*e-mail: wanchai.a@chula.ac.th

Abstract:

Since the beginning of the age of plastics in 1907 numerous different synthetic polymers have been created, and they are now widespread and essential in human life and, sadly, the environment. One of the most widely used plastics today is polyethylene terephthalate (PET), a synthetic polymer generated from crude oil. The features that have made plastic a desirable resource, however, are also to blame for the harm that is done once it becomes garbage since PET is a very stable polymer and resistant to hydrolytic or enzymatic destruction. Two-enzyme system is the main key to depolymerize PET into TPA and EG. BHET is broken down by PETase into MHET and EG, and MHETase then hydrolyzes the soluble MHET product to create TPA and EG. The main focus of this study will be the second enzyme (MHETase). By producing recombinant plasmid containing the gene encoding for MHETase and transforming this plasmid into *E. coli* strain Rosetta-gami 2(DE3) pLysS for the protein expression, our recombinant protein that was designed to be released in the culture media was successfully expressed. Beside optimizing the expression conditions by varying the IPTG concentration at which MHETase gives the highest expression which was found to be at concentration 0.3 mM. These technologies are likely to play a role in the near future in bio recycling of used PET, bioconversion of the monomer TPA to PCA, PET surface treatment, and techniques for the degradation of PEF as well as microplastics and plastic microbeads.

Introduction:

Due to their exceptional durability, low cost, and wide range of flexibility, synthetic polymers are used in every facet of modern life. Initially created to replace animal-based goods, they have since spread so far that, in addition to being plentiful in the biosphere and accumulating in landfills, they are also resistant to hydrolytic or enzymatic degradation, which is creating a global environmental disaster. Today, polyethylene terephthalate (PET), a synthetic polymer made from crude oil, is one of the most extensively used polymers.[1] Only a very small fraction of plastics are recycled at all, and the processes used to do so are expensive and energy-intensive, provide poor quality items, or are dependent on the addition of "new" crude oil.[2]

To make poly (ethylene terephthalate) PET, terephthalic acid (TPA) and ethylene glycol (EG) can be polycondensed, or dimethyl terephthalate and EG can be transesterified **(Figure 1)**.[3]

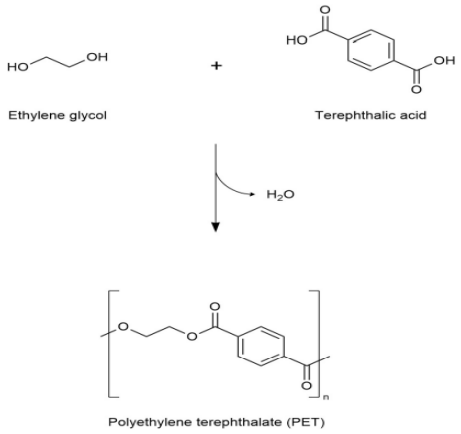

Figure 1.
Structure of PET polymer. Polycondensation reaction of ethylene glycol (EG) and terephthalic acid (TPA) monomers gives polymeric polyethylene terephthalate (PET), with water as a byproduct.[4]

PET, which was previously believed to be resistant to microbial degradation, thanks to recent research, the world knows now that it can be altered or broken down by some bacteria due to the development of their hydrolase enzymes. [5,6]

Researchers from Japan discovered PET-degrading bacteria in the culture of environmental materials, containing PET waste.[7,8] They identified that the bacterium possesses two distinct enzymes named PETase and MHETase that can degrade the PET plastic polymers. A bacterial species that can metabolize amorphous PET independently of the other organisms in the consortium was discovered after more investigation. *Ideonella sakaiensis* 201-F6 is the name of a strain of gram-negative, aerobic, rod-shaped bacteria that have been discovered as a unique species of the genus *Ideonella*.[9]

In April 2018, the PETase structure was finally solved, although PETase is only one part of the answer. It is equally important to describe the structure of the second enzyme, the MHETase. It has been established that the two enzyme parts of the system that degrades PET are PETase and MHETase. PETase hydrolyzes the ester links within the PET polymer to produce TPA, bis(2-hydroxyethyl) TPA, and mono(2-hydroxyethyl) MHET as it catalyzes the depolymerization of PET. It was found that MHETase can hydrolyze MHET and BHET releasing EG and TPA[10] (**Figure 2**).[11]

The crystal structure showed MHET hydrolase (MHETase), which consists of a lid domain and an α-β hydrolase domain.[2] The α-β hydrolase domain has amino acid residues required for catalysis, while the lid domain provides substrate selectivity **(Figure 3)**.[12] With the help of recombinant DNA technology and gene editing, it has been investigated if hazardous wastes can be broken down by bacteria. By identifying the genes for detoxifying the xenobiotic chemicals and transforming them into suitable host microorganisms using appropriate vectors under the strict control of promoters, genetic engineering assists in the evolution of the microbial ability and can lead to enhanced activity and reaction conditions tolerance.

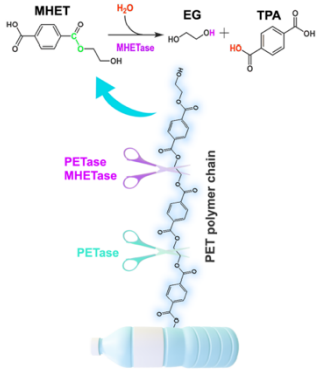

Figure 2.

Proposed mechanism for PET processing in *Ideonella sakaiensis*. Extracellular PETase enzyme acts on PET polymer chains to give oligomeric mono-(2-hydroxyethyl) terephthalate (MHET), the monoester of terephthalic acid (TPA) and ethylene glycol (EG). Intermediates are transported through a membrane protein before reaching MHETase, which degrades MHET into TPA and EG. Finally, monomers are transported into the cytoplasm to be metabolized.[11]

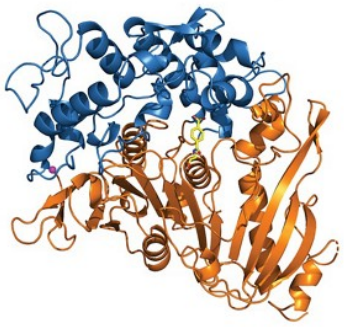

Figure 3.

MHETase has a lid (blue) and a hydrolase domain (orange) that work together to split MHET (yellow).[2]

To test the impact of the two enzyme systems PETase and MHETase, the hydrolysis of a commercial amorphous PET substrate was measured over 96 hours at 30 °C using PETase and MHETase at various doses. The overall pattern of degradation across the measured range of enzyme loadings, which shows increasing levels of monomers released as the concentration of both enzymes increases, points to the possibility that these reactions are enzyme-limited under these circumstances rather than substrate-limited.[13] The synergy study shows that degradation scales with enzyme loading and that the presence of MHETase, even at low concentrations relative to PETase, increases overall degradation despite what ratio of PETase to MHETase yields optimal degradation over the enzyme loadings tested.[12]

Previously PETase gene has been recombinantly constructed in a plasmid with native signal peptide from *Ideonella sakaensis* and was successfully expressed in *Escherichia coli* BL21(DE3). The expression analysis was done by SDS-PAGE proved that PETase was sucessfuly expressed both intracellular and extracellular. Even so, fully degrading PET to it's constituent monomers, terephthalic acid (TPA) and ethylene glycol (EG), can only be accomplished by MHETase. Despite the key role that MHETase plays in PET plastic degradation, very limited studies has been conducted to study the possibility and the efficiency of the recombinant MHETase. Therefore, this study will focus on producing the second degrading enzyme MHETase by the extracellular expression of the recombinant protein.[14]

Methodology:

Construction of expression vectors

The recombinant codon-optimized gene containing signal peptide MHETase in pETDuet-1 expression vector (MHETase pETDuet-1) was synthesized by (GeneScript, Piscataway, NJ). The plasmid was then transformed into *E. coli* strain DH5α by heat shock. The transformed bacteria were spread on LB agar containing100 µg/ml ampicillin and 34 µg /ml chloramphenicol and incubated at 30°C for 16-18 h. Then a single colony of transformant

was inoculated at 30°C, 200 rpm for 16-18 h in LB broth containing the same antibiotic. Then centrifugating at 13,000 rpm for 2 min at ambient temperature, cell pellet was harvested and subjected to plasmid isolation using a Monarch® Plasmid Miniprep Kit (New England Biolabs, MA) according to the manufacturer's protocol. The nucleotide sequence of extracted plasmid was then confirmed by Sanger sequencing with primers listed in **Table 1** (Macrogen, Korea).

Table 1.
Oligonucleotides used in this study

Name	Sequences (5' – 3')
MHETase_internal 688	GCTACCGACGGACATGAC
MHETase_internal 1188	GACTGCAGCCAACCCAGCGAATG
DuetUP2	TTGTACACGGCCGCATAATC
T7 terminator	GCTAGTTATTGCTCAGCGG

Expression of MHETase

The isolated plasmid with a 100% similarity to the gifted synthesized one was chosen and transformed to *E. coli* strain Rosetta-gami 2(DE3) pLysS by heat shock. The transformant bacteria harboring the plasmid (MHETase pETDuet-1) was selected by culture on LB agar supplemented with 100 µg/ml ampicillin and 34 µg/ml chloramphenicol, then incubated at 30°C for 16 -18 h. A single colony inoculated in 5 ml of LB broth with the same antibiotics and incubated with vigorous shaking for 16-18 hour at 30°C. Then the growth rate was measured by using spectrophotometer at optical density 600 nm (OD_{600nm}). Roughly 0.2 OD_{600nm} was cultured in 30 ml of antibiotics added LB broth with vigorously shaking at 30°C until reaching 0.4-0.5 $OD_{600nm.}$ The expression of recombinant MHETase was then induced by 0.4 mM Isopropyl ß-D-1-thiogalactopyranoside (IPTG) at final concentration.[15]

Detecting the expression of MHETase by SDS-PAGE and western blot analysis

As the desired protein was designed to be excreted in the media, all proteins were precipitated by adding a trichloroacetic acid (TCA) at 10% of the final concentration then incubated on ice overnight. After centrifugating the sample at 13,000 rpm at 4 °C for 10-15 min, the precipitated protein was washed with acetone and prepared for the SDS-PAGE analysis. The protein sample was then prepared in a 50 µL of mixture containing 32.5 µL of 0.1 N NaOH, 5 µL of β-mercaptoethanol and 12.5 µL of 4X SDS-PAGE sample loading buffer, then analyzed by SDS-PAGE and western blotting. After loading protein samples on two gels and run the SDS-PAGE, one of the two gels stained with coomassie brilliant blue R-250 (Bio Basic, Canada), while the other used for western blot analysis.

The protein on the gel was transferred onto a PVDF membrane using a Trans-Blot® SD Semi-Dry Transfer cell (Bio-Rad, Hercules, CA). After transferring the protein, the membrane was incubated twice with a blocking solution (5% (w/v) skimmed milk in 1X PBS Tween-20), then incubate with the blocking solution with anti-6X Histidine antibody (1: 5000) (R&D System, Minneapolis, MN), then incubate with shaking at the room temperature for 2 hour then wash it 4 times with 1X PBS Tween-20 (each 15 min), later the membrane was incubated with Anti-Mouse IgG Secondary Antibody with blocking solution (1:5000) (Sigma Aldrich, Piscataway, NJ) for an hour in the room temperature with shaking, then again rinse 4 times with 1X PBST (each 15 min) with shaking. Finally, the membrane was submerged with the substrate solution (100 mM, Tris-HCl (pH 8.5), 250 mM Luminal, 90 mM Coumaric acid, 30% H_2O_2), for 30 second and visualized by Alliance Q9 Advanced Chemiluminescence Imager (UVITEC Cambridge Ltd, United Kingdom).[16]

Optimizing the protein expression by varying the IPTG concentrations

A single colony from the transformant holding our recombinant plasmid (MHETase pETDuet-1) was selected same way as described before, 0.5 OD $_{600nm}$ was calculated and cultured in 75 ml LB broth with antibiotics then incubated in the shaking incubator at 30°C until reaching 0.4-0.5 OD $_{600nm}$. After reaching 0.4-0.5 OD $_{600nm}$ the culture medium was divided on 6 small flasks each contained 10 ml of the media and induced with various doses of Isopropyl ß-D-1-thiogalactopyranoside (IPTG) (0.1, 0.2, 0.3, 0.4, 0.5) mM and one uninduced control (U).

Results and Discussion:

MHETase expression and detection by SDS-PAGE and western blot analysis

This study was based on the hypothesize that using genetic engineering to produce recombinant MHETase enzyme in a competent cell host could successfully express the recombinant protein. After transforming the synthesized plasmid into *E. coli* strain Rosetta-gami 2(DE3) pLysS by the heat shock and streak it on LB agar containing 100 µg/ml ampicillin and 34 µg/ml chloramphenicol. Then 0.2 OD $_{600nm}$ was calculated and cultured in 30 ml of antibiotic containing culture media and kept in the shaking incubator at 30°C. After reaching 0.4-0.5 OD $_{600nm}$ 10 ml was collected in a new flask and induced by 0.4 mM IPTG for 3 hours, while another 10 ml was the control without IPTG. The induced flask was slower in growth than the uninduced one, which was later indication for the protein expression as the bacteria consume most of the energy on expressing the large recombinant protein. After collecting and precipitating the culture media, with SDS-PAGE and western blot analysis we got a band at average size 69 kDa which was the expected average size for MHETase, so we could strongly confirm that our recombinant protein (MHETase) was expressed and thrived with IPTG presence (**Figure 4**).

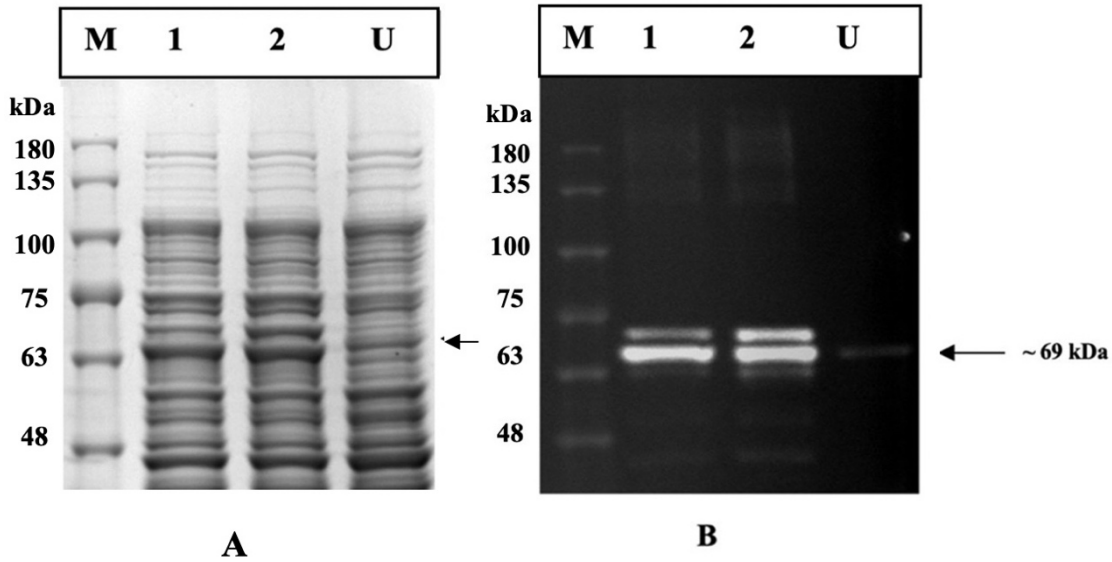

Figure 4.
(A) 12% SDS-PAGE and (B) western blot experiment, using anti-6X Histidine antibody. The M Lane is the TriColor Protein Ladder (10-180 kDa) (Biotechrabbit, Germany). the lanes number 1 and 2 are two clones of the induced recombinant bacteria while the third lane (U) is the un induced control of the second clone.

Varying IPTG experiment

To find the best IPTG concentration for our new recombinant and optimize the expression condition, varying IPTG experiment were conducted by using SDS-PAGE and western blot at IPTG concentrations (0.1, 0.2, 0.3, 0.4, 0.5) mM. The best expression for MHETase was observed at IPTG concentration 0.3 mM (**Figure 5).**

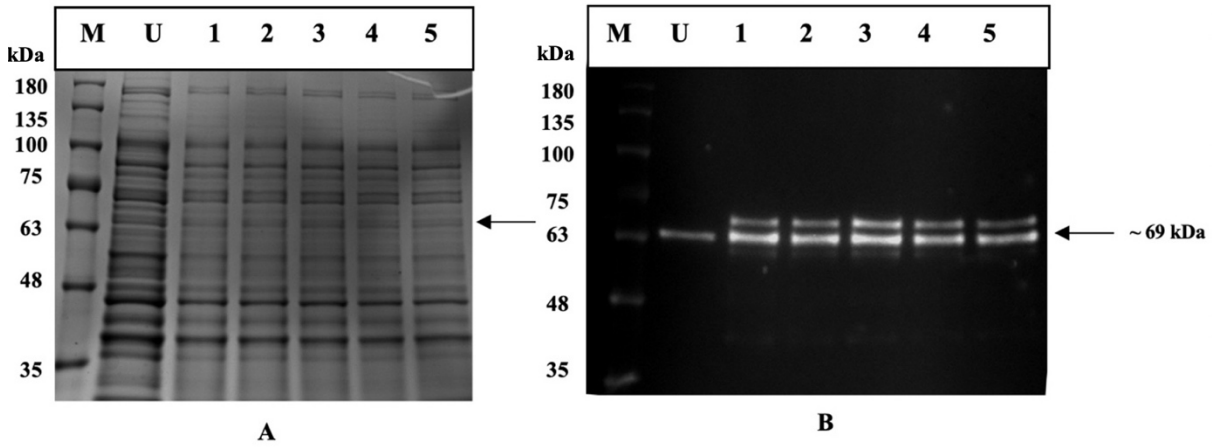

Figure 5.

(A) 12% SDS-PAGE and (B) membrane sheet from western blot varying IPTG experiment, The M Lane is the marker used TriColor Protein Ladder (10-180 kDa) (Biotechrabbit, Germany), the lanes number 1, 2, 3, 4, 5 are the IPTG concentrations 0.1, 0.2, 0.3, 0.4, 0.5 mM sequentially added to recombinant bacteria with MHETase. While the first lane (U) is the un induced control. The picture on the left-hand side is the SDS-PAGE gel.

Conclusion:

The urgent need to develop an environmentally friendly recycling method for PET plastics made it very important to understand and try to optimize the expression of the key enzymes for plastic degradation (PETase and MHETase). Now our recombinant protein (MHETase) can successfully be expressed, in the future we aim to use our technology to create PET degradation systems in which MHETase will work along with PETase to completely degrade PET plastic.

References:

1. Liu, C., Shi, C., Zhu, S., Wei, R., & Yin, C. C. *Biochem. Biophys. Res. Commun*. 2019; 508(1), 289-294. https://doi.org/10.1016/j.bbrc.2018.11.148
2. Palm, G. J., Reisky, L., Böttcher, D., Müller, H., Michels, E. A. P., Walczak, M. C., Berndt, L., Weiss, M. S., Bornscheuer, U. T., & Weber, G. *Nat. Commun*. 2019; 10(1), 1717. https://doi.org/10.1038/s41467-019-09326-3
3. Hiraga, K., Taniguchi, I., Yoshida, S., Kimura, Y., & Oda, K. *EMBO Rep*. 2019; 20(11), e49365. https://doi.org/10.15252/embr.201949365
4. Carr, C. M., Clarke, D. J., & Dobson, A. D. W. *Front. Microbiol.* 2020; 11, 571265. https://doi.org/10.3389/fmicb.2020.571265
5. Danso, D., Chow, J., Streit, W. R., & Drake, H. L. *Appl. Environ. Microbiol.* 2019; 85(19), e01095-01019. https://doi.org/doi:10.1128/AEM.01095-19
6. Taniguchi, I., Yoshida, S., Hiraga, K., Miyamoto, K., Kimura, Y., & Oda, K. *ACS Catal*. 2019; 9(5), 4089-4105. https://doi.org/10.1021/acscatal.8b05171
7. Kawai, F., Kawabata, T., & Oda, M. *Appl. Microbiol. Biotechnol*. 2019; 103(11), 4253-4268. https://doi.org/10.1007/s00253-019-09717-y

8. Yoshida, S., Hiraga, K., Takehana, T., Taniguchi, I., Yamaji, H., Maeda, Y., Toyohara, K., Miyamoto, K., Kimura, Y., & Oda, K. *Science.* 2016; 351(6278), 1196-1199. https://doi.org/10.1126/science.aad6359
9. Tanasupawat, S., Takehana, T., Yoshida, S., Hiraga, K., & Oda, K. *Int. J. Syst. Evol. Microbiol*. 2016; 66(8), 2813-2818. https://doi.org/10.1099/ijsem.0.001058
10. Sagong, H.-Y., Seo, H., Kim, T., Son, H., Joo, S., Lee, S., Kim, S., Woo, J.-S., Hwang, S., & Kim, K.-J. *ACS Catal*. 2020; 10 (8), 4805-4812. https://doi.org/10.1021/acscatal.9b05604
11. Pinto, A. V., Ferreira, P., Neves, R. P. P., Fernandes, P. A., Ramos, M. J., & Magalhães, A. L. *ACS Catal.* 2021; 11(16), 10416-10428. https://doi.org/10.1021/acscatal.1c02444
12. Maity, W., Maity, S., Bera, S., & Roy, A. *Appl. Biochem. Biotechnol.* 2021;193(8), 2699–2716. https://doi.org/10.1007/s12010-021-03562-4
13. Knott, B. C., Erickson, E., Allen, M. D., Gado, J. E., Graham, R., Kearns, F. L., Pardo, I., Topuzlu, E., Anderson, J. J., Austin, H. P., Dominick, G., Johnson, C. W., Rorrer, N. A., Szostkiewicz, C. J., Copié, V., Payne, C. M., Woodcock, H. L., Donohoe, B. S., Beckham, G. T., & McGeehan, J. E. *Proc. Natl. Acad. Sci. U. S. A.* 2020; 117(41), 25476-25485. https://doi.org/10.1073/pnas.2006753117
14. Janatunaim, R. Z., & Fibriani, A. *Recent Patent Biotechnol*. 2020; 14(3), 229–234. https://doi.org/10.2174/1872208314666200311104541
15. Seo, H., Kim, S., Son, H. F., Sagong, H. Y., Joo, S., & Kim, K. J. *Biochem. Biophys. Res. Commun*. 2019; 508(1), 250-255. https://doi.org/10.1016/j.bbrc.2018.11.087
16. Kim, J. W., Park, S.-B., Tran, Q.-G., Cho, D.-H., Choi, D.-Y., Lee, Y. J., & Kim, H.-S. *Microb. Cell. Fact*. 2020; 19(1), 97. https://doi.org/10.1186/s12934-020-01355-8

REMOVAL OF NITROGEN AND PHOSPHORUS FROM SYNTHETIC URINE WASTEWATER BY BIOCHAR AND ZEOLITE ADSORPTION

Thanaporn Chaihard[1,*], Tawan Limpiyakorn[1], Patiparn Punyapalakul[1], Jatuwat Sangsanont[2,3]
[1]Department of Environmental Engineering, Faculty of Engineering, Chulalongkorn University, Bangkok, Thailand
[2]Department of Environmental Science, Faculty of Science, Chulalongkorn University, Bangkok 10330, Thailand
[3]Water Science and Technology for Sustainable Environmental Research Group, Chulalongkorn University, Bangkok 10330, Thailand
*e-mail:
soe.thanaporn@gmai.com

Abstract:
Nowadays, nutrient recovery from urine is being studied for solving resource and environmental crises. Although only 1% of urine was in the total municipal wastewater, the found elements contain nutrients, both nitrogen and phosphorus in large quantities. In this research, 8 types of biochar and 5 types of zeolites were used to find the most efficient adsorbent for nitrogen and phosphorus removal from synthetic urine wastewater to develop alternative adsorbents for nutrients removal and recovery. The BC5 and ZL4 showed the highest adsorption capacity for biochar and zeolite. The maximum ammonium adsorption capacity reached 10.17 ± 0.79 and 12.45 ± 0.91 mg_N/g, respectively. However, both biochar and zeolite showed poor sorption capacity for phosphorus. Pseudo-second-order kinetics were proposed to fit the experimental data well for BC5 and ZL4, suggesting that the adsorption was controlled by chemical processes, which are driven by electrostatic attraction, ion exchange, and surface ligand exchange. For isotherm, BC5 data showed to fit with Langmuir isotherm though ZL4 data showed to fit with Freundlich isotherm. The morphology and elements of K, Mg, N, P and Ca were explored. BC5 was found to be morphos material. Conversely, ZL4 was found to be amorphous. Furthermore, the surface charge of BC5 was found to be positive at pH 9, which means that electrostatic was not the main force for ammonium adsorption in BC5. This is different from ZL4 that electrostatic was the main force according to the negative surface. Our findings showed that the original biochar and zeolite can be used as alternative adsorbents for ammonium adsorption in energy-saving treatment systems, but there are limitations in the absorption of phosphorus that may require surface improvement to suit its application beforehand.

Introduction:

In order to solve resource scarcity problem in sustainable way, the perspective for removing organic matter and nutrients in wastewater has been shifted from just removing to emphasizing the efficiency of post-treatment wastewater to the concept of wastewater resource recovery especially, in urine wastewater. In fact, urine wastewater accounts for 1% of the total municipal wastewater volume. Although the proportion is less than the wastewater from household activities and the total wastewater from toilets the constituents were found to contain large amounts of both nitrogen and phosphorus nutrients [1, 2]. Therefore, extraction of urine at the source is an easy approach and can be used as a model for the removal and recovery of nutrients.

In general, the treatment of nutrients in wastewater is either through a chemical process or biological processes. Various methods of reducing nitrogen and phosphorus removal processes are currently being developed. However, the use of absorbent materials like zeolite and biochar are commonly used in cation exchange processes [3, 4]. Previous studies showed that the removal of ammonium nitrogen by zeolite and biochar was up to 89% with a recovery rate of 96% [3, 5-8]. Biochar can also return nutrients in solid form. It can be used as a soil amendment without transformation and is also a carbon source for soil [9, 10].

From the above-mentioned information, both zeolite and biochar can be used for efficient energy-saving nutrient removal and recovery in wastewater, both in terms of reducing energy consumption and cost. Therefore, this research will focus on the idea of applying an efficient adsorption process to remove nutrients from urine wastewater which contains both nitrogen and phosphorus by using raw absorbent material.

Methodology:

- *Materials*

Biochar and zeolite were selected for the absorption of nutrients from synthetic urine wastewater, using 8 types of biochar and 5 types of zeolites which purchased from commercial store and agriculture place. Every biochar needs to sieve into 2 - 4 mm. before use.

For wastewater, initial concentrations of ammonium and phosphorus in a solution were 2000 mg_N/L and 125 mg_P/L, prepared from NH_4Cl and NaH_2PO_4, respectively. Synthetic hydrolyzed urine was from a previous study [11] and the chemical composition was showed in **Table 1.**, the initial concentrations of ammonium and phosphorus were 1750 mg_N/L and 155 mg_P/L, respectively. All wastewaters needed to adjust the pH to 8-9.

Table 1.
Chemical composition of synthetic hydrolyzed urine [11].

Chemical	Weight (g/L)
NaCl	0.8766
Na_2SO_4	0.5327
KCl	0.7455
NH_4Cl	3.1159
Na_2HPO_4	0.7098
NH_4HCO_3	5.2770
Citrate	0.0032

- *Adsorption experiment*

Nutrient removal capacity was evaluated for both for ammonium and phosphorus. Biochar and zeolites (1.0 g) were added to 50 mL prepared wastewater in a sealed flask. Then, the flask was shaken at 100 rpm at 25 (± 5 °C) for 20 h in a mechanical shaker. The wastewater sample was filtered through 0.45 μm membranes before analytical analyses.

- *Adsorption kinetics and isotherms*

Adsorption kinetics of ammonium and phosphate onto the biochar and zeolites were investigated. 1.0 g of biochar and 5.0 g of zeolite was added into 50 mL of the synthetic urine wastewater in a sealed flask. The wastewater samples were taken at appropriate time intervals during the adsorption experiment using the same shaking conditions as described above for 30 h Then, mathematical models were used to simulate the adsorption kinetics. The synthetic urine wastewater was diluted with deionized water to provide different concentrations of

ammonium for studying the adsorption isotherm, ranging 300-1750 mg_N/L. The experimental process was the same as for adsorption experiment for 25 h.

- *Analytical methods*

Ammonium concentration was measured colorimetrically at a wavelength of 640 nm according to salicylic acid method from Standard Methods, 4500-NH3, 1997 whereas phosphate concentration was measured colorimetrically at a wavelength of 880 nm according to the ascorbic acid method from EPA, Method 365.3, 1978

For physical and chemical characterization. Elemental composition of selected absorbents was analyzed with a Scanning Electron Microscope, FE-SEM, Quanta 250. FEG was used for high-resolution imaging and composition analysis by X-ray microanalysis (EDS) at magnifications ranging from 300x to 20,000x by analyzing Mg, Cl, P, N and Ca. And anion Exchange Capacity [12] was investigated.

Results and Discussion:

- *Adsorption capacity*

For ammonium adsorption capacity, **Figure 1a.** showed that biochar BC5 and zeolite ZL4 had the highest ammonium adsorption capacity with a mean value of 10.17 ± 0.79 and 12.45 ± 0.91 mg_N/g, respectively. The results showed that the adsorption capacity of ammonium on biochar was similar to the previous study [14]. For phosphorus adsorption capacity, **Figure 1b**. showed that both biochar and zeolites had low efficient to adsorb phosphorus compared to ammonium. Biochar BC5 showed the highest phosphorus capacity with an average value of 1.43 ± 0.26 mg_P/g. The results were similar to a previous study [15]. For zeolite, all type of zeolite had average phosphorus absorption capacity of 0.26 ± 0.03 mg_P/g, consistent with a previous study [16] .

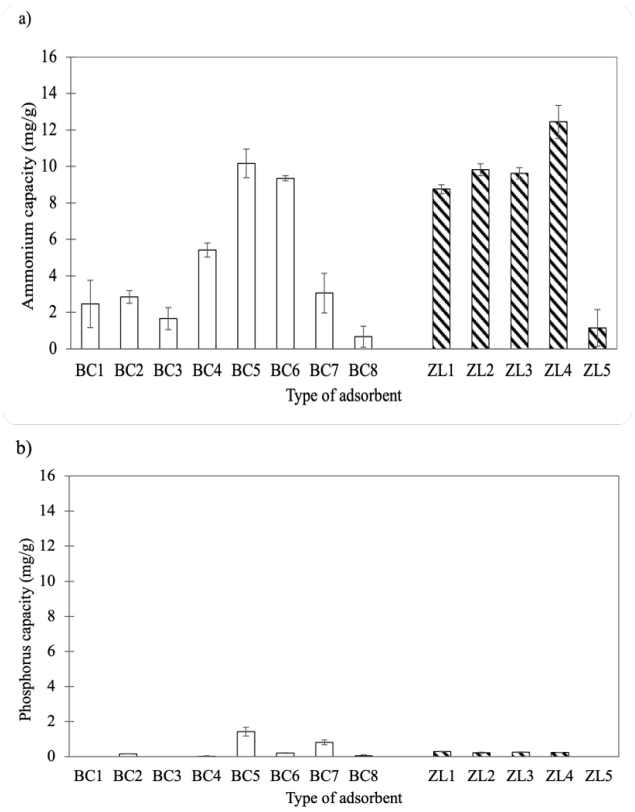

Figure 1.
Comparison of; a) ammonium adsorption capacity and b) phosphorus adsorption capacity of 13 adsorbents.

- *Adsorption kinetics*

The adsorption of the biochar BC5 reached the equilibrium after 12 h for ammonium **(Figure 2)**. Furthermore, kinetic adsorption was calculated according to mathematics calculations [2]. The data seemed to fit better with pseudo-second order reaction model ($R^2 \geq 0.99$) as showed in **Table 2**. It can be indicated that the ammonium adsorption on biochar BC5 is chemical adsorption in monolayer type which occurs under the effect of electrostatic attraction and active site [17].

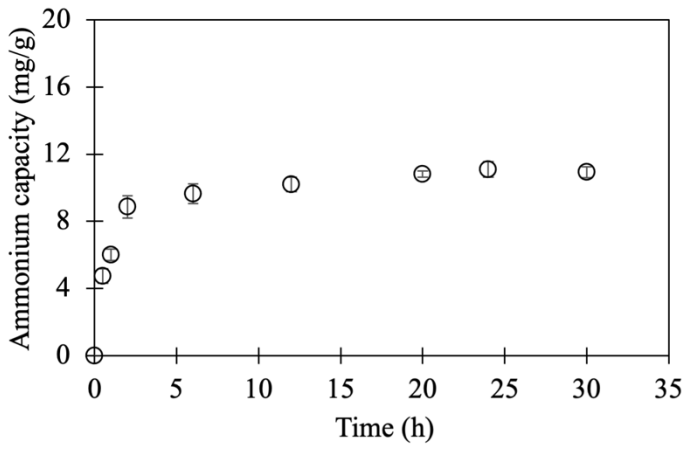

Figure 2.
Adsorption kinetic of BC5 for ammonium adsorption; with pH 8-9; Biochar content 1.0 g/50 mL.

In addition, adsorption kinetic of ZL4 reached the equilibrium after 20 h for ammonium **(Figure 3)**. It slightly fitted better with a pseudo-second order model with $R^2 \geq 0.98$ as showed in **Table 2**. This indicated that the adsorption of ZL4 in synthetic urine wastewater was chemical adsorption [17].

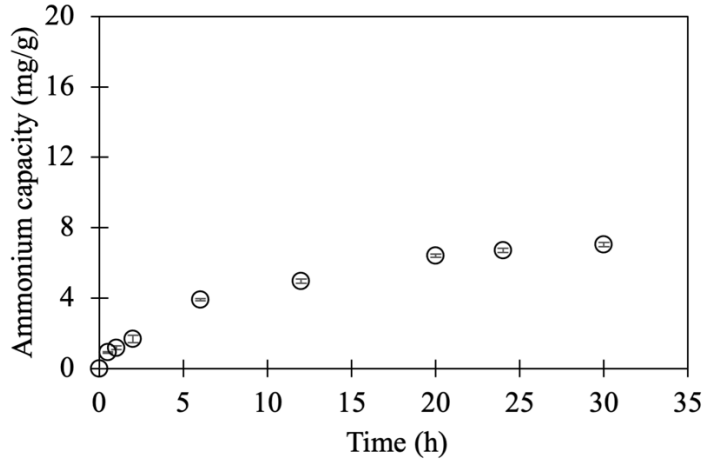

Figure 3.
Effect of time of biochar ZL4 for ammonium adsorption; with pH 8-9; zeolite content 5.0 g/50 mL.

Table 2.
Parameters for pseudo-first order and pseudo-second order models for BC5 and ZL4 ammonium adsorption in synthetic urine wastewater.

	Parameter	Ammonium adsorption	
		BC5	**ZL4**
pseudo-1st order	k_1 (h^{-1})	0.2327	0.1300
	q_e (mg/g)	4.20	7.46
	R^2	0.8806	0.9848
pseudo-2nd order	k_2(g/mg/h)	0.00181	0.00030
	q_e (mg/g)	11.27	8.46
	R^2	0.9994	0.9864

- *Adsorption Isotherm*

Adsorption isotherm data was analzyed by mathematics solutions [2]. It was found that the adsorption of biochar BC5 had Q_{max} equal to 17.30 mg_N/g and was consistent with the Langmuir adsorption isoterm as showed in **Figure 4a.** with R^2 = 0.9898 **(Table 2.).** This indicated that ammonium adsorption of BC5 was monolayer adsorption, which was agreeable with the adsorption kinetics [18]. R_L and 1/n, indicates that BC5 had a good adsorption with limited active site [2]. Otherwise, ZL4's data experiment in **Figure 4b.** was consistent with Freundlich adsorption isotherm (R^2 = 0.9899) **(Table 2.)** with Q_{max} equal to 17.37 mg_N/g. This type of isotherm hypothesized whether the adsorbent surface area was heterogeneous. This corresponds to the surface scanning image of ZL4 zeolite with SEM, and active site was limited [2].

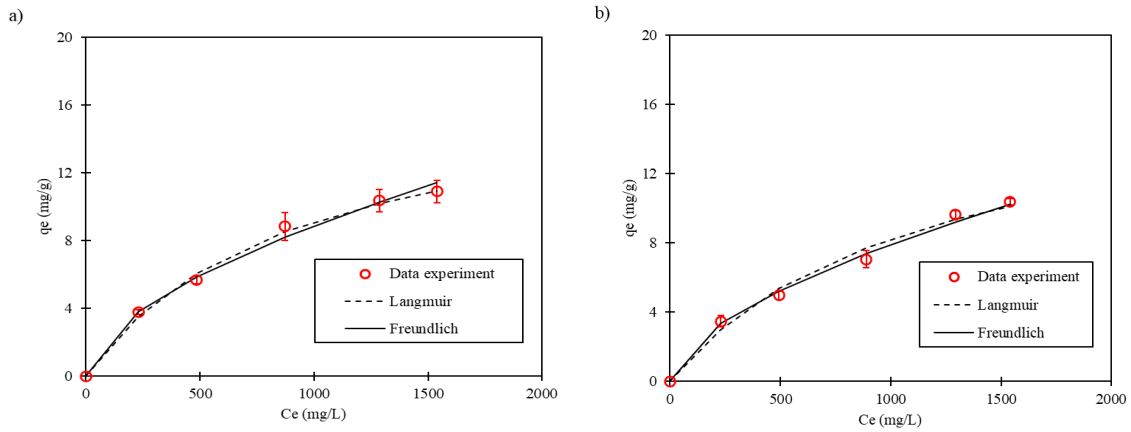

Figure 4.
Langmuir and Freundlich isotherm models for ammonium adsorption of a) BC5; b) ZL4 initial concentration = 300 - 2000 mgN/L; pH = 8 - 9; 25 h; adsorbent content 1 g/50 mL.

Table 3.
Langmuir and Freundlich isotherm models for ammonium adsorption on BC5 and ZL4.

	Parameter	BC5	ZL4
Langmuir	k_L (L/mg)	0.0011	0.0009
	Q_{max} (mg/g)	17.300	17.37
	R^2	0.9898	0.9246
Freundlich	k_f (L^n /mg $^{(1-n)}$ g)	0.1636	0.1350
	n	1.7287	1.6961
	R^2	0.9865	0.9899

- *Physical and chemical characterization*

The morphology and elements of BC5 were found to be morphos material that contained high K, Ca, and Mg **(Figure 5a-f.)**. The feedstock of BC5 was cassava, according to the importance of K and Mg on growth of cassava lead to high rates K and Mg in cassava and cassava rhizomes [19]. Conversely, ZL4 was found to be amorphous that contained high Si, followed by N, Al, Ca, K, Fe, Mg and Na **(Figure 6a-f.)**. Generally, there are many types of natural zeolite, for ZL4 which contains Si around 50.1 wt%, possibly in the high-silica zeolite class [20].

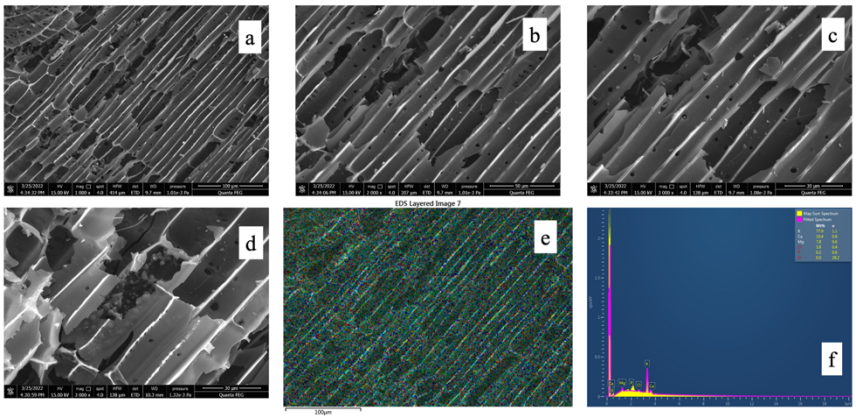

Figure 5a-f.
SEM image for BC5 at (a) 1,000x; (b) 2,000x; (c) 3,000x; (d) 5,000x; and (e and f) EDS Elemental Element Map on BC5.

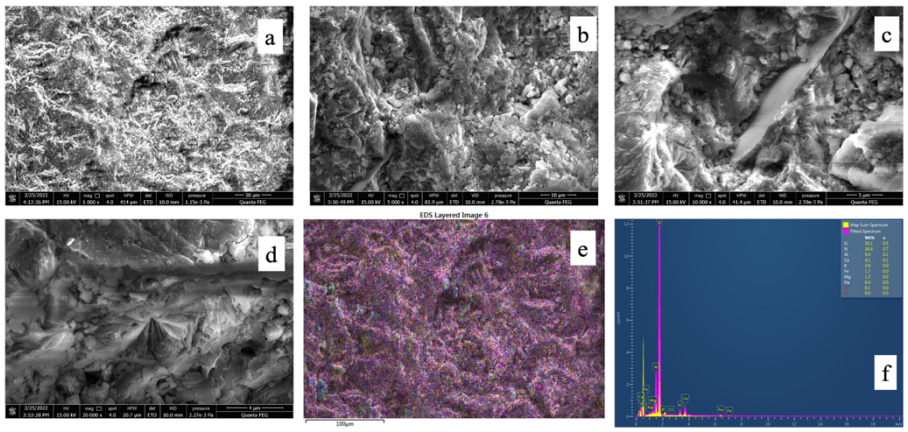

Figure 6a-f.
SEM image for ZL4 at (a) 1,000x; (b) 5,000x; (c) 10,000x; (d) 20,000x; and (e and f) EDS Elemental Element Map on ZL4.

For pH_{pzc} data showed that the surface charge at pH 9 for BC5 was positive and ZL4 was negative. Therefore, the main force of ammonium adsorption on BC5 is not an electrostatic force. The adsorption ability may be on the active site [17].

Conclusion

From the study of nutrient absorption in synthetic urine wastewater with 13 raw adsorbent materials, the BC5 and ZL4 showed the highest adsorption capacity for biochar and zeolite. However, both biochar and zeolite showed poor adsorption capacity for phosphorus. The adsorption kinetic and isotherm were performed in synthetic wastewater. Pseudo-second-order kinetics were proposed to fit the experimental data well for BC5 and ZL4, suggesting

that the adsorption was controlled by chemical processes, which are driven by electrostatic attraction, ion exchange, and surface ligand exchange. For isotherm, BC5 data fit with Langmuir isotherm though ZL4 fit with Freundlich isotherm. BC5 was found to be morphos material that contained high K, Ca, and Mg. Conversely, ZL4 was found to be amorphous, this can explain the Freundlich isotherm in ZL4. The study about the point of zero charge showed that the surface charge of BC5 was positive at pH 9, which means that electrostatic was not the main force for ammonium adsorption in BC5, which is different from ZL4 that electrostatic was the main force according to the negative surface. When the results of a study on nutrient absorption in synthetic urine wastewater with raw absorbents were considered, it was found that the original biochar and zeolite could be used as alternative adsorbents for ammonia nitrogen adsorption in energy-saving treatment systems (adsorption). However, there were limitations in the absorption of phosphorus because they had very low phosphorus absorption capacity that may be a result of positive-negative of surface charge. To absorb phosphorus, the surface of the absorbent material should be improved to suit its application beforehand.

Acknowledgement
This work was supported by National Research Council of Thailand (NRTC) (N25A640063).

Reference

1. Randall, D., *Urine – the liquid gold of wastewater.* Civil Engineering = Siviele Ingenieurswese, 2018. **2018**(5): p. 7-9.
2. Alaqarbeh, M., *Adsorption Phenomena: Definition, Mechanisms, and Adsorption Types: Short Review.* 2021. **13**: p. 43-51.
3. Beler-Baykal, B., A.D. Allar, and S. Bayram, *Nitrogen recovery from source-separated human urine using clinoptilolite and preliminary results of its use as fertilizer.* Water Sci Technol, 2011. **63**(4): p. 811-7.
4. Tarpeh, W.A., K.M. Udert, and K.L. Nelson, *Comparing Ion Exchange Adsorbents for Nitrogen Recovery from Source-Separated Urine.* Environmental Science & Technology, 2017. **51**(4): p. 2373-2381.
5. Allar Emek, A.D. and B. Beler-Baykal, *Stagewise processing of yellow water using clinoptilolite for N&P recovery and higher residual quality.* Water Science & Technology, 2015. **71**: p. 1869-1874.
6. B., A.E.A.D.a.B.B., *Stagewise processing of yellow water using clinoptilolite for N&P recovery and higher residual quality.* Water Sci. Technol, 2015. **71**: p. 1869-1874.
7. Xiaofeng, B., *Recovery of Ammonium in Urine by Biochar Derived from Faecal Sludge and its Application as Soil Conditioner.* Waste and biomass valorization, 2018. **v. 9**(no. 9): p. pp. 1619-1628-2018 v.9 no.9.
8. Gao, F., et al., *Removal of aqueous ammonium by biochars derived from agricultural residuals at different pyrolysis temperatures.* Chemical Speciation & Bioavailability, 2015. **27**(2): p. 92-97.
9. Yang, H., et al., *Utilization of biochar for resource recovery from water: A review.* Chemical Engineering Journal, 2020. **397**.
10. Shakoor, M.B., Z.L. Ye, and S. Chen, *Engineered biochars for recovering phosphate and ammonium from wastewater: A review.* Sci Total Environ, 2021. **779**: p. 146240.
11. Ronteltap, M., M. Maurer, and W. Gujer, *Struvite precipitation thermodynamics in source-separated urine.* Water Research, 2007. **41**(5): p. 977-984.
12. Lawrinenko, M. and D.A. Laird, *Anion exchange capacity of biochar.* Green Chemistry, 2015. **17**(9): p. 4628-4636.

13. Asgari, G. and A. Dayari, *Experimental dataset on acid treated eggshell for removing cyanide ions from synthetic and industrial wastewaters.* Data in brief, 2017. **16**: p. 442-452.
14. Park, M.H., S. Jeong, and J.Y. Kim, *Adsorption of NH3-N onto rice straw-derived biochar.* Journal of Environmental Chemical Engineering, 2019. **7**(2): p. 103039.
15. Sun, D., et al., *Phosphorus recovery and reuse by pyrolysis: Applications for agriculture and environment.* Chemosphere, 2018. **194**: p. 682-691.
16. Guaya, D., et al., *Modification of a natural zeolite with Fe(III) for simultaneous phosphate and ammonium removal from aqueous solutions.* Journal of Chemical Technology and Biotechnology, 2015. **91**.
17. Aydin, S., et al., *Modelling of Adsorption Kinetic Processes—Errors, Theory and Application*. 2018. p. 19.
18. Zhang, R., et al., *Biochar-activated peroxydisulfate as an effective process to eliminate pharmaceutical and metabolite in hydrolyzed urine.* Water Res, 2020. **177**: p. 115809.
19. Howeler, R., *Cassava Mineral Nutrition and Fertilization.* 1981.
20. Wise, W.S., *MINERALS | Zeolites*. 2013.

LOW-COST SUSTAINABLE ELECTROCATALYSTS OF ALLOY/CARBON-BASED NANOMATERIALS AND THEIR APPLICATION FOR Li-ION BATTERIES

Wongsathorn Kaewraung, Panitat Hasin

Department of Chemistry, Faculty of Science, Kasetsart University, Thailand

*e-mail: fscipths@ku.ac.th

Abstract:

Iron (Fe)-germanium (Ge)-based anode material has recently aroused great attention In lithium-ion batteries (LIBs), because of its high theoretical capacity and suitable lithium inserting potential. Nevertheless, because of large volumetric expansion and severe pulverization during lithiation/delithiation, the performance of Fe-Ge-based anode material is poor in LIBs. Herein, a composite with Fe-Ge alloy nanoparticles embedded in a multiwalled carbon nanotube matrix (Fe-Ge/MWCNT) is fabricated by a milling-assisted covalent-bonding method. The introduction of MWCNTs and Fe effectively suppresses the stress/strain originated from the volume change during charge/discharge processes. Excellent electrochemical performance is achieved as a LIB anode, which delivers a high reversible capacity of 502.0 mA h g^{-1} at 100 mA g^{-1}. Our findings not only propose a reasonable design of high-performance alloy-based anodes in LIBs but also promote the practical use of LIBs in large-scale energy storage.

Introduction:

Currently, humanity's use of fossil fuels is severely damaging our environment. Fossil fuels cause local pollution where they are produced and used, and their ongoing use is causing lasting harm to the climate of our entire planet. Nonetheless, meaningfully changing our ways has been very difficult. Moreover, CO_2 produced by human activities is the largest contributor to global warming. By 2020, its concentration in the atmosphere had risen to 48% above its preindustrial level (before 1750)[1]. With the huge consumption of traditional fossil fuels and the ensuing environmental issues mentioned above, the development of new energy storage technologies for renewable energy has been imperative.

At present, lithium-ion batteries (LIBs) are matured and widely used in the field of portable energy storage. They have many desirable characteristics such as high efficiencies, a long cycle life, high energy density, and high power density[2]. These characteristics, along with their capability for fast discharge, have made them nearly ideal for portable electronics applications.

When the ever-increasing demands in energy density and service environments, the currently available graphite-based anodes are incapable of satisfying requirements owing to their limited theoretical capacity and potential safety hazard at low temperatures[3]. Tremendous efforts have mainly optimized the structure and cycling stability of anodes over a wide temperature range. Alloy-type anodes exhibit high theoretical specific capacity and

appropriate lithiation potentials far from Li plating potential, which make them promising candidates for next-generation LIBs.

Among the potential alternative anode materials, group 14 elements, such as silicon (Si) and germanium (Ge), are very attractive candidates for high-capacity applications as they possess high theoretical capacities (3850 mA h g^{-1} for Si, 1568 mA h g^{-1} for Ge), because of their ability to alloy with as many as 4.4 Li atoms per Si or Ge atom (Figure 5). In particular, Ge is a promising candidate for fast-charging and high-capacity LIB application, with lithium diffusivity in Ge being 400 times higher than in Si, and higher intrinsic electronic conductivity compared to Si due to its smaller band gap[4,5].

However, similar to Si and Sn, Ge also suffers from large volume changes during Li alloying/de-alloying reactions on prolonged cycling. The increasing mechanical stress causes electrode pulverization, which leads to fast capacity fading. To improve the cycle stability of Ge-based electrodes and enhance lithium-ion transport, many efforts have been focused on designing new structures that are favorable for enduring volume changes, highly ionic conditions, and electronic transport, such as preparing nanosized Ge particles by high-energy mechanical milling or chemical reduction[6], synthesizing Ge particles with hollow structures[7], and embedding Ge nanoparticles in carbon fiber[8]. Another attractive approach to prepare high-performance anode materials is designing Ge-based binary or ternary alloys as the chemical architectures of the alloys, resulting in new physicochemical properties. Development of new Ge-based alloy systems with favorable electrochemical performance is of great importance from both scientific and technological points of views.

Various Ge-M (M = Cu, Ni, Sn, Co, and Mo) alloys have been used in attempts to alleviate the volume change during the lithiation/delithiation process to improve the cyclic stability of the electrode. However, the introduction of the second element into the system often shortens or even eliminates the plateau in the voltage profile of Ge, presenting a sloping voltage curve. To design high-performance Ge-M alloy anodes with a long flat voltage profile, high capacity, and stable cycle performance, a suitable metal element should be selected for the Ge-M alloy[9]. Among the transition metals, iron (Fe) has some marked advantages over the others due to its low cost, eco-friendliness, natural abundance, and high energy density. Moreover, nanosized iron also possesses high electrochemical capacities from the conversion mechanism instead of the intercalation reaction due to its rich redox reactions caused by abundant valence states (Fe^0, Fe^{2+}, and Fe^{3+}). However, there are still some challenges such as particle aggregation, low electronic conductivity, and other side reactions[10]. These unfavorable factors have largely limited the development of Ge-M alloy in the field of energy storage.

Several works have been devoted to address the above issues for improving the performances of LIBs. An ingenious strategy is to construct unique structures such as nanorods, nanospheres, nanosheets, nanotubes, and so on. These effective approaches can shorten the diffusion paths of ions/electrons and provide the large surface area. However, the low conductivity still leads to inferior electrochemical performance. A more effective method is to coat Ge-M alloy on the surface of the carbon materials so that it cannot only be used to segregate Ge-M alloy for avoiding the aggregation but also can largely improve the electrical and ionic conductivities. Based on this method, constructing a Ge-M alloy/carbon nanocomposite is an innovative strategy to eliminate the barrier for the application of Ge-M alloy/carbon. Moreover, the nanocomposite consisting of a carbon layer and an active

material has abundant space, which can accommodate the volume expansion during the lithiation/de-lithiation processes.

Based on the aforementioned consideration, we skillfully synthesized the Fe-Ge/multiwalled carbon nanotube (Fe-Ge/MWCNT) composite via a milling-assisted covalent-bonding method. Such a nanocomposite can not only tolerate the mechanical strain derived from the large volume change during charging/discharging but also enhance the electrical and ionic transport. Therefore, it showed excellent performance as an anode for LIBs.

Methodology:

Experimental details

Preparation of Fe-Ge alloy

The Fe-Ge alloy was synthesized by a solid-state synthesis method of mechanical ball milling. In a typical procedure as shown in Figure 16, 0.43 g of Fe powder was mixed with 0.57 g of Ge powder. The mixture was transferred to zirconia ball mill jar with the addition of the zirconia balls with five different sizes (15 mm, 12 mm, 10 mm, 8 mm, and 5 mm in diameter). The zirconia balls to sample ratio was 200:1 by weight. Then, the milling process was performed at the speed of 400 rpm for 40 h. After 40 h milling, the milled powder of Fe-Ge alloy was collected as a given Fe-Ge alloy product.

Preparation of Fe-Ge alloy/MWCNT nanocomposite

The Fe-Ge/MWCNT nanocomposite was prepared through a milling-assisted covalent-bonding method as shown in Figure 17. Typically, 0.50 g of the as-prepared Fe-Ge alloy was mixed with 0.25 g of MWCNTs, the mixture was then added into zirconia ball mill jar. The zirconia balls with five different sizes (15 mm, 12 mm, 10 mm, 8mm, and 5 mm in diameter) were added. All the mixture were milled at 750 rpm for 6 h. In this ball milling process, the Fe-Ge alloy molecules were tightly bonded to the commercial MWCNTs, thus forming a covalently bonded Fe-Ge/MWCNT nanocomposite.

Structural characterizations

All obtained samples were characterized with the combination techniques as follows. X-Ray fluorescence spectrometer (XPS) (S8 TIGER Series 2 by Sequential Type Spectrometry) was used to measure the element contents of the pristine Fe-Ge alloy. Thermogravimetric analysis (TGA) was performed on Perkin elmer model TGA8000. The amount of sample (4-5 mg) was introduced to an alumina pan. TGA analysis was consequently carried out under of O_2 atmosphere with the temperature range of 30 to 800 ^oC at a heating rate of 10 $^oC\ min^{-1}$. The structure of the prepared composite was characterized by X-ray diffractometer (XRD) (a Bruker D8 Advance) operated at 40 kV and 40 mA, scanning over between 20^o and 80^o. Cu K_α radiation was used as a light source. Raman spectroscopy (NT-MDT, model NTEGRA spectra) with an excitation wavelength of 532 nm was employed to analyze the structure of samples. The morphology of the prepared composite was characterized by Scanning electron microscope (SEM) (FEI model Quanta450) operated at an acceleration voltage of 25 kV.

Electrochemical measurements

The working electrode was prepared by mixing active materials, Super P conductive carbon black, and a binder (polyvinylidene fluoride) with a weight ratio of 8:1:1. The slurry was further coated on a copper foil. The mass loading of the electrode is about 0.29 mg cm^{-2}. Half cells (CR20302 coin-type) were assembled in an argon-filled glovebox. The electrolyte is 1 M $LiPF_6$ dissolved in ethylene carbonate, ethyl methyl carbonate, and dimethyl carbonate

(vol% 1:1:1). Lithium metal is used as a counter electrode and celgard 2320 microporous polypropylene/polyethylene/polypropylene is used as a membrane.

Results and Discussion:

The possibility of employing the ball-milling method to prepare Fe-Ge alloy was investigated. The ability of this method to coat Fe-Ge alloy with the MWCNTs was also proposed (**Figure 1**). This choice was selected because the ball-milling process is capable of preparing hard composite-based materials, which can be employed for coating purposes. During the first and intermediate stages of milling, the agglomerated Fe-Ge alloy powders were continuously disintegrated into smaller particles with fresh surface. Thus, Fe-Ge alloy nanoparticles have a much greater fresh surface with a large number of lattice defects and unstable dangling-bond electrons. Incorporation of Fe-Ge alloy nanoparticles into MWCNTs with abundant π-orbitals of unsaturated bonds, the covalent bonding of the Fe-Ge alloy nanoparticles and MWCNTs is obtained via the defect sites of Fe-Ge and π-orbitals of MWCNTs leading to an ideal dispersion of Fe-Ge on the surface of MWCNTs during ball-milling[10,11].

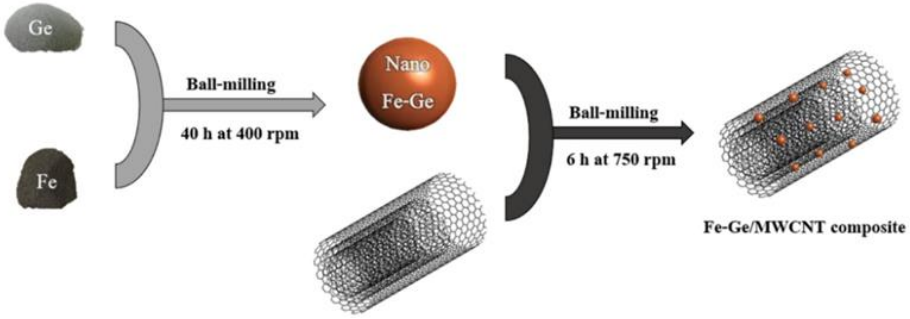

Figure 1. Schematic illustration of synthesis of Fe-Ge/MWCNT composite via milling-assisted covalent-bonding method.

In order to measure the contents of Fe and Ge in the Fe-Ge alloy, XRF results reveal that the weight ratio of Fe to Ge is about 1.0:1.1 as shown in **Table 1**, confirming 1.2:1.0 atomic ratio of Fe to Ge. As a result of XRF analysis, the Fe-Ge alloy with the atomic ratio of 1:1 was successfully synthesized by a milling-assisted covalent-bonding method.

Table 1. Chemical composition of the Fe-Ge nanoparticle measured by XRF.

Element	**Ge**	**Fe**	**Zr**	**Si**	**Other impurities**
Mass percentage(wt%)	48.4	43.5	1.20	0.127	0.176

Thermogravimetric analysis (TGA) was conducted to evaluate the covalent bond formed between the Fe-Ge particle and MWCNTs during ball-milling and the preservation of carbon after subsequent carbonization (**Figure 2a**). The carbon content in the Fe-Ge/MWCNT composite is calculated to be ~ 20.7 wt%, implying that the residual weight of the MWCNTs after carbonization is in a high level of ~ 12.6%. Nevertheless, the complete carbonization of pure MWCNTs can lead to the weight loss of about 99.6% as shown in **Figure 2b**. The covalent attachments of Fe-Ge alloy particles to the MWCNT surface can

cause the increased residual weight of carbon attributed to the presence of undecomposed or partially decomposed MWCNTs. This leads to the survival of MWCNTs during carbonization. An investigation of the weight change of the Fe-Ge/MWCNT composite at high temperature also reflects the covalent bonding. The weight increases of 32.0% observed in the pristine Fe-Ge alloy once the temperature was elevated to 900 °C is originated from the oxidation reactions of Fe-Ge alloy, whereas the corresponding sample of the Fe-Ge/MWCNT composite does not show the oxidation of Fe-Ge alloy particles, revealing the ability of MWCNTs to protect the surface of Fe-Ge alloy particles from oxidized environment. This indicates that the surface of Fe-Ge alloy particles is firmly bound to the MWCNTs[10].

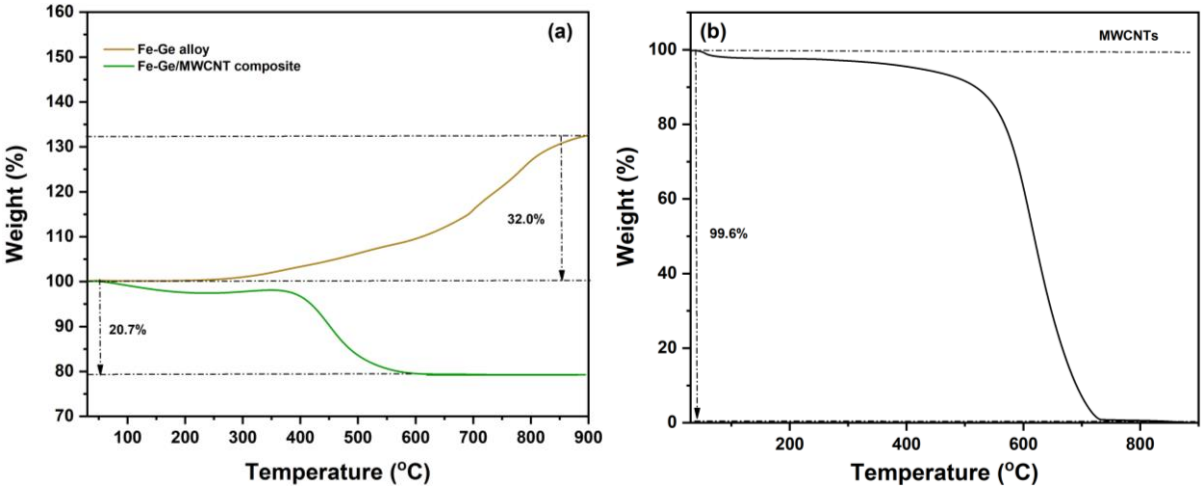

Figure 2. TG curves of (a) Fe-Ge alloy, Fe-Ge/MWCNT composite and (b) MWCNTs under O_2 atmosphere at 30-900 °C.

XRD patterns of the MWCNTs, Fe-Ge alloy, and Fe-Ge/MWCNT composite are presented in **Figure 3**. The Fe-Ge alloy shows XRD pattern, which can be assigned to FeGe phase. All XRD signals assigned to FeGe phase in the XRD pattern of Fe-Ge/MWCNT composite are preserved, which retains the original FeGe phase. Nevertheless, no diffraction peaks of MWCNTs can be observed in the XRD pattern, possibly due to its amorphous nature. This is evidenced by the XRD pattern of the MWCNTs, from which two slight diffraction peaks appear.

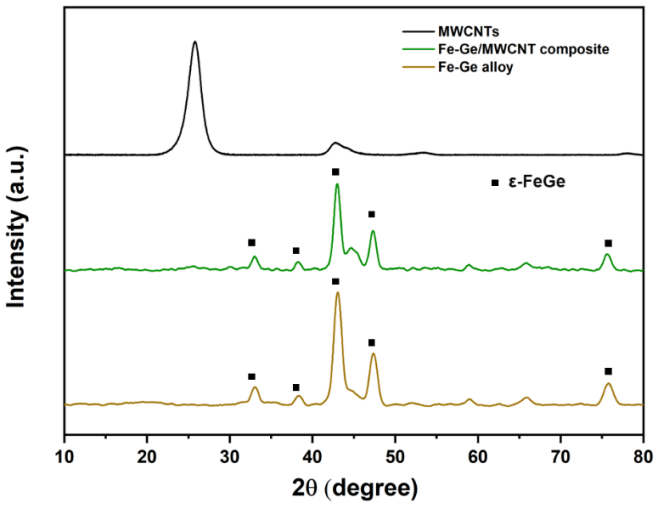

Figure 3. XRD patterns of MWCNTs, Fe-Ge alloy, and Fe-Ge/MWCNT composite.

The Raman spectrum of the Fe-Ge/MWCNT composite shows the bands at 1327 cm^{-1} and 1585 cm^{-1}, corresponding to the D and G bands of carbon, respectively (**Figure 4**). The intensity ratio between D and G bands (I_D/I_G) is calculated to be 2.79, suggesting that the MWCNTs in the Fe-Ge/MWCNT composite is highly amorphous, and Fe-Ge alloy nanoparticles are coated on the surface of MWCNTs. Compared to the peak intensity of alloy bands in the Raman spectrum of the Fe-Ge alloy, the alloy bands are not observed in the Raman spectrum of the Fe-Ge/MWCNT composite implying that the Fe-Ge alloy particles is uniformly coated on the surface of MWCNTs.

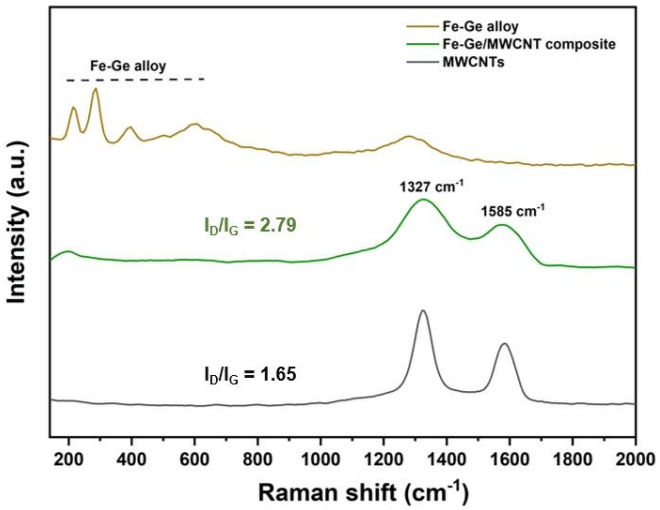

Figure 4. Raman spectra of MWCNTs, Fe-Ge alloy, and Fe-Ge/MWCNT composite.

The morphology and microstructure of the Fe-Ge/MWCNT composite are observed by scanning electron microscopy (SEM) measurement. As presented in **Figure 5b**, the nanoparticles of Fe-Ge alloy are well dispersed on the surface of MWCNTs, retaining the original tubular structure of MWCNTs[12] (**Figure 5a**). This indicates that the Fe-Ge alloy is present in the nanoparticle form tightly anchored to the MWCNTs. In addition, corresponding energy-dispersive spectroscopy (EDS) spectrum confirms the presence of Fe and Ge elements on MWCNTs (**Figure 5c**).

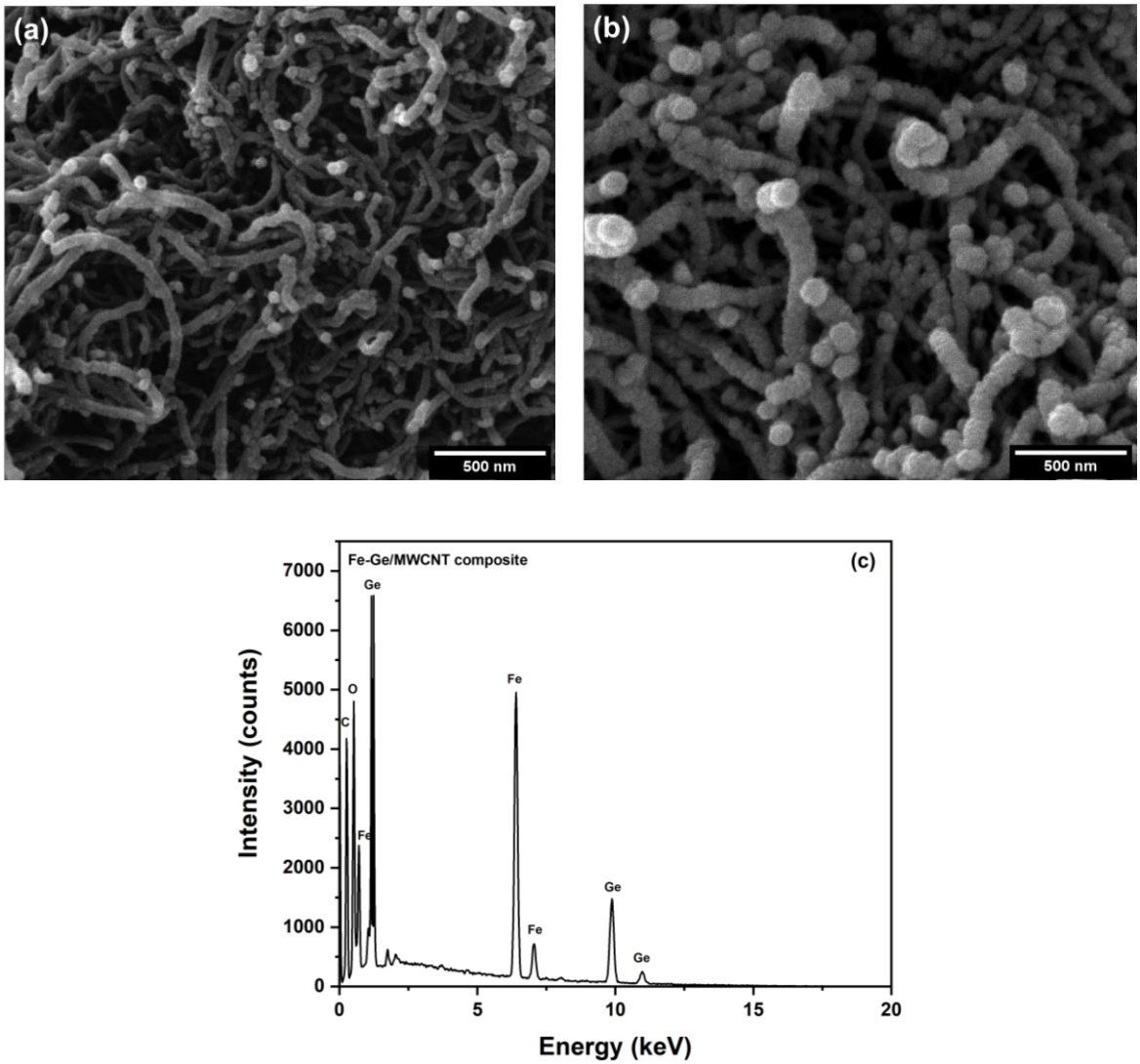

Figure 5. SEM images of (a) MWCNTs, (b) Fe-Ge/MWCNTs, and EDS spectrum of (c) Fe-Ge/MWCNT composite.

The electrochemical behavior of the Fe-Ge/MWCNT composite was investigated by cyclic voltammetry (CV) at 0.1 mV s^{-1} (**Figure 6**). In the first negative scan, a weak reduction current appears in the potential region of 0.8-0.3 V, representing the formation process of the surface SEI film. In the following cycles, an anodic peak is displayed at 0.45 V, which is associated with the delithiation reaction of Li_x(Fe-Ge) → (Fe-Ge). The CV curves are well overlapped, except the first scan, demonstrating a high reversibility and stability of the Fe-Ge/MWCNT composite anode[13,14].

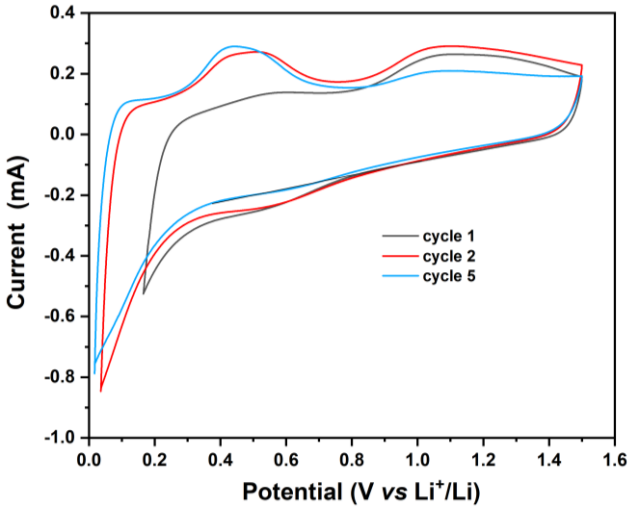

Figure 6. Cyclic voltammetry curves of the Fe-Ge/MWCNT composite anode from 0 V to 1.5 V vs. Li/Li^+ with a scan rate of 0.1 mV s^{-1}.

Figure 7a-c display selected charge/discharge profiles of the three samples at 100 mA g^{-1}. Similar voltage profiles are presented, indicating the same reversible lithiation/ delithiation reaction mechanism. The first discharge capacities are 501.3 mA h g^{-1} for MWCNTs, 288.6 mA h g^{-1} for Fe-Ge alloy, and 553.7 mA h g^{-1} for Fe-Ge/MWCNT composite with initial Coulombic efficiencies (CEs) of 118.2%, 92.0%, and 96.9%, respectively. It is interesting that the Fe-Ge/MWCNT composite shows CE close to 100% when compared to MWCNTs and Fe-Ge alloy, indicating a higher reversibility for the former one.

The rate capability of Fe-Ge/MWCNT composite was evaluated at different current densities (**Figure 7d**). When the current density increased from 100 to 10000 mA g^{-1}, reversible capacities of 502.0, 272.0, 150.3, 3.3, and 1.2 mA h g^{-1}, respectively, were delivered. A high capacity of 144.2 mA h g^{-1} was retained when the current density changed back to 1000 mA g^{-1}, demonstrating good rate capability. As a reference, the Ge/MWCNT anode without the Fe alloying was also tested at the same current densities. For the Ge/MWCNT electrode, although it has a high initial discharge capacity of 993.3 mA h g^{-1} for the first cycle at 100 mA g^{-1}, polarization becomes increasingly severe in the first few cycles, especially at high current densities because of the pulverization of Ge particles in the electrode caused by the large volume change. However, when the homogeneous Fe-Ge/MWCNT structure is formed, the electrode shows higher discharge capacity even at high current densities, indicating that the bonded Fe alloying of Ge structure builds a rather stable structure for the Fe-Ge/MWCNT composite. This will greatly increase the utilization efficiency of the lithium source of the anode in a cell. The electrochemical performance of the Fe-Ge/MWCNT composite outperforms MWCNTs, Fe-Ge alloy, and Ge/MWCNTs anode materials for LIBs, which is mainly attributed to the buffer effect of MWCNTs and Fe to Ge during the cycling process and the surface-bonded MWNCTs, which enhance the electrical conductivity and promote the Li ions into/out of alloy, thus accelerating the reaction kinetics of the Fe-Ge alloy with Li ions.[10,14]

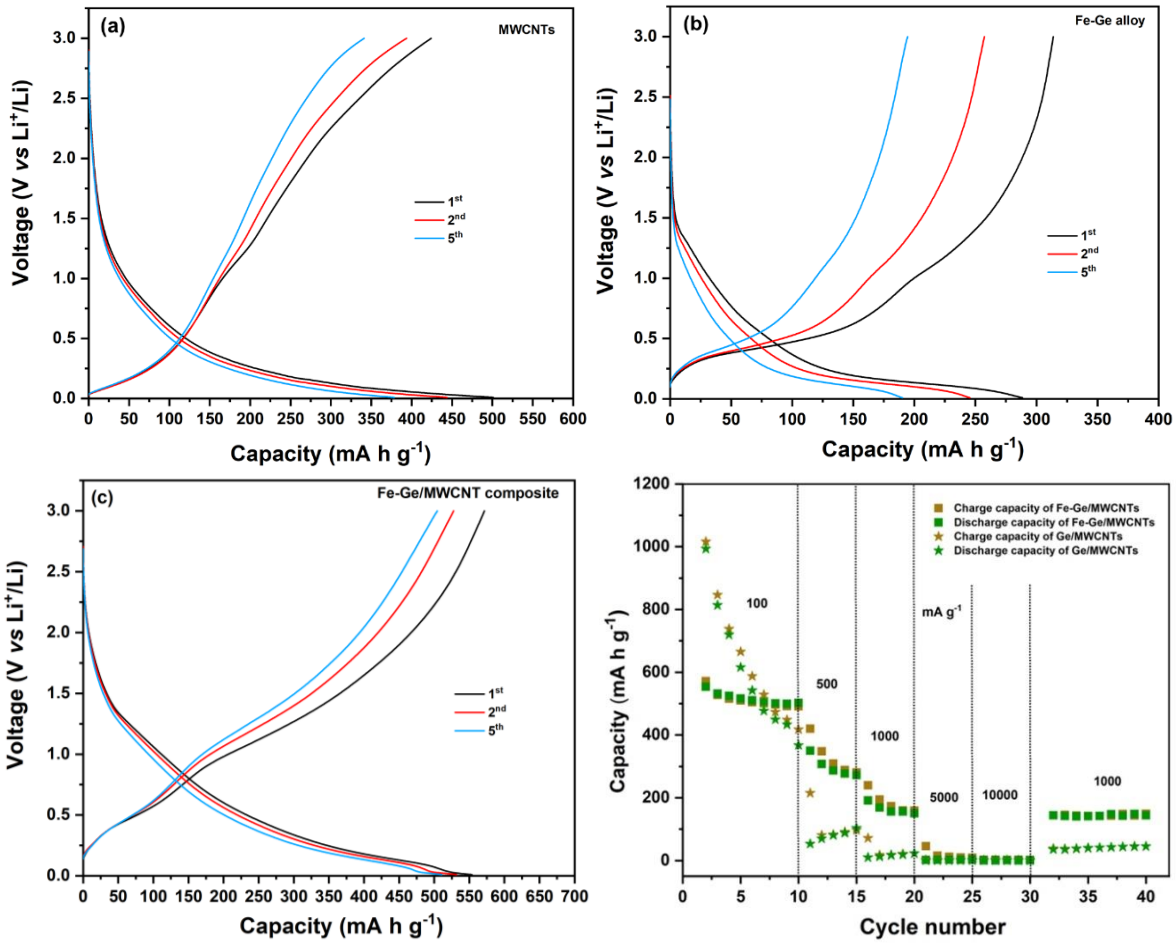

Figure 24. (a) Charging/discharging profiles of (a) MWCNTs, (b) Fe-Ge alloy, (c) Fe-Ge/MWCNT composite anode in the initial 5 cycle at 100 mA g^{-1}, and (d) rate performance of Ge/MWCNTs and Fe-Ge/MWCNTs composite anodes at different current densities (100-10000 mA g^{-1}).

Conclusion:

A composite with Fe-Ge alloy nanoparticles embedded in a MWCNT matrix was designed and synthesized using a milling-assisted covalent-bonding method. The characteristic structure with the introduction of Fe-Ge and MWCNTs can effectively buffer the volume change of Fe-Ge/MWCNT composite. Benefitting from the excellent structural features of the Fe-Ge/MWCNT composite, as an anode material for LIBs, excellent electrochemical performance was demonstrated with a high reversible capacity (502.0 mA h g^{-1} at 100 mA g^{-1}), relatively high initial Coulombic efficiency (102.0%), and good rate capability (144.2 mA h g^{-1} at 1000 mA g^{-1}). Our findings not only propose a reasonable design of high-performance alloy-based anodes in LIBs but also promote the practical use of LIBs in large-scale energy storage.

References:

1. Watts N, Adger WN, Agnolucci P, Blackstock J, Byass P, Cai W, et al. Lancet. 2015;386(10006):1861-914.
2. Liu Y, Zhang R, Wang J, Wang Y. iScience. 2021;24(4):102332.
3. Cheng H, Shapter JG, Li Y, Gao G. Energy Mater. 2021;57:451-68.
4. Tian H, Xin F, Wang X, He W, Han W. J. Materiomics. 2015;1(3):153-69.
5. Ocon J, Lee J, Lee J. J. Appl. Chem. 2014;25.

6. Wei Y, Huang L, Chen J, Guo Y, Wang S, Li H, et al. ACS Appl. Mater. Interfaces. 2019;11(44):41374-82.
7. Li L, Seng KH, Feng C, Liu HK, Guo Z. J. Mater. Chem. A. 2013;1(26):7666-72.
8. Liu J, Muhammad S, Wei Z, Zhu J, Duan X. NNOTER. 2020;31(1):015402.
9. Doherty J, McNulty D, Biswas S, Moore K, Conroy M, Bangert U, et al. NNOTER. 2020;31(16):165402.
10. Wang H, Fan S, Cao Y, Yang H, Ai X, Zhong F. ACS Appl. Mater. Interfaces. 2020;12(27):30503-9.
11. Chen Y, Qian J, Cao Y, Yang H, Ai X. ACS Appl. Mater. Interfaces. 2012;4(7):3753-827
12. Varzi A, Täubert C, Wohlfahrt-Mehrens M, Kreis M, Schütz W. J. Power Sources. 2011;196:3303-9.
13. Goriparti S, Gulzar U, Miele E, Palazon F, Scarpellini A, Marras S, et al. J. Mater. Chem. A. 2017;5(37):19721-8.
14. Wei D, Zeng S, Li H, Li X, Liang J, Qian Y. Electrochim. Acta. 2017;253:522-9.

ASSESSMENT AND ZONING OF SELF-CLEANING ABILITY OF NHIEU LOC-THI NGHE CANAL'S WATER IN HO CHI MINH CITY

Bui Viet Hung[1,*], Nguyen Ngoc Diep[2]

[1]*VNUHCM-University of Science, No.227 Nguyen Van Cu Street, District 5, Ho Chi Minh City 7000, Viet Nam*
[2]*University of Labors and Society of Ho Chi Minh City, To ky Street, District 12, Ho Chi Minh City 7000, Viet Nam*
[*]Emails: *bvhung@hcmus.edu.vn*

Received: xx xx xxxx; Accepted for publication: xx xx xxxx

Abstract. Assessment of self-cleaning capacity of water is interested in the environmental protection and management. Because this is the basis for the successful solutions to control and prevent a pollution and declination of water resources, when understanding the capacity of water to degrade the internal pollutants. This self-cleaning capacity is a ratio of the oxygen added (permeable) and losed (declining) for the redox reaction of pollutants in water. The processes of oxygen declining and permeable are expressed through the coefficients. The study has chosen the oxygen declining and dissolved coefficients according to the characteristics of water canal in Ho Chi Minh City to define the self-cleaning capacity the principle research of Nhieu Loc Thi Nghe canal (NLTN). Based on the assessment of water quality by index (WQI), the self-cleaning capacity classification of NLTN water, the study zoned the quality and self-cleaning capacity of water by maps. It also showed that the water quality of NLTN canal being variant, declined and demontrate the shock phenonminon of the water environment in the canal when the weather conditions change suddenly such as so hot or rainy on the season change.

Keywords: Oxygen declining coefficient, oxygen permeable coefficient, oxygen biological process, self-cleaning capacity, water quality index.

1. INTRODUCTION

Water can recover itself in a quantity, a quality and an energy. The quality recoverable capacity of water is often referred to as the self-cleaning process or the self-cleaning capacity. When analyzes the self-cleaning capacity of water, we often refer to the problem of pollution level and the dissolvent process of pollution substances. The rate of dissolution is referred to the selt-cleaning capacity.

The degree of self-cleaning capacity of water is often through a complex combination of biomechanical and biochemical processes taking place simultaneously in the water body. Depending on many specific events, some of these processes take place more prominently than others such as the mechanical and diluting processes take place strongly at the mountainous, midland areas; the biochemical and physical processes take place strongly such as deposition, chemistry, and biology at the delta and coastal zones. Water's self-cleaning capacity is limited and

requires some especial conditions. A water body has been exploited/polluted beyond its self-clealing capacity will be degraded, exhausted both quality and quantity, and loosed the capacity of exploitation.

Assessment of self-cleaning capacity of water body is usually based on the assessment of variations of the pollutants' concentrations. Water quality is referred to the suitability to maintain the balances of physical - chemical - biological cycles occurring in the water and for different uses. Water quality can be determined by a range of different parameters that determine the intended use of each water source. Otherwise, the water quality depends on the content of physical, chemical and biological parameters presenting in the water [1]. There are many approaches to assess the self-cleaning capacity of water in the relative studies. Such as:

- In the assessing of self-cleaning capacity of river water, the water quality parameters are often used such as dissolved oxygen, biochemical oxygen demand, organic nitrogen, ammonia, nitrate. and total phosphorus [2].

- The studying the self-cleaning capacity through the deposition of solid components in the flow have often focused on the sediment transportation in an open channel by the modelling this phenomenon. Flow with a ratio of current velocity with an erosional velocity (corresponding to some common concentration of suspended solids) will described the flow's settling or self-cleaning capacity [3]. These studies are usually applied for the mountain and highland regions.

- The self-cleaning capacity of a water represents the dissoluble rate to which the organic components are oxygenated in a unit of time (hours, days, ...) compared to the previous amount of these pollutant. Thus, the self-cleaning capacity of water is usually determined through the ratio of variation of pollutant concentration on time - the ratio of DOC/POC, where are the componenets DOC (a decomposed organic carbon) and POC (a previuos organic carbon) [4][2]. The ratio is also refered to the variation of dissolved oxygen component participating in organic cabon oxigenation in water [5][15][8]. The ratio formula is such as:

$$f = DO_{i+1} / DO_i \quad (1)$$

Where are: DO_i is an dissolved oxygen in water at time (i). f is a variation of oxygen concentration. If $f = 1$ (balance), $f > 1$ (good self-cleaning ability with pollution reduced), $f < 1$ (weak self-cleaning ability with pollution increaed).

Because the oxygen process (both the oxidation as well as the diffusion) being into the water depends greatly on the surrounding environmental conditions such as temperature, wind, etc. [14] [11]. The ratio number (f) in formula (1) is calculated according to the oxygen osmotic and reduction coefficients as follows:

$$f = k_2 / k_1 \quad (2)$$

Where are:

k_1 the coefficient of declining process due to the biological oxidation $k_1 = k_{1,T(20)} \, x \, f(T)$

k_2 the coefficient of oxygen permeability process into water and $k_2 = k_{2,T(20)} \, x \, f(T)$

$k_{1,T(20)}$, $k_{2,T(20)}$ are the declining and permeabillity numbers/experiential formulas determined at 20°C condition in a laboratory. They are often the experient formulas with flow components as velocity and depth.

The oxidations of different water quality elements occur under different conditions (oxidating veocity, temperature, pressure,…). So, each component of water quality, we have different above oxygen coefficients [11]. There are many kind of experient formuals to determine the k_1, k_2 coefficients. Such as below table.

Table 1. The summarization of oxygen declining and permeability coefficients

No	The experient formula of *k (1/date)*	Referrences	Note
1	$k_1 = 59{,}06\ Q^{-0,49}$	Wrigh and McDonnell [17]	The declining coeff. $Q(m^3/s) = 0{,}28\text{-}28{,}25$
	$k_1 = 0{,}25 – 0{,}35$	Wrigh and McDonnell [17]	The declining coeff. $Q(m^3/s) < 0{,}28$
2	$k_1 = 0{,}125\text{-}0{,}5\ (H/2{,}45)^{-0,434}(\theta)^{(T-20)}$	Hydroscience [19]	The declining coeff. h(m) < 2,45m
	$k_1 = 0{,}125\text{-}\ 0{,}5\ (\theta)^{(T-20)}$	Hydroscience [19]	The declining coeff. h(m) >= 2,45m
3	$k_1 = 0{,}15\ (\theta)^{(T-20)}$	Davis and Cornwell [18] Schroepfer, et al,, [23]	The declining coeff. $\theta = 1{,}135$ (4<T<20) $\theta = 1{,}056$ (20<T<30) $\theta = 1{,}047$ (T>30)
4	$k_1 = 0{,}3\text{-}0{,}4\ (\theta)^{(T-20)}$	Thomann and Mueller [21]	The declining coeff. $\theta = 1{,}047$
5	$k_2 = 5{,}026U^{0,969}H^{-1,673}(1{,}0241)^{(T-20°)}$	Churchill, Elmore, and Buckingham [6]	The permeability coeff. H=0,74-3,48 U=0,56 – 1,52
6	$k_2 = 5{,}344U^{0,67}H^{-1,85}(1{,}0241)^{(T-20°)}$	Owens, Edwards, and Gibbs [13]	The permeability coeff.
7	$k_2 = 3{,}053\ U\ H^{-3/2}\ (1{,}0241)^{(T-20°)}$	Isaacs and Gaudy [7]	The permeability coeff.
8	$k_2 = 6{,}77\ U\ H^{-3/2}\ (1{,}0241)^{(T-20°)}$	Isaacs and Gaudy [7] Churchill, Elmore, and Buckingham [6]	The pereability coeff. H=0,74-3,48 U=0,56 – 1,52
9	$k_2 = 4{,}419\ U\ H^{-3/2}\ (1{,}0241)^{(T-20°)}$	Isaacs and Gaudy [7] Krenkel's [24]	The permeability coeff.
10	$k_2 = 3{,}3\ U\ H^{-1,33}\ (1{,}0241)^{(T-20°)}$	Langbein and Durum [20]	The permeability coeff.
11	$k_2 = 3{,}93\ U^{1/2}\ H^{-3/2}\ (1{,}0241)^{(T-20°)}$	O'Connor and Dobbins [12]	The permeability coeff.
12	$k_2 = 2{,}33U^{0,608}H^{-1,689}(1{,}0241)^{(T-20°)}$	Bennett and Rathbun [9]	The permeability coeff.
13	$k_2 = 4{,}74\ U^{0,85}\ H^{-0,85}(1{,}0241)^{(T-20°)}$	Negulescu và Rojanski [10]	The permeability coeff.
14	$k_n = 0{,}005\text{-}1{,}0\ (1{,}0241)^{(T-20°)}$	Thomann, and Mueller [21]	The nitrogenous declining coeff.
15	$SOD = 1440\ x\ Slp\ x\ A$	Thomas A, Butts and Ralph L, Evans [14]	The Sediment oxygen damage
16	$SOD = 0{,}006\text{-}0{,}45\ (1{,}065)^{(T-20°)}$	Wei-Bo Chen, Wen-Cheng Liu and Li-Ting Huang [16]	The Sediment oxygen damage

Note: Q-discharge (m3/s); T-Temperature (oC); A-Bottom area (m2); Slp-bottom slope; U-flow velocity (m/s); H-flow depth (m).

HCMC has 5 inner urban canal systems. The Nhieu Loc – Thi Nghe (NLTN) is one of them with its basin being rather separated with others. The water quality of NLTN canal is affected strongly by domestic waste water and tidal regime. Although, NLTN canal was transformed and

improved flowing regime, but, its quality water still has declining phenomena such as a fish depth after rain, pollution smell occurred often. The NLTN canal with main and branches is showed below figure.

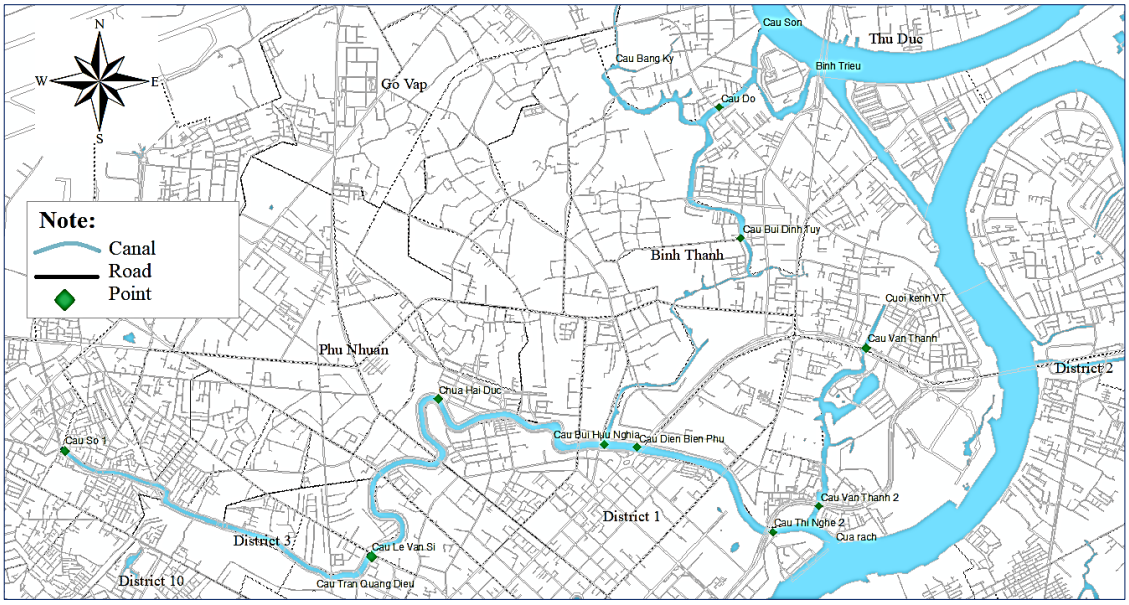

Figure 1. The NL-TL canal system and surveying locations, HCMC

The tidal prevention sluice is constructed at the outlet of NLTN canal. So, the operation process of sluice is for the flood prevention. But its operation have to not decline the water quality as well as its self-cleaning capacity. Therefore, the assessment of self-cleaning capacity of NLTN water canal is suitable and important informations to build or adjust the sluice's operation.

2. MATERIALS AND METHODS

The approachment is applied to assess the self-cleaning capacity of water at NLTN canal on period 2012 – 2021 (See below figure 2).

The surveying water quality points are located on NL-TN canal as below figure. There are 10 (ten) points near the bridges as So 1, Le Van Sy, Hai Duc Pagoda, Bui Huu Nghia, Dien Bien Phu, Van Thanh 2, Thi Nghe 2, Van Thanh, Bui Dinh Tuy and Do (See above figure 1).

The water quality data of NL-TN canal are surveyed on period 2012 – 2021 by the Central of Environment quality surveys of HCMC. The water quality data is surveyed in 2021 at Hai Duc Pagoda (example), which is summaried on below Table 2.

The model methods. The sudy applied the MIKE 11 to modify the hydraulic regime on NL-TN canal with some average flowing components such as the dischages (Q), velocity (U) and depth (H) determined at each surveying point. The river – canal system is showed below figure 3.

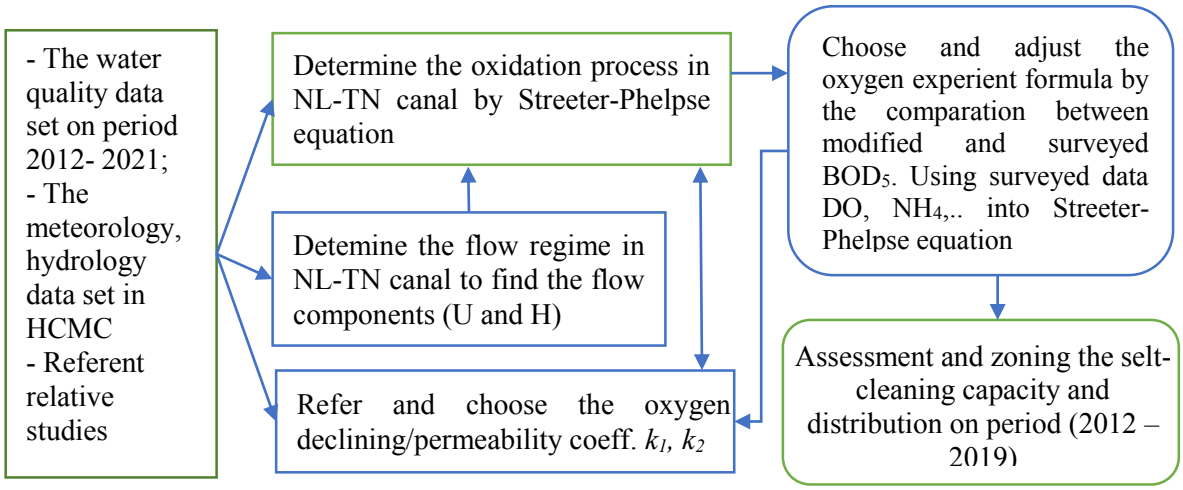

Figure 2. The approachment to assess and zone the self-cleaning capacity of NL-TN water

Table 2. The water quality data is surveyed at Cau So 1 in 2019 (Example)

Position	Process		T°C	pH	NH4	PO4	DO	COD	BOD5	Coliform	E. Coli
	Month	Tide			mg/l	mg/l	mg/l	mg/l	mg/l	MPN/ 100ml	MPN/ 100ml
Cau So 1	01	Lowest	29,8	6,98	2,55	0,00	0,33	22,60	8,18	14000	200
	02	Lowest	30,3	7,23	0,52	0,11	4,07	16,10	6,29	1300	500
	03	Lowest	30,2	7,14	0,39	0,02	2,33	19,25	7,11	38000	0
	04	Lowest	30,2	7,02	1,61	0,06	4,02	26,13	8,09	285000	3500
	05	Lowest	32,1	7,01	1,80	0,13	3,56	27,33	9,45	36000	0
	07	Lowest	30,5	7,06	9,24	0,23	0,2	88	38	43000	9300
	08	Lowest	29,58	7,26	7,84	0,43	0,53	38	14	29000	9300
	09	Lowest	30,13	7,22	7,65	0,28	2,1	41	15	43000	15000
	10	Lowest	31,5	7,32	5,69	0,43	2,64	30	10	93000	21000
	11	Lowest	30,4	7,06	13,63	1,07	0,2	51	20	75000	20000
	12	Lowest	31,43	7,5	8,4	0,26	2,51	30	15	64000	26000

The Streeter-Phelpse equation is applied to determine the oxygen declining/permeability coefficients with the concentrations of DO, NH_4, temperature, BOD_5 of the water quality surveying data set. The Streeter-Phelpse equation is:

$$D_t = \frac{k_1.L_0}{k_2 - k_1}\left(e^{-k_1.t} - e^{-k_2.t}\right) + \frac{k_3.N_0}{k_2 - k_3}\left(e^{-k_3.t} - e^{-k_2.t}\right) + \frac{SOD}{k_2 H}\left(1 - e^{-k_2.t}\right) + D_0 e^{-k_2.t} \quad (3)$$

Where are $D_0 = Ds - Dx$, the initial amount of oxygen declined in the stream, Dx is the oxygen concentration at a distance x from the discharge point. L_0 is an initial BOD_5 value; No is a nitrogenous substances (NH_4); SOD is an oxygen demand for the bottom mud/sludge.

The formulas of oxygen coefficient as k_1 *(Oxygen declining coefficient of* BOD_5 *oxidation process),* k_3 *(Oxygen declining coefficient of* NH_4 *oxidation process),* k_2 *(Oxygen permeable*

coefficient) and SOD (Sediment Oxygen Demand) are selected from the table 1. The assessment of self-cleaning capacity applied for NL-TN canal is implemented by the below tool.

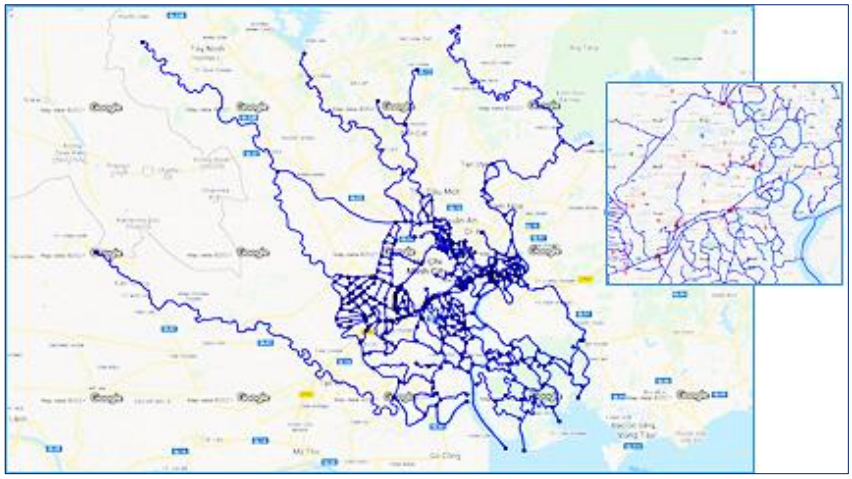

Figure 3. The River – canal systems are located in HCMC and Dong Nai Basin

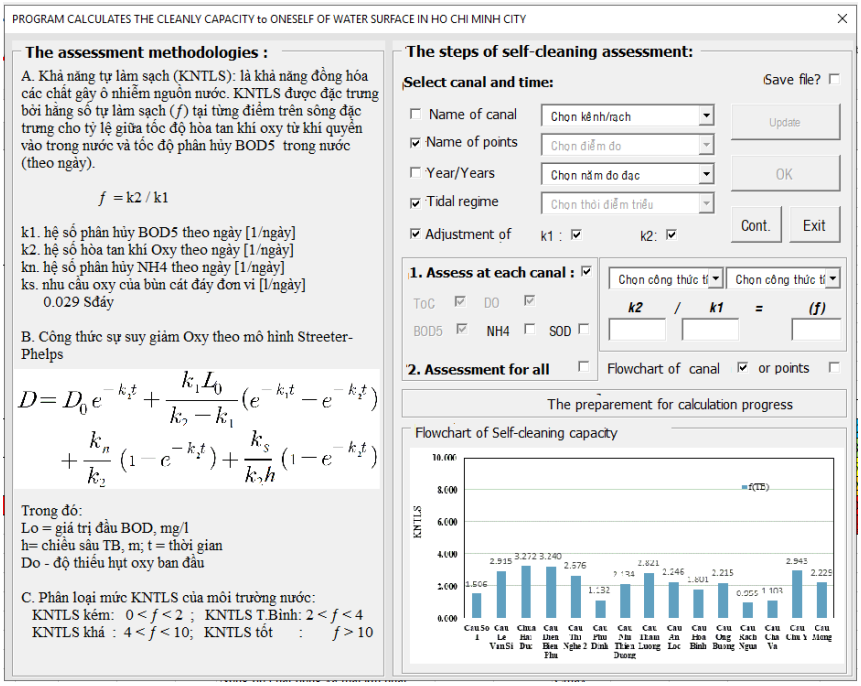

Figure 4. The interface of tool to assess the self-cleaning capacity of canal water

The above assessment tool of self-cleaning capacity, it applied the *Streeter-Phelpse equation* to simulate the BOD_5 components and adjust the values of oxygen coefficients with the oxygen declining quatity D_t, nitrogenous concentration NH_4 determined by the annual surveys and the hydraulic elements (velocity, depth) determined by MIKE 11 model. The assessment results are

accepted when the difference between simulated and surveyed BOD_5 values reasonable (The absolute different numbers are less than 5% - 10% per the surveys' value).

The results of above assessment tool are the values of oxygen coefficients (k_1 and k_2) and the their rate (f) used to find the self-cleaning capacities and levels.

The assessment of self-cleaning capacity of canal water:

- The self-cleaning capacity of water uses the rate formula (f) between two oxygen coefficients (the declining coefficient k and the permeable coefficient k_2) (Trinh, 2004). The relative researches often pointed that the biological oxygen demand is always larger the nitrogenous oxygen demand about several time in the organic decomposing process. Therefore, the oxygen declining coefficient (k) used in the rate formula (2) is often k_1 (*Oxygen declining coefficient of BOD_5 oxidation process*).

- The classification of self-cleaning capacity (level) referred to the relative research (Trinh, 2004) is divided into 4 ranges according to 4 levels such as (i) *weak level* ($f<2$), (ii) *normal level* ($2<f<4$), (iii) *pretty level* ($4<f<10$) and (iv) *good level* ($f>10$).

The zoning levels of self-cleaning capacity (the distribution map) on period 2012 - 2021. The study applied the MapInfor sofware with several GIS' layers (river-canal, administrative boundaries, resident areas,…) describes the self-cleaning capacity's levels of NLTN canal water. Besides, the distribution maps of self-cleaning capacity's levels will help to analysis as the consideration of affect figures to local water quality and its self-cleaning capacity and so on.

3. RESULTS AND DISCUSSION

The water quality in NLTN canal: Based on the measurement results of water quality in NLTN canal on period 2012 – 2021, (see example Table 2), it shows that the canal water quality has many fluctuations due to many reasons, including urban renovation and reclamation projects. The application of WQI equation (*Decision 1460/QD-TCMT of Viet Nam Ministry of Natural Resource Environment-MONRE*) determines the water quality on NLTN canal on period 2012 – 2021 as below figure 5.

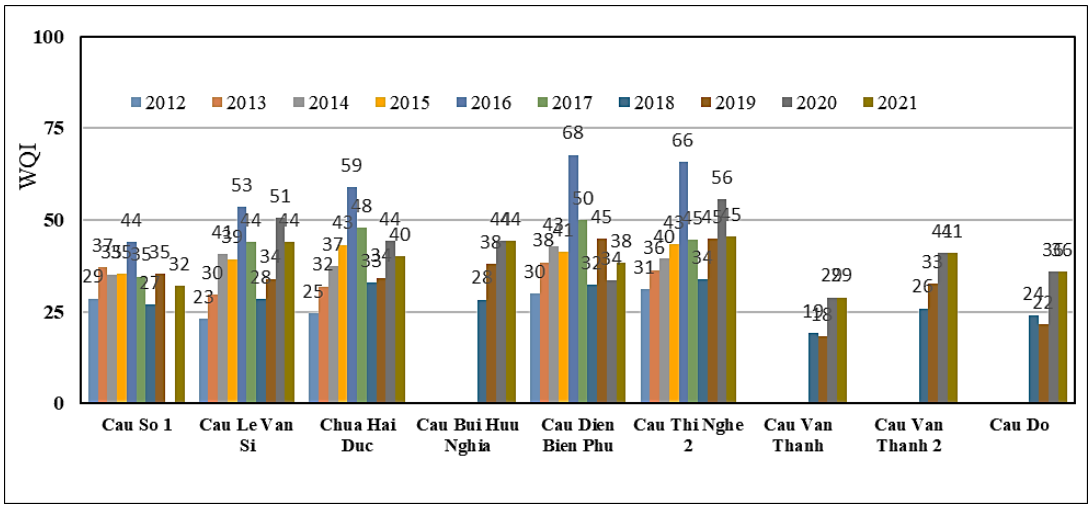

Figure 5. The water quality process on period 2012-2021 in NLTN canal

Plus, the measurement oxygen concentrations (DO) of water canal are very low in years. It means that the organic decomposing process is strongly affected in NLTN water canal lacked of oxygen. And, with the low oxygen concentration of flow, it affects adversely to the aquatic living situation and causes the pollution. the DO's concentrations were measured often below 2 mg/l and about less than 75% per all data set (See below figure 6).

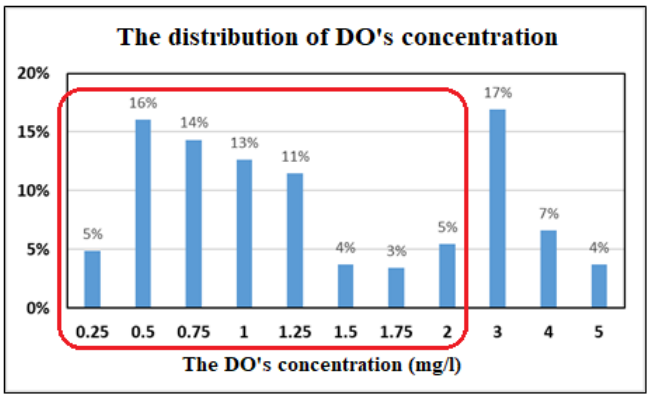

Figure 6. The distribution of DO's concentration per all water quality data set

The simulation of hydraulic regime in NLTN canal: MIKE 11 model is used to simulate the hydraulic regime on NLTN canal. The hydraulic components are determined as a discharge (m^3/s), velocity (m/s) and depth (m) on the high/low tidal periods and at each surveying point on NL-TN canal. The results are summarized in below Figure (Example for water level at Cau So 1 on NLTN canal).

Table 3. The average monthly values of hydraulic components at Cau So 1 of NLTN canal in 2019

Position	Month	Hydraulic components					
		Low tide			High tide		
		Q(m^3/s)	H (m)	U(m/s)	Q(m^3/s)	H (m)	U(m/s)
Cau So 1	01	0,81	1,75	0,264	0,79	2,77	0,262
	02	0,82	1,77	0,265	0,80	2,72	0,263
	03	0,92	1,77	0,276	0,82	2,70	0,265
	04	0,92	1,74	0,276	0,80	2,68	0,263
	05	0,86	1,68	0,270	0,77	2,63	0,259
	06	0,82	1,67	0,265	0,72	2,57	0,254
	07	0,78	1,67	0,260	0,72	2,54	0,253
	08	0,79	1,68	0,261	0,75	2,54	0,256
	09	0,86	1,70	0,270	0,78	2,61	0,260
	10	0,86	1,70	0,270	0,78	2,61	0,260
	11	0,79	1,68	0,261	0,75	2,54	0,256
	12	0,78	1,67	0,260	0,72	2,54	0,253

The assessment of self-cleaning capacity of NLTN canal water. See the interface tool to assess the self-cleaning capacity (Figure 4), all experiential formulas of oxygen declining and permeable coefficients (Table 1) used to compute are the functions of hydraulic components as velocity (U)

and depth (H) (Table 3). The assessment tool selects and uses the water quality components measured as DO, NH_4 and area of bottom channel into *Streeter-Phelpse equation* at considering time to detemine the BOD_5. After the trial and gradual computation by above assessment tool, the oxygen declining and permeable coefficients are determined by the condition of absolute different value between the computed and measured BOD_5 (values) about from 5% to 10% of the measurement value.

The computation results of above tool is summarized on below table with example at Cau So 1 position on NLTN canal.

Table 4. The value of BOD_5 and the oxygen coefficients (Example at CauSo1 position)

Position	Month	The concentration of Oxy, BOD_5; coefficient and self-cleaning capacity							
		T^OC	DObh	DO	BOD_5 (Measured)	BOD_5 (Simulated)	k_1	k_2	f
(1)	(2)	(3)	(4)	(5)	(6)	(7)	(8)	(9)	(10)
Cau So 1	01	29,8	7,5	0,5	7,7	8,2	0,256	0,371	*1,449*
	02	30,3	7,4	4,4	5,9	6,3	0,241	0,379	*1,576*
	03	30,2	7,4	2,3	7,1	7,6	0,240	0,390	*1,629*
	04	30,2	7,4	4,2	10,4	11,2	0,240	0,395	*1,648*
	05	32,1	7,1	3,8	11,7	12,7	0,261	0,421	*1,608*
	06	30,5	7,4	1,2	28,5	31,1	0,243	0,405	*1,668*
	07	29,4	7,5	1,1	12,0	13,0	0,250	0,394	*1,573*
	08	30,8	7,3	2,3	13,0	14,1	0,247	0,408	*1,655*
	09	31,4	7,2	3,0	11,5	12,4	0,253	0,412	*1,628*
	10	30,9	7,3	0,6	16,0	17,4	0,247	0,407	*1,648*
	11	30,1	7,4	1,8	11,0	11,9	0,239	0,401	*1,682*
	12	30,4	7,4	0,7	18,0	19,6	0,242	0,403	*1,667*
The average number of oxygen declining and permeable coefficients							***0,247***	***0,399***	***1,619***

The bottom row of above table means that the value of oxygen declining coefficient (k_1) is 0,247 and the oxygen permeable coefficient (k_2) is 0,399. The rate of two coefficients is 1,619 (it mean, in 2019, the level of self-cleaning capacity of NLTN canal water is weak level at Cau So 1 position).

The absolute different values between columns (6) and (7) are less than 10% of column (7) value. It means that the coefficients' values computed and formulas selected are reasonable and accepted. The values of oxygen coefficients and self-cleaning capacity of NLTN canal water on period 2012 – 2021 are summarized on below table.

Table 5. The values of k_1 , k_2 and f *at measurement positions and NLTN canal*

No	Position	k_1	k_2	f
1	Cau So 1	0,243	0,379	1,6
2	Cau Le Van Si	0,234	0,736	3,1
3	Chua Hai Duc	0,233	0,826	3,5
4	Cau Bui Huu Nghia	0,218	0,740	3,4

No	Position	k_1	k_2	f
5	Cau Dien Bien Phu	0,217	0,758	3,5
6	Cau Thi Nghe 2	0,192	0,556	2,9
7	Cau Van Thanh	0,197	0,612	3,1
8	Cau Van Thanh 2	0,205	0,725	3,5
9	Cau Do	0,193	0,568	2,9
10	NLTN canal	0,215	0,655	3,1

Table 5 shows that all measurement positions (exception the Cau So 1) and NLTN canal have the self-cleaning capacity of water at the normal level (it mean that their f – rate values are from 2 to 4). So that, the formulas of oxygen declining and permeable coefficients are selected such as:

- The oxygen declining coefficient k_1 is selected and inherited an relative research of Hydroscience (1971) such as:

$$k_1 = 0.15\ (H/2.45)^{-0.434}(\theta)^{(T-20)} \quad \text{when} \quad H < 2.45\text{m} \tag{4}$$

and $$k_1 = 0.15\ (\theta)^{(T-20)} \quad \text{when} \quad H \geq 2.45\text{m} \tag{5}$$

The element (θ) has a value according to the water temperature – T°C (Davis and Cornwell, 2008) such as:

$$\theta = 1.135\ (4<T<20) \tag{6}$$

$$\theta = 1.056\ (20<T<30) \tag{7}$$

$$\theta = 1.047\ (T>30) \tag{8}$$

- The oxygen permeable coefficient k_2 is selected and inherited an relative research of Langbein and Durum (1967) such as:

$$k_2 = 3{,}3\ U\ H^{1{,}33}\ (1{,}0241)^{(T-20°)} \tag{9}$$

- The nitrogenous declining coefficient k_3 is selected and inherited an relative research of Thomann, and Mueller (1987) such as:

$$k_3 = 0{,}025\ (1{,}0241)^{(T-20°)} \tag{10}$$

- The sediment oxygen demand *SOD* is selected and inherited an relative research of Wei-Bo Chen, Wen-Cheng Liu and Li-Ting Huang (2012) such as:

$$SOD = 0{,}015\ (1{,}065)^{(T-20°)} \tag{11}$$

The zoning of self-cleaning capacity level. With the self-cleaning capacity's results of table 5 are used to zone by MapInfo software with some GIS's layers at HCMC such as river-canal system, road-street system and administrative boundaries… The zoning map of self-cleaning capacity's levels of NLTN canal water is showed below figure 7.

Base on the methodologies and assessment results of self-cleaning capacity's levels of NLTN canal water, there are some summarizations such as:

- The research have inherited some results of the relative studies of international/national researchers. The research also have analyzed and selected the oxygen coefficients of the declining and permeable processes according to the water quality components as BOD_5, NH_4, bottom sediment/mud. They are applied into the *Streeter-Phelpse equation.*

- The research have applied directly the measurement water quality data into the *Streeter-Phelpse equation*. These water quality data sets are collected on the enough long period. It is very important for environmental management agencies when they can use directly their measurement

data of water quality to determine the level of self-cleaning water canal.

- The research have determined the reasonable and suitable formulas of oxygen declining and permeable coefficients for the hydraulic flow conditions. These formulas are the functions of the hydraulic flow's components such as velocity (m/s) and depth (m) surveyed or simulated by hydraulic models as MIKE 11.

- The zoning map of self-cleaning capacity's levels of NLTN canal water is reasonable when it shows that NLTN's branches and end of main channel have often weak self-cleaning capacity compared with main channel and channel outlets.

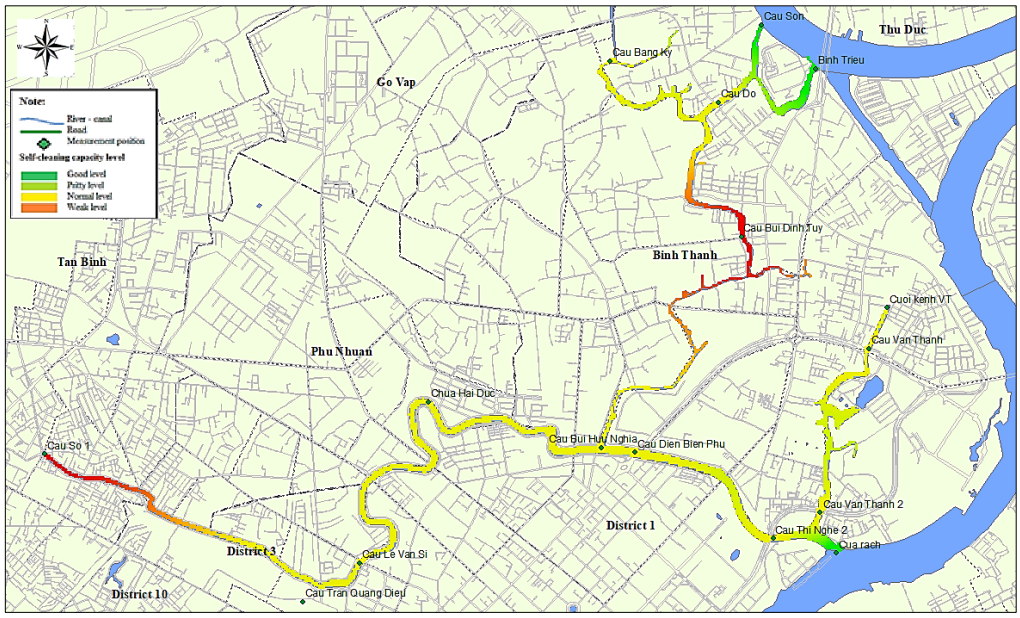

Figure 7. The zoning map of self-cleaning capacity's level on NLTN canal in 2012-2021

4. CONCLUSIONS

HCMC is in the rapid and hot urbanization period. Its socio-economic development and high population make a great pressure on the drainage infrastructure, especially wastewater collection and treatment. The adverse consequences are the quality of the environment, specifically the water quality of the inner urban canals, including NLTN canal, being get worse. Because, the NLTN canal basin is relatively closed, the level of self-cleaning capacity of the canal water fluctuates greatly with good levels at the outlets and weak levels in canal branches and dead-end canal.

The research inherited and selected suitable formulas to calculate the oxygen declining and permeable coefficients from related international/national studies for the NLTN canal. The research calculated and zoned the levels of self-cleaning capacity of NLTN canal water. Initially, the results show a reasonable level of self-cleaning capacity at the different areas of the canal.

Acknowledgements. The article is implemented with results from the research "Survey, assessment of water quality and self-cleaning capability, built an automatic water quality forecast system and proposed solutions for control of water quality management".

CRediT authorship contribution statement. Author 1: Methodology, Investigation, Funding acquisition. Author 2: Formal analysis.

Declaration of competing interest. We have no known competing financial interests or personal relationships that could have appeared to influence the work reported in this paper.

REFERENCES

1. Meybeck, M. (1996). River quality, Global ranges, time and space variabilities, proposal for some redefinitions. Verh. Internat. Verien. Limnol. 26 (in press).
2. Marcio R. S., Andrezza M. F., Carlos E. P. và Marcio A. R. S. (2014). Self-cleaning ability of the middle and lower courses of the uberaba river, UPGRH-GD8. Journal of Urban and Environmental Engineering , Vol. 8, No. 1 (2014), pp. 118-133.
3. Thanh L. M. (2015). Modeling the change of oxygen concentration in the aquatic environment under the influence of the bottom mud layer. Chemistry PhD. The Institute of Chemistry. Ministry of Education and Training of Vietnam.
4. Schiewer U. và Schernewski G. (2004). Self-purification capacity and management of Baltic coastal ecosystems. Journal of Coastal Conservation v.10, p. 25-32.
5. Mehrdadi N., Ghobadi M., Nasrabadi T. và Hoveidi H. (2006). Evaluation of the quality and self-purification potential of tajan river using qual2e model. Iranian Journal of Environmental Health Science & Engineering, Vol. 3, No. 3, pp. 199-204.
6. Churchill, M.A., H.L. Elmore, and R.A. Buckingham. 1962. The Prediction of Stream Reaeration Rates, ASCE, Journal Sanitary Engineering Division, Vol. No. 88, SA4, pp. 1-46.
7. Isaacs, W.P., and A.F. Gaudy, Jr. 1968. Atmospheric Oxygenation in a Simulated Stream, ASCE, J. Sanitary Engineering Division, Vol. 94, No. SA2, pp. 319-344.
8. Long B. T., Hieu N. D., Hien L. T. (2013). Determining the self-clean capacity of the canal and river system using the Saigon River as an example for research. Journal of Hydrometeorology February 2013 issue.
9. Bennett, J.P., and R.E. Rathbun. 1972. Reaeration. in Open-Channel Flow, U.S. Geological Survey Professional Paper 737.
10. Negulescu, M., và Rojanski, V., 1969, Recent research to determine reaeration coefficient: Water Research, v. 3, no. 3, p. 189-202.
11. Nuruzzaman Md., Al-Mamun A. và Salleh N. B. (2018). Experimenting biochemical oxygen demand decay rates of Malaysian river water in a laboratory flume. Environ. Eng. Res. 2018; 23(1). P.99-106.
12. O'Connor, D.J., and W.E. Dobbins. 1958. Mechanism of Reaeration in Natural Streams, ASCE Transactions, pp. 641-684, Paper No. 2934.
13. Owens, M., R.W. Edwards, and J.W. Gibbs. 1964. Some Reaeration Studies in Streams, Int. J. Air Wat. Poll., Vol. 8, pp. 469-486.
14. Thomas V. B., John A. M., Marc G. v. C. và Mani V. D. (2009). A Simple Field Technique For Accurate Reaeration Estimates in Aquatic Systems. Lake and Reservoir Management, 15:3, 185-199, DOI: 10.1080/07438149909354116
15. Tu N. T. T., Sy P. C. và Thang D. X. (2012). Study on self-cleaning capacity in CUDE river water environment. Journal of Hydrometeorology, September issue, 2012, p. 23-28.
16. Wei-Bo Chen, Wen-Cheng Liu & Li-Ting Huang, Measurement of sediment oxygen demand for modeling the dissolved oxygen distribution in a Subalpine lake, International Journal of Physical Sciences, 2012, 7 (27), 5036-5048.
17. Wright, R.M. and A.J. McDonnell. 1979. In-Stream Deoxygenation Rate Prediction. ASCE Jour. Env. Eng. 105:323-335.

18. Davis M.L., Cornwell D.A., (2008). Introduction to Environmental Engineering, 4th edition, 2008, McGraw – Hill, ISBN 978 – 0 – 07 – 242411 – 9.

19. Hydroscience, Inc., 1971. Simplified Mathematical Modeling of Water Quality, EPA-Water Programs.

20. Langbein, W.B., arid W.H. Durum. 1967. The Aeration Capacity of Streams. U. S. Geological Survey Circular S42.

21. Thomann R. V. và Mueller J. A., (1987), Principles of Surface Water Quality Modeling and Control, Harper International Edition, New York.

22. Trinh L., Hung N. Q. (2004). Environment in Dong Nai - Sai Gon River Basin, NXB KHKT, 2004.

23. Schroepfer, g. J.; rosins m. L.; susag, r. H. The research program on the Mississipi River in the vicinity of Minneapolis and St. Paul. Air and Water Polluttion International Journal, Dordrecht, v.7, p.373-391, 1964.

24. Krenkel, P. A., 1960, Turbulent diffusion and the kinetics of oxygen absorption: Berkeley, Calif., Univ. of California Dept. Sanitary Eng. Ph. D. dissert.

APPLICATION OF SEASONAL AUTOREGRESSIVE INTEGRATED MOVING AVERAGE MODEL IN FORECASTING THE SALINITY OF BANG PAKONG RIVER, THAILAND

Min Thura Mon,[1] Ratchanon Piemjaiswang,[2] Suthirat Kittipongvises,[2*]

[1]Graduate Student, International Program in Hazardous Substances and Environmental Management (IP-HSM), Graduate School, Chulalongkorn University, Bangkok, 10330, Thailand
[2] Environmental Research Institute, Chulalongkorn University, Bangkok, 10330, Thailand
*e-mail: suthirat.k@chula.ac.th

Abstract:
The Bang Pakong River (BPK) has annual salinity problem. The river is an important source of freshwater supply in the Eastern Economic Corridor (EEC) of Thailand, which has agricultural and industrial activities. Salinity is an essential parameter in the freshwater quality for irrigation purposes. Although there have been many applications of the Time Series Model in several research areas, the research approach to the salinity problem by using the Time Series Analysis—Seasonal Auto-regressive Integrated Moving Average (SARIMA) Model—in the BPK area is scarce. This research aimed to forecast the future concentration of salinity along the BPK river by using the SARIMA method for a better understanding of the salinity issue. The forecasted results show that the lower part of the BPK river has higher salinity values in both February-May and August-November periods, compared to the upper part. Moreover, it is forecasted that the salinity of the BPK river will have a seasonal pattern during the predicted time frame. This research also points out the future research opportunity on salinity forecasting using the combination of SARIMA and Machine Learning algorithms with other management approaches. Interlinkages between hydro-meteorological factors and anthropogenic factors affecting salinity distribution in different seasons should be further investigated.

Keywords: Time Series Analysis, SARIMA, Salinity, Bang Pakong River

Introduction:

Salinity has emerged as one of the most significant problems facing the Bang Pakong River (BPK) in Thailand. Geographically, the mouth of the BPK river is located on the Gulf of Thailand, indicating the potential inflow of saltwater into the river through the estuary. The BPK River is an important water source for residential, agricultural, and industrial activities in the Eastern Economic Corridor (EEC) of Thailand [1]. Salinity intrusion is also a widespread environmental problem that threatens the supply of fresh water in coastal areas, especially in Southeast Asia [2]. As a public health concern, drinking water salinity can be associated with hypertension, cardiovascular diseases, diarrhea, and also abdominal pain. Salinity exposure has also a long-term cancer risk because of chronic exposure to chlorinated water. This cancer risk is due the trihalomethanes (THM) and other disinfectants by-products, which are carcinogenic chemicals [3].

This condition leads to the need of predicting future salinity concentrations, in order to efficiently manage the salinity problem thereby preventing potential loss in agricultural

production. Among the forecasting methods, Time Series Analysis is the most common one, especially the Autoregressive Integrated Moving Average (ARIMA) model, one of the most popular linear models in time series forecasting during the past three decades [4]. Moreover, the Seasonal Autoregressive Integrated Moving Average (SARIMA) model is a variation of the ARIMA model for the seasonality nature of time series data. The popularity of the ARIMA model is due to its statistical properties as well as the well-known Box–Jenkins methodology in the model-building process [5]. In addition, various exponential smoothing models can be implemented by ARIMA models [6]. Although ARIMA models are quite flexible in that they can represent several different types of time series, i.e., pure autoregressive (AR), pure moving average (MA), and combined AR and MA (ARMA) series, their major limitation is the pre-assumed linear form of the model. That is, a linear correlation structure is assumed among the time series values, and therefore, no nonlinear patterns can be captured by the ARIMA model [4].

A wide range of ARIMA and SARIMA model applications can be observed from Energy Economics, Environmental Science and Management, Tourism to Climate, and Meteorology. Regarding the ARIMA and SARIMA model applications, Ediger and Akar (2007) used the Autoregressive Integrated Moving Average (ARIMA) and seasonal ARIMA (SARIMA) methods to estimate the future primary energy demand of Turkey from 2005 to 2020 [7]. Moreover, Mishra and Desai (2005) applied ARIMA and multiplicative SARIMA models to forecast droughts in the Kansabati river basin in India [8]. In addition, Al Shehhi and Kaya (2021) evaluated the performance of stochastic time series models: Seasonal Auto-regressive Integrated Moving Average (SARIMA) and nonlinear neural network (NN) to predict surface chlorophyll-α and sea surface temperature (SST) in coastal areas [9]. Moreover, Kbaier Ben Ismail, Lazure, and Puillat, (2016) observed the statistical properties and time-frequency analysis of temperature, salinity, and turbidity in the coastal waters of Boulogne-Sur-Mer, France [10].

However, in the case of the BPK river, there is a scarcity of literature on the application of the Time Series Model for assessing the concentration of salinity in freshwater. This research aims to employ the Time Series method (SARIMA) to forecast the future concentration of salinity for a better understanding of the salinity issue in the BPK River.

Methodology:

Study Area: The case study area is formed by the main Bang Pakong River (Fig. 1) that flows through Chachoengsao, Chonburi, Prachinburi, and Nakhon Nayok Provinces, with a total length of 122 km and an elevation range of 0 – 20 m above the sea level [1]. The BPK basin is characterized by rapid industrialization and facing one of the most pressing water problems in Thailand. In fact, the demand for water has already eclipsed its storage capacity. The water resources-related problems in the basin are in fact more developed making its situation relatively worse than the country's other basins [1].

Data Collection: The salinity time series data in terms of electrical conductivity (EC) in µS/cm unit from a total of 11 sampling stations along the river is applied in this research (Fig. 1). The data is collected quarterly in February, May, August, and November from 2010 to 2019 by the Pollution Control Department, Thailand.

SARIMA Model: In an autoregressive integrated moving average model, the future value of a variable is assumed to be a linear function of several past observations and random errors. That is, the underlying process that generates the time series has the form (in Eq.1):

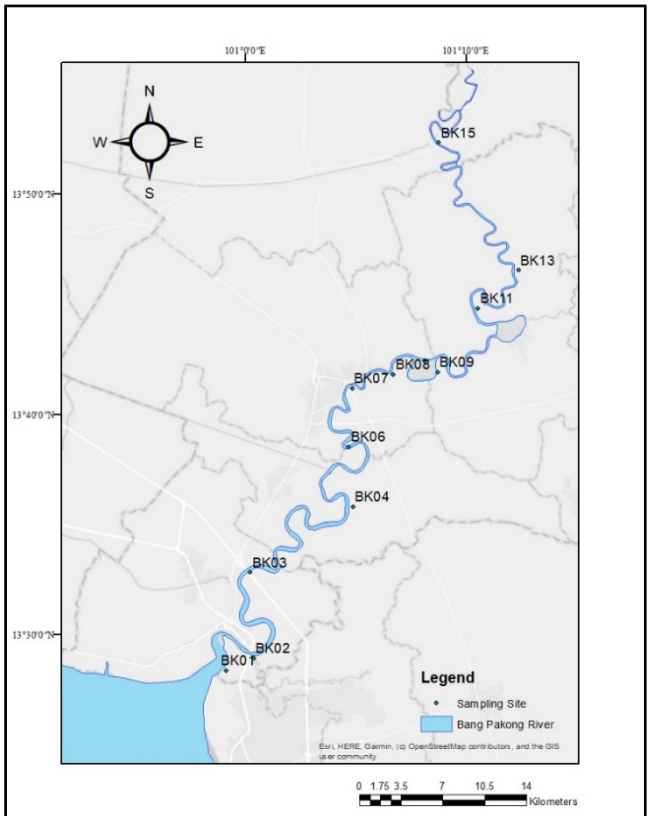

Figure 1. Location and sampling sites of Bang Pakong River

$$y_t = \theta_0 + \phi_1 y_{t-1} + \phi_2 y_{t-2} + \cdots + \phi_p y_{t-p} + \varepsilon_t - \theta_1 \varepsilon_{t-1} - \theta_2 \varepsilon_{t-2} - \cdots - \theta_q \varepsilon_{t-q}, \quad (1)$$

where y_t and ε_t are the actual value and random error at time period t, respectively; ϕ_i (i = 1; 2; : : : ; p) and θ_j (j = 0; 1; 2; : : : ; q) are model parameters. p and q are integers and often referred to as orders of the model. Random errors, ε_t, are assumed to be independently and identically distributed with a mean of zero and a constant variance of σ^2. Eq. (1) entails several important special cases of the ARIMA family of models. If $q = 0$, then 1 becomes an AR model of order p. When $p = 0$, the model reduces to an MA model of order q. One central task of the ARIMA model building is to determine the appropriate model order (p; q). Since the SARIM is a seasonal extension of ARIMA, thus, the formula of SARIMA can be simplified as the following (in Eq.2):

$$SARIMA(p,d,q)(P,D,Q)m \quad (2)$$

in which the non-seasonal part of the model is p: Trend autoregression order, d: Trend difference order, and q: Trend moving average order, meanwhile the seasonal part is P: Seasonal autoregressive order. D: Seasonal difference order, Q: Seasonal moving average order, and m: The number of time steps for a single seasonal period [12].

Model Development: There are three steps in developing the SARIMA model for the salinity forecasting of the BPK River. This study focuses on EC values of a total of 11 stations. This

study also uses the R software for the whole model processing. The following three stages are different steps of the salinity model: (a) Pre-model development, (b) Model development and selection, and (c) Forecasting future salinity (EC) value. The framework for the model development is shown in (Fig. 2).

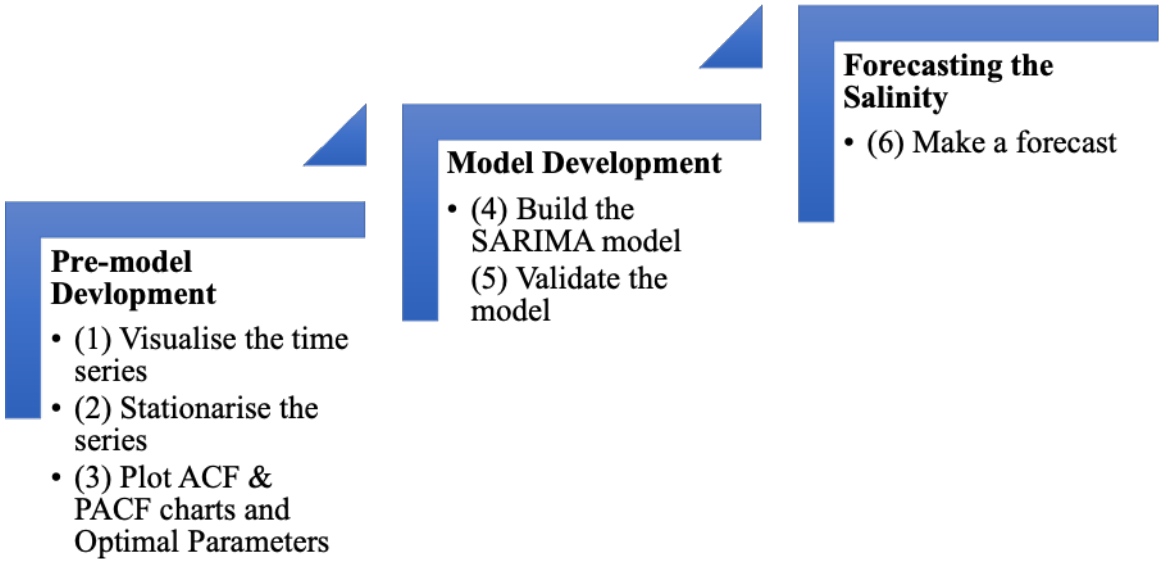

Figure 2. Framework for the SARIMA modeling processes.

Results and Discussion:

Firstly, quarterly EC time series data (2010-2019) is divided into testing and training; training is from 2010 to 2017 while testing is from 2018 to 2019 respectively. Each EC time series data from 11 stations are plotted, and possible outliers are searched using the 'ts' function in R. Plus, the normal distribution of the data is checked to represent real-valued random variables whose distributions are not known. After the screening of the data, the variance of the time series data is stabilized by the Box-Cox transformation, and the nature of the trend, in this case, the seasonality of the data is observed. In order to execute the time series analysis, the conversion of non-stationary to stationary is done through seasonal and regular differencing. The assumption for the Augmented Dickey-Fuller Test (ACF) on the original time series is as the following: the EC series is non-stationary (H0) while the EC series is stationary (H1), in which the p-value of the ADF result is greater than 0.05, it fails to reject the H0; so, the EC series is non-stationary. However, in this study, the values of ACF tests are less than the p-value of 0.05 where secondary differencing is not necessary.

Different SARIMA models are generated for different stations as the salinity values vary from one station to another, except for the stations: BPK-04, BPK-06, BPK-07, BPK-08, and BPK-09 which share the same model due to their geographical locations within the mid-stream part. However, in this paper, the results of stations: BPK-01, BPK-06, BPK-07, and BPK-11 are selected to represent the geographical distribution of stations—upstream station: BPK-11, mid-stream stations: BPK-06 and BPK-07, and downstream station: BPK-01—along the river. From Total Correlation Chart: Auto-correlation Function (ACF) and Partial Correlation Function (PACF) plots (Fig.3-6), all four stations fit well with non-seasonal part of the model (p,d, and q) equals to 0 suggesting that the salinity value is associated with seasonal pattern. All the values in the ACF and PACF plot fall within the 95% confidence band (Blue-dotted line). Detailed statistics of each selected station and their representative

model with the Akaike information criterion (AIC), the Bayesian information criterion (BIC), and the p-value of the Ljung-Box Test can be observed in Table.1.

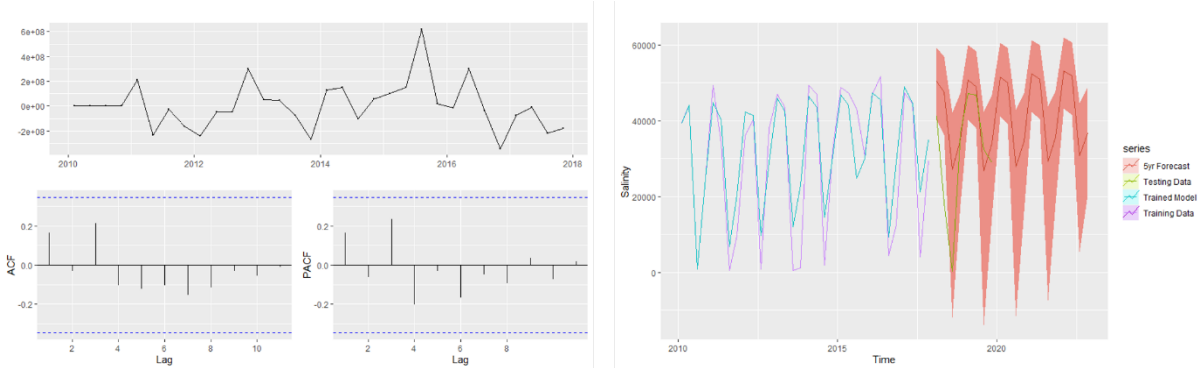

Figure 3. 3 ARIMA (0,0,0)(1,1,2)[4] of BPK-01 (left) and EC time series plot with 5-year forecasted values and testing data using the same model (right).

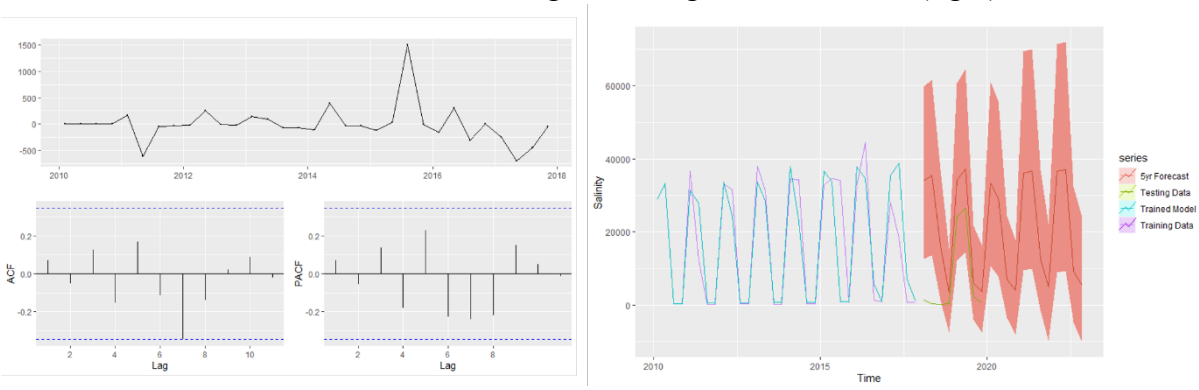

Figure 4. ACF and PACF plots of ARIMA (0,0,0)(2,1,0)[4] of BPK-06 (left) and EC time series plot with 5-year forecasted values and testing data using the same model (right).

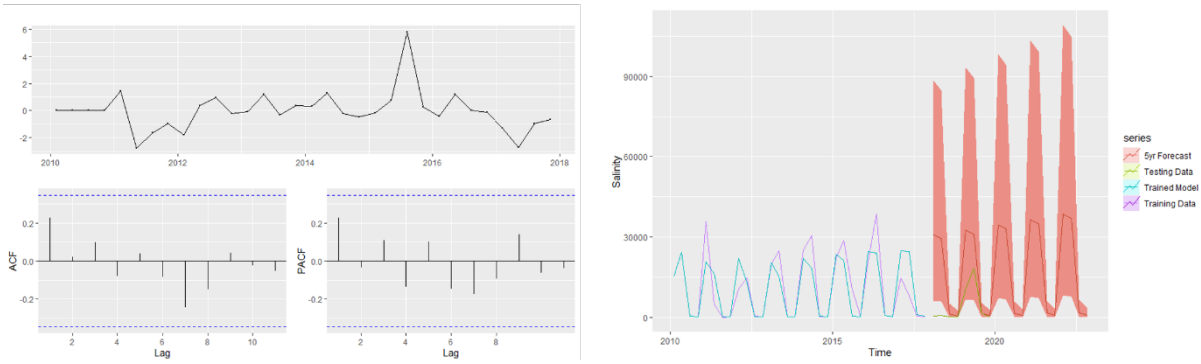

Figure 5. ACF and PACF plots of ARIMA (0,0,0)(2,1,0)[4] of BPK-07 (left) and EC time series plot with 5-year forecasted values and testing data using the same model (right).

The results of the 5-year forecasted values (from 2018-2022) are close enough to the actual salinity value, identified by the testing data from 2018-2019. The comparison of forecasted and actual salinity values can be observed together with the range of upper and lower 95 % confidence intervals in Table.2. Based on the forecasted result, the salinity of the BPK river has a similar pattern every year, high salinity is observed especially during quarters of February and May. These results are consistent with Yuenyong et al. [13] revealed that high

salinity in the BPK River was reported at the river mouth, especially in the dry season. This highlights the need to prepare salinity intrusion counter-measurement such as Watergate operation.

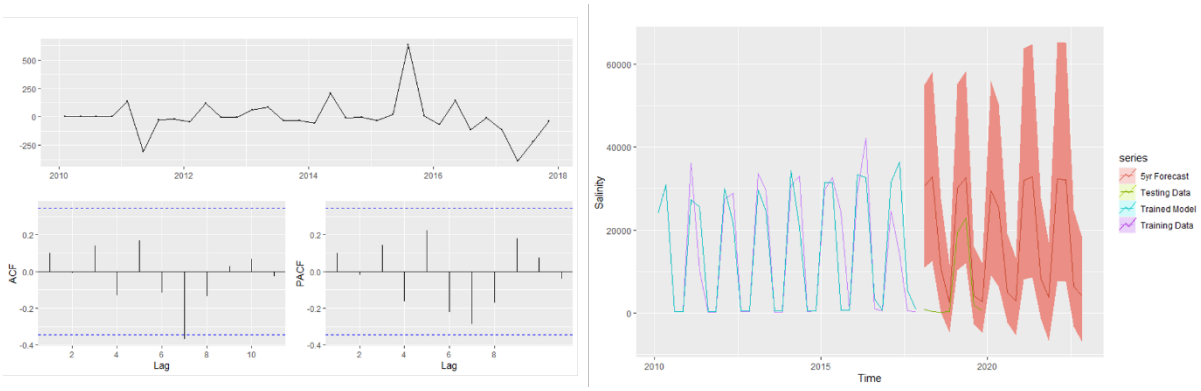

Figure 6. ACF and PACF plots of ARIMA (0,0,0) (0,1,1)[4] of BPK-11 (left) and EC time series plot with 5-year forecasted values and testing data using the same model (right).

Table 1. Statistics of each selected station along the BPK River

Station No	**SARIMA Model** *(p,d,q)(P,D,Q)(m)*	**AIC**	**BIC**	**Ljung-Box Test** *p-value*
BPK-01	(0,0,0)(1,1,2)[4]	1176.66	1183.32	0.1564
BPK-06	(0,0,0)(2,1,0)[4]	421.36	425.36	0.4836
BPK-07	(0,0,0)(2,1,0)[4]	377.93	381.93	0.4768
BPK-11	(0,0,0)(0,1,1)[4]	117.96	120.63	0.6472

Table 2. Actual vs forecasted salinity value of selected stations

Station No	**Year**	**Forecasted Value (µS/cm)**	**Actual Value (µS/cm)**	**Confidence Interval (95%)**	
				Lower	***Upper***
BPK-01	2019 Feb	50795.96	47200.00	40220.87	59927.47
	2019 May	48923.93	46700.00	37853.49	58364.93
	2019 Aug	26727.50	32400.00	-13942.35	42179.11
	2019 Nov	33885.54	28900.00	14618.24	46767.61
BPK-06	2019 Feb	34184.13	24200.00	12134.52	60722.38
	2019 May	37259.46	26600.00	14386.48	64475.08
	2019 Aug	5948.15	2240.00	-3907.01	21759.33
	2019 Nov	3767.99	634.00	-7450.56	16447.81
BPK-07	2019 Feb	30124.77	19480.00	10339.99	55132.52
	2019 May	32567.11	22900.00	11984.18	58283.62
	2019 Aug	4114.99	1965.00	-2471.72	16141.50
	2019 Nov	2731.63	615.00	-4810.33	12088.20
BPK-11	2019 Feb	32675.42	10590.00	6786.25	93170.08
	2019 May	31226.93	18340.00	6434.55	89360.01
	2019 Aug	1493.37	1481.00	161.63	5565.22
	2019 Nov	739.49	391.00	66.33	2949.94

Discussion and Limitations

(1) Identification of contributing factors: As this study aimed to explore salinity hotspots and forecast the future salinity trend along the BPK river both the upper and lower parts by employing the SARIMA method. However, it should be pointed out that there are many contributing factors affecting salinity distribution in the BPK in different seasons. Therefore, direct and indirect connections between the hydro-meteorological factors (i.e., run-off, precipitation, sea intrusion, dilution effect, etc.) and anthropogenic factors (i.e., the watergate operation, land-use, and river/coastal management) should be further and deeper investigated. For instance, Urat and Kanasut [14] applied a hydrodynamic MIKE 11 model for salinity intrusion analysis in the BPK river by considering the effects of run-off and the watergate management on salinity pollution.

(2) Prediction Uncertainty: Even though the SARIMA model can be used to predict salinity to a certain degree, it is learned that applying only the SARIMA can lead to uncertainty. As time series models are dependent on historical data, a longer duration of data can generate a better result. In addition, other influencing factors on salinity such as hydrological parameters, precipitation, and sea level rise should also be taken into account. Nowadays, there are also increasing applications of Machine Learning algorithms such as Artificial Neural Networks (ANN) can also provide future predictions, similar to the SARIMA.

Conclusion:

Time series analysis and forecasting are applicable to forecasting the salinity concentration of the BPK river. As salinity is an important water quality factor that has an impact on human health, agriculture and irrigation sectors, with the given geographically and economically important location, the salinity problem of BPK River in the EEC area should not be taken lightly. In addition, this research provides further research opportunities such as the integration of SARIMA and other forecasting methods such as ANN can lead to better prediction results. Both effects of all contributing factors and forecast uncertainty should be deeply investigated.

Acknowledgments:

The authors would like to thank the International Program on Hazardous Substances and Environmental Management (IP-HSM), Graduate School of Chulalongkorn University for the ASEAN and Non-ASEAN Scholarship program and research funding. In addition, the authors do acknowledge all contributors in terms of data, and suggestions for this paper.

References:

1. Chaiyarak B, Tattiyakul G, Karnsunthad N. Climate Change Vulnerability Assessment Bang Pakong River Wetland, Thailand. 2019;76.
2. Himi M, Tapias J, Benabdelouahab S, Salhi A, Rivero L, Elgettafi M, et al. Geophysical characterization of saltwater intrusion in a coastal aquifer: The case of Martil-Alila plain (North Morocco). Journal of African Earth Sciences. 2017;126:136–47.
3. Johnson J, Jensen. J. THM (TRIHALOMETHANES) and TOX (TOTAL ORGANIC HALOGEN) Formation: Routes, Rates, and Precursors. Washington, D.C.; 1986.

4. Zhang PG. Time series forecasting using a hybrid ARIMA and neural network model. Neurocomputing. 2003;50:159–75.
5. Box GEP, Jenkins G. Time Series Analysis, Forecasting and Control. San Francisco, CA: Holden-Day; 1970.
6. McKenzie E. General exponential smoothing and the equivalent arma process. J Forecast. 1984;3(3).
7. Ediger VŞ, Akar S. ARIMA forecasting of primary energy demand by fuel in Turkey. Energy Policy. 2007;35(3).
8. Mishra AK, Desai VR. Drought forecasting using stochastic models. Stochastic Environmental Research and Risk Assessment. 2005;19(5).
9. al Shehhi MR, Kaya A. Time series and neural network to forecast water quality parameters using satellite data. Cont Shelf Res [Internet]. 2021;231(July 2020):104612. Available from: https://doi.org/10.1016/j.csr.2021.104612
10. Kbaier Ben Ismail D, Lazure P, Puillat I. Statistical properties and time-frequency analysis of temperature, salinity and turbidity measured by the MAREL Carnot station in the coastal waters of Boulogne-sur-Mer (France). Journal of Marine Systems [Internet]. 2016;162:137–53. Available from: http://dx.doi.org/10.1016/j.jmarsys.2016.03.010
11. Okwala T, Shrestha S, Ghimire S, Mohanasundaram S, Datta A. Assessment of climate change impacts on water balance and hydrological extremes in Bang Pakong-Prachin Buri river basin, Thailand. Environ Res [Internet]. 2020;186(February):109544. Available from: https://doi.org/10.1016/j.envres.2020.109544
12. Cowpertwait PSP, Metacalfe A v. Introductory Time Series with R. 2009th ed. Springer; 2009.
13. Yuenyong, S. , Nimsuwan, N., Buranapratheprat, A., Gunboa, V., Jintasaeranee, P., Thaipichitburapa, P., and Suriyaphan, J. Water quality of the Bangpakong River during 2016 – 2018. Burapha Science Journal. 24(1)
14. Urat W, Kanasut J. Salinity intrusion analysis in Bangpakong River by Mathematical Model MIKE 11. The 13th Thai National Committee on Irrigation and Drainage (Thai CID) National Symposium, 2020

MODIFICATION OF CHARCOAL KILN VERTICAL TYPE FOR CHARCOAL PRODUCTION FROM BAMBOO WASTE

Kanatip Kumproa*, Rangsan Koodsamrong, Chaiyasit Kaewcharoon, Narumon Bunkrachang

Division of Agricultural Engineering and Technology, Faculty of Agriculture and Natural Resources, Rajamangala University of Technology Tawan-ok, Chonburi, Thailand

*e-mail: kenkanatip@gmail.com

Abstract:

The objective of the research aims to study the temperature profile of the vertical single wall kiln (V.S.K.) and double wall kiln (V.D.K.) covered with fiberglass as an insulator. Additionally, the research purposes to evaluate the bamboo waste as a raw material and to investigate the charcoal characteristic and charcoal yield with different design of kiln. The temperature profile for the kiln were collected by using thermocouples type K. The raw material and charcoal were determinded by proximate analysis, higher heating value (HHV) and heat utilization efficiency (HU). The results revealed that the maximum temperature of the V.S.K. and V.D.K. were occurred at the reactor (511.33ºC) and inner reactor (550.00ºC), respectively. It indicated that the vertical kiln covered with fiberglass as an insulator can be prevented heat loss. Furthermore, the charcoal from V.D.K. was highest fixed carbon content (68.63%), HHV (27.57 MJ/kg), charcoal yield (42.73%) and HU (18.08%), indicating that the carbonized kiln design and carbonization temperature affected proximate results, higher heating value, charcoal yield and heat utilization efficiency.

Keywords: Vertical kiln, Bamboo, Charcoal, Pyrolysis, Carbonization

Introduction:

Biomass is one of the main players in renewable resources of energy as it is made from agricultural wastes and waste from food processing, which are plentiful around 80 million tons per year due to Thailand's large agricultural industry [1-3]. It defines as hydrocarbon that consistes of carbon, hydrogen, oxygen and nitrogen with sulfur in less percentage [4]. Biomass conversion into valuable hydrocarbons could be achieved by three processes; biochemical, thermochemical and biological processes. Thermochemical process is the process that convert biomass into charcoal, bio-oil and non-condensable gas through gasification, liquefaction, combustion and pyrolysis. Among these processes, slow pyrolysis is aimed to produce charcoal as a main product [4-5].

Charcoal is an important renewable energy source for developing countries. It is the process of converting an organic substance into carbon or carbon-containing residues in the manufacture of carbonated charcoal. Charcoal is accomplished by burning the material to be charred to remove water content and other materials that are not needed by charcoal, such as hydrogen and oxygen or evaporating material [6-8]. Most people have used charcoal as the primary source of energy because charcoal allows convenient storage, is cheap, provides cleaner combustion and has higher heating value (HHV) than wood. Dry charcoal has a HHV of 31-33 MJ/kg compared to 15 MJ/kg for raw wood [9].

In Thailand, charcoal production can be divided into industrial scale and small scale. Brick kilns and metal kilns are produced charcoal at the industrial scale. Additionally, drum kilns and mound kilns are generally used for small scale in rural areas. It provides basic energy requirement for cooking and process heating in residential. Even though they are easy to construct and inexpensive, their thermal efficiency is very low for charcoal production [6].

Many carbonization kilns have been designed based on research to obtain higher efficiency of charcoal production and characteristic [9-16]. Jaisumroum, 2015 [10] studied on different types of charcoal kiln, including vertical kiln, horizontal kiln and mound kiln. The results revealed that the vertical kiln obtained the highest charcoal yield with faster time duration. Sinsaard, 2017 [11] focused on the development in the efficiency of producing charcoal from coconut shell by using drum kiln and mound kiln. The drum kiln shown the more efficient than mound kiln in terms of maximum temperature and heat utilization efficiency with faster heat duration. Homchat and Sucharitakul, 2011 [12] developed the pyrolysis of cassava rhizome by using a metal kiln with utilizing flue gas. In the experiment, the highest temperature of the pyrolysis process was 500ºC and the charcoal yield was 30.73%. Soka and Oyekola, 2020 [13] produced charcoal from corn stover by using the bench scale of slow pyrolysis process. They found the carbonized kiln design, carbonization process and process temperature had the most important factor on char HHV and yield. The HHV and yield of the charcoal were 26.25 MJ/kg and 34.50%, respectively with 453ºC for optimal condition. Sangsuk *et al*., 2018 [14] combined a heat distribution pipe into metal kiln covered with fiberglass and galvanized steel as an insulator for producing bamboo charcoal. The kiln was taken 27 h to reach 600ºC and the mass yield and HHV of the bamboo charcoal were 24% and 30.35 MJ/kg, respectively. Chandrasekaran *et al*., 2019 [15] developed a natural draft-improved charcoal retort system to produced charcoal. This system was made of mild steel with 3 mm thickness. The optimum temperature of the retort was 500ºC. The mass yield and HHV of charcoal was 29.60% and 30.8 MJ/kg, respectively. Sangsuk *et al*., 2020 [9] applied a heat distribution pipe to 200 l drum kiln for charcoal production from tamarind wood. Moreover, The drum was coated with fiberglass and galvanized steel as insulation. The process took 8 h to reach maximum temperature (430ºC) and obtained the tamarind wood charcoal. the mass yield and HHV of the product were 28% and 30 MJ/kg, respectively. Moreover, Laorach *et al*., 2021 [16] studied on the characteristics of wood charcoals burned using three burning process, including clay kiln, cement kiln and the metal kiln. The studied results shown that the carbon content (90.11%) and heating value (31.90 MJ/kg) of charcoal sample burned by the metal kiln process were the highest as compared to the charcoals obtained from two burning processes.

Therefore, this research focuses on the modification of charcoal kiln vertical type in terms of carbonized kiln design and carbonization process to obtain higher efficiency of charcoal production and characteristic. The bamboo waste from Nongmon market, Chonburi Province were used to produce charcoal. The carbonization temperature of kiln components were collected.Furthermore, the charcoal were characterized by the procedure of proximate analysis, heating value and heat utilization efficiency.

Methodology:

Material

Bamboo waste was collected from Nongmon market, Chonburi Province, Thailand. The biomass was dried at 103ºC for 24 h. Then, the sample was kept in the plastic zip lock bags until it was used.

Kiln system and charcoal production

The schematic diagrams of a vertical single wall kiln (V.S.K.) and a vertical double wall kiln (V.D.K.) are shown in Figure 1 and 2, respectively. The first one was made of 200 l of drum as a reactor with 30 cm of flue on the top of reactor for releasing gas. The bottom of the reactor is combustion chamber with 20 cm width and 25 cm length. The three thermocouples type K were located at the top, middle and bottom of the kiln to measure the carbonization temperature inside the flue, reactor and combustion chamber. In addition, the second one consists of 53 l of inner reactor that was made of metal sheet with 5 mm thickness, 200 l of drum as a outer reactor with 30 cm of flue on the top of reactor and combustion chamber with 20 cm width and 25 cm length in the bottom of the kiln. The inner reactor was covered with fiberglass (10 cm thickness) as an insulator. The four thermocouples type K were located at the flue, inner reactor, outer reactor and combustion chamber to measure the carbonization temperature.

The charcoal (Figure 3) was produced from dried bamboo waste by pyrolysis process for 120 min. The raw material was filled in the reactor in the V.S.K case and was filled in the inner reactor in the V.D.K. case. The fuel was ignited in the combustion chamber and the bamboo waste was carbonized to charcoal.

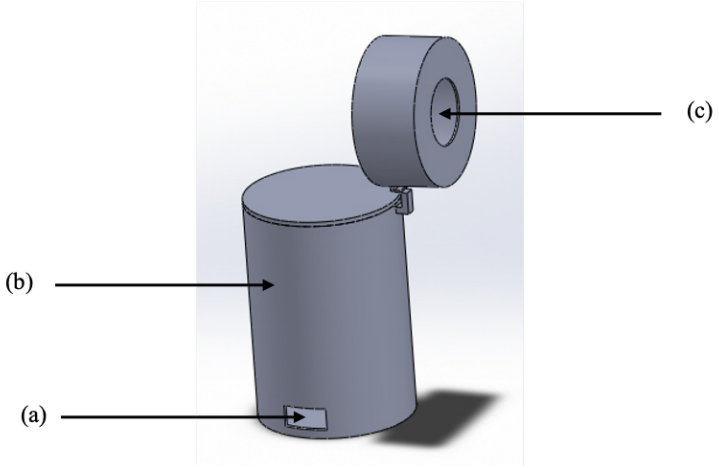

Figure 1. Schematic diagram of the vertical single wall kiln (V.S.K.); (a) combustion chamber, (b) reactor and (c) flue.

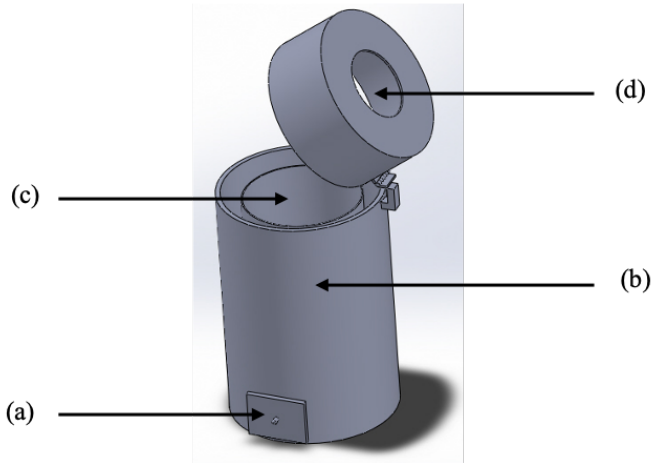

Figure 2. Schematic diagram of the vertical double wall kiln (V.D.K.); (a) combustion chamber, (b) outer reactor, (c) inner reactor and (d) flue.

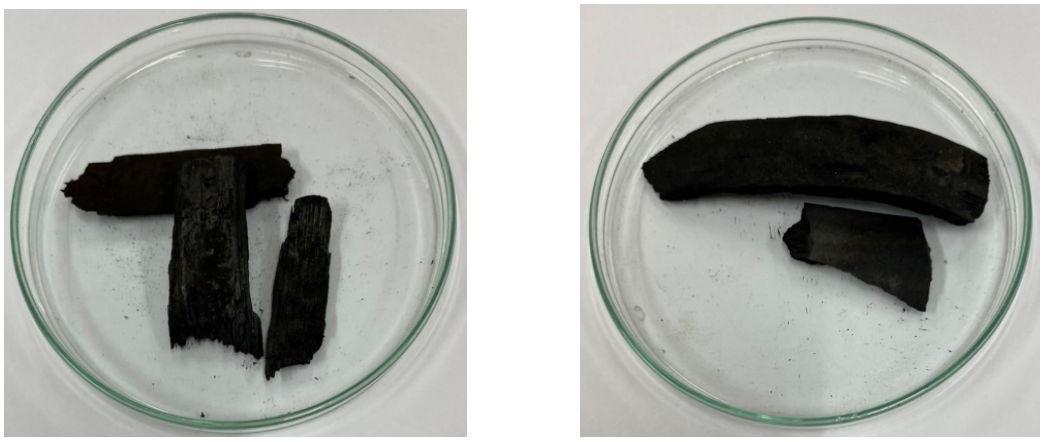

(a) (b)

Figure 3. Charcoal products; (a) bamboo charcoal in the V.S.K. and (b) bamboo charcoal in the V.D.K.

Proximate analysis and higher heating value

The percentage of the moisture, ash and volatile matter in bamboo waste and bamboo charcoal were analyzed by the major standards institutions, including, ASTM D3173, D3174 and D3175 [17].

Moisture content was analyzed based on ASTM D3173. Milled samples (3 g) in crucibles were dried at 110ºC for 2 h in an oven. The crucibles with samples were then cooled in a desiccator and weighted. The percentage of moisture content was calculated as percentage weight loss moisture content.

Ash content was analyzed based on ASTM D3174. Milled samples (3 g) in crucibles were heated in furnace at 500ºC for 1 h. Then, milled samples were heated at 750ºC for 2 h. The crucibles with samples were cooled in a desiccator and weighted. The percentage ash content was calculated.

Volatile matter was analyzed based on ASTM D3175. Milled samples (3 g) in crucibles were heated in furnace at 925ºC for 7 min and then cooled in a desiccator. The crucicles with samples were weighted as the percentage weight loss volatile matter.

Fixed carbon and higher heating value (HHV) were calculated based on Demirbas's equation [18]. The Demirbas's equation is shown in equation (1) and (2) respectively.

$$\% \text{ fixed carbon} = 100 - (\%\text{Moisture} + \%\text{Ash} + \%\text{Volatile matter}) \quad (1)$$

$$\text{Higher heating value} = (0.196 \times \%\text{fixed carbon}) + 14.119 \quad (2)$$

Carbon balance for the charcoal production

The carbon balance for the charcoal production by using both V.S.K. and V.D.K. can be calculated in equation (3) [19-20], where wood (W) is mass of raw material, charcoal (C) is charcoal yield, brands (B) mean partly carbonized wood product remaining in the reactor, condensable liquids (CL) mean liquid yield of pyrolysis, ash (A) is ash content from product remaining in the reactor. TNMOC is total nonmethane organic compounds, TSP is total suspended particulates. In addition, CO_2, CO and CH_4 are greenhouse gases.

$$W = C + B + CL + A + CO_2 + CO + CH_4 + TNMOC + TSP \quad (3)$$

Heat utilization efficiency

The heat utilization efficiency (HU) of the charcoal were calculated with standard water boiling test. The HU was evaluated in equation (4) [21], where M_w, C_p, T_b, T_0, M_c, L, M_f and H_f are mass of water (kg), specific heat of water (kJ/kg.^{o}C), boiling temperature of water (^{o}C), initial temperature of water (^{o}C), mass of water evaporated (kg), latent heat of evaporated (kcal/kg), mass of charcoal briquette burnt (kg) and heating value of charcoal briquette (kJ/kg) respectively.

$$HU = [M_wC_p(T_b - T_0) + M_cL]/M_fH_f \times 100 \quad (4)$$

Results and Discussion:

Temperature profile

The temperature profiles for bamboo pyrolysis in the V.S.K. and V.D.K. by reaction time are shown in Figure 4 and 5, respectively. Their shapes were similar, having a single peak in each components. The whole pyrolysis process took 120 min. They took 60 min to reach maximum temperature, 30 min to cool down to ambient temperature. The maximum temperature of the V.S.K. and V.D.K. were occurred at the reactor (511.33^{o}C) and inner reactor (550.00^{o}C), respectively. Furthermore, the carbonization temperature of inner reactor (550.00^{o}C) was higher than that of outer reactor (479.00^{o}C) in the V.D.K. It indicated that the vertical kiln covered with fiberglass as an insulator can be prevented heat loss. This result was similar to the result of Sangsuk *et al*., 2018 [14], Sangsuk *et al*., 2020 [9] and Manatura, 2021 [6]. Sangsuk *et al*., 2018 [14] studied the production of bamboo charcoal by using the metal kiln with heat distribution pipes and the reactor covered with fiberglass and galvanized steel as an insulator. Sangsuk *et al*., 2020 [9] produced charcoal from tamarind wood by using drum kiln with heat distribution pipes and the reactor covered with fiberglass and galvanized steel as an insulator. Manatura, 2021 [6] investigated the production of charcoal

from bamboo via retort with recirculating pyro-gas and reactor was covered by a ceramic insulator.

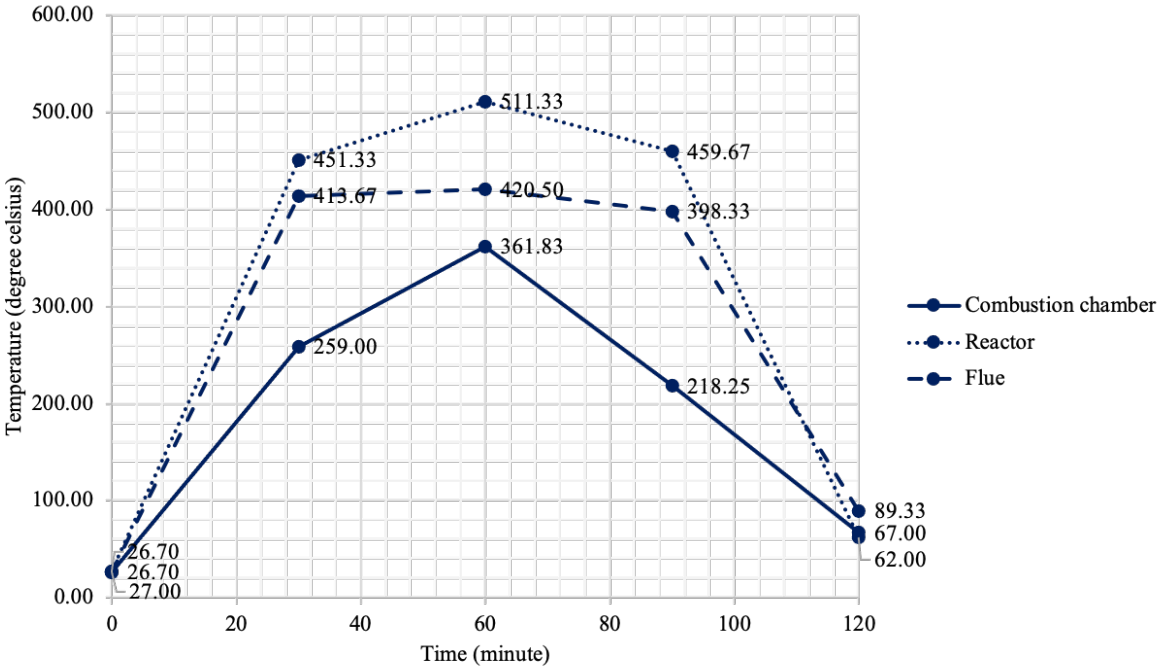

Figure 4. Temperature profiles for bamboo pyrolysis in the vertical single wall kiln.

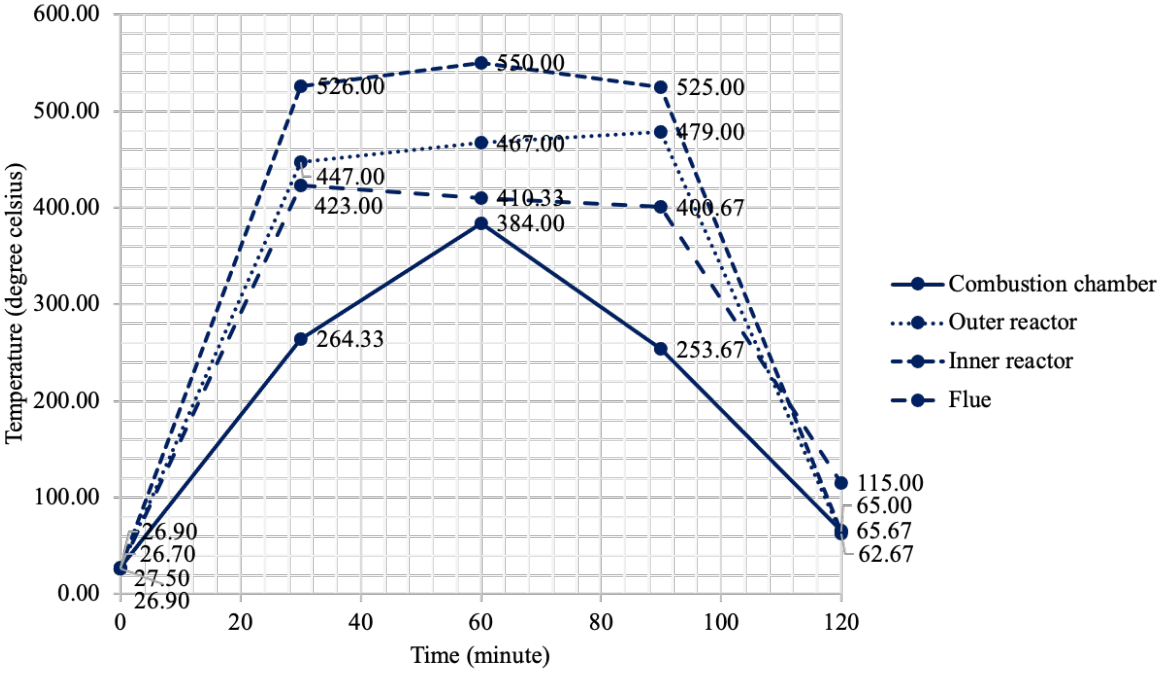

Figure 5. Temperature profiles for bamboo pyrolysis in the vertical double wall kiln.

Evaluation of bamboo waste as the raw material for charcoal production

Table 1 shows the characterization of bamboo waste as the raw material for charcoal production by the procedures of proximate analysis and HHV. According to Maiti *et al*., 2006 [22] and Demirbas's equation (2) [17], they described that the optimum HHV of biomass as a

feedstock for energy approximates 10-20 MJ/kg; moreover, HHV depends on fixed carbon content. However, high ash content and volatile matter could reduce HHV. Additionally, Higman and Burt, 2003 [17] described that the optimum moisture content for biomass as a raw material in biomass energy production should be less than 10%. In this research, the heating value and moisture content of bamboo waste was 18.55 MJ/kg and 6.94%, respectively. Therefore, the raw materials in this research contained the suitable heating value and moisture content in charcoal production.

Table 1. Proximate analysis and heating value of bamboo waste as the raw material.

Raw material	Proximate analysis (%)				HHV
	Fixed carbon	Volatile matter	Ash	Moisture	(MJ/kg)
Bamboo waste	20.93	70.06	2.11	6.94	18.55

Characterization of bamboo charcoal

The characterization of bamboo charcoal that were produced via the vertical single wall kiln (V.S.K.) and the vertical double wall kiln (V.D.K.) are summarized in Table 2. The results show the proximate analysis, HHV and yield of the bamboo charcoal. It found that the HHV, fixed carbon content and yield of the charcoal in the V.D.K. were higher than that of the charcoal in the V.S.K. The charcoal from V.D.K. was the highest HHV (27.57 MJ/kg), fixed carbon (68.63%) and yield (42.73%). The result in terms of fixed carbon content and HHV were higher than the result of Manatura, 2021 (64.36% and 23.74 MJ/kg, respectively). The yield result in this research was higher than the yield result of Chandrasekaran *et* al., 2019 [15]. However, the fixed carbon content (78.10%) and HHV (30.80 MJ/kg) results of Chandrasekran *et al.*'s research [14] were higher than this research. According to Community Product Standard Mor 657/2547 [19], the charcoal products showed the optimum HHV, volatile matter and moisture content which were higher than 25.12 MJ/kg, lower than 25% and lower than 10%, respectively. Although, the ash content of the charcoal in the V.D.K. was higher than that of the charcoal in the V.D.K., they were still higher than Community Product Standard Mor 657/2547 (8%)

Table 2. Proximate analysis, HHV and yield of bamboo charcoal.

Kiln type	Proximate analysis (%)				HHV	Yield
	Fixed carbon	Volatile matter	Ash	Moisture	(MJ/kg)	(%)
V.S.K.	62.08	16.24	19.36	2.58	26.29	31.08
V.D.K	68.63	16.58	12.83	2.22	27.57	42.73

The product yields of carbonization process by using both V.S.K. and V.D.K., including charcoal, brands, condensable liquids, ash, gaseous products (CO_2, CO and CH_4) and total suspended particulates, are summarized in Table 3. According to carbon balance's equation [19-20], the charcoal yield from V.D.K. was significantly higher than the charcoal yield from V.S.K. ($P<0.05$). Additionally, the amount of unwanted by-product from V.D.K., namely brands, condensable liquids, ash, gasous products and total suspended particulates

were lower than the by-product yields from V.S.K. It indicated that the charcoal production by using V.D.K. was more efficient than the charcoal production by using V.S.K. in terms of charcoal yield and the unwanted by-products. Furthermore, the charcoal yield from V.D.K. was higher than the theoretical yield of charcoal (30%).

Table 3. Product yields of carbonization process

Kiln type	Bamboo Waste (kg)	Product yield (kg)					
		Charcoal	Brands	Condensable liquids	Ash	Gases	suspended particulates
V.S.K.	23.75	7.38	3.46	3.08	1.44	7.13	1.26
V.D.K	23.23	9.93	2.19	2.86	1.27	5.81	1.17

Table 4 shows the heat utilization efficiency (HU) and boiling time of the bamboo charcoal that were produced in the V.S.K. and V.D.K. The results revealed that the HU of charcoal produced from V.D.K. (18.08%) was higher than the HU of charcoal produced from V.S.K. (14.20%); moreover, the boiling time of charcoal produced from V.D.K. (11.54 min) was shorter than the boiling time of charcoal produced from V.D.K. (13.92 min). It indicated that charcoal with higher HHV could be higher HU and shorter in boiling time.

According to the results of Figure 4-5 and Table 2-4, it indicated that the V.D.K. was more efficient than the V.S.K. in terms of maximum carbonization temperature, charcoal yield and charcoal characteristics including by covering the reactor with fiberglass as an insulator.

Table 4. Heat utilization efficiency and boiling time of bamboo charcoal.

Kiln type	Heat Utilization Efficiency (%)	Boiling time (minute)
V.S.K.	14.20	13.92
V.D.K	18.08	11.54

Conclusion:

The performance of the vertical single wall kiln (V.S.K.) and the vertical double wall kiln (V.D.K.) were evaluated the efficiency in terms of carbonization temperature, charcoal characteristic and charcoal yield. The results showed that the vertical kiln covered with fiberglass as an insulator can be generated higher carbonization temperature (550.00^{o}C) than the kiln without insulator covering. The charcoal characteristic and charcoal yield from the V.D.K. were more efficient than the results of charcoal from The V.S.K. Moreover, the amount of unwanted by-products from the V.D.K. were lower than the by-product yields from V.S.K. It indicated that the carbonized kiln design and carbonization process affected carbonization temperature, proximate results, higher heating value, charcoal yield, heat utilization efficiency and boiling time.

Acknowledgements:

The authors would like to knowledge Division of Agricultutal Engineering and Technology, Faculty of Agriculture and Natural Resources, Rajamangala University of Technology Tawan-ok, Chonburi province, Thailand for equipment and financial support of this work.

References:

1.Alejandro DAR, Aguilar AZ, Hernandez VHR, Arrigga AO. Biomass Bioenergy. 2018; 116: 80-88.
2. Restuccia F, Masek O, Hadden RM, Rein G. Fuel. 2019; 236: 201-213.
3. Ighalo J, Eletta OAA, Adeniyi AG. Bioresour Technol Rep. 2022; 17: 1-8.
4. Shoaib AM, Adly RAE, Hassanean MHM, Youssry A, Bhran AA. Egypt J Pet. 2018; 27: 1305-1311.
5. Solar J, Marco I, Caballero BM, Urionabarrenechea AL, Rodriguez N, Agirre I, Adrados A. Biomass Bioenergy. 2016; 95: 416-423.
6. Manatura K. Energy Sustain Dev. 2021; 64: 8-14.
7. Somerville M, Deev A. Renew Energy. 2020; 151: 419-425.
8. Antal MJ, Gronli M. Ind Eng Chem Res. 2003; 42: 1619-1640.
9. Sangsuk S, Buathong C, Suebsiri S. Energy Sustain Dev. 2020; 59: 1-7.
10. Jaisumroum N. RSU National Research Conference. 2015: 296-302.
11. Sinsaard A. ITECHJ. 2017; 10(2): 95-108.
12. Homchat K, Sucharitakul T. Energy Procedia. 2011; 9: 264-273.
13. Soka, Oyekola. Biomass Bioenergy. 2020; 6(7): 1-11.
14. Sangsuk S, Suebsiri S, Puakhom P. Energy Sustain Dev. 2018; 47: 149-157.
15. Chandrasekaran A, Subbiah S, Ramachandran S, Narayanasamy S, Bartocci P, Fantozzi F. Energy Fuels. 2019; 33: 111123-111124.
16. Laorach L, Jutajan W, Masakul P. J Phys Conf Ser. 2021; 2013(012003): 1-8.
17. Higman C, Burt MVD. 2003. Gasification. 1st edn. Gulf Professional Publishing, Burlington, United States of Amereica.
18. Ayhan D, Hilal AD. Energy Explor Exploit. 2004; 22(2): 135-143.
19. Heschel W, Klose E. Fuel. 1995; 74: 1786-1791.
20. Pennise DM, Smith KR, Kithinji JP, Rezende ME, Raad TJ, Zhang J, Fan C. J Geophys Res. 2001; 106(D20): 143-155.
21. Kritsada B, NirubolC, Naresuan Phayao J. 2020; 13(2): 51-56.
22. Maiti S, Dey S, Purakayastha S, Ghosh B. Bioresour. Technol. 2006; 97: 2065-2070..

SYNTHESIS OF METAL LOADING/ TITANIUM SILICATE CATALYSTS FOR HIGHLY SELECTIVE PALM OIL EPOXIDATION

Thanyarat Pakaew,[1,*] Chanatip Samart[1,2] Boonyawan Yoosuk[3] Suwadee Kongparakul,[1,2,*]
[1]Department of Chemistry, Faculty of Science and Technology, Thammasat University, Pathum Thani 12120, Thailand
[2]Bioenergy and Biochemical Refinery Technology Program, Faculty of Science and Technology, Thammasat University 12120, Thailand
[3]Clean Fuel Technology and Advanced Chemistry Research Team, National Energy Technology Center (ENTEC), Pathum Thani, 12120, Thailand
*e-mail: Thanyarat.P@sci.tu.ac.th, ksuwadee@tu.ac.th

Abstract:
The epoxidation reaction of vegetable oil using hydrogen peroxide is being intensively studied with a significant number of studies using homogeneous catalyst, however, there are some drawbacks might observe along the homogeneous catalytic process such as low epoxide rings selectivity, difficult to separate and recover the homogeneous catalyst, and extremely corrosive in the system, etc. Therefore, the heterogeneous catalyst has been used in this study. The titanium silicate catalysts (TS-1) were successfully synthesized by hydrothermal treatment followed by the wet impregnation method with transition metals such as Co, Fe, and Ni which named as Co/TS-1, Fe/TS-1, and Ni/TS-1, respectively. All prepared catalysts were characterized by X-ray powder diffraction (XRD), Fourier transform infrared spectroscopy (FTIR), N_2 adsorption-desorption. The structural properties of the TS-1 zeolites, Co/TS-1, Fe/TS-1, and Ni/TS-1 materials exhibited highly ordered porous structures with mordenite framework inverted (MFI) framework with surface area in the range of 401.8 to 481.4 m^2/g. The catalytic activity was investigated in the epoxidation of palm oil with hydrogen peroxide. The optimum condition to achieve 85.6% conversion of palm oil and 57.4% selectivity of epoxide ring was the ratio of palm oil to hydrogen peroxide of 1:8, 0.2 g of Ni/TS-1 and carried out at 80°C for 3h. The separation of catalyst was simply removed by filtration which environmentally benign compared to the convention homogeneous catalytic process for palm oil epoxidation.

Introduction:
The epoxidation process is one of the potential alternatives that could possibly transform biomass into more valuable compounds, therefore contributing to health benefits while being worth it in terms of cost-effectiveness and environmental friendliness. Epoxidation is the oxidation reaction that converts the carbon–carbon double bond into an epoxide ring by using acidic substances such as perbenzoic acid, perphthalic acid, peracetic acid, or formic peroxy acid that interact with hydrogen peroxide as an oxidant. The resultant epoxide rings from the epoxidation process can be used in a variety of applications, including PVC stabilizers, intermediates to produce polyurethanes and polyols, and lubricating components of pharmaceuticals and cosmetics. However, the epoxidation of vegetable oil with peroxide as the oxidant, which is formed in situ through the acid, is a conventional acid process. Even though the conventional process is simple to prepare, the main drawbacks of this process include low selectivity to the products' epoxide rings, difficult separation and recovery of the catalyst, and the acid system's highly corrosive nature. In the past few years, researchers have made many attempts to develop heterogeneous catalytic technologies for the epoxidation of vegetable oil, such as solid acid ion exchange resin**,** solid materials supported organic acid, zeolite, and cyclo-

oxygenase, which are applied in the epoxidation reaction to reduce the disadvantages that are present for conventional processes.

Therefore, in this research interested in TS-1 as a catalyst because of its unique structure and highly activated tetrahedral Ti centers within the skeleton, TS1 exhibits outstanding properties of shape-selective catalysis oxidation for epoxidation, which can be utilized as an environmentally safe catalyst in the oxidation. However, when used in an epoxidation process, the significant diffusion limitation of the vegetable oil, which has macromolecules, leads to the unavailability of the framework Ti on the internal surface and the low catalytic activity of TS-1. In this research, we designed a Co, Fe, and Ni-treated TS-1 catalyst with tetrahedral Ti species for the activity of palm oil epoxidation and the surface of species to understand the synergistic effect of TS-1 and achieve high-efficient epoxidation of palm oil.

Methodology:

Catalyst Preparation

The titanium silicalite-1 catalyst was synthesized in the following ratios: TiO_2: $0.24SiO_2$: 0.025 TPAOH: 1.75IPA: $26.3H_2O$. The first step is to combine the solution of Tetrapropylammonium hydroxide (TPAOH) with 40 deionized water under vigorous stirring at room temperature. Then, tetraethyl orthosilicate (TEOS) was added to the previously prepared tetrapropylammonium hydroxide (TPAOH) solution and aged for 30 min. Drops of solution were mixed with Tetrabutoxide monomer (TBOT) and isopropanol alcohol (IPA) and stirred for 2 hours. Heat to 80°C and keep it there for 1.5 h to evaporate the alcohol. The solution was transferred to the autoclave to transform the solution into crystals by utilizing high temperature and high pressure, which is known as the hydrothermal principle. Temperatures of 170°C were used in this study for 72 h. The materials were separated by centrifugation, the pH is neutralized with deionized water, and they are dried in an oven at 100°C for 12 hours. The catalyst's molecular sieve was generated by selecting a sieve smaller than 100 mesh and calcining it for 5 hours at 550°C under air flow. In this study, protons were added to the zeolite structure to increase the acidity of the catalyst by refluxing with 1M of ammonium chloride (NH_4Cl) for 20 ml and TS-1 zeolite as catalyst for 1 g.

Furthermore, the obtained TS-1 catalysts were modified via wet impregnation method with 3 transition metals such as Co, Fe,and Ni which named as Co/TS-1, Fe/TS-1, and Ni/TS-1, respectively. Cobalt(II) nitrate hexahydrate, ferric chloride hexahydrate, and nickel nitrate hexahydrate solutions for Co, Fe, and Ni were prepared in 10 mL of deionized water. The synthesized titanium silicalite-1 (TS-1) support was added to the solution and stirred at 800 rpm/min for 6 h at room temperature. Increase the temperature to 100 °C to evaporate the water from the solution until obtained solid form. Dried in an oven at 100°C for 24 hours before being transferred to the furnace and calcined for 5 hours at 550°C.

Activity test with epoxidation

The epoxidation of palm oil with hydrogen peroxide as an oxidizing agent was tested. Parameters such as temperature, ratios of palm and hydrogen peroxide, amount of catalyst (g), reaction time (h), and three kinds of catalysts such as Co/TS-1, Fe/TS-1, and Ni/TS-1 were investigated via epoxidation. The reaction temperatures were 40, 60, 80, and 100 °C, the mole ratios of palm oil and hydrogen peroxide were 1:2, 1:4, 1:6, 1:8, and 1:10, the amount of catalyst was 0.05, 0.2, 1, and 2 g, and the reaction time was 1, 3, 5, and 7h were investigated.

0.2 g of catalyst with 10 g of palm oil were combined at room temperature for 5 minutes. Add 30% hydrogen peroxide (H_2O_2) gradually. The reaction temperature was increased after adding 8 g of T-butanol. After the reaction, the catalyst was separated from the synthesized epoxidized palm oil by a separate funnel. Regeneration of catalyst undergoing calcination for 10 h at 550°C The product will be transported into a rotary-evaporation for 1 hour 30 minutes to remove residual water at 60°C at a pressure of 20 mbar before being treated with sodium sulfate anhydrous. Using a vacuum pump, filtrate the product to separate the epoxidized palm oil.

The epoxidized palm oil was evaluated through two methods: titration and nuclear magnetic resonance (NMR). The conversion of palm oil, which is the position of the double bond of palm oil converted to an epoxide ring or another group depending on control parameters of the reaction, was investigated by the titration method based on the standard method EN 1411. The iodine value is a measurement that indicates the quantity of double bonds in palm oil or raw material which can be determined using a conventional titration technique (EN 1411). Oxirane oxygen is oxygen found in products (epoxidized palm oil) which can be identified using a titration technique (AOCs Cd9-57). The selectivity of the epoxide ring, which is a specific epoxide ring that would appear in a product, was evaluated by nuclear magnetic resonance (NMR).

Results and Discussion:

Characterization results of catalyst samples

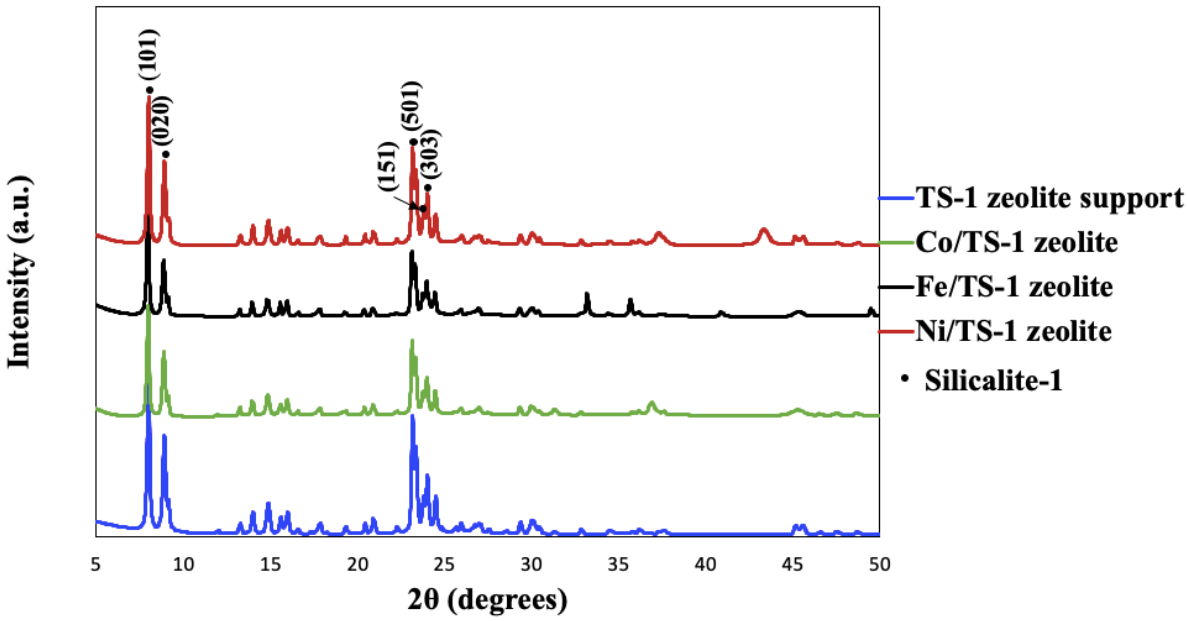

Fig. 1.

XRD diffraction patterns of the TS-1 zeolite support, Co/TS-1, Fe/TS-1, and Ni/TS-1samples.

X-ray difraction (XRD) of a titanium silicalite-1 zeolite (TS-1 zeolite), Co/TS-1, Fe/TS-1, and Ni/TS-1, as shown in Fig. 1, the x-ray diffraction patterns of catalysts treated with hydrothermal synthesis. The typically positions of all five major diffractions were found at 2θ of 7.9°, 8.8°, 23.1°, 23.9° and 24.4°, which are consistent with the topological spectra of the Mordenite Framework Inverted (MFI) following silicalite-1 structure. In particular, the diffraction peak was 24.4°, which was a good indication of the transition from monoclinic symmetry to orthogonal symmetry. The modificated titanium silicalite-1 with the transition metals at 2% concentrations of Co, Fe, and Ni were loaded onto the titanium silicalite-1 support via the wet impregnation method. The results indicate the x-ray diffraction pattern remains the same after loading transition metals on the support. Furthermore,transition metals such as Co, Fe, and Ni are well distributed on the surface of the TS-1 zeolite support. The diffraction pattern remained the same, but the signal intensity was slightly decreased because the external surface of the TS-1 zeolite support was covered with transition metals. FT-IR spectroscopy was used to examine the functional groups in the synthesized material. The results are exhibited in Fig. 2 were represent FTIR spectra after loading the 3 transition metals Co, Fe, and Ni onto the support. The spectra exhibited five main absorption functional groups at 450, 550, 800, 1100, and 1230 cm^{-1} are consistent with the characteristic bands of the MFI topology. 450 cm^{-1} and 550 cm^{-1} are bending vibration of the Si-O bond and the asymmetrical contractile vibration of SiO_4 and TiO_4 in the zeolite structure respectively. The symmetric and asymmetric stretching vibrations of the tetrahedral $(Si,Ti)O_4$ structure are represented by the characteristic peaks at 800 and 1110 cm^{-1}, respectively. And the position of the peak at 1230 cm^{-1} is considered to the asymmetric stretching vibration of the molecular sieve skeleton. Ti was successfully inserted into the TS-1 zeolite framework at the 960 cm^{-1} position, which represents the SiO_4-Ti tetrahedral bond. It is remarkable that this vibration peak at 960cm^{-1} almost remains unchanged after loaded of Co, Fe, and Ni to TS-1 which clearly shows that the introduction of the transition metals species does not change the existence state of the framework titanium.

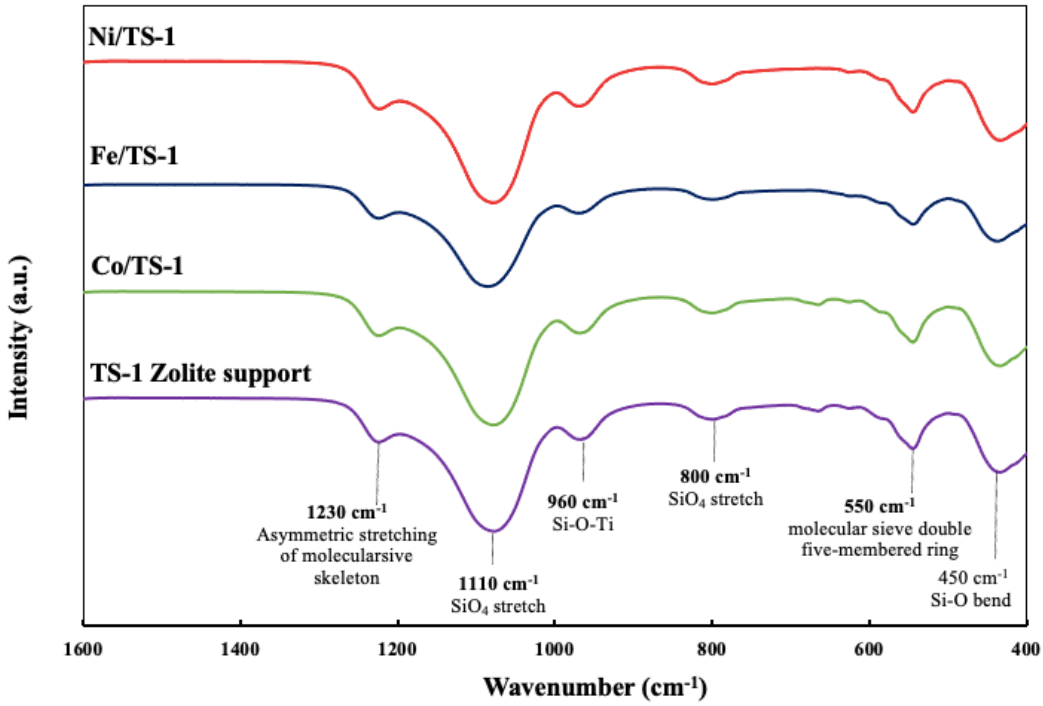

Fig. 2.

FTIR spectra of the TS-1 zeolite support, Co/TS-1, Fe/TS-1, and Ni/TS-1 samples.

The specific surface area, external surface area, internal surface area, pore volume and pore size of catalysts were investigated by N_2 adsorption-desorption technique. The samples are exhibited in **Fig. 3. and 4.** It can be seen from the N_2 adsorption isotherm that the structural properties of the TS-1 zeolites, Co/TS-1, Fe/TS-1, and Ni/TS-1 materials exhibited highly ordered porous structures with mordenite framework inverted (MFI) framework with surface area in the range of 401.8 to 481.4 m^2/g according to **Table 1,** which shown all samples still exhibit a similar type of adsorption desorption according to the International Union of Chemical and Applied Chemistry (IU-PAC), which is classified as a material in the microporous. The isotherms of micropores titanium silicalite-1 were also discovered when the 3 metals cobalt (Co), iron (Fe), and nickel were loaded (Ni) on support. Furthermore, all of Co, Fe and Ni have not impacted the structural integrity of the TS-1 zeolite support. This is compatible with the aforementioned experimental results from X-ray diffraction.

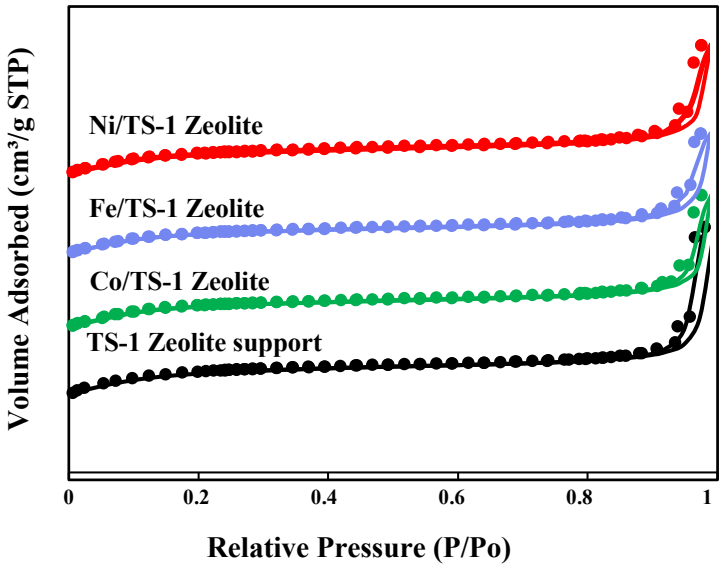

Fig. 3.

Nitrogen physisorption curves of the TS-1 zeolite support, Co/TS-1, Fe/TS-1 and Ni/TS-1

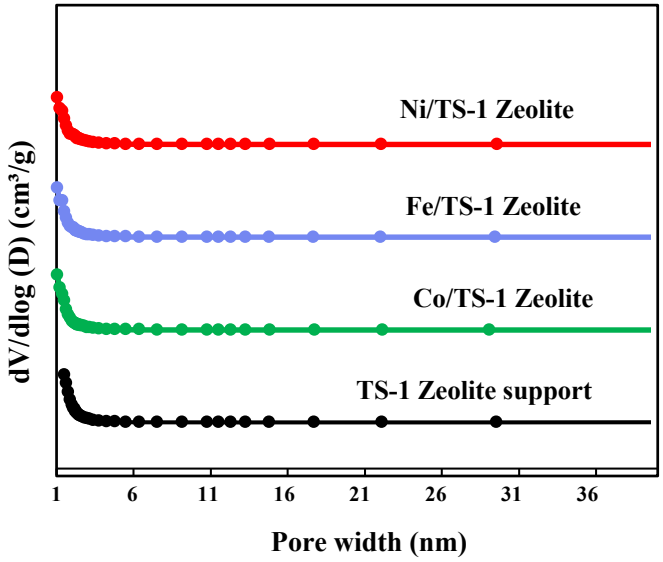

Fig. 4.

Pore size distribution curves of the TS-1 zeolite support, Co/TS-1, Fe/TS-1 and Ni/TS-1 .

Table 1.

The specific surface area, pore volumes and pore diameter of all catalysts.

Sample	S_{BET} [$m^2.g^{-1}$]	S_{EX} [$m^2.g^{-1}$]	S_{In} [$m^2.g^{-1}$]	$V_{Micropore}$ [cm^3g^{-1}]	$V_{Mesopore}$ [cm^3g^{-1}]	pore diameter (nm)
TS-1 support	481.4	96.2	385.2	0.15	0.20	3.37
Co/TS-1	427.4	72.8	354.5	0.14	0.15	3.35
Fe/TS-1	401.8	76.5	325.4	0.13	0.11	3.36
Ni/TS-1	410.1	80.2	329.9	0.14	0.21	3.46

Catalytic test results

Effect of reaction parameters

The parameter amount of catalyst was studied at 0.05, 0.2, 1, and 2 g. The experimental results are shown in **Fig. 5. and 6.** It was observed that the amount of catalyst of 0.2 g provided the highest percentage of oxirane oxygen, percentage of conversion of palm oil, and percentage of selectivity epoxide ring at 2.72, 77.36, and 57.76%, respectively. The increased amount of the catalyst has an increased active center, resulting in the conversion of palm oil significantly increasing. However, when the amount of catalyst was greater than 0.2 g, the percentage of oxirane oxygen and conversion of palm oil decreased to 1.70, 1.45%, and 49.23, 42.23%, respectively due to the excess catalytic concentration, which affected the epoxide ring deterioration. Therefore, it can be concluded that the optimal amount of titanium silicalite-1 catalyst is 0.2 g.

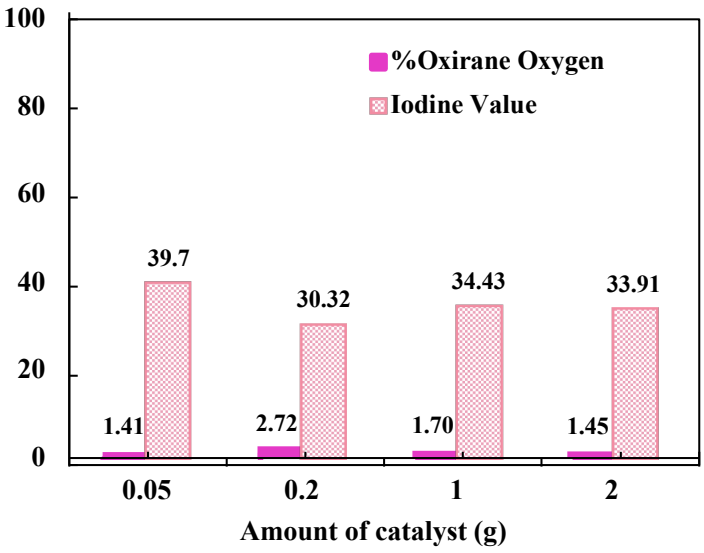

Fig. 5.

%Oxirane oxygen and iodine value from effect of amount of catalyst

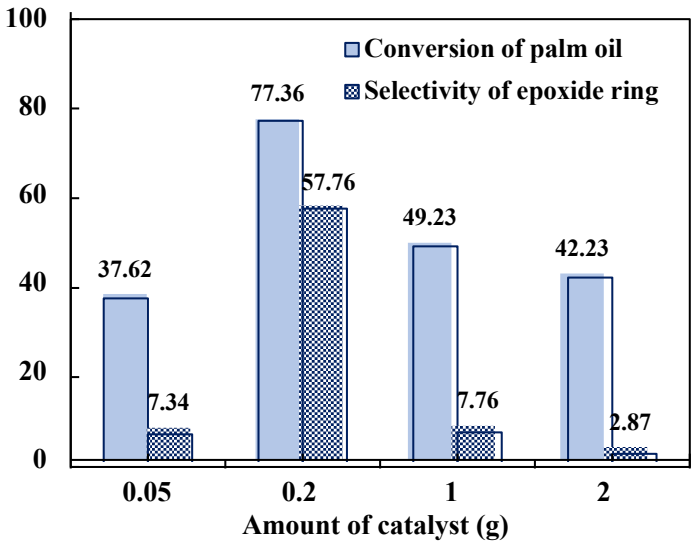

Fig. 6.

Conversion of palm oil and selectivity from effect of amount of catalyst

From the study on the effect of reaction times at 1, 3, 5, 7 and 24 h, it was found that the catalyst under the same conditions was the ratio of palm oil to hydrogen peroxide of 1:8, 80 °C and 0.2 g of TS-1 as catalyst. The results shown the percentage conversion of in the reaction increased significantly as the reaction time increased according to **Fig. 7. and 8**. From the principle of mass transfer and diffusion resistance, which is an important principle used to describe the relationship between molecules of palm oil and solid catalyst, In the case of the catalyst as a heterogenous catalyst, it can be observed that at the initial stage of the reaction times, the percentage conversion of palm oil and the selectivity of the epoxide ring are quite low values. After a period of reaction, the molecules of palm oil are adsorbed and react gradually at the active site of the catalyst. This has resulted in an increased conversion of palm oil. At the same time, the longer the reaction period, the more the epoxide ring products will undergo hydrolysis of the double bond position, generating hydroxyl or ether groups as a side product, reducing the selectivity of the epoxides. **Fig. 9. and 10.** shown the effect of

temperature, It was discovered that increasing the reaction temperature induced the molecules of palm oil move rapidly. As a consequence of the increased kinetic energy, the reaction rate correspondingly increases. However, from the experimental results, it was observed that the percentage conversion of palm oil had not significantly increased when the temperature was increased from 80 °C to 100 °C. The selectivity of epoxide ring was greatest at 80°C (57.8%) and gradually declined as temperature increased. This is attributed to the excess energy inducing a hydrolysis reaction that creates further side groups. As a result, the selectivity of epoxide ring decreased.

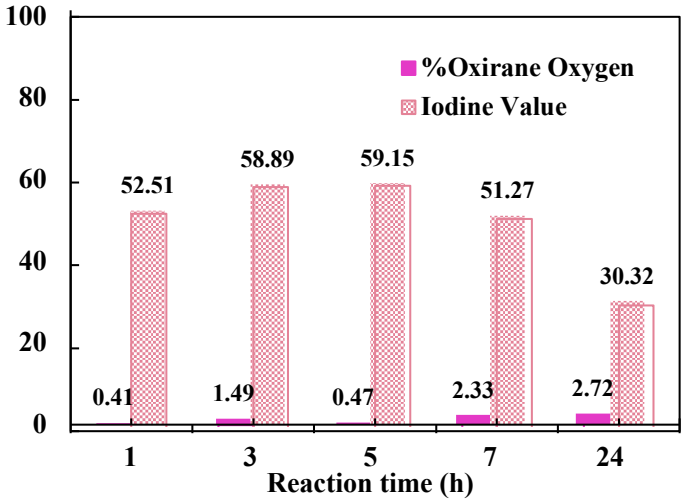

Fig. 7.

%Oxirane oxygen and iodine value from effect of reaction time

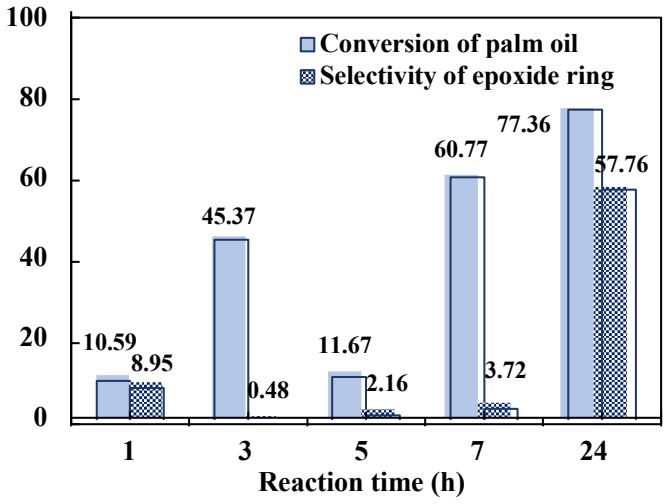

Fig. 8.

Conversion of palm oil and selectivity from effect of reaction time

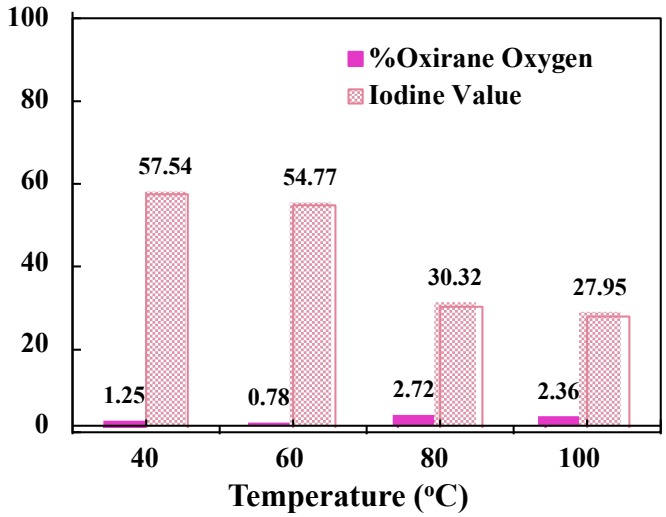

Fig. 9.

%Oxirane oxygen and iodine value from effect of temperature

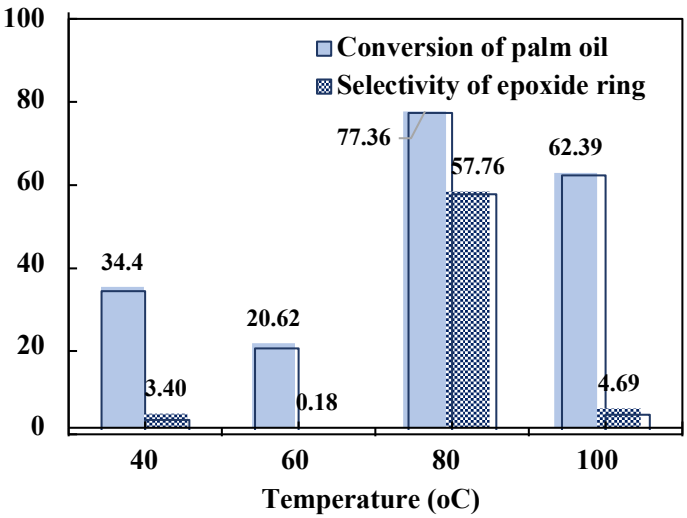

Fig. 10.

Conversion of palm oil and selectivity from effect of temperature

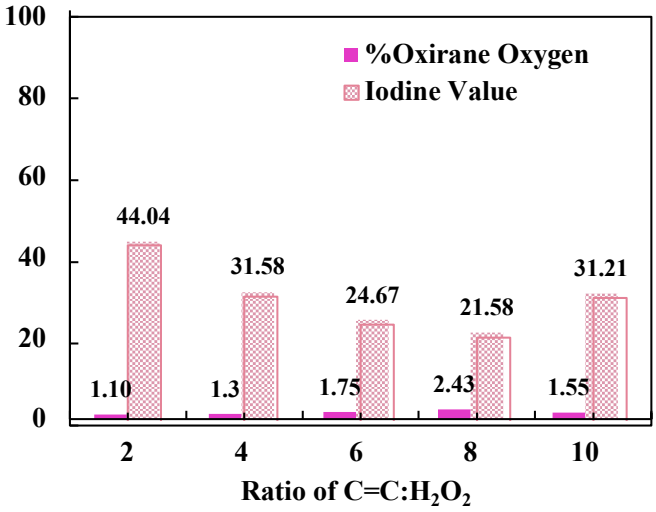

Fig. 11.

%Oxirane oxygen and iodine value from effect of ratio palm oil:H_2O_2

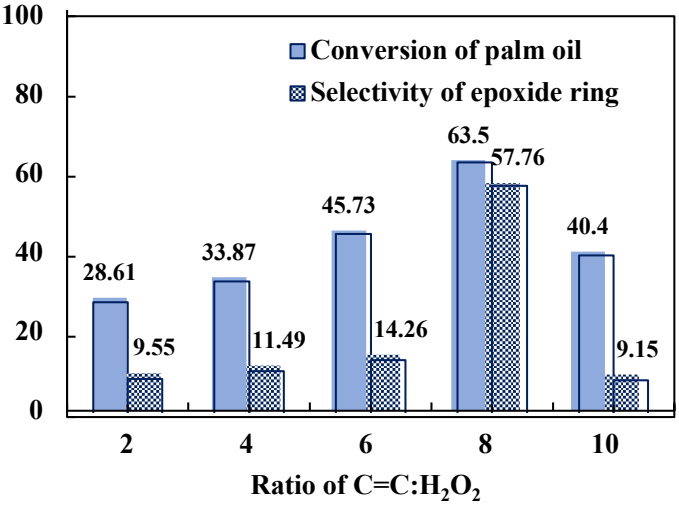

Fig. 12.

Conversion of palm oil and selectivity from effect of ratio palm oil:H_2O_2

According to **Fig. 11. and 12.** the experimental results of ratio between palm oil to hydrogen peroxide, the percentage change of palm oil tended to increase as the ratio of palm oil to hydrogen peroxide increased. However, the tendency for percentage conversion of palm oil and selectivity of epoxide ring decreased when the ratio of palm oil to hydrogen peroxide was increased by more than 1:8. The increased amount of hydrogen peroxide results in more hydrogen peroxide from the oxygen carrier at the double bond position (oxidizing agent). The amount of residual hydrogen peroxide in the system is greater than the utilization rate of hydrogen peroxide in the reaction. **Fig.13** As a result of the catalyst improvement, the metals were loaded cobalt (Co), iron (Fe), nickel (Ni), respectively. Nickel had the best performance in terms of conversion of palm oil and selectivity of epoxide ring. Transition metals, whose unoccupied 3d orbitals are good electron acceptors, display superior catalytic performance in redox reactions and TS-1 zeolite modified with metal effectively catalyzed in epoxidation. The interaction between metal and TS-1 changed the electronic environment of the Ti centers. The peripheral electronic cloud around the Ti center was attracted by an embedded 3d orbital of metal were loaded and the electrophilicity of the Ti center and active oxygen were enhanced this thing activated the double bond epoxidation of palm oil

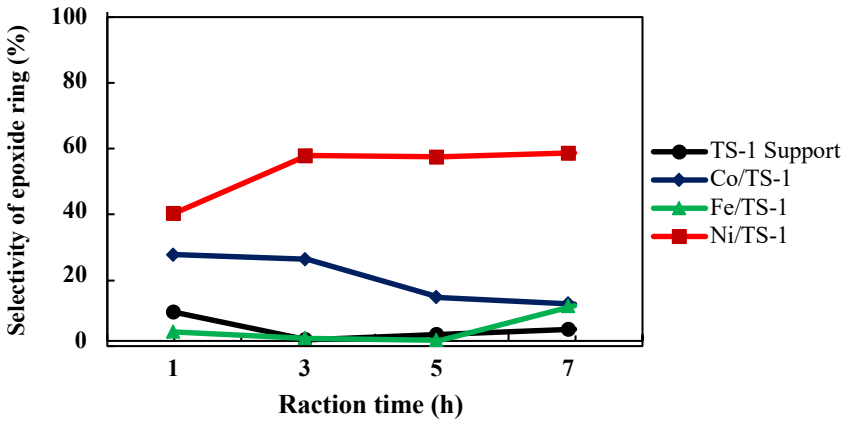

Fig. 13.

Selectivity of epoxide ring from TS-1 support, Co/TS-1, Fe/TS-1 and Ni/TS-1 of epoxidized palm oil

Conclusion:

The hydrothermal followed by the wet impregnation method successfully synthesized an acid-free and efficient epoxidation process for the production of epoxidized palm oil from palm oil and TS-1 supported with transitions such as Co, Fe, and Ni. The result showed all synthesized materials were characterized by X-ray diffraction, FTIR, and N2 adsorption-desorption. The experimental results in the epoxidation part showed that the optimum conditions to achieve 85.6% conversion of palm oil and 57.4% selectivity of the epoxide ring was the ratio of palm oil to hydrogen peroxide of 1:8, 0.2 g of Ni/TS-1, and carried out at 80°C for 3 hours. These observations will provide an environmentally friendly alternative in terms of the separation of catalyst, which is simply removed by filtration, which is more environmentally friendly than the conventional homogenous catalytic procedure for palm oil epoxidation.

Acknowledgements:

This work was supported by the Thailand Science Research and Innovation Fundamental Fund, Contract no. TUFF 09/2565, Thammasat University Research Fund, Contract no. TUFT-FF6/2565, and and Thammasat University Research Unit in Bioenergy and Catalysis (BCRU).

References:

1. Zhao, Liang, et al. "Alkali-treatment of ZSM-5 zeolites with different SiO_2/Al_2O_3 ratios and light olefin production by heavy oil cracking." *Fuel processing technology* 92.3 (2011): 414-420.
2. Koekkoek, Arjan JJ, et al. "Hierarchically structured Fe/ZSM-5 as catalysts for the oxidation of benzene to phenol." *Microporous and mesoporous materials* 145.1-3 (2011): 172-181.
3. Harris, James W., et al. "Propylene oxide inhibits propylene epoxidation over Au/TS-1." *Journal of Catalysis* 365 (2018): 105-114.
4. Hu, Tiejing, et al. "Synthesis of ZSM-5 monoliths with hierarchical porosity through a steam-assisted crystallization method using sponges as scaffolds." *Chinese Journal of Catalysis* 38.5 (2017): 872-877.
5. Li, Jiacheng, et al. "Size effect of TS-1 supports on the catalytic performance of PtSn/TS-1 catalysts for propane dehydrogenation." *Journal of catalysis* 352 (2017): 361-370.
6. Alfaro, S., Valenzuela, M. A., & Bosch, P. (2009). Synthesis of silicalite-1 by dry-gel conversion method: factors affecting its crystal size and morphology. *Journal of Porous Materials*, *16*(3), 337-342.
7. Xiong, G., Jia, Q., Cao, Y., Liu, L., & Guo, Z. (2017). The effect of acid treatment on the active sites and reaction intermediates of the low-cost TS-1 in propylene epoxidation. *RSC advances*, *7*(39), 24046-24054.
8. Alfaro, S., Valenzuela, M. A., & Bosch, P. (2009). Synthesis of silicalite-1 by dry-gel conversion method: factors affecting its crystal size and morphology. *Journal of Porous Materials*, *16*(3), 337-342.
9. Chen, C., Cai, L., Li, L., Bao, L., Lin, Z., & Wu, G. (2019). Heterogeneous and non-acid process for production of epoxidized soybean oil from soybean oil using hydrogen peroxide as clean oxidant over TS-1 catalysts. *Microporous and Mesoporous Materials*, *276*, 89-97.

WASTEWATER SURVEILLANCE OF SARS-CoV-2 FROM THE AIRCRAFT AND WASTEWATER TREATMENT PLANTS AT DOMESTIC AND INTERNATIONAL AIRPORTS, THAILAND

Chaw Su Thin,[1] Kwanrawee Sirikanchana,[2] Jatuwat Sangsanont [3,4]*
[1]International Program in Hazardous Substance and Environmental Management, Graduate School, Chulalongkorn University, Bangkok 10330, Thailand
[2]Research Laboratory of Biotechnology, Chulabhorn Research Institute, Bangkok 10210, Thailand
[3]Department of Environmental Science, Faculty of Science, Chulalongkorn University, Bangkok 10330, Thailand
[4]Water Science and Technology for Sustainable Environmental Research Group, Chulalongkorn University, Bangkok 10330, Thailand*
e-mail: chawsuthin18@gmail.com, jatuwat.s@chula.ac.th

Abstract:
Airports play a crucial role as the main entrance for each country. Since a variety of passengers come from different countries, it's more likely to have a higher chance of carrying infectious diseases and spreading them throughout the country. Wastewater-based epidemiology of SARS-CoV-2 is one of the reliable and cost-effective methods for virological surveillance. The aim of this study is to examine the applicability of wastewater surveillance of SARS-CoV-2 from aircraft and airport wastewater. The wastewater samples were collected from domestic and international airports in Thailand (A1 and A2) from March to June 2022. The adsorption-extraction by the electronegative membrane was used for viral concentration and continued RNA extraction and quantified by RT-qPCR assay with primers targeting nucleocapsid gene, N1. All wastewater samples from the aircraft and the airports' wastewater treatment plants were detected for N1 gene. High viral copies of SARS-CoV-2 RNA (267.84 to 6,874.79 copies/ml) were detected in aircraft wastewater from A2 airport, the airport for international travel, which was positively correlated with the number of infected cases from abroad at seven days lag (Pearson correlation = 0.984, $p>0.002$) during 21st March to 5th May 2022. The viral concentration from the aircraft's wastewater of A1 airport, the airport for domestic travel, varied from 164.57 to 10,986.71 copies/ml. No correlation was found between viral concentration and daily new cases in the city as well as from abroad. There was no significant difference in mean viral gene copies of SARS-CoV-2 RNA in aircraft wastewater at both airports from April to June. Moreover, since a high viral concentration of SARS-CoV-2 was detected from the aircraft compared to that from airport wastewater treatment plants, our results suggest that wastewater surveillance from the aircraft can also provide a cost-effective and alternative way to monitor the carriers of the SARS-CoV-2 virus at airports supporting public health decisions and responsive actions related to SARS-CoV-2 at the airports in the future.

Introduction:

Airports are the main entry into a country, which is necessary to be cautious about domestic infections. That is why every country tries to control diseases systematically at airports to prevent infection. When the COVID-19 waves are in severe conditions, air travel by flight has become the leading cause of the escalation of the COVID-19 infection from one country to another. In the past, to prevent coronavirus infection, the airline authorities in each country establish rules, laws, and policies such as RT-PCR test certificates, 10-14 days quarantine, etc.

In Thailand, due to the vaccine availability, the passengers were finally exempted from the quarantine and RT-qPCR tests at present. However, the virus can change into new variants by mutation over time and occur another COVID wave by domestic infection. Since the travelers come from different countries, there is a higher chance of carrying SARS-CoV-2 and its different variants, causing a high number of COVID-19 infection within a country. Moreover, it is imperative to track the viral trend of SARS-CoV-2 prevalence for the vaccination update according to the changes of the variants. Thus, airports have become a critical place where virological surveillance with effective and reliable methods should always be conducted.

Wastewater-based epidemiology (WBE) is an approach to use biological or chemical indicators in sewage to give health information on communities. It based on the principle that chemical or biological markers will be excreted to the sewage. It has successfully tracked SARS-CoV-2 from asymptomatic or symptomatic patients to the prevalence of the disease outbreak in the population[4,5]. The main advantage of the SARS-CoV-2 wastewater epidemiology method is that it can provide better evidence to inform pandemic and endemic disease surveillance to support management programs and other public health and social measures since it is independent of the diagnostic testing practices and capacity[6].

At the present, the SARS-CoV-2 WBE method has become a tool to detect the viral trends and changes at a population level correlated with hospitalizations in various countries[7,8]. In Thailand, SARS-CoV-2 was detected in wastewater treatment plants and showed the strongest correlation with COVID-19 daily new cases[9]. In addition, positive correlations were observed between the normalized viral RNA signal and both the number of new daily positive COVID-19 cases in Ottawa, Canada and clinical testing percent positivity[10].Furthermore, WBE has been shown to becomes one of the effective methods for the surveillance of the SARS-CoV-2. In addition, it can apply to monitor COVID-19 infection status and trends within populations of varying sizes and locations (scalable for catchment, postcode level, and building) [11]. This approach can be advantageous in areas with low or no existing active caseloads, including facilities such as nursing homes, prisons, universities, college campuses, and student dormitories, as well as ships, aircraft, resort hotel locations, and regional and remote vulnerable communities [12,13,14,15,16].

Early in the pandemic, SARS-CoV-2 RNA could be detected in wastewater collected from international flights and cruise ships [17, 18]. It was also observed that SARS-CoV-2 RNA was detected in 13.6 % of wastewater samples from 198 commercial aircraft arrived at Dubai Airport. Recently, the wastewater surveillance demonstrated 83.7% accuracy in detecting SARS-CoV-2 infections among passengers of international flights, all of whom had tested negative for COVID-19 before boarding [19]. Consequently, aircraft wastewater surveillance could offer a cost-effective method for screening onboard passengers to inform public health officials to manage passenger and crew well-being and prioritize clinical testing. The previous studies on WBE at the airport focused on the identification of infected person in the aircraft. However, the applicability of wastewater surveillance system for long term monitoring has not yet been clarified. The effectiveness of WBE for monitoring the spread of the disease would depend on the sampling site, frequency etc. Therefore, in this study, SARS-CoV-2 surveillance was carried out at airports to know the status of the SARS-CoV-2 within a country by focusing on the terminals and the aircraft wastewater. The information from the study can be contributed to the public and the Ministry of Health for the decision and responsive actions related to SARS-CoV-2 at the airports in future.

Methodology:

Study sites and Sample collection

A total of 56 samples of wastewater from the international airport (n=28) and the domestic airport (n=28) in Thailand were collected from March to June 2022. Five hundred mL of samples were collected every week from the two sampling sites of each airport: the wastewater from the airports' wastewater treatment plants and the aircraft. While collecting samples, the safety procedures were followed systematically. The samples were then brought with ice to the laboratory and continued for viral concentration within 24 hours.

Viral concentration

The samples (n=56) were subjected to the viral concentration method (Electronegative membrane filtration method)[20]. In this method, magnesium chloride ($MgCl_2$) powder were prepared to obtain the final concentration of 25 mM of $MgCl_2$ and then poured into the vacuum filtration installed with a 0.45 µm pore size integrated cellulose-ester membrane (HAWP04700, Merck Millipore, USA). After that, the filter was cut into pieces in a 5 ml tube and mixed with 1 ml of DNA/RNA shield solution (Zymo Research, USA). After that, 0.1 and 0.5 mm of the beads (P430010, ZR BashingBeads™ Lysis Tube, USA) were put into the tube, vortexed for around 20 minutes, and proceeded for RNA extraction.

RNA Extraction and RT-qPCR analysis

RNA extraction will be conducted using a QIAamp Viral RNA Mini Kit (Qiagen, Germany). The 140 µl of supernatant of the samples obtained from viral concentration were used for RNA Extraction. Finally, a final volume of 60 µl RNA were eluted and stored at –80ºC for further analysis. In the case of the quantification of SARS-CoV-2, the extracted RNA were continued with the one-step RT-qPCR with suitable primers and probes, as described by the Centers for Disease Control and Prevention (CDC) in the USA[21] (CDC N1 assay) (Table 1).

Table 1. Primers and probes for N1 genes

Primer/Probe		Sequence (5′-3')	
CDC	N1_F	GAC CCC AAA ATC AGC GAA AT	21
	N1_R	TCT GGT TAC TGC CAG TTG AAT CTG	
	N1_Probe	FAM-ACC CCG CAT TAC GTT TGG TGG ACC-BHQ1	

To prepare for the PCR components (10.0 µl), 2.5 µl of template RNA in 3.4 µl of distilled water were mixed with 0.6 µl of each primer N1 (Forward and Reverse Primers), 0.2 µl of probe and 2.5 µl of 4× Taq polymerase enzyme. The PCR conditions were 50°C for 15 minutes, 95°C for 20 seconds, 95°C for 3 seconds, and 55°C for 30 seconds. The qPCR for SARS-CoV-2 N1 gene was run for 45 cycles using the QuantStudio™ 6 Flex Real-Time PCR System (Applied Biosystems, Thermo Fisher Scientific, Waltham, MA, USA). The qPCR standard curves were constructed using linearized synthetic plasmid standards for N1 gene [22] (GeneArt ®, Invitrogen, Thermo Fisher Scientific, Waltham, MA USA).

Relationship between viral concentration and positive clinical cases

The relationship between the COVID-19 clinical positive patients from abroad and the presence of the SARS-CoV-2 RNA gene copies in the aircraft wastewater sample in the international airport, as well as the relationship between the daily COVID-19 cases and the viral gene copies of the aircraft wastewater in the domestic airport were also compared.

These clinical data were first obtained from the Department of Disease Control, Ministry of Public Health (https://covid19.ddc.moph.go.th/).

Data Analysis

A student's t-test was performed to compare viral concentration in wastewater from aircraft between two airports. Pearson's correlation analyses were used to correlate viral loads of aircraft wastewater from two airports, the number of COVID-19 positive individuals from abroad, and daily COVID-19 cases.

Results and Discussion:

All of the wastewater samples (n=56) from both international and domestic airports showed positive for RT-qPCR CDC N1 assay during the study periods. For the SARS-CoV-2 PCR assays, they were first developed against the E gene and N gene to detect the virus in patient samples and previous studies analyzing wastewater for SARS-CoV-2 surveillance [19,23,24]. Of the 28 samples from two airports' wastewater treatment plants, all samples were detectable for the N1 gene in this study. Whereas previous work on detecting SARS-CoV-2 RNA from aircraft wastewater demonstrated around 60% of the samples from Australia[26] and 13.6% of samples from Dubai[18] were positive, the present study has shown positive in all aircraft wastewater samples from both international and domestic airports with a high amount of viral copies. It may probably depend on the wastewater collection system and temporal variation of viral shedding[27] from the aircraft. If the wastewater from the aircraft which came directly from the passengers collected those samples, it would be more likely to have higher concentration and provide certain result for the surveillance. Remarkably, the viral concentration of the SARS-CoV-2 RNA was higher in the aircraft wastewater from both airports compared to the other sampling sites (Figure 1). In this study, the high viral copies of SARS-CoV-2 RNA in aircraft wastewater (267.84 to 6,874.79 copies/ml) and (164.57 to 10,986.71 copies/ml) were present in international and domestic airports, respectively (Figure 1). This finding may be explained by the idea that SARS-CoV-2 RNA could be detected in aircraft wastewater[17] and pointed as one of the critical sites for sample collection to trace the virus effectively.

In this study, SARS-CoV-2 RNA has been detected in all wastewater samples (100%) from the airports' wastewater treatment plants and aircraft. In wastewater surveillance, targeting confined sub-populations within high-risk facilities such as schools, dormitories, and nursing homes that entail frequent, prolonged close interactions between individuals has been shown to promote COVID-19 outbreaks[28,29,30]. Similar findings were reported that SARS-CoV-2 was detected in the target surveillance of hospitals (65.1%), university settings (27.7%), residential buildings (63.6%) and nursing homes (33.3%)[6]. This result highlights that little is known about the wastewater surveillance method, which could also be used at both sites to understand the viral trends at the airports; however, detecting SARS-CoV-2 RNA in wastewater could depend on factors for viral degradation such as viral shedding, duration, environmental factors and sewage system conditions[3].

Moreover, from April to June, there was no significant difference in mean viral gene copies of SARS-CoV-2 RNA of aircraft wastewater at both airports (Table 1). This may be due to the fact that there is dynamic air travel in both international and domestic travel. Starting from May, since there was no requirement for staying quarantined in Thailand, a lot of tourists came to Thailand and visited some famous destinations by domestic air travel. According to the data from AOT, Thailand, 41% and 76% of international aircraft movement increased from January to March and April to June, respectively. Likewise, 16% and 98% of domestic aircraft movement increased from January to March and April to June, respectively.

Interestingly, the viral gene copies of the SARS-CoV-2 RNA in aircraft wastewater were not much different in May and June; however, the daily COVID-19 cases in both months have vastly differed. This result suggests that this wastewater-based epidemiology method could also be used to indicate the viral trend of SARS-CoV-2 effectively, including

asymptomatic cases in both airports. In addition, some studies also reported that the high copies of the virus in wastewater might be related to asymptomatic cases and highlight the potential benefits of using wastewater surveillance as an early warning system[31].

Our data also agreed with the other studies that reported the positive correlation between the gene copies of the wastewater and the COVID-19 cases[32,33]. This study also found that the viral concentration of SARS-CoV-2 RNA in aircraft wastewater from international airports was correlated with a 7-days average number of SARS-CoV-2 infected persons from abroad (Figure 2a) by Pearson correlation analysis. Both were positively and significantly correlated at a 7-days lag (Pearson correlation = 0.984) from March 21 to May 5, 2022. However, there was no correlation between the aircraft wastewater from the domestic airport and the daily COVID-19 cases during this study (Figure 2b). Interestingly, the viral trends of the SARS-CoV-2 RNA of aircraft wastewater were similar to the clinical surveillance, which reflects that wastewater surveillance became essential to notice the viral circulation at the airports.

Nowadays, the Thailand government reduced the strict travel restriction for travelers at airports to welcome tourists back to come and visit Thailand. In addition, since the vaccinations are also improved more, there is unlikely to be an increase COVID-19 infection rate throughout the country. Nevertheless, the SARS-CoV-2 variant has many mutations, several of which are novel and a significant number of which affect the spike protein targeted by most COVID-19 vaccines at the time of discovering the Omicron variant[35]. This level of variation has led to concerns regarding its transmissibility, immune system evasion, and vaccine resistance. In addition, the variant makes concerns people about domestic infections of SARS-CoV-2 in a country. That is why monitoring SARS-CoV-2 should be done as routine testing in wastewater, particularly at airports and aircraft, which provides essential information such as early warning of COVID-19 waves to the public and the ministry of health.

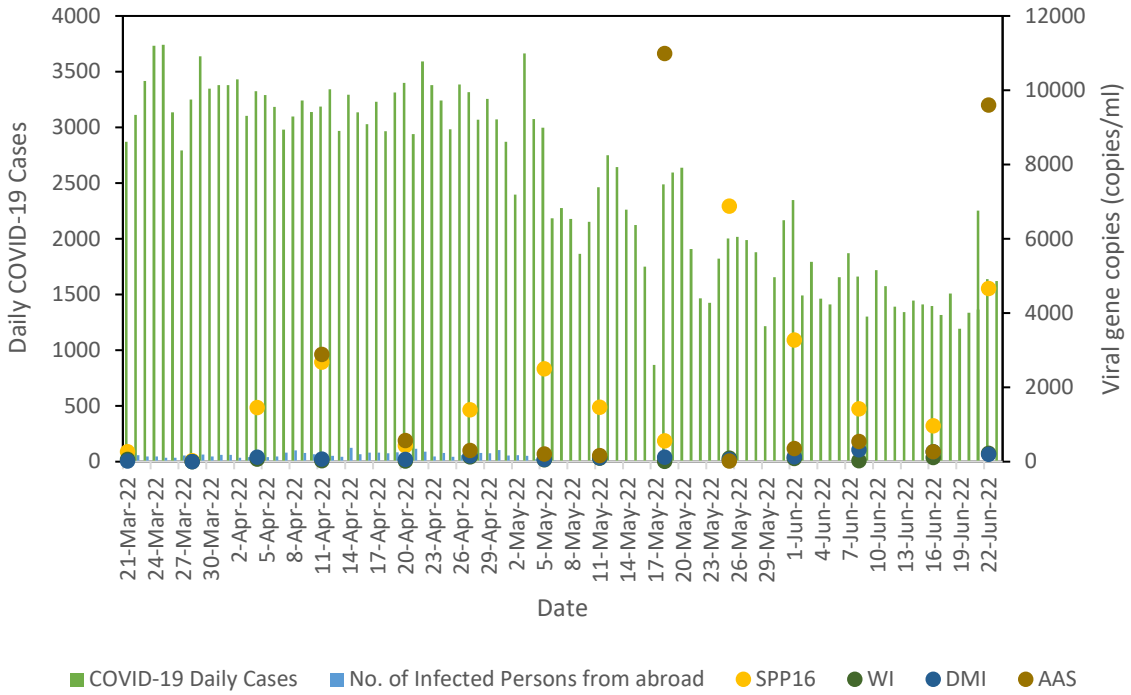

Figure 1.

The comparison between the SARS-CoV-2 RNA concentration in wastewater (copies/ml) from the aircraft and the airports' wastewater treatment plants (including daily COVID-19 cases and number of infected persons from abroad) from international and domestic airport. SPP16 and AAS refer to the aircraft wastewater from international and domestic airports, respectively. WI and DMI refer to the wastewater from international and domestic airports' wastewater treatment plants, respectively.

Table 1.
The mean viral gene copies of SARS-CoV-2 from aircraft wastewater of two airports and clinical COVID-19 Cases and that from abroad

Months	Mean viral copies (international) (copies/ml)[a]	Mean viral copies (domestic) (copies/ml)[a]	P (two tails)	Infected Persons from abroad	Daily COVID-19 Cases[c]
April	1493.084	1254.217	0.25	2,138	621,772
May	2850.405	2845.824	0.10	N/A	67,797
June	2582.302	2692.498	0.95	N/A	48,063

[a]Mean viral gene copies of SARS-CoV-2 RNA in aircraft wastewater in international and domestic airports
[b]Total number of infected persons from abroad per month [36]
[c]Total number of Daily COVID-19 cases per month [36]

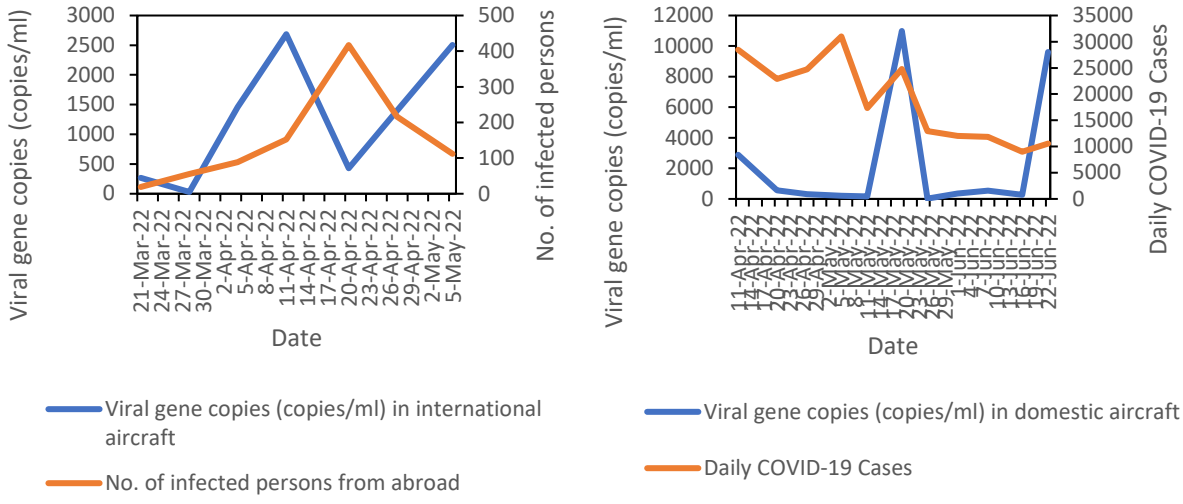

(a) **(b)**

Figure 2.
The comparison between the viral gene copies of the wastewater of total aircraft (copies/ml) (a), from the international airport and the number of infected persons from abroad (7-day lag) and (b), from the domestic airport and daily COVID-19 cases

Conclusion:

In the present study, the wastewater samples collected from the aircraft showed higher concentrations than those from the airports' wastewater treatment plants. Moreover, the international aircraft wastewater demonstrated that SARS-CoV-2 RNA concentration is

correlated with the number of COVID-19 infected persons from abroad. Our results suggest that the wastewater samples from the aircraft and airports' wastewater treatment plants are valuable sites for wastewater surveillance to monitor SARS-CoV-2 RNA circulations at the airports.

Acknowledgements:
This work was financially supported by the office of the Permanent Secretary, Ministry of Higher Education, Science, Research and Innovation (Grant No. RGNS-63-023), Kurita Overseas Research grant 2021 (Ref No. 21Pth012), Kurita Water and Environment Foundation, Japan, and Grants for Development of New Faculty Staff, Ratchadaphiseksomphot Endowment Fund, Chulalongkorn University, Thailand.

References:
1. Corman VM, Landt O, Kaiser M, et al. Detection of 2019 novel coronavirus (2019-nCoV) by real-time RT-PCR. *Euro Surveill* 2020;25:2000045.
2. Leung WK, To KF, Chan PK, et al. Enteric involvement of severe acute respiratory syndrome-associated coronavirus infection. *Gastroenterology* 2003;125:1011-1017.
3. Ahmed W, Bertsch PM, Bibby K, et al. Decay of SARS-CoV-2 and surrogate murine hepatitis virus RNA in untreated wastewater to inform application in wastewater-based epidemiology. *Environ Res* 2020;191:110092.
4. Maida CM, Amodio E, Mazzucco W, et al. Wastewater-based epidemiology for early warning of SARS-COV-2 circulation: A pilot study conducted in Sicily, Italy. *Int J Hyg Environ Health* 2022;242:113948.
5. Wannigama DL, Amarasiri M, Hurst C, et al. Tracking COVID-19 with wastewater to understand asymptomatic transmission. *Int J Infect Dis* 2021;108:296-299.
6. Shah S, Gwee SXW, Ng JQX, et al. Wastewater surveillance to infer COVID-19 transmission: A systematic review. *Sci Total Environ* 2022;804:150060.
7. Galani A, Aalizadeh R, Kostakis M, et al. SARS-CoV-2 wastewater surveillance data can predict hospitalizations and ICU admissions. *Sci Total Environ* 2022;804:150151.
8. Zhan Q, Babler KM, Sharkey ME, et al. Relationships between SARS-CoV-2 in Wastewater and COVID-19 Clinical Cases and Hospitalizations, with and without Normalization against Indicators of Human Waste. *ACS ES&T Water* 2022.
9. Sangsanont J, Rattanakul S, Kongprajug A, et al. SARS-CoV-2 RNA surveillance in large to small centralized wastewater treatment plants preceding the third COVID-19 resurgence in Bangkok, Thailand. *Sci Total Environ* 2022;809:151169.
10. D'Aoust PM, Graber TE, Mercier E, et al. Catching a resurgence: Increase in SARS-CoV-2 viral RNA identified in wastewater 48 h before COVID-19 clinical tests and 96 h before hospitalizations. *Science of The Total Environment* 2021;770:145319.
11. Huisman JS, Scire J, Caduff L, et al. Wastewater-Based Estimation of the Effective Reproductive Number of SARS-CoV-2
Environmental health perspectives 2022;130(5), 57011.
12. Betancourt WQ, Schmitz BW, Innes GK, et al. COVID-19 containment on a college campus via wastewater-based epidemiology, targeted clinical testing and an intervention. *Sci Total Environ* 2021;779,146408.
13. Hassard F, Lundy L, Singer AC, et al. Innovation in wastewater near-source tracking for rapid identification of COVID-19 in schools. *The Lancet Microbe* 2021;2:e4-e5.

14. Karthikeyan S, Ronquillo N, Belda-Ferre P, et al. High-Throughput Wastewater SARS-CoV-2 Detection Enables Forecasting of Community Infection Dynamics in San Diego County. *mSystems* 2021;6.
15. Spurbeck RR, Minard-Smith A, Catlin L. Feasibility of neighborhood and building scale wastewater-based genomic epidemiology for pathogen surveillance. *Sci Total Environ* 2021;789:147829.
16. Davo L, Segui R, Botija P, et al. Early detection of SARS-CoV-2 infection cases or outbreaks at nursing homes by targeted wastewater tracking. *Clin Microbiol Infect* 2021;27:1061-1063.
17. Ahmed W, Bertsch PM, Angel N, et al. Detection of SARS-CoV-2 RNA in commercial passenger aircraft and cruise ship wastewater: a surveillance tool for assessing the presence of COVID-19 infected travellers. *J Travel Med* 2020;27.
18. Albastaki A, Naji M, Lootah R, et al. First confirmed detection of SARS-COV-2 in untreated municipal and aircraft wastewater in Dubai, UAE: The use of wastewater based epidemiology as an early warning tool to monitor the prevalence of COVID-19. *Sci Total Environ* 2021;760:143350.
19. Ahmed W, Angel N, Edson J, et al. First confirmed detection of SARS-CoV-2 in untreated wastewater in Australia: A proof of concept for the wastewater surveillance of COVID-19 in the community. *Sci Total Environ* 2020;728:138764.
20. Ahmed W, Bertsch PM, Bivins A, et al. Comparison of virus concentration methods for the RT-qPCR-based recovery of murine hepatitis virus, a surrogate for SARS-CoV-2 from untreated wastewater. *Sci Total Environ* 2020;739:139960.
21. CDC. COVID-19: 2. Wastewater surveillance testing methods. 2021; https://www.cdc.gov/healthywater/surveillance/wastewater-surveillance/testing-methods.html Accessed December 10, 2021.
22. Kongprajug A, Mongkolsuk S, Sirikanchana K. CrAssphage as a Potential Human Sewage Marker for Microbial Source Tracking in Southeast Asia. *Environmental Science & Technology Letters* 2019;6:159-164.
23. Medema G, Heijnen L, Elsinga G, et al. Presence of SARS-Coronavirus-2 RNA in Sewage and Correlation with Reported COVID-19 Prevalence in the Early Stage of the Epidemic in The Netherlands. *Environmental Science & Technology Letters* 2020;7:511-516.
24. Wu Y, Guo C, Tang L, et al. Prolonged presence of SARS-CoV-2 viral RNA in faecal samples. *Lancet Gastroenterol Hepatol* 2020;5:434-435.
25. Herrera-Uribe J, Naylor P, Rajab E, et al. Long term detection and quantification of SARS-CoV-2 RNA in wastewater in Bahrain. *Journal of Hazardous Materials Advances* 2022;7:100082.
26. Ahmed W, Bivins A, Simpson SL, et al. Wastewater surveillance demonstrates high predictive value for COVID-19 infection on board repatriation flights to Australia. *Environ Int* 2022;158:106938.
27. Weidhaas J, Aanderud ZT, Roper DK, et al. Correlation of SARS-CoV-2 RNA in wastewater with COVID-19 disease burden in sewersheds. *Sci Total Environ* 2021;775:145790.
28. Daughton CG. Wastewater surveillance for population-wide Covid-19: The present and future. *Sci Total Environ* 2020;736:139631.
29. Koh D. Migrant workers and COVID-19. *Occup Environ Med* 2020;77:634-636.
30. Thompson DC, Barbu MG, Beiu C, et al. The Impact of COVID-19 Pandemic on Long-Term Care Facilities Worldwide: An Overview on International Issues. *Biomed Res Int* 2020;2020:8870249.

31. Gonçalves J, Koritnik T, Mioč V, et al. Detection of SARS-CoV-2 RNA in hospital wastewater from a low COVID-19 disease prevalence area. *Science of The Total Environment* 2021;755:143226.
32. Agrawal S, Orschler L, Lackner S. Long-term monitoring of SARS-CoV-2 RNA in wastewater of the Frankfurt metropolitan area in Southern Germany. *Scientific Reports* 2021;11:5372.
33. Mondal S, Feirer N, Brockman M, et al. A direct capture method for purification and detection of viral nucleic acid enables epidemiological surveillance of SARS-CoV-2. *Sci Total Environ* 2021;795:148834.
34. Xu Y, Li X, Zhu B, et al. Characteristics of pediatric SARS-CoV-2 infection and potential evidence for persistent fecal viral shedding. *Nat Med* 2020;26:502.
35. Torjesen I. Covid-19: Omicron may be more transmissible than other variants and partly resistant to existing vaccines, scientists fear. *BMJ* 2021;375:n2943.
36. Department of Disease Control MoPH, Thailand,. Daily COVID-19 Dashboard. 2022; https://ddc.moph.go.th/en/. Accessed March 1-June 22, 2022.

FACILE PREPARATION OF g-C_3N_4/$MgAl_2O_4$ NANOCOMPOSITE PHOTOCATALYST AND ENHANCED PHOTOCATALYTIC DEGRADATION

Worachita Wongtawee*, Pongsaton Amornpitoksuk, Sumetha Suwanboon
Division of Physical Science, Faculty of Science, Prince of Songkla University, Hat Yai, Songkhla, 90110 Thailand
*e-mail: worachita.mda@gmail.com

Abstract:

The pure $MgAl_2O_4$ spinel powder was synthesized by a co-precipitation method and the pure g-C_3N_4 was synthesized by a thermal decomposition method. The g-C_3N_4/$MgAl_2O_4$ nanocomposites were prepared by a grinding method for using as a photocatalyst in a photocatalysis process. The crystal structure and phase formation of the samples were characterized by X-ray diffractometry (XRD). The morphology of all samples was performed with scanning electron microscopy (SEM). The optical property of all samples was investigated by UV-Vis diffuse reflectance spectroscopy (DRS). The crystal structure of $MgAl_2O_4$ spinel powder unchanged when $MgAl_2O_4$ spinel powder was coupled with g-C_3N_4 powder. The g-C_3N_4/$MgAl_2O_4$ nanocomposite exhibited a cluster of agglomerated g-C_3N_4 and $MgAl_2O_4$ powders. The optical band gap energy of g-C_3N_4/$MgAl_2O_4$ nanocomposites decreased from 3.84 to 2.80 eV when the g-C_3N_4 increased from 0 to 25%. The photocatalytic degradation of MB solution increased when the g-C_3N_4 content increased. The highest photocatalytic degradation of about 83% over 25%g-C_3N_4/$MgAl_2O_4$ photocatalyst under UV irradiation was obtained in this study.

Introduction:

Dyes-contaminated wastewater from leather, printing and dyeing industries is a major environmental problem and it has been increasing exponentially due to it is difficult to degrade the dyes composition and ineffective wastewater treatment methods have been adopted.[1] Recently, dyes-contaminated wastewater was treated with several techniques such as adsorption, advanced oxidation processes, coagulation and membrane technology.[2] In recent years, photocatalysis, one of the advanced oxidation process, has been widely used to treat dyes-contaminated wastewater over other methods because it is a practical, environmentally-friendly, sustainable and affordable technique.[3]

Photocatalyst is one of an important parameter influencing the photocatalytic efficiency. Nowadays, the spinel powders such as $NiCo_2O_4$[4], $CuFe_2O_4$[5], $ZnCr_2O_4$[6], $CdCr_2O_4$[7], $ZnAl_2O_4$[8] and $MgAl_2O_4$[9] have been extensively used as a photocatalyst in a photocatalytic process in order to degrade the organic pollutants. Recently, $MgAl_2O_4$ spinel powder has been attracted attention, but it is greatly limited due to its wide band gap energy and low efficiency of charge carrier transfer.[10] Many researchers focused on this problem and they improved photocatalytic activity of $MgAl_2O_4$ powder by coupling with other compounds such as g-C_3N_4, CeO_2 and $Bi_7O_9I_3$.[9-12] Therefore, this research concentrated on the fabrication of g-C_3N_4/$MgAl_2O_4$ nanocomposite in order to use in degradation of methylene blue (MB) solution by photocatalytic test.

Methodology:

Preparation of $MgAl_2O_4$ spinel powder

In a typical procedure, 0.005 mol $Mg(NO_3)_2.6H_2O$ (Sigma-Aldrich) and 0.01 mol $Al(NO_3).9H_2O$ (Sigma-Aldrich) were dissolved in 100 mL distilled water under moderate

stirring. Then, the solution of 0.004 mol KOH (EMSURE) that dissolved in 100 mL distilled water was added dropwise to previous solution under continuous stirring. The white colloids formed and they were stirred at 70 ^{o}C for 1 h. The colloids were allowed to cool down to room temperature. The colloids were washed with RO water three times, filtered and dried at 80 ^{o}C in an oven overnight. The obtained powder was calcined at 800 ^{o}C for 1 h to produce the $MgAl_2O_4$ spinel powder.

Preparation of g-C_3N_4 powder

3 g of melamine were put in an alumina crucible and they were heated at 500 ^{o}C for 4 h. The obtained product was ground in an agate mortar to obtain g-C_3N_4 powder.

Preparation of g-C_3N_4/$MgAl_2O_4$ nanocomposite

A certain amount of g-C_3N_4 powder was mixed separately with $MgAl_2O_4$ spinel powder. Then, the mixed powders were ground for 15 min in an agate mortar to obtain g-C_3N_4/$MgAl_2O_4$ nanocomposites with different g-C_3N_4 contents.

Photocatalytic activity measurement

In this study, the photocatalytic activity of all samples was investigated through the degradation of MB solution. Briefly, 0.150 g of photocatalyst was dispersed in 150 mL of 1×10^{-5} M MB solutions. Before irradiation, suspension was kept in darkness for 30 min under continuous stirring to disperse the photocatalyst and achieve adsorption/desorption equilibrium. During photocatalytic testing, a 2 mL MB solutions were collected every 30 min and each soluton was centrifuged for 4 min with a speed of 4000 rpm to remove the photocatalyst. The absorbance of the supernatant was then measured by UV-Vis spectrophotometer (UV-Vis, Lambda25, PerkinElmer).

Characterization

Structural identification was performed with X-ray diffractometry (XRD, Empyrean, PANAlytical). Morphology of the samples was carried out on scanning electron microscopy (SEM, Quanta 400, FEI). UV-visible diffuse reflectance spectra were measured with UV-Vis diffuse reflectance spectrometer (DRS, UV2450, Shimadzu) using $BaSO_4$ as a reference.

Results and Discussion:

Structural investigation

The XRD technique was used to identify the crystal structure and phase formation. As shown in Figure 1, XRD pattern of $MgAl_2O_4$ powder was indexed to (111), (220), (311), (400), (551) and (440) planes, respectively. These peaks corresponded to the JCPDS card number 73-1959 and indicated a cubic structure. The XRD pattern of g-C_3N_4 powder was indexed to (100) and (002) planes, respectively. These two peaks corresponded to the JCPDS card number 87-1526.[9] For all g-C_3N_4/$MgAl_2O_4$ samples exhibited peaks of $MgAl_2O_4$ spinel powder as a major phase and peaks of g-C_3N_4 powder as a minor phase. The peak intensity of g-C_3N_4 of g-C_3N_4/$MgAl_2O_4$ samples increased as a function of g-C_3N_4 content. In this study, the peak positions of $MgAl_2O_4$ were unchanged, indicating that the crystal structure of $MgAl_2O_4$ was not deteriorated by g-C_3N_4.

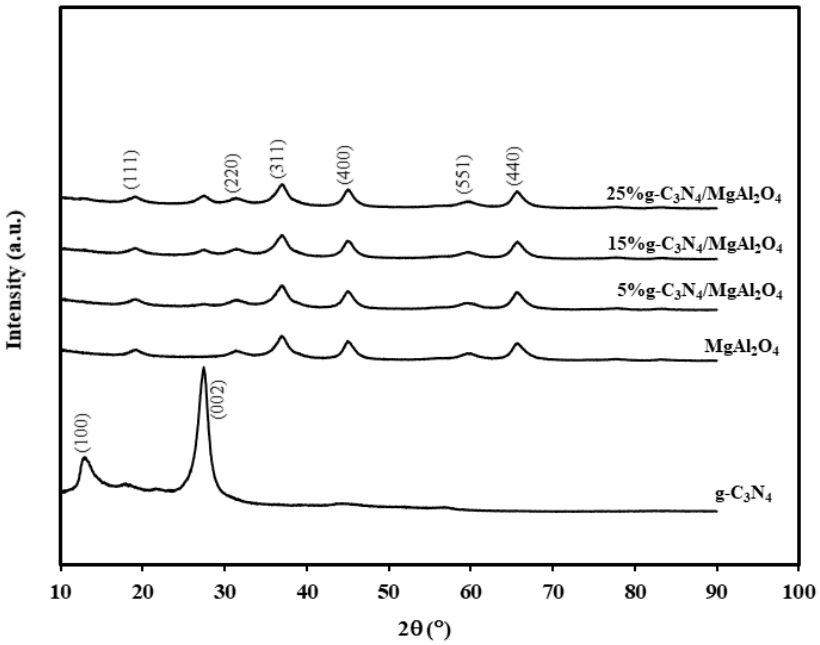

Figure 1.
XRD patterns of pure g-C_3N_4 powder, pure $MgAl_2O_4$ spinel powder and g-C_3N_4/$MgAl_2O_4$ nanocomposites at different g-C_3N_4 contents

Additionally, the morphology of pure g-C_3N_4 powder, pure $MgAl_2O_4$ spinel powder and g-C_3N_4/$MgAl_2O_4$ nanocomposite was studied by SEM and the results were shown in Figure 2. The g-C_3N_4 powder exhibited a dense agglomeration of layered structure. The $MgAl_2O_4$ spinel powder showed large clusters of agglomerated nanoparticles. All g-C_3N_4/$MgAl_2O_4$ nanocomposites showed an attachment of g-C_3N_4 on $MgAl_2O_4$ powders. This event could confirm a formation of nanocomposite between g-C_3N_4 and $MgAl_2O_4$ powders. The morphology of all g-C_3N_4/$MgAl_2O_4$ nanocomposites was similar.

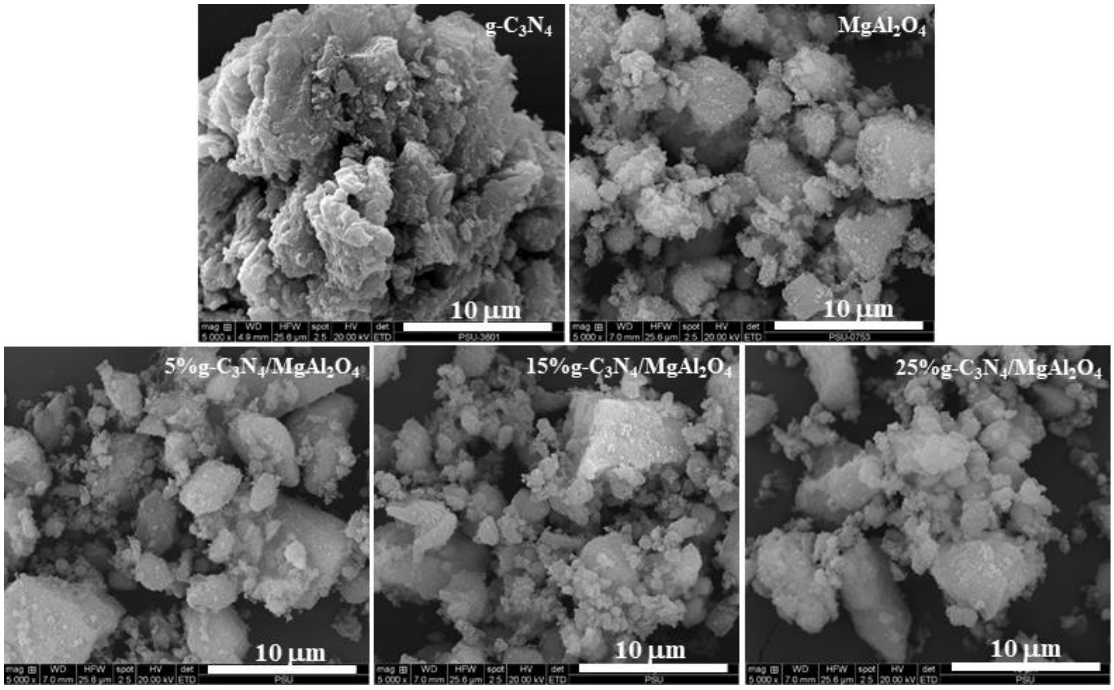

Figure 2.
SEM images of pure g-C_3N_4 powder, pure $MgAl_2O_4$ spinel powder and g-C_3N_4/$MgAl_2O_4$ nanocomposites at different g-C_3N_4 contents

Optical investigation

The optical property of pure g-C_3N_4 powder, pure $MgAl_2O_4$ spinel powder and g-C_3N_4/$MgAl_2O_4$ nanocomposites was investigated by DRS technique and the results were displayed in Figure 3.

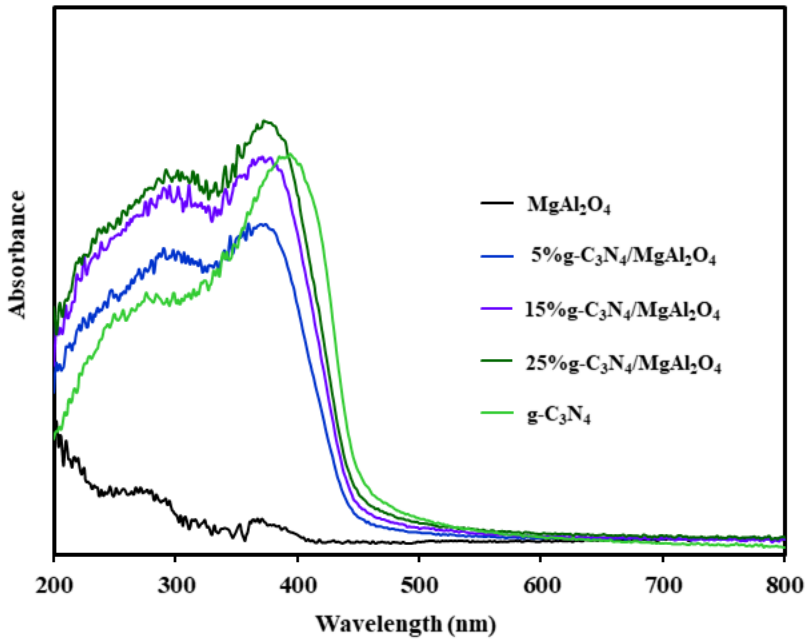

Figure 3.
DR spectra of pure g-C_3N_4 powder, pure $MgAl_2O_4$ spinel powder and g-C_3N_4/$MgAl_2O_4$ nanocomposites at different g-C_3N_4 contents

Considering the absorption spectra of all samples (Figure 3), it was found that the absorption edge of $MgAl_2O_4$ spinel powder was in UV region whereas the absorption edge of g-C_3N_4 powder was in visible region. The absorption edge of g-C_3N_4/$MgAl_2O_4$ nanocomposites was in visible region and it shifted to long wavelength when the g-C_3N_4 content increased. Moreover, the g-C_3N_4/$MgAl_2O_4$ nanocomposites exhibited higher absorption intensity at larger g-C_3N_4 content. This behavior could enhance the photocatalytic degradation of MB solution. The optical band gap energy of all samples was estimated using Tauc's formula as shown in equation (1).[9]

$$(\alpha E)^2 = A(E-E_g) \qquad (1)$$

where α is the absorption coefficient, E is the photon energy, A is a constant and E_g is the optical band gap energy. The absorption coefficient can be calculated by equation (2).[9]

$$\alpha = A/d \qquad (2)$$

where A is absorbance and d is the thickness (0.4 cm). The optical band gap energy can be approximated from the extrapolated linear parts of the Tauc plots as shown in Figure 4.

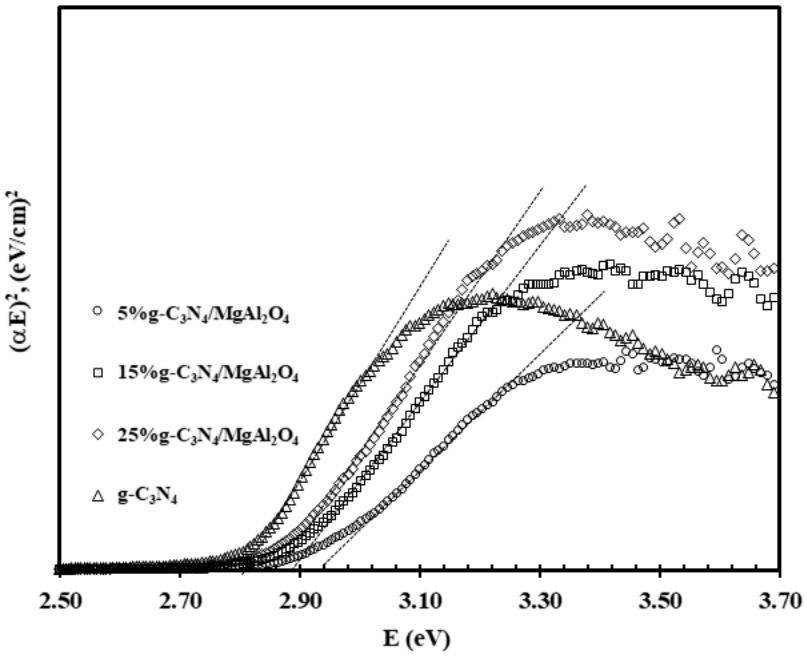

Figure 4.
Plot of $(\alpha E)^2$ versus E for evaluating E_g value of pure g-C_3N_4 powder and g-C_3N_4/$MgAl_2O_4$ nanocomposites at different g-C_3N_4 contents

The optical band gap energy of pure $MgAl_2O_4$ and pure g-C_3N_4 powder was 3.84 and 2.80 eV, respectively whereas the optical band gap energies of g-C_3N_4/$MgAl_2O_4$ nanocomposites were 2.92, 2.88 and 2.80 eV, respectively when the g-C_3N_4 content increased from 5-25%. In this study, it was found that the optical band gap energy of g-C_3N_4/$MgAl_2O_4$ decreased as a function of g-C_3N_4 content. The decrease in optical band gap energy of g-

$C_3N_4/MgAl_2O_4$ nanocomposites was due to formation of heterostructure between g-C_3N_4 and $MgAl_2O_4$ as occurred in a TiO_2@g-C_3N_4 composite.[13] In this study, the particle size of all g-$C_3N_4/MgAl_2O_4$ nanocomposites was similar. Therefore, the effect of particle size on optical band gap energy was ignored.

Photocatalytic activity investigation

The photocatalytic activity over pure $MgAl_2O_4$, pure g-C_3N_4 and all g-$C_3N_4/MgAl_2O_4$ nanocomposite photocatalysts was determined using MB solution as a dye model. The percentage of photocatalytic degradation was calculated using equation (3).[9]

$$\text{Photocatalytic degradation (\%)} = [(A_0-A_t)/A_0]\times 100 = [(C_0-C_t)/C_0]\times 100 \qquad (3)$$

where A_0 is the absorbance of MB solution before irradiation, A_t is the absorbance of MB solution after irradiation for time t, C_0 is the concentration of MB solution before irradiation and C_t is the concentration of MB solution after irradiation for time t. As shown in Figure 5, the photocatalytic degradation of MB solution over g-$C_3N_4/MgAl_2O_4$ nanocomposites increased as a function of g-C_3N_4 content. This event can be explained by a reduction in E_g value of g-$C_3N_4/MgAl_2O_4$ nanocomposites. When the E_g value decreased the electron in valence band can be excited to conduction band increasingly, giving rise to an improvement in photocatalytic degradation. Moreover, the photocatalytic degradation of MB solution was improved by synergistic effect between $MgAl_2O_4$ and g-C_3N_4.[9]

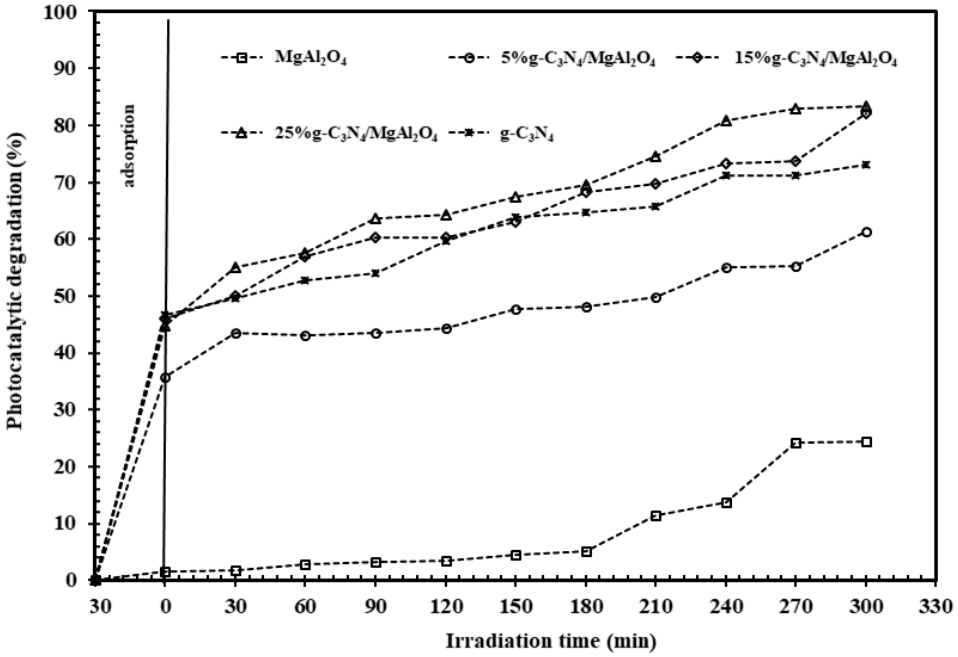

Figure 5.
Photocatalytic degradation of MB solution over pure $MgAl_2O_4$ spinel powder, pure g-C_3N_4 powder and g-$C_3N_4/MgAl_2O_4$ nanocomposites at different g-C_3N_4 contents

The possible mechanism for photocatalytic degradation of MB solution was presented in reaction (4-8).[9]

$$g\text{-}C_3N_4/MgAl_2O_4 + h\nu \longrightarrow g\text{-}C_3N_4/MgAl_2O_4(e^-) + g\text{-}C_3N_4/MgAl_2O_4(h^+) \qquad (4)$$

$$O_2 + e^- \longrightarrow {}^{\bullet}O_2^- \qquad (5)$$

$h^+ + OH^- \longrightarrow {}^{\bullet}OH$ (6)

$h^+ + H_2O \longrightarrow {}^{\bullet}OH + H^+$ (7)

MB + $^{\bullet}O_2^-$ / $^{\bullet}OH$ ⟶ degradation products (8)

Conclusion:

In summary, $MgAl_2O_4$ spinel powder was synthesized by a co-precipitation method, graphitic carbon nitride (g-C_3N_4) powder was prepared by a thermal decomposition and g-C_3N_4/$MgAl_2O_4$ nanocomposites were prepared by a grinding method. The photocatalytic activity of MB solution under UV irradiation over g-C_3N_4/$MgAl_2O_4$ nanocomposites was improved. The enhanced photocatalytic activity of g-C_3N_4/$MgAl_2O_4$ nanocomposites could be ascribed to the synergistic effect between $MgAl_2O_4$ and g-C_3N_4 powders. The synergistic effect can reduce the recombination rate of photo-excited electron-hole pairs and the 25%g-C_3N_4/$MgAl_2O_4$ nanocomposite photocatalyst provided the best photocatalytic activity.

Acknowledgements:

This research was supported by the National Science, Research and Innovation Fund (NSRF) and Prince of Songkla University (Grant No. TAE6505097M, TAE6505097b). W. Wongtawee wishes to thank the Development and Promotion of Science and Technology Talents Project (DPST) for the scholarship.

References:

1. Jiaojiao L, Zhanzhou L, Jiaojiao L, Ping L. Mater. Sci. Semi. Proc. 2018; 87: 24-31.
2. Rania E, Hanaa S, Zakaria K, Ahmed HM, Sadeek AS, Sharaa SI, Patrice R, Nada A. Environ. Tech. 2021; 23: 101710.
3. Zhang F, Wang X, Liu C, Wan Y, Long Y, Cai Z, Appl Sci. 2019; 9:2489.
4. Imranullah M, Hussain T, Ahmad R, Hwang JS, Ahmad S, Shakir I, Kang DJ. J. Mater. Res. Technol. 2021; 15: 623-632.
5. Keerthana SP, Yuvakkumar R, Ravi G, Pavithra S, Thambidurai M, Dang C, Velauthapillai D. Environ. Res. 2021; 200: 111528.
6. Palanisamy G, Pazhanivel T, Bhuvaneswari K, Bharathi G, Marimuthu G, Maiyalagan T. Colloids Surf. A. 2020; 590: 124505.
7. Abbasi A, Khojasteh H, Hamadanian M, Salavati-Niasari M. Sep. Purif. Technol. 2018; 195: 37-49.
8. Suwanboon S, Amornpitoksuk P, Rattana T, Randorn C. Ceram. Int. 2020; 46: 21958-21977.
9. Wongtawee W, Amornpitoksuk P, Randorn C, Rattana T, Suwanboon S. J. Indian Chem. Soc. 2022; 9: 100628.
10. Asl EA, Haghighi M, Talati A. Sol. Energy. 2019; 184: 426-439.
11. Li J, Wang S, Sun G, Gao H, Yu X, Tang S, Zhao X, Yi Z, Wang Y. Mater. Tod. Chem. 2021; 19: 100390.
12. Wang S, Gao H, Li J, Wang Y, Chen C, Yu X, Tang S, Zhao X, Sun G, Li D. J. Phys. Chem. Solid. 2021; 150: 109891
13. Toghan A, El-Lateef HMA, Taha KK, Modwi A. Diam. Relat. Mater. 2021; 118:108491.

DETERIORATION OF PALM-BASED BIOTRANSFORMER UNDER THERMAL AGING

Pornpong Siriratsakul,[1] Boonyawan Yoosuk,[2] Napida Hinchiranan [3,4,5*]
[1]Program in Petrochemistry and Polymer Science, Faculty of Science, Chulalongkorn University, Bangkok, Thailand
[2]National Energy Technology Center (ENTEC), Thailand Science Park, Pathumthani, Thailand
[3]Department of Chemical Technology, Faculty of Science, Chulalongkorn University, Bangkok, Thailand
[4]Center of Excellence on Petrochemical and Materials Technology (PETROMAT), Chulalongkorn University, Bangkok, Thailand
[5]Center of Excellence in Catalysis for Bioenergy and Renewable Chemicals (CBRC), Chulalongkorn University, Bangkok, Thailand
*e-mail: napida.n@chula.ac.th, pornpong45@gmail.com

Abstract:
Mineral oil, one of necessary components in an electrical transformer, is used as an insulating liquid and cooling medium. However, it is non-biodegradable, which can the adverse impact on the environment when it is spilled. Currently, there are many attempts to develop vegetable oils having biodegradability and non-toxicity to replace the use of the material oil. Palm-based oil is a good alternative insulating liquid for using as the transformer oil. However, the deterioration of palm oil for long-period aging during operation of the electrical transformer is the aim of this research. The characteristic deterioration of palm-based oil was monitored and compared to the mineral oil and a commercial natural ester (FR3) under thermal aging at 130˚C for 30 and 84 days. Before testing, palm oil was treated by removing moisture, reducing acidity, filling the additives, and it was called as ENPAT. It was observed that the moisture content, acidity, and dissolved decay content of aged ENPAT tended to be increased, which were similar to those of FR3, but the magnitude of these properties were less. Although the dielectric dissipation factor and resistivity of ENPAT were lower than those of mineral oil, the dielectric breakdown voltage of ENPAT was higher than that of the mineral oil and FR3.

Introduction:

The transformer is one of important pieces used for electric power transmission and distribution systems over a long distance[1]. The insulation system in the transformer is consisted of oil and insulating papers, which involve the performance of the transformers. Generally, the transformer is operated under thermal, electromechanical, and chemical stresses. Especially, thermal stress is a major cause for oil to lose insulation properties. Simultaneously, the degradation of the insulating paper affects the performance of the transformer by reducing its lifetime[2]. At present, mineral oil is used as the insulating oil for transformers because it has a low cost, good electrical properties, and good thermal stability. However, it has some drawbacks to adversely affect the environment due to its non-biodegradable property when it is leaked resulting the contamination in soil and river, which is dangerous for surrounding humans and animals existence. Thus, the natural oils derived from plants have potential to replace the mineral oil for using in the electrical transformer because it is eco-friendly, with high moisture tolerance, non-toxicity, and biodegradability.

Moreover, flash point and fire point of the plant oils are higher than 300˚C[3]. Therefore, it is safe and prevents fire during transformer.

Generally, vegetable oils or natural esters extracted from seeds and kernel of the plants i.e., soybeans, palm, rapeseed, and sunflower are consisted of triglycerides, which can be decomposed as glycerol and fatty acids. The fatty acids can be applied for synthesis of natural esters. However, its higher viscosity and pour point than those of mineral oil limit its application as the transformer oil. Hence, the improvement to achieve the desired properties for applying as the transformer oil is required. Nowadays, the natural esters under the trade name of Envirotemp FR3 is developed and commercialized by Cooper Power Systems. It is produced from soybeans filled with additives to improve its performance[4]. Apart from the natural esters, palm-based oil is another type of the vegetable oil that can be applied as the insulating oil for the transformers. The abundant of palm oil in Thailand is attractive for developing as the bio-transformer oil. However, the properties of the palm oil-based biotransformer oil after thermal aging for the given period are necessary for predicting its lifetime. Thus, this research work aimed to comparatively investigate the deterioration characteristics of the mineral oil, FR3, and palm oil-based biotransformer oil.

Methodology:

The procedure to test the thermal deterioration of each oil was consisted of 3 steps: pretreatment, thermal aging process, and properties measurement.

For the pretreatment step for the moisture removal, the silicon steel strip and copper strip were treated by heating at 105 ˚C for 24 h in a vacuum oven at 20 mbars. This condition was also applied for treating the insulating papers (0.13 mm., 0.18 mm., 0.18 mm. (diamond dot), and 0.5 mm. of thickness) for a long time to 48 h. The moisture in the treated insulating papers was controlled to achieve not over than 0.5 wt% according to IEEE C.57-100 before testing. Whereas, the pretreatment of the studied insulating liquids (MO, FR3, and ENPAT) were operated under vacuum at 50 ˚C for 48 h. The mineral oil and FR3 were received from Charoenchai Transformer Co., Ltd. (Bangkok, Thailand). For ENPAT sample, it was derived from palm oil, which was pretreated before use in order to remove moisture, decrease acidity and fill some additives. ENPAT was manufactured by National Energy Technology Center (Entec), National Science and Technology Development Agency (NSTDA, Pathumthani, Thailand)

For the procedure of the thermal aging process, the pretreated the silicon steel strip, copper strip, and insulating papers were immersed in each oil (mineral oil, FR3, and ENPAT). The proportion of the oil volume: paper volume: surface area of silicon steel: surface area of copper was controlled at 200 cm^3: 11.2 cm^3: 582.5 cm^2: 164.3 cm^2. When all components were loaded into the stainless steel cylinder reactor (2 L), they were heated at 50 ˚C for 24 h and then purged by nitrogen gas. This reactor was then placed in the oven at 130 ˚C for conducting thermal aging process for the given time (720 h and 2,016 h).

The properties of the aged oils were measured in terms of physical properties such as color (ASTM D1500), and viscosity (ASTM D445), chemical properties such as moisture content (ASTM D1533) acidity (ASTM D974), and dissolve decay content (ASTM D6802) and electrical properties such as dielectric breakdown voltage (IEC 60156), dielectric dissipation factor (IEC 60247), and resistivity (IEC 60247).

Results and Discussion:

Table 1 shows the physical, chemical, and electrical properties of oils analyzed following international standards for transformer oil. It was observed that the most properties of ENPAT could achieve the values according to the transformer oil standards. Therefore, the ENPAT had potential for using as the bio-transformer oil. Moreover, the water content and

acidity of ENPAT were lower than that of FR3, whereas the water content and acidity of the mineral oil were the lowest in all oils. However, the dielectric breakdown voltage of ENPAT and FR3 was higher than that of mineral oil. Whereas, the dielectric dissipation factor of that mineral oil was lower than that of FR3 and ENPAT.

Table 1.
The properties comparison of mineral oil, FR3, and ENPAT

Properties	Unit	Standard test methods	Limitation		MO	FR3	ENPAT
			ASTM D6871	IEC 62770			
Physical properties							
Color	-	ASTM D1500	≤ 1	-	< 0.5	< 0.5	1
Viscosity at 40 °C	mm^2/s	ASTM D445	≤ 50	-	8.1	32-33	40-41
Visual Examination	-	ASTM D1524	bright clear	-	bright clear	clear light green	clear yellow
Electrical properties							
Dielectric Breakdown: 2.5 mm gap	kV	IEC 60156	-	≥ 35	67.9	> 100	> 100
Dissipation Factor: 90°C	-	IEC 60247	-	≤ 0.05	0.69×10^{-3}	3.32×10^{-3}	16.6×10^{-3}
Chemical properties							
Water content	ppm	ASTM D1533	≤ 200	-	10	38	28
Acidity	mg•KOH/g	ASTM D974	≤ 0.06	-	0.009	0.029	0.021

The color of the insulating oils is the simple indicator to exhibit the degree of deterioration during accelerated thermal aging[5]. Table 2 shows the color change of mineral oil, FR3, and ENPAT aged at 130 ˚C at different aging time. Before aging, the color of the oils was bright and clear. After thermal aging, the color of all oils was changed to be darker because the oxidation of the insulating oils at high temperatures produced acidic products[6] and they were also contaminated by some chemical generated from the degradation of insulating papers.

Table 2.
The color change of oils before and after thermal aging at 130 ˚C for 30 and 84 days.

Types of oil	Before aging	Aging at 130˚C for	
		30 days	84 days
Mineral oil			
FR3			
ENPAT			

The viscosity, moisture content, and acidity of the insulating oils used in this experiment are shown in Table 3. The viscosity of mineral oil, FR3, and ENPAT remained constant throughout thermal aging. The viscosity of the mineral oil was in the range of 8.12-8.22 cSt, while the viscosity of FR3 and ENPAT was higher to the level of 32.3-32.6 and 40.6-41.1 cSt, respectively. Moreover, It was observed the viscosity of ENPAT was the highest than all oils due to the ENPAT contained to high content of saturated fatty acids[7]. However, the moisture content in all insulating oils was changed after thermal aging because

the water was a by-product released from the oxidation of insulating oil and the decomposition of the insulating paper[5]. It was noticed that the moisture content of FR3 and ENPAT decreased after aging for 84 days due to the effect to hydrolysis that consumed water to produce glycerol and fatty acids. Moreover, the acidity of aged oils significantly increased. The acidity of the aged mineral oil was 0.2-0.3 mg•KOH/g, which was less than that of aged FR3 and aged ENPAT having acidity in the range of 1.0-4.0 mg•KOH/g because those acids in the aged mineral oil had low molecular weight acids whereas, were generated by the oxidation and the degradation of insulating paper[8], whereas the acids of aged FR3 and aged ENPAT had high molecular weight acids. They were by oxidation and hydrolysis process. As a result, the lower acidity of age mineral oil than aged FR3 and aged ENPAT after aging.

Table 3.
The physical and chemical properties of oils before and after thermal aging at 130 ˚C for 30 and 84 days.

Samples	Viscosity (cSt)			Moisture content (ppm)			Acidity (mg•KOH/g)		
	Before aging	After aging		Before aging	After aging		Before aging	After aging	
		30 days	84 days		30 days	84 days		30 days	84 days
Mineral oil	8.22	8.20	8.12	13.2	18.6	29.9	0.009	0.260	0.241
FR3	32.6	32.3	32.6	37.8	108.9	73.2	0.029	1.094	3.777
ENPAT	40.7	40.6	41.1	28.2	124.8	33.2	0.021	0.996	2.836

The dissolved decay content is the by-products generated by the oxidation of the insulating oils. It was consisted of peroxides, aldehydes, ketones, and organic acids. These compounds could be absorbed by the insulating papers and caused the transformers to prematurely deteriorate[9]. After thermal aging, the dissolved decay content in all aged oils increased over aging period as shown in Table 4. Before aging, it was noticed the dissolved decay content in ENPAT was the highest of all oils due to the composition and the additive was filled in ENPAT that affected to the dissolved decay product was high value. However, the magnitude of dissolved decay content in aged ENPAT increased by 26.3% and 40.1%, which was less than that of aged mineral oil and aged FR3 after aging for 30 and 84 days because the ENPAT filled additive compound for enhance the oxidation stability. Therefore, the dissolved decay content in aged ENPAT was slightly increased.

Table 4.
The dissolved decay content in the oils before and after thermal aging at 130 ˚C for 30 and 84 days.

Samples	Dissolved decay content (a.u.)		
	Before aging	Aging at 130˚C for	
		30 days	84 days
Mineral oil	6.65	17.4 (161.7%)*	41.2 (519.5%)
FR3	24.0	83.6 (248.3%)	94.8 (295.0%)
ENPAT	128.3	162.1 (26.3%)	179.8 (40.1%)

* The value appeared in parentheses was the percentage of the change in the the dissolved decay content after thermal aging.

The dielectric breakdown voltage indicates the ability of insulating oil to withstand the electrical stress[10]. Figure 1a showed that, the dielectric breakdown voltage of the aged oils lower than that of the pristine ones due to the effect of contaminants generated during the thermal aging such as moisture, conductive particles, and acid by-products. However, the dielectric breakdown voltage of aged FR3 and aged ENPAT was still in the level of 55-80 kV, whereas this value for the aged mineral oil was dropped to 40-50 kV. Furthermore, the

dielectric breakdown voltage of both mineral oil and aged mineral oil was lower than those of FR3 and ENPAT before and after thermal aging because the mineral oil contained hydrocarbons, which were nonpolar, whereas water was polar. As a result, the mineral oil was vulnerable to changes in water level. Therefore, the dielectric breakdown voltage of the mineral oil was lower. The dielectric dissipation factor represents the quality and electrical loss of the insulating oils. From Figure 1b, it can be seen that the dielectric dissipation factor of the oils increased after thermal aging; especially, the dielectric dissipation factor of FR3 and ENPAT due to the formations of water, carbon black, and conductive particles dissolved in the oils[11]. This result was consistent to the higher resistivity as shown in Figure 1c. This was positive for applying in the transformer requiring the insulating oils having high resistivity[12]. It can be seen that the resistivity of oils gradually decreased during aging periods as shown in Figure 1c due to the formation of by-products that would encourage the conduction of insulating oil. However, the resistivity of aged mineral oil has still more than the fresh FR3 and ENPAT.

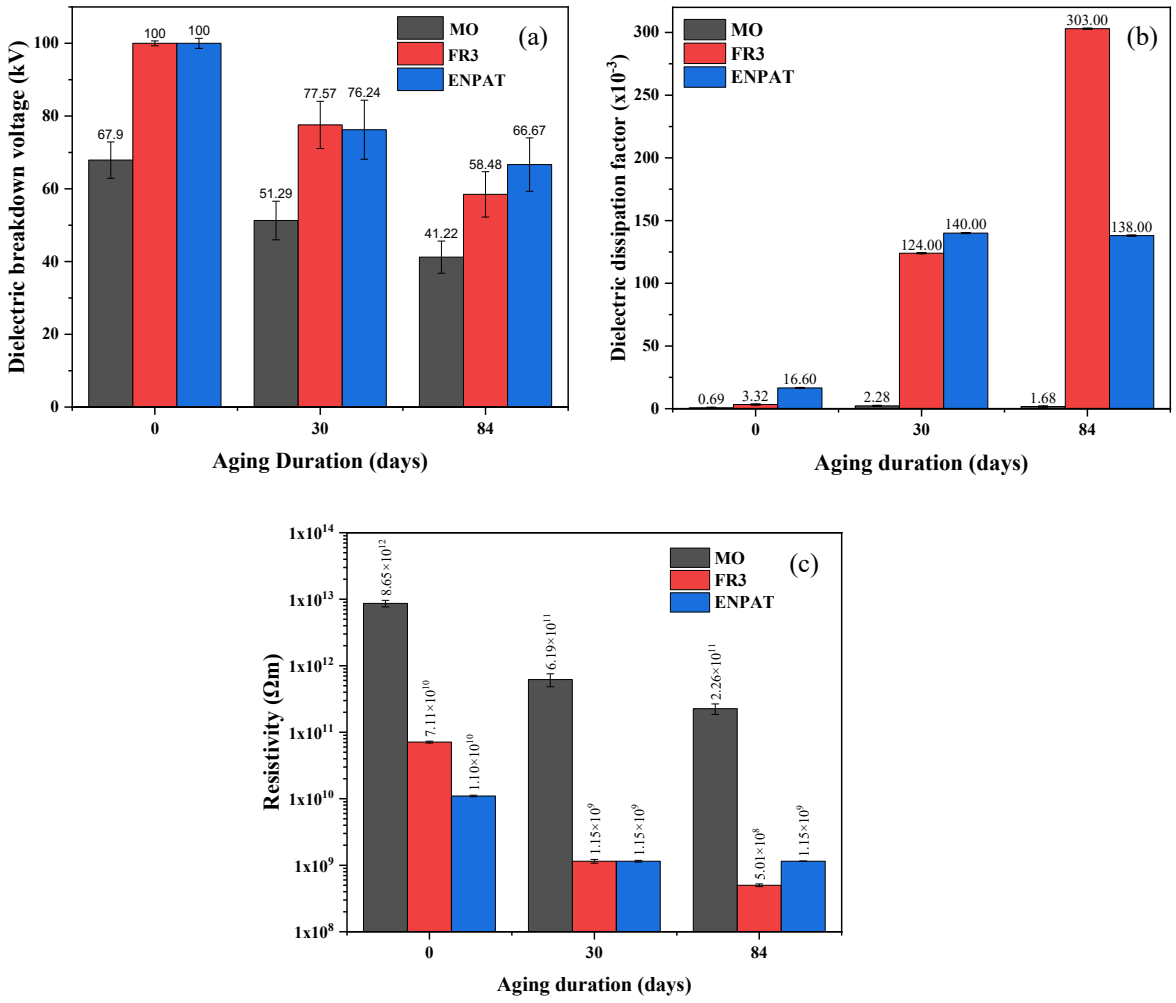

Figure 1.
Electrical properties of oils after thermal aging at 130˚C for 30 and 84 days:
(a) dielectric breakdown voltage, (b) dielectric dissipation factor and (c) resistivity.

Conclusion:

The characteristics of palm-based biotransformer oil (ENPAT) deteriorated under thermal aging at 130 ˚C for 30 and 84 days were investigated and compared to the mineral oil and natural ester (FR3). After thermal aging, the color of ENPAT becomes darker, but the moisture content and acidity of ENPAT were less than those of FR3. However, those properties were higher than those of mineral oil. The dissolved decay content generated from thermal aging of ENPAT was less than that obtained from the thermal aging of FR3 and mineral oil. Moreover, the ENPAT had the highest dielectric breakdown voltage. However, the dielectric dissipation factor and resistivity of ENPAT were lower than those of the mineral oil.

Acknowledgements:

The authors gratefully acknowledge the support of the National Energy Technology Center (ENTEC) through " P2150939 " project for providing materials and facilities to perform the experiments in this research.

References:

1. Coulibaly ML, Perrier C, Marugan M, Beroual A. IEEE Trans. Dielectr. Electr. Insul. 2013;20:1971-1976.
2. Mirzaie M, Gholami A, Tayebi HR. Turk. J. Electr. Eng. Comput. Sci. 2009;17:39-54
3. Srivastava M, Goyal SK, Saraswat A. Mater. Today: Proc. 2021;43:2850-2854
4. Tenbohlen S, Koch M. IEEE Trans. Power Deliv. 2010;25:825-830
5. Singha S, Asano R, Frimpong G, Claiborne CC, Cherry D. IEEE Trans. Dielectr. Electr. Insul. 2014;21:149-158
6. Abdi S, Boubakeur A, Haddad A, Harid N. Electr. Power Compon. Syst. 2011;39:1701:1711
7. Fernandez I, Ortiz A, Delgado F, Renedo C, Perez S. Electr. Power Syst. Res. 2013;98:58-69
8. Munster T, Werle P, Hamel K, Preusel J. Energies. 2021;14:3036
9. Ridzuan NLM, Bakar NA, Ghani SA, Chairul, IS, Aziz, NHA. Bull. Electr. Eng. Inform. 2019;8:735-743
10. Choi SH, Huh CS. Trans. Korean Inst. Electr. Eng. 2011;60:984-989
11. Trnka P, Hornak J, Prosr P, Michal O, Wang F. IEEE Access. 2020;8:61989-61998
12. Rafiq M, Shafique M, Azam A, Ateeq M, Khan IA, Hussain A. Molecules. 2020;25:3901

Session F:
FOOD SCIENCE AND TECHNOLOGY/ AGRICULTURAL SCIENCE/ (SEA) FOOD INNOVATION/ FOOD SAFETY AND PACKAGING

EFFECT OF ESSENTIAL OILS ON QUALITY AND VOLATILE COMPOSITION OF STERILIZED SMOKED MEAT (SE'I SAPI)

Ulil Afidah,[1] Safna Fauziah,[2] Thanakorn Wongprasert,[1] Pakavit Mathatheeranan,[1] Andi Febrisiantosa,[3] Endy Triyannanto,[2] Inthawoot Suppavorasatit [1,4,*]

[1] Department of Food Technology, Faculty of Science, Chulalongkorn University, Bangkok 10330, Thailand
[2] Departement of Animal Product Technology, Faculty of Animal Science, Universitas Gadjah Mada, Sleman, Daerah Istimewa Yogyakarta 55288, Indonesia
[3] National Research and Innovation Agency, Playen, Gunungkidul, Daerah Istimewa Yogyakarta 55288, Indonesia
[4] Special Task Force for Activating Research (STAR) in Flavor Science, Chulalongkorn University, Phayatai Road, Wangmai, Pathumwan, Bangkok 10330, Thailand
*E-mail: inthawoot.s@chula.ac.th

Abstract:

Indonesian smoked meat (se'i sapi) is one of traditional meat products that is normally degraded by both microorganisms and lipid oxidation. The aim of this study was to determine the effect of essential oils on quality and volatile compounds composition of sterilized se'i sapi. The se'i sapi was produced with the addition of 1000 ppm of cinnamon or nutmeg essential oil. The pH, color, water holding capacity (WHC), textural properties and volatile composition of essential oil treated samples were evaluated. From the study, it was found that addition of cinnamon or nutmeg oil did not affect pH, water holding capacity (WHC), moisture content, color, and texture of the se'i sapi samples. In addition, the volatile profiles of the samples evaluated by SPME/GC-MS were different among samples. It was found that pentadecanal, terpinen-4-ol, α-terpineol, 2,3-butanediol, and safrole were major compounds found in nutmeg oil treated sample. While, benzaldehyde, pentadecanal, eugenol, 1-methylindole, and caryophyllene were major compounds in cinnamon essential oil treated sample. It can be implied that the application of cinnamon or nutmeg oil help in providing the character aroma in each essential oil treated se'i sapi. Among more than twenty volatile compounds identified in nutmeg or cinnamon oil treated sample, methyl euganol and benzaldehyde were considered as the most impact odor-active compounds, which odor activity values (OAVs) of each sample were 97.85 and 69.65, respectively. In conclusion, the selected essential oils affected volatile aroma of se'i sapi samples.

Keyword: smoked meat, essential oil, cinnamon, nutmeg, volatile compounds

Introduction:

The global consumption of meat and meat products are increasing, which driven by population growth. [1] It might be due to its benefits to human body as primary source of proteins and essential amino acids. The main characteristics of meat and meat products are greatly considered by processing techniques such as smoking and sterilizing processes, the size of the meat, and the spices used in the process.[2] All of these could be factors that contribute to the quality of the processed meat products.[3] Moreover, Bosco et al. [4] stated that methods involved in the cooking process can also influence the quality of meat and meat products.

The se'i sapi is a smoked meat product originally from East Nusa Tenggara, Indonesia, specifically in the Rote Ndao district, traditionally cooked by smoking process.[5] In general, smoking process to make se'i sapi uses Kosambi wood as a fuel and utilizing the leaves to hold the heat.[6] This specific type of wood and leaves make a characteristic aroma and flavor of se'i sapi. However, too strong smoky aroma by smoking process or adding liquid smoke flavor in the product may affect consumers' acceptance. Therefore, adding aroma from other sources, such as essential oils, would help in lowering the power of smoky aroma while consuming the product. Essential oils contain volatile compounds that play an important role to improve product's aroma since they contain groups of compounds, including terpenes, aldehydes, organic acids, lactones, esters, furans, hydrocarbons and ketones.[7,8] In addition, the essential oil contains phenolic substances that can prevent the changes of the meat product due to the lipid oxidation processes during storage, especially in sterilized meat products.

Cinnamon (*Cinnamomum cassia*) is an evergreen tree under the Lauraceae family.[9] Cinnamon oils contains important compounds including cinnamic acid, cinnamaldehyde, coumarin, and cinnamyl alcohol.[10] Normally, cinnamon is applied to foods as a condiment, flavoring, and spice.[11] Another spice that usually used in meat product is nutmeg (*Myristica fragrans* Houtt). The nutmeg is usually used for medicinal and spice purposes.[12] Nutmeg composed of volatile oil (5-15%) which contains safrole, eugenol, isoeugenol, elemicin and myristin.[13] Adding cinnamon or nutmeg essential oils may give specific characters to the meat products due to the volatile aroma compounds containing in the oils. In addition, during sterilization might cause the changes of volatile aroma profiles in the products due to the high temperature and pressure conditions.

Up to now, available information on se'i sapi only refers to liquid smoke that is used as an alternative of smoking process. The information associated with essential oils in order to improve sterilized se'i sapi's qualities both in volatile aroma profiles and other physicochemical properties are still needed. Hence, the objective of this study was to evaluate the effect of essential oils (cinnamon and nutmeg) on the quality and volatile profiles of sterilized se'i sapi.

Methodology:

Sample preparation: Se'i sapi samples were prepared according to the method of Lopi et al.[14] with some modifications. Silverside of meat was cut into 10 × 3 × 2 cm pieces. Separately, 500 mL solution consisted of 0.05 % (w/v) potassium nitrate, 2 % (w/v) NaCl, 0.05 % (w/v) pepper, 1 % (v/v) liquid smoke, 1000 ppm cinnamon or nutmeg essential oils, and 0.1 % (v/v) Tween 80 was prepared. The solution was then homogenized at 10,000 rpm for 5 min (T18 digital ultra turrax, IKA, Belgium). The meat was then completely immersed in the marinade and then stored in the sterile trays wrapped with air-permeable polyethylene film at 4°C for 2 h. The marinated meat was then drained off and put in the oven at 140°C for 80 min. After that, the meat was then vacuum packed in retort pouch and then sterilized at 121°C for 15 min (F_0 = 5 min)

pH determination: pH of the sample was measured according to the method of Bakhsh et al.[15] The sample was weighed (3 g) and homogenized in 20 mL distilled water. The pH was measured using pH meter (Orion Star A111 Benchtop, Thermo Fisher Scientific Inc, Singapore).

Color determination: Color parameters (L*, a*, and b*) of the samples were determined using Konica Minolta® (spectrophotometer CM-5, U.S.A).

Water Holding Capacity (WHC) determination: WHC was evaluated according to the method described by Wilhelm et al.[16] Sample (2g) was placed between two pieces of filter papers, and put between two plexiglass plates. A weight of 10 kg was placed on the top of sample for 10 min. Final weight of each sample was recorded, and WHC was calculated as the following equation:

$$WHC\ (\%) = 100 - \left[\frac{(Initial\ weight\ of\ sample - final\ weight\ of\ sample)\ \times 100}{Initial\ weight\ of\ sample}\right]$$

Moisture content determination: Moisture content was evaluated following the AOAC method.[17]

Textural determination: Hardness, cohesiveness, and springiness of samples were measured using TA.TX plus texture analyzer (Stable Micro System Ltd., Godalming, UK) according to the published method.[18] Meat was cut into 15 mm cube shape (as the direction of the meat fiber), then pressing by 25 mm diameter cylindrical probe. The compression was 60% of its original height, pre-test speed of 3 mm s^{-1}, test speed of 1 mm s^{-1}, and post-test speed of 3 mm s^{-1}.

Volatile compounds analysis: Volatile compounds of smoked meat samples were analyzed using solid phase microextraction and gas chromatography-mass spectrometry (SPME-GC-MS) equipped with a DB-WAX column. One g of sample was blended with 2.5 mL saturated NaCl solution. Ten µL of each internal standard solution, (2-methyl-3-heptanone (100.870 µg/ml) and 2,4,6-trimethylpyridine (100.776 µg/ml)) was added for quantification purpose. The samples were then incubated at 60°C for 10 min while inserting SPME fiber coated with PDMS/CAR//DVB. Subsequently, the SPME fiber was desorbed in GC inlet at 220°C for 5 min. Helium gas was used as a carrier gas with a constant flow rate of 2 mL/min. Oven temperature was maintained at 40°C for 5 min, programmed to increase at 5°C/min to 220°C, the holding time was 5 min. The volatile compounds were identified using MS library (NIST 17) and calculated retention indices (RI). While, the RI was calculated as follows:

$$\text{Retention index (RI)} = 100Z + 100\left[\frac{RT_X - RT_n}{RT_N - RT_n}\right]$$

Where Z is the carbon number of n-alkane eluted before sample peak, RT_x is retention time of target peak, RT_n is retention time of n-alkane peak eluted before sample peak, and RT_N is retention time of n-alkane peak eluted after sample peak. The concentration of volatile compounds was calculated against the internal standard's peak areas. The odor activity value (OAV) of each compound was calculated by dividing the concentration of the compound by the threshold of the compound.

Results and Discussion:

pH: pH values of se'i sapi samples are shown in **Table 1**. There was no different found in the samples ($p>0.05$). This could be due to all samples passed through the same process and the amount of essential oils added was not enough to make a difference. However, it was observed that the pH value of smoked meat treated with cinnamon (5.85) and nutmeg (5.82) oils showed a bit lower in pH values than the control sample (5.86). The lower pH observed might be caused by organic acids contain in cinnamon and nutmeg oils[19]. Brilliana et al.[20] stated that the compounds present in the cinnamon essential oil is capable of lowering pH value of ground beef compared to control sample. The result from our study was in agreement with the work reported by Shaltout et al.[21], who treated minced meat with cinnamon and thyme essential oils and found that there was no difference on pH of minced meat product at the day of production.

Color: The color parameters of samples were measured and reported in **Table 1.** Overall, there is no significant difference found in all color parameter values among samples. This might be due to the small amount of essential oils added, thus the color of the all samples were not different ($p>0.05$). This finding is similar to the result of Siroli et al.[22], who reported that essential oils did not affect the color parameters of pork loin. The similar result was obtained by Kirkin et al.[23] and Lopez et al.[24], who stated that the addition of tarragon and oregano essential oils did not affect all color parameter of frankfurters and fermented sausage, respectively.

Table 1. pH and color parameters of sterilized se'i sapi treated with cinnamon (CEO) and nutmeg (NEO) essential oils

Samples	pH^{ns}	Color parameter		
		L^{*ns}	a^{*ns}	b^{*ns}
Control	5.86±0.01	47.26±0.61	6.29±0.70	15.19±0.38
CEO	5.82±0.03	46.94±0.90	6.67±0.62	16.06±0.52
NEO	5.85±0.02	46.05±1.35	6.76±0.35	15.43±0.25

ns: not significant, CEO: Cinnamon essential oil treated sample, NEO: Nutmeg essential oil treated sample.

WHC: **Table 2** showed WHC of the se'i sapi samples obtained from all treatments. It was found that there was no different in WHC among samples ($p>0.05$). Cheng and Sun[25] stated that factors affecting the development of WHC of meat were cooking techniques, cooking temperature, cooking rates, and cooling methods. The result of our study was in agreement with the study of Hijazeen et al[26] who reported that the immersion of cooked chicken meat in *Origanum syriacum* L. essential oil did not give significant difference in the WHC value. However, our result differed

from the result obtained by Patriani et al.[19] who reported that marinate chicken meat using *Gracinia atroviridis* extract was significantly different from the control sample.

Moisture: Moisture content of se'i sapi with all treatments was shown in **Table 2**. It was found that there was not significantly different ($p>0.05$) among treatments. Our result was comparable to the report by Zahra et al.[27] who used *Myristica fragrance* essential oil on beef and found that there was no significant difference on moisture content in the early day of evaluation. Gök and Bor.[28] also reported that the application of fruit and vegetable juice on turkey breast meat had no significant difference on moisture content at day-0 of evaluation. The result of moisture content was related to the ability of meat to absorb water (WHC). Moreover, the amount of water trapped in the muscles and changes occurred in muscle cells affect the ability of muscle cells to retain water.[19]

Table 2. Moisture, water holding capacity (WHC), and texture parameters of sterilized se'i sapi treated with cinnamon (CEO) and nutmeg (NEO) essential oils

Samples	Moisture ^{ns}	WHC ^{ns}	Texture ^{ns}		
			Hardness	Cohesiveness	Springiness
Control	59.78±1.62	95.66±2.71	35.91±1.79	0.25±0.03	35.36±6.27
CEO	61.69±0.69	96.00±0.52	33.71±3.25	0.30±0.02	35.31±0.88
NEO	61.26±1.25	95.94±0.53	33.71±3.25	0.27±0.02	33.02±1.74

ns: not significant, CEO: Cinnamon essential oil treated sample, NEO: Nutmeg essential oil treated sample.

Texture: The texture (hardness, cohesiveness, and springiness) of se'i sapi samples were determined and shown in **Table 2.** In fact, phenolic compounds in the samples may cause the fragmentation of myofibril protein and thus improve meat tenderness.[29] However, it was revealed that both cinnamon and nutmeg essential oils did not impact in our smoked meat texture ($p>0.05$). This could be because all samples passed through the same heating and sterilizing processes. In addition, the action of phenolic compounds did not affect the texture at early stage after process. The changes in texture might be apparently occurred after storage for a certain period of time. In addition, our result was similar to the study reported by Noshad et al.[30] who stated that lemon essential oil did not affect buffalo meat texture. This finding was in agreement with the study conducted by Siroli et al.[22] who reported that marinade solution applied with essential oil can increase meat tenderness by reducing shear force in pork loin.

Table 3. Volatile compound composition of se'i sapi treated with essential oils

No.	RI	RI lit*	Compound	Relative concentration (μg/kg)			Threshold	OAV**		
				Control	NEO***	CEO***	(ppb)	Control	NEO	CEO
1	<1100	-	Dimethylamine	964.85±301.41	-	114.42±16.62	59[a]	16.35	-	1.94
2	<1100	-	2,3-Pentanedione	96.94 ±30.47	-	-	10[b]	9.69	-	-
3	<1100	-	2,3-Butanedione	205.77±65.82	-	-	6[c]	34.30	-	-
4	<1100	-	2-Methyl-2-propenoic acid	237.78±93.36	-	-	4.5[a]	52.84	-	-
5	1104		Allyl mercaptan	263.25±99.02	-	-	2.4[d]	109.69	-	-
6	1121	1106	Hexanal	219±98.06	-	78.14±19.38	2.4[e]	91.25	-	32.56
7	1176	-	2-Hydroxy-3-pentanone	387.18±112.93	-	-	2500[f]	0.15	-	-
8	1177	1153	β-Myrcene	-	125.87±43.28	-	112.5[g]	-	1.12	-
9	1182	-	Acetic acid methyl ester	428.32±59.85	-	323.62±103.78	5100[a]	0.08	-	0.06
10	1208	1210	α-Phellandrene	424.39±191.36	380.04-83.83	-	160[f]	2.65	2.38	-
11	1231	1266	β-Ocimene	-	264.41±76.98	-	18.7[g]	-	14.14	-
12	1251	1230	3-Methyl-1-butanol	-	353.14±33.10	-	220[e]	-	1.61	
13	1289	1290	Acetoin	376.28±119.22	757.70-190.91	195.06±10.45	14[f]	26.88	54.12	13.93
14	1303	1280	*p*-cymene	-	1380.48±157.45	-	100[k]	-	13.80	-
15	1470	1479	Benzaldehyde	695.28±93.53	-	4179.24±728.44	60[n]	11.59	-	69.65
16	1471	-	2-Ethyl-1-hexanol	430.19±39.07		-	-	-	-	-
17	1476	-	3-Ethyl-2,4-pentanedione	1247.04±169.93	-	-	-	-	-	-
18	1514	1563	Terpinen-4-ol	-	15852.63±4262.38	452.94±100.35	3100[l]	-	5.11	0.14
19	1514	-	Butyrolactone	112.33±1.98	-	-	1000[o]	0.11	-	-
20	1518	-	(*R*)-(-)-2-Pentanol	264.18±158.76	-	-	-	-	-	-
21	1550	1542	2,3-Butanediol	-	1887.30±227.20	-	20000[m]	-	0.09	-
22	1556	1548	Linalool	-	840.37±264.28	-	37[p]		22.71	-
23	1574	1568	2-Furanmethanol	163.90±2.06	-	-	1900[o]	0.09	-	-
24	1594	-	5-Methyl-2-furanmethanethiol	164.66±4.44	124.42±11.25	100.10±18.99	-	-	-	-
25	1598	1566	2-Methyl-1H-pyrrole	-	298.50±60.06	-	-	-	-	-
26	1607	1595	Isobornyl acetate	-	261.00±79.46	581.71±129.66	1380[q]	-	0.18	0.42
27	1636	-	Methoxypyrazine	-	266.91±81.07	-	400[r]	-	0.66	-
28	1746	1728	α-Terpineol	-	2821.99±804.09	566.82±160.11	1000[s]	-	2.82	0.56
29	1753	-	1-Benzylindole	-	278.86±56.09		-	-	-	-
30	1787	-	2-Methoxy-phenol	-	-	-	-	-	-	-

*: data from literatures[31-33] **: Odor Activity Value, ***: Nutmeg essential oil treated sample, ****: Cinnamon essential oil treated sample
a-z = data from published literatures[34-59]

Table 3. Volatile compound composition of se'i sapi treated with essential oils (cont.)

No.	RI	RI lit*	Compound	Relative concentration (μg/kg)			Threshold	OAV*		
				Control	NEO**	CEO***	(ppb)	Control	NEO	CEO
31	1817	-	α-Cubebene	-	545.93±167.13	-	6[q]	-	90.98	-
32	1820	1861	Phenylethyl alcohol	-	390.52±18.63	-	12[t]	-	32.54	-
33	1830	-	*trans*-β-Farnesene	608.58±30.72	-	649.12±37.75	87[u]	7	-	7.46
34	1889	-	Caryophyllene	-	-	584.45±94.50	1540[k]	-	-	0.37
35	1903	1876	Safrole	-	1769.74±622.42	-	160[v]	-	11.06	-
36	1922	-	2(1H)-Pyridinone	-	206.55±22.27	-	-	-	-	-
37	1937	-	*p*-Cresol	269.64±25.02	-	-	68[w]	3.97	-	-
38	1995	-	Hexanoic acid	-	196.55±33.30	-	1800[k]	-	0.1	-
39	2011	2015	Methyl eugenol	624.56±9.07	978.52±244	367.04±51.93	68[x]	14.39	97.85	5.40
40	2036	-	Benzoyl isothiocyanate	-	-	253.76±49.07	-	-	-	-
41	2094	2140	Eugenol	860.38±7.08	855.44±155.96	920.62±181.35	470[y]	1.82	1.82	1.96
42	2117	-	cinnamyl scetste	-	-	501.67±83.28	150[z]	-	-	3.34
43	2143	-	3-Methyl-1H-pyrazole	-	-	467.79±71.62	-	-	-	-
44	2220	-	2-Ethyl- thiazole	-	-	606.08±110.42	-	-	-	-
45	2243	-	Pentadecanal	2741.29±375.17	1866.45±169.46	1373.50±248.30	1000[u]	2.74	1.86	1.37
46	2244	-	1-Methyl-1H-indole	1948.19±240.20	-	732.97±135.88	-	-	-	-

*: data from literatures[31-33] **: Odor Activity Value, ***: Nutmeg essential oil treated sample, ****: Cinnamon essential oil treated sample
a-z = data from published literatures[34-59]

Volatile compound composition: GC-MS was applied to investigate the differences of volatile compounds in samples and the information regarding all compounds in the samples was shown in **Table 3**. Volatile compounds in cinnamon (CEO) or nutmeg (NEO) oil treated and control samples were divided into the following groups: alcohols (9), esters (3), ketones (7), aldehydes (4), hydrocarbon (13), furan (2), acids (2) and others (7). The se'i sapi treated with nutmeg oil showed twenty five volatile compounds, among them, terpinen-4-ol (15,852.63 μg/kg) was found to be a major compound, followed by α-terpineol (2,821.99 μg/kg), 2,3-butanediol (1,887.30 μg/kg), pentadecanal (1,866.45 μg/kg), and safrole (1,769.74 μg/kg). In addition, there was no terpinen-4-ol, α-terpineol, 2,3-butanediol, and safrole in the control sample, while the pentadecanal concentration was higher in the control sample. This result was supported by previous research which found that terpinen-4-ol and safrole were the major compounds in nutmeg oil.[60] Some studies found that sabinene was the major compound presented in nutmeg oil, followed by terpinen-4-ol, safrole, α-pinene, β-phellandrene, and γ-terpinene.[61-62] In this study, pentadecanal is one of the major compounds in nutmeg oil treated sample, in which was also detected in the control sample. This might be one of the compounds that was naturally occurring in meat. This was proved by previous study reported that pentadecanal also has been detected in jerked beef product.[63] Additionally, it was also found that pentadecanal has been detected as meat flavor compound in Xiangxi yellow cattle.[64] However, the terpine-4-ol was not affect much in aroma of se'i sapi treated with nutmeg essential oil, since the odor activity value (OAV) of this compound was 5.11, which was less than methyl eugenol that showed the highest OAV (97.85). This could be implied that high concentration of volatile compounds found in samples might not impact in overall aroma of the sample. In contrast, low concentration, but very low in odor threshold giving high OAV. This compound would important and impact the overall aroma of the product. From OAV, the methyl eugenol, α-cubebene, and phenylethyl alcohol were first three aroma active compounds in se'i sapi treated with nutmeg essential oil.

In contrast, twenty-one volatile compounds were identified in cinnamon oil treated sample. The dominant volatile compounds of cinnamon oil treated sample were benzaldehyde (4,179 μg/kg), pentadecanal (1,373 μg/kg), eugenol (920 μg/kg), 1-methylindole (732.97 μg/kg), and caryophyllene (584.45 μg/kg). Meanwhile, only benzaldehyde and pentadecanal were found in the control sample. This result is according to the previous study which reported that major volatile compounds observed in cinnamon oil were eugenol, caryophyllene, trans-3-ceren-2-ol, benzyl benzoate, eugenyl acetate, α-pinene, and α-phellandrene.[65] The result of our study was also comparable to the result of another study which reported that eugenol as one of the abundant compounds found in cinnamon oil.[66] In addition, benzaldehyde exhibited the highest concentration of volatile compounds and this compound also contributed the highest effect in aroma of se'i sapi since it also showed the highest odor activity value (69.65). Meanwhile, even though some compounds that showed high concentration in the sample treated with cinnamon essential oil, such as caryophyllene (584.45 μg/kg), but it showed the odor activity value only 0.37, which is less than 1. This could be indicated that the compound cannot be detected by human nose. Based on the OAV, benzaldehyde, acetoin and *trans*-β-Farnesene were the top three aroma active compounds in se'i sapi treated with cinnamon essential oil.

Conclusion:

The addition of nutmeg and cinnamon essential oils had no effect on pH, water holding capacity (WHC), moisture content, color, texture (hardness, cohesiveness and springiness), but influenced the volatile compounds composition of se'i sapi. Terpinen-4-ol, α -terpineol, 2,3-butanediol, pentadecanal, and safrole were the major compounds found in nutmeg oil. While, benzaldehyde, pentadecanal, eugenol, 1-methylindole, and caryophyllene were the dominant volatile compounds observed in cinnamon oil. Odor activity value (OAV) indicated the important aroma active compounds contributed to the se'i sapi, and it was shown that methyl euganol had the highest OAV (97.85) in nutmeg oil treated sample. Meanwhile, benzaldehyde was the compound with the highest OAV (69.65) in cinnamon oil treated sample.

References:

1. Godfray HCJ, Aveyard P, Garnett T, Hall JW, Key TJ, Lorimer J, Jebb SA. Science. 2018;361:1-8.
2. Leroy F, Geyzen A, Janssens M, De VL, Scholliers P. Trends Food Sci Technol. 2013;3:130-137.
3. Gómez M, Domínguez R, Fonseca S, Lorenzo JM. Austin J Nutr Food Sci. 2015;3:1-12
4. Bosco AD, Castellini C, Bernardini M. J Food Sci. 2001;66:1047-1051.
5. Hutasoit K, Suarjana IGK, Suadda IK. Indones Med Vet. 2013;2:248–260.
6. Buntu Y, Sinaga S, Suradi K. J Ilmu Tek Peternakan. 2020;8:37–44.
7. Patel S. Food Addit Contam. 2015;32:1049-1064.
8. Vandendriessche T, Nicolai BM, Hertog MLATM. Food Anal Methods. 2013;6:512–520.
9. Zhang C, Fan L, Fan S, Wang J, Luo T, Tang Y, Yu L. Phytochemis Pharmacol Toxicol. 2019;24:1-31.
10. Ranasinghe P, Pigera S, Premakumara GA, Galappathty P, Constantine GR, Katulanda P. BMC Complement Altern Med. 2013;13:1-10.
11. Kowalska J, Tyburski J, Matysiak K, Jakubowska M, Lukaszyk, Kryminska J. Mol. 2021;26:1-13.
12. Capasso R, Pinto L, Vuotto ML, Carlo G. Fitoterapia. 2000;71:131–137.
13. Janssen J, Laeckman GM. J Ethnopharmacol. 1990;29:179-188.
14. Lopi F, Sipahelut GM, Sabtu B. J Nukleus Peternakan. 2014;1:117-122.
15. Bakhsh A, Lee SJ, Lee EY, Hwang YH, Joo ST. Food Sci Anim Resour. 2021;41:983-996.
16. Wilhelm AE, Maganhini MB, Hernández-Blazquez FJ, Ida EI, Shimokomaki M. Food Chem. 2010;119:1201-1204.
17. AOAC, 1999. Official Methods of Analysis. 16th edn. Association of Official Analytical Chemists Washington USA.
18. Choe JH, Choi MH, Rhee MS, Kim BC. Asian-Aust J Anim Sci. 2015;29:1029–1036.
19. Patriani P, Hafid H, Sepriadi S. IOP Publishing. 2021;782:1-6.
20. Brilliana IN, Manuhara GJ, Utami R, Khasanah LU. IOP Publishing. 2017;193:1-6.
21. Shaltout FA, Koura HA. Benha Vet Med J. 2017;33:351-364.
22. Siroli L, Baldi G, Soglia F, Bukvicki D, Patrignani F, Petracci M, Lanciotti R. Foods. 2020;29:1-21.
23. Kirkin C, Inbat SM, Nikolov D, Yildirim S. AIMS Agric Food. 2019;4:244–250.

24. Chaves-López C, Martin-Sánchez AM, Fuentes-Zaragoza E, Viuda-Martos M, Fernández-López J, Sendra E, Pérez Alvarez JA. J Food Protec. 2012;75:104–111.
25. Cheng Q, Sun DW. Crit Rev Food Sci Nut. 2008;48:137-159.
26. Al-Hijazeen, M. Brazilian J Poultry Sci. 2019;21:1-9.
27. Zahra K, Hojjati M, Behbahani BA, Noshad M. J Food Safety. 2020;40:1-14.
28. Gok V, Bor Y. Brazilian J Poult Sci. 2016;18:481-488.
29. Zhong RZ, Li HY, Fang Y, Sun HX, Zhou DW. Meat Sci. 2015;105:1–7.
30. Noshad M, Alizadeh BB, Jooyandeh H, Rahmati-Joneidabad M, Hemmati KME, Ghodsi SM. Food Sci Nut. 2021;9(3):1625-1639.
31. Miyazawa M, Nakashima Y, Nakahashi H, Hara N, Nakagawa H, Usami A, Chavasiri W. J Oleo Sci. 2015;64:999–1007.
32. Naspi C, Costa A, Lucia A, Audino P, Masuh H. J Braz Chem Soc. 2017;29:419-429.
33. Arn H, Acree T. 2004. Datu Inc. Accessed 08 Sept 2018. http://flavornet.org/flavornet.html
34. Nagata Y. Minis Environ Gov Jpn. 2003;118-127.
35. Blank I, Sen A, Grosch W. Lebensm Unters Forsch. 1992;195:239-245.
36. Leksrisompong P, Barbamo DM, Barbano AF, Foegeding P, Gerard, Drake M. J Sens Stud. 2010;25:347-370.
37. Katz SH, Talbert. US Bureau Mines Technol Report. 1930;480:1-40.
38. Czerny M, Christlbauer, Fischer A, Granvogl, Hammer M, Hartl C. Eur Food Res Technol. 2008;228:265-273.
39. Neuser F, Zorn H, Berger RG. J Agric Food Chem. 2000;48:6191-6195.
40. Guntert M, Krammer G, Lambrecht S, Sommer H, Surburg H, Werkhoff P. ACS Symp. 2001;794:119-137.
41. Buttery RG, Orts WJ, Takeoka GR, Nam Y. J Agric Food Chem. 1999;47:4353-4356.
42. Pino JA, Mesa J. Flvour Fragr J. 2006;21:207-213.
43. Cain WS, Schmidt R, Wolkoff P. Indoor Air. 2007;17:337-347.
44. Boonbumrung S, Tamura H, Mookdasanit J, Nakamoto H, Ishihara M, Yoshizawa T, Varanyanond W. Food Sci Technol. 2001;7:200-206.
45. Maas BA, Dietrich A, Mosandl A. Naturwiss. 1993;80:470-472.
46. Schnabel KO, Belitz HD, Vonrason C. Lebensm Unters Forsch. 1988;187:215-223.
47. Garcia GDL, Tena N, Aparicio-ruiz R, Morales MT. Meat Sci. 2008;80:315-325.
48. Buttery RG, Guadagni DG, Ling LC. J Agric Food Chem. 1973;21:198-201.
49. Zea L, Moyana L, Moreno J, Cortes B, Medina M. Food Chem. 2001;75:79-84.
50. Masuda H, Mihara S. J Agric Food Chem. 1998;36:584-587.
51. Elss S, Kleinhenz S, Schreier P. Food Sci Technol. 2007;40:1826-1831.
52. Dalton P, Lees PSJ, Gould M, Dilks D, Stefaniak A, Bader M, Ihrig A, Triebig G. Chem Senses. 2007;739-747.
53. Tamura H, Nakamoto H, Yang RH, Sugisawa H. Nippon. Shokuhin Kagaku Kogaku Kaishi. 1995;42:887-891.
54. Tamura H, Pradayuttawat A, Tokunaga T. Food Sci Technol.1999;5:156-160.
55. Appell. Perfum. Cosmet. 1969;84:45-50.
56. Frauendorfer F, Schieberle. J Agric Food Chem. 2006;54:5521-5529.
57. Takeoka GR, Güntert M, Engel KH. ACS Symp. 2001;794:138-148.
58. Bonfils P, Faulcon P, Avan P. Acta Otolaryngol. 2004;124:1063-1071.

59. Sinuco DC, Steinhaus P, Schieberle, Osorio C. Eur Food Res Technol. 2010;230:859-864.
60. Zhao X, Wu H, Wei J and Yang M. Ind Crops Prod. 2019;130:137–145.
61. Matulyte I, Marksa M, Ivanauskas L, Kalveniene Z, Lazauskas R and Bernatoniene J. Mol. 2019;24:1–12.
62. Sipahelut SG, Patty JA, Patty Z, Kastanja AY, Lekahena VNJ. Eurasia J Biosci. 2019;13:93–98.
63. Freixo APA, Silva ACR, Castro MLR, Quiterio SL, Raices RSL. Food Sci. Tech. 2022; 42:1-7.
64. Chen D, Wang X, Guo Q, Deng H, Luo J, Yi K, Sun A, Chen K, Shen Q. Animals. 2022;12:1-15.
65. Unlu M, Ergene E, Unlu GV, Zeytinoglu HS and Vural N. Food Chem Toxicology. 2010;48:3274–3280.
66. Simić A, Soković MD, Ristić M, Grujić-Jovanović S, Vukojević J, Marin PD. Phythother Res. 2004;18:713–717.
67. Gotmare S, and Tambe E. Glob J Sci Front Res. 2019;19:1-10.

EFFECT OF PECTIN AS WALL MATERIAL ON THE PROBIOTIC SURVIVAL OF MICROENCAPSULATED *Lactobacillus plantarum*

Nurul Hasniah[1], Varin Titapiwatanakun[2] Sarisa Suriyarak[1,*]

[1]Department of Food Technology, Faculty of Science, Chulalongkorn University, Bangkok 10330, Thailand
[2]Department of Pharmaceutics and Industrial Pharmacy, Faculty of Pharmaceutical Sciences, Chulalongkorn University, Bangkok 10330, Thailand

[*]e-mail: sarisa.s@chula.ac.th

Abstract:

The microencapsulation, a promising technology, can offer maintain the viability of probiotics during processing, storage, and delivery to gastrointestinal tract. However, the loss of probiotic occurs with insufficient covering up through the heat at the atomizer of the spray dryer. Therefore, this study aimed to evaluate the impact of high and low methoxyl pectin as wall material with maltodextrin DE 10-12 on the survival of *Lactobacillus plantarum* and its physicochemical properties. The *L. plantarum* cells were added into maltodextrin 10%, maltodextrin 9% + low methoxyl pectin 1%, maltodextrin 8% + low methoxyl pectin 2%, maltodextrin 9% + high methoxyl pectin 1%, and maltodextrin 8% + high methoxyl pectin 2% solutions, followed by spray drying at an air inlet temperature of 120 ± 4 °C. The cell viability, spray drying yield, moisture, color, and bulk density of microencapsulated *L. plantarum* were evaluated. The results showed that the powders produced with a combination of low methoxyl pectin 1% and maltodextrin 9% had the highest bacterial survival (9.94 ± 0.14 log CFU/g) due to its gelation property. The microencapsulated powders with high and low methoxyl pectin were more yellow than with maltodextrin only. The bulk density of spray-dried probiotics with the addition of low methoxyl pectin was higher than high methoxyl pectin and maltodextrin only. This study presented that low methoxyl pectin can be used to produce spray-dried probiotic products with higher survivability.

Keywords: encapsulation, spray drying, pectin, maltodextrin, probiotic

Introduction:

Recently, the global market for probiotics has increased significantly each year, predicted at USD 61.1 billion in 2021, and is projected to be valued at 91.1 billion by 2026 due to increasing consumer awareness about healthy diets.[1] Probiotic encapsulation appears as a strategy to protect probiotics from environmental stress, improving the viability of probiotics during processing, storage, and delivery to the gastrointestinal tract. Spray drying is a common technique in the food industry that is low cost, low energy consumption, fast processing, and high productivity.[2] However, during spray drying, high temperatures reduce the viability of probiotics. Probiotic powders contained higher than 10^6 CFU/g after drying, as a minimal dose recommended for probiotic products.[3] Therefore, it is important to select material that can provide maximum protection of the probiotics against environmental conditions, such as heat, oxygen, light, and humidity.

Encapsulating materials or wall materials can be obtained from a wide range of natural and synthetic polymers. Pectin is a negatively charged polysaccharide

abundantly found in the cell walls of plants which can be extracted from fruit, waste, etc.[4] Pectin can be used as wall materials in oil/water microencapsulation due to its gelation property [5]. Pectin carboxyl groups and calcium can form ionic bridges, leading to the arrangement of molecular chains and gel formation.[6] Pectins are subdivided into high-methoxyl pectins (HM pectins) and low methoxyl pectins (LM pectins) according to the percentage of carboxyl groups esterified with methanol or known as degree of methylation (DM). The gel formation of HM pectins (more than 50% DE) are affected by the type of pectin, pH (generally to pH 2.5-3.8), the concentration of water-binding components, such as sugar (55%-85%, generally about 65%), and temperature (35 °C-90 °C).[7,8] LM pectins (less than 50% DE) do not require sugar, but the presence of divalent cations, such as calcium, to form gel and provide cross-bridge.[7,8]

Pectin can act as an emulsion stabilizer, having gelling properties and binding abilities [8]. Pectin can encapsulate the bioactive compounds using nanospray drying, nano complex formation, or coacervation.[9] Besides, in upper GIT conditions, pectin is poorly absorbed, but, it is absorbed entirely in the colon which pectinolytic enzymes can digest by colonic microflora.[10] As a prebiotic, pectin increases the fecal bulk, enhancing the survivability of probiotics in the gut.[11]

This study aimed to study the effect of pectin on spray-dried probiotics (*L. plantarum*) using different concentrations and physical properties of the products. The development of wall materials is expected to be a potentially protective barrier for probiotic application.

Methodology:

Probiotic cultivation and preparation

One ose of the *L. plantarum* was cultivated in 10 mL of sterile MRS broth at 37 °C for 24 h, and then 10 Ml of culture was transferred into 90 mL of sterile MRS broth and incubated at 37 °C for 24 h. The cells were harvested by centrifugation using 4,500 rpm at 4 °C for 5 min. After that, the cells were washed twice with sterile saline solution (8.5 g L^{-1}).

Preparation of the wall material

The wall material combinations were presented in Table 1. The wall materials were mixed and sterilized at 121 °C for 15 min, and then it was cooled down to 25 °C. After harvesting, the *L. plantarum* cell was inoculated into wall material solutions.

Table 1. Composition of feed solutions.

Wall material Formulation	Pectin (% w/v)	Maltodextrin 10-12 DE (% w/v)
Maltodextrin (M)	-	10
Low-methoxyl pectin + maltodextrin (LPM1)	1	9
Low-methoxyl pectin + maltodextrin (LPM2)	2	8
High-methoxyl pectin + maltodextrin (HPM1)	1	9
High-methoxyl pectin + maltodextrin (HPM2)	2	8

Microencapsulation by spray drying

Microencapsulation of probiotics was conducted using a mini-spray dryer (BÜCHI B-290, Flawil, Switzerland). This spray drying was performed at an air inlet temperature of 120 ± 4 °C and outlet temperature of 64 ± 5 °C with pump at 15%, aspirator of 90%, and the drying airflow rate of 35 m^3 h^{-1}. The feed solution was agitated at room temperature, followed by feeding into the spray chamber through a peristaltic pump. From the bottom of cyclone, the spray-dried probiotic was collected, then packed in sealed aluminium foil and

stored at 4 °C. The moisture content and viability cells before and after spray drying were analyzed immediately.

Viability and physical properties of microencapsulated L. plantarum

Spray drying yield

Drying yield was determined as the ratio of the dry matter content in probiotic powder to the dry matter content of the feed solution.[12]

Survivability of microencapsulated *L. plantarum*

Encapsulation efficiency (*EE*) was calculated as the fraction of viable cells of microencapsulated probiotics over the viable cells in the feed before spray drying.[13] One gram of probiotics powder was prepared in 9 mL of sterile peptone water, preparing serial dilutions from the initial suspension and using pour plate method in MRS agar. After that, the samples were incubated at 37 °C for 48 h and calculated as colony-forming units per gram (CFU g^{-1}).

.

Moisture

Moisture content was calculated by evaporating water in the powder at 105 °C until constant mass (gravimetry).[14]

Bulk density

The sample was poured into a measuring cylinder and the volume and weight of the sample was recorded. Bulk density (g/cm^3) was the net weight of the sample over the volume occupied by the sample in the cylinder.

Color

Color parameters were determined in a colorimeter and expressed according to the CIELAB color system (*L**, *a**, and *b**).

Data Analysis

The data was analyzed by Analysis of variance (ANOVA) at $p < 0.05$ using the software SPSS 17.0. Differences between means were determined by using Duncan's test.

Results and Discussion:

Spray drying yield

The yield is an important parameter for spray-dried powder. The result varied between 64.03-73.04% depending on maltodextrin and pectin concentration as wall material. The highest yield was obtained for the combination of pectin 1% and maltodextrin 9% (73.04 ± 1.63%), but it was not significantly different with maltodextrin only (72.82 ± 2.48%), whereas the lowest yield was a combination of HM pectin 2% and maltodextrin 8% (64.03 ± 1.24%), as presented in Table 2. Different parameters influence the yield of the spray-dried products, such as the inlet temperature, feed flow rate, and wall material concentration.[15] The low yield obtained is probably caused by its high viscosity, at higher feed viscosity causes solids to stick to the main chamber wall, thus it will reduce the process yield.[15] Drying yield significantly increased with an increase in maltodextrin concentration. The maltodextrin can

increase the glass transition temperature of the food components, reduce the stickiness problem of the powder, and increase the powder yield.[16,17]

Table 2. Yield of microencapsulated probiotic powders after spray drying

Sample	Yield (%)
M	72.82 ± 2.48^{b}
LPM1	69.25 ± 2.57^{b}
LPM2	72.04 ± 0.77^{b}
HPM1	73.04 ± 1.63^{b}
HPM2	64.03 ± 1.24^{a}

Survivability of LGG after spray-drying

Survivability is associated with probiotic viability as an important factor in developing a target delivery system. During spray drying, high temperatures cause osmotic, heat, and oxidative stress for probiotics, affecting the cytoplasmic membrane, cell wall, DNA, and RNA of cells.[18–20] Heat can cause cell damage or the leakage of intracellular substances. The death of the microorganism can be caused by unfolding thermally labile proteins, such as the α- and β-subunits of RNA polymerase at a higher temperature.[21–24] Therefore, high temperatures are detrimental to probiotics due to sub-lethal thermal shock during spray drying.

The initial count of viable bacteria in feed solutions for all the treatments was almost similar (10 log CFU/g) as presented in Table 3. The survival ratio ranged between 12.98-49.72%. This study obtained the maximum survival ratio of 49.72% with a combination of LM pectin 1% and maltodextrin 9%, followed by maltodextrin only (31.49 ± 28.28%), whereas the lowest survival ratio was at 12.98 ± 4.10% from HM pectin. Pectin can be used as encapsulating agent due to its gelling properties and binding ability, thus it can protect probiotics from high temperature and dehydration during spray drying. In a previous study, the addition of pectin and maltodextrin to the Ca-alginate microcapsule preparation gave higher thermal resistance.[25] From the results, it was suggested that LM pectin was better to encapsulate the probiotics due to its higher carboxyl group content. Another study reported that LM pectin had a higher capacity than HM pectin to encapsulate native lactoferrin and can be used as a better encapsulating agent candidate to interact with and stabilize lactoferrin because of its higher carboxyl group content. [26]

Table 3. Survivability of microencapsulated probiotic powders after spray drying

Sample	Before spray drying (log CFU/g)	After spray drying (log CFU/g)	Survival ratio (%)
M	10.25 ± 0.22^{a}	9.78 ± 0.17^{b}	31.49 ± 28.28^{ab}
LPM1	10.27 ± 0.18^{a}	9.94 ± 0.14^{b}	49.72 ± 19.57^{b}
LPM2	10.09 ± 0.05^{a}	9.36 ± 0.25^{a}	21.72 ± 16.06^{ab}
HPM1	10.05 ± 0.06^{a}	9.28 ± 0.14^{a}	18.22 ± 7.09^{ab}
HPM2	10.19 ± 0.09^{a}	9.30 ± 0.13^{a}	12.98 ± 4.10^{a}

Physical properties of spray-dried probiotic

Moisture content

Moisture content of probiotic powder affects the product stability and probiotic viability during storage.[27] It affects the water activity and powder flow properties. At low moisture content, it can offer better stability and longer shelf life. The moisture content of encapsulated probiotic powders varied from 4.58% to 6.47% (Table 5). From Tables 4 and 5, maltodextrin contained the lowest moisture content before spray drying and after spray drying, 4.58 ± 0.21% and 4.87 ± 0.08%, respectively due to the differences between the chemical structures of the carrier agents. The wall materials and drying conditions affect the moisture content. In a previous study, the moisture content of the powder decreased with an increase in maltodextrin concentration.[12] The higher moisture content was observed for the combination of HM pectin 2% and maltodextrin 8% before and after spray drying (6.40 ± 0.10% and 6.47 ± 0.30%, respectively) than the LM pectin 2% and maltodextrin 8% (6.11 ± 0.14% and 6.34 ± 0.14%, respectively). The moisture content of spray-dried powders should be below 5% for storage stability.[28] At higher viscosity of the feed, it can reduce the heat and mass transfer, thus reducing the evaporation of water.[15]

Table 4. Physical properties of wall material before spray drying

Sample	Moisture content (%)	Viscosity (cP)	Color			Bulk density (g/cm^3)
			L*	a*	b*	
M	4.87 ± 0.08^a	24.03 ± 0.06^a	96.13 ± 0.36^e	0.10 ± 0.02^e	0.39 ± 0.01^a	0.47 ± 0.01^a
LPM1	5.31 ± 0.20^b	66.43 ± 0.80^b	95.09 ± 0.06^d	0.88 ± 0.02^d	4.82 ± 0.01^b	0.47 ± 0.01^a
LPM2	6.11 ± 0.14^d	134.53 ± 4.00^c	92.63 ± 0.06^c	1.58 ± 0.03^c	7.94 ± 0.10^c	0.50 ± 0.02^b
HPM1	5.80 ± 0.11^c	70.43 ± 0.40^b	91.76 ± 0.13^b	1.84 ± 0.01^b	7.70 ± 0.10^c	0.47 ± 0.02^a
HPM2	6.40 ± 0.10^e	155.37 ± 4.75^d	87.99 ± 0.48^a	2.67 ± 0.03^a	10.59 ± 0.31^d	0.48 ± 0.00^a

Color

The color and the visual appearance of the probiotic product are an important factors affecting customer preference or consumer buying behavior.[29] The color of the spray-dried products is associated with the natural color, carrier material concentration, and inlet temperature.[30] The microencapsulated probiotic colors were evaluated based on the color components (L*, a*, b*) as presented in Table.

The L* values of encapsulated probiotic powder varied from 95.08 ± 0.01 to 99.50 ± 0.20 at different combinations (Table 5), whereas the L* values of raw material or wall materials before spray drying were lower than after spray drying (from 87.99 ± 0.48 to 96.13 ± 0.36). It can be caused by pectin can stick to the chamber during spray drying, reducing pectin concentration in final products. In addition, it was observed that the L* values of probiotic powder slightly decreased with an increase in pectin concentration. *L** was different between wall materials with the higher concentration of the maltodextrin was lighter, thus it

showed greater values of luminosity due to the carrier or maltodextrin is white. The white color of maltodextrin affects the final color of the product (Figure 1). Besides, the lowest *L** value was the combination of HM pectin 2% and maltodextrin 8% among all samples.

Table 5. Physical properties of microencapsulated probiotic powders after spray drying

Sample	Moisture content (%)	Color			Bulk density (g/ cm^3)
		L*	a*	b*	
M	4.58 ± 0.21^{a}	99.50 ± 0.20^{e}	-0.52 ± 0.08^{a}	0.08 ± 0.16^{a}	0.30 ± 0.00^{a}
LPM1	5.88 ± 0.13^{b}	98.35 ± 0.23^{d}	-0.07 ± 0.02^{b}	1.47 ± 0.09^{b}	0.36 ± 0.01^{d}
LPM2	6.34 ± 0.14^{c}	96.98 ± 0.12^{b}	0.06 ± 0.01^{c}	2.66 ± 0.16^{d}	0.41 ± 0.01^{e}
HPM1	5.73 ± 0.17 ^{b}	97.19 ± 0.20^{c}	0.65 ± 0.04^{d}	1.79 ± 0.20^{c}	0.32 ± 0.01^{b}
HPM2	6.47 ± 0.30^{c}	95.08 ± 0.01^{a}	1.11 ± 0.01^{e}	3.41 ± 0.06^{e}	0.34 ± 0.01^{c}

The parameters a* and b* showed significant differences among wall material combinations. The *a** coordinate varying from green (−) to red (+). Parameter *b** is defined as the difference between blue (−) and yellow (+).[31] The samples with a higher concentration of pectin presented an increase in these parameters, the yellow color (*b**) due to the carrier responsible for this color, especially HM pectin.

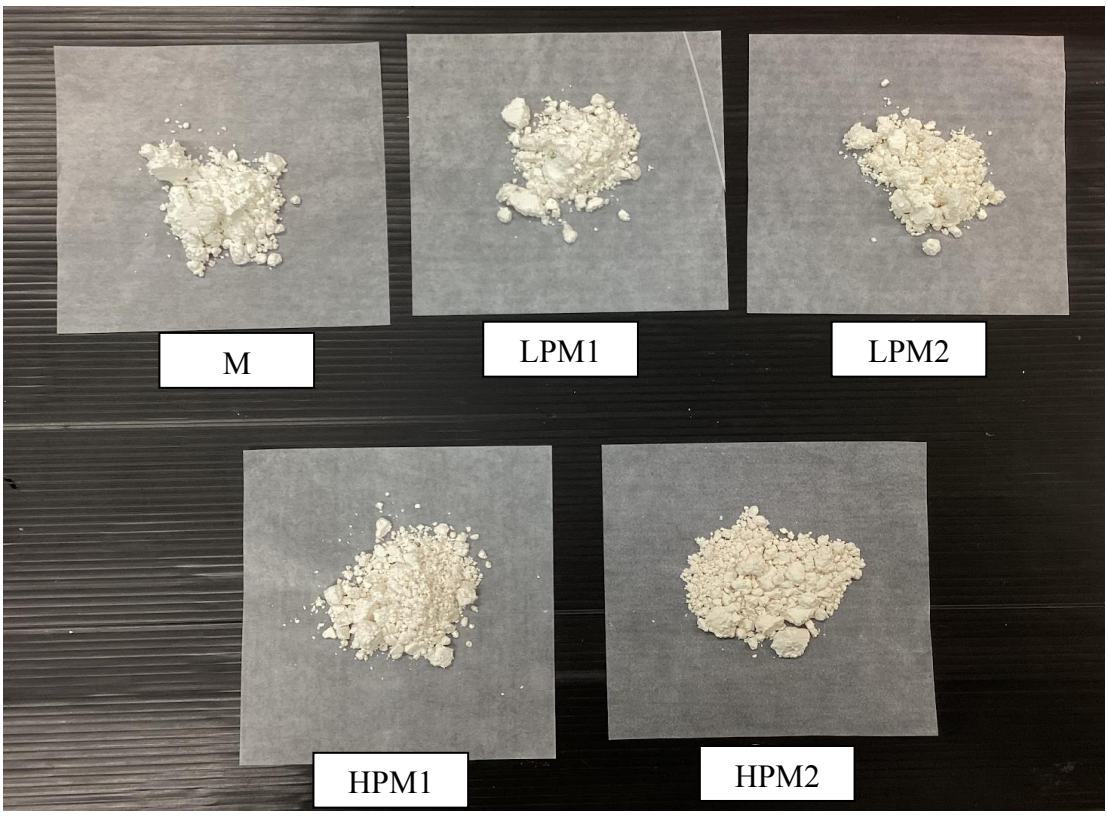

Figure 1. Microencapsulated probiotic after spray drying

Bulk density

One of important factors for transport and packaging is bulk density. High bulk density results in higher packing due to the lower volume occupied per mass unit. Lower bulk density values may increase the possibility of product oxidation, due to a large amount of air

within the powder, reducing storage stability. The bulk density values of the encapsulated probiotics ranged from 0.30 to 0.41 g/cm^3 (Table 5). In this study, maltodextrin showed the lowest bulk density (0.30 ± 0.00 g/cm^3), whereas at a higher concentration of pectin, it increased the bulk density. Low methoxyl pectin gave higher bulk density than high methoxyl pectin.

Conclusion:

Pectin and maltodextrin were easily found in the market for food product development. The encapsulated probiotic showed levels of *L. plantarum* viable cells above 9 log CFU/g after spray drying. The combination of LM pectin 1% and maltodextrin 9% was wall material with the highest number of viable cells after spray-drying. Probiotic powders produced with maltodextrin resulted in higher yield and moisture contents lower than 5%. This study demonstrated that LM pectin can be used to produce spray-dried probiotic products. The formulation of microencapsulating agent and its interaction between wall material and probiotics formulation and encapsulation technique should be studied further to produce probiotic products with higher survivability during processing, storage, and delivery to gastrointestinal tract.

References:

1. Research and Markets. https://www.globenewswire.com/en/news-release/2021/07/23/2268057/28124/en/Global-Probiotics-Market-2021-to-2026-Probiotics-Can-Replace-Pharmaceutical-Agents-Presenting-Opportunities.html
2. Tao T, Ding Z, Hou D, et al. *J Food Eng*. 2019;252:10-17.
3. Hill C, Guarner F, Reid G, et al. *Nat Rev Gastroenterol Hepatol*. 2014;11:506-514.
4. Mohnen D. *Curr Opin Plant Biol*. 2008;11:266-277.
5. Noh J, Kim J, Kim JS, Chung YS, Chang ST, Park J. *Carbohydr Polym*. 2018;182:172-179.
6. Zhao S, Zhang Y, Liu Y, et al. *Int J Biol Macromol*. 2018;115:29-34.
7. BeMiller JN. In: BeMiller JNBTCC for FS (Third E, ed. *Carbohydrate Chemistry for Food Scientists (Third Edition)*. AACC International Press; 2019:303-312.
8. Rehman A, Ahmad T, Aadil RM, et al. *Trends Food Sci Technol*. 2019;90:35-46.
9. Fathi M, Martín Á, McClements DJ. *Trends Food Sci Technol*. 2014;39:18-39.
10. Shishir MRI, Xie L, Sun C, Zheng X, Chen W. *Trends Food Sci Technol*. 2018;78:34-60.
11. Nazzaro F, Fratianni F, Nicolaus B, Poli A, Orlando P. *Anaerobe*. 2012;18:280-285.
12. Vivek K, Mishra S, Pradhan RC. *Int J Fruit Sci*. 2021;21:193-204.
13. Arepally D, Goswami TK. *LWT-Food Sci Technol*. 2019;99:583-593.
14. AOAC. In: sixteenth. Association of Official Analytical Chemist, Maryland; 1995.
15. Tonon R V, Brabet C, Hubinger MD. *J Food Eng*. 2008;88:411-418.
16. Barbosa J, Teixeira P. *Food Rev Int*. 2017;33:335-358.
17. Can Karaca A, Guzel O, Ak MM. *J Sci Food Agric*. 2016;96:449-455.
18. Paéz R, Lavari L, Vinderola G, et al. *Food Res Int*. 2012;48:748-754.
19. Perdana J, Bereschenko L, Fox MB, et al. *Food Res Int*. 2013;54:1351-1359.
20. Tripathi MK, Giri SK. *J Funct Foods*. 2014;9:225-241.
21. Anekella K, Orsat V. *LWT-Food Sci Technol*. 2013;50:17-24.
22. Santivarangkna C, Kulozik U, Foerst P. *J Appl Microbiol*. 2008;105:1-13.

23. Smelt J, Brul S. *Crit Rev Food Sci Nutr*. 2014;54:1371-1385.
24. Šipailienė A, Petraitytė S. *Probiotics Antimicrob Proteins*. 2018;10:1-10.
25. Dong LM, Luan NT, Thuy DTK. *Microbiol Biotechnol Lett*. 2020;48:113-120.
26. Niu Z, Loveday SM, Barbe V, Thielen I, He Y, Singh H. *Food Hydrocoll*. 2019;93:120-130.
27. Guerin J, Petit J, Burgain J, et al. *J Food Eng*. 2017;193:10-19.
28. Ghandi A, Powell IB, Chen XD, Adhikari B. *Dry Technol*. 2012;30:1649-1657.
29. Shenoy P, Innings F, Lilliebjelke T, Jonsson C, Fitzpatrick J, Ahrné L. *J Food Eng*. 2014;128:140-145.
30. Obón JM, Castellar MR, Alacid M, Fernández-López JA. *J Food Eng*. 2009;90:471-479.
31. de Souza VB, Thomazini M, Balieiro JC de C, Fávaro-Trindade CS. *Food Bioprod Process*. 2015;93:39-50.

TOTAL PHENOLIC AND ANTHOCYANIN CONTENTS OF BLACK RICE WINE FERMENTED WITH *Saccharomyces cerevisiae* SC90 AND M30

Aung Pyae[1], Warawut Krusong [2], Poke Gadpoca[3], Sarisa Suriyarak [1]*
[1]Department of Food Technology, Faculty of Science, Chulalongkorn University, Phayathai Road, Wangmai, Pathumwan, Bangkok, 10330, Thailand
[2]Faculty of Food Industry, King Mongkut's Institute of Technology, Ladkrabang, Bangkok, 10520, Thailand
[3] Program in Biotechnology, Faculty of Science, Chulalongkorn University, Phayathai Road, Wangmai, Pathumwan, Bangkok, 10330, Thailand
*e-mail: sarisa.s@chula.ac.th

Abstract:

Black rice (*Oryza sativa L.indica*) is known for its unique flavor and color, high in protein, fiber, minerals and vitamins. It also contains the abundant presence of phenolics related to its color and antioxidant activity. These compounds are mostly from the complex in the bran layer of rice grains which could be liberated by fermentation. The study, thus, aimed to determine the total phenolic and anthocyanin contents of black rice wine fermented with 2 strains of *Saccharomyces cerevisiae* (SC90 and M30) in the course of 10-day fermentation. Black rice powder was fermented in a liquid state of 5w/v%, adjusted pH to 4.5±0.2 and incubated at 20°C and 40°C, and 6 LogCFU/ml inoculation. The CFU count, pH, Brix, color, total phenolic, total monomeric anthocyanin content and antioxidant activity were evaluated. The results showed that the 20°C incubation was more suitable for both strains of *S.cerevisiae* SC90 and M30 at pH 4.5±0.2 compared to the fermentation at 40°C. The total phenolic contents during the fermentation period were not altered by both yeast strains, 578.18±2.75 GAE mg/L. However, total monomeric anthocyanin contents were significantly decreased by the yeasts over the course of fermentation which in turns negatively affect the overall anti-oxidant activity and significantly decrease the color values especially the redness of the wine.

Keywords: Black rice wine, Fermentation, Phenolic, Anthocyanin

Introduction:

Fermented rice beverages have been one of the most popular beverage among Asian countries and various types of rice wine have been developed through different microbial cultures.[9,21,28] Several studies have learnt the increased in anti-oxidant properties and bioaccessiblity of phenolic compounds and flavonoids upon the fermentation process, which are believed to be the primary contributors of the health benefits and the nutritional value expressed by rice wine.[13,14,17]

In addition to common white-rice varieties, there are some speciality rices such as the colored ones (black, also known as purple, brown and red). Colors in the rice are due to the deposition of large amounts of anthocyanin pigment in the rice coat or rice bran.[8] The phytochemical constituents of pigmented rice are flavonoids, phenolics, tannin, sterols, tocols, γ-oryzanols, amino acids, and essential oils.[19,20] Choi et al. (2007a) and Shen et al. (2009) also reported the variations in phenolics content, flavonoid and antioxidant properties among the cereal grains with special emphasis on black rice, brown rice, red

sorghum, and white rice. Anthocyanins (cyanidin-3-O-β-glucoside and peonidin-3-O-β-glucoside) and tocols were identified in black rice which proved that they have aldose reductase inhibitory activity.[29]

Black rice (*Oryza sativa L.indica*) is known for its unique flavor and color, high in protein, fiber, minerals and vitamins. It also contains the abundant presence of phenolics and flanonoids, especially anthocyanins which related to its color and antioxidant activity.[16,25] Choi et al. (2007b) reported that the pigments of colored rice bran inhibit allergic reactions *in vitro*. The prevention of cancer-cell invasion property of peonidin, peonidin 3-glucoside, cyanidin 3-glucoside, and other major anthocyanins of black rice has been reported by Chen et al. (2006). Ichikawa et al. (2001) also reported that black rice are efficient, and two fold stronger, with respect to antioxidant activities of blueberries. These compounds are mostly form the complex in the bran layer of rice grains which could be liberated by fermentation. The work of Chaiyasut et al. (2017) claimed that the antioxidant properties of black rice bran were slightly enhanced after 24 h of fermentation by *Saccharomyces cerevisiae*. If *S.cerevisiae* could ferment the rice media, the phenolics and flavonoids of black rice could be extracted into the liquid medium and hence increase the overall anti-oxidant activity. The study, thus, aimed to analyze the total phenolic contents, total monomeric anthocyanin contents and the antioxidant properties of black rice wine fermented with 2 strains of *Saccharomyces cerevisiae* (SC90 and M30) over the course of 10-day fermentation.

Methodology:

Preparation of black rice flour

Black rice was purchased from a local market. The rice grains were washed thoroughly for several times with tap water and dried in hot air oven at 50°C until the moisture percent reach below 6%. Then dried rice grains were grinded to 60 mesh size and black rice flour was stored in vacuum sealed aluminum bag at -40°C until further analysis.

Proximate analysis

Moisture contents of black rice flours was determined according to AOAC approved standard method 925.09 and crude fat was analyzed by Soxhlet method by extraction with petroleum ether as described by AOAC 920.85.[2] Crude protein was determined according to the ICC standard method 105/2 using the factor 5.95 × N for conversion.[15] The carbohydrate content (estimated total carbohydrate content) was determined by difference from the analysis of moisture, protein and fat.

Preparation of black rice media

Black rice media (5% w/v) was prepared by mixing black rice flour with distilled water in amber colored Duran™ bottles. The pH was adjusted to 4.7 with food grade lactic acid. Then, they were autoclaved at 121°C at 15 min. After sterilization, aliquots of 80ml were made with sterile 125ml PP bottles. Then, cooled down in ice-water bath and prepared for inoculation with yeast.

Preparation of yeast inoculum

Two strains of *Saccharomyces cerevisiae* SC90 and M30 were provided by Warawut Krusong (Faculty of Food Industry, King Mongkut's Institute of Technology). A loop of yeast was taken from the slant agar tube into 250ml flask with 50 ml YM broth and incubated at 30°C for 24h. Second activation step was done by taking 10 ml of aliquot into 500ml flask with 90 ml YM broth (1:10) and incubate at 30°C for 16h. Then, the yeast cells were harvested by centrifuging at 4000 rpm for 10 min at room temperature. The cell mass was washed two times and re-suspended with peptone water.

Fermentation of black rice wine

The prepared cell suspension was inoculated (at least 10^6 CFU/ml) into the previously prepared black rice media. The inoculated black rice media was incubated at 20°C and 40°C

for 10 days. The rice wine samples are collected and then centrifuged at 6000 rpm for 10 min at room temperature and supernatants are used for further analysis.

Viable CFU count

The yeast count was determined just after inoculation and every 24 h until 10 days of fermentation by the spread plate method of Wise (2006). The samples were prepared with ten-fold dilution series with peptone water to get appropriate CFUs (20-300) per plate. Then 100 microliters of diluted sample was used to spread on the YM agar plates. Two replicates were done for each sample. Then the agar plates were incubated at 30°C until the colonies are clearly visible to be counted (24-48h).

Determination of pH, Brix and color

The pH, Brix and color were determined just after inoculation and every 24 h until 10 days of fermentation. The pH levels were determined by using the pH/Ion bench-top meter (S220 model, Mettler Toledo, Columbus, OH, US) before centrifuge. The soluble solids (Brix %) was determined with the Master™ refractometer (Atago, TYO, JP) before centrifuge. The color differences were determined by using CIE L*a*b* coordinates with a D_{65} light source from the colorimeter (CR-400/410 model, Konica Minolta, Marunouchi, CHY, JP) before and after centrifuging of the samples as mentioned previously.

Determination of total phenolic content

A modified version of the Folin-Ciocalteu assay[24] was used to determine the total phenolic content in the supernatant from the fermented rice samples. Gallic acid standard curve was made with appropriate concentrations of aqueous gallic acid solution. For the analysis, 40µl each of sample, gallic acid standard or blank (distilled water) were taken in separate test tubes and to each 1.56 ml of distilled water was added, followed by 100 µl of Folin-Ciocalteu reagent, mixed well and within 8 min, 300 µl of 20% sodium carbonate was added. The samples were mixed immediately via vortex mixer and allowed to incubate in dark at 40°C for 30 min. The absorbance was measured at 765 nm. The phenolic content was expressed in GAEmg/L.

Determination of total monomeric anthocyanin pigment content

Total monomeric anthocyanin pigment content of fermented rice wine samples was determined with slight modifications of the pH differential methods of Lee et al. (2019). Briefly, 0.8 ml of the sample was mixed thoroughly with 3.2 ml of 0.025M potassium chloride buffer (pH1). The mix was then allowed to stand for 20 min in dark. The absorbance was then measured at 515 and 700 nm against distilled water in a visible spectrophotometer (model). The same amount of sample was also mixed similarly with 0.025M sodium acetate buffer (pH 4.5), and the absorbance was measured at the same wavelength after standing in dark for 20 min. The results were calculated and expressed as mg of cyaniding-3-glucoside equivalent/L, as follows:

$$\mathrm{TAC} = \frac{\mathrm{A} \times \mathrm{MW} \times \mathrm{DF} \times 1000}{\varepsilon \times \mathrm{l}}$$

where A (Absorbance) = $(A_{515}\text{-}A_{700})$at pH1-$(A_{515}\text{-}A_{700})$at pH4.5; MW (molecular weight) = 449.2 g/mol for cyaniding-3-glucoside; DF = dilution factor of tested sample; l = pathlength of cuvette in cm (1 cm); ε = 26,900 molar extinction coefficient, in $\mathrm{L} \times \mathrm{mol}^{-1} \times \mathrm{cm}^{-1}$, for cyaniding-3-glucoside; and 10^3 = factor for conversion from g to mg.

Determination of DPPH radical scavenging activity

Free radical scavenging activity was measured by 1,1-diphenyl-2-picryl-hydrazil ($DPPH^{\cdot}$) using the method of Carmona- Jiménez et al. (2014) with minor modifications. Briefly, 200 µl of diluted sample or EtOH (blank) were added to 3.3 ml of 50 µM solution of DPPH in ethanol which was prepared daily (0.069 ppm of initial DPPH) in centrifuge tubes. Then, the tubes were kept in dark at room temperature for 30 min and centrifuged at 6000 rpm for 3 min. The supernatants were used to measure the absorbance at 515 nm. The initial

amount of DPPH was chosen to obtain initial and final absorbance values within the range of accuracy of spectrophotometry (0.221- 0.698). The inhibition percentage of DPPH is determined using the following equation:

$$I\% = \frac{(A_{blank} - A_{sample})}{A_{blank}} X\ 100$$

Results and Discussion:

Table 1. Proximate composition of Black rice flour before fermentation (g/100g DM basis)

Composition			
Moisture	**Fat**	**Protein**	**Total carbohydrate**
3.96±0.001	3.22±0.01	9.42±0.09	83.40±0.08

Results shown in average ± standard deviation.

The proximate composition of black rice flour before fermentation is presented in Table 1. The viable counts of two strains of *Saccharomyces cerevisiae* yeasts (SC90 and M30) in black rice solution were determined at 20°C and 40°C (Figure 1). Both strains showed significant growth ($p<0.05$) after 10 days of fermentation at 20°C but decreased in viable count significantly ($p<0.05$) at 40°C. However, the pH and %Brix changes over the fermentation period showed no difference ($p>0.05$) from starting pH 4.5±0.2 and %Brix 2.7±0.25 for both strains at both 20°C and 40°C temperatures; which means the effect of temperature is significant and in given conditions, 20°C is the better fermentation temperature in terms of the growth of both yeast strains.

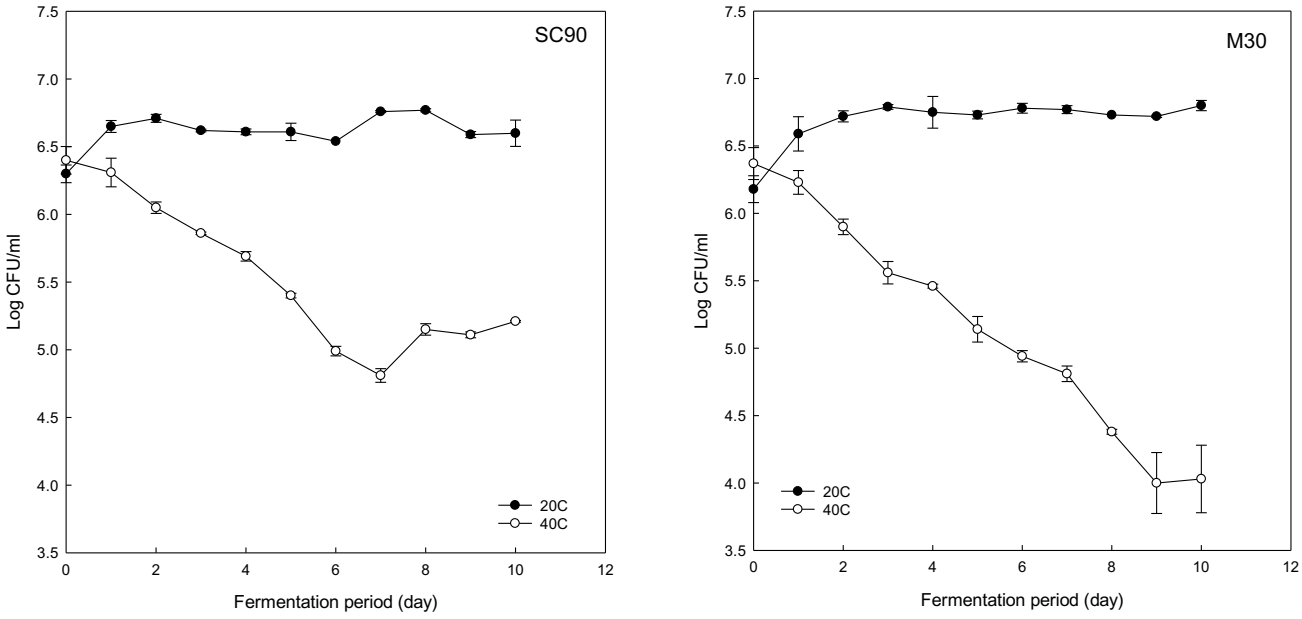

Figure 1. Changes in total yeast counts of two *Saccharomyces cerevisiae* strains SC90 and M30 at the fermentation temperatures of 20°C and 40°C in the black rice media. Error bars represent standard deviation.

The changes in total phenolic contents during fermentation of black rice media is presented as gallic acid equivalent (GAE mg/L) in Figure 2. Both strains of yeast (SC90 and

M30) did not change the total phenolic contents in the supernatant of black rice solution at 20°C. However, there was a significant ($p<0.05$) dropped of total phenolic contents; 17% and 19% after 10 days of incubation with SC90 and M30 at 40°C, respectively.

The changes in total phenolic contents may greatly depend on the enzyme profile of the yeast strains during fermentation. Asides from the soluble phenolic compounds that were compartmentalized within the cell vacuoles, a considerable portion of phenolics in rice were linked to cell wall structures, the hemicellulosic, cellulosic and protein components, as insoluble form Adom & Liu. (2002). The esterase and xylanase secreted by microbes can hydrolyse the covalent bond to release the bound phenolics, meanwhile the secreted protease and cellulase can hydrolyse the structural components to make the esterase and xylanase more available to release phenolics. Therefore, the more free phenolics in *S.cerevisiae* fermented rice may be largely attributed to the abundant enzymes produced by *S.cerevisiae*, including protease, cellulase and esterase.[4] The results showed that with the growth of the yeast strains at 20°C, the phenolic compounds were sustained at a constant concentration throughout the fermentation period by the yeasts. Overall, the changes in total phenolic contents after fermentation were not significant between the strains of SC90 and M30 which states that the different strains may not affect the phenolics in the rice wine as they were mainly derived from their plant materials.

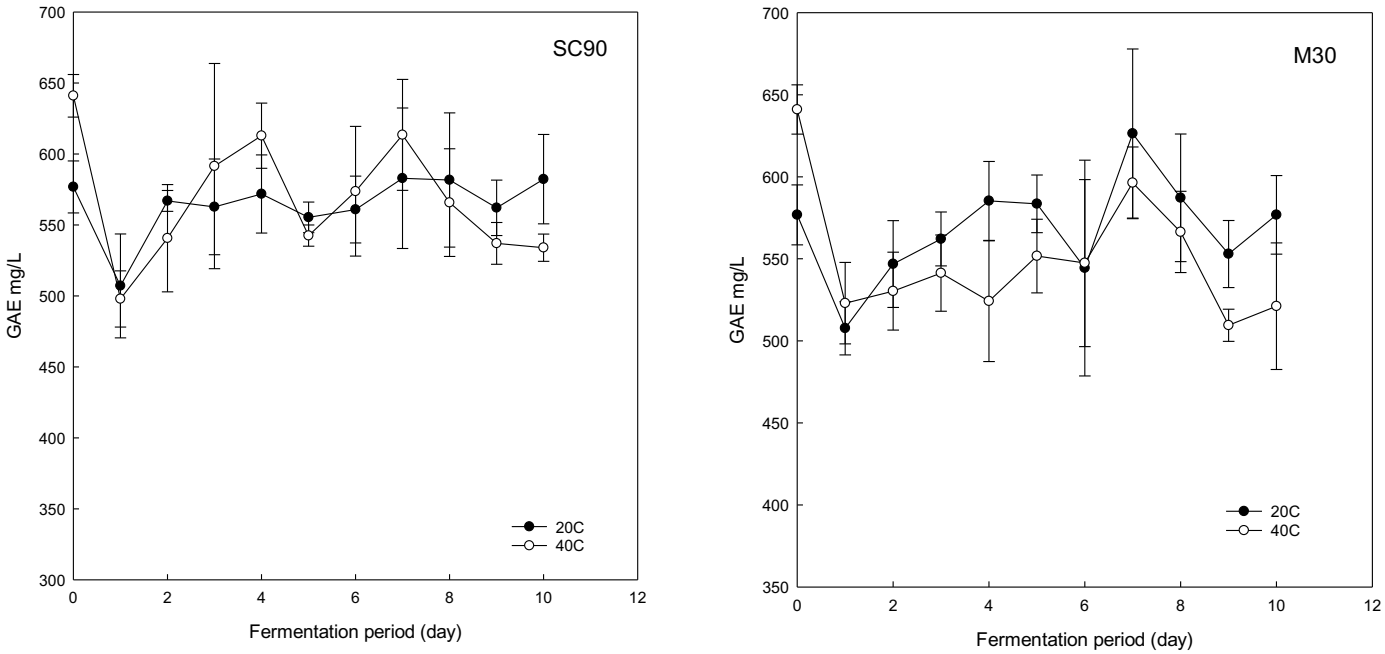

Figure 2. Total phenolic contents represented as gallic acid equivalent (GAE mg/L) in supernatant black rice solution fermented with two *Saccharomyces cerevisiae* strains SC90 and M30 at the fermentation temperatures of 20°C and 40°C. Error bars represent standard deviation.

The changes in total monomeric anthocyanin contents during fermentation period were shown in Figure 3. All experimental treatments showed the same trend with significant decreased ($p<0.05$) in monomeric anthocyanin contents. There was a strong negative correlation ($r = -5.10$, $p<0.05$) between overall color changes ΔE^* and decreased in total

monomeric anthocyanin contents, which directly correlates ($r = 0.738$, $p<0.01$) largely due to lowered red value (a*) during fermentation as shown in Table 2.

Pengkumsri et al. (2015) stated that the anthocyanin contents in black rice were mainly due to high amount in cyanidin-3-glucoside and peonidin-3-glucoside which give the color in the outer rice coat. These anthocyanins (cyaniding-3-glucoside and peonidin-3-glucoside) can be transformed to anthocyanidins (cyaniding and peonidin); also known as aglycon forms, by the extracellular β-glucosidases enzyme from *S.cerevisiae*, which breaks the glycosidic bond of anthocyanins and release the glucose group.[7] Additionally, Berenguer et al. (2016) also reported the decreased in anthocyanin contents during 14 days of wine fermentation with different yeast strains of *S.cerevisiae*. The results also showed similar trend in degradation of anthocyanins during fermentation (Figure 3).

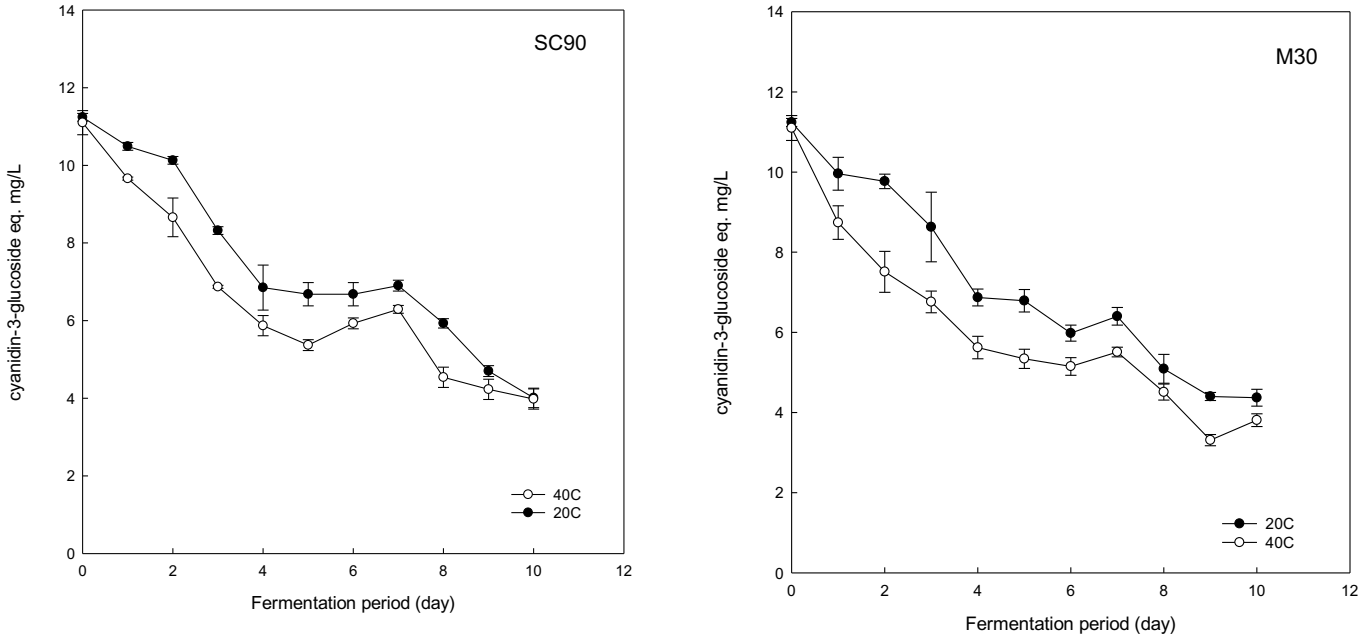

Figure 3. Total monomeric anthocyanin contents represented as cyaniding-3-glucoside equivalent (mg/L) in supernatant black rice solution fermented with two two *Saccharomyces cerevisiae* strains SC90 and M30 at the fermentation temperatures of 20°C and 40°C. Error bars represent standard deviation.

Table 2. Color values represented by CIEL*a*b* coordinates of supernatant black rice wine during fermentation under D_{65} light source

Fermentation period (day)	S20[1)] L*	a*	b*	S40 L*	a*	b*
0	30.09±0.37[2)]	6.37±0.37	5.18±0.15	29.72±0.37	6.65±0.37	5.36±0.15
3	29.80±0.74	6.10±0.19	4.41±0.80	29.99±0.84	6.49±0.06	5.48±0.77
7	30.40±0.84	5.76±0.41	4.89±0.31	29.75±0.80	6.04±0.26	5.28±0.53
10	30.40±0.95	5.49±0.27	5.05±1.61	29.36±0.82	5.65±0.18	4.69±0.64
Fermentation period (day)	**M20 L***	**a***	**b***	**M40 L***	**a***	**b***
0	29.84±0.37	6.52±0.37	5.10±0.15	29.86±0.37	6.79±0.37	5.35±0.15
3	30.42±0.68	6.38±0.13	5.28±0.67	30.05±1.37	6.05±0.31	5.28±0.67
7	30.31±0.20	5.71±0.31	4.54±0.21	29.67±0.74	6.06±0.03	5.19±0.63
10	30.40±0.78	5.23±0.02	4.18±1.29	29.80±0.96	5.77±0.18	5.13±1.00
Fermentation period (day)	**C20 L***	**a***	**b***	**C40 L***	**a***	**b***
0	31.25±0.37	6.26±0.37	6.70±0.15	30.51±0.37	7.00±0.37	6.40±0.15
3	31.05±0.01	6.26±0.06	6.91±0.16	31.03±0.01	6.15±0.05	6.60±0.16
7	30.46±0.06	6.45±0.20	5.49±0.50	30.58±0.06	6.06±0.20	6.49±0.50
10	30.94±0.30	5.84±0.21	5.17±0.84	31.54±0.30	5.42±0.21	6.85±0.84

[1)]Strain and Temperature; S=SC90, M=M30, C=Control
[2)]Average ± standard deviation

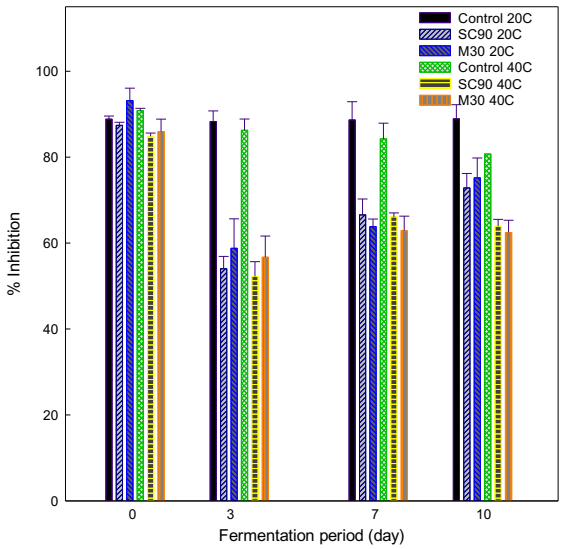

Figure 4. The antioxidant activity represented by DPPH radical savaging activity as inhibition % in supernatant black rice solution fermented with two *Saccharomyces cerevisiae* strains SC90 and M30 at the fermentation temperatures of 20°C and 40°C. Error bars represent standard deviation.

The DPPH free radical scavenging ability represented as %inhibition was used to assess the antioxidant activity of the black rice wine during fermentation period (Figure 4). After the 10 days fermentation period, the initial inhibition % (84.89±0.72, 85.97±2.88, 87.41±0.72 and 93.17±2.88) was dropped significantly ($p<0.05$) to 63.89±1.62, 62.45±2.86,

72.86±3.36 and 75.19±4.62 for SC90 at 40°C, M30 at 40°C, SC90 at 20°C and M30 at 20°C, respectively. Although, the anti-oxidant activity at Day 10 was increased by 16% up to 18% compared to the values at Day 3 for all experiment expect M30 at 40°C, it is still lowered compared to the control samples with no inoculation of yeast. Additionally, the anti-oxidant activity was also directly correlate ($r = 0.264$, $p<0.05$) to the total monomeric anthocyanin content; and no significant correlation with the total phenolic content the black rice wine. This showed that the anti-oxidant activity was mainly related upon the concentration of anthocyanins rather than phenolics compound in this study which is not align with the claim of Cai et al., (2019); that the free radical scavenging abilities of rice wine are mainly associated with their total polyphenol contents. It could be due to the fact that the complexity of enzymes from numerous microbial flora in the rice wine starters that could hydrolyze the plant materials releasing the phenolic compounds. Whereas in this study, a single strain of *S.cerevisiae* was used to ferment the black rice media, in which the yeasts tend to hydrolyze the glucosidic bonds of anthocyanin compounds that are solubilized in the suspension; leading to further degradation of anthocyanins and decreased in overall anti-oxidant activity of the black rice wine. However, it is undeniable that there was a significant increasing trend of anti-oxidant activity from Day 3 to Day 10 ($p<0.05$) which could be due to the formation of primary phenolic degradation products that align with the analysis of total phenolic results as mentioned.

Conclusion:

In summary, with regard to the fermentation temperature, 20°C was more suitable for the strains of *S.cerevisiae* SC90 and M30 at pH 4.5±0.2 compared to the fermentation at 40°C. The total phenolic contents during the fermentation period were not altered by both yeast strains. However, total monomeric anthocyanin contents were significantly decreased by the yeasts over the course of fermentation which in turns negatively affect the overall anti-oxidant activity and significantly decrease the color values especially the redness of the wine. This could be due to the fact that the simplification on the preparation step of black rice media leads to lack of sufficient carbon source that is solubilized in the water for the uptake of yeasts. Therefore, it could be concluded that even though there was a growth of yeasts in the black rice media, in terms of enhancing the anti-oxidant activity of the rice wine is still not promising. But with the combination of hydrolyzing the black rice and optimizing the fermentation conditions, there is a possibility of increased anti-oxidant activity in the final product.

References:

1. Adom KK, Liu RH. Antioxidant activity of grains. Journal of agricultural and food chemistry. 2002;50(21):6182-7.
2. AOAC, Association of Analytical Communities. Official methods of analysis. 2006.
3. Berenguer M, Vegara S, Barrajón E, Saura D, Valero M, Martí N. Physicochemical characterization of pomegranate wines fermented with three different Saccharomyces cerevisiae yeast strains. Food Chemistry. 2016;190:848-55.
4. Bintsis T, Vafopoulou-Mastrojiannaki A, Litopoulou-Tzanetaki E, Robinson R. Protease, peptidase and esterase activities by lactobacilli and yeast isolates from Feta cheese brine. Journal of Applied Microbiology. 2003;95(1):68-77.
5. Cai H, Zhang Q, Shen L, Luo J, Zhu R, Mao J, et al. Phenolic profile and antioxidant activity of Chinese rice wine fermented with different rice materials and starters. Lwt. 2019;111:226-34.

6. Carmona-Jiménez Y, García-Moreno MV, Igartuburu JM, Barroso CG. Simplification of the DPPH assay for estimating the antioxidant activity of wine and wine by-products. Food chemistry. 2014;165:198-204.
7. Chaiyasut C, Pengkumsri N, Sirilun S, Peerajan S, Khongtan S, Sivamaruthi BS. Assessment of changes in the content of anthocyanins, phenolic acids, and antioxidant property of Saccharomyces cerevisiae mediated fermented black rice bran. AMB Express. 2017;7(1):114.
8. Chaudhary R. C. Speciality rices of the world: Effect of WTO and IPR on its production trend and marketing. Journal of Food Agriculture and Environment, 2003;1(2):34-41.
9. Chay C, Dizon E, Elegado F, Norng C, Hurtada W, Raymundo L. Isolation and identification of mold and yeast in medombae, a rice wine starter culture from Kompong Cham Province, Cambodia. Food Research. 2017.
10. Chen PN, Kuo WH, Chiang CL, Chiou HL, Hsieh YS, Chu SC. Black rice anthocyanins inhibit cancer cells invasion via repressions of MMPs and u-PA expression. ChemicoBiological Interactions, 2006;163(3):218-229.
11. Choi SP, Kang MY, Koh HJ, Nam SH, Friedman M. Antiallergic activities of pigmented rice bran extracts in cell assays. Journal of Food Science, 2007b:72(9), S719-S726.
12. Choi Y, Jeong HS, Lee J. Antioxidant activity of methanolic extracts from some grains consumed in Korea. Food Chemistry, 2007a:103(1),130-138.
13. Ghosh K, Ray M, Adak A, Dey P, Halder SK, Das A, et al. Microbial, saccharifying and antioxidant properties of an Indian rice based fermented beverage. Food Chemistry. 2015;168:196-202.
14. Hur SJ, Lee SY, Kim YC, Choi I, Kim GB. Effect of fermentation on the antioxidant activity in plant-based foods. Food chemistry. 2014;160:346-56.
15. ICC. Standard Methods, Edition 2001. 2001.
16. Ichikawa H, Ichiyanagi T, Xu B, Yoshii Y, Nakajima M, Konishi T. Antioxidant activity of anthocyanin extract from purple black rice. Journal of Medicinal Food, 2001;4(4)-211-218.
17. Khan SA, Zhang M, Liu L, Dong L, Ma Y, Wei Z, et al. Co-culture submerged fermentation by lactobacillus and yeast more effectively improved the profiles and bioaccessibility of phenolics in extruded brown rice than single-culture fermentation. Food Chemistry. 2020:126985.
18. Lee J, Durst RW, Wrolstad RE, Collaborators:. Determination of Total Monomeric Anthocyanin Pigment Content of Fruit Juices, Beverages, Natural Colorants, and Wines by the pH Differential Method: Collaborative Study. Journal of AOAC INTERNATIONAL. 2019;88(5):1269-78.
19. Min B, Chen MH, Green BW. Antioxidant activities of purple rice bran extract and its efect on the quality of low-NaCl, phosphate-free patties made from channel catfsh (Ictalurus punctatus) belly fap meat. J Food Sci. 2009;74:268–277.
20. Nakornriab M, Sriseadka T, Wongpornchai S. Quantifcation of carotenoid and favonoid components in brans of some Thai black rice cultivars using supercritical fuid extraction and high-performance liquid chromatography-mass spectrometry. J Food Lipids. 2008; 15:488–503.

21. Park KH, Liu Z, Park C-S, Ni L. Microbiota associated with the starter cultures and brewing process of traditional Hong Qu glutinous rice wine. Food Science and Biotechnology. 2016;25(3):649-58.
22. Pengkumsri N, Chaiyasut C, Saenjum C, Sirilun S, Peerajan S, Suwannalert P, et al. Physicochemical and antioxidative properties of black, brown and red rice varieties of northern Thailand. Food Science and Technology. 2015;35:331-8.
23. Shen Y, Jin L, Xiao P, Lu Y, Bao J. Total phenolics, flavonoids, antioxidant capacity in rice grain and their relations to grain color, size and weight. Journal of Cereal Science. 2009;49(1):106-111.
24. Slinkard K, Singleton VL. Total phenol analysis: automation and comparison with manual methods. American journal of enology and viticulture. 1977;28(1):49-55.
25. Sompong R, Siebenhandl-Ehn S, Linsberger-Martin G, Berghofer E. Physicochemical and antioxidative properties of red and black rice varieties from Thailand, China and Sri Lanka. Food Chemistry, 2011;124(1);132-140.
26. Wise K, Preparing spread plates protocols. Am. Soc. Microbiol. Microbe Libr. 2006; 3085.
27. Wise K. Preparing spread plates protocols. Am. Soc. Microbio.l Microbe. Libr. 2006; 3085.
28. Yang S, Lee J, Kwak J, Kim K, Seo M, Lee Y-W. Fungi associated with the traditional starter cultures used for rice wine in Korea. Journal of the Korean Society for Applied Biological Chemistry. 2011;54(6):933-43.
29. Yawadio R, Tanimori S, Morita N. Identification of phenolic compounds isolated from pigmented rices and their aldose reductase inhibitory activities. Food Chemistry. 2007;101(4):1616-1625.

MICRONEEDLES FOR BORAX TESTING IN FOOD

Suratwadee Sriwarom,[1] Thanachita Sumontha,[1] Jeerapond Leelawattanachai,[2*] Darapond Triampo[1*]
[1] Department of Chemistry and Center of Excellence for Innovation in Chemistry, Faculty of Science, Mahidol University, Nakhon Pathom, 73170, Thailand
[2] National Nanotechnology Center (NANOTEC), National Science and Technology Development Agency (NSTDA), Pathum Thani 12120, Thailand
*e-mail: darapond.tri@mahidol.edu, jeerapond@nanotec.or.th

Abstract:

Borax is a dangerous carcinogenic substance that, if taken in a large dosage, can risk human health. Borax is used as a food additive to create a crisp, chewy texture, and extend the shelf life of the product. This study aims to test borax in food by using microneedles. The microneedles (MNs) prepared from 11.1 % w/w of poly(methyl vinyl ether-alt-maleic acid)(PMVE/MA) and 5.6 % w/w of poly(ethylene glycol)(PEG) with varying 10 mg, 30 mg, and 50 mg of curcumin was to investigate an appropriate method of borax detection. The MNs could absorb liquid containing borax and react with the curcumin embedded in the upper layer of the MNs. Agar gel was prepared with varying concentrations of borax 0, 5, 20, 50, 100, 200, and 500 ppm to be used as test samples. The MNs applied time in the sample was varied with the best time of 60 mins at 60°C. The MNs drying time was also determined for best color observation. The MNs were dried at 60°C for 24 hours. The color change of the MNs can be observed with the naked eye. The detection limit of this MNs-based technique is 5 ppm. The advantages of the MNs-based technique are one-step sample preparation and not having to use strong acids, like, hydrochloric acid.

Introduction:

Borax is an ionic compound of boron and oxygen with the chemical formula $Na_2H_{20}B_4O_{17}$ often written in terms of $Na_2B_4O_7{\cdot}10H_2O$. Borax can easily be converted to boric acid when react with hydrochloric acid. Boric acid is a well-known borate that forms red complexes. Two red complexes formed between borate and curcumin are rosocyanine and rubrocurcumin. [1] Borax is a toxic substance that may be used as a food additive to enhance its crispness and chewiness and is also used as a food preservative. Foods that are commonly found to contain borax include meat products such as meatballs, sausages, canned fruits, and pickled vegetables. In Thailand Notification of Ministry of Public Health No. 151 in 1993 states that borax is a substance that is forbidden to be used as an additive in food. Violators are punished with a fine of not more than 20,000 Baht. According to the World Health Organization (WHO), experimental research for short-term intake of borax in rats exhibits an effect on reduced testicular weights. Additionally, for long-term intake, it is reported an increase in mortality rate. Moreover, the effect on humans reported in the lowest reported lethal doses of boric acid is 640 mg/kg body weight (oral), 8600 mg/kg body weight (dermal), and 29 mg/kg body weight (intravenous injection). Borax can affect the risk of human health to cause carcinogens such as renal failure, cerebral edema, fatty liver, and gastroenteritis and cause human chromosome abnormalities which lead to genetic defects. Immediate symptoms when consuming contaminated a large amount of borax are squeamishness, severe stomach pain, gastrointestinal irritation, and vomiting. These symptoms will occur when adults receive 15 grams of borax, and 5 grams for children. [2-6]

As in China, boric acid and borate have been found in beans, rice, and aquatic products. [7] In Malaysia, noodles and fish-based processed food have also been detected with boric acid. [8] Caviar and dried apricot produce have also found boric acid in the United States and China. [9-10] The methods for the determination of boric acid in food are using of the titration technique of mannitol and the colorimetric method using curcumin, which was detected in pickled mango, noodles, and prawns. [11] It has been reported, the detection of borax with the use of a fiber optic sensor as a detector for borax content in meat. [12] Curcumin paper-based test kit has been used as a simple colorimetric method to determine the amount of borax in food. Curcumin is a substance that is found in turmeric (Curcuma longa). Curcumin can react with borate compounds to create a red color compound. However, the curcumin paper-based technique involved many steps of sample preparation and it must be prepared under acidic conditions with concentrated hydrochloric acid (HCl) which is rather dangerous and highly corrosive. HCl is used to convert borax to boric acid. [13-16] Microneedles (MNs) contain micron-sized needles ranging in height from 25 to 2000 μm. The essential parameters to design and fabricate MNs are their shape and geometry. MNs are divided into five types included solid, coated, dissolving, hollow, and hydrogel-forming MNs. [17] Hydrogel-forming MNs are prepared from swellable polymers that have water absorption ability. Hydrogels are hydrophilic crosslinked polymers that are able to absorb a large amount of water in their 3-dimensional networks. [18] In this work, we developed MNs patches based on PMVE/MA and PEG containing curcumin for borax testing in food. The MNs could absorb liquid containing borax and appear red in color with curcumin after drying the MNs. The change in color can be observed with the naked eye. The hydrophilic polymer served as an acid bed and react with borax to convert to boric acid and generated the red compound. The application of this MNs-based technique helps reduced the use of hydrochloric acid and reduced the many steps of sample preparation.

Methodology:

Materials

Chemicals used in this study were curcumin powder, di-sodium tetraborate decahydrate (Borax) (QRec New Zealand), poly(methyl vinyl ether-co-maleic anhydride) (PMVE/MA) (Sigma-Aldrich), poly(ethylene glycol) (PEG) (Sigma-Aldrich), agar powder (Sigma-Aldrich), and distilled water (DI water).

Fabrication of MNs containing curcumin by double layers casting method

MNs patches were prepared using 11.1 % (w/v) of PMVE/MA. It was added into DI water and stirred vigorously to make certain good wetting and to inhibit aggregation. The temperature of the mixture was maintained between 95 to 100 °C until a clear solution was obtained. Then, 5.6% (w/v) of PEG at room temperature was added to the PMVE/MA gel. The polymer mixture was centrifuged at 5000 rpm for 5 mins to get rid of bubbles.

Four hundred microliter of the polymer mixture was cast onto poly(dimethyl siloxane) (PDMS) MNs molds having a hexagon curvature of pyramidal shape. The vacuum was applied to the molds for 45 mins to force the polymer solution to fill into the PDMS molds channels. The casted solution was dried in the molds for 24 hours at room temperature.

After the first layer of MNs patches was dried. The second layer was added curcumin to the polymer solution with varying concentrations of 10, 30, and 50 mg which act as the analyte reagent to detect the borax. Then, the second layer of solution was poured onto the casted first layer and was dried at room temperature for 24 hours. After drying, the patches were cured at 80°C for 24 hours to crosslink the polymers between PMVE/MA and PEG. The MNs were carefully removed from the molds. The fabrication of MNs patches revealed

that the incorporation of curcumin into the second layer of the polymeric matrix of the MNs did not result in any changes in MNs morphology, as can be shown in the digital microscope image of MNs patches in Figure. 1 (a).

Borax testing of MNs in agar gels

Agar gel was prepared with varying concentrations of borax 0, 5, 20, 50, 100, 200, and 500 ppm to be used as test samples. Agar plates were prepared by adding 0.1 g of agar powder in DI water which has a total volume of 20 mL. The agar solution was heated at 100 °C. After a clear agar solution was obtained, the solution was left to cool down then 20 µL, 80 µL, 200 µL, 400 µL, 800 µL, and 2000 µL, of 5000 ppm of the borax solution were added to 20 mL total volume of agar solution to obtain agar gel with the borax concentration of 5, 20, 50, 100, 200, and 500 ppm, respectively. The mixtures with varying borax concentrations were poured into a petri dish and cooled in the refrigerator to allow the agar gel to set.

To investigate a suitable concentration of curcumin in the MNs patches for borax detection, first, we varied the curcumin concentrations of 10 mg, 30 mg, and 50 mg which were tested in an agar gel with borax at the concentration of 0, 5, 20, 50, 100, 200, and 500 ppm. The MNs patches were applied into agar gel at room temperature for 90 mins to absorb the borax solution. Then, MNs patches were incubated into agar gel at 60 °C in the oven for another 60 mins. After that, MNs patches were removed from the agar gel and were heated in an oven at 60 °C for 24 hours to dry.

Then, we observed the applied times for MNs on the top of agar gel at 60 °C was observed at 60 mins, 90 mins, and 120 mins. Which were tested with MNs containing curcumin 10 mg in borax concentrations of 0, 5, 20, 50, 100, and 200 ppm. The MNs patches were applied into agar gel at 60 °C for 60 mins, 90 mins, and 120 mins to absorb the borax solution. After that, the MNs patches were removed from the agar gel and were heated in an oven at 60 °C for 24 hours to dry. In this method, we also observed drying times of 120 mins, 150 mins, 180 mins, and 24 hours.

Water absorption

The MNs patches having a round shape with a dimension of 1.45 cm were prepared for the water absorption evaluation. The MNs patches were immersion in 15 mL DI water at room temperature for 0, 1, 2, 3, and 24 hours. Then, the MNs patches were removed from DI water to stop the water absorption. After that, remove the excess water on the MNs patches surface with tissue paper by gently blotting. The MNs patches were weight before immersion which is measured as W_0 and W_1 were measured as the weight of MNs patches after being immersed in water for 0, 1, 2, 3, and 24 hours at room temperature that is following as Eq 1.

$$\text{Water Absorption, \%} = \frac{W_1 - W_0}{W_n} x100 \qquad \text{Eq 1.}$$

Where,

W_0 = weight of MNs patches before immersion

W_1 = weight of MNs patches after 0, 1, 2, 3, and 24 hours of immersion in DI water

Diameter length swelling

The MNs patches having a round shape with a dimension of 1.45 cm were prepared for the thickness swelling evaluation. The MNs patches were immersion in 15 mL DI water at room temperature for 0, 1, 2, 3, and 24 hours. Then, the MNs patches were removed from DI

water to stop the water absorption. After that, remove the excess water on the MNs patches surface with tissue paper by gently blotting. The MNs patches were measured diameter length of the MNs patches before immersion which was measured as L_0 and L_1 were measured as the diameter length of MNs patches after being immersed in water for 0, 1, 2, 3, and 24 hours at room temperature that is following in Eq 2.

$$\text{Diameter length swelling, \%} = \frac{L_1 - L_0}{L_0} x100 \quad \text{Eq 2.}$$

Where,

L_0 = the diameter length of MNs patches before immersion

L_1 = the diameter length of MNs patches after 0, 1, 2, 3, and 24 hours of immersion in DI water

Results and Discussion:

Fabrication of MNs containing curcumin by double layers casting method

A double-layer casting method was prepared from 11.1% (w/v) of PMVE/MA and 5.6% (w/v) of PEG in DI water using double layers casting method and crosslinking at 80°C for 24 hours. The double layer MNs patches, in the dry state, the average patches base thickness of 233 µm, the dimension of the patches base is 1.45 cm and each needle measured 122 µm in width, 361 µm in length, and 344 µm inter-needle spacing (the distance between each edge to edge of the needle) and schematic diagram of the side view of MNs patches shown in Figure 1 (b).

Borax detection of the MNs patches in agar gels

To investigate an appropriate method of MNs patches for borax detection, we observed different conditions including various curcumin concentrations, times of applied into agar gel at 60 °C, and times for drying MNs patches at 60 °C. To testing of MNs patches is able to detect borax by observing the color change from yellow color to orange color. From the result in Figure 2, it can be seen that 5 ppm of borax in agar gel the MNs patches with 10 mg of curcumin to change color from yellow to slightly orange color, which can see the orange color shape in the middle of MNs patches as shown in Figure 2 (c). As in 30 mg and 50 mg of curcumin are also observed darker yellow color to orange color with a darker color in 5 ppm due to the greater concentration of curcumin as shown in Figure 2 (b).

On the other hand, the color change from yellow color to orange color of MNs patches at borax concentration 20, 50, 100, and 200 ppm can be seen as the color increase darker orange with increasing borax concentrations respectively, which are noticeable all in 10 mg, 30 mg and 50 mg of curcumin concentrations as shown in Figure 2(a). This indicates that MNs patches can detect the borax in agar gel. According to the curcumin in MNs patches can react with borax to produce the orange color complex. The color change of the MNs patches can be observed with the naked eye. The orange color is a product of the reaction between borax and curcumin under the acid condition to change borax to borate. These MNs patches based on PMVE/MA and PEG can generate the acid condition. The anhydride ring of the PMVE/MA copolymer must be opened by hydrolysis in an aqueous solution in order to release the free carboxylic acid (COOH) groups needed to react with polyols. The crosslink reaction occurred at 80 °C with PEG. The PMVE/MA crosslink with PEG consists of the carbonyl group, which is an acid state. [19]

According to the color of the result in Figure 2, 10 mg of curcumin is appearing from yellow to orange which can be easily observed by a color change and used 10 mg of curcumin MNs patches to investigate the times for applying the MNs patches into agar gel.

Figure 3 investigated times for applying the MNs patches into agar gel and incubating at 60 °C with varying times of 60 mins, 90 mins, and 120 mins. The results are at 60 mins, 90 mins, and 120 mins, and then remove MNs patches and dry for 180 mins, 150 mins, and 120 mins respectively. The color changes from yellow to orange are still unclear due to the MNs patches being moisture, not completely dry as exhibited in Figure 3 (a). and after drying at 24 hours in the oven for 24 hours, the MNs patches changed color from yellow to a darker orange. In addition, the MNs patches incubated at 60 °C can reduce the time of applied MNs patches in agar gel which takes 60 mins when there are compared with MNs patches applied into agar gel at room temperature which takes 90 mins.

Water absorption

To determine the water absorption of MNs patches were immersed in DI water at room temperature for 0, 1, 2, 3, and 24 hours. The results of water absorption of curcumin 10 mg are 0, 374.12%, 483.13%, 493.15%, and 554.01%. As 30 mg are 0, 315.96%, 393.42%, 379.94%, and 524.53%. And the results of water absorption of 50 mg are 0, 274.47%, 290.94%, 314.38%, and 419.29%. From Figure 4, it can be seen that the MNs patches can absorb water which can indicate that the MNs patches can absorb the borax solution. According to borax can dissolve in water and react with curcumin in the MNs patches.

Diameter length swelling

To determine the water absorption of MNs patches were immersed in deionized water at room temperature for 0, 1, 2, 3, and 24 hours. From Figure 5, the diameter length of curcumin at 10 mg, 30 mg, and 50 mg has a similar average starting size of 1.45 cm, and after immersion in DI water has a size of 2.35 cm. The diameter length of the MNs patches after immersion in DI water was not different in 10 mg, 30 mg, and 50 mg due to the same crosslinking densities, since they were prepared from the same amount of PMVE/MA and PEG, resulting in the same percentage of swelling which is equal to 62.07%.

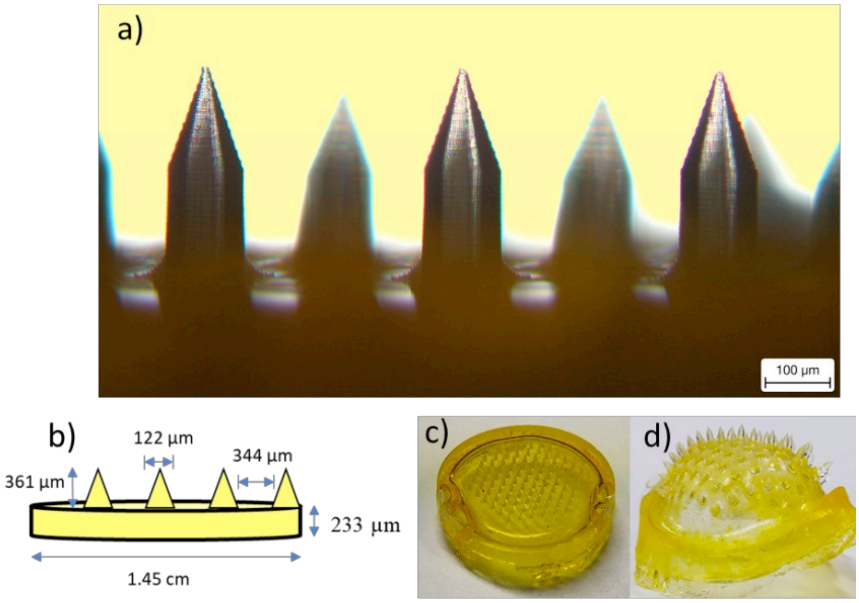

Figure 1.

Digital images of poly(methyl vinyl-alt-maleic acid) and poly(ethylene glycol) MNs (a) the average base thickness of 233 µm, the dimension of patches is 1.45 cm and each needle measured has a size of 122 µm in width, 361 µm in length, and 344 µm in the inter-needle spacing (the distance between each edge to edge of the needle) (b) Schematic diagram of a side view of MNs patches (c) MNs patch with 10 mg of curcumin appeared yellow in color. (d) MNs patch after swelled in DI water.

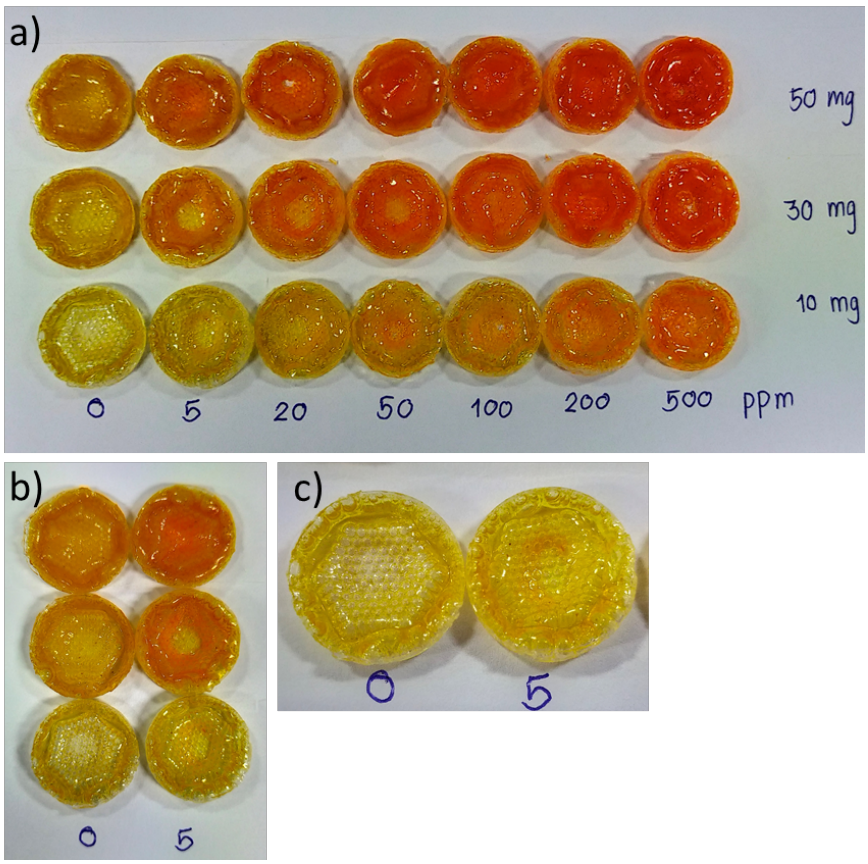

Figure 2.

MNs patches containing 50 mg, 30 mg, and 10 mg of curcumin are applied into the agar gel containing 0, 5, 20, 50, 100, 200, and 500 ppm of borax for 90 mins at room temperature and incubated in agar gel at 60°C for another 60 mins. Then, removed the MNs patches from the gel and heat to dry at 60°C for another 24 hours.

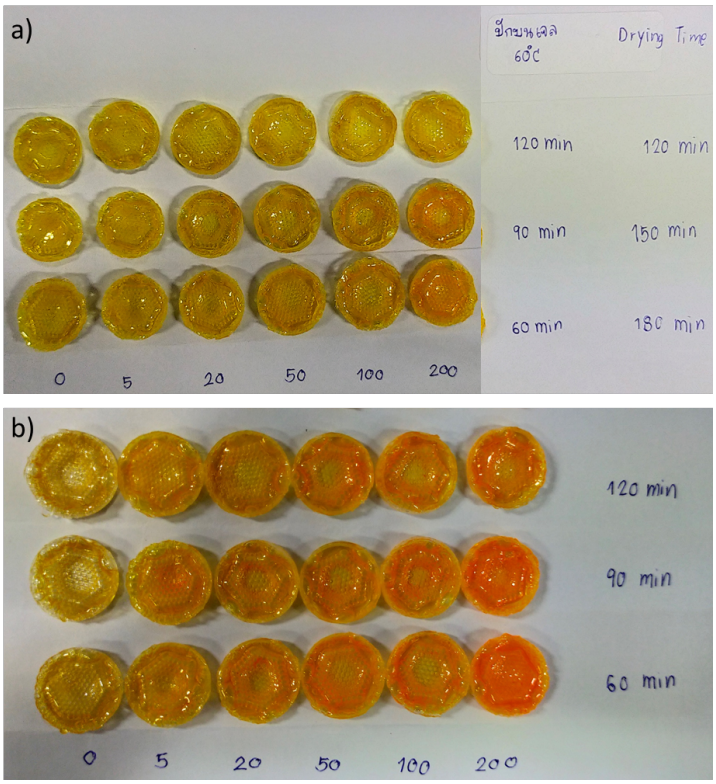

Figure 3.

Borax detection upon MNs patches was applied into an agar gel containing 0, 5, 20, 50, 100, and 200 ppm of borax. MNs patches contained 10 mg of curcumin and heat in an oven at 60°C for 60 mins, 90 mins, and 120 mins. (a) the MNs patches were removed from the gel and heated at 60°C for 120 mins, 150 mins, and 180 mins. (b) the MNs patches were removed from the agar gel and heated at 60°C for 24 hours to dry.

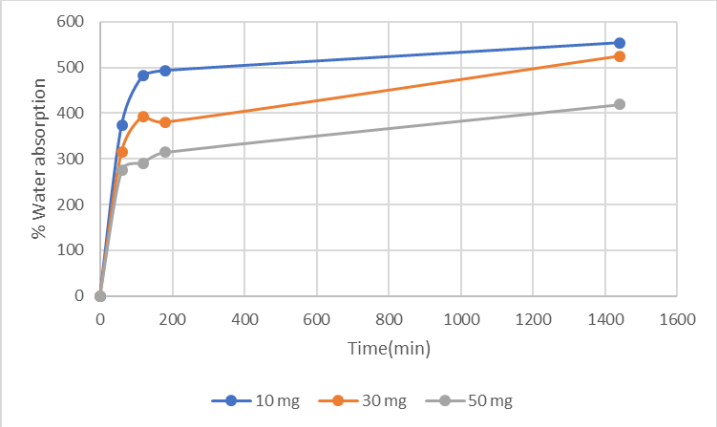

Figure 4.

% Water absorption of MNs patches.

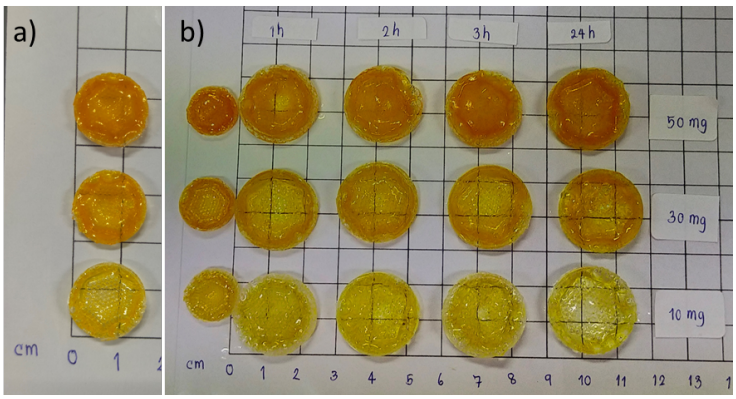

Figure 5.
Swelling of MNs patches made of hydrophilic polymers of PMVE/MA and PEG, (a) in the dry state of MNs patches. (b) Upon immersion in water for 0, 1, 2, 3, and 24 hours. L_0 = 1.45 cm and L_1 = 2.35 cm.

Conclusion:

Hydrogel MNs patch-based can be used to detect borax in both liquid samples and moist solid samples. According to the MNs patches are made from PMVE/MA and PEG which have a good water absorption capability with a high percentage of water absorption. The MNs patch borax detection changed color from yellow to orange due to reacting with curcumin inside the MNs patches that can be observed with the naked eye. The minimum time that the MNs needed to be applied into the sample was at least 60 mins at 60°C in the oven and remove MNs patches to dry for 24 hours. The detection limit of borax is 5 ppm. The use of MNs patch help reduced the many steps of sample preparation and avoid the use of concentrated hydrochloric acid which is a hazardous chemical.

Acknowledgements:

This research was financially supported by the Thailand Graduate Institute of Science and Technology (TGIST, SCA-CO-2563-12174-TH), the National Nanotechnology Platform (NPT, P185171), National Nanotechnology Center (NANOTEC), the National Science and Technology Development Agency (NSTDA), Thailand, and the Department of Chemistry, Faculty of Science, Mahidol University, Thailand

References:

1. PubChem. "Borax". pubchem.ncbi.nlm.nih.gov. Retrieved December 27, 2021.
2. World Health Organization. Boron in drinking-water: Background document for development of WHO Guidelines for Drinking-water Quality. No. WHO/HSE/WSH/09.01/2. World Health Organization, 2009.
3. Hadrup, Niels, Marie Frederiksen, and Anoop K. Sharma. Regul Toxicol Pharmacol. 2021; 121: 104873.
4. Pongsavee M. Southeast Asian J. Trop. Med. 2009; 40(2): 411.
5. Donoiu, Ionuţ, Trace Elem. Med Biol. 2018; 50: 47-56.
6. Ermawati F U. J Phys. Conf. Ser. 2021; 2110(1).
7. Wen Zhu Z, Yi Z and Yu GJ. Food Saf. Qual. 2020; 11: 4242
8. Amit Z Borneo. J. Resour. Sci. Technol. 2020; 10: 70
9. Holak W. J. Assoc. Off. Anal. Chem. 1972; 55: 890

10. Laura R. After China turned it into a cheap snack, caviar is at risk of losing its status as a luxury good. The Washington posts. 2019.
11. Siti-Mizura S, Tee E and Ooi H. J. Sci. Food Agric. 1991; 55: 261
12. Yunianto M, Andaresta D, Anwar F and Saraswati T 2021 J. Phys. Conf. Ser. 1825 12078
13. Rahma C, Hidjrawan Y. Journal Pangan dan Agroindustri. 2021; 9(1): 56-63
14. Ratnarathorn N, Dungchai W. J Anal Chem. 2020; 75(4): 487-494.
15. Wen Xian. Simple qualitative detection method of borax in food (C.N. Patent No.104020166) Nanjing Mai Side Catering Management Co Ltd. 2014.
16. Wen Xian. Kit for detecting sodium borate in food. (C.N. Patent No.104007111 Nanjing Mai Side Catering Management Co Ltd. 2014.
17. Aldawood F K, Andar A, Desai, S. Polymers. 2021; 13(16): 2815.
18. Turner.; Joseph G., et al. Macromol. Biosci. 2021; 21(2): 2000307.
19. Singh, Thakur Raghu Raj, et al. European Polymer Journal, 2009; 45(4): 1239-1249.

Session SP2:
SCIENCE EDUCATION: CHALLENGES TOWARDS VUCA ERA

DETECTION OF ELECTROMAGNETIC WAVES BY A HOMEMADE HERTZ EXPERIMENT KIT

Chakrit Smarnrak,* Thanyanan Somnam
Department of Physics, Mahidol Wittayanusorn school, Salaya, Phutthamonthon, Nakhon Pathom 73170, Thailand
*e-mail: chakrit.man@mwit.ac.th

Abstract:

It is well-known that electromagnetic waves were first experimentally generated and detected by Heinrich Rudolf Hertz in 1887 in order to clarify Maxwell's equations. He built an apparatus which consists of a transmitter, involving an induction coil and a capacitor to create electromagnetic waves, and a receiver in form of wire loop containing a gap between two brass spheres to detect the waves. To study this topic by imitating the original Hertz experimental setup is still difficult and dangerous due to high voltage generator. Therefore, this work aims at demonstrating the detection of electromagnetic waves using a simple homemade apparatus. We use a gas lighter gun which cannot produce fire as transmitter to generate electromagnetic wave signal. The receiver is made by a fluted polypropylene sheet covered with aluminum foil which is kept distant from the ground. To detect the existence of electromagnetic waves from the transmitter and their propagation through free space, a light-emitting diode (LED) is used. One LED pin (anode) is connected to the foil via electric alligator clips, while the other one (cathode) is held by hand in order to be connected to the ground. Each time the lighter gun is pressed, the LED glows within the signal period of 0.1 s. This can be explained by the electric field created in the foil by the radiation of electromagnetic waves from the transmitter. This makes higher potential difference between the foil and the ground, yielding enough amount of current to light the LED. No matter the size of LED, our study gives the best observation during daylight when both 3 mm and 5 mm clear green LEDs are used. Our homemade Hertz experiment kit costs less than 100 Thai baht. This work could be improved and designed to be an experimental setup for studying other aspects of electromagnetic waves. In conclusion, our work presents a simple and low-cost way to set up Hertz experiment in high schools, universities, and even at home.

Introduction:

Studying the properties of electromagnetic waves is one of the most difficult physics topics for students and undergraduates. In 1861-1862, James Clerk Maxwell proposed four fundamental field equations interpreting the electromagnetic field and showed that electromagnetic waves are a natural consequence of these equations, known as Maxwell's equations. To confirm Maxwell's equations, Heinrich Rudolf Hertz was the first physicist who demonstrated the existence of electromagnetic waves in 1887 by inventing an apparatus which is composed of a transmitter to generate electromagnetic waves, and a receiver to detect the waves.[1,2] Figure 1 shows the arrangement of Hertz experiment. The transmitter involves an induction coil (L) and two spherical electrodes separated by a narrow gap acting as a capacitor (C). From a circuit viewpoint, this can be considered as an LC circuit. The induction coil provides short voltage surges to the electrodes, then the spark or the discharge between the electrodes exhibits an oscillatory behavior of electric and magnetic fields at a very high frequency. The electric and magnetic fields are perpendicular to each other. The receiver in form of wire loop containing a gap between two brass spheres detects induced

sparks across the gap. Note that the detection only occurs when the frequency of the receiver is adjusted to match that of the transmitter.

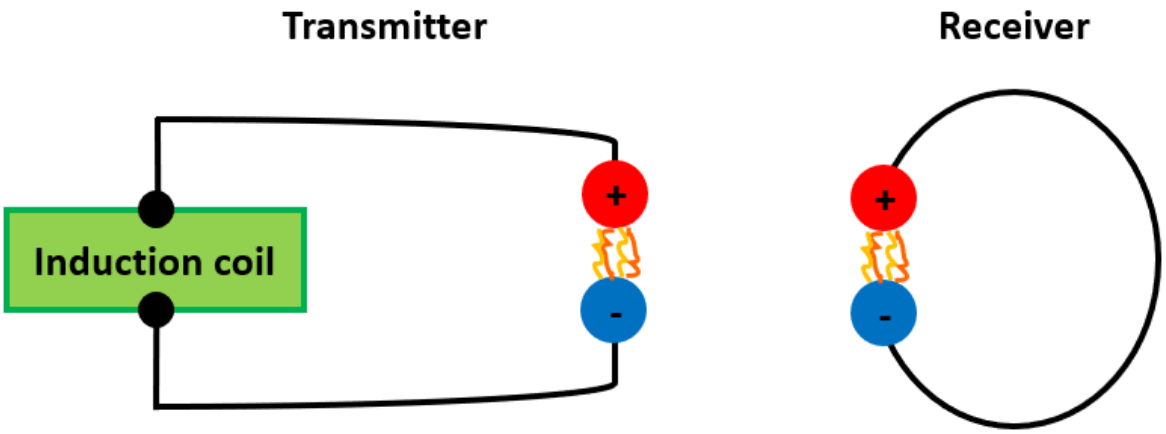

Figure 1.
Scheme of the arrangement of Hertz experiment.

Imitating the original Hertz experimental setup as previously mentioned is still complicated for instructors and dangerous when using due to high voltage generator. Several studies have shown modified Hertz experimental setups which allow to study various aspects of electromagnetic waves.[3] However, they are still complicated and some specific techniques are required. Therefore, the present work aims to demonstrate the use of a simple homemade apparatus to detect electromagnetic waves. Our own apparatus is composed of a transmitter and a receiver which are made of simple materials that can be easily found in laboratory and at home. It differs from the original Hertz experimental setup because the receiver can detect electromagnetic waves immediately without tuning its frequency to that of the transmitter. This important point makes the apparatus inexpensive and easy to use. The invention of our homemade Hertz experiment kit and obtained experimental results will be described in detail in the following parts.

Methodology:

We used simple materials and apparatus shown in Figure 2 (Left) to set up Hertz experiment: 1. gas lighter gun used as transmitter, 2. receiver made by a fluted polypropylene sheet covered with aluminum foil, 3. Plasticine, 4. LED, and 5. Alligator clips. In this work, electromagnetic waves are created by pressing the gas lighter gun (number 1) of which the gas tube is removed in order to prevent fire when pressing as presented in Figure 2 (Right). As shown in Figure 2 (Left), the signal receiver (number 2) can be made from aluminum foil of dimension 30 cm × 30 cm which covers a fluted polypropylene board of dimension 30 cm × 33 cm. Note that the foil is kept distant from the ground to ensure that a short circuit between the foil and the ground cannot occur. Plasticine or any non-conducting materials (number 3) is used for maintaining the board in vertical position. When the lighter gun is pressed, an electromagnetic wave signal is emitted and travels through space to the receiver. The signal will be detected by the receiver and can be observed by the glowing of the LED (number 4). One LED pin (anode) is connected to the foil via electric alligator clips (number 5), while the other one (cathode) is held by hand in order to be connected to the ground as shown in Figure 3 (Left).

Figure 2.
(Left) Materials and apparatus used to make our Hertz experimental setup: 1. gas lighter gun used as transmitter 2. receiver made by a fluted polypropylene sheet covered with aluminum foil 3. Plasticine 4. LED 5. Alligator clips. (Right) Gas lighter gun without fire when pressing due to the removal of gas tube as shown in dashed circle.

Figure 3 (Right) presents the diagram of our homemade Hertz experimental setup. In this experiment, the lighter gun was set far of about 1 cm from the foil. The intensity of LED glowing is defined based on the observation with naked eyes in three levels: level 0 (LV0) means light cannot be observed, level 1 (LV1) means light is dim and barely visible, and level 2 (LV2) means light is the brightest and can be clearly observed. We tested several LEDs in order to find the best specification of the LED that makes the experiment easy to use. Moreover, we used the brightest LED (glowing at level 2) in the arrangement of the apparatus to find the best orientation of the lighter gun to the foil.

To find which specification of LED is best suited to this experiment, several LEDs of different sizes (3 mm and 5 mm in diameter), different optical properties (clear and diffused LEDs), and different colors (red, green, blue, yellow, and white) were tested. The light from LED was observed both in lighted room and darkened room. We also did experiment in lighted room with 9 participants to minimize errors from bare eye observation. In this experiment, the intensity level of LEDs will be turned to score i.e. LV0 = 0, LV1 = 1 and LV2 = 2. The summation of scores from all participants will lead to find the most suitable LED which has the maximum scores.

The orientation of the lighter gun was also tested with the brightest LED found previously. The lighter gun was placed about 1 cm from the foil in 4 orientations: perpendicular to the foil (in front of and behind the foil) and parallel to the foil (the tip of the lighter gun points towards the saddle of the foil). We also tried to press the lighter gun and rotate its tip simultaneously around the lighter gun rod by 0, 90, 180 and 360 degrees. This could generate electric signal in different directions.

Moreover, in the last experiment we tested the signal detection by covering the receiver with paper as shown in Figure 3 (Right).

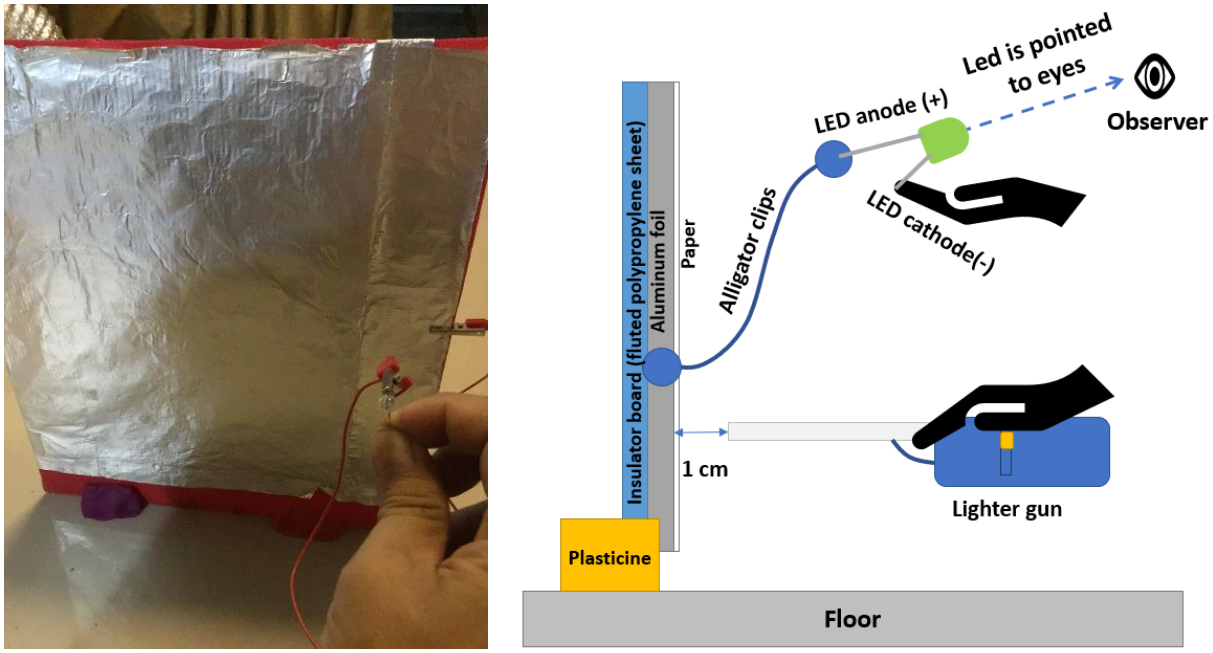

Figure 3.
(Left) Photo and (Right) diagram of our homemade Hertz experimental setup. Anode LED pin is connected to the foil of the receiver via electric alligator clips, while the cathode LED pin is held by hand in order to be connected to the ground. In some experiments, the receiver is covered with paper on top of aluminum foil for preventing electron jumping from the lighter gun to the foil.

Results and Discussion:

We set up our experiment as shown in Figure 3 (Right). The lighter gun was set far of about 1 cm from the foil. The tested LED was connected to the receiver and one hand of the observer. One LED pin (anode) is connected to the foil of the receiver via electric alligator clips, while the other one (cathode) is held by hand in order to be connected to the ground. Note that all the tested LEDs were set to point towards the observer's eyes since most of LEDs exhibit the maximum intensity of light in this direction, and the position of the alligator clips was unchanged through all experiments. When pressing the lighter gun, electromagnetic waves are generated and emitted to the receiver. The LED of the receiver glows immediately within the signal period of 0.1 s and disappears suddenly. Here, the signal period is defined to be the duration between the pressing of the lighter gun and the glowing of the LED. This can be explained by the electric field created in the foil by the radiation of electromagnetic waves from the transmitter. This makes higher potential difference between the foil and the ground, yielding enough amount of current to light the LED. Figure 4 presents examples of experimental results of the LED specification test on the 5 mm clear LEDs of five different colors in lighted room. After pressing the lighter gun, the LEDs glow immediately with different intensities: (A) red LED of level 1, (B) green LED of level 2, (C) blue LED of level 1, (D) yellow LED of level 1, and (E) white LED of level 2.

Figure 4.
Examples of results of the LED specification test on the 5 mm clear LEDs of five different colors in lighted room. After pressing the lighter gun, the LEDs glow with different intensities: (A) red LED of level 1, (B) green LED of level 2, (C) blue LED of level 1, (D) yellow LED of level 1, and (E) white LED of level 2.

All the experimental results of the LED specification test are presented in detail in Table 1 for 3 mm diameter LEDs and Table 2 for 5 mm diameter LEDs. All the LEDs were tested both in lighted room and darkened room.

Table 3 and Table 4 show respectively experimental results of 3 mm and 5 mm diameter LEDs of different optical properties and different colors tested in lighted room by 9 observers. According to the LED intensity level, numbers in the table show number of participants. The interval of total scores ranges from 0 to 18.

Table 1.
Experimental results of 3 mm diameter LEDs of different optical properties and different colors. All the LEDs were tested both in lighted room and darkened room.

LEDs of 3 mm in diameter	Lighted room	Darkened room
Clear Red LED	LV1	LV2
Clear Green LED	LV2	LV2
Clear Blue LED	LV1	LV2
Clear Yellow LED	LV1	LV2
Clear White LED	LV2	LV2
Diffused Red LED	LV1	LV2
Diffused Green LED	LV0	LV0
Diffused Blue LED	LV1	LV2
Diffused Yellow LED	LV1	LV2

Table 2.
Experimental results of 5 mm diameter LEDs of different optical properties and different colors. All the LEDs were tested both in lighted room and darkened room.

LEDs of 5 mm in diameter	Lighted room	Darkened room
Clear Red LED	LV1	LV2
Clear Green LED	LV2	LV2
Clear Blue LED	LV1	LV2
Clear Yellow LED	LV1	LV2
Clear White LED	LV2	LV2
Diffused Red LED	LV1	LV2
Diffused Green LED	LV0	LV0
Diffused Blue LED	LV2	LV2
Diffused Yellow LED	LV1	LV2

Table 3.
Experimental results of 3 mm diameter LEDs of different optical properties and different colors tested in lighted room by 9 observers. According to the LED intensity level, numbers in the table show number of observers. The range of the scores is between 0 and 18.

LEDs of 3 mm in diameter	LV0 (score 0)	LV1 (score 1)	LV2 (score 2)	Total scores
Clear Red LED	2	7	0	7
Clear Green LED	0	0	9	18
Clear Blue LED	3	6	0	6
Clear Yellow LED	2	7	0	7
Clear White LED	0	1	8	17
Diffused Red LED	5	4	0	4
Diffused Green LED	9	0	0	0
Diffused Blue LED	7	2	0	2
Diffused Yellow LED	7	2	0	2

Table 4.
Experimental results of 5 mm diameter LEDs of different optical properties and different colors tested in lighted room by 9 observers. According to the LED intensity level, numbers in the table show number of observers. The range of the scores is between 0 and 18.

LEDs of 5 mm in diameter	LV0 (score 0)	LV1 (score 1)	LV2 (score 2)	Total scores
Clear Red LED	0	8	1	10
Clear Green LED	0	0	9	18
Clear Blue LED	3	5	1	7
Clear Yellow LED	0	9	0	9
Clear White LED	0	1	8	17
Diffused Red LED	5	4	0	4
Diffused Green LED	9	0	0	0
Diffused Blue LED	6	2	1	4
Diffused Yellow LED	6	3	0	3

From the obtained results, it is clear that both 3 mm and 5 mm clear green LEDs are the most suitable for our Hertz experiment because they exhibit the highest total score of 18. When they receive a signal, they are brightest and can be clearly observed by all observers. In addition, both 3 mm and 5 mm clear white LEDs have similar results as clear green LEDs and could be used as an alternative when clear green LEDs are not available. A diffused LED is not recommended to use in the experiment during daylight since some participants cannot detect the LED glowing. However, all the LEDs except diffused green LEDs can be used when the experiment is set in dark environment.

It is interesting that diffused green LEDs of both diameter sizes do not emit light (light intensity of level 0) even in darkened room. One of the reasons could be the fact that the diffused green LEDs of both diameter sizes are made of AlGaInP or InGaN which differ from the material of clear green LEDs.

Once the best specification of LED was found, we used the 5 mm clear white LED in the experiment to test the best orientation of the lighter gun. For all the orientations and the rotations described previously, we found that there is no change in light intensity (level 2) emitted from the LED.

Our last experiment is the test of the signal detection of the LEDs. We used A4 paper to cover the receiver to prevent electron jumping directly from the lighter gun to the receiver. We found that all the LEDs glow as the same as the case of the uncovered receiver. This implies that the glowing of LEDs is directly the result of electromagnetic waves, but not the electron jumping.

Conclusion:

In conclusion, we present in this work a simple way to demonstrate the existence of electromagnetic waves by creating a new arrangement of experimental homemade apparatus. Our homemade Hertz experiment kit illustrates the propagation of electromagnetic waves through empty space. Each time the lighter gun acts as the transmitter, the LED of the receiver glows within the signal period of 0.1 s, indicating the arrival of electromagnetic waves traveling without medium. We found that the best observation during daylight occurs when clear green LEDs were tested. Both 3 mm and 5 mm size of the clear green LEDs give the same results. The materials used to make our apparatus cost less than 100 Thai baht. Our present work shows a simple and low-cost way for instructors to set up Hertz experiment in educational institutes and even at home. Moreover, this work could pave the way to design various experimental setups for studying other properties of electromagnetic waves.

Acknowledgements:

We are grateful for the financial support and the facilities at the workshop and the physics laboratory of Mahidol Wittayanusorn school.

References:

1. Trouton FT. Nature. 1889;39:391-393.
2. Adawi I. American Journal of Physics. 1989;57:125-127.
3. Faccio D, Clerici M, Tambuchi D. American Journal of Physics. 2006;74(11):992-994.

Poster Session

Session A: PHYSICS / APPLIED PHYSICS

NUMERICAL ANALYSIS OF COVID-19 SILVA DISPERSION IN AN AIR-CONDITIONED ROOM

Sirikul Siriteerakul[1], Chainarong Chaktranond[2,*]
[1]Department of Mathematics, Faculty of Science, King Mongkut's Institute of Technology Ladkrabang, Thailand
[2]Department of Mechanical Engineering, Faculty of Engineering, Thammasat University, Thailand
*e-mail: cchainar@engr.tu.ac.th

Abstract:
This study numerically explores the dispersion and fall distance of saliva droplets released from the mouth of a COVID-19 infected person sneezing in an air-conditioned restaurant through two-dimensional numerical simulations of air stream and saliva droplets. Parameters studied are the positions of cold-air outlet (E_{supply} = 1.4 and 6.4 m), velocity of supply air (0.125, 0.25 and 0.5 m/s), and angle of supply air leaving from the outlet (45, 60, and 90 degree). The saliva droplets are assumed as spherical particles and exit continuously from the mouth of the infected person at a speed of 8.5 m/s during the first 0 – 0.5 s. It is found from numerical results that when the outlet is placed near the infected person at E_{supply} = 1.4 m, the particles drift and drop farther than when the outlet is at E_{supply} = 6.4 m. In addition, in case of the air outlet at E_{supply} = 1.4 m, the less angle is less than 90 degree, the more particles can drop further away from the infected person. However, when the outlet is at E_{supply} = 6.4 m, the angle does not much affect the fall distance of particles. Moreover, at the angle of 90 degree in both cases of the outlet at E_{supply} = 1.4 and 6.4 m, particles drop near the infected person. It is because the supply cold-air streams, which are injected vertically downwards, block the particle movement. By considering the outlet at E_{supply} = 1.4 m and the angle of 90 degree, it is found that varying the supply-air velocities do not significantly affect the fall distance of particles away from the infected person.

Introduction:
The crisis of the epidemic of the Covid-19 virus has affected the economy population health and the lifestyle of people around the world. Numerous researchers have attempted to study the dispersion and transmission behaviors caused by aerosols of respiratory secretions when sneezing, coughing, and breathing. These results would help us find strategies to protect and reduce the risk of infection. These studies are performed through experiment or simulation.

Since 2011, Gralton et.al [1] have been suggests that droplet size is the main factor affecting the transmission of pathogens and relative humidity also affect the size of the excreted particles. Lin et.al [2] studied air distribution patterns inside classroom using ANSYS Fluent software. In 2020, the start of the Covid-19 coronavirus pandemic, there are a lot of interests in doing research in this area. Kohanski et.al [3] and Santos, et.al [4] showed that the air movement affects the distribution of saliva particles and good HVAC (Heating, ventilation, and air conditioning) system design can reduce the risk of COVID-19 infection within an indoor environment. Dbouka and Drikakisb [5] studied the effect of wind speed on the distribution of saliva in the air in a 3-D model room. In the same year, Merghani et.al [6] compiled research experiment parameters to see the flow direction and the diffusion angle of the aerosol. In 2021, Bazant and Bush [7] said that pathogens can be transmitted from person to person through the air. Mariam et.al [8] studied the airborne transmission distance of Covid-19 released from the respiratory tract from one person to another nearby by simulating

flow patterns that Different ventilation in the working room. Shao et.al [9] studied the risk of spreading corona virus while people talk or breathe in elevators, small classrooms and in supermarkets. They concluded that the design of the ventilation system was a priority to reduce the risk of exposure to coronavirus particulates. However, the spread of infection in a wider area, as well as the residual aerosol particles on a large number of surfaces on objects such as floors and air vents must also be considered. In addition, Mahamadi and Fazeli [10] have compiled and summarized research on the epidemic model of COVID-19 in various situations. The wind affects the particle's ability to travel long distances despite social distancing. Berry et al. [11] showed that pathogens enter the body through the mouth, nose, or eyes through contact with infected saliva that falls on walls or surfaces, especially in closed, air-conditioned rooms.

Studying the spread of COVID-19 has been received attentions and made important in guiding ways to reduce the spread of the disease. This study simulated the distribution of COVID-19 viral particles by studying the movement and range of saliva particles released from an infected person's mouth while sneezing under the ventilation system in various types of restaurants. The positions, directions and velocities of supply air leaving from the outlet are considered. Results of this research can be used to guide the placement of the dining table and setting of air conditioning systems to reduce the spread of germs.

Methodology:

In this study, the model of the room was 13 m (length) × 3 m (height) as showed in **Figure 1**. The infected person was seated at position A (x = 0.2 m), with B being the normal person's position and C and D is the position of the person sitting next table. In this research, we will simplify by using rectangle instead of sitting people to reduce unnecessary mesh resolution. The cooling air outlet position was tested at x = 1.4 and 6.4 m, and F is the position of the outflow. The air coming out of the air conditioner was tested at angles of 45, 60 and 90 degree with velocities of 0.125, 0.25 and 0.5 m/s. The 1000 particle 80 μm center has constant properties throughout the calculation. The temperature of the saliva particles exiting the infected mouth was 37ºC with a speed of 8.5 m/s [5] for the first 0–0.5 seconds to represent the sneezing behavior.

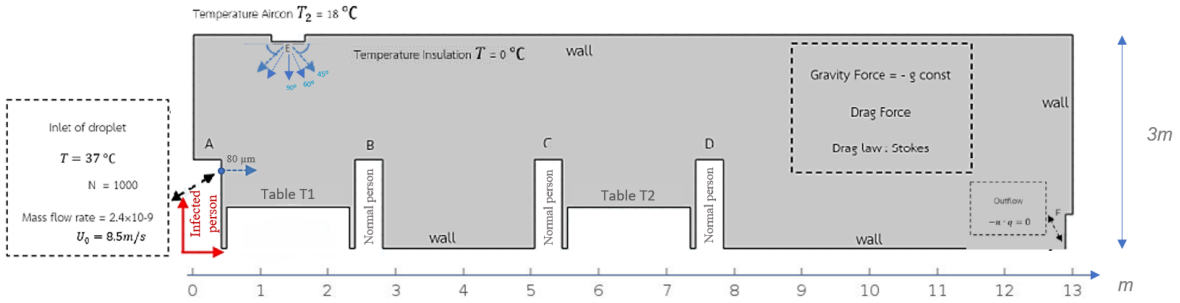

Figure 1.
Computational Domain.

The air flow is incompressible flow, calculated through Navier-Stoke Equation, continuity equation, energy equation and equation of particle motion as shown in Equations (1) to (5), the particle motion is Lagrangian. The physical laws, such as Newton's laws and conservation of mass and energy, apply directly to each particle. The governing equations can be expressed as:

$$\nabla \cdot \vec{u} = 0 \quad (1),$$

$$\rho\left(\frac{\partial \vec{u}}{\partial t} + \vec{u} \cdot \nabla \vec{u}\right) = -\nabla p + \mu \nabla^2 \vec{u} + \rho g \quad (2),$$

$$\rho c\left(\frac{\partial T}{\partial t} + \vec{u} \cdot (\nabla T)\right) = k \nabla^2 T \quad (3),$$

where $\vec{u}$ is the velocity vector, ρ is the fluid density (1.276 kg/m^3), p is the pressure, g is the gravitational acceleration (9.81 m/s^2), T is the temperature, c is specific heat of air (1.006 kJ/(kg.K)), k is the thermal conductivity (24.35×10^{-3} W/(m.K)) and μ is the dynamic viscosity (17.22×10^{-6} Pa.s)

Equation of particle motion is considered. Drag force and gravitational force shown as

$$m_p \frac{d\vec{u}_p}{dt} = \frac{1}{\tau_p} m_p \left(\vec{u} - \vec{u}_p\right) + \left(m_p - m\right)\vec{g} \quad (4),$$

where τ_p is particle relaxation time is given in the form

$$\tau_p = \frac{\rho_p d_p^2}{18\mu} \quad (5),$$

Where subscript p means particle, m is the mass, ρ_p is the particle density (1000 kg/m^3) ,and d_p is the particle of diameter (80×10^{-6} m).

In the calculations, the air velocity is zero at the wall (No-slip condition) and zero pressure gradient at the outlet and no heat transfer at the wall. The temperature of the cold air which is supplied from the outlet was 18ºC, and the initial room temperature was 25ºC, and the temperature of the saliva particles at the time of exiting the infected mouth was 37ºC. Heat transfer from people at positions B, C, and D is not considered. Calculations were done using COMSOL Multiphysics 5.3. The domain for computational are divided into the unstructured triangular-elements fine-mesh as shown in **Figure 2**. The mesh is finer around the edges and corners of objects. The number of computational meshes are approximately not less than 73,000 elements in all cases. In addition, increasing the number of meshes are tested and shown no noticeable difference.

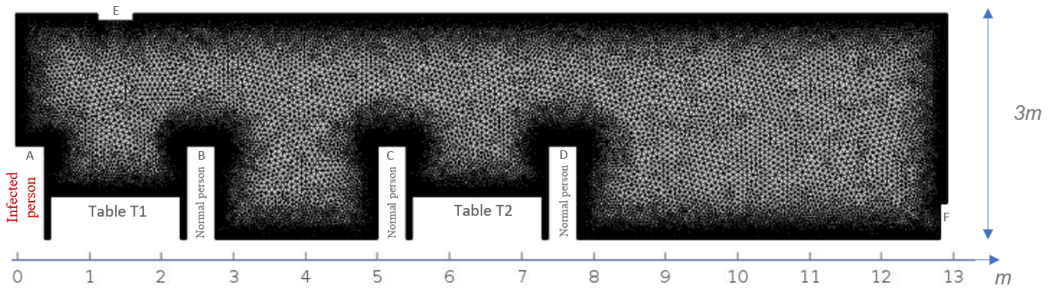

Figure 2.
Domain with the unstructured triangular-elements fine-mesh.

Results and Discussion:

The research is a numerical study to observe the distribution and fall of saliva droplets released from the mouths of COVID-19 patients while sneezing in an air-conditioned restaurant through a two-dimensional simulation of air currents and droplets. The studies are divided into 3 issues as follows:

3.1 Effect of the position of the air outlet (diffuser)

In this study, the effect of the position of cold air outlet to the dispersion distance of infected saliva particles was investigated.

The air conditioner is installed at two locations (one at a time) where E_{supply} = 1.4 m was the located above the infected person's table and E_{supply} = 6.40 m was the located away from the infected person's table. The air velocity leaving the diffuser is 0.5 m/s and the air supply angle is 90 degree (V90 = 0.5 m/s).

From **Figure 3**, defined as Case 1, presents the distribution of particles without supply air from the outlet in various time (no air outlet). In the beginning, most of the particles were found floating around the infected person's table (Table T1) and the person sitting opposite which sitting at the same table as the infected person. At 10 seconds, we can clearly see the particles floating in the air. After that, the particles will gradually fall to the bottom on objects. At 30 seconds, some particles are still floating. From 60 seconds, no more particles are floating in the air.

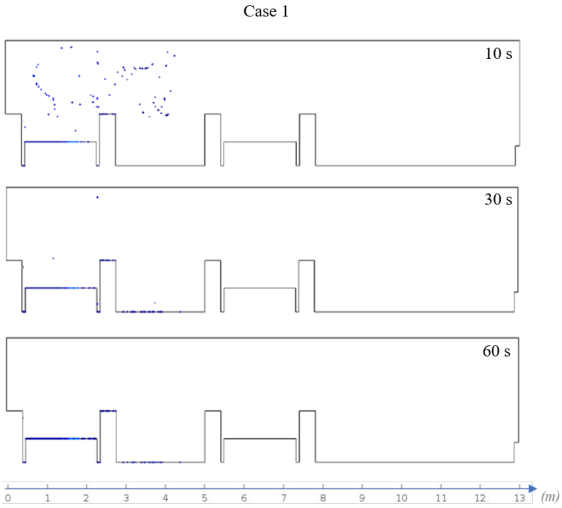

Figure 3.

Particle locations at different times(10 s, 30 s and 60 s), Case 1, no air outlet.

In this case (no air outlet), most of the particles were found to land on the object at a distance of 0.5-2 m near the seat of the infected person (x = 0.2 m) and from a distance of x = 4 m, there were very few particles.

Figure 4 (left) shows the case of air flow from the air supply installed at position 1.4 m, velocity of supply air = 0.5 m/s with the angle of 90 degree (Case 2). It was found that the majority of particles were floating around the infected person's table more than in Case 1 (without the effect of air supply). This is because the airflow from the air supply was directing it down to the area near the infected person sitting. It prevents the flow of particles to the side table. At a distance of x = 1.4 m, this is the center of the table where the infected person sits, most of the particles are somewhat oriented towards the infected person. At distances from x = 4 m, the number of particles falling on the object is very small.

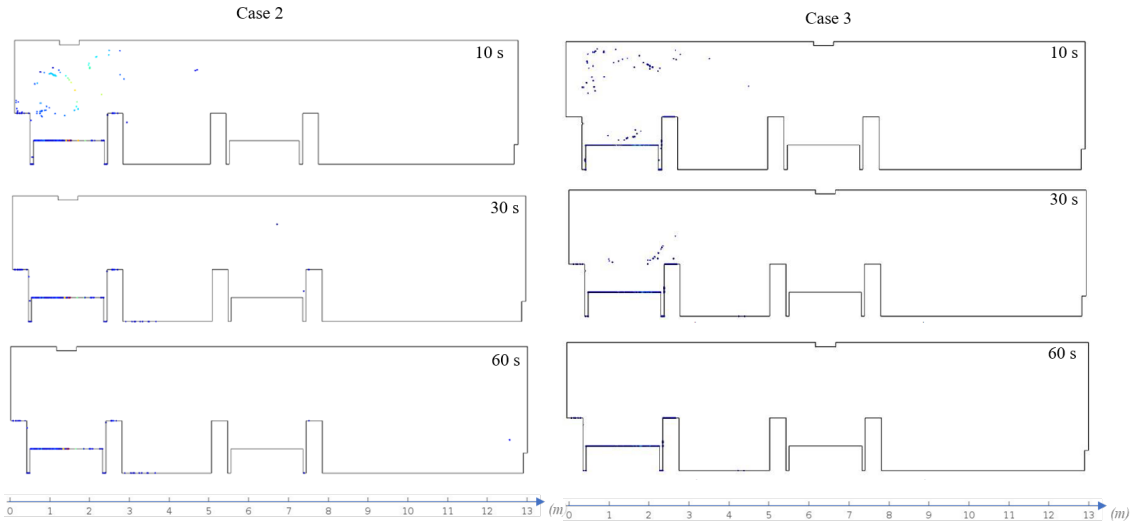

Figure 4.
Particle locations at different times (10 s, 30 s and 60 s),
of Case 2 (E_{supply} = 1.4 m) (left) and Case 3 (E_{supply} = 6.4 m) (right)

Figure 4 (right) shows the case of air flow from the air supply installed at position 6.4 m, velocity of supply air = 0.5 m/s with the angle of 90 degree (Case 3). It was found that the majority of particles were floating around the infected person's table and the person sitting opposite him. This is because the airflow exiting the diffuser at E_{supply} = 6.4 m pushes the air out, and preventing particles from moving to the table where the diffuser is located. Very few particles fall on the object at a distance from x = 3 m. A comparison of the number of particles falling on objects in Case 1, 2, and 3 is shown in **Figure 5.**

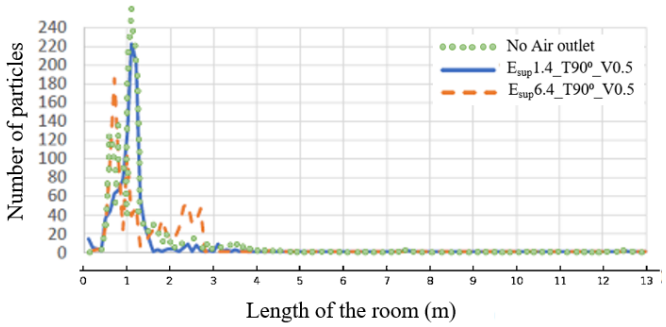

Figure 5.
Comparison the number of particles falling on objects in Case 1, 2, and 3.

3.2 Effect of the supply air direction

Particle locations at different times are shown in **Figure 6**, Case 4, which E_{supply} = 1.4 m, velocity of supply air = 0.5 m/s with the angle of 45 degree is on the left and Case 5 which E_{supply} = 1.4 m, velocity of supply air = 0.5 m/s with the angle of 60 degree is on the right.

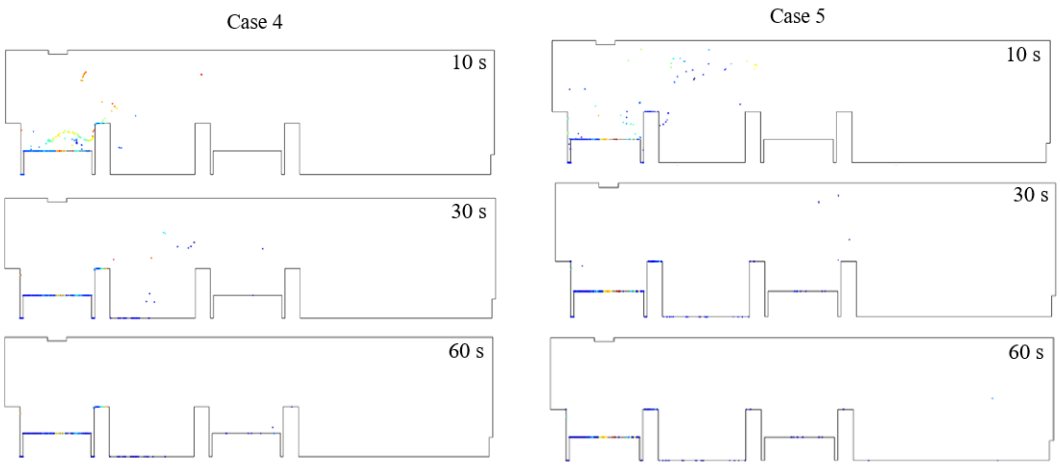

Figure 6.
Particle locations at different times (10 s, 30 s and 60 s) which E_{supply} = 1.4 m, Case 4 (the angle is 45 degree) (left) and Case 5 (the angle is 60 degree) (right)

Figure 6 both cases show the majority of particles were floating around the infected person's table and the person sitting opposite him. Very few particles fall on the object at a distance from x = 3 m. The comparison the number of particles falling on objects in Case 2, 4, and 5 are shown in **Figure 7**. It can be seen that the angle of the air flow from the diffuser is reduced, which means that the particles will fall farther on the surface of the object.

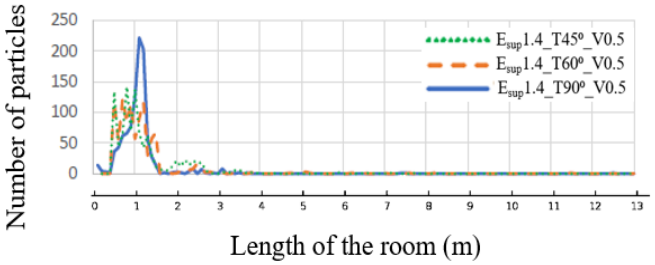

Figure 7.
Comparison the number of particles falling on objects in Case 2, 4, and 5.

Particle locations at different times are shown in **Figure 8**, Case 6 which E_{supply} = 6.4 m, velocity of supply air = 0.5 m/s with the angle of 45 degree is on the left and Case 7 which E_{supply} = 6.4 m, velocity of supply air = 0.5 m/s with the angle of 60 degree is on the right. Both cases show the majority of particles were floating around the infected person's table and the person sitting opposite him. Very few particles fall on the object at a distance from x = 4m. The comparison the number of particles falling on objects in Case 3, 6, and 7 are shown in **Figure 9**. Overall, it can be seen that the angle does not greatly affect the particle's fall distance. In the range of 3 to 4 meters, the angle of the air flow from the diffuser is reduced, the particles will fall slightly farther on the surface of the object. The same is the case with the diffuser at the 1.4 m position. At the angle of 90 degree, the particles float no more than 3 meters. It is because the supply cold-air streams, which are injected vertically downwards, block the particle movement. However, in Case 7, the particles drifted longer.

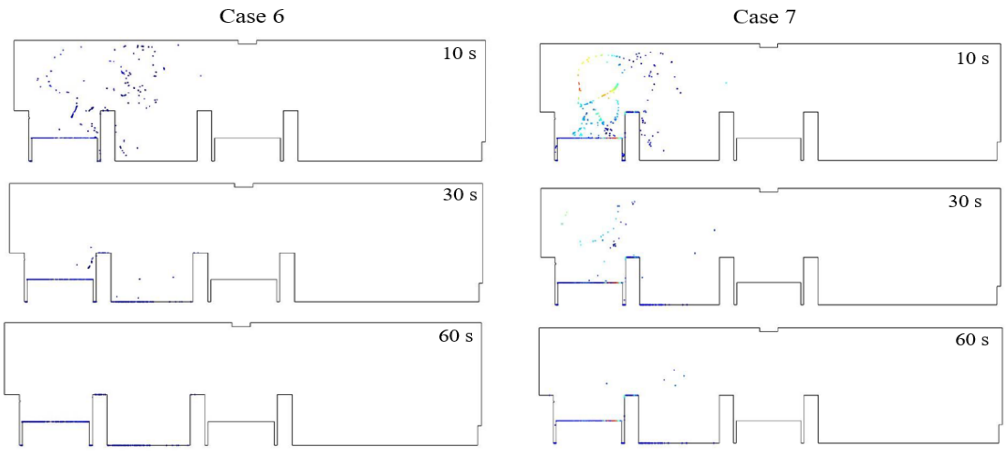

Figure 8.
Particle locations at different times (10 s, 30 s and 60 s) which E_{supply} = 6.4 m, Case 6 (the angle is 45 degree) (left) and Case 7 (the angle is 60 degree) (right)

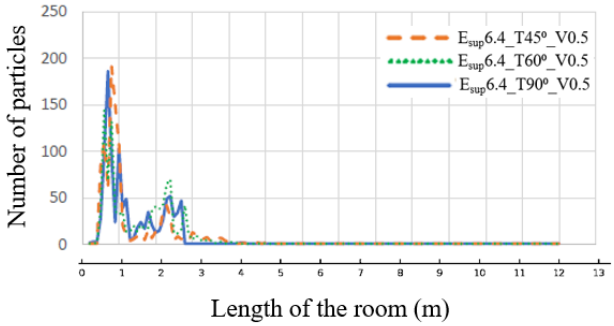

Figure 9.
Comparison the number of particles falling on objects in Case 3, 6, and 7.

3.3 Effect of supply-air velocity

As addressed above, it was found that Case 3, when the air outlet is installed at E_{supply} = 6.4 m and the angle of air diffuser is 90 degree, the particles land on the surface closest to the infected person. Next, with these conditions, we will consider the effect of supply air velocity on particle positions as shown in **Figure 10.**

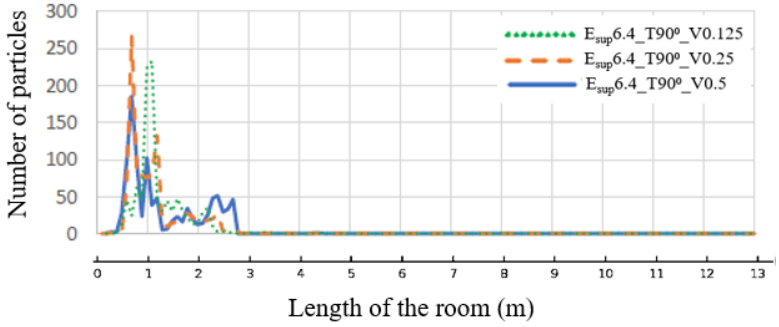

Figure 10.
Comparison the number of particles falling on objects when change wind speed.

It was found that if the supply-air velocity was reduced (V90 = 0.125 and 0.25 m/s), the particles would fall on the surface of the object further away from the infected person.

However, when compared to Case 2, the particles continued to settle on the surface of objects closer to the infected person than in Case 2 (V90 = 0.5 m/s and E_{supply} = 1.4 m). The velocity of the air leaving the diffuser has a slight effect on the particle fall. The speed of air flow reduces, the particles will fall on the surface closer to the infected person. Very few particles fall on the object at a distance from x = 3 m.

Conclusion:

Two-dimensional laminar flow and one-way coupling Lagragian particle simulations are performed to investigate the motion and fall distance of saliva droplet. The remarking conclusions are following:

1. Installing the supply air outlet near the table of infected person causes the droplet to move and fall farther. On the other hand, the airflow exiting the diffuser at above the other table pushes the air out and preventing particles from moving to the table where the diffuser is located.

2. When the supply air leaves from the outlet with lower angle, the air streams carry the droplets to drift longer, resulting in farther fall distance. However, when the outlet is at E_{supply} = 6.4 m, the angle does not much affect the fall distance of particles. Moreover, at the angle of 90 degree in both cases of the outlet at E_{supply} = 1.4 and 6.4 m, particles drop near the infected person. It is because the supply cold-air streams, which are injected vertically downwards, block the particle movement.

3. By considering the outlet at E_{supply} = 1.4 and the angle of 90 degree, it is found that varying the supply-air velocities do not significantly affect the fall distance of particles away from the infected person.

Therefore, the position and angle of the air outlet directly affects the spreading distance of the pathogen. The results of this research could help guide table placement and air conditioning installations restaurants to reduce the spread of germs.

Acknowledgements:

This research was supported by a research grant from Faculty of Engineering Thammasat University, Rangsit Campus. We are grateful to Mr. Suphakorn Tong-Aon and Mr. Patawee Laosutthiwat for data preparation.

References:

1. Gralton, J., Tovey, E., McLaws, M.L., and Rawlinson, W.D. (2011) The role of particle size in aerosolized pathogen transmission: A review, J. Infection, Vol.62, pp.1 -13.
2. Lin S., Tee B.T., Tan C.F. (2015) Indoor Airflow Simulation inside Lecture Room: A CFD Approach, IOP Conf. Series, Mater. Sci. Eng., Vol. 88, 012008.
3. Kohanski, M.A., Lo, L.J., and Waring, M.S. (2020) Review of indoor aerosol generation, transport, and control in the context of COVID-19, Int. Forum Allergy Rhinol., Vol. 10 (10), pp.1173 – 1179.
4. Santos, A.F., Gaspar, P.D., Hammandosh, A., Aguiar, E.B., Filho, G.A.C., and Souza, H.J.L. (2020) Best practices on HVAC design to minimize the risk of COVID-19 infection within indoor environments, Braz. Arch. Biol. Technol., Vol.63, e20200335.
5. Dbouk, T., and Drikakis, D. (2020) On coughing and airborne droplet transmission to humans, Phys. Fluids, Vol.32, pp.053310-1 – 053310-10.
6. Merghani K.M.M, Sagot B., Gehin E., Da G., Motzkus C. (2021) A review on the applied techniques of exhaled airflow and droplets characterization, Wiley, pp. 7-25.
7. Bazant, M.Z., and Bush, J.W.M. (2021) A guideline to limit indoor airborne transmission of COVID-19, Proceedings of the National Academy of Sciences (PNAS), Vol.118 (17), e2018995118

8. Mariam, Magar A., Joshi M., Rajagopal P.S., Khan A., Rao M.M., Sapra B.K. (2021) CFD Simulation of the Airborne Transmission of COVID-19 Vectors Emitted during Respiratory Mechanisms: Revisiting the Concept of Safe Distance, OCS Omega, ACS Publications, Vol. 6, 16876-16889.
9. Shao, S., Zhou, D., He, R., Li, J., Zou, S., Mallery, K., Kumar, S., Yang, Su., and Hong, J. (2021) Risk assessment of airborne transmission of COVID-19 by asymptomatic individuals under different practical setting, J. Aero. Sci, Vol. 151, 105661.
10. Mohamadi F. and Fazeli A. (2022) A Review on Applications of CFD Modeling in COVID-19 Pandemic, Springer, Archives of Computational Methods in Engineering, Springer, s11831-021-09706-3.
11. Berry, G., Parsons, A., Morgan, M., Rickert, J., and Cho, H. (2022) A review of methods to reduce the probability of the airborne spread of COVID-19 in ventilation systems and enclosed spaces, Environmental Research, Vol. 203, 111765.

PERSISTENCE EXPONENTS OF A PARTICULAR HEIGHT FLUCTUATION IN MOLECULAR BEAM EPITAXY MODEL

Pipitton Sanseeha, Rangsima Chanphana* and Patcha Chatraphorn
Department of Physics, Faculty of Science, Chulalongkorn University, Bangkok, 10330 Thailand
*Corresponding author. E-mail: rangsima.c@chula.ac.th

Abstract:

In this work, we investigate height fluctuations, $h(t)$, in thin film growth of the molecular-beam epitaxy model [1,2] via the study of steady-state persistence probability, $P^S(t)$, and interface width, w. $P^S(t)$ is the chance that $h(t)$ of each site does not cross to its value at the initial time, denoted h_0, throughout a specific time interval [3]. When averaged over all values of h_0, $P^S(t)$ decreases with time as a power-law. The decay rate is the persistence exponent, θ^S. However, results from earlier studies [4,5] suggest that when only a specific value of h_0 is considered, $P^S(h_0,t)$ does not always exhibit a power law behavior. We identify conditions on the value of h_0 that lead to the power-law decay of $P^S(h_0,t)$. The dependence of θ^S on h_0 is studied. We also found that long diffusion length arising from growth with high substrate temperature results in an increase in θ^S. Finally, our investigation of how the persistence probability scales with h_0, the system size, and the discrete sampling time is included.

Introduction:

Steady-state persistence probability, $P^S(t)$, of height fluctuations, $h(t)$, in thin films simulated by the molecular-beam epitaxy (MBE) model [1,2] is investigated in this work. The MBE model is associated with the molecular beam epitaxy growth technique which consists of three fundamental processes: the deposition process, the diffusion process, and the desorption process. Height profile of simulated films are obtained and the interface width, denoted $w(t)$, and $P^S(t)$ are calculated. $P^S(t)$ is the probability that $h(t)$ does not cross to its initial value, h_0, over a certain period of time [3]. In earlier research, it was discovered that when averaged over all h_0, $P^S(t)$ decays as a power law in time [3-5]. The exponent showing the decay rate is the persistence exponent, θ^S. However, when examining the persistence probability of a particular value of h_0, $P^S(h_0,t)$, it was noted that only a certain set of conditions on h_0 can lead to a power law decay in $P^S(h_0,t)$. In this work, we identify those conditions and investigate effects of h_0 on $P^S(h_0,t)$. Another quantity of interest in this study is the interface width. $w(t)$ is the root-mean-squared height fluctuations which can be used to describe the roughness of a growing thin film. It increases as a power law in time with the exponent β at the early stage, then tapering off to a saturated value, w_{sat}, in the steady-state. We also study effects of the diffusion length, l, on the values of β and θ of the simulated films. The diffusion length is the distance deposited atoms can diffuse on the surface. It can be varied in simulations to reflect changes in substrate temperature in MBE growth process. In the last section, the scaling behavior of the persistence probability is investigated.

Methodology:

The molecular-beam epitaxy (MBE) model

For MBE model, an atom is deposited on a substrate at a random site. After deposition, the atom can hop away to another site on the substrate if it has enough energy to break atomic

bonds at its deposition site. The energy of the atom depends on the growth temperature while the amount of energy required to break the bonds depends on the number of bonds at that site and the bonding energy. After the atom breaks its initial bond, its leftover energy determine how far it can diffuse on the surface before being incorporated as part of the grown film. This distance is l. It is one of the parameters that characterize the grown film. It can be calculated from the deposition rate (F), substrate size (L), growth temperature (T), atomic vibration period (t_0), activation energy (E_0), bonding energy (E_b) and the number of bond (n):

$$l = \left(\frac{1}{F \times L^{Dimension}}\right) / \left(t_0 \exp\left(\frac{E_0 + nE_b}{k_B T}\right)\right). \quad (1)$$

In this work, dimension = 2 while the deposition rate is fixed at $F = 1$ ML/s and the unit of t is monolayer (ML) which is the time it takes for the film to grow one complete atomic layer. Note that each surface atom also has a chance to desorb from the surface. However, desorption occurs with much less probability compared to the deposition and diffusion processes when the growth temperature is not too high, so it is neglected in this work.

Steady-state persistence probability

There are 2 types of steady-state persistence probability i.e., the positive persistence probability, P_+^S, which is the probability that $h > h_0$, and the negative persistence, P_-^S, which is defined in the opposite way. For the steady-state probabilities, t_0 is chosen after the interface width reaches w_{sat}. The initial height fluctuation of every site, $h_0(x, t_0)$, is then measured. At time $t_0 + 1$ ML, the height fluctuation of each site is compared to $h_0(x, t_0)$. The sites with $h(x,t) > h_0(x,t_0)$, are counted for P_+^S while the site with $h(x,t) < h_0(x,t_0)$ are counted for P_-^S. Afterward, height fluctuations are checked after every 1 ML deposition. For the positive persistence, when the condition $h(x,t) > h_0(x,t_0)$ is satisfied, P_+^S of that site is increased, otherwise $P_+^S = 0$ at that site. The negative persistence is calculated in the same method except that the condition is $h(x,t) < h_0(x,t_0)$.

Usually, if only a specific value of h_0 is used in the calculation, the persistence probability is denoted by $P_+^S(h_0)$. However, when the probabilities are averaged over all values of h_0, they are denoted by P_+^S. From previous studies [3-5], the averaged steady state persistence probabilities exhibit a power law decay with time: $P_+^S \propto t^{-\theta_\pm^S}$, where θ_+^S are the steady-state positive and negative persistence exponents. The lack of up-down symmetry in the MBE model causes the decay rates in P_+^S and P_-^S to be different.

Results and Discussions:

Effects of initial height fluctuation on steady-state persistence probability

The steady-state persistence probabilities of a specific value of h_0, $P_+^S(h_0, t)$ are studied. It has been shown in the literature [4,5] that positive persistence probabilities of positive value of h_0, $P_+^S(+|h_0|, t)$, decrease very quickly over time. Similar fast decay is observed in $P_-^S(-|h_0|, t)$. As a result, we do not study these two probabilities here. We aim to find conditions for the positive persistence probability of negative value of h_0, $P_+^S(-|h_0|, t)$, and the negative persistence probability of positive value of h_0, $P_-^S(+|h_0|, t)$, to exhibit power law decay in time.

Our simulation results show that $P_+^S(-|h_0|, t)$ exhibit the desired power law decay only when $|h_0| \gg w_{sat}$. In contrast, $P_-^S(+|h_0|, t)$ shows the power law decay when $|h_0| \gtrsim w_{sat}$. Figure 1 (a) and (b) show plots of $P_+^S(-|h_0|, t)$ and $P_-^S(+|h_0|, t)$ from the system of $L \times L = 50 \times 50$ sites. For the same value of $w_{sat} \approx 2.9$ in this system size, it can be seen from the figures that at $|h_0| = 4$, the plot of $P_+^S(-|h_0|, t)$ in (a) does not exhibit a power law decline whereas the plot of $P_-^S(+|h_0|, t)$ in (b) clearly does. From (a), only P_+^S of very large $|h_0|$, i.e., $|h_0| = 10$ shows an approximate straight line in the log-log scale. Moreover, we observe that both $P_+^S(-|h_0|, t)$ and $P_-^S(+|h_0|, t)$ with larger value of $|h_0|$ decrease slower in

time when compared to those with smaller $|h_0|$. This result indicates that stronger fluctuations on the film surface persist longer than weaker ones. Our findings are similar to those of the Das Sarma–Tamborenea (DT) model in [5].

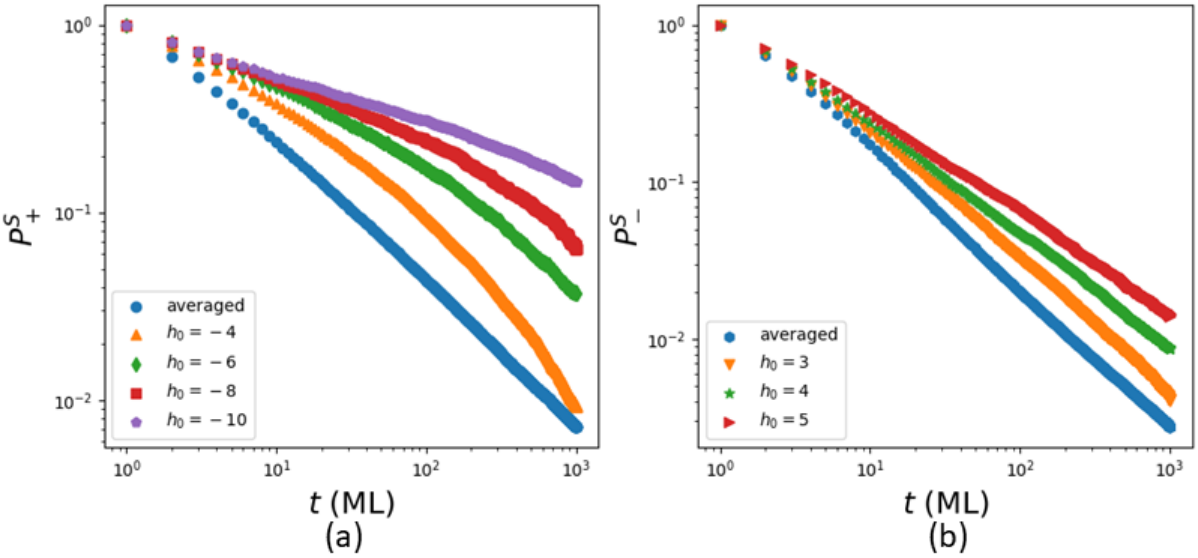

Figure 1. (a) $P_+^S(-|h_0|, t)$ and (b) $P_-^S(+|h_0|, t)$ with varying h_0 from the system of $L \times L = 50 \times 50$ sites

Effects of diffusion length on persistence and growth exponents

From equation (1), increasing growth temperature (T) leads to the increase in diffusion length (l). This means as the temperature is increased, the atom can search further for the stable site to be incorporated, thus the film is smoother. Figure 2 shows that when the temperature rises from T =700 K to T =750 K, corresponding to the increase from l = 1 to l = 5, the surface morphology becomes smoother. When the film is smoother, w saturates faster, so β decreases as shown in figure 3. In addition, h returns to h_0 faster for a smoother surface. As a result, both P_+^S (averaged over all h_0) decrease more quickly, resulting in an increase in θ_+^S as shown in figure 4. It is worth pointing out that the morphology in figure 2(a) is quite similar to that of the DT model with deep grooves and smooth top surface [6] so it is not surprising that the persistence probabilities of the MBE model have similar behavior to those of the DT model.

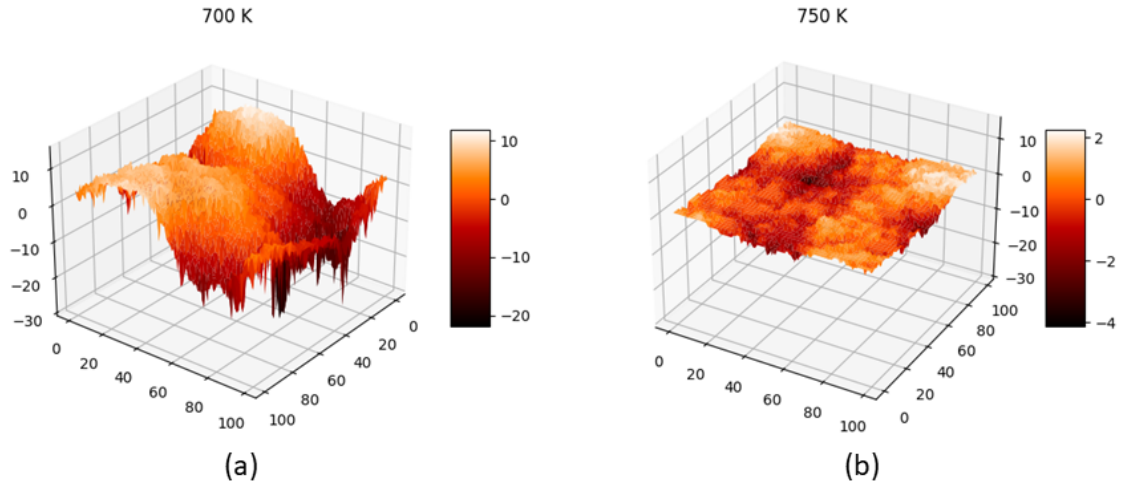

Figure 2. Morphology of the MBE model with $L \times L = 100 \times 100$ sites at steady-state with temperature: (a) $T = 700$ K ($l = 1$) and (b) $T = 750$ K ($l = 5$).

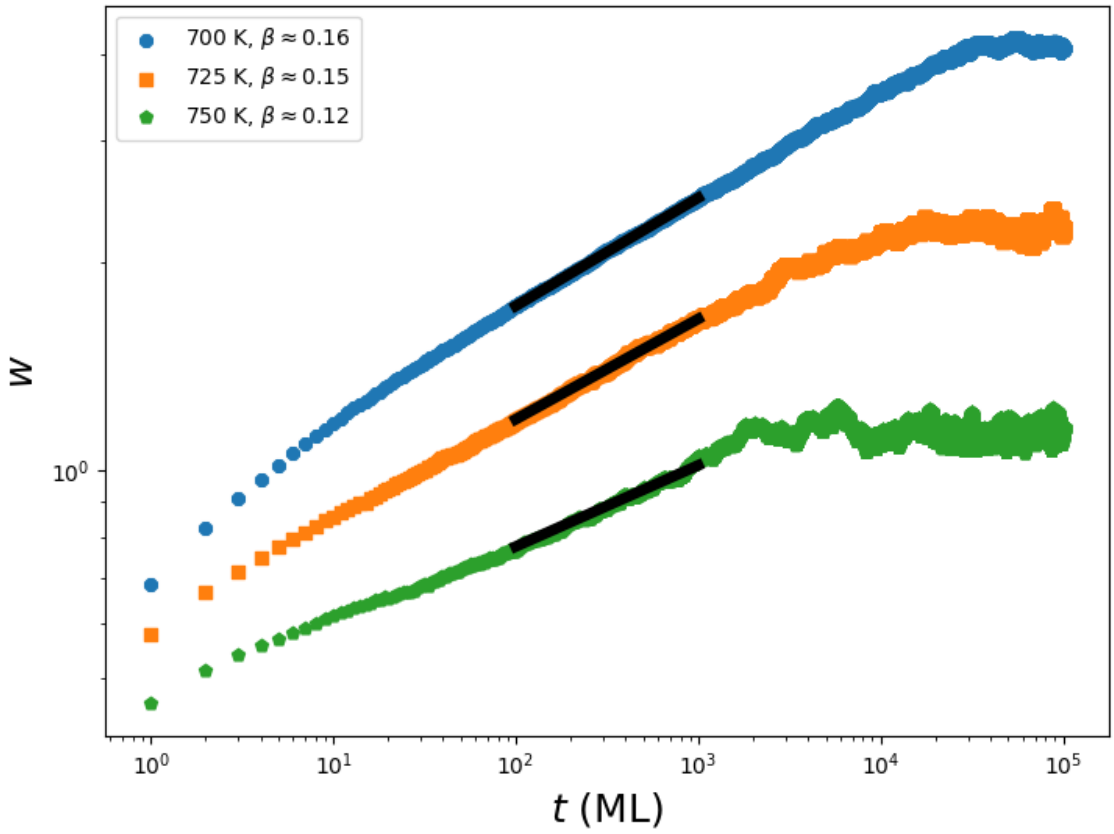

Figure 3. $w(t)$ with varying temperature. The solid black lines are fitting lines for β.

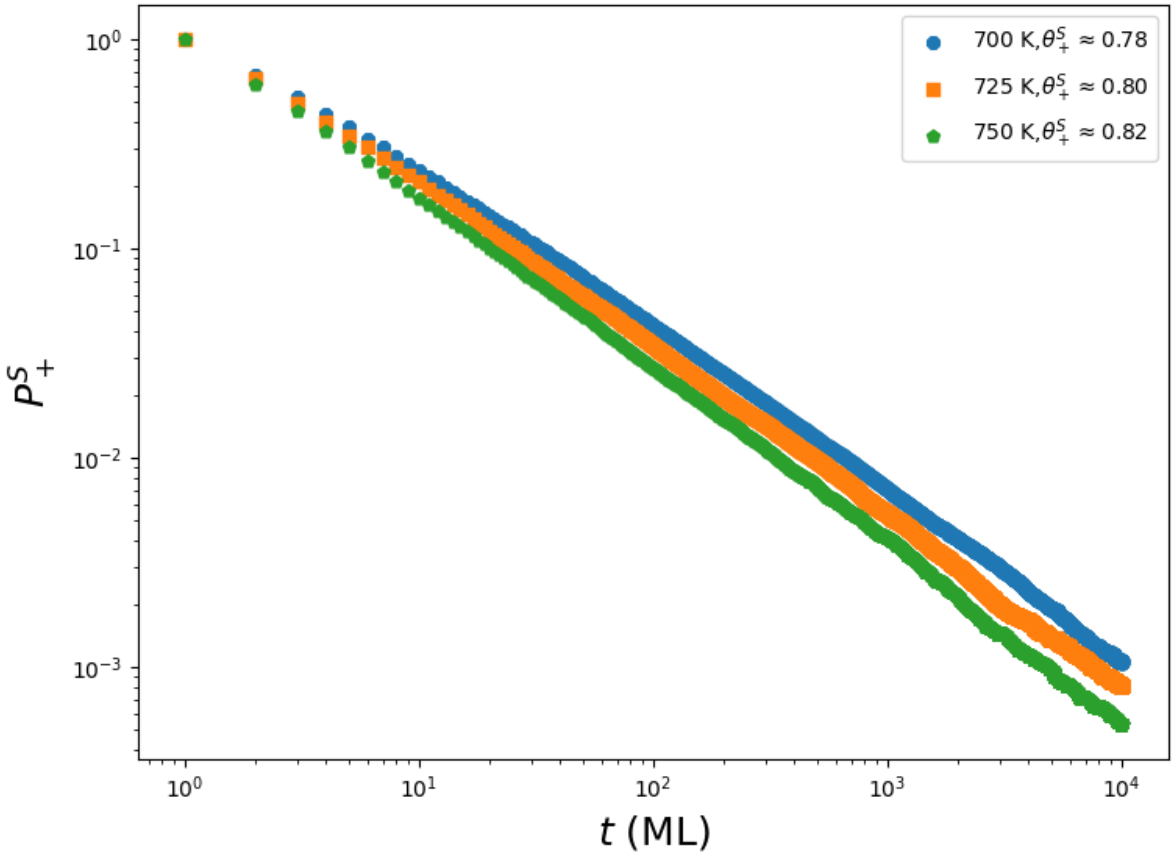

Figure 4. (a) P_+^S and (b) P_-^S of averaged height fluctuations with varying temperature. θ_+^S is calculated from t= 20-1,000 ML interval.

Scaling behavior

Our works indicate that shape and decay rate of persistence probability depend on h_0. According to R. Chanphana et. al. [4], $P_+^S(h_0, t)$ also depend on the sampling time (δt) and the substrate size (L). δt is the discrete time interval between two measurements of $P_+^S(h_0, t)$. (For results shown in previous figures, $\delta t = 1$). Since the saturation time scales with the substrate size as L^z when z is the dynamical exponent, δt should scale with L^z as well. Additionally, when L is varied, w_{sat} and range of possible h_0 are changed. From these behaviors, the expected scaling ratios are $\frac{\delta t}{L^z}$ and $\frac{|h_0|}{w_{sat}}$. In this work, we set the diffusion length condition to $l = 1$ and use the obtained value of the dynamical exponent of the MBE model; $z = 3.3$. Plots with different $\delta t, h_0$ and L, but fixed ratios $\frac{\delta t}{L^z}$ and $\frac{|h_0|}{w_{sat}}$ show power law decay with approximately the same slope (see Figures 5). The graphs effectively collapse into a single curve after time in the horizontal axis is scaled with δt. As a result, the persistence probability of the MBE model follows the relation established in prior researches [4,5].

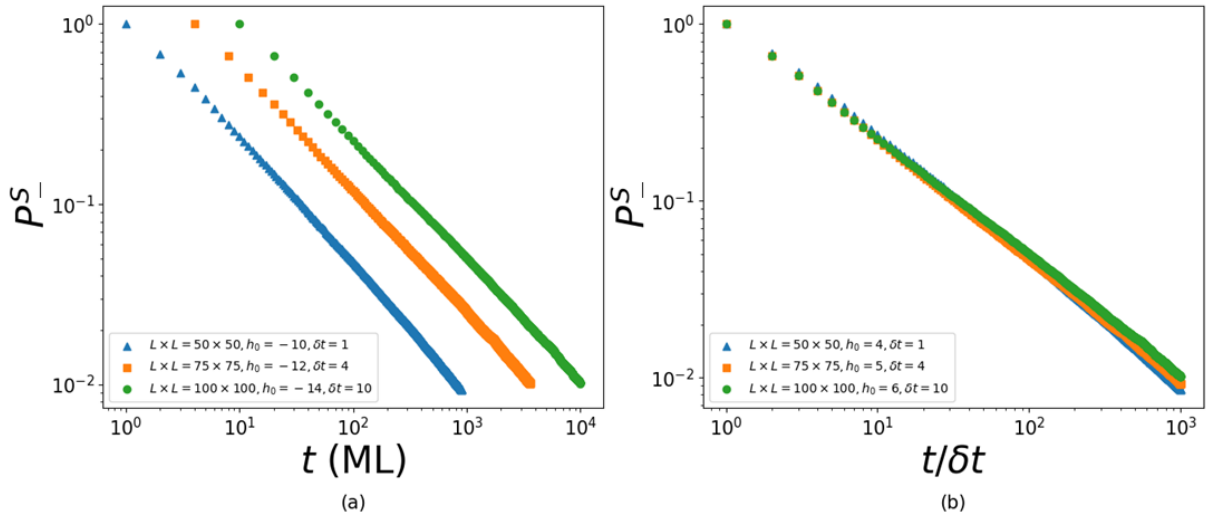

Figure 5. (a) $P_-^S(+|h_0|, t)$ with different $\delta t, h_0$ and L. The fixed ratios are $\frac{\delta t}{L^z} \approx 2.47 \times 10^{-6}$ and $\frac{|h_0|}{w_{sat}} \approx 1.41$. (b) Scaling collapse of $P_-^S(t, L, \delta t, |h_0|)$.

Conclusion:

Positive and negative persistence probabilities of height fluctuation in the MBE model have different behavior with $\theta_+^S \neq \theta_-^S$. From the growth mechanism in the model, deposited atoms prefer to stick to the nearest hill rather than fill up the deep grooves. This makes P_-^S decay faster than P_+^S. $P_+^S(\mp|h_0|, t)$ are observed to decrease with slower rate for larger h_0. $P_+^S(-|h_0|, t)$ does not show power law decay unless $h_0 \gg w_{sat}$ while the condition for $P_-^S(+|h_0|, t)$ to have a power law decay is $|h_0| \gtrsim w_{sat}$. We found that the surface morphology is smoother for larger l. Increasing l also leads to the increase in θ_+^S and the decrease in β. Finally, we also found that the steady-state persistence probability is a function of three parameters: $f\left(\frac{t}{L^z}, \frac{\delta t}{L^z}, \frac{|h_0|}{w_{sat}}\right)$.

References:

1. Sarma, S. Das. Computational Materials Science. 1996;6:149-157.
2. Sarma, S. Das, et al. Physical Review E. 1996;53:359-388.
3. Krug, J., et al. Physical Review E. 1997;56:2702.
4. Chanphana, R., et al. Physical Review E. 2013;88:062402.
5. Chanphana, R., and Chatraphorn, P. Indian Journal of Physics. 2021;95:187-193.
6. Sarma, S. Das, and Tamborenea, P. Physical review letters. 1991;66:325.; Sarma, S. Das, and Tamborenea, P. Physical Review E. 1993;48:2575.

Session B:
BIOLOGICAL SCIENCES

OPTIMIZATION OF THE EXTRACELLULARLY EXPRESSED PETASE PRODUCED FROM *Escherichia coli* FOR PET PLASTIC BIODEGRADATION

Phatpimol Kitchanakan,[1] Sucharat Suksai,[2] Kitipong Angsujinda [3] and Wanchai Assavalapsakul [1,4*]

[1]Department of Microbiology, Faculty of Science, Chulalongkorn University, Bangkok, Thailand

[2]Program in Biotechnology, Faculty of Science, Chulalongkorn University, Bangkok, Thailand

[3]Aquatic Resources Research Institute, Chulalongkorn University, Bangkok, Thailand

[4]Center of Excellence in Microbial Technology for Marine Pollution Treatment (MiTMaPT), Department of Microbiology, Faculty of Science, Chulalongkorn University, Bangkok, Thailand

[*]e-mail: wanchai.a@chula.ac.th

Abstract: Polyethylene terephthalate (PET) is one of the plastic types that can be found in daily life and become a huge accumulation in the environment. A biodegradation breaking the chemical molecule of PET polymer to monomer can decrease the period of PET degradation. Even secreted enzyme, namely PETase, was found from *Ideonella sakaiensis* 201-F6, its secretion mechanism is still unclear, and it is difficult to directly apply in the environment. In this study, *I. sakaiensis*' PETase gene linked with a signal peptide in the expression plasmid was synthetically constructed and the expression of its counterpart was conducted and optimized in *E. coli* strain Rosetta-gami DE3(pLysS) by using various isopropyl β-d-1-thiogalactopyranoside (IPTG) concentration. SDS-PAGE and Western blot analysis showed the recombinant PETase, roughly 30 kDa in size, was present in the culture medium with the highest expression level when inducing the recombinant bacteria at 0.5 mM IPTG final concentration. Anyhow the function in PET degradation of this recombinant enzyme needs further investigation.

Introduction:

Plastics are widely used and have become a global issue due to the accumulation in ecosystems[1,2]. One of the most common plastics found in everyday life is polyethylene terephthalate (PET), a polyester with thermoplastic and semi-aromatic properties. The main components of PET plastic are terephthalic acid (TPA) and ethylene glycol (EG), which give it appealing properties such as colorlessness, rigidity, lightweight, impact resistance, and transparency[3]. However, the accumulation of PET plastic waste is found in many areas and exponentially increased causing a negative impact on the environment, wildlife, and human health[4,5]. The COVID-19 pandemic has not only resulted in a dramatic loss of human life worldwide, but it has also affected all our lifestyles, including social, economic, public health, and the entire food system[6]. The limited contact area between people contributes to an increase in PET plastic waste. The management of PET plastic waste requires appropriate strategies, that should be cost-effective, energy-efficient, and environmentally friendly[7,8,9].

PET plastic-degrading bacteria, *Ideonella sakaiensis* 201-F6 was discovered and isolated from soil collected from the PET plastic factory and this isolate used PET plastic as a major carbon and energy[10]. The researchers identified two PET hydrolases in *I. sakaiensis* 201-F6 that are involved in the biodegradation of PET plastic. First, PET-digesting enzyme (PETase) can convert PET molecule to mono(2-hydroxyethyl)-terephthalic acid (MHET) with TPA and bis(2-hydroxyethyl)-terephthalic acid (BHET) as secondary products which can convert to MHET as well. Second, MHET-digesting enzyme (MHETase) break the MHET molecule to TPA and EG[11,12]. The degradation of PET plastic using an engineered bacteria secreting PET degrading enzyme might be promising in PET waste management[13,14]. However, many engineered bacterial hosts are limited in non-pathogenic strain, genetic background, and manipulation methods[15,16].

E. coli is a diverse engineered bacterial host with a comprehensive genetic background and a simple inclination for recombinant protein production due to the remarkable effectiveness of DNA molecules instruction into cells[17]. Most PET-hydrolases found in plastic-degrading microbes, including lipases, esterases, carboxylesterases, and cutinases can cleave the ester bond linkage of PET plastic polymer[18]. Among PET plastic-degrading enzymes, PETase has a unique structure, distinct properties, and degrading capacity [19,20,21]. The PETase enzyme from *I. sakaiensis* 201-F6 could be improved by using a secretion system of *E. coli* to induce its secretion into the culture medium and efficiently contribute to PET plastic-degradation activity. In this study, extracellular PETase encoded by a synthetic gene from *E. coli* strain Rosetta-gami could be produced and secreted out into a culture medium. In addition, the optimization for extracellularly expressed PETase secretion was conducted with various IPTG concentrations.

Methodology:

Plasmid and Expression of recombinant PETase

The pRSFDuet-1 harboring a PETase gene of *Ideonella sakaiensis*, (*Is*PETase) coupled signal peptide (pRSFDuet-1-PETase; U7734DJ300-4) was ordered for synthesizing by GenScript (Piscataway, NJ). The plasmid was transformed into *E. coli* strain Rosetta-gami (pLysS) by heat shock and spread on Luria-Bertani (LB) agar containing 34 mg/L chloramphenicol and 50 mg/L kanamycin. A selected transformant was cultured in LB broth supplemented with the same antibiotics at 30 °C for 14-16 hrs, with vigorous shaking. The transformant culture was then transferred into a 300 mL of LB broth supplemented with the same antibiotics and incubated at 30 °C, 200 rpm until the optical density at 600 nm reached 0.4-0.5. To determine the optimal condition for recombinant PETase expression, the bacterial culture was equally divided and then induced with 0.1, 0.2, 0.3, 0.4 and 0.5 mM IPTG at final concentration at 30 °C for 3 hrs.

Culture medium collection and protein preparation

After induction for 3 hrs, the culture medium of each IPTG concentration was collected and cell debris removed by centrifugation at 13,000 rpm for 15 min at 4 °C. The protein in harvested supernatant was precipitated by an addition of trichloroacetic acid at 10% final concentration. The solution was incubated on ice overnight and protein was then pelleted by centrifugation at

13,000 rpm for 15 min at 4 °C. The protein pellet was washed with acetone, protein sample prepared and analyzed by SDS-PAGE and Western blotting.

SDS-PAGE and Western blot analysis

In brief, the protein in the first gel was stained with Coomassie brilliant blue R-250 (Bio Basic, Canada), while protein in the other was transferred onto a PVDF membrane using a Trans-Blot SD Semi-Dry Transfer Cell (Bio-Rad, Canada). The transferred membrane was blocked with a blocking solution (5% skim milk in 1X PBS-Tween 20; PBST) for 15 min twice, followed by an incubation with anti His Tag (R & D System, Minneapolis, MN) (1:5000) at ambient temperature for 1 hr. After washing with PBST, the membrane was incubated with goat anti-mouse IgG HRP (Sigma Aldrich, Piscataway, NJ) (1:5000) at ambient temperature for 1 hr. The membrane was finally submerged in chemiluminescent substrates and visualized by using Alliance Q9 Advanced Chemiluminescence Imager (UVITEC Cambridge Ltd, United Kingdom) following washing with PBST.

Bradford assay

Control LB broth, uninduced culture medium, culture medium in each IPTG concentration and gradient concentration of bovine serum albumin (BSA) 1, 0.5, 0.25, 0.125, 0.0625, 0.0312, 0.0156, 0.0078, 0.0039, 0.00195, 0.000975, 0.0004875 mg/mL (Pierce, Rockford, IL) as a standard protein concentration were added in 96 well plate and mixed with Bio-Rad Protein Assay (Bio-Rad Laboratories Inc., Canada). Thereafter, the protein concentration was determined by using microplate reader (PerkinElmer, Waltham, MA) at the optical density at 595 nm (OD_{595}).

Results and Discussion:

Up to date, PET degradation studies were mostly carried out with cutinase and lipase family enzyme. These enzymes were ineffective and had low PET affinities. However, *Is*PETase from *I. sakaiensis* has been shown to have a higher PET degradation efficiency than other enzymes in the same family[22]. To investigate and optimize the expression of recombinant signal peptide linked *Is*PETase in the culture medium, the recombinant bacteria was induced by the addition of 0.1, 0.2, 0.3, 0.4 or 0.5 mM IPTG at final concentration. The culture medium in each treatment was collected and then examined by SDS-PAGE and Western blot analysis. The result showed the distinct protein band was observed from all sources of protein analyzed except that from the uninduced control (**Figure 1a**). Western blot analysis using anti His Tag confirmed the induced protein, approximately at 30 kDa was the recombinant *Is*PETase (**Figure 1b**). The result further indicated that the recombinant *Is*PETase was produced and released into the culture medium in the presence of IPTG with the highest extent at 0.5 mM final concentration. According to previous research, recombinant *Is*PETase could be also expressed in *E. coil* strain SoluBL21 after induction with 0.5 mM IPTG at 22 °C for 16 hrs. The SDS-PAGE further demonstrated its molecular weight was roughly at 30 kDa similarly to our protein[23]. To select the high proficiency of IPTG concentration for inducing the

extracellular PETase expression produced from *E. coli* should examine the SDS-PAGE and Western blot analysis to check the quantity and position of the secreted PETase and the Bradford assay to speculate the potential induction of various IPTG concentration.

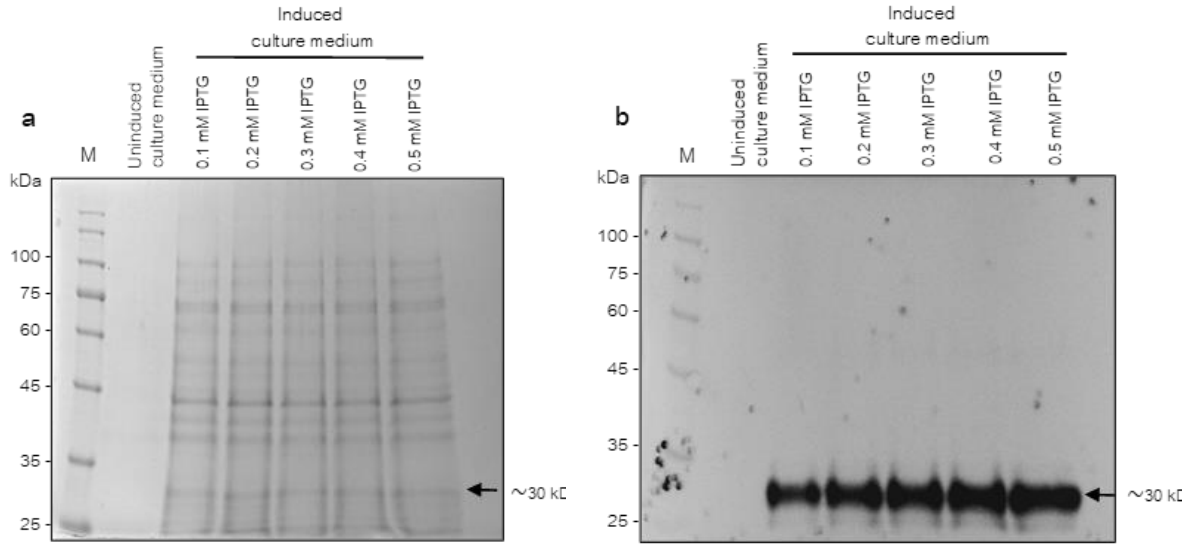

Figure 1.
Evaluation of the extracellular PETase expression induction under various IPTG concentration with SDS-PAGE (a) and Western blot analysis (b)

To determine the protein concentration, culture media from different IPTG treatments were analyzed by Bradford assay. BSA standard curve in relation to OD_{595} (**Table 1**) was used to determine the amount of secreted PETase after inducing with various IPTG concentration compared with the absence IPTG controls. The results showed the amount of protein concentration ranged from 0.0 to 29.0 µg/mL. The highest protein concentration from recombinant PETase induction with 0.5 mM IPTG was 29.0 µg/mL, whereas no protein was detected in LB broth and uninduced culture medium which are the control treatments.

Table 1.
Comparison of the OD_{595} average and calculated protein concentration from linear equilibrium in protein concentration standard curve of each treatment

Sample	$OD_{595\ nm}$ Average	Protein concentration (µg/mL) [a]
LB broth	0.365	0.0
Uninduced culture medium	0.366	0.0
0.1 mM IPTG	0.425	24.0
0.2 mM IPTG	0.427	25.0
0.3 mM IPTG	0.431	26.0
0.4 mM IPTG	0.436	28.0
0.5 mM IPTG	0.437	29.0

[a] Calculating protein concentration from linear equilibrium in protein concentration standard curve

Conclusion:
Under an induction by IPTG, the recombinant PETase can be produced from *E. coli* Rosetta-gami DE3 (pLysS) containing the recombinant plasmid. The extent of released protein in culture medium is positively related to the amount of IPTG. The higher concentration of IPTG added, the higher level of recombinant PETase obtained. Additional research pertaining to PET degradation by recombinant *Is*PETase requires investigation.

Acknowledgements:
This research was funded by Center of Excellence on Hazardous Substance Management, HSM, Chulalongkorn University, Bangkok, Thailand and 90th Anniversary of the Chulalongkorn University Fund (Ratchadaphiseksomphot Endowment Fund) from Graduate School, Chulalongkorn University, Bangkok, Thailand (Batch No.52 (2/65)). We would like to thank the member of WA2014 laboratory, Department of Microbiology, Faculty of Science, Chulalongkorn University, Thailand for their technical support in the laboratory.

References:
1. Papadopoulou A, Hecht K, Buller R. Enzymatic PET degradation. *Chimia (Aarau)*. 2019;73:9:743-749.
2. Carr C. M, Clarke D. J, Dobson A. D. W. Microbial polyethylene terephthalate hydrolases: current and future perspectives. *Front Microbiol*. 2020;11:571265.
3. Hiraga K, Taniguchi I, Yoshida S, Kimura Y, Oda K. Biodegradation of waste PET: a sustainable solution for dealing with plastic pollution. *EMBO Rep*. 2019;20:11:e49365.

4. Sinha V, Patel M.R, Patel J.V. PET waste management by chemical recycling: a review. *J Polym Environ*. 2010;18:8–25.
5. Liu B, He L, Wang L, Li T, Li C, Liu H, Luo Y, Bao R. Protein crystallography and site-direct mutagenesis analysis of the poly (ethylene terephthalate) hydrolase PETase from *Ideonella sakaiensis*. *Chembiochem*. 2018;19:14:1471-1475.
6. Tsai W. T. Analysis of plastic waste reduction and recycling in Taiwan. *Waste Manag Res*. 2021;39:5:713-719.
7. Liu C, Shi C, Zhu S, Wei R, Yin C. C. Structural and functional characterization of polyethylene terephthalate hydrolase from *Ideonella sakaiensis*. *Biochem Biophys Res Commun*. 2019;508:1:289-294.
8. Maurya A, Bhattacharya A, Khare S. K. Enzymatic remediation of polyethylene terephthalate (PET)-based polymers for effective management of plastic wastes: an overview. *Front Bioeng Biotechnol*. 2020;8:602325.
9. Wei R, Zimmermann W. Microbial enzymes for the recycling of recalcitrant petroleum-based plastics: how far are we?. *Microb Biotechnol*. 2017;10:6:1308-1322.
10. Janatunaim R. Z, Fibriani A. Construction and cloning of plastic-degrading recombinant enzymes (MHETase). *Recent Pat Biotechnol*. 2020;14:3:229-234.
11. Yoshida S, Hiraga K, Takehana T, Taniguchi I, Yamaji H, Maeda Y, Toyohara K, Miyamoto K, Kimura Y, Oda K. A bacterium that degrades and assimilates poly (ethylene terephthalate). *Science*. 2016;351:6278:1196-1199.
12. 12. Fecker T, Galaz-Davison P, Engelberger F, Narui Y, Sotomayor M, Parra L. P, Ramírez-Sarmiento C. A. Active site flexibility as a hallmark for efficient PET degradation by *I. sakaiensis* PETase. *Biophys J*. 2018;114:6:1302-1312.
13. Kim J. W, Park S. B, Tran Q. G, Cho D. H, Choi D. Y, Lee Y. J, Kim H. S. Functional expression of polyethylene terephthalate-degrading enzyme (PETase) in green microalgae. *Microb Cell Fact*. 2020;19:1:97.
14. Wang N, Guan F, Lv X, Han D, Zhang Y, Wu N, Xia X, Tian J. Enhancing secretion of polyethylene terephthalate hydrolase PETase in Bacillus subtilis WB600 mediated by the SP_{amy} signal peptide. *Lett Appl Microbiol*. 2020;71:3:235–241.
15. Huang X, Cao L, Qin Z, Li S, Kong W, Liu Y. Tat-independent secretion of polyethylene terephthalate hydrolase PETase in *Bacillus subtilis* 168 mediated by its native signal peptide. *J Agric Food Chem*. 2018;66:13217–13227.
16. Seo H, Kim S, Son H. F, Sagong H. Y, Joo S, Kim K. J. Production of extracellular PETase from *Ideonella sakaiensis* using sec-dependent signal peptides in *E. coli*. *Biochem Biophys Res Commun*. 2019;508:1:250-255.
17. Selas Castiñeiras T, Williams SG, Hitchcock AG, Smith DC. *E. coli* strain engineering for the production of advanced biopharmaceutical products. *FEMS Microbiol Lett*. 2018;365:15.
18. Chen C. C, Han X, Ko T. P, Liu W, Guo R. T. Structural studies reveal the molecular mechanism of PETase. *FEBS J*. 2018;285:20:3717-3723.
19. Wei R, Oeser T, Zimmermann W. Synthetic polyester-hydrolyzing enzymes from thermophilic actinomycetes. *Adv Appl Microbiol*. 2014;10:6:1308-1322.
20. Verger R. 'Interfacial activation' of lipases: facts and artifacts. *Trends Biotechnol*. 1997:15:1:32-38.

21. Austin H. P, Allen M. D, Donohoe B. S, Rorrer N. A, Kearns F. L, Silveira R. L, Pollard B. C, Dominick G, Duman R, El Omari K, Mykhaylyk V, Wagner A, Michener W. E, Amore A, Skaf M. S, Crowley M. F, Thorne A. W, Johnson C. W, Woodcock H. L, McGeehan J. E, Beckham G. T. Characterization and engineering of a plastic-degrading aromatic polyesterase. *Proc Natl Acad Sci USA*. 2018;115:19:E4350-e4357.
22. Joo S, Cho I.J, Seo H. Structural insight into molecular mechanism of poly (ethylene terephthalate) degradation. *Nat Commun*. 2018;9:382.
23. Puspitasari N, Tsai SL, Lee CK. Fungal Hydrophobin RolA Enhanced PETase Hydrolysis of Polyethylene Terephthalate. *Appl Biochem Biotechnol*. 2021;193: 1284–1295.

CHARACTERIZATION OF A NOVEL MIRNA IN DENGUE VIRUS SEROTYPE 2 INFECTED HEK293T CELLS

Maliha Sharmin,[1] Kitipong Angsujinda,[2] and Wanchai Assavalapsakul[1*]
[1]Department of Microbiology, Faculty of Science, Chulalongkorn University, Bangkok, Thailand 10330
[2]Aquatic Resources Research Institute, Chulalongkorn University, Bangkok, Thailand 10330
[*]e-mail: wanchai.a@chula.ac.th

Abstract:
Dengue virus (DENV), a common mosquito-borne viral species that belongs to the Flaviviridae family, is responsible for causing dengue fever (DF) and dengue hemorrhagic fever/dengue shock syndrome (DHF/DSS) in people in tropical and subtropical areas. The single-stranded RNA virus has four different serotypes: DENV 1, DENV 2, DENV 3, and DENV 4. The host's innate and adaptive immune responses are essential for determining the viral infection's history. Even though most illnesses are subclinical, they can nevertheless cause a variety of symptoms. Although a DENV vaccination has already been developed, its effectiveness against the four DENV serotypes varies greatly. We evaluated a few potential miRNAs for changes in expression levels after DENV 2 infection of HEK293T (embryonic kidney) cells to better understand the role that miRNAs play in DENV 2 replication. At every time studied, it was confirmed that one miRNA, miR-MS, showed bands at all time points tested. Moreover, our research is ongoing, and the outcome is not yet achieved. However, from our results so far, we can assume that miR-MS can have the capability in inhibiting dengue virus serotype 2 replication. This study will aid in our ongoing investigation into the function of miRNA in the replication of DENV 2 and fathom the function of microRNA as a therapeutic component in DENV 2 replication.

Introduction:

The etiologic agent of dengue fever (DF), dengue virus (DENV), a member of the Flaviviridae family, can initially present as a non-specific febrile illness called dengue. However, it can then progress to a more complicated and potentially fatal clinical form called severe dengue, which includes dengue hemorrhagic fever (DHF) and dengue shock syndrome (DSS). The four DENV serotypes are antigenically different (DENV1-4). A 390 million dengue infections are thought to occur annually, 96 million of which are thought to be symptomatic. In endemic places, dengue illness has reemerged as a significant public health risk.[1,2] There is currently no known cure for dengue virus (DENV) infection, despite the recent advent of a vaccine to prevent infection in several countries.[3,4]

Uncertainties exist regarding the pathophysiology of DENV infection. Given that severe dengue frequently exhibits vascular leakage and hemorrhage, which are common clinical symptoms, this raises the possibility that vascular endothelial cells (VECs) may function as a target for DENV and contribute to the pathogenesis of the illness.[5] However, it is yet ambiguous how the infection changes endothelial function and/or morphology. Though the method by which the infection modifies endothelial function and/or morphology is yet unclear. Specific elements of the host cells cause the process of DENV infection. Infected cells have reportedly been shown to contain DENV virions between the rough endoplasmic reticulum and the Golgi.[6] Some viral particles are transported to the Golgi system for maturation before being released by exocytosis once the nucleocapsids have been formed, acquired their envelopes, and related structures. The specific regulator or host cell component that participates in the DENV

replicative cycle throughout this phase is still unknown and knowing this information will help us better understand DENV infection and dengue therapies.[7]

MicroRNA (miRNA) is a family of single-stranded, conserved, short non-coding RNA molecules, which are roughly 18 to 22 nucleotides long, can modulate gene expression by RNA silencing and post-transcriptional alterations. miRNAs can silence genes by either perfectly binding to the coding region of messenger RNA (mRNA), which causes degradation, or by imperfectly binding to the 3' untranslated region (3'UTR) of the mRNA, which causes translational repression.[7,8] One-third of human genes are regulated by miRNA, which also influences several biological processes, including immune cell differentiation, immune regulation, and central nervous system regulation. As a result, miRNA has emerged as a new tool for the detection and management of a variety of human diseases.[9,10]

According to several research, host-cellular miRNAs regulate the expression of viral genes, which has a profound impact on how the host and pathogen interact. However, viruses have developed a method to evade the host immune response, and they may potentially control the cellular miRNA pathway for their own interests.[11] Studies have been conducted to date to show the importance of flaviviruses in altering the host miRNAs' expression. The dengue virus has also been observed to change the expression of numerous miRNAs in mosquitoes and humans.[12] Zhu *et al*. showed that miR-30e inhibits dengue viral replication by upregulating the production of IFN and IFN-stimulated genes (ISG).[13] In peripheral blood mononuclear cells infected with DENV 2, 11 upregulated and 4 downregulated miRNAs were reported to be found. It was hypothesized that miRNAs may target cytokines and epigenetic regulators as a result.[14] It was shown Wu *et al.* that miR-223 targets the 3'UTR of the STMN1 gene to downregulate the expression of STMN1 (Stathmin 1) and so prevent DENV 2 replication.[15] miRNAs play an active role in the interaction between hosts and viruses during viral infection, from viral attachment to disease progression.[15,16] However, there hasn't been any clinical research done to date connecting the therapeutic function of miRNA in DENV infection. It has become essential to identify a variety of miRNAs that may be candidates for regulation during dengue viral infection. Understanding the roles that miRNAs play and how they are expressed during dengue viral infection can help us better understand in developing miRNA-based treatments that can either act as miRNA antagonists or miRNA mimics.[17]

Methodology:

Cells and culture conditions:

The mosquito cell line C6/36 (ATCC® CRL-1660™) was cultured in Minimum Essential Medium-MEM (Gibco™ Invitrogen, Carlsbad, CA) using 10% FBS and incubated at 28° C. The human embryonic kidney cell line HEK293T (ATCC® ACS-4500™) was cultured in Dulbecco's Modified Eagle's Medium-DMEM (Gibco™ Invitrogen, Carlsbad, CA) using 10% heat-inactivated fetal bovine serum (FBS; Gibco™ Invitrogen, Carlsbad, CA), and incubated at 37° C with 5% CO2. The monkey kidney cell LLC-MK2 (ATCC® CCL-7™) was cultured in DMEM with 5% FBS at 37° C with 5% CO_2.

Virus and viral titer:

Dengue virus serotype 2 (DENV 2) strain 16681 was used for this study and propagated in C6/36 cells at 28° C for 6 days (without CO_2). After 6 days, the culture medium was centrifuged to exclude cell debris. A day with a maximal virus titer was chosen for collecting the virus-containing media[18] and centrifuged afterwards to exclude cell debris. The viral stock was kept at -80° C until use. A plaque assay on LLC-MK2 cells was used to measure the virus titer as

mentioned in previous research.[19,20] Samples of the viral supernatant were serially diluted and inoculated on LLC-MK2 cells at the concentration that the cells become confluent and cover all the area within 24 hrs. On the following day of the incubation, the cells were treated with 1X overlay and incubated at 37° C with 5% CO_2. After 5 days of 1X overlay, 2X overlay was added and incubated again at 37° C with 5% CO_2. Plaques were visualized within 14 hours for cytopathic effect (CPE) by staining with 1.5% neutral red, and the viral titer was calculated.

HEK293T cell-based dengue virus production:
HEK293T cells were grown in 75 cm^2 containing tissue culture flasks. Prior to confluence, when the cell number reached 2 x 10^7, the cells were washed with PBS and trypsinized with 0.25% Trypsin-EDTA at RT for 3-6 minutes followed by the addition of a fresh culture medium to inactivate trypsin. The cell suspension was transferred to 50 mL centrifuge tube and centrifuged at 1500 rpm for 5 minutes. The cell supernatant was discarded, and the cell pellet was re-suspended in 10 mL complete growth medium. The cells were seeded in 6 wells of a 12-well plate for further viral infection. The experiment was done in triplicates.

Oligonucleotide:
The primer specific to hsa-miR-MS employed in this study was designed and modified (Integrated DNA Technologies, Coraville, IA). The pair of primers were resuspended in nuclease-free water to prepare a stock with a final concentration of 100 mM. The stock was then used to prepare 5 mM for the experiment. The stock and newly prepared (5 mM) pair of primers were stored at -20° C.

miRNA expression profile:
For evaluating miRNA expression profile, viral suspension was prepared within 18-24 hours after HEK293T cell seeding on a 12-well plate. Cells were mock-infected or infected with DENV 2 at a MOI of 5 for 2 h. The culture medium was then replaced with a fresh medium and the cells were cultured at 0, 6, 12, 24, and 48 h post-infection (h.p.i). At the appropriate time point, all the cells were lysed, and RNA was extracted by TRI-reagent® (MRC, Cincinnati, OH) following the manufacturer's guidelines. A Nanodrop 2000 (Eppendorf AG, Germany) was used to quantify the amount of RNA.

To detect miRNA expression, 250 ng of total RNA was used as a template to synthesize cDNA using RevertAid™ Premium Reverse Transcriptase (Thermo Fisher Scientific Inc., Waltham, MA) as discussed by others.[21] Each PCR was conducted at 94° C for 3 min, 94° C for 15 s, followed by 35 cycles at 62° C for 5 s, and 72° C for 45 s **(Table 1)**. The U6 small RNA was used to standardize all data. Polyacrylamide gel electrophoresis was used to visualize the result.

Table 1.
Steps and conditions for thermal cycling in PCR for both miR-MS and U6.

Steps	Temperature (° C)	Time (Min)	Cycles
Initial denaturation	94	3:00	
Denaturation	94	0:15	35
Annealing	62	0:05	
Extension	72	0:45	
Final extension	72	7:00	

Results

Evaluation of CPE of DENV 2 in HEK293T cells:

HEK293T cells were cultured in 75 cm^2 flask. The infection with DENV 2 was performed and kept at 37° C with 5 % CO_2 for 5-7 days. The virus infection of permissive cells caused the productive infection and cytopathic effect (CPE) was observed under an inverted microscope (Olympus CKX53, Japan) **(Figure 1).**

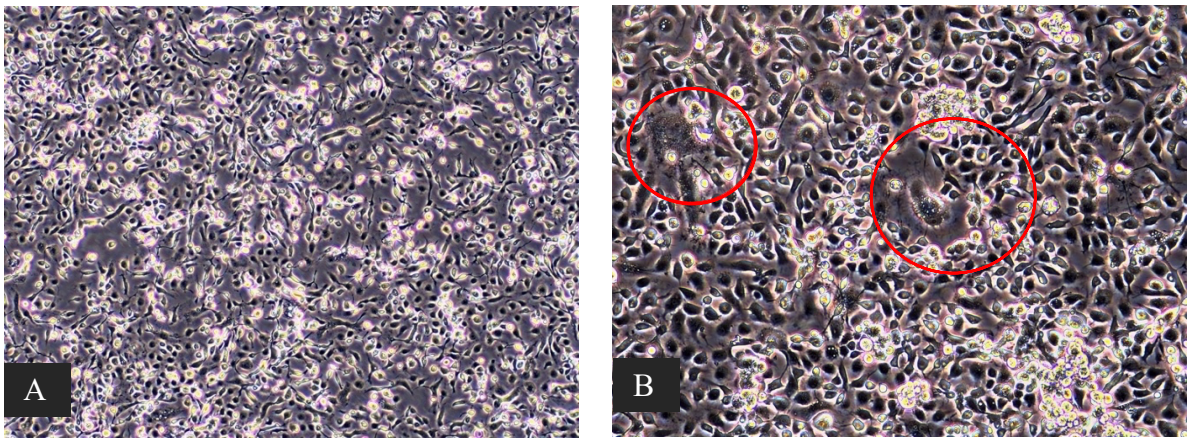

Figure 1. Observation of cytopathic effect (CPE) in DENV 2 infected HEK293T cells. Representative DENV 2 cytopathic responses of HEK293T cells in 100X visualization. (A) Uninfected HEK293T cells 4d post subculture at 37° C with 5% CO_2. (B) CPE of HEK293T cells infected with DENV 2 4d post-infection. The red circles (B) showing the CPE of HEK293T cells post-infection with DENV 2; whereas there was no CPE observed in normal cultured cells (A).

miRNA regulation in DENV 2-infected HEK293T cells:

A panel of miRNAs preselected based on existing information (miRBase and research work) was assessed for amplification from HEK293T cells to pin down those miRNAs that may have a potential function in DENV infection. Numerous potential miRNAs (hsa-miR-Tobby, hsa-miR-Turbo) failed optimization due to issues like nonspecific bands, multiple bands, and failure in amplification. One miRNA, hsa-miR-MS, however, had a profile that was suitable for amplification.

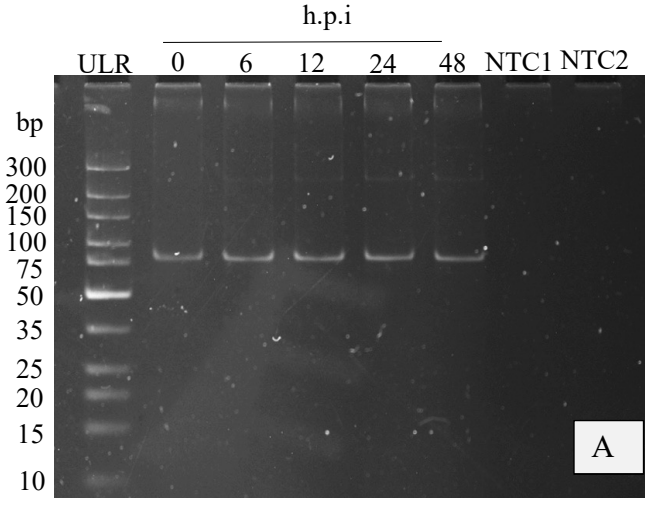

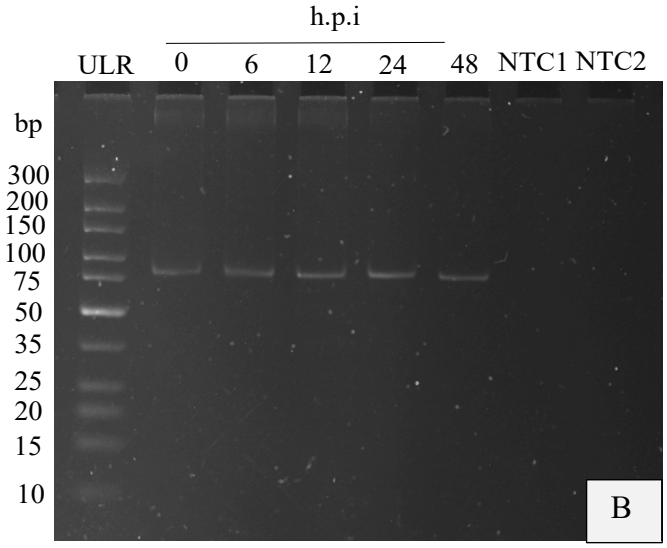

Figure 2. Gel image of miR-MS in DENV-infected and mock-infected HEK293T cells
RT-PCR of miR-MS in DENV-infected HEK293T cells followed by polyacrylamide gel electrophoresis. ULR (Ultra low range ladder) was used for the quantification of the DNA. (A) miRNA expression of DENV-infected cells of all time points. Negative control 1 (NTC1) was for RT and negative control 2 (NTC2) was used for PCR for the verification purpose which did not show any band. (B) Gel image of miRNA expression in mock-infected cells of all time points. Both NTC1 and NTC2 did not show any band for mock-infected samples.

To study the regulation of these miRNAs during DENV 2 infection, HEK293T cells were infected with DENV 2 or mock-infected, and at each time point (0, 6, 12, 24, and 48 h.p.i), the regulation of these 3 miRNAs in viral treated cells was analyzed. The results showed that among these 3 miRNAs, only miR-MS was expressed at all time points of infection **(Figure 2)**. All the results were standardized against U6 small RNA **(Figure 3).** Therefore, based on this result we can say that this miRNA is a candidate for further research in DENV 2.

Discussion and Conclusion:
It is now thought that viruses, which take advantage of a variety of host gene expression mechanisms, have the capacity to encode miRNAs in their genomes. Viral miRNAs have been shown to play several significant roles in studies during the past ten years.[22,23] Numerous biological processes are known to be modulated by miRNAs,[24] which are known to exert their effects through controlling mRNA translation[25] as well as by interacting with mRNA binding proteins.[26]

Although significant progress has been made, it is still unclear how miRNA might be involved in dengue virus infections. In one study, miR-133a was downregulated in DENV infection, and they proposed that the 3′UTR of DENV inhibits the expression of miRNA-133a during the initial hours of infection in Vero cells.[27] Upon DENV infection, miR-146a expression was markedly elevated in primary human monocytes and THP-1 cells. When miR-146a was overexpressed, DENV 2 replication increased; when miR-146a was inhibited, viral replication altered.[28]

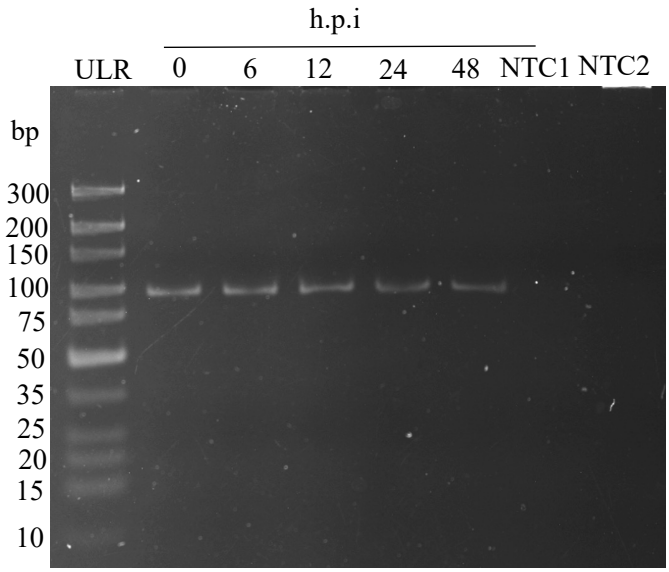

Figure 3. Gel image of U6 small RNA in DENV-infected HEK293T cells
RT-PCR of U6 small RNA in DENV-infected HEK293T cells followed by polyacrylamide gel electrophoresis.

Our result showed that miR-MS was expressed at every time point of dengue virus infection, which will help us continue our further research. Until now, no study has been done on miR-MS in terms of viral infection. Even after this, our results so far are in consonance with another research.[29]

Previous research has demonstrated that miRNAs can influence DENV infection by either directly targeting the DENV genome or targeting genes involved in the innate immune system.[30,28,13] Although the scope of our research is limited, additional research on miR-MS may be useful in determining the direct miRNA target in the dengue virus genome. This may therefore be a novel microRNA that can be employed as an antiviral treatment against DENV infections.

References:

1. Guzman M, Halstead S, Artsob H, Buchy P, Farrar J, Gubler D, *et al. Nat Rev Micro.* 2010;8:S7e16
2. Bhatt S, Gething PW, Brady OJ, Messina JP, Farlow AW, Moyes CL, *et al*. *Nature.* 2013;496:504e7
3. Runge-Ranzinger S, McCall PJ, Kroeger A, Horstick O. *Trop Med Int Health.* 2014;19(9):1116e1160.
4. World Health Organization, 2016. *Wkly Epidemiol Rec*. 2016;91(30):349e364.
5. Basu A, Chaturvedi UC. *FEMS Immunol Med Microbiol*. 2008;53:287e99.
6. Kuhn RJ, Zhang W, Rossmann MG, Pletnev SV, Corver J, Lenches E, *et al*. *Cell.* 2002;108:717e25.
7. Bartel DP. *Cell.* 2004;116:281e97.
8. Reis LO, Pereira TC, Lopes-Cendes I, Ferreira U. *Urology.* 2010;76:521e7.
9. De Rie D, Abugessaisa I, Alam T, Arner E, Arner P, Ashoor H, *et al*. *Nat Biotechnol*. 2017;35:872–878
10. Kim YK, Kim VN. *EMBO J*. 2007;26:775–783.
11. Ghosh Z, Mallick B, Chakrabarti J. *Nucleic Acids Res. 2009*;37, 1035-48.
12. Slonchak A, Shannon RP, Pali G, Khromykh AA. *J Virol.* 2015;90:2388-402.
13. Zhu X, He Z, Hu Y, Wen W, Lin C, Yu J, et al. *PLoS Negl Trop Dis*. 2014;8(8):e3088.
14. Qi Y, Li Y, Zhang L, Huang J. *Mol Med Rep.* 2013;7(3):791–8.
15. Wu N, Gao N, Fan D, Wei J, Zhang J, An J. *Microbes Infect.* 2014;16(11):911–22.
16. Wong RR, Abd-Aziz N, Affendi S, Poh CL. *J Biomed Sci.* 2020;27(1):4.
17. Bader AG, Brown D, Stoudemire J, Lammers P. *Gene Ther.* 2011;18(12):1121–6.
18. Sakoonwatanyoo P, Boonsanay V, Smith DR. *Intervirology*. 2006;49(3):161-172.
19. Panyasrivanit M, Greenwood MP, Murphy D, Isidoro C, Auewarakul P, Smith DR. *Virol*. 2011;418(1):74-84.
20. Sithisarn P, Suksanpaisan L, Thepparit C, Smith DR. *J Med Virol.* 2003;71(4):532-539.
21. Varkonyi-Gasic E, Wu R, Wood M, Walton EF, Hellens RP. *Plant Methods,* 2007;3:12.
22. Nahand JS, Mahjoubin-Tehran M, Moghoofei M, Pourhanifeh MH, Mirzaei HR, Asemi Z, Khatami A, Bokharaei-Salim F, Mirzaei H, Hamblin MR. *Epigenomics*. 2020;12:353–70.
23. Sadri NJ, Shojaie L, Akhlagh SA, Ebrahimi MS, Mirzaei HR, Bannazadeh Baghi H, Mahjoubin-Tehran M, Rezaei N, Hamblin MR, Tajiknia V, Rahimian N, Mirzaei H. *Mol Ther Nucleic Acids*. 2021;24:487-511.
24. Harfe BD. *Curr. Opin Genet Dev*. 2005;15:410e415.
25. Felekkis K, Touvana E, Stefanou Ch, Deltas C. *Hippokratia*. 2010;14 (4):236e240.
26. Ciafre SA, Galardi S. *RNA Biol*. 2013;10(6):934e942.
27. Castillo JA, Castrill JC, Diosa-Toro M, Betancur JG, St Laurent G, Smit JM, Urcuqui-Inchima S. *BMC Infect Dis.* 2016;16(29).
28. Wu S, He L, Li Y, Wang T, Feng L, Jiang L, Zhang P, Huang X. *J Infect*. 2013;67(4):329e341.
29. Kanokudom S, Vilaivan T, Wikan N, Thepparit C, Smith DR, Assavalapsakul W. *Antiviral Res.* 2017;142:169–77.
30. Chen RF, Yang KD, Lee IK, Liu JW, Huang CH, Lin CY, Chen YH, Chen CL, Wang L. *J Infect.* 2014;69(4):366e374.

SULFATED GALACTANS PROMOTE MIGRATION OF KERATINOCYTE CELLS

Palarat Atsatit, Jinchutha Duangdara, Apinya Sayinta, Boottoh Nambunruang, Kanokpan Wongprasert*
Department of Anatomy, Faculty of science, Mahidol university, Bangkok, Thailand
*e-mail: kanokpan.won@mahidol.ac.th

Abstract:

Currently, the ineffective treatment of wounds and the delay wound healing in the elderly people with comorbidities illness is an increasing health-economic burden on healthcare systems, thus, there is a growing interest in effective treatment of wound repair. Keratinocytes and fibroblasts are critical players for skin repair after injury. During the wound healing process, proliferation, migration, and differentiation of these cells are the major mechanisms leading to tissue repair. Previously, sulfated galactans (SG) isolated from red seaweed *Gracilaria fisheri* has been shown to stimulate fibroblast migration and proliferation. In this study, we therefore, aimed to explore whether SG displays effects on the migration of a human keratinocyte cell line (HaCaT) using scratch wound healing assay. SG was tested for cytotoxicity and proliferation effects on keratinocyte cells. Expressions of migration associated proteins including E-cadherin, p-FAK and p-NF-κB were investigated by Western blot analyses. The results demonstrated that SG at the tested concentrations showed no toxicity and proliferation effects on keratinocyte cells. SG significantly accelerated HaCaT cell migration in a concentration-dependent manner at 24 h exposure. Furthermore, SG was found to significantly downregulate the expression E-cadherin and upregulate the expression of p-FAK and p-NF-κB. The present findings demonstrate that SG may be a promising compound to promote the migration of keratinocytes for skin wound treatment. Further studies are still required to confirm the underlined wound healing property of SG.

Introduction:

Cutaneous wound closure is a complex biological process that needs the concerted action of activated keratinocytes and dermal fibroblasts to resurface and close the wound. Re-epithelialization process, which resurfaces the wound with new epithelium, is a critical step to reform an epidermal permeability barrier function. The activated keratinocytes participate in re-epithelialization through a series of cellular activities, including cell proliferation and migration[1]. Failure of keratinocytes to maintain the epidermal barrier is a risk for wound infection and may contribute to wound reoccurrence. To facilitate migration, cells alter their gene expression program to transition from a tissue-resident to a migratory cell type, such as downregulating expression of cell-cell adhesion gene E-cadherin and upregulating the expression of genes involved extracellular matrix breakdown, matrix metalloproteinase (MMPs)[2]. It has been reported that increased expression of MMPs in migrating keratinocytes is regulated through the transcriptional factor NF-κB[3] and focal adhesion kinase (FAK)[4].

Numerous polysaccharides isolated from seaweed have attracted great interest as sources of functional foods, nutrition, and bioactive compounds for pharmaceuticals [5]. Their important biological activities include immunomodulatory, antitumor, antiviral, antioxidant, hypolipidemic[5], anti-inflammatory, antibiotic[6], and wound healing[7]. In recent years, sulfated polysaccharides (SPs) are emerging as high-value drugs and biomaterials for use in

wound management and tissue engineering[8]. Many naturally derived SPs used in wound healing are derived from plants, and macroalgae, in which compounds show low toxicity and good biocompatibility with human tissue[9].*Gracilaria fisheri (G. fisheri*) is a red seaweed widely found in the southern *p*art of Thailand[10]. It is commonly used as feed for fish and shellfish, and components in nutrition. Recently, sulfated galactans (SG) isolated from *G. fisheri* has been shown to promote migration of fibroblast in wound model[11]. In the present study, we, therefore, aimed to explore wound healing property of SG by investigating the effects of SG on keratinocyte cells migration.

Methodology:

Sulfated galactans (SG)

SG was extracted from red seaweed *G. fisheri* as previously described[12].The structure of SG consists of a linear backbone of alternating 3-linked β-D-galactopyranose (G) and 4-linked 3,6-anhydro- α-L-galactopyranose (LA) or α-L-galactose 6-sulfate (L6S) units. Stock solution of SG (10 mg/mL) was dissolved in 3D water, heated at 37°C, and kept at -20°C until used.

HaCaT cells culture

Human keratinocyte cells, HaCaT cells (Addex Bio, California, USA) were cultured in Dulbecco's modified Eagle's medium (DMEM) with 10% fetal bovine serum (FBS), 3.7 g/L sodium bicarbonate and 1% anti-antibiotic. Cells were maintained at 37°C in a humidified incubator containing 5% CO_2.

Cell viability assay

Cytotoxicity of SG on HaCaT cells was evaluated using the 3-(4,5-Dimethylthiazol-2-yl)-2,5-Diphenyltetrazolium bromide (MTT) assay. Cells were seeded at a density of $5x10^3$ cells/well in a 96-well plate for overnight. The cells were then treated with various concentrations of SG (0, 10, 20, 40, 80 and 125 μg/mL) for 24 and 48 h. The 100 μl of MTT solution (Sigma, New York, USA) was added to each well and the plate incubated in the dark at 37°C for 2 h. The solution was removed and 100 μl of DMSO (Merck, Darmstadt, Germany) was added to lyse the cells. The formazan product was measured using a Versamax microplate reader (SoftMax® Pro 4.8 analysis software, Molecular Devices, USA) at OD 490 nm. The viability of cells was expressed as a percentage of control.

Scratch wound healing assay

HaCaT cells were cultured in a wound condition and determined for the cell migration activity. Cells were seeded in 6-well plates with a density of $9x10^5$ cells/well and cultured for 24 h. The cell monolayer was scratched with a sterile pipette tip to create the wound and followed by treatment with different concentrations of SG (0, 10, 20, 40 μg/mL). The wound closure was examined and photographed at 0, 12, 18 and 24 h after scratching under an inverted phase contrast microscope (Olympus, Hamburg, Germany). The percentage of distance wound closure was calculated, using the data from time 0 (*T*0), the wound area (*Tt*: 12,18 and 24 h) by the following formula:

Percentage of distance wound closure = [(wound area at *T*0 – wound area at *T*t)/ wound area at *T*0]x100

Western blotting

Cellular proteins in the scratch wound cultures were extracted using a lysis buffer containing protease inhibitor solution. Protein lysate was separated in 10% SDS-PAGE gel electrophoresis and transferred to nitrocellulose membranes (Merck, Darmstadt, Germany). Each membrane was incubated with specific primary antibodies including anti-E-cadherin, anti-p-FAK and anti-p-NF-κB antibodies, followed by the HRP-conjugated secondary antibodies. Immunoreactive proteins were detected using a Chemiluminescence ECL Western

blotting detection kit (Cell signaling Technology, Massachusetts, USA). The expression of protein was quantified relatively to β-actin using Image J software (National Institutes of Health, Maryland, USA).

Statistical analysis

All data were presented as mean ± the standard error of the mean (SEM). One-way analysis of variance, followed by LSD post hoc test was used for testing the differences in the mean values among groups. The statistically significant difference between treatments was considered with *p*-value less than 0.05.

Results and Discussion:

SG showed no cytotoxicity on keratinocyte cells culture

Treatment of HaCaT cells with the SG ranging from 10-125 µg/mL for 24 and 48 h showed no significant reduction of cell viability compared to those of control (Figure 1). Our finding was in line with previous studies for no toxicity of SG in fibroblast cells[11] and in other marine algae such as SPs from *Codium tomentosum*[13] and *Caulerpa cupressoides*[14]. The results suggest that SG is a safe compound for further scratch wound healing study.

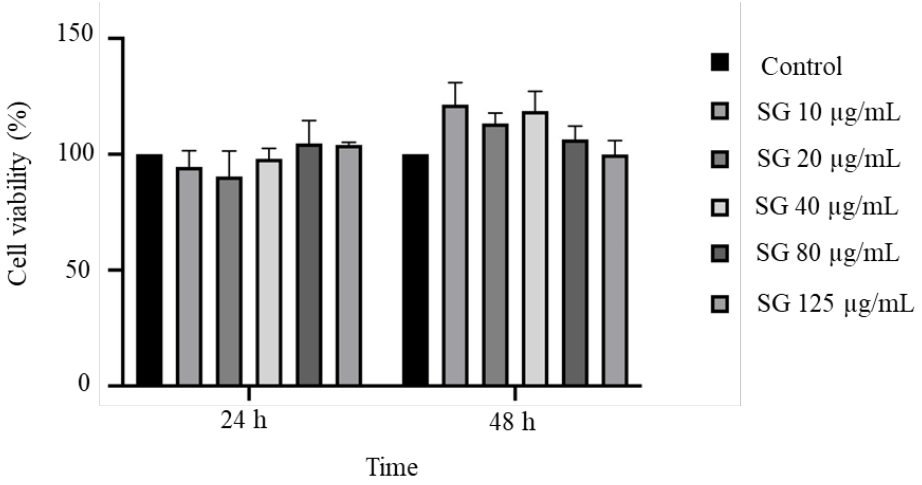

Figure 1. Percentage of viable HaCaT cells after treatment with different concentrations of SG for 24 h and 48 h compared to untreated control. Values are mean ± SEM of three independent experiments.

SG promoted keratinocytes migration

In the re-epithelialization stage of wound healing process, migration of keratinocytes at the wound edge are important for wound closure[15]. Thus, the enhanced keratinocytes migration for proper wound healing process is considered as an indicative of faster wound healing. The effect of different concentrations of SG on HaCaT cells migration was investigated at 12, 18, and 24 h exposure time in a scratch wound healing model. The results showed that SG at the concentrations of 10, 20, and 40 µg/mL apparently accelerated wound closure in a time- and dose-dependent manner, with a notably improvement of wound gap closure from control at 24 h exposure (Figure 2). These results indicate that SG promoted wound closure through increased migration rate of keratinocyte cells.

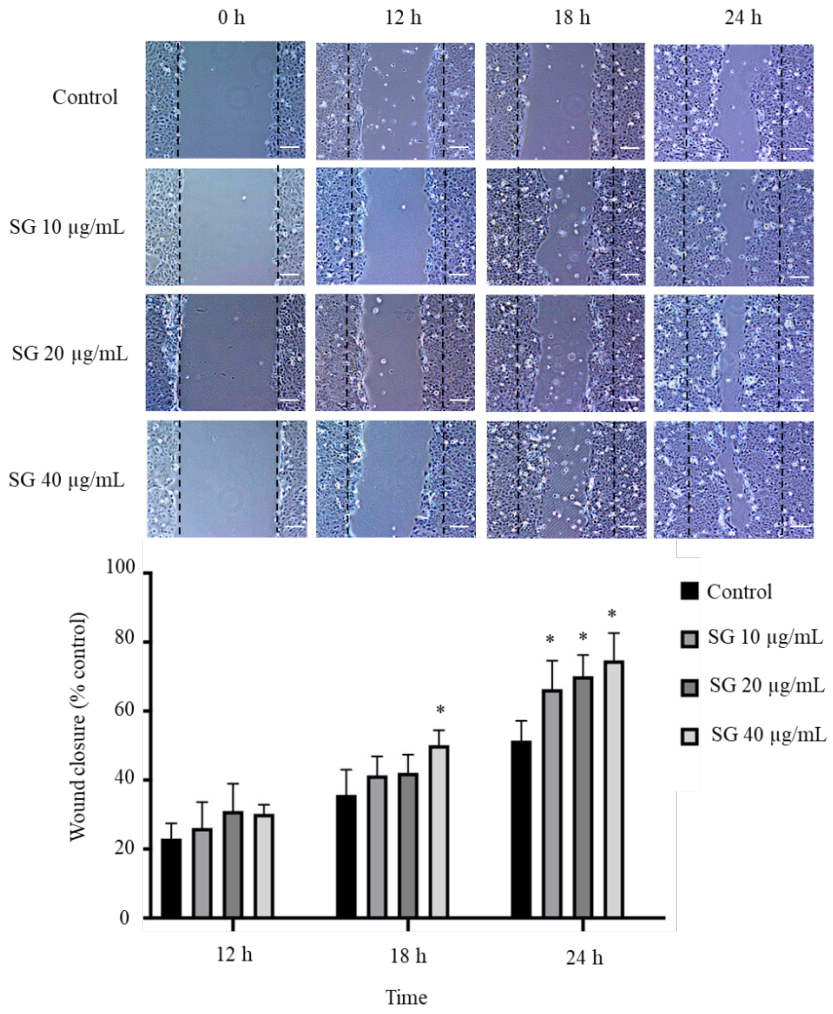

Figure 2. The effect of SG on migration of HaCaT cells in a scratch wound healing assay. Phase contrast micrographs showing the distance of scratch wound in different treatment groups. Percentage of wound closure compared to control at 12, 18, 24 h after wound scratching. Cells were scratched wound and followed with SG treatments (10, 20, 40 µg/mL), photographed at 0, 12, 18 and 24 h. Values are mean ± SEM of three independent experiments.
*indicates a significant difference from control, $p < 0.05$. Scale bar =100 µm

SG induced keratinocyte cells migration via down regulation of E-cadherin expression and upregulation of p-FAK and p-NF-κB expression

Western blot analysis was employed to determine the effect of SG on major proteins regulating cell migration. E-cadherin is a protein biomarker of epithelial cells and its downregulation could be used as a marker for epithelial cells migration/invasion[15]. Our results revealed that cells treated with SG had a dose-dependent decrease in the expression of E-cadherin compared to control group (Figure 3). These findings appear to be corroborated by a previous study which showed that polysaccharides from medicinal mushroom promoted wound healing via increased epithelial cell migration and downregulation of E-cadherin [16].

During re-epithelialization process of wound healing, migrating cells secrete MMPs to breakdown the ECM leading to cell migration. Expression of MMPs is mediated via NF-κB[3] and FAK activation[4]. We further investigated the effects of SG on the expression of p-FAK and p-NF-κB in HaCaT cells. Our results revealed that SG induced increased expression of p-FAK and p-NF-κB over control cells (Figure 3). FAK activation and

phosphorylation was found to be significant in keratinocytes migration in epidermal wound healing[17] and involved in the secretion of MMPs[11]. Phosphorylated NF-κB modulates expression of MMPs resulting in breaking down of the basement membrane leading to cell migration[18]. Our results agree with the previous study which demonstrated that SG promoted fibroblast cells migration via activation of NF-κB signaling and increased MMP-2 activity[11]. A study in neural stem cell also reported that SPs from the *Stichopus japonicas* activated NF-κB signaling and induced MMP-2 expression during cells migration[19]. Taken together, our present results demonstrate an initial observation that SG promotes FAK and NF-κB activation which signaling is crucial for keratinocyte migration. Further investigation is required to understand the underlined cellular and molecular mechanisms of the wound healing property of SG in keratinocyte cells.

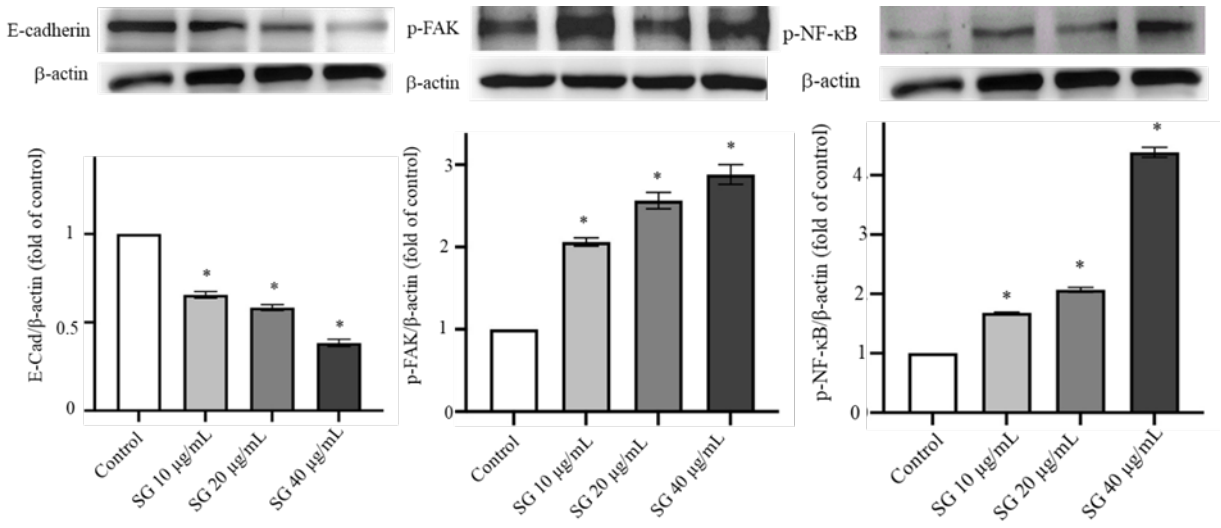

Figure 3. Western blot analysis showing the effect of SG on the level of E-cadherin, p-FAK and p-NF-κB proteins in HaCaT cells. Histogram showing quantitative fold change in protein expression normalized to β-actin expression by Image J analysis. Values are mean ± SEM of three independent experiments. *indicates a significant difference from control, $p < 0.05$

Conclusion:

The present study investigated the effect of SG from red seaweed *G. fisheri* on keratinocyte cells migration using the in vitro scratch wound model. The results showed that SG promoted cells migration and improved wound closure, in part, via modulating the migration associated proteins which includes downregulated E-cadherin expression and upregulated p-FAK and p-NF-κB expressions. SG shows potential as a wound healing therapeutic agent for future drug development.

Acknowledgement:

This research was supported by Mahidol University, and the Central Instrument Facility (CIF) and Center of Nanoimaging (CNI) grant, Faculty of Science, Mahidol University.

References:

1. Eming S A, P Martin,M Tomic-Canic. *Sci Transl Med*. 2014;6(265):265sr6.
2. Kuwahara M. *J Cutan Pathol*. 2001;28(4):191-9.
3. Na J. *J Invest Dermatol*. 2016;136(4):847-858.
4. Gates R E. *Cell Growth Differ*. 1994; 5(8): 891-9.
5. Xu S -Y, X Huang, K-L Cheong. *Marine Drugs*. 2017;15(12):388.
6. Dang HT. *Journal of Natural Products*. 2008;71(2):232-240.
7. Premarathna AD. *Wound Medicine*. 2019;24(1):1-7.
8. Kuznetsova TA. *Journal of Marine Science and Engineering.* 2020; 8(7): 481.
9. Holdt S,S Kraan. *Journal of Applied Phycology*. 2011;23:543-597.
10. Tseng, C K, B.-M Xi. *Botanica marina.* 1999;42(3):209-218.
11. Pariwatthanakun C. *Songklanakarin Journal of Science and Technology*. 2021;43:1374-1381.
12. Wongprasert K, T Rudtanatip. *Fish Shellfish Immunol.* 2014;36(1):52-60.
13. Navya P, SS. Khora. *Journal of Applied Pharmaceutical Science*. 2017;7(6):033-036.
14. Barbosa JdS. *Marine Drugs*. 2019;17(2):105.
15. Broughton G, II J E Janis, C.E. Attinger. *Plastic and Reconstructive Surgery.* 2006; 117(7S)
16. Mapoung S. *Journal of Fungi*. 2021;7(4):247.
17. Petpiroon N. *J Nat Med*. 2015;69(3):340-8.
18. Na, J. *Journal of Investigative Dermatology*. 2016;136(4):847-858.
19. Syarina, PN. *Excli j*. 2015;14:385-93.

APPLICATION OF THERMAL INSULATOR FOR HEAT STORAGE IN CATFISH PONDS

Shewin Attasat *, Pavinee Pattanachan, Bundit Tirachulee, Chanakon Upajak

Pilot Plant Development and Training Institute, King Mongkut's University of Technology Thonburi, Thailand
*e-mail: shewin.att@kmutt.ac.th

Abstract:

Water temperature was an important factor influencing the livelihood of aquatic animals including fishes. The low water temperature resulted in reduced feed intake and growth and lead to a shortage of fish production during the winter, as well as in the highlands region such the northern of Thailand, which the air temperature probably dropped below 15 degrees Celsius. For this reason, many researches had been done into finding methods for increasing the water temperature in aquaculture ponds, such using fish pond heaters, or using greenhouses to prevent heat loss from ponds. In this study, the using of pond insulation together with pond covering in order to store solar heat inside hybrid catfish (*Clarias macrocephalus* x *C. gariepinus*) ponds were conducted and evaluated the performance in increasing water temperatures. The results showed that using insulation together with pond covering not only increased the average water temperatures up to 6.3 degrees Celsius higher than the control, but also reduced the daily water temperature fluctuation. In addition, the catfish raised in the insulated ponds had better growth performances. The growth rates and survival rates were higher than the control up to 34 and 91 percent, respectively, while the feed conversion ratio was lower about 30 percent.

Keywords: Catfish, Water temperature, Thermal insulator, Aquaculture

Introduction:

At present, catfish farming in Thailand had been very successful due to the development of breeding technology with high growth rate and resistant to disease. A high annual production of 97,200 tons and valued of 4,477 million baht [1] made it to become one of the high economic value freshwater fish in Thailand. However, the catfish production depends on number of factors such as pond preparation, water quality management and the weather conditions. The later directly affected water temperatures including fish activities. The low water temperature resulted in reduced feed intake, slow growth and less productive. It becomes a problem for grow-out fish during the winter, as well as in some areas such the northern of Thailand which air temperature probably dropped below 15 degrees Celsius and the difference of temperature in the day and night was about 15-20 degrees Celsius. The optimum water temperature for production of tropical aquatic animals should be in the range of 25-32 degrees Celsius, which achieved the best growth and increased the productivity [2] and provided high growth rate, low feed conversion ratio, shorten grow-out period and reduce feed cost [3]. The optimum growth temperature for hybrid catfish was 27 degrees Celsius [4] and water temperatures had profound effects on the growth of catfish. The growth rate of catfish fry at 21 and 27 degrees Celsius increased 6 times and 20 times, respectively, compared to those raised at 17 degrees Celsius [5].

The utilizing sunlight was one of the popular methods in increasing water temperature in aquaculture ponds. Sunlight or solar radiation was a form of thermal energy. It was the major source of heat transferred to water, and then be absorbed by body of water and increased the temperature. This heat eventually lost to the atmosphere through convection and radiation.

Some of them lost to the ground by conduction. For this reason, finding the way to store the solar heat efficiently would maximize the benefits of using of solar energy to increase water temperatures in aquaculture ponds.

In the past, various methods had been studied to increase and control water temperature in aquaculture ponds. For example, using greenhouses to store and prevent heat loss from fish ponds during the winter, could increase water temperatures up to 3-4 degrees Celsius and provided better fish growth rates than those of outdoor ponds [6]. Wudtigid (2010) [7] found that using Solar-Heat pump system in winter and rainy season could increase and control the water temperature in earthen catfish ponds within ranges of 30-32 degrees Celsius, compared to the ranges of 25-29 degrees Celsius for the control group without using Solar-Heat pump system. In addition, the higher temperature also gave significantly better growth rates about 1.6-1.7 times higher. In an attempt to store solar heat, Mohapatra *et al*. (2015) [8] found that using 0.2 mm thickness LDPE plastic sheet covered fish ponds during the winter could increase water temperatures higher than the control and also controlled the physical properties of water within the suitable range for aquaculture. Jadrnicek (2016) [9] suggested that using 1 inch thickness polystyrene insulation covered at pond bottom could reduce heat loss to the ground. Bozkurt *et al*. (2016) [10] had determined the efficiency in reduction heat loss of the different insulation materials, i.e. foam, glass wool, and rock wool, installed on the floor and walls of the solar pond and found that foam had the best efficiency in reduction heat loss followed by glass wool and rock wool respectively. In this study, the efficiency of using thermal insulators and pond covering to store the solar heat in catfish ponds were evaluated.

Methodology:

1. Experimental ponds

The experimental ponds were rectangular concrete ponds (width 2 m x length 2 m x height 1 m and wall thickness 10 cm, contained water with the depth of 50 cm) and placed in a shed with transparent roof and without wall. The experiments were conducted during January - May 2022 at the KMUTT Coordinating Center, Nan Province and were divided into 2 parts;

2. Determination for the efficiency of using thermal insulators and pond covering in increasing water temperatures

The polyethylene foam was installed on the 4 sides of the pond wall and/or the bottom of the pond with the 3 cm thickness of insulator on each side. The water was filled to the pond to the water depth of 50 cm. The transparent plastic sheet with 0.15 mm of thickness was covered on the surface of the pond to retain heat (Figure 1). The experimental ponds were set into 3 groups as follows:

1) Control 1 (0-Cover): No insulation and no covering.
2) Experiment 1 (4+Cover): Insulation on 4 walls and covering.
3) Experiment 2 (5+Cover): Insulation on 4 walls and pond bottom, and covering.

Experimental pond Pond insulation Pond covering

Figure 1.
Experimental pond, Pond insulation and Pond covering

3. Determination for the efficiency of using thermal insulators and pond covering in raising catfishes.

The hydrid catfishes, with the average size of 9.5 g individual, were raised in a 500 liter plastic pond for 1 week before the experiment for acclimating. The healthy fishes were selected and stocked in the experimental ponds at the rate of 200 fish each pond. The 30% protein content floating diet was fed twice a day at a rate of 3-4% of their body weight per day. The experimental ponds were set into two groups as follows:

1) Control 2 (0-Cover+Fish): Raising fishes in ponds with neither insulation nor covering.

2) Experiment 3 (4+Cover+Fish): Raising fishes in ponds with insulation on 4 walls and covering.

4. Measurement Methods

4.1 Water temperatures

Water temperatures were measured by using Type-K thermocouples at the depth of 10 and 40 centimeters below a water surface and recorded every 30 minutes with the data logger (Model: dataTaker DT85). During the experiment period, average daily water temperatures were calculated, and the daily water temperature fluctuation was showed in term of the coefficient of variation (CV), which was calculated from the equation below.

CV = (Standard deviation of daily water temperature / Average daily water temperature) x 100%

4.2 Growth performance parameters

The 20 fish samples were taken randomly from each treatment and determined individual weight every 15 days. The growth performance parameters were calculated at the end of experiments as follows.

a. Average daily growth (g/d)
= (Final fish weight – Initial fish weight) / Grow-out period

b. Specific growth rate (%/d)
= (ln (Final fish weight) - ln (Initial fish weight)) / Grow-out period x 100%

c. Survival rate (%)
= (Initial fish number – Final fish number) / Initial fish number x 100%

d. Feed conversion ratio
= Total weight of feed used / Total weight of fish produced

4.3 Statistical Analysis

A One-Way ANOVA was performed to compare mean values of each treatment using SPSS Statistics software version 16.0 (SPSS Inc., US) at 95% confidence level ($P<0.05$).

Results and Discussion:

1. The efficiency of using thermal insulators and pond covering in increasing water temperatures

The experimental results showed that using thermal insulators together with pond covering (4+Cover and 5+Cover) was effective on increasing average water temperatures compared to the control (0-Cover) (Figure 2-3). It was presumed that thermal insulators could prevent heat loss to the atmosphere and the ground from walls and bottom of the pond, while the hot air above the water surface under the plastic sheet prevented heat loss from the water surface. The highest average water temperature was found in the pond insulated on 4 walls and pond bottom and covering (5+Cover), which was higher than that of the control about 6.3 degrees Celsius (Table 1). Moreover, using thermal insulators together with pond covering

could control water temperatures above 18.9 degrees Celsius throughout the experimental period, which was determined to be lethal for catfish during the larval period [11].

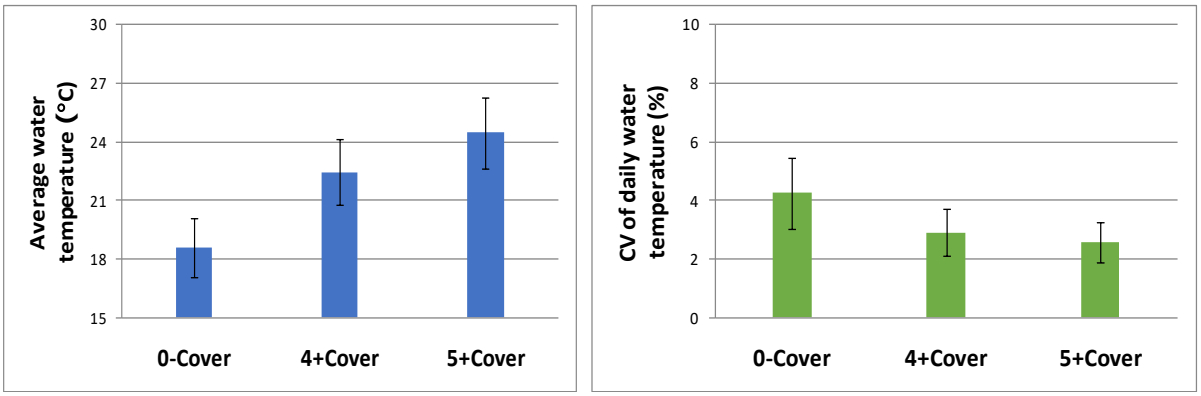

Figure 2.
Average water temperatures and CV of daily water temperatures in the first experiment (during January – February 2022, the average air temperature was 19.0 ± 5.4 degrees Celsius)

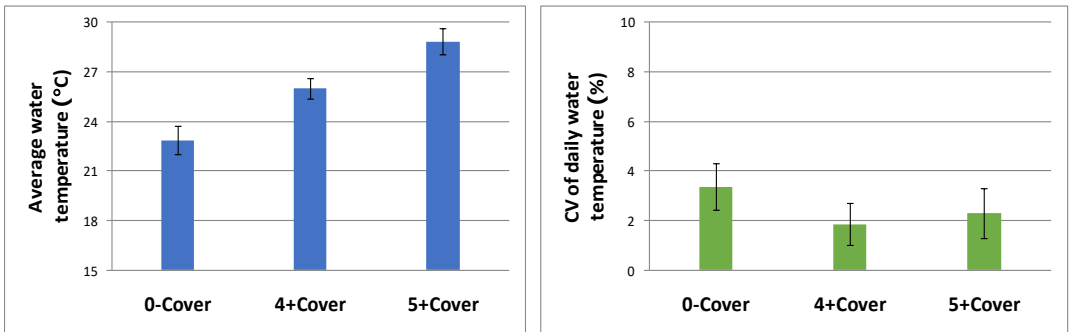

Figure 3.
Average water temperatures and CV of daily water temperatures in the second experiment (during March 2022, the average air temperature was 23. 6 ± 4.4 degrees Celsius)

Table 1.
Comparison of average water temperatures in each treatment

Treatment	January – February 2022		March 2022	
	Range (Min - Max)	Mean ± SD	Range (Min - Max)	Mean ± SD
0-Cover	16.40 – 20.73	$18.60^{a} \pm 0.98$	21.18 – 24.35	$22.87^{a} \pm 0.87$
4+Cover	20.70 – 24.02	$22.46^{b} \pm 0.76$	24.80 – 27.07	$25.99^{b} \pm 0.63$
5+Cover	22.80 – 26.13	$24.46^{c} \pm 0.71$	27.45 – 30.41	$28.84^{c} \pm 0.80$

*Mean values with different characters in columns were statistically significant at the 95% Confidence level (P≤0.05).

In addition, it was found that using thermal insulators together with pond covering also reduced the daily water temperature fluctuation compared to the control (Fig. 2-3). This was probably due to the less heat loss to the environment. The less temperature fluctuation also had a positive effect on fishes. The change of water temperature might cause of stress from adaption to new environment. This stress could reduce immunity thus allowing pathogen invasion and disease incidence [12, 13, 14].

2 The efficiency of using thermal insulators and pond covering in raising catfishes

This experiment was conducted to compare growth of catfishes in the experimental ponds with insulation and covering (4+Cover+Fish) to the control (0-Cover+Fish). The average water temperatures and the growth performance parameters are shown in Figure 4 and Table 2.

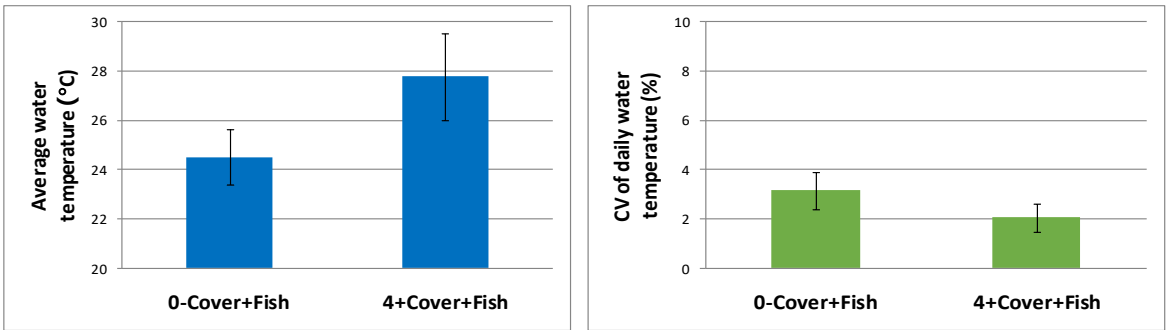

Figure 4.
Average water temperatures and CV of daily water temperature in catfish ponds (during March - May 2022)

Table 2.
Data on growth and growth performance parameters of catfishes in each treatment

Parameters	Unit	Control (0-Cover+Fish)	Experiment (4+Cover+Fish)
Grow-out period	day	60	60
Pond size	m^3	2	2
Initial fish number		200	200
Initial fish size	g/fish	9.7	9.2
Harvested fish size	g/fish	75.5	97.5
Survival rate	%	51.5	98.5
Average daily growth	g/d	1.10	1.47
Specific growth rate	% /d	3.42	3.94
Feed conversion ratio		1.81	1.26

It was found that using thermal insulators together with pond covering not only increased the average water temperature and reduce the daily water temperature fluctuation compared to the control, but it also provided better the growth performance parameters with a higher growth rate and a lower feed conversion ratio. Moreover, catfishes raised in the control had a high mortality rate especially during the first week of the experiment. That probability resulted from the temperature was lower than their optimum range (25 - 30 degree Celsius), and a higher daily water temperature fluctuation might cause stress to fishes and lead to their weakness and dead.

Conclusion:

The resulted from this study indicated that using thermal insulators together with pond covering could increase water temperatures higher than the control. The insulation on walls and pond bottom was the most effective in increasing water temperatures, up to 6.3 degree

Celsius higher than the control, and also reduce the daily change water temperature fluctuation. In addition, catfishes raised in the insulated ponds had better growth performances than the control. The growth and survival rates increased by 34 and 91 percent, respectively, and the feed conversion ratio decreased by 30%. Therefore, this technology tended to be an option for improvement the production of catfish in winter or in the highlands region.

Acknowledgements:

This work was supported by Thailand Science Research and Innovation (TSRI) and Program Management Unit on Area Based Development (PMU A) (grant number : A13F640044)

References:

1. Department of Fisheries. Fisheries statistics of Thailand. 2019;Document No. 2/2019 [in Thai]
2. Duangsawat M, Somsiri J. Water Attributes and Procedures for Fishery Research. 1985; 115 p [In Thai]
3. Taemprasit W. Master's Thesis in Science (Fisheries Technology), Maejo University. 2014 [In Thai]
4. Visoottivisetha P, Chanwanna N. ScienceAsia. 2001;27:75-81.
5. Li M, Robinson E, Peterson B, Bates T. N.Am.J.Aquac. 2008;70(3):347-352.
6. Tiwari G, Das T, Sarkar B. Int. J. Agric. Res. 2006;1(5):406-419.
7. Wudtigid K. Master's Thesis in Engineering (Energy Engineering) Chiangmai University. 2010; [in Thai]
8. Mohapatra B, Mahanta S, Sahu H., Sahoo P, Mandal P, Kisku S, Majhi D. Int.j.fish.aquat. 2015;3(1):269-275.
9. Jadrnicek S. Chelsea Green Publishing. 2016
10. Bozkurt I, Sogukpinar H, Karakilcik M. JMEST. 2016;2(6):1378-1382.
11. Prokesova M, Drozd B, Kouril J, Stejskal V, Matoušek J. J.Appl.Ichtyol. 2015;31(4).
12. Lafferty K. Ecology. 2009;90:888-900.
13. Mariana S, Badr G. J.Surv.Fish.Sci. 2019;5(2):149-159.
14. Chirapongsatonkul N, Wattitum S, Srichanun M, Nganwisutthiphun T, U-taynapun K. Khon Kaen Agr.J. 2021;1:611-617 [In Thai].

GENERATION OF A CRISPR-Cas9 MUTAGENESIS SYSTEM FOR GENERATING LYTIC PHAGE VARIANTS FROM *Clostridioides difficile* PROPHAGE

Thapakorn Trirasspanich,[1] Phurt Harnvoravongchai,[1] Tavan Janvilisri,[2] Surang Chankhamhaengdecha [1,*]
[1] Department of Biology, Faculty of Science, Mahidol University
[2] Department of Biochemistry, Faculty of Science, Mahidol University
*e-mail: surang.cha@mahidol.edu

Abstract:

The clustered regularly interspaced short palindromic repeats (CRISPR) and CRISPR-associated protein (Cas) is known to be an adaptive immunity in prokaryotes. Due to its accuracy and efficacy, the CRISPR-Cas system has been widely used to edit the genome of several organisms as well as viruses. In this study, the CRISPR-Cas9 system for the disruption of integrase gene (*int*) in the *C. difficile* prophage genome was created. PAM sequences in the *int* gene of phage ΦHN10 were located to retrieve the potential guide RNA (gRNA) sequences. The protocols used the CRISPR-Cas9 gRNA expression plasmid pJK02 and *in vivo* assembly for cloning and expressing the *int* sequence. The repair fragment was subsequently subcloned to replace the upstream and downstream regions of the pJK02 for homology-directed repair after Cas9 cut the target. The gRNA and upstream/downstream homology arms in the constructed plasmid were verified by restriction digestion and sequencing to ensure the joining and preservation of the local sequence context. The system reported here is an applicable, efficient, and simpler procedure to construct expression clones for CRISPR/Cas9-mediated phage genome editing.

Introduction:

Clostridioides, formerly *Clostridium*, *difficile* is a Gram-positive, spore-forming, anaerobe, and toxin-producing bacterium (1). Gut microbiome dysbiosis induced by antibiotic exposure is a factor that allows *C. difficile* to colonize at epithelium cells of the large intestine and releases protein toxins, toxin A and toxin B, which consequently cause diarrhea and pseudomembranous colitis. *C. difficile* infection (CDI) is classified as an urgent threat in the United States, where more than 200,000 cases of gastrointestinal infection and 12,000 deaths in 2017 were reported (2, 3). Antibiotics that are used to treat CDI are vancomycin, fidaxomicin, and metronidazole. However, high levels of antibiotic resistance CDI and treatment failures have been reported. In 2005, the European survey of *C. difficile* infection showed that 55% of resistant clinical isolates were multidrug-resistant (4). Thus, alternative treatment for CDI is needed to get more attention for tackling the disease.

Bacteriophage or phage is a virus that capable of infecting a specific bacterial host. Generally, phage has two types of life cycles, which are lytic and lysogenic cycles. In the lytic cycle, the phage replicates, reproduces new progeny virions, and lyses the host cell. While in the lysogenic cycle, phage DNA is incorporated into the host genome without the production of phage progeny. In contrast, a phage that can proceed with both types of cycles is classified as a temperate phage. For the process of phage genome integration into the host genome, phage integrase is necessary for site-specific recombination (5). In therapeutic use, obligated lytic phages are required for effectiveness and to avoid horizontal gene transfer. However, all *C. difficile* phages discovered to date are considered temperate and this contributed to the difficulties with their therapeutic utilization. To remove the impact of

lysogeny on the therapeutic efficacy, modern genome engineering tools can convert temperate phages into obligated lytic phage phages by disrupting the integrase gene.

The clustered regularly interspaced short palindromic repeats (CRISPR) – CRISPR-associated nuclease (Cas) systems are adaptive immunity that protects bacteria and archaea from invading genetic elements such as bacteriophage (6). CRISPR-Cas system is generally used in several aspects of biology including genome editing. CRISPR-Cas9 system can break double-stand DNA using the Cas9 endonuclease (7), detects the target by guide RNA (gRNA) which is about 20 – 40 bp of RNA that was combined with Cas9 for recognition and cut the target. CRISPR-Cas9 can rapidly and efficiently edit the genome in various organisms (8).

Previously, *C. difficile* phage ΦHN10 has been induced from *C. difficile* HN10 lysogen by our research group (9). ΦHN10 is considered temperate as its genome encodes an integrase and lysogen-associated proteins to control the switch between lytic and lysogenic infection cycles. This study aims to establish the streamlined method for the efficient generation of the CRISPR-Cas9 system for further use in the disrupting integrase gene in the genome of *C. difficile* HN10 prophage.

Methodology:

Bacterial strains and growth conditions

Escherichia coli strains were grown in lysogenic broth (LB) at 37 °C, 20 µg/mL chloramphenicol was supplied when needed. *C. difficile* was growth in brain heart infusion (BHI) medium or TY medium (3% tryptone, 2% yeast extract, 10 mM $CaCl_2$ and 10 mM $MgCl_2$) at 37 °C under anaerobic (10% H_2, 5% CO_2, 85% N_2) conditions.

Bacteriophage propagation

C. difficile HN21 colony that is propagate host for ΦHN10 was picked into BHI broth and incubated at 37 °C, in an anaerobic chamber overnight. And then 150 µL of overnight culture was transferred to 3 mL TY broth and incubated in 37 °C, in anaerobic chamber for 4 h. After that, 10^4-10^6 pfu of phage ΦHN10 were added to the culture and incubated for 4 h. To eliminate bacteria, the culture was centrifuged at 10,000 *x g* for 1 minute and the supernatant was filtered by a 0.2 µm syringe filter. To measure phage titer, *C. difficile* strain HN21 was cultured in a BHI medium and incubated overnight in an anaerobic chamber at 37 °C. 5% of HN21was transferred into TY medium and incubated for 8 h or until OD 1.4. 1.5 mL of HN21 was mixed with 3 mL TY soft agar (0.6% agar (w/v)) and poured into the BHI agar plate. Phage was diluted by SM buffer, after that 10 µL of phage dilution was spot on the BHI agar plate and incubated overnight in anaerobic condition at 37 °C. After that, plaques were observed and calculated by the formula,

$$\frac{pfu}{ml} = \frac{number\ of\ plaque}{dilution * phage\ volume\ (10\ uL)}$$

Bacteriophage genome extraction

1 mL of phage lysate solution 10^8-10^{10} pfu was added DNase and RNase and was incubated for 1 h for bacterial DNA and RNA elimination. 8 µL of 5 M $ZnCl_2$ was added to phage lysate solution as a final concentration of 40 mM and was mixed by inversion at room temperature for 1 min. After that, the solution was centrifuged at 14,000 *x g* for 1 minute. The supernatant was removed and suspended with 1 mL of sterile water and 8 µL of 5 M $ZnCl_2$ as a final concentration 40 mM. The solution was centrifuged at 14,000 *x g* for 1 min and removed supernatant. The pellet was suspended by 100 µL of 0.25 M EDTA pH8. After that, 300 µL of protein solubilizing buffer (250 mM Tris-HCl pH6.5, 7% SDS, 2M urea and 20% glycerol) and mixed by inversion for 2 min. To remove protein, 500 µL of phenol/chloroform/isoamyl alcohol (25:24:1 v/v) was added and shaken vigorously. Then, it

was centrifuged at 14,000 *x g* for 2 min. The aqueous phase around 300 – 400 µL was collected and transferred to a new tube. After that, 950 µL cold absolute ethanol was added, mixed gently, and incubated for 2 minutes on ice. The solution was centrifuged at 14,000 *x g* for 2 min at 4 °C and the supernatant was removed. The pellet was washed twice with 75% cold ethanol, dried and suspended with 50 µL TE buffer.

Design gRNA oligonucleotides and construct plasmid

Plasmid pJK02 containing CRISPR-Cas9 was purchased from Addgene (Figure 1A) (10). To specify the target region for CRISPR-Cas9, the integrase gene specific guide RNA (gRNA) sequences were designed manually using the plasmid editor ApE (A plasmid Editor; https://jorgensen.biology.utah.edu/wayned/ape/). Briefly, protospacer adjacent motif (PAM) sequences (NGG) for Cas9 in the integrase gene (*int*) of phage ΦHN10 were located and a 20-bp gRNA upstream of each PAM was extracted. The phage genome ΦHN10 was annotated by Prokka. The gRNAs were aligned with reference phage genome sequences, ΦHN10, on a homology basis to avoid off-target cuts by Vector NTI. The list of gRNAs was then analyzed to contain GC content lower than 10% or can form secondary structure were filtered out. The most potential gRNA for all criteria was selected for specific prophage *int* gene disruption. To construct a CRISPR-Cas9 expression plasmid (expressing Cas9 and *int* specific gRNA), primers IVA_gRNA_F and IVA_gRNA_R (Table 1) were designed. These primers consist of a 20 bp gRNA overhang and 15 bp sequences complement with pJK02 plasmid (Figure 2A). Primers IVA_gRNA_F and IVA_gRNA_R were used to amplify a CRISPR-Cas9 plasmid, pJK02 by Phusion DNA polymerase. The PCR products were digested with *Dpn*I to remove the original template DNA and then transformed into *E. coli* DH5α for circularization by homologous recombination *in vivo*. The resulting plasmid was designated as pJK03. The homologous region in pJK03 was then removed and replaced with the up and downstream regions of the *int* gene for homologous repairing by splicing with overlap extension PCR (SOE-PCR). In brief, up- and down downstream regions of *int* gene were amplified by F1/R1 and F2/R2 primers and Phusion DNA polymerase, respectively. Then, up and downstream were fused by F1/R2 primers and Phusion DNA polymerase, SOE-PCR (Figure 2B, Table 1). After that, pJK03 was pJK03 was amplified by IVA_UP_R, IVA_DOWN_F primers (Table 1) and Phusion DNA polymerase. The PCR products were verified by agarose gel electrophoresis. The original template plasmids were digested by *Dpn*I. The PCR products, pJK03 amplification and up-downstream, were then introduced into *E. coli* DH5α for circularization *in vivo*. The resulting plasmid was designated as pJK04 (Figure 2C).

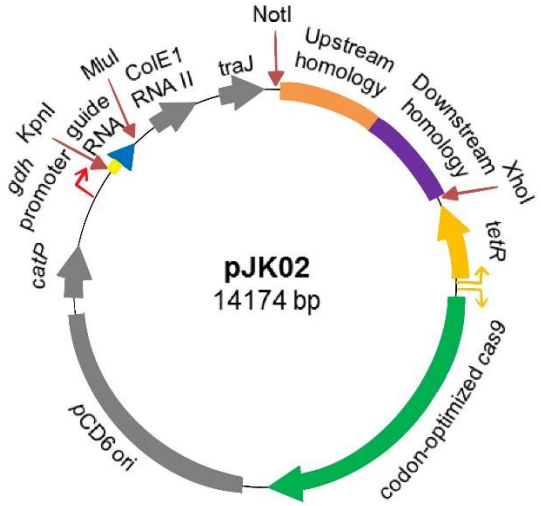

Figure 1 *C. difficile* CRISPR-Cas9 plasmid map. The pMTL84151 backbone, denote in gray, consists of the pCD6 *oriV*, the thiamphenicol resistance marker *catP*, *colE1* and *traJ*. gRNA (yellow) and tracrRNA (blue) under the *gdh* promoter. gRNA specifies the *selD* gene. Up-down stream homology region for homologous repairing *selD* deletion. *Streptococcus pyogenes cas9* gene that was codon optimized for expression in *C. difficile* under *tetR* promoter (10).

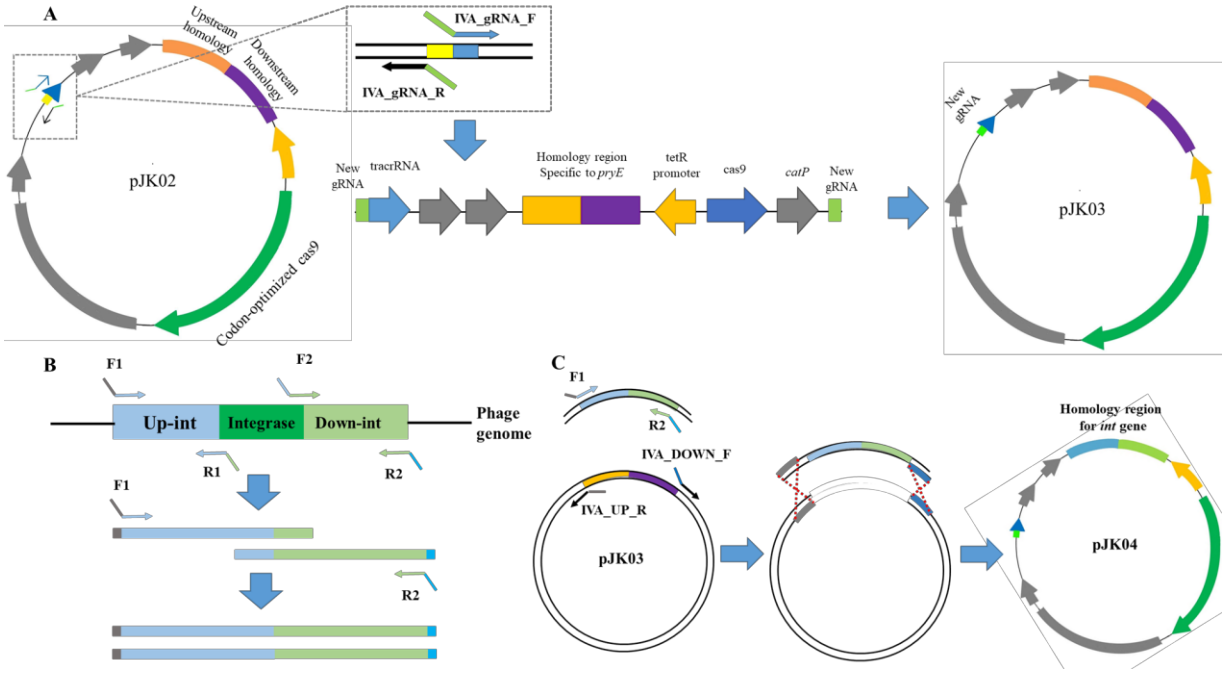

Figure 2 Method overview and primer design. A) Schematic of gRNA editing by IVA, pJK02 was amplified by IVA_gRNA primers that have new gRNA 20 bp overhang (light green). The PCR product was linear DNA, and this linear DNA was transformed into *E. coli* DH5α. After that, linear DNA was assembled to circular DNA that join at new gRNA, called pJK03. B) Schematic of SOE-PCR. C) Schematic of homology region editing by IVA, called pJK04 (11).

Validate the sequence of gRNA expression plasmid and homology region

To confirm the accuracy of gRNA editing, pJK03 was amplified by gRNA_F and ori_pMTL84151_R primer, that recognize gRNA and ori of pMTL84151. Moreover, pJK03 was cut by *Kpn*I, *Not*I and *Xho*I restriction enzymes and gRNA was verified sequence by

sequencing. In the same way, pJK04 was checked by PCR, restriction enzymes (*Kpn*I, *Not*I and *Xho*I) and up-downstream was verified sequence by sequencing.

Table 1 Primer list

Primer name	Purpose	Sequence
F1	Upstream amplification	5'-ATAAGAATGCGGCCGCTAAACTATACAAGAGTATGACACTATTTGTAATG-3'
R1	Upstream amplification	5'-ATTTAACTAGCCCCCTTTTATACCTCCCCTTTCCAG-3'
F2	Downstream amplification	5'-CTGGAAAGGGGAGGTATAAAAGGGGGC TAGTTAAATGAATAC-3'
R2	Downstream amplification	5'-CCGCTCGAGCGG TTATTCAACTGGCATTTC-3'
IVA_DOWN_F	IVA homology region	5'-AAATGCCAGTTGAATAACCGCGAGGCCTGCAG ACATGCGC-3'
IVA_UP_R	IVA homology region	5'-GAACTCTATAGTTTAGCGGCCGCGGTCATAGCT GTTTCC-3'
IVA_gRNA_F	*In Vivo* assembly (IVA)	5'GAAAGCTGGATATACAGTAAGTTTTAGAGCTAGA AATAGCAAGTT-3'
IVA_gRNA_R	*In Vivo* assembly (IVA)	5'-TTACTGTATATCCAGCTTTCCCAACAATGCATCA CTTTTC-3'
gRNA_F	Check IVA gRNA	5'- GAAAGCTGGATATACAGTAAGTTTTAGAG -3'
Ori_pMTL84151_R	Check IVA gRNA	5'-TTTCCATAGGCTCCGCCC-3'
UP_F	Check IVA homology region	5'-AGAGTTCTTTTCTTAACTAATTCAAATT-3'
DOWN_R	Check IVA homology region	5'- TTATTCAACTGGCATTTCAAAC-3'

Results and Discussion:

Result of gRNA design

CRISPR-Cas9 system is an interesting choice, high efficiency, and consist of 2 major components, which are DNA nuclease Cas9 and single-guide RNA (sgRNA, gRNA + tracrRNA). Tran-activating crRNA is a scaffold for gRNA and Cas9 and gRNA is the recognition target part. Cas9 can break double-stand DNA at a target locus with a protospacer adjacent motif (PAM) (12, 13). To design gRNA, PAM sequence (5'-NGG-3') and 20 bp upstream of PAM (N-20 NGG principle) were investigated by the ApE-A plasmid editor. Seven sequences of N-20 were designed. To avoid off-target mutations of the gRNA on a given genome, redundant sequences with other genes in *C. difficile* HN10 were filtered out by BLASTN. Four gRNA candidates were then retrieved. Further considerations need to be taken for designing of gRNAs. The %GC content and secondary structure of gRNA are factors that influence gRNA efficiency. Therefore, the gRNA candidates were further investigated for their GC content and secondary structure using Vector NTI software. Due to the limited range of effective binding sites and optimal parameters, only one gRNA candidate (5'- GAAAGCTGGATATACAGTAA-3') was selected.

Construction and fusion of upstream and downstream components of the integrase gene

After cleavage of the target gene by the Cas9-gRNA complex, the Cas9-induced double-strand breaks need to be subsequently repaired. The two major pathways for the repair of DSB, are non-homologous end joining (NHEJ) and homologous recombination (HR). NHEJ modifies the broken DNA ends and ligates them together with no consideration for homology, generating deletions or insertions. On the other hand, HR uses an undamaged DNA template to repair the break, leading to the reconstitution of the original sequence (14). Therefore, the homologous region of the *int* gene was constructed for the reparation template. 1 kb of upstream and downstream regions of the integrase gene was amplified by PCR using F1/R1 and F2/R2 primers, respectively. The annealing temperature for PCR amplification was optimized (Figures 3A and 3B). The optimal annealing for up and downstream fragments is 43 °C, since up- and downstream can amplify together in this temperature and do not have non-specific band. After that, PCR products were used for up-downstream fragments fusion to acquire the product of 2 kb (Figure 4A). In the general PCR condition, without adding DMSO, the fusion reaction generated the non-specific amplification produces at all annealing temperatures (Figure 4A). Addition of DMSO to a final concentration of 5% was used to improve the quality of the DNA amplification, however, non-specific bands were still also presented (Figure 4B). PCR products of both up and downstream amplifications were then purified using a PCR clean-up kit to eliminate small DNA fragments or carried-over primers. Then, purified up and downstream fragments from 5% DMSO at 68 °C were fused by F1/R2 primer by PCR technique. As a result, a clear band of 2 kb was obtained from the fusion reaction with no non-specific band detected (Figure 4C). PCR technique that was used for homology fusion is an easy, fast and cheap method. DMSO that was added into homology fusion can decrease non-specific bands by inter and intra-strand re-annealing (15). In plasmid construction, a restriction enzyme was used with IVA because increasing IVA fragments can decrease the efficiency of IVA (11).

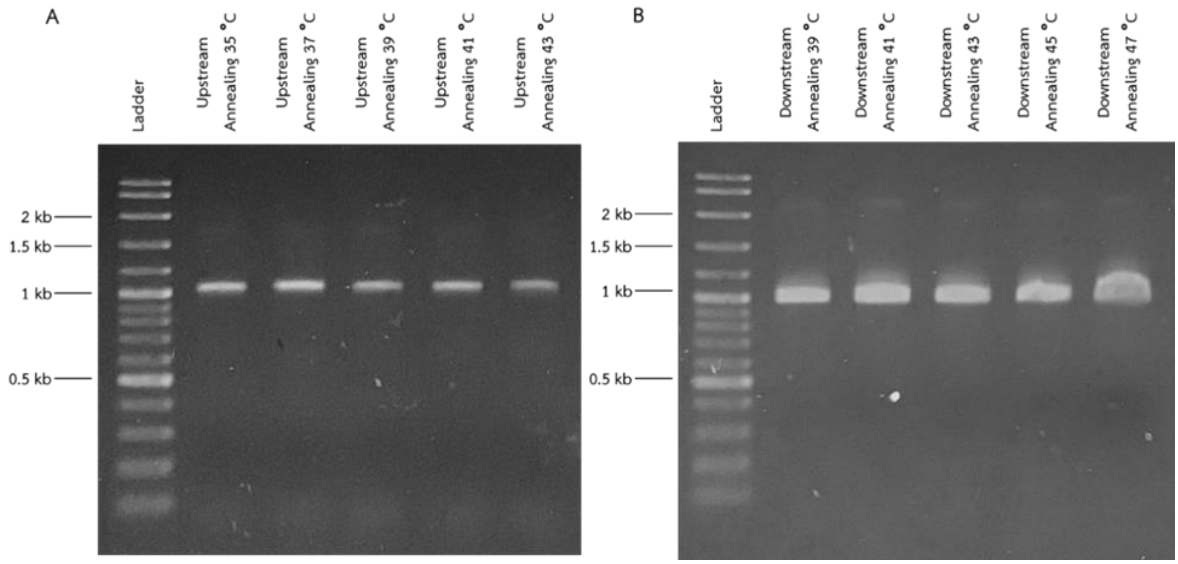

Figure 3 Upstream (A) and downstream (B) regions of integrase gene amplification, annealing temperatures varied from 35 °C to 47 °C. The amplicon size of upstream and downstream regions is 1,000 bp. The annealing temperatures were optimized for amplification.

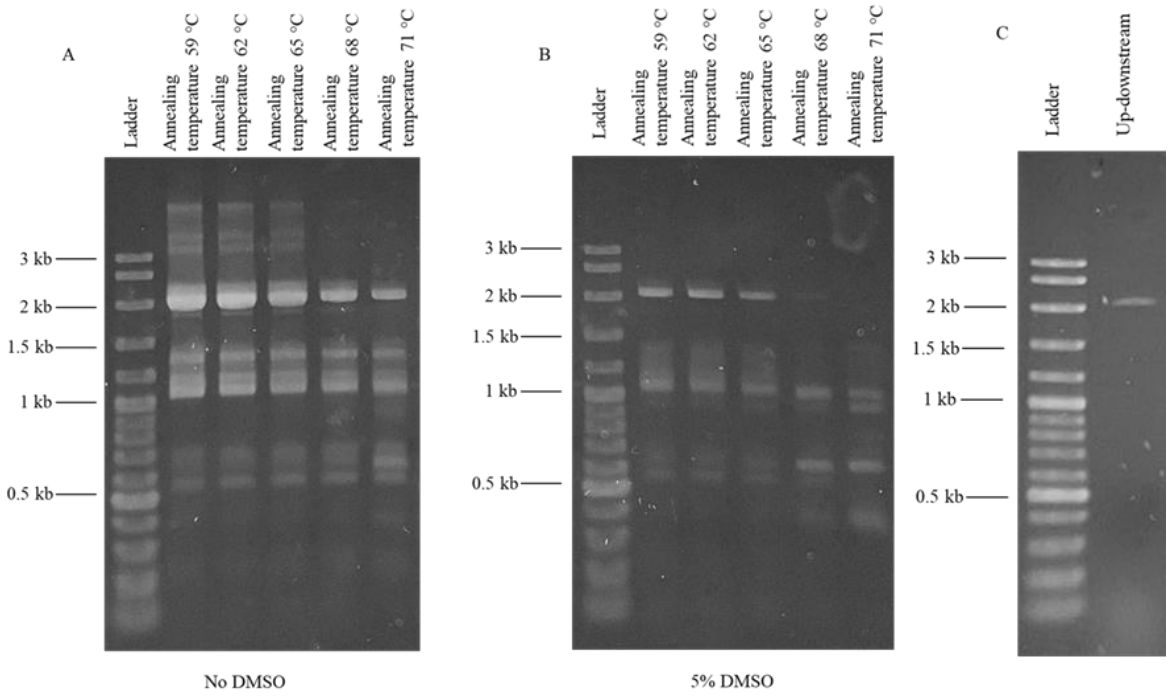

Figure 4 Upstream and downstream fragments fusion by PCR, annealing temperatures were varied from 59 °C to 71 °C. A) DMSO was not added to the PCR reaction. B) 5% DMSO was added to the PCR reaction. C) Up-downstream fusion products

Plasmid construction

pJK02 contains *S. pyogenes* Cas9, that codons were already optimized for expression in *C. difficile*. For expression plasmid in *C difficile*, pJK02 contains pCD6 *C. difficile* (Gram-positive) replicon. To edit gRNA of pJK02, primers for PCR were designed to have non-homologous regions at the 5′ end that contain the recognition sequence for the gRNA of the *int* gene. The amplified linear fragments were then joined by IVA to generate the plasmid pJK03 (Figure 5) which contains a new gRNA sequence that direct Cas9 to the *int* gene. After that, this linear fragments were transformed to *E. coli* DH5α and plasmid pJK03 were extracted to check accuracy. The accuracy of the construct was determined by PCR analysis (Figure 6A) and restriction enzyme (RE) digestion using enzymes *Kpn*I, *Not*I and *Xho*I (Figure 6B). The 881 bp PCR fragment and RE digestion pattern were obtained as expected indicating the correct insert orientation.

The up-downstream homology regions of pJK03 were then edited to homology region of the *int* gene to induce a site-specific DNA repairing (pJK04). pJK04 was then verified by PCR analysis (Figure 7A), RE digestion (Figure 7B) and DNA sequencing to confirm the accuracy of the construction. RE digestion confirms the link between plasmid and new homology region. Until then, *C. difficile* was considered genetically intractable, genetic engineering in this organism is largely delayed due to the lack of efficient genome editing tool. The CRISPR-Cas9-based genome editing tool, pJK04 developed in this study will facilitate *int* gene knockout for *C. difficile* prophage carriage strain in the future.

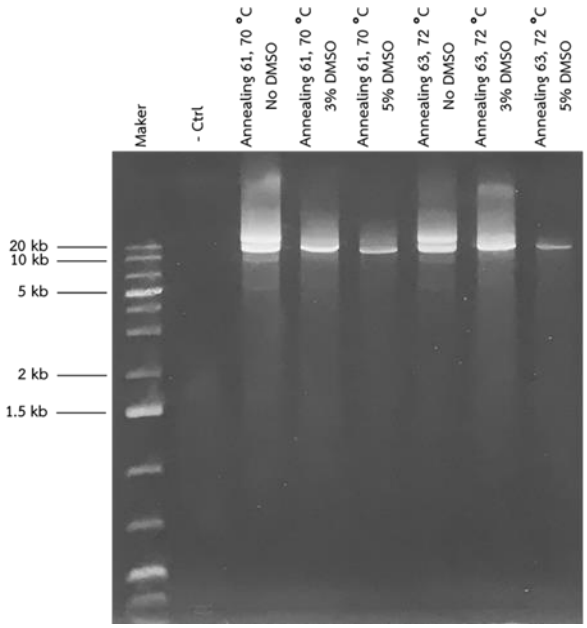

Figure 5 gRNA editing by IVA. Annealing temperature and concentration of DMSO for the PCR reaction varied from 61 °C to 72 °C and 0% to 5% DMSO.

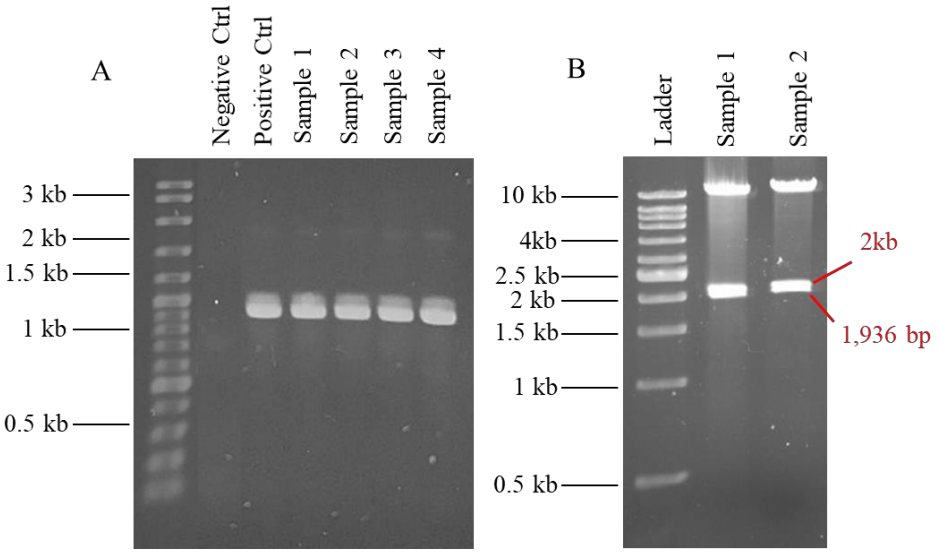

Figure 6 IVA that edited gRNA was verified by colony PCR and restriction enzyme digested, A) the product size is 881 bp. Lane 1 was ladder 100 bp. Lane 2, negative control, add pMTL84151 which is a backbone of pJK02. Lane 3 was a positive control. Lane 4 -7 were *E. coli* DH5α transformants. B) pJK03 was digested by *Kpn*I, *Not*I and *Xho*I restriction enzyme. The product has 3 bands, which are 10,229, 2,000 and 1,936 bp.

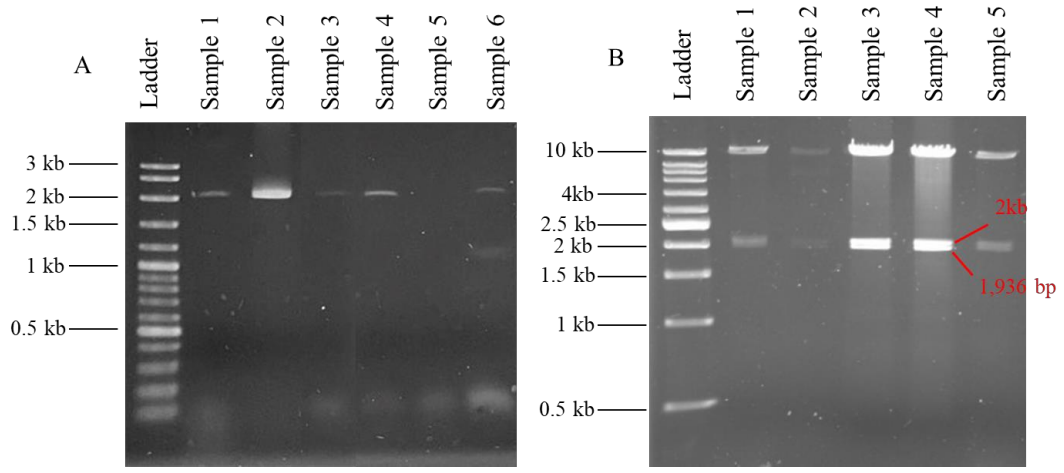

Figure 7 pJK04 verification. A) Up-downstream in pJK04 was amplified by colony PCR, product size 2 kb. B) pJK04 was digested by *Kpn*I, *Not*I and *Xho*I restriction enzyme. The product has 3 bands, which are 10,229, 2,000 and 1,936 bp.

Conclusion:

In summary, we got pJK04 that gRNA specifics to ΦHN10 *int* gene. pJK04 was edited by *in vivo* assembly (IVA) and splicing with overlap extension PCR (SOE-PCR). These methods save time and save cost more than traditional method.

The CRISPR-Cas9 system used in this study was derived from *Streptococcus pyogenes* (10). This system has a larger range of mutation, deletion, insertion, and point mutations, that have many benefits for improvement therapy, industry, etc.

For the future work, pJK04 was transformed into *C. difficile* HN10 for *int* gene deletion in prophage.

Acknowledgments:

This project is funded by the National Research Council of Thailand (NRCT) and Mahidol University (NRCT5-RSA63015) to S.C. and Research Cluster: Multi-generation Researchers Grant from Mahidol University to S.C., P.H. and T.J.

References:

1. Lyras D, O'Connor JR, Howarth PM, Sambol SP, Carter GP, Phumoonna T, et al. Nature. 2009;458(7242):1176-1179.

2. Heuler J, Fortier LC, Sun X. FEMS Microbiol Rev. 2021;45(5).

3. Semon AK, Keenan O, Zackular JP. J Pediatric Infect Dis Soc. 2021;10(Supplement_3):S3-S7.

4. Spigaglia P, Mastrantonio P, Barbanti F. Cham: Springer International Publishing; 2018 2018//. 137-159 p.

5. Karow M, Calos MP. Expert Opinion on Biological Therapy. 2011;11(10):1287-1296.

6. Maikova A, Kreis V, Boutserin A, Severinov K, Soutourina O. Appl Environ Microbiol. 2019;85(20).

7. Jiang F, Doudna JA. Annual Review of Biophysics. 2017;46(1):505-529.

8. Ma Y, Zhang L, Huang X. FEBS J. 2014;281(23):5186-5193.

9. Phothichaisri W, Ounjai P, Phetruen T, Janvilisri T, Khunrae P, Singhakaew S, et al. Front Microbiol. 2018;9:1701.

10. McAllister KN, Bouillaut L, Kahn JN, Self WT, Sorg JA. Sci Rep. 2017;7(1):14672.

11. Garcia-Nafria J, Watson JF, Greger IH. Sci Rep. 2016;6:27459.

12. Liang Y, Wei Y, Jiao S, Yu H. Synth Syst Biotechnol. 2021;6(3):200-208.

13. Scott T, Urak R, Soemardy C, Morris KV. Scientific Reports. 2019;9(1):16104.

14. Mao Z, Bozzella M, Seluanov A, Gorbunova V. DNA Repair (Amst). 2008;7(10):1765-1771.

15. Jensen MA, Fukushima M, Davis RW. PLoS One. 2010;5(6):e11024.

A STUDY OF DYS612 MUTATION IN THAI FATHER-SON PAIRS

Tamonwan Chotikorn,[1*] Kornkiat Vongpaisarnsin,[1,2]

[1] Department of Forensic Medicine, Faculty of Medicine, Chulalongkorn University, Bangkok 10330, Thailand.
[2] Forensic Serology and DNA Unit, Department of Forensic Medicine, Faculty of Medicine, Chulalongkorn University, Bangkok 10330, Thailand.

*e-mail: 6370018730@student.chula.ac.th

Abstract:

Y chromosomal short tandem repeat (Y-STR) was a common DNA marker for investigation of paternal lineage, to identify male contributor in sexual assault specimen, and other forensic interests. However, the Y-STRs that contained in recent commercial kits was designed to answer common scenarioes for paternal lineage. These markers were selected as their low to moderate mutation rate. However, these markers could not discriminate closely related male individuals. DYS612 was one of rapidly mutating Y-STRs (RM Y-STRs) that possessed higher discrimination power when compared to commercial kits. The mutation rate of this RM Y-STR differed in each ethnic population. Threfore, this study aimed to determine mutation rate of DYS612 in Thai father-son pairs. Among 150 Thai father-son pairs, 4 mutations were observed and the mutation rate was 2.67×10^{-2}. If DYS612 was added for Y-STR analysis, our data will be important for Y-STR kinship index, as the mutation rate of DYS612 is effect to forensic genetic statistics.

Introduction:

The Y chromosome is a male-chromosome with 50 million bases in length [1-3]. There are two of male-chromosomal parts. Five percentage of total is called pseudoautosomal region (PAR) that showed recombination with X chromosome and other 95% is a non-recombining portion (NRY) or a male-specific region (MSY), which inherit through paternal lineages and is preserved except the mutation occurs [4].

Y chromosomal short tandem repeat (Y-STR) is a repetitive base that located in the NRY region. In forensic applications, Y-STR was commonly used to determine paternity relationship, to investigate male contributor DNA in sexual assault evidence and to study evolutionary[5]. At present, Y-STR markers had been studied throughout and several Y-STRs commercial kits are available. These kits contained Y-STRs with low to medium mutation rate and can be used with most common scenarioes for paternal lineage. However, these markers in commercial kits are unable to distinguish between closely related males if the perpetrator is a male family member, such as a father, brother, or man with a paternal linage. To resolve this scenario, rapidly mutating Y-STRs (RM Y-STRs) had been studied and verified.

Ballantyne et al. studies the mutation rate of 186 Y-STRs and identified 13 Y-STRs of total which had a highly mutation (> 1.0 x 10^{-2} per locus per generation). Therefore, 13 Y-STR markers were termed "Rapidly mutating Y-STRs or RM Y-STRs". In addition, the major molecular factors that effect to Y-STR mutation including in number of repeats, complexity of repetitive structure and length of repetitive motif [2]. In recent years, many studies investigated mutation rate of RM Y-STR in different groups of population and showed different mutation rate in each population group[6-12].

DYS612 is one of the 13 RM Y-STR markers and has been selected in this study. First, DYS612 showed high mutation rate in Asian population. Second, this marker was complex trinucleotide repeat unit and thus tended to have high mutation rate. Moreover, at present, there is no data of this marker in Thai population and thus, become our purpose of this study. Primer was newly designed and validated to analyzed on capillary electrophoresis. Validation study included sensitivity to define the lowest DNA input and specificity test to demonstrate the usable in forensic investigation.

Methodology:

Primer design

FASTA file of DYS612 was from UCSC Genome browser, and Primer 3 software [13]was used to design the DYS612 primer. In silico PCR was performed by UCSC In silico PCR, and size of PCR product was checked by agarose gel electrophoresis. The DYS612 primer was show in **Table 1**.

Table 1: Primer sequence of DYS612

Marker	Forward primer	Reverse primer	Expected size
DYS612	**VIC**-CCCCATGCCAGTAAGAATAAAA	CTAGAGCCAAAAAGGGAACTGA	204-240 bp

Then, PCR condition was validated, and DYS612 primer was labeled with green fluorescent dye [14] for capillary electrophoresis detection.

Validation study

To test the sensitivity of the DYS612 primer, 2800M control DNA were diluted to 1, 0.1, 0.01, and 0.001 ng /µL was used in the PCR reaction.

To test specificity of DYS612 primer, Human and non-human was tested. Female DNA was used for male specific primer test, and animal DNA (a rat, a mouse, and a pig) was used for cross-species test.

Collection of blood on FTA card

Total of 300 blood FTA card samples were from 150 Thai father-son pairs. All samples were confirmed by paternity testing from the forensic serology unit, Faculty of Medicine, Chulalongkorn university which the results showed that half of the son's allele were similar to his father. The samples were selected and analyzed approved by the Institutional Review Board of the Faculty of Medicine, Chulalongkorn University, Bangkok, Thailand.

FTA card purification

Blood on FTA card was punched by 1.2 mm puncher. Then FTA card purification reagent [3] 100 µL was added to remove a PCR inhibitor after 100 µL TE buffer [3] was added and discarded. The FTA card which completely purifies were dried at 65ºC.

PCR

DYS612 forward primer was conducted fluorescent dye (Thermo Fisher Scientific). The PCR amplification was performed in total volume of 25 µL that consisted of Amplitaq gold 360 master mix [3] 1X , nuclease-free water, forward primer 0.15 µM, reverse primer 0.15 µM and one purified 1.2 mm FTA disc. Thermal cycling was performed on the ProFlex™ 3x32-Well PCR (Thermo Fisher Scientific) and conditions were pre-denaturation at 95ºC for 5 min and 30 cycles of denaturation at 95ºC for 30 sec, annealing at 58ºC for 30 sec, extension 72ºC for 1 min and final extension 72ºC for 1 hr[15].

Capillary electrophoresis

PCR product was analyzed by capillary electrophoresis[16]. The master mix were contained: 1 µL aliquot of PCR Product, 8.7 µL of HiDi-formamide and 0.3 µL of GeneScan™ 600 LIZ™ Size Standard v2.0 [3]. Then, CE master mix was denatured at 95ºC for 3 min. The injection protocol was performed 8 sec for injection time, 15 kVolts of run voltage on ABI3500xl Genetic Analyzer [3] with 36 cm capillary and POP-4 polymer. Raw data was analyzed with GeneMapper ID-X v1.4 [3]. The analytical threshold was assigned to 50 RFU for peak calling.

Data analysis

Mutation rate was calculated as number of mutations divide by number of meiosis and mutation rate of DYS612 were compared with other population[17].

Results and Discussion:

Validation study

Validation study was one of important task that needed to be carried out when new method or new technique was established. When serial dilution of DNA input was used in the reaction, allele dropout was detected in reaction with 0.01 ng /µL of DNA input and was used to define analytical threshold of this study[18] that show in **Figure 1**. **Figure 2 (a-b)** demonstrate specificity of primers showed specificity to only male DNA sample as the expected peak was showed in male DNA sample in electropherogram.

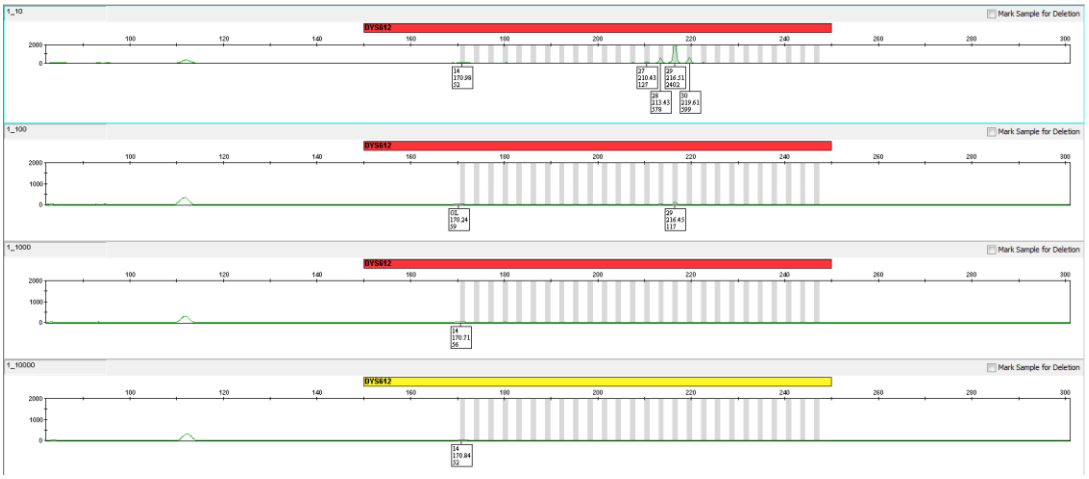

Figure 1 The electropherogram of DYS612 sensitivity test.

a. Animal DNA

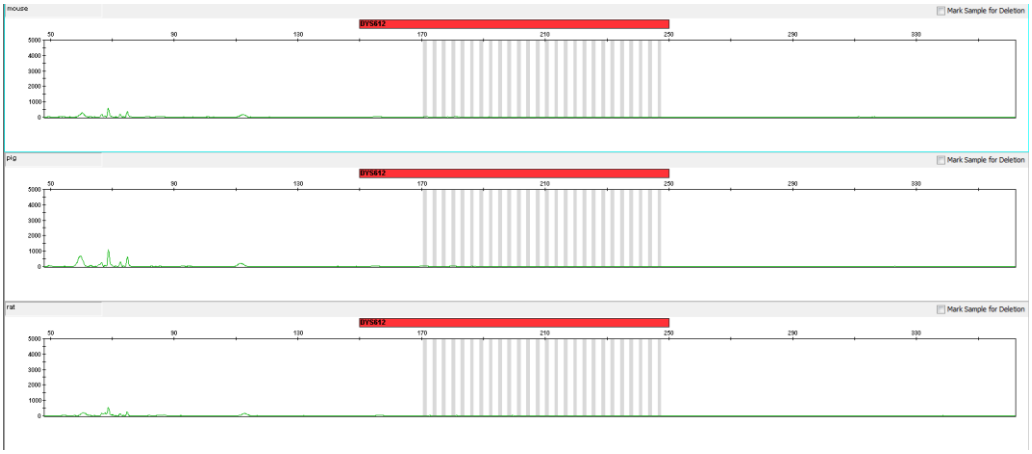

b. Female DNA

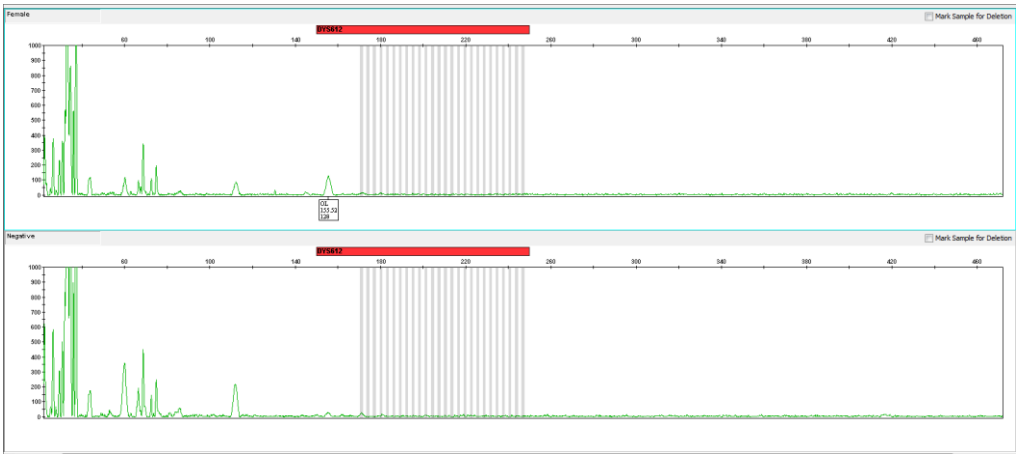

Figure 2 The electropherogram of DYS612 specificity test.

DYS612 Mutation Characteristics

Table 2 summarize the genotype result of DYS612 mutation samples. The findings showed that four mutations were found to be repeat gains. **Figure 3(a-d)** demonstrates the electropherogram of DYS612 mutations. For example, **Figure 3(a)** offspring allele was changed from allele 31 to allele 32 which repeat unit was added one repeat. These results were in accord with the previous study [19] which carried out in Poland population. The study reported five mutations with 4 single-step and one multi-step mutations from 361 father-son pairs and total mutation results were repeat gains. The different findings of our study and the previous study [20]might cause from the different number of sample and the different ethnic group of population[14].

Table 2: Genotype result of 4 mutation pair of samples

Sample No.	Father allele	Offspring allele	Pattern of mutation
A	31	32	+1
B	29	30	+1
C	32	33	+1
D	33	34	+1

a. Sample A

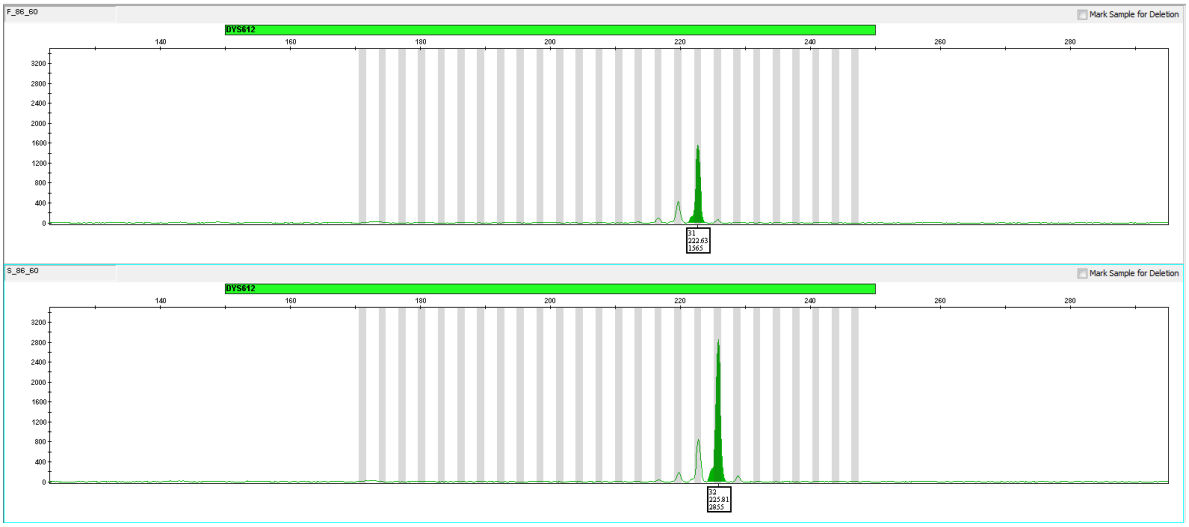

b. Sample B

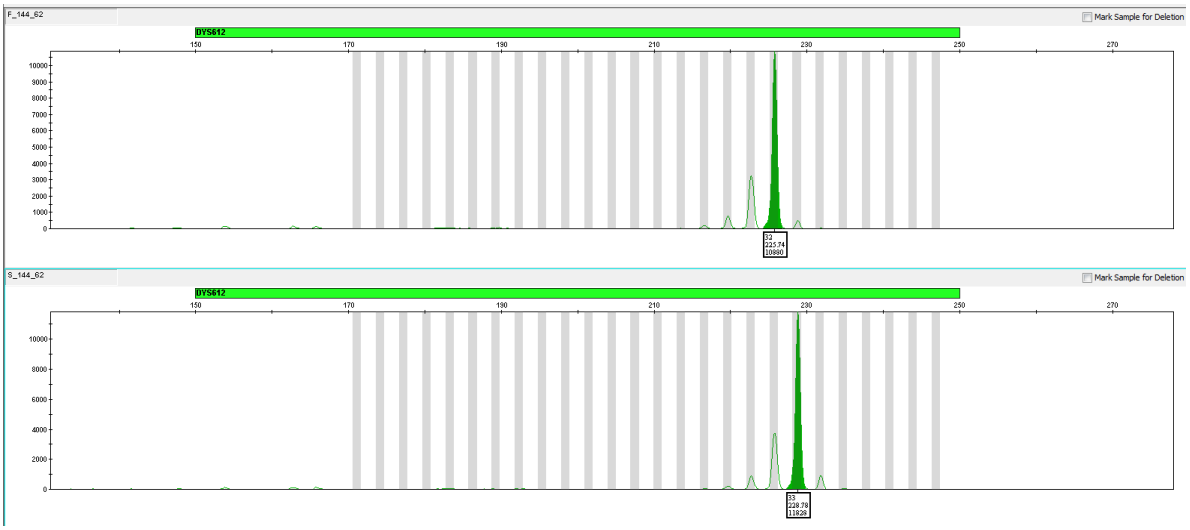

c. Sample C

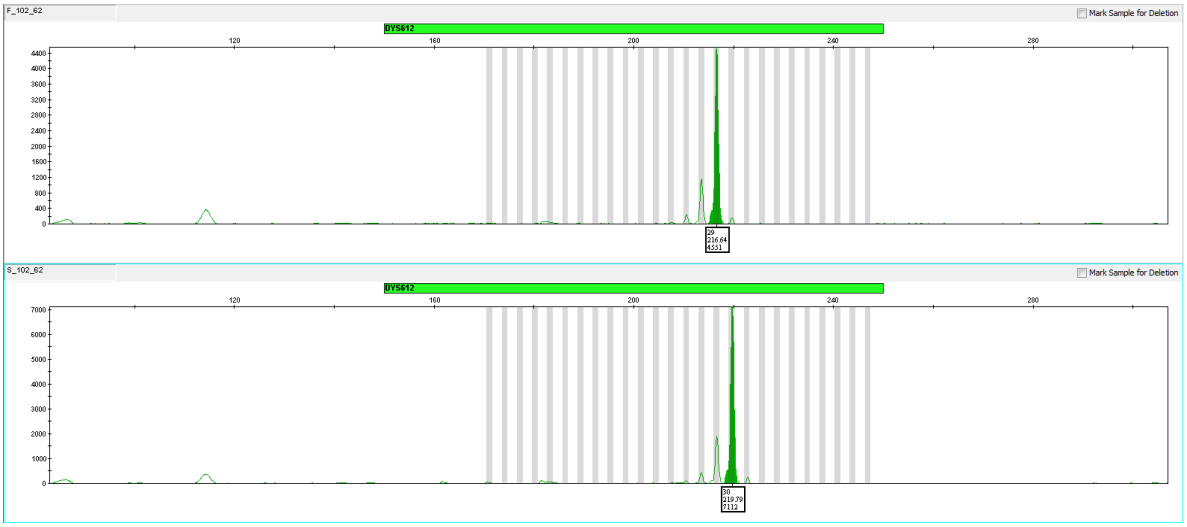

d. Sample D

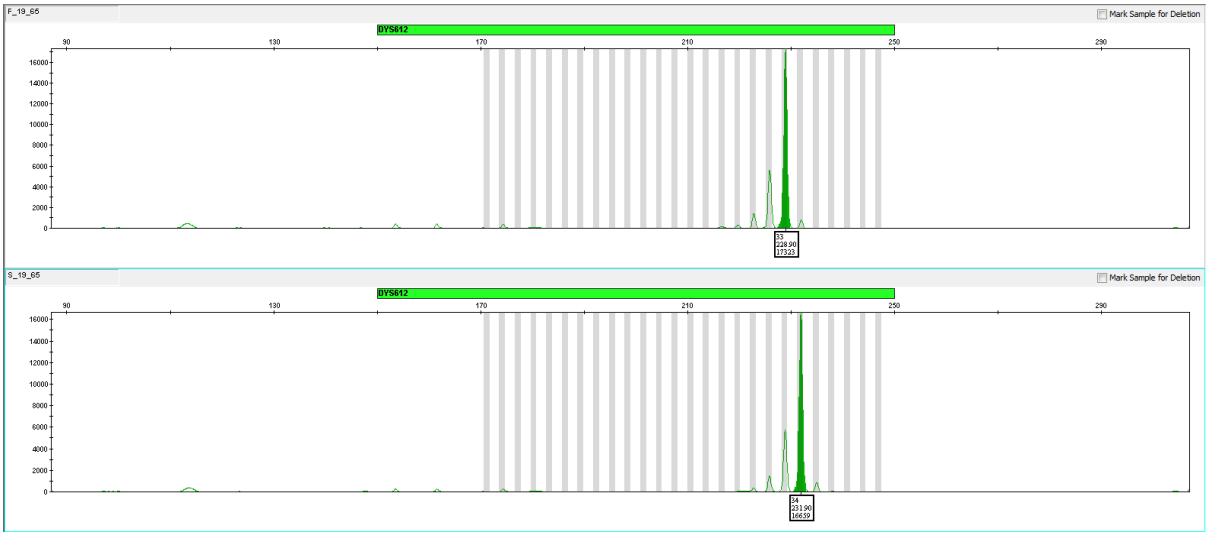

Figure 3 The electropherogram of DYS612 mutation in 4 pair of samples.

Mutation rate of DYS612

The Y-STR DYS612 has mutation rate 2.67 x 10^{-2} per gamete per generation. According to DYS612 sequence, DYS612 is a trinucleotide repeat which has three base pair each repeat unit[21]. Our finding confirmed previous reports that length in base pair of the repetitive motif decrease in mutation rate as the repeat length increased[2,22]. In addition, DYS612 is a complex repeat, and this data is supported by a number of studies[23]. They reported that complex Y-STR expressed a higher average mutation rate than simple and compound repeat Y-STR [2,22].

Comparison of mutations

When compared DYS612 mutation rate in this study with other studies, the mutation rate in this study was lower than Pakistani population[10,12] , 260 father-son pairs of Chinese Yi[8] and Europe population[2], but was higher than father-son pairs in Chinese Han[6,7,11]. However, these mutation rates were more than 1 x 10^{-2}. Accordingly, DYS612 in Thai population tended to be highly mutation.

Conclusion:

In this study, DYS612 mutation was investigated in 300 Thai father-son pairs. Mutation of DYS612 was the single repeat mutation and all samples were found one repeat gain. The mutation rate of DYS612 was 2.67 x 10^{-2} in this study. The result of this study will be useful for calculating Y-STR kinship index. Therefore, it is essential to conduct research on RM Y-STR mutation in Thai population.

References:

1. Skaletsky H, Kuroda-Kawaguchi T, Minx PJ, et al. The male-specific region of the human Y chromosome is a mosaic of discrete sequence classes. *Nature.* 2003;423(6942):825-837.
2. Ballantyne KN, Goedbloed M, Fang R, et al. Mutability of Y-chromosomal microsatellites: rates, characteristics, molecular bases, and forensic implications. *Am J Hum Genet.* 2010;87(3):341-353.
3. Biosystems A. *GeneMapper® ID-X Software manual.* 2019.
4. Delbridge ML, Graves JA. Origin and evolution of spermatogenesis genes on the human sex chromosomes. *Soc Reprod Fertil Suppl.* 2007;65:1-17.
5. Kayser M. Forensic use of Y-chromosome DNA: a general overview. *Hum Genet.* 2017;136(5):621-635.
6. Zhang W, Xiao C, Yu J, et al. Multiplex assay development and mutation rate analysis for 13 RM Y-STRs in Chinese Han population. *Int J Legal Med.* 2017;131(2):345-350.
7. Yuan L, Chen W, Zhao D, et al. Mutation analysis of 13 RM Y-STR loci in Han population from Beijing of China. *Int J Legal Med.* 2019;133(1):59-63.

8. Wang Q, Jin B, An G, et al. Rapidly mutating Y-STRs study in Chinese Yi population. *Int J Legal Med.* 2019;133(1):45-50.
9. Rakha A, Oh YN, Lee HY, et al. Discriminating power of rapidly mutating Y-STRs in deep rooted endogamous pedigrees from Sindhi population of Pakistan. *Leg Med (Tokyo).* 2018;34:17-20.
10. Javed F, Sumbal S, Shafique M, et al. Male individualization using 12 rapidly mutating Y-STRs in Araein ethnic group and shared paternal lineage of Pakistani population. *Int J Legal Med.* 2018;132(6):1621-1624.
11. Chen Y, Zhou W, Li M, et al. Mutation rates of 13 RM Y-STRs in a Han population from Shandong province, China. *Forensic Science International: Genetics Supplement Series.* 2017;6:e346-e348.
12. Adnan A, Ralf A, Rakha A, Kousouri N, Kayser M. Improving empirical evidence on differentiating closely related men with RM Y-STRs: A comprehensive pedigree study from Pakistan. *Forensic Science International: Genetics.* 2016;25:45-51.
13. Untergasser A, Cutcutache I, Koressaar T, et al. Primer3—new capabilities and interfaces. *Nucleic Acids Research.* 2012;40(15):e115-e115.
14. Ballantyne KN, Ralf A, Aboukhalid R, et al. Toward male individualization with rapidly mutating y-chromosomal short tandem repeats. *Hum Mutat.* 2014;35(8):1021-1032.
15. Butler JM. Chapter 4 - PCR Amplification: Capabilities and Cautions. In: Butler JM, ed. *Advanced Topics in Forensic DNA Typing: Methodology.* San Diego: Academic Press; 2012:69-97.
16. Butler JM. Chapter 6 - Capillary Electrophoresis: Principles and Instrumentation. In: Butler JM, ed. *Advanced Topics in Forensic DNA Typing: Methodology.* San Diego: Academic Press; 2012:141-165.
17. Kayser M, Roewer L, Hedman M, et al. Characteristics and frequency of germline mutations at microsatellite loci from the human Y chromosome, as revealed by direct observation in father/son pairs. *Am J Hum Genet.* 2000;66(5):1580-1588.
18. Butler JM. Chapter 2 - Data, Models, Thresholds. In: Butler JM, ed. *Advanced Topics in Forensic DNA Typing: Interpretation.* San Diego: Academic Press; 2015:25-46.
19. Rogalla U, Woźniak M, Swobodziński J, et al. A novel multiplex assay amplifying 13 Y-STRs characterized by rapid and moderate mutation rate. *Forensic Sci Int Genet.* 2015;15:49-55.
20. Otagiri T, Sato N, Shiozaki T, et al. Mutation analysis for 25 Y-STR markers in Japanese population. *Legal Medicine.* 2021;50:101860.
21. Butler JM. Chapter 8 - Short Tandem Repeat Markers. In: Butler JM, ed. *Fundamentals of Forensic DNA Typing.* San Diego: Academic Press; 2010:147-173.
22. Fan H, Chu JY. A brief review of short tandem repeat mutation. *Genomics Proteomics Bioinformatics.* 2007;5(1):7-14.
23. Ballantyne KN, Keerl V, Wollstein A, et al. A new future of forensic Y-chromosome analysis: rapidly mutating Y-STRs for differentiating male relatives and paternal lineages. *Forensic Sci Int Genet.* 2012;6(2):208-218.

AN ALTERNATIVE APPROACH FOR SCREENING MICROSATELLITE MARKERS FROM TRANSCRIPTOME OF *ACHETA DOMESTICUS* LINNAEUS, 1758

Thawatchai Thoradit, Somjit Homchan, Yash Munnalal Gupta*

Department of Biology, Faculty of Science, Naresuan University, Thailand

*e-mail: yashmunnalalg@nu.ac.th

Abstract:
Simple sequence repeats (SSRs), also known as microsatellites, are highly polymorphic genetic markers found in both genomic and transcriptomic sequences. The conventional methods for developing SSR markers can be laborious, time consuming and less efficient. Therefore, the transcriptome sequences were employed in this study to find polymorphic SSRs, construct microsatellite markers, and assess their transferability using the Basic Sequence Alignment Tool (BLAST). The transcriptomic sequences of *Acheta domesticus* were used to search polymorphic SSR against raw sequences from transcriptomes. The focus of the study was on perfect trinucleotide SSRs, and their variation was observed based on stepwise mutation model. Total 26 polymorphic SSRs out of 200 sequences from transcriptome were identified by *in silico* method. Additionally, five (42%) out of 12 designed primers pairs from 26 polymorphic SSRs were successfully amplified by PCR. Moreover, their transferability was also checked using transcriptome datasets from different species. Two microsatellite markers (50%) out of four primer pairs showed successful amplification with expected size from *Gryllus bimaculatus* DNA samples. *In silico* analysis using BLAST (megablast) and raw sequence databases can be used to screen for polymorphic microsatellite makers and their transferability using the alternative methods proposed in this study. Furthermore, the *in silico* approach provided detailed data of each SSR-containing sequence in the form of alignment, which can be extremely useful for SSR scouring error correction, primer design, and a better knowledge of SSR-containing sequences in general.

Introduction:

Insects have been recognized as novel dietary nutrition in the twenty-first century. Food for human consumption and animal feed for farm livestock have created variety of views regarding insects as a nutritious diet. This is especially as a result of rising animal protein costs, food and feed insecurity, especially an increase in population growth and demand for protein [1]. According to World Health Organization (WHO) and Food and Agriculture Organization (FAO), an insect diet can provide a healthy diet with high fat, protein, vitamins, fiber, and mineral content [2]. According to the nutritional value of an edible insect diet offers, it is being as an alternative protein source. Moreover, the nutritional benefits of edible insects are particularly diverse because of the wide range of edible insect species. Approximately 2,000 insect species are consumed globally, and the number is constantly increasing [3]. Among these Orthoptera, (crickets and grasshoppers) have a higher protein content than other edible insect species [2]. However, there are still many obstacles. Despite the commercial success of the crickets as food, genetic information on these insects remains limited. It is necessary to examine the genetic structure of cricket populations since these crickets are numerous in the environment and are highly widespread in Thailand [4].

Researchers have focused on deeper study of these insect species. When investigating a species, genome, or attempting to understand the genetic structure of insects. Lacking background knowledge of some species is still challenging. If a new approach or genetic marker is being used for the first time, the genetic composition of all taxon species should be established [5]. Furthermore, studying the genetic structure of insect populations demands gathering a vast number of samples of each species [4]. When high-resolution DNA markers are employed in genetic studies to evaluate the structure of insect populations, determine haplotypes, reconstruct present or former gene flow patterns, and provide information on the insect's origin and extension pathways [6], the researchers are able to identify and quantify the genetic structure of a particular species. Molecular markers, especially microsatellites, offer useful information on population genetics in aphids, hymenopteran insects, mosquitoes, moths, and butterflies [7]. In addition, gene flow estimation, using genetic markers like SSRs, has been investigated before with mite research, which offers information on the mite's population structure and dispersal patterns [8].

Among the many molecular markers available, microsatellites are extremely popular in population genetics research, They are also highly powerful in determining genetic diversity, and have spawned a wide variety of genetic investigations [9, 10]. Microsatellite, also known as Simple Sequence Repeats (SSRs), are DNA segments made up of tandemly repeating mono-, di-, tri-, tetra-, or penta-nucleotide units (e.g., three repeat of trinucleotide $(ATA)_3$, five repeat of tetranucleotide $(CATA)_5$) that are scattered in the genome on all regions of the chromosome, which is mostly found in eukaryotic organisms [7]. In addition, SSRs also have been found in gene coding regions, and non-coding sequences. Microsatellite mutation rates as high as 10^{-2} per generation have been observed and are hypothesized to be generated by polymerase slippage during DNA replication, leading to variations in the number of repeat units [11]. The mutational model used for the molecular markers of choice has a significant impact on estimates of population parameters such as structure, number of migrants, and effective population size. Due to the obvious high mutation rate at these loci, this dependence is considered to be particularly strong for microsatellites [11]. Traditional mutation models for microsatellite have suggested a stepwise mutation model (SMM; Kimura and Ohta 1978) could more accurately describe the evolution of these loci [12]. Furthermore, if an allele state is due to mutation, the model predicts the abnormalities in repetitive of regions in the genome which will increase or decrease based on the insertion and deletion of mutation that can be easily identified by a single repeat unit at a fixed rate, and these changes in allele states are demonstrated by an integer shown in Equation 1 [13].

$$(\ldots, X-1, X, X+1, \ldots) \quad (1)$$

In addition, the stepwise mutation can be detected by Basic Local Alignment Search Tool (BLAST) in the gaps pattern caused by mechanism of insertion or deletion mutation in the sequences.

BLAST is a program that compares a query to a database of sequences via web interface or as a standalone application [14]. The BLAST programs is one of the most broadly employed bioinformatics research tool [15] which are commonly used to find sequence similarities in protein and DNA databases [14]. Moreover, BLAST is extremely sensitive over greater evolutionary distances between a query sequence and the database, but it is also somewhat slow. In general, BLAST displays those databases that adequately match a query sequence to within a given level of quality [16].

When working with microsatellite markers, researchers frequently encounter problems during the screening process. As a result, the number of working primer pairs for amplifying the target DNA template decreases. This also reduces the number of polymorphic

primer pairs that could be used in research [17]. SSR marker screening has been a difficult and time-consuming process due to their manual development process [17]. Therefore, to reduce laboriously, and less SSR scoring errors, an efficient method for screening markers *in silico* before employing them in the lab (*in vitro*) must be developed. According to the BLAST's aspects, we realized that BLAST algorithm has a potential which can be used to mine the SSRs loci from assembled sequences (even genomes or transcriptomes) by BLAST against Sequence Read Archive (SRA, unassembled reads). In this study, we have proposed a novel concept of a *in silico* screening of polymorphic SSR using BLAST algorithm. SSR studies will be benefited by *in silico* analysis given in present research to increasing accuracy and reproducibility along with reducing the labor and cost.

Methodology:

SSR sequence detection and isolation from transcriptome datasets

The reads of unassembled female *Acheta domesticus* transcriptome was downloaded from SRA database (NCBI), (Accession number: SRR7692603) and assembled into contigs by the Trinity assembler pipeline [18]. The assembled nucleotide sequence contigs of transcriptome was used to search SSR loci using Phobos software [19]. The parameters followed: Repeat unit size range were defined from 3-3 for mining only trinucleotides. The search was also limited to identify perfect microsatellites. For *in silico* analysis, only 200 sequences from transcriptome dataset contained SSR loci were used to search for polymorphic SSR in the sequences.

SSR sequence similarity search (in silico screening for polymorphism) and SSR Primer designing

The 200-transcriptomics containing SSR were used to find polymorphic SSR by BLAST (megablast algorithm) against SRA databases. 200 transcriptomic sequences containing SSR were compared with SRA datasets of *A. domesticus* (**Table 1**). The 26 sequences containing polymorphic SSR were used to design the primers via Primer3 (version 0.4.0). The parameters used in the Primer3 tool were used as follow: (i) PCR product size range of 200 to 400 bp, (ii) Primer optimal size was set to 20 bp, (iii) Annealing temperature ranged from 57°C to 63 °C, (iv). The raged of GC concentration was set 20%-80%.

Table 1. The SRA accession list of *A. domesticus* transcriptomes

Sample Types	Accession List
Wild-caught individuals	SRX9979741
reared individuals	SRX9979739
1 day nymph	SRX4552071
Embryo	SRX4552070
2 weeks nymph	SRX4552069
1 week nymph	SRX4552068
Adult female	SRX4552067
4 weeks nymph	SRX4552066

Assessment of the transferability of microsatellite markers

To verify the transferability of sequences containing SSR loci, the SSR sequences containing polymorphic loci was used to investigate the variation in the conservativeness of SSR flanking regions using the BLAST algorithm (megablast algorithm) [20]. In *A. domesticus* transcriptomes, the transferability of the SSR sequences containing polymorphic loci were compared with seven SRAs from different life stages of *Gryllus bimaculatus* (**Table 2**).

Table 2. The SRA accession of *G. bimaculatus* transcriptomes

Sample Types	**Accession List**
1st instar	SRX10403327
2nd instar	SRX10403328
3rd instar	SRX10403329
Juvenile (size 6-10mm)	SRX10403330
Juvenile (size 10-15mm)	SRX10403331
Juvenile (size 15-20mm)	SRX10403332
Adult	SRX10403333

Sample collection, DNA extraction, DNA barcoding for extracted DNA samples of A. domesticus

The DNA samples from 30 individuals of house cricket from Sukhothai farm were used for DNA extraction and SSR primer screening. Ten samples of edible cricket; *G. bimaculatus* were collected from farm at Phitsanulok to verify transferability of SSR markers. Genomic DNA was isolated from hind leg of *A. domesticus* using a conventional method developed by Anleitner and Haymer [21]. The DNA extracted from adult female and male house crickets was used for microsatellite marker screening. Similarly, genomic DNA from two-spotted crickets (*G. bimaculatus*) was also extracted and used for cross-amplification test. DNA quality was checked by electrophoresis on a 0.8% agarose gel. Additionally, to identify the cricket species, DNA barcoding was performed using the primer design from *A. domesticus* cytochrome c oxidase subunit I (COI) (accession: MG458975.1).

Microsatellite markers and transferability screening

Twelve primer pairs were used to amplify DNA from five *A. domesticus* individuals for the initial microsatellite marker screening. The PCRs were carried out with 25 µl reaction mixtures: 10 X Taq buffer, 0.2 µl Taq DNA polymerase, 0.8 mM dNTPs, 1.2 mM of MgCl2, 10 µM of each primer, and 1 µl of DNA template followed by nuclease-free water to make up volume to 25 µl in reaction tube. All PCRs were carried out with the following conditions for each primer pairs: initial denaturation at 95°C for 3 minutes followed by 35 cycles of denaturation, annealing, and extension at 95°C for 30 seconds, range from 54.9°C to 60.6°C for 30 seconds, 72°C for 40 seconds, respectively with a final extension at 72°C for 5 minutes. All PCRs were performed with Biometra TOne Thermal Cyclers by Analytik Jena, Germany. The primers that showed positive results from transferability assessment screening are also used for checking transferability features of polymorphic SSR primers using extracted DNA from *G. bimaculatus*.

Results and Discussion:

It is essential to use genetic markers in population genetic structure and diversity studies [22, 23]. Markers based on transcriptome sequences are being used to identify functional variation and perform genetic analysis on genes [24]. Because SSR markers produced from the transcriptome are found in coding regions of the genome, they are particularly functional and interesting. As a result, they frequently demonstrate a high level of transferability to related species [25, 26].

SSR sequence detection and isolation from transcriptome datasets

The Phobos software was used for SSR mining, in which 90,401 SSR loci were detected from 141,666 contigs. Among those SSR containing sequences, 200 randomly selected sequences were employed for *in silico* analysis using BLAST (megablast algorithm) against eight transcriptomes of *A. domesticus,* and 26 SSRs were found to be polymorphic.

Development, validation, and transferability of microsatellite markers using BLAST (megablast algorithm)

Out of 26 primers, 12 primer pairs were manufactured and employed to amplify DNA samples for screening. To verify the accuracy of BLAST results, the twelve polymorphic SSR primers were selected to conduct PCR amplification with *A. domesticus* DNA samples. Out of these, only five primer pairs were able to amplify the house cricket DNA in the experimental validation. While other primers were failed to amplify DNA, which may have been caused by the absence of primer binding sites in DNA sequences. Although there were one primer pair that was amplified a fragment showed a bigger than expected size which is probably due to an insertion mutation or nonspecific amplification. Furthermore, this study also showed that the five (~42%) among twelve primers pairs revealed polymorphism in SSR sequence, suggesting that BLAST (megablast algorithm) had the potential of mining polymorphic SSR in the sequences. Additionally, the transferability of sequence containing SSRs were examined using the four polymorphic loci, from BLAST (megablast algorithm) polymorphic SSR finding. Two (~50%) were successfully amplified in *G. bimaculatus* with expected fragment sizes. Furthermore, only one primer pair amplified a shorter than expected fragment size, indicating that the amplified DNA would have deletion mutation. Moreover, the transferability assessment using the BLAST *in silico* procedure can be employed to check the transferability within known polymorphic microsatellite primers, which is a highly potential source of codominant markers for population genetic and genetic diversity studies in crickets.

Discussion in in silico technique

The current availability of massive sequencing data from a large number of eukaryotic genomes has accelerated research towards better understanding of microsatellite evolution and the exploration of novel applications for sequence analysis [27]. Currently, the use of bioinformatics tools, sequence data, and *in silico* mining of SSR markers from sequence databases for genetic investigations is displacing traditional SSR development approaches [28, 29].

Although various software tools for mining SSRs from assembled sequences have been established, the precision, rapidity, and flexibility of these systems must be altered to fit the user requirements. MISA can distinguish between perfect microsatellites, and compound microsatellites which are disrupted by a number of bases [30, 31]. Additionally, Msatfinder is

a program that explores for perfect repetitions in sequence files that are either annotated (e.g., GenBank, Swiss-prot, EMBL) or unannotated (FASTA, raw). The SSRIT Software detects regular SSRs in the sequence using a Perl script and inputs data in FASTA format. Moreover, the motif threshold in GMATA and Kmer-SSR were inflexible, and these two programs had to employed in several works in order to obtain SSRs [28]. However, among these various software tools for searching, SSRs are shown to be inadequate for polymorphic SSR loci mining in the sequences. Herein, we have presented in silico methodology based on the BLAST algorithm for mining polymorphic SSR by input FASTA to compare with the FASTAQ file format (Sequence Read Archive datasets). On the other hand, SSRMD is a tool that searches for polymorphic SSR loci in nucleotide sequences [28], but the limitations in a command-based tool require a massive memory and multiple threads of the computational process.

In contrast, the presented in silico workflow is based on the BLAST algorithm, which can be accessed directly from the NCBI website. As a result, researchers can effortlessly use the tool and dataset for variation analysis. In general, default nucleotide BLAST compares a query sequence against nucleotide collection, which consist of annotated sequences to find sequence similarities. Herein, we have compared SSR containing query sequences with SRA datasets (raw sequence data: FASTAQ) to investigate the variation in SSR loci in a particular query sequence. The advantage of using SRA datasets is that they contain unassembled raw sequence data. While the sequences from nucleotide collections (GenBank) are assembled sequences, they may contain assembly errors caused by repeats in the assembly process. Therefore, the present study has utilized BLAST (megablast algorithm) to find polymorphic SSR loci by comparing SSR containing sequences to unassembled sequences from different individuals to visualize the perfect gaps in alignment.

Conclusion:

The preliminary study showed an alternative approach to searching for polymorphic microsatellites based on the BLAST (megablast algorithm). In this study, SSR containing sequences from the transcriptome of *A. domesticus* was used to generate alignments against raw sequence reads from SRA, NCBI. Furthermore, we found that the polymorphism existed in the SSR locus could be checked and visualized in the form of gaps in the sequence alignment. These findings are encouraging in terms of creating polymorphic SSR *in silico* for *in vitro* testing.

Furthermore, experimental validation utilizing 12 primer pairs for polymorphic SSR markers screening revealed that five (42%) primer pairs amplified PCR products successfully. In addition, two (50%) of the four primer pairs from the transferability assessment were positive in PCR amplification with related species. To conclude that a novel *in silico* workflow based on the BLAST algorithm provides a reproducible and faster procedure for microsatellite marker development. The given methodology can be used in research that needs the development of microsatellite markers for genetic studies of any organism.

References:

[1] van Huis, A., Potential of Insects as Food and Feed in Assuring Food Security. *Annual Review of Entomology*, 2013. **58**(1): p. 563-583.

[2] Ordoñez-Araque, R. and E. Egas-Montenegro, Edible insects: A food alternative for the sustainable development of the planet. *International Journal of Gastronomy and Food Science*, 2021. **23**: p. 100304.

[3] Prósper Ortega, L., *Seguridad alimentaria y calidad nutricional del uso de insectos en la dieta*. 2020.

[4] Gupta, Y.M., S. Tanasarnpaiboon, K. Buddhachat, S. Peyachoknagul, P. Inthim, and S. Homchan, Development of microsatellite markers for the house cricket, Acheta domesticus (Orthoptera: Gryllidae). *Biodiversitas Journal of Biological Diversity*, 2020. **21**(9).

[5] Filipe, P., C. Joao, and A. Antonio, Identification of Species with DNA-Based Technology: Current Progress and Challenges. *Recent Patents on DNA & Gene Sequences*, 2008. **2**(3): p. 187-200.

[6] Bossart, J.L. and D. Pashley Prowell, Genetic estimates of population structure and gene flow: Limitations, lessons and new directions. *Trends in Ecology & Evolution*, 1998. **13**(5): p. 202-206.

[7] Singh, S., V. Mishra, and T.K. Bhoi, Insect molecular markers and its utility-a review. *International Journal of Agriculture, Environment and Biotechnology*, 2017. **10**(4): p. 469-479.

[8] Hinomoto, N., Y. Todokoro, and T. Higaki, Population structure of the predatory mite Neoseiulus womersleyi in a tea field based on an analysis of microsatellite DNA markers. *Experimental and Applied Acarology*, 2011. **53**(1): p. 1-15.

[9] Liu, Z.J. and J. Cordes, DNA marker technologies and their applications in aquaculture genetics. *Aquaculture*, 2004. **238**(1-4): p. 1-37.

[10] Arif, I. and H. Khan, Molecular markers for biodiversity analysis of wildlife animals: a brief review. *Animal biodiversity and conservation*, 2009. **32**(1): p. 9-17.

[11] Estoup, A., P. Jarne, and J.-M. Cornuet, Homoplasy and mutation model at microsatellite loci and their consequences for population genetics analysis. *Molecular ecology*, 2002. **11**: p. 1591-604.

[12] Oppen, M.J.H.v., C. Rico, G.F. Turner, and G.M. Hewitt, Extensive Homoplasy, Nonstepwise Mutations, and Shared Ancestral Polymorphism at a Complex Microsatellite Locus in Lake Malawi Cichlids. *Molecular Biology and Evolution*, 2000. **17**(4): p. 489-498.

[13] Valdes, A.M., M. Slatkin, and N.B. Freimer, Allele frequencies at microsatellite loci: the stepwise mutation model revisited. *Genetics*, 1993. **133**(3): p. 737-749.

[14] Altschul, S.F., T.L. Madden, A.A. Schäffer, J. Zhang, Z. Zhang, W. Miller, and D.J. Lipman, Gapped BLAST and PSI-BLAST: a new generation of protein database search programs. *Nucleic acids research*, 1997. **25**(17): p. 3389-3402.

[15] Johnson, M., I. Zaretskaya, Y. Raytselis, Y. Merezhuk, S. McGinnis, and T.L. Madden, NCBI BLAST: a better web interface. *Nucleic Acids Research*, 2008. **36**(suppl_2): p. W5-W9.

[16] Shah, N., M.G. Nute, T. Warnow, and M. Pop, Misunderstood parameter of NCBI BLAST impacts the correctness of bioinformatics workflows. *Bioinformatics*, 2018. **35**(9): p. 1613-1614.

[17] Mariotti, R., et al., Development, evaluation, and validation of new EST-SSR markers in olive (Olea europaea L.). *Tree Genetics & Genomes*, 2016. **12**(6): p. 1-14.

[18] Grabherr, M.G., et al., Full-length transcriptome assembly from RNA-Seq data without a reference genome. *Nat Biotechnol*, 2011. **29**(7): p. 644-52.

[19] Mayer, C., Phobos, a tandem repeat search tool for complete genomes. *Version*, 2008. **3**: p. 12.

[20] Altschul, S.F., W. Gish, W. Miller, E.W. Myers, and D.J. Lipman, Basic local alignment search tool. *J Mol Biol*, 1990. **215**(3): p. 403-10.

[21] Anleitner, J. and D. Haymer, Y enriched and Y specific DNA sequences from the genome of the Mediterranean fruit fly, Ceratitis capitata. *Chromosoma*, 1992. **101**: p. 271-8.
[22] Wu, Q., F. Zang, Y. Ma, Y. Zheng, and D. Zang, Analysis of genetic diversity and population structure in endangered Populus wulianensis based on 18 newly developed EST-SSR markers. *Global Ecology and Conservation*, 2020. **24**: p. e01329.
[23] Wang, W., et al., Genetic diversity and population structure analysis of Lateolabrax maculatus from Chinese coastal waters using polymorphic microsatellite markers. *Scientific Reports*, 2021. **11**(1): p. 15260.
[24] Vasemägi, A., J. Nilsson, and C.R. Primmer, Expressed Sequence Tag-Linked Microsatellites as a Source of Gene-Associated Polymorphisms for Detecting Signatures of Divergent Selection in Atlantic Salmon (Salmo salar L.). *Molecular Biology and Evolution*, 2005. **22**(4): p. 1067-1076.
[25] Gupta, P.K., S. Rustgi, S. Sharma, R. Singh, N. Kumar, and H.S. Balyan, Transferable EST-SSR markers for the study of polymorphism and genetic diversity in bread wheat. *Mol Genet Genomics*, 2003. **270**(4): p. 315-23.
[26] Zheng, X., C. Pan, Y. Diao, Y. You, C. Yang, and Z. Hu, Development of microsatellite markers by transcriptome sequencing in two species of Amorphophallus (Araceae). *BMC genomics*, 2013. **14**(1): p. 1-11.

EXPLORING ANTIMICROBIAL ACTIVITIES OF NUCLEOSIDE ANALOGS AGAINST FOODBORNE PATHOGENS

Peenalin Loyma[1], Methinee Pipatthana[2], Matthew Phanchana[3], Jamorn Somana[1], Surang Chankhamhaengdecha[4], Tavan Janvilisri[1] Phurt Harnvoravongchai [4]*
[1]Department of Biochemistry, Faculty of Science, Mahidol University, Thailand
[2] Department of Microbiology, Faculty of Public Health, Mahidol University, Thailand
[3] Department of Molecular Tropical Medicine and Genetics, Faculty of Tropical Medicine, Mahidol University, Thailand
[4] Department of Biology, Faculty of Science, Mahidol University, Thailand
*e-mail: phurt.har@mahidol.ac.th

Abstract:

Foodborne illness is a major health concern of human diseases across the world. Treatment of foodborne illness is limited as the emergence of antibiotic resistance is increasing. To tackle antibiotic resistance, novel antimicrobial compounds must be identified. Drug library screening is an approach for discovering novel drugs with a simple, rapid, efficient, and reliable strategy. Therefore, this study aims to explore the antimicrobial activity of compounds against 7 common foodborne pathogens using in vitro screening of the nucleoside analog compounds library. A total of 290 nucleoside analogs was screened for the inhibitory effect against foodborne pathogens using single concentration screening of compounds with a cutting point of 20 μM. From the total of 290 compounds, floxuridine and zidovudine were found to inhibit *Staphylococcus aureus* (MRSA), *Salmonella* Typhimurium, *Listeria monocytogenes*, and *Shigella sonnei*. MIC values of floxuridine were 0.019 μg/ml and 0.308 μg/ml for MRSA and *L. monocytogenes*, respectively. Whereas zidovudine was found to inhibit *S.* Typhimurium and *S. sonnei* with MIC values of 0.01μg/ml and 0.042 μg/ml, respectively. To extend an understanding of the candidate drugs, a further experiment is required to elucidate the mechanism of action.

Keyword: foodborne pathogens, nucleoside analogs, antimicrobial activity.

Introduction:

Foodborne infections create a huge economic impact since illnesses burden healthcare systems, resulting in a loss of production, and impact on tourism and trade. The estimated global foodborne illness is approximately 600 million cases and 420,000 deaths each year in 2010 according to World Health Organization (WHO) (1). Foodborne illness is commonly caused by chemicals, toxins, especially by foodborne pathogens in contaminated foods (2). Illnesses treatment depends on identification of the responsible pathogen; however, most common foodborne diseases are usually caused by bacteria. Most pathogen are mesophile including *Staphylococcus aureus*, *Salmonella* Typhimurium, *Shigella sonnei,* and *Pseudomonas aeruginosa*. Some bacteria can produce spores and withstand extreme temperatures; *Clostridioides difficile* and *Clostridium perfringens*. Moreover, some of the foodborne pathogens, such as *Listeria monocytogenes* is psychrotrophs which can survive in very low temperature (3,4). Foodborne bacteria can also be classified into oxygen sensitive, such as *C. difficile* and *C.* perfringens, and those which are insensitive to oxygen, such as methicillin-resistant *S. aureus* (MRSA), *S.* Typhimurium, *L. monocytogenes, S. sonnei,* and *P. aeruginosa.* Foodborne pathogens have been detected in a variety of food sources. Raw meat, processed food, and water normally contaminated with *C. difficile, C. perfringens S. aureus*, *S.*

Typhimurium, and *P. aeruginosa* (5,6). Whereas, *L. monocytogenes* has been also found in the fishery products, fermented sausages as well as dairy products (7).

Nowadays, the emergence of antibiotic resistance has been occurred worldwide, resulting in a decrease in the efficiency of antibiotics and a severity of the disease (8). Antibiotic resistance threats reported by CDC in 2019 revealed that antibiotic-resistant infections occurred more than 2.8 million cases, and more than 35,000 people die per year (9). This implying that an antibiotic is less effective for treating infections caused by those bacteria. As antibiotic resistant incidences have been increasing, alternative treatment is urgently needed. Compounds library screening is a feasible and reliably strategy for developing novel drug through high-through method (10). A previous study has demonstrated screening of 1,600 Food and Drug Administration (FDA) approved drugs against *Enterococcus faecium*, *S. aureus*, *Klebsiella pneumoniae*, *Acinetobacter baumannii*, *P. aeruginosa*, and *Enterobacter cloacae* (ESKAPE) pathogens; resulting in identified 49 non-antimicrobial drugs that were active against at least one species of ESKAPE pathogen (11).

Nucleoside analogues are a group of synthetic compounds structurally similar to natural nucleosides. This group of compounds is commonly used to treat fungal infections, viral infections, cancers, and even some bacterial infections (12,13). Nucleoside analogues can mimic endogenous nucleosides and exploit the metabolism of cells that interferes with DNA or RNA synthesis (14). Moreover, previous studies demonstrated that the nucleoside analogue, azathioprine, is able to modulate cell aggregation and inhibit the biosynthesis of biofilm formation in *C. difficile* (15). The different modes of action of the compound can be observed depending on the compounds' type and structure. Herein, we aim to screen for promising compounds that are capable of inhibiting foodborne pathogens from the nucleoside analogues library as well as to provide a glimpse of the action.

Methodology:

Bacterial strains and culture conditions

Seven selected strains of pathogenic bacteria, *C. difficile* R20291, *C. perfringens*, *S. aureus* (MRSA) DMST 20646, *S.* Typhimurium DMST 23566, *L. monocytogenes* DMST 21164, *S. sonnei*, and *P. aeruginosa* were used in this study. Brain heart infusion (BHI) broth was used to anaerobically culture *C. difficile* and *C. perfringens*, while *L. monocytogenes* was cultured under aerobic condition at 37ºC. *S. aureus*, *S.* Typhimurium, *S. sonnei*, and *P. aeruginosa* were cultured in Luria-Bertani (LB) broth at 37ºC. All bacterial strains were initially recovered from -80ºC storage, grown on an agar plate before sub-cultured into corresponding broth for a downstream experiment.

Single concentration screening of compounds for antimicrobial activity

The 290 compounds of Enamine nucleoside mimetics (NML-290-X-50) library were screened using single concentration screening assay at the threshold concentration of 20 µM. Original stock of the compounds was used to prepare working stocks by dissolving the compound in DMSO to the final concentration 4 mM. The working stock was stored at -20 ºC until use. For screening against anaerobic bacteria, an amount of 90 µl of test compounds pre-dissolved in MHB broth were prior added into each well in a 96-well plate and kept in an anaerobic chamber for at least 8 hours to deplete oxygen level for anaerobe bacterial.

For inoculation preparation, single bacterial colony was selected from agar plate then inoculated into BHIY medium for 24- hour incubation. Subsequently, the bacterium was sub-cultured in BHIY medium (anaerobic condition) or Mueller Hinton Broth (MHB) (aerobic condition) for 6 hours to reach mid-log phase. Bacterial suspensions were adjusted with MHB to obtain a final inoculum of 1×10^7 CFU/ml. Consequently, the wells were filled with 10 µl bacterial inoculum. Additionally, a negative control with a culture medium was included. After

48 hours of incubation at 37ºC under appropriate condition for each bacterium, the inhibitory effect of the compound was determined by microplate reader. The compounds that exhibit 75% growth reduction compared to the control were considered hit compounds and selected for further investigation.

Antimicrobial susceptibility

To determine the antimicrobial susceptibility of nucleoside analogue candidate compounds on foodborne pathogens, the minimum inhibitory concentrations (MICs) of candidate compounds were evaluated using broth microdilution assay according to the CLSI M45 guideline (16). Firstly, the candidate nucleoside analogues compounds were prepared with two-fold serial dilution ranging from 20 to 0.0195 µM then added in duplicates into each well in a 96-well plate. Using antibiotic treating each bacterium as a positive control; vancomycin, ampicillin, chloramphenicol, and ciprofloxacin for *S. aureus* (MRSA), *L. monocytogenes*, *S.* Typhimurium and *S. sonnei*, respectively. After that the bacterial colonies were picked and then cultured in a corresponding condition. Three percent of the overnight culture was transferred to BHIY (anaerobic) or MHB (aerobic) broth and incubated for 6 hours at 37ºC. The bacterial culture was adjusted to a final concentration 1×10^6 CFU/ml in a 96-well plate, and optical density at 600 nm (OD_{600}) values was measured after 24 hours or 48 hours of incubation at 37°C. The MIC values were determined to be the lowest concentration of antimicrobial agent required to prevent bacterial growth. Minimum Bactericidal Concentration (MBC) was determined using a 96 pin multi-blot replicator to directly stamp the treated bacterial culture from MIC assay onto tryptic soy agar (TSA) plate. The plates were incubated at 37°C for 18-24 hours; eventually, the results were observed and recorded. MBC was effectively determined to be the lowest antimicrobial concentration capable of inactivating more than 99.99% of bacterial growth.

Time-kill kinetic assay

In brief, overnight culture of bacterial inoculum at ~1.5×10^8 CFU/ml was exposed with 4x MIC, 2x MIC, 1x MIC, or 0.5x MIC of the drug. Later, bacterial growth was monitored by measuring OD_{600} every 30 min interval for 24 hours at 37°C using a microplate reader (Tecan) under aerobic conditions. The relative growth was plotted using the ratio of OD_{600} at time compared the initial OD_{600} (T_n/T_0). Our assay was performed with three replicates of each drug against each bacterial.

Results and Discussion:

Screening of nucleoside analog compounds against foodborne pathogens

Total of 290 compounds nucleoside analogs library was screened against 7 foodborne pathogens at the cutting point of 20 µM as summarized in the workflow (**Figure 1**). According to the screening result, 2 candidates; floxuridine and zidovudine exhibited antimicrobial with more than 75% of growth inhibition. Floxuridine has shown inhibitory effect against *S. aureus* (MRSA) DMST 20646, and *L. monocytogenes* DMST 21164 (**Figure 2a and 2b**). Whereas, zidovudine was effective against growth of *S.* Typhimurium DMST 23566 and *S. sonnei* at the concentration of 20 µM with more than 75% of bacterial growth inhibition (**Figure 2c and 2d**). Floxuridine was the most active with more than 99% inhibition of *L. monocytogenes*, followed by zidovudine inhibited *S.* Typhimurium growth by 94.7%. Subsequently, floxuridine inhibited *S. aureus* (MRSA) by 86.4%, and zidovudine inhibited *S. sonnei* growth by 78.1%. Nevertheless, none of nucleoside analog in the library showed an inhibitory property against

C. difficile, *C. perfringens*, or *P. aeruginosa*. Our results coincide with prior studies that reported antimicrobial activity of floxuridine has been found to inhibit *S. aureus* (17) and zidovudine was effective against *S.* Typhimurium (19).

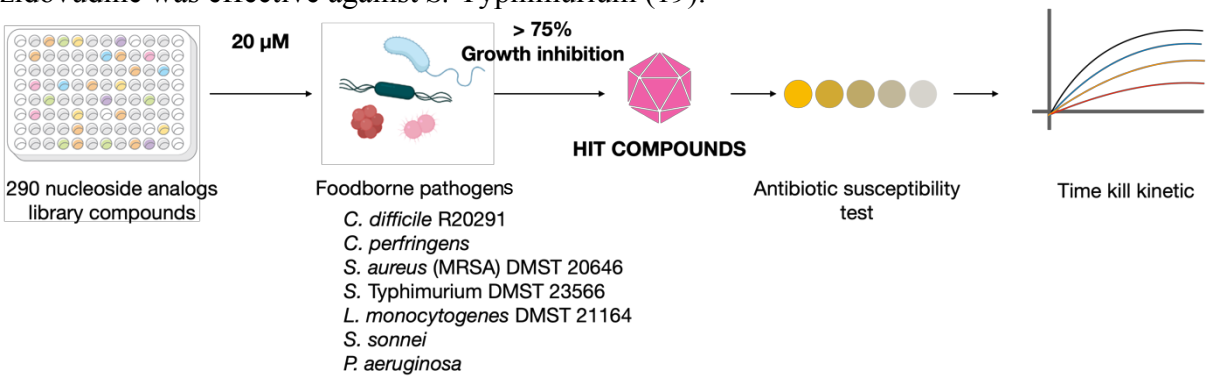

Figure 1. Schematic diagram illustrated nucleoside analogues library screening workflow. Nucleoside analogs library screening at 20 µM led to identification of antimicrobial compounds against foodborne pathogens.

Antimicrobial susceptibility of candidate compounds

As the MIC and MBC values were determined by broth microdilution assay, floxuridine and zidovudine were examined antimicrobial activity against 4 selected pathogens. Floxuridine had antimicrobial effect on *S. aureus* (MRSA) DMST 20646 and *L. monocytogenes* DMST 21164 with MIC values of 0.019 µg/ml and 0.308 µg/ml, respectively. Compared with 0.25 - 4 µg/ml vancomycin and 0.5 µg/ml for ampicillin, positive control of MRSA and *L. monocytogenes*, respectively (**Table 1**). The results are commensurate with nearby range MIC of floxuridine against bacteria in previous studies; floxuridine had been previously found to potentially inhibit staphylococcal growth with MIC 0.025 - 0.00313 µM (0.00077 - 0.00616 µg/ml) (17), another study reported a slight antimicrobial effect on *S. aureus* USA300 with the MIC of 0.0625 µg/ml (18). These inconsistencies could be attributed to variances in the test strain and the assay conditions used. Since our bacterial strain is methicillin-resistant specie; thus, it might harbor unknown resistant mechanism resulting in less susceptibility to the drugs. Moreover, floxuridine was also reported to repress SaeRS two-component system (TCS), that regulates virulence factors of *S. aureus* bacteria (18). However, our result is the first report to show an antimicrobial activity of floxuridine against *L. monocytogenes*. Zidovudine showed an inhibitory effect on *S.* Typhimurium and *S. sonnei* with MIC values of 0.01 µg/ml and 0.042 µg/ml, respectively. Compared with 1 µg/ml chloramphenicol and 0.063 µg/ml for ciprofloxacin, positive control of *S.* Typhimurium and *S. sonnei*, respectively (**Table 1**).

The results related with similar range MIC of zidovudine against various bacteria in previous study; 0.0025 – 25 µg/ml (19). Zidovudine has been shown to have specific antibacterial activity only on gram-negative bacteria (19). Our result showed to be consistency with the previous finding that zidovudine activity is limited to only gram-negative bacteria, *S.* Typhimurium and *S. sonnei*. The explanation that Gram-positive bacteria is not inhibited by zidovudine may be due to lack of dThd kinase activity resulted in zidovudine insusceptible (18). The antibacterial mechanism of zidovudine on *S.* Typhimurium, has been examined zidovudine-triphosphate incorporate into DNA could be expected to result in DNA chain termination since zidovudine lacks 3'hydroxyl necessary for DNA polymerase-mediate DNA chain elongation (20). For *S. sonnei*, this is the first time to report antimicrobial activity of zidovudine against this foodborne pathogen.

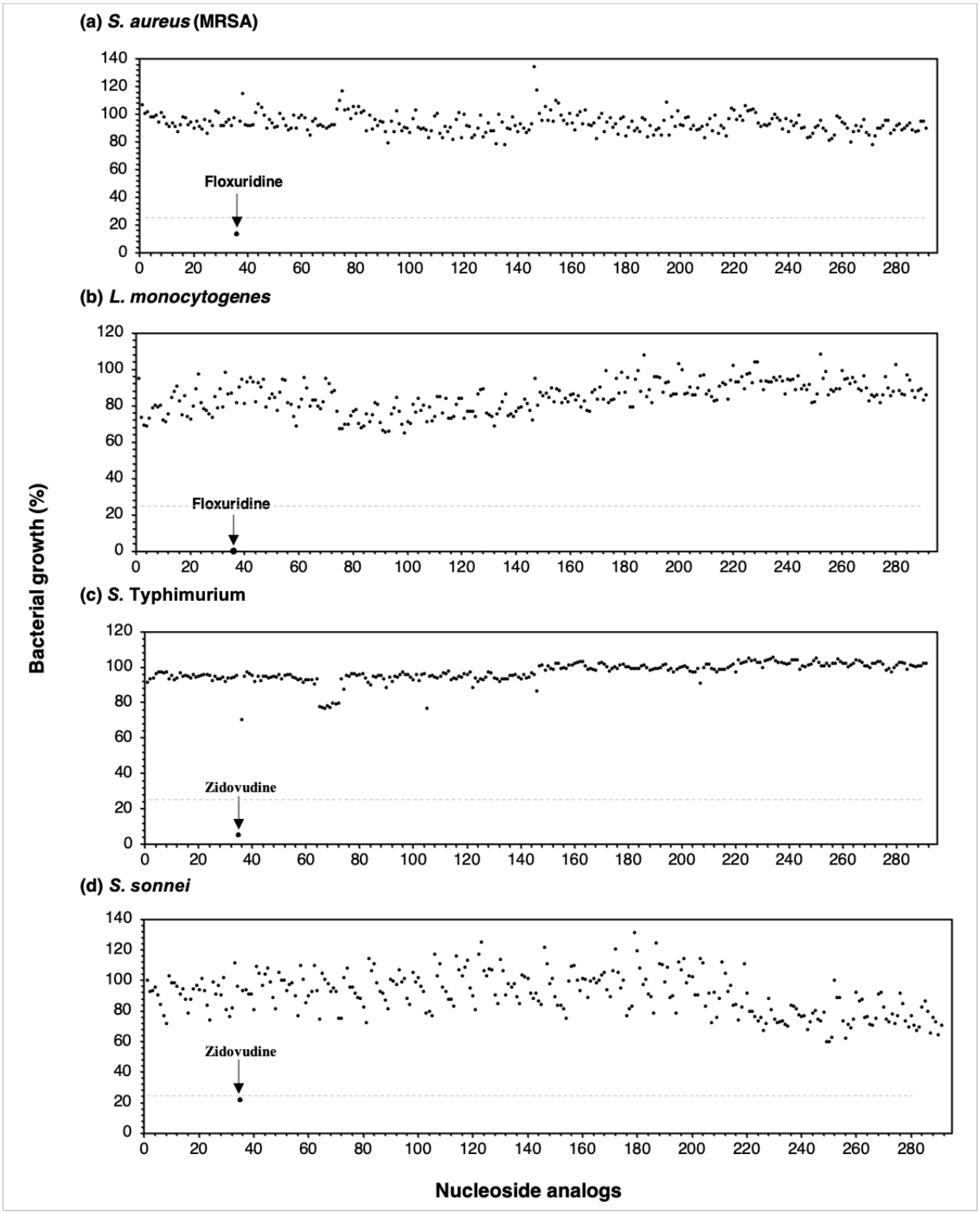

Figure 2. Plot of bacterial growth upon challenging with 20 µM of nucleoside analogs compounds; (a) *S. aureus* (MRSA) DMST 20646, (b) *L. monocytogenes* DMST 21164, (c) *S.* Typhimurium DMST 23566, and (d) *S. sonnei*. Dotted line represented growth inhibition of more than 75%.

The values noted for MBC were greater than 4 times of MIC, floxuridine represented MBC against *L. monocytogenes* 1.231 μg/ml, and zidovudine show 0.669 μg/ml against *S. sonnei*. These results can be interpreted that both preferentially exhibit bacteriostatic activity against *L. monocytogenes* and *S. sonnei*. Accordingly, our result shows that floxuridine may inhibit gram-positive bacteria through specific mechanism rather than gram-negative bacteria, while zidovudine probably has a unique mechanism for inhibiting gram-negative bacteria.

Table 1. Drugs susceptibility against of tested foodborne pathogens

Foodborne pathogens	Drugs	MIC (μg/ml)	MBC (μg/ml)
***S. aureus* (MRSA)**	Floxuridine	0.019	N/A[a]
	Vancomycin	0.25	N/A
L. monocytogenes	Floxuridine	0.308	1.231
	Ampicillin	0.5	>1
***S.* Typhimurium**	Zidovudine	0.01	N/A
	Chloramphenicol	1	N/A
S. sonnei	Zidovudine	0.042	0.669
	Ciprofloxacin	0.063	<0.063

[a] N/A, not applicable

Time-kill kinetics

Time-kill assay has been used to measure the kinetics of in vitro bacterial killing but not generally to determine whether an antibacterial agent is bacteriostatic or bactericidal (21). For investigation of the killing kinetics of these compounds, growth kinetic was measured upon compound incubation. From these time-kill curves, both bacteria showed normal exponential growth without the test compound. Both compounds hindered the growth of the bacteria during the first 4 hours. Floxuridine caused an *L. monocytogenes* growth reduction when drug concentrations increased after 5 hours (**Figure 2a**). In comparison, zidovudine could effectively inhibited the growth of *S. sonnei* as growth curve of the bacteria was shown to be steady after 4 hours (**Figure 2b**). The result indicated that floxuridine and zidovudine are effective antimicrobial agents against *L. monocytogenes* and *S. sonnei*. Although, floxuridine and zidovudine-treated bacterial cells were recovered at around 18 and 17 hours, but the bacterial growth was relatively low compared to those of negative control. Despite the studies of drug mechanism in floxuridine and zidovudine on *S. aureus* and *S.* Typhimurium, no mechanism of action of these drugs is now understood for *L. monocytogenes* and *S. sonnei*. Hence, the further experiment should be conducted to comprehend the possible mechanism of action.

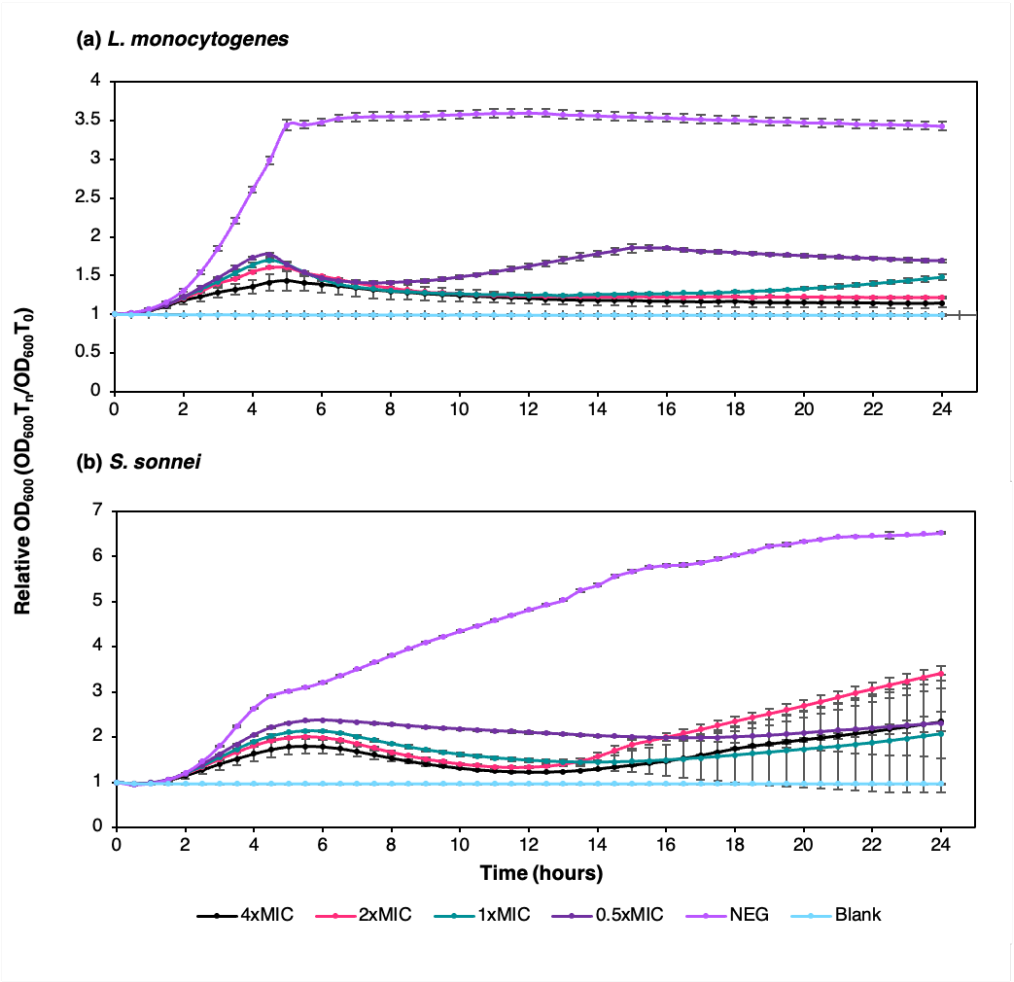

Figure 3. Time-kill kinetics assay of *L. monocytogenes* and *S. sonnei.* (a) Time-kill kinetics floxuridine against *L. monocytogenes* was represented in a relation to the initial OD_{600} over 24 h exposure to various concentrations. (b) Time-kill kinetics of zidovudine against *S. sonnei* was represented in a relation to the initial OD_{600} over 24 hours exposure to various concentrations Error bar is measured by standard deviation.

Conclusion:

Our screening campaign revealed floxuridine has a potent antimicrobial activity against gram-positive bacteria including *S. aureus* (MRSA) DMST 20646 and *L. monocytogenes* DMST 21164. While zidovudine exhibited effective antimicrobial activity against *S.* Typhimurium DMST 23566 and *S. sonnei*. The MIC values are diverse from previous studies on other pathogens; thus, the different mode of actions of each bacterium may be implied. Due to the structural similarity to nucleic acid, DNA interfering mechanism could be the most probable assumption, and it is needed to be proven.

Acknowledgements:

This research project is supported by Mahidol University.

References:

1. Havelaar AH, Kirk MD, et al. PLOS Medicine. 2015;12(12).
2. Lee H, Yoon Y. Food Sci. Anim. Resour. 2021;41(1):1–7.
3. Bacon RT, Sofos JN. Food Safety Handbook. 2003;157–195.
4. Bintsis T. AIMS Microbiol. 2017;3(3):529-563.
5. Lessa FC, Mu Y, et al. N Engl J Med. 2015;372(9):825–34.
6. Grass JE, Gould LH, Mahon BE. Foodborne Pathog Dis. 2013;10:131–136.
7. European Food Safety Authority, & European Centre for Disease Prevention and Control. EFSA journal.2017;15(12).
8. Ventola CL. P T. 2015;40(4):277–83.
9. Antibiotic resistance threats in the United States, 2019. Atlanta, Georgia. 2019.
10. Cunningham BT, Laing LG. Expert Opin Drug Discov. 2008;3(8):891-901.
11. Younis W, AbdelKhalek A, et al. Curr Pharm Des. 2017;23(14):2147-2157.
12. Thomson JM, Lamont IL. Front. Microbiol. 2019;10.
13. Galmarini C, Mackey J, Dumontet C. Leukemia. 2001;15(6):875–90.
14. Serpi M, Ferrari V, Pertusati F. J. Med. Chem. 2016;59(23):10343–82.
15. Shad AA, Shad WA. Arch. Microbiol. 2021;203(1):45–58.
16. Clinical and Laboratory Standards Institute. CLSI. 2015;44-46.
17. Lau QY, et al. Antibiotics (Basel). 2015;4:424–434.
18. Yeo WS, Arya R, Kim KK, et al. Sci Rep. 2018;8(1):2521.
19. Elwell LP, Ferone R, Freeman GA, et al. Antimicrob. Agents and chemother. 1987;31(2):274-80.
20. Herrmann JL, Lagrange PH. Antimicrob Agents Chemother. 1992;36(5):1081-1085.
21. Pankey G. A., Sabath L. D. Clin. Infect. Dis. 2004;38(6):864–870.

A PROTEOMIC APPROACH FOR IDENTIFYING POTENTIAL DRUG'S MECHANISM OF ACTION IN *Clostridioides difficile*

Supassara Klinsrisuk[1], Matthew Phanchana[2], Methinee Pipatthana[3], Patompon Wongtrakoongate[1], Surang Chankhamhaengdecha[4], Tavan Janvilisri[1], Phurt Harnvoravongchai[4*]

[1] Department of Biochemistry, Faculty of Science, Mahidol University, Bangkok 10400, Thailand
[2] Department of Molecular Tropical Medicine and Genetics, Faculty of Tropical Medicine, Mahidol University, Bangkok 10400, Thailand
[3] Department of Microbiology, Faculty of Public Health, Mahidol University, Bangkok 10400, Thailand
[4] Department of Biology, Faculty of Science, Mahidol University, Bangkok 10400, Thailand
*email: phurt.har@mahidol.ac.th

Abstract:

The gram-positive anaerobic bacterium *Clostridioides difficile* is the major cause of diarrhea and enteritis in human. Vancomycin, metronidazole, and fidaxomicin are the mainstay for the treatment of *C. difficile* infection (CDI). However, the incidence of treatment failure and high recurrent rate caused by antibiotics resistance in *C. difficile* have been continuously reported. Several researches have been seeking novel anticlostridial agents, but less is studied on how these compounds are working. Under an antibiotic exposure, alteration of protein expression in the bacteria is unique corresponding to each type of cellular damages. The change in the protein pattern is useful for exploring the mode and/or mechanism of action of antibiotics. Therefore, a mass spectrometry-based proteomic approach was used to analyze changes in the *C. difficile* proteome when challenging with antibiotics. Our study revealed that metronidazole, vancomycin, and fidaxomicin modified number of marker proteins involved in biosynthesis of protein, nucleic acid, as well as in cell wall. This established pipeline can be used to further predict mode and/or mechanism of action of unknown drugs in *C. difficile*.

Introduction:

Clostridioides difficile is a rod-shaped, anaerobic gram-positive bacterium that exists both in spore and vegetative form[1]. *C. difficile* is the major cause of diarrhea and enteritis, which can be severe and caused considerable harm to patients. There have been reported that about 15,000 patients died from CDI per year in the US[2]. In Asia, about 2.7 per 1,000 admission cases were reported to have CDI in Korea, and 1.7 per 1,000 admission cases were also associated with CDI in China[3]. Generally, three antibiotics are served as a primary treatment for CDI, which are vancomycin, metronidazole, and fidaxomicin[4]. Metronidazole has previously been recommended as the first-line treatment for CDI[4]. Until 2018, Infectious Diseases Society of America (IDSA) recommended to replace metronidazole with either vancomycin or fidaxomicin for the initial infection[5]. However, in 2021, IDSA have recently updated a new guideline for CDI treatment by recommending prescribing fidaxomicin rather than vancomycin as it shows high risk of relapse[6]. Based on mode of action (MOA) of antibiotic, these three antibiotics harbor difference target and MOA including the inhibition of DNA synthesis and disruption of cell wall synthesis. Metronidazole targets to DNA, resulting in inhibition of DNA synthesis and breaking DNA strand[7]. Vancomycin kills the bacterium by inhibiting cell wall biosynthesis through the binding of peptidoglycan at D-Ala D-Ala terminal

site[8]. For the MOA of fidaxomicin, it firstly binds to the DNA strand-RNA polymerase complex, which eventually prevent the initiation of transcription through the inhibition of DNA strand separation[9]. Although these three CDI drugs have been widely used and studied on their action, some limitations on reducing their effectiveness continuously documented. Increasing in treatment failures, rising of recurrence rate, and emerging of drug resistance strain led to an urgent need on seeking novel antibiotic against *C. difficile*. Several studies have been seeking for novel anticlostridial agents, but less of them are looking into their MOA[10,11,12]. Understanding drug's MOA could be useful for monitoring dose and effectiveness, as well as, understanding on how the bacteria themselves develop a resistance mechanism to the corresponding drug[13].

A proteomic approach is used as a tool for quantification and identification of proteins in the cell, which can be widely applied in many fields such as basic cell biology, agriculture, biotechnology, and healthcare. As proteomics can provide functional and mechanistic perspectives to the cell stress response, it is therefore applied to elucidate the mechanisms of drugs[14]. In 2020, Senges et al. established the proteomic responses of *Bacillus subtilis* against 91 drugs. Interestingly, their findings from comparative proteomic and protein profiling uncovered not only crucial protein markers but also mechanisms of action of the given drug[15]. This supports the reliability of proteomics to use as a tool to identify the marker proteins under antibiotic treatment for further explanation on biological association of drug and its target.

In this study, we aim to use proteomic approach to study the proteomic profile for further establishing a pipeline for prediction of drug's MOA in *C. difficile*. Alteration of protein profile of *C. difficile* after challenging with well-studied CDI antibiotics including metronidazole, vancomycin, and fidaxomicin was investigated. Our pipeline could potentially be an alternative approach for further use to predict MOA of a novel anti-*C. difficile* drug.

Methodology:

Construction of antibiotics-related marker library in C. difficile

The sets of protein marker responded for different MOA of antibiotic in *B. subtilis*[15] were used as a model for reconstruction in *C. difficile*. Candidate protein markers from *B. subtilis* strain 168 were firstly searched in *C. difficile* based on protein annotation. To avoid missing of unannotated proteins, amino acid sequence of each *B. subtilis* protein marker was subjected to BLAST (Basic Local Alignment Search Tool) against all *C. difficile* R20291 proteins through KEGG (Kyoto Encyclopedia of Genes and Genomes) and NCBI (National Center for Biotechnology Information) databases to retrieve a homologous protein.

Bacterial culture and minimal inhibitory concentration (MIC) determination

Antibiotic susceptibility of *C. difficile* strain R20291 (ribotype 027) under antibiotic treatments was determined using broth microdilution method regarding to the CLSI M11-A6[16] guideline. *C. difficile* was cultured in brain heart infusion (BHI) broth supplemented with 0.5 % yeast extract (BHIY) under anaerobic condition at 37°C for overnight. Bacterial culture was then transferred to fresh BHIY broth and incubated for further 6 hours. Bacterial culture was adjusted to obtained final 1 x 10^5 CFU/well in 96-well plate containing varied concentration of antibiotic. Metronidazole was prepared in the range of 0.0625 to 8 µg/ml, fidaxomicin in the range of 0.001953 to 0.25 µg/ml, and vancomycin in the range of 0.25 to 32 µg/ml. The MIC values were determined after 48 hours of incubation by measuring the OD_{600} of viable cells using a microplate reader (BioTek). The MIC value is defined by the lowest concentration of a compound at which no growth is shown. All treatment conditions were performed in triplicates.

Time-kill assay

Time-kill assay was performed to determine the killing kinetics of the antibiotics toward *C. difficile* R20291. Briefly, bacterial inoculum at ~6×10^8 CFU/ml was incubated with varied inhibitory concentrations of metronidazole, fidaxomicin, and vancomycin. The bacterial growth was observed by measuring OD_{600} every 10 minutes interval for 12 hours at 37°C using a microplate reader (BioTek) under anaerobic conditions. The relative growth was calculated as a ratio of OD_{600} measured at times T_n to T_0. 2.5% DMSO was used as a negative control as it was used for the preparation of the antibiotics. All treatment conditions were performed in triplicates.

Proteomic analysis

Preparation of protein extract

Three percent of overnight cultured was transferred to BHIY broth and incubated for 6 hours at 37°C under anaerobic condition to enter mid log-phase. The bacterium was challenged with antibiotic at 2xMIC concentration for 30 min. Cultured bacterial cells were harvested by centrifugation, and pellets were washed of Phosphate-buffered saline (PBS). The pellet will be resuspended in 500 µl of ice-cold RIPA lysis buffer followed with sonication on ice with the following pulse sequence; 10s/10s (on/off cycle), 2 minutes timer, and amplitude 20% was applied. After cell disruption, the suspension was centrifuged to collect and transferred to the new tube.

Protein concentration determination and visualization

Amount of total protein was quantified using a Bicinchoninic Acid (BCA) Protein Assay Kit, with bovine serum albumin (BSA) as standard. The proteins profile was determined using SDS-PAGE.

Sample clean-up and digestion

To perform gel-free based proteomics, a total protein (100 µg) was precipitated using acetone/5mM DTT (1:5, (v, v) ratio) at -20°C for 3 hours or -80°C for 1 hour. After that, the protein pellet was collected by centrifugation at 10,000g for 10 minutes at 4°C. After precipitation, the protein pellet was resolubilized with 50-75 µl of 0.2% RapidGest SF, 10mM NaCl in 10mM Ammonium bicarbonate by using a probe tip sonication at a frequency of 20 kHz and 80% amplitude for 2 seconds. To break disulfide bonds in proteins, DTT solution (20mM DTT in 10mM Ammonium bicarbonate) was added to the solubilized proteins (to obtain a final concentration of 5 mM DTT) and incubated at 90°C for 15 minutes. After that, to add the acetamide group to the reduced proteins, IAA solution (100 mM IAA in 10mM Ammonium bicarbonate) was added to obtain a final concentration of 25 mM IAA and incubated at room temperature (in the dark) for 25 minutes. The solution was cleaned up using a Desalting Zebra-spin column and the flow-through fraction was collected. The Rapidgest solution (0.5% RapidGest SF in 10mM ammonium bicarbonate) and the trypsin solution (100 ng/µl trypsin in Ammonium bicarbonate) was added to the solution. After that, the digested solution was incubated at 37°C for 3-4 hours, add the 1% formic acid to terminate the reaction and dried the tryptic peptides before LC-MS/MS analysis.

LC-MS/MS analysis of peptide

A total of 1.6 µg peptides were subjected to LC-MS/MS using an Orbitrap HF hybrid mass spectrometer combined with and EASY-nLC1000 nano-liquid chromatography (LC) system (Thermo Fisher Scientific) with a nano C18 column. The LC conditions were used as the following: mobile phase A and B were used, with mobile phase A being composed of 0.1% formic acid in water and mobile phase B comprising 95% acetonitrile with 0.1% formic acid.

Data processing and analysis

Three independent experiments were done to assure data reproducibility. Thermo Proteome Discoverer 2.4 with identified against the Uniplot protein database were be used to process and interpret all MS/MS raw spectra. The false discovery rate (FDR) was set to 1%. The proteins with a fold change higher or lower than ± 1-folds with a significant difference of p-value < 0.05 were selected. Microsoft Excel and Perseus software were used to analyze the data.

Results and Discussion:

Construction of antibiotics-related marker library in C. difficile

Figure 1 is an experimental pipeline of using proteomic profile for predicting MOA of antibiotics in *C. difficile*. First, the marker proteins known to be altered upon antibiotic exposures from *B. subtilis* strain 168 were used as a reference for *C. difficile* R20291. Based on protein sequence homology, all 36 protein markers were successfully retrieved from *C. difficile* R20291 and classified into seven groups corresponding to MOA of antibiotics.; inhibition of fatty acid biosynthesis, inhibition of protein biosynthesis, protein stress, effect on nucleic acid, inhibition of cell wall biosynthesis, structural integrity of membrane, and membrane (associated functions). Clostridial protein markers for each MOA of antibiotic were listed in **Table 1**. The result showed that most of homologous proteins found in *C. difficile* contained more than 30% sequence similarity to the markers of *B. subtilis*. The most common proteins that share among the two species are those in the group of protein stress and protein synthesis. Whereas protein markers belong to the group of "effect on nucleic acid" are diverse between two species. Although genome size of *B. substilis* and *C. difficile* are similar (4.2 and 4.3 mbp, respectively), GC content in *B. substilis* is shown to be relatively higher than those of *C. difficile*[17, 18]. Moreover, the major difference could also come from the fact that *C. difficile* harbors multiple mobile genetic elements[19].

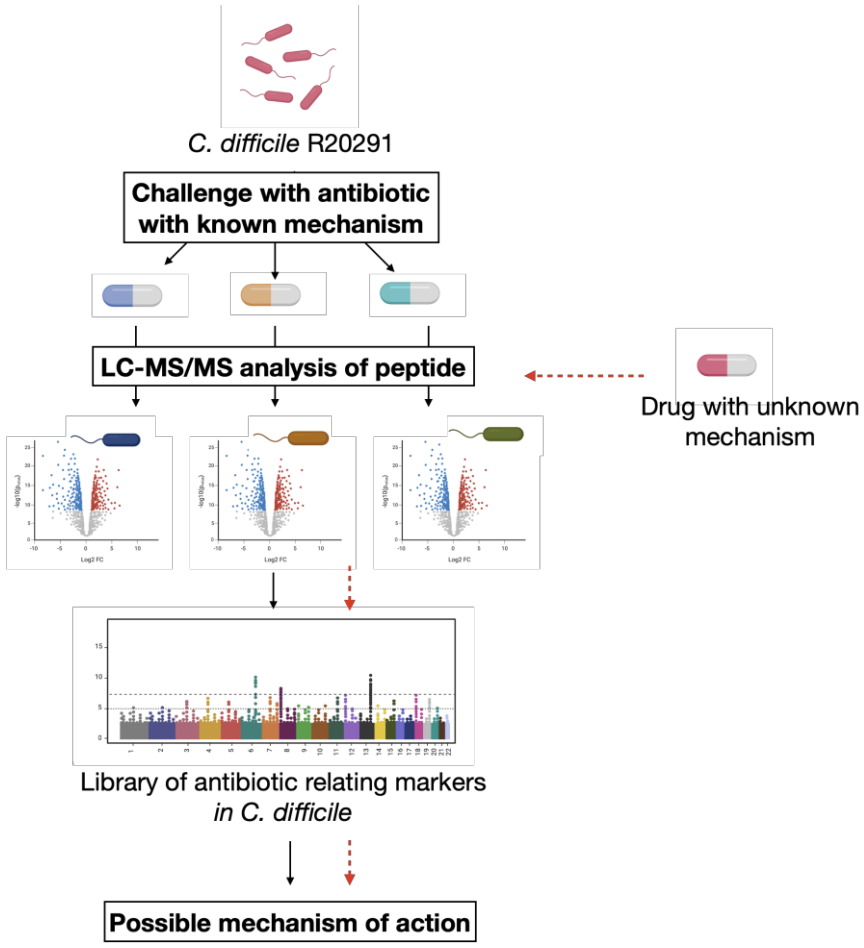

Figure 1. Overview of the workflow to establish proteomic-based platform for identifying antibiotic action.

Table 1. Comparison of antibiotic-relating marker in *B. subtilis* 168 and *C. difficile* R20291

Inhibition of fatty acid biosynthesis						
***Bacillus subtilis* 168**				***Clostridioides difficile* R20291**		
Gene	Annotation	AA seq	% Identities	Gene	Annotation	AA seq
FabHA	3-oxoacyl-[acyl-carrier-protein] synthase III	312	53%	FabH	3-oxoacyl-[acyl-carrier-protein] synthase III	328
FabHB	3-oxoacyl-[acyl-carrier-protein] synthase III	325	40%	FabH	3-oxoacyl-[acyl-carrier-protein] synthase III	328
FabI	enoyl-[acyl-carrier protein] reductase I	258	25%	CDR20291_2463	3-oxoacyl-[acyl-carrier protein] reductase	245
FabF	3-oxoacyl-[acyl-carrier-protein] synthase II	413	63%	FabF	3-oxoacyl-[acyl-carrier-protein] synthase II	412
PanB	3-methyl-2-oxobutanoate hydroxymethyltransferase	277	48%	PanB	3-methyl-2-oxobutanoate hydroxymethyltransferase	275
PlsX	phosphate acyltransferase	333	46%	PlsX	phosphate acyltransferase	340

Protein stress						
***Bacillus subtilis* 168**				***Clostridioides difficile* R20291**		
Gene	Annotation	AA seq	% Identities	Gene	Annotation	AA seq
GroEL	chaperonin GroEL	544	74%	GroEL	chaperonin GroEL	542
ClpC	ATP-dependent Clp protease ATP-binding subunit ClpC	810	60%	ClpC	ATP-dependent Clp protease ATP-binding subunit ClpC	749
ClpE	ATP-dependent Clp protease ATP-binding subunit ClpE	699	56%	ClpC	ATP-dependent Clp protease ATP-binding subunit ClpC	749
DnaK	molecular chaperone DnaK	611	68%	RpsF	30s ribosomal protein S6	615
GroES	chaperonin GroES	94	60%	GroES	chaperonin GroES	94
ClpP	ATP-dependent Clp protease, protease subunit	197	75%	clpP1	ATP-dependent Clp protease, protease subunit	194
PtsH	phosphocarrier protein HPr	88	44%	PtsH	phosphocarrier protein HPr	86

Inhibition of protein biosynthesis						
***Bacillus subtilis* 168**				***Clostridioides difficile* R20291**		
Gene	Annotation	AA seq	% Identities	Gene	Annotation	AA seq
RplJ	50s ribosomal protein L10	166	47%	RplJ	50s ribosomal protein L10	168
TufA	elongation factor Tu	396	78%	FabH	3-oxoacyl-[acyl-carrier-protein] synthase III	397
RpsB	30s ribosomal protein S2	246	71%	RpsB	30s ribosomal protein S2	237
RpsF	30s ribosomal protein S6	95	41%	RpsF	30s ribosomal protein S6	92
Adk	adenylate kinase	217	57%	Adk	adenylate kinase	221
PyrAA	carbamoyl-phosphate synthase pyrimidine-specific small chain	364	51%	pyrAA 1	carbamoyl-phosphate synthase, pyrimidine-specific, small chain	364

Effects on nucleic acid						
***Bacillus subtilis* 168**				***Clostridioides difficile* R20291**		
Gene	Annotation	AA seq	% Identities	Gene	Annotation	AA seq
YvyD	sigma-54 modulation protein	189	37%	CDR20291_0141	putative sigma-54 modulation protein	143
KatA	catalase	483	48%	CDR20291_1707	putative two-component system response regulator	132
AhpF	NADH-dependent peroxiredoxin subunit F	509	32%	CDR20291_2024	thioredoxin reductase	302
AhpC	NADH-dependent peroxiredoxin subunit C	187	26%	CDR20291_1282	putative bifunctional protein: peroxiredoxin/chitinase	709
MrgA	metalloregulation DNA-binding stress protein	153	30%	CDR20291_1620	probable acyltransferase	254
YtxH	hypothetical protein	151	37%	CDR20291_1815	putative membrane protein	127
YuaE	hypothetical protein	162	33%	BirA	BirA bifunctional protein	325

Inhibition of cell wall biosynthesis						
***Bacillus subtilis* 168**				***Clostridioides difficile* R20291**		
Gene	Annotation	AA seq	% Identities	Gene	Annotation	AA seq
YtrB	acetoin utilization transport system ATP-binding protein	292	31%	CDR20291_1516	ABC transporter, ATP-binding protein	241
YtrE	acetoin utilization transport system ATP-binding protein	231	41%	CDR20291_1377	putative ABC transport system ATP-binding protein	224
TrmB	tRNA guanine-N(7)-methyltransferase	213	53%	CDR20291_1865	tRNA guanine-N(7)-methyltransferase	227
Nad-E	NH(3)-dependent NAD(+) synthetase	272	36%	NadE	NH(3)-dependent NAD(+) synthetase	251
LiaH	lia operon expression modulator LiaH	225	26%	CDR20291_1226	putative transporter	834
YceC	stress response protein SCP2	199	62%	CDR20291_1534	tellurium resistance protein	209
YceH	hypothetical protein	363	41%	CDR20291_1537	putative tellurite resistance protein	378

Membrane (structural integrity)						
***Bacillus subtilis* 168**				***Clostridioides difficile* R20291**		
Gene	Annotation	AA seq	% Identities	Gene	Annotation	AA seq
LiaH	lia operon expression modulator LiaH	225	26%	CDR20291_1226	putative transporter	834
PspA	phage shock protein A homolog	227	30%	CDR20291_1408	conserved hypothetical protein	289
YceC	stress response protein SCP2	199	62%	CDR20291_1534	tellurium resistance protein	209
YvlB	hypothetical protein	365	27%	CDR20291_0501	putative uncharacterized protein	345
YceH	hypothetical protein	363	41%	CDR20291_1537	putative tellurite resistance protein	378
Abh	transition state regulator Abh	92	42%	spoVT	stage V sporulation protein T	185
YfmS	sensory transducer protein YfmS	286	38%	CDR20291_0463	putative methyl accpeting chemotaxis protein	567

Membrane (associated functions)						
***Bacillus subtilis* 168**				***Clostridioides difficile* R20291**		
Gene	Annotation	AA seq	% Identities	Gene	Annotation	AA seq
YceC	stress response protein SCP2	199	62%	CDR20291_1534	tellurium resistance protein	209
NadE	NH(3)-dependent NAD(+) synthetase	272	36%	NadE	NH(3)-dependent NAD(+) synthetase	51
PspA	phage shock protein A homolog	227	30%	CDR20291_1408	conserved hypothetical protein	289
LiaH	lia operon expression modulator LiaH	225	26%	CDR20291_1226	putative transporter	834
RacX	amino-acid racemase	227	51%	RacX	amino-acid racemase	232
Spo0M	sporulation-control protein spo0M	258	30%	AddA	ATP-dependent nuclease subunit A	1275

Antibiotic susceptibility test

Antimicrobial activity of metronidazole, vancomycin, and fidaxomicin against *C. difficile* R20291 were identified. Our data revealed that metronidazole had a MIC range between 0.5-1 μg/ml. The MIC of vancomycin was in the range of 0.5-2 μg/ml. Our data were in agreement with previous studies that reported the MIC of metronidazole against *C. difficile* was in a range of 0.125-0.5 μg/ml, and vancomycin was in a range of 1-2 μg/ml [7,20]. For fidaxomicin, the MIC was in a range of 0.03125-0.125 μg/ml, which was in a good association with the previous study, 0.06-0.25 μg/ml [21,22].

Time-kill assay

Killing actions of metronidazole, vancomycin, and fidaxomicin on *C. difficile* R20291 were investigated. The results revealed that all drugs showed a concentration dependent manner in inhibiting the growth of *C. difficile* (**Figure 2**). Metronidazole exhibited a rapid killing profile, which was in agreement with the previous study[20]. Metronidazole reduced the number of bacteria after 1 hour (h) of incubation. In contrast, vancomycin and fidaxomicin showed a slower decline in growth compared to metronidazole. As vancomycin targets cell wall biosynthesis, the action may not be as fast as metronidazole, which targeting DNA. The similar explanation could also be implied for fidaxomicin since the drug acts to inhibit protein synthesis.

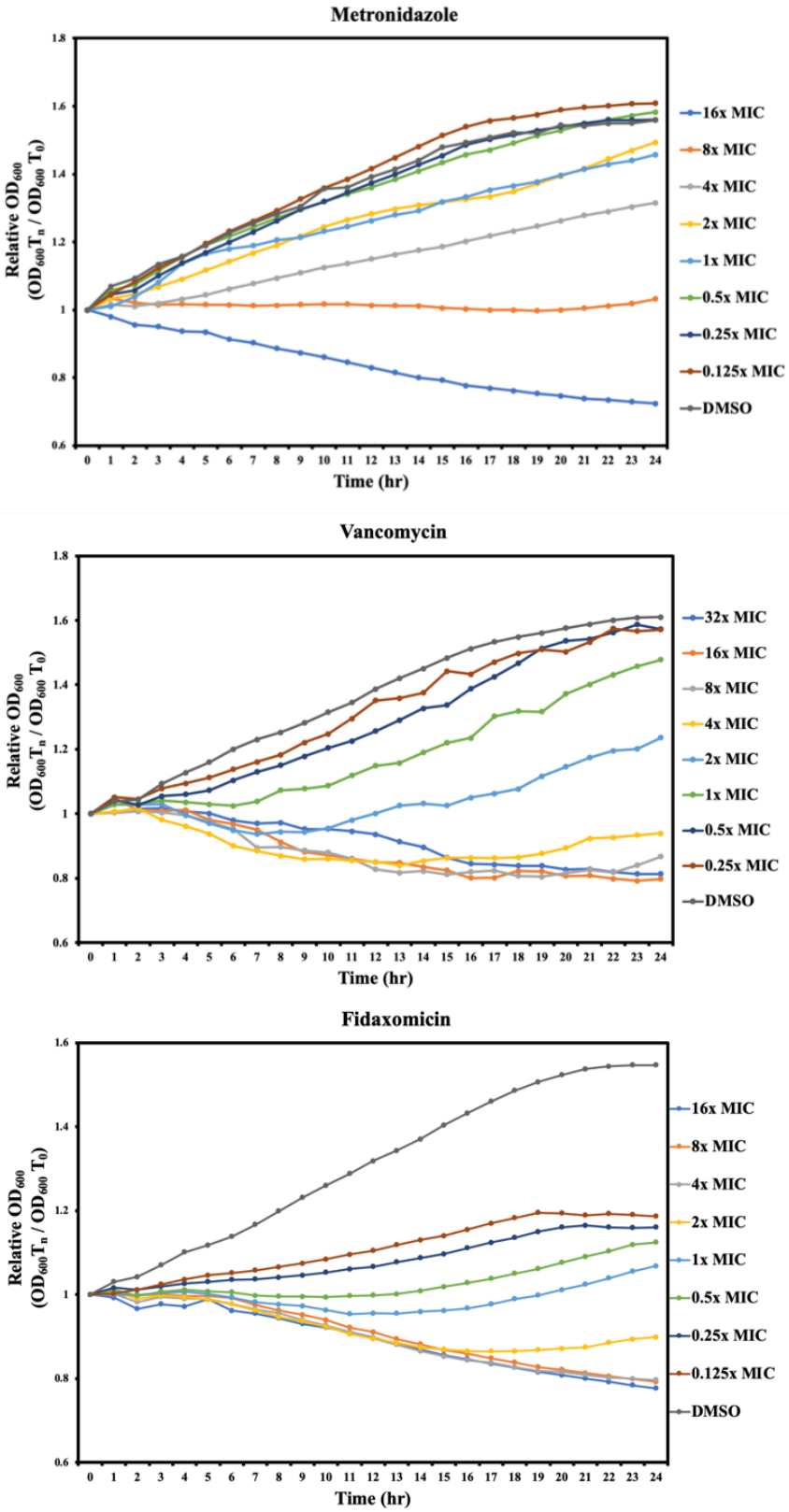

Figure 2.

Time-kill kinetics the candidate drugs against *C. difficile* R20291 followed for 12 h. (a); Metronidazole, (b); Vancomycin, and (c); Fidaxomicin.

Proteomic analysis

Proteomic analysis was used to analyze changes in *C. difficile* proteins when challenged with candidate repurposing drugs against *C. difficile*. The raw mass spectra (raw file) were processed by Proteome Discoverer 2.4 and used Perseus software platform for analysis. According to the normalized proteomic analysis, the volcano plot of the differential protein expression identifying the most significant protein expression changes is described in Figure 3. Each spot represents the protein expression ratio (drug: control) according to their log10p values. The differentially expressed proteins associated with these spots are listed in the Table 2.

The LC-MS/MS analysis revealed a total number of 1785 proteins among the antibiotics and the control groups. We identified 88 significantly different proteins, compared between the metronidazole and control groups. Specifically, 57 significantly different proteins were up regulated (Cut-off criteria: p-value < 0.05 and |log2FC|>0.1) and 31 protein were found to be down regulated (Figure 3 (a)). For fidaxomicin, the volcano plot showed that 279 proteins showed significantly altered in protein expression, which 182 proteins and 97 proteins were up and down regulated, respectively (Figure 3 (c)) and mostly were up regulated (blue region, Figure 3 (c)). Furthermore, we found 850 significantly different proteins expression, compared between the vancomycin and control groups. The proteins expression changes were mostly up regulated, 714 significantly different proteins were up regulated (blue region, Figure 3 (b)) whereas 136 were down regulated (red region, Figure 3 (b)). Considering antibiotics toward mode of action in *C. difficile*, data of protein expression was mapped to the constructed marker proteins as shown in Table 2. According to the results, most of marker proteins for "Inhibition of cell wall biosynthesis" and "Effects on nucleic acid" are missing for vancomycin and metronidazole. Although, most of the marker proteins could be retrieved from the proteomic analysis of fidaxomicin treatment, but the relatively fold changes were not considerably different.

The difference of protein expressions among these experimental groups was clustered, as represented in the heatmap in Figure 4. The top of the heatmap presents the names of the proteins, and the left side shows the three-drug including metronidazole, vancomycin, and fidaxomicin, with proteins expressed with a maximum distance of 0.5.

There are some non-marker proteins, which showed significantly changed in protein expression (|log2FC|> 1, 0.05≤ p-value). Six of these proteins were found when *C. difficile* was challenged with vancomycin, while one of each protein was found for metronidazole and fidaxomicin treatment. This data suggested the novel possible marker for predicting. Asparagine synthase showed more than 2-fold change, when *C. difficile* encountered with vancomycin. This protein was reported *in Lactococcus lactis* to involve with amidation of d-Asp for peptidoglycan crosslink[23].

In this study, precise protein markers still have not been identify, for different mode of action. Novel markers or pattern could be established to be unique in *C. difficile*, however, further experiment with more type of antibiotics and protocol optimization should be continued.

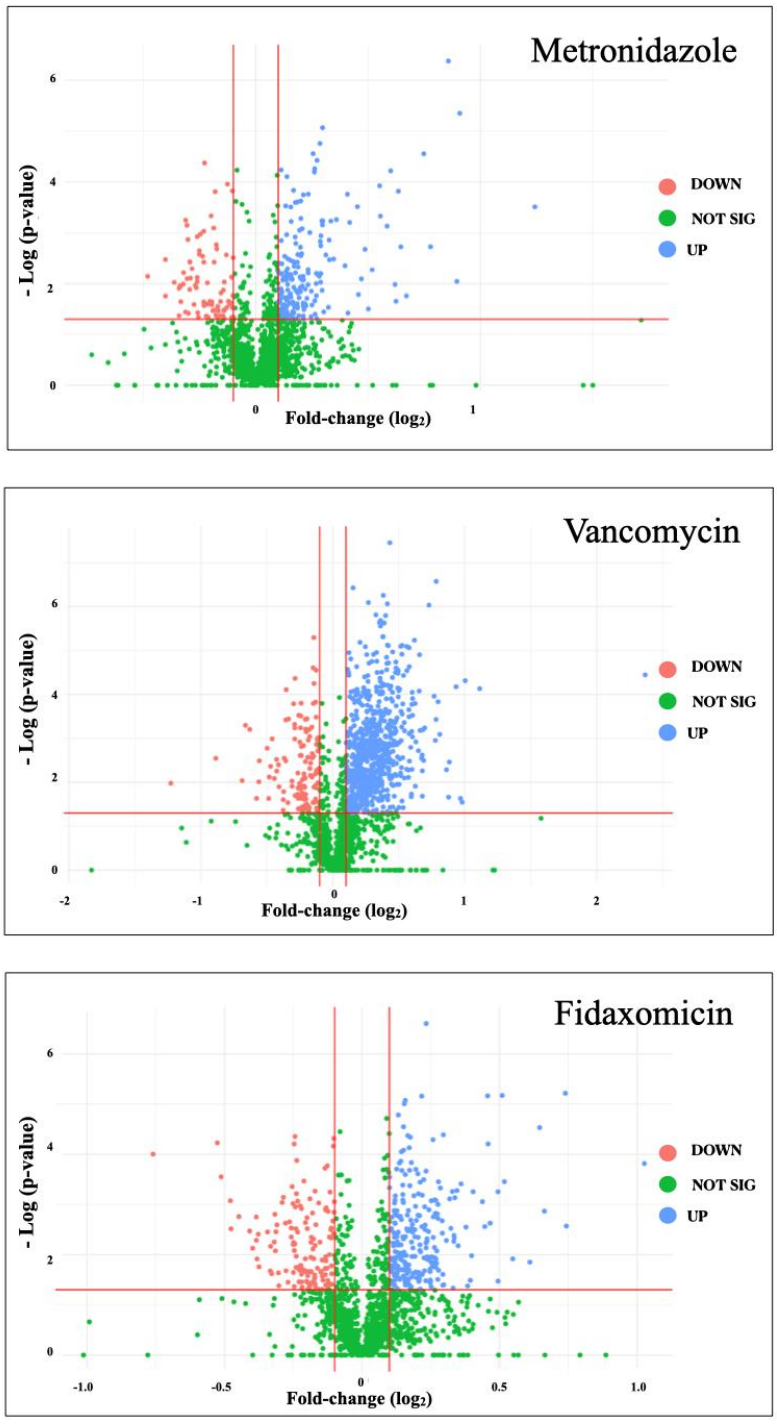

Figure 3

Quantitative proteomic analysis visualized by a volcano plot. The plot shows a negative natural log of the p-values plotted against the base2 logs of the change in each protein compared between the (a); Metronidazole, (b); Vancomycin, and (c); Fidaxomicin and control groups. Statistically significant results ($p < 0.05$) are plotted above the dashed line in the blue and red regions. Proteins significantly up- and down-regulated upon the antibiotics treatment are shown as blue and red dots, respectively.

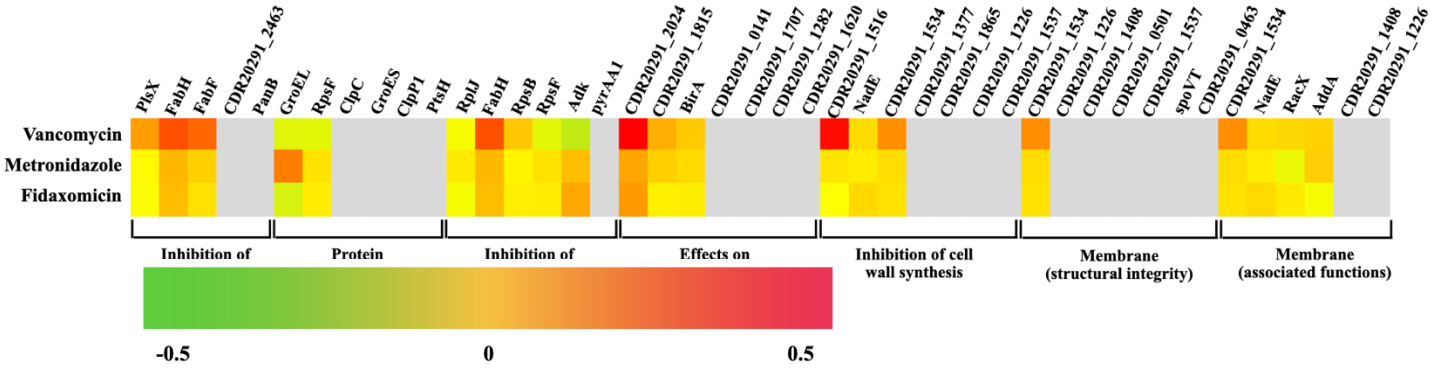

Figure 4

Heat map presenting differentially expressed of the proteins uniquely identified in the antibiotics treatment group. This information was obtained from KEGG database.

Table 2

The list of marker protein when *C. difficile* was challenged with antibiotic.
Vancomycin

Inhibition of cell wall biosynthesis			
Marker	Annotation	Fold change (log_2)	p-value
CDR20291_1516	ABC transporter, ATP-binding protein	0.4819	≤0.05
CDR20291_1377	putative ABC transport system ATP-binding protein	ND	ND
CDR20291_1865	tRNA guanine-N(7)-methyltransferase	ND	ND
NadE	NH(3)-dependent NAD(+) synthetase	0.0707	≤0.05
CDR20291_1226	putative transporter	ND	ND
CDR20291_1534	tellurium resistance protein	0.2213	≤0.05
CDR20291_1537	putative tellurite resistance protein	ND	ND
Other proteins (non-marker)			
AsnB	Asparagine synthase (Glutamine-hydrolyzing)	2.36621	≤0.05
HprK	HPr kinase/phosphorylase	1.5771	≤0.05
	SpoIIE family protein phosphatase	1.1124	≤0.05
	Polysaccharide biosynthesis protein	1.0024	≤0.05
	PTS system tagatose-specific transporter subunit IIABC	-1.1465	≤0.05
	Polyamine aminopropyltransferase	-1.2289	≤0.05

Metronidazole

Effects on nucleic acid			
Marker	Annotation	Fold change (log_2)	p-value
CDR20291_0141	putative sigma-54 modulation protein	ND	ND
CDR20291_1707	putative two-component system response regulator	ND	ND
CDR20291_2024	thioredoxin reductase	0.1760	≤0.05
CDR20291_1282	putative bifunctional protein: peroxiredoxin/chitinase	ND	ND
CDR20291_1620	probable acyltransferase	ND	ND
CDR20291_1815	putative membrane protein	0.0926	≤0.05
BirA	BirA bifunctional protein	0.0754	≤0.05
Other proteins (non-marker)			
	Amidohydrolase	1.2428	≤0.05

Fidaxomicin

Inhibition of protein biosynthesis			
Marker	Annotation	Fold change (log_2)	p-value
RplJ	50s ribosomal protein L10	-0.0184	≤0.05
CDR20291_0065	3-oxoacyl-[acyl-carrier-protein] synthase III	0.1287	≤0.05
RpsB	30s ribosomal protein S2	0.0317	≤0.05
RpsF	30s ribosomal protein S6	0.0375	≤0.05
Adk	adenylate kinase	0.1711	≤0.05
pyrAA1	carbamoyl-phosphate synthase, pyrimidine-specific, small chain	ND	ND
Other proteins (non-marker)			
	SpoIIE family protein phosphatase	1.0264	≤0.05

*ND represents Not detect.

Acknowledgements:

This study was supported by Mahidol University. The equipment was facilitated by Central Instrument Facility (CIF) at Faculty of Science, Mahidol University.

References:

1. Kachrimanidou M, Malisiovas N. Crit. Rev. Microbiol. 2011;37(3):178–87.
2. Lessa FC, Mu Y, Bamberg WM, et al. N Engl J Med. 2015;372(24), 2368–2370.
3. Burke KE, Lamont JT. Epub. 2014;8(1):1–6.
4. Doan T-H-D, Yen-Nicolaÿ S, Bernet-Camard M-F, Martin-Verstraete I, Péchiné S. PLoS One. 2020;15(11).
5. McDonald, L. C., Gerding, D. N., Johnson, S., et al. Clin. Infect. Dis. 2018;66(7).
6. Johnson, S., Lavergne, V., Skinner, A. M., et al. Clin. Infect. Dis. 2021;73(5).
7. Sigeti JS, Guiney DG Jr, Davis CE. J Infect Dis. 1983;148(6):1083-9.
8. Wang F, Zhou H, Olademehin OP, Kim SJ, Tao P. ACS Omega. 2018;3(1):37-45.

9. Artsimovitch, I., Seddon, J., & Sears, P. Clin. Infect. Dis. 2012;55.
10. Pal, R., & Seleem, M. N. PLoS One. 2022;17(8).
11. Petrosillo, N., Granata, G., & Cataldo, M. A. Front. Med. 2018;5.
12. Pal, R., Dai, M. & Seleem, M.N. Sci Rep. 2021;11(10913).
13. Nat Med. 2010;16(4), 347.
14. Aslam, B., Basit, M., Nisar, M. A., Khurshid, M., & Rasool, M. H. J. Chromatogr. Sci. 2016;55(2), 182–196.
15. Senges CH, Stepanek JJ, Wenzel M, Raatschen N, Ay Ü, Märtens Y, et al. Antimicrob. Agents Chemother. 2020;65(1).
16. CLSI document M11-A6. 2004.
17. Kunst, F., Ogasawara, N., Moszer, I. et al. 1997; 390, 249–256.
18. Wang J., Yang C., Zhang C., et al. Bioengineered. 2021; 12(1):745-754.
19. Brouwer, M. S., Warburton, P. J., Roberts, A. P., et al. PLoS One. 2011;6(8).
20. Phanchana, M., Phetruen, T., Harnvoravongchai, P., et al. Sci Rep. 2020;10(6497)
21. Bassères, E., Endres, B. T., Montes-Bravo, N., et al. Anaerobe. 2020;69(102352).
22. Corbett, D., Wise, A., Birchall, S., et al. J Antimicrob Chemother. 2015;70(6), 1751–1756.
23. Veiga, P., Erkelenz, M., Bernard, E., et al. J. Bacteriol. 2009;191(11), 3752–3757.

IDENTIFICATION OF POTENTIAL DRUG CANDIDATES FOR CHOLANGIOCARCINOMA FROM A META-ANALYSIS OF TRANSCRIPTOMIC PROFILES

Jakkapath Puriteerangkul[1], Titipatima Sakulterdkiat[2], Brinda Balasubramanian[1], Chawalit Ngernsombat[3], Rutaiwan Tohtong[1], Tavan Janvilisri[1]*
[1]Department of Biochemistry, Faculty of Science, Mahidol University, Thailand
[2]Department of Pathobiology, Faculty of Science, Mahidol University, Thailand
[3]Department of Preclinical Science, Faculty of Medicine, Thammasat University, Thailand

*E-mail: tavan.jan@mahidol.ac.th

Abstract:

Cholangiocarcinoma (CCA) is an epithelial carcinoma of the bile duct that can be distinguished into distinct subtypes based on anatomical sites. These CCA subtypes have genetic variability but lack a stereotyped genetic profile, resulting in the challenges of diagnosis and treatment. The obstacles in the diagnosis process result in a low survival rate for the patients with late stages of malignancies since CCA are unresponsive to conventional treatment. Therefore, finding the genetic profile of CCA is crucial for developing effective therapy. Several studies have used meta-analysis to extract novel insights into cancers from the data on available databases. In this study, we performed a meta-analysis of gene expression in CCA to identify candidate genes as a target for the treatment. The RNA-sequencing (RNA-seq) and array-based gene expression data of CCA and bile duct were retrieved from public databases, Gene Expression Omnibus (GEO) and European Bioinformatics Institute (EBI). The differentially-expressed genes (DEGs) presented in both platforms were used for downstream analysis. A total of 250 significant DEGs were identified that distinguished between CCA and adjacent normal tissues. Potential drug candidates based on DEGs were retrieved through Enrichr. We hope that our pipeline will lead us to identify novel therapeutic candidates for CCA.

Keywords: Meta-analysis, cholangiocarcinoma, transcriptomics, microarray, RNA-sequencing

Introduction:

Cholangiocarcinoma (CCA) is a cancer that develops from the epithelial layers of the bile ducts. It is a multifactorial disease with multiple risk factors, such as but not limited to, hepatitis C virus (HCV) infection, alcohol, and liver fluke infection, which account for less than 30% of all cases (1-3). The early stages of CCA are primarily asymptomatic leading to late diagnosis as the growth of the tumor mass causes bile duct obstruction leading to symptomatic presentation of painless jaundice or even palpable mass on the abdomen. The expression of upregulated CEA or CA19-9 antigen could aid in CCA diagnosis, however, this approach is not specific to only CCA since other benign diseases, such as cholangitis can also test positive for antigen detection (4). The difficulty of early CCA diagnosis results in lower survival rates for CCA patients. CCA are divided histologically into three subtypes based on anatomical origin and genetic stereotypes but research of these differences are severely lacking (5). The current curative approach for CCA patients is surgery, which is only limited to about one-third of the patients and is most effective in the early stages of diagnosis (6, 7). Advance stages of CCA require chemotherapy in combination with surgery to increase survival. Due to

these challenges in diagnosis and treatment options, identification of the genetic stereotypes of CCA could provide crucial information and novel insight for CCA diagnosis and treatment strategies.

Promising approaches, such as precision medicine and targeted therapy, are being developed to identify new therapeutic targets in CCA, especially for advanced-stage treatment. Differentially expressed genes (DEGs), which are responsible for aberrant phenotypes of CCA, pose as a potential target. The changes in gene expression trigger alteration in various pathways and cancer phenotypes, which could lead to aberrant cell cycle regulation, vascularization, metastasis and cancer aggressiveness. Therefore, identifying transcriptomic changes in CCA could provide vital insights and potential target candidates for CCA treatment.

At present, transcriptomic cancer profiles are accumulating and readily available. These data can be pooled and evaluated together on a large-scale to identify patterns and new insights (8, 9). Many studies have used transcriptomic analysis to determine the potential candidate that could be used as therapeutic targets (10). This study, therefore, aims to find novel therapeutic targets by performing a meta-analysis of DEG genes in CCA and to identify potential therapeutic candidates for CCA.

Methodology:

Data retrieval

RNA-seq and array-based transcriptome data of CCA and normal bile duct were retrieved from publicly available databases, Gene Expression Omnibus (GEO) (11) and European Bioinformatics Institute (EBI) (12), using search terms "cholangiocarcinoma", "human", and "tissue". The retrieved gene expression data of each platform were analyzed separately. For RNA-seq, the raw data were downloaded using SRA tools. The quality of the reads was evaluated by FastQC. The low-quality reads were trimmed using *trimmomatic* (13). The trimmed reads were aligned against *Homo sapiens* Genome Reference Consortium Human Build 38 by STAR (14). The mapped reads were summarized by featureCounts in Subread package (15). The RNA-seq data were normalized using the DEseq2 package (16). For array-based data, RStudio 2022.02.1+461 "Prairie Trillium" was used. The gene expression data were downloaded and extracted using *GEOquery* and *Biobase* package (17). Quantile normalization was performed on each dataset. Each probe was annotated based on the respective platform of each dataset using the *AnnotationDbi* package. The genes with multiple probes were averaged to obtain the representative expression of each gene. Subsequently, the normalized datasets were combined, and quantile normalized. The batch effect was also removed using the *limma* package (18).

Gene ontology (GO) analysis

Functional identification of DEGs was annotated by g:Profiler (19). Statistically significant genes were filtered using FDR-adjusted p-value < 0.05. The information on biological processes, cellular compartment, molecular function, and related pathways was retrieved. The enriched terms were then ranked based on the FDR-adjusted p values, and the top five terms in each category were shown.

Hierarchical clustering

The DEGs were clustered and visualized by the *pheatmap* package in R. The unsupervised hierarchical clustering was performed against array-based data using the DEGs obtained from DEG analysis. The PCA plot were generated by R and missing values were imputed by *missMDA* package (20).

Drug enrichment analysis

The upregulated and downregulated DEGs profile of CCA were analyzed using Drug Perturbations from GEO via Enrichr to find the enriched drugs (21). The top-ten ranked enriched drugs by *p*-values were presented.

Statistical analysis

The DEG analysis was performed to identify differentially expressed genes. The samples were compared between CCA and normal tissues. For RNA-seq data, DEGs were identified using the DEseq2 package. For array-based data, DEGs were identified using the *limma* package. The gene with FDR-adjusted *p*-value < 0.05 was considered as significantly differentially expressed between CCA and normal tissue. The genes considered significant in both RNA-seq, and array-based analysis were selected for further analysis.

Results and Discussion:

Identification of DEGs from a meta-analysis of RNA-seq and microarrays

The alterations in gene expression of CCA cause phenotypic changes and cancer progression. These alterations can result in the aggressiveness of cancer and poor prognosis in the patients. To identify DEGs in CCA, we manually curated transcriptomic data based on RNA-seq and microarrays from NCBI GEO and EBI. We retrieved 60 and 854 samples for RNA-seq and array-based data, respectively. The datasets consisted of 35 CCA and 25 normal tissues for RNA-seq data and 655 CCA and 199 normal tissues for array-based data.

Following the data retrieval, the RNA-seq and array-based transcriptomic data were analyzed separately. The normalization within and between samples was performed to confirm the validity of the comparison between each study. Subsequently, the DEG analysis between CCA and normal tissue samples was performed using the normalized data. As a result, 1,832 and 575 DEGs from RNA-seq-based and array-based analysis were detected, respectively. Among the total 2,157 DEGs found from both platforms, only 250 DEGs were found in both RNA-seq and array-based data (Figure 1A). We selected these overlapping DEGs with $\log_2$ fold change > 1 and *p*-values < 0.05 for further downstream analysis (Figure 1B).

Clustering CCA into molecular subtypes based on the DEGs

As previous studies have reported on the heterogeneity of CCA, we expected that the identified DEGs may be able to distinguish between CCA and normal tissues. Furthermore, we anticipated that the DEGs could differentiate CCA into different subtypes. To evaluate the subtypes that could be distinguished by the DEGs, we performed unsupervised hierarchical clustering using the identified DEGs based on our RNA-seq and array-based analysis against the array-based expression data. In the results, we found that the DEGs could be used to differentiate between CCA and normal samples. Furthermore, the CCA cohorts were further divided into five different subtypes, including subtype 3, which were clustered with the normal samples (Figure 2A). To validate that the identified DEGs could cluster the intrinsic molecular subtypes of these samples, we performed the PCA analysis using both DEGs and the whole transcriptomics against the microarray data. The PCA plot generated from both DEGs and the whole transcriptome could also distinguish the CCA into five subtypes (Figure 2B and C). These results revealed different molecular subtypes of CCA based on our DEGs. Our results coincided well with a previous study that distinguished CCA into five distinct subtypes based on the receptors tyrosine kinases profiles (22).

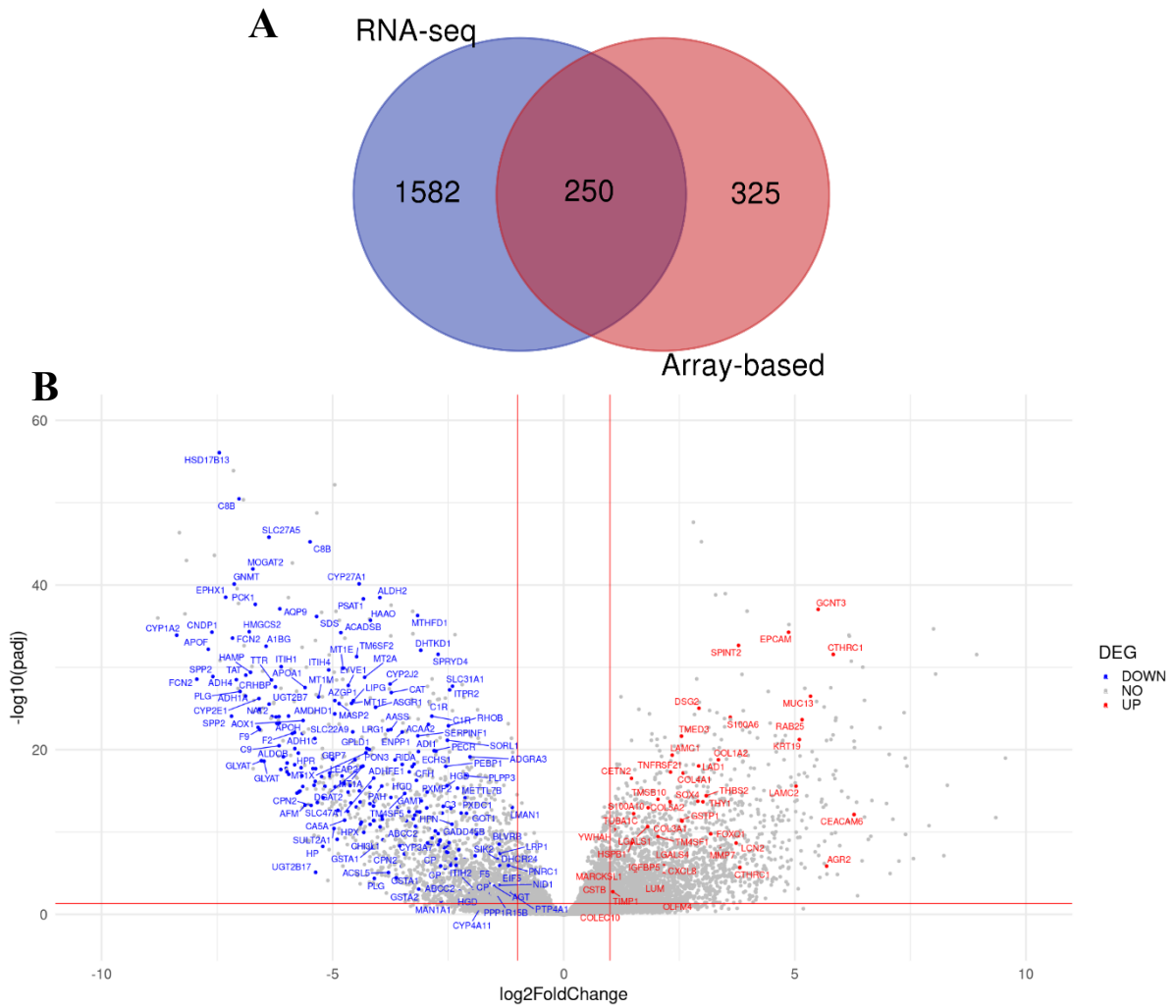

Figure 1. Differential gene expression analysis of RNA-seq-based and array-based data between CCA and normal tissues; (A) A Venn diagram represents the DEGs from both platforms. (B) The volcano plot represents significant DEGs between CCA and normal tissues in both RNA-seq-based and array-based data. The red line indicates the FDR-adjusted *p*-values <0.05 and $\log_2$ fold change > 1 and < -1. The method for differential gene analysis is the Wald test with FDR-adjusted p-values, **p* <0.05.

Gene ontology and pathway enrichment analysis

To assign the associated functional role of the DEGs, we performed the enrichment analysis via g:Profiler. The enriched term with FDR-adjusted *p*-values less than 0.05 were considered significant. The enriched terms were ranked by the FDR-adjusted *p*-values in which the top five enriched terms in Molecular Function, Cellular Compartment, Biological Process, and KEGG were presented. Some examples of the enriched pathways from the DEGs include "Complement and coagulation cascades" and "Metabolic pathways", suggesting that these pathways may play a critical role in CCA (Figure 3). Moreover, a previous study reported that the coagulation cascades, such as platelets, might also influence the circulating tumor cells, including their metastatic ability (23). These associated pathways could serve as a therapeutic target for CCA in the future.

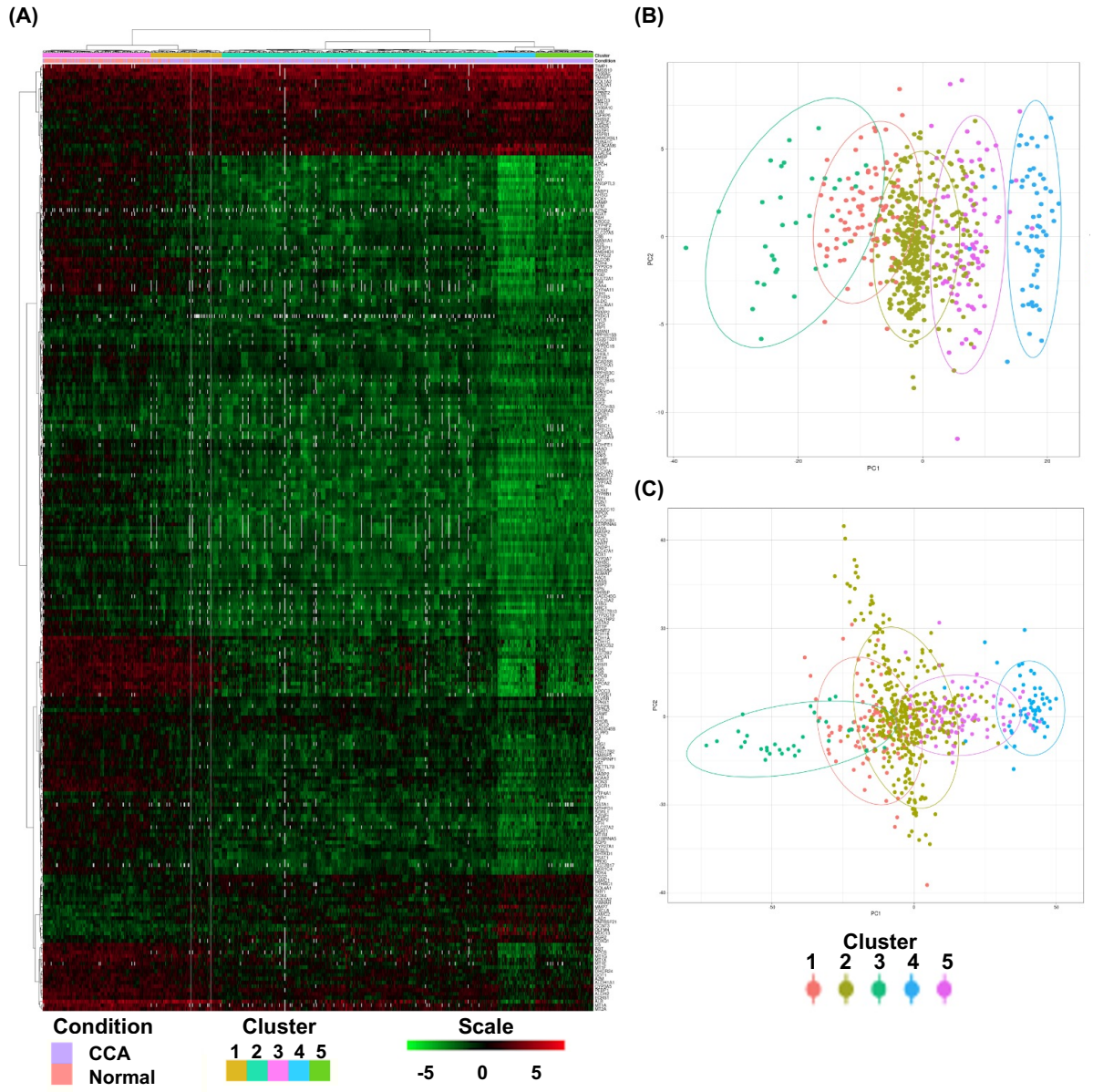

Figure 2. Clustering CCA into five different molecular subtypes; (A) The unsupervised hierarchical clustering using the DEGs. (B) The PCA plot of the CCA cohorts using the DEGs. (C) The PCA plot of the CCA cohorts using the whole transcriptome.

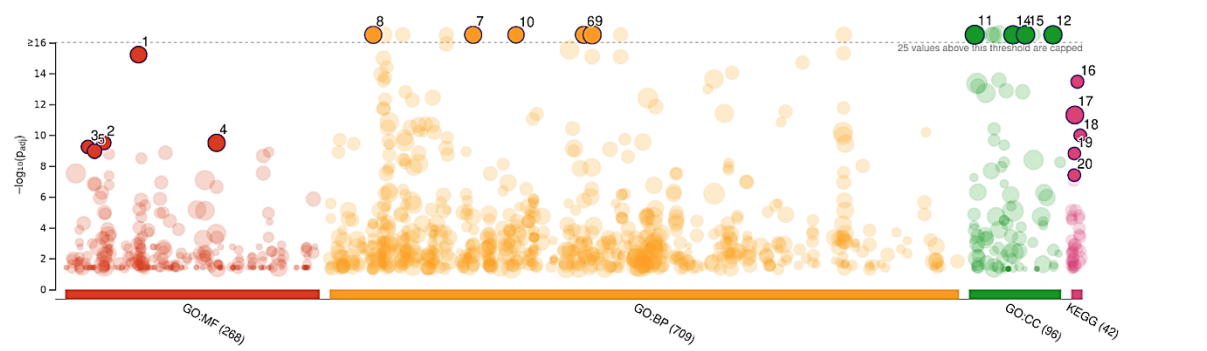

ID	Source	Term ID	Term Name	p_{adj} (query_1)
1	GO:MF	GO:0016491	oxidoreductase activity	6.178×10^{-16}
2	GO:MF	GO:0005506	iron ion binding	3.174×10^{-10}
3	GO:MF	GO:0004497	monooxygenase activity	5.851×10^{-10}
4	GO:MF	GO:0046914	transition metal ion binding	3.217×10^{-10}
5	GO:MF	GO:0004866	endopeptidase inhibitor activity	1.113×10^{-9}
6	GO:BP	GO:0043436	oxoacid metabolic process	1.502×10^{-38}
7	GO:BP	GO:0019752	carboxylic acid metabolic process	1.502×10^{-38}
8	GO:BP	GO:0006082	organic acid metabolic process	3.365×10^{-38}
9	GO:BP	GO:0044281	small molecule metabolic process	3.163×10^{-33}
10	GO:BP	GO:0032787	monocarboxylic acid metabolic process	1.570×10^{-29}
11	GO:CC	GO:0005615	extracellular space	8.181×10^{-38}
12	GO:CC	GO:1903561	extracellular vesicle	8.181×10^{-38}
13	GO:CC	GO:0065010	extracellular membrane-bounded organelle	8.181×10^{-38}
14	GO:CC	GO:0043230	extracellular organelle	8.181×10^{-38}
15	GO:CC	GO:0070062	extracellular exosome	1.621×10^{-37}
16	KEGG	KEGG:04610	Complement and coagulation cascades	3.461×10^{-14}
17	KEGG	KEGG:01100	Metabolic pathways	5.023×10^{-12}
18	KEGG	KEGG:05204	Chemical carcinogenesis - DNA adducts	1.035×10^{-10}
19	KEGG	KEGG:00982	Drug metabolism - cytochrome P450	1.557×10^{-9}
20	KEGG	KEGG:00980	Metabolism of xenobiotics by cytochrome P450	3.938×10^{-8}

Figure 3. The gene ontologies and pathways were enriched by the identified DEGs. The top five enriched terms in each category are shown in the figure. The enriched terms with FDR-adjusted p-values < 0.05 were considered significant. The numbered dots were labeled with the term ID, term name, and FDR-adjusted p values below.

Identification of drugs candidate from DEGs

To find the drug candidates that could serve as an alternative treatment to CCA. We used Enrichr to identify the drug candidates that may reverse the aberrant phenotypes of CCA cells. In Enrichr, the "Drug perturbations from GEO" contains gene sets that have been compared before and after drug treatment in the GEO database. The enriched drugs were ranked by the *p*-values. In our analysis, the candidate drugs including carbidopa, pioglitazone and caerulein from the upregulated DEGs (Figure 4A), and imatinib, rosiglitazone and PLX 4720 for downregulated DEGs in CCA (Figure 4B). Interestingly, carbidopa has been used for treating Parkinson's disease, but has also been reported to have anticancer effects in many cancers, such as pancreatic cancer and melanoma (24, 25). This evidence supports that this framework may provide screening for potential drug candidates that could serve as an alternative therapeutic compound for CCA.

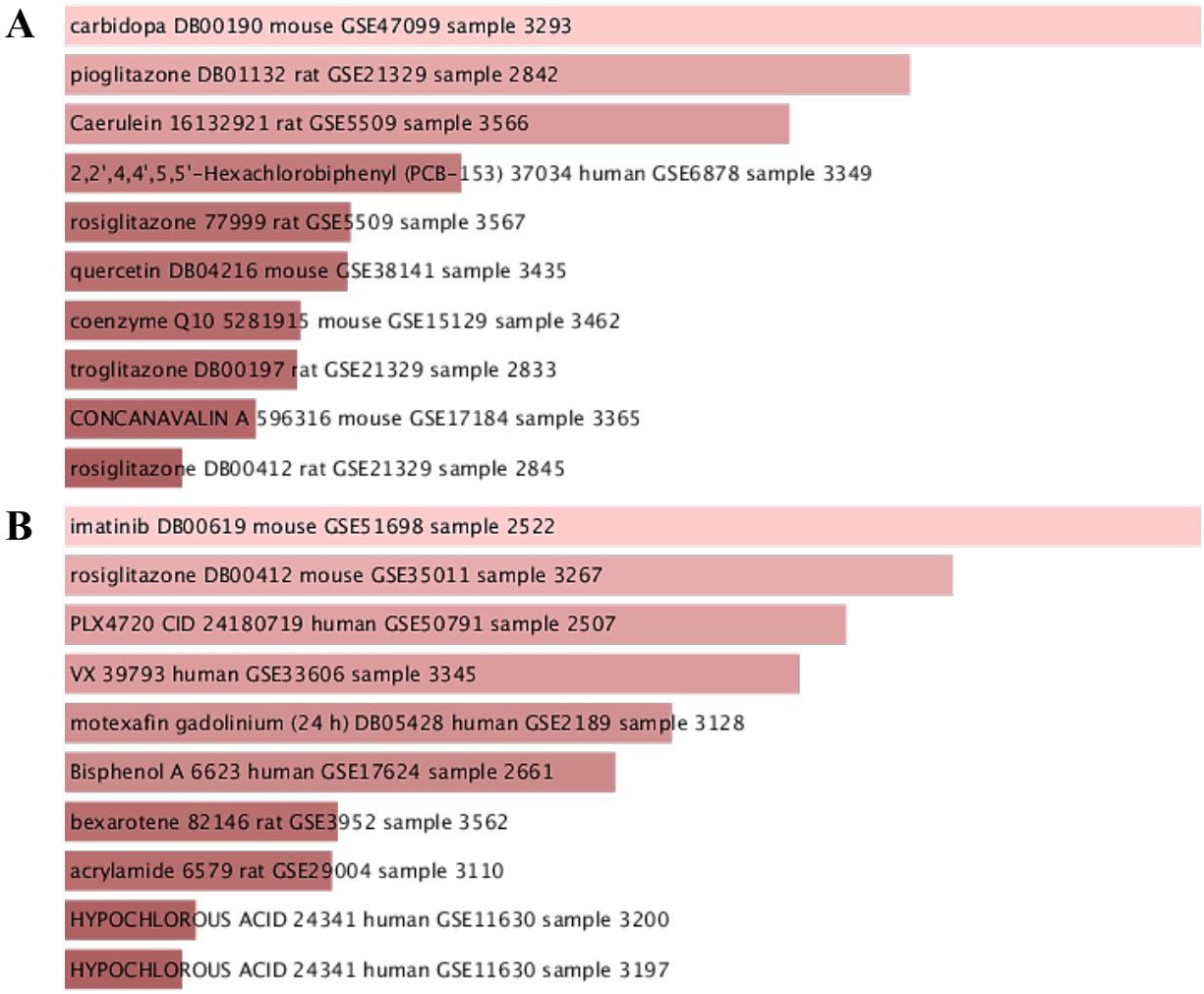

Figure 4. The top ten enriched drugs were ranked by p-values and shown as (A) enriched drugs from upregulated DEGs (B) and downregulated DEGs.

Conclusion:

The aberrant gene expression in CCA contributes to carcinogenesis, progression, and cancer aggressiveness, all of which leads to poor prognosis. There is still a lack of a stereotyped genetic profile for CCA that is necessary to identify its heterogeneity and genetic variability of CCA. In this study, we performed bioinformatics analysis framework to explore the genetic implication of CCA (Figure 5). We successfully identified the DEGs of CCA using the publicly available transcriptomic data in various databases, which are composed of both RNA-seq and array-based data via a meta-analysis approach. We identified 250 DEGs that were significant in both RNA-seq and array-based data. In addition, these DEGs could distinguish the CCA into five subtypes. We also found these subtypes were distinguishable in the CCA cohorts using the whole transcriptome analysis. Furthermore, we also discovered an association of the DEGs to the molecular function, cellular compartment, biological process, and associated pathways, indicating the vital role of these DEGs in contributing to the alterations of the enriched

pathways. Finally, we used the determined DEGs to propose the candidate drugs that could reverse the aberrant expression of CCA. In conclusion, we established the pipeline of identifying potential therapeutic targets and drug candidates that may reverse the abnormal expression of CCA. These targets and drug candidates are warranted for further investigations.

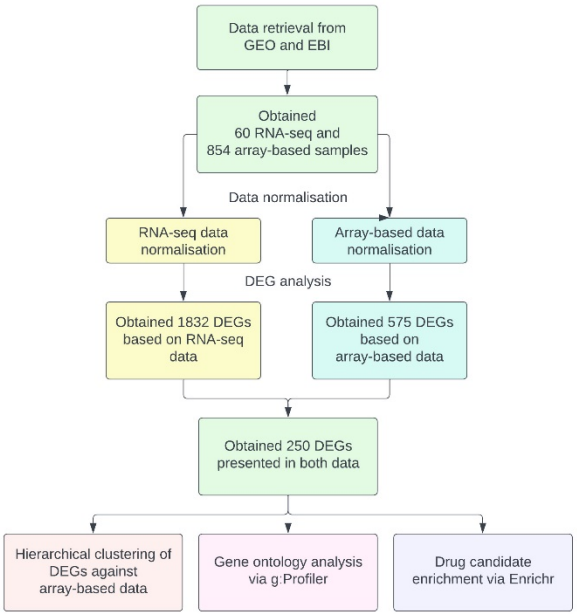

Figure 5. The overall framework in this study.

Acknowledgements:
This work is supported by Mahidol University.

References:

1. Shin HR, Lee CU, Park HJ, Seol SY, Chung JM, Choi HC, et al. Int J Epidemiol. 1996;25(5):933-40.
2. Lim MK, Ju YH, Franceschi S, Oh JK, Kong HJ, Hwang SS, et al. Am J Trop Med Hyg. 2006;75(1):93-6.
3. Sripa B, Kaewkes S, Sithithaworn P, Mairiang E, Laha T, Smout M, et al. PLoS Med. 2007;4(7):e201.
4. Metzger J, Negm AA, Plentz RR, Weismüller TJ, Wedemeyer J, Karlsen TH, et al. Gut. 2013;62(1):122-30.
5. Nakamura H, Arai Y, Totoki Y, Shirota T, Elzawahry A, Kato M, et al. Nat Genet. 2015;47(9):1003-10.
6. Khan SA, Davidson BR, Goldin RD, Heaton N, Karani J, Pereira SP, et al. Gut. 2012;61(12):1657.
7. Blechacz B, Gores GJ. Hepatology (Baltimore, Md). 2008;48(1):308-21.
8. Lee YH. Annals of laboratory medicine. 2015;35(3):283-7.
9. Deelen J, Evans DS, Arking DE, Tesi N, Nygaard M, Liu X, et al. Nature Communications. 2019;10(1):3669.
10. Bell R, Barraclough R, Vasieva O. Current molecular medicine. 2017;17(3):200-10.
11. Barrett T, Wilhite SE, Ledoux P, Evangelista C, Kim IF, Tomashevsky M, et al. Nucleic Acids Research. 2012;41(D1):D991-D5.
12. Kanz C, Aldebert P, Althorpe N, Baker W, Baldwin A, Bates K, et al. Nucleic Acids Res. 2005;33(Database issue):D29-33.

13. Bolger AM, Lohse M, Usadel B. Bioinformatics. 2014;30(15):2114-20.
14. Dobin A, Davis CA, Schlesinger F, Drenkow J, Zaleski C, Jha S, et al. Bioinformatics. 2013;29(1):15-21.
15. Liao Y, Smyth GK, Shi W. Bioinformatics. 2014;30(7):923-30.
16. Love MI, Huber W, Anders S. Genome Biology. 2014;15(12):550.
17. Davis S, Meltzer PS. Bioinformatics. 2007;23(14):1846-7.
18. Ritchie ME, Phipson B, Wu D, Hu Y, Law CW, Shi W, et al. Nucleic Acids Res. 2015;43(7):e47.
19. Raudvere U, Kolberg L, Kuzmin I, Arak T, Adler P, Peterson H, et al. Nucleic Acids Research. 2019;47(W1):W191-W8.
20. Josse J, Husson F. Journal of Statistical Software. 2016;70.
21. Kuleshov MV, Jones MR, Rouillard AD, Fernandez NF, Duan Q, Wang Z, et al. Nucleic Acids Res. 2016;44(W1):W90-7.
22. Balasubramanian B, Venkatraman S, Janvilisri T, Suthiphongchai T, Jitkaew S, Sripa J, et al. Pharmaceuticals (Basel). 2021;14(9).
23. Ward MP, E. Kane L, A. Norris L, Mohamed BM, Kelly T, Bates M, et al. Molecular Cancer. 2021;20(1):59.
24. Chen Z, Cai A, Zheng H, Huang H, Sun R, Cui X, et al. Oncogenesis. 2020;9(5):49.
25. Ganapathy V, Babu E, Ramachandran S, Bhutia YD. Cancer Research. 2016;76(14_Supplement):1015.

THE DESIGN OF A PLATELET-DERIVED GROWTH FACTOR DECOY

Chatcharee Lohanoot , Thaned kangsamaksin*

Department of Biochemistry, Faculty of Science, Mahidol University, Bangkok 10400, Thailand
*E-mail: thaned.kan@mahidol.ac.th

Abstract:

The platelet-derived growth factor (PDGF) family plays an essential role in controlling cell-to-cell communication and mediating complex biological processes including cell growth, differentiation, and motility of connective tissue cells. It consists of five ligand isoforms namely PDGF-AA, PDGF-AB, PDGF-BB, PDGF-CC, PDGF-DD and three receptor tyrosine kinase isoforms which are PDGFR-αα, PDGFR-αβ, and PDGFR-ββ. Previous evidence showed that PDGF signaling irregularity was involved in several types of cancer. Thus, inhibition of the PDGF-PDGFR interaction might serve as a potential therapeutic target for cancer therapy. In this study, we designed and developed a biologic PDGF inhibitor based on the structure of PDGFR-alpha (PDGFR-α) and fused with a heavy chain of immunoglobulin (Fc) or "PDGF decoy" to use it as a trap for PDGF ligands and block the PDGF-PDGFR signaling.

Introduction:

The platelet-derived growth factor (PDGF) family plays an essential role in cell growth and division. It is expressed in many cells such as fibroblasts, vascular smooth muscle, and endothelial cells. This family consists of five types of ligands namely PDGF-AA, AB, BB, CC, and DD and three receptor tyrosine kinases which are PDGFR-αα, αβ and ββ. Structure of PDGF polypeptide chains begin with signal peptide sequence (SP) that is used for protein navigation. The following part is pro-peptide sequence (PRO) that helps the protein transportation across endoplasmic reticulum. In addition, PDGF-C and PDGF-D also contain Complement subcomponents (CUB) that regulate the extracellular distribution of latent forms. Next, it is protease-recognition sequences that offers substantial structural stability and promotes the formation of homodimers or heterodimers. All PDGF ligands contain a cystine-knot motif that is responsible for recruiting their receptor interaction. To maintain flexible structure, PDGF-A and PDGF-B adopt positively charged amino acids such as arginine and lysine in their tails while PDGF-C and PDGF-D lack a tail section.

Their two receptors, namely PDGFR-α and PDGFR-β, belong to the class III receptor tyrosine kinases (RTKs). The coding sequences of PDGFR-α and PDGFR-β start with a signal peptide of different length followed by five extracellular immunoglobulin (Ig)-like domains, the single transmembrane (TM) helix and the kinase domain which carry auto-phosphorylation sites for phosphorylation of downstream molecules. In general, each dimer of PDGF ligands will bind differently to their receptors. For PDGF-AA, it can only bind to the homodimer of PDGFR-α while PDGF-AB can interact with either PDGFR-αα or PDGFR-αβ. For PDGF-BB, it can bind all types of PDGF receptors but preferentially bind with PDGFR-ββ. For PDGF-CC and PDGF-DD, they can bind to PDGFR-αα and PDGFR- ββ respectively; however, some studies found that they have weak interaction with PDGFR-αβ[1,4]. Once the PDGF ligands and receptors are bound to each other, the kinase domain will phosphorylate downstream molecules that regulate cell survival and growth in several cell types such as fibroblasts, vascular smooth muscle, and glial cells. Apart from the regulation of survival and growth in normal cells, the PDGF signaling also has been reported to be involved in many types of cancer cells. As their

substrate protein signaling molecules such as SRC tyrosine kinase subfamily, phospholipase C gamma (PLC-γ), phosphatidylinositol 3-kinase (PI3-K) play a role in cell membrane serine threonine residues which resulting in a variety of gene regulation and protein phosphorylation so, they can trigger normal cells to become abnormal or cancer cells when they are not well-regulated[3].

In this study, we aimed to design and develop an effective and specific inhibitor of PDGF signaling based on the structure of PDGFR-α and fused with a heavy chain of immunoglobulin (Fc) or "PDGF decoy" for serving as an alternative tool of anti-cancer drugs and improve cancer therapeutic strategies.

Methodology:

Cell culture

The Chinese hamster ovary (CHO) cell line was obtained from the American Type Culture Collection (ATCC). CHO cells were cultured in Nutrient Mixture F-12 Ham (Ham's F-12) medium under 5% CO_2 atmosphere at 37 ˚C. The medium was renewed once or twice between subcultures.

PDGF decoy plasmid amplification

Lyophilized PDGF decoy plasmid (GenScript) was added into *E. coli* XL 1 blue competent cells and incubated on ice 30 min then, heated at 42°C for 1.30 min before placing back on ice 2-3 min. 900 µL of LB Broth was added into the cells and incubated at 250 rpm, 37 °C for 60 min. After LB agar with 100 µg/mL of Ampicillin (AMP) antibiotic plate was prepared, the cells were transferred into the plate and incubated for 16 hours. The next day, the three single colonies of each plasmid were selected and incubated in a shakable incubator at 180 rpm, 37 °C overnight. After inoculation, 200 mL of LB broth with AMP was transferred into a flask and incubated at 180 rpm, 37 °C overnight. The DNA plasmids were extracted following the manufacturer's instructions and the DNA concentrations were measured by using nanodrop 2000 UV-Vis spectrophotometer at OD 260 nm.

PDGF decoy plasmid transfection and selection

1.8 x 10^6 cells of Chinese Hamster Ovary (CHO) cells were seeded into a 6-well plate and incubated overnight. On the following day, 5 µg of DNA plasmid was prepared in Opti-MEM medium with P3000 reagent and Lipofectamine® LTX in ratio 1:1 then, gently dropped 250 µL of the the DNA-Lipofectamine® LTX mixture solution into each well and the plate was incubated at 37°C under a 5% CO_2 atmosphere for 48 hours before subculture into 10-cm dish. Then, the transfected cells were selected by Geneticin (G418) treatment for 18-19 days or until the colonies were observed.

Protein extraction and Western blotting

The transfected cells were trypsinized and centrifuged at 17,000 rpm for 5 min. After removing supernatant, the cell pellet was resuspended by 1X PBS and transferred into the microtube then subsequently centrifuged at 5,000 rpm 5 min. The cell pellet was lysed by using Tris-EDTA-NaCl (TENT), pH 8.0 and Protease inhibitor (PI) mixture buffer together with centrifugation at 13,000 rpm at 4 °C for 15 min. Collect the supernatant in a new tube on ice and discard the pellet. Western blotting was performed following standard techniques. 8% separating gel and 5% stacking gel were applied for western blotting. Protein 30 µg was loaded into each well. 5% BSA and 2% BSA in 2% skim milk were used as blocking buffer and the blotted was washed with 1X PBST 3 times and subsequently incubated with 1° Anti-Human IgG (Fc specific)−Peroxidase antibody (1:10,000), β-actin mouse monoclonal antibody

(1:1,000) overnight and 2° antibody for beta-Actin : Anti-HRP mouse monoclonal antibody (1:1,000) for 1 hour.

Protein purification

Protein A HP SpinTrap (Cytiva, USA) columns were applied for the protein of interest purification. After column equilibration, cell lysate was diluted in 20 mM sodium phosphate, pH 7 (binding buffer) and subsequently loaded into the column. Next, the column was rinsed through 3 times by using the binding buffer. The protein of interest was eluted from the column by 0.1 M glycine-HCl, pH 2.7 (elution buffer) and kept in 1 M Tris-HCl, pH 9.0 (neutralizing buffer) at 20°C fridge. Centrifugation at 1,000 rpm for 2 min was involved in every step in the protein purification.

Coomassie staining

Coomassie Brilliant Blue R-250 (Biorad, USA) was used for gel staining. Coomassie stain was added into the gel and incubated for 1 hr on the shaker. Then, the gel was destained until the clear gel was observed.

Results and Discussion:

Design of the PDGF decoy structure

Many studies indicated that PDGFR-α can be associated with all types of PDGF ligands except PDGF-DD[4]. Therefore, we adopted PDGFR-α construction (figure 1A) to generate PDGF decoy. The previous study showed that only Ig 1 to 3 domains could sufficiently bind to PDGF-BB ligands with high affinity[5]. In addition, several monoclonal antibodies (mAbs)-based therapeutic in the markets required Crystallizable fragment (Fc) region of IgG for biological functions such as stability, aggregation, and immunogenicity[6]. Thus, we designed the PDGF decoy by assembling the sequences of the signal peptide (SP) section to Ig-like domain 1 to 3 and fused with Fc segment (Figure 1B). SP-(Ig1-3)-Fc fragment was constructed into a mammalian expression vector which is pcDNA3.1(+) and tagged with C-Myc. After we designed the composition of the PDGF decoy, we provided the outline to GenScript for lyophilized PDGF plasmid construction.

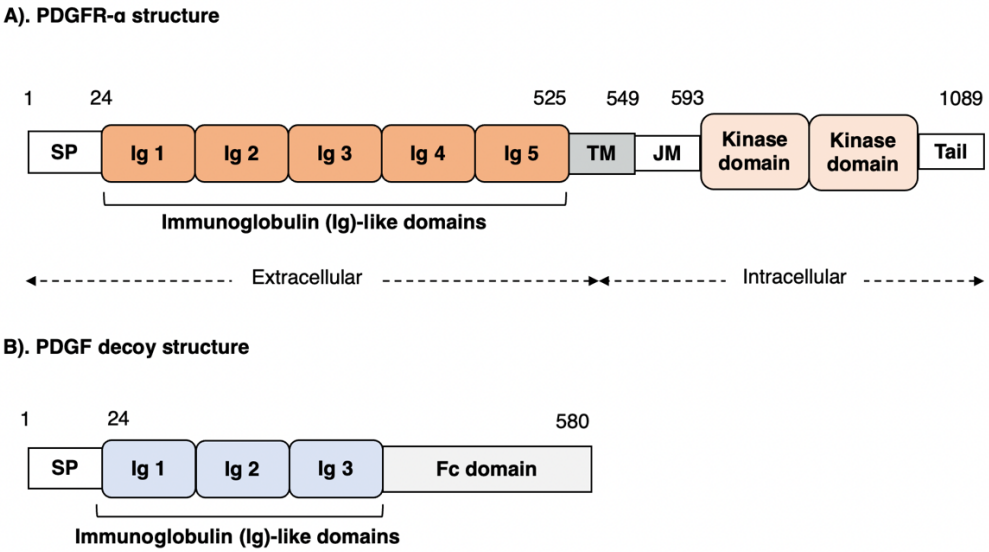

Figure 1. Schematic of full length of (A) PDGFR-α started with signal peptide (SP) part followed by Immunoglobulin (Ig)-like domain (Ig) 1 to 5, The single transmembrane helix (TM), Juxtamembrane domain (JM), The kinase domain and tail. (B) PDGF decoy**,** we designed to fuse Ig domain 1 to 3 with signal peptide (SP) together with Fc domain to stabilize the structure. The number represents amino acid sequences.

Transfection of the PDGF decoy expression plasmid in Chinese Hamster Ovary (CHO) cells

After transformation of *E. coli* with lyophilized PDGF decoy plasmid and extraction was carried out following the manufacturer's instructions. The DNA concentration was measured and further used for transfection into the CHO cell line. After seeding CHO cell line at 1.8 x 10^6 cells into each well of 6-well plate and incubated overnight, then the DNA-Lipofectamine® LTX mixture solution was transfected into CHO cell line by using Lipofectamine™ 3000 Reagent followed Thermo Fisher's protocol. After 2 days from transfection, we subcultured the transfected cells into a 10-cm dish and placed them under a 5% CO_2 atmosphere at 37 °C overnight. On the following day, Geneticin (G418) which is an aminoglycoside antibiotic was used for selection of the transfected cells due to the plasmid consists of Neomycin resistance (NeoR) gene (figure 2) thus, the transfected cells could resist and survive in the presence of G418 while the normal cells did not survive due to polypeptide synthesis inhibition from G418. In the presence of G418, the transfected cells could grow normally, and we could observe their colonies under microscope after treatment for 2 weeks; however, the normal cells gradually floated and died from days 4-5 of the treatment. We continued to subculture the transfected cells in the presence of G418 and harvested the pellet for protein purification.

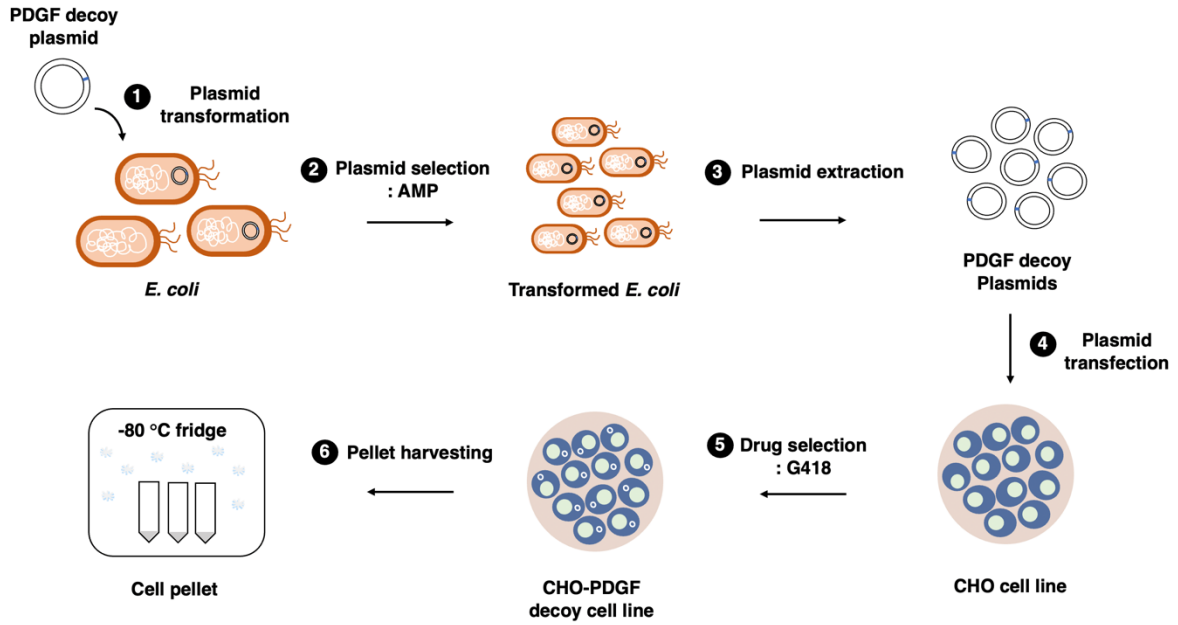

Figure 2. Schematic of PDGF decoy transformation and transfection into *E. coli* and CHO cell line. PDGF decoy plasmid was transformed into *E. coli* by heat shock method and subsequently, selected the transfected cells by using Ampicillin (AMP). After PDGF decoy plasmids were extracted following the manufacturer's instructions. The PDGF decoy plasmids were transfected into the CHO cell line by Lipofectamine™ 3000 Reagent following Thermo Fisher's protocol. 400 µg/mL of G418 drug was used for CHO cell line expressing PDGF decoy (CHO-PDGF decoy cell line) selection. The pellet was kept in the fridge until use.

PDGF decoy could be purified by using Protein A HP SpinTrap

After we could verify and extract cell lysate from CHO-PDGF decoy cell line, we further purified the decoy by using Protein A HP SpinTrap that is prepacked with Protein A Sepharose High Performance, a proven medium with strong affinity for IgG subclasses. After we equilibrated and washed the column with a binding buffer, the protein of interest was eluted for 3 times. Then, we performed gel electrophoresis (SDS-PAGE) and stained the gel with Coomassie Brilliant Blue R-250 (Biorad, USA). After washing the gel, we could not visualize the band on elution fractions (figure 3A) however, the specific bands on the elution fractions after performing the western blotting were observed (figure 3B). This might result from the quantity of our protein of interest being too low and unable to detect from Coomassie Stain.

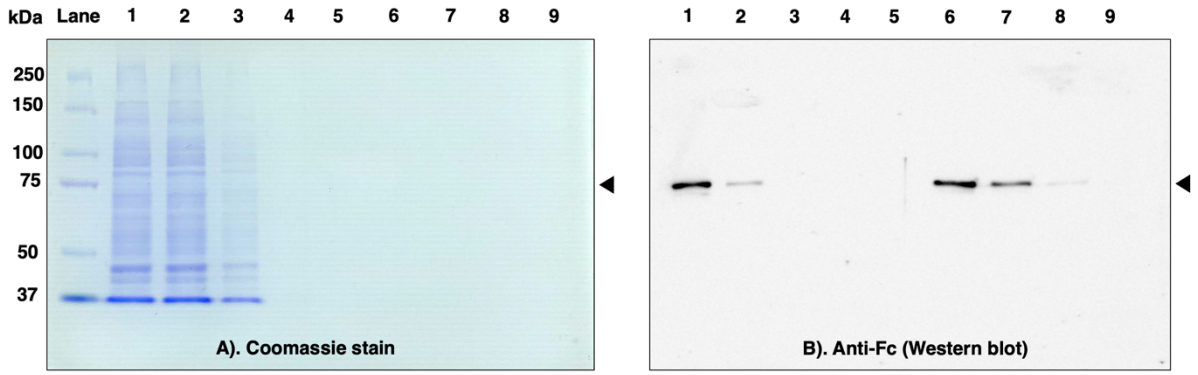

Figure 3. Gel electrophoresis. After purification using the Protein A HP SpinTrap, gel electrophoresis was performed and subsequently stained with (A) Coomassie or (B) probed with an anti-Fc antibody. Lane numbers represent different purification fractions: cell lysate (1), flow-through (2), wash (3-5), and elution (6-9) respectively. Arrows indicate PDGF decoy.

Conclusion:

In this study, we successfully designed the PDGF decoy by using the PDGFR-α as a template and fused with the Fc fragment to stabilize the structure. We chose CHO cells as a host to produce the decoy, and G418 was applied to select transfected cells. Then, we used the Protein A HP SpinTrap column for decoy purification and obtained the purified protein with correct size, which will be further tested in subsequent experiments for their physical and biological activities. However, the purification method used in our study might not be appropriate for large-scale applications.

Acknowledgements:

This work was financially supported by Mahidol University (T.K.). We would like to thank Ruchanok Tinikul, Jirundon Yuvaniyama, Philaiwarong Kamutira, and Chanisara Kaewsasan for technical assistance.

References:

1. Tallquist M, Kazlauskas A. Cytokine Growth Factor Rev. 2004;15(4):205-13.
2. Farooqi AA, Siddik ZH. Cell Biochem Funct. 2015;33(5):257–265.
3. Huang F, Wang D, Yao Y, Wang M. Int J Clin Exp Med. 2017;10(7):9918-9929.
4. Evrova O, and Buschmann J. Eur. Cells Mater. 2017;34:15-39.
5. Heidaran M.A, Mahadevan D, and Larochelle W.J. FASEB J. 1995;9:140-145.
6. Li W, Zhu Z, Chen W, Feng Y, Dimitrov DS. Front. Immunol. 2017;8:1554

PREDICTING SPECIES DISTRIBUTION USING MAXENT – CASE OF THE SIMPLE THALLOID LIVERWORT GENUS *Aneura* Dumort. IN THAILAND

Nopparat Anantaprayoon[1] and Ekaphan Kraichak[1, 2, *]
[1] Department of Botany, Faculty of Science, Kasetsart University, Bangkok 10900, Thailand
[2] Biodiversity Center Kasetsart University (BDCKU), Bangkok 10900, Thailand
*e-mail: ekaphan.k@ku.th

Abstract

Aneuraceae is the largest family of the simple thalloid liverworts. Member of Aneuraceae is well-known for its unique ecological habitat, cryptic diversity, and species-rich lineages. Many of its members, such as the genus *Aneura*, have cosmopolitan distributions. However, the environmental factors associated with such distributions are poorly studied. In this study, we used the maximum entropy (MaxEnt) species distribution modeling (SDM) to predict potential locations and relevant ecological factors of *Aneura in an* area of Thailand. The results showed that the important variables were the maximum temperature of warmest month, annual precipitation, and precipitation of the warmest quarter. Thus, the possible locations for future exploration would be the north-to-southwestern and peninsular regions of Thailand, together with some major mountain ranges. The MaxEnt SDM performed equally well with only the three most important variables. Our results demonstrated the possibility of using SDMs in further explorations of bryophytes in Thailand.

Introduction

Among the simple thalloid liverworts, the Aneuraceae is the most species-rich number within this group[1, 2]. This family comprises over 360 taxa from 5 genera. Members of Aneuraceae are often challenging to work with for several reasons. First, only a small number of morphological traits are available to examine due to their simple life form. Second, one of the taxonomically essential characters is oil bodies. These structures disappear rapidly in a few days or weeks and cannot be used for identifying specimens from the herbarium[3]. Therefore, a complete taxonomic work will require the examination of fresh specimens in the field.

The genus *Aneura* Dumort. is among the most difficult to study taxonomically and ecologically. So far, a total of 49 species have been reported worldwide, many of which have cosmopolitan distributions. Two species have been reported in Thailand, including *A. pinguis* (L.) Dumort.[4] and *A. maxima* (Schiffn.) Steph.[5]. The *A. pinguis*, also known as the "Greasewort", has been recognized for its complication with species delimitation and cryptic speciation[2, 6, 7, 8]. A lack of specimens and ecological data has made it challenging to clarify the taxonomic status of this genus.

Species distribution models (SDMs) have been widely used for predicting potential habitats for a taxon. They have become a tool for identifying potential conservation sites, informing sustainable forest management, and studying more profound questions in biogeography, ecology, and biodiversity[9, 10, 11]. These models are implemented only with observational data and environmental or physical factors. Biologists have increasingly applied these approaches to their study organisms to lower the time and effort in finding and collecting specimens[12, 13] and further their understanding of their organisms' ecology.

In this study, we focused on species distribution modeling with the maximum entropy (MaxEnt) algorithm for the liverwort genus *Aneura*, based on collected specimens or occurrences that are available in major bryophyte herbaria of Thailand. Specifically, we aimed

1) to identify potential distributions of *Aneura* in Thailand for future exploration and 2) to determine the important climatic variables associated with the distribution of *Aneura*. The results from this study will help us identify the potential areas for future research and deepen our understanding of the ecology of the poorly known genus for conservation purposes in the future.

Methodology

Data collection

We searched for the plant specimens and records of *Aneura* from all major herbaria in Thailand with databases of bryophyte collection. Identification has been made but verified by the curators and bryologists from each herbarium (CMUB, PSU, Department of Biology of Burapha University). Additional specimens were collected from our own field trips across the country. A total of 43 liverwort records were compiled and georeferenced to yield the coordinates (latitude and longitude) for each specimen.

Species distribution model analysis

All the analyses were conducted with the R environment 4.2.1[14]. We used commands from package 'raster'[15] to obtain bioclimatic variables (Table 1) from the WorldClim Database[16]. The climate dataset was cropped to the extent of the political boundary of Thailand. Occurrence data were randomly partitioned into training and testing sets at 70 and 30 percent, respectively. To apply the MaxEnt model to our occurrence dataset, we used the 'maxent' command from the package 'dismo'[17] with the pseudo-absence from 1,000 random points within the map extent. We calculated the threshold-independent area under the curve (AUC) with the receiver operating characteristic (ROC) plot as a criterion for the model performance. The AUC of 0.7 or greater is considered a reasonably good model[18].

To determine the importance of each climatic variable, we used the Jackknife test to determine if regularized training gain changed in the absence of a particular variable and the presence of only that variable in the model[19]. We also repeated modeling with only the three most important variables (the reduced model). We computed the AUC values to see whether a smaller set of climatic variables could perform sufficiently well compared to the full model.

Finally, we plotted variable response curves and predicted occurrences maps from the full and the reduced models to examine the differences in resulting predictions and important environmental variables for distributions of *Aneura* in Thailand.

Results and Discussion

Model performance and variable importance

The full MaxEnt model with all 19 climatic variables yielded the AUC value of 0.903. The variables bio5, 7, 8, 12, 17, and 18 contributed the most to the prediction of the *Aneura* distribution (Table 1). However, the permutation tests showed that only three variables contributed substantially to the model, including bio5, 12, and 18, which were maximum temperature of warmest month, annual precipitation, and precipitation of warmest quarter, respectively (Figures 1, 2). The results suggested strong autocorrelations among the 19 climatic variables and the possibility of a better-performing model with fewer variables.

We performed the analysis on the reduced model with only bio5, 12, and 18. The AUC value of the reduced model was 0.904, similar to that of the full model. The resulting predicted distributions of the two models were almost identical (Figure 3). The results suggested that these three variables were sufficient in creating a distribution model of *Aneura* in Thailand and potentially important ecological variables for this genus. This combination of climate variables was also the top three most contributing variables from a MaxEnt modeling study in

Hypopterygium tamarisci, a pleurocarpous moss species in Central and South America[20]. Many bryophyte groups likely share a similar set of climate requirements at this data resolution.

Response curves and Predicted occurrences

The response curve for the maximum temperature in the warmest month (bio5) showed a rapid decrease in predicted value when the temperature exceeded 30 °C. The response curves of precipitation variables (bio12 and 18) predicted a higher probability when annual precipitation was lower than 1,200 mm, and the precipitation of the warmest quarter was between about 200–400 mm (Figure 2). The response to the temperature was consistent with our personal observation, as we often found *Aneura* in colder areas. The precipitation responses were atypical for most bryophytes which generally require more rainfall. However, our specimen collection showed that these specimens were often found in moist areas but not necessarily the areas with heavy rainfall. Additional factors, such as relative humidity (RH) and Vapor Pressure Deficit (VPD), could be more relevant variables for future species distribution modeling studies of bryophytes.

The predicted distribution in both models showed potential occurrences in the North- and Southwestern, spanning from Tak, Kanchanaburi, Phetchaburi, Prachuap Khiri Khan to Peninsular Thailand, and mostly mountain ranges like Phetchabun, middle Tenasserim, and San Kala Khiri (Figure 3). In our datasets, no specimens have been collected from the Western mountains and Phetchaburi areas before. These areas should be a priority for the next expedition for this genus in Thailand.

Although, *Aneura* has been described as cosmopolitan, the global records are surprisingly lacking even in the Global Biodiversity Information Facility (GBIF) database, which did not contain a single record of this genus in Thailand. Missing data points result from taxonomical and geographical biases in database participation, which can dramatically affect the model's accuracy. When the observation is spatially clustering or filtering, the prediction seems to be overfitting[21]. Fortunately, we were able to obtain the occurrence data from the local herbaria across the country and less likely to be affected by the geographical clustering of the occurrence data.

The accuracy of the SDM is highly dependent on the environmental variables, ecological niche, and reproductive biology of the study organisms[20]. Most SDM methods focus on the presence or absence of the organisms in conjunction with environmental factors at a broader scale. Abundances, colony size, the existence of host species, and the microclimatic conditions cannot be directly incorporated into the current modeling techniques. While a model might appear incomplete, the broad-scale prediction from the SDM techniques can help us narrow down the study areas and reduce the collecting efforts for many taxa that quickly disappear from land use global climate changes.

Table 1 Environmental variables in this study, percentage contribution and permutation importance through the MaxEnt model for predicting species occurrence.

Codes	Variables[a]	Percent contribution	Permutation importance
bio1	Annual Mean Temperature	0	0
bio2	Mean Diurnal Range	0	0
bio3	Isothermality	0	0.1
bio4	Temperature Seasonality	0	0
bio5	Max Temperature of Warmest Month	3	7.1
bio6	Min Temperature of Coldest Month	0	0
bio7	Temperature Annual Range	0.6	3.3
bio8	Mean Temperature of Wettest Quarter	76.3	16.7
bio9	Mean Temperature of Driest Quarter	0	0
bio10	Mean Temperature of Warmest Quarter	0.6	0
bio11	Mean Temperature of Coldest Quarter	0.4	0.4
bio12	Annual Precipitation	2.1	39.7
bio13	Precipitation of Wettest Month	0	0.2
bio14	Precipitation of Driest Month	1.4	1.9
bio15	Precipitation Seasonality	0.7	0
bio16	Precipitation of Wettest Quarter	7	0
bio17	Precipitation of Driest Quarter	1.6	13.6
bio18	Precipitation of Warmest Quarter	1.6	14
bio19	Precipitation of Coldest Quarter	4.7	3.1

[a]https://www.worldclim.org/data/bioclim.html

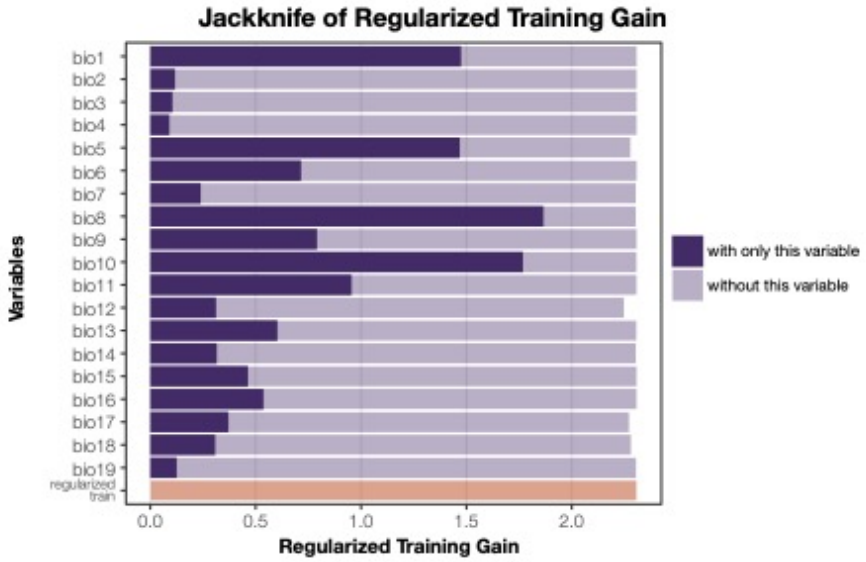

Figure 1 Jackknife test of regularized training gain shown effect of presence and absence each parameter in this MaxEnt modeling. The performance of the full model with all variables is displayed as the orange bar.

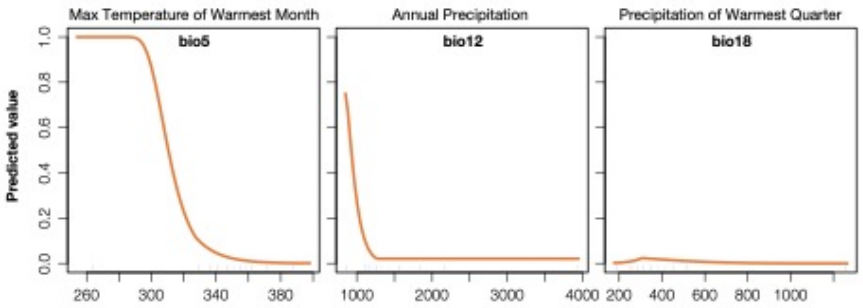

Figure 2 The response curves of the three most influential variables from the permutation and Jackknife tests.

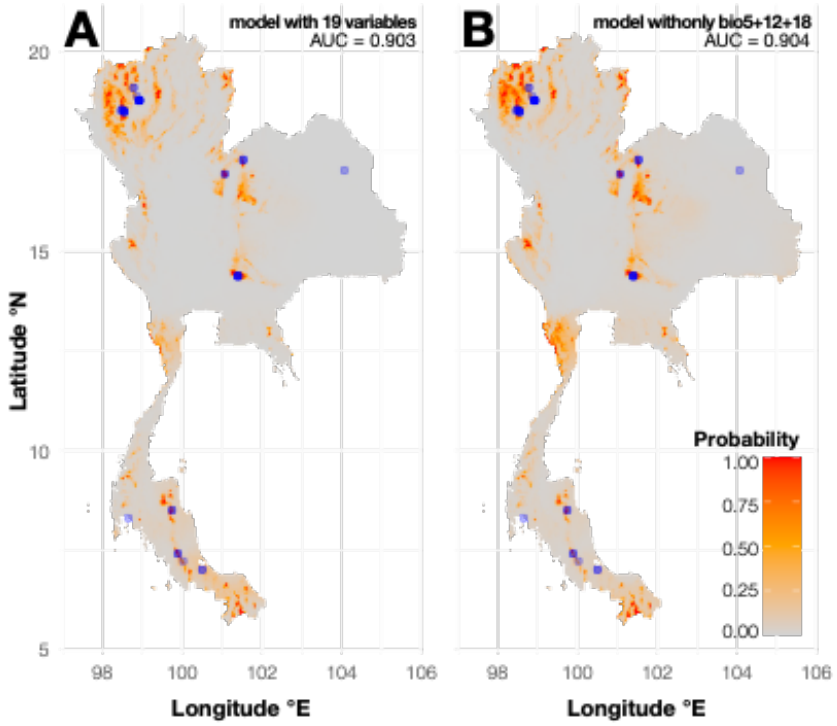

Figure 3 Predicted species distribution of the genus *Aneura* in Thailand (A) with 19 bioclim variables, and (B) with only the three most influential variables (bio5, 12, and 18) along with their respective area under curves (AUCs).

Conclusion

Species distribution modeling of Thai *Aneura* records with the MaxEnt algorithm showed predicted occurrences under the important variables are the max temperature of warmest month, annual precipitation, and precipitation of warmest quarter. Thus, the probable regions for future exploration would be the north-to-southwestern and peninsular regions of Thailand, together with some mountain ranges.

Acknowledgements

We would like to thank with gratefulness to the following colleagues for their supports with the specimens: Sahut Chantanaorrapint and Jiroat Sangrattanaprasert from Department of Biology, Prince of Songkla University, Phiangphak Sukkharak from Department of Biology, Burapha University, and Narin Printarakul from Department of Biology, Chiang Mai University. Nopparat Anantaprayoon's graduate program was supported by the Graduate Program Scholarship from the Graduate School, Kasetsart University. This project was financially supported by the Office of the Ministry of Higher Education, Science, Research, and Innovation, and the Thailand Science Research and Innovation through the 2021 Kasetsart University Reinventing University Program, Thailand, and by National Research Council of Thailand (NRCT), 2022 annual funding under Thailand Science Research and Innovation (TSRI).

References

1. Furuki T. The Journal of the Hattori Botanical Laboratory. 1991;70:293-397.
2. Preußing M, Olsson S, Schäfer-Verwimp A, Wickett NJ, Wicke S, Quandt D, Nebel M. Taxon. 2010;59(5):1424-1440.
3. Bakalin VA. Botanica Pacifica: a Journal of Plant Science and Conservation. 2018;7(2):3-21.
4. Lai MJ, Zhu RL, Chantanaorrapint S. Annales botanici fennici. 2008;45(5):321-341.
5. Frahm JP, Pollawatn R, Chantanaorrapint S. Tropical bryology. 2009;30(1):17-18.
6. Bączkiewicz A, Szczecińska M, Sawicki J, Stebel A, Buczkowska K. PLOS one. 2017 ;12(12):e0188837.
7. Polok K, Zielinski R. Cryptogamie, Bryologie. 2008;29(1):3-21.
8. Wachowiak W, Bączkiewicz A, Chudzińska E, Buczkowska K. Botanical Journal of the Linnean Society. 2007;155(2):273-282.
9. Srivastava V, Lafond V, Griess VC. CABI Reviews. 2019:1-3.
10. Guisan A, Tingley R, Baumgartner JB, Naujokaitis-Lewis I, Sutcliffe PR, Tulloch AI, Regan TJ, Brotons L, McDonald-Madden E, Mantyka-Pringle C, Martin TG. Ecology letters. 2013;16(12):1424-1435.
11. Cayuela L, Golicher DJ, Newton AC, Kolb M, De Alburquerque FS, Arets EJ, Alkemade JR, Pérez AM. Tropical Conservation Science. 2009;2(3):319-352.
12. Mi C, Huettmann F, Guo Y, Han X, Wen L. PeerJ. 2017;5:e2849.
13. Newbold T. Progress in Physical Geography. 2010;34(1):3-22.
14. R Core Team. R Foundation for Statistical Computing, Vienna, Austria. https://www.R-project.org/.
15. Hijmans RJ, Van Etten J, Cheng J, Mattiuzzi M, Sumner M, Greenberg JA, Lamigueiro OP, Bevan A, Racine EB, Shortridge A, Hijmans MR. R package. 2015;734.
16. Fick SE, Hijmans RJ. International journal of climatology. 2017;37(12):4302-4315.
17. Hijmans RJ, Phillips S, Leathwick J, Elith J, Hijmans MR. Circles. 2017;9(1):1-68.
18. Warren DL, Seifert SN. Ecological applications. 2011;21(2):335-342.
19. Wildt AR, Lambert ZV, Durand RM. Journal of Marketing Research. 1982;19(1):99-107.
20. Kruijer H, Raes N, Stech M. Nova Hedwigia. 2010;91(3):399.
21. Promnikorn K, Jutamanee K, Kraichak E. Agriculture and Natural Resources. 2019;53(1):44-48.

EFFECTS OF CANNABINOID RECEPTOR AGONISTS ON BREAST CANCER AND OSTEOBLAST INTERACTION

Janjira Kanjanapipak,[1] Chartinun Chutoe,[1] Ingon Inson,[1] Kanlaya Katewongsa,[1] Kornkamon Lertsuwan[1,2]*
[1]Department of Biochemistry, Faculty of Science, Mahidol University, Bangkok, Thailand
[2]Center of Calcium and Bone Research (COCAB), Faculty of Science, Mahidol University, Bangkok, Thailand
*e-mail: kornkamon.ler@mahidol.edu

Abstract:

Breast cancer is one of the biggest global health concerns. Bone has been reported as a frequent site of breast cancer metastasis resulting in bone pain, bone fracture and hypercalcemia. Cannabinoid receptor (CB) agonists are synthetic cannabinoids that exhibit cannabimimetic effect and have shown the anticancer activity against multiple types of malignant tumors. However, the effect of CB agonists on breast cancer and bone interaction is still unclear. The purpose of this research is to determine the effect of CB agonists on breast cancer-induced osteoblastic cell death. The IC_{50} values of CB agonists, ACEA and GW405833 in breast cancer cell lines were obtained by performing MTT assay. At 48 h after the treatment, the IC_{50} values of ACEA were 41.23 µM and 225.9 µM in MDA-MB-231 and MCF-7, respectively. The IC_{50} values of GW405833 were 24.23 µM and 88.39 µM for MDA-MB-231 and MCF-7, respectively. Moreover, osteoblast (UMR-106) cell viability was decreased significantly upon the exposure of breast cancer conditioned media. Interestingly, negative effect of conditioned medium derived from MDA-MB-231 cells was also recovered by the pretreatment of GW405833 on MDA-MB-231. To explore the potential breast cancer-derived factor(s) affected from GW405833 treatment, qRT-PCR was used. Our results revealed that GW405833 did not suppress IL6 expression, but upregulated the expression of Wnt signaling inhibitor, sclerostin (SOST). Taken together, our results suggested that CB agonists induced breast cancer cell death and GW405833 improved viability of osteoblastic cell in breast cancer and bone interaction.

Introduction:

Breast cancer has emerged as one of the major health issues worldwide.[1] The significant risk factors reported for breast cancer development include age, genetic, reproductive factors, hormones, and lifestyle.[2] Due to the different molecular subtypes, various treatment options have been used for the patients with breast cancer. Nevertheless, the treatment of metastatic breast cancer is still challenging and typically done to improve quality of life and extend survival period.[3,4] Majority of advanced breast cancer patients were more likely to have osteolytic bone metastases, which contributed to bone-related diseases such as pain, pathologic fractures, spinal cord compression and hypercalcemia.[5] Therefore, understanding the relationship between breast cancer and bone is crucial for developing the effective therapeutic strategy.

Upon entering bone microenvironment, breast cancer cells release several factors, such as interleukins (IL-6, IL-8 and IL-11) and tumor necrosis factor-α (TNF-α) to disrupt bone forming cell (osteoblast) function by altering the protein expressions produced by osteoblasts, including osteoprotegerin (OPG) and receptor activator of nuclear factor-κB ligand (RANKL).

Consequently, high level of RANKL results in activation and differentiation of bone-resorbing cells (osteoclasts) to promote bone loss.[6] So, targeting those factors may be beneficial for bone metastatic breast cancer patients.

The use of cannabinoids for medical purposes have increased over the past decade. Diverse effects, including anti-cancer activity, were demonstrated when cannabinoid receptors (CB1 or CB2) were activated.[7] Synthetic cannabinoids are a subclass of cannabinoids that typically have higher affinity to cannabinoid receptors than plant-derived cannabinoids.[8] For our study, arachidonyl-2'-chloroethylamide (ACEA) and GW405833 were used as selective agonists for CB1 and CB2 receptors, respectively. Although these CB agonists have been reported to inhibit cancer cell growth and invasion in several cancers.[9,10,11] However, the roles of ACEA and GW405833 on breast cancer and bone interaction is still unclear. Hence, the objective of this work was to examine the effect and underlying mechanism of CB agonists on breast cancer and osteoblast interaction.

Methodology:

Cell line and culture condition

Breast cancer cell lines used in this study including MCF-7 and MDA-MB-231 and mouse osteoblastic cells (UMR-106) were obtained from ATCC. All cells were cultured in DMEM medium supplemented with 10% heat-inactivated fetal bovine serum (FBS) and 1% penicillin-streptomycin (Gibco, Texas, USA). Cells were kept at 37°C in an incubator with 5% CO_2 and saturated humidity.

CB agonists used in this study

Arachidonyl-2'-chloroethylamide (ACEA) as a selective CB1 agonist and GW405833 (Sigma-Aldrich, MO, USA) as a selective CB2 agonist were dissolved in DMSO.

MDA-MB-231 conditioned medium collection

MDA-MB-231 cells were seeded into 6-well plate at $5x10^5$ cells/well in complete media as described previously. Cells were incubated in an incubator for 24 h. After that, complete medium was removed and serum free medium with or without treatment for 48 h was replaced into the well. The treatment included DMSO, 30 μM ACEA, 15 μM GW405833. Forty-eight hours after treatment, the new serum free medium was then replaced and incubated for 48 h. Next, conditioned medium was filtered with 0.2 μm syringe filter and placed in -80 °C refrigerator until use.

Cell viability assay

Breast cancer and osteoblast cell viabilities were examined by MTT assay. Briefly, in the first experiment, MDA-MB-231 and MCF-7 cells with the density of 1×10^4 cells/well were seeded into 96-well plates. Then, MDA-MB-231 were treated with different concentrations of ACEA and GW405833 (0, 1, 3, 10, 30, and 100 μM) for 48 h. Concentrations of ACEA up to 1,000 μM were used in MCF-7. For second experiment, UMR-106 cells (1×10^4 cells/well) were seeded into 96-well plate. After that, cells were treated with conditioned medium of breast cancer pretreated with ACEA (30 μM) and GW405833 (15 μM) in complete medium for 48 h. For both experiments, cells were incubated with 0.5 mg/ml MTT in a serum free medium for 3 h. Then, formazan crystals were solubilized in 100 μL of 10% SDS and 50% N, N-dimethyl-formamide. The mixture was spectrophotometrically measured at 595 nm.

Quantitative real-time PCR

MDA-MB-231 cells were seeded into 6-well plate ($3.3x10^5$ cells/well) for 24 h. After that, cells were treated with ACEA 30 µM and GW405833 15 µM in culture medium without FBS for 48 h. Then, cells were trypsinized and harvested for RNA extraction by Trizol (Invitrogen, MA, USA). An iScript RT Supermix (Bio-Rad, CA, USA) was used to convert total RNA to cDNA and then qRT-PCR was performed in CFX Connect Real-Time System (Bio-Rad). The relative mRNA expression was normalized with housekeeping gene (β-actin).

Statistical analysis

The data were represented as mean ± standard deviation (SD). Statistical tests were performed using one-way ANOVA. The value of significance for statistical analysis was p-value < 0.05.

Results and Discussion:

CB agonists suppressed breast cancer cell viability

For our study, we investigated the direct effect of ACEA and GW405833 in MDA-MB-231 and MCF-7 cells, which known as highly and non-metastatic breast cancer cells, respectively. The results revealed that ACEA and GW405833 significantly reduced viability of MDA-MB-231 and MCF-7 cells (Figure1 and 2). The IC_{50} values of ACEA and GW405833 in the two cell lines were shown in Table 1. According to our results, CB agonists have lower IC50 values for MDA-MB-231 cells than MCF-7 cells, suggesting that metastatic breast cancer cells had higher sensitivity to CB agonists treatment as compared to the non-metastatic cells.

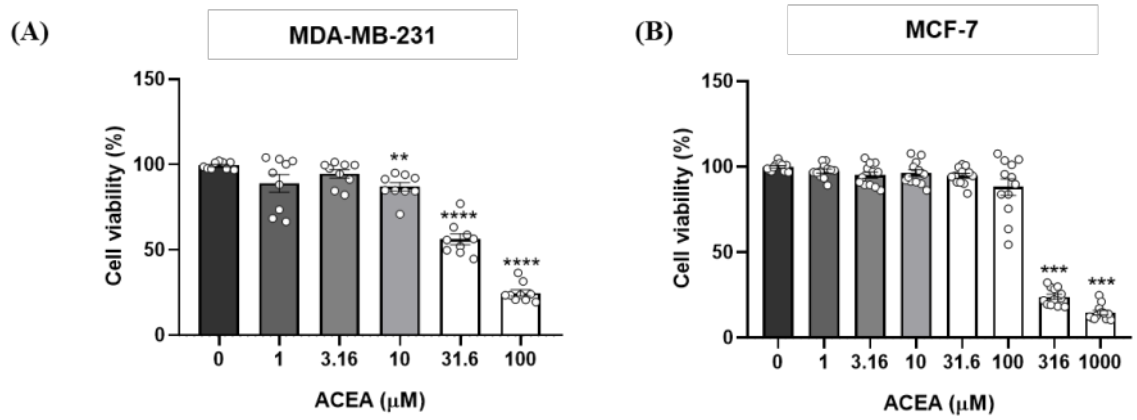

Figure 1. Cytotoxic effects of ACEA on breast cancer cell viability, (A) MDA-MB-231 (B) MCF-7. The data were presented as mean ± SD of three independent experiments with internal triplicate each. **p < 0.01, ***p < 0.001 and ****p < 0.0001.

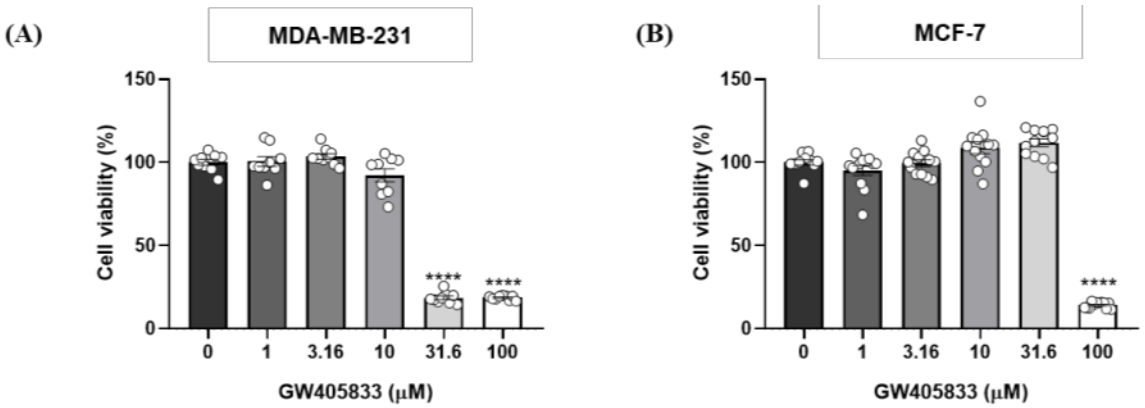

Figure 2. Cytotoxic effects of GW405833 on the viability of breast cancer cells, (A) MDA-MB-231 (B) MCF-7. The data were presented as mean ± SD of three independent experiments with internal triplicate each. ****$p < 0.0001$.

Table 1. IC_{50} values of CB agonists in breast cancer cells

Cell line	IC_{50} values (μM)[a]	
	ACEA	GW405833
MDA-MB-231	41.23	24.23
MCF-7	225.9	88.39

[a]IC_{50} values as means from three independent experiments with internal triplicate each

CB agonists recovered breast cancer-induced osteoblast cell death

In this study, MTT assay was used to study the effect of CB agonists on breast cancer-induced osteoblast suppression. As shown in Figure 3, cell viability of untreated osteoblastic UMR-106 cells was set to 100% as a control. The results showed that MDA-MB-231 conditioned medium reduced UMR-106 cell viability by almost 50%. Even though the result was not statistically significant, preexposure of GW405833 to MDA-MB-231 altered this activity. When osteoblastic cells were treated with conditioned media from MDA-MB-231 cells previously pretreated with 15 μM GW405833, the viability of UMR-106 cells was shown to be increased by 7.18% as compared to conditioned media derived from untreated MDA-MB-231. Our results revealed that the osteoblastic cell viability was decreased by factors from breast cancer cells, but this phenomenon was recovered by GW405833. From this result, we found that only GW405833 recovered breast cancer-induced osteoblast cell death. It has been reported that CB2 receptor expression was significantly higher than CB1 receptor in breast cancer specimen.[12] Therefore, this could explain the higher sensitivity of breast cancer to CB2 agonist than CB1 agonist and only CB2 agonist could partially recover breast cancer-mediated osteoblast suppression.

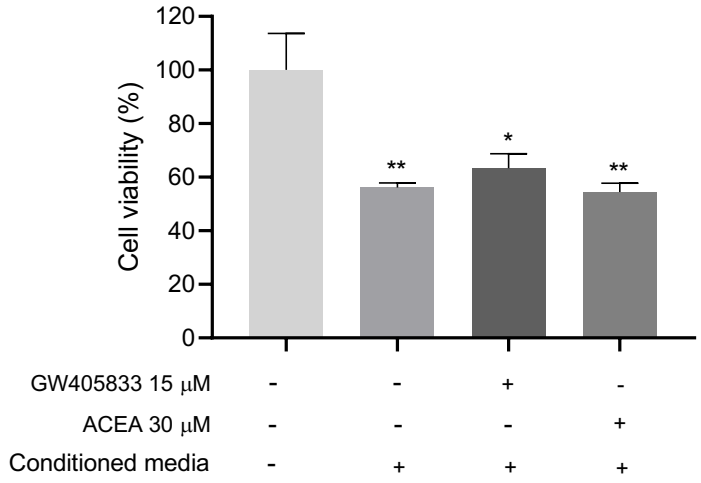

Figure 3. Effect of CB agonists pretreatment on breast cancer-mediated osteoblast suppression. Cell viability of UMR-106 was determined using MTT assay. The data were represented as mean ± SD of one independent experiment with internal triplicate each. *$p < 0.05$ and **$p < 0.01$.

CB2 agonist did not change IL-6 mRNA level but increased mRNA level of SOST expressed in breast cancer cells

Various cytokines and growth factors can be released from breast cancer, and act as the suppressive factors for osteoblasts.[13] So, the effects of GW405833 on the expression of potential breast cancer-derived factor(s) that negatively affected osteoblast in MDA-MB-231 were studied. SOST is an inhibitor of Wnt signaling pathway that has necessary role in bone homeostasis. The loss of bone mass can be caused by SOST dysregulation.[14] It has been demonstrated the anticancer activity of SOST by suppression of growth and migration in osteosarcoma.[15] As the inhibitor of Wnt signaling pathway, the expression of sclerostin (SOST) in MDA-MB-231 upon GW405833 treatment was investigated. As shown in Figure 4A, SOST was upregulated in MDA-MB-231 after GW405833 treatment. In contrast, IL-6 is important for breast cancer metastasis to the bone by promoting breast cancer colonization and bone destruction.[16] In this study, expression of IL-6 in MDA-MB-231 exposed to GW405833 was also determined. The results showed that GW405833 did not alter IL-6 level in MDA-MB-231 (Figure 4B). Our findings demonstrated that SOST level was elevated by GW405833, but not IL-6. However, further works are still needed to explore the mechanism underlying the recovery effect of CB agonists.

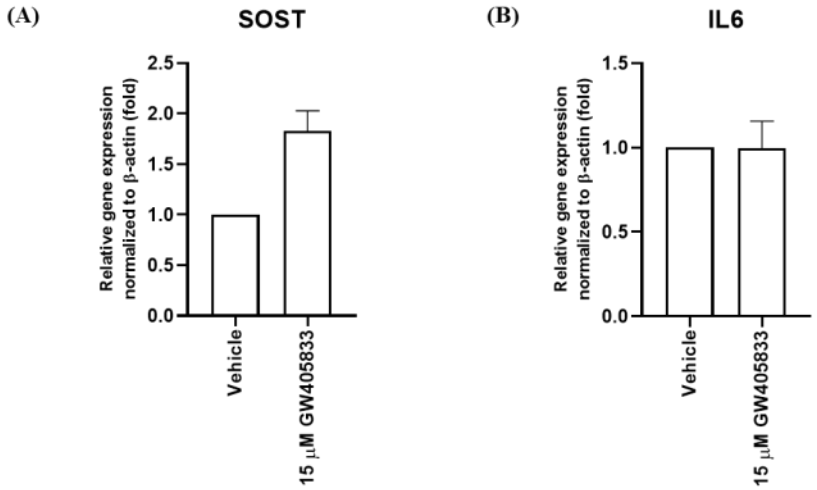

Figure 4. Effect of GW405833 on mRNA expression of (A) SOST (B) IL-6 in MDA-MB-231 cells. mRNA expression was analyzed by q-PCR and normalized with β-actin. The data were represented as mean ± SD of two independent experiments with internal duplicates each.

Conclusion:

Taken together, our findings suggested that CB agonists induced breast cancer cell death and had ability to recover breast cancer-mediated osteoblast suppression, potentially through upregulation of SOST.

Acknowledgements:

This work was supported by Mahidol University under the New Discovery and Frontier Research Grant and the CIF/CNI grant, Faculty of Science, Mahidol University (to KL).

References:

1. Wilkinson L, Gathani T. Br J Radiol. 2022;95:20211033.
2. Sun YS, Zhao Z, Yang ZN, Xu F, Lu HJ, Zhu ZY, Shi W, Jiang J, Yao PP, Zhu HP. Int. J. Biol. Sci. 2017;13:1387-97.
3. Abotaleb M, Kubatka P, Caprnda M, Varghese E, Zolakova B, Zubor P, Opatrilova R, Kruzliak P, Stefanicka P, Büsselberg D. Biomed. Pharmacother. 2018;101:458-77.
4. Cherny NI, Paluch-Shimon S, Berner-Wygoda Y. Breast Cancer (Dove Med Press). 2018;10:231-43.
5. Tahara RK, Brewer TM, Theriault RL, Ueno NT. Springer, Cham. 2019;105-29.
6. Chen Y-C, Sosnoski DM, Mastro AM. Breast Cancer Res. 2010;12:215.
7. Sarfaraz S, Adhami VM, Syed DN, Afaq F, Mukhtar H. Cancer Res. 2008;68:339-42.
8. Castaneto MS, Gorelick DA, Desrosiers NA, Hartman RL, Pirard S, Huestis MA. Drug Alcohol Depend. 2014;144:12-41.
9. Mohammadpour F, Ostad SN, Aliebrahimi S, Daman Z. Iran J Pharm Res. 2017;16:1479-86.
10. Dando I, Donadelli M, Costanzo C, Dalla Pozza E, D'Alessandro A, Zolla L, Palmieri M. Cell Death Dis. 2013;4:e664-e.
11. Khunluck T, Lertsuwan K, Chutoe C, Sooksawanwit S, Inson I, Teerapornpuntakit J, Tohtong R, Charoenphandhu N. Sci Rep. 2022;12:7398.
12. Kisková T, Mungenast F, Suváková M, Jäger W, Thalhammer T. Int J Mol Sci. 2019;20.

13. Wu X, Li F, Dang L, Liang C, Lu A, Zhang G. Front Cell Dev Biol. 2020;8.
14. Delgado-Calle J, Sato AY, Bellido T. Bone. 2017;96:29-37.
15. Ideta H, Yoshida K, Okamoto M, Sasaki J, Kito M, Aoki K, Yoshimura Y, Suzuki S, Tanaka A, Takazawa A, Haniu H, Uemura T, Takizawa T, Sobajima A, Kamanaka T, Takahashi J, Kato H, Saito N. Cancers. 2021;13.
16. Salamanna F, Borsari V, Contartese D, Costa V, Giavaresi G, Fini M. Cancers. 2019;11.

INHIBITORY EFFECTS OF BREAST CANCER-DERIVED FACTOR(S) ON OSTEOBLAST SURVIVAL AND FUNCTION AND THE DEVELOPMENT OF GELATIN-BASED 3D SCAFFOLD FOR 3D BONE CELL CULTURE SYSTEM

Thanayuth Jenpichitkulchai[1], Chartinun Chutoe[1] and Kornkamon Lertsuwan[1,2*]

[1]Department of Biochemistry, Faculty of Science, Mahidol University, Thailand
[2]Center of Calcium and Bone Research (COCAB), Faculty of Science, Mahidol University, Bangkok, Thailand
*e-mail: kornkamon.ler@mahidol.edu

Abstract:

The most common secondary site for breast cancer metastasis is bone. After the metastatic tumor has colonized the bone, the tumor produces factors that stimulate bone degradation that eventually leads to bone osteolytic lesion. Our study showed that conditioned media (CM) from MDA-MB-231 (MDA-MB-231 CM) also suppressed a bone forming cell (osteoblast; UMR-106) survival. The objectives of this study are to elucidate the effects of breast cancer-derived conditioned media in osteoblast cell survival and function and to develop gelatin-based 3D bone cell culture model for further study. Our results from the mineralization assay revealed that MDA-MB-231 CM significantly decreased the mineralization activity of UMR-106. To access the potential mechanisms involved, genes related to differentiation and mineralization in osteoblasts were analyzed by qRT-PCR. The results indicated a decrease in alkaline phosphatase (ALP), Collagen type I (Col 1) & Osteocalcin (OCN), which imply a reduction in osteoblast activity. Furthermore, to better mimic bone environment in the future study, 3D culture GelMA-based model was also developed.

Introduction:

The most common type of breast cancer bone metastatic is an osteolytic lesion, resulting from the increased osteoclast activity and decreased osteoblast activity.[1, 2] Bone metastasis is a multistep process that involves interaction between cancer cells and host cells.[3] One of the first steps of metastasis involves tumor invasion of the surrounding tissues. The cancer cells eventually intravasate into the blood circulation or newly formed vessels and extravasate to other tissues in the body. After the extravasation, cancer cells can remain dormant or develop into a secondary tumor.[4] Studies have shown that breast cancer produce the most metastases.[5] Metastases generated from breast cancer cells can travel to tissues in the body. The most common metastatic site for breast cancer is bone.[6] Bone is a metabolic tissue with cytokines and other secreted proteins in its environment.[7] Several studies shown that secreted cytokines and proteins provide fertile soil for cancer cell growth.[3] After the tumor has colonized the bone, the environment drastically adjusted to meet the high needs of the tumor. It has been shown that the change in bone environment is also mediated by the tumor-derived factors to reprogram bone remodeling process. The reprogramming of bone function includes physical changes, increased

hormone production, metabolic states, and environmental stimulation that eventually led to osteolytic lesion.[2, 8]

Bone remodeling is process composed of two main cell types. Osteoblast is responsible for synthesizing bone matrix and facilitating/governing the mineralization of the skeleton.[9] Osteoclasts are responsible for bone resorption activity. Osteoblast differentiation and function are regulated by several transcription factors and proteins. In addition, osteoblasts can regulate osteoclast differentiation by expressing receptor activator of nuclear factor κ-B ligand (RANKL) that binds to receptor activator of nuclear factor κ-B (RANK) to up regulate osteoclast differentiation from osteoclast precursors. Moreover, osteoblast could also express osteoprotegrin (OPG), a decoy receptor for RANKL, to inhibit RANKL which prevent osteoclast maturation. Thus, RANKL/OPG ratio determines whether bone formation or bone resorption is presently favorable.[10] Next, this study used three markers of osteoblast differentiation and functions. Type I collagen (Col 1) is the most abundant protein in bone extracellular matrix. Col 1 functions mainly as mechanical support for the bone.[11] Another important player in bone formation and mineralization is Alkaline phosphatase (ALP). ALP hydrolyzes pyrophosphate and provides inorganic phosphate to osteoblast, where the mineralization process will proceed.[12] Osteocalcin (OCN) is exclusively produced in mature osteoblast.[13] OCN functions in aligning calcium ions in hydroxyapatite which account for 65 to 70% of the bone weight.[14, 15]

Cell culture models are divided into two-dimensional (2D) and three-dimensional (3D) models. Cultures that grow on flat surfaces, such as Petri dishes or flasks, are classified as 2D cultures.[16] Many well-known techniques allow 2D culture to be universal, but the techniques do not provide a realistic environment to represent the natural cells' environment.[17] On the other hand, three-dimensional models were found to better mimic native tissue.[18] Moreover, several studies have shown that cells in 3D models exhibit cell morphology closer to *in vivo* than the 2D model.[19, 20] However, the effective of 3D bone cell culture model is still being sorted.

Gelatin is a natural hydrogel with bioactive motifs to promote cells adhesion and growth in many cell types.[21] However, Gelatin only undergoes physical gelation at low temperatures, which will be unable to maintain its physical characteristics at physiological temperatures.[22] On the contrary, gelatin methacryloyl (GelMA) was found to control the level of stiffness in the hydrogel, which affects cell viability, cell morphology, and preservation of the chondrogenic phenotype after seeding.[23] Moreover, many studies have widely used GelMA-based hydrogels containing cells for 3D-culture.[23] Bone mesenchymal stem cells (BMSCs) encapsulation by GelMA was found to enhance bone formation, ossification and have biocompatibility.[24, 25] In addition to the hydrogel, hydroxyapatite has been used as an component because HA is a natural component of bone and its biocompatibility, osteoconductivity and biodegradability.[26, 27] Hydroxyapatite is a native component of bone.[27] Moreover, a study by Zhou et al. (2016) showed that osteoblast proliferation was increased in a 3D culture with HA rather than in a 3D culture without HA. Therefore, this study also aims to develop GelMA-based bone cell 3D culture with HA to be used as the tool in bone metabolism and cancer.

Methodology:

Cell culture and reagents

Two cell lines were used in this study: breast cancer cell line (MDA-MB-231) (American Type Culture Collection (ATTC), VA, USA, catalog no. HTB-26) and osteoblast cell line (UMR-106) (American Type Culture Collection (ATTC), catalog no. CRL-1661). They were maintained in Dulbecco's modified Eagle's medium (DMEM) (Sigma, MO, USA, catalog no. 12800-017) supplemented with 10% v/v fetal bovine serum (FBS) (Gibco, NY, USA, catalog no. F5724) and 1% v/v penicillin-streptomycin (Pen Strep) (Gibco, catalog no. 15140-122). All cells were incubated at temperature of 37 ^{o}C with 5% CO_2.

MDA-MB-231 conditioned media collection

MDA-MB-231 cells were seeded into a 6-well plate (Corning, NY, USA, catalog no. 3516) at cell density of 5.0 x 10^5 cells/well in complete media and incubated at 37^{o}C with 5% CO_2. After 48 hours, the media was replaced with complete media. The media was replaced with serum-free media 24 hours later and continued to incubate for 48 hours before the conditioned media collection. The media was collected and filtered through 0.22 µm filter (Jet Biofil, Guangzhou, China, Catalog no. FPE-204-030). The conditioned media was separated for one-time use in different container and stored at -20 ^{o}C until usage.

Cell viability assay by MTT

UMR-106 cells were seeded into a 96-well plate at cell density of 5,000 cells/well in complete media and incubated at 37 ^{o}C with 5% CO_2. Conditioned media was combined with complete media to 50% v/v. After 72 hours of treatment, the media is replaced 1 ml of 0.5 mg/ml MTT (3-(4,5-dimethylthiazol-2-yl)-2,5-diphenltetrazolium bromide) then incubate at 37^{o}C with 5% CO_2 for 3 hours. After that, formazan dissolving solution containing 10% SDS (Sigma, catalog no. L4390) in 50% *N,N*-dimethyl-formamide is added to dissolve MTT product, formazan. The absorbance is measured at 595 nm by using microplate reader.

Bone mineralization determination by Alizarin red S staining

UMR-106 cells were seeded into a 24-well plate (Corning, catalog no. 3524) at cell density of 2 x 10^4 cells/well. Conditioned media was combined with complete media supplemented with 50 mM ß-glycerophosphate and 50 µM/ml ascorbic acid (Sigma, catalog no. A8960) to 50 % v/v. The treatment was replaced every other day. On the 6th day after the 1st treatment, cells were visualized with 38 mM alizarin red S (ARS) staining (Fluka, NC, USA catalog no. 05600). The image was quantified by ImageJ.

Quantitative real-time PCR (qRT-PCR)

UMR-106 cells were seeded in a 6-well plate (Corning, catalog no. 3516) at density of 4.2 x 10^5 then incubated at 37 ^{o}C with 5% CO_2. After 24 hours, cells were treated with CM 50% v/v to complete media for 72 hours. The total RNA from osteoblast cell line was extracted by TRIzol reagent (Invitrogen, catalog no. 15596026). After the extraction, RNA was converted into cDNA by iScript^{TM} reverse transcription supermix (Bio-rad, CA, USA, catalog no. 1708841).

Quantitative real-time polymerase chain reaction (qRT-PCR) was performed by using iTaq (Bio-rad, catalog no. 1725121).

GelMA synthesis

Type A porcine skin (Sigma, catalog no. G2500) was dissolved in demineralized water to 10% w/v at 50 ºC with a stir bar. After the solution had become homogeneous, methacrylic anhydride (Sigma, catalog no. 276685) was added dropwise to a weight ratio of 3:5, methacrylic anhydride to type A porcine skin. The solution was kept stirring and heated for 1 hour. The solution was then transferred to a 50 ml test tube and centrifuge at 3,500 G for 3 minutes at room temperature. The supernatant was collected and diluted with 2x of the supernatant volume with preheated 40 ºC demineralized water and transfer to 10 kDa SnakeSkin™ Dialysis Tubing (Thermo, MA, USA, catalog no. 68100). Dialysis was performed for 8 days in a hotplate at 40 ºC with magnetic bar stirring during the day and with hotplate off at night. The fluid was replaced every morning with demineralized water. After dialysis is completed, pH of the solution was adjusted to 7.2 by $NaHCO_3$ (PanReac AppliChem, Darmstadt, Germany, catalog no. A0384) and transferred to 50 ml tube then snap-freeze in a -80 ºC freezer overnight. Lyophilization was performed by freeze-dryer (Labconco, KC, USA). The samples were stored at -20 ºC until use.

Ninhydrin assay

Type A porcine skin (Sigma, catalog no. G2500) was dissolved in PBS from 0 – 10 mg/ml concentration. Synthesized GelMA was dissolved at 10 mg/ml. Ninhydrin (Sigma, catalog no. N4876) 20 mg/ml in absolute ethanol (Fulltime, Anhui, China, catalog no. B6531) was added to gelation solution in 1:8 ratio. The samples were heated at 70 ºC for 30 minutes and plate in a 96-well plate (NEST, Jiangsu, China, catalog no. 1205B). The absorbance was measured at 570 nm by Multiskan SkyHigh Microplate Spectrophotometer (Thermo, catalog no. A51119500C). Linear pattern from gelatin standard (2 mg/mL – 8 mg/mL) were used to obtain a standard linear regression graph and to generate a linear equation, which was used to calculate GelMA apparent concentration.

$$Fraction\ of\ free\ amines = \frac{Apparent\ sample\ conc.}{Nominal\ sample\ conc.}$$

Degree of functionalization (DoF) was calculated by using the following formula:

$$DoF = 100 * (1 - \frac{Apparent\ sample\ conc.}{Nominal\ sample\ conc.})$$

The apparent sample concentration refers to apparent detected absorbance of GelMA sample obtained from a linear regression equation. Nominal sample concentration refers to the prepared concentration of the sample.

3D culture by GelMA

Gelatin methacrylate (GelMA) was in-lab synthesized according to protocol mentioned earlier. GelMA was dissolved in auto-cleaved PBS. UMR-106 was mixed into GelMA following

by 2-Hydroxy-4'-(2-hydroxyethoxy)-2-2methylpropiophenone (Irgure2959) (Sigma, catalog no. 410896) to the final concentration of 0.5% w/v. The solution was added into silicone isolators (Sigma, catalog no. GBL664215-25EA) pressed together. The cross-linking was process was initiated by UV radiation at 355 nm for 15 minutes. The solidified gel was transferred into a 24-well plate and incubate in complete media at 37 ^{o}C with 5% CO_2. For the hydrogel containing hydroxyapatite (HA), HA was pre-weighted and auto-cleaved for decontamination before GelMA, photo-initiator and cells were added into the container.

Results & Discussion:

Cell viability of UMR-106 decreased after CM treatment

To investigate cell growth of osteoblasts after MDA-MB-231 derived CM treatment, UMR-106 were selected as the model. Cells viability was normalized to control which had 50% v/v complete media and serum-free media. After 72 hours of treatment, the result showed that cell viability decreased by 25% on average when compared to control (**Fig 1**). The decreased in cell viability indicated that CM treatment negatively affected UMR-106 functions which hindered cells differentiation and cells' growth.

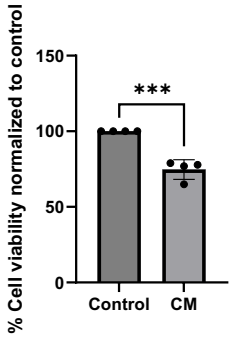

Figure 1. Cell viability assay of UMR-106 after MDA-MB-231 derived CM treatment. Cell viability of UMR-106 decreased after 72 hours of CM treatment.
***P < 0.001 as compared to control

qRT-PCR on differentiation markers

To examine known differentiation markers of osteoblasts, the relative expression of OPG and RANKL of UMR-106 cells after MDA-MB-231 derived CM treatment were investigated by qRT-PCR. After 72 hours of CM treatment, OPG and RANKL showed signs of bone modeling reprogramming (**Fig 2**). OPG expression, associated with preventing bone resorption, decreased by 39.1% while, RANKL expression, associated with upregulating bone resorption, increased by 29.0%. This suggested that MDA-MB-231 CM treatment may inhibit osteoblast differentiation.

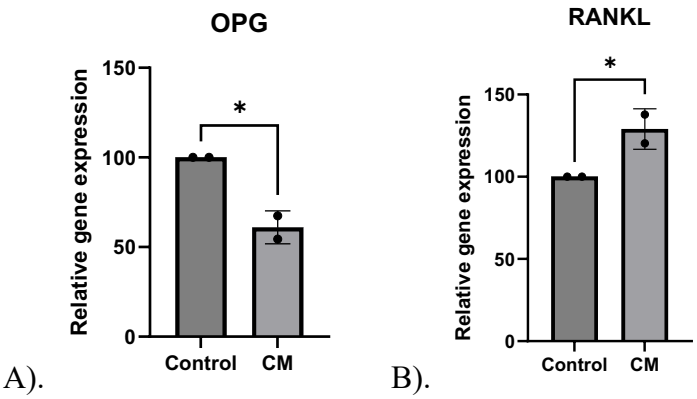

A). B).

Figure 2. The expression of differentiation markers of osteoblast by UMR-106 cells. **A**). OPG. **B**). RANKL. *P<0.1, **P < 0.01, ***P < 0.001 as compared to control

Mineralization activity decreased after MDA-MB-231 derived CM treatment.

To investigate the effect of CM on osteoblast functions, CM was used as treatment. Osteoblasts were treated with CM 50% v/v in complete media, while the control group had serum-free media instead of CM. After five days of CM treatment, Calcium deposition in extracellular matrix and osteoblast cells were detected by ARS staining. Our result indicated that UMR-106 cells exposed to CM showed significantly lower calcium deposition in osteoblast culture represented in **Figure 2A**. The quantitative data showed that alizarin-positive area in CM treated osteoblast was reduced by 87% when compared to the control group (**Fig 2B**). The result indicated that CM negatively and significantly affected the mineralization process of osteoblast.

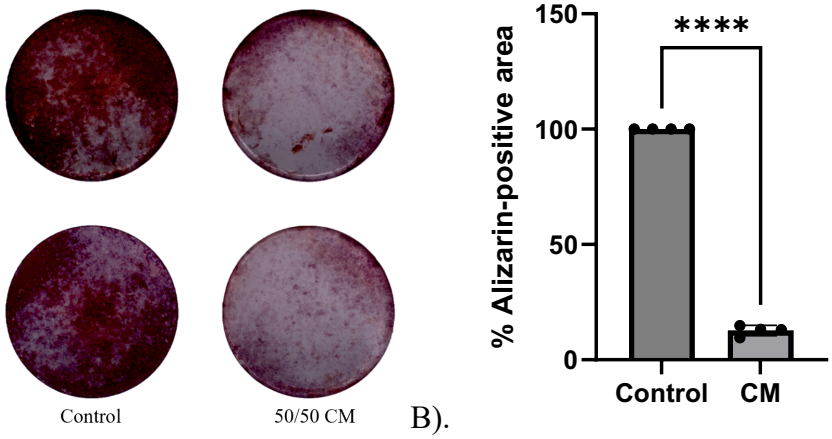

A). B).

Figure 2. UMR-106 mineralization activity was visualized by Alizarin red S staining and quantified by ImageJ **A)**. Gross appearance **B)**. Quantified data by ImageJ representing mineralization area by % alizarin-positive area. ****P < 0.0001 as compared to control

qRT-PCR result indicated a decrease in osteoblast function after CM treatment.

Next, to investigate the affected function of osteoblasts after CM treatment, osteoblasts were treated with CM and then analyzed by qRT-PCR. The relative expression of genes involved in mineralization was analyzed. After 72 hours of CM treatment, RNA was extracted and converted to cDNA. ALP, Col 1 & OCN were found to decrease by 23%, 31%, & 5% respectively (**Fig 3**). Although OCN relative expression decreased only slightly, ALP and Col1 reduced moderately. A decrease in relative gene expression of these genes confirmed a previous result from ARS staining. The dense amount of % alizarin-positive area could be due to the accumulation of mineralization deposition over the five days.

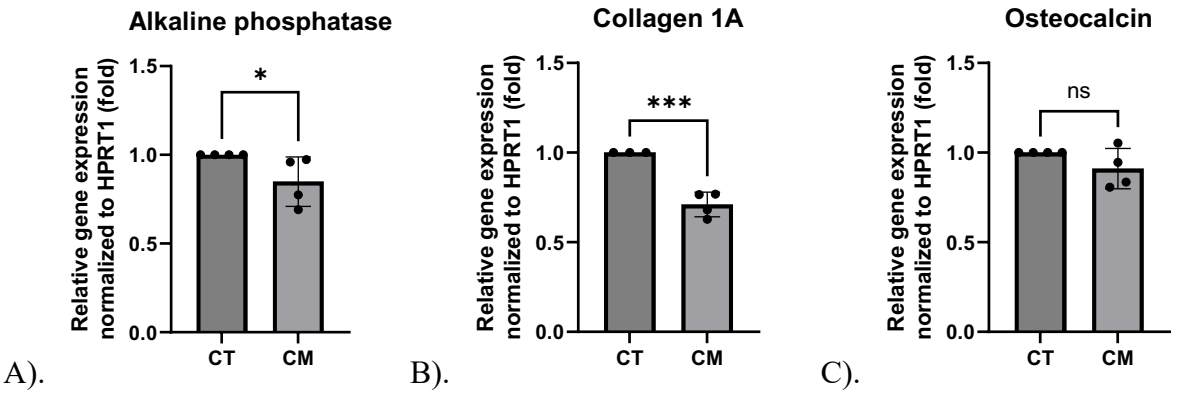

Figure 3. The expression of osteoblasts genes related to mineralization and differentiation was reduced by MDA-MB-231 CM treatment (**A**) ALP, (**B**) Col1, and (**C**) OCN. *P<0.1, **P < 0.01, ***P < 0.001 as compared to control

Modification of gelatin hydrogel into full GelMA for further study was accomplished

Ninhydrin assay revealed that the Degree of Functionalization (DoF) of in-lab synthesized GelMA would be able to generate GelMA-based hydrogel. **Figure 4A** showed an overall illustration of GelMA synthesis. Gelatin contains amines group and hydroxyl as its functional groups. When gelatin reacts with methacrylic anhydride, methacryloyl couples with free-amine and carboxyl group resulting in methacrylamide and methacrylate, respectively (**Fig 4B**). Ninhydrin is an assay performed to detect amine groups. Ninhydrin compound reacts with amines group to produce a deep blue color compound called Ruhemann's purple (**Fig 4C**). Thus, Ruhemann's purple formation will not occur if the amines group is occupied. In other words, ninhydrin assay could detect available amines group in GelMA. **Figure 5A** showed plotted gelatin and GelMA concentration against absorbance which were used to generate a linear regression equation. Gelatin functional group availability could also be referred to as the degree of functionalization (DoF). High DoF suggest that methacrylation of gelatin have converted most amines and hydroxyl group to methacryloyl, while low DoF indicate high availability of free-amine and hydroxyl groups in GelMA. DoF is crucial in determining the physical properties of GelMA-based hydrogel since achievable cross-linking density, mechanical properties, stiffness,

and porosity depend significantly on DoF. Our samples had 71% DoF on average, calculated from linear regression equation (**Fig 5B),** shown in **Table 1.**

To investigate the 3D culture models for osteoblasts, GelMA was used as the main component. The hydrogel concoction comprised of GelMA, UMR-106 cells, and a photo-initiator (Irgure2959) with and without hydroxyapatite. Photo-crosslinking was initiated by UV radiation at 355. After 15 minutes, each gel was carefully transferred to a 24-well plate and incubated with complete media at 37°C with 5% CO_2. **Figure 6** showed the hydrogels taken out of the 24-well plate after 24 hours of incubation. All of the hydrogels were able to maintain their cuboid shape. Initially, hydrogels without hydroxyapatite were clear and transparent after photo-crosslinking. However, all of the hydrogels turned pinkish after incubating in complete media. The color change indicated that media could penetrate the hydrogel, which would be essential for cell proliferation and differentiation.

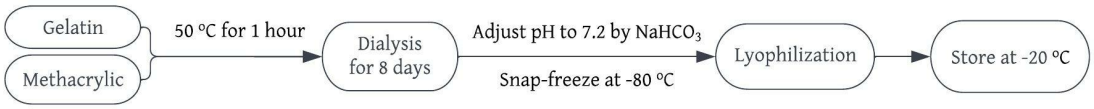

A).

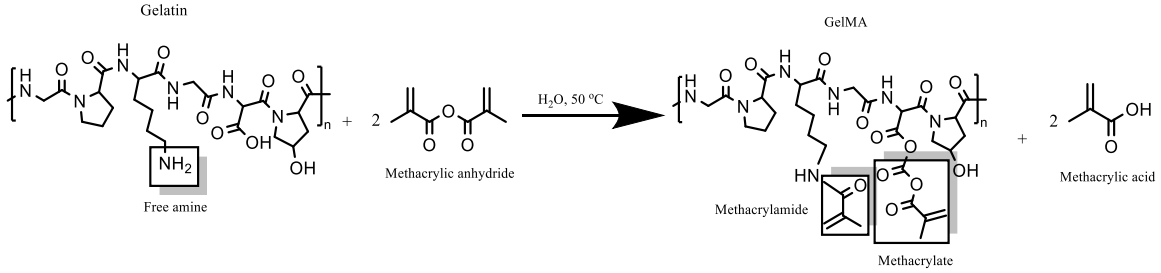

B).

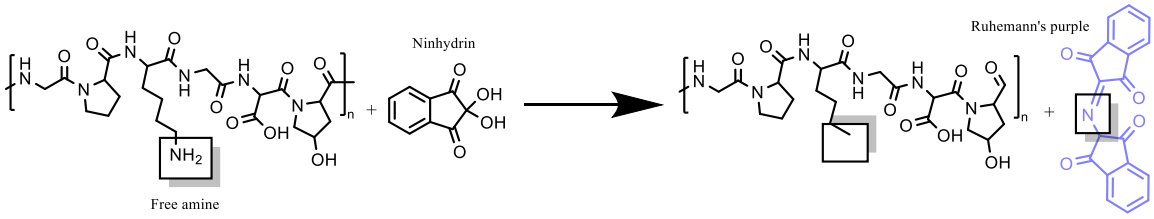

C).

Figure 4. GelMA functionalization and characterization A). summary of GelMA synthesis. Gelatin and methacrylic anhydride reacting through stirring and heating was crucial in methacrylation process. After this process, dialysis was essential in removing unreacted methacrylic anhydride, hydrogen ion and methacrylic acid. Lyophilization was performed to solidify GelMA for shelf life. **B**). GelMA synthesis by methacrylation and methacrylic anhydride in demineralized water at 50 °C. **C**). Ninhydrin reaction with gelatin functional group to generate Ruhemann's purple.

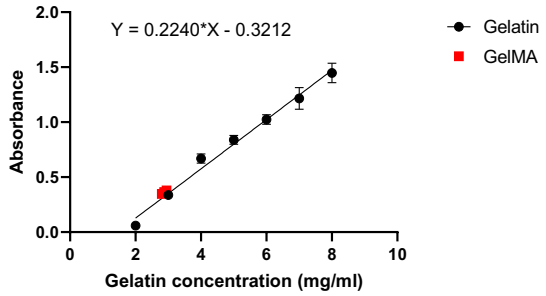

A).

$$DoF = 100 * (1 - \frac{Apparent\ sample\ conc.}{Nominal\ sample\ conc.})$$

B).

Figure 5. Determination of DoF by ninhydrin assay. A). Gelatin concentration from 2-8 mg/mL were selected for a standard linear regression. Linear regression equation was obtained from ninhydrin assay of gelatin. **B**). Degree of functionalization determination. *Apparent sample concentration* was calculated from experimental value of GelMA sample absorbance from ninhydrin linear regression equation. *Nominal sample concentration* refers to the actual GelMA concentration

Table 1. Degree of functionalization of GelMA sample. After lyophilization, GelMA samples were dissolved in 1X PBS in 10 mg/ml as nominal concentration. Linear regression analysis from ninhydrin assay was used to determine DoF of the GelMA samples.

Absorbance	Concentration	DoF
0.3067	2.8031	71.969
0.3385667	2.9454	70.546
0.3226667	2.8744	71.256

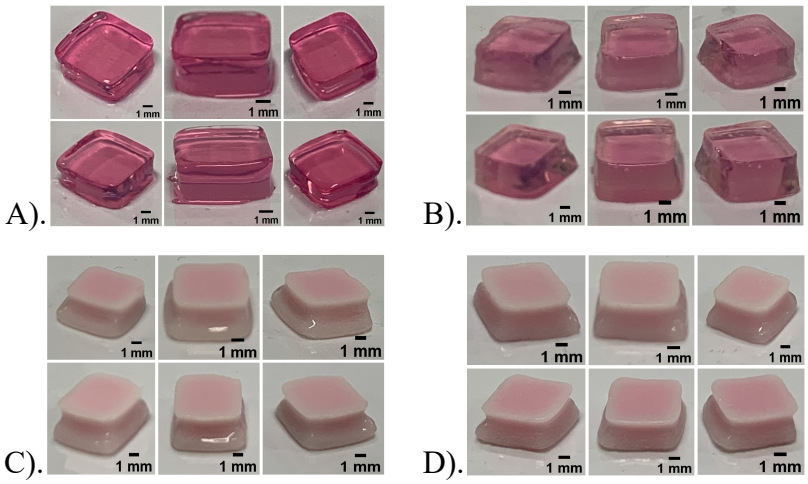

Figure 6. 3D culture by GelMA. A). 10% w/v GelMA B). 15% w/v C). 10% w/v GelMA + 10% w/v HA D). 15% w/v GelMA + 10% w/v HA. Both hydrogels with and without hydroxyapatite were able to retain their cuboid shape after photo-cross-linking.

Conclusion

Derived MDA-MB-231 conditioned media treatment on osteoblasts hinders osteoblast functions. The result from cells viability and ARS confirmed that MDA-MB-231 derived CM treatment were able to inhibit UMR-106 cells' growth. Moreover, CM treatment also induce bone resorption suggested from increased RANKL as compared to decreased OPG (**Fig 2)**. Likewise, further investigation in osteoblast differentiation markers by qRT-PCR implied similar effects of CM treatment to ARS and MTT results. Future experiments could include cell encapsulation within GelMA based hydrogel followed with biocompatibility test to determine whether GelMA-hydrogel based could be used as for 3D culture. In addition to 3D-culture future development, endothelial cells could also be included to model metastatic process via constructed vessels from endothelial cells.

Funding: This research was supported by Research grant for New Discovery and Frontier Research from Mahidol University, Mid-career research grant from National Research Council of Thailand (NRCT) and Mahidol University (N42A650356) and CIF and CNI grant, Faculty of Science, Mahidol University (to K.L.).

Acknowledgements: This study was supported by Research grant for New Discovery and Frontier Research from Mahidol University, Mid-career research grant from National Research Council of Thailand (NRCT) and Mahidol University (N42A650356) and the CIF and CNI grant, Faculty of Science, Mahidol University, Thailand awarded to Assistant Professor Dr. Kornkamon Lertsuwan.

References:

1. Komori, T., *Functions of Osteocalcin in Bone, Pancreas, Testis, and Muscle.* Int J Mol Sci, 2020. **21**(20).
2. Guise, T.A., et al., *Basic mechanisms responsible for osteolytic and osteoblastic bone metastases.* Clin Cancer Res, 2006. **12**(20 Pt 2): p. 6213s-6216s.
3. Mundy, G.R., *Mechanisms of bone metastasis.* Cancer, 1997. **80**(8 Suppl): p. 1546-56.
4. Geiger, T.R. and D.S. Peeper, *Metastasis mechanisms.* Biochim Biophys Acta, 2009. **1796**(2): p. 293-308.
5. Disibio, G. and S.W. French, *Metastatic patterns of cancers: results from a large autopsy study.* Arch Pathol Lab Med, 2008. **132**(6): p. 931-9.
6. Barney, L.E., et al., *The Predictive Link between Matrix and Metastasis.* Curr Opin Chem Eng, 2016. **11**: p. 85-93.
7. Shupp, A.B., A.D. Kolb, and K.M. Bussard, *Novel Techniques to Study the Bone-Tumor Microenvironment.* Adv Exp Med Biol, 2020. **1225**: p. 1-18.
8. Riquelme, M.A., E.R. Cardenas, and J.X. Jiang, *Osteocytes and Bone Metastasis.* Front Endocrinol (Lausanne), 2020. **11**: p. 567844.
9. Florencio-Silva, R., et al., *Biology of Bone Tissue: Structure, Function, and Factors That Influence Bone Cells.* Biomed Res Int, 2015. **2015**: p. 421746.
10. Boyce, B.F. and L. Xing, *Biology of RANK, RANKL, and osteoprotegerin.* Arthritis Res Ther, 2007. **9 Suppl 1**: p. S1.
11. Saito, M. and K. Marumo, *Effects of Collagen Crosslinking on Bone Material Properties in Health and Disease.* Calcif Tissue Int, 2015. **97**(3): p. 242-61.
12. Orimo, H., *The mechanism of mineralization and the role of alkaline phosphatase in health and disease.* J Nippon Med Sch, 2010. **77**(1): p. 4-12.
13. Wei, J. and G. Karsenty, *An overview of the metabolic functions of osteocalcin.* Curr Osteoporos Rep, 2015. **13**(3): p. 180-5.
14. Moriishi, T., et al., *Osteocalcin is necessary for the alignment of apatite crystallites, but not glucose metabolism, testosterone synthesis, or muscle mass.* PLoS Genet, 2020. **16**(5): p. e1008586.
15. Habibah, T.U., D.V. Amlani, and M. Brizuela, *Hydroxyapatite Dental Material*, in *StatPearls*. 2022: Treasure Island (FL).
16. Xie, M., et al., *Facile 3D cell culture protocol based on photocurable hydrogels.* Bio-Design and Manufacturing, 2021. **4**(1): p. 149-153.
17. Duval, K., et al., *Modeling Physiological Events in 2D vs. 3D Cell Culture.* Physiology (Bethesda), 2017. **32**(4): p. 266-277.
18. Haycock, J.W., *3D cell culture: a review of current approaches and techniques.* Methods Mol Biol, 2011. **695**: p. 1-15.
19. Krishnan, V., et al., *Dynamic interaction between breast cancer cells and osteoblastic tissue: comparison of two- and three-dimensional cultures.* J Cell Physiol, 2011. **226**(8): p. 2150-8.
20. Fontoura, J.C., et al., *Comparison of 2D and 3D cell culture models for cell growth, gene expression and drug resistance.* Mater Sci Eng C Mater Biol Appl, 2020. **107**: p. 110264.

21. Xiao, S., et al., *Gelatin Methacrylate (GelMA)-Based Hydrogels for Cell Transplantation: an Effective Strategy for Tissue Engineering.* Stem Cell Rev Rep, 2019. **15**(5): p. 664-679.
22. Zhu, M., et al., *Gelatin methacryloyl and its hydrogels with an exceptional degree of controllability and batch-to-batch consistency.* Sci Rep, 2019. **9**(1): p. 6863.
23. Dong, Z., et al., *Gelatin methacryloyl (GelMA)-based biomaterials for bone regeneration.* RSC Adv, 2019. **9**(31): p. 17737-17744.
24. Zhao, X., et al., *Injectable Stem Cell-Laden Photocrosslinkable Microspheres Fabricated Using Microfluidics for Rapid Generation of Osteogenic Tissue Constructs.* Advanced Functional Materials, 2016. **26**(17): p. 2809-2819.
25. Li, J., et al., *Biomimetic Methacrylated Gelatin Hydrogel Loaded With Bone Marrow Mesenchymal Stem Cells for Bone Tissue Regeneration.* Front Bioeng Biotechnol, 2021. **9**: p. 770049.
26. Zhou, X., et al., *3D Bioprinting a Cell-Laden Bone Matrix for Breast Cancer Metastasis Study.* ACS Appl Mater Interfaces, 2016. **8**(44): p. 30017-30026.
27. Mahammod, B.P., et al., *Investigation of Physico-mechanical Behavior, Permeability and Wall Shear Stress of Porous HA/PMMA Composite Bone Scaffold.* Arabian Journal for Science and Engineering, 2020. **45**(7): p. 5505-5515.

GENE ISOLATION FROM MANGO RELATED *Colletotrichum gloeosporioides* INFECTION

Kultida Pantayak and Maliwan Nakkuntod*
Department of Biology, Faculty of Science, Naresuan University, Phitsanulok, Thailand
*e-mail: maliwann@nu.ac.th

Abstract:

Mango is an important export fruit of Thailand, so the high quality and safety of mangoes are required. The major plant disease of mango is anthracnose that gardeners should monitor carefully after post harvesting. The objectives of this research were to isolate *Colletotrichum gloeosporioides* causing anthracnose in mango, to clone genes related defense mechanism and to investigate gene expression in mango fruit after *C. gloeosporioides* infection. The results showed that four genera of pathogenic fungi, namely *Colletotrichum, Neoscytalidium, Lasiodiplodia* and *Pseudofusicoccum*, were identified using morphological and molecular data. From all of 7 genes related fungal infection, only 4 genes were successful to amplify by PCR method and only 3 genes (actin, chitinase and PR-1) were detected in right clones. After that, RNA samples from mango fruit after anthracnose fungi infection for 0, 24, 48, 72, 96, 120 and 144 hours were extracted and examined quantity and purity. All RNA solutions presented high concentration but low purity; hence, the gene expression could not be detected. Therefore, specific primer design and purity of RNA are important criteria for development of anthracnose detection system in mango further to control mango quality before export.

Introduction:

Mango is a fruit that the government has a policy to promote production potential for export and at present, Udon Thani province is the number 1 exporter of Nam Dok Mai Golden Mango in the Northeast. Due to the large area of cultivation There is a safe and standard planting system. As a result, mangoes are high quality therefore it's required by the international market to get quality produce match the market demand farmers should especially be on the lookout for the most damaging anthracnose diseases. (Rattiya Ngamrabam, 2018)

Anthracnose disease of mango Caused by fungi *Colletotrichum gloeosporioides* this fungus is common in tropical landscapes and subtropical regions (Wittaya Aphai, 1998). The symptoms are young leaves are distorted, leaves are brown spots, young branches are brown-black lesions, looks like a hardened wound that collapses slightly. The result is a black lesion of an unstable shape. In the middle of the lesion, red-brown mucus may be found in a circle. (Department of Agriculture, 2007) resulting in difficult disease control and is a major obstacle for distribution to both domestic and international markets Especially mangos that are eaten with ripe fruit and thin skins are easily destroyed by the infection. Farmers therefore need to use chemical fungicides after each harvest. Chemical fungicides, such as benomyl or carbendazim, may affect the environment and produce toxic residues within the produce (Niphon Wisartanon, 1997). can be observed from the lesions which makes it too slow to control resulting in damage to the production Therefore, early detection of plant infection is necessary. There are a variety of methods, such as dissection for examination by culture, etc., but can only be detected when there is a sufficient amount of infection. Another interesting

method is investigating the expression of genes that plants produce when they are infected. This will enable farmers to deal with the disease in a timely manner.

There are studies of gene expression of Pathogenesis-related (PR) in vaporized avocados of thyme oil. It was found that thyme oil vapors significantly reduced avocado incidence of anthracnose. Induced gene expression ß-1,3-glucanase and the chitinase gene were increased (Bill et al., 2015), which the enzyme produced was resistant to fungi (Suvita Saphaisan, 2011). The objective of this study was to study the expression of genes such as ß-1,3-glucanase, chitinase, Pathogenesis-related (PR) genes within mangoes to guide the development of a coating that slows down the symptoms of pathogens. *Colletotrichum gloeosporioides* reduce the problem of using fungicides and can keep mangoes longer.

Methodology:

1.Fungal isolation and fungal identification by tissue transplanting method.

In the first step, plant specimens are cut from the junction of normal and symptomatic tissues approximately 0.5×0.5 cm in size. The external surface is sterilized with 15% sodium hypochlorite for 5 minutes, and patted dry on sterile tissue. The tissue was then cultured on potato dextrose agar (PDA) medium at 25 ± 2 °C for 7-10 days and subculture until the fungi were pure. The fungi were then identified by microscopic morphology.

2. DNA extraction by CTAB method. Crous et al. (2000)

Scrape the fungus fibers and grind with liquid nitrogen. Add 1 ml of CTAB and 10 mg of PVP. Incubated at 55 °C for 30 min, then centrifuged at 13,000 rpm for 10 min. Aspirate the 700 µL volume of solution into a new tube, then add chloroform: isoamylalcohol (24:1), approximately 1 time the volume. Centrifuge at 13,000 rpm for 10 min. Aspirate the solution into a new tube, add 2 times the volume of absolute ethanol, chill for 30 minutes and centrifuge at high speed at 13,000 rpm for 10 minutes, pour out the top solution and add 70% ethanol 2 times, suck out the top solution. Leave to dry and fill TE buffer 30 µL and store at -20 °C.

3. DNA enrichment at ITS area by Polymerase Chain Reaction (PCR) technique

Increase the amount of DNA in the Internal Transcribed Spacer (ITS) with ITS1 primers (5'TTTCCGTAGGTGAACCTGC3') and ITS4 (5'TCCTCCGCTTATTGATATGC) by increasing the amount of rDNA region during ITS1-5.8S rDNA-ITS2. Purification of DNA fragments using a PCR Clean-Up & Gel Extraction Kit (Puredirex, Taiwan) and the obtained products were analyzed results with electrophoresis on 1% agarose gel in 0.5XTBE buffer under UV transilluminator. Analyze the sequencing at Macrogen, South korea and compare with the database reported in GenBank.

4. Studies on gene expression in mangoes.

DNA was extracted from young leaves of Nam Dok Mai mango by CTAB method modified from Agrawal et al. (1992). Endochitinase, β-1,3-glucanase, Phenylalanine ammonia (PAL), Lipoxygenase (LOX), PR-1, Thaumatin-like protein (TLP) As in Table 1, from the central NCBI database, web Primer 3 was used for design and DNA quantification was obtained with the designed primer. DNA fragments were purified using a PCR Clean-Up & Gel Extraction Kit (Puredirex, Taiwan). Connect the DNA fragment to the vector. Plasmids were then injected into host cells by heat shock method. DNA amplification using M13 primer and primer for the gene to be studied.

Table 1. Primers used to enrich DNA regions.

Primer	Sequence	Accession number	Source
Actin_RICE	5’ – TCC ATC TTG GCA TCT CTC A – 3’ 5’ – GTA CCC TCA TCA GGC ATC TG – 3’	-	rice
Endochitinase	5’- TGC AGC AAA CTC CTT CAA TG -3’ 5’- GAA AGC AAT ATC CCC AAG CA -3’	Z78202.1	avocado
β-1,3-glucanase	5’- ATG CAT GGG TCC AAA ACA AT–3’ 5’– AAG TAC TCC GGT GTC GAT GG–3’	U49454.1	peach
Phenylalanine ammonia (PAL)	5’- AGG TCA GGG TGG AGT TGT CT -3’ 5’- GGC TCC TCC TTG CTT GGT TC -3’	U16130.1	avocado
Lipoxygenase (LOX)	5’- CCC AGC TCC AGA CCC TTC TT – 3’ 5’- ACT GGT CGT CGT CGT TCA TC -3’	AD001673	avocado
PR-1	5’- TGG TGT CGG CCC TAT GAC A -3’ 5’- GGC CAC CAG AGT GTT GCA T -3’	AY560589	Sweet pepper
Thaumatin-like protein (TLP)	5’- TGC TGT AAA GTG CCC ACA ACA -3’ 5’- TGT CGA AAC AAT GAC CAT CTT CA -3’	AF297646	Sweet pepper

5. Gene expression

Cultivation of test fungus on mango skin. Prepare mangoes by selecting mangoes with size, color. and no lesions to be cleaned with 15% sodium hypochlorite, 5 min, blot dry on sterile paper and inoculate on mango skin by inoculating. The pole area and the tribute area of the mango fruit then cover each mango with a plastic bag. incubated at 25 °C by giving light to dark. Mango Sampling Fruit collection was started at 0, 24, 48, 72, 96, 120 and 144 hours (6 days) after inoculation using cork borer 5 mm in diameter, plant samples were cut around the inoculation site, extracted samples were obtained for RNA extraction number 3 repetitions. RNA extraction by modified method from (Ploypailin Thanikkul, 2012) and cDNA synthesis by SensiFASTTM cDNA Synthesis Kit, UK as recommended by the company.

Results and Discussion:

1.Fungal isolation and fungal identification by tissue transplanting method.

Fungus isolates from mango by tissue transplanting method. and classified by morphological characteristics A total of 7 fungal isolates were distinguished, for example M1, M2, M3, M4, M5, M6 and M7. The mycelium characteristics of the M1 sample were white. full of petri dishes conidia are colorless, rounded cylindrical in shape conidia are approximately 3 × 14 µm in size, M2 specimens. Fungal mycelium is white conidia are rounded cylindrical, colorless, and, for example, M7, fungal mycelium is white grow into a circle conidia are rounded cylindrical, colorless, for example M3 to M5. Fungal mycelium is gray-black in color conidia have a short oval shape when in adulthood, conidia are black. It took a long time to create conidia. The culture medium turned black and the mycelium M6 specimen was grey-black in color grow into a circle conidia is elongated in shape (Figure 1).

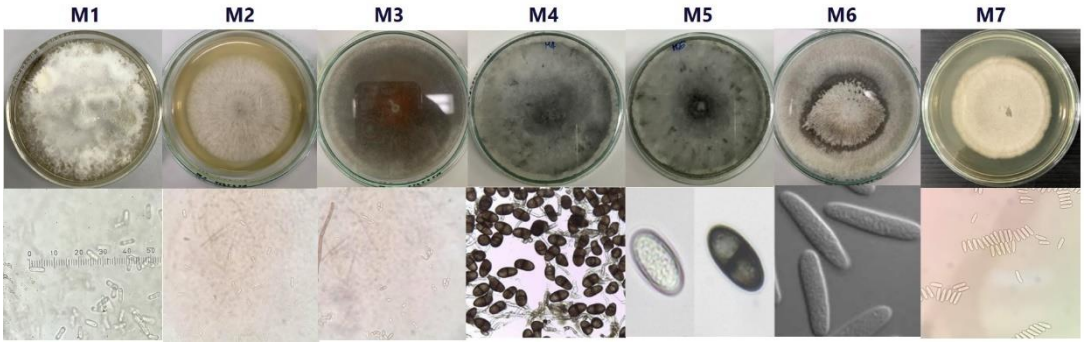

Figure 1. Morphology of fungi isolated from mango (Suvita, 2020; Draginja, 2008).

2.Fungal identification by increasing the amount of DNA around ITS.

A study of fungal 7 isolates by DNA extraction by CTAB method modified from Crous et al. (2000) showed that the extracted fungal DNA exceeds 10,000 base pairs. The amplified DNA was approximately 500-550 base pairs, and when nucleotide sequencing was compared with the GeneBank database, fungal nucleotide sequences from the M1 samples contained nucleotide sequences. The cletide is the same as the nucletide sequence of Colletotrichum gloeosporioides at ITS1-5.8SrDNA-ITS2 At 100% similarity (MW131601.1), the M2 sample has the same nucletide sequence as the nucletide sequence of MW131601.1. Colletotrichum coffeanum at ITS1-5.8SrDNA-ITS2 At a 99.80% similarity percentage (KP174769.1), the M3 sample had the same nucletide sequence as the nucleotide sequence of Neoscytalidium dimidiatum at ITS1-5.8SrDNA-ITS2 At 100% similarity (MG865987.1), the M4 sample has the same nucletide sequence as the nucletide sequence of Lasiodiplodia theobromae at ITS1-5.8SrDNA-ITS2 At 99.72% similarity percentage (MZ496574.1), the M5 sample had the same nucletide sequence as the nucleotide sequence of Lasiodiplodia pseudotheobromae at ITS1-5.8SrDNA-ITS2 At a 99.56% similarity percentage (MT913570.1), the M6 sample had the same nucletide sequence as the nucleotide sequence of M6. Pseudofusicoccum kimberleyense region of ITS1-5.8SrDNA-ITS2 at 99.32% similarity percentage (MW251929.1) and the M7 sample had the same nucletide sequence as the nucletide sequence of Collectotrichum gloeosporiodes at ITS1-5.8SrDNA-ITS2 at 100% similarity percentage (MK215707.1)

3. Studies on gene expression in mangoes.

Increasing the amount of DNA at Actin, Endochitinase, β-1,3-glucanase, Phenylalanine ammonia (PAL), Lipoxygenase (LOX), PR-1 and Thaumatin-like protein (TLP) by polymerase chain reaction (PCR) was found to be able to Can only increase the amount of DNA in 4 regions: Actin, Endochitinase, β-1,3-glucanase and PR-1. The size of the DNA fragment is about 700 base pairs. The DNA region PR-1 is the size of the DNA fragment about 800 base pairs. β-1,3-glucanase There are different sizes of DNA fragments which shows that the primer β-1,3-glucanase There is no specificity to the DNA of mangoes (Figure 2).

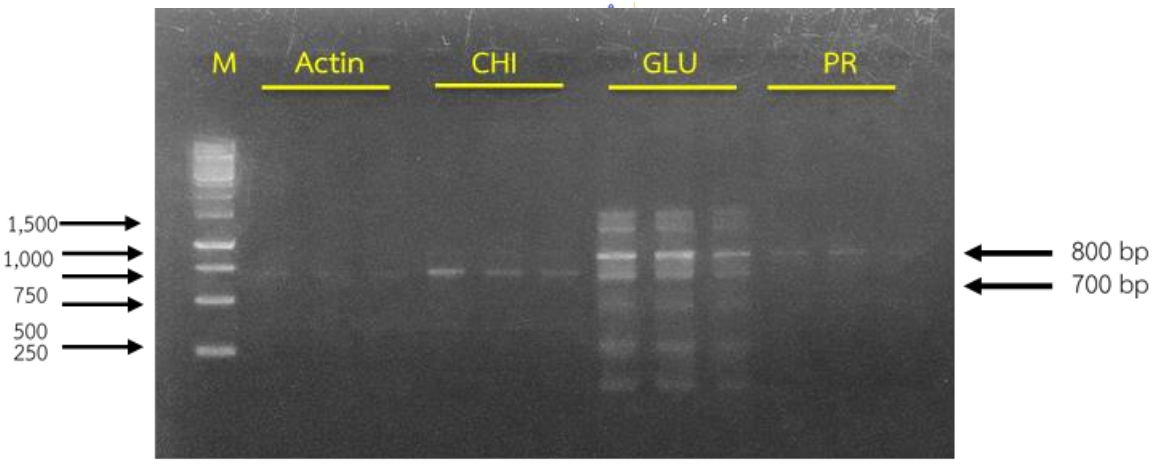

Figure 2. DNA enrichment at Actin, Endochitinase, β-1,3-glucanase and PR-1 sites. (M = 1Kb DNA ladder Themo Scientific)

Actin, Endochitinase, β-1,3-glucanase and PR-1 genes were purified and linked to pT257R/T plasmids, then transferred to *E. coli* DH5α by heat shock method, and then plasmid extracted. plasmid and DNA fragments were examined with specific cutting enzymes *Bam*HI and *Eco*RI in 1% gel agarose. All three white colonies were formed: Actin, β-1,3-glucanase and PR-1 (Figure 3) White colonies were selected from all Actin genes, 3 colonies β-1,3-glucanase 5 colonies, 4 PR-1 colonies and plasmid extraction was performed. They were then examined with 1 percent agarose gel for preliminary screening of gene-infiltrated plasmids. The plasmids obtained using the M13 primer DNA amplification were examined. Four of the correct sized clones were Actin clone 1, β-1,3-glucanase clone 2. , 3 and PR-1 clones at 2 (Figure 4) were then re-validated by DNA quantification with the Actin primer, β-1,3-glucanase, and PR-1. Four clones of the correct size were also found: Actin clone 1, β-1,3-glucanase clone 2, 3 and PR-1 clone 2 (Figure 5). Samples were sent for sequencing. The next nucleotide

The results of RNA extraction from mango fruit after inoculation for 0, 24, 48, 72, 96, 120 and 144 h were examined with 1 percent agarose gel to determine RNA content. A It was found that large amounts of RNA could be extracted. But there is also contamination resulting in low purity. Affects the detection of gene expression. As a result, this study was unable to verify gene expression.

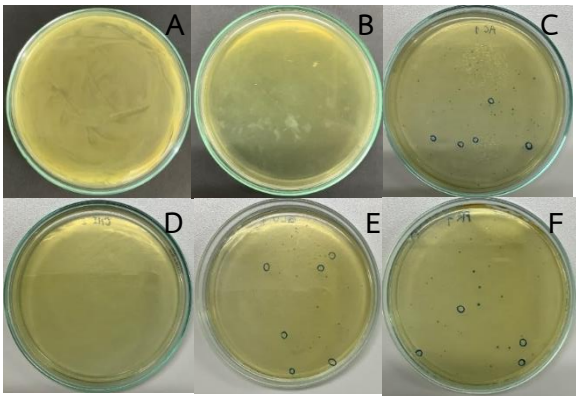

Fig. 3. Blue-white colonies on Ampicillin-added culture medium of Actin, Endochitinase, β-1,3-glucanase and PR-1 genes.
A; Negative control No Amp,X-gal,IPTG, B; Negative control with Amp,X-gal,IPTG, C; Actin, D; Endochitinase, E; β-1,3-glucanase, F; PR-1

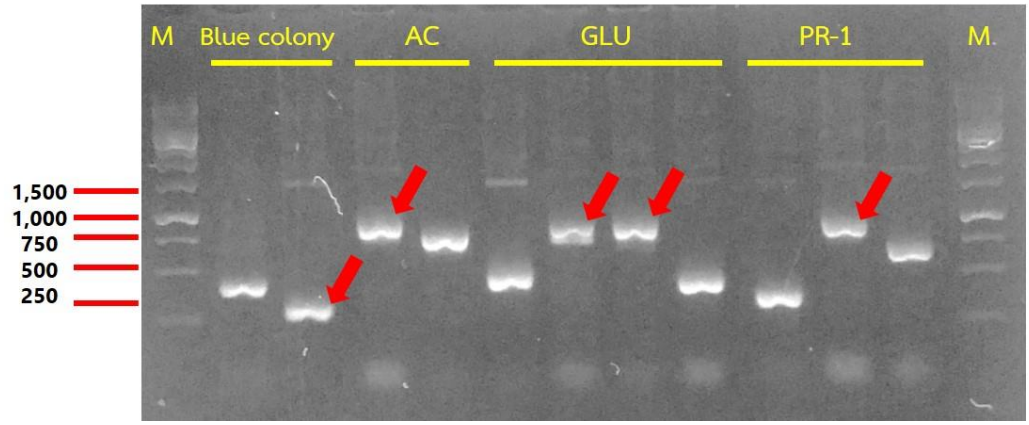

Figure 4 Examination of the plasmid obtained by DNA enrichment with an M13 primer.
(M = 1Kb DNA ladder Themo Scientific)

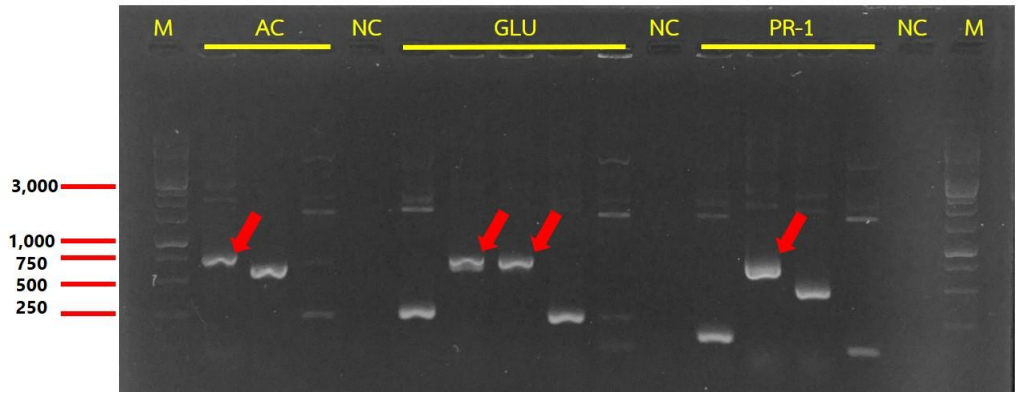

Figure 5 Examination of plasmids obtained by DNA enrichment with Actin primers, β-1,3-glucanase and PR-1.
(M = 1Kb DNA ladder Themo Scientific, NC = Negative control)

From the morphological observations of the fungi, samples 1, 2 and 7 had white filaments conidia are cylindrical with rounded ends and approximately 3 × 14 µm in size, consistent with a study by Rungthip Sankhphueak (2014). *Colletotrichum gloeosporioide* is approximately 3.23 × 13.4 µm. The fungi in samples 1, 2 and 7 are believed to be *C. gloeosporioides*. who want to study when taken for genetic testing to confirm the type of fungi by increasing the amount of DNA in the Internal Transcribed Spacer (ITS) by PCR technique, the resulting DNA fragments were between 500-550 base pairs. The nucleotide sequence data was analyzed with the NCBI database. Types of fungi samples 1 and 7 are considered fungal species. *Colletotrichum gloeosporioide* and the second sample was a type of fungi *Colletotrichum coffeanum*

The results of DNA extraction from mango leaves showed a large amount of DNA and low contamination. Agrawal et al. (1992)'s CTAB method was therefore an appropriate method. The amount of DNA was then added to the Actin, Endochitinase, β-1,3-glucanase, Phenylalanine ammonia (PAL), Lipoxygenase (LOX), PR-1 and Thaumatin-like protein (TLP) sites. Actin, Endochitinase, β-1,3-glucanase and PR-1 genes, but does not increase the amount of DNA around the gene. Phenylalanine ammonia (PAL), Lipoxygenase (LOX) and Thaumatin-like protein (TLP) can be obtained because the temperature used in the annealing procedure is not suitable as a primer. The DNA fragments of the Actin, Endochitinase, β-1,3-glucanase and PR-1 genes were then linked with pT257R/T plasmids and transferred to *E. coli* DH5α by heat shock method and then screened. Blue/white colony cloning results showed that plasmid containing DNA fragments in the Actin, β-1,3-glucanase and PR-1

genes was successfully transfected, but plasmid containing DNA fragments in the gene region was not transfected. Endochitinase was possible due to the plasmid transfection process into *E. coli* DH5α by heat shock method, a low efficiency method (Matsumura, 2015). White colonies were selected from the Actin gene, 3 colonies β-1,3-glucanase 5 colonies 4 PR-1 colonies and plasmids were extracted. The extraction results revealed that very small amounts of plasmid were obtained. This may be due to the bacterial extraction age beyond the log phase. Bacterial waste may inhibit the effectiveness of the plasmid extraction agent. This allows the extraction of plasmids in small quantities. After that, take it to check. Plasmids obtained using a DNA enrichment method with primers M13, Actin, β-1,3-glucanase and PR-1 were found to be 4 clones of the correct size, Actin clones at 1 β. -1,3-glucanase clones 2, 3 and PR-1 clones 2, other clones that do not have the expected size may be due to in cloning, there may be DNA fragments of various sizes. but cannot be examined by gel electrophoresis. As a result, those DNA fragments could be enriched with primers M13, Actin, β-1,3-glucanase and PR-1. Therefore, nucleotide sequencing samples were sent to verify the validity of the genes. Next

RNA extraction results showed that the resulting RNA was abundant. but also contaminated low purity This may be due to the fact that in the grinding process the samples are not yet thoroughly grinded. And the sample contains a lot of polysaccharides. The substance does not react at full efficiency making it impossible to extract RNA in large quantities each suction may be contaminated with substances in the phenol group. The resulting RNA was therefore of low purity and could not be used for gene expression testing. Therefore, this method of RNA extraction is not yet appropriate.

Conclusion: From the isolation of fungi that cause plant diseases Classification of fungi by morphology. Fungi were identified by genetic characteristics by increasing the DNA content at the Internal Transcribed Spacer (ITS) by PCR technique. The results of this study were able to identify all four genera of mango fungi, namely *Colletotrichum*, *Neoscytalidium*, *Lasiodiplodia* and *Pseudofusicoccum*. Fungus Two samples of *Colletotrichum gloeosporioides* were extracted from mango leaf DNA and cloned 7 genes. Three genes, actin, chitinase and PR-1 were successfully cloned by extracting RNA from mango after extraction. Infected for 0, 24, 48, 72, 96, 120 and 144 hours, it was found that large quantities of RNA could be extracted. but low purity When investigated for the expression of different genes, it has not been successful. Therefore, the design of a specific primer and pure RNA is an important factor in the further development of the anthracnose detection system in mangoes to lead to quality control of mangoes for export.

Acknowledgements:

The researcher would like to thank Asst. Prof. Dr.Maliwan Nakkunthod, advisor who advises and Ms.Sunisa Lunglue, who has always supported the research and thanked the Department of Biology, Faculty of Science, Naresuan University that supports equipment and places to do research

References:

1. Bill, M., Sivakumar, D., Beukes, M., & Korsten, L. (2016). Expression of pathogenesis-related (PR) genes in avocados fumigated with thyme oil vapours and control of anthracnose. *Food chemistry*, *194*, 938-943.

2. Lin, J., Gong, D., Zhu, S., Zhang, L., & Zhang, L. (2011). Expression of PPO and POD genes and contents of polyphenolic compounds in harvested mango fruits in relation to Benzothiadiazole-induced defense against anthracnose. *Scientia Horticulturae*, *130*(1), 85-89.
3. Matsumura, I. (2015). Why Johnny can't clone: Common pitfalls and not so common solutions. *BioTechniques*, *59*(3), IV-XIII. https://doi.org/10.2144/000114324
4. Niphon Visarathanonth, (1997). Elevation of carbendazim and mancozeb efficacies with fulvic acid to control anthracnose disease of 'Nam Dokmai' mango leaves and fruits by artificial inoculation studies. *Proceedings of the 35th Kasetsart University Annual Conference: Plant, Agricultural Extension and Communication and Agro-Industry*
5. Tovar-Pedraza, J. M., Mora-Aguilera, J. A., Nava-Díaz, C., Lima, N. B., Michereff, S. J., Sandoval-Islas, J. S., Câmara, M. P. S., Téliz-Ortiz, D., & Leyva-Mir, S. G. (2020). Distribution and Pathogenicity of Colletotrichum Species Associated With Mango Anthracnose in Mexico. *Plant Disease*, *104*(1), 137-146. https://doi.org/10.1094/pdis-01-19-0178-re
6. Wittaya Aphai, (1998). Chemical efficacy test in mango anthracnose control. Master of Science Thesis Department of Plant Pathology, Faculty of Agriculture, Kasetsart University.
7. Zhang, Z., Yang, D., Yang, B., Gao, Z., Li, M., Jiang, Y., & Hu, M. (2013). ß-Aminobutyric acid induces resistance of mango fruit to postharvest anthracnose caused by Colletotrichum gloeosporioides and enhances activity of fruit defense mechanisms. *Scientia Horticulturae*, *160*, 78-8

THE EFFECT OF AIR TEMPERATURE RISES INSIDE OPEN TOP CHAMBERS (OTCs) ON THE PHOTOSYNTHETIC ACTIVITY OF LICHEN *Heterodermia flabellata* AT DOI INTHANON, THAILAND.

Mongkol Phaengphech,[1,] Kruewan Pipatsawasdikul,[2] Wetchasart Polyiam,[1]*

[1]Lichen research unit, Department of Biology, Faculty of Science, Ramkhamhaeng University, Bangkok, 10240.
[2]Inthanon Lady's Slipper Orchid Under Initiative Conservation Project, Ban Luang, Chom Thong District, Chiang Mai 50160, Thailand.
*e-mail: wetchasart1p@gmail.com

Abstract:
Climate change is threatening lichen around the world, especially species growing at high elevations and in cool areas. This study aims to investigate the efficiency of photosynthetic activity of *Heterodermia flabellata* impacted by increased air temperature inside Open Top Chambers (OTCs). Five OTCs were installed for lichen experiments under field conditions at Doi Inthanon, Thailand. Our results found that the mean air temperature in the photosynthesis active and maximum air temperature inside OTCs has higher than 1.1 and 4.5°C, and relative humidity is lower than 4% compared with the references site (outside OTCs). The response of photosynthetic activity (Φ_{PSII} and ETR value) of *H. flabellata* related to thallus water content. Lichens growing inside OTCs had photosynthetic efficiency lower than lichens growing outside OTCs. Moreover, after three months of long-term monitoring, the Fv/Fm value of *H. flabellata* shows Fv/Fm value inside OTCs recorded at 0.535 lower than that outside OTCs recorded at 0.560. Therefore, the mean air temperature increases to 1.1°C could be affected to reduce photosynthetic efficiency and growth rate of lichens. In addition, the projection of increasing temperature results that endemic lichens having a high risk of extinction and deterioration of the lichen community under global warming.

Introduction:
Climate change is predicted as a great disaster thorough on all life on the earth and it will occur in the future. The Intergovernmental Panel on Climate Change (IPCC, 2022) reports that if global warming reaches 1.5 degrees Celsius (°C) in the near term, causing a loss of biodiversity in forest ecosystems. This risk was classified as moderate to high levels.
Lichens are diverse at 13,500-20,000 species worldwide.[1] Some species growing in cold areas and on top of high mountains are being affected by climate change.[2] However, many lichens had tolerant to high temperatures differently. Some species of lichen can be grown in high temperatures up to 50-70°C and are resistant to dry conditions.[3] But in wet conditions some lichens are a very low tolerance to high temperatures, which results in algae in lichens undergoing heat stress at 35-46°C. *Trebouxia* algae adapt very slowly to rising temperatures, and if sudden global warming occurs, many lichens are unable to adapt to new conditions.[4] Moreover, higher temperatures affected the photosynthesis process by reducing the efficiency of photosystem II (PSII). The lichens incubated under 45°C resulted in the photosystem II being damaged and inactive. Especially, at a position of Mn-cluster in photosystem II was destroyed.[5]
Climate changes were simulated by air temperature rise in Open Top Chambers (OTCs). This method can increase air temperature by 1-5°C, in the long-term experiment the lichen that

growing in OTCs may cause by reducing photosynthesis efficiency and increasing invasions by other vegetation.[7] For example, an increase in mosses population leads to a decline in lichen populations in the same areas.[8] Therefore, non-adaptive lichens in high temperatures may be a risk of extinction, while the heat-adapted lichens show tend to increase in population size and are invasive to native lichens. These results in the ecosystem balance being altered.[2]

Thus, the lichens inhabitant in the high mountain of Thailand, such as Doi Inthanon, Chiang Mai province, could be affected by climate change as found in another high mountains around the world. The specific lichen species growing in such conditions of high altitudes may disturb. Especially, *Heterodermia flabellata* is a common species in the area. This lichen is possible to be affected by climate change in the future. In this study, we aimed to observe the response to the efficiency of photosynthetic activity of *H. flabellata* under the microclimate variations at Doi Inthanon, which were affected by OTCs. Those simulated the future effect of climate changes on the adaptation of lichen communities inhabited at a high mountain.

Methodology:

Study area: The study site is in the Inthanon Lady's Slipper Orchid Under Initiative Conservation Project, Chiang Mai province, Thailand, which has an elevation between 1,600 and 1,700 m.a.s.l. This area used to be hill evergreen forests, and then it was converted into a botanical garden and orchid cultivation plot. The physiological data of lichen *Heterodermia flabellata* were selected and investigated in Open Top Chambers (OTCs) under the field condition (Figure 1.). *H. flabellata* is a common species in the study site, it's most distributed on the rocks.

An Open Top Chamber system (OTCs): The OTCs are the simulation of global warming, which could increase the air temperature by 2-3ºC. The OTC was made from six acrylic sheets, which were 3 mm thick with a trapezoid shape by the size of 25x20 cm. The acrylic sheets joined together to form a hexagonal box with an internal area of 1,623.8 cm^2. The complete OTCs were set up on rock surfaces where lichen grows (Figure 1).

Monitoring the photosynthetic activity of lichens: Responses of lichen inside and outside OTCs measured by using the chlorophyll fluorescence technique, and we divided into two experiments were studied as follows:

1). *The response of photosynthetic activity of lichens in the diurnal*: Ten thalli of *H. flabellata* at inside and outside OTCs were selected for measuring Φ_{PSII} and ETR, while five transferred thalli of each inside and outside OTCs used for measurements of thallus water content (TWC). Lichen thalli were monitored every 30 minutes during the day-times (5.30 a.m. to 9.30 p.m.) under climate inside and outside OTCs on 18 December 2021. The microclimate data was composed of light intensity, air temperature, and relative humidity inside and outside OTCs measured every 5 minutes from 17-21 December 2021 (Figure 1c).

2). *The response of the maximum efficiency of photosystem II of lichens under the simulation of climate change inside OTCs*: Five thalli of *H. flabellata* inside and outside OTCs selected for measurement of the Fv/Fm value, and these values compared at the start (September 2021) with three months after installed OTCs (December 2021).

Data analysis: The Φ_{PSII}, ETR values, and microclimate data were analyzed by made into graphs with SigmaPlot V.14.0 (Systat Software, Inc. Germany). The Fv/Fm values of lichens at the start and three months after installing OTCs, and inside and outside OTCs analyzed by pair t-test and comparing the differences between groups of OTCs analyzed by F- test (one-way anova) with SPSS version 26 (SPSS Inc. USA). The relationship between microclimates and photosynthetic efficiency of lichens was predicted by trends in survival and extinction risk of these lichens under climate changes.

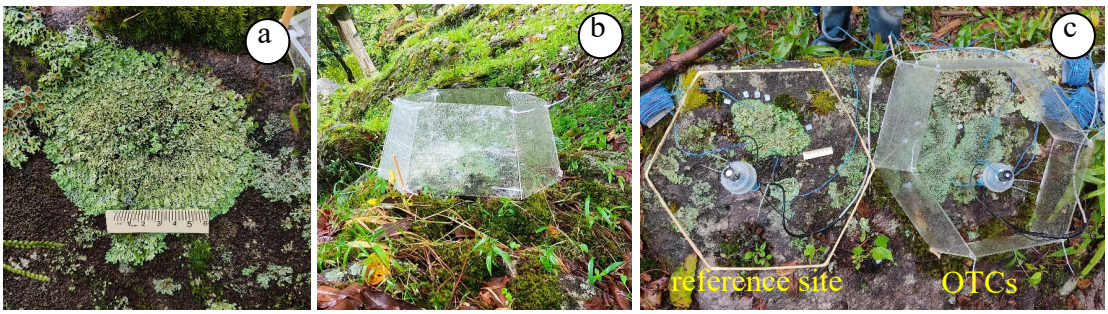

Figure 1. Field investigation of lichen physiology. The thallus of *Heterodermia flabellata* (a), Vertical view of an OTCs located on the rock surface where lichens grow (b), and Horizontal view of an OTCs (right) and a reference site (left), showing the *H. flabellata* thalli and microclimate sensors, which were installed inside OTCs and reference site (c). The OTCs were set up on rocks from 28 September to 21 December 2021.

Results and Discussion:

Microclimates inside OTC and reference site

The microclimate data inside and outside OTC were measured in mid-December 2021, the variation of microclimates during the observation period was shown in figure 2. Our results showed mean air temperature during the photosynthetic active period (6-10 a.m.) inside OTC had higher than outside at 1.1°C. While the maximum air temperatures inside OTC had higher than outside at 4.5°C. In addition, the thallus temperature of lichen inside OTC was slightly higher than outside (0.3-0.5°C). The relative humidity inside OTC is lower than outside about 4% during photosynthesis activity. The light intensity inside and outside OTC was no different.

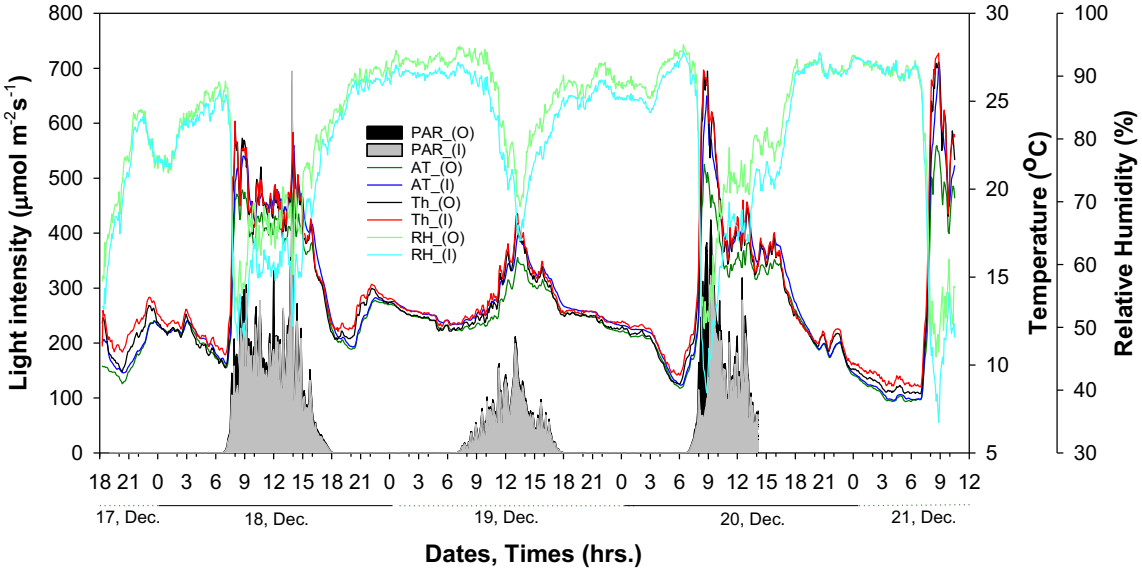

Figure 2. The microclimatic data includes light intensity (PAR), air temperature (AT), thallus temperature (Th), and relative humidity (RH) Inside (I) and Outside (O) of OTCs; data were recorded between 17 and 21 December 2021.

Physiology of *Heterodermia flabellata*

The physiological responses of lichen related to microclimate variation inside and outside OTCs, these consisted of the thallus water content (TWC) and the photosynthesis activity (Φ_{PSII}, ETR) (Figure 3). The highest TWC in lichen measured at 11-12% around 6.30 a.m., and the lichens thalli were dried after 10 a.m. (Figure 3a). The TWC in lichen was increased by the rehydration when high air humidity occurred during 5 p.m. of the day, which is no photosynthesis. The TWC of *H. flabellata* growing outside OTCs is slightly higher than inside OTCs, recorded at 1.1%. This result relates to an increase in air temperature resulting in a decrease in air humidity leading to reduced TWC.

The chlorophyll fluorescence method showed Φ_{PSII} and ETR values of the lichen. The Φ_{PSII} value outside OTCs at the photosynthesis pried had higher than inside OTCs, indicating that lichen was affected by higher temperature stress (Figure 3b). The highest Φ_{PSII} was recorded at 6.30 a.m. then decrease until 9:30 a.m. showing that the lichen thallus was dried out and the photosynthesis is inactive (Figure 3b), which this event corresponds to TWC. The ETR values showed that the photosynthesis activity of *H. flabellata* at outside OTCs has higher than inside OTCs, were indicated that lichen outside OTCs has a growth capacity than inside OTCs (Figure 3c).

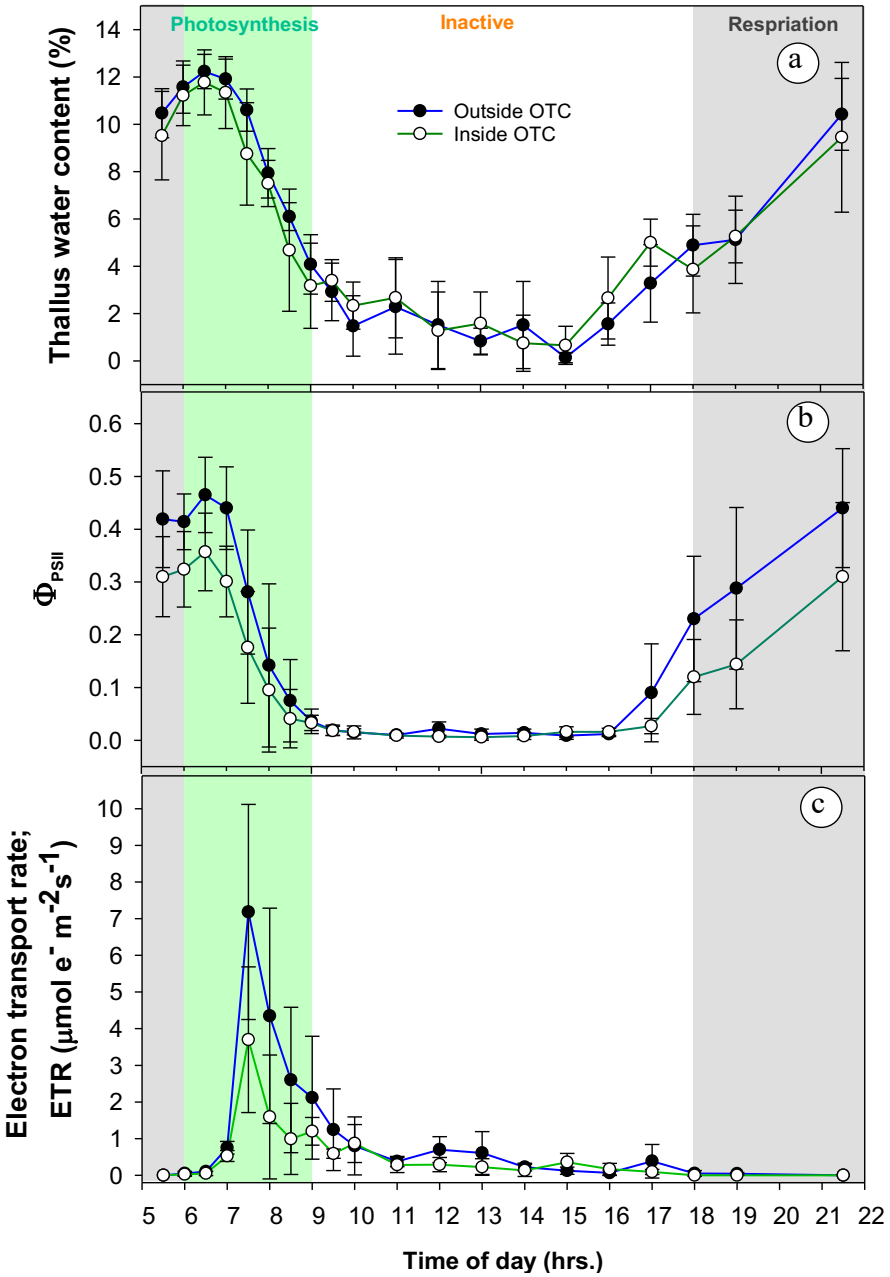

Figure 3. Variation of thallus physiology of *H. flabellate* with inside and outside OTCs, Thallus water content; TWC (a) quantum yield of PSII or Φ_{PSII} (b) and Electron transport rates; ETR (c). All parameters were measured every 30 minutes from 5.30 a.m. to 9.30 p.m. on 18 December 2021.

After 3 months of long-term monitoring, the lichen *H. flabellata* grew inside and outside OTCs (references site) were investigated the response of maximum quantum yield of PSII (Fv/Fm), as shown in Table 1. The decline of Fv/Fm value could be indicated that the photochemical processes in photosystem II of lichen occur under heat stress.[5] Our results found that the mean values of Fv/Fm of lichens growing outside and inside OTCs was 0.723, which was no difference in the beginning (September 2021). However, Fv/Fm values of outside OTC_3 and inside OTC_2 are different from other OTCs. After 3 months (in December

2021), all lichen experiments were adjusted to the stress conditions of the cool season. Mean values of Fv/Fm showed a decrease significantly at inside and outside OTCs accounting for 0.535 and 0.560 respectively.

The mean values of Fv/Fm of lichen outside and inside OTCs were not significantly different (Table 2.), but Fv/Fm value at inside OTCs have lower than outside OTCs at 4.5% approximately. Thus, the decreasing Fv/Fm value inside OTCs indicated that the lichens are affected by the unsuitable microclimate within OTCs, which simulated to increase in air temperature (>1-2°C) in the future. This study indicated that the rising air temperature can be affected the efficiency of photosystem II, especially the Mn-cluster in photosystem II were destroyed.[5] Thus, this result may be a long-term impact on lichens by reducing growth rate and thallus deterioration.[7]

Table 1.

The maximum quantum yield of PSII (Fv/Fm) of lichen *Heterodermia flabellata* was shown by Fv/Fm value. The Fv/Fm value inside with outside OTCs, and value at the start with 3 months after installed OTCs, were compared by t-test and F-test.

No. OTC	Fv/Fm value of lichen *Heterodermia flabellata* outside and inside OTCs							
	Start (Sep. 2021)		After 3 months (Dec. 2021)		*t-test*			
	Outside (1)	Inside (2)	Outside (3)	Inside (4)	(1)x(2)	(3)x(4)	(1)x(3)	(2)x(4)
OTC_1	0.732^{ab}	0.746^{a}	0.594	0.541^{ab}	1.74	0.65	5.70**	3.95*
OTC_2	0.752^{a}	0.716^{b}	0.633	0.572^{a}	-7.84***	3.92**	17.36***	10.26***
OTC_3	0.676^{b}	0.732^{ab}	0.473	0.438^{c}	1.89	0.451	3.53*	15.04***
OTC_4	0.723^{ab}	0.723^{ab}	0.589	0.572^{ab}	-0.03	0.64	5.04**	25.31***
OTC_5	0.758^{a}	0.723^{ab}	0.512	0.551^{bc}	-5.12***	-1.33	11.09***	9.83***
Mean(*F-test*)	$0.728^{(p=0.011)}$	$0.728^{(p=0.011)}$	$0.560^{(p=0.137)}$	$0.535^{(p<0.001)}$	0.06	0.84	11.78***	10.96***

Significant level; * is <0.05, ** is <0.01, *** is <0.001 (t-test), and ^{a,b,c} is different between groups of OTCs (F-test).

Further predicting of lichen communities

Our results found that lichen grows inside OTCs limited by an unsuitable microclimate. This condition is global warming simulation by increasing temperature and decreasing humidity causing in lower photosynthesis rate and slow growth of lichens.

Thus, this study revealed that lichens living under the conditions of OCTs probably in long term resulted in a lower growth rate and death in the future. In addition, the higher temperature inside OTCs could changes to a suitable condition for the warming lichens, mosses, and other bryophytes.[8] Whenever global warming occurs, our results predicted that the endemic lichens in high altitude areas or cool climates substituted for warming lichens studied in the polar and reported that the lichen community in that area has changed.[2]

Conclusion:

Open Top Chambers (OTCs) could simulate climate change with a 1.1°C increase in air temperature and 4% decrease in relative humidity, reducing the daily photosynthetic efficiency of lichen *H. flabellata*. The high-temperature effects that occur in the long-term can lead to decreasing in Fv/Fm, which this event may affect the growth of lichens in the future. Especially, endemic species that grow in highlands maybe change in lichens community. As well as lichens growing in lowlands move to higher lands and replace the native lichens.

Acknowledgments:

We would like to thank staff members of Inthanon lady's slipper orchid under the initiative conservation project for assistance in fieldwork, and our colleagues at the Lichen Research Unit, Ramkhamhaeng University. This study was funded by the National Research Council of Thailand (NRCT).

References:

1. Feuerer, T., & Hawksworth, D. L. Biodiversity and Conservation. 2007; 16: 85-98.
2. Aptroot, A., Stapper, N. J., Košuthová, A., & van Herk, K. Climate Change. 2021; 483-497.
3. Gauslaa, Y. J Exp Bot. 1999; 50: 697-705.
4. Nelsen, M. P., Leavitt, S. D., Heller, K., Muggia, L., & Lumbsch, H. T. Frontiers in Microbiology. 2022; 13:1-14
5. Bednaříková, M., Folgar-Cameán, Y., Kučerová, Z., Lazar, D., Spundova, M., Hájek, J., & Bartak, M. Photosynthetica. 2020; 58: 646-656.
6. Bokhorst, S., Huiskes, A., Aerts, R., Convey, P., Cooper, E., Dalen, L., Erschbamer, B., Gudmundsson, J., Hofgaard, A., Hollister, R., Johnstone, J., Jónsdóttir, I., Lebouvier, M., Van de Vijver, B., Wahren, C. H., & Dorrepaal, E. Global Change Biology. 2013; 19: 64-74.
7. Casanova-Katny, A., Bartak, M., & Gutierrez Campos, C. Czech Polar Reports. 2019; 9: 61-77.
8. Maphangwa, K. W., Musil, C. F., Raitt, L., & Zedda, L. Oecologia. 2012; 169: 257-268.

REDUCTION OF CISPLATIN RESISTANCE OF HUMAN ORAL SQUAMOUS CELL CARCINOMA CELL SPHEROIDS USING COLD ATMOSPHERIC PLASMA

Krittaya Aksonnam[1], Pimpon Uttayarat[2], Pimchanok Pimton[3]*
[1] Department of Immunology, Faculty of Medicine Siriraj Hospital, Mahidol University, Bangkok, Thailand
[2] Thailand Institute of Nuclear Technology (Public Organization), Nakhon Nayok, Thailand
[3] Biology Department, School of Science, Walailak University, Nakhon Si Thammarat, Thailand
*e-mail: pimchanok.pi@mail.wu.ac.th

Abstract:
Cold atmospheric plasma (CAP) has gained increasing attention in the treatment of cancer due to its controllable production of reactive oxygen and nitrogen species. In this study, we examined the effect of combined CAP-activated phosphate buffered saline (cPBS) and cisplatin-mediated chemotherapy *in vitro* on oral squamous cell carcinoma (OSCC) cells by using two-dimensional (2D) and three-dimensional (3D) culture models. The cPBS was generated by irradiation of PBS with plasma jet under room temperature. The 2D monolayers and 3D spheroids of OSCC cell line CLS-354 were then treated with gradient dilutions of cPBS, gradient concentrations of cisplatin or cPBS + cisplatin. The resulting cytotoxicity was monitored using MTT assay to obtain the half-maximal inhibitory concentration (IC_{50}) of cPBS and cisplatin. Our results demonstrated that the viability of CLS-354 monolayers and spheroids was inhibited by cPBS and cisplatin with a dose-dependent manner. However, CLS-354 spheroids exhibited lower IC_{50} to cPBS with higher IC_{50} to cisplatin than 2D cells, suggesting that spheroids were more sensitive to cPBS but resistant to cisplatin. IC_{50} values of cisplatin in CLS-354 spheroids were decreased in cPBS pretreated sequential combined treatments, indicating that chemosensitivity of CLS-354 spheroids to cisplatin was improved. Collectively, our data reinforced the importance of combination therapy to increase the effectiveness of chemotherapeutic drugs and suggested that resistance of CLS-354 spheroids to cisplatin could be reduced when used in combination with cPBS.

Introduction:

Oral squamous cell carcinoma (OSCC) is one of the most diagnosed cancers worldwide with the highest number recorded in Asia in 2020 [1]. It is associated with high rate of mortality and morbidity. Cisplatin is a front-line chemotherapy used in the treatment of OSCC [2]. The cytotoxicity of the drug is shown by its ability to bind to the OSCC cells' DNA and cause the formation of DNA adducts, which result in cell death. Unfortunately, the resistance to cisplatin persists in most patients, rendering them less responsive to further therapy [3]. Therefore, any new treatment is required to overcome the OSCC's resistance to cisplatin.

For the past decade, cold atmospheric plasma (CAP) has been regarded as a novel and promising modality for cancer treatment[4–6]. CAP is generally described as a room temperature ionized gas generated when feeding an inert gas with electrical energy, resulting in the production of several reactive oxygen species such as hydroxyl radical, superoxide, hydrogen peroxide, and ozone, and also reactive nitrogen species, such as nitric oxide, nitrite, and nitrate. Among these reactive species, hydrogen peroxide, nitrite, and nitrate play an important role in the mechanisms of CAP therapy [7–9].

The CAP-activated culture solution is a new anticancer agent and produced using CAP irradiation to the culture solution. In addition, CAP-activated culture solution is more advantageous than CAP irradiation because the solution can be administered just like chemotherapeutic agent. Currently, both CAP and CAP-activated solution provide new approaches for cancer treatment owing to its selective killing of cancer cells without damaging the neighboring normal cells [10–14]. Several studied have demonstrated that both CAP and CAP-activated culture solution have a selective effect toward several cancers including OSCC cells [15–17].

Combination therapy has recently gained a recognition as a cornerstone of cancer treatment [18]. It is an approach that combines two or more therapeutic agents to combat cancer. When agents with different mechanism are combined, each agent can be used at its optimal dose, without causing unendurable side effects. A less explored application of CAP is its use in combined therapy with cisplatin for OSCCs. Recently, Lee et al. demonstrated the synergistic effect of cisplatin and CAP treatment against human OSCC cells SCC-15 with low cytotoxicity against normal cells *in vitro* [15]. However, the study was done using traditional two-dimension (2D) cell culture, which might not reproduce the *in vivo* cell behavior in 3D tissue microenvironments. For this reason, many anticancer agents evaluated in 2D cell culture model have been considered clinically irrelevant [19].

To overcome the limitation of 2D cell culture model, spheroids have gained considerable attention as an alternative *in vitro* model that can mimic some aspects of 3D *in vivo* tumor tissues [20]. In this study, we proposed to evaluate the CAP-activated solution in combination with cisplatin using 3D spheroid model. By comparing the 3D spheroid with 2D monolayer of human OSCC cells CLS-354, we showed that spheroids were more resistant to cisplatin therapy and the resistance can be overcome by CAP-activated solution-pretreated sequential combined treatment.

Methodology:

Cell culture

Human OSCC cell line CLS-354[21] used in this study was kindly provided by Assoc. Prof. Dr. Warangkana Chunglok, School of Allied Health Sciences, Walailak University. They were grown in complete medium composed of RPMI-1640 basal medium (Corning, USA) supplemented with 10% fetal bovine serum, 2mM L-glutamine and 1% penicillin/streptomycin (Gibco, USA). The cells were maintained in the monolayer at 37°C in a humidified atmosphere with 5% CO_2.

CAP source and preparation of CAP-activated culture solution

The cold atmospheric plasma jet system was developed by the Plasmas and Electromagnetic Wave Science Center of Excellence, Walailak University, Thailand (Figure 1A). The operating condition of the plasma jet included argon gas flow rates at 5 SLM and input power of 22.5 W. In this study, a phosphate buffered saline (PBS) solution (Gibco, USA) was selected instead of cell culture media to produce CAP-activated culture solution because of its simple composition and similar osmolarity to the clinically accepted solution of normal saline [22]. Moreover, it has been shown to be more stable and as effective as CAP-activated media in killing cancer cells[22,23]. The PBS solution was prepared to 6 mL in sterile 50-mL beaker and activated by CAP for 120 sec. The distance between the open end of the quartz tube and the surface of the PBS solution was fixed at 4 mm during CAP treatment. From this point onward, the CAP-activated PBS was referred as cPBS.

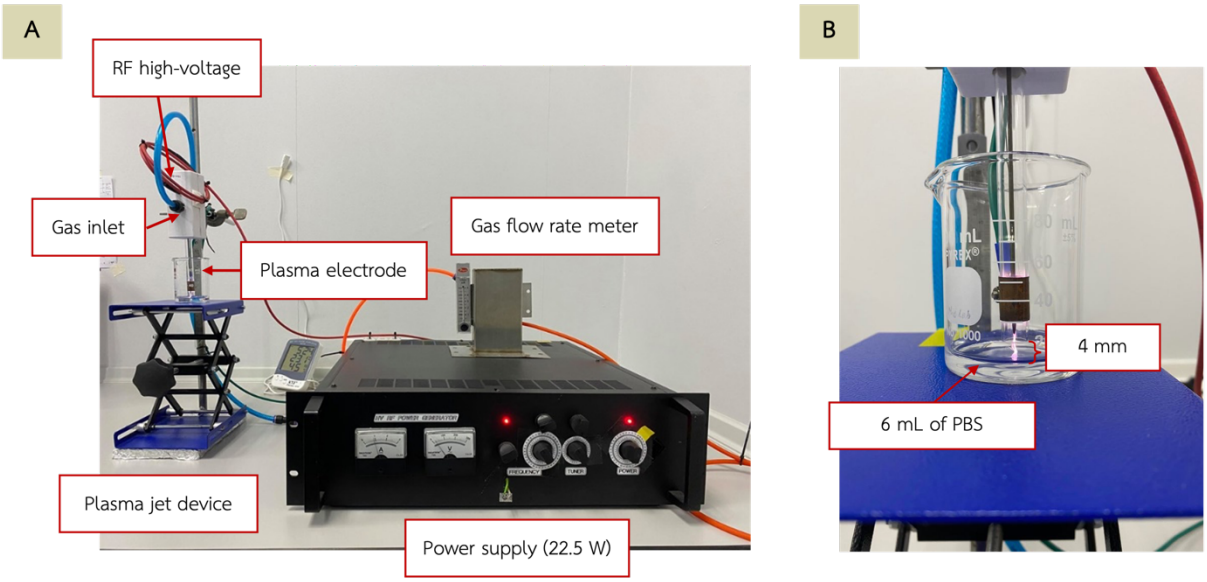

Figure 1.
The setup of (A) plasma jet system and (B) cPBS preparation.

Cell treatment with cPBS and ciplatin

For the 2D monolayer culture, a 100 µL of 1×10^4 CLS-354 cell solution was seeded in 96-well plates and incubated in CO_2 incubator at 37 ºC for 24 h before the treatment. For 3D spheroid generation, a 100 µL of 1×10^3 CLS-354 cell solution was seeded into ultralow attachment U-bottom 96-well plate and incubated in CO_2 incubator at 37 ºC for 3 days before the treatment. The cPBS was prepared immediately before the treatment and then diluted in complete medium (concentrations ranged from 3.52% to 64% cPBS). Cisplatin (Sigma, USA) stock solution prepared in normal saline were also diluted in complete media (concentrations ranged from 0.98 uM to 1000 uM cisplatin). For single agent treatment, the media on top of the cells grown in plates were carefully removed and replaced by complete media containing different concentration of cPBS or cisplatin. Cells were incubated for 24 h in CO_2 incubator at 37 ºC and then evaluated for their viability.

The half-maximal inhibitory concentration (IC_{50}) of cPBS and cisplatin was determined using the Quest Graph™ IC50 Calculator. AAT Bioquest, Inc. (Available online: https://www.aatbio.com/tools/ic50-calculator) [24].

For the combined cPBS + cisplatin treatment, the concentrations that caused 65% cell viability (IC_{65}) of single cPBS in monolayer cells was first determined. The IC_{65} was chosen to avoid drastic oxidative damage of cPBS + cisplatin to the cells. Additionally, to prevent possible interactions between cPBS and cisplatin, the combined treatments were designed to pretreat the cells with one agent at its IC_{65} for 12 h, then sequentially treated with another agent at varying concentrations for another 12 h. Thus, 2D monolayers or 3D spheroids of CLS-354 cells were first pretreated with a fixed IC_{65} concentration of cPBS, then replaced with the complete medium that contained varied concentrations of cisplatin (0.98 uM to 1000 uM). Cells replaced with complete media were served as control in all experiments.

Cell viability assay

To study the cytotoxicity of cPBS and cisplatin on CLS-354 cells, the viability of CLS-354 cells in response to different cPBS and cisplatin concentration were evaluated, and the levels of cytotoxicity were characterized according to guideline in previous report[25]: cell viability above 80% are considered as non-cytotoxicity; within 80%-60% weak; 60%-40% moderate and below 40% strong cytotoxicity, respectively[25].

After a total treatment time of 24 h, the treatment media were removed. Then, 50 µL of freshly prepared 0.5 mg/ml MTT was added to the control and treated cells in 2D culture and incubated for 3 h in CO_2 incubator at 37 ºC. Later, the formazan crystal was dissolved in 100 µL of isopropanol and incubated for 30 min at room temperature. Absorbance of the formazan solution was measured at a wavelength of 570 nm and 670 nm with an Eon Microplate Reader (BioTek, USA). Each treatment was repeated three times (n = 3).

Cell viability in the spheroid culture was detected using modified MTT assay. Briefly, after 24 h of incubation, 10 µL of 5 mg/mL MTT solution was added to the control and treated spheroids and the spheroids were incubated for 3 hours in CO_2 incubator at 37 ºC. Later, the formazan crystal was dissolved in 100 µL of 10% SDS in 10 mM HCl and incubated overnight at room temperature to allow the formazan crystal inside spheroids to be completely dissolved. Absorbance of the formazan solution was measured at a wavelength of 570 nm and 690 nm with an Eon Microplate Reader (BioTek, USA). Each treatment was repeated three times (n = 3).

Statistical analysis

All data were expressed as mean ± SD from triplicate samples collected from three independent experiments. Statistical significances were analyzed using the Student's t- test. P values of < 0.05 were considered statistically significant.

Results and Discussion:

Cytotoxicity of cisplatin alone to CLS-354 cells in 2D monolayer and 3D spheroid system

In this study, cisplatin alone exhibited the ability to decrease the viability of CLS-354 cells. In the 2D culture system, cisplatin concentration lower than 7.81 uM did not cause any toxicity to the cells. However, at higher concentration from 7.81 to 1000 µM, the cell viability was shown to be inhibited in a dose dependent manner (Figure 2). In 3D culture system, CLS-354 spheroids were able to tolerate cisplatin up to 125 µM. The cisplatin concentrations of 250 µM, 500 µM and 1,000 µM exhibited weak, moderate, and strong cytotoxicity, respectively (Table 1). Half maximum inhibitory concentration (IC_{50}) is essential for comparison of cytotoxicity and can be obtained using CompuSyn software[26]. The result from CompuSyn software showed that IC_{50} of cisplatin in 2D and 3D culture system was at 17.76 µM and 480.39 µM, respectively. The IC_{50} values determined with cells cultured in spheroids were approximately 27-fold higher than that of cells grown in a monolayer. The data demonstrated that 3D spheroid culture of CLS-354 cells were less susceptible to cisplatin than their 2D counterpart. This indicated that 3D cells exhibited resistant to cisplatin. Concurrently, cisplatin resistance was reported in the treatment of oral cancer in 3D microenvironment. Dasari *et al.* [27] reported that cisplatin alone was not an effective drug in treating the head and neck squamous cell carcinoma. Additionally, cisplatin resistant was reported to be due to the increased expression of Nanog and Sox1[28]. Therefore, many studies aimed to find more effective therapy to substitute or use in combination with cisplatin to increase the efficiency of the treatment. Several evidence has shown higher efficiency of combination of cisplatin with other therapies in overcoming drug resistance[29].

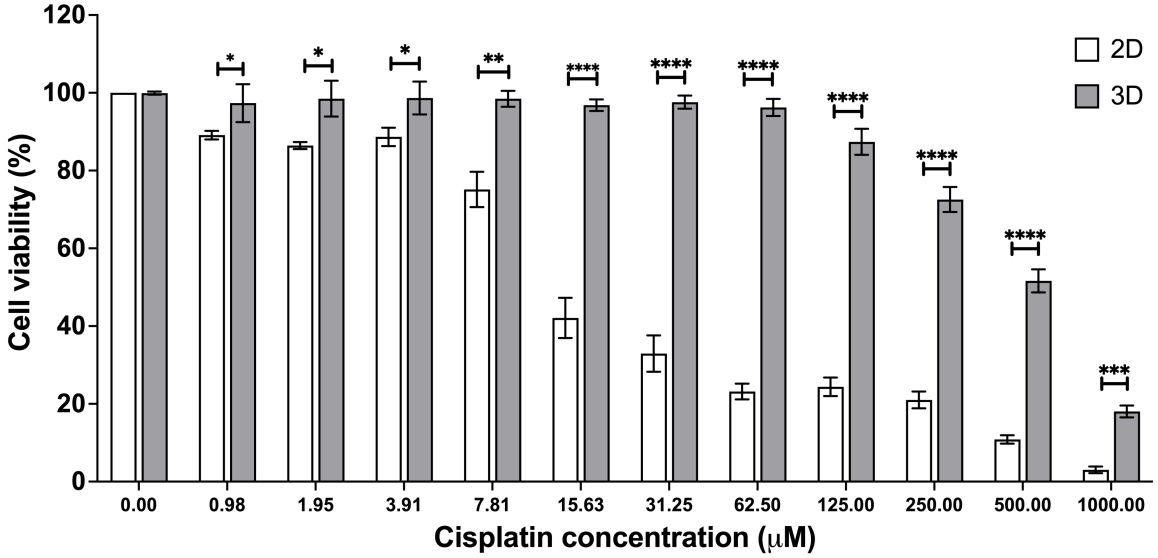

Figure 2.

CLS-354 cell viability in 2D and 3D culture systems after treated for 24 h with cisplatin concentration ranging from 0.98 uM to 1000 μM. Data are expressed as means ± SD.

Table 1. Different cytotoxicity levels of cisplatin in 2D and 3D culture systems

System	Cisplatin concentrations (μM) and corresponding cytotoxicity levels				IC_{50} (uM)
	None	Weak	Moderate	Strong	
2D	0 - 3.91	7.81	15.63	31.25 - 1000	17.76
3D	0 - 125	250	500	1000	480.39

Cytotoxicity of cPBS alone to CLS-354 cells in 2D monolayer and 3D spheroid system

Treatment with cPBS has shown to decrease the viability of CLS-354 cells in both 2D and 3D culture systems in dose dependent manner. In the 2D culture system, cPBS concentration lower than 32.77% exhibited no toxicity as cell viability remained above 80%. At higher concentrations, cPBS exhibited weak, moderate, and strong cytotoxicity at 32.77% - 40.96%, 51.2% and 64%, respectively (Table 2). For the 3D culture system, cPBS decreased the viability of CLS-354 spheroid in a dose dependent manner and cell viability was significantly lower compared to the 2D system (Figure 3). The cPBS concentration higher than 10.74% exhibited toxicity to CLS-354 spheroids (Table 2). The IC50 of cPBS in CLS-354 cells in 2D and 3D culture was at 47.80% and 35.48%, respectively. These IC50 values indicated that CLS-354 spheroids were more sensitive to cPBS than CLS-354 cells in 2D culture system. Based on these results, cPBS exhibited a better potential for killing oral cancer cell when cultured in 3D. Moreover, as spheroid exhibited a resistant to cisplatin, it would be better to use cPBS together with cisplatin to help reduce the viability of CLS-354 cells in 3D environment.

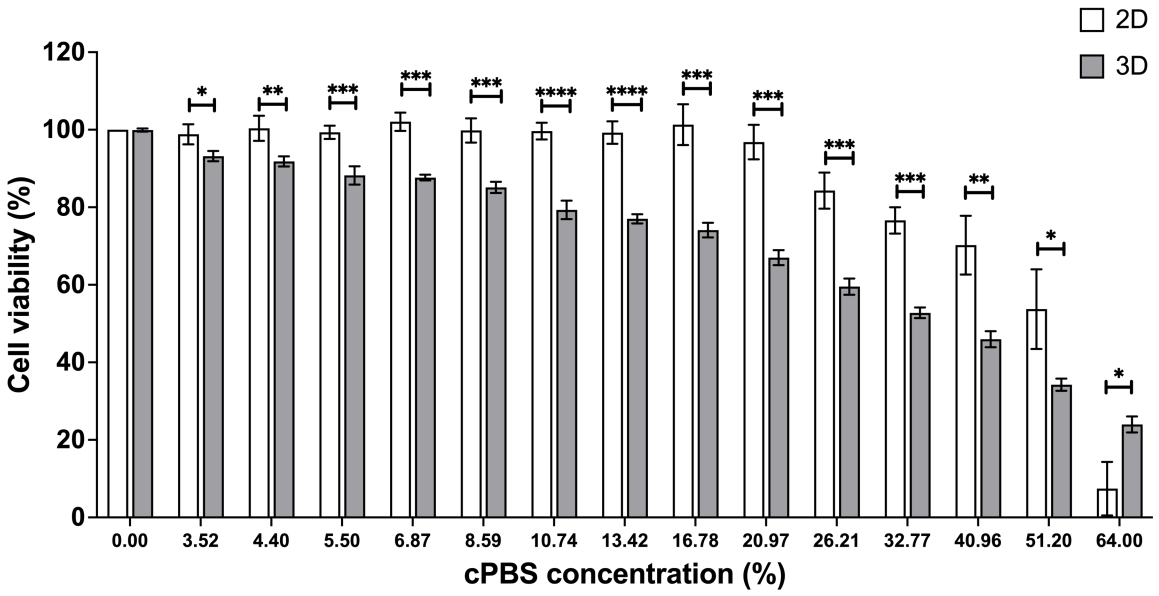

Figure 3.
CLS-354 cell viability in 2D and 3D culture system when treated for 24 h with pPBS concentration ranging from 3.52% to 64%. Values are expressed as means ± SD.

Table 2. Different cytotoxicity levels of cPBS in 2D and 3D culture system

System	cPBS concentration (%) and corresponding cytotoxicity levels				IC_{50} (%)
	None	Weak	Moderate	Strong	
2D	0 - 26.21	32.77 - 40.96	51.2	64	47.80
3D	0 - 8.59	10.74 - 20.97	21.21 - 40.96	51.2 - 64	35.48

Sequential combinations of cPBS and cisplatin against CLS-354 cells in 2D monolayer and 3D spheroid system

The IC_{65} of cPBS in monolayer cells was 42%. When sequential combination was tested in 2D system, dose dependent response to varying cisplatin concentration did not establish (Figure 4). The cisplatin concentration ranging from 0.98 to 62.5 μM exhibited weak cytotoxicity (Table 3). Cisplatin concentration higher than 62.5 μM exhibited moderate cytotoxicity. No strong cytotoxicity was observed. The IC_{50} values of cisplatin obtained for sequential combined treatment in CLS-354 cells in 2D was above 600 μM, which was relatively higher than that of single cisplatin treatment.

When cPBS pretreatment was sequentially combined with cisplatin in the 3D system, the viability of CLS-354 spheroid was decreased in dose dependent manner with the concentration of cisplatin ranging from 62.5 to 1000 μM (Figure 4). Cisplatin concentration ranging from 0.98 to 62.5 μM was non-cytotoxic. Cisplatin concentration at 125 and 250 uM exhibited weak cytotoxicity. Cisplatin concentration at 500 and 1000 μM developed strong cytotoxicity. The IC_{50} of cisplatin for this sequentially combined treatment in CLS-354 spheroids was at 465.26 μM, which was relatively lower than that of single cisplatin treatment in 3D culture system. These results indicated that in contrast to the 2D culture system, cPBS might facilitate the effect of cisplatin on the CLS-354 spheroids.

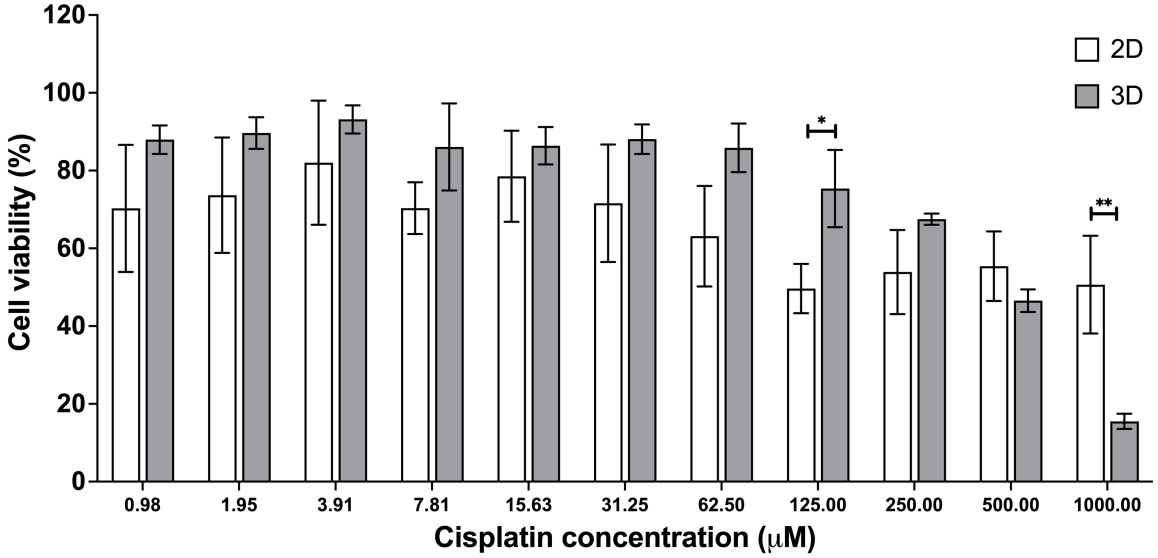

Figure 4.
CLS-354 cell viability in 2D and 3D culture systems after treated for 12 h with 42% cPBS followed by 12 h with cisplatin with concentration ranging from 0.98 – 1000 μM. Values are expressed as means ± SD.

Table 3. Different cytotoxicity levels of cPBS + cisplatin in the sequentially combined treatment in 2D and 3D culture systems

System	Cytotoxicity levels corresponded to cisplatin concentration (μM) in sequential combined treatment				IC_{50} (μM)
	None	Weak	Moderate	Strong	
2D	-	0.98 – 62.5	125 - 1000	-	> 600
3D	0.98 to 62.5	125 - 250	-	500 - 1000	465.26

Conclusion:

The effects of cisplatin activated plasma in the form of cPBS, and sequentially combined cPBS + cisplatin approach on OSCC cells cultured in 2D vs. 3D systems were established. Cytotoxicity evaluation showed that cell monolayer was more sensitive to cisplatin, whereas cells in spheroid was more sensitive to cPBS. For the sequentially combined approach, cells cultured in spheroids were also shown to be more sensitive to the treatment at lower concentration. These results showed that cPBS alone was more effective than cisplatin in combating cancer cells in 3D environment and therefore had the potential to serve as an anticancer agent against OSCCs.

References:

1. Oral cancer - the fight must go on against all odds…. Evid Based Dent2022; 23.
2. Chen S, Hu H, Miao S, Zheng J, Xie Z, Zhao H. Anti-tumor effect of cisplatin in human oral squamous cell carcinoma was enhanced by andrographolide via upregulation of phospho-p53 in vitro and in vivo. Tumor Biology 2017; 39.

3. Wu T, Jiao Z, Li Y, Su X, Yao F, Peng J, Chen W, Yang A. HPRT1 Promotes Chemoresistance in Oral Squamous Cell Carcinoma via Activating MMP1/PI3K/Akt Signaling Pathway. Cancers (Basel) 2022; 14.
4. Ratovitski EA, Cheng X, Yan D, Sherman JH, Canady J, Trink B, Keidar M. Anti-cancer therapies of 21st century: Novel approach to treat human cancers using cold atmospheric plasma. Plasma Processes and Polymers2014;
5. Yan D, Sherman JH, Keidar M. The Application of the Cold Atmospheric Plasma-Activated Solutions in Cancer Treatment. Anticancer Agents Med Chem 2017;
6. Yan D, Sherman JH, Keidar M. Cold atmospheric plasma, a novel promising anti-cancer treatment modality. Oncotarget2017;
7. Ahn HJ, Kim K il, Hoan NN, Kim CH, Moon E, Choi KS, Yang SS, Lee JS. Targeting cancer cells with reactive oxygen and nitrogen species generated by atmospheric-pressure air plasma. PLoS One 2014;
8. Stoffels E, Sakiyama Y, Graves DB. Cold atmospheric plasma: Charged species and their interactions with cells and tissues. IEEE Transactions on Plasma Science 2008;
9. Bauer G, Sersenová D, Graves DB, Machala Z. Cold Atmospheric Plasma and Plasma-Activated Medium Trigger RONS-Based Tumor Cell Apoptosis. Sci Rep 2019;
10. Li Y, Tang T, Lee HJ, Song K. Selective anti-cancer effects of plasma-activated medium and its high efficacy with cisplatin on hepatocellular carcinoma with cancer stem cell characteristics. Int J Mol Sci 2021; 22.
11. Subramanian PSG, Jain A, Shivapuji AM, Sundaresan NR, Dasappa S, Rao L. Plasma-activated water from a dielectric barrier discharge plasma source for the selective treatment of cancer cells. Plasma Processes and Polymers 2020; 17.
12. Bisag A, Bucci C, Coluccelli S, Girolimetti G, Laurita R, de Iaco P, Perrone AM, Gherardi M, Marchio L, Porcelli AM, et al. Plasma-activated ringer's lactate solution displays a selective cytotoxic effect on ovarian cancer cells. Cancers (Basel) 2020; 12.
13. Li Y, Tang T, Lee H, Song K. Cold atmospheric pressure plasma-activated medium induces selective cell death in human hepatocellular carcinoma cells independently of singlet oxygen, hydrogen peroxide, nitric oxide and nitrite/nitrate. Int J Mol Sci 2021; 22.
14. Harley JC, Suchowerska N, McKenzie DR. Cancer treatment with gas plasma and with gas plasma–activated liquid: positives, potentials and problems of clinical translation. Biophys Rev2020; 12.
15. Lee CM, Jeong Y il, Kook MS, Kim BH. Combinatorial effect of cold atmosphere plasma (Cap) and the anticancer drug cisplatin on oral squamous cell cancer therapy. Int J Mol Sci 2020; 21.
16. Ramireddy L, Lai CH, Low BS, Li C, Hsieh JH, Lee JW, Wu HY. Induction of apoptosis by cold atmospheric pressure plasma for oral squamous cell carcinoma cells. Plasma Med 2018; 8.
17. Ramireddy L, Lai CH, Low BS, Li C, Hsieh JH, Lee JW, Wu HY. Cold atmospheric helium plasma induces apoptosis by increasing intracellular reactive oxygen and nitrogen species. Plasma Med 2020; 10.
18. Mokhtari RB, Homayouni TS, Baluch N, Morgatskaya E, Kumar S, Das B, Yeger H. Combination therapy in combating cancer. Oncotarget2017; 8.
19. Weiswald LB, Bellet D, Dangles-Marie V. Spherical Cancer Models in Tumor Biology. Neoplasia (United States)2015; 17.
20. Filipiak-Duliban A, Brodaczewska K, Kajdasz A, Kieda C. Spheroid Culture Differentially Affects Cancer Cell Sensitivity to Drugs in Melanoma and RCC Models. Int J Mol Sci 2022; 23.

21. Utaipan T, Sattayakhom A, Prachongsai I, Charong N, Chunglok W. Reduction of intracellular-reactive oxygen species and diminished mitogen-activated protein kinases (MAPKs) activation are associated with oral squamous cell carcinoma cell aggressiveness. Walailak J Sci Technol 2018;
22. Freund E, Liedtke KR, van der Linde J, Metelmann HR, Heidecke CD, Partecke LI, Bekeschus S. Physical plasma-treated saline promotes an immunogenic phenotype in CT26 colon cancer cells in vitro and in vivo. Sci Rep 2019;
23. Freund E, Liedtke KR, Gebbe R, Heidecke AK, Partecke L-I, Bekeschus S. In Vitro Anticancer Efficacy of Six Different Clinically Approved Types of Liquids Exposed to Physical Plasma . IEEE Trans Radiat Plasma Med Sci 2019;
24. Almosa H, Alqriqri M, Denetiu I, Baghdadi MA, Alkhaled M, Alhosin M, Aldajani WA, Zamzami M, Ucisik MH, Damiati S. Cytotoxicity of standardized curcuminoids mixture against epithelial ovarian cancer cell line SKOV-3. Sci Pharm 2020; 88.
25. López-García J, Lehocký M, Humpolíček P, Sáha P. HaCaT Keratinocytes Response on Antimicrobial Atelocollagen Substrates: Extent of Cytotoxicity, Cell Viability and Proliferation. J Funct Biomater 2014; 5.
26. Tun JO, Salvador-Reyes LA, Velarde MC, Saito N, Suwanborirux K, Concepcion GP. Synergistic cytotoxicity of renieramycin M and doxorubicin in MCF-7 breast cancer cells. Mar Drugs 2019; 17.
27. Dasari S, Bernard Tchounwou P. Cisplatin in cancer therapy: Molecular mechanisms of action. Eur J Pharmacol2014; 740.
28. Melissaridou S, Wiechec E, Magan M, Jain MV, Chung MK, Farnebo L, Roberg K. The effect of 2D and 3D cell cultures on treatment response, EMT profile and stem cell features in head and neck cancer. Cancer Cell Int 2019; 19.
29. Aldossary SA. Review on pharmacology of cisplatin: Clinical use, toxicity and mechanism of resistance of cisplatin. Biomedical and Pharmacology Journal 2019; 12.

EFFECT OF MAGNETIC FIELD STIMULATION COMPARED WITH SALICYLIC ACID ELICITATION ON BACOSIDE A ACCUMULATION IN *Bacopa monnieri* (L.) Wettst.

Lalin Tunprasert, Narisa Kunpratum, Marootpong Pooam*
Department of Biology, Faculty of Science, Naresuan University, Phitsanulok, Thailand
*e-mail: marootpongp@nu.ac.th

Abstract:
The bioactive compound which is recognized as a memory enhancer found in *Bacopa monnieri* is called Bacoside A. This study aims to find a way to induce this compound by using 1 mM salicylic acid treating after 4 weeks of culture and using 2 mT magnetic field elicitations (static magnetic field and pulsed electromagnetic field) treating 10 minutes every day for 4 weeks. These two elicitors can cause stress by increasing reactive oxygen species (ROS) production in plant cells and leading to an increase in some antioxidant enzymes and secondary metabolites. After detecting ROS production and DPPH antioxidant activity using a spectrophotometer, detecting Bacoside A using High-performance liquid chromatography (HPLC), we found that magnetic field elicitation can increase ROS production, and both elicitors can increase the antioxidant enzyme activity. However, the Bacoside A production tends to decrease in all treatments. This result suggests that the plant synthesizes other antioxidant enzymes or secondary metabolites instead of Bacoside A in response to the stress, because Bacoside A is not involved in plant defense mechanisms.

Introduction:

Bacopa monnieri (L.) Wettst. (Brahmi) has been widely used in Ayurvedic medicine as a memory enhancer and to cure some pharmacological disorders. The chemical components in Brahmi include various classes of secondary metabolites such as sterols, flavonoids, and saponins called bacosides, which are the main components of its enhancing properties.[1] Because of its pharmaceutical and medicinal treatment importance, the need for this plant has been increasing for many years. Many people find a way to expand bacosides production by using plant culture techniques along with the elicitors. Elicitors are the chemical compounds from abiotic sources (physical, chemical, and hormonal) or biotic sources (polysaccharides, yeast extract, fungal and bacterial) that can cause stress and activate the plant defense mechanism. After that stress, the plant will produce and accumulate more secondary metabolites to protect itself. Numerous studies have found that plant hormones can be an excellent elicitor to get more medicinal compounds. For example, salicylic acid (SA) is a plant hormone that acts as a signaling molecule to activate plant defense responses. It can also act as a stimulator through the signal transduction pathway to synthesize the secondary metabolites, including the bacosides in Brahmi.[2] Furthermore, the study reveals that elicitation with salicylic acid can also stimulate the production of reactive oxygen species (ROS) by inhibiting the catalase, which converts H_2O_2 to H_2O. These ROS will activate PR gene expression and induce the plant defense mechanism. However, if ROS is accumulated at a higher level and excess over the plant defense mechanism, it can lead to oxidative stress.[3,4]

Interestingly, the magnetic field, an abiotic source, can also cause the formation of free radicals and oxidative stress in living organisms. In which, magnetic field is one of the fundamental forces in the universe that can be generated from the Earth, called the Earth's magnetic field. Moreover, the rapid development of technology in telecommunication

contributes to the generation of electromagnetic fields with a wide range of frequencies and intensities in the environment, called Man-made magnetic fields. Thus, from prokaryote-like bacteria to eukaryotes like us, the organisms on this planet are surrounded by magnetic fields. Hence, magnetic fields could influence living organisms. For almost a century, it has been known that some migratory animals, for example, the European robin can use the Earth's magnetic field as a compass for navigation. In humans, the biological effect of electromagnetic fields in the environment is a public concern since some reports have shown the involvement of electromagnetic fields in increasing health risks such as childhood leukemia.[5] However, some researchers have discovered that electromagnetic fields can be beneficial to human health. For example, the application of pulsed electromagnetic fields (PMF), a discontinuous pulsed magnetic generator, has been used in regenerative medicine and the treatment of different types of pain as therapeutic tools, especially in the field of orthopedics and neurological diseases.[6] In plants, magnetic fields can also affect the rate of seed germination and plant development.[7] The use of magnetic fields has been recently proposed for the enhancement of secondary metabolite production. The treatments of cell suspension-cultured, the static magnetic field (SMF) at specific intensities, and magnetite nanoparticles as abiotic elicitors can increase the total secondary metabolites, and they are less hazardous for the environment.[8]

For the mechanism, there is a candidate biological magnetoreceptor in living organisms called cryptochromes, which is the flavoprotein photoreceptor and can be sensitive to blue light. Cryptochromes can undergo redox reactions while activating the synthesis of ROS, which are the regulators in cellular signaling functions of the plant stress response.[9] The level of ROS production could be regulated by the generation of magnetic fields and then affect the other signaling pathways. For example, the low level of ROS formation by magnetic fields could induce some protective mechanisms in living organisms. In this case, ROS might trigger some antioxidant genes or be involved in some secondary metabolite production. Furthermore, a study shows that magnetic field treatment of maize seeds in optimal concentration can enhance growth and photosynthesis under soil stress, and a significant increase in ROS after magnetic fields treatment shows an essential change in the initial stage of seed development by having longer hypocotyls, roots, and thus greater vigor.[10] It was illustrated that ROS formation stimulated by magnetic fields could induce plants to produce more antioxidant enzymes or secondary metabolites after activating their protective mechanisms, which consequently help them to survive in an unsuitable environment.

According to the effect of both elicitors on plant defense mechanisms, this study aims to enhance the production of bacoside A, a secondary metabolite in *B. monnieri*, by using magnetic field stimulation (both SMF and PMF) individually and in combination with salicylic acid (SA). This plant hormone is very well documented for increasing secondary metabolites. The magnetic fields can be elicitors, which are less harmful and save cost more than the plant hormones.

Methodology:

Magnetic fields preparation

The static magnetic field (SMF) was generated by Helmholtz coils with magnetic field strength (2–60 mT), and a gap of 10 cm between coils was fabricated. The diameter of each coil is 9 cm and the number of turns per coil is 50. A DC power supply 5A (Spectrum, Thailand) with continuous variable output current was used for the electromagnet. A digital Gauss meter model U1300 (3B-Scientific, Hamburg, Germany) was used to calibrate and set up the magnetic intensity for the experiment. The intensity is 2 mT.[10]

The pulsed electromagnetic field (PMF) was generated using repetitive low-intensity magnetic stimulation from medical therapeutic tools, which is used for the treatment of bone-

related diseases (EC10701; GEM Pty Ltd., Perth, Western Australia). The coil in the device is 9 x 5.5 cm and the number of turns per coil is 200. The samples were placed in the petri dish, distancing them 1 cm from the device. The highest intensity is 2 mT, and the intensity will change at a frequency 10 Hz.

Plant materials and treatments

The shoots of *B. monnieri* were cultured under Deep Flow Technique hydroponics system in 50% Hoagland Solution for 4 weeks. During the growth, the plants were treated with the magnetic fields and salicylic acid as the following,

Treatment 1 – no elicitation (Control)
Treatment 2 – 1 mM Salicylic acid (SA)
Treatment 3 – Pulsed electromagnetic field (PMF)
Treatment 4 – Static magnetic field (SMF)
Treatment 5 – Pulsed electromagnetic field + 1 mM Salicylic acid (PMF+SA)
Treatment 6 – Static magnetic field + 1 mM Salicylic acid (SMF+SA)

The magnetic field treatments (Treatment 3,4) were treated with the magnetic field generators for 10 minutes every day until harvesting. Unlike the salicylic acid treatment (Treatment 2), it was sprayed on the plant only in week 4 after culture. The volume is 10 ml/ sample. For the combination treatment (Treatment 5,6), the plants were treated with magnetic field generators for 10 minutes every day. After that, the plants were sprayed with salicylic acid in week 4 after culture, and they continued to be treated with magnetic fields until harvesting. All the treatments were harvested on day 2 after salicylic acid treatment. The plant materials were dried in a hot air oven at 40 ºC until the weight was stable.

Reactive Oxygen Species (ROS) detection

0.1 g dried powder of *B. monnieri* was dissolved in 0.1% Trichloroacetic acid (TCA) 1 ml, mixed with a vortex, and centrifuged at 10,000 rpm for 20 minutes. The supernatants were collected into a new tube for 300 µl, added more than 300 µl of 0.1% TCA and 300 µl of 1M Potassium iodide (KI). The samples were mixed and incubated for 20 minutes. The absorbance of ROS was detected at 267 nm by using a UV/Visible spectrophotometer (Jenway 7415). The results of ROS production were calculated from the standard curve of hydrogen peroxide (H_2O_2).

Antioxidant activity analysis using DPPH

0.01 g dried powder of *B. monnieri* was dissolved in 1 ml absolute ethanol, mixed with a vortex for 1 minute, and centrifuged at 6,000 rpm for 30 minutes. After that, 100 µl of extracts and 100 µl of DPPH were transferred into a 96-well microplate. The samples were mixed and incubated for 30 minutes in the dark. The absorbance was measured at 515 nm by using a multimode microplate reader (BioTek Synergy H1). The scavenging activity was calculated as a percentage of oxidative inhibition in the formula below:

% Oxidative inhibition = [(OD515 control – OD515 sample) / OD515 Control] x 100

Bacoside A detection using High-performance liquid chromatography (HPLC)

B. monnieri needs to be extracted to get the bacoside A content before detection with HPLC. 1 ml methanol (HPLC grade) was added to 0.1 g dried powder of *B. monnieri*, mixed with a vortex for 1 minute, sonicated at 40ºC for 15 minutes, and centrifuged at 8,000 rpm for 3 minutes. After that, the supernatant was collected into a new tube, and the residue was used to extract again. The extraction is repeated two times, and the last collected solution is about 3 ml. The solution was diluted ¼ times before being filtered through a 0.45 m filter membrane into a 1.5 ml vial, with the caps wrapped in Parafilm tape and kept at -20ºC until the injection into HPLC.

High-Performance Liquid Chromatography (HPLC) Agilent 1100 Series was used to analyze the bacoside A content at the conditions in the following table. The results of bacoside A content were calculated from the standard curve of bacoside A.

Table 1. HPLC analysis condition[11]

Stationary phase	Purospher® STAR RP-18 column (C18, 250 x 4.6 mm, 5µm particle size, column temperature 35ºC)
Mobile phase	0.2% phosphoric acid : acetonitrile (65:35 %v/v)
Injection (flow rate)	10 µL (1.0 mL/min) running for 50 minutes
Detector	UV-205 nm

Statistical Analysis

All the experiments were repeated three times. Data were analyzed by comparing the different using T-test analysis through Microsoft Excel.

Results and Discussion:

Effect of elicitors on reactive oxygen species (ROS) production and antioxidant activity of B. monnieri

The ROS production was detected by measuring the concentration of H_2O_2. The results show that ROS production in all treatments is not significantly different compared with the control, unless the combination treatment of salicylic acid (SA) and static magnetic field (SMF). The individual SMF treatment also increases ROS production similar to the combination treatment. Due to the high standard deviation, the result of SMF treatment is not significant (Figure 1).

In cases that cells produce radicals at a higher level, the antioxidant enzymes will be produced more to maintain the oxidative status. Even though there are no significant results of oxidative inhibition in every treatment, the SMF treatments tend to induce oxidative inhibition both individually and in combination with SA (Figure 2). These results follow the ROS production (Figure 1) and also follow the previous reports from Maffei (2014) and Sherrard et al. (2018).[7,9] Under the work of a magneto sensor called cryptochrome, ROS will be produced, and then it will induce the production of antioxidant enzymes to protect cells from oxidative stress.

The results of pulsed electromagnetic field (PMF) treatment are not similar to those of SMF treatment. There is a slight decrease in ROS production but not significant (Figure 1), and the result of antioxidant activity is not different compared with the control (Figure 2). Pooam et al. (2020) reported that the effect of SMF and PMF on ROS production under the work of cryptochrome protein is not different in animal cells.[12] However, there is still no report comparing the effects of SMF and PMF in plant cells. So, these results indicate that the work of cryptochrome in animal cells and plant cells may be different.

For the individual SA treatment, the trend of ROS production is not different compared with the control (Figure 1). The trend of oxidative inhibition still increases (Figure 2). This can be assumed that ROS production is increasing due to the increase of antioxidant enzymes. Nevertheless, the ROS increase may be in other molecules such as superoxide (O_2^-) or hydroxyl radical (OH), which have not been measured. According to the report from La et al. (2018), salicylic acid (SA) can improve drought-stress tolerance in *Brassica rapa* through the regulation of redox status, including the increase of superoxide.[13] In this case, the increase in antioxidant enzymes during SA treatment in *B. monnieri* may be due to superoxide production rather than hydrogen peroxide.

Effect of elicitors on bacoside A accumulation of B. monnieri

The bacoside A accumulation was detected by High-Performance Liquid Chromatography (HPLC). The results show that the control treatment has the highest level of bacoside A. There are three treatments that can significantly decrease bacoside A content compared with the control, the PMF, SMF and PMF+SA treatment. The results obviously show that all

elicitors can decrease the accumulation of bacoside A, especially in the SMF treatment (Figure 3).

Typically, if the plant is stimulated by abiotic stress or the elicitors that can act as stressors, they will produce some antioxidant enzymes or secondary metabolites involved in plant defense mechanisms to survive in an unsuitable environment.[14] The result of antioxidant activity shows that the SA, SMF, and combination treatment induce oxidative inhibition (Figure 2), which means that there is the synthesis of the antioxidant enzymes or secondary metabolites involved in plant defense mechanisms. Bacoside A is the saponin compounds that plays a role as an anti-feedant.[15] Therefore, the decrease of bacoside A in all treatments indicate that it may not be involved in plant defense mechanisms.

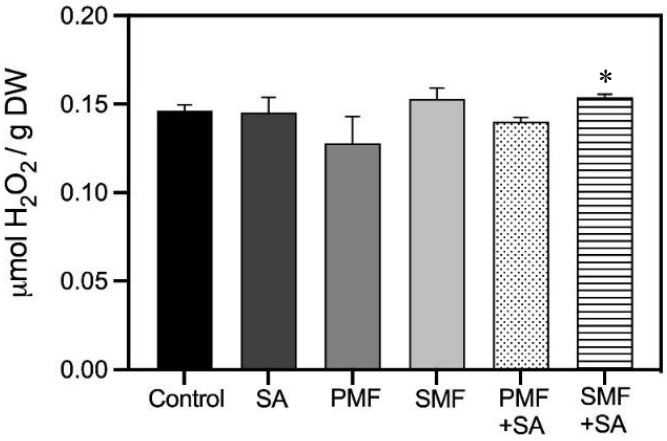

Figure 1. Effect of elicitors on reactive oxygen species (ROS) production

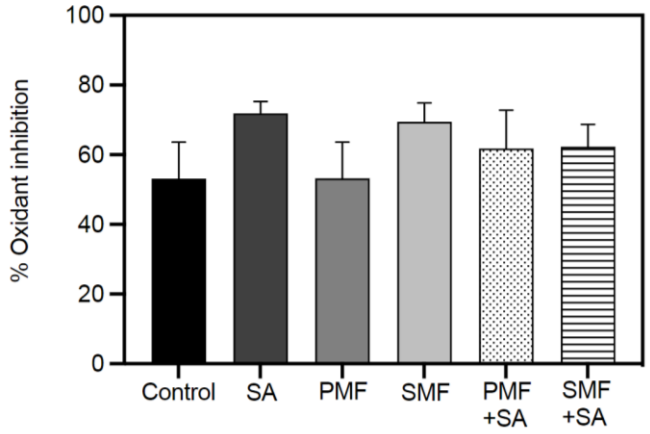

Figure 2. Effect of elicitors on DPPH antioxidant activity

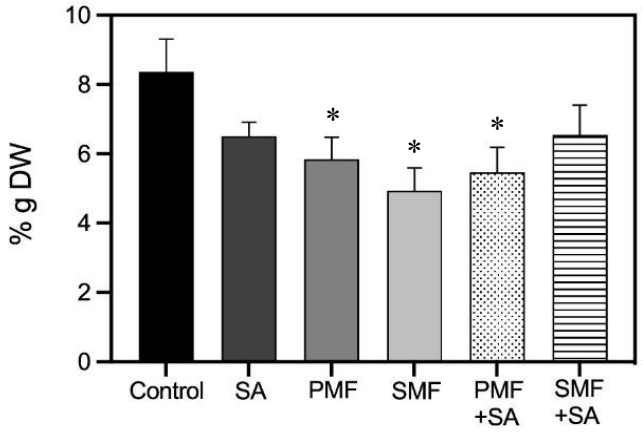

Figure 3. Effect of elicitors on bacoside A accumulation detected by HPLC

Conclusion:

Bacopa monnieri (L.) Wettst. were grown under a Deep Flow Technique hydroponics system for 4 weeks and treated with elicitors, which are salicylic acid, static magnetic field, and pulsed electromagnetic field individually and in combination. Salicylic acid and static magnetic field can induce the antioxidant enzymes for plant defense mechanisms. Nevertheless, salicylic acid and static magnetic fields cannot elicit bacoside A production under these research conditions because bacoside A may not be involved in plant defense mechanisms.

Acknowledgements:

The success of this thesis can be attributed to the extensive support and assistance of the thesis advisor, Dr. Marootpong Pooam, and the co-advisor, Assistant Professor Dr. Narisa Kunpratum. I am deeply thankful for the valuable advice and warm guidance, suggestions and encouragement throughout this study. I would also like to thank the Department of Biology, Naresuan University for sponsoring my research and the staff of the department for helping. Thanks to Sirikwan Wongwanich and Siriporn Senajumnong for teaching me to use HPLC. Thanks to my seniors, Chutiporn Maneeply and Thidarat Maitham, for all the useful suggestions and encouragement. Thanks to Chatchai Palawat, Sawanya Yodjun, and all of my friends for the help, support, and friendship.

References:

1. Saesong T, Temkitthawon P, Nangngam P, Ingkaninan K. Songklanakarin J Sci Technol. 2019;41:397–404.
2. Largia MJV, Pothiraj G, Shilpha J, Ramesh M. Plant Cell, Tissue and Organ Culture. 2015;122:9–20.
3. Klessig DF, Durner J, Noad R, Navarre DA, Wendehenne D, Kumar D, Zhou JM, Shah J, Zhang S, Kachroo P, Trifa Y, Pontier D, Lam E, Silva H. PNAS. 2000;97:8849–8855.
4. Ho T, Murthy HN, Park S. International Journal of Molecular Sciences. 2020;21:1–18.
5. Brain JD, Kavet R, McCormick DL, Poole C, Silverman LB, Smith TJ, Valberg PA, Etten RAV, Weaver JC. Environmental health perspectives. 2003;111:962–970.
6. Markov MS. Environmentalist. 2007;27:465–475.
7. Maffei ME. Frontiers in Plant Science. 2014;5:1–15.
8. Taghizadeh M, Nasibi F, Kalantari KM, Ghanati F. Plant Cell, Tissue and Organ Culture (PCTOC). 2019;136:489–498.

9. Sherrard R, Morellini N, Jourdan N, El-Esawi M, Arthaut L, Niessner C, Rouyer F, Klarsfeld A, Doulazmi M, Witczak J, d'Harlingue A, Mariani J, Mclure I, Martino C, Ahmad M. PLOS Biology. 2018;16:1–17.
10. Kataria S, Baghel L, Guruprasad KN. Biocatalysis and Agricultural Biotechnology. 2017;10:83–90.
11. Phrompittayarat W, Putalun W, Jetiyanon K, Ingkaninan K. Naresuan University Journal. 2007;15:29–34.
12. Pooam M, Jourdan N, El-Esawi M, Sherrard R, Ahmad M. PLOS ONE. 2020;15:1–11.
13. La VH, Lee BR, Zhang Q, Park SH, Islam MT, Kim TH. Horticulture, Environment, and Biotechnology. 2018;60:31–40.
14. Ramakrishna A, Ravishankar GA. Plant Signaling and Behavior. 2011;6:1720–1731.
15. Hussain M, Debnath B, Qasim M, Bamisile BS, Islam W, Hameed MS, Wang L, Qiu D. Molecules. 2019;24:2067

THE EFFECT OF ACTINOMYCETE AND SELENIUM NANOPATICLE ON RICE AGAINST SALT STRESS.

Sukanya Phusing,[1] Karan Lohmaneeratana,[1] Weerasin Sonjaroon,[2] Nuttaporn Pimpha,[3] Natthika Saengkrit,[3,*] Arinthip Thamchaipenet[1,*]
*e-mail: nattika@nanotec.or.th, arinthip.t@ku.ac.th

[1] Department of Genetics, Faculty of Science, Kasetsart University, Bangkok 10900, Thailand
[2] School of Integrated Science, Kasetsart University, Bangkok 10900, Thailand
[3] National Nanotechnology Center (NANOTEC), National Science and Technology Development Agency (NSTDA), Pathum Thani 12120, Thailand

Abstract:

This study aims to use an endophytic *Streptomyces* sp. GKU 895 together with selenium nanoparticle (SeNP) as plant biostimulant. *Oryza sativa* L. cv. KDML105 was used to study the effect of biostimulant on plant physiologies and gene expression. The effects of SeNP and *Streptomyces* sp. GKU 895 on growth were evaluated in rice under salt stress condition by immersion of 7-days germinated seed with 10 mg L^{-1} SeNP solution and 10^8 spores mL^{-1} of *Streptomyces* sp. GKU 895 for 4 h. The results indicated that the biostimulant significantly increased plant growth of shoot, root, and chlorophyll, but decreased ethylene when compared to the control group. At 5 days post-induction of salt stress, the growth of the treatment group was normal when compared to the control group. Gene related to ethylene production *EREBP1* was down-regulated, whereas genes encoding antioxidant enzymes, *CuZn-SOD1* and *CATb*, were up-regulated. Therefore, SeNP and *Streptomyces* sp. GKU 895 are verified to be the biostimulant for rice under salt stress condition.

Keywords: biostimulant, endophyte, actinomycete, rice, selenium nanoparticle.

Introduction:

Rice is an important food crop for the entire world population. *Oryza sativa* L. cv. KDML105 is commonly known in food markets as Khao Dok Mali 105 or Thai jasmine rice. It is one of the most popular rice cultivars in the world. It was also found that this rice cultivar is salt-sensitive. As a result, the rice cannot grow well when it is grown under saline soil.[31,33,37]

Salinity is one of the major yield restricted factors that reduce plant growth and productivity. Soil with an excess salt concentration may affect inhibition of root water uptake by osmotic pressure. Furthermore, the effect of specific ions directly causes toxicity which competes with nutrient absorption in plants.[2,4] In addition, saline soil is a major problem for rice plantations in many areas in Asia, particularly in southeast Asia.[21]

Endophytes are groups of microorganisms living together within plant tissues and provide benefits to plants. Plant growth promoting (PGP) bacteria is able to produce (i) indole-3-acetic acid (IAA) which is the most common plant hormone of the auxin. IAA has many effects that are related to cell division and elongation with subsequent results for plant growth and development; (ii) 1-aminocyclopropane-1-carboxylate (ACC) deaminase which can degrade ACC, a precursor for ethylene, and resulting in decreasing of the ethylene content in plants and help plant thrive in an extreme condition; (iii) siderophore which can uptake iron from environment; (iv) phosphate solubilization which can solubilize rock

phosphate into a soluble form. *Streptomyces* sp. GKU 895 is an endophytic actinomycete associated with sugarcane roots carrying several PGP traits and promoting sugarcane growth.[21]

Selenium nanoparticle (SeNP) is an essential trace element and has great properties including abiotic stress resistance, plant growth regulator, stress modulator, antioxidant agent and pathogenic defenses. SeNP improves plant growth better than normal and the ability to withstand stress. It has excellent biological properties, low toxicity, and is environment friendly.[6,25,36]

Actinomycetes and SeNP have been reported to promote plant growth as well as alleviate various abiotic stresses including salinity, drought, heat, and osmotic stress.[1,5,14,43] ACC deaminase trait found in several PGP-bacteria including *Bacillus, Enterobacter, Pseudomonas* and *Streptomyces* which improved tolerance of drought, flooding, salinity, and phytopathogens in plants.[12,19,27,34] Interestingly, increasing level of ACC deaminase activity by overexpression of the corresponding gene in PGP-bacteria remarkably facilitated growth and alleviated environmental stresses of host plants more than that of wild type strains.[10,17,32,40]

This research aims to study the plant growth promoting effect of *Streptomyces* sp. GKU 895 and SeNP on salt stress response in rice. Plant physiological traits were measured and transcriptional analysis was analyzed using real time PCR on stress response genes.

Methodology:

Rice growing condition. Rice seeds of *O. sativa* L. cv. KDML105 were surface sterilized and germinated according to Jaemsaeng *et al.,* (2018). The roots of seedlings were cut to the same length and soaked in an individual sterile glass beaker containing 10^8 spores mL^{-1} of *Streptomyces* sp. GKU 895 and 10 mg L^{-1} of SeNP for 4 hours as defining the condition in Table 1. The seedlings were re-located to a moist sponge support before transferring to a 20-L container filled with ½ Yoshida solution[41] for 7 days and replaced with Yoshida solution for 7 days. Next, the nutrient solution was changed to Yoshida solution supplemented with 150 mM NaCl for 5 days. The pH of the nutrient solution was maintained between 5.0–5.5 throughout the growth period.

Table 1 Rice treatment in this experiment.

Unsalted condition	Salted condition
Rice control	Rice + Salt
Rice + SeNP	Rice + SeNP + Salt
Rice + GKU 895	Rice + GKU 895 + Salt
Rice + SeNP + GKU 895	Rice + SeNP + GKU 895 + Salt

Note: control, rice without treatment; GKU 895, rice inoculated with *Streptomyces* sp. GKU 895; SeNP, rice treated with selenium nanoparticle; GKU 895+ SeNP, rice inoculated with *Streptomyces* sp. GKU 895 and treated with SeNP.

Determination of chlorophyll, ethylene, and hydrogen peroxide. Ten rice samples were taken to measure chlorophyll with a chlorophyll meter SPAD-502. One sample was measured in 3 areas, and each area was measured 3 times to calculate the average values. Ethylene was measured by putting the whole rice plants into a 250-mL sealed glass container which contained 10 mL acetylene for 1 hour. A 10 mL gas sample was withdrawn and quantified by gas chromatography at PGPR Biofertilizer and Aerated Compost Soil Microbiology Research Group, Soil Science Division, Department of Agriculture, Ministry of Agriculture and Cooperatives, Bangkok, Thailand. Hydrogen peroxide (H_2O_2) was extracted and measured

from the whole rice plants according to Önder *et al.* (2020). Rice was ground with liquid nitrogen and 5 ml 0.1% (w/v) trichloroacetic acid. The mixture was centrifuged at 15.000 rpm. for 15 min at 4 °C. Supernatant (0.5 ml) was aliquoted and added one ml of 1 M KI and 0.5 ml of 10 mM K_2HPO_4 buffer (pH 7.0). The reaction mixture was subjected to dark conditions for 60 min. The absorbance values of the samples were read at 390 nm. H_2O_2 amount was calculated with a standard curve.

RNA extraction and qRT-PCR analysis. Total RNA was extracted from the whole rice plants following the manufacturer's protocol for GF1 total RNA extraction kit (Vivantis, Malaysia). cDNA was synthesized using the Revert Aid First strand cDNA synthesis Kit (Thermo Scientific). Maxima SYBR qPCR master mix (Thermo Scientific) was used for quantification in Master Cycler Realplex 4 (Eppendorf). The mean value was calculated and normalized with actin (*act1*) as an internal control.

Results and Discussion:

Physiological properties of rice. The physiological effects of rice in each condition after 5 days of salt stress treatment were compared. *Streptomyces* sp. GKU 895, SeNP, and mixture of *Streptomyces* sp. GKU 895 and SeNP inoculated to the rice showed better growth of shoot length, root length, fresh weight, and dry weight than the control group (Figure 1 and Figure 2).

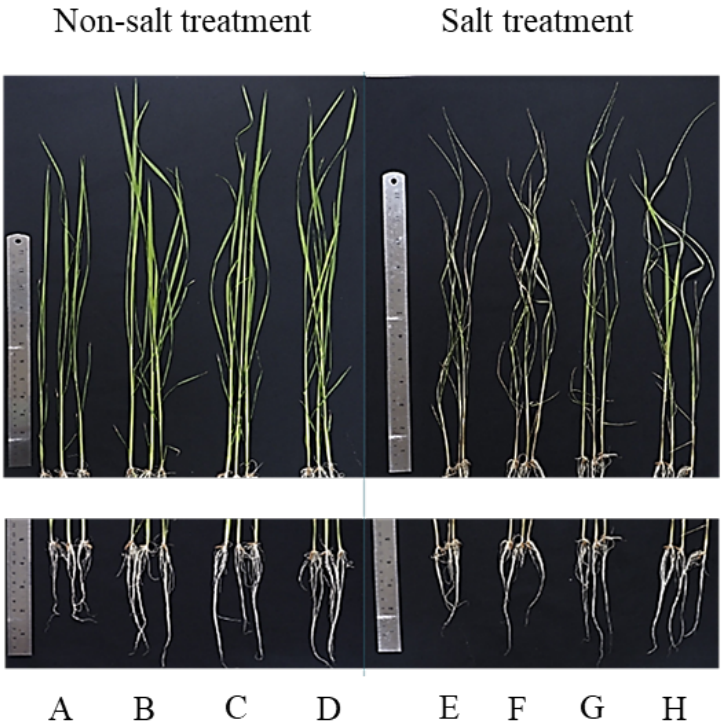

Figure 1. Comparison of shoot and root length of rice plants under non-salted treatment (A-D) and salted treatment (E-H) with and without the addition of stimulants. (A, E) Control, (B, F) *Streptomyces* sp. GKU 895, (C, G) SeNP, (D, H) *Streptomyces* sp. GKU 895 + SeNP.

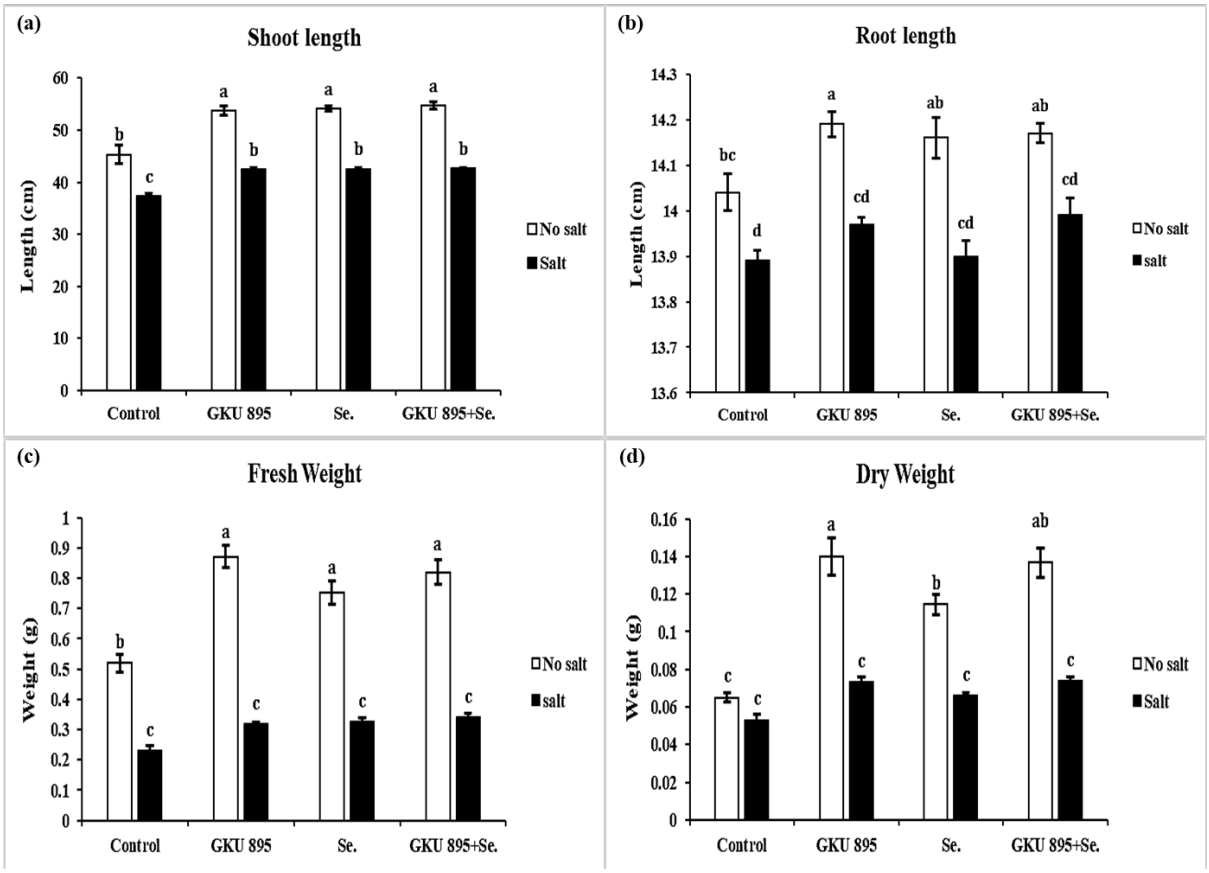

Figure 2. Effect of *Streptomyces* sp. GKU 895 and SeNP on the physiology of *O. sativa* L. cv. KDML105 after 5 days of salt stress under hydroponic conditions. (a) Shoot length; (b) root length, (c) fresh weight; (d) dry weight. Values are the mean of ten replicates±standard error of the mean. Different letters indicated statistically significant differences between treatments (Tukey's test, $P<0.05$). Control, rice without treatment; GKU 895, rice inoculated with *Streptomyces* sp. GKU 895; Se, rice treated with SeNP; GKU 895+Se, rice treated with *Streptomyces* sp. GKU 895 and SeNP; white bar, non-salt treatment; black bar, salt treatment (150mM NaCl).

Under salt stress conditions, *Streptomyces* sp. GKU 895, SeNP, and mixture of *Streptomyces* sp. GKU 895 and SeNP inoculated rice plants showed enhancement in growth parameters including shoot and root length compared to those of uninoculated controls. However, fresh and dry weight parameters were not significantly higher than uninoculated plants. Our results were congruent with previous work that an ACC deaminase-producing *Streptomyces* increased shoot and root growth of halophytic *Ligustrum sinense* under salt-stress treatment[24] and ACC deaminase-producing *Bacillus* significantly increased seed germination and promoted growth of KDML105 rice[28] and indica rice.[22]

Effects of *Streptomyces* sp. GKU 895 and SeNP on plant physiology. Indices of plant physiology including chlorophyll, ethylene, and hydrogen peroxide (H_2O_2) were investigated. The chlorophyll content of rice inoculated with *Streptomyces* sp. GKU 895, SeNP, and the mixture of both was significantly higher, whereas ethylene content was significantly lower than those of uninoculated control (Figures 3a, c). Under salt-stress conditions, the chlorophyll content of all treatments was significantly decreased while ethylene and H_2O_2 were highly increased when compared to those of non-salt conditions. However, the

chlorophyll content of the treated rice samples was significantly higher, whereas ethylene and H_2O_2 were significantly lower than those of uninoculated control under salt treatment (Figure 3).

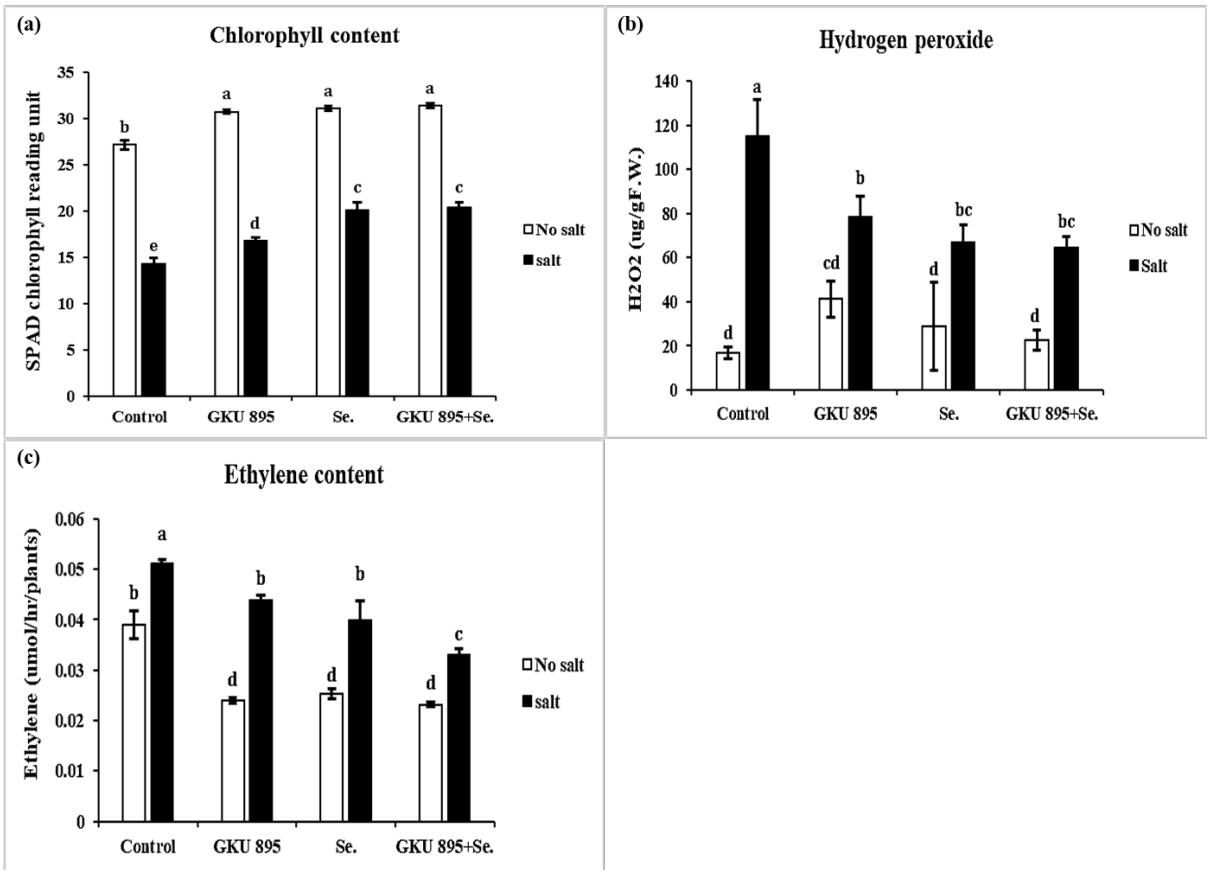

Figure 3. Effects of *Streptomyces* sp. GKU 895 and SeNP on the physiology of *O. sativa* L. cv. KDML105 after 5 days of salt stress under hydroponic conditions. (a) Chlorophyll content; (b) hydrogen peroxide, (c) ethylene content. Values are the mean of ten and three replicates±standard error of the mean. Different letters indicated statistical differences between treatments (Tukey's test, $P<0.05$). Control, rice without treatment; GKU 895, rice inoculated with *Streptomyces* sp. GKU 895; Se, rice treated with SeNP; GKU 895+Se, rice treated with *Streptomyces* sp. GKU 895 and SeNP; white bar, non-salt treatment; black bar, salt treatment (150mM NaCl).

The reduction of total chlorophyll of plants is generally the first notable effect of salt stress, such as those reported in black gram and rice.[13,35,39] In this work, the total chlorophyll in all treatments of rice plants was significantly increased under salt treatment, when rice was inoculated with *Streptomyces* sp. GKU 895, SeNP, and the mixture of both. The results were congruent with other studies in which ACC deaminase-producing *Enterobacter* sp. SBP-6 in wheat,[29] *Bacillus subtilis* RJ46, *Ochrobactrum pseudogrignonense* RJ12, and *Pseudomonas* sp. RJ15 in black gram and pea[26] increased chlorophyll level more than those of non-inoculated plants under salt stress.

It is generally known that ethylene is a main plants response to stress environment. Salinity induced a high level of ethylene production via the actions of ACC synthase and ACC oxidase towards ACC, an ethylene precursor. Whereas, ACC deaminase of bacteria assists plants by conversion of ACC into ammonia and α-ketobutyrate, thus reducing ethylene as a consequence.[9] In this work, ethylene levels were significantly lower when rice was associated with *Streptomyces* sp. GKU 895, SeNP, and the mixture of both compared to that of uninoculated control. Our results were similar to previous reports that ethylene levels in rice and sugarcane were reduced by ACC deaminase-producing *Streptomyces* sp. GMKU 336[13] and *Enterobacter* sp. EN-21,[19] respectively. In addition, a lower amount of ACC was observed in tomatoes inoculated with ACC deaminase-overexpressed psych tolerant bacteria under chilling stress.[30]

The excellent application potential of plant-mediated SeNPs against salinity stress is due to the reduction ability of H_2O_2 content in the plants that caused oxidative damage.[42] Moreover, selenium can help plants cope with stress by stimulating antioxidant capacity through the enhancement of the activity of antioxidant enzymes (SOD, CAT and glutathione peroxidase, GSH-Px).[7] Antioxidant enzymes convert H_2O_2 to H_2O and O_2 which induce the spontaneous dismutation of the superoxide radical ($O2^{-\bullet}$) into H_2O_2 and consequently increase antioxidant defense systems.[7,8] In this work, *Streptomyces* sp. GKU 895, SeNP, and the mixture of both help reduce H_2O_2 in rice under salt stress.

Effects of *Streptomyces* sp. GKU 895 and SeNP on the expression of salt-stress responsive genes. Three candidate genes of rice-encoded proteins involved in salt stress response namely, ethylene responsive element binding proteins (*EREBP1*), catalase (*CATb*), and superoxide dismutase (*CuZn-SOD1*) were transcriptionally analyzed in all treatments. Gene expression profiles were observed at similar basal level in plant grown under non-salt conditions. When the rice was exposed to salt, *EREBP1* in inoculated rice was significantly down-regulated better than in the control plants (Figure 4a).

Genes encoding antioxidant enzymes, *CATb* and *CuZn-SOD1* were up-regulated in salt-stress rice higher than the non-salt treatments and uninoculated plants. The expression levels were significantly high in rice treated with *Streptomyces* sp. GKU 895 and mixture of *Streptomyces* sp. GKU 895 and SeNP compared to the un-inoculated and inoculated with *Streptomyces* sp. GKU 895, and SeNP (Figures 4b and c). All of these results indicated that rice treatment with *Streptomyces* sp. GKU 895, SeNP, and the mixture of both illustrated a positive influence against salt stress response gene expression in rice by down-regulation of *EREBP1* while up-regulation of *CATb,* and *CuZn-SOD1* which improved salt tolerance in rice as a consequence.

The gene-encoding ethylene responsive element binding protein (*EREBP1*) was up-regulated in all salt-treated plants. EREBP is a member of the ethylene-response factor (ERF) family[3] which plays an important role in abiotic stress response.[16] Up-regulation of *EREBP1* was observed in tobacco during drought and salt stress.[38] Here, we report that the expression profile of *EREBP1* was significantly up-regulated in all salt-stress treated rice but lower expression in KDML105 inoculated with *Streptomyces* sp. GKU 895, SeNP, and the mixture of both. Selenium partially inhibited ethylene biosynthesis in roots of rice seedings.[20] Likewise, selenium inhibited 1-aminocyclopropane-1-carboxylate synthase (ACS) activity in wheat which is involved in the main limiting step of ethylene production in higher plant.[11]

The transcription levels of superoxide dismutase (*CuZn-SOD1*) and catalase (*CATb*) genes were significantly up-regulated in rice treated with *Streptomyces* sp. GKU 895 and the mixture of *Streptomyces* sp. GKU 895 and SeNP under salt stress condition, except for rice inoculated with SeNP. The results indicated that *Streptomyces* sp. GKU 895 and the mixture

of *Streptomyces* sp. GKU 895 and SeNP promoted salt tolerance in rice by promoting plant growth and inducing of antioxidant enzymes.

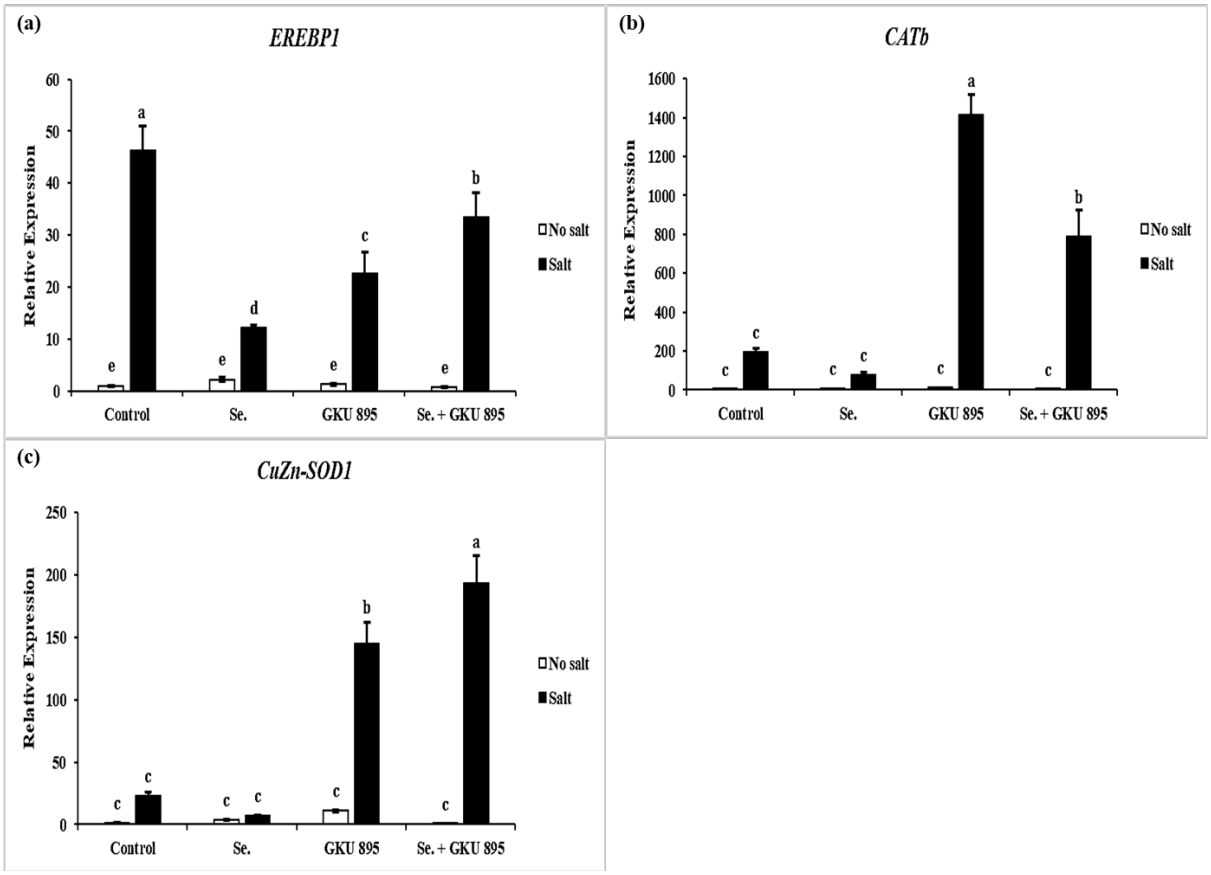

Figure 4. Transcriptional analysis of genes involved in salt stress response in *O. sativa* L. cv. KDML105 associated with *Streptomyces* sp. GKU 895 and SeNP. (a) *EREBP1*; (b) *CATb*; (c) *CuZn-SOD1*. The histogram represents the mean of the expression ratio, relative to the actin gene (*act*). Values are the mean of three replicates±standard error of the mean. Different letters indicated statistical differences between treatments (Tukey's test, $P<0.05$); Control, rice without treatment; GKU 895, rice inoculated with *Streptomyces* sp. GKU 895; Se, rice treated with SeNP; GKU 895+Se, rice treated with *Streptomyces* sp. GKU 895 and SeNP; white bar, non-salt treatment; black bar, salt treatment (150 mM NaCl).

Conclusion:

All of the experimental data indicated that *Streptomyces* sp. GKU 895 and SeNP promoted growth and protected *O. sativa* L. cv. KDML105 from salt stress damage. This endophyte and SeNP enhanced salt tolerance in rice by lowering stress-induced ethylene, and reduction of hydrogen peroxide (H_2O_2) but increased chlorophyll content. The plants physiology also correlated with expression profiles of stress responsive genes in rice associated with *Streptomyces* GKU 895 and SeNP. Down-regulation of *EREBP1* implicated in the reduction of ethylene production in rice which plays a role in salt tolerance. In addition, the antioxidant defense system showed up-regulation of *CuZn-SOD1* and *CATb* gene expression resulting in the increasing of antioxidant enzymes which subsequently inhibits

H_2O_2 production. Noticeably, rice treated with *Streptomyces* sp. GKU 895, SeNP, and the mixture of both exhibited plant growth promotion, physiology, and expression of plant stress responsive genes.

It is clearly demonstrated for the *Streptomyces* sp. GKU 895 and SeNP enhance plant growth and salt tolerance by regulation of stress responsive genes in plants under salt-stress treatment. Knowledge of the interaction is crucial to understand the relationship between rice, endophytic actinomycete, and SeNP for further applications of potential environmentally friendly biofertilizers in saline soil.

Acknowledgements:

SP was granted an MSc scholarship from the Thailand Graduate Institute of Science and Technology (TGIST), NSTDA. We give special thanks to PGPR Biofertilizer and Aerated Compost Soil Microbiology Research Group, Soil Science Division, Department of Agriculture, Bangkok, Thailand for ethylene determination. This research was funded by Kasetsart University Research and Development Institute (KURDI), grant No. FF(KU)5.64.

References:

1. Bano I, Skalickova S, Sajjad H, Skladanka J, Horky P. J. Agron. 2021;11.
2. Bartels D, Sunkar R. Crit. Rev. Plant Sci. 2005;24:23-58.
3. Chen YY, Wang LF, Dai LJ, Yang SG, Tian WM. Arg. Mol. Biol. Rep. 2012;39:3713-3719.
4. Clarkson DT, Hanson JB. Annu. Rev. Plant Physiol. 1980;31:239-298.
5. El-Tarabily KA. Plant Soil. 2008;308:161-174.
6. Fairweather-Tait SJ, Bao Y, Broadley MR, Collings R, Ford D, Hesketh JE, Hurst R. Antioxid. Redox Signal 2011;14:1337-1383.
7. Feng R, Wei C, Tu S. Environ Exp Bot 2013;87:58–68.
8. Foyer CH, Noctor G. Plant Cell Environ 20012;35:199–201.
9. Glick BR. Adv. Appl. Microbiol. 2004;56:291-312.
10. Grichko VP, Glick BR. Plant Physiol Biochem. 2001;39:11-17.
11. Iqbal M, Hussain I, Liaqat H, Arslan AM, Rasheed R, Ur Rehman A. Plant Physiol. Biochem. 2015;94:95-103.
12. Jaemsaeng R, Jantasuriyarat C, Thamchaipenet A. Agri. Nat. Resour. 2018;52:330-334.
13. Jaemsaeng R, Jantasuriyarat C, Thamchaipenet A. Sci. Rep. 2018;8:1950.
14. Jozwiak W, Politycka B. Plants. 2019;8:217.
15. Kamran M, Malik Z, Parveen A, Zong Y, Abbasi GH, Rafiq MT, Shaaban M, Mustafa A, Bashir S, Rafay M, Mehmood S, Ali M. Plant Physiol. Biochem. 2019;250:109500.
16. Kizis D, Lumbreras V, Pages M. FEBS Lett. 2001;498:187-789.
17. Kong Z, Glick BR, Duan J, Ding S, Tian J, McConkey BJ, Wei G. Plant Soil 2015;391:383-398.
18. Kruasuwan W, Thamchaipenet A. J. Plant Growth Regul 2016;35:1074-1087.
19. Kruasuwan W, Thamchaipenet A. J. Plant Growth Regul 2018;37:849-858.
20. Malheiros RS, Costa LC, Avila RT, Pimenta TM, Teixeira LS, Brito FA, Zsögön A, Araújo WL, Ribeiro DM. Planta 2019;1:333-345.
21. Martinez-Beltran J, ManzurCL, Proc Int Saline 2005:311-313.
22. Nautiyal CS, Srivastava S, Chauhan PS, Seem K, Mishra A, Sopory SK. Plant Physiol. Biochem. 2013;66:1-9.
23. Önder S, Önder DG, Tonguç MJ. Nat. Appl. Sci. 2020;24:681–688.
24. Qin S, Zhang Y-J, Yuan B, Xu P-Y, Xing K, Wang J, Jiang J-H. Plant Soil 2014;374:753-766.
25. Rayman MP. Lancet 2012;379:1256-1268.

26. Saikia J, Sarma RK, Dhandia R, Yadav A, Bharali R, Gupta VK, Saikia R. Sci. Rep. 2018;8:3560.
27. Saleem MR, Brunetti C, Khalid A, Rocca GD, Raio A, Emiliani G, Carlo AD, Mahmood T, Centritto M. PloS One. 2018;13.
28. Sapsirisopa S, Chookietwattana K, Maneewan K, Khaengkhan P. As. J. Food Ag-Ind. 2009:S69-S74.
29. Singh RP, Jha PN. Acta Physiol. Plant. 2016;38:110.
30. Subramanian P, Krishnamoorthy R, Chanratana M, Kim K, Sa T. Plant Physiol. Biochem. 2015;89:18-23.
31. Summart J, Thanonkeo P, Panichajakul S, Prathepha P, McManus MT. Afr. J. Biotechnol. 2010;9:145-152.
32. Tavares MJ, Nascimento FX, Glick BR, Rossi MJ. Lett. Appl. Microbiol. 2018;66:252-259.
33. Theerakulpisut P, Bunnag S, Kong-ngern K. Asian J. Plant Sci. 2005;4:562-573.
34. Toklikishvili N, Dandurishvili N, Vainstein A, Tediashvili M, Giorgobiani N, Lurie S, Szegedi E, Glick BR, Chernin L. Plant Pathol. 2010;59:1023-1030.
35. Turan S, Tripathy BC. Physiol. Plant. 2015;153:477-491.
36. Wang H, He Y, Liu L, Tao W, Wang G, Sun W, Wang M. Oxid. Med. Cell. Longev. Oxid Med Cell Longev 2020;14.
37. Wanichananan P, Kirdmanee C, Vutiyano C. Sci. 2003;29:333-339.
38. Wei W, Zhang Y, Han L, Guan Z, Cha T. Plant Cell Rep. 2008;27:795-803.
39. Win K, Fukuyo T, Keiki O, Ohwak Y. Plant Physiol. Biochem. 2018;127:599-607.
40. Yoolong S, Kruasuwan W, Phạm HTT, Jaemsaeng R, Jantasuriyarat C, Thamchaipenet A. Sci. Rep. 2019;9:1-10.
41. Yoshida S, Forno DA, Cock JH, Gomez KA. 1976.
42. Zahedi SM, Abdelrahman M, Hosseini MS, Hoveizeh NF, Tran LSP. Env Poll. 2019;253:246–58.
43. Zohra E, Ikram M, Omar AA, Hussain M, Satti SH, Raja NI, Mashwani Z-U-R, Ehsan M. Green Process. Synth. 2021;10:456-475.

TRANSCRIPTOME PROFILES OF *Streptomyces* sp. GKU 223 IN DIFFERENT GROWTH PHASE

Pattamaporn Pumpong,[1] Karan Lohmaneeratana,[1] Aiyada Aroonsri,[2] Vanicha Vichai,[2] Arinthip Thamchaipenet[1,*]

[1]Department of Genetics, Faculty of Science, Kasetsart University, Chatuchak, Bangkok 10900, Thailand
[2]National Center for Genetic Engineering and Biotechnology, National Science and Technology Development Agency, Pathum Thani, Thailand
*email : arinthip.t@ku.ac.th

Abstract:

Streptomyces have the ability to produce a multitude of varied and complex secondary metabolites through a shift from primary to secondary metabolism, which is regulated by activated complex networks after growth termination. This work is aimed to understand the regulatory elements of gene expression related to primary and secondary metabolism in a marine actinomycete, *Streptomyces* sp. GKU 223. Transcriptome profiles were performed from *Streptomyces* sp. GKU 223 growing at three different growth phases to analyze the differentially expressed genes (DEGs) during cell growth. In the lag vs exponential phases (L/E), cellular growth functions, including carbon source consumption and energy production, were up-regulated, while in the lag vs stationary phases (L/S), a general decreasing trend in cell growth and energy production; and an increasing trend of precursors expected leading in the production of secondary metabolism were observed. These transcriptome analyses of *Streptomyces* sp. GKU 223 provided a valuable genetic resource for understanding metabolism during the growth phases and may contribute to facilitating the rational engineering of secondary metabolite production.

Keywords: RNA-seq, *Streptomyces* sp. GKU 223, Gene expression, Growth phase

Introduction:

Actinomycetes are generally found in various environments. They are renowned as proficient producers of bioactive natural products. Therefore, they have been used for insecticides and herbicide production by replacing harmful chemicals to reduce the problem of residue chemicals in both plants and the environment. *Streptomyces* is Gram-positive bacteria that typically colonize terrestrial and marine soils as free-living saprophytes.[1] *Streptomyces* is a member of the largest genus of actinobacteria with over 900 described species.[2] They have linear chromosome with a high GC content as important genomic features.[3] The most interesting property of *Streptomyces* is the ability to produce secondary metabolites, such as antifungals, antivirals, anticancer, anti-hypertensives, and immunosuppressants.[4] More than two-thirds of natural antibiotics are in the pharmaceutical industry.[2,5] These secondary metabolites are synthesized by secondary metabolite biosynthesis gene clusters, which depend on the supply of precursor molecules from primary metabolisms such as acetyl-CoA and amino acids.[6] Secondary metabolism is usually activated after vegetative growth terminates through a metabolic transition from primary to secondary metabolism, accompanied by morphological differentiation.[7] Thus, understanding the complex regulatory systems of the metabolic transition is important for enhancing

secondary metabolite production. To understand the underlying molecular mechanisms of metabolic transitions, alterations of transcriptional that occur between growth phases have been studied.

Streptomyces sp. GKU 223 is a marine actinomycete isolated from Ranong province, Thailand (Leetanasaksakul and Thamchaipenet, 2018). This strain produced protease and antibiofilm formation against *Staphylococcus aureus*.[8] In this study, RNA-seq was performed from *Streptomyces* sp. GKU 223 at three different growth phases. Pathway enrichment of differentially expressed genes was investigated. These analyses of *Streptomyces* sp. GKU 223 provided a valuable genetic resource for understanding metabolism during the growth phases.

Methodology:

Strains cultivation and growth curves

Streptomyces sp. GKU 223 was grown on mannitol-soybean (MS) agar (20 g soybean/l, 20 g mannitol/l and 20 g agar/l; at 28°C for 4 days. Single colony was transferred into LS2 medium (20 g mannitol/l, 20 g soytone/l, 1 ml trace solution/l (0.4% $CaCl_2$, 0.2% $ZnSO_4$, 0.01% $Na_2B_4O_7$, 0.5% $FeSO_4$, 0.005% KI, 0.05% $CoCl_2$, 0.02% CuSO4, 0.2% $MnCl_2$, 0.005% Na_2MoO_4, 95–97% p.a. H_2SO_4) containing 2 ml vitamin complex solution/l pH 6.2; at 28 °C, with shaking incubator at 200 rpm until stationary phase. Cells were collected for the growth curve determination by counting colony-forming units at each time point. The growth curve progresses through three growth stages: lag (L), exponential (E) and stationary (S) phases. All three stages were performed in triplicate.

RNA extraction and sequencing

Cells were collected from 50 ml of culture in LS2 medium at 3-time points for three growth phases by vacuum filtration at 48 h, 78 h, and 96 h. Cells were flash-frozen in liquid nitrogen and ground into a fine powder, then resuspended in 0.5 ml TRIzol™ Reagent (Ambion, USA), incubated at room temperature for 15 min before adding 0.1 ml chloroform. The cell suspension was mixed thoroughly and then centrifuged at 12,000 rpm, 4°C for 5 min. The top aqueous layer (~200 µl) was carefully removed and added with an equivalent volume of isopropanol. Samples were then centrifuged at 12,000 rpm, 4°C for 10 min to pellet the total RNA. Isopropanol was removed, and the pellet was washed with 1 ml 75% EtOH, then centrifuged again at 12,000 rpm, 4°C for 5 min. The residue of 75% EtOH was removed, and the pellet was air-dried for 30 min, then resuspended in 35 µl RNase-free H_2O. RNAs were quantified using a NanoDrop spectrophotometer and quality-assessed on 0.8% agarose gel electrophoresis. RNA integrity was assessed using the RNA Nano 6000 Assay Kit of the Agilent Bioanalyzer 2100 system (Agilent Technologies, CA, USA).

The RNA samples with RNA Integrity Number (RIN) higher than 9 were processed for library preparation. Totally, 9 samples of RNA (3 samples for each growth phase) were analyzed. RNA samples were purified to remove genomic DNA using the DNase I, RNase-free (Thermoscientific), and RNA Clean-up and Concentrator™ -5 kit (Zymo Research). RNA-seq was performed by the Illumina Novaseq 6000 platform (Illumina technology) by Novogene (Beijing, China) to generate 150 bp paired-end reads.

Identification of Differentially Expressed Genes (DEGs)

The raw reads were uploaded to Galaxy Project (usegalaxy.org) for RNA-seq data analysis. Sequence quality was performed on fastq files by using FastQC (Version 0.73).[9] Raw FASTQ data were trimmed for low-quality bases and sequencing adapters (5'-AGATCGGAAGAGCGTCGTGTAGGGAAAGAGTGTAGATCTCGGTGGTCGCCGTAT CATT-3') using Trimmomatic (Version 0.38)[10] in paired-end mode, retaining reads with a

minimum Phred quality score of 20. The clean read for each sample was mapped to the *Streptomyces* sp. GKU 223 reference genome using Bowtie2 (Version 2.4.2) with default parameters.[11] The number of reads mapped to each gene was calculated based on the BAM alignment result file and the GTF file of the gene structure to obtain a count matrix for differential expression analysis. Differential gene expression was carried out using Cuffdiff (Version 2.2.1.6).[12]

Differential expressed genes were cut-off at logarithmic fold change (log2FC) ≥ 1 and *p*-value < 0.05 at false discovery rate (FDR) <0.05. Kyoto Encyclopedia of Genes and Genomes (KEGG) pathways were used for annotations of all genes of *Streptomyces* sp. GKU 223 genome. KEGG pathway enrichment analysis was performed using piano in R package. KEGG was used for systematic analysis of gene functions, linking genomic information with higher order functional information of the DEGs.[13]

Results and Discussion:

Growth phase of Streptomyces sp. GKU 223

Growth of *Streptomyces* sp. GKU 223 in liquid LS2 medium at 0-54 h was in the lag phase, at 54-96 h was in the log phase and at 96–102 h was in the stationary phase (Figure 1.). RNA was isolated from GKU 223 cultures harvested at 48 h, 78 h and 96 h, which represent the lag (L), exponential (E) and stationary (S) phases, respectively. To identify the differentially expressed genes between each growth phase at the transcription levels, RNA-seq was performed using Next generation sequencing technology.

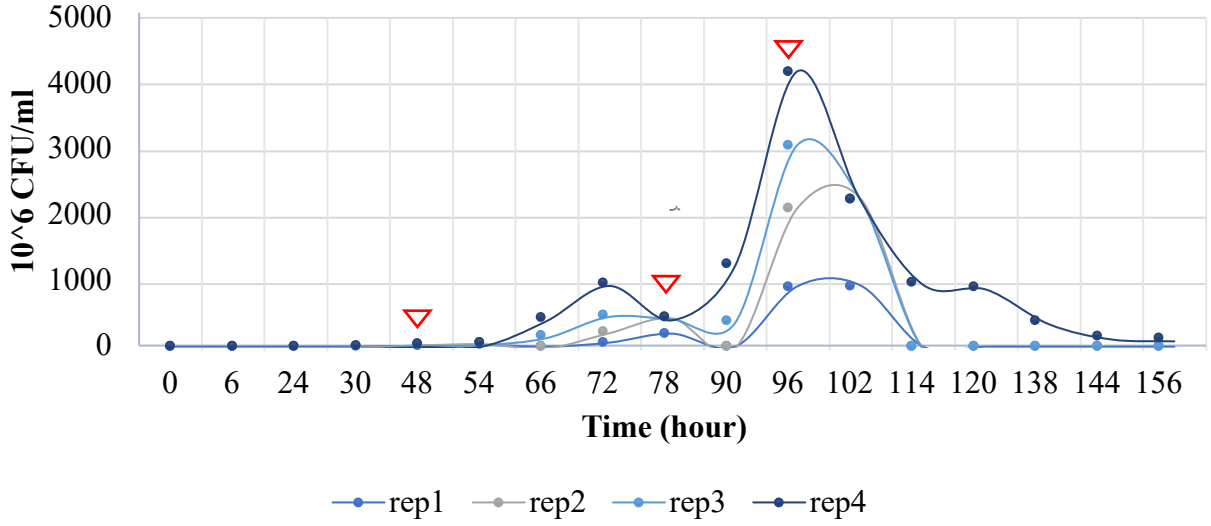

Figure 1.
Growth of *Streptomyces* sp. GKU 223 in liquid LS2 medium. Cell growth was assessed based on a colony forming unit (CFU). Red triangles denote the three-time points selected for preparing RNA for transcriptome analysis.

Sequence quality control and quantification of gene expression levels

The results of sequence quality assessment for all samples are summarized. The average raw reads obtained by sequencing was 23,999,897, while the average clean reads

after filtration was 23,918,691. The base error rate of each sample was 0.03%, Q20 was greater than 97.62%, Q30 was greater than 93.44%, and GC content was 67.1– 69.12%. The average mapping rates are 97.47% (Table 1.)

Table 1.
Overview of basic quality of read counts.

Sample	Raw reads	Clean reads	Q20(%)	Q30(%)	Mapped reads	GC(%)	%map
S48_4	22,291,716	22,217,754	97.62	93.44	21,626,762	68.94	97.34
S48_5	22,096,468	22,001,466	97.69	93.74	21,506,492	68.15	97.33
S48_6	23,430,804	23,345,816	97.62	93.52	22,759,836	68.14	97.49
S78_4	24,054,410	23,946,600	97.69	93.77	23,206,650	69.12	96.91
S78_5	23,155,450	23,078,502	97.79	93.58	22,490,000	68.11	97.45
S78_6	29,688,130	29,604,454	97.94	94.08	28,920,591	68.04	97.69
S96_4	22,245,140	22,173,874	97.70	93.67	21,619,527	67.74	97.50
S96_5	23,981,808	23,917,598	97.83	93.87	23,312,483	68.01	97.47
S96_6	25,055,152	24,982,156	97.80	93.84	24,502,498	67.10	98.08

Differential gene expression analysis and gene function annotation

Differentially expressed genes (DEGs) were calculated according to the gene expression count matrix using Cuff package. 339 DEGs with log2FC ≥ 1 and *p*-value < 0.05 at FDR <0.05 were obtained from the exponential phase compared with the lag phase (L/E), among which 189 DEGs were up-regulated and 150 DEGs were down-regulated. 2,049 DEGs were obtained from the stationary phase compared with the lag phase (L/S), among which 986 DEGs were up-regulated and 1,063 DEGs were down-regulated. Among the genes with a significant difference in both L/E and L/S, A total of 115 out of 339 DEGs and 558 out of 2,049 DEGs were annotated with KEGG pathway, including 77 and 295 DEGs were up-regulated and 38 and 263 DEGs were down-regulated, respectively (Table 2.). Differentially transcribed genes showed a higher proportion of up-regulated genes than down-regulated genes in both comparisons of L/E and L/S phases.

Table 2.
Number of DEGs in KEGG pathway comparative of different growth phases.

Category	Number of DEGs	
	Lag phase vs Exponential phase (L/E)	Lag phase vs Stationary phase (L/S)
Significantly expressed gene (*p*-value < 0.05)[a]	1,663	3,411
|log2FC| ≥ 1.0[b]	339	2,049
- Up-regulated gene	189	986
- Down-regulated gene	150	1,063
KEGG pathway	115 (36.98%)	558 (27.23%)
- Up-regulated gene	77	295
- Down-regulated gene	38	263

[a]When the *p*-value of the expression level in the same gene between the two groups was less than 0.05, the difference was significant, and the number was indicated.
[b]Among the genes with significant differences between the two phases, the number of genes whose *p*-value is less than 0.05 and log2FC > 1 is indicated.

The top 10 up-regulated DEGs and the top 10 down-regulated DEGs in L/E and L/S, respectively, are shown in Tables 3. and 4. In the L/E phase, most of the genes involved in nitrogen metabolism (e.g. TCONS_00000808 and TCONS_00003577) and carbohydrate metabolism (e.g. TCONS_00005566, TCONS_00000935 and TCONS_00005567) were up-regulated, as they are an important source of energy for the growth and viability of microorganisms.[14] For example, *tpiA_2* gene (TCONS_00005567) encoding triosephosphate isomerase converts dihydroxyacetone phosphate into glyceraldehyde-3-phosphate, which is the substrate in the successive step of the glycolysis pathway, tpiA_2 oxidizes glucose to ATP.[15] During the exponential phase of growth, bacterial cells produce metabolites that are necessary for growth.[7,16] On the opposite, amino acid metabolism (e.g. TCONS_00002685 and TCONS_00001489) was down-regulated. In the L/S phase, most the gene related to amino acid metabolism were up-regulated. Once essential nutrients are depleted, cells switch to a stationary phase, stop growing and often start producing secondary metabolites to increase the probability of long-term survival.[17] Amino acids are key precursors for the biosynthesis of many secondary metabolites.[18] For example, *pccA* gene (TCONS_00004536) encoding propionyl-CoA carboxylase (PCC) catalyzes the carboxylation of propionyl-CoA to methylmalonyl-CoA[19], which is part of a subgroup of biotin-dependent carboxylases which also includes acetyl-CoA carboxylase (ACC), 3-methylcrotonyl-CoA carboxylase (MCC) (TCONS_00004537), and pyruvate-CoA carboxylase[20], which are key enzymes in the metabolism of fatty acids, carbohydrates, and amino acids.[21] In some microorganisms, these enzymes have important functions in CO_2 fixation[22], mycolic acid and methyl-branched fatty acid biosynthesis[23], urea utilization as a nitrogen source[24], polyketide biosynthesis[25], and metabolism of terpenoids.[26] The late sporulation protein WhiD belonging to a protein family unique to actinomycetes[18] encoded by *whiD* gene (TCONS_00004075) was higher expressed in the exponential phase and stationary phase. This is because both sporulation and secondary metabolism are required to survive competition with other microorganisms under limited nutrient conditions.[6] However, carbohydrate metabolism and glycan biosynthesis and metabolism were down-regulated. The cAMP phosphodiesterase hydrolyzes 3',5'-cyclic AMP (cAMP) to 5′-adenosine monophosphate (AMP), which in this experiment, the most down-expressed gene was 3',5'-cyclic-AMP phosphodiesterase (cAMP phosphodiesterase) (TCONS_00005031) encoded by *cpdA*, which repressed expression of β-galactosidase, a product of the *lacZ* gene.[27] In the case of media containing both glucose and lactose, bacteria break down glucose for use in cells first. When cells enter the stationary phase, nutrients begin to be depleted and, glucose levels decreasethe expression of this gene decreases in order to switch to other carbon sources.

Table 3.
The fold change of the top 10 up-regulated DEGs and down-regulated DEGs in the exponential phase compared with the lag phase.

Gene ID	Gene name	log2FC	*p*-value
Up-regulated genes in Lag phase vs Exponential phase (L/E)			
TCONS_00000808	release factor glutamine methyltransferase (*prmC*)	5.08178	2.60×10^{-3}
TCONS_00005566	6-phospho-3-hexuloisomerase (*hxlB*)	4.38229	5.00×10^{-5}
TCONS_00004075	family transcriptional regulator, redox-sensing transcriptional regulator (*whiD*)	3.312	5.00×10^{-5}
TCONS_00000580	bifunctional lysine-specific demethylase and histidyl-hydroxylase (*NO66*)	3.21582	5.00×10^{-5}
TCONS_00005567	triosephosphate isomerase (TIM) (*tpiA_2*)	3.16669	5.00×10^{-5}
TCONS_00004038	acetyl esterase (*aes*)	3.03491	5.00×10^{-5}
TCONS_00000455	ATP-dependent Clp protease ATP-binding subunit ClpC (*clpC*)	3.0205	5.00×10^{-5}
TCONS_00000935	alcohol dehydrogenase, propanol-preferring (*adh_2*)	2.81612	5.00×10^{-5}
TCONS_00005569	putative hydrolase of the HAD superfamily	2.67414	5.00×10^{-5}
TCONS_00003577	L-asparaginase (*ansA*)	2.66856	5.00×10^{-5}
Down-regulated genes in Lag phase vs Exponential phase (L/E)			
TCONS_00002685	4-hydroxyphenylpyruvate dioxygenase (*hppd*)	-2.33214	5.00×10^{-5}
TCONS_00003147	aminopeptidase S (*lieA*)	-1.63067	5.00×10^{-5}
TCONS_00001494	2-amino-4-deoxychorismate synthase (*phzE*)	-1.61781	1.50×10^{-4}
TCONS_00004514	polyketide synthase PksL (*pksL*)	-1.53242	5.00×10^{-5}
TCONS_00005252	two-component system, NarL family, response regulator DevR (*devR*)	-1.50956	5.00×10^{-5}
TCONS_00003408	viologen exporter family transport system permease protein (*evrB*)	-1.4458	1.22×10^{-2}
TCONS_00001489	3-deoxy-7-phosphoheptulonate synthase (*aroG*)	-1.43855	5.00×10^{-5}
TCONS_00005113	xanthine dehydrogenase YagT iron-sulfur-binding subunit (*yagT*)	-1.38625	6.00×10^{-5}
TCONS_00004506	MFS transporter, DHA2 family, multidrug resistance protein (*lfrA*)	-1.35441	5.00×10^{-5}
TCONS_00004272	cold shock protein (*cspA*)	-1.32818	5.50×10^{-4}

Table 4.
The fold change of the top 10 up-regulated DEGs and down-regulated DEGs in the stationary phase compared with the lag phase.

Gene ID	Gene name	log_2 FC	*p*-value
Up-regulated genes in Lag phase vs Stationary phase (L/S)			
TCONS_00005638	multiple sugar transport system substrate-binding protein	6.73752	5.00×10^{-5}
TCONS_00002843	2-oxoisovalerate dehydrogenase E1 component alpha subunit (*bkdA*)	5.75185	5.00×10^{-5}
TCONS_00000205	urease subunit gamma/beta (*ureAB*)	4.71149	5.00×10^{-5}
TCONS_00000207	agmatine deiminase (*aguA*)	4.6453	5.00×10^{-5}
TCONS_00003476	superoxide dismutase, Fe-Mn family (*sodF1*)	4.37561	5.00×10^{-5}
TCONS_00003585	P-type Cu+ transporter (*ctpA_2*)	4.17948	5.00×10^{-5}
TCONS_00005395	glutamine-fructose-6-phosphate transaminase (isomerizing) (*glmS_2*)	4.17821	5.00×10^{-5}
TCONS_00004536	propionyl-CoA carboxylase, biotin carboxylase, biotin carboxyl carrier protein (*pccA*)	3.88292	5.00×10^{-5}
TCONS_00004537	3-methylcrotonyl-CoA carboxylase beta subunit (*mccb*)	3.7136	5.00×10^{-5}
TCONS_00004075	family transcriptional regulator, redox-sensing transcriptional regulator (*whiD*)	3.45258	5.00×10^{-5}
Down-regulated genes in Lag phase vs Stationary phase (L/S)			
TCONS_00005031	3',5'-cyclic-AMP phosphodiesterase (*cpdA*)	-8.41681	5.00×10^{-5}
TCONS_00000938	PhoX family protein	-8.34277	5.00×10^{-5}
TCONS_00005505	glycerophosphoryl diester phosphodiesterase (*glpQ_3*)	-7.71615	5.00×10^{-5}
TCONS_00005126	polyene glycosyltransferase (*amphDI, nysDI, fscMI, pimK*)	-7.43699	5.00×10^{-5}
TCONS_00004311	crotonyl-CoA carboxylase/reductase (*ccr_1*)	-7.38895	5.00×10^{-5}
TCONS_00003154	DeoR family transcriptional regulator, fructose operon transcriptional repressor (*fruR*)	-7.18085	5.00×10^{-5}
TCONS_00001936	undecaprenyl-diphosphatase (*bacA*)	-7.1258	5.00×10^{-5}
TCONS_00002582	lipoyl-dependent peroxiredoxin subunit D (*ahpD_2*)	-6.93992	5.00×10^{-5}
TCONS_00003776	GDPmannose 4,6-dehydratase (*gmd*)	-6.75024	5.00×10^{-5}
TCONS_00005133	ABC-2 type transport system ATP-binding protein (*drrA_7*)	-6.71479	5.00×10^{-5}

KEGG pathway enrichment analysis

Pathway enrichment analysis was performed using piano in R package (Varemo et al, 2013). Significant enrichment pathways were considered pathways with a *p*-value <0.05. To understand the biological context of DEGs, pathway enrichment analysis was ensued. In the L/E phase, the pathways for valine leucine and isoleucine biosynthesis, C5-branched dibasic

acid metabolism, butanoate metabolism, arginine and proline metabolism, and glycolysis/gluconeogenesis were significantly up-regulated. In contrast, the pathways for valine, leucine and isoleucine degradation, arginine biosynthesis, phenylalanine metabolism, phenazine biosynthesis, phenylalanine, tyrosine and tryptophan biosynthesis were significantly down-regulated. In the L/S phase, valine leucine and isoleucine degradation, lysine degradation, pyruvate metabolism, fatty acid degradation, and glycolysis/gluconeogenesis were significantly up-regulated, whereas the pathways in oxidative phosphorylation, citrate cycle (TCA cycle), phenylalanine, tyrosine and tryptophan biosynthesis, arginine biosynthesis, and sulfur metabolism were significantly down-regulated (Table 5.).

Table 5.
Significant enrichment pathway comparison between the exponential phase, the lag phase, and the stationary phase.

Up-regulated pathway	**(*p*-value)**	**Down-regulated pathway**	**(*p*-value)**
Lag phase vs Exponential phase (L/E)			
Valine leucine and isoleucine biosynthesis	9.99×10^{-4}	Valine leucine and isoleucine degradation	2.90×10^{-2}
C5-Branched dibasic acid metabolism	2.00×10^{-3}	Phenylalanine tyrosine and tryptophan biosynthesis	1.42×10^{-1}
Butanoate metabolism	6.00×10^{-3}	Arginine biosynthesis	2.90×10^{-2}
Arginine and proline metabolism	1.47×10^{-2}	Phenylalanine metabolism	2.90×10^{-2}
Glycolysis/Gluconeogenesis	2.43×10^{-2}	Phenazine biosynthesis	4.50×10^{-2}
Lag phase vs Stationary phase (L/S)			
Valine leucine and isoleucine degradation	3.33×10^{-4}	Oxidative phosphorylation	$3.33x\ 10^{-4}$
Lysine degradation	3.33×10^{-4}	Citrate cycle (TCA cycle)	6.66×10^{-4}
Pyruvate metabolism	3.33×10^{-4}	Phenylalanine tyrosine and tryptophan biosynthesis	7.00×10^{-3}
Fatty acid degradation	3.33×10^{-4}	Arginine biosynthesis	1.10×10^{-2}
Glycolysis / Gluconeogenesis	6.66×10^{-4}	Sulfur metabolism	1.10×10^{-2}

Conclusion:

The results of this study showed the difference in expressed genes of the metabolism in *Streptomyces* sp. GKU 223 at different growth phases. The KEGG pathway analysis was annotated at the primary metabolite level. However, further studies from other databases should expand the understanding of secondary metabolism. This may contribute to facilitating the rational engineering of secondary metabolite production.

Acknowledgements:

PP has been granted a Master Scholarship of Graduate Institute of Science and Technology (TGIST), National Science and Technology Development Agency. This research was funded by Kasetsart University Research and Development Institute (KURDI) project FF(KU)5.64.

References:

1. Dyson P. Elsevier Inc. 2019;334-345.
2. Kim JN, Kim Y, Jeong Y, Roe JH, Kim BG, Cho BK. J. Microbiol. Biotechnol. 2015;25:1599–1605.
3. Bentley SD, Chater KF, Cerden AM, Challis GL, Thomson NR, James KD, Harris DE, Quail MA, Kieser H, D. Harper, Bateman A, Brown S, Chandra G, Chen CW, Collins M, Cronin A, Fraser A, Goble A, Hidalgo J, Hornsby T, Howarth S, Huang C, Kieser T, Larke L, Murphy L, Oliver K, O'Neil S, Rabbinowitsch E, Rajandream M, Rutherford K, Rutter S, Seeger K, Saunders D, Sharp S, Squares R, Squares S, Taylor K, Warren T, Wietzorrek A, Woodward J, Barrell BG, Parkhill J, Hopwood DA. NATURE. 2002;417:141-147.
4. Omura S, Ikeda H, Ishikawa J, Hanamoto A, Takahashi C, Shinose M, Takahashi Y, Horikawa H, Nakazawa H, Osonoe T, Kikuchi H, Shibai T, Sakaki Y, Hattori M. PNAS. 2001;98:12215-12220.
5. Chandra G, Chater KF. FEMS Microbiol Rev. 2014;38:345–379.
6. Hodgson DA. Adv. Microb. Physiol. 2000;42:47-238.
7. Alam MT, Merlo ME, Hodgson DA, Wellington EM, Takano E, Breitling R. BMC Genomics. 2010;11.
8. Leetanasaksakul K, Thamchaipeneta A. Agric. Nat. Resour. 2018;52:228-233.
9. Kroll KW, Mokaram NE, Pelletier AR, Frankhouser DE, Westphal MS, Stump PA, Stump CL, Bundschuh R, Blachly JS, Yan P. Cancer Informatics. 2014;13:7-14.
10. Bolger AM, Lohse M, Usadel B. Bioinformatics. 2014;30:2114-2120.
11. Langmead B, and Salzberg SL. Nature Methods. 2012;9:357-359.
12. Trapnell C, Hendrickson DG, Sauvageau M, Goff L, Rinn JL, Pachter L. Nat Biotechnol. 2013;31:46-53.
13. Kanehisa M, Goto S, Kawashima S, Okuno Y, Hattori M. Nucl Acids Res. 2004;32:277-2780.
14. Nieselt K, Battke F, Herbig A, Bruheim P, Wentzel A, Jakobsen M, Sletta H, Alam M , Merlo M, Moore J, Omara W, Morrissey E, Juarez-Hermosillo M, Rodríguez-García A , Nentwich M, Thomas L, Iqbal M, Legaie R, Gaze W, Challis G, Jansen R, Dijkhuizen L, Rand D, Wild D, Bonin M, Reuther J, Wohlleben W, Smith M, Burroughs N, Martín J, Hodgson D, Takano E, Breitling R, Ellingsen T, Wellington E. BMC Genomics 2010;11.
15. Williams J, Zeelen J, Neubauer G, Vriend G, Backmann J, Michels P, Lambeir AM, Wierenga R. Protein engineering. 1999;12:243-250.
16. Saraireh H, Wael A. Zereini A, Tarawneh K. Jordan J. Biol. Sci. 2015;8:127-132.
17. Komatsu M, Uchiyama T, Ōmura S, Cane D, Ikeda H. PNAS. 2010;107:2646-2651.
18. Keulen G, Dyson P. Adv. Appl. Microbiol. 2014;89:217-266.
19. Hou J, Xiang H, Han J. Appl. Environ. Microbiol. 2015;81:794-804.
20. Tong J. Cell. Mol. Life Sci. 2013;70:863-891.
21. Zempleni J, Mock D. J. Nutr. Biochem. 1999;10:128-138.
22. Pratscher J, Dumont MG, Conrad R. Proc Natl Acad Sci USA. 2011;108:4170-4175.

23. Gago G, Diacovich L, Arabolaza A, Tsai S-C, Gramajo H. FEMS Microbiol Rev. 2011;35:475-497.
24. Zhang H, Boghigian BA, Pfeifer BA. Biotechnol Bioeng. 2010;105:567-573.
25. Strope PK, Nickerson KW, Harris SD, Moriyama EN. BMC Evol Biol. 2011;11.
26. Fromme K, Jendrossek D. Appl. Microbiol. Biotechnol. 2010;87:859-869.
27. Imamura R, Yamanaka K, Ogura T, Hiraga S, Fujita N, Ishihama A, Niki H. J. Biol. Chem. 1996;271:25423-25429.

CHARACTERIZATION OF DISSOLVABLE MICROARRAY PATCHES BASED CARBOXYMETHYLCELLULOSE, POLYVINYLPYRROLIDONE AND CHITOSAN CROSS-LINKED WITH HYALURONIC ACID

Julinthip Puttawong,[1] Suchera Thananimit[2,3,*]

[1]Biomedical Science and Biomedical Engineering, Faculty of medicine, Prince of Songkla University, Songkhla, Thailand 90112
[2]Center for Genomics and Bioinformatics Research, Faculty of Science, Prince of Songkla University, Songkhla 90112, Thailand
[3]Division of Biological Science, Faculty of Science, Prince of Songkla University, Songkhla 90112, Thailand
*e-mail: s.thananimit@yahoo.com

Abstract:

Due to the excellent barrier properties of the upper most layer of the skin, the stratum corneum (SC), microneedle (MN) arrays/microarray patches has been proposed as a method to overcome the SC barrier and to enhance the transdermal transport of bioactive substances/molecules therapeutics. In the present study, three biocompatible and biodegradable materials, carboxymethylcellulose (CMC), polyvinylpyrrolidone (PVP), and chitosan (CS), cross-linked with hyaluronic acid (HA) were characterized for dissolvable microarray patch (DMP) fabrication. The comparative studies were examined by the following parameters: integrity of DMP fabrication, viscosity, and dissolution rate. The analysis showed that the percentage integrity of DMP fabrication for CMC-HA is relatively higher (90 %) than that for PVP-HA, which is as well higher than that for CS-HA. In addition, the dissolution duration of PVP-HA is shorter compared to that of CMC-HA; however, compared to CMC-HA (7 h), PVP-HA formulation requires a longer time for microneedle formation (12 h). Therefore, the DMPs based CMC cross-linked with HA were selected for further experiment (3% CMC + HA). Based on this fabrication, the formulation of CMC-HA was also carried out via chemical structure analysis, and solution viscosity was considered for specific quality control that are suitable for production processes. Additionally, the cell cytotoxicity test was examined to assess the safety and biocompatibility of the CMC-HA combination used for DMP preparation, including 3 % CMC+HA (microneedle layer) and 6 % CMC+HA (backing layer). From these findings, it can be inferred that the fabrication of DMPs is biocompatible and efficacious/safe as potential transdermal drug delivery strategy/system.

Keywords: Drug Delivery System; Dissolvable Microneedle Patch; Microneedle; Hyaluronic Acid; Carboxymethylcellulose

Introduction:

Dissolvable microneedles are mainly developed and widely used for drug delivery or cosmetic purposes. They are needlelike structures of micron-scale lengths (<1000 μm), typically assembled as arrays with desirable potential of piercing into the skin in a minimally invasive and painless manner[1]. Transdermal drug delivery system has several advantages, including its ease of application, non-invasiveness, and painless therapeutic effect in biomedical[2] and personal cosmetic application[3]. Furthermore, the microneedle/microarray patch could be integrated with other targeted compounds; thus, microneedle-assisted transdermal delivery allows the coadministration of several bioactive substances/molecules[4].

Dissolvable microneedles are usually fabricated from various biodegradable/biocompatible polymers. Among the numerous polymers, carboxymethyl cellulose (CMC), chitosan (CS), and polyvinylpyrrolidone (PVP) are used for the fabrication of microneedles due to their low cost. Therefore, we collectively analyzed three biocompatible and biodegradable materials, carboxymethyl cellulose (CMC), chitosan (CS), and polyvinylpyrrolidone (PVP), cross-linked with hyaluronic acid (HA)[5]. Comparing their overall properties including geometrical parameters after molding, dissolution duration, viscosity, structural interaction, and cytotoxicity will aid the identification of the most suitable material for microarray preparation. Therefore, we investigated the characterization of dissolvable microarray patches (DMPs) with distinct formulations.

Methodology:

Fabrication and design

Three polymers–CMC, PVP, and CS–were cross-linked with HA to yield the respective formulations (CMC-HA, PVP-HA, and CS-HA). For this purpose, 1 % HA solution was prepared in deionized water and mixed with different types of microneedle solutions prepared from CMC, PVP, and CS at percentage concentrations of 3, 3, and 0.5 % (w/v), respectively. Subsequently, the volume ratios of the individual formulations (CMC-HA, PVP-HA and CS-HA) were independently evaluated as 3:1. Lastly, the backing layer of microneedle patch was 6 % CMC-HA, formulated at a ratio of 3:1.

Moreover, the viscosity of the three formulations was measured via digital Viscometer *(Model LVDV-I Primer, Brookfield, USA),* at 25.0±1.0 °C. Specifically, 20 mL of solution was measured with spindle number S00 (shear rate, 0.6 rpm) in triplicate to primarily establish the optimal standards, which would thus yield satisfactory results towards the formulation of dissolvable microneedle.

The fabrication process was conducted with a pyramidal (needle-like) silicone template/mold (Needle array of dimensions; 25 x 90 x 300 μm) using CMC-HA, PVP- HA, and CS-HA as a base material (needle), following which 6 % CMC-HA was used as the splice on the needle. Further, 2 mL of each formulation was dropped onto the silicone mold, dripping through the pinhole, and subsequently dried for 9 h while ensuring it is airtight. Subsequently, 6 % CMC-HA was added onto the pinhole layer of silicone template to form a needle splicer. A microneedle patch was baked in a desiccator with silica gel and allowed to dry for 24 h prior to its removal from the silicone mold.

Morphology

The DMPs were visualized via scanning electron microscopy (SEM) to further examine the shape and morphology of the surfaces (*TM3030 plus tabletop scanning electron microscope, Hitachi, Tokyo, Japan)*. To ensure a thorough fabrication of the microneedle patches, all formulations were analyzed. Notably, the SEM was employed at a beam voltage of 5.0 kV, and the images were visualized at magnifications of 60 and 250×.

Solubility

The dissolution rates of the microneedle arrays are dependent on the properties of their relative precursor polymer. Thus, the dissolution time of the DMPs developed from CMC, PVP, and CS with cross-linked HA was evaluated. Further, DMP samples (1 × 1 cm) were added to a 1 mL phosphate buffered saline (PBS; pH 7.4), followed by specific time evaluations and recordings until complete dissolution.

Fourier-transform infrared spectroscopy (FTIR)

Fourier-transform infrared spectroscopy (FTIR) spectra of CMC-HA, PVP- HA, and CS-HA were analyzed using Fourier transform infrared spectrometer, VERTEX 70, Bruker, Germany, in the region of 4000–400 cm^{-1}, and results were collected at 64 scans with a resolution of 4 cm^{-1}.

Cytotoxicity

An *in vitro* cytotoxicity analysis was performed on PCS-201-010 fibroblast primary cell line, using the 3-(4,5-dimethylthiazol-2-yl)-2,5-diphenyltetrazolium bromide (MTT) assay[6]. Cells were cultured in Dulbecco's modified Eagle's medium (DMEM) containing 10 % fetal bovine serum (FBS), 1 % penicillin-streptomycin (Penstrep), and 1 % L-glutamine. Then, the cells were seeded into a 96-well plate, immersed in DMEM medium containing 10 % FBS, at a plating density of 5000 cells/well, and incubated at 37 °C in 5 % CO_2 for 24 h, prior to the test. Subsequent to culture, polymers were dissolved in media. After 24 h, 10 µL of the medium containing the test compounds at concentrations of 3 and 6 % (CMC-HA) were added and incubated at 37 °C in 5 % CO_2 for 48 h. Experiments were performed thrice, and cells containing no test compounds served as the control. Cytotoxicity was qualified subjectively and quantitatively using an Invitrogen LIVE/DEATHTM cell imaging kit and the MTT assay. After the cells medium was removed, staining solution (100–200 µL) was immediately applied to the cells at a volume ratio of 1:1 (DMEM:dye). Prior to fluorescence microscopy, the resulting stained solution was incubated at 20–25 °C for 30 min. After 48 h, 110 µL of MTT solution (5 mg mL^{-1}) in PBS was added to each well and incubated at 37 °C for 4 h. After removing the medium containing the MTT, the resulting formazan crystals were solubilized in 110 µL of DMSO, and the absorbance at 570 nm was measured using a microplate reader. The cell viability was calculated using the following formula: % Cell viability = Abs (treated CMC+HA)/Abs (untreated; UT) ×100.

Results and Discussion:

Morphology of DMPs

Various characterizations should be analyzed since the unique properties, which are based on the type of microneedle formulation, can considerably determine the application efficacy and quality fabrication[7]. DMPs were fabricated using a variety of polymer solutions, including a combination of CMC-HA, PVP-HA, and CS-HA. DMPs are pyramidal, have a needle height of 300 µm, and the density of microneedles is approximately 500 needles per cm² **(Fig. 1)**. To ensure a thorough/complete DMPs fabrication, the integrity percentages of the 3 different formulations were independently calculated per 1 square millimeter as the complete microneedles/total microneedles × 100. The percentage integrity of the different dissolvable microneedles prepared from CMC-HA, PVP-HA and CS-HA are 91.2±1.1, 91.1±0.9 and 87.3±0.8, respectively.

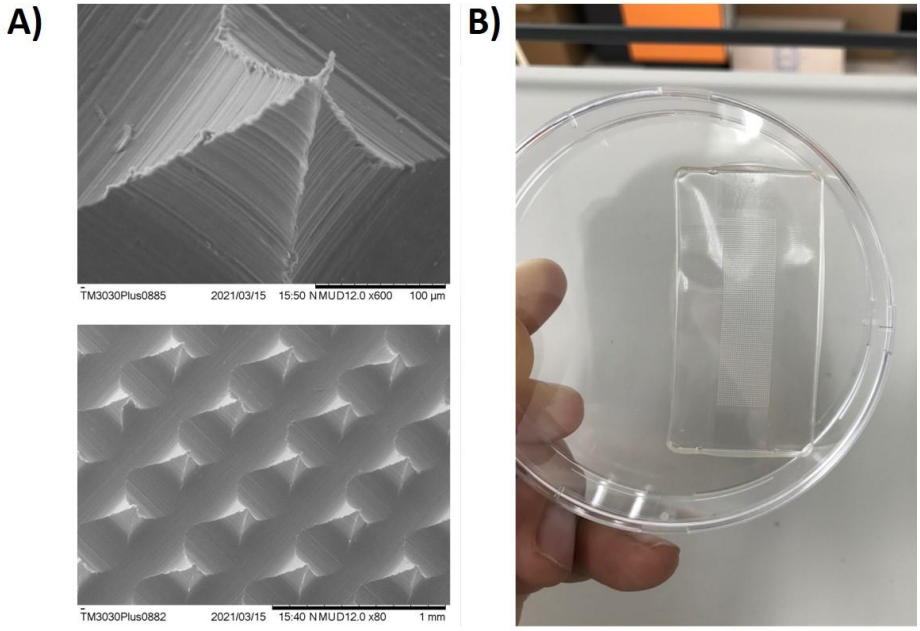

Fig. 1 (a) SEM images of the internal surfaces of CMC-HA in form of single and array and (b) DMPs based CMC cross-linked with HA.

Investigation and selection of material for DMP fabrication

Dissolution analyses of the three formulations were performed to predict the time required for drug release from each DMPs. The solubility time of DMPs formulated from CMC-HA, PVP-HA, and CS-HA was investigated. The DMPs formulated from PVP-HA completely dissolved within a short period (9 min) of immersion in PBS (pH 7.4), followed by durations for CMC-HA and CS-HA. In addition, the viscosity of all formulations were studied to evaluate the influence to the DMP fabrication. The solution viscosity of DMP fabrication prepared from CMC-HA, PVP-HA and CS-HA are 209.1±0.1, 37.7±0.1 and 52.2±0.1 cP, respectively. These results indicate that the high viscosity of CMC-HA confers it a slightly longer dissolution time than PVP-HA. However, the CMC-HA formulations were selected for DMP fabrication in the following experiment since its baking time towards the DMP formulation is 7 h lesser than that of PVP-HA (12 h) at the needle layer. Meanwhile, CS-HA takes 4 h to dry, while the upper layer of the needle takes 24 h. Furthermore, the

obtained viscosities for the needle and upper layers were considered as established standards for future DMP fabrication. In order to demonstrate intermolecular interaction between components in polymer mixture, three different FTIR spectra of pure CMC and HA, as well as CMC-HA combination, are shown in **Fig. 2**. Comparing the IR spectra, it can be found that the specific peaks of pure CMC and pure HA all appeared in the spectrum of CMC-HA composite shown in **Fig. 2c**. Therefore, the spectra retain the original identity of CMC and HA, which suggests that there is no change in the two compositions subsequent to crosslinking with HA.

The advantages of this fabricated DMP include simple production and low or no risk for the reproducible application, since the biocompatible properties of dissolvable polymeric microneedle and the pharmaceutical active ingredient/drug could be loaded for many purposes[8].

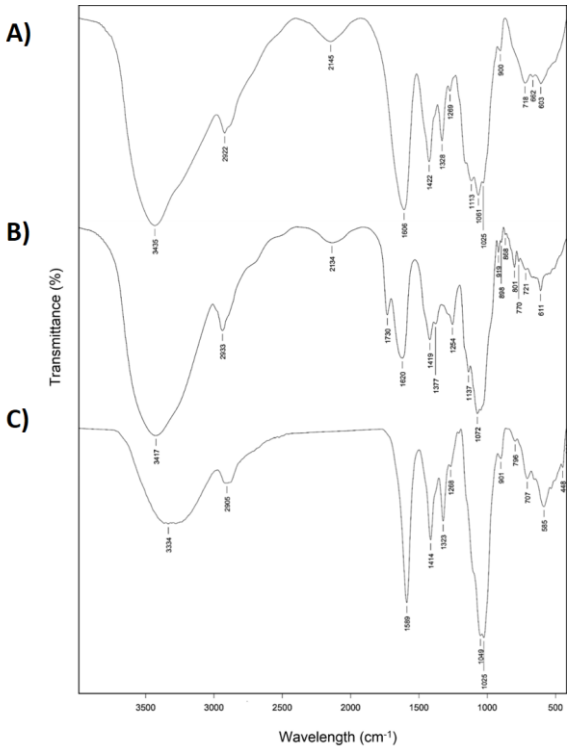

Fig. 2 FTIR spectra of (a) CMC, (b) HA, and (c) CMC-HA.

Biocompatibility

The PCS-201-010 fibroblast primary cell line was cultivated with dissolvable DMP, in both the needle and backing layers, 3 % CMC+HA and 6 % CMC+HA, respectively, to assess the biocompatibility and biosafety of DMPs[9]. The results **(Table 1)** showed that the cell viability following treatment with CMC-HA formulation was relatively good (100–132 %), following incubation at 48 h indicating that the CMC-HA combination used in this study is highly biocompatible.

Table 1 The cell viability of DMPs via MTT assay on fibroblasts cell.

Samples	Cell Viability Percentage
UT	100.0±9.3
6%CMC+HA	110.7±15.2
3%CMC+HA	132.0±6.2

Conclusion:

Microfabrication of dissolvable and biodegradable polymeric microneedle arrays were extensively investigated based on micromolding technique. The aim of this study was to describe the polymer selection and optimize formulation compounding parameters for various polymeric DMPs. The polymeric DMPs were subsequently assembled and physicochemically characterized. DMPs were constructed at a depth of 300 μm with 3 % CMC+HA for needle tip, and 6 % CMC+HA for base layer. Micromolding sequence also aided in the formulation of DMPs with high precision and accuracy. Based on the obtained results, our developed formulation of DMPs is promising for constructing these polymeric types of matrix devices that have further application in biomaterial/bio-medical research.

Acknowledgements

This work was supported by Center for Genomics and Bioinformatics Research, Faculty of Science and Biomedical Science and Biomedical Engineering, Faculty of medicine, Prince of Songkla University for facilitating all equipment.

References

1. Sartawi Z, Blackshields C, Faisal W. J Control Release. 2022;348:186–205.
2. Tariq N, Ashraf M W, Tayyaba S. J Pharm Innov. 2021;doi:10.1007/s12247-021-09586-x.
3. Huang Y. European Polym J**.** 2022;163:110942.
4. Dugam S, Tade R, Dhole R, Nangare S. Future J Pharm Sci. 2021;7:19.
5. Aldawood F K, Andar A, Desai S. Polymers (Basel). 2021;13:2815.
6. Ghasemi M, Turnbull T, Sebastian S, Kempson I. Int J Mol Sci. 2021;22:12827.
7. Waghule T. Biomed Pharmacother. 2019;109:1249–1258.
8. Wang R. Macromol Rapid Commun. 2022;43:2200037.
9. Donnelly R F, Raj Singh T R, Woolfson A D. Drug Deliv. 2010;17:187–207.

DEVELOPMENT OF DNAZYME-BASED BIOSENSOR FOR CIRCULATING TUMOR DNA

Sutida Chimasungkanun[1], Benjamaporn Sriwilai[1], Anuttara Udomprasert[2,*], Thaned Kangsamaksin[1,*]
[1] Departmet of Biochemistry, Faculty of Science, Mahidol University, Bangkok 10140, Thailand
[2] Departmet of Biochemistry, Faculty of Science, Burapha University, Chonburi 20131, Thailand
*e-mail: anuttara@go.buu.ac.th, thaned.kan@mahidol.ac.th

Abstract:

Liquid biopsy is one of the promising techniques that can be used in cancer diagnosis. This technique detects circulating tumor DNA (ctDNA), circulating tumor cells (CTCs), exosomes and miRNA. ctDNA and CTCs are released from tumor cells and exist in the bloodstream. However, ctDNA concentration is higher than the other components, thus ctDNA is mostly used for cancer diagnosis in liquid biopsy. Our research team aimed to develop a colorimetric DNAzyme-based biosensor that can detect ctDNA containing gene mutation. Our biosensor was designed by using G-quadruplex/hemin DNAzyme mimicking horseradish peroxidase (HRP) enzyme which catalyzes H_2O_2 and $ABTS^{2-}$ and changed the color from light green to visible green. In this study, we investigated and optimized the catalytic activity of G-quadruplex/hemin DNAzyme in various conditions. To immobilize onto nanoparticles for signal amplification, DNAzyme has to be modified with NH_2. Thus, the catalytic activity of G-quadruplex/hemin 5'NH_2- and 3'NH_2-modified DNAzymes were compared. Our results showed that the highest catalytic activity was obtained when using the ratio of DNAzyme:hemin at 1:20. Furthermore, the higher DNAzyme concentration exhibited the stronger color change signal. In addition, DNAzyme with NH_2 modification at 5' end showed higher catalytic activity. These results should be appropriate for further development of the ctDNA biosensor.

Introduction:

Liquid biopsy is one of the techniques that diagnose cancer by using body effluent, mainly blood. The advantage of this technique is a less-invasive procedure when compared with the standard technique or biopsy which requires surgery.[1] Therefore, liquid biopsy is an alternative technique that diagnoses and monitors cancer. In the formation of cancer, circulating tumor DNA (ctDNA) and circulating tumor cells (CTCs) are released into the bloodstream. CTCs are cells that are released from tumor cells and ctDNA is a single- or double-stranded DNA containing gene mutation released from tumor cells. However, ctDNA was found in higher concentration than CTCs. In addition, ctDNA contains highly specific and sensitive genetic mutation therefore ctDNA is mostly used as biomarkers for cancer diagnosis in liquid biopsy.[2] Nowadays, the Next-generation sequencing (NGS) technology has been used for gene mutation analysis.[3] However, there are some limitations such as expensive reagent and chemical for normal people that would like to diagnose cancer. Therefore, many studies have been proposed and developed biosensors for the cancer diagnosis. The biosensor divides into two parts. First, the bioreceptor part specifically binds with target molecule, then the signal transducer part creates the signal for signal measurement.[4] To detect specific DNA target, a DNA-based biosensor would be an excellent alternative for detection. Moreover, the

colorimetric biosensor is one of the biosensor types that is mostly used in the biomedical field such as cancer diagnosis. This type of biosensor is observed in the change of color when the target molecule binds with the biosensor.[5] Thus, we would like to develop the colorimetric biosensor for ctDNA detection. Our biosensor is designed by using the color change signal from G-quadruplex/hemin DNAzyme as a part of a signal transducer part in the biosensor. DNAzyme is an oligonucleotide that can catalyze the reaction of the substrate-like enzyme. G-quadruplex/hemin DNAzyme is one of the DNAzyme type which is guanine-rich oligonucleotides. The G-tetraplex could form from four guanine bases via Hoogsteen base-pairing and then fold into a quadruplex secondary structure (Figure 1a). In addition, this structure requires a co-factor or hemin to act as DNAzyme. Hemin could form stable complex with G-quadruplex DNA structure and enhance the catalytic activity of DNAzyme. The G-quadruplex/hemin DNAzyme mimics the catalytic activity of horseradish peroxidase (HRP) enzyme which catalyzes substrate, H_2O_2 and $ABTS^{2-}$, and the color changes into visible green (Figure 1b).[6-9] This DNAzyme has been utilized in biosensors for signal amplification.[7]

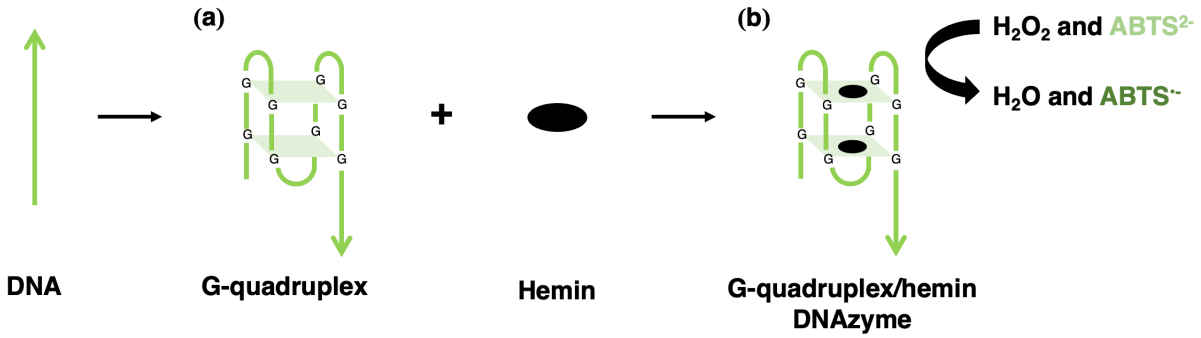

Figure 1. (a) The G-quadruplex structure, four guanine bases complementary via Hoogsteen base-pairing to form G-tetraplex and fold into a quadruplex secondary structure. (b) Hemin binds with G-quadruplex structure and form G-quadruplex/hemin DNAzyme which catalyzes H_2O_2 and $ABTS^{2-}$ and generates $ABTS^{\bullet-}$ and H_2O.

Therefore, our biosensor platform is developed by using the G-quadruplex/hemin DNAzyme immobilized nanoparticles in the signal transducer part. As the bioreceptor part of the biosensor, the capture probe binds with the target ctDNA (Figure 2a), then the signal transducer part of biosensor, the signal probe- and DNAzyme-immobilized nanoparticles (Figure 2b), will be captured and catalyzes the substrate resulting in the change of color (Figure 2c). In this study, we investigated the catalytic activity of five reported G-quadruplex/hemin DNAzymes to find the highest catalytic activity, and then the highest catalytic activity of G-quadruplex/hemin DNAzymes was selected for condition optimization for further used in the development of the ctDNA biosensor.

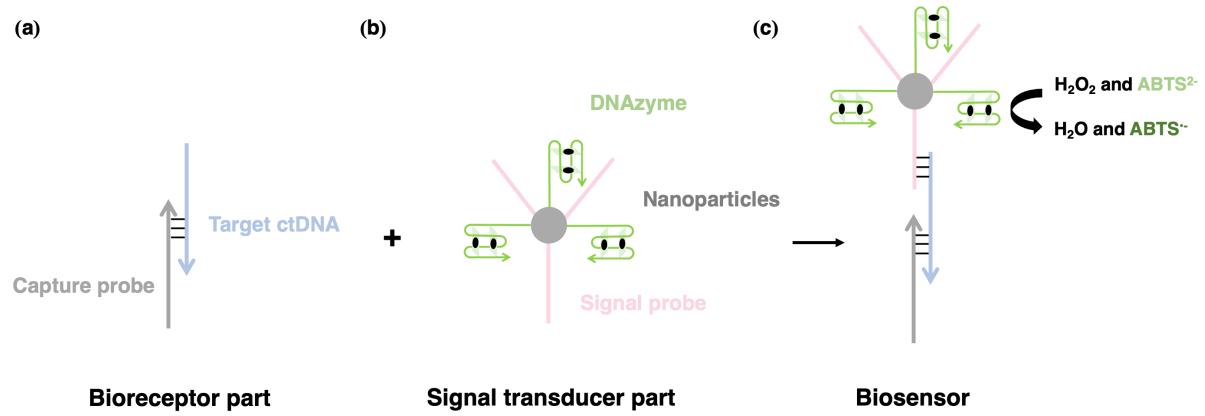

Figure 2. To construct a DNAzyme-based biosensor, (a) the capture probe binds with target ctDNA as part of the bioreceptor part, (b) then the signal probe- and DNAzyme-immobilized nanoparticles as part of the signal transducer part are added into the biosensor. (c) Finally, the signal transducer part will be captured and catalyzes the substrate resulting in the change of color.

Methodology:

The catalytic activity of five different G-quadruplex/hemin DNAzymes (DNAzymes 1–5)

The catalytic activity of G-quadruplex/hemin DNAzyme was determined by a microplate reader. First, 0.1 µM DNAzyme in 10 mM Tris-HCl, pH 8.0 containing 50 mM KCl were annealed by heating at 95 °C for 5 minutes, then cooling down at room temperature for 2 hours. After annealing, the solution was incubated in 1X MES buffer, pH 5.0 (25mM MES, pH 5.0 containing 200 mM NaCl, 10 mM KCl, 1% DMSO and 0.05% Triton X-100) with various concentrations of hemin (0.1, 0.5, 1, 1.5, 2 µM) for 30 minutes. Then, 2 mM ABTS and 2 mM H_2O_2 were added to the solution. Finally, the absorbance was recorded at 415 nm every 10 minutes.

The catalytic activity of DNAzyme 2 at DNAzyme:hemin ratio of 1:20

The catalytic activity of DNAzyme 2 was determined by a microplate reader. First, the various concentrations of DNAzyme 2 (25, 50, 75, 100 nM) in 10 mM Tris-HCl, pH 8.0 containing 50 mM KCl were annealed by heating at 95 °C for 5 minutes, then cooling down at room temperature for 2 hours. After annealing, the solution was incubated in 1X MES buffer, pH 5.0 (25mM MES, pH 5.0 containing 200 mM NaCl, 10 mM KCl, 1% DMSO and 0.05% Triton X-100) with various concentrations of hemin (0.5, 1, 1.5, 2 µM) for 30 minutes. Then, 2 mM ABTS and 2 mM H_2O_2 were added to the solution. Finally, the absorbance was recorded at 415 nm every 10 minutes.

The catalytic activity of NH_2-modified DNAzyme 2

The catalytic activity of NH_2-modified DNAzyme 2 was determined by a microplate reader. First, 0.1 µM DNAzyme in 10 mM Tris-HCl, pH 8.0 containing 50 mM KCl were annealed by heating at 95 °C for 5 minutes, then cooling down at room temperature for 2 hours. After annealing, the solution was incubated in 1X MES buffer, pH 5.0 (25mM MES, pH 5.0 containing 200 mM NaCl, 10 mM KCl, 1% DMSO and 0.05% Triton X-100) with 2 µM hemin 30 minutes. Then, 2 mM ABTS and 2 mM H_2O_2 were added to the solution. Finally, the absorbance was recorded at 415 nm every 10 minutes.

Results and Discussion:

The catalytic activity of five G-quadruplex/hemin DNAzymes at various ratios

To select G-quadruplex/hemin DNAzyme to be applied in our biosensor, all five reported G-quadruplex/hemin DNAzymes from previous research [10-13] were investigated for the highest catalytic activity. The catalytic activity of each DNAzyme in various concentration ratios of DNAzyme:hemin was examined. Since only G-quadruplex DNA itself cannot act as DNAzyme. However, after binding with hemin, the stable G-quadruplex/hemin DNAzyme complex forms and enhance the catalytic activity.[9] Thus, hemin concentrations were varied in our study for catalytic activity optimization. The concentration ratios of DNAzyme:hemin in the reactions were varied at 1:1, 1:5, 1:10, 1:15 and 1:20 (Figure 3a-3e). The result showed that the catalytic activity of five DNAzymes increased with increasing hemin concentrations. In addition, all five DNAzymes exhibited higher catalytic activity at DNAzyme:hemin ratio of 1:20 (Figure 3e). Moreover, DNAzyme 2 showed the highest catalytic activity among five DNAzymes.

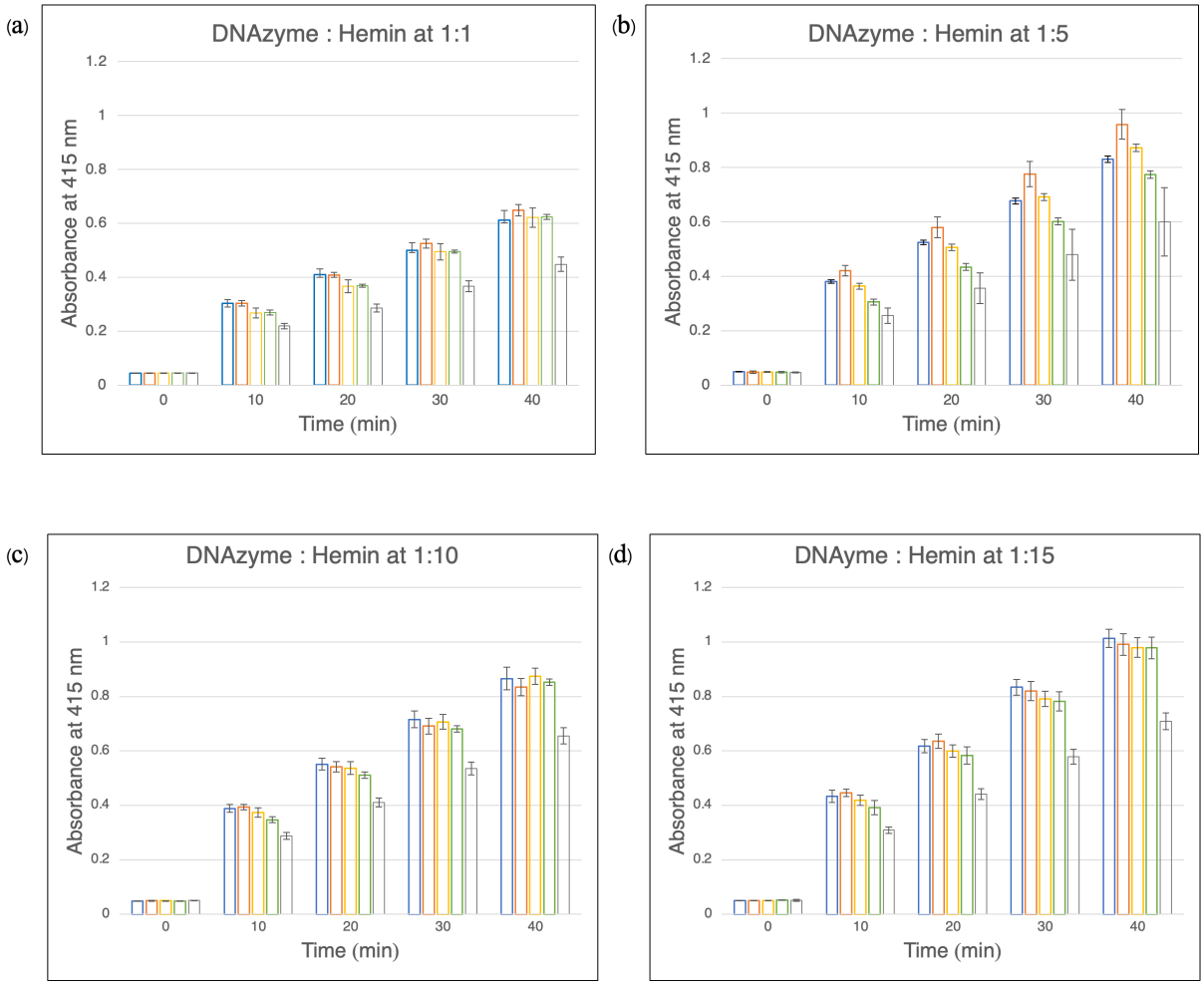

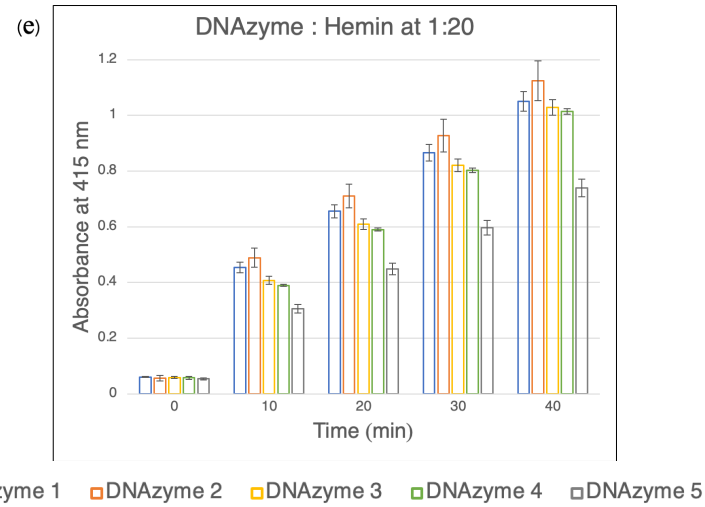

Figure 3. The catalytic activity of DNAzyme 1-5 at various DNAzyme:hemin concentration ratios. (a) the DNAzyme and hemin concentration ratio at 1:1, (b) 1:5, (c) 1:10, (d) 1:15 and (e) 1:20. DNAzyme 1 (blue bar), DNAzyme 2 (orange bar), DNAzyme 3 (yellow bar), DNAzyme 4 (green bar) and DNAzyme 5 (grey bar).

The catalytic activity of DNAzyme 2 at DNAzyme:hemin ratio of 1:20

From the previous result, DNAzyme 2 with the concentration ratio of DNAzyme:hemin at 1:20 exhibited the highest catalytic activity among five DNAzymes. In this experiment, different concentrations of DNAzyme 2 were utilized for the catalytic activity investigation with the concentration ratio of DNAzyme:hemin at 1:20 concentrations (25 nM DNAzyme:0.5 µM hemin, 50 nM DNAzyme:1 µM hemin, 75 nM DNAzyme:1.5 µM hemin and 0.1 µM DNAzyme:2 µM hemin). The result showed that the catalytic activity increased with increasing DNAzyme concentrations (Figure 4). Thus, DNAzyme concentration at 0.1 µM and hemin concentration at 2 µM will be used in the further experiments.

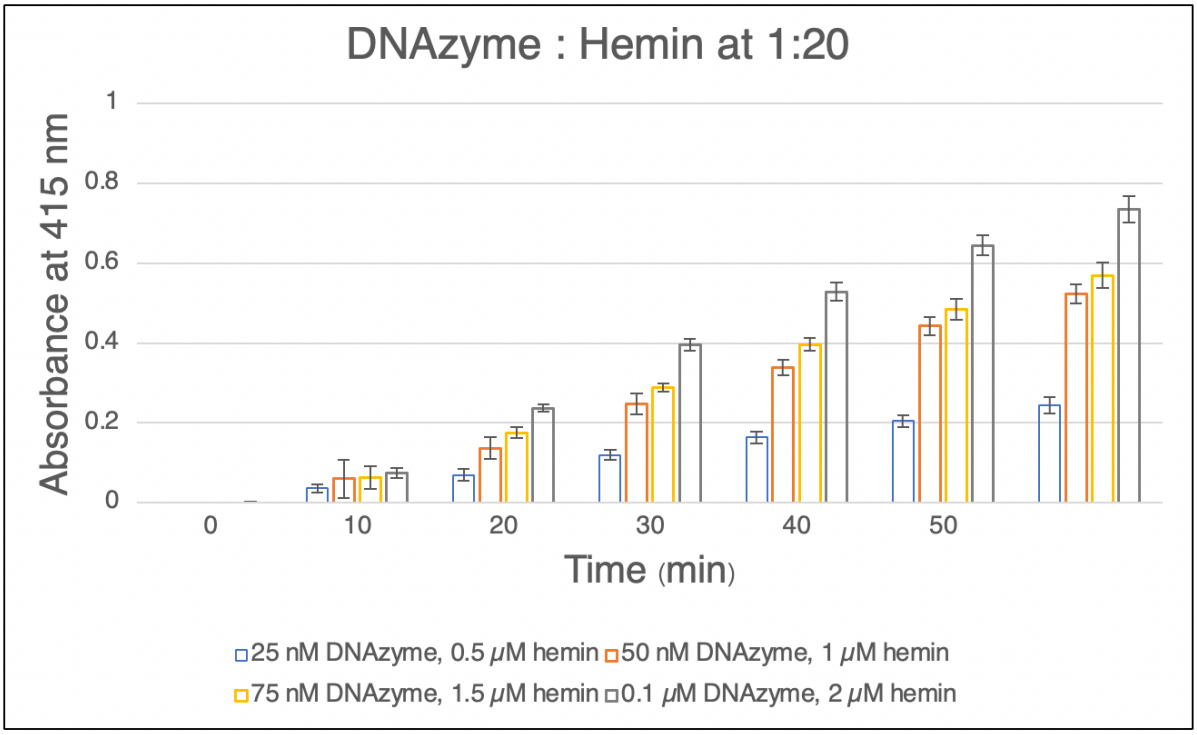

Figure 4. The catalytic activity of DNAzyme 2 at DNAzyme:hemin ratio of 1:20. 25 nM DNAzyme:0.5 µM hemin (blue bar), 50 nM DNAzyme:1 µM hemin (orange bar), 75 nM DNAzyme:1.5 µM hemin (yellow bar) and 0.1 µM DNAzyme:2 µM hemin (grey bar).

The catalytic activity of NH_2-modified DNAzyme 2

To enhance the signal, NH_2-modified DNAzyme will be immobilized onto nanoparticles with 3-aminopropryltriethoxysilane (APTES) functional group modification via covalent bond as shown in previous research.[14-15] As DNAzyme is required to be modified with $-NH_2$ for immobilization, the catalytic activity of DNAzyme modified with $-NH_2$ at 5' and 3' end was compared. The result showed the catalytic activity of NH_2-modified DNAzyme 2 at 5' end has higher catalytic activity than that of NH_2-modified DNAzyme 2 at 3' end (Figure 5) . Thus, NH_2-modified DNAzyme 2 at 5' end was selected to be immobilized onto nanoparticles for enhancing signal in the colorimetric ctDNA biosensor.

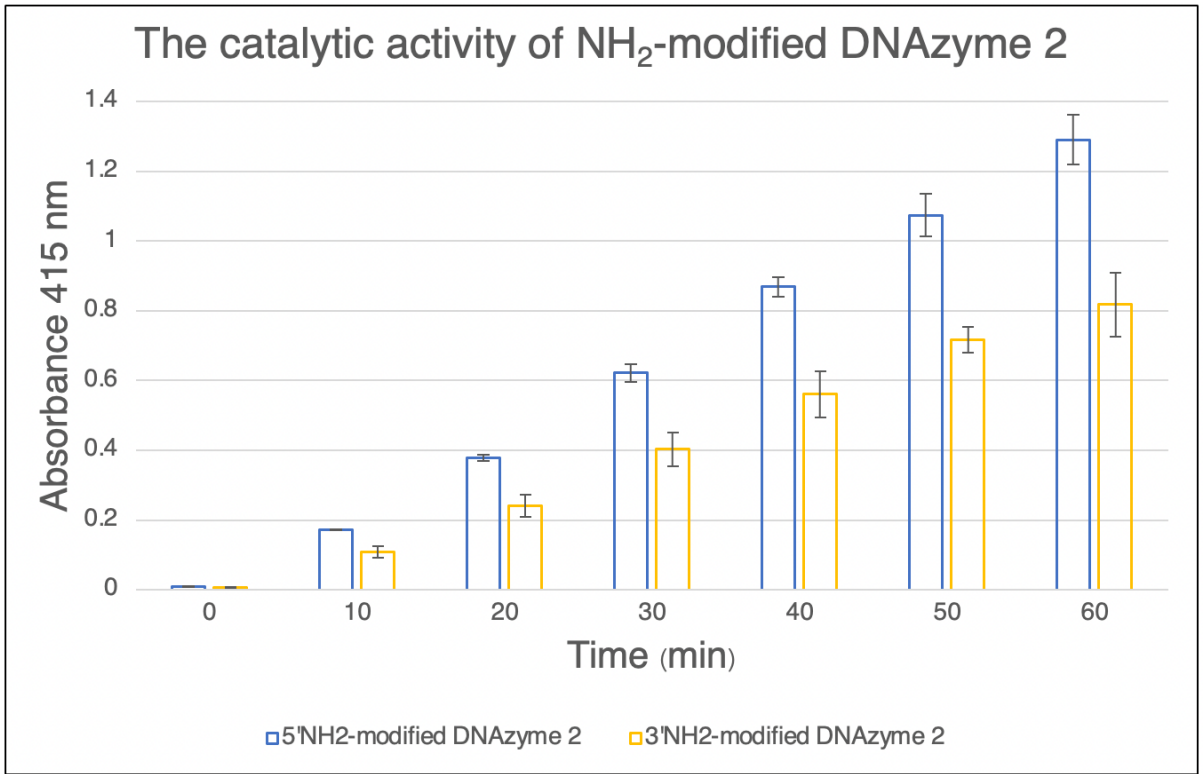

Figure 5. The catalytic activity of NH_2-modified DNAzyme 2.

Conclusion:

Our results showed that increasing hemin concentration ratio enhanced the catalytic activity of G-quadruplex/hemin DNAzyme. DNAzyme 2 at the concentration ratio of DNAzyme:hemin at 1:20 when using 0.1 µM DNAzyme and 2 µM hemin exhibited the highest catalytic activity among five DNAzymes. The catalytic activity of 5'NH_2-modified DNAzyme 2 was higher than that of 3'NH_2-modified DNAzyme 2. Therefore, 5'NH_2-modified DNAzyme 2 will be immobilized onto nanoparticles and the catalytic activity after the immobilization will be further examined for the development of the colorimetric ctDNA biosensor.

Acknowledgments:

This study was financially supported by the Office of the Permanent Secretary, Ministry of Higher Education, Science, Research and Innovation (Grant No. RGNS63-141) (A.U.) and Mahidol University (T.K.). We also thank the Central Instrumental Facility (CIF), Faculty of Science, Mahidol University for technical assistance.

References:

1. Poulet G, Massias J, Taly V. Acta Cytol. 2019;63:449-55
2. Cheng F, Su L, Qian C. Oncotarget. 2016;07:48832-41
3. Chen M, Zhao H. Hum Genomics. 2019;13:34
4. Srinivasan B, Tung S. J Lan Autom. 2015;20:365-89
5. Bai Y, Li H, Xu J, Huang Y, Zhang X, Weng J, Li Z, Sun L. Biosens Bioelectron. 2020;166:112424

6. Bhattacharyya D, Mirihana Arachchilage G, Basu S. Front Chem. 2016;4:38.
7. Spiegel J, Adhikari S, Balasubramanian S. Trends Chem. 2020;2:123-136
8. Li W, Liu Z, Lin H, Nie Z, Chen J, Xu X, Yao S. Anal Chem. 2010;82:1935-41
9. Alizadeh N, Abdollah S, Rahman H. Adv Biochem Eng Biotechnol. 2020;170:85-106
10. Li W, Li Y, Liu Z, Lin B, Yi H, Xu F, Nie Z, Yao S. Nucleic Acids Res. 2016;44:7373-7384
11. Tang G, Zhao C, Gao J, Tan H. Sens Actuators B. 2016;237:795-801
12. Wang Z, Zhao J, Bao J, Dai Z. ACS Appl Mater Interfaces. 2015;8:827-833
13. Liu B, Li D, Shang. Chen Cen J. 2014;8:57
14. Akahori R, Yanagi I, GOTO Y, Harada K, Yokoi T, Takeda. Sci Rep. 2017;7:9073
15. Udomsom S, Mankong U, Paengnakorn P, Theera-Umpon N. Coatings. 2021;11:595

COMPARATIVE STUDY OF THE MORPHOLOGICAL AND METAPHASE CHROMOSOME NUMBER OF *Centella asiatica* (L.) URBAN FROM UTTARADIT, PHITSANULOK AND SOME PROVINCES IN THE NORTHEAST OF THAILAND

Thararat Yimcharoen and Somjit Homchan*

Department of Biology, Faculty of Science, Naresuan University, Phitsanulok, Thailand

* e-mail : somjitt@nu.ac.th

Abstract:

Centella asiatica (L.) Urban or Asiatic pennywort belongs to the family Apiaceae. It has been widely used in medicine and cosmetic productions. In Thailand, pennywort have been found in every part of the country with highly diverse in morphology, particularly size of leaves. Some samples show very big leaves while some of them show very small leaves. The sample with a big size of leaf may hypothesized that is a polyploidy plant. However, there was no report or evidence to confirm that the different size of leaves were effected by ploidy level or environment. Therefore, the purpose of this study was to compare the metaphase chromosome number of *C. asiatica* in different areas in Thailand with morphology of leaves. In this study, chromosomes were studied using cell maceration enzymes and aceto-orcein staining. It was found that all samples from different locations are diploid (2n=2x=18) but different in size and shape of metaphase chromosomes. From this study, the correlation between karyotype of each sample and leaf morphology was not found. However, the type or shape of chromosomes have to be confirmed with centromere staining for clearly conclusion that the variation of metaphase chromosome types are found in pennyworth or not.

Introduction:

Centella asiatica, commonly known as Gotu kola, kodavan, Indian pennywort and Asiatic pennywort, is an herbaceous, perennial plant in the flowering plant family Apiaceae. It is native to the wetlands in Asia. It is used as a culinary vegetable and as a medicinal herb. It is reproduced through seeds or roots and must be planted in direct sunshine to thrive. It is found in Europe, South Africa, India, Pakistan, and Sri Lanka (Piriyaphattarakit. et al., 2018).

Thais have consumed *C. asiatica* for a long time. It is eaten as a side dish with various dishes in the shape of fresh vegetables. It contains the triterpenoid glycosides asiatic acid, asiaticoside, and medecassic acid or medecassol which displays antioxidant activity. As a potent antioxidant it is effective in the protection of cells and organs against oxidative damage. Thus, *C. asiatica* is a valuable herb (Thong Ekkaew, 2013).

Because of *C. asiatica* is a common vegetable. It is found throughout the world's tropical and subtropical climates. It is sometimes commercially grown for its immense therapeutic and economic value.

In Thailand, *C. asiatica* is highly diverse. Each area in *C. asiatica* has a distinct shape, as observed. The leaves range in size from small to large. There is no proof that the different sizes of leaves are the result of a set of chromosomes or environment. In the field of genetics, almost all the previous research on *C. asiatica* possesses different somatic chromosome number such as $2n = 18$, $2n = 22$, $2n = 33$, $2n = 36$, $2n = 54$ and $2n = 76$ according to available literatures (Dash. et al., 2019) and the chromosomes found are metacentric, submetacentric and acrocentric (Warasy, 2015). Rakotondralambo et al. (2013) reported some diploids and tetraploid populations of *C. asiatica* from Madagascar.

As a result, the researcher has objectives. To study type and number of metaphase chromosomes in *C.asiatica* and compare the morphology and number of metaphase chromosomes in *C. asiatica*.

This data will be important in the development and promotion of economic crops for consumption. As well as a raw for cosmeceutical and herbal medical applications in the future.

Methodology:

In this study, *Centella asiatica* (L.) Urban were used as materials. These plants were maintained in Uttaradit, Phitsanulok, Sakon Nakhon, Si Sa Ket, Nakhon Ratchasima and Roi Et.

Morphological investigation

The leaves morphological characteristics and differences of *C.asiatica*in different areas were studied. These characters consist of leave shape, size, margin, color and length of petioles.

Chromosome research

Young healthy roots were cut ca. 0.5 cm away from the tip by a sharp blade. The optimum time of collection was 10.15 am during summer, pretreated with 2 mM 8-hydroxyquinoline for 3 h at 20–25 °C followed by 15 min fixation in 45% acetic acid at 4 °C. Wash roots in water for 10–30 min. Dissect meristems and transfer them into 0.1M citric buffer, pH 4.8 at 20–25 °C and Transferred into enzyme 2% Cellulase- RS (W/V) 1.5% Macerozyme R-10 (W/V) for 15 min at 37 °C. Wash roots in water for 10–30 min to inactivate the enzyme. One drop of 1% aceto orcein was added to the materials and then the slides are kept in an acetic acid chamber for overnight. Then the slides were observed under microscope. To get an accurate measurement of lengths, chromosomes from five metaphase plates were measured for each case. The karyotypes and idiograms were made based on chromosome size in decreasing order. The short arm placed on the upper side of the axis and long arm on the lower side and comparison the morphological and number of metaphase chromosomes.

Results and Discussion:

Table 1

The morphology of *C.asiatica* leaf.

Sample collections	leaf diameter on average (cm)	The appearance of leaves
Uttaradit	3.03	
Phitsanulok	4.05	
Sakon Nakhon	2.29	
Nakhon Ratchasima	5.7	
Si Sa Ket	2.5	
Roi Et	3.87	

Table 2
Metaphase chromosomes, karyotype and arrangement for diploid chromosomes (2n).

Sample collections	karyotype formula	Karyotype
Uttaradit	$2n(18) = L_6^m+L^{sm}_2+L^t_2+M^t_4+S^t_4$	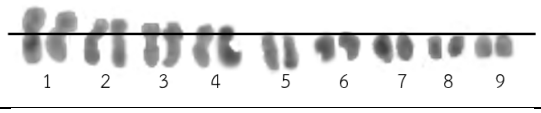
Phitsanulok	$2n(18) = L^m_4+L^{sm}_2+L^t_2+M^t_8+S^t_2$	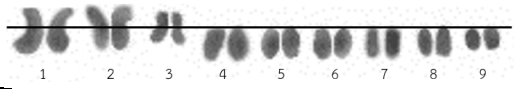
Sakon Nakhon	$2n(18) = L^m_2+L^{sm}_2+L^t_2+M^t_8+S^t_4$	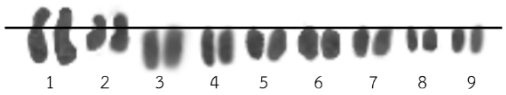
Nakhon Ratchasima	$2n(18) = L^{sm}_4+M^m_2M^{sm}_2+M^a_2++S^t_8$	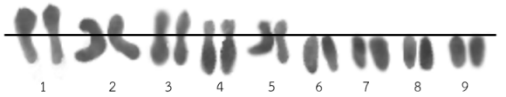
Si Sa Ket	$2n(18) = L^m_2+L^a_2+L^t_8+M^t_4+S^t_2$	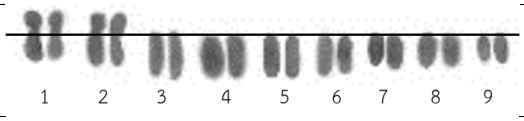
Roi Et	$2n(18) = L^m_6+L^{sm}_4+M^{sm}_2+M^t_4+S^t_2$	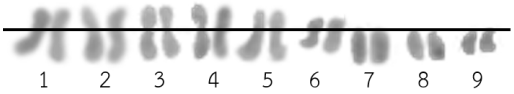

* L = Large chromosomes, M = Medium chromosomes, S = Small chromosomes
m = Metacentric, sm = Submetacentric, a = Acrocentric, t = Telocentric

In this study, 2n = 18 somatic chromosomes were observed in *C. asiatica* (Table 2). However, the size and shape of the metaphase chromosomes varied between samples (Table 1). Similar chromosome count was reported earlier (Warasy, 2015, Dash. et al., 2019). Therefore, the present findings support the earlier report on 2n chromosome number.
The phenotypes obtained from polyploid plants were different from the diploids. The polyploidy plant had big leaf and the number of chloroplasts in the guard cell were higher than the diploids plant. However, the number of chromosomes in plants cannot be determined. This is due to the small size of the chromosomes and the small number of plants thought to be polyploids. As a result, the number of chloroplasts was employed instead to compare (Chulalaksananukul and Chimnoi, 2001). The distribution of genetic relationships in *C.asiatica* was not compatible with its location, according to an assessment of its genetic diversity using Random Amplified Polymorphic DNA (RAPD). It can occur for a variety of reasons, including infections of various species resulting from intraspecific hybridization within different cytotypes (Phothong, 2018).

According to the findings of this study, the staining technique should be added in the field of chromosomal staining. C-banding and G-banding are two more approaches used to identify chromosomes. to check chromosomal shape or type Each source area has a different base and centromere position (Chaithiangtham and Patawang, 2019).

Conclusion:

The studied *Centella asiatica* (L.) Urban was diploid with chromosome number of 2n =2x=18. However, the size and shape of the metaphase chromosomes varied between samples and according to leaf size, *C. asiatica* can be divided into 2 groups, small leaf and large leaf. The studied discovered no link between karyotype and leaf shape.

Acknowledgements:

The success of this thesis can be attributed to the extensive support and assistance of the thesis advisor, Assistant Professor Dr. Somjit Homchan and Assistant Professor Dr. Kittisak Buddhachat for assisting in a variety of subjects, offering advice and guidance on completing proper research I would also like to thank the Department of Biology, Naresuan University for sponsoring my research and the staff of the department for helping. and all of my friends for the help, support, and friendship.

References:

1. Piriyaphattarakit A, Ruploet P, Amprayn A, Chanchula, N. Thai Journal of Science and Technology. 2019;8:54-65.
2. ThongEkkaew J. Journal of Science and Technology, Ubon Ratchathani University. 2013;15:70-75.
3. Warasy, A. A. Jahangirnagar University Journal of Biological Sciences. 2015;4:81-84.
4. Dash, C. K., Rahman, M. S., Afroz, M., Sultana, S. S. Journal of Applied Research on Medicinal and Aromatic Plants. 2019;14:100221
5. ThongEkkaew J. Journal of Science and Technology, Ubon Ratchathani University. 2013;15: 70-75.
6. Chulalaksananukul W, Chimnoi W. Research report, Chulalongkorn University, Bangkok. 2001.
7. Phothong S. Master thesis, M.S., Naresuan Uphiniversity, Phitsanulok. 2018.
8. Chaithiangtham P., Patawang I. Journal of Science and Technology MSU. 2020;39

Session C:
CHEMISTRY (Analytical Chemistry)

IDENTIFICATION OF VOLATILE COMPOUNDS IN GREEN CURRY USING COMPREHENSIVE HEARTCUT TWO-DIMENTIONAL GAS CHROMATOGRAPHY-MASS SPECTROMETRY

Sudarat Arunmongkon, Palathip Kakanopas, Pannipa Janta, Chadin Kulsing, Thumnoon Nhujak*
Chromatographic Separation and Flavor Chemistry Research Unit, Department of Chemistry, Faculty of Science, Chulalongkorn University, Bangkok 10330, Thailand
*e-mail: Thumnoon.N@chula.ac.th

Abstract:
In this study, comprehensive heart cut two-dimensional gas chromatography hyphenated with mass spectrometry (CH/C 2DGC-MS) was used for identification of volatile compounds in a Green curry sample. The system utilized the first and second dimensional (^{1}D and ^{2}D) columns of 5MS (30 m × 0.25 mm × 0.25 µm) and DB-WAX (60 m × 0.25 mm × 0.25 µm), respectively, connected via a Deans switch. The compound identification approach was based on matches with MS and ^{1}D retention index (^1I) data obtained from the NIST17 library. The analysis offered the approximated total peak capacity of 5840. The Green curry sample was found to contain 93 volatile compounds with the major components of tumerone (14.9%peakarea), β-cubebene (8.7%), cyclopropylbenzene (8.4%) α-ocimene (8.0%) and terpinen-4-ol (5.3%).

Introduction:

Green curry is one of the most famous Thai dishes containing the main ingredients of coconut milk and green chilies with the characteristic pastel green color. Apart from the conventional recipes, a simple method to cook the dish is to add instant green curry paste mix into boiled water. The paste is considerably complex sample since it is composed of the chemical components extracted from herbs, chilies, kaffir lime skins and galangal with several hundred volatile compounds such as terpenes, aldehydes, ketones and esters.[1] Gas chromatography (GC) can be used to separate and analysis of volatile compounds in the food or herbs in the curry paste based on their different interactions with stationary phase inside a column. This technique is commonly hyphenated with mass spectrometry (MS) which can identify compounds by comparing the experimental *m/z* and retention index values with that from the National Institute of Standards and Technology (NIST) library. This technique shows difficulty in analyzing a complex food sample containing several hundred volatile compounds. [2]

Multidimensional gas chromatography (MDGC) is a powerful separation technique providing high peak capacity for improved analysis of complex samples such as food, waste water, petrochemical, essential oil, or pharmaceutical or biological samples[2, 3]. The technique uses two columns having different separation mechanisms [4]. and can be performed using different modulation approaches such as cryogenic modulation, flow modulation or valve-based modulation [5]. An alternative type of MDGC called as comprehensive heart-cut two-dimensional GC (CH/C 2DGC) has been reported using a flow switching device [6, 7] in order to transfer all components of a sample within narrow bands obtained from ^{1}D separation to undergo ^{2}D separation. Coupling with mass spectrometry could further allow identification of several hundred volatile compounds within the analysis [4]. In this study, CH/C 2DGC-MS was applied for improved analysis of a Green curry paste sample. The compound profile was discussed and the peak capacity was reported.

Methodology:

Materials and chemicals

Alkane standards (C8 to C20) were purchased Sigma-Aldrich co. LLC. (Singapore) and hexane was purchased RCI Labscan Limited co., Ltd. (USA).

Extraction of Green curry

Green curry paste (1 g) was dissolved in 2 mL of *n*-Hexane. The extracted sample was filtered through 0.2 μm of PTFE syringe filter prior to analysis with CH/C 2DGC-MS instrumentation.

CH/C 2DGC analysis

An Agilent 7890A gas chromatography and MS Model 7000 (CA, USA) were applied in this study. The system contains two analytical columns and a restrictor column (1.5 m × 0.1 mm; Agilent technologies Inc.). ^{1}D and ^{2}D columns were semi-nonpolar HP-5MS capillary column (30 m × 0.25 mm × 0.25 μm; J&W Scientific, USA) and polar DB-WAX(60 m × 0.25 mm × 0.25 μm; J&W Scientific, USA), respectively. A Dean switch (DS, Agilent technologies Inc.) was applied as the interface connecting all the columns. This device was performed in off and on modes to diverge the flow from ^{1}D column to a flame ionization detector (FID) via the restrictor or to MS via the ^{2}D column, respectively. The alkane mixture (100 ppm in hexane) or the sample was injected (1 uL) at 240 °C under splitless mode. Flow rates of carrier gas (He 99.999% purity) on ^{1}D and ^{2}D columns were 2.0 and 4.0 mL/min, respectively, using a constant flow mode. The GC oven temperature program was set at 40 °C, raised to 250 °C (6 °C/min) and hold at 250 °C for 15 min. This leads to the total runtime of 50 min per injection. A constant H/C window of 0.20 min was applied to sample peaks from ^{1}D column outlet. Several H/C were periodically performed within every 5 min. 25 injections were performed in order to complete the CH/C analysis.

MS was operated in full scan mode with the ion source temperature and electron ionization voltage of 250 °C and -70 eV, respectively.

Data analysis

Data analysis was performed using Agilent MassHunter and Microsoft Excel. A peak of interest was identified according to comparison of the experimental MS spectrum and ^{1}I with that from the NIST17 library. The criteria were MS match scores of >650 and ^{1}I differences of ±40 compared with the database values.

Results and Discussion:

CH/C 2DGC was applied to analyze the Green curry paste sample. Liquid injection was performed to introduce the sample into the analysis system. The approach applied multiple injections and periodic multiple H/C methods as previously discussed in [6]. In our study, a constant H/C window of 0.20 min was applied to sample peaks covering ^{1}D separation time range from 3.0 to 33.0 min. 25 injections were required to complete the comprehensive analysis corresponding to the total analysis time of 20.8 h. Within each injection after solvent delay for 8 min, each H/C run was periodically performed within every 5 min which is equivalent to modulation period in conventional comprehensive 2DGC analysis (GC×GC). The examples of periodic H/C chromatograms are provided in **Figure 1**. The profiles of the identified compounds are provided in **Table 1**. Based on the peak area percentages, the major components obtained include tumerone (14.90%), β-cubebene (8.73%), cyclopropylbenzene (8.44%) α-ocimene (8.05%) and terpinen-4-ol (5.30%).

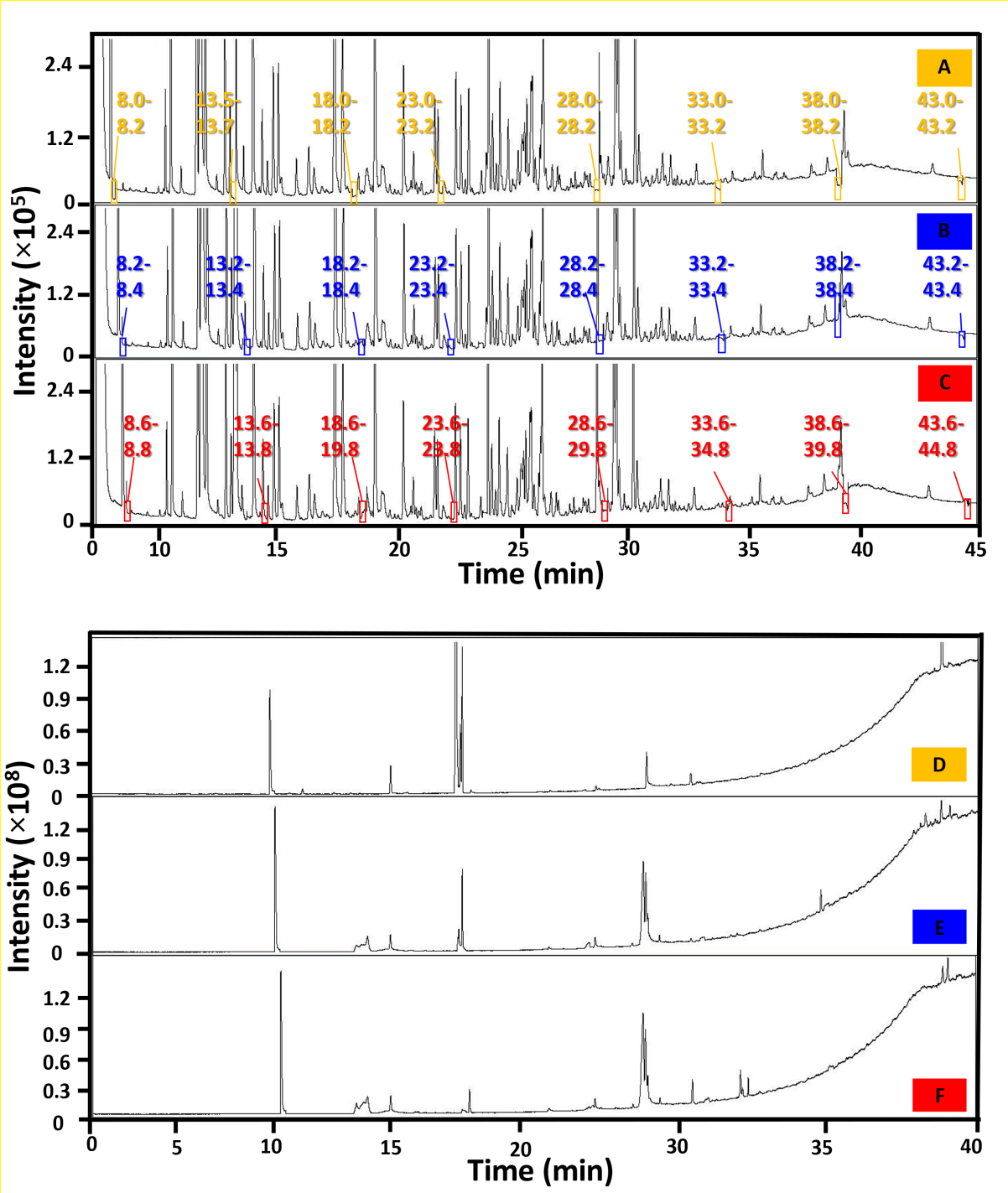

Figure 1. CH/C 2DGC chromatograms of the Green curry paste sample from 1st, 2nd and 3rd injections for ^{1}D separation-FID of A, B and C resulting in ^{1}D + ^{2}D separation-MS showing D, F and F, respectively.

Total peak capacity ($n_{c,total}$) is calculated based on the total number of peaks with the average peak width at baseline of $w_{b,ave}$ which fully occupy (baseline separation) a 2D separation space between the first and the latest eluting peaks with the retention times of $t_{R,first}$ and $t_{R,last}$, respectively. This is according to the relationships of 1) $n_{c,total} = {}^{1}n_c \times {}^{2}n_c$, 2) ${}^{1}n_c =$

($^1t_{R,first}$ - $^1t_{R,last}$)/ $^1w_{b,ave}$ and 3) ^2n_c = Period between each H/C/$^2w_{b,ave}$. The superscripts 1 and 2 indicate that the parameters are in ^{1}D or ^{2}D separation, respectively. The period between each H/C of 5 min was applied in this study. The CH/C 2DGC analysis showed $n_{c,total}$ of 5,840. This corresponds to 245 identified compounds, while these correspond to 93 compounds identified according to the comparison with both the MS spectra and ^1I library.

Table 1. Volatile compound profiles with literature/experimental retention indices and MS match scores of the Green curry paste sample analysed by CH/C 2DGC-MS.

No.	^1t_R (min)	^2t_R (min)	Compound	% Area	MS match	I_{lit}/I_{exp}[a]	ΔI
1	11.66	3.56	limonene	0.37	850	1030/842	-188
2	13.49	5.39	*p*-cymene	0.02	786	1025/842	-183
3	13.73	5.43	2-propenylbenzene	0.43	833	934/858	-76
4	13.87	4.17	α-thujene	0.39	892	929/941	12
5	14.10	3.80	α-pinene	1.66	860	937/969	14
6	14.80	4.30	camphene	0.08	702	952/979	27
7	14.99	2.90	cyclopropylbenzene	8.44	816	1032/1048	16
8	15.00	4.10	1-propenylbenzene	0.32	821	934/998	13
9	15.65	4.40	sabinene	3.21	874	974/1015	32
10	15.77	4.47	β-pinene	0.23	795	979/1015	36
11	15.84	3.94	4-methylene-1-(1-methylethyl)-cyclohexane	0.72	857	1182/1039	11
12	16.03	4.93	β-phellandrene	1.51	792	1031/1006	-25
13	16.06	4.36	β-myrcene	1.36	922	991/1031	40
14	16.67	5.17	α-phellandrene	0.07	783	1005/1023	18
15	16.87	3.17	2,4,6-trimethyl-decane	1.05	712	1121/1114	-7
16	17.03	4.53	β-terpinene	1.21	782	1028/1064	36
17	17.48	4.78	α-ocimene	8.05	748	1047/1073	26
18	17.64	7.34	2-thujene	0.38	877	966/969	3
19	17.59	5.09	γ-terpinene	1.59	767	1060/1064	4
20	17.73	4.43	trans-sabinene hydrate	*0.53*	721	1070/1097	27
21	17.88	4.18	1-methyl-4-(1-methylethenyl)-cyclohexanol acetate	*0.12*	788	1317/1114	-211
22	17.90	7.20	sulcatone	0.47	*904*	986/988	2
23	17.99	5.49	2-ethyl-*p*-xylene	0.58	865	1074/1064	-10
24	18.00	6.30	trans-β-ocimene	0.21	877	1049/1031	-18
25	18.04	4.94	benzene, 2-ethyl-1,4-dimethyl-	0.03	835	1074/1089	10
26	18.43	5.33	terpinolene	3.09	865	1088/1089	1
27	19.05	5.15	benzenepropanal	3.26	765	1162/1122	-40
28	19.39	9.69	terpinolene	0.54	909	1088/1064	-24
29	20.69	7.99	cis-linalool oxide	*0.81*	875	1074/1073	-1
30	20.79	6.69	*p*-menth-8-en-1-ol, stereoisomer	0.39	*837*	1161/1130	-31

31	21.02	12.52	2-heptanol	0.04	690	900/874	-26
32	21.27	8.57	trans-linalool 3,7-oxide	*0.23*	849	1086/1073	-13
33	21.45	7.15	(1*Z*)-1-propen-1-yl 2-propen-1-yl disulfide	0.17	738	1107/1139	32
34	21.83	7.73	(1*E*)-1-propen-1-yl2-propen-1-yl disulfide	0.04	764	1103/1130	27
35	21.97	8.67	linalool	0.76	892	1099/1097	-2
36	22.41	7.51	cis-2-*p*-menthen-1-ol	*0.05*	680	1161/1163	2
37	22.78	9.68	acetophenone	*0.84*	835	1065/1089	24
38	22.75	8.28	1-phenyl-1,2-propanedione	0.03	755	1175/1147	-28
39	22.94	8.44	isopulegol	0.21	682	1146/1147	1
40	23.05	3.35	2,6,10-trimethyl-dodecane	0.05	732	1366/1371	15
41	23.61	4.51	*N*,*N*-diethyl-4-methyl-benzenamine	0.06	769	1343/1344	1
42	23.60	8.86	di-isopulegol	0.09	684	1163/1134	-29
43	24.00	7.70	methyl 2-propenyl trisulfide	0.04	770	1142/1222	80
44	24.27	9.17	terpinen-4-ol	5.30	855	1177/1171	-6
45	24.30	6.60	3-*p*-merthen-7-al	0.10	698	1169/1282	113
46	24.58	6.68	4-ethyl-3-methyl-phenol	0.10	705	1237/1209	-28
47	24.69	8.59	dimethyl acetal benzaldehyde	0.41	721	1200/1239	39
48	24.70	11.60	α,α-dimethyl-benzene methanol	1.77	822	1090/1089	-1
49	24.97	8.67	2-91-methylethyl-phenol	0.02	662	1199/1222	23
50	25.15	2.25	2-(1-methylethyl)-, methylcarbamate phenol	0.13	673	1532/1525	-7
51	25.31	11.41	1-ethyl-4-methoxy-benzene	0.15	707	1110/1122	12
52	25.46	5.76	1-(4-methoxyphenyl)-2-propanone	0.34	659	1384/1371	-13
53	25.51	10.41	α-terpineol	1.18	838	1189/1171	-18
54	25.53	8.23	α,α,4-trimethyl-3-cyclohexene-1-methanethiol	1.12	694	1283/1265	-18
55	26.09	5.19	β-cubebene	0.04	682	1389/1481	29
56	26.38	12.28	tetrahydro-4-methyl-2-(2-methyl-1-propenyl)-2*H*-pyran	0.15	676	1110/1130	20
57	26.48	10.18	citronellol	0.22	710	1228/1239	11

58	26.92	12.42	trans-verbenol	0.41	660	1144/1147	3
59	26.99	6.89	copaene	0.95	870	1376/1389	13
60	27.03	7.53	citronellol acetate	0.60	808	1354/1362	8
61	27.42	4.72	germacrene	0.71	712	1481/1514	33
62	27.43	7.13	β-cubebene	8.73	734	1389/1399	10
63	27.45	6.95	β-copaene	0.57	683	1432/1408	-24
64	27.63	8.73	mesitaldehyde	2.83	696	1337/1335	-2
65	27.72	6.22	γ-elemene	0.37	681	1433/1456	23
66	27.72	5.02	1,2,3,5,6,7,8,8a-octahydro-1,4-dimethyl-7-(1-methylethenyl)-, [1*S*-(1α,7α,8aβ)]-azulene	0.14	701	1505/1514	9
67	27.87	11.17	geraniol	1.03	717	1255/1239	-16
68	27.97	8.87	1,2-diol limonene	0.13	685	1321/1344	23
69	28.31	5.81	β-guaiene	0.25	702	1490/1504	14
70	28.34	7.24	neryl propanoate	0.77	766	1455/1437	-18
71	28.39	9.89	α-cubebene	0.92	721	1351/1317	-34
72	28.41	5.71	α-farnesene	0.83	826	1508/1514	6
73	28.63	6.13	valencene	1.59	792	1492/1504	12
74	28.75	5.25	germacrene B	0.15	689	1557/1555	-2
75	28.77	4.87	(*E*,*E*)-1,5-cyclodecadiene, 1,5-dimethyl-8-(1-methylethylidene)	0.38	773	1557/1575	18
76	28.84	5.94	β-bisabolene	0.69	707	1509/1525	16
77	29.72	6.62	trans-α-bisabolene	0.48	673	1512/1535	23
78	30.00	10.10	copaene	0.18	*776*	1376/1344	-32
79	30.16	9.26	α-cedrene	0.22	*680*	1411/1427	15
80	30.45	7.55	β-sesquiphellandrene	0.57	679	1524/1525	1
81	30.65	8.35	β-eudesmene	0.21	728	1486/1494	-8
82	30.76	8.46	α-selinene	0.15	686	1494/1494	0
83	31.06	10.16	cedrene	0.37	666	1422/1427	5
84	31.13	7.83	α-cadinene	0.92	747	1538/1545	7
85	31.17	9.67	γ-muurolene	0.38	679	1477/1456	-21
86	31.35	8.85	2-methylpropionate cuminyl alcohol	0.33	680	1511/1504	-7
87	32.92	9.02	cetene	0.37	725	1592/1575	-17
88	35.89	11.79	carotol	0.33	682	1594/1585	-9
89	35.91	12.61	ledol	3.07	778	1565/1585	20
90	36.83	12.53	spirojatamol	0.16	761	1592/1596	4
91	37.07	11.73	a*R*-tumerone	0.11	687	1664/1649	-15
92	37.25	13.15	globulol	0.48	822	1580/1585	5
93	37.47	12.37	tumerone	14.90	717	1632/1638	6

[a] I_{lit} and I_{exp} refer to the values of literature and experimental indices, respectively

Conclusion:
CH/C MDGC employing a DS as the flow diverging device was demonstrated for analysis of the Green curry paste sample. The system with automated operation was stable with good repeatability. The application of a narrow H/C window (0.2 min) allows sampling of significantly sharp bands of the components from a ^{1}D column outlet before undergoing ^{2}D separation. This avoids use of a cryogenic trapping device which is environmentally friendly. The effective separation of the peaks also improved confidence in compound identification. This technique is thus expected to be simple and applicable for high resolution separation of food samples in the future.

Acknowledgements:
We would like to gratefully acknowledge the financial support from the Chulalongkorn University's Ratchadapisek Sompot Fund [DNS_62_025_23_003_1] and [GCURP_59_02_23_01] for the research project.

References:
1. Forero M.D, Quijano C.E, Pino J.A. Flavour Fragr J. 2009;24:25-30.
2. Nolvachai Y, Kulsing C, Marriott P.J. Trends Analyt Chem. 2017;96:124-137.
3. Marriott P.J, Chin S.-T, Maikhunthod B, Schmarr H.-G, Bieri S. Trends Analyt Chem. 2012;34:1-21.
4. Kulsing C, Nolvachai Y, Marriott P.J. Trends Analyt Chem. 2020;130:115995.
5. Adahchour M, Beens J, Vreuls R.J.J, Brinkman U.A.T. Trends Analyt Chem. 2006;25:540-553.
6. Thongdorn N, Nhujak T, Janta P, Rueangthaweep A, Hinchiranan N, Kulsing C. Anal. Methods. 2020;12:5160-5167.
7. Janta P, Pinyo D, Yodta Y, Vasasiri P, Weidenbach M, Pursch M, Yang X, Kulsing C. Anal. Methods. 2021;13:124-132.

QUALITY CONTROL OF PROXIMATE ANALYSIS AND HEAT COMBUSTION IN PALM KERNEL SHELLS

Songpol Homutai*,Patchara Sukonrat, Siriwan Pongprueksapattana

Office of Scientific Instrument and Testing, Prince of Songkla University, Hat Yai Campus, Songkhla, 90110 Thailand
*e-mail: Songpol.h@psu.ac.th

Abstract:

Proximate analysis and calorific value are the common method that is used to observe the quality of coal and biomass as renewable energy source. This study aims to develop the control chart of coal used as quality control for determining the proximate analysis in palm kernel shells (PKS) and studying the heat combustion by a bomb calorimeter. Proximate analysis determines moisture, ash, volatile matter, and fixed carbon content. The percent of volatile dried coal is between 47.61 and 50.02 used for quality control in this study. This control chart is suitable for monitoring processes, identifying causes of variability, and confirming the results of PKS samples in this study. Sixteen palm kernel shell samples were studied proximate analysis by Macro-TGA instrument based on ASTM D7582-15. The data for proximate analysis in PKS showed moisture content in dried was around 6.87±0.06%. The volatile fraction, fixed carbon, and ash content were found at 69.43±0.33%, 20.98±0.27%, and 2.72±0.19%, respectively. Its higher heating values determined by the bomb calorimetric method show 4482.56±73.69 Kcal/kg in the drying process. These results provided useful information about PKS as a raw material for the renewable energy industry and to compare the further studies of properties such as torrefaction and fast pyrolysis in the future.

Introduction:

The extensive use of fossil fuels for energy has become a major cause of global warming due to increasing of carbon dioxide into the atmosphere. Especially the coal for power generation, the toxic inorganic heavy metals is released into the environment. Therefore, to maintain the sustainability of the environment and to prevent the health risk, the alternative energy sources which is renewable.[1] In the South of Thailand, the rubber industry is a major contributor to economic growth, followed by the palm oil industry. Typically, the main products from the palm oil industry are crude palm oil and palm kernel oil. Nowadays, the demand for these products continuously increases due to population growth. The increase of palm oil wastes after harvesting, such as empty fruit bunches and palm kernel shells, also causes palm oil processing growth. Importantly, PKS is typical plant material. It contains carbohydrates such as cellulose, hemicelluloses, and lignin in composition[4]. Therefore, to properly eliminate this waste of palm kernel shells, we need to use it for the renewable energy industry. Generally, there are many methods to study the energy and power of biomass that are used for renewables, such as proximate analysis and high heating value. The Standard Test Methods for Proximate Analysis of Coal and Coke by Macro Thermogravimetric Analysis (ASTM D7582-15)[2] is used to study the proximate analysis of coal. This method separates the products into four groups such as moisture, volatile matter (consist of gases and vapors), fixed carbon (the nonvolatile fraction of coal), and ash (the inorganic residue remaining after combustion). The data is used to characterize and study the composition of coal. Moreover, the fixed carbon value is one of the values used in determining the efficiency of coal-burning equipment as well. The following study of the

calorific value is normally the essential item specified in contracts for coal to be used in steam plants. It is the most important value determined for coal to be used for heating purposes. This study aims to develop the control chart of coal used as quality control for determining the proximate analysis in palm kernel shells and studying the heat combustion of palm kernel shells by a bomb calorimeter. These results provided useful information on palm kernel shells as a raw material for the renewable energy industry. The data collected in this study can be used to support research development on thermochemical processes such as torrefaction and fast pyrolysis in the future.

Methodology:

Palm kernel shell preparation

Palm kernel shell wastes were obtained from customer that tested samples to OSIT in year 2020-2021. Before experiment, palm kernel shells were oven-dried at 105 °C for 24 hours to remove unbound water. After that the samples were ground with a grounding machine (Retsch, MM 400, Germany) and sieved process. The particles in the range of 30-60 μm were collected.

Proximate analysis test

The grinding of coal was oven-dried at 105 °C for 1 hour before testing used for quality control in this study. The method of proximate analysis was conducted according to the American Society for Testing and Material standards (ASTM D7582-15). Moisture content was calculated using Eq (1). The volatile matter and ash content were calculated using Eq (2) and Eq (3) while the fixed carbon content was calculated using Eq (4).

Moisture content (%) $M = [(W-B)/W] \times 100$ (1)

W = sample weight (g)

B = sample weight after dried at 107.00°C

Volatile matter (%) $V = [(B-C)/W] \times 100$ (2)

C = sample weight after heated at 950.00°C

Ash (%) $A = [(F-G)/W] \times 100$ (3)

F = weight of crucible + ash

G = weight of crucible

Fixed Carbon (%) $H = 100-(M+A+V)$ (4)

One gram of coal sample was tested proximate analysis and the control chart was collected from September 16, 2020 to May 6, 2021 of 25 data before testing palm kernel shell sample. Sixteen palm kernel shell samples that were collected from the different months were studied proximate analysis by Macro-TGA instrument (TGA7, LEGO, USA). One gram of the sample grinding and sieving process was uses in triplication. The Macro-TGA condition in this study started with moisture content; the program was heating from 25°C to 107°C at 6°C/min and held in 107°C for 15 mins until the constant weight in nitrogen gas then heated from 107°C to 950°C at 50°C/min and held in 950°C for 7 mins. The last step was heating the program from 600°C to 750°C at 3°C/min in oxygen gas and held for 15 mins at 650°C until the constant weight. The result will be calculated following the equation above in automatically.

Determination of heating value

In order to measure the higher heating value (HHV) of sixteen palm kernel shell samples, the bomb calorimeter (C5000, IKA, Germany) was used. The sample in triplication was first weighed accurately at approximately 0.2 g, and then it was placed into the sampling cup. The sampling cup was then placed inside the bomb. After inserting all the required data regarding the sample on the screen, the bomb was placed inside the bomb calorimeter. The sample inside the bomb was ignited using an electrical circuit. As the fuel was burned, the heat generated was transferred into the surrounding water. The water

temperature provided the necessary data to calculate the calorific value of the sample. After around 15 mins, the analysis was completed, and the calorific value was obtained directly from the instrument monitoring screen in terms of Kcal/kg. The energy equivalent of the calorimeter is determined by burning standard samples of benzoic acid.

Results and Discussion:

The result of percent volatile dried of coal in different days used to study the control chart was shown in **Table 1.** There were twenty-five data to establish the control chart. The average data (X) showed percent volatile dried was 48.82±0.40, and use this data to develop the control chart by calculating the upper control limit (UCL) and lower control limit (LCL) by mean ± 3SD. The control chart of coal represented percent volatile dried was shown in **Figure 1.** The data showed that percent volatile dried in between 47.61 to 50.02 was used as quality control of proximate analysis in PKS samples. This control chart is good for monitoring processes, identifying causes of variability and confirming the results of PKS samples in this study.

Table 1.

Percent volatile dried of coal in different day used for established control chart in this study

No.	Date of collection	% Volatile dried
1	16/9/2020	49.13
2	28/10/2020	48.25
3	29/10/2020	48.78
4	10/11/2020	48.45
5	18/11/2020	48.82
6	25/11/2020	49.56
7	3/12/2020	48.45
8	8/12/2020	48.31
9	8/1/2021	48.23
10	28/1/2021	49.17
11	4/2/2021	48.63
12	9/2/2021	49.54
13	10/2/2021	48.40
14	11/2/2021	49.14
15	24/2/2021	49.17
16	4/3/2021	49.50
17	10/3/2021	49.13
18	1/4/2021	48.90
19	8/4/2021	48.83
20	9/4/2021	48.40
21	22/4/2021	48.65
22	23/4/2021	48.60
23	26/4/2021	48.54
24	27/4/2021	49.08
25	6/5/2021	48.79

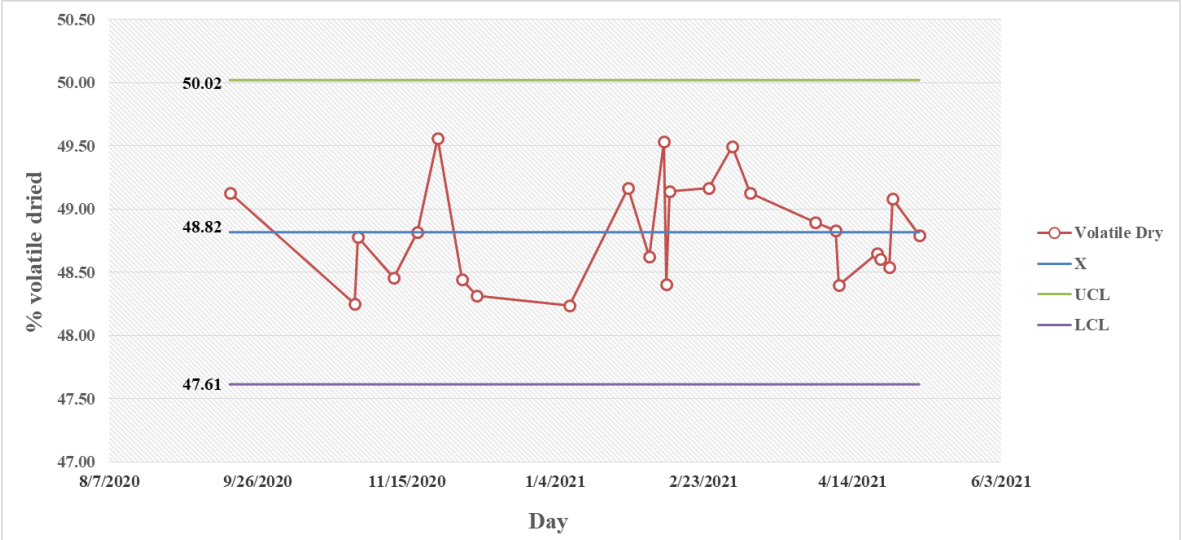

Figure 1.
Control chart of coal in value of percent volatile dried, the average data (X), upper control limit (UCL) and lower control limit (LCL)

Sixteen palm kernel shell samples collected in the different months were dried and ground with a grinding machine and studied proximate analysis and calorific value. Proximate analysis of palm kernel shell that indicated in terms of moisture content, volatile matter, fixed carbon, ash, and higher heating value is shown in **Table 2.** The moisture content of most of the samples appears to be higher than expected. The moisture may be generated by grinding the sample in the grinding machine and may have resulted in moisture increase.

Table 2.
Proximate analysis and calorific value of sixteen palm kernel shells

Sample	Proximate analysis				Calorific value (Kcal/Kg)
	Moisture	Volatile matter	Fixed carbon	Ash	
PKS 1	6.09±0.01	69.16±0.60	21.61±0.52	3.13±0.12	4,447.67±157.58
PKS 2	7.43±0.02	68.85±0.10	20.74±0.14	2.97±0.04	4,315.67±16.01
PKS 3	5.75±0.04	70.93±0.30	21.31±0.25	2.01±0.07	4,481.00±177.03
PKS 4	6.22±0.11	71.15±1.34	20.74±0.30	1.89±1.17	4,462.00±12.49
PKS 5	6.38±0.01	69.69±0.33	20.70±0.46	3.23±0.17	4,450.33±8.96
PKS 6	7.00±0.01	69.64±0.08	21.00±0.08	2.37±0.04	4,462.33±33.53
PKS 7	8.43±0.01	68.96±0.03	19.83±0.07	2.78±0.02	4,411.00±41.58
PKS 8	8.15±0.02	69.22±0.46	20.34±0.49	2.30±0.04	4,367.67±36.17
PKS 9	8.42±0.01	68.31±0.28	20.86±0.34	2.41±0.09	4,396.67±30.99
PKS 10	5.92±0.01	69.51±0.46	21.52±0.08	3.06±0.08	4,593.33±95.05
PKS 11	5.50±0.02	69.79±0.27	20.70±0.25	4.00±0.11	4,533.00±43.92
PKS 12	5.79±0.03	69.05±0.14	21.62±0.20	3.54±0.36	4,602.00±190.73
PKS 13	5.52±0.07	69.19±0.18	22.48±0.27	2.81±0.30	4,641.67±125.06
PKS 14	8.03±0.02	69.19±0.40	20.25±0.58	2.53±0.32	4,471.00±80.58
PKS 15	7.99±0.03	69.64±0.11	20.03±0.12	2.34±0.03	4,551.67±90.39
PKS 16	7.28±0.59	68.64±0.55	21.87±0.22	2.21±0.14	4,532.67±38.45

The average results of proximate analysis of PKS showed percent moisture, volatile matter, fixed carbon, and ash content in 6.87±0.06, 69.43±0.33, 20.98±0.27 and 2.72±0.19, respectively and the higher heating values determined by bomb calorimetric method showed 4,482.56±73.69 Kcal/kg in the drying process, which was shown in **Table 3**. Palm kernel shell showed high fixed carbon and small of ash approximate 3% which was a good material used for pelletization and as a feed for the boiler to generate electrical power. The higher heating value of PKS was almost equal to coal that good for renewable energy. HHV was utilized as the higher heating value criterion to divide the lignite qualities into 2 groups, standard and desirable groups depending on HHV values. Desirable groups indicated the HHV values more than 4,000 Kcal/kg.[3] Moreover, the higher heating values of PKS higher than lignite and rubber sawdust that showed 3,582.69 Kcal/kg and 4,060.38 Kcal/kg respectively.[5] Therefore, the quality of PKS samples in this study showed a good model to be a tool for suitability of palm oil wastes as raw materials for renewable energy in the future.

Table 3.
Average physical properties of the PKS and coal sample

Proximate analysis	% By mass		Calorific value by bomb calorimeter (Kcal/kg)	
	PKS	Coal	PKS	Coal
Moisture	6.87±0.06	2.56±2.31	4,482.56±73.69	5,829.50±21.58
Volatile matter	69.43±0.33	47.56±1.09		
Fixed carbon	20.98±0.27	41.90±1.32		
Ash	2.72±0.19	7.97±0.22		

Conclusion:

In this study, the control chart is good for monitoring processes in identifying causes of variability and confirming the results of the proximate analysis in PKS. The PKS showed high fixed carbon, high HHV and small ash, approximately less than 3%, that was used as plant material for pelletization and as a feed for the boiler to generate electrical power. Moreover, the PKS is a valuable model as a tool for the suitability of palm oil wastes for renewable energy in the future.

Acknowledgements:

This research has been successful due to the support of Office of Scientific Instrument and Testing, Prince of Songkla University, for all instruments testing and financial support.

References:

1. Asadullah M, Adi AM, Suhada N, Malek NH. Energy Convers. Manag.2014;88:1086-1093.
2. ASTM D7582-15. ASTM International.2015:1-9.
3. Charoensiri T, Mekparyup J, Sithanu K. SWU Sci. 2016;32(1):72-82.
4. Chen WH, Kuo PC. Energy.2010;35: 2580-2586.
5. Kan R, Kaosol T, Tekasakul P. KKU EN J. 2016;43(S2):259-262.

METHOD VALIDATION OF THE DETERMINING PROTEIN IN LATEX GLOVES BY USING UV-Vis SPECTROPHOTOMETER

Siriwan Pongprueksapattana, Supaporn Chinpha*

Office of Scientific Instrument and Testing, Prince of Songkla University, Hat Yai Campus, Songkhla, 90110

*e-mail: supaporn.chinpha@gmail.com

Abstract:

Protein is a contaminant substance in latex gloves. In the manufacturing process of latex gloves, where protein is not completely removed and a large amount of protein residue remains, it can cause an allergic reaction to the user, which can be life threatening. Therefore, the FDA organization has established the optimal protein content in such gloves. The determination of protein residues in latex gloves was performed using the Modified Lowry Method, based on ASTM D5712 testing with an UV-Vis spectrophotometer. This research aims to study the method validation of the ASTM D5712-standard protein quantitation test method to improve the protein content test results. According to AOAC guideline, the linearity (R^2-value) was found to be 0.9980. The accuracy was reported as the recovery being 98.88%, which is in the acceptable range of 80%-110%. Moreover, it showed good precision with the RSD at 4.74%. The limits of detection (LOD) and the limits of quantitation (LOQ) were 2.49 µg/mL and 7.54 µg/mL, respectively.

Introduction:

Rubber is an economic crop in Thailand. Nowadays, it is found that natural latex is used to produce many products, such as gloves, condoms, cleaning sponges, and dolls, etc. The natural latex, similar in appearance to milk, contains rubber in the serum part, and the non-rubber part includes proteins, carbohydrates, fats, and other inorganic substances such as potassium, zinc, copper, magnesium, and iron, etc. Protein is a substance that is found in latex gloves and condoms made from natural latex. There are many reports of allergic reactions to natural latex proteins.[1] One of the reports showed that the protein content in gloves was recommended at 30 µg/g.[2] In addition, the corn starch used in the manufacturing of rubber gloves has also been found to cause allergic reactions. The most common allergic reaction including irritant contact dermatitis (ICD),[3] Allergic contact dermatitis (ACD),[4] and type I IgE-mediated hypersensitivity reaction, with allergic reactions ranging from erythema to life-threatening.[5] The effect of protein allergies on natural latex gloves has led users to use nitrile gloves, made from synthetic rubber that does not contain latex and are safe for contact with people suffering from latex allergies, instead of latex gloves. The advantage of latex gloves is that they are more resistant and flexible than nitrile gloves,[7] which are especially useful for medical purposes, making them still essential. In addition, researchers tend to study the methods that can reduce the protein content in latex gloves to ensure the safety of users. A suitable standardized method for the determination of residue protein in the production process is required.[8] The method that is commonly used is the modified Lowry method according to ASTM D5712 (Standard test method for analysis of aqueous extractable protein in natural rubber and its products using the modified Lowry method)[9] according to which the US Food and Drug Administration (FDA) specifies that the latex gloves must contain a protein content of not more than 200 µg/g to avoid allergic reactions. The reaction equation for this method is as follows.[9]

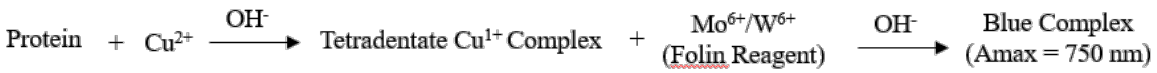

The ASTM D5712-standard method is used to quantify soluble proteins in gloves by extracting with buffer solution and then precipitating, adding alkaline copper reagent, reacting with Folin-Ciacateau reagent, and then measuring the absorbance at 750 nm with a UV-Visible spectrophotometer. The purpose of this research was to study the validation of the ASTM D5712-standard protein quantification test methods, including linearity, limit of detection (LOD), limit of quantitation (LOQ), accuracy, and precision, which are suitable for use as a test method to determine the protein content in gloves.

Methodology:

Reagents and materials

All chemicals and reagents were purchased from commercial sources. Sodium hydroxide (NaOH), Trichloroacetic acid (TCA), Anhydrous sodium carbonate (Na_2CO_3) were obtained from Merck (Darmstadt, Germany). Phosphate buffer saline (extraction buffer) and Folin-ciacateau reagent were bought from Sigma-Aldrich (St. Louis, MO, USA). Phosphotungstic acid (PTA) and cupric sulfate pentahydrate were purchased from Loba chemie. Sodium deoxycholate (DOC) and sodium tartrate were obtained from HiMedia (India) and Qrec (New Zealand), respectively. All reagents were analytical grade. Standard albumin was purchased from Sigma-Aldrich.

A standard protein solution was prepared by dissolving 100 mg of albumin in 100 mL of extraction buffer for 2 hours at 25°C ± 5°C. Filter and determine the absorbance at 280 nm using a UV spectrophotometer (V770, JASCO, Japan) to calculate the actual concentration of the stock solution. All glove samples were obtained from the office of Scientific Instrument and Testing, Prince of Songkla University.

Extractable and Assay Procedures

The tests were performed in accordance with ASTM D5712. All glove samples were extracted by adding the buffer solution in the ratio of 1 g : 10 mL at 25°C ± 5°C for 120 min ± 5 min and shaking at the start, in the middle, and after 120 min, and then filtered through a 0.45 mm pore size filter. 1 mL each of the reagent blank (extraction buffer), standard protein solutions, and the extractable samples were used. In brief, the precipitation step was performed by first adding 0.1 mL of DOC, mixing and standing for 10 minutes, and then adding 0.2 mL of freshly mixed 50:50 TAC and PTA. Centrifuge after mixing well and standing for 30 minutes at 10,000 x g for 15 minutes, removing any remaining liquid, and adding 0.25 M NaOH in each tube to dissolve the precipitated protein. The coloration procedure was prepared in the last step by adding 1 mL of alkaline copper reagent, waiting for 15 minutes, and reacting with 0.15 mL of the Folin-Ciacateau reagent. Then the absorbance was measured with the UV-Vis spectrophotometer after standing for 30 minutes.

Method validation

The validation method in this study includes linearity, limit of detection (LOD), limit of quantitation (LOQ), accuracy, and precision as defined by the protocol from International Conference of Harmonization (ICH)[10] and AOAC guidelines.[11]

For the linearity, the protein standard solutions for calibration curves ranging from 2 μg/mL to 100 μg/mL were prepared by diluting the protein stock solution with extract buffer three times at each of the multiple protein standard amounts: 2, 5, 10, 20, 50, and 100 μg/mL. The test results are plotted on a standard curve, where the x-axis is the protein

concentration in µg/mL unit, and the y-axis is the absorbance. The best fit line for the average value plotted had an R^2 value of at least the average 0.9950.

The LOD is the lowest concentration of an analyze in a sample that can be detected and calculated by the calibration curve as follows: 3.3×σ/S where S is the slope of the calibration curve and σ is the standard error of the response. This standard deviation can be determined by using the calibration regression line. The LOQ is the lowest level that can be quantified in a sample. The determination of LOQ can be estimated by the equation that is expressed as ten times the standard error of the y-intercept of the calibration regression line divided by the slope of the calibration line. It is common that LOD and LOQ are reported together in µg/mL units.

Accuracy expresses the familiarity of conformity between the value obtained and the value which is accepted either as a predictable true value or an accepted reference value. The accuracy was calculated as the percentage of the recovery by adding the known amount of albumin standard in the sample. The sample concentrations were determined with the standard calibration curve. Seven replicates of the 82.03 µg/g concentration level were spiked into the glove sample (Glove O). It should be shown that samples are accurately recovered and the recovery in the range of 80%-110% is acceptable.

The precision of the modified Lowry method was determined by the repeatability of the glove sample and calculated the relative standard deviation (RSD) of the mean concentration from calibration curves. The calculated %RSD should not be greater than 5.3%.

Results and Discussion:

Linearity

The results of the linearity study gave linear relationships over the concentration range of 0, 2, 5, 10, 20, 50, and 100 µg/mL by diluting the stock standard solution in extract buffer. The results showed that the average coefficient R^2 value was considered to be 0.9980, which is acceptable in the criteria of AOAC guideline requiring that the R^2 value must be greater than 0.995. The results can explain a linear relationship between the standard protein concentration and the absorbance, which can be predicted with a linear equation of y = 0.0082x + 0.0100. The calibration curve of standard albumin is shown in **Figure 1**.

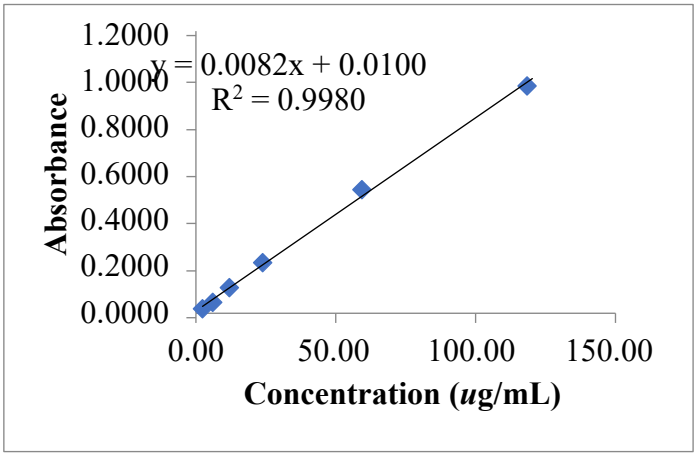

Figure 1.
The linearity results

Limit of Detection (LOD) and Limit of quantitation (LOQ)

The LOD and LOQ parameters were calculated based on the analysis of three replicates of six different concentration levels. The values of LOD and LOQ obtained with this method were found to be 2.49 µg/mL and 7.54 µg/mL, respectively, based on the analytical method validation assay[10] (See **Table 1**).

Accuracy

From the test results of the accuracy of the analytical method, this study used a standard addition method and determined the accuracy by analyzing the recovery value. Seven replicates of Glove O with spiked the concentration level of 82.03 µg/g was used as a study sample. The test results showed that the recovery value is between 89.62%-107.62% with an average value of 98.88% as shown in **Table 1**. Therefore, the test result was acceptable with the criteria range of 80%-110%.

Precision

The precision of the method was tested by prepared seven repeatability of Glove O sample. The %RSD value was 4.74%, indicating the high precision of the method. An acceptance criterion is %RSD that is not more than 5.3% (See **Table 1**).

Table 1.
Method validation results of the analytical method for latex gloves (n = 7)

Parameter	Results
Linear equation	y = 0.0082x + 0.0100
Linearity (R^2)	0.998
LOD (µg/mL)	2.49
LOQ (µg/mL)	7.54
% Recovery	98.88 ± 5.79
Precision (%RSD)	4.74

Protein content in Glove samples

The levels of protein content in different six glove samples were determined using this validated method. The results showed that some of the glove samples obtained the extractable protein content in a range of more than 200 µg/g that causes the allergic reactions referred to the FDA certificate. The quantities of protein tested are shown in **Table 2**.

Table 2.
The results of the protein content in glove samples (n=3)

Sample	Protein content[a] ± SD (µg/g)	Concentration added[b] (µg/g)	Protein content found[c] (µg/g)	%Recovery
Glove A	66.25 ± 1.98	81.11	140.04	90.98
Glove B	24.40 ± 0.91	119.57	134.53	92.11
Glove C	746.70 ± 9.13	116.00	858.92	96.75
Glove D	16.25 ± 0.98	102.22	112.24	93.91
Glove E	184.49 ± 1.99	99.63	282.70	98.57
Glove F	451.54 ± 17.43	83.43	539.68	105.64

[a]The initial protein concentration in glove sample and SD is the standard deviation.
[b]The concentration of the protein standard that added in to the glove sample depended on the concentration in each sample and the dilution factor.
[c]The final concentration of the protein that found in each sample.

Conclusion:

This study was to investigate a method validation including the linearity, LOD, LOQ, accuracy, and precision to improve the quality of determining protein content in gloves according to ASTM D5712. All required parameters complied with the ICH and AOAC guidelines. The analytical range was 2 µg/mL to 100 µg/mL with good linearity (R^2 = 0.9980). The LOD and LOQ were 2.49 µg/mL and 7.54 µg/mL, respectively. The accuracy and precision of the method were also good, with the RSD lower than 5.3%.

Acknowledgements:

This research has been successful due to the support of the director of the office of scientific instrument and testing, Prince of Songkla university, who encourages personnel to develop our knowledge and extend our routine work to research.

References:

1. Kolarich D, Weber A, Turecek PL, Schwarz HP, Altmann F. Proteomics. 2006;6:3369-3380.
2. Gathen YVD, Sander I, Flagge A, Bruning T, Raulf-Heimsoth M. Allergologie select. 2019;1(2):109-119
3. Brehler R, Kutting B. Arch Intern Med. 2001;161(8):1057-1064.
4. Cohen DE, Scheman A, Stewart L. J Am Acad Dermatol. 1998;39:98–106.
5. Baur X, Chen Z. Allergology International. 1999;48:31-36.
6. Baur X, Chen Z, Allmers H. J Allergy Clin Immunol. 1998;101:24–7.
7. Kovuttikulrangsie S, Khongkot T. J. Sci. Technol. 2004;26(4):577-593.
8. Chin PS, et al. Proceeding Rubber Research Institute of Malaysia, Planters'Conference, 1974;252-262.
9. Lowry OH, Rosebrough NR, Farr AL, Randall RJ. J Biol Chem. 1951;196:265-275.
10. International Council for Harmonisation of Technical Requirements for Pharmaceuticals for Human Use, ICH Harmonised Tripartite Guideline. Methodology, 6 November 1996.
11. Guidelines for standard Method Performance Requirements, AOAC Official Methods for Analysis. 2016;1-18

DIFFERENTIATION OF ORIGINS OF THAI COFFEES BY CHEMOMETRIC ANALYSIS OF AROMA PROFILES FROM GAS CHROMATOGRAPHY – MASS SPECTROMETRY

Rujirat Pumbua,[1] Thanit Praneenararat,[2,*]
[1] Department of Petrochemistry and Polymer Science, Faculty of Science, Chulalongkorn University, Phayathai Rd., Pathumwan, Bangkok, 10330, Thailand
[2] Department of Chemistry, Faculty of Science, Chulalongkorn University, Phayathai Rd., Pathumwan, Bangkok, 10330, Thailand
*e-mail: Thanit.P@chula.ac.th

Abstract:

Coffee is one of the most important agricultural commodities, and the demand for specialty coffee and single-origin coffees is also increasing significantly. Methods that can effectively differentiate the origins of coffee is tremendously beneficial. In this work, headspace solid-phase microextraction (HS-SPME) in combination with gas chromatography-mass spectrometry (GC-MS) was used as a tool for differentiating coffee origins. The acquired data was then processed by principal component analysis (PCA) and linear discriminant analysis (LDA), resulting in successful identification of the origins of coffee with prediction accuracies of 65-100%. Studies with the aforementioned performance include the discrimination of Arabica vs Robusta, Arabica coffees from different geographical origins, Robusta coffees from different geographical origins, and geographical origins of Arabica coffees within each province in Thailand. In brief, the overall workflow is simple, free of sample pre-treatment, but yet effective for distinguishing origins of coffee.

Introduction:

Coffee is one of the world's most traded products with considerable economic importance on the global market. *Coffea Arabica* and *Coffea Canephora (Robusta)* are most widely cultivated coffee species in the world. Coffee varieties are known to have distinct flavor profiles due to their geographical origins.[1,2] With the growing interest in specialty coffee and single-origin coffees, accurate representation of origins of coffee has become a topic of interest, and as such methods that can efficiently distinguish origins of coffee has gain significant interest. Clearly, analytical instrumentations that can unbiasedly reveal chemical profiles of food samples are a method of choice for such differentiation study.

Several analytical techniques, in combination with chemometrics, have been utilized for coffee studies. For example, nuclear magnetic resonance (NMR) spectroscopy was used to accurately discriminate roasted Colombian coffee from other types of coffee.[3] Dicaffeoylquinic acids analysis by ultra-performance high-pressure liquid chromatography coupled with mass spectrometry (UPLC-MS) has been used to distinguish samples grown in subregions of Ethiopia.[4] Phenolic compounds have also been studied by high-performance liquid chromatography (HPLC) to separate different chemical species based on their geographical origin.[5] Gas chromatography-mass spectrometry (GC-MS) has been widely applied in the characterization of the geographical origin of coffee based on the analysis of volatile and semi-volatile compounds. Coffee samples were also prepared by a solvent extraction method followed by direct liquid injection into the GC column[6,7], resulting in an additional process prior to sample analysis. However, some volatile and semi-volatile compounds may be evaporated during the coffee sample preparation process. The application of headspace solid phase microextraction (HS-SPME) in combination with gas chromatography-mass

spectrometry (GC-MS)[8,9] has been widely recognized to extract volatile compounds from coffee samples because it is a non-destructive method in the determination of volatile and semi-volatile compounds. Furthermore, it is simple, fast, and free from pre-treatment processes.

In this study, coffee samples originating from different origins in Thailand were analyzed using headspace solid phase microextraction (HS-SPME) in combination with gas chromatography-mass spectrometry (GC-MS) as the analytical method. The results from this study demonstrate that coffee samples can be rapidly discriminated by evaluating volatile species using chemometric analysis. The methodology was successfully applied to differentiate 1) the types of coffees (Arabica vs Robusta), 2) geographical origins of Arabica coffees, 3) geographical origins of Robusta coffees, and 4) geographical origins of Arabica coffees within the same province of Thailand.

Methodology:

Coffee bean samples

The coffee bean samples were acquired from different regions of Thailand. All samples are listed in **Table 1**. All coffee samples were light roasted with either natural, honey or washed processing. Samples were stored in a freezer at -20 °C until used.

Table 1.
List of coffee samples from different origins in Thailand.

ID	Name	Type	Processing	Location
C1	Doi Pha Hee	Arabica	Washed	Chiang Rai, Thailand
C2	Doi Pang Khon	Arabica	Washed	Chiang Rai, Thailand
C3	Robusta Chiang Rai	Robusta	Washed	Chiang Rai, Thailand
C4	Doi Chang	Arabica	Washed	Chiang Rai, Thailand
C5	Mae Ton Luang	Arabica	Natural	Chiang Mai, Thailand
C6	Om koi	Arabica	Honey	Chiang Mai, Thailand
C7	Thep Sadet	Arabica	Natural	Chiang Mai, Thailand
C8	Manipruek	Arabica	Natural	Nan, Thailand
C9	Doi Sakad	Arabica	Washed	Nan, Thailand
C10	Huai Wai	Arabica	Natural	Mae Hong Son, Thailand
C11	Dulapur	Arabica	Natural	Mae Hong Son, Thailand
C12	Robusta Chumphon	Robusta	Washed	Chumphon, Thailand
C13	Robusta Krabi	Robusta	Washed	Krabi, Thailand

Gas chromatography-mass spectrometry Experiments

Three grams of each source of coffee bean was ground by a handheld grinder and placed in a 20 mL headspace vial, which was then closed tightly by an aluminum cap lined with a PTFE/silicone septum.

The analysis was performed using a 7697A headspace autosampler connected to a 7890B GC system and a 5977B mass spectrometer (Agilent Technologies, USA). The GC-MS system was controlled by Agilent MassHunter GC-MS Acquisition software, version B.07.04. The sample vials were heated at 70 °C for 10 minutes to reach sample headspace equilibrium. The volatile compounds were extracted using a SPME fiber (DVB/C-WR/PDMS). The fiber was inserted into the vial and exposed to the headspace above the coffee sample for 30 minutes at 70 °C. After the extraction, the fiber was desorbed into the GC injection port for 5 minutes. GC-MS analysis was performed in split ratio mode at 10:1. The oven temperature program was set as 40 °C, held for 2 minutes, increased to 240 °C at a rate of 5 °C/min, and finally held for 5 minutes. The preparation of each coffee sample was repeated in triplicates.

Chemometrics

Chemometric analysis on the percentage of the relative peak area (%RPA) was performed using MATLAB software, version R2022a. The %RPA was calculated by the peak area divided by the total peak area of all identified peaks in each chromatogram. The data was centered over all samples prior to principal component analysis (PCA). In this study, PCA was applied to visualize the clusters of samples, using PCs with the maximum variances (PC1-PC3). To obtain the classification performance, Linear Discriminant Analysis (LDA) was applied to construct classification models useful for the prediction of the geographical origin of the coffee samples.

Results and Discussion:

Chemical Profile of Volatiles in Coffee Beans

In this study, the grounded coffees from various regions were analyzed by HS-SPME/GC-MS technique. All the coffee samples revealed similar volatile profiles with differing intensities. The representative total ion chromatogram (TIC) of the Doi Pha Hee coffee (C1) is shown in **Figure 1**. The tentative identification of the volatile compounds in the coffee samples were identified according to a comparison of their mass spectra and the linear retention index (LRI) with those present in the NIST 14 database. The list of volatile metabolites extracted and identified is summarized in **Table 2**. All compounds detected in the GC-MS chromatograms have also been reported by several research groups that analyzed coffee by HS/GC-MS.[10,11] Overall, the volatile profiles of coffee samples provide enough features that may lead to effective differentiation of coffee origins.

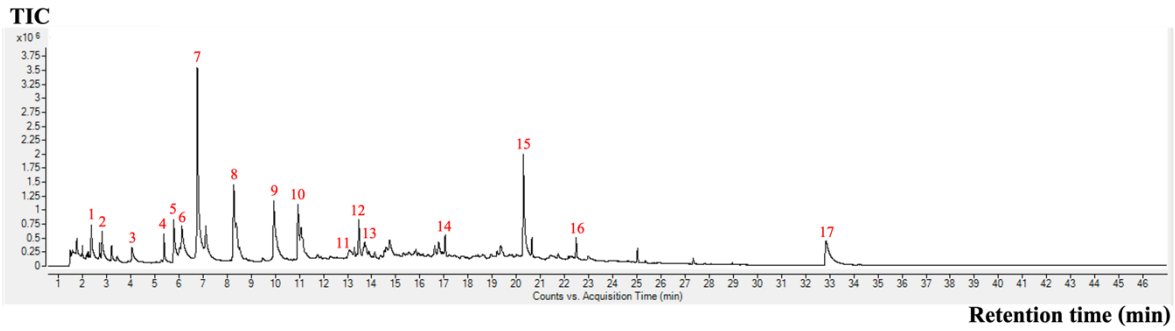

Figure 1.
Representative total ion chromatogram (TIC) of Doi Pha Hee coffee (C1).

Table 2.
Volatile compounds of Doi Pha Hee coffee (C1) obtained by HS-SPME GC-MS.

Peak No.	RT (min)	Compound	CAS No.	LRI	
				Exp[a]	Database[b]
1	2.375	Acetic acid	64-19-7	<800	610±10
2	2.806	2-Methylbutanal	96-17-3	<800	662±8
3	4.055	Pyridine	110-86-1	<800	746±7
4	5.378	Dihydro-2-methyl-3(2H)-furanone	3188-00-9	825	809±3
5	5.783	2-Methylpyrazine	109-08-0	836	831±7
6	6.120	Furfural	98-01-1	846	833±4
7	6.765	2-Furanmethanol	98-00-0	865	859±6
8	8.280	2,6-Dimethylpyrazine	108-50-9	910	917±7
9	9.933	5-Methyl-2-furancarboxaldehyde	620-02-0	964	965±5
10	10.941	Furfuryl acetate	623-17-6	996	995±4
11	13.070	2,5-Dimethyl-4-hydroxy-3(2H)-furanone	3658-77-3	1065	1070±10
12	13.464	2,5-Dimethyl-3-ethylpyrazine	13360-65-1	1085	1082±3
13	13.704	2-Ethyl-3,5-dimethylpyrazine	13925-07-0	1078	1084±3
14	17.043	Dodecane	112-40-3	1196	1200
15	20.290	2-Methoxy-4-vinylphenol	7786-61-0	1311	1317±5
16	22.477	Tetradecane	629-59-4	1392	1400
17	32.848	Caffeine	58-08-2	1855	1835±7

[a] Exp : Experimental linear retention indices calculated using *n*-alkane standards.
[b]Database : Linear retention indices obtained from NIST 14 database.

Comparison of Volatile Compounds in Arabica and Robusta coffees

Chemometric analysis was performed using the %RPA of 17 volatile compounds (variables) from 13 coffee samples as an input dataset for calculation. The dataset was subjected to an unsupervised analysis by PCA to evaluate the possibility of discriminating Arabica with Robusta coffee. The PCA score plot is shown in **Figure 2**. The result indicated a clear separation between the coffee species. This is also reflected in the classification accuracy by LDA, where the overall predictive ability of the constructed model was 92%. Therefore, the result from this initial study confirms that this method has potential to classify coffee samples based on their origins.

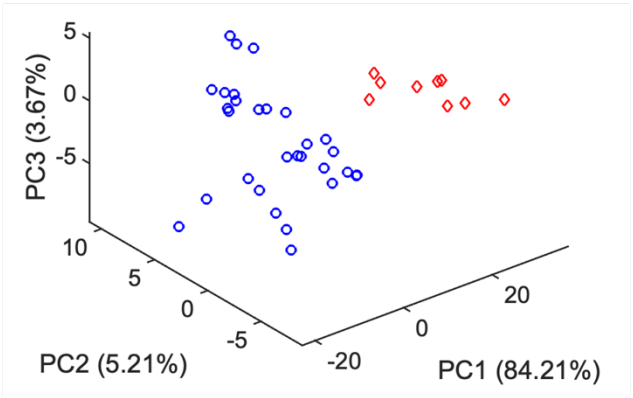

geographical origin	% correct classification
Arabica	100
Robusta	67
Overall	92

Figure 2.
PC score plots of the first 3 principal components to visualize the cluster relationship of types of coffees, along with percentage of correct classifications from LDA.

Discrimination of Coffees based on Geographical Origins

Encouraged by the initial result, we also studied the differentiation of coffees based on geographical origins. First, we analyzed different sources of Arabica coffee within certain provinces of Thailand. The resulting PCA score plot is shown in **Figure 3A**. The first 3 PCs (PC1-PC3) were chosen in order to represent the data objects with the highest variation (34.98%, 29.10%, and 14.98% of the variation). The results showed that these coffee samples can be separated into four groups according to the provinces of origin. The PCA grouping result was in agreement with that obtained using LDA, with classification rates of 56%, 67%, 83%, 67%, and 67% from Chiang Rai, Chiang Mai, Nan, Mae Hong Son, and overall, respectively. Interestingly, lower classification accuracies among the provinces of Chiang Rai, Chiang Mai, and Mae Hong Son may probably due to their closer proximities in comparison to Nan.

The case of Robusta coffees also showed good differentiation performance with the first 3 PCs (**Figure 3B**). The first 3 PCs gave great prediction accuracies by reaching 100% accuracy in all cases.

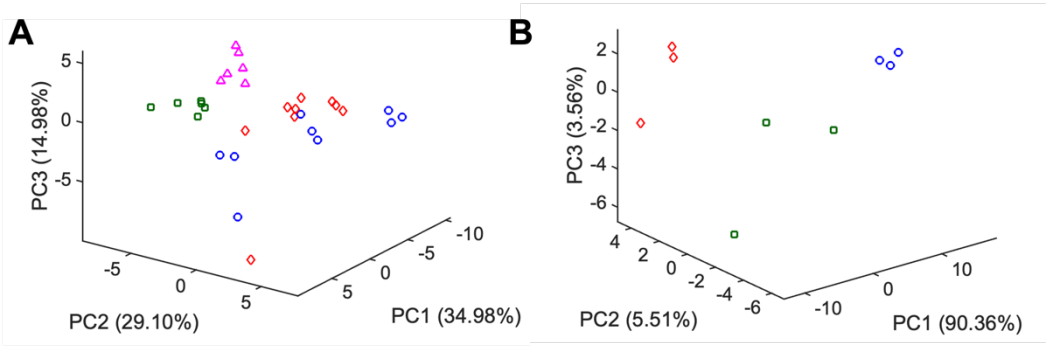

geographical origin	% correct classification
Chiang Rai	56
Chiang Mai	67
Nan	83
Mae Hong Son	67
Overall	67

geographical origin	% correct classification
Robusta Chiang Rai	100
Chumphon	100
Krabi	100
Overall	100

Figure 3.
PC score plots of the first 3 principal components in all Arabica coffee sources (A) and PC score plots of the first 3 principal components in all Robusta coffee sources (B).

After successfully distinguishing coffees based on their provinces of origin as discussed above, we studied the differentiation of the sources of Arabica coffee within the same province. This study was more challenging because the chemical profiles are expected to be more similar due to their closer locations of origin. The PCA score plot of all sources within the provinces of Chiang Rai, Chiang Mai, Nan, and Mae Hong Son indicated successful discrimination of origins using only the first 3 PCs, with most of the prediction accuracies reaching 100% (**Figure. 4A-D**). Thus, HS-SPME/GC-MS, which requires no solvent and free from pre-treatment processes, is an attractive and convenient method to uncover geographical indications of coffees.

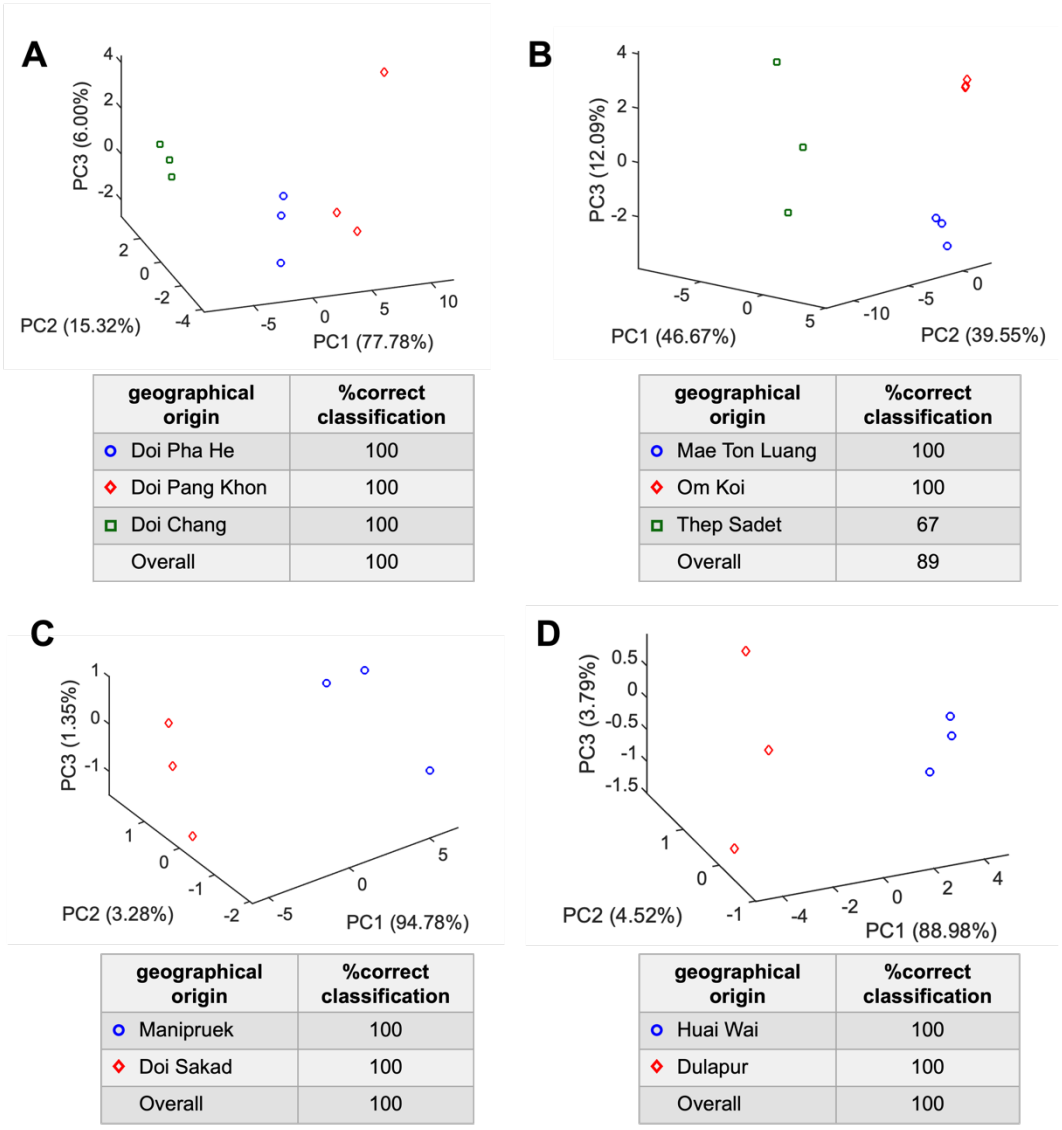

geographical origin	%correct classification
Doi Pha He	100
Doi Pang Khon	100
Doi Chang	100
Overall	100

geographical origin	%correct classification
Mae Ton Luang	100
Om Koi	100
Thep Sadet	67
Overall	89

geographical origin	%correct classification
Manipruek	100
Doi Sakad	100
Overall	100

geographical origin	%correct classification
Huai Wai	100
Dulapur	100
Overall	100

Figure 4.
PC score plots of Arabica coffees within the same province of Chiang Rai (A), Chiang Mai (B), Nan (C), and Mae Hong Son (D).

Conclusion:

In this work, profiles of volatiles in a variety of coffee samples were obtained by HS-SPME/GC-MS. The resulting data were used for PCA and LDA, which successfully discriminate (in the range of 65-100% accuracies except in one case) a variety of coffees based on 1) the coffee species, 2) geographical origins of Arabica coffees, 3) geographical origins of Robusta coffees, and 4) geographical origins of Arabica coffees within the same province of Thailand. Hence, this study clearly illustrated that the combination of HS-SPME/GC-MS with chemometric analysis is effective in discriminating coffee samples based on their origins, which can be further adopted as a tool that aids the registration of GI.

Acknowledgements:

The authors thank Associate Professor Dr. Kanet Wongravee (Sensor Research Unit (SRU), Department of Chemistry, Faculty of Science, Chulalongkorn University) for his support in chemometric analysis.

References:

1. Cheng B, Furtado A, Smyth HE, Henry RJ. Trends Food Sci Technol. 2016;57:20–30.
2. Sunarharum WB, Williams DJ, Smyth HE. Food Res Int. 2014;62:315–325.
3. Arana VA, Medina J, Alarcon R, Moreno E, Heintz L, Schäfer H, Wist J. Food Chem. 2015;175:500–506.
4. Mehari B, Redi-Abshiro M, Chandravanshi BS, Combrinck S, Atlabachew M, McCrindle R. J Food Compos Anal. 2016;45:16–25.
5. Babova O, Occhipinti A, Maffei ME. Phytochemistry. 2016;123:33–39.
6. Mehari B, Redi-Abshiro M, Chandravanshi BS, Combrinck S, McCrindle R, Atlabachew M. J Sci Food Agric. 2019;99:3811–3823.
7. Putri SP, Irifune T, Yusianto, Fukusaki E. Metabolomics. 2019;15:77–87.
8. Ongo EA, Montevecchi G, Antonelli A, Sberveglieri V, Sevilla Iii F. Food Res Int. 2020;134:109227.
9. Zakidou P, Plati F, Matsakidou A, Varka EM, Blekas G, Paraskevopoulou A. Molecules. 2021;26:4609.
10. Amanpour A, Selli S. J Food Process Preserv. 2016;40:1116–1124.
11. Ochiai N, Tsunokawa J, Sasamoto K, Hoffmann A. J Chromatogr A. 2014;1371:65–73.

DEVELOPMENT OF SAMPLE PREPARATION AND ANALYTICAL METHOD FOR THE DETERMINATION OF ANDROGRAPHOLIDE IN *Andrographis paniculata* EXTRACT

Watchara Kaewsuwan, Songsuda Promthong*
Office of Scientific Instrument and Testing, Prince of Songkla University, Hat Yai Campus, Songkhla, 90110, Thailand
*e-mail: songsuda.p@psu.ac.th

Abstract:
The objective of this work was developed sample preparation and analytical method using HPLC-DAD system for the quantification of andrographolide in *Andrographis paniculata* extract. The chromatographic HPLC-DAD system for the separation of andrographolide was carried out using a reverse phase LiChrospher 100 RP-18 (4.0 x 250 mm, 5µm particle size) column at 40 degrees Celsius using isocratic elution of mobile phase consisted of Methanol:Deionized water in the ratio of 80:20, v/v at a flow rate of 0.80 mL/min, and the absorption wavelength was monitored at 220 nm with a run time of 10 minutes. Under the optimum conditions, the linearity was obtained in the concentration range of 0.4-40 mg/g. The limit of detection (LOD) was 0.02 mg/g, limit of quantification (LOQ) was 0.04 mg/g, the accuracy and precision were (100.1±4.2) %recovery and 1.1 %RSD (n=10), respectively with acceptable criteria. This method was simplicities of extraction procedure, good accuracy and precision. Moreover, the developed method for the andrographolide detection in *Andrographis paniculata* extract was successfully and can be applied to the new service at the Office of Scientific Instrument and Testing, Prince of Songkla University, Songkhla, Thailand.

Introduction:

Andrographis paniculata is commonly used as a medicinal herb in traditional medicine.[1] This plant has been widely used for treating sore throat, flu, and upper respiratory tract infections.[5] Andrographolide (Figure 1.) is a major bioactive chemical constituent of the plant. Its exhibiting a wide spectrum of biological activities, including anti-inflammatory, antibacterial, anticancer properties, antidiabetic, antimalarial and hepatoprotective, etc.[1,5]

Consequently, the suitable method was used for the separation and quantification of andrographolide in *Andrographis paniculata* extract. High-performance liquid chromatography (HPLC) method is extensively used for the determination of andrographolide because of its high sensitivity, good resolution and precision.[3,8]

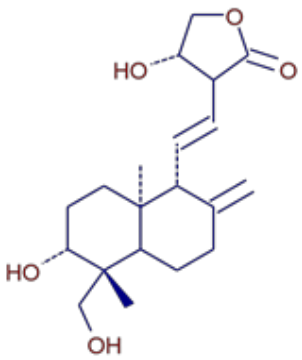

Figure 1. The chemical structure of andrographolide.

In addition, a sample preparation technique was required prior to instrumental analysis. Various sample preparation techniques have been reported for the extraction of andrographolide from *Andrographis paniculata* extract, such as conventional reflux,[6] solvent extraction,[7] and solid phase extraction.[9,11] These methods take long extraction time, required a large volume of organic solvent, expensive and tedious steps. To overcome these drawbacks, alternative sample extraction procedure using ultrasonic extraction[1,4,10] was investigated for the extraction of andrographolide from *Andrographis paniculata* extract as shown in Figure 2.

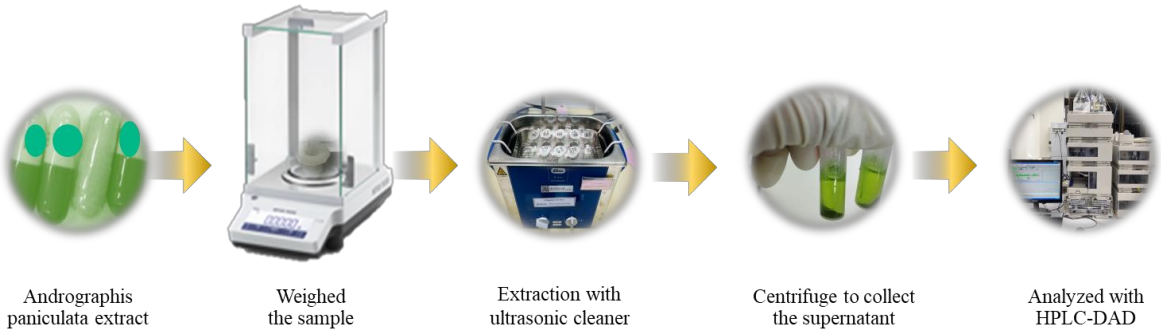

Figure 2. The extraction procedure of andrographolide from *Andrographis paniculate* extract using ultrasonication.

Methodology:

Standard and solvent: Andrographolide standard (purity ≥ 98%) was purchased from Pharmaceutical Laboratory Service Center Faculty of Pharmaceutical Sciences Prince of Songkla University, Songkhla, Thailand. Methanol (HPLC grade) was purchased from RCI Labscan, Bangkok, Thailand.

Instruments: High Performance Liquid Chromatograph (HPLC), 1200 series, Agilent Technologies, Germany. Analytical balance 5 digits, Mettler Toledo XP205, Switzerland. Vortex mixture, Vortex Genie 2 G560E, United States. Ultrasonic Cleaners, Elma sonic e30H, United States. Centrifuge, eppendorf Centrifuge 5430R, Germany. Deionized (DI) water system was purchased from Human Corporation ZENEER NAVI UP 900, Korea.

Mobile phase preparations: Methanol (HPLC grade) and Deionized water were filtered through 0.2 µm or 0.45 µm of nylon membrane before use, under the isocratic elution.

Preparation of stock standard and calibration curve: 10 mg of andrographolide standard was dissolved in methanol to obtain a stock standard solution (1,000 mg/L) and kept in freeze (-20 ºC). Dilute stock solution with a mobile phase to obtain at least 5 concentrations having known concentration of 1.0, 5.0, 10, 25, 50, 100 mg/L that, called working standard solution to achieve a calibration curve.

Sample preparations:[1] 5.0 mg of *Andrographis paniculata* extract were added in microcentrifuge tubes and 1.0 mL of methanol was added to extract andrographolide with ultrasonic cleaners for 30 min., then centrifuged at 10,000 rpm for 5 min. The supernatant was collected and the extraction was repeated twice. The extracted sample solution was filtered through 0.2 µm of nylon membrane filter before inject to HPLC-DAD system, if necessary, dilute the sample with a mobile phase.[1]

Analytical performance and method validation:[2] The analytical performance of the developed method was based on AOAC Official Methods of Analysis (AOAC, 2016)[2] including;

Linearity: The linearity of the andrographolide was investigated, the calibration curve was plotted between the peak area and the concentration of andrographolide to obtain the linearity; it was determined by considering the correlation coefficient (R) greater than 0.995.

Limit of detection (LOD): The LOD is generally determined at the lowest concentration of the standard that can be distinguished between signal response and baseline noise to establish the minimum concentration that gave the signal to noise ratio greater than or equal to 3 (S/N ≥ 3).
Limit of quantification (LOQ): The LOQ is generally performed by comparing measured signal response and baseline noise to establish the minimum concentration that gave the signal to noise ratio greater than or equal to 10 (S/N ≥ 10).
Accuracy: The recovery was investigated to evaluate the accuracy of the developed method. *Andrographis paniculata* extract was spiked with andrographolide standard to obtain the final concentration of 12.5 mg/L.
Precision: The precision of the developed method was also investigated by considering the relative standard deviation (%RSD) within ten replicates (n=10).

Results and Discussion:

Optimization of HPLC-DAD conditions

The optimum conditions of HPLC-DAD system for the determination of andrographolide as shown in Table 1.

Table 1. The optimum conditions of HPLC-DAD system for the determination of andrographolide.

High Performance Liquid Chromatograph-Diode Array Detector (HPLC-DAD)	
Mobile phase:	Methanol:Deionized water, (80:20, v/v)
Flow rate:	0.80 mL/min
Injection volume:	20 µL
Column details:	LiChrospher 100 RP-18 (4.0 x 250 mm, 5µm)
Column temperature:	40 ºC
Detector:	Diode Array Detector (DAD), Wavelength 220 nm
Run time:	10 min.

Under the optimum conditions, the chromatogram of andrographolide exhibited good peak symmetry and short analysis time (Figure 3).

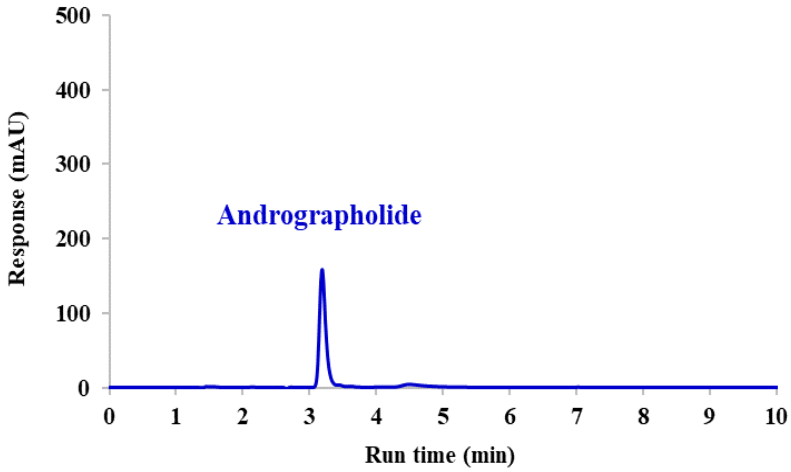

Figure 3. The chromatogram of andrographolide at 25 mg/L.

Optimization of amount of sample

The preliminary experiment, to check the extraction efficiency of andrographolide in different amount of sample. The amount of sample was investigated in the range of 2.0 to 10.0 mg (Figure 4). The extraction efficiency of andrographolide increased with increasing amount of sample from 2.0 to 5.0 mg, and then remained almost constant. Therefore, 5.0 mg of the sample was chosen for further study.

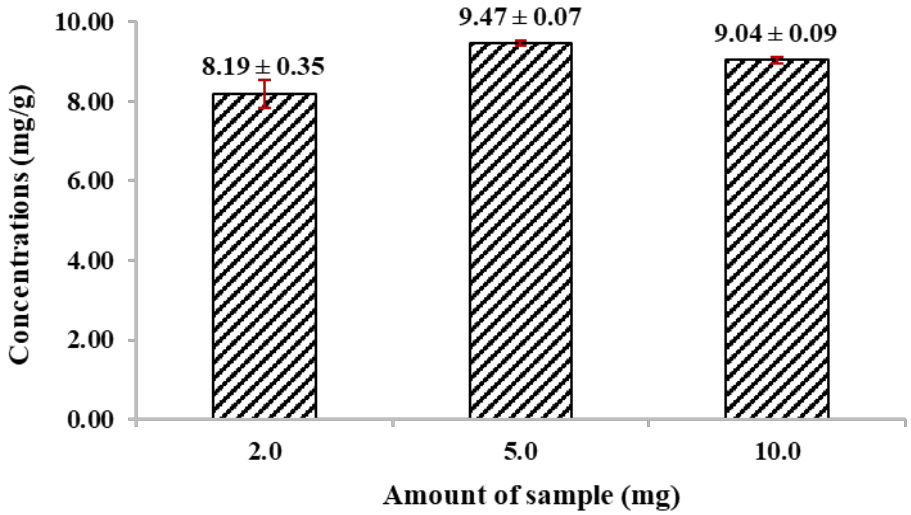

Figure 4. The effect of amount of sample on the extraction efficiency of andrographolide from *Andrographis paniculata* extract (n=2).

Analytical performance and method validation[2]

Linearity: The linearity of the developed method was obtained in the range of 0.4-40 mg/g with correlation coefficient (R) of 0.99995.

Limit of detection (LOD): The LOD of the developed method based on S/N ≥ 3 was 0.02 mg/g.

Limit of quantification (LOQ): The LOQ of the developed method based on S/N ≥ 10 was 0.04 mg/g.

Accuracy: The accuracy of the developed method was evaluated in term of recovery. Satisfactory recoveries were achieved between 93.8 and 105.4 % (acceptable recovery of 80 to 110 % AOAC, 2016).[2]

Precision: The precision of the developed method was evaluated from the relative standard deviation (%RSD). The RSD of the developed method was 1.1 % (n=10) with was acceptable % RSD ≤ 5.3, recommended by AOAC, 2016.[2]

Under the optimum conditions of HPLC-DAD system, the analytical performance and method validation of the developed method are summarized in Table 2.

Table 2. The summarized of the analytical performance and method validation.

Parameters	Criteria (AOAC, 2016)[2]	Optimum conditions
Linearity of instrument, method	-	1.0-100 mg/L, 0.4-40 mg/g
Correlation coefficient (R)	R > 0.995	0.99995
LOD of instrument, method	S/N ≥ 3	0.05 mg/L, 0.02 mg/g
LOQ of instrument, method	S/N ≥ 10	0.10 mg/L, 0.04 mg/g
Accuracy	% Recovery (80-110)	100.1 %
Precision	% RSD ≤ 5.3 (n=10)	1.1 %

Real samples analysis: The developed method was successfully applied for the determination of andrographolide in a various *Andrographis paniculata* extracts and the results are showed in Table 3. The recovery of andrographolide in real samples were obtained in the range of (93.7-99.7) % with acceptable criteria of AOAC.[2] Under the optimum conditions, the peak of andrographolide in *Andrographis paniculata* extracts could be separated from the other interferences (Figure 5).

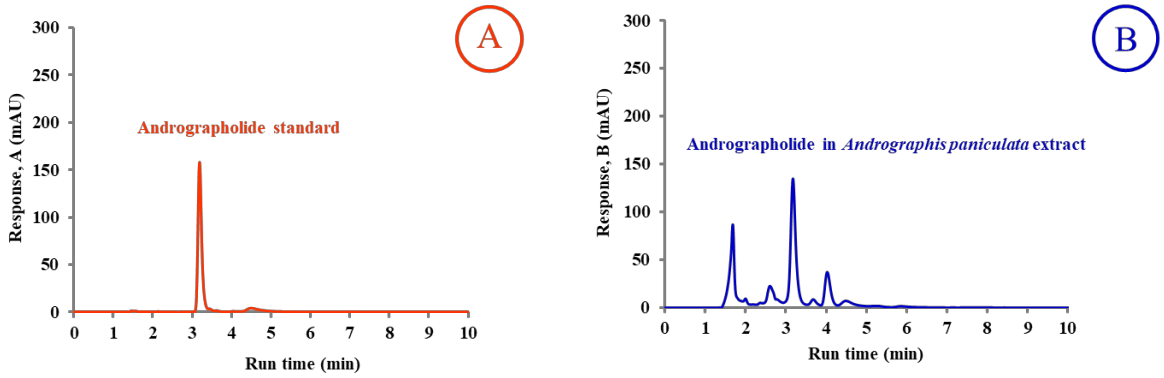

Figure 5. The chromatograms of andrographolide standard (A) and andrographolide in *Andrographis paniculata* extract (B).

Table 3. The recovery of andrographolide in *Andrographis paniculata* extract (n=3).

No. of samples	Andrographolide[a] ± SD (mg/g)	Concentration added[b] (mg/g)	Andrographolide found[c] ± SD (mg/g)	%Recovery ± SD[d]
Extract #1	6.6 ± 0.1	3.9	10.4 ± 0.0	95.1 ± 3.3
Extract #2	40.2 ± 0.9	19.5	59.6 ± 0.0	99.7 ± 4.4
Extract #3	32.1 ± 0.4	19.6	51.5 ± 0.2	99.0 ± 1.2
Extract #4	44.7 ± 0.1	19.0	62.5 ± 0.1	93.7 ± 0.6
Extract #5	40.1 ± 0.2	19.8	59.7 ± 0.0	99.3 ± 1.1
Extract #6	17.4 ± 0.1	19.3	36.3 ± 0.0	97.7 ± 0.3
Extract #7	54.3 ± 1.7	39.5	93.6 ± 0.6	99.5 ± 3.2

[a]The initial andrographolide concentration in the *Andrographis paniculata* extract.
[b]The concentration of andrographolide standard was added into the sample, it depended on the concentration in each sample and dilution factor.
[c]The final concentration of andrographolide was found in each sample.
[d]The standard deviation.

Conclusion:

The developed sample preparation and analytical method were successfully established for the determination of andrographolide in *Andrographis paniculata* extract. The developed sample preparation using ultrasonic extraction with several advantages including; simplicity of extraction procedure, low consumption of organic solvent, good accuracy and precision. The linearity was obtained in the concentration range of 0.4-40 mg/g, the limit of detection (LOD) and limit of quantification (LOQ) were obtained at 0.02 mg/g and 0.04 mg/g, respectively. The accuracy and precision were (100.1±4.2) % recovery and 1.1 %RSD (n=10), respectively with acceptable criteria.[2] Moreover, the developed sample extraction can

be applied to the new service at the Office of Scientific Instrument and Testing, Prince of Songkla University, Songkhla, Thailand.

Acknowledgements:
This work was supported by the financial of Office of Scientific Instrument and Testing, Prince of Songkla University. We would like to thanks, Director of Office of Scientific Instrument and Testing and Head of Scientific Research Equipment Services for a consultant and support the personnel of Office of Scientific Instrument and Testing to develop the knowledge from a routine work to a research work.

References:

1. Emmanuelle V.-P, Véronique F, Joana F. C, Emilie D, Chantal P, Sabine B.-R. Foods. 2019;8:1-11.
2. Guidelines for Standard Method Performance Requirements, AOAC Official Methods of Analysis. 2016:1-18.
3. Rashmi P, Vandana J. J. Chromatogr. Sci. 2021;59:191-203.
4. Muhammad D, Erindyah R. W, Andi S, Indah H. Int. J. Pharm. Sci. Rev. Res. 2015;35:140-143.
5. Thanasekaran J, Cheng-Y. H, Jie-J. L, Joen-R. S. Evid. Based Complementary Altern. Med. 2013;2013:1-16.
6. Kotagiri R, Anil K, Parveen S, Deepak T. Int. J. Pharm. Sci. Res. 2013;4:2623-2628.
7. Rafi M, Devi1 F. A, Syafitri D. U, Heryanto R, Suparto H. I, Amran B. M, Rohman A, Prajogo B, Lim W. L. BMC Res Notes. 2020;13:1-6.
8. Mrinalini D, Namrata G. Int. j. pharm. res. scholars. 2016;5:47-53.
9. Ligang C, Aimin Y, Xiaodong Z, Kui Z, Xiupin W, Lan D, Hanqi Z. Talanta. 2007;74:146-152.
10. Bachtiar R. P. I, Achmad F. H, Riesta P, Aty W, Mochammad Y. Research J. Pharm. and Tech. 2020;13:4291-4296.
11. Jinda W, Supawadee D, Kanokwan J, Bung-orn S. Thai Pharm Health Sci J. 2006;1:209-218.

DEVELOPMENT OF AN ENZYME-FREE HYDROGEN PEROXIDE SENSOR USING DUAL-SHAPED SILVER NANOPARTICLES

Charles Oliver Avenido,[1,3] Kanet Wongravee,[2] Monpichar Srisa-Art[1,*]

[1] Electrochemistry and Optical Spectroscopy Center of Excellence (EOSCE), Department of Chemistry, Faculty of Science, Chulalongkorn University, Bangkok 10330, Thailand

[2] Sensor Research Unit, Department of Chemistry, Faculty of Science, Chulalongkorn University, Bangkok 10330, Thailand

[3] Chemical Testing Laboratory, Technical Services Division, Philippine Textile Research Institute, Department of Science and Technology, Bicutan, Taguig City 1633, Philippines

*e-mail: Monpichar.S@chula.ac.th

Abstract:
In the past decade, silver nanoparticles (AgNP) facilitate the enzyme-free measurement of hydrogen peroxide owing to its unique optical properties. Decomposition-based colorimetric sensing with silver nanoparticles have been reported previously for various analytes including hydrogen peroxide. However, this technique continues to suffer disadvantages such as low selectivity and sensitivity. Thus, an alternative method is necessary to address these concerns. Herein, we report the development of a silver nanospheres (AgNS) and citrate-capped silver nanoprisms (AgNPr) mixture as a highly selective and sensitive sensor for hydrogen peroxide. Etching of the silver nanospheres by hydrogen peroxide releases Ag^+ which is sequentially reduced by excess H_2O_2 to silver metal that deposits anisotropically at the edges of the citrate-capped nanoprisms. A reduction of plasmon band intensity at around 400 nm, a red shift, and an increase in intensity of the in-plane dipole plasmon resonance peak were observed corresponding to a multi-color change with varying H_2O_2 concentrations. Quantitative analysis has been accomplished by tracking the changes in peak intensities of the nanospheres and nanoprisms. Using the AgNS/NPr sensor, a sub-micromolar limit of detection was achieved. Growth-based sensing using dual-shaped silver nanoparticles is a potential alternative for hydrogen peroxide determination as it enables a highly selective and sensitive colorimetric and naked-eyes approach with high accuracy and precision.

Introduction:
Hydrogen peroxide is a common cleaning or bleaching agent at home and in various industries. Amid the Covid-19 pandemic, it is widely used as a disinfectant in the form of mouthwash, nasal spray, hand sanitizers and aerosol mist.[1-5] In biological systems, H_2O_2 is a representative reactive oxygen species (ROS), which is an end result of aerobic respiration.[6, 7] Several oxidase enzymes generate H_2O_2 from a wide range of biological substrates or biomarkers that can reveal health conditions such as glucose or cholesterol.[8-11]Abnormal levels or buildup of this small molecule can cause oxidative damage to cells and tissues that may lead to serious human diseases, such as, lupus, ulcerative colitis, diabetes, cancer, and neurodegenerative diseases, namely, Alzheimer's. Parkinson's and Huntington's diseases.[6, 7, 12] Hence, hydrogen peroxide detection attracted a great deal of research interest in recent years.

Traditional methods of hydrogen peroxide detection include titrimetry[13], spectrophotometry[14], electrochemical[15], and luminescence techniques[16, 17]. Several drawbacks, such as low selectivity, sensitivity and resolution, long detection time, and costly and complicated instrumentation, have been reported for these conventional methods.[18] Colorimetric detection offers a great alternative in H_2O_2 determination being simple, instrument-free, and able to attain even ultra-low sensitivity.[19] Typical materials used for optical detection are horseradish peroxidase (HRP) and chromogenic dyes, for example, 3,3',5,5'-Tetramethylbenzidine (TMB), 3,3'-Diaminobenzidine (DAB) or ortho-phenylenediamine (OPD) that change in color in the presence of H_2O_2.[20, 21] Natural enzymes, such as HRPs, are costly and require a highly controlled environment making them unsuitable for routine analysis. If the conditions are not maintained, enzyme activity is reduced permanently, introducing errors to the system.[22, 23] Nanozymes or artificial enzymes that have peroxidase-like activity emerged as a promising substitute by addressing these shortcomings. However, they also present some challenges like limited selectivity, unclear mechanisms, potential toxicity, and still require the aforementioned dyes. [20]

In addition to enzyme-mimicking properties of nanoparticles, common strategies for colorimetric detection include an etching-based approach and growth or aggregation of gold or silver nanoparticles.[24] Unique plasmonic properties of silver nanoparticles (AgNPs) from the visible to the near infrared have been broadly explored for H_2O_2 analysis. One of the advantages in using AgNPs is that it enables label-free or enzyme-free detection, which does not require chromogenic dyes and HRP, reducing the cost and use of reagents while providing a simple and quick method of detection. Several works describe the decomposition of silver nanoplates, nanoprisms or nanospheres to detect hydrogen peroxide.[25-29] However, selectivity of these methods remains a challenge since many other substances can etch AgNPs. The colors produced are limited to one or two colors, and the color transition as the concentration of the analyte changes may not be easily deduced with the naked eyes. Growth-based detection, on the other hand, is more commonly employed in plasmonic enzyme-linked immunoassays or ELISA with hydrogen peroxide and gold nanoparticles. This method has a proven sensitivity and exhibits multi-color transition.[19] As of this writing, only a handful of research describe sensors based on seed-mediated growth of silver nanoparticles.

In this study, we exploit the concept of transformation of silver nanospheres to nanoprism and nanoplates with hydrogen peroxide.[30] The growth-based mechanism that is unique in the presence of H_2O_2 was investigated to develop a novel, quick, and highly selective plasmonic sensor using a mixture of silver nanospheres (AgNSs) and silver nanoprisms (AgNPrs). The reduced silver from etched silver nanospheres assemble at the edges of the citrate-capped AgNPrs allowing the lateral growth of the nanoprism. This increase in size can be observed as a red shift and amplified intensity of the in-plane dipole plasmon resonance band, and a distinctive color change from yellow, orange, red, purple to blue. Accordingly, determination of H_2O_2 concentration can then be achieved with spectrophotometry and naked eyes detection.

Methodology:

Chemicals

Hydrogen peroxide (30% w/w H_2O_2), Silver nitrate ($AgNO_3$), trisodium citrate, and soluble starch were purchased from Merck. Sodium borohydride ($NaBH_4$) was acquired from Sigma-Aldrich. All chemicals were analytical reagent (AR) grade and were used as received. Ultrapure water taken from Milli-Q system was used in the preparation of all aqueous solutions.

Synthesis of silver nanospheres

Starch-stabilized silver nanospheres and its transformation to nanoprisms were done following earlier works with some modifications.[25, 30] Briefly, 3.71 mM or 400 ppm silver nanospheres were prepared by dissolving 126 mg of silver nitrate in a 100 mL of 2% starch solution. In a separate beaker, 63 mg of $NaBH_4$ was mixed with the starch solution until completely dissolved. The $AgNO_3$ solution was injected immediately to the $NaBH_4$ solution at a rate of 2 mL s^{-1} while stirring vigorously for 30 minutes. The colorless solution immediately turns to yellow and then deep brown, which indicates the development of silver nanospheres. The colloid was gently boiled for 1.5 h and then cooled at room temperature before adjusting the total volume to 200 mL using MilliQ water. The solution was aged overnight in an amber bottle at room temperature to make sure that there will be no residual $NaBH_4$ before being transformed to silver nanoprisms.

Synthesis of citrate-capped AgNPrs

Silver nanospheres were transformed to silver nanoprisms using a 1:10 molar ratio of silver to 30% hydrogen peroxide (9.79 M). The red wine colloid was diluted with MilliQ water to 65 ppm and incubated with 100 ppm sodium tricitrate in a 1.5 mL microcentrifuge tube for three hours to allow the self-assembly of citrate onto the silver nanoprism surface. It was then centrifuged, washed twice, and redispersed in MilliQ water.

Hydrogen peroxide detection

Citrate capped nanoprisms (1.5 mL, 65 ppm) were transferred to a cuvette and mixed with silver nanospheres with a 1:2 ratio of silver nanoprisms to nanospheres to be used as a sensor (AgNS/NPr). MilliQ water was added to make up a total volume of 2.5 mL. The effect of the increasing hydrogen peroxide to the sensor was studied by adding the concentrated H_2O_2 from 0.1 to 30 µL yielding a final concentration of 0.39 mM to 117.5 mM. The AgNS/NPr sensor and hydrogen peroxide were mixed for 15 seconds by pipetting up and down until the colloid turns completely dark. Contact time ranging from one minute to 30 minutes was investigated to optimize the reaction time. Since there were no significant changes in the peak intensity and λ_{max} after a minute, one minute reaction time was chosen for the rest of the experiments. The sensor was diluted five times with ultrapure water before analyzing with a UV-Vis Spectrophotometer. Images of the solution in the cuvettes were captured with a Samsung S21 smartphone camera in ambient lighting.

Selectivity

Common ions were evaluated against the selectivity of the silver nanoparticle sensor. Initially, 100 µM solutions were prepared and 50 µL was mixed with the sensor. Extinction spectra were measured before and after addition of hydrogen peroxide to observe the change in intensity of the dipole plasmon resonance (DPR) and In-plane dipole plasmon resonance (IPDPR) bands.

Accuracy and Precision

To evaluate the accuracy and precision of the sensor, hydrogen peroxide solutions of 5.0 mM and 11.0 mM concentrations were prepared and reacted with the AgNS/NPr sensor. %Recovery and %RSD (n=5) were calculated from the results.

Results and Discussion:

Characterization

To confirm the successful synthesis of the silver nanoparticles, UV-Vis Spectrophotometry (Agilent HP8453) and TEM (JEOL JEM-1400 Flash Electron Microscope) imaging were employed. ImageJ software was used to measure the mean diameter of the AgNPs. The synthesized silver nanospheres registered a sharp dipole plasmon resonance (DPR) band at 403 nm and a yellow color of the diluted solution is observed (**Figure 1a**). The presence of out-of-plane quadrupole resonance (OPQPR) at 339 nm and in-plane dipole plasmon resonance (IPDPR) at 487 nm (**Figure 1b**) signify the successful synthesis of silver nanoprisms as described in the literature.[31] The color of the diluted silver nanoprism colloid is pinkish purple. TEM imaging confirmed the presence of both silver nanospheres and nanoprisms with an average diameter of 6.4 ± 2.5 nm and 14.2 ± 3.6 nm respectively, in the sensor (**Figure 1c**).

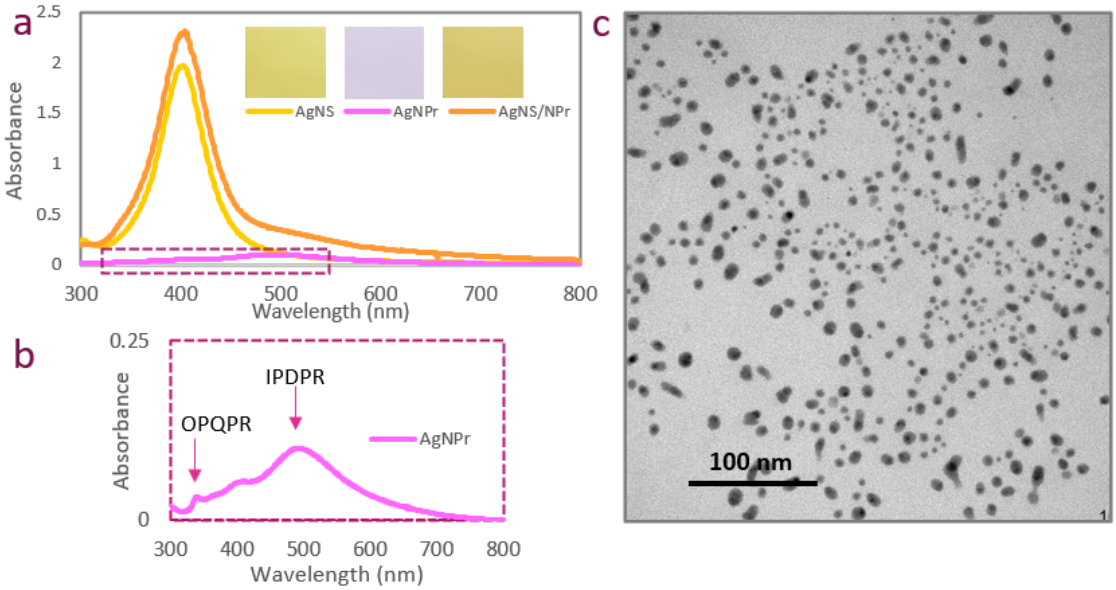

Figure 1.

(a) Extinction spectra of silver nanospheres (AgNSs), nanoprisms (AgNPrs) and the mixture of both (AgNS/NPr) (b) the enlarged spectra of the silver nanoprisms (c) A TEM image of the sensor containing AgNSs and AgNPrs.

Sensing Mechanism

Hydrogen peroxide can oxidize silver nanospheres to silver ions and subsequently reduce these ions to silver metal.[30] Citrate molecules preferably coordinate to the {111} facet of the nanoprism protecting it from oxidation by H_2O_2. Ag^0 then binds to the anisotropic edges of the nanoprism, facilitating the enlargement of the AgNPrs. (**Figure 2a**) The enlargement of the nanoprism is corroborated by a red shift and enhancement of the plasmon intensity of the nanoprism λ_{max} (IPDPR), and a decrease of the nanosphere λ_{max} intensity (DPR), which can be correlated to the H_2O_2 concentration in the system (**Figure 2b**). TEM images as presented in **Figures 2c** and **2d** also reveal the reduction of the number of silver nanospheres and the development of larger AgNPrs.

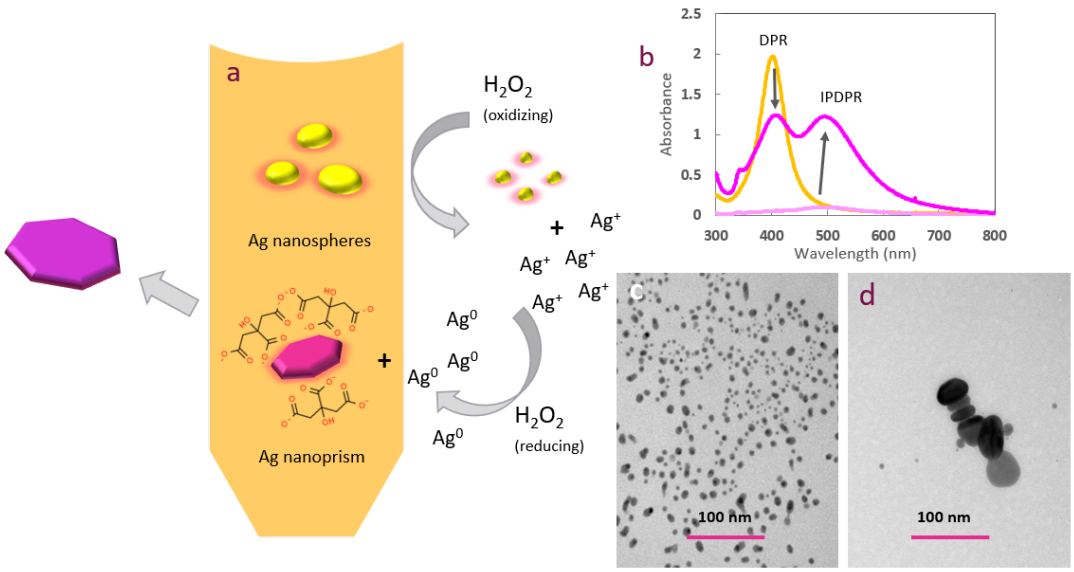

Figure 2.

(a) Schematic diagram of the growth-based mechanism of the dual nanoparticle sensor in the presence of H_2O_2 (b) the change of extinction spectra of the AgNS/NPr sensor after addition of hydrogen peroxide and the corresponding TEM images of the sensor before (c) and after (d) addition of H_2O_2.

Upon addition of hydrogen peroxide, the plasmonic sensor turned darker in color indicating an intensified extinction band due to the growth of the particles. **Figure 3a** illustrates the changes of the IPDPR λ_{max} and their respective intensities as hydrogen peroxide volume was increased, producing multiple hues (**Figure 3b**). Greatest intensity change and red shift were recorded at 4 µL and 20 µL respectively, corresponding to the red violet and light blue colors.

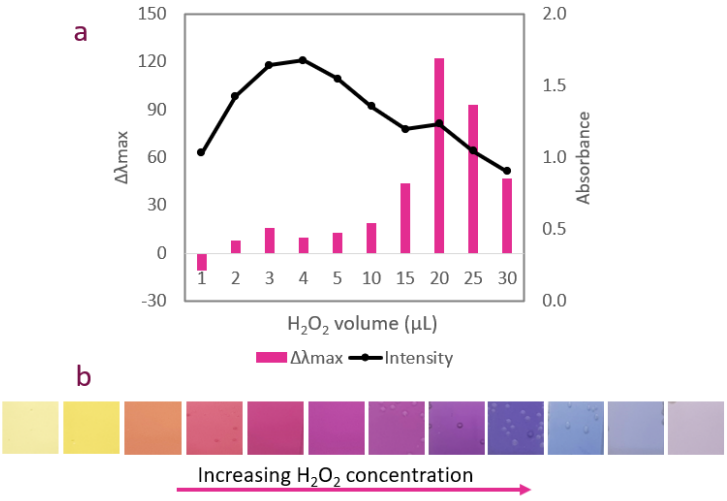

Figure 3.

(a) Effect of increasing hydrogen peroxide to the IPDPR and absorbance intensities with respect to the $\lambda_{max\ AgNPr}$ and (b) the colors produced by the AgNS/NPr sensor.

An increase in the extinction spectra of the IPDPR λ_{max} while the DPR decreases clearly suggests that oxidative etching of the nanospheres and growth of the nanoprisms have occurred (**Figure 4a**). Furthermore, these data points can enable ratiometric response for the detection of H_2O_2 extending the linear range from 0.39 mM to 11.75 mM and lowering the detection limit to 4.8 µM (**Figure 4b**) based on the 3σ/slope, where σ was the standard deviation of blank samples. **Figure 4c** displays the color transition from yellow, orange, to red making naked eye detection possible at this range.

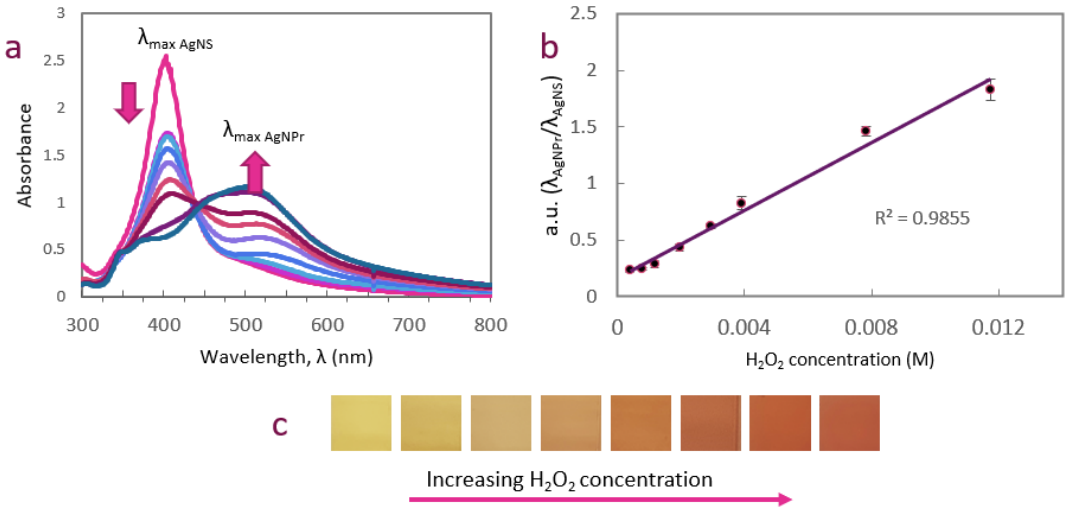

Figure 4.

(a) Extinction spectra of the AgNS/NPr sensor treated with increasing hydrogen peroxide concentrations (0.39 mM to 11.75 mM) (b) A plot of the relationship of the ratio of the IPDPR and DPR, and H_2O_2 concentrations.

Selectivity

We initially investigated the effect of halides on the sensor since they are known to either transform silver nanoparticles into nanoplates through etching or form insoluble compounds with silver.[32] Change in the mean intensities at the extinction bands of the nanospheres and nanoprisms were calculated as follows: $\Delta I = I_{tested\ species} - I_{blank}$ where the blank is the AgNS/NPr sensor before incubating with different species. As shown in **Figure 5a**, halides did not cause notable change with the plasmon band intensities compared to how hydrogen peroxide shifted absorbances at the DPR at and IPDPR bands. Among the tested species, Only H_2O_2 was able to generate a visible color change from yellow to red (**Figure 5b**). Although, minimal etching was observed, halides were not able to promote the growth of the nanoprism in the system. Other inorganic ions specifically $H_2PO_4^-$, CO_3^{2-} and SO_4^{2-} present in biological samples were also tested against the sensor. Since these species also resulted in minimal shift in intensities, we can deduce that these will not affect the hydrogen peroxide measurement if applied in biological matrices in the future.

Figure 5.
Interference test of the AgNS/NPr sensor (a) A plot of the intensity changes at the $\lambda_{max\ AgNS}$ and $\lambda_{max\ AgNPr}$ (b) Digital images of the sensor before (blank) and after incubation with H_2O_2 and different common anions.

Accuracy and Precision

As shown in Table 1, recoveries of 102.3% and 100.0% were obtained for the 5- and 11-mM samples respectively. Repeatability of the measurement of H_2O_2 from the two samples is less than 2% indicating that the developed plasmonic sensor has a great potential as an alternative to hydrogen peroxide determination in water samples.

Table 1.
Accuracy and Precision (n=5) of the sensor for analysis of hydrogen peroxide in water

Sample	$H_2O_{2\ spiked}$ (mM)	H_2O_{2found} (mM)	Recovery (%)	RSD (%, n=5)
1	5.0	5.1 (±0.1)	102.3	1.6
2	11.0	11.0 (±0.1)	100.0	0.6

Conclusion:

In summary, silver nanospheres and silver nanoprisms were successfully synthesized and mixed to produce a plasmonic hydrogen peroxide sensor which is simple, sensitive, and selective based on the growth of etched silver nanospheres on citrate-capped silver nanoprism. The growth of the nanoparticles was validated using UV-Vis spectrophotometry and TEM imaging. The advantages of the AgNS/NPR sensor are the high selectivity of the nanoprism growth in the presence of hydrogen peroxide resulting to a highly sensitive detection, and the distinct multi-color transition enabling optical read out with the naked eyes, compared to a single color of etching-based silver nanoparticle sensors. A linear range within 0.4 mM and 11.8 mM was achieved with a corresponding limit of detection of 4.8 µM. High precision and accuracy suggests that the developed sensor is a feasible alternative to hydrogen peroxide detection in water samples. In the future, this novel strategy will be further studied for the detection of H_2O_2 in food or biological samples, such as to measure biomarker substrates of oxidase enzymes, such as glucose and cholesterol.

Acknowledgments:
This work was partially funded by the National Research Council of Thailand (NRCT): N41A640073. The author would also like to thank the Chulalongkorn University Office of Academic Affairs for providing the Graduate Scholarship Program for ASEAN or Non-ASEAN Countries.

References

1. Dutta, A.; Maitra, U. *ACS Sensors* **2022,** 7, (2), 513-522.
2. Stathis, C.; Victoria, N.; Loomis, K.; Nguyen, S. A.; Eggers, M.; Septimus, E.; Safdar, N. *Future Microbiology* **2021,** 16, (2), 119-130.
3. Krishnan, J.; Subhash, N. N.; Muraleedharan, C. V.; Mohanan, P. V.; Nandakumar, M.; Neethu, S.; Rethnagireeshwar, R. *Transactions of the Indian National Academy of Engineering* **2020,** 5, (2), 289-294.
4. Mohanan, P. V.; Sangeetha, V.; Sabareeswaran, A.; Muraleedharan, V.; Jithin, K.; Vandana, U.; Varsha, S. B. *Environmental Science and Pollution Research* **2021,** 28, (47), 66602-66612.
5. Arunwuttipong, A.; Jangtawee, P.; Vchirawongkwin, V.; Kangwansupamonkon, W.; Asavanant, K.; Ekgasit, S. *Open Access Macedonian Journal of Medical Sciences* **2021,** 9, (E), 847-856.
6. Sies, H. *Redox Biology* **2017,** 11, 613-619.
7. Grisham, M. B. *Comparative Biochemistry and Physiology Part A: Molecular & Integrative Physiology* **2013,** 165, (4), 429-438.
8. de la Rica, R.; Stevens, M. M. *Nature Nanotechnology* **2012,** 7, (12), 821-824.
9. Wang, L.; Kang, X.; Pan, D. *Inorganic Chemistry* **2017,** 56, (11), 6122-6130.
10. Xu, J.; Jiang, D.; Qin, Y.; Xia, J.; Jiang, D.; Chen, H.-Y. *Analytical Chemistry* **2017,** 89, (4), 2216-2220.
11. Pratsinis, A.; Kelesidis, G. A.; Zuercher, S.; Krumeich, F.; Bolisetty, S.; Mezzenga, R.; Leroux, J.-C.; Sotiriou, G. A. *ACS Nano* **2017,** 11, (12), 12210-12218.
12. Veal, E. A.; Day, A. M.; Morgan, B. A. *Molecular Cell* **2007,** 26, 1-14.
13. Klassen, N. V.; Marchington, D.; McGowan, H. C. E. *Analytical Chemistry* **1994,** 66, (18), 2921-2925.
14. Rubio, C. P.; Cerón, J. J. *BMC Veterinary Research* **2021,** 17, (1), 226.
15. Luo, C.; Liu, X.; Liu, F.; He, N.; Yu, R.; Liu, X. *Journal of Electroanalytical Chemistry* **2022,** 904, 115930.
16. Lee, Y.-D.; Lim, C.-K.; Singh, A.; Koh, J.; Kim, J.; Kwon, I. C.; Kim, S. *ACS Nano* **2012,** 6, (8), 6759-6766.
17. Liu, J.; Dong, Z.-Z.; Yang, C.; Li, G.; Wu, C.; Lee, F.-W.; Leung, C.-H.; Ma, D.-L. *Scientific Reports* **2017,** 7, (1), 8980.
18. Gaikwad, R.; Thangaraj, P. R.; Sen, A. K. *Scientific Reports* **2021,** 11, (1), 2960.
19. Wu, S.; Tan, S. Y.; Ang, C. Y.; Luo, Z.; Zhao, Y. *Chemical Communications* **2016,** 52, (17), 3508-3511.
20. Liang, M.; Yan, X. *Accounts of Chemical Research* **2019,** 52, (8), 2190-2200.
21. Peng, W.; Li, W.; Han, H.; Liu, H.; Liu, P.; Gong, X.; Chang, J. *VIEW* **2022,** 3, (1), 20200191.
22. Neal, C. J.; Gupta, A.; Barkam, S.; Saraf, S.; Das, S.; Cho, H. J.; Seal, S. *Scientific Reports* **2017,** 7, (1), 1324.
23. Li, Y.; Wang, Y.; Fu, C.; Wu, Y.; Cao, H.; Shi, W.; Jung, Y. M. *Analyst* **2020,** 145, (2), 607-612.
24. Xue, M.; Mao, W.; Chen, J.; Zheng, F.; Chen, W.; Shen, W.; Tang, S. *Analyst* **2021,** 146, (22), 6726-6740.

25. Nitinaivinij, K.; Parnklang, T.; Thammacharoen, C.; Ekgasit, S.; Wongravee, K. *Analytical Methods* **2014,** 6, 9816–9824.
26. Nguyen, N. D.; Nguyen, T. V.; Chu, A. D.; Tran, H. V.; Tran, L. T.; Huynh, C. D. *Arabian Journal of Chemistry* **2018,** 11, (7), 1134-1143.
27. Lertvachirapaiboon, C.; Maruyama, T.; Baba, A.; Ekgasit, S.; Shinbo, K.; Kato, K. *Analytical Sciences* **2019,** 35, (3), 271-276.
28. Tran, H. V.; Nguyen, T. V.; Nguyen, L. T. N.; Hoang, H. S.; Huynh, C. D. *Journal of Science: Advanced Materials and Devices* **2020,** 5, (3), 385-391.
29. Yoon, S.-J.; Nam, Y.-S.; Lee, H.-J.; Lee, Y.; Lee, K.-B. *Sensors and Actuators B: Chemical* **2019,** 300, 127045.
30. Parnklang, T.; Lertvachirapaiboon, C.; Pienpinijtham, P.; Wongravee, K.; Thammacharoen, C.; Ekgasit, S. *RSC Advances* **2013,** 3, (31), 12886-12894.
31. Pastoriza-Santos, I.; Liz-Marzan, L. M. *Journal of Materials Chemistry* **2008,** 18.
32. Phoonsawat, K.; Ratnarathorn, N.; Henry, C. S.; Dungchai, W. *Analyst* **2018,** 143, (16), 3867-3873.

APPLICATION OF TWO-DIMENSIONAL THIN-LAYER CHROMATOGRAPHY FOR IMPROVED ANALYSIS OF AGARWOOD OIL

Phawida Yodthongchai[1], Isaya Thaveesangsakulthai[1], Charoenkwan Kraiya[1], Thumnoon Nhujak[2], Chadin Kulsing[2] * and Luxsana Dubas[1]*

[1]Department of Chemistry, Faculty of Science, Chulalongkorn University, Bangkok 10330, Thailand

[2]Chromatographic Separation and Flavor Chemistry Research Unit and Center of Molecular Sensory Science, Department of Chemistry, Faculty of Science, Chulalongkorn University, Bangkok 10330, Thailand

*e-mail: ckulsing@gmail.com and luxsana.l@chula.ac.th

Abstract: Agarwood oils are considerably one of the most valuable essential oils which requires efficient essential oil analysis to investigate the adulterants and qualities of genuine agarwood oil. TLC has been recognized as a simple and effective approach to perform this task. This study developed comprehensive two dimensional thin-layer chromatography (TLC×TLC) technique for an agarwood sample. The system employed a single stationary phase of silica gel 60 and two different mobile phase systems. Gas Chromatography-Mass Spectrometry (GC-MS) analysis was applied to investigate the agarwood sample. The best mobile phase system is dichloromethane for the first dimensional and 9:1 (v:v) hexane/ethyl acetate in second dimensional separations. This showed the greater separation with the orthogonality (A_0) of 0.6636 based on the asterisk approach separating 14 spots of the agarwood sample compared with 9 spots separated by the conventional one dimensional TLC analysis using 1:1 (v:v) hexane/dichloromethane. The developed TLC×TLC is expected to be applicable as an effective method providing a fingerprint of essential oils in the future.

Introduction:

The resinous heartwood of Aquilaria trees which is formed as a result of infection or injury-induced defense is known as agarwood.[1] Agarwood oil is in high demand on the present global market which has been used as an ingredient in perfumes, traditional medical preparations, or incense in religious ceremonies (Buddhism, Hinduism, and Islam).[2] Agarwood oil consists of a complex mixture of chemicals such as sesquiterpenes, oxygenated sesquiterpenes and chromone derivatives.[3] Thin layer chromatography (TLC), as a convenient, simple, fast, and cost-efficient separation technique, is also an indispensable tool for the separation of complex mixtures in organic synthesis, pharmaceutical, industrial, environmental, toxicology or food analysis. TLC has widely been applied for separation of terpenoids in herb samples[4-8] including agarwood analysis.[9-11] Due to the composition of Agarwood that there are various components, the capacity to examine the samples using one dimensional TLC separation is frequently limited. The TLC×TLC has been used to separate several chemicals that cannot be separated using a single dimension TLC.[12] Multiple stationary or mobile phases with different selectivities were used in each dimensional separation to create TLC×TLC [14,15] which offers improved number of separated components within a 2D separation space. For instance, the separation of a mixture of 2,4-dinitrophenylhydrazine derivatives and hydroxy carbonyl compounds using two different stationary phases was reported.[16] In addition, two different

mobile phase systems can also be applied as illustrated in the analysis of hydroxy carbonyl compounds in the essential oils obtained from the mentha samples.[17]
Therefore, separation using a single stationary phase and two different mobile phase systems in each dimensional separation was developed in this study to improve separation of agarwood oil and avoid complexity in use of two stationary phase.

Methodology:
Materials and chemicals: The sample of agarwood oil was kindly given by Almas Oudh Al manufacturer, Thailand. The retention index (*I*) of the analyte peaks was calculated using a mixture of C8-C20 n-alkanes (purchased from Sigma Aldrich) as a reference. Vanillin was purchased from TCI, and hexane (Hex), dichloromethane (DCM), acetonitrile (ACN), sulfuric acid, ethanol, and ethyl acetate (EtOAc) were all purchased from Sigma Aldrich. TLC silica gel 60 were purchased from Merck.
GC-MS: The agarwood sample was injected (1 µL) into GC Model 7890A and MS Model 7000 (Agilent Technologies CA, USA) which consists of autosampler and column oven. The MS system consists of electron ionization (EI) and triple quadrupole mass analyzer operated in single quadrupole mode. The HP-5MS capillary column (30 m × 0.25 mm i.d., 0.25 µm film thickness; J&W Scientific, USA) was applied to separate the agarwood sample using ultra-high purity helium (99.999 %, Linde), as the carrier gas with a flow rate of 1.0 mL min^{-1}. The extracted sample was injected under splitless mode. The GC oven temperature was programmed to increase from 40 to 260 °C at a rate of 7 °C min^{-1}. The temperature of the ion source in the MS was set at 230 °C. The electron ionization voltage was - 70 eV. The mass spectra were acquired over the mass range of 30-300 Da with a scan time of 100 ms.
1D TLC separation: The 0.5 µL of agarwood sample (diluted 200 times in ACN) was loaded onto a TLC plate (1 cm × 5 cm) by using a micropipette. A 10 mL of 9:1 Hex/EtOAc, 1:1 Hex/DCM, DCM and ACN were used as the mobile phases and the separation continued until the mobile phase level reaching 4.5 cm from the bottom of a TLC plate. Vanillin solution was used to detect the spot components after the separation. The plate treated with vanillin was heated at 65 °C for 4 min resulting in the separated spot colors.
TLC×TLC separation: Before use, TLC plates were cut into the dimension of 5 cm × 5 cm. 0.5 µL of sample (diluted 200 times in ACN) was loaded at the TLC plate corner using a micropipette. ^{1}D separation on the plate was performed using the same mobile phases as in the previous section TLC separation. The plate was then dried by using dryer and turned 90 degrees for performing ^{2}D separation. The vanillin solution was used to visualize. The separation method was show in **Figure 1**.

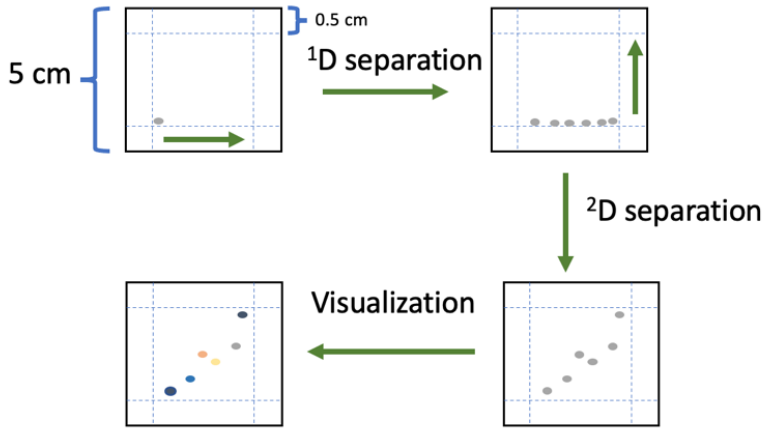

Figure 1. TLC×TLC separation method

Data processing: Data analysis and compound identification in GC-MS were performed using Agilent MassHunter software. A peak of interest was identified by the comparison of the experimental MS spectrum with the spectra from the NIST17 library (National Institute of Standards and Technology). The compounds were identified with match scores of >650 and differences of <20 units between the experimental retention indices (*I*) and the literature values on the semi-nonpolar column. The experimental *I* was obtained by comparison of the peak retention time with that of the alkanes bracketing this peak under the same experimental conditions based on the Van den Dool and Kratz relationship[13] according to equation 1.

$$I = 100n + 100\left[\frac{t_{R(i)} - t_{R(n)}}{t_{R(n+1)} - t_{R(n)}}\right] \quad (1)$$

where t_R is the retention time, n is the number of carbons of the lesser retained alkane standard and $n + 1$ is the number of carbons of the more retained alkane standard bracketing analyte i.

Orthogonality calculation: TLC×TLC separation results in this study were evaluated according to the following approach to calculate orthogonality scales which measure the quality of spot distributions in 2D spaces. Initially, a TLC×TLC result was normalized by normalizing each analyte spot position as described in equation 2.

$$^{i}D_{\text{normalized}} = \frac{^{i}d - {}^{i}d_{\min}}{^{i}d_{\max} - {}^{i}d_{\min}} \quad (2)$$

where $^{i}d_{\min}$ and $^{i}d_{\max}$ are minimum and maximum distances from the loaded position of the most and least strongly retained analytes which could be visualized using the vanillin solution. The superscript i indicates each dimensional separation, 1D or 2D. Plots between $^{1}D_{normalized}$ and $^{2}D_{normalized}$ were then constructed. The normalized results were required to further calculate orthogonality according to the asterisk equations[16] which is based on orthogonality (A_0) scale (equation 3). This is the scale considering the spots distribution in a normalized chromatogram compared with four main asterisked axes in a 2D space. A completely orthogonal separation will have A_0 of 1.[18] The higher the value of the Z parameters is the higher the A_0 value. The Microsoft Visual Basic script was developed for the calculation of A_0 values.

$$A_0 = \sqrt{Z_- \cdot Z_+ \cdot Z_1 \cdot Z_2} \quad (3)$$

where Z_-, Z_+, Z_1 and Z_2 are parameters linked to the spot distribution around the x, y, and other two diagonal lines in a two-dimensional (2D) space in **figure 2**. The standard deviation of these distances is calculated and describes the standard deviation of the spots around the Z line. By taking the standard deviation of these distances in effect determining the degree of spreading of spots around the four Z lines. The S_{Zx} refers to "spreading" around line Z_x as demonstrated.

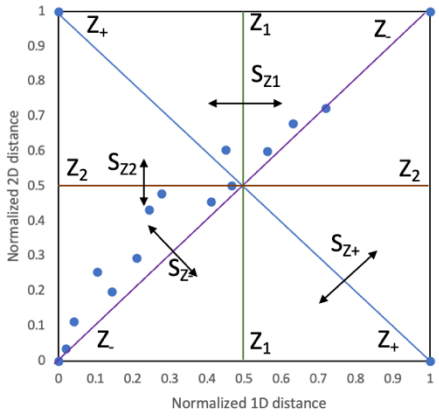

Figure 2 Normalized TLC×TLC result of the agarwood oil with the lines used for orthogonality calculation

In addition, number of separated spots and bin coverage (number of spots to be resolved) were calculated according to the previously reported approaches.[19] Bin coverage is an alternative parameter to measure which measure the quality of spot distributions in 2D spaces. Further data analysis was performed using Microsoft Excel.

Results and Discussion:

GC-MS analysis

Volatile compounds of the agarwood sample were analyzed using GC-MS. Table 1 showed the major compounds of β-guaiene, dehydrofukinone, 2,2,7,7-tetramethyltricyclo[6.2.1.0(1,6)]undec-4-en-3-one, eudesm-7(11)-en-4-ol and khusimone.

Table 1. Volatile compound profiles of the agarwood sample with the literature retention indices and peak areas analyzed by GC-MS.

#	Compound	I_{Lit} [a]	Peak area (×10^5 counts·s)
1	4-Phenyl-2-butanone	1232	352
2	β-Guaiene	1490	7001
3	β-Vetispirene	1495	341
4	β-Vetivenene	1540	313
5	Spathulenol	1576	559
6	(-)-Globulol	1580	1197
7	Caryophyllene oxide	1581	238
8	Khusimone	1605	2710
9	γ-Eudesmol	1631	1188
10	Isospathulenol	1638	451
11	Agarospirol	1645	1587
12	α-Bisabolol oxide B	1655	236
13	Valerianol	1661	1411
14	2,4,5,6,7,7α-Hexahydro-3-(1-methylethyl)-7α-methyl-1H-2-indenone	1663	235
15	Khusimyl methyl ether	1680	935
16	Eudesm-7(11)-en-4-ol	1692	2977

#	Compound	I_{Lit} [a]	Peak area (×10^5 counts·s)
17	α-Costal	1695	452
18	Valerenal	1716	1761
19	2,2,7,7-Tetramethyltricyclo[6.2.1.0(1,6)]undec-4-en-3-one	1730	3754
20	Valerenol	1736	621
21	15-Hydroxy-α-muurolene	1777	1051
22	Eremophila-1,11-dien-9-one, 8α-hydroxy-	1777	242
23	Dehydrofukinone	1817	6661
24	trans-Valerenyl acetate	1832	263
25	10-Epigazaniolide	1833	1366
26	Hydroxyeremophilone	1865	257
27	Columellarin	1958	248
28	n-Hexadecanoic acid	1968	446
29	3-Pentanone, 1,5-diphenyl-	2029	346
30	9-Octadecenamide, (Z)-	2386	310

[a] Literature retention index obtained from NIST17.

One dimensional TLC

One dimensional (1D) TLC was applied to separate the same agarwood sample using four different mobile phases. The results after dyeing with the vanillin solution were shown in **Figure 3**. The mobile phase polarity decreased from ACN, DCM, 1:1 Hex/DCM and 9:1 Hex/EtOAc with the results shown in **Figures 3A-D**, respectively. For example, the decreasing polarity led to the greater separation of the lower polarity (grey,1) and the higher polarity (pink, 2) spots in **Figure 3D**, by comparing the separated spots circled in each figure. To this end, the separated numbers of spots were ~ 3, ~ 6, ~ 9 and ~ 8 with the mobile phases ACN, DCM, 1:1 Hex/DCM and 9:1 Hex/ EtOAc, respectively. The greater separation (higher selectivity and more separation space) could be obtained using 1:1 Hex/DCM. However, the number of separated spots were <10 spots using 1D TLC.

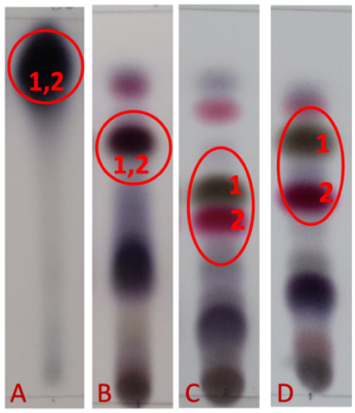

Figure 3. TLC result of the agarwood oil obtained by using different mobile phases: (A) ACN, (B) DCM, (C) 1:1 Hex/DCM and (D) 9:1 Hex/ EtOAc.

Comprehensive two-dimensional TLC

TLC×TLC approach using different combination of any two mobile phase systems in ^{1}D and ^{2}D separations based on the list of four mobile phases applied in 1D TLC. The separation results with the calculated orthogonality values (A_0) are shown in **Figure 4**. From the aspect of selectivity, the greater difference between ^{1}D and ^{2}D mobile phase polarities could be expected to provide greater A_0. This could be expected for the combination of ACN and 9:1 hexane/ethyl acetate. However, the corresponding result in **Figure 4B** did not show the greatest separation (~10 separated spots and $A_0 = 0.52$). This is due to the low separation power of ACN. In **Figure 4A** ACN used as ^{1}D mobile phase did not show the better separation. DCM with the second highest polarity but with the higher separation power (~6 spots in **Figure 3B**) thus showed the greatest result (~14 separated spots $A_0 = 0.66$, **Figure 4D**). Alternatively, combination of the two mobile phases: 1:1 Hex/DCM and 9:1 Hex/ EtOAc which the polarities are relative similar with the higher separation power (both with ~9 spots in 1D TLC **Figures 3C-D**) also provided good separation result (~12 separated spots $A_0 = 0.59$, **Figure 4F**).

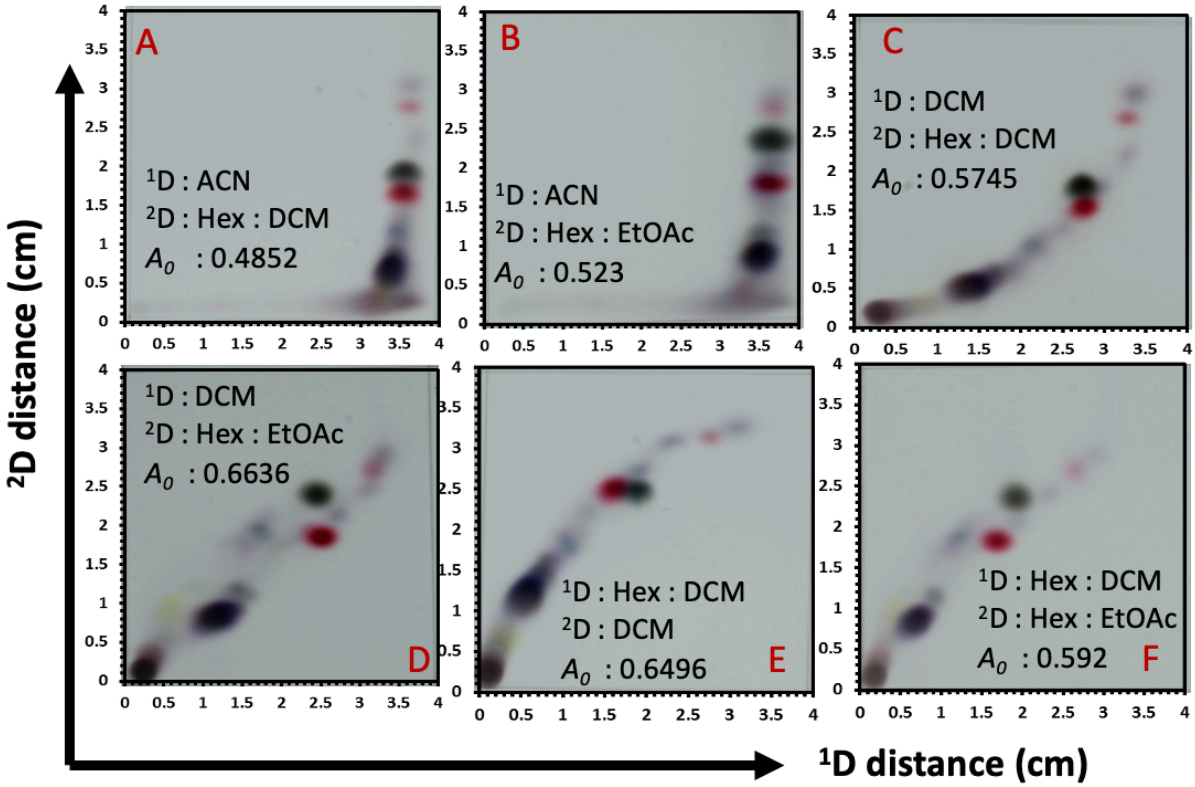

Figure 4. TLC×TLC result of the agarwood oil obtained by using different mobile phase system provided in Table 2.

Table 2. Mobile phase systems applied in TLC×TLC analyses with the corresponding separation results.

Fig.	Mobile phase system		Separation results		
	^{1}D mobile phase	^{2}D mobile phase	A_0	Bin coverage	#Separated spots
2A	ACN	1:1 Hex:DCM	0.49	7	11
2B	ACN	9:1 Hex:EtOAc	0.52	6	10
2C	DCM	1:1 Hex:DCM	0.57	7	12
2D	DCM	9:1 Hex:EtOAc	0.66	9	14
2E	1:1 Hex:DCM	DCM	0.65	9	13
2F	1:1 Hex:DCM	9:1 Hex:EtOAc	0.59	8	12

Conclusion: TLC×TLC technique was developed employing a single stationary phase with two different mobile phases in ^{1}D and ^{2}D separations. The suitable conditions were demonstrated to provide the greater results compared with the conventional 1D TLC analysis with more separated components and more separation space. These are expectedly applicable for separation and fingerprinting based analyses of other types of agarwood oils in the future.

Acknowledgements: This research was supported by the Development and Promotion of Science and Technology Talents Project (DPST). Also, thanks to Almas Oudh Al manufacturer, Thailand for supporting the agarwood oil sample.

References:

1. Kim Ngan TT, Thu Thuy DT, Tuyen TT, Inh CT, Bich HT, Long PQ, et al. Asian J Chem. 2019;32:36-40.
2. Nizam TS, Nurlaila I, Ali NAM, Mailina J, Hezri FRM, Nasir TM. Malaysian J. Anal. Sci. 2013 17 403-413
3. Ismail N, Ali N, Jamil M, Rahiman M, Taib M, Tajuddin S. Chem. Nat. Compd. 2015;51:776-779.
4. Ahadi A, Partoazar A, Abedi-Khorasgani MH, Shetab-Boushehri SV. J Biomed Res. 2011;25:362-367
5. Pittet A, Royer D. J Agric Food Chem. 2002;50:243-247.
6. Sajewicz M, Wojtal Ł, Natić M, Staszek D, Waksmundzka-Hajnos M, Kowalska T. J Liq Chromatogr Relat Technol. 2011;34:848-863.
7. Sajewicz M, Staszek D, Natić M, Wojtal Ł, Waksmundzka-Hajnos M, Kowalska T. J Liq Chromatogr Relat Technol. 2011;34:864-887.
8. Zhang Y, Chen R, Ma H, Chen S. J Agric Food Chem. 2015;63:8819-8828.
9. Zhang XL, Liu YY, Wei JH, Yang Y, Zhang Z, Huang JQ, Chen HQ, Liu YJ. Chin Chem Lett. 2012;23:727-730.
10. Chong S, Osman MF, Bahari N, Nuri EA, Zakaria R, Rahim K. J Agrobiotechnol. 2015; 5:1-16.
11. Liu Y, Chen H, Yang Y, Zhang Z, Wei J, Meng H, Chen W, Feng J, Gan B, Chen X, Gao Z, Huang J, Chen B, Chen H. Molecules. 2013;18:3086-3106.

12. Gocan S. J Liq Chromatogr Relat Technol. 2004;27:1105-1113.
13. Jiang M, Kulsing C, Nolvachai Y, Marriott P. J Anal Chem. 2015;87:5753-5761.
14. Petkova Z, Antova G, Bulg Chem Commun. 2014;46:100–105.
15. Rabel F, Sherma J. J Liq Chromatogr Relat Technol. 2016;39:627-639.
16. Anet EFLJ. J Chromatogr, A. 1962;9:291-294.
17. Hawryl M, Swieboda R, Hawryl A, Niemiec M, Stepak K, Waksmundzka-Hajnos M, Szymczak G. J Liq Chromatogr Relat Technol. 2015;38:1794–1801.
18. Camenzuli M, Schoenmakers PJ. Anal Chim Acta. 2014;838:93-101.
19. Kulsing C, Nolvachai Y, Rawson P, Evans DJ, Marriott PJ. Anal Chem. 2016;88:3529-3538.

Session C:
CHEMISTRY
(Organic & Medicinal Chemistry)

SYNTHESIS OF ENAMINE DERIVATIVES OF USNIC ACID AS α-GLUCOSIDASE INHIBITORS

Nhung Nguyen Thi My, Hoa Tai Xuan Hang, Warinthorn Chavasiri*
Department of Chemistry, Faculty of Science, Chulalongkorn University, Bangkok 10330, Thailand
*E-mail: warinthorn.c@chula.ac.th

Abstract:

Usnic acid, a secondary metabolite of lichens with a unique dibenzofuran scaffold distributed in various lichen species, was structurally modified to enamine derivatives **1**–**14**. All derivatives were evaluated for their α-glucosidase inhibitory activity. Most of the derivatives displayed potent inhibition with the IC_{50} values ranging from 16.56 to 43.29 μM in comparison with acarbose as the standard inhibitor (IC_{50} = 100.00 μM). Compound **5** was revealed as the strongest derivative with IC_{50} = 16.56 ± 1.05 μM.

Introduction:

Diabetes mellitus is a chronic disease characterized by hyperglycemia, which is described as irregularities in glucose, lipid, and protein metabolism in the body.[1] α-Glucosidase, which is an important carbohydrate hydrolyzing enzyme located in the small intestine, could convert carbohydrates into monosaccharides to provide energy for the body. α-Glucosidase inhibitors can delay carbohydrate digestion by inhibiting enzymes in the stomach, lowering postprandial blood glucose and insulin levels.[2] To the best of our knowledge, acarbose, miglitol, and voglibose are known as the best α-glucosidase commercial inhibitors. However, they have many side effects.[3] Therefore, more potent, less toxic α-glucosidase inhibitors are required.

Usnic acid is a naturally occurring dibenzofuran derivative distributed in various lichen species including *Usnea* (Usneaceae), *Parmelia* (Parmeliaceae), *Cladonia* (Cladoniaceae), *Lecanora* (Lecanoraceae), and *Ramalina* (Ramalinaceae). Usnic acid attracts much attention due to its wide range of biological activities, including anticancer, antifungal, antiviral, antibacterial, anti-inflammatory, insecticidal, as well as antidiabetic activities.[4,5,6,7] According to the structure-activity relationships (SARs) study, usnic acid enamine derivatives demonstrated better biological activities comparing to the original compound.[8] Previous reports indicated that some usnic acid benzylidene derivatives[6] and usnic acid ester derivatives[7] were potent α-glucosidase inhibitors. On the other hand, the study on α-glucosidase inhibitory activity of a series of thiobarbituric enamine derivatives and barbituric acid derivatives found that a hydrogen bond was observed between the nitrogen atom of enamine moiety with amino acid Thr215.[9] Furthermore, many articles on α-glucosidase inhibition showed that halogen substituents gave strong inhibition when they were introduced into the starting material.[10,11]

From the idea of enamine moiety and halogen-containing derivatives that enhanced usnic acid biological properties, a series of halogen-containing usnic acid enamine derivatives were synthesized and evaluated for α-glucosidase inhibitory activity.

Methodology:

The general procedure of the synthesis of halogen-containing usnic acid enamine derivatives

The synthetic route of halogen-containing usnic acid enamine derivatives **1**–**14** is shown in **Scheme 1** while their structures are displayed in **Table 1**. Specifically, a mixture of

(+)-usnic acid (1 mmol) and amine (1.5 mmol) in EtOH (12 mL) was heated under reflux conditions.[12] Thin-layer chromatography (TLC) was used to assess the reactions. After finishing, the reaction mixture was cooled, and then 10 mL of distilled water was added. The precipitate was collected, washed with cold water, and dried in air. The precipitation was chromatographed on a silica gel column by a mixture of *n*-hexane and ethyl acetate to obtain desirable products. The structures of these compounds were characterized by using ^{1}H, ^{13}C NMR, and HRMS data.

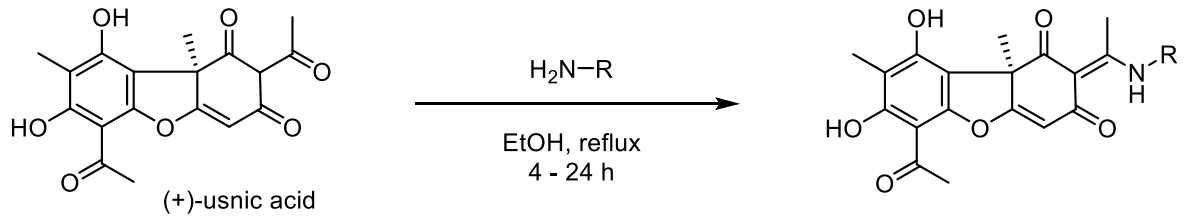

Scheme 1. General procedure of the synthesis of halogen-containing usnic acid enamine derivatives

(R,E)-6-acetyl-2-(1-((4-fluorophenyl)amino)ethylidene)-7,9-dihydroxy-8,9b-dimethyldibenzo[b,d]furan-1,3(2H,9bH)-dione (**1**): yellow solid; 50.12%; ^{1}H NMR (500 MHz, $CDCl_3$): δ 11.76 (s, 1H), 7.18 (d, *J* = 7.5 Hz, 4H), 5.87 (s, 1H), 2.68 (s, 3H), 2.56 (s, 3H), 2.09 (s, 3H), 1.75 (s, 3H). ^{13}C NMR (125 MHz, $CDCl_3$): δ 200.8, 198.9, 174.4, 163.7, 163.1, 161.1, 158.2, 155.9, 132.1, 127.7, 127.7, 117.0, 116.8, 108.3, 104.9, 102.4, 101.5, 57.6, 32.1, 31.4, 20.7, 7.6.

(R,E)-6-acetyl-2-(1-((2-chlorophenyl)amino)ethylidene)-7,9-dihydroxy-8,9b-dimethyldibenzo[b,d]furan-1,3(2H,9bH)-dione (**2**): yellow solid; 60.08%; ^{1}H NMR (500 MHz, $CDCl_3$): δ 11.76 (s, 1H), 7.55 (d, *J* = 9.5 Hz, 1H), 7.37 (dd, *J* = 9.5, 2.5 Hz, 1H), 7.37 (t, *J* = 2.5 Hz, 1H), 7.27 (d, *J* = 2.5 Hz, 1H), 5.90 (s, 1H), 2.69 (s, 3H), 2.52(s, 3H), 2.10 (s, 3H), 1.77(s, 3H). ^{13}C NMR (125 MHz, $CDCl_3$): δ 200.8, 199.0, 191.3, 175.1, 174.9, 163.7, 158.2, 155.9, 134.0, 131.1, 130.8, 129.7, 128.1, 127.9, 108.4, 105.0, 103.0, 102.4, 101.5, 57.7, 32.0, 31.5, 20.7, 7.6.

(R,E)-6-acetyl-2-(1-((3-chlorophenyl)amino)ethylidene)-7,9-dihydroxy-8,9b-dimethyldibenzo[b,d]furan-1,3(2H,9bH)-dione (**3**): yellow solid; 57.44%; ^{1}H NMR (500 MHz, $CDCl_3$): δ 11.71 (s, 1H), 7.42 (t, *J* = 8.0 Hz, 1H), 7.39 (d, *J* = 8.0 Hz, 1H), 7.23 (s, 1H), 7.42 (d, *J* = 7.5 Hz, 1H), 5.88 (s, 1H), 2.68 (s, 3H), 2.59 (s, 3H), 2.10 (s, 3H), 1.75 (s, 3H). ^{13}C NMR (125 MHz, $CDCl_3$): δ 200.8, 199.1, 191.2, 175.1, 174.1, 163.7, 158.2, 155.9, 137.4, 135.5, 130.8, 128.6, 126.2, 124.2, 108.4, 104.9, 132.0, 102.3, 101.5, 57.8, 32.0, 31.5, 20.8, 7.6.

(R,E)-6-acetyl-2-(1-((4-chlorophenyl)amino)ethylidene)-7,9-dihydroxy-8,9b-dimethyldibenzo[b,d]furan-1,3(2H,9bH)-dione (**4**): yellow solid; 49.10%; ^{1}H NMR (500 MHz, $CDCl_3$): δ 13.23 (s, 1H), 11.60 (s, 1H), 7.36 (d, *J* = 8.0 Hz, 2H), 7.13 (d, *J* = 8.0 Hz, 2H), 5.73 (s, 1H), 2.54 (s, 3H), 2.51 (s, 3H), 1.94 (s, 3H), 1.62 (s, 3H). ^{13}C NMR (125 MHz, $CDCl_3$): δ 200.3, 198.6, 190.7, 174.4, 173.7, 163.4, 157.9, 155.5, 134.6, 133.8, 129.7, 126.9, 107.9, 104.6, 102.7, 101.9, 101.1, 57.4, 31.7, 31.0, 20.3, 7.4

(R,E)-6-acetyl-2-(1-((4-bromophenyl)amino)ethylidene)-7,9-dihydroxy-8,9b-dimethyldibenzo[b,d]furan-1,3(2H,9bH)-dione (**5**): yellow solid; 54.04%; ^{1}H NMR (500 MHz, $CDCl_3$): δ 13.33 (s, 1H), 11.66 (s, 1H), 7.59 (d, *J* = 8.0 Hz, 2H), 7.08 (d, *J* = 8.0 Hz, 2H), 5.85 (s, 1H), 5.29 (s, 1H), 2.66 (s, 3H), 2.57 (s, 3H), 2.07 (s, 3H), 1.73 (s, 3H). ^{13}C NMR (125 MHz, $CDCl_3$): δ 200.7, 199.0, 174.0, 163.7, 158.2, 155.9, 135.2, 133.0, 127.5, 122.2, 108.4, 104.9, 102.4, 101.5, 53.5, 32.0, 31.3, 29.8, 20.6, 7.6.

(R,E)-6-acetyl-2-(1-((2,3-dichlorophenyl)amino)ethylidene)-7,9-dihydroxy-8,9b-dimethyldibenzo[b,d]furan-1,3(2H,9bH)-dione (**6**): yellow solid; 45.11%; ^{1}H NMR (500 MHz, $CDCl_3$): δ 11.65 (s, 1H), 7.53 (d, *J* = 8.0 Hz, 1H), 7.33 (t, *J* = 8.0 Hz, 1H), 7.20 (d, *J* = 8.0 Hz, 1H), 5.90 (s, 1H), 2.69 (s, 3H), 2.52 (s, 3H), 2.09 (s, 3H), 1.76 (s, 3H). ^{13}C NMR (125 MHz, $CDCl_3$): δ 200.8, 199.1, 191.3, 175.3, 174.7, 163.7, 158.2, 157.6, 155.8, 135.8, 134.8, 130.4, 127.9, 126.2, 108.5, 104.9, 103.1, 102.3, 98.5, 57.8, 32.0, 28.1, 20.7, 7.6.

(R,E)-6-acetyl-2-(1-((2,4-dichlorophenyl)amino)ethylidene)-7,9-dihydroxy-8,9b-dimethyldibenzo[b,d]furan-1,3(2H,9bH)-dione (**7**): yellow solid; 48.91%; ^{1}H NMR (500 MHz, $CDCl_3$): δ 11.65 (s, 1H), 7.57 (d, *J* = 2.0 Hz, 1H), 7.37 (dd, *J* = 8.5, 2.5 Hz, 1H), 7.2 (d, *J* = 8.5 Hz, 1H), 5.90 (s, 1H), 2.69 (s, 3H), 2.52 (s, 3H), 2.10 (s, 3H), 1.76 (s, 3H). ^{13}C NMR (125 MHz, $CDCl_3$): δ 200.8, 199.1, 191.3, 175.3, 174.9, 163.7, 158.2, 155.8, 135.0, 132.8, 131.8, 130.6, 128.8, 128.3, 108.5, 104.9, 103.2, 102.3, 101.5, 57.8, 32.0, 31.5, 20.7, 7.7.

(R,E)-6-acetyl-2-(1-((2,5-dichlorophenyl)amino)ethylidene)-7,9-dihydroxy-8,9b-dimethyldibenzo[b,d]furan-1,3(2H,9bH)-dione (**8**): yellow solid; 50.21%; ^{1}H NMR (500 MHz, $CDCl_3$): δ 11.62 (s, 1H), 7.48 (d, *J* = 9.0 Hz, 1H), 7.34 (dd, *J* = 9.0, 2.5 Hz, 1H), 7.30 (d, 1H, *J* = 2.5 Hz), 5.90 (s, 1H), 2.69 (s, 3H), 2.54 (s, 3H), 2.10 (s, 3H), 1.76 (s, 3H). ^{13}C NMR (125 MHz, $CDCl_3$): δ 200.8, 199.1, 191.3, 175.3, 174.8, 163.8, 158.2, 155.8, 135.1, 133.6, 131.5, 129.8, 129.6, 128.1, 108.5, 104.9, 103.2, 102.3, 101.6, 57.9, 32.0, 31.5, 20.7, 7.6.

(R,E)-6-acetyl-2-(1-((2,6-dichlorophenyl)amino)ethylidene)-7,9-dihydroxy-8,9b-dimethyldibenzo[b,d]furan-1,3(2H,9bH)-dione (**9**): yellow solid; 44.10%; ^{1}H NMR (500 MHz, $CDCl_3$): δ 11.69 (s, 1H), 7.49 (dd, *J* = 8.0, 1.0 Hz, 1H), 7.47 (dd, *J* = 1.0 Hz, 1H), 7.33 (t, *J* = 8.0 Hz, 1H), 5.93 (s, 1H), 2.69 (s, 3H), 2.44 (s, 3H), 2.10 (s, 3H), 1.78 (s, 3H). ^{13}C NMR (125 MHz, $CDCl_3$): δ 200.8, 199.1, 191.5, 176.2, 175.3, 163.7, 158.3, 155.8, 133.7, 133.6, 132.5, 130.2, 129.1, 129.0, 108.5, 105.0, 102.8, 102.4, 101.5, 57.8, 32.0, 31.5, 20.2, 7.7.

*(R,E)-6-*acetyl-*2-(1-((3,4-dichlorophenyl)amino)ethylidene)-7,9-dihydroxy-8,9b-dimethyldibenzo[b,d]furan-1,3(2H,9bH)-dione* (**10**): yellow solid; 54.77%; ^{1}H NMR (500 MHz, $CDCl_3$): δ 11.62 (s, 1H), 7.56 (d, *J* = 8.5 Hz, 1H), 7.35 (d, *J* = 2.5 Hz, 1H), 7.07 (dd, *J* = 8.5, 2.5 Hz, 1H), 5.88 (s, 1H), 2.68 (s, 3H), 2.59 (s, 3H), 2.10 (s, 3H), 1.75 (s, 3H). ^{13}C NMR (125 MHz, $CDCl_3$): δ 200.8, 199.1, 191.2, 174.0, 163.8, 158.2, 155.8, 135.6, 134.0, 132.8, 131.5, 127.9, 125.3, 108.5, 104.8, 103.2, 102.3, 101.6, 77.4, 77.2, 76.9, 57.8, 32.0, 31.5, 20.7, 7.7.

(R,E)-6-acetyl-2-(1-((3,5-dichlorophenyl)amino)ethylidene)-7,9-dihydroxy-8,9b-dimethyldibenzo[b,d]furan-1,3(2H,9bH)-dione (**11**): yellow solid; 63.09%; ^{1}H NMR (500 MHz, $CDCl_3$): δ 11.57 (s, 1H), 7.41 (t, *J* = 2.0 Hz, 1H), 7.14 (d, *J* = 2.0 Hz, 2H), 5.89 (s, 1H), 2.69 (s, 3H), 2.60 (s, 3H), 2.10 (s, 3H), 1.75 (s, 3H). ^{13}C NMR (125 MHz, $CDCl_3$): δ 200. 8, 199.2, 191.3, 175.3, 173.9, 163.8, 158.2, 155.8, 138.2, 136.2, 128.6, 124.7, 115.1, 110.6, 108.6, 102.3, 101.6, 57.9, 31.9, 31.5, 29.8, 7.7.

(R,E)-6-acetyl-2-(1-((3,4-difluorophenyl)amino)ethylidene)-7,9-dihydroxy-8,9b-dimethyldibenzo[b,d]furan-1,3(2H,9bH)-dione (**12**): yellow solid; 70.01%; ^{1}H NMR (500 MHz, $CDCl_3$): δ 11.64 (s, 1H), 7.30 (d, *J* = 9.0 Hz, 1H), 7.09 (t, *J* = 9.0 Hz, 2H), 6.97 (d, *J* = 9.0 Hz, 1H), 5.87 (s, 1H), 2.67 (s, 3H), 2.57 (s, 3H), 2.08 (s, 3H), 1.74 (s, 3H). ^{13}C NMR (125 MHz, $CDCl_3$): δ 200.8, 199.1, 191.2, 175.1, 174.3, 163.7, 158.2, 155.8, 151.5, 149.6, 132.5, 122.5, 118.5, 115.8, 108.4, 104.9, 103.0, 102.3, 101.5, 57.8, 32.0, 31.4, 20.6, 7.6.

(R,E)-6-acetyl-2-(1-((4-chloro-3-hydroxyphenyl)amino)ethylidene)-7,9-dihydroxy -8,9b-dimethyldibenzo[b,d]furan-1,3(2H,9bH)-dione (**13**): yellow solid; 73.33%; ^{1}H NMR (500 MHz, $CDCl_3$): δ 11.72 (s, 1H), 7.41 (d, *J* = 8.5 Hz, 1H), 6.89 (d, *J* = 2.5 Hz, 1H), 6.72 (dd, *J* = 8.5 Hz, 2.5 Hz, 1H), 5.88 (s, 1H), 2.68 (s, 3H), 2.58 (s, 3H), 2.09 (s, 3H), 1.74 (s, 3H). ^{13}C NMR (125 MHz, $CDCl_3$): δ 200.8, 199.0, 191.3, 175.2, 174.1, 163.7, 158.2, 155.9, 152.6, 136.1, 130.1, 120.1, 118.6, 113.9, 108.4, 105.0, 102.9, 102.3, 101.5, 57.8, 32.0, 31.5, 20.8, 7.6.

(R,E)-6-acetyl-2-(1-((2-chloro-4-hydroxyphenyl)amino)ethylidene)-7,9-dihydroxy-8,9b-dimethyldibenzo[b,d]furan-1,3(2H,9bH)-dione (**14**): yellow solid; 78.71%; ^{1}H NMR (500 MHz, $CDCl_3$): δ 11.97 (s, 1H), 7.38 (d, J = 8.5 Hz, 1H), 7.02 (d, J = 2.5 Hz, 1H), 6.86 (dd, J = 8.5 Hz, 2.5 Hz, 1H), 6.00 (s, 1H), 2.65 (s, 3H), 2.45 (s, 3H), 1.97 (s, 3H), 1.70 (s, 3H). ^{13}C NMR (125 MHz, $CDCl_3$): δ 201.4, 198.5, 175.3, 174.2, 162.9, 158.6, 157.8, 156.0, 130.1, 129.6, 124.7, 116.7, 115.5, 106.9, 105.4, 102.7, 102.6, 101.3, 57.1, 32.0, 31.5, 20.6, 7.9.

α-Glucosidase inhibition assay

This activity was performed by the method described by Ramadhan and coworkers.[13] Briefly, α-glucosidase (0.1 U/mL) and substrate (1 mM *p*-nitrophenyl-α-*D*-glucopyranoside) were dissolved in 0.1 M phosphate buffer (pH 6.9). A 10 µL test sample was pre-incubated with α-glucosidase (40 µL) at 37 ºC for 10 min. A substrate solution (50 µL) was then added to the reaction mixture and incubated at 37 ºC for an additional 20 min and terminated by adding 1 M Na_2CO_3 solution (100 µL). Enzymatic activity was quantified by measuring the absorbance at 405 nm (ALLSHENG AMR-100 microplate reader). The percentage inhibition was calculated as follows: % Inhibition = $[(A_0-A_1)/A_0]$ x 100, where: A_0 is the absorbance without the sample; A_1 is the absorbance with the sample. The IC_{50} value was deduced from the plot of % inhibition versus concentration of the test sample. Acarbose was used as standard control and the experiment was performed in triplicate.

Results and Discussion:

As shown in **Table 1**, among the mono-halogenated derivatives (**1**–**5**), compound **4** having chlorine group at 4-position was found to be the most active derivative. The inhibitory activity decreased when chloro substituent shifted from 4-position in compound **4** to 2- and 3-position, compounds **2** and **3**, respectively. This may be explained that the chloro substituent at 3-position did not have the conjugation with the enamine moiety, it just had the inductive effect. Therefore, it slightly affected on the aromatic ring, which led to a less electron deficiency in the comparison with the substituent at 4-position. Besides, among 3 halogen atoms (fluorine, bromine, and chlorine), compounds bearing bromine and chlorine substituents were found to display better inhibitions in the comparison with that containing fluorine. Compound **5** with a bromine atom at 4-position was the most active derivative with IC_{50} = 16.56 ± 1.05 µM.

In addition, with the di-halogenated derivatives (**6**–**12**), the presence of two adjacent substituents or two substituents located one carbon apart contributed to increasing the activity, as in compounds **6**, **7**, **10**, and **11**. Compound **14** bearing two fluoro atoms at 3- and 4-positions also gave no good inhibition, which was consistent with that observed from the mono-halogenated derivatives. Replacing one chlorine substituent with one hydroxyl group as in compounds **13** and **14** gave the same inhibition.

Table 1. α-Glucosidase inhibitory activity of halogen-containing usnic acid enamine derivatives.

Compound	R	% Inhibition at 50 µM	IC_{50} (µM)[a]
1	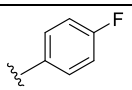	65.97	43.29 ± 2.01

2		16.70	-[b]
3	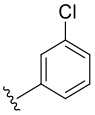	28.17	-
4	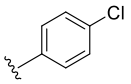	78.33	18.59 ± 0.65
5	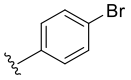	99.06	16.56 ± 1.05
6	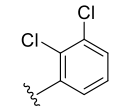	97.59	20.29 ± 1.16
7	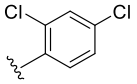	81.96	27.41 ± 1.40
8	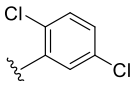	26.69	-
9	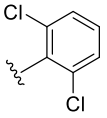	33.78	-
10	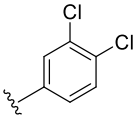	84.83	24.94 ± 0.99
11	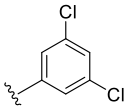	82.48	28.54 ± 1.65
12	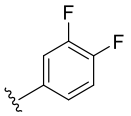	16.02	-
13	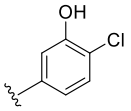	88.14	25.07 ± 1.57
14	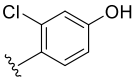	71.70	29.40 ± 2.08
Usnic acid			>200
Acarbose			100.00 ± 0.95

[a]IC_{50} value was expressed as mean ± SD from three independent experiments.
[b]IC_{50} value was not tested if the inhibition rate was less than 50% at 50μM.

Conclusion:

Fourteen halogen-containing usnic acid enamine derivatives were successfully synthesized, characterized, and evaluated for α-glucosidase inhibitory activity. Most derivatives displayed potential inhibition with the IC_{50} values ranging from 16.56 to 43.29 μM better than the original usnic acid and the positive control, acarbose. The SARs indicated that usnic acid enamine derivatives with halogenated phenyl moiety were the potent inhibitors. The slight difference on α-glucosidase inhibitory activity was mainly affected by the position as well as the number of halogen substituents.

Acknowledgements:

NNTM is grateful thank to the Chulalongkorn University's Graduate Scholarship Programme for ASEAN or Non-ASEAN Countries.

References:

1. Roglic G. Int J Non-Comm. Dis. 1. 2016;1:3-8.
2. Hollander P. Diabetes Spectr. 2007;20:159-165.
3. Aoki K, Muraoka T, Ito Y, Togashi Y, Terauchi Y. Int Med. 2010;49:1085-1087.
4. Guo L, Shi Q, Fang JL, Mei N, Ali AA, Lewis SM, Leakey JEA, Frankos VH. J Environ Sci Health A. 2008;26:317-338.
5. Araújo AAS, de Melo MGD, Rabelo TK, Nunes PS, Santos SL, Serafini MR, Santos MRV, Quintans-Júnior LJ, Gelain DP. Nat Prod Res. 2015;29:2167-2180.
6. Nguyen HT, Asshaima PD, Nguyen TVA, Chavasiri W, Pham DD, Sichaem J, Nguyen NH, Huynh BLC, Nguyen VK, Duong TH. Chem Biodivers. 2021, 18.
7. Pham DD, Duong TH, Nguyen VK. Sci & Technol Dev J. 2020;23:590-597.
8. Beata GK, Katarzyna G, Anna HA, A. Curr Pharmacol Rep. 2019;5:429-439.
9. Ali M, Barakat A, El-Faham A, Al-Rasheed H, Dahlous K, Al-Majid M, Sharma A, Yousuf S, Sanam M, Ul-Haq Z, Iqbal-Choudhary M, Torre B, Albericio F. J Enzyme Inhib Med Chem. 2020; 35:692-701.
10. Peytam F, Takalloobanafshi G, Saadattalab T, Norouzbahari M, Emamgholipour Z, Moghimi S, Firoozpour L, Reza-Bijanzadeh H, Ali-Faramarzi M, Mojtabavi S, Rashidi-Ranjbar P, Karima S, Pakraad R, Foroumadi A. Sci Rep. 2021;11:11911.
11. Madiha SK, Munawar AM, Mohammad A, Umber A, Athar A, Abdullah MA, Samina K, Misbahul AK. Bioorg Med Chem. 2014;22:1195-1200.
12. Tazetdinova AA, Luzina OA, Polovinka MP, Salakhutdinov NF, Tolstikov GA. Chem Nat Compd. 2009;45(6):800-804.
13. Ramadhan R, Phuwapraisirisan P. Bioorg Med Chem Lett. 2015;25:4529-4533.

BROMINATION OF 2-AMINOPYRAZINE: THE EXPERIMENTAL AND COMPUTATIONAL STUDIES

Thanyaporn Phongphankhum, Poomsith Thangsan, Kanyapat Yiamsawat, Pitak Chuawong*
Department of Chemistry and Center of Excellence for Innovation in Chemistry, Faculty of Science, Special Research Unit for Advanced Magnetic Resonance (AMR), Kasetsart University, Bangkok 10900, Thailand
*e-mail: Pitak.C@ku.ac.th

Abstract:

Bromination of 2-aminopyrazine was conducted using *N*-bromosuccinamide (NBS). Two brominated products, 2-amino-5-bromopyrazine (**1**) and 2-amino-3,5-dibromopyrazine (**2**), were obtained in 79% and 9% yields, respectively. Density functional theory calculations provided insight into the selectivity of the bromination process. A comparison of intermediate energies indicates a more favored pathway leading to the major monobrominated product. Moreover, natural bond orbital (NBO) charge analysis revealed that the site of bromination was determined by the intrinsic electronic influence of the reactant. This work highlights our effort to theoretically describe the selectivity of the bromination reaction using the computational method.

Introduction:

Pyrazines are heterocyclic aromatic compounds containing two sp^2 nitrogen atoms at the *para*-position relative to one another (**Figure 1**). In nature, pyrazine-containing compounds were found in peppers, green peas, and insects.[1] Various pyrazine derivatives have been commercialized as pharmaceutically active drugs, such as antitumor,[2] antiplasmodial,[3] antimicrobial,[4] and anti-influenza drugs[5] (**Figure 1**).

Pyrazine analogs bearing an electron-donating group, such as 2-aminopyrazine, readily undergoes electrophilic aromatic substitution at low temperature. In particular, bromination is one of the most frequently utilized methods to generate bromopyrazine analogs, which can be used as precursors for syntheses of biologically active molecules (**Scheme 1**). Several bromine sources are utilized, for example, molecular bromine,[6] *N*-bromosuccinamide,[7] and tetrabutylammonium tribromide.[8] Generally, two bromopyrazinamine products are obtained, including 2-amino-5-bromopyrazine **1** and 2-amino-3,5-dibromopyrazine **2**. Previously, Lizano and co-workers reported that the bromine source, solvent, and brominating agent impacted the reaction efficiency and selectivity. Additionally, they demonstrated that chlorination and iodination were less effective than bromination. [9]

Herein, we employed Density Functional Theory (DFT) calculations to shed light on the selectivity of the bromination reaction. Our computational results are in agreement with the experimental data. The selectivity of the reaction depends on the nucleophilicity of the sp^2 carbon atoms on the pyrazine ring. The reaction preferentially proceeds via the pathway with more stable reaction intermediates.

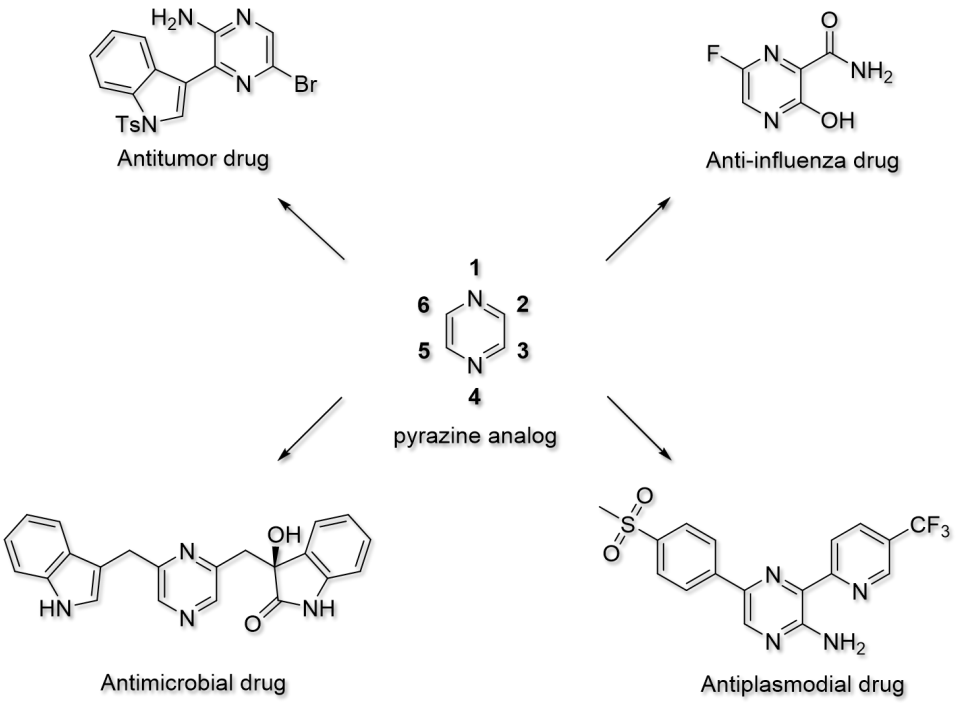

Figure 1. Pharmaceutically significant pyrazine analogs.

Scheme 1. Bromination of 2-aminopyrazine.

Methodology:

Materials and General Procedure

All chemicals were purchased from commercial sources and used without further purification. Thin-layer chromatography (TLC) was conducted on Merck® aluminum-backed 0.2 mm thick silica gel 60 F254 plates, Germany. The plates were visualized under a 254 nm and 356 nm UV lamp and sprayed with a solution of vanillin followed by heating. Flash column chromatography was performed on SiliCycle® silica gel 60 70-230 mesh), Canada. The ^{1}H and proton-decoupled ^{13}C NMR spectra were obtained at 400 and 100 MHz, respectively, using DMSO-d_6 as a solvent on a Bruker 400 MHz AVANCE III HD spectrometer. The peak residue of $(CH_3)_2SO$ (2.50 ppm for ^{1}H and 39.52 ppm for ^{13}C) was used as an internal reference.

Synthesis of 2-amino-5-bromopyrazine and 2-amino-3,5-dibromopyrazine

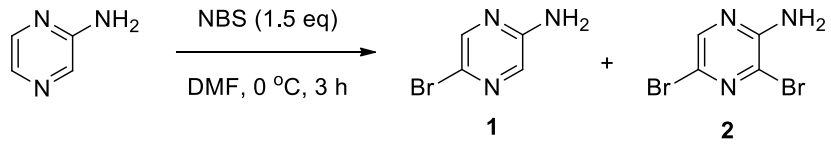

Scheme 2. Bromination conditions in this study.

To a solution of 2-aminopyrazine (0.85 mg, 9.0 mmol) in DMF (43 mL) was added NBS (1.60 g, 9.0 mmol) at 0 °C (**Scheme 2**). The reaction mixture was allowed to stir at room temperature for 2 h. Subsequently, NBS (801.0 mg, 4.5 mmol) was added, and the reaction was stirred for a further 1 h. After the substrate was consumed completely, DMF was removed *in vacuo* using a high vacuum pump. The residue was filtered through short-plug silica gel using 0-30% MeOH/EtOAc and concentrated under reduced pressure. The crude reaction mixture was purified by flash column chromatography using 20-50% EtOAc/hexane to provide 2-amino-5-bromopyrazine **1** and 2-amino-3,5-dibromopyrazine **2**.[10]

Compound **1** was obtained as a yellow solid (1.231 g, 79%); ^{1}H NMR (400 MHz, DMSO-d_6) δ 8.02 (d, J = 1.4 Hz, 1H), 7.68 (d, J = 1.4 Hz, 1H), 6.63 (s, 2H); ^{13}C{^{1}H} NMR (100 MHz, DMSO-d_6) δ 155.3, 143.6, 132.2, 123.7. The NMR spectroscopic data match those previously reported.[11]

Compound **2** was obtained as a pale-yellow solid (163.0 mg, 7%); ^{1}H NMR (400 MHz, DMSO-d_6) δ 8.12 (s, 1H), 6.96 (s, 2H); ^{13}C{^{1}H} NMR (100 MHz, DMSO-d_6) δ 153.3, 143.1, 123.0, 120.1. The NMR spectroscopic data match those previously reported.[12]

Computational details

The structures of bromination intermediates were optimized using the hybrid density functional B3LYP method with a 6-31G(d,p) basis set, implemented in Gaussian 09W.[13] The polarizable continuum model (PCM) was applied to simulate the solvent (DMF) effect, similar to the experimental conditions. The free energies of all optimized structures at 373.15 K and 1 atm were obtained via single point calculations at the same level of theory.

Results and Discussion:

Initially, we planned to synthesize 2-amino-5-bromopyrazine **1** and 2-amino-3,5-dibromopyrazine **2** via bromination reaction. Then, the mono-brominated pyrazine **1** will be utilized as the starting material in the Sonogashira coupling reaction to synthesize arylpyrazinyl acetylene derivatives. These acetylenes will be used as precursors in the Larock indole synthesis. Therefore, we plan to maximize the formation of **1** without any by-products. Previously, Isobe and co-workers reported that only mono-brominated product (compound **1)** was obtained in good yields when 0.9 equivalent of the NBS was used.[10] Therefore, we performed the reaction according to Isobe's conditions. Unfortunately, the reaction proceeded slowly, forming a small portion of the mono-brominated product. Then, the bromination reaction of 2-aminopyrazine was performed again using 1.5 equivalents of NBS in DMF at 0 °C, and compounds **1** and **2** were obtained in 79% and 7% yields, respectively. The reaction proceeded more effectively but with the formation of the di-brominated product. The excess equivalent of NBS was responsible for the di-bromination reaction but also progressively pushed the reaction forward. Therefore, an intricate balance should be achieved between the reagent equivalent, reaction temperature, and time to maximize the desired brominated products.

According to the previous report and our experimental results, the electrophilic bromine atom is more selective toward the 5-position of the 2-aminopyrazine ring rather than the 3-position. To elucidate the selectivity of the bromination reaction, density functional theory (DFT) calculations were performed. It is worth noting that our attempt to locate the transition states was unsuccessful. Besides, there is no report on the theoretical study of the bromination reaction of pyrazine. Therefore, a similar transition state structure is unavailable as an initial guess structure for the transition state optimization in our computational study.

Therefore, the energy of intermediates was analyzed to infer the favorable pathway of the bromination reaction.

All three possible mono-bromination pathways are shown in **Scheme 3**. Routes I, II, and III proceed through intermediates **INT1a**, **INT1b**, and **INT1c** to provide mono-brominated compounds **1**, **3**, and **4**, respectively. The calculated electronic and thermal free energies of the optimized mono-brominated intermediates are shown in **Table 1**. A reaction preferably proceeds via the intermediate with lower energy, leading to the major product. Evidently, **INT1a** possesses the lowest energy among all intermediates. Therefore, **INT1a** is the most stable, leading to 2-amino-5-bromopyrazine **1** as a particular mono-brominated product. These computational results agree with the experimental data where compound **1** is obtained initially.

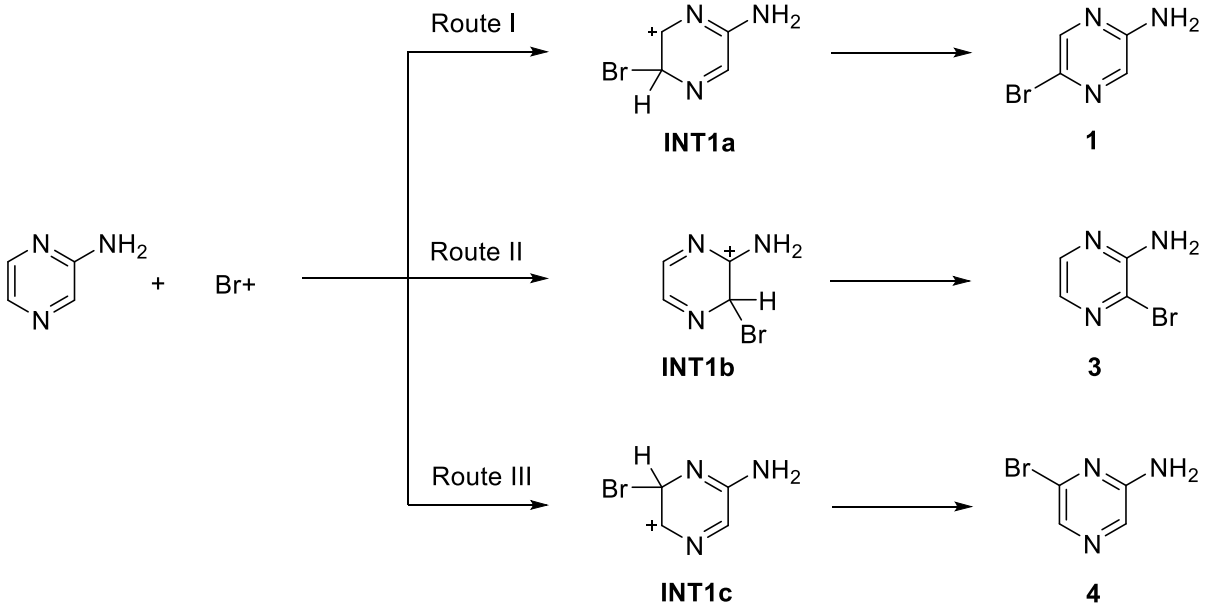

Scheme 3. Three possible routes of monobromination.

Table 1. The free energy of intermediates in the monobromination reaction.

Entry	Code	Free energy (kcal/mol)	Relative energy (kcal/mol)	Optimized structure
1	**INT1a**	-1814193.645	0.00	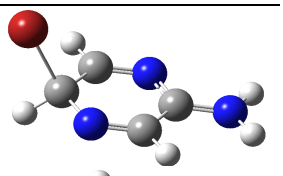
2	**INT1b**	-1814190.968	2.68	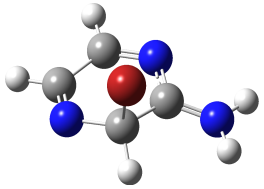
3	**INT1c**	-1814163.907	29.74	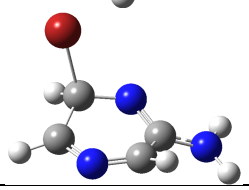

Subsequently, the second bromination reaction was investigated. Compound **1** was considered as the reactant for the second bromination due to its preferred formation described above. Two possible di-brominated pathways are shown in **Scheme 4**. Routes I and II are the pathways proceeding through intermediates **INT2a** and **INT2b** to provide di-brominated compounds **2** and **5**, respectively. The calculated energy and optimized structure of di-brominated intermediates are shown in **Table 2**. The relative energy comparison indicates that the energy of **INT2a** is lower than **INT2b** by 18.75 kcal/mol. The **INT2a** is more stable due to the direct stabilization of the sigma complex by the amino group. In addition, steric hindrance between the two bromine atoms also renders **INT2** unstable. Thus, route I is a more favorable pathway yielding the di-brominated product **2**, consistent with our experimental observation.

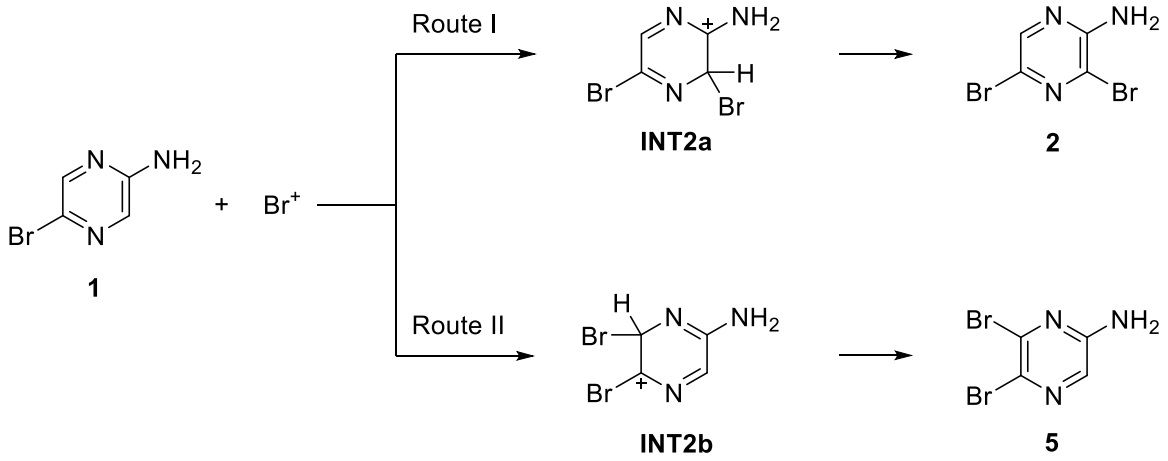

Scheme 4. Two possible routes of the second bromination.

Table 2. The free energy of intermediates in the second bromination reaction.

Entry	Code	Free energy (kcal/mol)	Relative energy (kcal/mol)	Optimized structure
1	**INT2a**	-3427571.729	0.00	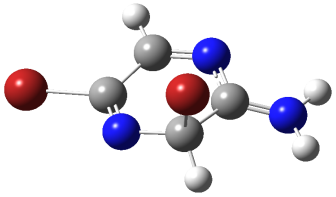
2	**INT2b**	-3427552.980	18.75	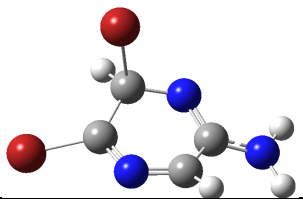

The optimized structures of the first and second bromination reactions, 2-aminopyrazine and 2-amino-5-bromopyrazine **1**, were chosen for the NBO charge analysis, and the results are illustrated in **Table 3**. Electrophiles react with the aromatic ring at the position with the greatest electron density. The NBO charge at the C5 of 2-aminopyrazine is

considerably more negative than the C3 and C6. Therefore, the reactant is preferably brominated at the C5, resulting in compound **1** as a product. Meanwhile, the highest electron density at the C3 of compound **1** reveals that the reaction is selective at the 3-position, leading to compound **2** as a product. Indeed, the NBO charge analysis demonstrates that the selectivity of the bromination reaction can be quantitatively rationalized from the resonance effect of the amino group in 2-aminopyrazine and 2-amino-5-bromopyrazine **1**.

Distinctly, DFT calculations, including the relative energy of intermediate and NBO charge analyses, reflect the experimental observation. The bromination reaction preferentially proceeds through the pathway with a lower energy intermediate, while the brominium ion selectively reacts with the pyrazine reactant at the sp^2 carbon bearing greater electron density. Consequently, the selective bromination of 2-aminopyrazine undergoes **INT1a** to provide the mono-brominated compound **1**, followed by **INT2a** to give the di-brominated compound **2**.

Table 3. Selected NBO charges of 2-aminopyrazine and 2-amino-5-bromopyrazine (**1**)

Reactant	**NBO charge**		
	C3	**C5**	**C6**
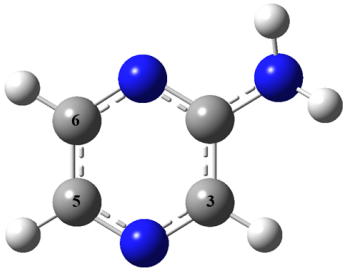 2-aminopyrazine	-0.052	-0084	-0.008
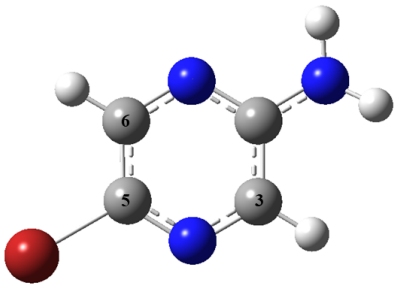 2-amino-5-bromopyrazine (**1**)	-0.039	0.042	-0.006

Conclusion:

In conclusion, we have reported the computational investigation on the selectivity of the bromination reaction of 2-aminopyrazine. Our calculations reveal that the electronic properties of 2-aminopyrazine and 2-amino-5-bromopyrazine **(1)** reactants govern the selectivity of the mono- and di-bromination reactions. Furthermore, the calculated intermediate energy suggests the favorable reaction pathway, leading to the major product. The calculation results are also in agreement with our experimental observation. This work highlights a successful utilization of theoretical study on the electrophilic aromatic substitution of a pyrazine core structure.

Acknowledgements:

This project was supported by the Kasetsart University Research and Development Institute (KURDI), the Faculty of Science, Kasetsart University, and financial support from

the Center of Excellence for Innovation in Chemistry (PERCH-CIC), Ministry of Higher Education, Science, Research, and Innovation is gratefully acknowledged.

References:

1. Attygalle AB, Morgan ED. Chem Soc Rev. 1984;13:245.
2. Jiang B, Yang CG, Xiong WN, Wang J. Bioorg Med Chem. 2001;9: 1149.
3. Younis Y, Douelle F, González Cabrera D, Le Manach C, Nchinda AT, Paquet T, Street LJ, White KL, Zabiulla KM, Joseph JT, Bashyam S, Waterson D, Witty MJ, Wittlin S, Charman SA, Chibale K. J Med Chem. 2013;56:8860.
4. Anjum K, Kaleem S, Yi W, Zheng G, Lian X, Zhang Z. Mar Drugs. 2019;17:89.
5. Guo Q, Xu M, Guo S, Zhu F, Xie Y, Shen J. Chem Pap. 2019;73:1043.
6. Kokatla HP, Thomson PF, Bae S, Doddi VR, Lakshman MK. J Org Chem. 2011;76: 7842.
7. Sato N, Takeuchi R. Synthe. 1990;659.
8. Nakamura H, Takeuchi D, Murai A. Synlett. 1995;1227.
9. Lizano E, Grima J, Pujol MD. Synlett. 2019;30:2000.
10. Chou CM, Tung YW, Lin MI, Chan D, Phakhodee W, Isobe M. Heterocycles. 2012;86:1323.
11. Zhu W, Wu C, Xu S, Wang M, Wang W, Le C, Xia H, Zheng P. Adv Mater Res. (Durnten-Zurich, Switz.) 2015;1081:67.
12. Sato N. J Heterocycl Chem. 1982;19:673.
13. Frisch MJ, Trucks GW, Schlegel HB, Scuseria GE, Robb MA, Cheeseman JR, Scalmani G, Barone V, Petersson GA, Nakatsuji H et al. Gaussian, Inc, Wallingford CT, USA. 2009.

SYNTHESIS OF 5-ARYLBENZO[*a*]PHENAZINE DERIVATIVES AND THEIR PHOTOPHYSICAL PROPERTIES

Natthapat Pitakwong, Watcharapon Prasitwatcharakorn, Chaiwat Rujirasereesakul, Pipat Pobpimai, Torsak Luanphaisarnnont*
Department of Chemistry and Center of Excellence for Innovation in Chemistry, Faculty of Science, Mahidol University, Bangkok 10400, Thailand
*e-mail: torsak.lua@mahidol.ac.th

Abstract:
An efficient, simple, and low-cost synthesis of 5-arylbenzo[*a*]phenazine derivatives was reported. A condensation reaction between 4-aryl-1,2-naphthoquinone derivatives and 1,2-phenylenediamine under mild reaction conditions afforded the corresponding products in good to excellent yields. Absorption and fluorescence emission spectra of 5-(2,4,6-trimethoxyphenyl)benzo[*a*]phenazine were also reported. The result suggested that the compound exhibited solvatochromic behavior.

Introduction:
Polycyclic aromatic compounds are an important class of compounds that exhibit interesting biological and photophysical properties due to their extended π systems. Benzo[*a*]phenazines (**Figure 1**) are a subclass of polycyclic aromatic compounds containing four consecutive aromatic rings with two nitrogen atoms in a middle ring. Benzo[*a*]phenazine derivatives are present in the core structure of many important lead compounds for development of pharmaceutic drugs. These compounds have been studied for their antitumor activity as they can inhibit topoisomerases, enzymes that are excessively produced in cancer cells.[1,2] Examples of these benzo[*a*]phenazine derivatives are XR-11576,[3] NC-182,[4] and NC-190.[5]

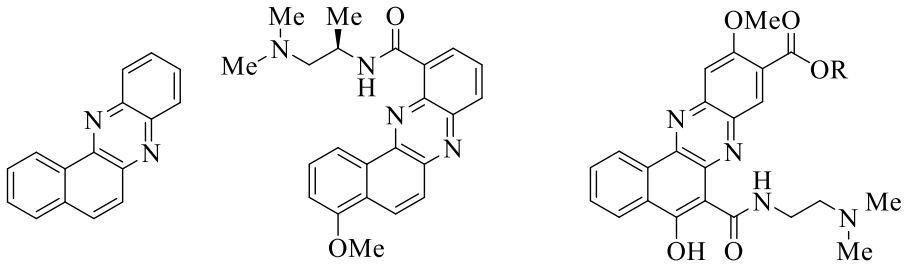

benzo[*a*]phenazine XR-11576 NC-182: R = CH_3
NC-190: R = Na

Figure 1. Structures of benzo[*a*]phenazine and examples of benzo[*a*]phenazine derivatives with antitumor activity

In addition to their biological activity, benzo[*a*]phenazines are also present as a core structure of various compounds with interesting photophysical properties. Examples of these compounds are shown in **Figure 2**. Tetrahydrobenzo[*a*]chromeno[2,3-*c*]phenazinone was reported to show solvatochromic behavior in its fluorescence spectra.[6] Halochromism of styryl-dihydrobenzo[*a*]phenazines was also reported.[7] Its absorption spectra showed bathochromic shift in acidic condition and hypsochromic shift in basic condition. Carbazole-substituted benzo[*a*]phenazines showed both acidochromism in excitation spectra and

solvatochromism in emission spectra.[8] Zwitterionic pyridine-substituted benzo[*a*]phenazines have been used as a photoinitiator for polymerization reactions.[9]

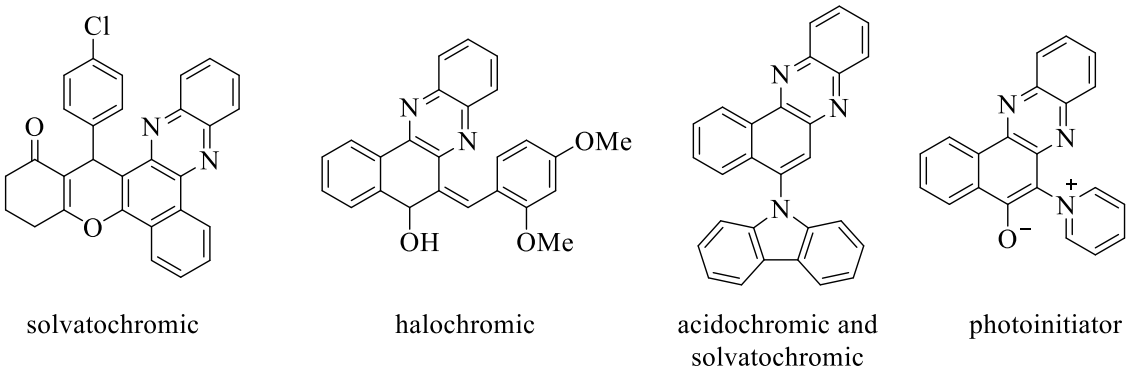

solvatochromic | halochromic | acidochromic and solvatochromic | photoinitiator

Figure 2. Examples of benzo[*a*]phenazine derivatives with photophysical properties

Previous methods to synthesize benzo[*a*]phenazines have been reported (**Scheme 1**). Selected examples of such methods are: acid-catalyzed and acid-mediated condensation reaction between naphthoquinone derivatives and 1,2-phenylenediamines,[10–13] one-pot oxidative cyclization of 1,4-napthoquinones,[14,15] one-pot cyclization-reduction of 1,2,4-triketonapthoquinones and 1,2-phenylenediamines,[7] intramolecular Heck reaction,[16] and intramolecular hydroarylation of 2-aryl-3-ethynylquinoxalines.[17] Although many methods have been reported, these methods have limitations such as the use of transition metal catalysts, the use of mediator, and/or lengthy synthesis preparation of starting materials. Development of a simple and efficient method to synthesize this class of compounds is therefore important. Moreover, exploration of benzo[*a*]phenazines with electron-rich aryl substituents on the position 5 has not been reported despite the potential push-pull electronic effect in the molecule that may result in interesting photophysical properties of this class of compounds. Herein, we reported a simple and efficient metal-free cyclization between naphthoquinones and 1,2-phenylenediamine under mild reaction conditions to yield 5-arylbenzo[*a*]phenazine derivatives. The photophysical property of the synthesized derivatives was also reported.

Previous work

i) Condensation

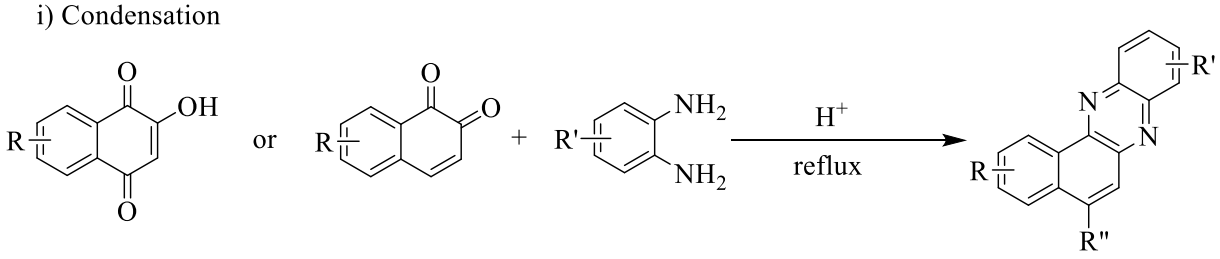

R" = H or OH

ii) One-pot oxidative cyclization

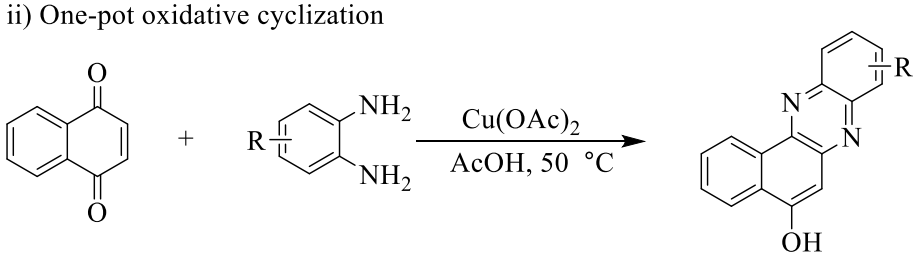

iii) Intramolecular Heck reaction

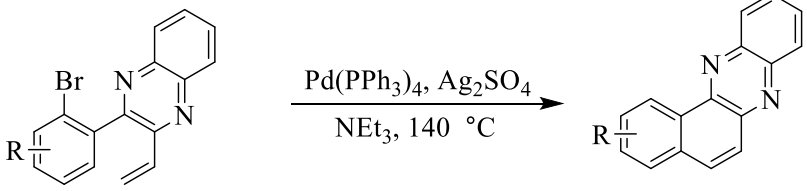

iv) Intramolecular hydroarylation

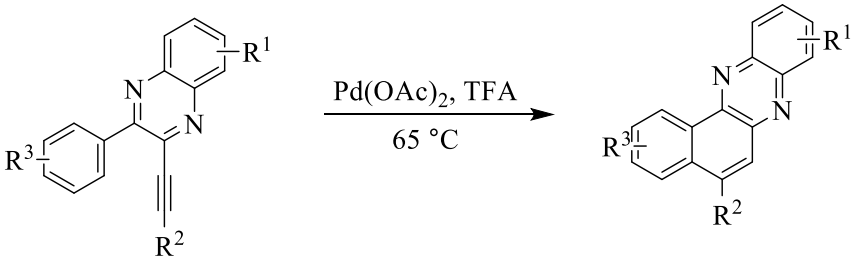

This work

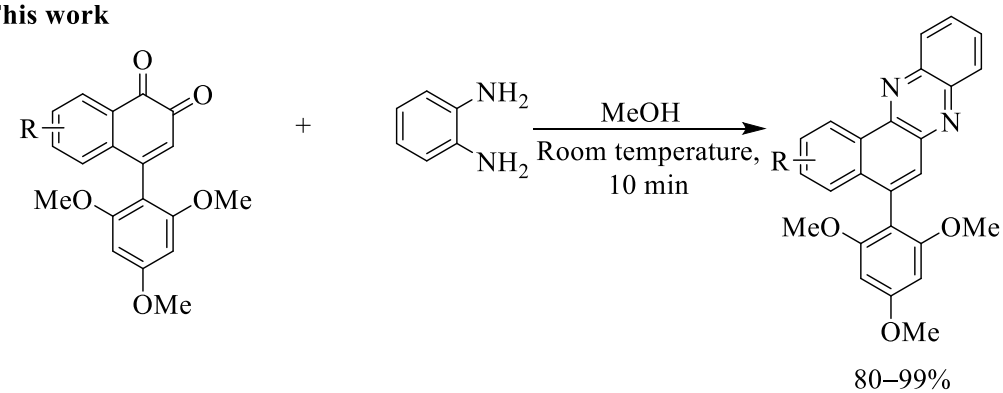

80–99%

Scheme 1. Previous work and this work on the synthesis of benzo[*a*]phenazine derivatives

Methodology:
1,2-Phenylenediamine and organic solvents were purchased from commercial sources (Sigma Aldrich,TCI, Merck, and Alfa Aesar), and were used without further purification. All reactions were performed under an ambient atmosphere in oven-dried glassware with magnetic stirrer at room temperature. 4-(2,4,6-Trimethoxyphenyl)-1,2-naphthoquinone derivatives were synthesized following Prasitwatcharakorn's method.[18] Analytical thin layer chromatography (TLC) was performed on alumina sheets pre-coated with a Merck silica gel 60 F254 plate and compounds were visualized under UV light. Flash chromatography was performed with silica gel 60 (particle size 40−60 μm) from Merck. ^{1}H and ^{13}C NMR spectra were recorded on a Bruker Avance 400 MHz NMR spectrometer in $CDCl_3$. The chemical shifts were recorded in part per million (ppm) relative to the resonance of the residual protonated solvent (^{1}H: $CDCl_3$, δ = 7.26 and ^{13}C: $CDCl_3$, δ = 77.00). Data are reported as following: (s = singlet, d = doublet, t = triplet, and m = multiplet; coupling constants, J, in Hz, integration). IR spectra were recorded on a Perkin Elmer Frontier FT-IR spectrometer. Absorption and emission spectra were measured using a standard quartz cell with 1 cm path length. Absorption spectra were recorded on Shimadzu UV-1800 on wavelength between 300 and 700 nm. Emission Spectra were recorded on Fluoromax Horiba on wavelength between 400 and 700 nm.

General procedure for the synthesis of 5-arylbenzo[a]phenazines (3) 4-Aryl-1,2-naphthoquinone (**1**, 0.1 mmol, 1.0 equiv.) and 1,2-phenylenediamine (**2**, 0.15 mmol, 1.5 equiv.) were dissolved in methanol (1 mL). The reaction was stirred for 10 minutes at room temperature. Water (5 mL) was added to the reaction. The mixture was extracted with EtOAc (3 x 3 mL). The combined organic layers were washed with brine, dried over anhydrous Na_2SO_4, and concentrated. The residue was purified by column chromatography to yield the desired product.

5-(2,4,6-Trimethoxyphenyl)benzo[*a*]phenazine (3a)

The title compound was synthesized following the general procedure using 4-(2,4,6-trimethoxyphenyl)-1,2-naphthoquinone as the starting material. The product was obtained in 96%. The NMR spectra of compound **3a** were identical to those reported in the literature.[18]

Yellow solid; 38.0 mg (96%).

Melting point 205–208 °C.

R_f = 0.30 (EtOAc/Hexanes, 1/3, v/v).

IR (KBr): 2999, 2937, 2837, 1607, 1583, 1490, 1413, 1336, 1225, 1205, 1157, 1126 cm^{-1}.

^{1}H NMR (400 MHz, $CDCl_3$) δ 9.49 (d, *J* = 8.0 Hz, 1H), 8.43–8.34 (m, 1H), 8.32–8.23 (m, 1H), 7.89 (s, 1H), 7.87–7.81 (m, 2H), 7.77 (td, *J* = 8.0, 1.2 Hz, 1H), 7.66 (td, *J* = 8.0, 1.2 Hz, 1H), 7.58 (dd, *J* = 8.2, 1.4 Hz 1H), 6.33 (s, 2H), 3.94 (s, 3H), 3.66 (s, 6H).

^{13}C NMR (100 MHz, $CDCl_3$) δ 161.4, 158.9, 143.6, 142.7, 141.8, 138.5, 133.8, 131.0, 129.6, 129.6, 129.3, 129.3, 129.0, 129.0, 127.2, 126.5, 125.2, 108.9, 90.7, 55.7, 55.4.

2-Methoxy-5-(2,4,6-trimethoxyphenyl)benzo[*a*]phenazine (3b)

The title compound was synthesized following the general procedure using 7-methoxy-4-(2,4,6-trimethoxyphenyl)-1,2-naphthoquinone as the starting material. The product was obtained in 99%.

Yellow solid; 42.3 mg (99%).

Melting point 198–201 °C.

R_f = 0.33 (EtOAc/Hexanes, 1/3, v/v).

IR (KBr): 3010, 2938, 2836, 1611, 1534, 1499, 1468, 1337, 1226, 1205, 1126, 1058 cm^{-1}.

^1H NMR (400 MHz, $CDCl_3$) δ 8.93 (d, J = 2.7 Hz, 1H), 8.43–8.34 (m, 1H), 8.31–8.22 (m, 1H), 7.88–7.79 (m, 2H), 7.76 (s, 1H), 7.50 (d, J = 8.8 Hz, 1H), 7.25 (dd, J = 9.1, 2.5 Hz, 1H), 6.32 (s, 2H), 4.12 (s, 3H), 3.93 (s, 3H), 3.66 (s, 6H).

^{13}C NMR (100 MHz, $CDCl_3$) δ 161.3, 158.9, 158.8, 143.9, 142.7, 142.1, 141.4, 138.2, 132.6, 129.5, 129.4, 129.0, 128.8, 128.0, 126.5, 119.1, 109.1, 106.0, 90.7, 55.7, 55.5, 55.2.

3-Bromo-5-(2,4,6-trimethoxyphenyl)benzo[*a*]phenazine (3c)

The title compound was synthesized following the general procedure using 6-bromo-4-(2,4,6-trimethoxyphenyl)-1,2-naphthoquinone as the starting material. After purification of the product by column chromatography, the product was further purified by recrystallization using DCM:MeOH (1:10) solvent mixture to yield the title compound in 80%.

Yellow solid; 37.9 mg (80%).

Melting point 240–243 °C.

R_f = 0.33 (EtOAc/Hexane, 1/3, v/v).

IR (KBr): 3001, 2930, 2836, 1590, 1466, 1415, 1358, 1333, 1226, 1203, 1131, 1038 cm^{-1}.

^1H NMR (400 MHz, $CDCl_3$) δ 9.35 (d, J = 8.6 Hz, 1H), 8.40–8.31 (m, 1H), 8.3–8.22 (m, 1H), 7.90 (s, 1H), 7.88–7.82 (m, 3H), 7.70 (d, J = 2.0 Hz, 1H), 6.33 (s, 2H), 3.95 (s, 3H), 3.68 (s, 6H).

^{13}C NMR (100 MHz, $CDCl_3$) δ 161.8, 158.9, 143.4, 143.0, 142.2, 142.0, 137.4, 135.4, 130.6, 130.4, 130.0, 129.9, 129.7, 129.7, 129.2, 129.1, 127.0, 124.4, 108.2, 90.9, 55.8, 55.5.

Results and Discussion:

To begin the reaction optimization (**Table 1**), 4-(2,4,6-trimethoxyphenyl)-1,2-naphthoquinone[18] (**1a**) and 1,2-phenylenediamine (**2**) were used as model substrates. Various solvents including non-polar solvents, polar aprotic solvents, and polar protic solvents were screened. n-Hexane did not give any desired product (entry 1) possibly due to the poor solubility of **1a** in the solvent. Toluene (PhMe) gave the desired cyclized product in good yield (73%, entry 2), which may be explained by the higher solubility due to the π–π stacking interaction between the starting materials and the solvent. Polar aprotic solvents such as dichloromethane (DCM), acetonitrile (MeCN), and acetone gave the products in low to good yields (80, 60, and 24%, respectively, entries 3–5). When methanol (MeOH) was used as the solvent, the product was obtained in 96% (entry 6). H-bonding may help to stabilize the intermediate and/or transition state, resulting in a more efficient reaction. Changing the solvent to other polar protic solvents (water and ethanol), however, led to a drastic decrease in the product yields (0 and 10 %, respectively, entries 7 and 8). These low yields could be attributed to the poor solubility of **1a** in the solvents. Methanol was chosen as the optimal solvent for further investigation.

Table 1. Reaction optimization[a]

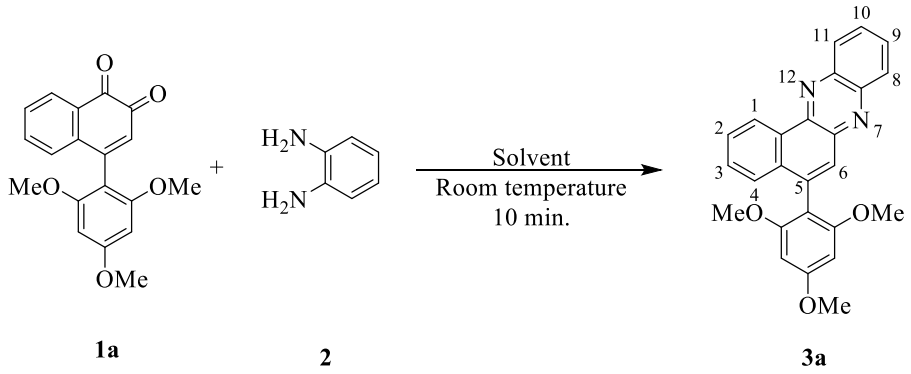

1a **2** **3a**

Entry	Solvent	Yield (%)[b]
1	n-Hexane	0
2	PhMe	73
3	DCM	80
4	MeCN	60
5	Acetone	24
6	**MeOH**	**96**
7	H_2O	0
8	EtOH	10

[a] Reaction conditions: 4-(2,4,6-trimethoxyphenyl)-1,2-naphthoquinone (**1a**) (32.4 mg, 0.1 mmol, 1.0 equiv.), 1,2-phenylenediamine (**2**) (16.2 mg, 0.15 mmol, 1.5 equiv.) in solvent (1 mL) at room temperature for 10 minutes.
[b] Isolated yields.

Using the optimal reaction conditions, the substrate scope of the reaction was investigated (**Table 2**). 4-(2,4,6-Trimethoxyphenyl)-1,2-naphthoquinone derivatives with different substituents at different positions were studied. A substrate with an electron donating methoxy group worked well in the reaction. 7-Methoxy-4-(2,4,6-trimethoxyphenyl)-1,2-naphthoquinones gave the desired product (**3b**) in 99%. A substrate with a bromo substituent also worked well in the reaction *albeit* a slightly lower yield. 6-Bromo-4-(2,4,6-trimethoxyphenyl)-1,2-naphthoquinone gave the product (**3c**) in 80%. It should be noted that the bromo substituent could act as a handle for further functionalization to install other substituents through a cross-coupling reaction.

Table 2. Substrate scope[a]

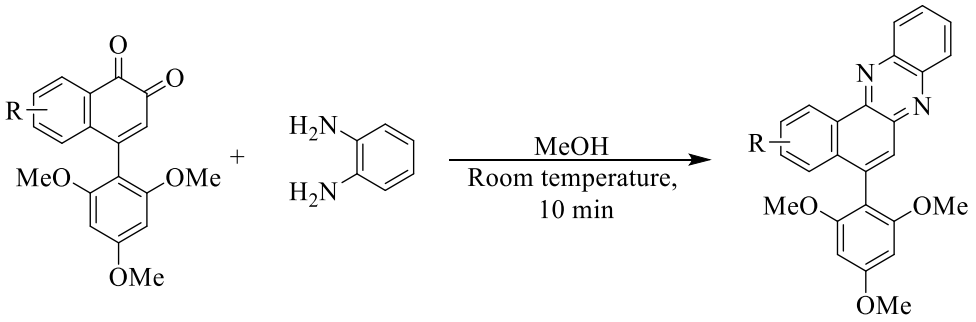

1 **2** **3**

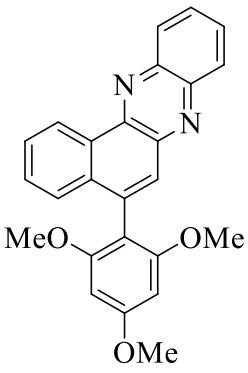

3a
96%

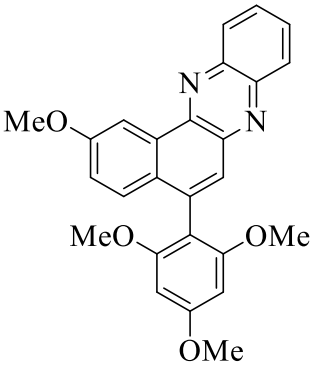

3b
99%

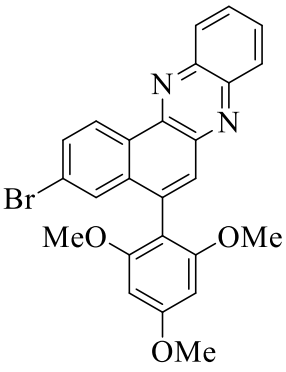

3c
80%

[a] Reaction conditions: 4-(2,4,6-trimethoxyphenyl)-1,2-naphthoquinone derivatives (0.1 mmol, 1.0 equiv.), 1,2-phenylenediamine (**2**) (16.2 mg, 0.15 mmol, 1.5 equiv.) in methanol (1 mL) at room temperature for 10 minutes. All yields were isolated yields.

The absorption and emission spectra of compound **3a** were investigated as a representative for this class of compounds (**Figure 3**). The absorption spectra exhibit similar patterns in different solvents. The wavelengths for maximum absorption in acetonitrile and toluene were 407 and 388 cm^{-1}; and 409 and 388 cm^{-1}, respectively. The difference in the wavelength was minimal. In contrast, the nature of the solvents had a large impact on the emission spectra. The fluorescence emission spectra had the highest intensity at 535 and 457 cm^{-1} in acetonitrile and toluene, respectively. The Stork shift for **3a** was dependent on the nature of the solvent. The compound exhibited solvatochromic behavior, which could be used for further applications of this class of compounds.

a)

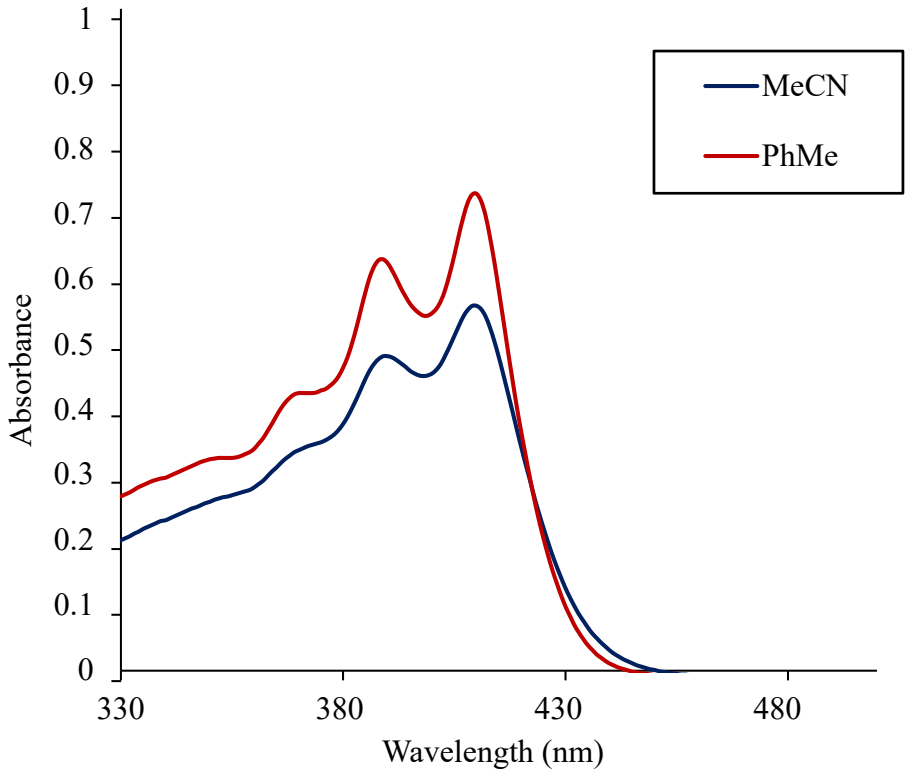

b)

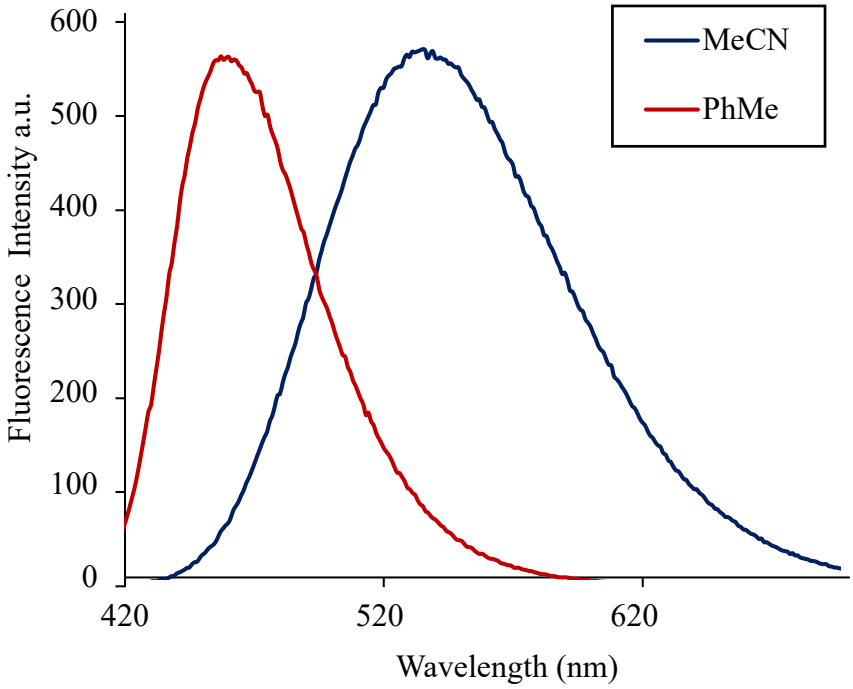

Figure 3. a) Absorption and b) emission spectra of 5-(2,4,6-trimethoxyphenyl)benzo[*a*]phenazine (**3a**) in MeCN (blue) and PhMe (red).

Conclusion:

In summary, we have developed an efficient synthesis of 5-arylbenzo[*a*]phenazine derivatives *via* a condensation reaction between 4-aryl-1,2-naphthoquinones and 1,2-phenylenediamine. The reaction was accomplished under mild reaction conditions, and the reaction time was short. The desired products were obtained in good to excellent yields. Investigation of the photophysical properties of **3a** revealed that the maximum wavelength of the fluorescence emission spectra depended on the solvent. Photophysical properties of **3b** and **3c** are currently under investigation. Further mechanistic study, and application of this efficient method are currently undergoing and will be reported in due course.

Acknowledgements:

This research was supported by the Center of Excellence for Innovation in Chemistry (PERCH-CIC), Ministry of Higher Education, Science, Research and Innovation; and the Department of Chemistry, Faculty of Science, Mahidol University. We also thank the Central Instrumental Facility (CIF) at the Faculty of Science, Mahidol University for research facilities.

References:

1. Wang JC. Annu Rev Biochem. 1996;65:635-692.
2. Vos SM, Tretter EM, Schmidt BH, Berger JM. Nat Rev Mol Cell Biol. 2011;12:827-841.
3. Vicker N, Burgess L, Chuckowree IS, Dodd R, Folkes AJ, Hardick DJ, Hancox TC, Miller W, Milton J, Sohal S, Wang S, Wren SP, Charlton PA, Dangerfield W, Liddle C, Mistry P, Stewart AJ, Denny WA. J Med Chem. 2002;45:721-739.
4. Tarui M, Doi M, Ishida T, Inoue M, Nakaike S, Kitamura K. Biochem J. 1994;304:271-279.
5. Yamagishi T, Nakaike S, Nanauni K, Otomo S, Tsukagoshi S. Cancer Chemother Pharmacol. 1993;32:249-253
6. Khurana JM, Chaudhary A, Lumb A, Nand B. Green Chem. 2012;14:2321-2327.
7. Patil SR, Choudhary AS, Sekar N. Tetrahedron. 2016;72:7968-7974.
8. Singh P, Baheti A, Thomas KRJ. J Org Chem. 2011;76:6134-6145.
9. Podemska K, Podsiadły R, Orzeł A, Kowalska A, Maruszewska A, Marcinek A, Sokolowska J. Color Technol. 2014;130:250-259.
10. Choudhary AS, Malik MK, Patil SR, Prabhu KH, Deshmukh RR, Sekar N. Can Chem Trans. 2014;2:365-380.
11. Hahn S, Biegger P, Bender M, Rominger F, Bunz UHF. Chem Eur J. 2016;22:869-873.
12. Kaupp G, Naimi-Jamal MR. Eur J Org Chem. 2002;2002:1368-1373.
13. Rehberg GM, Rutherford JL. J Heterocycl Chem. 1995;32:1643-1644.
14. Kour H, Paul S, Singh PP, Gupta R. Synlett. 2014;25:495-500.
15. Paul M, Teubner M, Grimm-Lebsanft B, Buchenau S, Hoffmann A, Rübhausen M, Herres-Pawlis S. J Inorg Biochem. 2021;224:111541.
16. Lou S-J, Xu D-Q, Shen D-F, Wang Y-F, Liu Y-K, Xu Z-Y. Chem Comm. 2012;48:11993-11995.
17. Kumar S, Saunthwal RK, Mujahid M, Aggarwal T, Verma AK. J Org Chem. 2016;81:9912-9923.
18. Prasitwatcharakorn W, Rujirasereesakul C, Luanphaisarnnont T. Results Chem. 2022;4:100319.

BIOASSAY-GUIDED ISOLATION AND IDENTIFICATION OF BIOACTIVE COMPOUNDS FROM *Leonurus japonicus* HOUTT. EXTRACT

Trirath Sukthawee,[1,2,3] Wuttichai Jaidee,[3] Narawadee Rujanapun,[3] Surat Laphookhieo,[1,2,3] Rawiwan Charoensup,[3,4] and Tharakorn Maneerat[1,2,3,*]
[1]School of Science, Mae Fah Luang University, Chiang Rai 57100, Thailand
[2]Center of Chemical Innovation for Sustainability (CIS), Mae Fah Luang University, Chiang Rai 57100, Thailand
[3]Medicinal Plants Innovation Center of Mae Fah Luang University, Mae Fah Luang University, Chiang Rai 57100, Thailand
[4]School of Integrative Medicine, Mae Fah Luang University, Chiang Rai 57100, Thailand
*e-mail: wisanu.man@mfu.ac.th

Abstract:

Leonurus japonicus (*L. japonicus*) is widely used in folk medicine to treat diabetes, menstrual irregularities, and bronchitis. This study evaluated the *α*-glucosidase inhibitory and anti-inflammatory activity of the crude extract, semi-purified fractions, and isolated compounds from the aerial of *L. japonicus* through bioassay-guided isolation. The crude ethanolic extract was partitioned with ethyl acetate. Bioassay-guided fractionation of an EtOAc-soluble extract led to the isolation of six known compounds (**1-6**). Their structures were elucidated based on data analysis, including ^{1}H NMR data, LC-QTOF-MS, ECD, UV, and FT-IR. Compounds **1-6** exhibited *α*-glucosidase inhibitory and anti-inflammatory activities in range IC_{50} values at 143.9 - 598.4 μM and 66.9 – 285.8 μM, respectively, when compared with the positive control.

Introduction:

The *Leonurus japonicus* (*L. japonicus*) is a native plant in Asia, Europe, and Africa. It belongs to the *Lamiaceae* family and is known as Gun-Cha-Ted in Thailand. It is categorized as a herbaceous plant. *L. japonicus* was used extensively in Traditional Chinese Medicine (TCM) to treat blood disorders and diseases affecting women. This plant displayed anti-oxidative, anti-cancer, cardioprotective, and neuroprotective properties. Approximately 282 substances have been isolated and identified from *L. japonicus*. Alkaloids, diterpenes, and flavones have been identified as major constituents in *L. japonicus*.[1] So, *L. japonicus* has been the subject of numerous reviews over time, primarily concentrating on its chemical constituents and pharmacological properties. In our screening, the EtOAc-soluble part of *L. japonicus* inhibited *α*-glucosidase and nitric oxide (NO) production with percent inhibition of 86% and 88%, respectively. Bioassay-guided isolation is the method that increases the likelihood of discovering potent bioactive compounds and novel compounds.[2] Therefore, we adopted bioassay-guided investigation to discover active compounds that inhibited *α*-glucosidase and NO production.

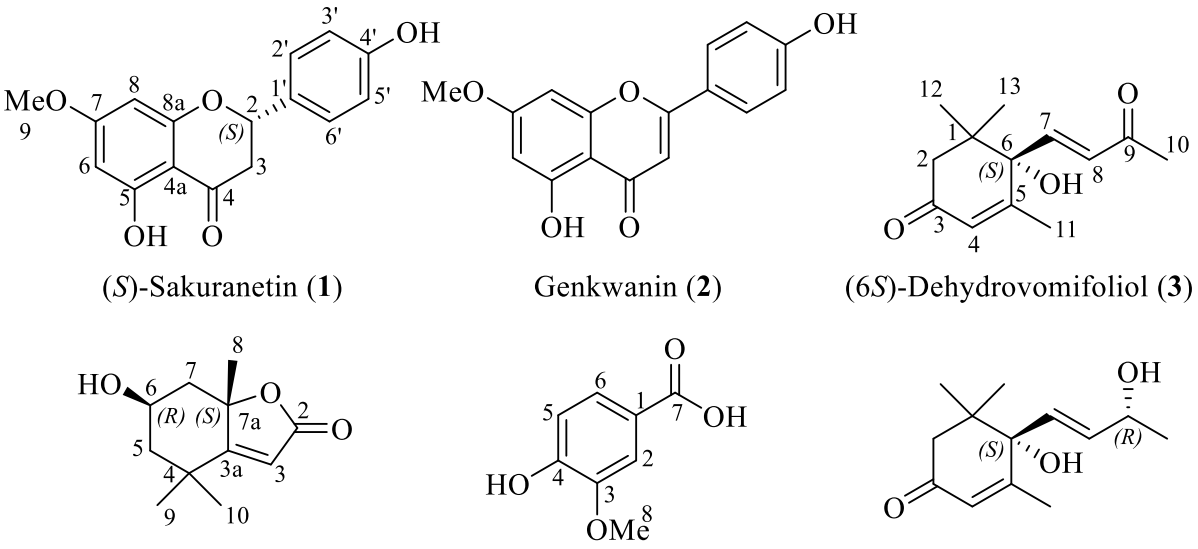

(*S*)-Sakuranetin (**1**) Genkwanin (**2**) (6*S*)-Dehydrovomifoliol (**3**)

(-)-Loliolide (**4**) Vanillic acid (**5**) (6*S*, 9*R*)-Vomifoliol (**6**)

Figure 1. Structure of compounds (**1**-**6**)

Methodology:

Instrument and Chemical:

The UV and ECD spectra were recorded with a JASCO J-1500 spectrophotometer. FT-IR spectra were recorded on a Thermo Scientific Nicolet IS50. ^{1}H NMR spectra were obtained using Bruker AVANCE NEO, 500 MHz. LC-QTOF-MS were recorded with Agilent 1290 infinity II/G6545B QTOF/MS. Flash column chromatography (FCC) was performed with a Pure C-815 Flash (BUCHI, Japan). High-Performance Liquid Chromatography (HPLC) was done with Agilent 1260 Infinity II. Column chromatography (CC) and quick column chromatography (QCC) were performed on Merck silica gel 100 (0.063-0.200 mm), Merck silica gel 60 (40-63 mm), and Merck silica gel C_{18}, respectively. Thin layer chromatography (TLC) aluminum sheets of silica gel 60 F_{254} (20×20 cm) layer thickness 0.2 mm, (Merck), Germany, were used for analytical purposes. Organic solvents for extraction and isolation were hexane, dichloromethane (DCM), acetone, ethyl acetate (EtOAc), methanol (MeOH), ethanol (EtOH), and distilled water. Besides the normal phase silica gel, the reverse phase C_{18} silica gel and Sephadex LH-20 were also employed to isolate crude extract.

Plant Material:

The dried plants of *L. japonicus* were received from Lanna herb, Chiang Mai, Thailand, in July 2018. To estimate the reliability of species identification using DNA barcoding regions, the sequence from ITS2 gene had 482 bp and was compared in the NCBI database. The result showed 92% query coverage and 100% identification of *L. japonicus*.

Extraction and Isolation:

The dried plants of *L. japonicus* (1.20 kg) were soaked in EtOH at room temperature for three days. The solvent was evaporated using a rotary evaporator under reduced pressure. This extraction method was done in triplicate. The ethanolic extract (TA10N 72.05 g) from plants of *L. japonicus* was partitioned with ethyl acetate (4 x 500 ml each) to obtain TA10N EtOAc (42.97 g). The aqueous phase was lyophilized and kept in the fridge for further studies. The crude ethyl acetate extract (TA10N EtOAc, 42.97 g) was subjected to quick column chromatography (QCC) (silica gel 60, 20:80 Acetone/Hexane) to give ten fractions (TA10N 01A-01J). Fraction TA10N 01H (696.6 mg) was subjected to flash column chromatography

(FCC), using gradient elution with Acetone/Hexane (10-30%) to give eight fractions (TA10N 40A-40H). Fraction TA10N 40C (211.4 mg) was further subjected to FCC (80:20 MeOH/water) to give five fractions (TA10N 44A-44E). Fraction TA10N 44A (72.8 mg) was further subjected to Sephadex LH-20 (MeOH) to give five fractions (TA10N 47A-47E). Compound **1** (0.8 mg) was obtained from fraction TA10N 47D. Fraction TA10N 44D (30.8 mg) was further subjected to Sephadex LH-20 (MeOH) to give four fractions (TA10N 48A-48D). Compound **2** (1.8 mg) was obtained from fraction TA10N 48D. Fraction TA10N 48A.2 was precipitated from fraction TA10N 48A to afford compound **3** (4.9 mg). Fraction TA10N 40F (1.68 g) was further purified by RP C_{18} column chromatography (60:40 MeOH/water) to give six fractions (TA10N 52A-52F). Fraction TA10N 52B (203.6 mg) was further purified by RP C_{18} HPLC (50:50 MeOH/water, 1.5 mL/min) to afford compound **4** (3.6 mg, R_t 16.8 min). Fraction TA10N 52A (200.8 mg) was further purified by CC (5:95 MeOH/DCM) to give five fractions (TA10N 59A-59E). Fraction TA10N 59D (45.70 mg) was further purified by column chromatography (CC) (15:85 Acetone/Hexane) to give three fractions (TA10N 65A-65C). Fraction TA10N 65B (10.2 mg) was further purified by CC (30:70 EtOAc/Hexane) to afford compound **5** (1.0 mg). Fractions TA10N 59E (35.40 mg) was further purified by CC (10:90 MeOH/DCM) to give four fractions (TA10N 67A-67D). Fraction TA10N 67A (18.1 mg) was further purified by CC (10:90 Acetone/Hexane) to give six fractions (TA10N 70A-70F). Fraction TA10N 70F (3.3 mg) was further subjected to RP C_{18} HPLC (80:20 MeOH/water, 1.5 mL/min) to afford compound **6** (1.2 mg, R_t 8.1 min).

α-Glucosidase inhibitory assay:

Briefly, the α-glucosidase assay was carried out using the technique that was previously reported.[3] The samples were dissolved in DMSO and diluted solutions with potassium phosphate buffer (100 mM KH_2PO_4, pH 6.8-7.0) to a concentration of 10% DMSO. The 1.5 mM of the substrate, *p*-nitrophenyl-D-glucoside (Sigma, St. Louis, USA; CAS No. N1377) was dissolved in phosphate buffer. The sample of 50 µL was added to 100 µL of α-glucosidase enzyme solution (0.35 U/mL, Sigma, St. Louis, USA, CAS No. G5003) and pre-incubated the combination at 37°C for 10 minutes. 100 µL of 1.5 mM substrate was added to the mixture to begin the enzymatic reaction, which was then given 20 minutes of incubation at 37°C. After that, the reaction was stopped by using 1 mL of 1 M Na_2CO_3. As an absorption indicator, the amount of *p*-nitrophenol produced from the substrate was measured at 405 nm.

Nitric Oxide production inhibitory and cell viability assay:

RAW 264.7 cells were plated in 96-well plates at a density of 5.0×10^5 and cultured for 24 hours at 37°C with 5% CO_2. After that, the culture supernatant from each well was discarded with samples and then stimulated with 1 µg/mL LPS. In incubation for 24 hours at 37°C, the supernatant was treated with 50 µL of a Griess reagent at room temperature for 10 minutes and measured the absorbance at 570 nm. Cell viability was performed using the MTT assay.[3]

Results and Discussion:

Structure elucidation:

(*S*)-Sakuranetin (**1**) was isolated as white crystals. The molecular formula of compound **1** was $C_{16}H_{14}O_5$; the HRMS data displayed a molecular ion at *m/z* $[M+H]^+$ 287.2769 (calculated $[M+H]^+$ $C_{16}H_{14}O_5$, 287.2754). The UV (MeOH) spectrum showed two maxima absorption bands at 358 and 287 nm. The FT-IR spectrum presented absorption in the broadband at 3379 cm^{-1}, indicating O-H stretching (hydroxy group), the narrow band at 2923 cm^{-1}, indicating

aromatic, the narrow band at 2863 cm^{-1}, indicating C=C-H stretching (aromatic), and the sharp band at 1639 cm^{-1}, indicating C=O stretching (ketone group). Compound **1** was a flavonoid derivative based on ^{1}H NMR spectroscopic data, which showed signals for chelated hydroxy proton [δ_H 12.03 (1H, *s*, 5-OH)], a set of AA'BB' aromatic protons [δ_H 7.33 (2H, *d*, *J* = 8.7 Hz, H-2' and H-6') and 6.88 (2H, *d*, *J* = 8.7 Hz, H-3' and H-5')], *ortho*-coupled aromatic protons [δ_H 6.08 (1H, *d*, *J* = 2.3 Hz, H-8) and 6.06 (1H, *d*, *J* = 2.3 Hz, H-6)], one oxy-methine proton [δ_H 5.35 (1H, *dd*, *J* = 3.0 and 13.0 Hz, H-2)] coupled with nonequivalent methylene protons [δ_H 3.08 (1H, *dd*, *J* = 13.0 and 17.1 Hz, H_a-3) and 2.80 (1H, *dd*, *J* = 3.0 and 17.1 Hz, H_b-3)], and one methoxy group [δ_H 3.81 (3H, *s*, 7-OMe). In this study, the absolute configuration of the chiral center at position C-2 of compound **1** was identified by the specific rotation presented by levorotation ($[\alpha]_D^{25}$ -4.64°, *c* = 0.0028, MeOH). The ECD spectrum presented two Cotton effects at 288 nm (Δε -5.6) and 330 nm (Δε +1.16). A positive Cotton effect at ~330 nm (n→π* transition; cinnamoyl system) and a negative effect at ~280–290 nm (π→π* transition; benzoyl system) indicated the absolute configuration at C-2 to be *S*. Consequently, the structure of the compound **1** was identified as (*S*)-sakuranetin.[4-7]

Genkwanin (**2**) was isolated as white crystals. The molecular formula of compound **2** was $C_{16}H_{12}O_5$; the HRMS data displayed a molecular ion at *m/z* $[M+H]^+$ 285.0642 (calculated $[M+H]^+$ $C_{16}H_{12}O_5$, 285.0652). The UV (MeOH) spectrum showed three maxima absorption bands at 267, 303 (sh), and 335 nm. The FT-IR spectrum presented absorption in the broadband at 3371 cm^{-1}, indicating O-H stretching (hydroxy group), the narrow band at 2919 cm^{-1}, indicating aromatic, the narrow band at 2850 cm^{-1}, indicating C=C-H stretching (aromatic), and the sharp band at 1588 cm^{-1}, indicating C=O stretching (ketone group). Compound **2** was also a flavonoid derivative based on ^{1}H NMR spectroscopic data and showed similar signals to compound **1**, except for the displacement of signals for the oxy-methine proton (H-2) and one set of methylene protons (H_{ab}-3) in compound **1** with that of one olefinic proton [δ_H 6.54 (1H, *s*, H-3)] in compound **2**. Thus, the structure of compound **2** was identified as genkwanin.[6,8-9]

(*6S*)-Dehydrovomifoliol (**3**) was isolated as a yellow viscous oil. The molecular formula of compound **3** was $C_{13}H_{18}O_3$; the HRMS data displayed a molecular ion at *m/z* $[M+H]^+$ 223.1329 (calculated $[M+H]^+$ $C_{13}H_{18}O_3$, 223.1316). The UV (MeOH) spectrum showed maxima absorption band at 233 nm. The FT-IR spectrum presented absorption in the broadband at 3430 cm^{-1}, indicating O-H stretching (hydroxy group), the narrow band at 2924 cm^{-1}, indicating aromatic, the narrow band at 2853 cm^{-1}, indicating C=C-H stretching (aromatic), and the sharp band at 1662 cm^{-1}, indicating C=O stretching (conjugated ketone). Compound **3** was a sesquiterpene derivative based on ^{1}H NMR spectroscopic data, which showed *trans* olefinic protons [δ_H 6.86 (1H, *d*, *J* = 15.6 Hz, H-8), and 6.49 (1H, *d*, *J* = 15.6 Hz, H-7)], one olefinic proton of trisubstituted alkene [δ_H 5.96 (1H, *s*, H-4)], nonequivalent methylene protons [δ_H 2.53 (1H, *d*, *J* = 17.2 Hz, H_a-2), and 2.36 (1H, *d*, *J* = 17.2 Hz, H_b-2)], together with four methyl groups [δ_H 2.31 (3H, *s,* H-10), 1.89 (3H, *s,* H-11), 1.11 (3H, *s,* H-12), and 1.03 (3H, *s,* H-13)]. In this study, the configuration at C-6 of compound **3** was identified by the specific rotation presented by levorotation ($[\alpha]_D^{25}$ -1.81, *c* = 0.022, MeOH). The ECD spectrum presented a positive Cotton effect at 247 nm (Δε +22.7). A positive Cotton effect at ~250 nm (π→π* transition; enone system) indicated the absolute configuration at C-6 to be *S*. Consequently, the structure of the compound **3** was identified as (*6S*)-dehydrovomifoliol.[10-12]

(–)-Loliolide (**4**) was isolated as a yellow viscous oil. The molecular formula of compound **4** was $C_{11}H_{16}O_3$; the HRMS data displayed a molecular ion at *m/z* $[M+H]^+$ 197.1169 (calculated $[M+H]^+$ $C_{11}H_{16}O_3$, 197.1173). The UV (MeOH) spectrum showed maxima absorption band at 206 nm. The FT-IR spectrum presented absorption in the broadband at 3360 cm^{-1}, indicating O-H stretching (hydroxy group), the narrow band at 2924 cm^{-1}, and the sharp band at 1726 cm^{-1} indicating C=O stretching (carbomethoxy group). Compound **4** was a

benzofuran derivative based on ^{1}H NMR spectroscopic data, which showed signals for one olefinic proton of trisubstituted alkene [δ_H 5.70 (1H, *s*, H-3)], one oxygenated methine [δ_H 4.34 (1H, *m*, H-6)], two sets of nonequivalent methylene protons [δ_H 2.46 (1H, *dd*, *J* = 14.1, and 4.0 Hz, H_a-7), and 1.80 (1H, *dd*, *J* = 14.1, and 4.0, H_b-7), and δ_H 1.98 (1H, *dt*, *J* = 14.1 and 2.7 Hz, H_a-5), and 1.52 (1H, *dt*, *J* = 14.1 and 2.7 Hz, H_b-5)], together with three methoxy groups [δ_H 1.79 (3H, *s*, H-9), 1.47 (3H, *s*, H-10), and 1.28 (3H, *s*, H-8)]. In this study, the absolute configuration at C-7a of compound **4** was identified by the specific rotation presented by the levorotation ($[\alpha]_D^{25}$-3.57, *c* = 0.0028, MeOH). The ECD spectrum presented two Cotton effects at 227 nm (Δε -54.8) and 257 (Δε +5.8). A negative Cotton effect at ~230 nm (π→π* transition; acyl system) and a positive Cotton effect at 260-270 nm (n→π* transition; C-C to C=C) established the 6*R*,7a*S* configuration. Consequently, compound **4** was identified as (–)-loliolide.[13-15]

Vanillic acid (**5**) was isolated as a brown viscous oil. The molecular formula of compound **5** was $C_8H_8O_4$; the HRMS data displayed a molecular ion at *m/z* [M-H]$^-$ 167.0648 (calculated [M-H]$^-$ $C_8H_8O_4$, 167.0653). The UV (MeOH) spectrum showed two maxima absorption bands at 292 and 259 nm. The FT-IR spectrum presented absorption in the broadband at 3479 cm^{-1}, indicating O-H stretching (hydroxy group), the narrow band at 2924 cm^{-1}, indicating O-H stretching (carboxylic group), the medium band at 1680 cm^{-1}, indicating C=O stretching (carboxylic group), the narrow band at 1376 and 910 cm^{-1}, indicating O-H bending (hydroxy group), and the narrow band at 1273 cm^{-1} indicating C-O stretching (carboxylic group). Compound **5** was also a phenol derivative based on ^{1}H NMR spectroscopic data, which showed signals for a 1,3,5-trisubstituted benzene [δ_H 7.72 (1H, *dd*, *J* = 8.3 and 2.0 Hz, H-5), 7.58 (1H, *d*, *J* = 2.0 Hz, H-2), and 6.97 (1H, *d*, *J* = 8.3 Hz, H-6)], together with one methoxy group [δ_H 3.97 (3H, *s*, -OCH_3)]. Thus, compound **5** was identified as vanillic acid.[16-17]

(*6S*,*9R*)-Vomifoliol (**6**) was isolated as a yellow viscous oil. The molecular formula of compound **6** was $C_{13}H_{20}O_3$; the HRMS data displayed a molecular ion at *m/z* [M-H]$^-$ 223.6024 (calculated [M-H]- $C_{13}H_{20}O_3$, 223.6012). The UV (MeOH) spectrum showed maxima absorption band at 235 nm. The FT-IR spectrum presented absorption in the broadband at 3417 cm^{-1}, indicating O-H stretching (hydroxy group), the narrow band at 2924 cm^{-1}, indicating aromatic, the narrow band at 2853 cm^{-1}, indicating C=C-H stretching (aromatic), and the narrow band at 1655 cm^{-1}, indicating C=C stretching (alkene-cis). Compound **6** was also a sesquiterpene derivative based on ^{1}H NMR spectroscopic data showed similar signals to compound **3,** except for one additional signal for one oxygenated methine proton [δ_H 5.91 (1H, *t*, *J* = 1.4 Hz, H-9)] in compound **6**. In this study, the absolute configuration at C-6 and C-9 of compound **6** was identified by the specific rotation presented by dextrorotation ($[\alpha]_D^{25}$ +7.17, *c* = 0.0053, MeOH). The ECD spectrum presented two Cotton effects at 242 nm (Δε +94.8) and 321 nm (Δε -9.36). A positive Cotton effect at ~250 nm (π→π* transition; enone system) and a negative Cotton effect at ~320 nm (n→π* transition; conjugated carbonyl system) established the *6S*,*9R* configuration. Consequently, compound **6** was identified as (*6S*,*9R*)-vomifoliol.[18-21]

Table 1.
α*-Glucosidase inhibitory and NO production inhibitory activities of fractions isolated from *L. japonicus

Fractions	*α*-Glucosidase inhibitory activity	NO production inhibitory activity
	IC_{50} Values (μg/mL)	IC_{50} Values (μg/mL)
EtOAc-soluble[a]	72.8 ± 1.9	20.7 ± 2.2
A	Inactive[c]	75.5 ± 4.0
B	Inactive[c]	51.2 ± 3.4
C	Inactive[c]	39.8 ± 4.6
D	Inactive[c]	49.4 ± 2.9
E	49.4 ± 1.5	29.0 ± 3.2
F	72.8 ± 1.0	59.8 ± 3.8
G	Inactive[c]	toxic[d]
H	27.9 ± 0.1	34.3 ± 3.5
I	Inactive[c]	toxic[d]
J	Inactive[c]	54.4 ± 5.2
Acarbose[b]	115.4 ± 0.6	-
Indomethacin[b]	-	78.3 ± 2.4

[a]Concentration of the extract or fraction was 200 μg/mL
[b]Compound used as a positive control
[c]Inactive at >200 μg/mL
[d]The percentage of cell viability is less than 80%

α*-Glucosidase and NO production inhibitory activities-guided fractionation of the extract of *L. japonicus

α-Glucosidase and NO production inhibitory activities of the EtOAc-soluble part and its semi-purified fractions of *L. japonicus* were summarized in Table 1. Fractions E, F, and H exhibited stronger inhibitory *α*-glucosidase activity than the EtOAc-soluble part and positive control (acarbose). However, for NO production inhibitory activity, the EtOAc-soluble part was more active than all of fractions and positive control (indomethacin).

Table 2.
α*-Glucosidase inhibitory and NO production inhibitory activities of compounds isolated from *L. japonicus

Compounds	*α*-Glucosidase inhibitory activity	NO production inhibitory activity
	IC_{50} Values (μM)	IC_{50} Values (μM)
1	143.9 ± 0.6	214.8 ± 3.3
2	367.5 ± 0.6	66.9 ± 3.7
3	408.5 ± 1.9	70.6 ± 3.8
4	434.7 ± 1.1	187.5 ± 3.7
5	598.4 ± 0.6	285.8 ± 2.5
6	192.2 ± 0.5	toxic[b]
Acarbose[a]	157.1 ± 0.1	-
Indomethacin[a]	-	32.7 ± 3.9

[a]Compound used as a positive control.
[b]The percentage of cell viability is less than 80%

α-Glucosidase and NO production inhibitory of isolated compounds from *L. japonicus*

Compounds **1-6** were tested for α-glucosidase and NO inhibitory production activities (Table 2). Many flavonoid compounds have antidiabetic properties, according to *in vitro* studies.[22] Compound **1** showed stronger inhibitory activity against α-glucosidase activity than other compounds and positive control. Compound **1** exhibited effective α-glucosidase activity with an IC_{50} value of 143.9 μM, and compound **2** showed lower activity with IC_{50} value of 367.5 μM. The main flavonoid subclasses are flavones, flavonols, flavanones, and isoflavones. In many studies, numerous members of these groups have proved to be effective α-glucosidase inhibitors.[22-23] The result agreed with that of previously reported that the flavanone showed stronger inhibitory α-glucosidase activity than the flavone skeleton.[23] From the above data, it can be deduced that the main components responsible for the α-glucosidase activity of *L. japonicus* were flavonoids.

However, compounds **2** and **3** showed the strongest anti-inflammatory activity with IC_{50} values of 66.9 and 70.6 μM, respectively. These data demonstrated that the main components responsible for the anti-inflammatory activity of *L. japonicus* were the flavone and terpenoid derivatives.

Conclusion:

In the course of our ongoing research project on bioactive natural products from aerial of *L. japonicus*, an EtOAc-soluble part of the EtOH extract of the arial of *L. japonicus* displayed α-glucosidase and NO production inhibitory activities. This prompted us to perform detailed bioassay-guided isolation from this plant, which led to the isolation of six known compounds. (*S*)-sakuranetin (**1**) showed the highest efficacy in inhibiting α-glucosidase enzyme with the IC_{50} values of 143.9 μM. However, genkwanin (**2**) and (*6S*)-dehydrovomifoliol (**3**) showed moderate anti-inflammatory with IC_{50} values of 66.9 and 70.6 μM, respectively. These findings support that *L. japonicus* is a good source of bioactive compounds.

Acknowledgments:

This work was supported by Medicinal Plants Innovation Center (MPIC), and Mae Fah Luang University were acknowledged for its laboratory facilities. In addition, my parents and the Center of Chemical Innovation for Sustainability (CIS) partially financially support me.

References:

1. Shang X, Pan H, Wang X, He H, Li M. J Ethnopharmacol. 2014;152:14-32.
2. Queiroz SC, Cantrell CL, Duke SO, Wedge DE, Nandula VK, Moraes RM, Cerdeira AL. J Agric Food Chem. 2012;60:5893-5898.
3. Suthiphasilp V, Maneerat W, Rujanapun N, Duangyod T, Charoensup R, Deachathai S, Laphookhieo S. Bioorg Med Chem. 2020;28:115462.
4. Grecco SD S, Dorigueto AC, Landre IM, Soares MG, Martho K, Lima R, Lago JH G. Molecules. 2014;19:7528-7542.
5. Takemoto JK, Remsberg CM, Yáñez JA, Vega-Villa KR, Davies NM. J Chromatogr A. 2008;875:136-141.
6. Yamashita Y, Hanaya K, Shoji M, Sugai T. Chem Pharm Bull. 2016;64:961-965.

7. Zainullin RA, Kunakova RV, Gareev VF, Galyautdinov IV, Sadretdinova ZR, Muslimov ZS, Odinokov VN. Chem Nat Compd. 2018;54:975-977.
8. Bosabalidis A, Gabrieli C, Niopas I. Phytochemistry, 1998;49:1549-1553.
9. Ray G, Leelamanit W, Sithisarn P, Jiratchariyakul W. J Pharm Sci. 2014;41:54-8.
10. Yang Y, Bakri M, Gu D, Aisa HA. J Liq Chromatogr. 2013;36:573-582.
11. Aishan H, Baba M, Iwasaki N, Kuang H, Okuyama T. Pharm Biol. 2010;48:577-583.
12. Kobayashi N, Muranaka A. RSC Adv. 2011.
13. Gangadhar KN, Rodrigues MJ, Pereira H, Gaspar H, Malcata FX, Barreira L, Varela J. Mar Drugs. 2020;18:567.
14. Bich TTN, Kato-Noguchi H. Bot Stud. 2014;55:1-5.
15. Vingre da Silva Mota G, Costa FLP. J Mol Model. 2021;27116.
16. Chang SW, Kim KH, Lee IK, Choi SU, Ryu SY, Lee KR. Nat Prod Sci. 2009;15:234-240.
17. González-Baró A.C, Parajón-Costa BS, Franca CA, Pis-Diez R. J Mol Struct. 2008;889:204-210.
18. Maria S, Islam F, Qais N, Hasan CM. Asian J Chem. 2013;25:3533.
19. Yamano Y, Ito M. Chem Pharm Bull. 2005;53:541-546.
20. Grayer RJ, Thabrew MI, Hughes RD, Bretherton S, Lever A, Veitch NC, Simmonds MS. Pharm Biol. 2008;46:154-161.
21. Snatzke G. Angew Chem Int Ed Engl. 1979;18:363-377.
22. Proença C, Freitas M, Ribeiro D, Oliveira EF, Sousa JL, Tome SM, Fernandes E. J Enzyme Inhib Med Chem. 2017;32:1216-1228.
23. Şöhretoğlu D, Sari S, Barut B, Özel A. Bioorg Chem. 2018;79:257-264.

α-GLUCOSIDASE INHIBITORY ACTIVITY OF CHEMICAL CONSTITUENTS FROM *Premna herbarcea* Roxb. ROOT EXTRACT

Angkana Doungsanit[1-4], Passakorn Teerapongpisan[1,2], Wutthichai Jaidee[3,4], Virayu Suthiphasilp[3,4], Surat Laphookhieo[1-4], Rawiwan Charoensup[3,4], Tharakorn Maneerat[1-3,*]
[1]Department of Applied Chemistry, School of Science, Mae Fah Luang University, Chiang Rai 57100, Thailand
[2]Center of Chemical Innovation for Sustainability (CIS), Mae Fah Luang University, Chiang Rai 57100, Thailand
[3]Medicinal Plant Innovation Center of Mae Fah Luang University, Chiang Rai 57100, Thailand
[4]Department of Thai Traditional Medicine, School of Integrative Medicine, Mae Fah Luang University, Chiang Rai 57100, Thailand
*e-mail: wisanu.man@mfu.ac.th

Abstract:

Premna herbacea Roxb. or Khao Yen Tai in Thailand, is used in the Ayurvedic traditional Thai medicine system as an ingredient formula for treating several ailments, especially diabetes. Nevertheless, the antidiabetic against α-glucosidase enzyme of chemical components from this plant remains unknown. In this study, four diterpenoid quininemethides were isolated and identified as known compounds: bharangin (**1**), bharangi-δ-lactone (**2**), salvilenone (**3**), and sapriolactone (**4**) from the EtOAc extract of *P. herbacea* roots. Their chemical structures were determined by analysis of spectroscopic methods and by comparison with literature data. Crude extracts and all isolated compounds were screened at a concentration of 200 μg/mL and evaluated the IC_{50} values in a series of concentrations for α-glucosidase inhibitory activity. Compounds **1**, **3,** and **4** showed significant inhibitory activity against α-glucosidase with IC_{50} values of 67.9, 30.9, and 44.4 μM, respectively, while compound **2** showed the weakest activity with an IC_{50} value of 282.5 μM.

Introduction:

Diabetes mellitus (DM) is one of the most serious chronic diseases,[1] which is a metabolic disease characterized by high blood glucose that results from decreased insulin production (type 1) and decreased tissue response to insulin action (type 2).[2] Over 10% of the world's population is estimated to have DM or be at high risk of developing DM, according to the report of the World Health Organization. Thailand is among the Asian countries with a high prevalence of diabetes.[3] The value of public health policy is greatly diminished by incomplete registration of death and by concerns about the quality of cause-of-death information. Research Estimated causes of death in Thailand in 2005, therefore, examined the deaths to eliminate misclassification and derive the best estimate of national mortality patterns by age, sex, and cause of death. Almost 400,000 deaths are registered each year, showing the percentage of death in DM of women and men was 8.2% and 3.3%, respectively.[4] DM is a leading cause of the cardiovascular disease (primarily heart disease and stroke), renal failure, and blindness (due to diabetic retinopathy).[5]

Medicinal plants have long been used in traditional medicine. In Thailand, many medicinal plants from the Lamiaceae family are used as herbal medicines such as antiallergenic, antidiabetic, antioxidant, antimutagenic, anticarcinogenic, antimicrobial, and anti-inflammatory agents, enhancers of the gastrointestinal function, immune-modulators and stimulators as well as blood pressure and cholesterol reducing agents.[6] The Lamiaceae family

is a rich source of terpenoids, quinonemethides,[7] and coumarin.[8] *Premna herbacea* Roxb. a small herb like an undershrub, belongs to the family of Lamiaceae.[7] In Thailand, *P. herbacea* locally known as "Khao-Yen-Tai", has mostly been used in the Ayurvedic traditional Thai medicine system as an ingredient formula for the treatment of several ailments.[9] About 2449 preparations for "Hua-Khao-Yen" were registered at the Ministry of Public Health of the Thai government in 1986.[10] These preparations have been used to treat leprosy, venereal diseases, inflammations, bacterial infections, and cancers.[11] However, a survey of 23 traditional Thai doctors nationwide discovered the use of five species of "Hua-Khao-Yen" including *Dioscorea birmanica*, *Dioscorea membranacea, Premna herbacea, Smilax corbularia,* and *Smilax glabra* for the treatment of cancers, AIDS, septicemia and lymphatic diseases.[12] In the previous research, the ethanolic extract of the root and root nodules of *P.herbacea* exhibited many activities such as antipyretic activity, antipyretic activity, and anti-inflammatory activity.[13] Moreover, ethanolic and water extracts of the rhizome of *P. herbacea* were treated with anti-HIV activity,[14] and cytotoxic activity.[15] In addition, ethanol, ethyl acetate, butanol, and water extracts from root nodules of *P.herbacea* displayed i*n vitro* cytotoxicity in MCF-7 cell (Human Breast adenocarcinoma cells) by MTT assay with IC_{50} values of 75.51, 84.04, 269.12 and 12032.20 µg/mL, respectively and *in vivo* antitumor activity on brine shrimp lethality bioassay with LC_{50} (lethal concentration) values of 7.82, 2.05, 364.24 and 648.65 µg/mL, respectively.[16] Our initial studies showed that the ethyl acetate extract of the roots of *P.herbacea* showed strong α-glucosidase inhibitory activity (99% inhibition at 200 µg/mL). The current study investigated the chemical constituents of *Premna herbacea* Roxb. root extracts and evaluated their antidiabetic activity *via* the α-glucosidase inhibitory pathway. The project aimed to discover primary bioactive compounds for developing antidiabetic therapeutic drugs in the future.

Methodology

General experimental procedure

1D and 2D NMR spectra were recorded with Bruker AVANCE NEO NMR spectrometers operating at 500 MHz. High-resolution mass spectra (HRESIMSQTOF) were recorded using a Liquid Chromatography Quadrupole Time-of-Flight Mass Spectrometer; LC-QTOF with Agilent technologies Agilent 1290 Infinity II G6545B QTOF/MS mass spectrometer. Circular Dichroism and UV-Visible spectra were recorded with JASCO J-1500 spectrophotometer. Fourier Transform Infrared Raman (IR) spectra were recorded with Thermo scientific Nicolet iS50 Spectrometer. Analytical thin-layer chromatography (TLC) was performed with Merck silica gel 60 F_{254} plates (0.25 mm for thick layer). Column chromatography was performed with Merck silica gel 60 (70-230 mesh).

Plant material

The dried plant of *P. herbacea* was bought from drugstore in Phichit Province, Thailand in October 2020 by the Medicinal Plants Innovation Center of Mae Fah Luang University. The plant was identified by Assoc. Prof. Dr. Surat Laphookhieo at the Natural Products Research Laboratory of Mae Fah Luang University

Extraction and isolation

The dried root of *P. herbacea* (3 kg) was ground and extracted by acetone (3×20 L) to give an acetone extract. The acetone extract was partitioned with water, and ethyl acetate to give ethyl acetate extract (SGA), and water extract (SGA.H_2O). The solvent was evaporated in a vacuum using a rotary evaporator to obtain the crude extracts. The ethyl acetate extract (24.5 g) was separated by quick column chromatography (silica gel, acetone-hexane, a

gradient of 0:100 to 100:0) to give 7 fractions (SGA1A-SGA1G). Fraction SGA1B (3.5596 g) was recrystallized to afford compound **1** (4.6 mg) as yellow crystals. Fraction SGA1C (4.1938 g) was separated by normal-phase flash column chromatography (FCC) using a mobile phase of acetone-hexane (1:4, v/v) collecting 9 subfractions (SGA2A-SGA2I). Subfraction SGA-2B (252.6 mg) was separated by normal-phase FCC using a mobile phase of DCM-hexane (3:1, v/v) collecting 8 subfractions (SGA7A-SGA7H). Compound **2** (7.4 mg) was obtained by purification of subfraction SGA-7F (17.8 mg) with column chromatography (CC) using DCM-hexane (3:1, v/v). Compound **3** (3.0 mg) was obtained by purification of subfraction SGA-7H (18.8 mg) with CC using acetone-hexane (1:4, v/v). Fraction SGA1D (855.2 mg) was separated by normal-phase FCC using a mobile phase of acetone-DCM (a gradient of 0:100 to 100:0) collecting 9 subfractions (1DSGA1A-1DSGA1I). Subfraction 1DSGA-1E (101.4 mg) was separated by normal-phase FCC using a mobile phase of acetone-DCM (1:9, v/v) collecting 4 subfractions (1DSGA2A-1DSGA2D). Compound **4** (1.4 mg) was obtained by purification of subfraction 1DSGA-2B (8.7 mg) with CC using MeOH-DCM (1:19, v/v).

α-Glucosidase inhibition assay

The α-glucosidase inhibitory activity was performed using the same methodology as in the previous study.[3,17] After preparing a series of concentrations of samples and positive control (acarbose) in 5% DMSO with phosphate buffer saline (PBS) (pH 6.8, 50 µL) to obtain the extract solution with a final concentration in a range of 1.25-250 µg/mL, then was combined in a 96-well microplate with 50 µL of the α-glucosidase enzyme (0.05 U/mL). After leaving the sample mixtures at 37°C for 5 minutes, 50 µL of 1 mM *p*-nitrophenyl-α-D-glucopyranoside in buffer was added to each well. Then, the reaction was further incubated at 37 °C for 30 min. The reaction was stopped by adding 50 µL of Na_2CO_3 (0.3 M), and the absorbance at 400 nm was measured using a microplate reader.[17] The procedure was carried out in triplicate. Acarbose was used as a positive control with an IC_{50} value of 374.6 µM. The process was repeated in triplicate and the percent inhibition was calculated with the following equation:

$$\text{Percent inhibition (\%)} = [((A - B) - (C - D)) / (A - B)] \times 100$$

where,

A is the absorbance of a blank reaction containing only 5% DMSO in phosphate buffer,

B is the absorbance of the control reaction containing 5% DMSO in phosphate buffer and α-glucosidase enzyme,

C is the absorbance of sample reaction containing sample solution and α-glucosidase enzyme,

D is the absorbance of the control sample containing only the sample solution.

The concentration of samples that inhibited α-glucosidase activity by 50% was defined as the IC_{50} value.[3]

Results and Discussion:

Purification and investigations of ethyl acetate extract from *P. herbacea* led to the isolation of four known compounds (**Figure 1**). The structures of these isolated compounds were characterized by analysis of their 1D NMR, IR, UV, MS data and the comparison with the previous reports.

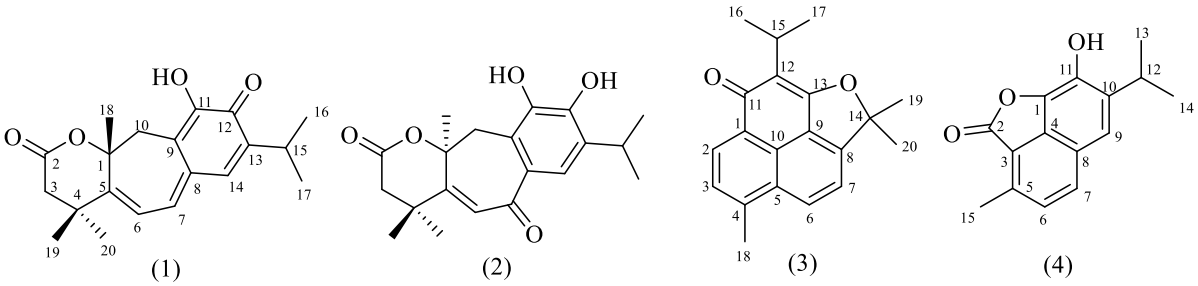

Figure 1.
The structures of isolated compounds

Bharangin (**1**) was isolated as yellow crystals; mp. 213-214 ºC; $[\alpha]_D^{25}$+378º (*c* 0.1, MeOH). HRESIMSQTOF analysis of molecular was determined as $C_{20}H_{24}O_4$ at *m/z* 329.1750 $[M+H]^+$ (calcd for $C_{20}H_{25}O_4$ 329.1747). The IR spectrum absorption showed the absorption for hydroxyl at 3334 cm^{-1}, ν_{max} 1730 cm^{-1} presence of carbonyl on δ-lactone, and carbonyl showed the absorption at 1600 cm^{-1}, and the UV spectrum showed absorption maxima at λ_{max} 386 nm. The ^{1}H NMR (500 MHz, $CDCl_3$) showed a diterpenoid skeleton incorporating an extended quinonemethide core structure at the assignable signals to two sets of the methylene protons in AB doublets at δ_H 3.67 (1H, d, *J* = 15.3 Hz, H-10) and δ_H 2.90 (1H, d, *J* = 15.3 Hz, H-10) and δ_H 2.60 (1H, d, *J* = 16.4 Hz, H-3) and δ_H 2.47 (1H, d, *J* = 16.3 Hz, H-3)[18], the signal at δ_H 3.10 (1H, p, *J* = 6.9 Hz, H-15) corresponding to a methine proton of an isopropyl group and two doublets for two methyls of isopropyl group at δ_H 1.18 (3H, d, *J* = 6.9 Hz, H-16) and δ_H 1.16 (3H, d, *J* = 6.9 Hz, H-17) and three singlets at δ_H 1.43 (3H), δ_H 1.34 (3H), δ_H 1.28 (3H). Furthermore, the ^{13}C NMR spectrum showed signals for two carbonyls δ_C 179.2 (saturated carbonyl) and δ_C 170.4 (δ-lactone), eight carbon signals in the aromatic and ten carbon signals in the aliphatic region. The presence of four methines, two methylene, and five methyl signals was differentiated in its DEPT 135º spectrum. Among the four methine carbons, one was in the aliphatic (δ_C 26.8) region and three in the aromatic (δ_C 138.0, δ_C 137. 9, and δ_C 117. 1). Two methylene carbons (δ_C 42. 5 and δ_C 38. 6) and the remaining five methyl carbons showed signals at δ_C 29.7 (C-19), δ_C 28.5 (C-20), δ_C 23.7 (C-18), δ_C 21. 8 (C-16) and δ_C 21. 7 (C-17) were in the aliphatic region. These data were confirmed by HMBC correlations between 3.67 and 2.90 (H-3) with C-2 (δ_C 170.4), C-4 (δ_C 37.7), C-5 (δ_C 159.3), C-19 (δ_C 29.7), 6.50 (H-7) with C-5 (δ_C 159.3), C-8 (δ_C 134.0), C-14 (δ_C 137.9), and 6.79 (H-14) with C-8 (δ_C 134.0), C-12 (δ_C 179.2), C-14 (δ_C 137.9). Thus from the preceding spectral studies, the structure of **1** was elucidated as bharangin.[9,18,19]

Bharangi-*δ*-lactone (**2**) was isolated as a yellow powder; mp. 242–244 ºC; $[\alpha]_D^{25}$-39º (*c,* 0.1, MeOH). HRESIMSQTOF analysis of molecular was determined as $C_{20}H_{24}O_5$ at *m/z* 344.1621 $[M-H]^-$ (calcd for $C_{20}H_{23}O_5$ 344.1624). The IR spectrum displayed absorption bands at ν_{max}: 3357, 1733 and, 1636 cm^{-1} indicating the presence of hydroxyl group, carbonyl on γ-lactone and carbonyl, respectively. The UV spectrum showed absorption maxima at λ_{max} 246 and 328 nm. The ^{1}H NMR (500 MHz, $CDCl_3$) spectroscopic data suggested that the structure of **2** had a quinonemethides core structure, which was closely related to that of **1**. The major difference between compounds **2** and **1** was the replacement of hydroxyl group (δ_C 190.1) and carbonyl group (δ_C 146.1) at C-7 and C-12 of **2**, respectively. This structure was confirmed by HMBC spectrum correlation between the signal of 6.34 (H-6) with C-5 (δ_C 160.7), C-7 (δ_C 190.1), and C-8 (δ_C 128.8) and 7.61 (H-14) with C-9 (δ_C 121.2), C-12 (δ_C

146.6), and C-14 (δ_C 121.5). Thus from the preceding spectral studies, the structure of **2** was elucidated as bharangi-δ-lactone.[9]

Salvilenone (**3**) was isolated as a yellow gum; mp. 141.2 ºC. HRESIMSQTOF analysis of molecular was determined as $C_{20}H_{20}O_2$ at *m/z* 293.1538 $[M+H]^+$ (calcd for $C_{20}H_{21}O_2$ 293.1542). The IR spectrum displayed absorption bands at ν_{max}: 1658, 1634, 1607 cm^{-1} and, 1372 cm^{-1} indicating the presence of phenyl ring and gem-dimethyl, respectively. The UV spectrum showed absorption maxima at λ_{max} 332 nm. The ^1H NMR (500 MHz, $CDCl_3$) showed a diterpenoid skeleton incorporating an extended phenalenone core structure,[20] which phenalenone is an aromatic ketone that constitutes an unusual class of nonbenzenoid aromatic compounds, and it has remarkable stability of phenalenyl radicals, anions, and cations.[21] The presence of phenalenone core structure showed in the signals of two sets of *ortho* aromatic proton at δ_H 8.37 (1H, d, J = 7.4 Hz, H-2), δ_H 7.58 (1H, d, J = 7.4 Hz, H-3), and δ_H 8.14 (1H, d, J = 8.4 Hz, H-6), δ_H 7.46 (1H, d, J = 8.5 Hz, H-7). The isopropyl group showed a signal of methine proton at δ_H 3.45 (1H, hept, J = 7.1 Hz) and two doublets for two methyls at δ_H 1.35 (6H, d, J = 7.1 Hz). The positions of which were confirmed by HMBC correlation between δ_H 3.45 (H-15): C-11 (δ_C 185.8), C-12 (δ_C 119.6), C-13 (δ_C 165.1), C-16,17 (δ_C 21.0). Furthermore, the ^{13}C NMR spectrum showed the signals of quaternary and carbonyl carbons at C-13 (δ_C 165.7) and C-11 (δ_C 185.8), respectively. The position of the methyl group attached to the aromatic ring position was confirmed by HMBC that correlated between δ_H 2.81 (H-18) to C-2 (δ_C 129.6), C-3 (δ_C 128.8), and C-4 (δ_C 140.1) and carbonyl between δ_H 3.45 (H-15) and δ_H 8.37 (H-2). Thus from the preceding spectral studies, the structure of 3 was elucidated as salvilenone.[22,23]

Sapriolactone (**4**) was isolated as a white powder; mp. p 123-124 ºC HRESIMSQTOF analysis of molecular was determined as $C_{15}H_{14}O_3$ at *m/z* 242.0934 $[M+H]^+$ (calcd for $C_{15}H_{15}O_3$ 242.1021). The IR spectrum displayed absorption bands at ν_{max}: 3260 cm^{-1}, 1746 cm^{-1} and 1652, 1476, 1462 cm^{-1}, indicating the presence of hydroxyl group, carbonyl group, and conjugated naphthalene, respectively. The spectrum showed absorption maxima at λ_{max} 347 nm. The ^1H NMR (500 MHz, $CDCl_3$) showed a diterpenoid skeleton incorporating an extended norditerpene core structure[24] at the signals of *ortho* aromatic proton at δ_H 7.91 (1H, d, J = 8.1 Hz, H-7) and δ_H 7.40 (1H, d, J = 8.2 Hz, H-6). The signal of methine proton at δ_H 3.48 (1H, p, J = 6.9 Hz, H-12) indicated the existence of one aromatic isopropyl group at δ_H 1.36 (6H, d, J = 6.9 Hz, H-13,14). Furthermore, the position of aromatic methyl was confirmed by HMBC that correlated between δ_H 2.81 (H-15): C-3 (δ_C 116.1), C-5 (δ_C 129.7), and C-6 (δ_C 141.0). The aromatic protons were confirmed by COSY and HMBC that correlated between the signal of 7.40 (H-6) with C-3 (δ_C 116.1), C-8 (δ_C 123.2), and C-15 (δ_C 17.7), 7.91 (H-7) with C-5 (δ_C 141.0), C-6 (δ_C 129.7), and C-9 (δ_C 117.8) and 7.47 (H-9) with C-6 (δ_C 129.7), C-7 (δ_C 131.6), C-11 (δ_C 134.5), and C-12 (δ_C 28.2). Thus from the preceding spectral studies, the structure of **4** was elucidated as sapriolactone.[24]

All isolated compounds were assayed for their α-glucosidase inhibitory activity with acarbose as a positive control. The result is reported in **Table 1**. The highest α-glucosidase inhibitory activity was shown by salvilenone (**3**), with an IC_{50} value = 30.9 μM, followed by sapriolactone (**4**) (IC_{50} value = 44.4 μM) and bharangin (**1**) (IC_{50} value of 67.9) μM. The acarbose showed an IC_{50} value of 190.4 μM. Compounds **1**, **3**, and **4** also showed inhibitory activity better than acarbose, while of the compound **2** showed the weakest activity.

Table 1.
α-glucosidase inhibitory effect of isolated compounds

Compound	IC_{50} (μM)
Bharangin (**1**)	67.9 ± 0.8
Bharangi-δ-lactone (**2**)	282.5 ± 2.6
Salvilenone (**3**)	30.9 ± 0.02
Sapriolactone (**4**)	44.4 ± 0.9
Acarbose	190.4 ± 3.6

Conclusion:

In conclusion, this paper described the isolation of four compounds, including bharangin (**1**), bharangi-δ-lactone (**2**), salvilenone (**3**), and sapriolactone (**4**), isolated from *P.herbacea*. The compounds were identified as two quinonemethides (**1-2**) and two diterpenoids (**3-4**). All isolated compounds were evaluated for α-glucosidase inhibitory activity, while compound **3** showed the best α- glucosidase inhibition activity.

Acknowledgment:

We would like to thank the Department of Applied Chemistry School of Science, Center of Chemical Innovation for Sustainability (CIS), Medicinal Plants Innovation Center for its laboratory facilities, and Department of Thai Traditional Medicine, School of Integrative Medicine of Mae Fah Luang University, Chiang Rai, Thailand.

References:

1. Kim, Y. M., Wang, M. H., & Rhee, H. I. Carbohydrate research. 2004;339.3:715-717.
2. Sharma, B. R., Park, C. M., Kim, H. A., Kim, H. J., & Rhyu, D. Y. Phytotherapy Research. 2019;33.10:2765-2774.
3. Phukhatmuen, P., Raksat, A., Laphookhieo, S., Charoensup, R., Duangyod, T., & Maneerat, W. Heliyon. 2020;6.4:e03625.
4. Porapakkham, Y., Rao, C., Pattaraarchachai, J., Polprasert, W., Vos, T., Adair, T., & Lopez, A. D. Population Health Metrics. 2010;8.1:1-11.
5. Sun, H., Saeedi, P., Karuranga, S., Pinkepank, M., Ogurtsova, K., Duncan, B. B., ... & Magliano, D. J. Diabetes research and clinical practice. 2022; 183:109-119.
6. Carović-StanKo, K., PeteK, M., Grdiša, M., Pintar, J., Bedeković, D. A. L. I. B. O. R., & Satovic, Z. Czech journal of food sciences. 2016;34.5:377-390.
7. Satish, K., Srihari, G., Sudhakar, G., Narsimha, K., Rao, T. P., & Murthy, M. M. Phytochemistry Letters. 2015; 12:129-132.
8. Meng, Q., & Chen, W. Planta medica. 1988;54.01:48-49.
9. Srihari, G., Vishnuvardhan, M. V. P. S., Satish, K., Subrahamanyam, M., Raju, T. V., Prabakar, T., & Murthy, M. M. Phytochemistry Letters. 2011;4.2:109-112.
10. Division of Medical Research, Department of Medical Sciences, (1986). Report of studi and analysis of the status and potential of the production and utilization of medicinal plants and the need for research and development in Thailand. Ministry of Public Health, Bangkok.
11. Itharat, A., Singchangchai, P., & Ratanasuwan, P. Wisdom of southern Thai traditional doctors. Prince of Songkla University, Songkhla. 1998:126

12. Thongdeeying, P. Doctoral dissertation, THAMMASAT UNIVERSITY. 2016.
13. Narayanan, N. , Thirugnanasambantham, P. , Viswanathan, S. , Reddy, M. K. , Vijayasekaran, V., & Sukumar, E. Fitoterapia. 2000;71.2:147-153.
14. Tewtrakul, S., Itharat, A., & Rattanasuwan, P. ethnopharmacology. 2006;105(1-2) : 312-315.
15. Itharat, A., Houghton, P. J., Eno-Amooquaye, E., Burke, P. J., Sampson, J. H., & Raman, A. ethnopharmacology, 2004;90(1):33-38.
16. Dhamija, I., Kumar, N., Manjula, S. N., Parihar, V., Setty, M. M., & Pai, K. S. R. Experimental and Toxicologic Pathology. 2013;65(3):235-242.
17. Kittiwisut, S., Amnuoypol, S., Pathompak, P., & Setharaksa, S. Sci. Asia. 2021; 48:175-184.
18. Sankaram, A. V. B., Murthi, M. M., Bhaskaraiah, K., Rao, G. N., Subrahmanyam, M., & Shoolery, J. N. Tetrahedron letters. 1988;29(2):245-248.
19. Srihari, G., Vishnuvardhan, M. V. P. S., Satish, K., Subrahamanyam, M., Raju, T. V., Prabakar, T., & Murthy, M. M. Phytochemistry Letters. 2011;4(2):109-112.
20. Phatangare, K. R., Lanke, S. K., & Sekar, N. fluorescence. 2014;24(6):1827-1840.
21. Danheiser, R. L., & Helgason, A. L Journal of the American Chemical Society. 1994;116(21):9471-9479.
22. Kusumi, T., Ooi, T., Hayashi, T., & Kakisawa, H. Phytochemistry. 1985;24(9):2118-2120.
23. Lin, L. Z., Wang, X. M., Huang, X. L., Huang, Y., & Yang, B. J. Planta medica. 1985;54(05):443-445.
24. Long-ze, L. , Xiao-Ming, W. , Xiu-Lan, H. , Yong, H. , & Cordell, G. A. Phytochemistry 1989;28(12):3542-3543.

IN VITRO FREE RADICAL SCAVENGING AND α-GLUCOSIDASE INHIBITORY ACTIVITIES OF *Ludwigia adscendens* EXTRACTS

Kavisara Srithadindang, Nungruthai Suphrom*
Department of Chemistry, Faculty of Science, Naresuan University, Phitsanulok 65000, Thailand
*e-mail: nungruthais@nu.ac.th

Abstract:

The objective of this research was to study the *in vitro* free radical scavenging and α-glucosidase inhibitory activities of *Ludwigia adscendens* (phaeng phuai nam) extract. In the study, fresh shoots of *L. adscendens* were extracted with 95% ethanol. The crude ethanolic extract was then partitioned with ethyl acetate and water to provide ethyl acetate and aqueous extracts. The abilities of both extracts to scavenge DPPH radical and inhibit α-glucosidase were investigated. The preliminary isolation of active compounds based on bioassay-guided fractionation was performed. The determination of total flavonoids of crude extracts and their fractions was also studied. Sub-fractions of ethyl acetate extract and aqueous extract exhibited DPPH radical scavenging activity with IC_{50} values of 4.43-5.11 µg/mL and 10.38 µg/mL, respectively. At the concentration of 80.70 µg/mL, ethyl acetate and aqueous extracts inhibited α-glucosidase activity to a comparable level (98.16 and 97.75 %, respectively). A phenolic compound, ethyl gallate, was identified through preliminary study on the isolation of chemical constituents. Moreover, total flavonoid content in other active fractions was detected. Our findings provide basic information about active fractions; however, further research is required to identify bioactive compounds.

Introduction:

Chronic diseases tend to occur in the elderly and are important for action in the health sector. The most common types of chronic disease include cancer, heart disease, stroke, diabetes, and arthritis. Therefore, there is a lot of research which aimed at the prevention and treatment of health problems. Free radicals are unstable atoms that can cause damage to cells and lead to the aging process and illnesses. The development of natural and synthetic antioxidants that can bind to free radicals and form new free radicals that are more stable is gaining a lot of attention.

Diabetes (Diabetes mellitus) is a metabolic disease that causes high blood glucose levels. The prevalence of diabetes is increasing and is still a top health problem for Thai people in terms of disease status and mortality. There are two main types of diabetes, type 1 and type 2 diabetes. In particular, type 2 diabetes is the most prevalent type of diabetes in Thailand. Type 2 is characterized by insulin resistance, which may be combined with relatively reduced insulin secretion. Besides adjusting exercise behavior and diet in diabetic patients, drugs that can inhibit the α-glucosidase activity, resulting in a lower blood sugar level, are also approved for treatment. However, the α-glucosidase inhibitor drugs (acarbose, miglitol, and voglibose) have some side effects such as flatulence, abdominal distention and diarrhoea.[1] Therefore, this enzyme is one of the important models for the search for new alternative sources for the prevention and treatment of diabetes. In recent years, numerous antioxidants and α-glucosidase inhibitors have been isolated from plants, including flavonoids, alkaloids, terpenoids,

anthocyanins, glycosides and phenolic compounds.[2] Therefore, the natural sources with antioxidant and α-glucosidase inhibiting properties might fulfill this requirement.

Ludwigia adscendens (L.) H. Hara, local Thai name "Phaeng phui nam", is an aquatic plant which belongs to Onagraceae family. The common scientific synonym name of this plant is *Jussiaea repens* L. In some parts of Thailand, people boiled and cooked the young part of shoots, leaves and stems as salad and also dipped them with chili paste. This plant is used traditionally as a poultice to treat ulcers and skin disorders, as an astringent, as a diuretic and for scalp, skin, eye and throat complaints, as well as for its anti-inflammatory properties. According to research reports on *L. adscendens* and its synonym *Jussiaea repens*, some biological activities such as antibacterial, antioxidant, inhibitory (against the proliferation of 3T3–L1 adipocyte cells), anti-inflammatory, and hepatoprotective activities have been reported. The phytochemical investigation of *L. adscendens* has reported the presence of several alkanes, flavonoids, phenolic acids, polyphenols, saponins, sterols, tannins, and triterpenoids.[3] Recently, our research group has preliminary investigated antioxidant properties of some aquatic plant extracts. Among 20 extracts, crude *L. adscendens* ethanolic extract displayed potent DPPH free radical scavenging activity (IC_{50} = 39.57 ± 2.60 μg/mL) and has high content of total phenolic compounds (56.62 ± 9.47 mg GAE/g extract). In the present study, a new lot of fresh shoots was extracted and partially isolated the chemical constituents. The objective was to investigate the *in vitro* DPPH free radical scavenging and α-glucosidase inhibitory activities of crude extracts and their fractions.

Methodology:

Preparation of L. adscendens extract

L. adscendens was collected from the area around Mani Rattana pool, Naresuan University, Phitsanulok. Fresh shoots of *L. adscendens* (LA) were washed and cut it into small pieces. LA fresh shoots (1800 g) were soaked with 95% ethanol (6.3 L) for 3 days at room temperature. The solution was filtered and marc was re-macerated with 95% ethanol with the same procedure for another two times. The resulting solution was pooled and evaporated by rotary evaporator to provide the crude ethanolic extract. Small volume of water was added into the obtained extract and was then partitioned with ethyl acetate. Two soluble parts were obtained; namely ethyl acetate extract (LAE, 122.63 g) and aqueous extract (LAA, 1.1410 g) and kept at -20 ºC before use.

Isolation and identification of chemical constituents in L. adscendens extract

Ethyl acetate extract (LAE, 32.32 g) was dissolved in hexane to give the hexane soluble part (LAEH, 23.48 g). The residue extract (non-soluble part) was then dissolved in dichloromethane and methanol, respectively. Two soluble parts; a dichloromethane soluble part (LAED, 0.27 g) and a methanol soluble part (LAEM, 0.48 g) were obtained. Their chemical profiles were then studied using Thin Layer Chromatography (TLC) and Proton Nuclear Magnetic Resonance spectroscopy (^{1}H NMR) techniques.

A part of hexane soluble part (LAEH, 1.68 g) was isolated using a Sephadex LH-20 column (i.d. 2.5 x 68 cm) and methanol as a mobile phase. A total of 8 fractions were obtained (LAEH.A-LAEH.H). Fraction LAEH.G (0.0236 g) was separated using a reverse phase C18 column (i.d. 2 x 23 cm) and methanol as the mobile phase to obtain 6 sub-fractions (LAEH.G(A)-LAEH.G(F)). Sub-fraction LAEH.G(B) (0.0044 g) which was obtained as a mixture of white-green solid, was separated using the same procedure as fraction LAEH.G to give 3 fractions (LAEH.G(B).1 - LAEH.G(B).3). The comparative studies of their chemical profiles were done by TLC, ^{1}H NMR and LC-MS techniques. A pure compound (3.8 mg) was obtained from fraction LAEH.G(B).2 as a white solid. The structure of this pure compound was identified using spectroscopy techniques.

For the isolation of aqueous extract (LAA), 50 mL of aqueous solution from the partitioning step was dried by freeze dry to obtain an aqueous crude extract (LAAF, 1.1410 g). The remainder solution was fractionated using Dianion HP-20 column (i.d. 3 x 62 cm) and distilled water was used as the initial mobile phase followed with gradient elution by reducing the polarity of the eluents; 50% distilled water (in methanol), and methanol, respectively. Based on the TLC and ^{1}H NMR profiles of obtained fractions, a total of 8 fractions (LAA.A-LAA.H) were obtained.

Determination of total flavonoids using aluminum chloride colorimetric method [4]

The aqueous crude extract (LAAF), three soluble parts (LAEH, LAED and LAEM) at a final concentration of 50 µg/mL, and eight fractions from the aqueous extract (LAA.A - LAA.H) at a final concentration of 500 µg/mL were determined for total flavonoid content using microplate absorbance measurements compared to a standard flavonoid, quercetin. The reaction of a mixed solution of tested sample and 10% $AlCl_3$ in a 96-well microplate was kept and protected from light for 30 min at room temperature. The absorbance was measured with a microplate reader at a wavelength of 415 nm. The absorbance values were then analyzed for total flavonoid content by comparing the absorbance of the sample with quercetin hydrate standard curve and expressed as milligram equivalent of quercetin per a gram of sample (mg QE/ 1 g of sample).

2-Dihenyl-2-pipyrylhydrazyl (DPPH) free radical scavenging activity assay [5]

Various concentrations of 12 samples including a crude extract, three soluble parts and eight fractions as mentioned above were tested for DPPH free radical scavenging activity. The solution of 500 µM DPPH solution (in ethanol) and 100 µL of sample (in appropriate solvent i.e., ethanol, 10%DMSO, distilled water) was mixed into 96-well microplate and kept in the dark for 30 min at room temperature. The absorbance of reaction was measured at a wavelength of 515 nm using a microplate reader. The absorbance values were then calculated to determine the percentage of radical scavenging activity compared to two positive standards; L-ascorbic acid and trolox. Determinations were done in triplicate and the radical scavenging activity values were then plotted against the final concentrations of tested samples in reaction. The half maximal inhibitory concentration (IC_{50}) were determined using GraphPad Prism program.

α-Glucosidase assay

Samples were tested on the inhibition of α-glucosidase activity by monitoring the release of *p*-nitrophenol from the *p*-nitrophenyl-β-D-glucopyranoside (*p*-NPG) substrate. The assay was performed according to the assay previously described [6,7] with slight modifications. Each of LAE and LAA extracts was prepared with a stock concentration of 183 µg/mL in 5%DMSO solvent (in 0.1 M phosphate buffer (pH 6.8). In the assay, the 96-well microplate containing 60 µL sample and 50 µL of 0.2 U/mL α-glucosidase (in 0.1 M phosphate buffer (pH 6.8)) was incubated at 37 ºC for 10 min. After that, 50 µL of 2.5 mM *p*NPG (in 0.1 M phosphate buffer (pH 6.8)) was added and re-incubated at 37 ºC for 20 min. The reaction was stopped with 40 µL of 0.2 M solution of Na_2CO_3 (in distilled water). Then, the mixture was measured at 405 nm by microplate reader. Acarbose was used as a positive control. A solution of 5% DMSO in 0.1 M phosphate buffer (pH 6.8) without sample was used as a control. The inhibition of tested sample was determined by measuring the absorbance and calculated the enzymatic reaction inhibition.

Results and Discussion:

The fresh shoots of *L. adscendens* were extracted with 95% ethanol and was then partitioned with ethyl acetate, resulting two extracts (LAE and LAA) for the initial study. The extraction yield (% weight of fresh weight) were 6.81 (for LAE) and 0.67 (for LAA). The results of DPPH radical scavenging activity and total flavonoid content of LAAF, LAEH, LAED and LAEM are shown in **Table 1**. The aqueous extract (LAAF) exhibited comparable

DPPH radical scavenging activity to that of two positive standards; L-ascorbic acid and trolox. Three soluble parts (LAEH, LAED, and LAEM) exhibited approximately twofold greater DPPH radical scavenging activity than LAAF and two positive controls, IC_{50} values ranging from 4.4-5.1 µg/mL. For the analysis of total flavonoid content, LAEM and LAED had comparable flavonoid levels, while LAAF had the lowest flavonoid content.

Table 1. IC_{50} values of DPPH radical scavenging activity and total flavonoid content of tested extracts. The data were done in triplicate and expressed as mean ± SD.

Samples	**IC_{50} (µg/mL)**	**Total flavonoid content (mg QE/g extract)**
LAAF	10.38 ± 3.15	91.34 ± 0.02
LAEH	4.94 ± 0.69	272.84 ± 0.09
LAED	5.11 ± 1.33	308.80 ± 0.03
LAEM	4.43 ± 0.36	311.24 ± 0.06
L-ascorbic acid	10.17 ± 0.32	n.d.
Trolox	10.99 ± 0.83	n.d.

n.d = not tested

In this study, the preliminary focus was on the soluble part LAEH, which has the highest yield among the three soluble parts and possesses potent DPPH radical scavenging properties. Afterward, a portion of LAEH was fractionated using chromatographic techniques. When the isolation of LAEH was performed, sub-fraction LAEH.H was obtained as a white-green solid. Chromatographic fractionation and purification of the sub-fraction LAEH.G(B).2 resulted in the isolation of a known compound; namely ethyl gallate. The structure (**Figure 1**) was initially elucidated on the basis of ^{1}H NMR, mass spectroscopy and data from literature.[8] Interestingly, ethyl gallate is a natural phenolic antioxidant, anti-inflammatory and antimicrobial agent, and often used as an additive in food, pharmaceutical and cosmetics industry. Therefore, this compound could be used as one of markers for the further study of this plant.

Ethyl gallate: white solid; ESI-MS *m/z*: 197 $[M–H]^–$; ^{1}H NMR (400 MHz, acetone-d_6, δ) 7.12 (2H, *s*, H-2 and H-6), δ 4.25 (2H, *q*, *J* = 7.1 Hz, H-7), 1.31 (3H, *t*, *J* = 7.1 Hz, H-8).

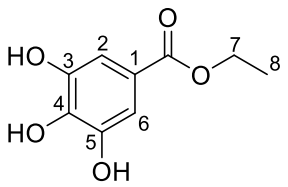

Figure 1. Chemical structure of ethyl gallate isolated from *L. adscendens* extract

In the experiment, some sub-fractions that contained the interested compounds has low amount. To obtain the higher content of compounds, the aqueous extract (LAA) was then focused to isolate using column chromatography technique. After 8 fractions (LAA.A – LAA.H) were obtained, the bioassay-guided fractionation using DPPH radical scavenging activity was applied. The DPPH radical scavenging activity of the sub-fractions is shown in **Figure 2**. At 500 µg/mL, it can be seen that each fraction has a high antioxidant activity.

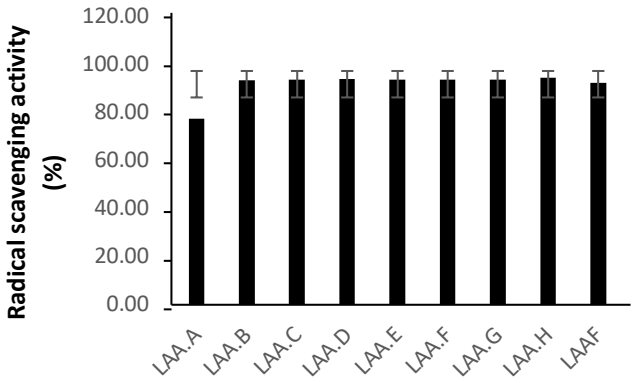

Figure 2. DPPH radical scavenging activity of fractions LAA.A – LAA.H and LAAF which were tested at a concentration of 500 µg/mL (n = 3)

The total flavonoid content was also analyzed and the result showed that LAA.F had the highest total flavonoid content (27.33 ± 0.00 mg QE/g extract) followed by LAA.G (26.97 ± 0.01 mg QE/g extract). For the investigation of α-glucosidase inhibition test, at a concentration of 100 µg/mL of the ethyl acetate (LAE) and aqueous (LAAF) extracts inhibited the activity of enzyme at the same level (97.8-98.2%). As shown in **Table 3**, both extracts showed stronger inhibitory effect on α-glucosidase activity than the standard drug at concentration of 80.70 µg/mL. However, it is still necessary to determine the efficacy of the two extracts and positive drug in terms of IC_{50} in our assay. Moreover, the tests for three soluble parts (LAEH, LAED, and LAEM) are interesting and necessary for the future plan to guide and identify the active soluble part. Unfortunately, the amount of pure ethyl gallate available for testing in our experiment was limited.

Table 3. α-Glucosidase inhibitory activity of extracts at a concentration of 100 µg/mL and the standard drug acarbose at a concentration of 80.70 µg/mL (n=3).

Samples	Inhibitory activity (%)
LAE	98.16 ± 0.23
LAAF	97.75 ± 0.27
Standard drug; acarbose	13.61 ± 7.08

As the results of total flavonoid content and the antioxidant and α-glucosidase inhibitory activity of our extracts, the results corresponded to other published data. Flavonoids isolated from many plants have been reported as antioxidant and α-glucosidase inhibitor.[9] Moreover, some publish data also reported the chemical constituents from watercress and found that methanol and ethanol extracts which rich in flavonoid glycosides and tannins showed good antibacterial, anti-inflammation, antioxidant, anti-diabetic, and α-glucosidase inhibitory activities.[10,11] This present study provides a preliminary information for the further study on the active constituents of this plant.

Conclusion:

The ethyl acetate extract of *L. adscendens* (in terms of three soluble parts LAEH, LAED and LAEM) exhibited potent DPPH radical scavenging, with approximately twice the DPPH radical scavenging activity of LAAF and two positive controls. Sub-fractions LAA.B – LAA.H also showed the promising DPPH radical scavenging activity which should be studied further in the future. Ethyl gallate was isolated and identify from ethyl acetate extract and it may serve

as an antioxidant marker for this plant. Moreover, LAEM and LAED had comparable flavonoid levels, while LAAF had the lowest flavonoid content. Both LAE and LAAF extracts inhibited α-glucosidase activity at tested concentration more effectively than the standard drug. In order to confirm the IC_{50}, the inhibitory potency of each extract against α-glucosidase should be determined in future research. Our findings provide basic information about active fractions, but additional research is necessary to identify bioactive compounds.

Acknowledgments:

This work was supported by Development and Promotion of Science and Technology Talents Project (DPST) and by a partial grant from Department of Chemistry, Faculty of Science, Naresuan University.

References:

1. Hillebrand I, Boehme K, Graefe KH, Wehling K. Klin Wochenschr. 1986;64(8):393–396.
2. Kumar S, Narwal S, Kumar V, Prakash O. Pharmacogn Rev. 2011;5(9):19–29.
3. Shilpi JA, Gray A, Seidel V. Biochem. Syst Ecol. 2010; 38:106–109.
4. Sembiring EN, Elya B, Sauriasari R. Pharmacogn J. 2018;10(1): 123–127.
5. Piangpraichom S, et al. The 4th Conference on Taxonomy and Systematics in Thailand. May 23 – 25 Phitsanulok, Thailand; 2014, 8-14.
6. Dong H-Q, Li M, Zhu F, Liu F-L, Huang J-B. Food chem. 2012;130(2):261–266.
7. Matsui T, Yoshimoto C, Osajima K, Oki T, Osajima Y. Biosci Biotechnol Biochem. 1996; 60(12): 2019-2022.
8. Sato Y, Oketani H, Singyouchi K, Ohtsubo T, Kihara M, Shibata H, Higuti T. Biol Pharm Bull. 1997; 20(4):401–404.
9. Hong HC, Li SL, Zhang XQ, Ye WC, Zhang QW. Chin Med. 2013; 8(1):19.
10. Marzouk MS, Soliman FM, Shehata IA, Rabee M, Fawzy GA. Nat Prod Res. 2007; 21(5):436–443.
11. Orabi MA., Bayoumi S A, Sayed HM, Huseein EA, Khedr AI, Hatano T. J Appl Pharm Sci. 2020; 10(03): 022 –038.

Session C:
CHEMISTRY
(Physical & Theoretical Chemistry)

EFFECT OF RICE HUSH BIOCHAR ON THE REMOVAL OF Pb^{2+} FROM AQUEOUS SOLUTION

Panita Kongsune,[1,*] Maedah Kueji,[1] Somkait Kongsune[2]
[1] Department of Chemistry, Faculty of Science, Thaksin University, Phattalung, 93210, Thailand
[2]The Center for Scientific and Technological Equipment, Walailak University, Nakhon Si Thammarat, Thailand, 80160
*e-mail: dpanita@tsu.ac.th, +66-74609600 ext 2362

Abstract:

Nowadays, lead contamination in water has become an environmental problem of worldwide concern due to its poisoning in humans cause severe damage to many organs or death. The use of organic amendments, especially biochar, can decrease the decrease of Pb^{2+} in aqueous solution. The aims of this work were to investigate the adsorption capacity and isotherm of Pb^{2+} by biochar prepared from rice husk (RH). The RH was combusted at 500 °C for 4 h. The maximum adsorption capacity at equilibrium (q_e) of Pb^{2+} equal 45.64 mg•g^{-1} was achieved when using RHBC adsorbent, Pb^{2+} concentration of 30 mg•L^{-1}, pH of 5, adsorbent dose of 0.25 g and contact time of 60 min. The isotherm adsorption was found to fit well with the Freundlich isotherm, indicating that the adsorption of Pb^{2+} onto RHBC adsorbent has a high degree of heterogeneity on the surface. The B_1 of Temkin isotherm indicated that the adsorption reaction was an exothermic process. The value of E obtained from D-R isotherm plot was 1.138 kJ•mol^{-1}, indicating that the adsorption process was a physical adsorption.

1. Introduction:

Contamination of soil and water by lead (II) ion (or Pb^{2+}) released from many industrial activities leads to severe problems of soil and water pollution. It is well-known that free Pb^{2+} and its compounds can cause lead prisoning. Noticeably, many attempts have been made to remove Pb^{2+} in ground water and wastewater. Such methods as precipitation, ion exchange, biochar adsorption have been applied [1].

Utilization of biochar (BC) derived from dead biomass and agricultural wastes as a potential absorbent for heavy metal removal from metal contaminated medium is of great interests. This is due to the fact that the derived BC has high porosity and adsorption capacity. Moreover, preparation of BC is cheap and not complicated. Furthermore, reuse and recycle of biomass and agricultural wastes to prepare the derived BC can also reduce wastes from factories and agricultural activities [2].

Various studies of adsorption of heavy metal ions onto BC has been improved and many kinds of the derived BC have been proposed [3]. It was revealed that adsorption capacity of BC depends on many factors. Types of precursors used for BC preparation are also the main factor. Among biomass and agricultural wastes, a rice hush (RH) is the best alternative low-cost materials for BC preparation. This is because RH has a high amount of organic and Si content [4], is locally available and there is a high amount of waste material from rice crop that can be transformed to be a value-added product. A large amount of rice hush waste from consumption should be transformed to be a value-added product.

In this study, RHBC was prepared and applied as absorbent for sorption of Pb^{2+} from aqueous solution. The properties of RHBC were analyzed using various experimental

techniques such as scanning electron microscopy (SEM), energy dispersive X-ray spectrometer (EDS), Fourier Transform Infrared spectroscopy (FT-IR) and Brunauer–Emmett–Teller (BET). For adsorption of Pb^{2+} onto MPAC, the batch experiment was applied and effects of adsorbent dosage, contact time, pH and concentration of Pb^{2+} on adsorption activity of RHBC were also investigated. The equilibrium isotherms, kinetics, and thermodynamics of Pb^{2+} adsorption from aqueous solution were also studies.

2. Methodology:

2.1 Preparation of biochar

The rice hush was collected from rice crop at Papayom district, Phatthalung Province, Thailand. The collected rice hush was dried at 100 ◦C in the heating oven for 24 h. The dried sample was ground to small size and the sample was placed in the porcelain crucibles and tightly covered. The porcelain crucibles were sealed with tin foil paper in order to isolate oxygen and then it was placed into a high temperature furnace (Carbolite CWF 13/23, England). The sample inside the furnace was combusted in air atmosphere at 500 °C for 4 h and then cooled to room temperature. The biochar samples were ground, sieved with mesh No. 200 to a particle size of 0.25 mm and was dried in an oven at 105 °C for 3 hours to remove moisture. Finally, the RHBC stored in the glass bottle for determining the physical and chemical properties.

2.2 Characterization of RHBC

The approximation properties RHBC were analyzed. The FT-IR spectra of RHBC was recorded in a range of 4000-400 cm-1 (G8044AA, Agilent Technologies). The SEM in conjunction with EDS was applied for surface morphology and elemental analysis RHBC (Oxford, Merlin compact).

2.3 Surface acidity/basicity

The surface acidity was estimated by mixing 0.20 g of each adsorbent with 25 cm^3 of 0.05 M NaOH solution in a conical flask for 48 h at room temperature. After the mixtures separated the filtrates were titrated with 0.05 M HCl. The surface basicity was obtained by a similar procedure, while 0.05 M HCl solution was contacted with 0.20 g of adsorbents and the titration solution was 0.05 M NaOH.

2.4 Batch adsorption experiment

The adsorption capacity of RHBC was tested for the removal of Pb^{2+} from aqueous solution. The effects of absorbent dosage, pH of Pb^{2+} solution, contact time, and initial concentration of Pb^{2+} solution on absorption equilibrium were studied and optimism, respectively. The RHBC of 0.25 - 2.50 g were soaked in 150 mL of 5-60 $mg \bullet L^{-1}$ of Pb^{2+} solution (pH 2-8) for 180 min at 30 °C in a shaker bath at the 240 rpm. The initial and final concentrations of Pb^{2+} were analyzed by atomic adsorption spectrophotometer (AAS, Perkin Analyst 700). The percentage of Pb^{2+} removed from the solution (%Pb^{2+} removal) was calculated using equation (1).

$$\%Pb^{2+}\ removal = \left(\frac{C_0 - C_e}{C_0} \right) \times 100 \qquad (1)$$

Where C_0 and C_e are the initial and equilibrium concentrations ($mg \bullet L^{-1}$) of Pb^{2+}.
The adsorption capacity at equilibrium (q_e) in $mg \bullet g^{-1}$ unit of Pb^{2+} was calculated as equation (2).

$$q_e = \left(\frac{C_0 - C_e}{W} \right) \times V \quad (2)$$

Where W, and V are mass of RHBC (g) and volume of the solution (L), respectively.

3. Results and Discussion

3.1 FTIR, SEM and EDS analyses of the RHBC

Adsorption capacity of BC does not depend on only its pore structure but also by the chemical nature of its surface. Many atoms such as oxygen, hydrogen, nitrogen and others exist as single atoms and/or in the form of functional groups on the surface of BC structure. The functional groups of the surface adsorbents were analysed by the FT-IR technique and the FTIR spectra of RH and RHBC are displayed in Fig.1(a). The spectrum of RH and RHBC were displayed very similarly. However, RH adsorbent, which was not subjected to heat treatment and hence, contains especially volatile compounds, is the richest in terms of functional groups compared to other RHBC adsorbent. The wide absorbance band in the range of 3600-3200 cm^{-1} correspond to O-H stretching arising from moisture as well as hydroxyl (-OH) groups present in the sample. Structures containing hydroxyl were phenols, alcohols and carboxylic structures. Relatively long peaks at 1030 cm^{-1} were C-O stretching peaks. The peak at 896 cm^{-1} of RHBC adsorbent also indicated C-O-H group.

SEM photographs of rice hush biochar were observed for visualizing their surface structures and displayed in Fig1(b), the result shows that the surface of the material was smooth with less porous structures, channels or voids. The result of element analysis of RHBC by EDS is shown in Fig.1(c). The EDS data indicated that RHBC has a high carbon, oxygen and silicon contents, hence causing an increase in graphitization and removal of the volatile compound.

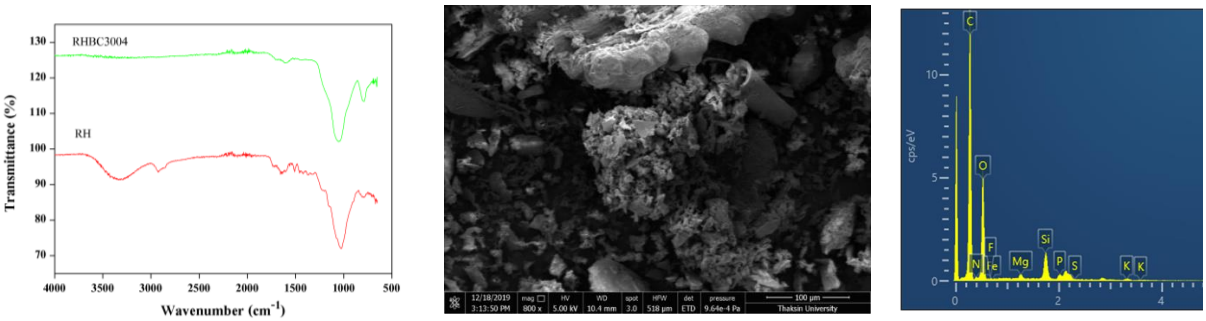

Fig. 1 The (a) FTIR spectrum (b) SEM photograph and (c) EDS spectrum of RHBC adsorbent.

3.2 Boehm titration of the adsorbents

As mentioned before, oxygen and nitrogen atoms are important factors that affect the surface property of biochar. The oxygen containing functional groups such as hydroxyl and the nitrogen containing functional groups such as amine are commonly located on the surface. The higher the oxygen contents the more acidic whereas the higher the nitrogen contents the more basic the surface. Acidic and basic surface functionalities are determined by Boehm titration and summarized in Table 1. The total amount of surface of RH and

RHBC were acidic than that of basic because it contained higher oxygen contents. In addition, the value of the acidic groups of the RHBC sample was higher than that of RH. Carbonization process decreased the volatile compounds on the structure of the RH. This result was consistent with the EDS and pH results. Therefore, the activating agent the arrangement of surface functional groups.

Table 1 The pH, %Yield, acidic and basic values of RH and RHBC adsorbents

Adsorbent	pH	% Yield	Acidic site (mmol/g)	Basic site (mmol/g)
RH	5.15	-	2.62	0.84
RHBC	4.95	75.99	3.39	0.98

3.3 Effects of parameters on Pb^{2+} adsorption

Results from studying the effects of adsorbent dosage, pH of Pb^{2+} solution, initial concentration of Pb^{2+} solution, and contact time on Pb^{2+} adsorption are displayed in Fig. 2a-2d, respectively. Fig.2a presents the effect of the adsorbent dose on the adsorption of the Pb^{2+} by varying the adsorbent amount from 0.25 to 2.5g for RHBC at fixed times of 180 min, pH values of 7, temperatures of 30 ºC, and initial concentrations of 5 ppm. It was observed that the amount of Pb^{2+} adsorbed per unit weight of adsorbent (q) decreased with an increase in adsorbent dose while the removal percentage of Pb^{2+} by RHBC slightly increased with an increase in adsorbent dose. This suggests that using 0.25 g of RHBC can yield a high value of q and $\%Pb^{2+}$ removal.

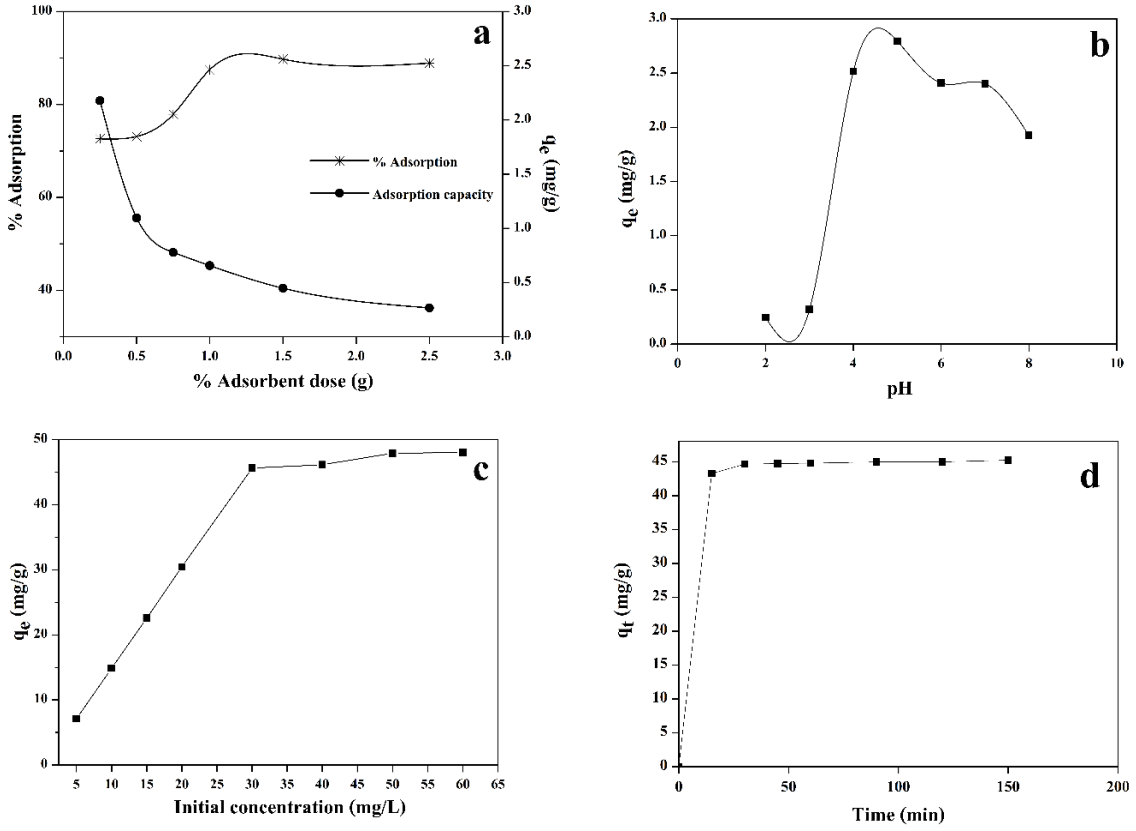

Fig.2 The effects of (a) adsorbent dosage (b) pH of pb^{2+} solution (c) initial pb^{2+} concentration, and (d) contact time on the adsorption capacity of pb^{2+} onto the RHBC.

Effect of pH is considered to be one of the key parameters in the adsorption process of metal ions from an aqueous solution because it affects the surface charge of adsorbents and also the chemical speciation of the adsorbate. The adsorption experiments were conducted in the initial pH range of 2-8 (Fig.2b). The maximum adsorption capacity of RHBC was obtained at pH5 and there was a little drop when the pH of Pb^{2+} solution was increased to be 6-8. At low pH, the competition of H^+ or H_3O^+ ions with the metal ions and hence H^+ or H_3O^+ ions reacted with the RHBC surface [5], which led to the decrease in the adsorption yield of RHBC surface and Pb^{2+}. At higher pH values, the adsorption capacity was slightly decreased. The precipitation of metal hydroxides may account for metal removal [5]. Thus, a pH values of 5 was used as the optimum pH value throughout the tests.

The initial concentration of Pb^{2+} in the aqueous solution, as one of the affecting parameters for adsorption, was investigated using a range of 5, 10, 15, 20, 30, 40, 50 and 60 $mg•L^{-1}$ of Pb^{2+} solution (see Fig.2c). The adsorption capacities were increased when the initial concentration was increased from 10 to 30 $mg•L^{-1}$ and there was no significant change in the Pb^{2+} concentration after 30 $mg•L^{-1}$. Such a pattern can be predicted because at a lower concentration, the ratio of Pb^{2+} over the adsorption surface is low. So, the Pb^{2+} quickly adheres to the available adsorption sites, resulting in the higher adsorption efficiency. Correspondingly, the higher amount of adsorbate encounters a limited availability of active sites on the adsorbent surface. Therefore, more Pb^{2+} are left unadsorbed in the solution due to the saturation of the binding sites, and consequently, the adsorption efficiency decreases.

The effect of contact time was studied using a function of time in the range of 5-180 minutes at a constant adsorbent dose of 0.25 $g•L^{-1}$ and Pb^{2+} solution pH of 5 with initial concentrations of 30 ppm. The effect of contact time on the adsorption capacity of RHBC is depicted in Fig.2d. It is obviously seen that there was a rapid uptake of Pb^{2+} within the first 30 min, the apparent adsorption equilibrium was usually established within 60 min and no significant change in the amount of Pb^{2+} adsorbed was observed after 60 min. The maximum adsorption capacity at equilibrium (q_e) of Pb^{2+} was 45.65 $mg•g^{-1}$.

3.4 The adsorption isotherms

The adsorption isotherms reveal the specific relation between adsorption capacity and concentration of the remaining adsorbate at constant temperature. Freundlich and Langmuir are the two most frequent used models. Freundlich isotherm describes the heterogeneous surface energies by multilayer adsorption [6]. and is expressed by the following equation:

$$\log q_e = \frac{1}{n}\log C_e + \log K_F \qquad (3)$$

where K_F and n are constants of Freundlich isotherm incorporating adsorption capacity (mg g^{-1}) and intensity.

Langmuir isotherm is based on the monolayer sorption [7] and is represented by the following equation:

$$\frac{1}{q_e} = \frac{1}{K_L q_m}\frac{1}{C_e} + \frac{1}{q_m} \qquad (4)$$

where q_m indicates the maximum monolayer adsorption capacity $(mg•g^{-1})$ and K_L indicates Langmuir constant or capacity factor.

In addition, the Temkin isotherm that is based on the assumption that the heat of adsorption is due to adsorbate–adsorbent interactions [8] was also studied. This isotherm is

applicable for chemical adsorption on solid adsorbents and liquid adsorbates. The linearized mathematical form of isotherm is described as follows:

$$q_e = B_1 \ln k_T + B_1 \ln C_e \quad (5)$$

where K_T is the Temkin equilibrium isotherm constant ($L \cdot g^{-1}$) and B_1 is the constant related to the heat of adsorption. In exothermic and endothermic adsorption reactions, the value of B_1 is higher and lower than unity, respectively. Values of K_T and B_1 were calculated from the plot of q_e and $\ln C_e$.

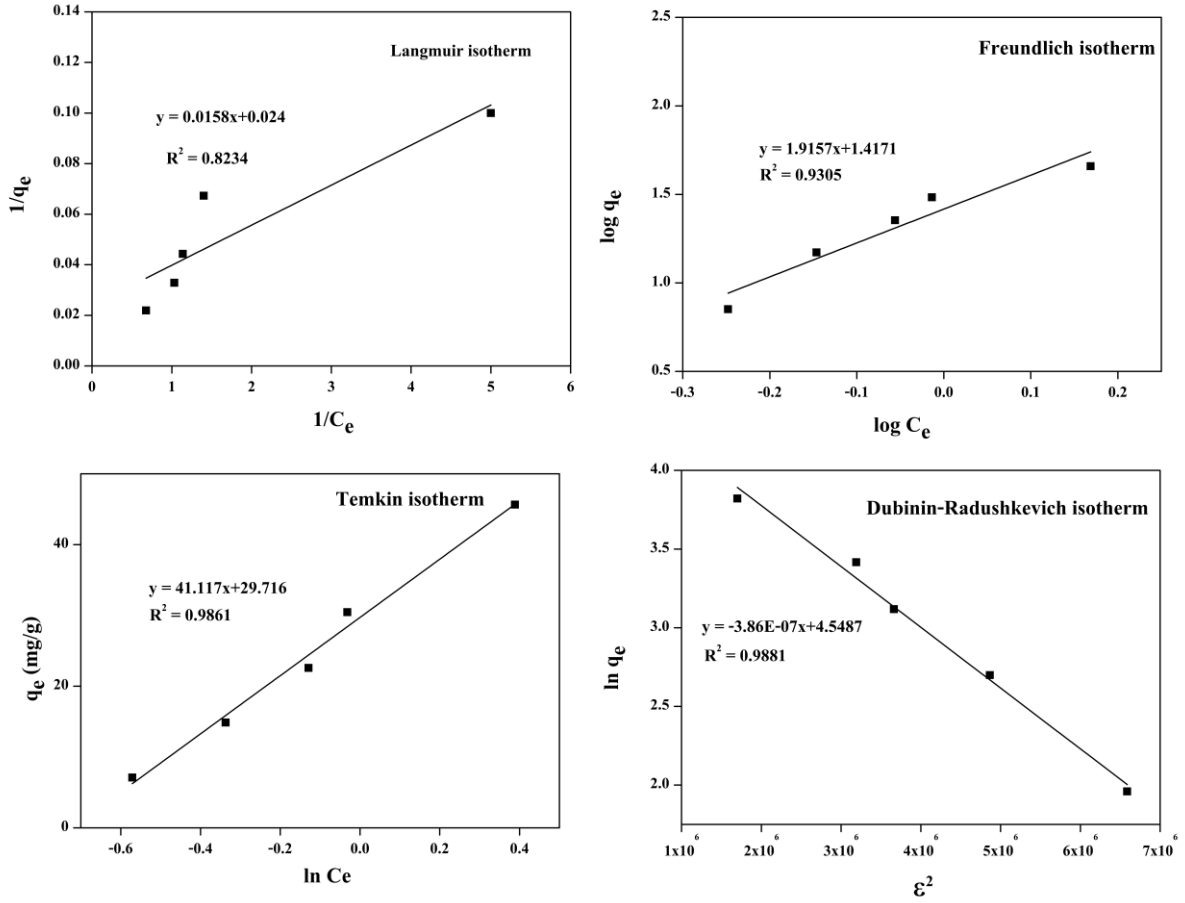

Fig.3 Isotherm plots of (a) Langmuir, (b), Freundlich, (c) Temkin and (d) Dubinin–Radushkevich models on the adsorption capacity of pb^{2+} onto the MPAC adsorbent.

Moreover, the Dubinin–Radushkevich (D–R) isotherm [9] that was used for understanding the type of bonding between Pb^{2+} and MPAC i.e. physical or chemical was also considered. D–R isotherm is presented as follows:

$$\ln q_e = \ln q_m - K_D \varepsilon^2 \quad (6)$$

where K_D is a constant which is related to the mean free energy of adsorption per mole of the adsorbate ($mol^2 \cdot J^{-2}$) and ε is the Polanyi potential that is logarithmic function of adsorbate concentration, which is given by

$$\varepsilon = RT \ln\left(1 + \frac{1}{C_e}\right) \quad (7)$$

Where R is ideal gas constant (8.314 J mol^{-1}•K^{-1}), and T is the absolute temperature in Kelvin (K). The mean free energy of adsorption (E) is defined as the free energy change, required when 1 mol of ions is transferred from solution to solid surfaces. The value of E can be calculated from K_D values, which is given as follows:

$$E = \frac{1}{\sqrt{2K_D}} \quad (8)$$

The value of E can be used to estimate the type of adsorption. The E value less than 8 kJ•mol^{-1} indicates physical adsorption. When the value of E falls between 8 to 16 kJ•mol^{-1}, it signifies a chemical ion exchange. Chemical adsorption is indicated by E values range from 20 to 40 kJ•mol^{-1} [10, 11].

The Freundlich, Langmuir, Temkin and D-R isotherms plot of Pb^{2+} adsorption onto RHBC adsorbent are shown in Figure 3a-3d, respective when their parameters are shown in Table 2. The applicability of isotherm equation is compared on the basis of correlation coefficients R^2. The best fit of the experimental data was obtained by the Freundlich isotherm (Figure 3d), indicating that the adsorption of Pb^{2+} onto RHBC adsorbent has a high degree of heterogeneity on the surface. According to R^2 values of Temkin isotherm plot in Fig.3d (0.9861), Temkin isotherm fit to the experimental data well by linear analysis. The reported values of B_1 in Table 2 equal 41.117 that higher than unity indicating that the adsorption reaction of Pb^{2+} onto RHBC was an exothermic process. The value of E obtained from D-R isotherm plot was 1.138 kJ•mol^{-1}, indicating that the adsorption process was a physical adsorption.

Table 3 Parameters of the Langmuir, Freundlich, Temkin and Dubinin–Radushkevich (D-R) isotherms of Pb^{2+} adsorption on RHBC adsorbent.

Langmuir isotherm			Freundlich isotherm			Temkin isotherm			D–R isotherm		
K_L	q_m	R^2	K_F	1/n	R^2	K_T	B_1	R^2	K_D	E	R^2
1.5192	41.66	0.8812	26.1517	1.9157	0.9305	1.96	41.117	0.9861	$3.86x10^{-7}$	1.138	0.9881

4. Conclusions

The findings of this work indicated the basic conditions such as adsorbate concentration, contact time, and adsorbent dosage influence the removal of pb^{2+} from aqueous solutions by adsorbent prepared from rice hush biochar (RHBC). The RH was combusted at 500 °C for 4 h. The maximum adsorption capacity at equilibrium (q_e) of Pb^{2+} equal 45.64 mg•g^{-1} was achieved when using Pb^{2+} concentration of 30 mg•L^{-1}, pH of 5, adsorbent dose of 0.25 g and contact time of 60 min. The isotherm adsorption was found to fit well with the Freundlich isotherm, the adsorption of Pb^{2+} onto RHBC adsorbent has a high degree of heterogeneity on the surface. The B_1 of Temkin isotherm indicated that the adsorption reaction of Pb^{2+} onto RHBC was an exothermic process. The value of E obtained from D-R isotherm plot was 1.138 kJ•mol^{-1}, indicating that the adsorption process was a physical adsorption.

Acknowledgements

This work was supported by National Higher Education, Science, Research and Innovation Policy Council, Thaksin University (Fundamental Research Fund; TSU-65A105000002) Fiscal Year 2022. The authors would like to thank the Department of Chemistry, Faculty of Science, Thaksin University, for providing research facilities.

References:

1. Oladoye, P.O. Chemosphere. 2022; 287:132130.
2. Wijeyawardana, P., Nanayakkara, N., Gunasekara, C., Karunarathna, A., Law, D., Pramanik, B.K. Environ. Technol. Innov. 2022; 28: 102640.
3. Dinh, V.-P., Nguyen, D.-K., Luu, T.-T., Nguyen, Q.-H., Tuyen, L.A., Phong, D.D., et al. Mater. Chem. Phys. 2022; 285:126105.
4. Huong, P.T., Jitae, K., Al Tahtamouni, T.M., Le Minh Tri, N., Kim, H.-H., Cho, K.H. J. Water Process. Eng. 2020; 33:101037.
5. Kongsune, P., Rattanapan, S., Chanajaree, R. Groundw. Sustain. Dev. 2021; 12: 100524.
6. Freundlich, H.M.F. J. Phy. Chem. 1906; 57:385-470.
7. Langmuir, I. J. Am. Chem. Soc. 1918; 40: 1361-403.
8. Temkin, M.J., Pyzhev, V. Acta Physiochim URSS. 1940; 12:217- 25.
9. Dubinin, M.M., Radushkevich, L.V. Proc. Acad. Sci. USSR Phys. Chem. Sec. 1947; 55:331-7.
10. Foo, K.Y., Hameed, B.H. Chem. Eng. J. 2012; 180:66-74.
11. Chaudhry, S.A., Ahmed, M., Siddiqui, S.I., Ahmed, S. J. Mol. Liq. 2016; 224:431-41.

MOLECULAR DYNAMICS SIMULATION STUDY OF NEWLY DESIGNED GELDANAMYCIN ANALOGUES FOR TARGETED CANCER-CAUSING Hsp90 INHIBITOR

Satipat Suttayasorranakhom, [1] Chanjira Jaramornburapong,[2] Waya S. Phutdhawong,[1] Jitnapa Sirirak[1,*]
[1]Department of Chemistry, Faculty of Science, Silpakorn University, Nakhon Pathom 73000, Thailand;
[2]Program of Chemistry, Faculty of Science and Technology, Nakhon Pathom Rajabhat University, Nakhon Pathom, Thailand 73000;
*e-mail: sirirak_j@silpakorn.edu, +66-34255797

Abstract:

Heat shock protein 90 (Hsp90) is one of the attractive molecular targets for the development of anticancer drugs because it contributes to cancer incidence or maintains cancer persistence based on the GDM derivatives such as alvespimycin (17-DMAG). Herein, using in-silico approaches, molecular docking was performed to gain insights into the binding between Hsp90 and our newly designed geldanamycin derivative, **F1**, compared with 17-DMAG. Moreover, to observe its physical movements and molecular interactions, molecular dynamics simulation was conducted for 200 ns using Amber20. The results show that **F1** is located in the active site of Hsp90 throughout 200 ns of simulations. Amine and amide groups of indole derivative substitution group at the C17 position of **F1** can interact with amino acid side chains outside the cavity of Hsp90 including Asp47, Asp50, and Ser46, leading to lower binding energy than 17-DMAG. This indicates that these substitution groups could play a significant role in the Hsp90 binding site and **F1** could be the potential anticancer drug.

Introduction:

Cancer, a silent threat that most people do not expect, is a vital issue that has received increasing attention worldwide. To design anti-cancer drugs, heat shock protein 90 (Hsp90) is one of the promising targets. Heat shock protein 90 (Hsp90) is a chaperone protein responsible for the folding, stability, and activity of the oncoproteins that promote the proliferation and survival of cancer.

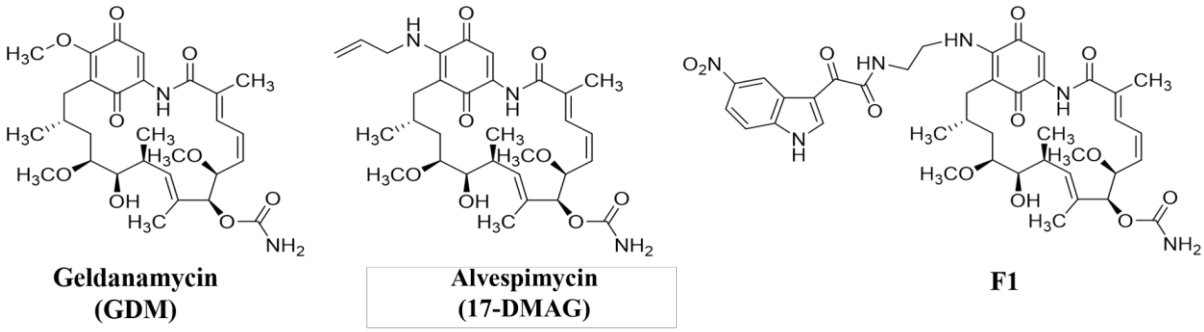

Figure 1. The 2D structure of geldanamycin (GDM), alvespimycin (17-DMAG) and the novel geldanamycin derivative (**F1**)

Geldanamycin (GDM) as shown in Figure 1, a naturally occurring benzoquinone ansamycin antibiotic [1], is the first known Hsp90 inhibitor drug created by *Streptomyces*

hygroscopicus [2]. It binds directly to the ATP binding site in the N-terminal of Hsp90 and blocks nucleotides from binding to Hsp90, rendering the conformational change of Hsp90 which cannot cling to client protein [3-5]. However, the major problem with GDM is its hepatotoxicity and poor water solubility, resulting in its unavailability as a clinical drug [6]. As a result, there are many GDM derivatives developed as anti-cancer drugs [7, 8] including alvespimycin (17-DMAG) which is applied for the treatment of chronic lymphocytic leukemia (CLL) [9]. This indicates that the modifications to the GDM structure can be the way to increase the inhibitory efficiency, reduce side effects, and provide guidelines for designing a new generation of drugs for Hsp90 and other cancer treatments.

Herein, novel geldanamycin derivatives, **F1** was designed as a potential Hsp90 cancer drug by against oncogenic client protein. The binding of **F1** in the cavity of Hsp90 was explored by molecular docking using the iGEMDOCK v2.1 software [10]. The molecular dynamics simulation was then performed to investigate its binding stability using Amber20 software [11] for 200 ns. Additionally, its root-mean-square displacement (RMSD) and radius of gyration (R_g), and important distances between the amino acids of Hsp90 and ligand were investigated and compared with those of 17-DMAG.

Methodology:

F1 was designed by adding the indole derivative substitution group at the C17 position and its optimized 3D structure was obtained at the B3LYP/6-311g* level. A molecular docking study was then performed using iGEMDOCK v.2.1. with accurate docking with population size (N=800), 80 generation and 10 solutions, and Hsp90 (PDB ID: 1OSF) was selected as protein. Moreover, the dynamic behavior of ligand-complex of **F1** and Hsp90 was investigated using molecular dynamics (MD) simulation using AMBER20. The CPPTRAJ module of AMBER20 was employed to analyze: the system stability factors including Root-Mean-Square Displacement (RMSD) and Radius of Gyration (R_g), and Important distances between the amino acids of Hsp90 and ligand. All images were prepared using BIOVIA Discovery Studio Visualizer.

Results and Discussion:

As can be seen in Figure 2, **F1** effectively bound and formed H-bond with amino acid residues in the binding pocket of Hsp90 with more or less the same position as 17-DMAG. Moreover, the binding energy of **F1** (-169.70 kcal/mol) was much lower than that of 17-DMAG (-145.57 kcal/mol) as shown in Table 1, indicating that **F1** was the interesting compound for the development of the potential anticancer drug. Thus, the molecular dynamics simulation of the **F1**-Hsp90 complex was then performed to explore the binding stability and important interaction of **F1** in Hsp90.

Table 1. The binding energies, amino acid interactions, and hydrogen bond lengths of newly designed geldanamycin derivative (**F1**) and 17-DMAG in molecular docking studies.

Compounds	Binding energy (kcal/mol)	VDW (kcal/mol)	H-Bond (kcal/mol)	Amino acid residue	H-bond length (Å)
F1	-169.70	-132.52	-36.31	ASP54, ASP93, ASN106, LYS112, PHE138	3.09, 2.26, 2.25, 2.58, 1.95
17-DMAG	-142.57	-114.18	-28.39	ASP93, LYS112, PHE138, GLY135	2.33, 2.78, 2.37, 2.85

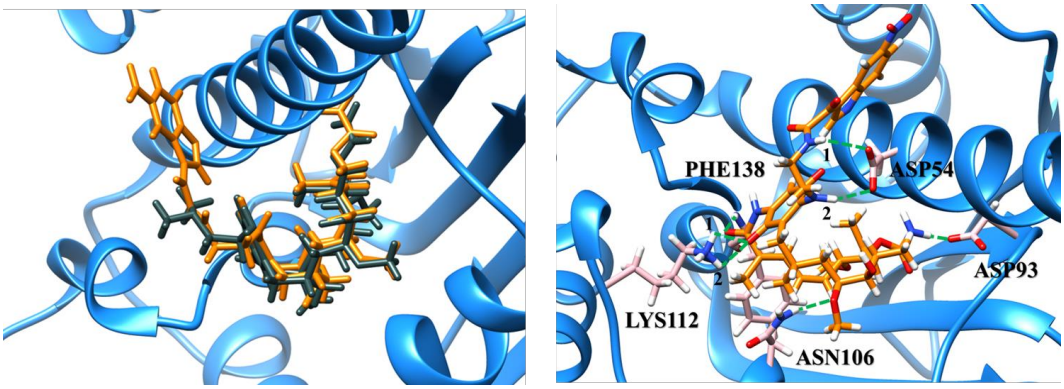

Figure 2. The comparison of binding positions of the novel geldanamycin analogue **F1** (orange) and 17-DMAG (green) (left), and hydrogen bond of **F1** (right) in the cavity of Hsp90 (PDB ID: 1OSF).

The molecular dynamics simulation of **F1**-Hsp90 complex was performed for 200 ns using Amber20. Its RMSD, radius of gyration (R_g), the distance of center of mass between Hsp90 and ligand, and important distances between ligand and the amino acid residues of Hsp90 were then explored using the CPPTRAJ module of AMBER20 and compared with those of 17-DMAG-Hsp90 complex.

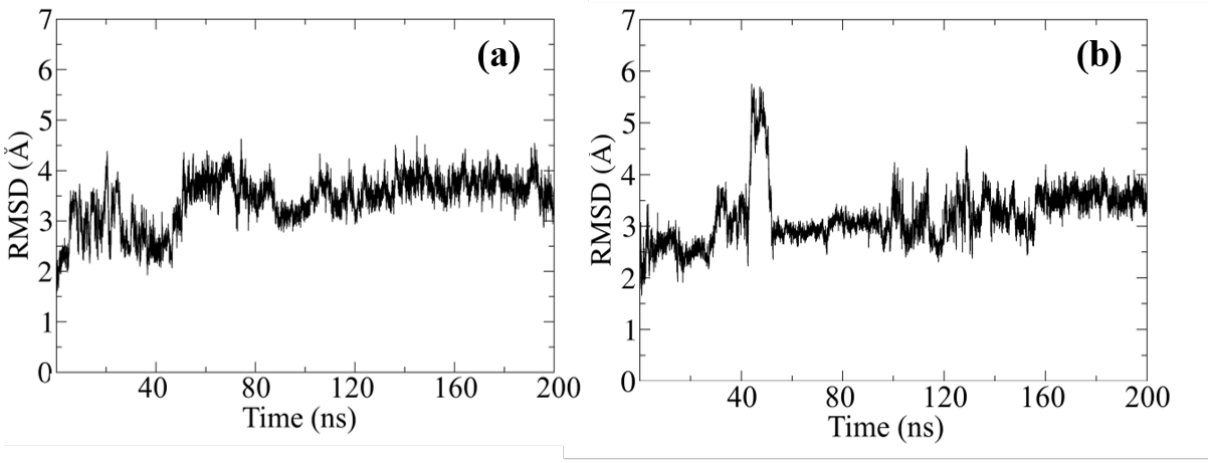

Figure 3. RMSD of **F1**-Hsp90 complex (a) and 17-DMAG-Hsp90 (b) during 200 ns of molecular dynamics simulations.

Figure 3 displayed that, throughout 200 ns of the simulation, the RMSD of **F1** in the **F1**-Hsp90 complex had slightly fluctuated from 0.5 to 2.0 Å with the average of 1.66 Å, which was a little higher than that of 17-DMAG (0.5 to 1.5 Å and the average of 0.93 Å). Moreover, both RMSD of 17-DMAG-Hsp90 complex and **F1**-Hsp90 complex were fluctuated at the beginning of the simulation and become approximately 3 to 4 Å after 50 ns. This indicated the stability of the complex without any variation of conformational changes during MD simulation. Additionally, as shown in Figure 5, the radius of gyration (R_g) of the 17-DMAG-Hsp90 complex and the **F1**-Hsp90 complex were similar and within the range of 17-18 Å, indicating the similarity of the compactness of these two complexes during the MD simulation.

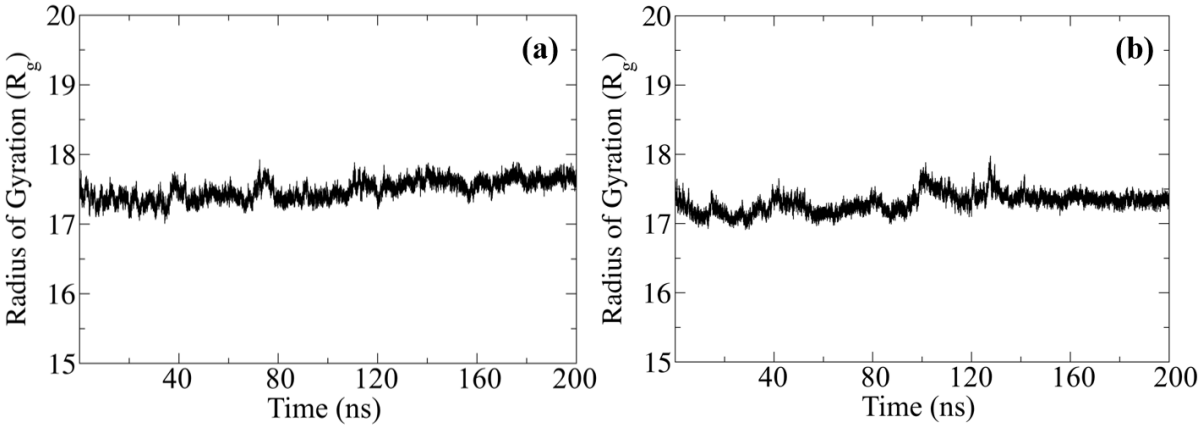

Figure 4. Radius of gyration (Rg) of **F1**-Hsp90 complex (a) and 17-DMAG-Hsp90 complex (b) during 200 ns of molecular dynamics simulations.

The distance between the center of mass of Hsp90 and ligand observed in both **F1**-Hsp90 complex and 17-DMAG-Hsp90 complex were rather constant around 9 and 9.5 Å, respectively, with small fluctuations throughout simulations. This confirmed that **F1** was in the active site throughout 200 ns which agreed with the snapshots of MD simulations over a period of 200 ns of the **F1**-Hsp90 complex shown in Figure 5.

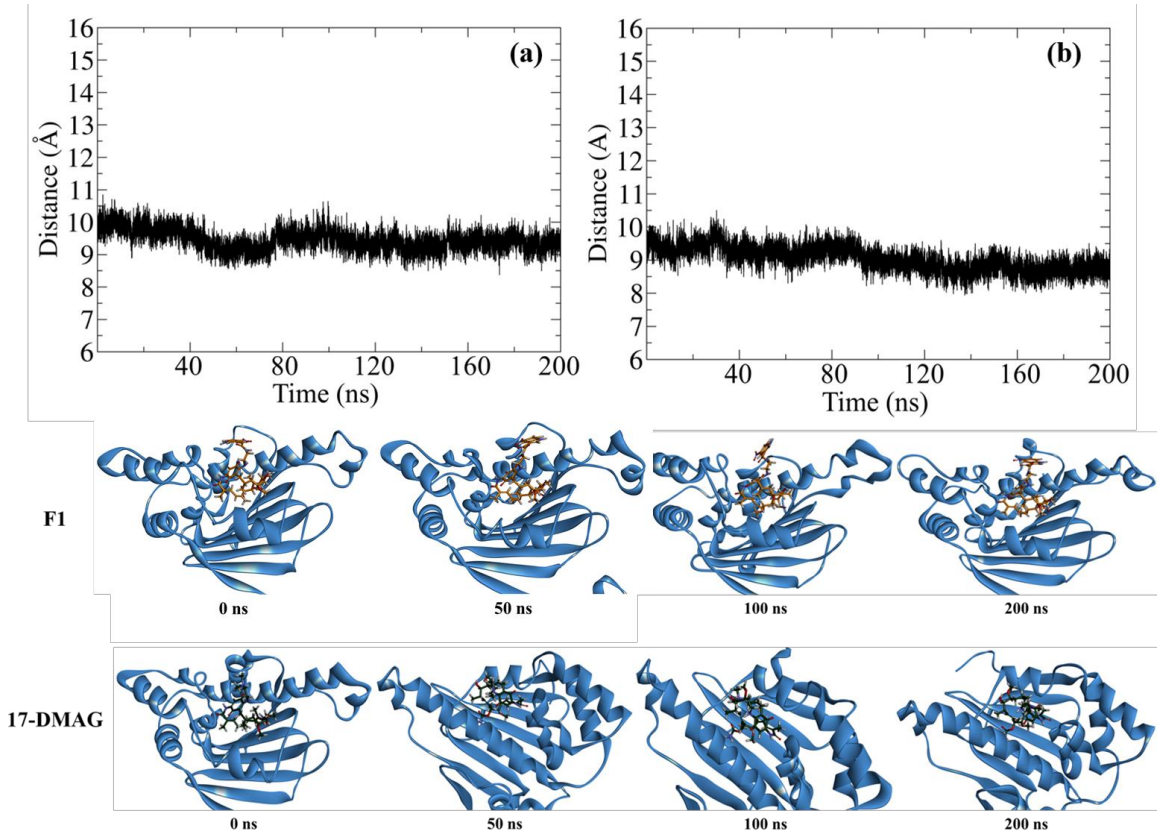

Figure 5. Distance of center of mass between Hsp90 and ligands: **F1** (a) and 17-DMAG (b) and the snapshot at 0, 50, 100 and 200 ns during MD simulation time of **F1**-Hsp90 complex and 17-DMAG-Hsp90 complex.

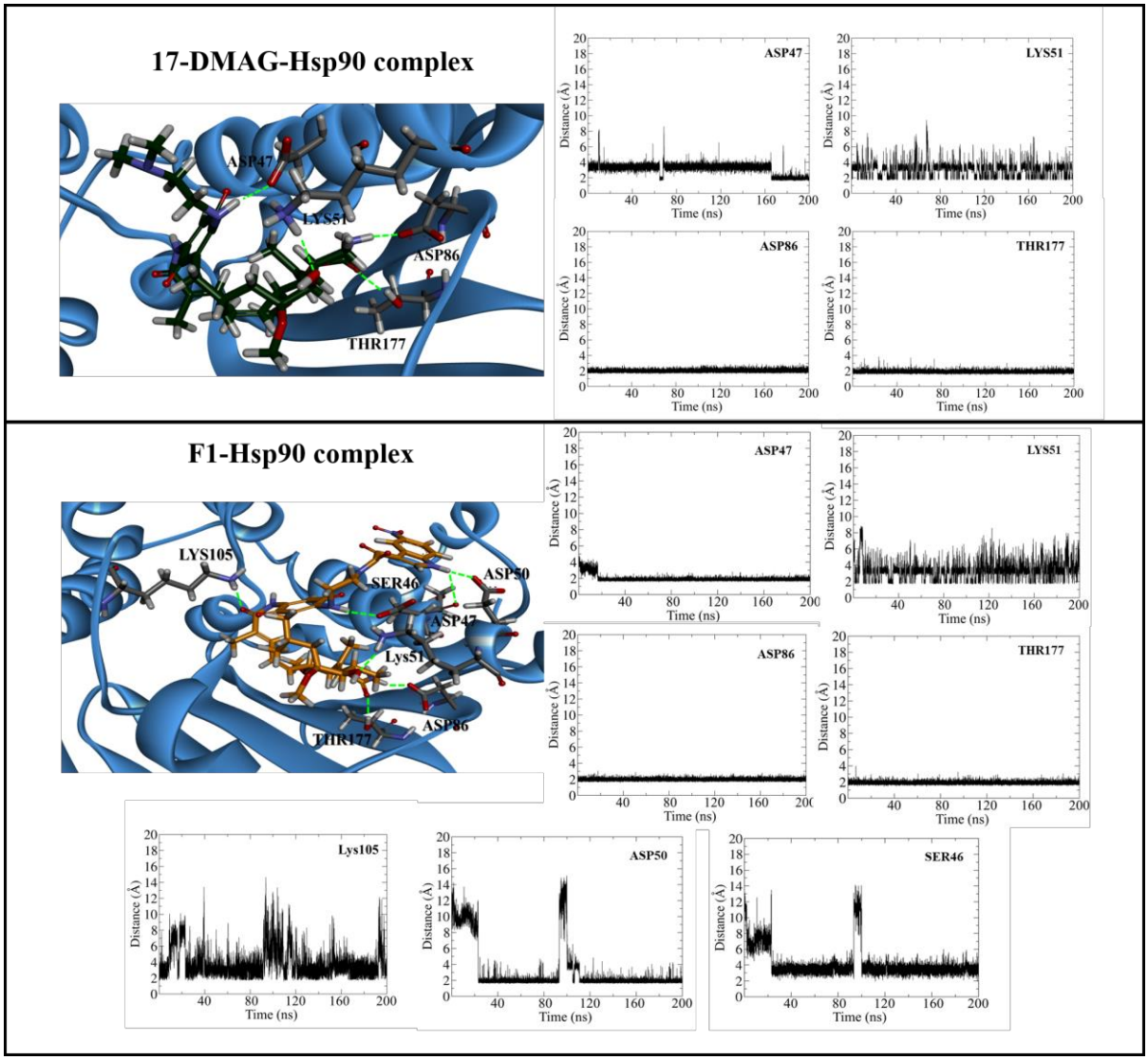

Figure 6. Important distances between the amino acid residues of Hsp90 and **F1** during 200 ns of molecular dynamics simulations.

As shown in Figure 6, for both complexes, the distances between Asp86 and ligand were rather constant at 2 Å, indicating that the ligands were located in the active site of Hsp90 throughout 200 ns of simulations. Moreover, the length of the side chain and the number of amine and amide groups of the indole derivative substitution group at the C17 position of geldanamycin (GDM) analogue on the binding in the cavity of Hsp90 resulted in the binding with the amino acid residues of Hsp90, including Asp47, Asp50, and Ser46. These amino acid residues effectively interacted with amide groups of the indole derivative substitution group at the C17 position of **F1**. Thus, the amide groups of the indole derivative substitution group at the C17 position of geldanamycin (GDM) analogue played a vital role in Hsp90 binding site.

Conclusion:

Newly designed GDM analogue: **F1** containing amine group of indole derivative substitution group at C17 position of GDM could effectively bind in the active site of Hsp90 throughout 200 ns. This additional substitution of **F1** also interacted with amino acid residues in the binding pocket of Hsp90 including Asp47, Asp50, and Ser46 which could be the key to

inhibiting the Hsp90 protein involved in anti-cancer activities. Our results, thus, would be useful for the development of new promising anti-cancer drugs in the future.

Acknowledgements:

This research was financially supported Faculty of Science, Silpakorn University (Grant Number SRIF-JRG-2564-28).

References:

1. Biebl, M.M. and J. Buchner. Cold Spring Harbor perspectives in biology. 2019; 11(9), p. a034017.
2. Hermane, J., et al. ChemBioChem. 2015; 16(2), p. 302-311.
3. Kyle Hadden, M., D.J. Lubbers, and B.S. J Blagg. Current topics in medicinal chemistry. 2006; 6(11), p. 1173-1182.
4. Blagg, B.S. and T.D. Kerr. Medicinal research reviews. 2006; 26(3), p. 310-338.
5. Neckers, L. Molecular chaperones in health and disease. 2006; p. 259-277.
6. Neckers, L., T.W. Schulte, and E. Mimnaugh. Investigational new drugs. 1999; 17(4), p. 361-373.
7. Kitson, R.R. and C.J. Moody. Chemical communications. 2013; 49(76), p. 8441-8443.
8. Hermane, J., et al. Organic & Biomolecular Chemistry. 2019; 17(21), p. 5269-5278.
9. Rao, R., et al. Cancer biology & therapy. 2009; 8(13), p. 1273-1280.
10. Hsu, K.-C., et al. BMC bioinformatics. 2011; 12(1), p. 1-11.
11. Case, D.A., et al. 2021; University of California, San Francisco.

Session D:
MATHEMATICS / STATISTICS / COMPUTER SCIENCE / DATA SCIENCE / AI

THE ENHANCEMENT OF TOURISM STAFF IN KHANOM FOR GOOGLE TRANSLATE APPPLICATION TO PROMOTE LOCAL TOURISM: NAKHON SI THAMMARAT

Sirilak Intasaro,[1,*] Wanwisa Phetcharatmunee[2]
[1] Assistant Professor, Information Technology, Faculty of Science and Technology, Rajamangala University of Technology Srivijaya
[2]Assistant Professor, English, Faculty of Science and Technology, Rajamangala University of Technology Srivijaya
*e-mail: sirilak.i@rmutsv.ac.th

Abstract:
This research aims to study the difficulties in the translation of tourism personnel in Khanom District. Learn about attitudes and acceptance of google translation technology. Learn about the basic readiness of using google translation applications. Study and analyze the feasibility of using the application. Google Translate of travel personnel in Khanom District and to provide guidance on how to elevate tourism personnel in Khanom district to use the application. Translate from Google to support secondary city tourism The sample is a tourism worker in Khanom District. 140 persons

The findings It found that the percentage of problem-solving conditions in translation of the most people was ignorance of vocabulary, 86.43% of english grammar, 72.86% and the least percentage of problems: embarrassment, fear and nervousness in Speaking English, 16.43%. Google's application attitude ($\overline{X}$ = 4.21), application usage feasibility ($\overline{X}$ = 3.85) and the elevated approach that people need to use the application ($\overline{X}$ = 4.12) are very high. Application Acceptance Section ($\overline{X}$ = 3.36) and application availability ($\overline{X}$ = 3.42) moderate

Introduction:

According to the policy, the government has supported tourism in 55 secondary cities, with the south having 9 secondary cities, namely Nakhon Si Thammarat, Nakhon Si Thammarat, Phatthalung, Trang Satun, Chumphon, Ranong, Narathiwat, Yala, Pattani.In addition, the government has promoted tourism to the secondary city, which includes Nakhon Si Thammarat province, where Khanom district is located in the northernmost part of the province. It is bordered by the following neighbouring subdivisions, the north contacts the Gulf of Thailand. The east contacts the Gulf of Thailand. To the south, it contacts Sichon District. To the west, it connects with Donsak District (Surat Thani Province), which can be connected to the main city of Surat Thani Province. Khanom district is a district with beautiful beaches and the longest beaches in Nakhon Si Thammarat province. Surrounded by mountains, the beach is visited by many foreign tourists, as well as buying houses (long-term rentals), and there are many beautiful and quiet beaches that have been developed to be popular with tourists, such as Thong Yi Beach, Andhra Pradesh Beach, Andhra Pradesh In front of the checkpoint, Khanom beach, Kho Khao beach , etc. In addition, Khanom district has an old temple, the Kradangga Temple. Not far from Wat Kradangga, samet chun waterfall and Khao Phra are scenic spots overlooking the district and the sea of Khanom Bay. Located 4 kilometers from the beach, it is private, but permission can be obtained from the owner of the area to see it. Nowadays, one of the things that attracts tourists is the fact that they come to see the pink dolphins that come for food in many areas of Khanom Bay. In this regard, the bustling and continuous tour of secondary cities and communities is a tool to

stimulate the preparation and development of the area into a balanced tourist attraction in all dimensions.

Communication is considered one of the activities of the human being that is important. Whether it's verbal or nonverbal communication, it's an activity that's intended to convey. The thoughts or needs of the messenger to the listener's destination. At present, communications It is not limited to a particular group. But there is also cross-group communication, which uses different languages. Hence the translation of the language for communication. Learning and exchanging sciences with each other plays an important role. Effective translation requires people with knowledge of the language. However, online tools and applications are now widely popular with the rapidly changing technology. The development of translation innovations has given rise to several translation aids, one of which is "Google Translate" (GT), a widely popular Google add-on today that relies on the principle of working with statistics referenced in translations. This makes it convenient and fast to translate text automatically within a short time. Effective translation must take into account the text or language of origin and destination. Meanings that require interpretation, transmission of the source language. Once translated, it must not be contrary to the nature of the destination language.

Nowadays, many foreign tourists come to Visit Thailand. This can cause communication problems when using multiple foreign languages, which may require a translation application to communicate and translate in order to communicate with surfers.Today, the evolution of the world is changing rapidly. It's now the age of digital. It has played an important role in human life and has caused many changes to society with only the advancement of modern technology and information. Tourism personnel rely on modern technology and applications. Nowadays, technology is being developed rapidly. It has evolved to be more consistent with its use. The use of smartphones and tablets has played a huge role in people's daily lives. As evidenced by the constant portability of the user, the translation application running on smartphones and tablets is constantly being developed to meet the needs of users. Nowadays, the internet system is involved in the use of technology to make it more convenient to use. Therefore, Google Translate has played a huge role in the lifestyle of people and tourism personnel. It can be seen that those applications can help tourism personnel perform their work activities in various fields more efficiently compared to the past. Without sufficient knowledge, it would not be possible to use the application to its fullest potential and maximum benefit.

Therefore, the researchers are interested in studying ways to upgrade tourism personnel in Khanom. To use google translation application to promote tourism in Secondary Cities, Nakhon Si Thammarat province, to study the problem of translation of tourism personnel in Khanom District. To study the attitudes and acceptance of google translate technology to study the fundamental readiness of the application. To study and analyze the feasibility of using the Google Translate application to provide guidance on how to upgrade tourism personnel in Khanom. Tourism personnel can elevate themselves by developing themselves using the Google Translate application and contributing to the promotion of tourism in secondary cities, Nakhon Si Thammarat provinces.

Objectives of research

1. To study the problem of translation of tourism personnel in Khanom District.

2. To study attitudes and acceptance of the use of translation technology. Google Translate of tourism personnel in Khanom

3. To study the fundamental readiness of the application. Google Translate of tourism personnel in Khanom

4. To study and analyze the feasibility of using the application. Google Translate of tourism personnel in Khanom

5. To obtain guidelines for upgrading tourism personnel in Khanom district to use the application. Google Translate to support secondary city tourism

Methodology:

1. Study populations and samples

Population is 220 personnel employed in accordance with the standard jobs of tourism personnel in the accommodation branch (Hotel Services), who are personnel working in hotels or resorts in tourist destinations in Khanom District, Nakhon Si Thammarat Province.

An example is tourism personnel in Khanom District, Nakhon Si Thammarat Province. 140 out of a population of 220, compared from the prefabricated table of Krejcie and Morgan' tables, divided the number of samples according to the size of the establishment.

2. Survey the establishments used in the research.

Conducted a survey of hotel or resort establishments located in Khanom district and selected to group a sample of 140 people.

3. Create tools used in research

Tools used to collect data as questionnaires

Divide the question into 2 parts as follows:

Part 1 General information of respondents includes gender, age, status, maximum education. Foreign language proficiency job Work experience and average monthly income level

Part 2 divides the questions into 6 issues:

1) Difficult conditions in the translation of personnel
2) Attitude to using Google Translate application
3) Acceptance of use of the Google Translate application
4) Fundamental availability of Google Translate applications
5) Possibility of using the Google Translate application
6) The elevated approach that personnel need to use the Google Translate application.

The following are the issues of studying ways to enhance tourism personnel's use of google translation applications:

1) Difficult conditions in the translation of personnel

- Lack of opportunity to speak English.
- Do not practice speaking English.
- Shyness, fear, and nervousness in speaking English
- Ignorance of words
- Don't know English grammar.
- Lack of knowledge of English in hospitality
- Lack of knowledge of English on tourism

2) Studied issues of google translate application usage

- Attitudes to using Google Translate applications
- Acceptance of the use of the Google Translate application
- Fundamental availability of google translate applications
– Possibility of using the Google Translate application
- The elevated approach that personnel need to use the Google Translate application.

3)Tool Quality Inspection

Perform a tool quality check by taking the questionnaire to an expert to verify its accuracy and can be used to complete the questionnaire.

4) Instrument testing

(1) Finding validity by taking the questionnaire to 3 experts to check for accuracy in order to correct the defect.

(2) Reliability test of the revised questionnaire, whereby the researcher performs a pre-test on a non-sample group to test the confidence of the questionnaire.

4. Create a guide to using google translate application to find ways to raise the bar.

The Google Translate application manual was created for samples to study the way tourism personnel are raised.

5. Collect Information

In the collection of this research, a total of 140 questionnaires were collected from tourism personnel.

6. Analyze data

Measuring using statistics, the average is calculated for arithmetic mean using the following:

An average of 4.50 – 5.00 means the highest level.
An average of 3.50 – 4.49 means extreme level.
An average of 2.50 – 3.49 means moderate.
An average of 1.50 – 2.49 means small.
An average of 1.00 – 1.49 means minimal level.

Results and Discussion:

The results of the study of the problem of translation of languages of tourism personnel.

Table 1.

Percentage of problems in the translation of personnel

Problem condition	Samples (Freq:140)	Percent of problem condition.
Lack of opportunity to speak English	40	28.57
Do not practice speaking English	95	67.85
Shyness, fear, and nervousness in speaking English	23	16.43
Ignorance of words	121	86.43
Don't know English grammar	102	72.86
Lack of knowledge of English in hospitality	36	25.71
Lack of knowledge of English on tourism	26	18.57

According to Table 2, the results of the study of the problem in the translation of tourism personnel in Khanom District. It was found that the highest percentage of people's translation problems were vocabulary ignorance, followed by ignorance of English grammar, and the least percentage of problems were shyness, fear and nervousness in speaking English.

Levels of use of the Google Translate application

Table 2.

Levels of usage of the Google Translate application

Issues studied	average	level
Attitudes to using the Google Translate application	4.21	very
Acceptance of use of the Google Translate application	3.36	moderate
Fundamental availability of the Google Translate application	3.42	moderate
Possibility of using the Google Translate application	3.85	very
The elevated approach that people need to use the Google Translate application.	4.12	very

According to Table 3, the attitude to using Google Translate applications, the possibility of using Google Translate applications, and the elevated approach that personnel want to use Google Translate applications are very high. Acceptance of Google Translate applications and fundamental availability of Google Translate applications are moderate.

Conclusion:

The results of the study of the problem of translation of languages of tourism personnel in Khanom District. It was found that the highest percentage of problems in translating personnel was vocabulary ignorance, accounting for 86.43 percent, followed by ignorance of English grammar, which accounted for 72.86 percent, and the least problematic condition was shyness, fear and nervousness in speaking English, which was 16.43 percent.

Attitudes to using Google Translate applications (average of 4.21), the possibility of using Google Translate applications (average of 3.85), and the elevated approach that personnel need to use Google Translate applications (average of 4.12) are very high. Acceptance of Google Translate applications (average of 3.36) and fundamental availability of Google Translate applications (average of 3.42) are moderate.

Discuss the results:

The results of the study of the problem of translation of languages of tourism personnel in Khanom District found that the problem of translating languages influenced the use of the Google Translate application.

Results of the study on attitudes and acceptance of the use of Google Translate technology found to influence the use of Google Translate translation technology.

Fundamental readiness study on the use of Google Translate applications found to influence the use of Google Translate translation technology.

Results of the study and analysis of the feasibility of using the Google Translate application found that the possibility influences the use of Google Translate translation technology.

Get guidelines for upgrading tourism personnel in Khanom district to use the application. Google Translate to support secondary city tourism. Guidelines for upgrading tourism personnel in Khanom District In order to use Google Translate applications, conduct specific studies on the use of Google Translate applications and feasibility studies to analyze the feasibility of using Google Translate applications and to obtain ways to upgrade tourism personnel in Khanom District. To use the Google Translate application

Acknowledgements:

The researchers would like to thank the Faculty of Science and Technology, Rajamangala University of Technology Srivijaya, Nakhon Si Thammarat Campus for their generous equipment and research facilities, and thank Rajamangala University of Technology Srivijaya for supporting the budget for this research study.

References:

1. Arisara S. Attitudes and behaviors of students in using the Google Translate program. 2013.

2. Kamol K, and Saraporn S. Behavior and problems using "Google Translate" by English major students. 2016; Journal of Arts, PSU Hat Yai Campus, Vol. 8, No. 1, January-June.

3. Iladda M, Abhijat D. Teen translation applications on Android operating systems. 2015; 1st National Symposium on Technology and Innovation Management, Mahasarakham Rajabhat University, 12-13 May.
4. Theerasak K. A study of employee satisfaction using mobile delivery applications: a case study of Seoul stores in Chonburi province. 2015; Master of Business Administration, Graduate School, Bangkok University.

SOME CONTINUED FRACTIONS WITH PARTIAL QUOTIENTS 1 OR 2, AND RECURRENCE

Worarat Srisurat, Arjuna Chaiyasena
School of Mathematics, Suranaree University of Technology, Nakhon Ratchasima 30000, Thailand
*E-mail: apc@sut.ac.th

Abstract:

Guy [3] mentions that not every number n can be expressed as the sum of two positive integers $n = a + b$ where $\frac{a}{b}$ is written as a continued fraction with partial quotients 1 or 2 only; for example, $5 = 3 + 2$ and $\frac{3}{2} = [1; 2]$ and $7 = 5 + 2$ and $\frac{5}{2} = [2; 2]$. However, he does mention that 23 cannot be so expressed. We consider only bump sequences that are close to Fibonacci sequence in their continued fraction expansion. We can use basic recurrence techniques.

First, we show that $[1;1,1,\dots,1] = \frac{F_{n+1}}{F_n}$, where F_n is the nth Fibonacci Number. Then, we consider $[2;1,1,1,1,\dots]$, a *1*- Bump Sequence of continued fraction $[2;1,1,1,1,\dots] = \frac{p_n}{q_n} = \frac{F_{n+2}}{F_n}$ is true for all positive integers. Next, we will consider $[1;2,1,1,1,\dots]$, a *2*- Bump Sequence: $[1;2,1,1,1,\dots] = \frac{p_n}{q_n} = \frac{(\frac{1+\sqrt{5}}{2})^n + (\frac{1-\sqrt{5}}{2})^n}{F_n}$. Moreover, we consider $[1;1,2,1,1,\dots]$ *3*- Bump Bumped Sequence. $[1;1,2,1,1,\dots] = \frac{p_n}{q_n} = \frac{(\frac{7}{2\sqrt{5}} - \frac{1}{2})(\frac{1+\sqrt{5}}{2})^n - (\frac{7}{2\sqrt{5}} + \frac{1}{2})(\frac{1-\sqrt{5}}{2})^n}{(\frac{\sqrt{5}}{2} - \frac{1}{2})(\frac{1+\sqrt{5}}{2})^n - (\frac{\sqrt{5}}{2} + \frac{1}{2})(\frac{1-\sqrt{5}}{2})^n}$; $n \geq 2$.

Finally, we consider $[2], [2;2], [2;2,2], \dots$ obtaining the pattern $\frac{p_n}{q_n} = \frac{\frac{\sqrt{2}}{4}(1+\sqrt{2})^n - \frac{\sqrt{2}}{4}(1-\sqrt{2})^n}{(\frac{1}{2} - \frac{\sqrt{2}}{4})(1+\sqrt{2})^n + \frac{1}{4-2\sqrt{2}}(1-\sqrt{2})^n}$.

Introduction:

The general form of simple continued fractions is

$$\frac{a}{b} = [a_0; a_1, a_2, \dots] = a_0 + \cfrac{1}{a_1 + \cfrac{1}{a_2 + \cfrac{1}{a_3 + \cfrac{1}{a_4 + \cdots}}}}$$

with the assumption that all the elements a_i that $i \geq 1$ are positive integers.

The Fibonacci numbers, commonly denoted F_n, form a sequence called the Fibonacci sequence, such that each number is the sum of the two preceding ones, starting from 0 and 1. That is, $F_0 = 0, F_1 = 1$ and $F_n = F_{n-1} + F_{n-2}$ for $n > 1$. The first few terms of the sequence are $0, 1, 1, 2, 3, 5, 8, 13, 21, 34, 55, 89, 144, \dots$

Guy mentions that not every number n can be expressed as the sum of two positive integers $n = a + b$ where $\frac{a}{b}$ is written as a continued fraction with partial quotients 1 or 2 only; for example, $5 = 3 + 2$ and $\frac{3}{2} = [1; 2]$ and $7 = 5 + 2$ and $\frac{5}{2} = [2; 2]$.

However, he does mention that 23 cannot be expressed. Thus, we want to study those fractions with partial fractions consisting of 1 or 2 only. In the process of investigation, we came up with linear second order homogenous recurrences very naturally to find convergents. Thus, we want to present some of our explorations.

THEOREM1

(a) If the characteristic equation $x^2 - r_1 x - r_2 = 0$ of the recurrence relation $a_n = r_1 a_{n-1} + r_2 a_{n-2}$ has two distinct roots, s_1 and s_2,
then $a_n = \mu s_1^n + \vartheta s_2^n$ where μ and ϑ depend on the initial conditions, is the explicit formula for the sequence.

(b) If the characteristic equation $x^2 - r_1 x - r_2 = 0$ has a single root s, the explicit formula is $a_n = \mu s^n + \vartheta n s^n$, where μ and ϑ depend on the initial conditions.

LEMMA2 for $n \geq 1$, we have the relations

$p_n = a_n p_{n-1} + p_{n-2}, \qquad q_n = a_n q_{n-1} + q_{n-2}$

(For a proof, see [5], p. 20 – 21).

Methodology:

1. We started with the problem as stated by Guy , considering some continued fractions with Partial Quotients 1 or 2, and their Recurrences. We came up with linear second order homogenous recurrences very naturally with convergents.
2. We consider only bump sequences that differ from the continued fraction of the Fibonacci sequence by 1.

Results and Discussion:

We begin to write $[1] = 1, [1;1] = \frac{2}{1}, [1;1,1] = \frac{3}{2}, [1;1,1,1] = \frac{5}{3}$ so we have $[1;1,1,\ldots,1] = \frac{F_{n+1}}{F_n}$ where F_n is the nth Fibonacci Number; $F_0 = 0$ $F_1 = 1$ and so on. Thus, we can see that the numbers m which can be expressed as the sum of two positive integers $m = a + b$ are precisely the Fibonacci numbers in this case.

	-1	0	1	2	3	4	5	...
a_i			1	1	1	1	1	...
p_i	0	1	1	2	3	5	8	...
q_i	1	0	1	1	2	3	5	...

$\frac{p_1}{q_1} = \frac{F_2}{F_1}$, $\frac{p_2}{q_2} = \frac{F_3}{F_2}$,… $\frac{p_n}{q_n} = \frac{F_{n+1}}{F_n}$

We would like to show that $\frac{p_n}{q_n} = \frac{F_{n+1}}{F_n}$ *is true for all positive integers by induction.*

1. *Basis step: When* $n = 1$, *then it true as by the table.*
2. *Induction hypothesis: Assume* $n = k$ *such that* $\frac{p_k}{q_k} = \frac{F_{k+1}}{F_k}$ *is true when* $k \geq 1$
3. *We want to show that* $n = k + 1$ *is also true when* $k \geq 1$

$$\frac{p_{k+1}}{q_{k+1}} = \frac{p_{k-1} + p_k}{q_{k-1} + q_k} = \frac{F_k + F_{k+1}}{F_{k-1} + F_k} = \frac{F_{(k+1)+1}}{F_{k+1}}$$

so $k + 1$ is true. By induction we have shown $\frac{p_n}{q_n} = \frac{F_{n+1}}{F_n}$ is true for all *positive integers.*

Now define a "Bumped" sequence of a Fibonacci sequence to be a sequence that is different from that of the Fibonacci in one continued fraction term ; for example, $[2;1,1,1,1,\ldots]$ is a 1- Bump Sequence of continued fraction. It differs from $[1;1,1,\ldots,1]$ in the first term.

	-1	0	1	2	3	4	5	...
a_i			2	1	1	1	1	...
p_i	0	1	2	3	5	8	13	...
q_i	1	0	1	1	2	3	5	...

So $\frac{p_1}{q_1} = \frac{F_3}{F_1} = \frac{2}{1}$, $\frac{p_2}{q_2} = \frac{F_4}{F_2} = \frac{3}{1}, \ldots \frac{p_n}{q_n} = \frac{F_{n+2}}{F_n}$

We would like to show $\frac{p_n}{q_n} = \frac{F_{n+2}}{F_n}$ is true for all positive integers by induction. The case $n = 1$ is true as by the table. Assuming $n = k$ such that $\frac{p_k}{q_k} = \frac{F_{k+2}}{F_k}$ is true when $k \geq 1$, we want to show that $n = k + 1$ is also true when $k \geq 1$:

$$\frac{p_{k+1}}{q_{k+1}} = \frac{p_{k-1} + p_k}{q_{k-1} + q_k}$$
$$= \frac{F_{k+1} + F_{k+2}}{F_{k-1} + F_k}$$
$$= \frac{F_{k+3}}{F_{k+1}} = \frac{F_{(k+1)+2}}{F_{k+1}}$$

so $k + 1$ is true. By induction we have shown $\frac{p_n}{q_n} = \frac{F_{n+2}}{F_n}$ is true for all *positive integers.*

Next step, we will consider $[1;2,1,1,1,\ldots]$ *2*- Bump Sequence.

	-1	0	1	2	3	4	5	...
a_i			1	2	1	1	1	...
p_i	0	1	1	3	4	7	11	...
q_i	1	0	1	2	3	5	8	...

So; $p_1 = 1, p_2 = 3$ and $p_{n+2} = p_n + p_{n+1}$.

By THEOREM 1, the recurrence relation $p_{n+2} = p_n + p_{n+1}$ is a linear homogeneous relation of degree 2. Its associated equation is $x^2 = 1 + x$

$$x^2 - x - 1 = 0$$
$$x = \frac{1+\sqrt{5}}{2}$$

So $p_n = \vartheta\left(\frac{1+\sqrt{5}}{2}\right)^n + \mu\left(\frac{1-\sqrt{5}}{2}\right)^n$

From $p_1 = 1, p_2 = 3$ *then,*

$p_1 = \vartheta\left(\frac{1+\sqrt{5}}{2}\right)^1 + \mu\left(\frac{1-\sqrt{5}}{2}\right)^1 = 1$ ----------*(1)*

$p_2 = \vartheta(\frac{1+\sqrt{5}}{2})^2 + \mu\left(\frac{1-\sqrt{5}}{2}\right)^2 = 3$ ----------*(2)*

We find ϑ *and* μ to be

$$\vartheta\left(\frac{1+\sqrt{5}}{2}\right) + \mu\left(\frac{1-\sqrt{5}}{2}\right) = 1$$
$$\vartheta(1+\sqrt{5}) + \mu(1-\sqrt{5}) = 2$$

$$1\vartheta + \sqrt{5}\vartheta + 1\mu - \sqrt{5}\mu = 2$$

$\vartheta + \mu + (\vartheta - \mu)\sqrt{5} = 2$ ------ (3)

from (2) we get $3(\vartheta + \mu) + (\vartheta - \mu)\sqrt{5} = 6$ --------(4)

Next step, we choose (4)-(3) for will have coefficients of $(\vartheta - \mu)\sqrt{5}$ and $-(\vartheta - \mu)\sqrt{5}$ which is what we need for this method. Here is the work for this step.

$$[3(\vartheta + \mu) + (\vartheta - \mu)\sqrt{5}] - [\vartheta + \mu + (\vartheta - \mu)\sqrt{5}] = 6 - 2$$

$$2(\vartheta + \mu) = 4$$

$$\vartheta + \mu = 2$$

$\vartheta = 2 - \mu$ --------*(5)*

Now, substitute ϑ *from (5) into (3)* $\vartheta + \mu + (\vartheta - \mu)\sqrt{5} = 2$

$$2 - \mu + \mu + (2 - \mu - \mu)\sqrt{5} = 2$$

$$2 + (2 - 2\mu)\sqrt{5} = 2$$

$$(2 - 2\mu)\sqrt{5} = 0$$

$$2 - 2\mu = 0$$

$$2\mu = 2$$

$$\mu = 1$$

So $\vartheta = 1$ *(confirm by python calculator)*

So, the solution is $p_n = 1(\frac{1+\sqrt{5}}{2})^n + 1\left(\frac{1-\sqrt{5}}{2}\right)^n$

And we known $q_n = F_n$

$$\therefore \quad \frac{p_n}{q_n} = \frac{(\frac{1+\sqrt{5}}{2})^n + \left(\frac{1-\sqrt{5}}{2}\right)^n}{F_n}$$

In the same way, we consider $[1;1,2,1,1,\ldots]$ *3-* Bump Sequence.

	-1	*0*	*1*	*2*	*3*	*4*	*5*	...
a_i			*1*	*1*	*2*	*1*	*1*	...
p_i	*0*	*1*	*1*	*2*	*5*	*7*	*12*	...
q_i	*1*	*0*	*1*	*1*	*3*	*4*	*7*	...

So $\frac{p_1}{q_1} = 1$ $\frac{p_2}{q_2} = 2$ *and* $p_{n+2} = p_n + p_{n+1}$ *when* $n \geq 2$ *and* $p_2 = 2, p_3 = 5$

we get $\therefore \frac{p_n}{q_n} = \frac{(\frac{7}{2\sqrt{5}} - \frac{1}{2})(\frac{1+\sqrt{5}}{2})^n - (\frac{7}{2\sqrt{5}} + \frac{1}{2})\left(\frac{1-\sqrt{5}}{2}\right)^n}{(\frac{\sqrt{5}}{2} - \frac{1}{2})(\frac{1+\sqrt{5}}{2})^n - (\frac{\sqrt{5}}{2} + \frac{1}{2})\left(\frac{1-\sqrt{5}}{2}\right)^n}$; $n \geq 2$

The last case, we consider $[2],[2;2],[2;2,2],\ldots$

	-1	*0*	*1*	*2*	*3*	*4*	*5*	...
a_i			*2*	*2*	*2*	*2*	*2*	...
p_i	*0*	*1*	*1*	*2*	*5*	*12*	*29*	...
q_i	*1*	*0*	*0*	*1*	*2*	*5*	*12*	...

The truncations $[a_0; a_1, a_2, \ldots, a_n]$ are plainly rational numbers $\frac{p_n}{q_n}$.

Indeed, the continuants p_n and q_n are defined by the matrix identities.

$(p_n\ p_{n-1}\ q_n\ q_{n-1}) = \prod_{j=0}^{n}(a_j\ 1\ 1\ 0)$

Follows immediately from $(p_0\ p_{-1}\ q_0\ q_{-1}) = (2\ 1\ 1\ 0)$

$$(p_1\ p_0\ q_1\ q_0) = (2\ 1\ 1\ 0)(2\ 1\ 1\ 0) = (5\ 2\ 2\ 0)$$
$$(p_2\ p_1\ q_2\ q_1) = (5\ 2\ 2\ 0)(2\ 1\ 1\ 0) = (12\ 5\ 5\ 0)$$
$$(p_3\ p_2\ q_3\ q_2) = (12\ 5\ 5\ 0)(2\ 1\ 1\ 0) = (29\ 12\ 12\ 0)$$
$$\dots$$
$$\dots$$

$$(p_n\ p_{n-1}\ q_n\ q_{n-1}) = (p_{n-1}\ p_{n-2}\ q_{n-1}\ q_{n-2})(2\ 1\ 1\ 0)$$
$$= (2p_{n-1} + p_{n-2}\ p_{n-1}\ 2q_{n-1} + q_{n-2}\ q_{n-1})$$

Hence $p_n = 2p_{n-1} + p_{n-2}$

$q_n = 2q_{n-1} + q_{n-2}$

So, we get $\frac{p_n}{q_n} = \frac{\frac{\sqrt{2}}{4}(1+\sqrt{2})^n - \frac{\sqrt{2}}{4}(1-\sqrt{2})^n}{(\frac{1}{2} - \frac{\sqrt{2}}{4})(1+\sqrt{2})^n + \frac{1}{4-2\sqrt{2}}(1-\sqrt{2})^n}$

Conclusions:

Now we have the new results of some continued fractions. First, we know $[1;1,1,\dots,1] = \frac{F_{n+1}}{F_n}$ where F_n is the nth Fibonacci Number; $F_0 = 0\ F_1 = 1$. Then we consider $[2;1,1,1,1,\dots]$ is a 1- Bump Sequence of continued fraction. $[2;1,1,1,1,\dots] = \frac{p_n}{q_n} = \frac{F_{n+2}}{F_n}$ is true for all positive integers. Next, we will consider $[1;2,1,1,1,\dots]$ *2*- Bump Sequence. $[1;2,1,1,1,\dots] = \frac{p_n}{q_n} = \frac{(\frac{1+\sqrt{5}}{2})^n + (\frac{1-\sqrt{5}}{2})^n}{F_n}$. In the same way, we consider $[1;1,2,1,1,\dots]$ *3*- Bump Sequence.

$[1;1,2,1,1,\dots] = \frac{p_n}{q_n} = \frac{(\frac{7}{2\sqrt{5}} - \frac{1}{2})(\frac{1+\sqrt{5}}{2})^n - (\frac{7}{2\sqrt{5}} + \frac{1}{2})(\frac{1-\sqrt{5}}{2})^n}{(\frac{\sqrt{5}}{2} - \frac{1}{2})(\frac{1+\sqrt{5}}{2})^n - (\frac{\sqrt{5}}{2} + \frac{1}{2})(\frac{1-\sqrt{5}}{2})^n}$; $n \geq 2$. The last case, we consider $[2], [2;2], [2;2,2], \dots$ so we found that the the pattern was $\frac{p_n}{q_n} = \frac{\frac{\sqrt{2}}{4}(1+\sqrt{2})^n - \frac{\sqrt{2}}{4}(1-\sqrt{2})^n}{(\frac{1}{2} - \frac{\sqrt{2}}{4})(1+\sqrt{2})^n + \frac{1}{4-2\sqrt{2}}(1-\sqrt{2})^n}$.

In the future, we will consider the sums $p_n + q_n$ to address the original problem which numbers are not included.

References:

[1] JONATHAN BORWEIN, ALF VAN DER POORTEN, JEFFREY SHALLIT, WADIM ZUDILIN. (2014). Australian Mathematical Society Lecture Series: 23 (Neverending Fractions: An Introduction to Continued Fractions). Crawley, Australia.

[2] Timothy J. Barth Michael Griebel David E. Keyes Risto M. Nieminen Dirk Roose Tamar Schlick. Programming for Computations – Python Second Edition. (2018). Fac of Tech, Natural Sci & Maritime Sci University of South-Eastern Norway Porsgrunn, Norway.

[3] Richard K. Guy. Unsolved problems in number theory. Third Edition. P. cm.- (Problem books in mathematics). Includes bibliographical reference and index.

[4] A.YA. KHINCHIN. CONTRINUED FRACTION. The third edition. State publishing house of physical-mathematical literature, Moscow, 1961.
[5] C.D. OLDS san jose state college. (1963). CONTRINUED FRACTIONS. (3). NEW YOK:
RANDOM HOUSE THE L.W. SINGER COMPANY.
[6] Arturo Presa, Andy Hayes, Calvin Lin, and 3 others contributed. Linear Recurrence Relations[online].
https://brilliant.org/wiki/linear-recurrence relations/?fbclid=IwAR3SDDV66jdV7vuYn4jMGyK2xnaJIe8yiz-lo5H2MjaHjbQAh3SGk-ckmAI#definition
[20 October 2564]

Session E:
ENERGY / ENVIRONMENTAL & EARTH SCIENCE / MATERIALS SCIENCE / SPIN CROSSOVER

PETROGRAPHY OF XENOLITHS IN BASALT FROM THE CHANTHABURI-TRAT GEM FIELDS, THAILAND

Apichet Boonsoong
Department of Geological Sciences, Faculty of Science, Chiang Mai University, Chiang Mai, Thailand
*e-mail: Siamsapphire@hotmail.com, Apichet.b@cmu.ac.th

Abstract:
In the Chanthaburi-Trat basalts, xenoliths are composed of essentially ultramafic xenoliths (particularly spinel lherzolite) with a few of an aggregate of feldspar. Modal compositions of the ultramafic nodules vary with olivine (60-75%), clinopyroxene (20-30%), orthopyroxene (0-15%), minor spinel (1-3%) and plagioclase (<1%). The essential minerals form an equigranular, medium- to coarse-grained, granoblastic texture, and all are in mutual contact indicating attainment of equilibrium. Reaction rims are common along the nodule margins and in some are also present along grain boundaries. Zoning occurs in clinopyroxene, and to a lesser extent in orthopyroxene. The equilibration temperatures of these xenoliths are estimated to be in the range 973 to 1063°C. The general mineral assemblage of the lherzolite xenoliths and the absence of garnet indicate a pressure range of approximately 12–19kbar, which is equivalent to depths approximately of 38 to 60km.

Introduction:

Ultramafic xenoliths of mantle origin are common in alkali basalts around the world (e.g., Frey and Green, 1974; Frey and Prinz, 1978; Press *et al*., 1986) and provide direct and valuable insights into processes controlling the geochemical evolution of the upper mantle and its composition. In Thailand, ultramafic xenoliths are found in the Late Cenozoic basaltic volcanics and attempts to understand the sub-lithospheric processes and the composition of the mantle beneath Thailand have been done by studies of host basalts and their megacrysts (e.g., Barr and MacDonald. 1981; Barr and Dostal, 1986; Intasopa *et al*., 1995; Mukasa *et al*., 1996; Zhou and Mukasa, 1997). In this current article, the petrography of the xenoliths in the Chanthaburi-Trat gem fields will be outlined and related to their petrogenesis.

The xenoliths in Thai basalts consist mainly of ultramafic xenoliths with less-abundant metamorphic rocks, other igneous rocks and sedimentary rocks. They are for example peridotite and related rocks, quartzite, gabbro, tuff, feldspathic aggregate etc. The majority of the ultramafic xenoliths are spinel lherzolites with lesser harzburgite, and rare websterite, dunite and pyroxenite. They are accompanied by a variety of megacrysts of pyroxene, spinel, olivine, garnet, zircon, magnetite, nepheline, ilmenite, feldspar, quartz, biotite, and corundum (Vichit *et al*., 1979; Barr and Dostal, 1986). Some diabasic and gneissic fragments have been reported from the Bo Ploi area, Kanchanaburi province (Barr and Dostal, 1986).

The Chanthaburi-Trat Basalts:

In Chanthaburi and Trat provinces the basalts are Pleistocene in age. They occur as scattered masses, of highly variable sizes, covering an area of approximately 320km^2 in Amphoe Tha Mai, Amphoe Pong Nam Ron, Amphoe Khlung, Chanthaburi Province and Amphoe Bo Rai, Trat Province (Figure 1). The basalts are largely of subaerial flows which have largely been extensively weathered, giving rise to brown and brownish yellow soil. The least-altered basalts are medium dark grey to dark grey, and are dense, fine-grained, with phyric to microphyric textures. The most common phenocryst assemblage for basanites/nepheline

basanites is olivine + clinopyroxene + ulvöspinel, and olivine + clinopyroxene + plagioclase ± ulvöspinel for the trachybasalts/basalt. In addition to these assemblages, chromium-rich spinel may be present as megacrysts. The most abundant phenocrysts are olivines. The groundmass commonly shows felty texture and uncommon trachytic texture. The primary groundmass constituents are made up largely of plagioclase laths with subordinate intergranular olivines and pink clinopyroxenes, and minor ulvöspinel; many samples have variable amounts of brown glass and quenched crystals. A few of the basalts exhibit subophitic textures. Amygdales and veinlets are rarely present. Lherzolite and feldspathic xenoliths have been sporadically detected in some samples; quartz xenocrysts are rare in trachybasalts.

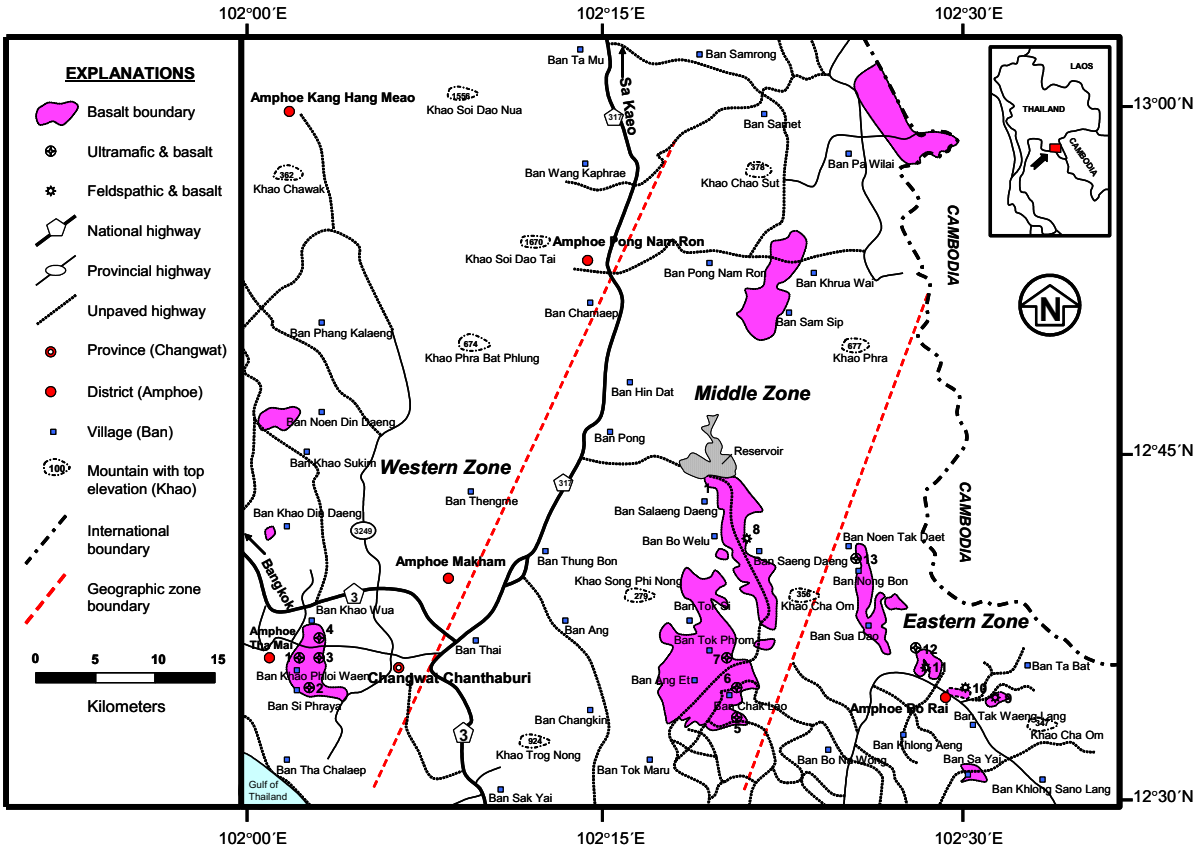

Figure 1. Schematic map sample to show locations for basalts with ultramafic and feldspathic xenoliths in the Chanthaburi-Trat gem fields.

In the Chanthaburi-Trat gem fields, xenoliths are composed of essentially ultramafic xenoliths (particularly spinel lherzolite) with a few of an aggregate of feldspar. Ultramafic xenoliths are found throughout the study area, and are more abundant in the western zone than the middle and the eastern zones, whereas the feldspathic xenoliths are found only in the middle and the eastern zones (Figure 1 and Table 1).

Methodology:

Some 19 ultramafic xenoliths were collected from 13 different locations (Figure 1 and Table 1). They range in size from 3.5 to 60mm across. Most are weathered and oxidized on the surface but fresh samples are obtained from cut surfaces. Thin sections were made of the least-altered basalts for petrographic study.

Table 1. Xenoliths from Chanthaburi-Trat gem fields and their host rocks.

Geographic Zone	Sample No.	Location	Xenolith	Host Rock
Western Zone (Chanthaburi province)	CT 1	Ban Khao Phloi Waen,	Spinel lherzolite	Nepheline basanite
	CT 2	Ban Bo Phu	Spinel lherzolite	Nepheline basanite
	CT 3	Ban Khao Phloi Waen	Spinel lherzolite	Nepheline basanite
	CT 4	Ban Khao Wua	Spinel lherzolite	Nepheline basanite
Middle Zone (Between Chanthaburi and Trat provinces)	CT 5	Ban Na Ta Mi	Spinel lherzolite	Nepheline basanite
	CT 6	Ban Chak Lao	Sp-plag lherzolite	Trachybasalt
	CT 7	Ban Sato Noi	Spinel lherzolite	Basanite
	CT 8	Ban Saeng Som	Feldspathic rock	Trachybasalt
Eastern Zone (Trat province)	CT 9	Ban Ta Bat	Feldspathic rock	Basanite
	CT 10	Ban Thung Satharana	Feldspathic rock	Nepheline basanite
	CT 11	Ban Sua Dao	Feldspathic rock	Nepheline basanite
	CT 12	Ban Nong Bon	Spinel lherzolite	Basanite
	CT 13	Ban Noen Tak Daet	Sp-plag lherzolite	Basanite

Petrography:

Ultramafic Xenoliths

In hand specimen, these are light green to dark green in colour, and range in size from 0.3 to 10cm. They have flattened, rounded and oval shapes, and are found throughout the study area but mainly in the western zone. In thin section, they are seen to consist of variable amounts of olivine, clinopyroxene, orthopyroxene with minor spinel and plagioclase, and are classed as lherzolite (Streckeisen, 1976). The modal compositions vary between xenoliths with olivine (60-75%), clinopyroxene (20-30%), orthopyroxene (0-15%), with minor spinel (1-3%) and plagioclase (<1%).

The essential minerals usually form equigranular, medium- to coarse-grained mosaics of anhedral to subhedral crystals with granoblastic texture. Reaction rims are common along the xenolith margins (Figure 2a) and in some these also occur along grain boundaries. Triple-junctions between minerals, especially olivines (Figure 2a) are common. All the primary phases are in mutual contact suggesting attainment of equilibrium. Olivines in the majority of samples range in size from 0.1 to 4.2mm with most between 0.5 to 1.6mm. In some, olivines display weak kink bands and undulatory extinction. Small (0.1 to 0.3mm), round olivines also occur as inclusions in both clinopyroxenes and chromium-rich spinel (Figure 2a). In places replacement by chlorite/serpentine and iron oxides/hydroxides occurs. Clinopyroxenes are light pinkish brown to light green in colour and occur as anhedral to subhedral (0.2 to 2.8mm) crystals. In some samples particularly in the eastern zone, clinopyroxene grains have a sieve-textured and/or thin reaction rims consisting of secondary clinopyroxene (Figure 2b). Orthopyroxenes appear pale brown in thin sections, and only present in the xenoliths from Ban Chak Lao (Sample no. CT 6) in the middle zone and at Ban Khao Phloi Waen (Sample no. CT 1) and Ban Khao Wua (Sample no. CT 4) in the western zone. They occur as anhedral to subhedral grains, with grain sizes between 0.3 and 3.5mm. In some xenoliths, a symplectite texture occurs in orthopyroxenes where they are in contact with the host basalt. This consists of secondary clinopyroxene and olivine with some apatites. Spinels vary between brown (chromium-rich spinel) and green (ferroan spinel). They occur as an

interstitial phase, with a grain size of 0.1 to 1.6mm, and commonly as inclusions in orthopyroxene, clinopyroxene and olivine. They most commonly have sharp contacts with other grains, though in some, reaction rims are found around small (< 0.5mm) irregular spinels. Anhedral plagioclases (sizes up to 0.8mm) occur are accessory minerals, and are present only in two xenoliths from Ban Chak Lao (Sample no. CT 6) and at Ban Noen Tak Daet (Sample no. CT 13) in the middle and eastern zones respectively.

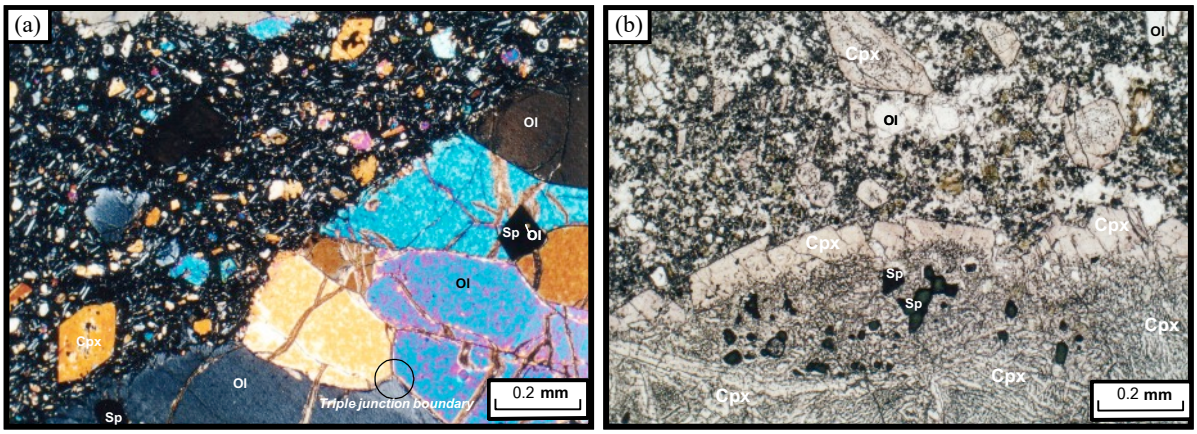

Figure 2. (a) Spinel lherzolite xenolith (Sample no. CT 7) with corroded edges at contact with host basalt, and showing elongate grains with equilibrium 120-degree triple-junction grain boundaries. Crossed polars. (b) Sieve-textured clinopyroxenes (Cpx) in spinel lherzolite xenolith with dark green ferroan spinel (Sp) (Sample no. CT 12). Plane polarised light. Abbreviations: Ol = olivine.

Feldspathic Xenoliths

These xenoliths are found only in the basalts from the middle and the eastern zones (Table 1). They have flattened, round, and oval shapes with sizes ranging from 3.0 to 6.5mm. In thin section, they display two textural types; a crystalline texture and a quenched one. The crystalline texture is mostly composed of alkali feldspar and accessory amounts of plagioclase, with or without quartz. Feldspars within this occur as anhedral to subhedral crystals, with average grain sizes between 0.1 and 0.8mm, showing zoning along the edges of some grains. Those with the quench texture are largely of plagioclase, alkali feldspar and glass with subordinate small, light-green clinopyroxenes. The quench-feldspars are characterised by small skeletal crystals.

Conclusion:

The xenoliths from Chanthaburi-Trat basalts are predominantly ultramafic nodules (particularly spinel lherzolite). In addition, there are a small number consisting of feldspar aggregates. The ultramafic nodules are found throughout the study area in the more alkalic basalt and are more abundant in the western zone than in the middle and the eastern zones. The feldspathic xenoliths are found only in the middle and the eastern zones. Modal compositions of the ultramafic nodules vary with olivine (60-75%), clinopyroxene (20-30%), orthopyroxene (0-15%), minor spinel (1-3%) and plagioclase (<1%). The essential minerals form an equigranular, medium- to coarse-grained, granoblastic texture, and all are in mutual contact indicating attainment of equilibrium. Reaction rims are common along the nodule margins and in some are also present along grain boundaries. Zoning occurs in clinopyroxene, and to a lesser extent in orthopyroxene. The mineral assemblage and the absence of garnet indicates a pressure range of 12–19kbar, equivalent to depths between 38

and 60km. The presence of spinel lherzolites and the absence of garnet lherzolite in the alkali-basalt mantle xenoliths may indicate thinning of the lithospheric mantle which may have resulted from thermal erosion by the ascent of hot asthenosphere at the base of the lithosphere.

References:

1. Barr SM, Dostal L. J Southeast Asian Earth Sci. 1986;1(2):107-116.
2. Barr SM, MacDonald AS, Geol. Soc. Amer. Bull. 1981; 92 (Part 2):1069-1142.
3. Brey GP, Kohler T. J. Petrol. 1990;31:1353-1378.
4. Frey FA, Green HD. Earth Planet. Sci. Lett. 1974;38:1023-1059.
5. Frey FA, Prinz M. Earth Planet. Sci. Lett. 1978;38:129-176.
6. Green DH, Hibberson W. Phys. Earth Planet. Inter. 1970;3:247-254.
7. Green DH, Ringwood AE. Phys. Earth Planet. Inter. 1970;3:359-371.

DEVELOPMENT OF A CAPACITIVE DEIONIZATION STACK FOR BRACKISH WATER DESALINATION

Kunchaya Thungsuai, Eknarin Thanayupong, Nuttaporn Pimpha, and Saowaluk Chaleawlert-umpon*
National Nanotechnology Center, National Science and Technology Development Agency, Thailand Science Park, Pathum Thani 12120, Thailand
*e-mail: saowaluk@nanotec.or.th

Abstract:
Capacitive deionization (CDI) as a promising desalination technology has attracted wide attention with a cost-effectiveness in brackish water treatment. In this study, we aimed to develop a scale-up CDI stack with a coconut shell-based carbon electrode to desalinate brackish water. The optimal operational parameters such as flow rate and concentration of NaCl solution were symmetrically investigated in terms of the CDI performances: salt removal efficiency (R) and salt adsorption capacity (SAC). The results demonstrated that a low flow rate caused an enhancement of the overall CDI performance due to a sufficient contact time for ions on the electrode surface. The initial feed concentration had a direct effect on EDL formation in terms of a high ion concentration gradient resulting in an increase in salt adsorption capacity. However, a reduction in salt removal efficiency was obtained with increasing of salt concentration. It was because of the fixed mass loading and surface area of the CDI electrode with 10 stacks. Finally, the data in this study can be used as guidance for further improvement of CDI system for practical applications in brackish groundwater desalination.

Introduction:
Water shortage has much gained attention in the world issue which has been rising due to the depletion of freshwater resources. Climate change is one of the causes of drought and progress seawater ingress leading to the availability and quality of freshwater for daily life. Desalination of brackish water is one of the promising technologies to provide abundant freshwater. Among traditional desalination technologies (ion exchange, electrodialysis, reverse osmosis, etc.), capacitive deionization (CDI) is an alternative desalination technology that claimed as a more effective approach for water with low and moderate salt content.[1] CDI is based on an electrochemically controlled process *via* an electrical double layer (EDL) mechanism, like a capacitor. It operates at a relatively low electrical voltage (typically 0.8-1.6 V) to polarize a pair of porous carbon electrodes allowing charged ions adsorption by electrostatic force attraction safely and easily, resulting in the removal of ions. The advantage including low-voltage and low-pressure operation and high-water recovery makes CDI an attractive energy efficient and environmentally friendly approach for brackish water desalination.[2-3] Furthermore, the ability to recover some of the energy (from energy consumption in the adsorption step) by the desorption step of CDI makes it an additional benefit over others.[4-5]

Since the CDI performances mainly depend on nature electrode materials. The effect of the novel carbon-based materials towards the adsorption of ions was investigated.[6-11] However, large-scale production for CDI applications is cost limit so activated carbon made from biomass are the

most cost-effective material and a potential choice for the fabrication of CDI electrodes. Furthermore, operational conditions such as applied voltage, feed flow rate, and initial concentration also affect to the adsorption capacity and energy consumption.[6,12-16] In a lab scale test, a batch mode operation is simply operated by recycling feed with the limited quantity until the steady state condition is reached to study the possibility and efficiency of desalination system.

This study aims to scale up a lab scale CDI in a batch mode system with a stacked electrode (16 x 16 cm^2) to investigate the adsorption capacity. The operational conditions in terms of flow rate and initial concentration of feed water were optimized in 2,000 ppm NaCl solution which is a model for medium brackish groundwater. This finding will provide a possible operational condition for further pilot scale CDI devices in brackish groundwater desalination applications.

Methodology:

Electrode preparation

Carbon electrodes were prepared from a commercial coconut shell-based carbon powder (YAO) (Right solution, Thailand), conductive graphite (MTI Corporation, USA), and Polytetrafluoroethylene (PTFE) (60 wt% solution dispersion on water, Aldrich, USA) in a mass ratio of 80:5:15, respectively. The viscous homogeneous slurry was formed in EtOH solvent and spread onto a graphite current collector with a thickness of 600 μm (approximately). The prepared electrodes were dried in an oven at 120°C for 24 h. A geometric active surface area of each electrode was 16×16 cm^2. The total weight of the 20 electrodes (10 pairs) was 118 g, when all the components were considered (YAO, PTFE, and conductive graphite).

CDI-based system setup

The CDI electrodes were fabricated into a self-made CDI apparatus as shown in Figure 1. Symmetric electrodes were used with similar mass (<10 wt% difference). All experiments were carried out in a NaCl solution (1 L) with various concentrations and flow rates. A direct voltage at 1.2 V was applied on the opposite electrodes in an adsorption step and -0.3 V in a desorption step. An ion conductivity meter was used to monitor and measure the concentration of NaCl solution. The NaCl concentration obtained by using a standard calibration curve between the conductivity and the concentration of NaCl solutions. For our analyses, the percentage of salt removal efficiency (R) and the salt adsorption capacity (SAC, mg/g) were defined from the eqns (1) and (2), respectively:

$$R(\%) = \frac{(C_0 - C_e) \times 100}{C_n} \quad (1)$$

$$SAC = \frac{(C_0 - C_e) \times V}{m} \quad (2)$$

where C_0 and C_e are the initial and final NaCl concentrations (mg/L), V is the volume of the NaCl solution (L), m is the total mass of the electrodes (g), and t is the electrosorption time (min).

Results and Discussion:

CDI stack assembly

The assembled CDI stack and a diagram showing the system setup as depicted in Figure 1. We investigated the CDI performance through a batch mode which cycling feed water with a specific volume through CDI cell was operated. The experiment setup (Figure 1a) composed of a reservoir, peristaltic pump, CDI stack cell, and power supply. The assembled CDI unit cell (Figure 1b) was composed of two parallel similarly carbon electrodes separated by a silicone sheet spacer acting as a channel for feed water. The stainless-steel sheets were used as a supporter for graphite-based current collectors. The CDI stack was bolted together using end plates of polyethylene sheet (photograph in Figure 1a).

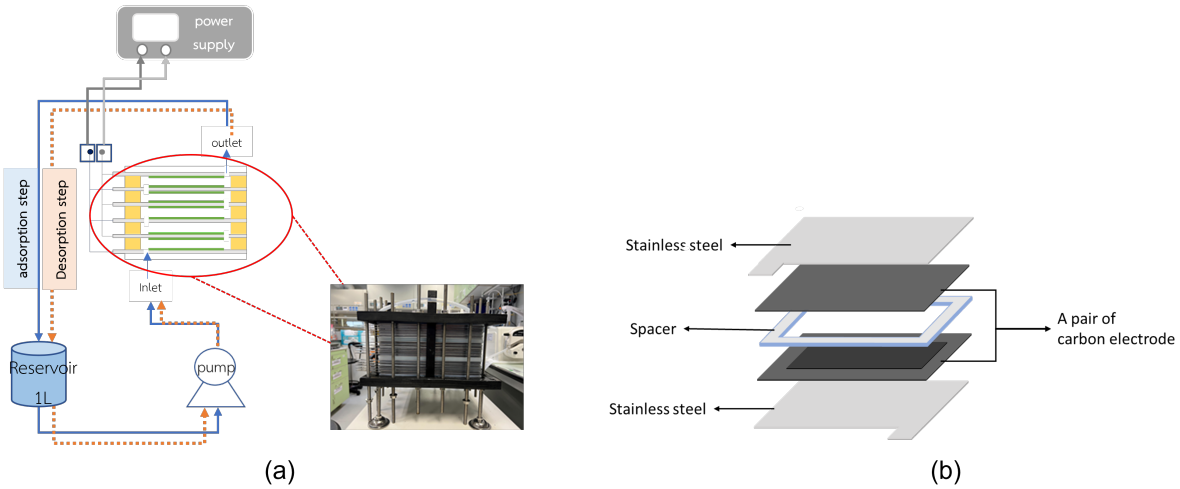

Figure 1. (a) diagram for CDI-based system in a batch mode and photograph of the CDI stack and (b) CDI unit cell configuration.

CDI performances

The CDI stack with 10 pairs of carbon electrodes were first operated in 500 ppm NaCl solution for adsorption/desorption process. Our previous study, the operational applied voltage (an adsorption step at 1.2 V and the reverse voltage at -0.3 V for a desorption step) were optimized (the data was not shown). In this study, the CDI stack will be operated under this constant voltage.

An influence of feed water flow rate was investigated in terms of CDI performances. Figure 2a presents the changes in the feed water conductivity as a function of time with different flow rates. The solution conductivity quickly dropped at the initial time (5-10 min) indicating the fast ions adsorption on the electrode when applying voltage. After 20-30 min, the conductivity remained constant indicating saturated ion adsorption on the electrode. It was resulted in the removal of the ions from the feed solution in the adsorption process. A lower flow rate induced a higher change of solution conductivity in a shorter operating time. However, the final conductivities of the outlet stream (after saturated adsorption) were almost similar. The results of CDI performances: salt removal efficiency and salt adsorption capacity are summarized in Figure 2b.

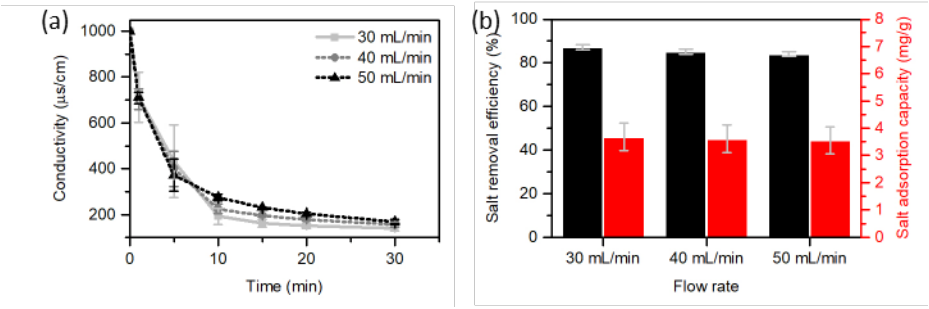

Figure 2. (a) conductivity profile during adsorption process and (b) the results of salt removal efficiency and salt adsorption capacity of the CDI stack obtained in a 500 ppm NaCl solution at different flow rates.

As expected, the salt removal efficiency slightly decreased from 87% to 84% when the flow rate increased from 30 to 50 mL/min. In the same way, the salt adsorption capacity had slightly decreased from 3.68 to 3.55 mg/g. This statement was in agreement with the literatures[12,14-16] generally reported that adsorption capacity increased when the flow rate increased. It was due to a sufficient adsorption time of ions on the electrode surface with a low flow rate operation resulted in a higher adsorption capacity (or removal efficiency). Nevertheless, the CDI stack was operated in the low initial concentration of NaCl solution (500 ppm) so this phenomenon was not obviously observed. This was because of enough active sites on the carbon electrode for almost all ion adsorptions in a low salt concentration.

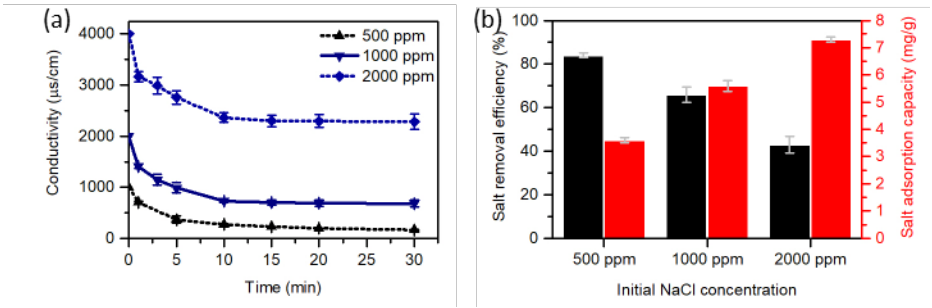

Figure 3. (a) conductivity profile during adsorption process and (b) the results of salt removal efficiency and salt adsorption capacity of the CDI stack operated at a flow rate of 50 mL/min in various initial concentrations of NaCl solution.

The effect of the initial concentration was further studied. The CDI stack was performed at 50 mL/min of flow rate for a high-water production. The observed conductivity profiles are exhibited in Figure 3a, showing the solution conductivity was reduced in the same pattern for all salt concentrations. The summarized results of the CDI performances are presented in Figure 3b. We noted that increasing the initial feed concentration reduced the salt removal efficiency but enhanced the salt adsorption capacity.[14,17] As the concentration increased from 500 to 2,000 ppm, the salt removal efficiency decreased from 84% to 43% while the salt adsorption capacity increased from 3.55 to 7.3 mg/g. The EDL formation would be greatly facilitated by the lower resistance (in

the higher concentration gradient), suggesting the improvement of salt adsorption capacity.[18-19] In contrast, salt removal efficiency relied on the active sites of the electrode for adsorption. So, the salt removal efficiency would relatively reduce with the increase of feed salt concentration when the mass and interfacial surface area of the electrode were fixed. This result confirmed that the electrosorption capacity of the CDI electrode was concentration dependent.

Conclusion:

This study demonstrated two optimized operational parameters: feed flow rate and initial salt concentration for the scale-up CDI stack in batch mode. Firstly, we found that the low feed flow rate caused the enhancement of CDI performance due to more residence time of ions adsorption on the electrode surface. Secondly, the initial salt concentration induced a better EDL formation at the interface of the electrode and feed water from the higher concentration gradient resulted in a greater salt adsorption capacity. This indicated the salt adsorption capacity was ion concentration dependent. While the salt removal efficiency related to the mass loading and the active surface area of the electrode for the highest salt adsorption. We believed that this operational finding will be beneficial for further improvement CDI device to desalinate brackish water in a salinity range of 2,000 ppm.

Acknowledgements:

This work was funded by National Research Council of Thailand (NRCT, 2021).

References:

1. Anderson MA, Cudero AL, Palma J. Electrochim. Acta 2010;55:3845-3856.
2. Porada S, Zhao R, van der Wal A, Presser V, Biesheuvel PM. Prog. Mater. Sci. 2013;58:1388-1442.
3. Yu T-H, Shiu H-Y, Lee M, Chiueh P-T, Hou C-H. Desalination. 2016;399:53-60.
4. Długołęcki P, van der Wal A. Environ. Sci. Technol. 2013;47:4904-4910.
5. García-Quismondo E, Santos C, Lado J, Palma J, Anderson MA. Environ. Sci.Technol. 2013;47:11866-11872.
6. Elisadiki J, Kibona TE, Machunda RL, Saleem MW, Kim W-S, Jande YAC. Biomass Convers. Biorefin. 2020;10:1327-1356.
7. Chaleawlert-umpon S, Pimpha N. New J. Chem. 2020;44:12058-12067.
8. L. Chao L, Liu Z, Zhang G, Song X, Lei X, Noyong M, Simon U, Chang Z, Sun X. J. Mater. Chem. A. 2015;3:12730-12737.
9. Jagiello J, Olivier JP. Carbon 2013;55:70-80.
10. Nita C, Bensafia M, Vaulot C, Delmotte L, Ghimbeu CM. Carbon. 2016;109:227-238.
11. Oladunni J, Zain HZ, Hai A, Banat F, Bharath G, Alheinat E. Sep. Purif. Technol. 2018;207:291-320.
12. Jande YAC, Kim WS. J. Ind. Eng. Chem. 2014;20:3356-3360.
13. Jia B, Zhang W. Nanoscale Res. Lett. 2016;11:64.
14. Mossad M, Zou L. J. Hazard. Mater. 2012;213-214:491-497.
15. Wang C, Song H, Zhang Q, Wang B, Li A. Desalination. 2015;365:407-415.
16. Xu D, Tong Y, Yan T, Shi L, Zhang D. ACS Sustain. Chem. Eng. 2017;5:5810-5819.

17. Li G-X, Hou P-X, Zhao S-Y, Liu C, Cheng H-M. Carbon. 2016;101:1-8.
18. Lado JJ, Zornitta RL, Calvi FA, Tejedor-Tejedor MI, Anderson MA, Ruotolo LAM. J. Anal. Appl. Pyrolysis. 2016;120:389-398.
19. Zhao S, Yan T, Wang Z, Zhang J, Shi L, Zhang D. RSC Adv. 2017;7:4297-4305.

EFFECTIVENESS ON THE STRATUM CORNEUM LAYER AFTER USING NANOEMULSIONS FROM HONEYSUCKLE FLOWERS ESSENTIAL OILS

Natnicha Phungsara[1], Wannisa Keawbankrud[2]*

[1]Mahidol Bumrungrak Nakhonsawan Medical Center, Nakhonsawan, Thailand
[2]Health Science and Aesthetic Program, Faculty of Science and Technology, Rajamangala University of Thechnology Krungthep, Bangkok, Thailand

*Corresponding author. E-mail: wannisa.k@mail.rmutk.ac.th

Abstract:

The objective of this research was to study the efficacy of a nanoemulsion containing honeysuckle essential oil on Tween 80 at a ratio (1:2) in 10 volunteers for 8 weeks. Stratum corneum measurements revealed that After using the nanoemulsion, wrinkles were reduced and the indentation index was at 9.621 ± 0.11, the deepest groove was reduced at 0.098 ± 0.19 mm, elevations were reduced at 8.54 ± 0.41 mm^3, roughness was reduced at 9.676 ± 0.24. It also resulted in increased hydration at 3.79 ± 0.85 uS, Transepidermal water loss (TEWL) was reduced at 2.1 ± 0.62 $g/m^2/h$, and the elasticity could be increased. The total value between skin tightening and recovery was at 11.4 ± 0.42 MPa. Young's elasticity modulus increased to 5.9 ± 0.05 MPa. Therefore, this nanoemulsion is effective in reducing wrinkles, roughness, and TEWL as well as stimulating the skin to be more hydrated and elastic. It is an alternative product for people who focus on skin care.

Introduction:

Stratum corneum has properties to retain and prevent transepidermal water loss. But it has been found that daily transepidermal water loss is on average 400 ml, and the transepidermal water loss may be higher than normal by various factors. For example, the humidity of the air. In winter, when relative humidity is low, the skin tends to lose moisture more easily than usual. Body washes such as soap, shampoo, or even a touch of dishwashing detergent can accelerate the stratum corneum's loss of NMF and lipids in this skin layer, which can lead to dry skin. Even in the case of some skin diseases, the stratum corneum can be peeled more often than usual. Therefore, a moisturizer that has the property of preventing or retaining hydration in this layer of skin was invented.

There are 3 types of skin moisturizers. It contains Occlusives, which are water-repellent substances such as petroleum jelly, wax, paraffin, lanolin, etc. It will coat in a thin film to prevent water from evaporating from the stratum corneum. Humectants are substances that have the property of retaining water from evaporating from the skin such as water, glycerin, urea, pyrrolidone, carboxylic acid (PCA), etc. This substance will attract water from the dermis to the stratum corneum and can also attract water from the airborne moisture to the stratum corneum. Lastly, emollients are substances that can smoothen and soften the skin by fulfilling in the gaps between corneocyte cells such as Glycerol, isopropyl myristate, keratin, collagen, elastin and oil, etc.

Nanoemulsions are oil-in-water dispersion systems with droplets smaller than microns in size. In general, it is popular in the range between 20-200 nm. Nanoemulsions are also kinetic stability, low viscosity, and translucency. Therefore, it is applied in the system for delivering drugs and cosmetic substances through the skin. It can enhance the therapeutic effect of the

drug, increase the stability of the important drug and deliver the drug to its target, as well as increase the moisture content of the skin. The nanoemulsion droplets adhere to the skin and form a strong film. therefore, it can inhibit transepidermal water loss There are capillary forces of nanometer-scale holes between the nanoemulsion droplets to form a strong hydrating film to the skin[1].

Methodology:

2.1 Materials and instrumentation

The material was nanoemulsion containing honey suckle essential oil. The chemicals included Tween 80 (Krungthep Chemi), DI water (Chemipan)[2]. The equipment included Multi-parameter skin analysis (Dermalab Combo), Antera 3D CS Version 2.0 (Miravex), Digital Microscope Premier (Dino-Lite).

The Nanoemulsion included honey suckle essential oil was extracted from honey suckle flowers on supercritical CO_2 extraction equipment, Guangzhou Heaven-Sent Industrial Co., Ltd., Tween 80 and DI water. The preparing of nanoemulsion on an ultrasonic sonicator, Cole-parmer, CP-750. with a maximum power output of 750 W. Particle size and size distribution of the nanoemulsion were determined by scanning electron microscope (SEM), JEOL, JSM-6610LV. The nanoparticle size distribution was determined on a particle analyzer, Beckman counter, Delsa Nano C. The stability of nanoemulsion was tested on a centrifuge equipment, Hettich mikro 22r[2], Appearance and particle size of nanoemulsions showed in Figure 1. Previous research has shown that honeysuckle flowers have many pharmacological effects including hepatoprotective, cytoprotective, antimicrobial, antioxidative, antiviral, anticancer[3], anti-inflammatory, tyrosinase-inhibitory properties[4] and healing effects in wound-induced rats.[5]

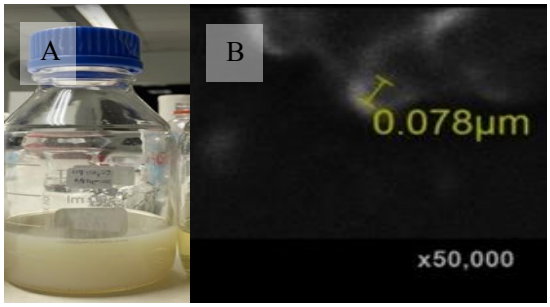

Figure 1 Appearance and particle size of nanoemulsions[2]
A = Appearance of nanoemulsions B = Particle size of nanoemulsions

2.2 Testing in volunteers

Population determination and sample selection population included Thai population in Rajamangala University of Technology Krungthep, aged between 30-60 years old, both female and male with healthy skin, no underlying disease, and not taking drugs or supplements selected 10 samples who voluntarily participated in the research project of both males and females with healthy skin by Convenient Sampling.

Inclusion criteria included volunteers who voluntarily consented to the research project and signed the consent form, 30-60 years old and No gender limits

Exclusion criteria included volunteers had a skin pathology in the area to be examined, chronic disease, taking drugs or supplements and used topical skin moisturizing product 30 days prior to the examination.

Method of testing in volunteers included

1. Volunteers took the questionnaire.

2. The researcher brought the volunteers into the room provided for the volunteers to rest for 30 minutes.

3. The researcher brought the volunteers into the examination room with internal temperature control at 18-22ºC.

4. The researcher measured hydration, TEWL, and skin elasticity by using Dermalab Combo on the forehead area. The frequency of measurement before using the product was after 4 weeks and 8 weeks of using the cream.

5. The researcher measured wrinkles, elevations, and roughness using Antera 3D CS Version 2.0 on the forehead. The frequency of measurement before using the product was after 4 weeks and 8 weeks of using the cream.

6. The researcher measured the skin condition by Digital Microscope Premier (Dino-Lite) with 50x magnification of the forehead area. The frequency of measurement before using the product was after 4 weeks and 8 weeks of using the cream.

Results and Discussion:

1. Allergy test of honeysuckle essential oil facial cream[2]

In this test, 2% sodium lauryl sulfate (SLS) was used as a positive control and Glycerin was used as a negative control for 4 hours and 24 hours with the patch test. It was an allergic reaction test on 10 healthy volunteers without allergies to essential oils and pollen. It consisted of 8 females and 2 males aged between 22-61 years. The volunteers had a mean age of 34.18 ± 02.29 years. All volunteer's patch test sensitization results showed that the honeysuckle essential oil-derived nanoemulsion formulation had zero scores on the ICDRG standard at 4 hours and 24 hours. In other words, no rashes or allergic reactions were found. Whereas, negative control (2% SLS) reported localized sensitization rash 24 hours after patch test with a score of 1-3 volunteers with a mean score of 1.5±0.71 as shown in Table 1. The researcher found symptoms such as mild itching in the test area in 8 volunteers and redness in the test area in 2 volunteers. It demonstrated the normal response of all volunteers to the sensitization effect of the negative control. The honeysuckle essential oil nanoemulsion formulation showed no skin symptoms in the volunteers with a score of 0. In other words, all volunteers tested for allergy to product containing honeysuckle essential oil nanoemulsion at a maximum concentration of 3 percent did not reveal redness or abnormality on healthy skin.

Table 1 the results of the allergy irritant test of nanoemulsion in volunteer[2]

Fomula	ICDRG Score	
	4 hours	24 hours
Nanoemulsion	0	0
2% SLS (positive control)	0	1.5±0.71
Glycerin (negative control)	0	0

Note : SLS was sodium lauryl sulfate

2. Effectiveness of nanoemulsions on Stratum corneum

To test the efficacy of the product in 10 volunteers, the stratum corneum depth (0.1 - 1 mm) was measured using Antera 3D CS Version 2.0 on the volunteers' forehead. Measurements were divided into before & after 4 weeks and 8 weeks of product use to compare the effectiveness of the skin in each range.

2.1 Roughness

The results of the roughness measurement test before and after using the nanoemulsion product as shown in Figure 2 showed that before using the nanoemulsion product, the roughness mean of the measured skin area was 10.397 ± 0.53 and after using the nanoemulsion product, the roughness mean was reduced by 9.676 ± 0.24 as shown in Table 2. Previous research has shown that honeysuckle flower oil contains polysaccharides, which have a soothing effect on allergic contact dermatitis in mice induced by picryl chloride[6] and studies on its cosmetic pharmacological effects. Ethanol extract from honeysuckle flowers has anti-inflammatory and wound-healing effects in mice[7], has a reducing effect on the enzymes tyrosinase, tyrosinase-related protein-1 (TRP-1), and tyrosinase-related protein-2 (TRP-2), has a reducing effect on the melanin pigment content of the skin[8-9].

Table 2 Showed the average roughness of the skin on the forehead. (n=10)

Factor	Roughness Ra*	Roughness Rq*	Elevation span (mm)
W_0	10.397 ± 0.53	13.878 ± 0.43	0.167 ± 0.20
W_4	9.982 ± 0.30	13.030 ± 0.39	0.158 ± 0.50
W_8	9.676 ± 0.24	12.530 ± 0.93	0.143 ± 0.36

Note : W_0 = Before using the product.
W_4 = After using nanoemulsion products 4 weeks.
W_8 = After using nanoemulsion products 8 weeks.
Ra* = Roughness Average. (The average surface roughness of the measured surface area)
Rq* = Roughness mean square. (The squared average surface roughness value of the measured surface roughness)

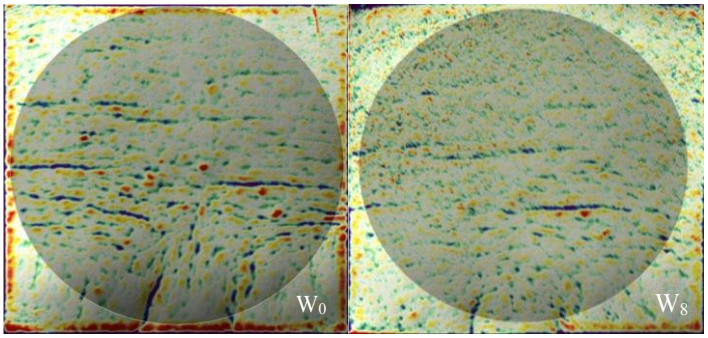

Figure 2 Showed roughness of the skin on the forehead of the volunteer.
W_0 = Before using the product
W_8 = After using nanoemulsion products 8 weeks

2.2 Wrinkles

The results of the wrinkles measurement test before and after using the nanoemulsion product as shown in Figure 3 showed that the indentation index of the nanoemulsion product was 9.963 ± 0.08. At 8 weeks of use, the indentation index reduced to 9.621 ± 0.11. The deepest groove before the nanoemulsion product was averaged 0.121 ± 0.02 mm. After 8 weeks of using the nanoemulsion product, the mean values were 0.098 ± 0.19 mm as shown in Table 3.

Table 3 Showed wrinkles on the forehead (n=10)

Factor	Indentation index	Maximum depth (mm)
W_0	9.963 ± 0.08	0.121 ± 0.02
W_4	9.821 ± 0.21	0.104 ± 0.13
W_8	9.621 ± 0.11	0.098 ± 0.19

Note : W_0 = Before using the product.
W_4 = 4 weeks after using nanoemulsion products.
W_8 = 8 weeks after using nanoemulsion products.

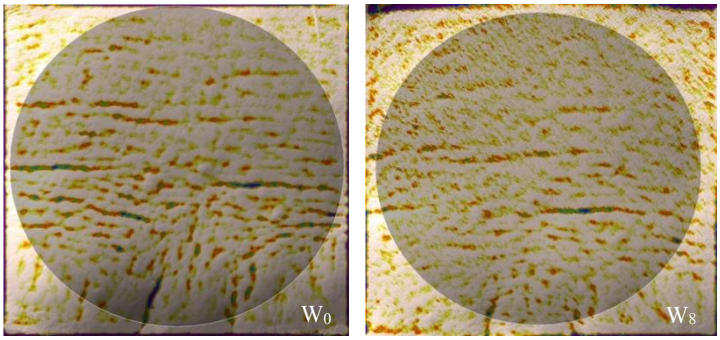

Figure 3 Showed wrinkles on the forehead of the volunteer
W_0 = Before using the product
W_8 = After using nanoemulsion products 8 weeks

2.3 Elevations

The results of the elevations measurement test before and after using the nanoemulsion product as shown in Figure 4 showed that before using the nanoemulsion product, the elevations was at 12.93 ± 0.07 mm^3, after using the nanoemulsion product for 8 weeks, the elevations was at 8.54 ± 0.41 mm^3 The area with all elevations on the forehead before using the product was at 397.2 ± 0.18 mm^2, after using the nanoemulsion product, the elevations was reduced at 291.0 ± 0.39 $mm^{2,}$ the maximum elevations before using the nanoemulsion product was at 0.111 ± 0.94 mm and after using the nanoemulsion product, the elevations was reduced at 0.100 ± 0.73 mm as shown in Table 4.

Table 4 Showed Elevations on the forehead. (n=10)

Factor	Volume (mm^3)	Affected area (mm^2)	Maximum height (mm)
W_0	12.93 ± 0.07	397.2 ± 0.18	0.111 ± 0.94
W_4	11.72 ± 0.19	301 ± 0.82	0.106 ± 0.26
W_8	8.54 ± 0.41	291.0 ± 0.39	0.100 ± 0.73

Note: W_0 = Before using the product.
W_4 = After using nanoemulsion products 4 weeks
W_8 = After using nanoemulsion products 8 weeks

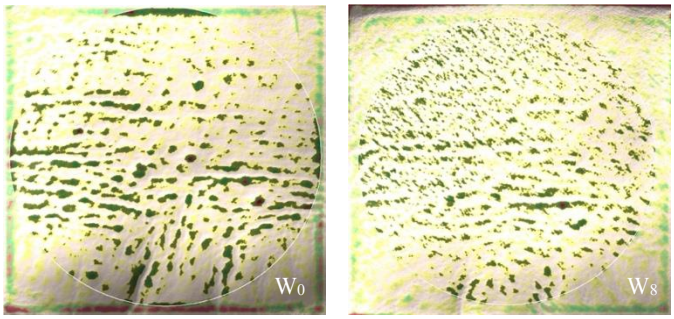

Figure 4 Showed elevations on the forehead of the volunteer
W_0 = Before using the product W_8 = After using nanoemulsion products 8 weeks

2.4 Hydration, TEWL and Elasticity

Product efficacy test in 10 volunteers by measuring the Stratum corneum depth (0.1 - 1 mm) using the Dermalab Combo on the volunteers' forehead (before & after using the product for 4 weeks and after using the product for 8 weeks) to compare the effectiveness of the skin after using the product, it was found that after using the product, the hydration was at 379 ± 0.85 uS, TEWL was at 2.1 ± 0.62 g/m^2/h and the skin was more elastic. When assessed, the total value between skin tightening and recovery (VE) increased to 11.4 ± 0.42 MPa and Young's elasticity modulus (E) increased to 5.9 ± 0.05 MPa as shown in Table 5. Therefore, when using the product for 4 weeks, the skin was hydrated and more elastic. In addition, the skin had less transepidermal water loss. After using the product for 8 weeks, the skin is hydrated and more elastic. In addition, the skin had significantly less transepidermal water loss as shown in Figure 6. When comparing moisture and TEWL, it was found that when using the nanoemulsion for 8 weeks, the skin was more hydrated and the transepidermal water loss value reduced as shown in Figure 5. It was consistent with the previous research studied on skin pathology. The results revealed that hydration was inversely proportional to the TEWL[10] value in some groups, for example: people with scaly dermatoses had low skin hydration and high TEWL. As a result, the skin of this group would be dry because the stratum corneum lost its ability to retain moisture effectively[11]. According to previous research, Honey suckle essential oils can enter the body through the skin in terms of good skin permeability and relatively high contents[12]. According to previous research, Honey suckle essential oil can improve skin moisture content, maintain skin health and skin moisturizing natural raw materials.[13] In addition, Previous research has shown that the honey suckle essential oil was effective in external treatment for wounds. The mechanism of action was postulated to involve angiogenesis, collagen deposition, granulation tissue formation, epithelization, and wound contraction at the proliferative stage, and these actions are attributed to the synergistic effects of the strong antibacterial and anti-inflammatory effects of the active compounds in the extract such as chlorogenic acid.[14]

Table 5 Showed the hydration, TEWL and Elasticity value of the skin on the forehead. (n=10)

Factor	Hydration value (x100 uS)	TEWL value (g/m^2/h)	Elasticity value	
			VE (MPa)	E (MPa)
W_0	2.37 ± 0.24	4.7 ± 0.23	8.3 ± 0.04	3.5 ± 0.12
W_4	3.13 ± 0.43	3.2 ± 0.92	9.6 ± 0.23	4.8 ± 0.32
W_8	3.79 ± 0.85	2.1 ± 0.62	11.4 ± 0.42	5.9 ± 0.05

Note: W_0 = Before using the product, W_4 = After using nanoemulsion products 4 weeks.
W_8 = After using nanoemulsion products 8 weeks.
VE = ViscoElasticty (The total value between skin tightness and regeneration.)
E = Young's elasticity modulus (The height of the surface pulled up in the set vacuum pressure.)
Mpa = mega Pascal, uS = Micro siemens, g/m^2/h = Evaporation of water in the skin per hour.

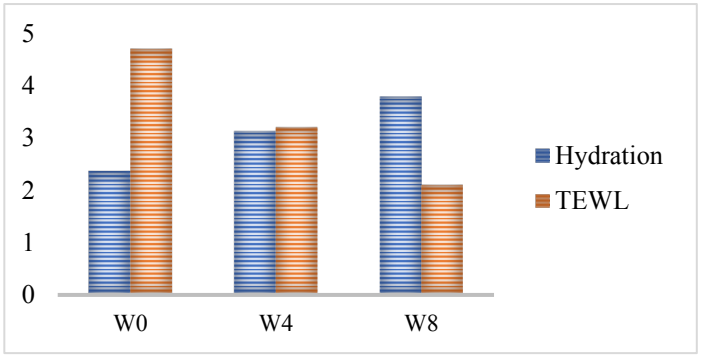

Figure 5 Showed comparison of TEWL and hydration of the skin on the forehead
W_0 = Before using the product
W_4 = After using nanoemulsion products 4 weeks.
W_8 = After using nanoemulsion products 8 weeks.

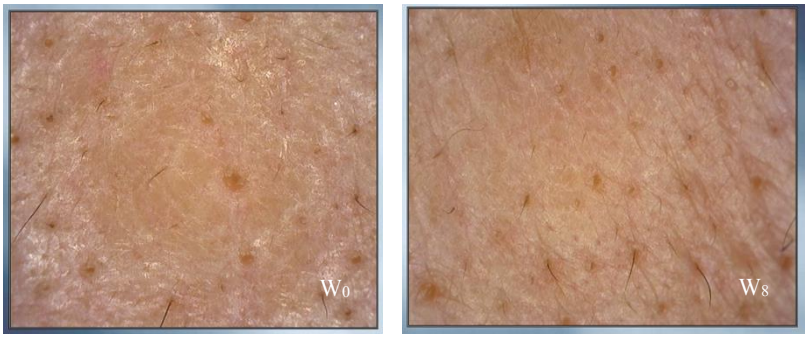

Figure 6 Showed hydration of the skin on the forehead in volunteer with Digital Microscope Premier (Dino-Lite),50x W_0 = Before using the product W_8 = After using nanoemulsion products 8 weeks.

The research tested for acute toxicity in mice using 5,000 mg/kg honeysuckle extract by mouth once, it was found that it did not cause rat death, the behavior of mice and internal organs did not cause any changes, and the subacute toxicity test in mice using 1,000 mg/kg honeysuckle extract by mouth for a period of 14 days showed no toxicity, hematological values and clinical chemical values showed no indication of toxicity. According to histological examination, no changes were found[15].

Conclusion:

In this research, a nanoemulsion containing honeysuckle essential oil to Tween 80 at a ratio (1:2) was prepared by magnetic stirrer. It was stirred for 15 min, then the particle size was reduced by an ultrasonic reducer for 30 min. The appearance emulsion was opaque white with a size of 71.1 ± 0.42 nm and a zeta potential of 31.35 ± 2.56 $mV^2$to test the efficacy of the nanoemulsion on 10 volunteers using the nanoemulsion product on the forehead for 8 weeks. Then, the researchers measured the stratum corneum depth (0.1 - 1 mm) before 4 weeks and 8 weeks and found that wrinkles reduced with the indentation index at 9.621 ± 0.11. The deepest groove reduced at 0.098 ± 0.19 mm. reduced at 8.54 ± 0.41 mm^3. Roughness reduced at 9.676 ± 0.24. Moreover, hydration increased at 379 ± 0.85 uS. TEWL reduced at 2.1 ± 0.62 $g/m^2/h$. The elasticity was increased significantly. When assessed, the total value between skin

tightening and recovery (VE) increased to 11.4 ± 0.42 MPa and Young's elasticity modulus (E) increased to 5.9 ± 0.05 MPa. When comparing moisture and TEWL, it was found that when using the nanoemulsion for 8 weeks, the skin was more hydrated and the TEWL reduced. It was consistent with the previous research studied on skin pathology[4]. The results revealed that hydration was inversely proportional to the TEWL value in some groups, for example: people with scaly dermatoses had low skin hydration and high TEWL. As a result, the skin of this group would be dry because the stratum corneum lost its ability to retain moisture effectively

Acknowledgements:

The researcher would like to appreciate the Department of Health and Beauty Science, the Faculty of Science and Technology for providing the research facility.

References:

1. Zhou H, Yue Y, Liu G, Li Y, Zhang J, Gong Q, Yan Z, Duan M. Nanoscale Res Lett. 2010;5:224–30.
2. Keawbankrud W, Meenongwa A. PACCON. 2022;728–733.
3. Zhang B, Yang RY, Liu CZ. Sep. Purif. Technol 2008;62:480–483.
4. Shang X, Pan H, Li M, Miao X, Ding H. J Ethnopharmacol. 2011;138:1–21.
5. Won, J.-H., & Woo, C.-H. J. Korean Med. Rehabil. 2020;30:47–61.
6. Tian J, Che H, Ha D, Wei Y, Zheng S. Carbohydr Polym. 2012;90:1642–7.
7. Chen WC, Liou SS, Tzeng TF, Lee SL, Liu IM. BMC Complement Altern Med. 2012;12:226.
8. Fan Z, Li L, Bai X, Zhang H, Liu Q, Zhang H, et al. Food Sci Nutr. 2019;7:1786–94.
9. Jeong YT, Jeong SC, Hwang JS, Kim JH. Chem Biol Interact. 2015;238:33–9.
10. Nuttapon P. Master Thesis. M.S. Dermatology. 2006;2–86.
11. Berardesca E, Maibach HI. Dermatosen 1990;38:50–64.
12. Zhang, K., Sun, W., Fahr, A., Zeng, X., Ge, L., Chen, M., Yang, L., Wu, S., Fei, J., & Zhou, B. New J. Chem. 2019;43:12538–12547.
13. Han, S., Lee, S., & Ha, H. MDPI Processes. 2021;9: 321.
14. Chen, W.-C., Liou, S.-S., Tzeng, T.-F., Lee, S.-L., & Liu, I.-M. BMC Complement Altern. Med. 2012;12.
15. Thanabhorn S, Jaijoy K, Thamaree S, Ingkaninan K, Panthong A. J Ethnopharmacol. 2006;107:370–3

EXPERIMENTAL HEAT TREATING OF YELLOW JADEITE JADE FROM MYANMAR

Chanthaphon Tan,[1] Kanyarat Kwansirikul,[1,*] Phisit Limtrakun,[1]
[1]Department of Geological Sciences, Faculty of Science, Chiang Mai University, Chiang Mai, Thailand 50200
*e-mail: kanyarat.k@cmu.ac.th

Abstract:
Jadeite has been one of the popular gemstones in the gems and jewelry market because of its distinct toughness and various colors. In this study, twenty yellow jadeite beads from Myanmar were experimentally heat treated to change their color and characterized gemological properties using gemological standard methods, and some advanced techniques. Specific gravities of the samples were in the range of 3.31 to 3.33. The refractive index tested by spot reading method was in the range of 1.64-1.67. They were inert under short-wave and long-wave UV radiation. The samples were heated at a maximum temperature of 400, 450, 500, and 550°C in oxidizing conditions and soaking time for 1 hour at each temperature. The result of the heating experiments revealed that the optimum temperature to change from yellow to red color without transparency decreasing was between 450°C and 500°C. Chemical composition analysis using WD-XRF showed major elements of Na, Al, and Si while trace elements comprised Fe and Ca. The mineral compositions of the studied samples analyzed by XRD before and after heat treatment consisted mainly of jadeite, hematite, and goethite. The hematite content was likely to increase after heat treatment when the sample's color changed from yellow to red. FTIR absorption spectra showed the characteristic peaks in the range of 3200-3600 cm^{-1} which related to the mineral compositions of natural jadeite. The UV-Visible-NIR absorption spectra exhibited a broad absorption between 400 - 490 nm due to Fe^{3+} ion. After heating, the yellow samples changed to red or reddish brown, and the absorption between 400 - 490 nm was intensified.

Introduction:

The gemstone that is commonly called jade is two separated and distinct materials: jadeite and nephrite. These materials have more simulants than most other gems[1]. Modern gemologists use the word "jade" as a generic term for both nephrite and jadeite. These gems have been linked throughout history. The term jade has also been applied to several gems and ornamental materials that resemble jade, and even some manmade equivalents resembling jadeite and nephrite. Both jadeite and nephrite are actually metamorphic rocks made up of tiny interlocking mineral crystals. These interlocking crystals make both gems exceptionally tough. Jadeite shows a wide range of attractive colors such as shades of green, yellow, reddish orange, white, gray, black, brown, and lavender. The coloration is often streaked or mottled, giving jadeite gemstones an interesting visual texture that carvers can use to create imaginative and intriguing effects. Nephrite is also accepted as jade in the international gem and jewelry industry. It ranges from translucent to opaque and can be light to dark green, yellow, brown, black, gray, or white. Its colors tend to be more muted than jadeites, and they're often mottled or streaked.

Nephrite jade which consists of minerals in the amphibole group has a chemical composition of calcium magnesium silicate ($Ca_2(Mg,Fe)_5Si_8O_{22}(OH)$) and it crystalizes in a monoclinic crystalline system. Typical crystal textures of nephrite are finely felted fibrous. Jadeite, which is more expensive than nephrite jade, contains minerals in the pyroxene group. Its chemical composition is sodium aluminum silicate ($NaAlSi_2O_6$) and it also crystalizes in a

monoclinic crystalline system similar to nephrite jade. The jadeite often shows fine-*grained* with inter-locking texture[2]. Fine-quality jadeite with colorful and near-transparent pieces, especially jadeite from Myanmar, has the highest market value. Although green jadeite is more popular than other colors, some colors of jadeite are rarer such as red and purple or lavender jade. In the gems market nowadays, color-enhanced jadeites are often available to increase jadeite's value. Filling and dyeing methods have been used for decades to modify jadeite's color, but these methods can damage the texture of jadeite and decrease its value[3].

Heat treatment without adding other chemical materials is one of the enhancement methods that can also change jadeite's color. In other gemstones, heat treatment to change the gem's colors is accepted in the market because the changing colors are permanent and become desirable colors. For jadeite jade, color improvement by heat treatment has rarely been reported, especially changing to red jadeite. Therefore, this study aims to experimentally heat yellow jadeite from Myanmar under oxidizing conditions to observe the change of color after heating. The study also characterizes the gemological properties of the studied samples.

Methodology:

Twenty bead-cut yellow jadeite jade from Myanmar with a diameter of each bead of approximately 10 mm, ranging from 2.483 to 7.660 ct. were studied. The samples were cut into half and kept one half for comparison of color changes before and after heat treatment. Another part was heated under oxidizing conditions and analyzed for the gemological properties, chemical compositions, and spectroscopic features. The analytical gemological techniques included specific gravity, refractive index, fluorescence, and internal features using standard gemological instruments. Nine samples were selected for chemical composition analysis by Philips Magix PRO PW 2400 X-ray fluorescent spectrometer (XRF) spectrometer (wavelength dispersive system). The obtained chemical data were measured from single crystal samples. Ultraviolet-visible-near infrared (UV-Vis-NIR) absorption spectra for all twenty samples were recorded throughout of 250 - 800 nm before and after heat treatment using a Hitachi U4001 spectrophotometer, with a slit width of 2 mm and a scan speed of 300 nm/min. The Ultraviolet-Visible-Near infrared absorption spectra can give information related to electron transitions of trace elements or other structural defects. Infrared spectra were collected in the 500 - 3500 cm^{-1} range using a Bruker Tensor 27 Fourier Transform Infrared (FTIR) Spectrophotometer. X-ray diffraction (XRD) pattern was also recorded using an AXS D8 Advance X-ray Diffractometer manufactured by Bruker for mineral composition analysis. Heat treating experiments were carried out with a SANTE electric furnace, under oxidizing conditions at 400, 450, 500, and 550 °C soaked for 1 hour at each temperature. The furnace was slowly cooled down to room temperature before samples removing. All experiments and analysis methods were done at the Department of Geological Sciences, Faculty of Science, Chiang Mai University, Chiang Mai, Thailand.

Results and Discussion:

The studied twenty jadeite beads from Myanmar were yellow and semi-translucent (Figure 1). The samples were classified into three groups depending on their appearance colors viewed under a daylight fluorescence lamp. They consisted of yellow-brown, yellowish-brown, and light-yellow sample groups. The specific gravity of all samples ranged from 3.30 to 3.34 (average 3.32) and the refractive index investigated by spot reading was 1.66 which was consistent with the jadeite jade[4]. The samples were inert under short-wave and long-wave

ultraviolet radiation. For internal features observed under a gemological microscope, uneven color distribution and fractures or healed fractures were found in every sample (Figure 2). Some samples showed yellowish-brown stains along healed fractures. However, the studied samples exhibited poor transparency, clear internal features were difficult to see.

Nine samples for chemical analysis were selected from the three color groups. The chemical data of the studied samples were summarized in Table 1. The samples revealed major elements of Na_2O (14.334 - 17.094 wt%), Al_2O_3 (20.102 - 23.216 wt%), and SiO_2 (59.615 - 63.181 wt%). Minor and trace elements detected were composed of CaO (0.01 - 1.247 wt%) and total Fe_2O_3 (0.01 - 0.0892 wt%). The obtained chemical compositions corresponded to the general chemical formula of jadeite; $NaAl_2SiO_4$. Ferric iron (Fe^{3+}) which was the coloring element could affect the intensity or lightness of the pure yellow color of the yellow jadeite jade. The brownish-yellow samples contained greater amounts of total iron than the samples in the yellow-brown group and light-yellow group, respectively[5].

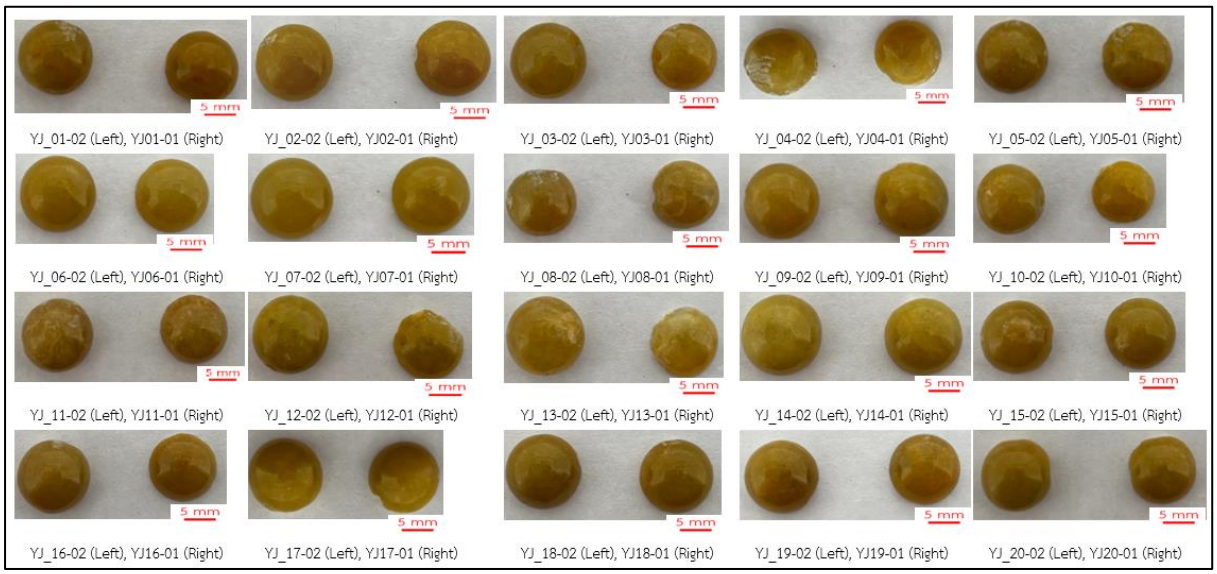

Figure 1. Twenty yellow jadeite jade from Myanmar cutting into two parts for each sample.

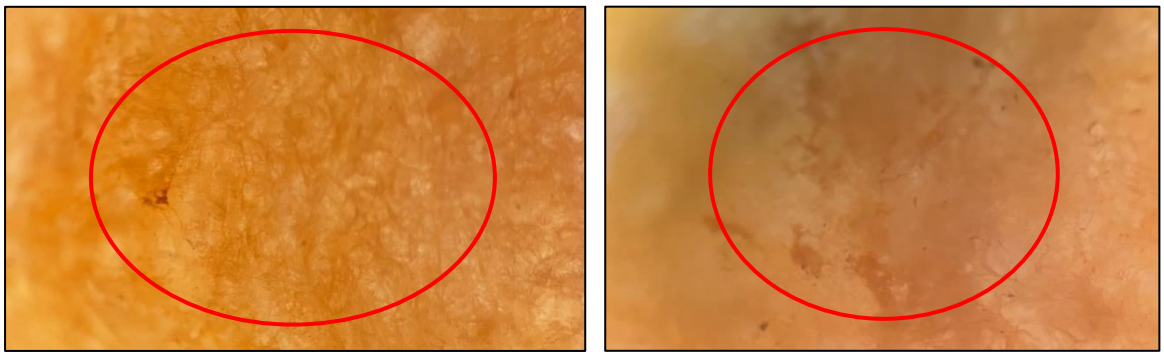

Figure 2. Representative of internal features found in the yellow jadeite jade samples showing uneven color distribution and fractures or healed fractures (red circle in both figures).

The 20 yellow jadeite samples were heated under oxidizing conditions at 400, 450, 500, and 550 °C with soaking time for 1 hour at each maximum temperature. Change of the colors of the samples were compared before and after heat treatment (Table 2). The heating experiment showed that most samples of the three color groups changed their yellow color to three main colors including dark brown, brown, and red after heating at 400°C. After heating at 450 °C and higher temperatures, the samples showed brown discoloration and some samples turned into reddish-brown to red. The samples which exhibited red color after heating at 400 °C remained unchanged. After heat treatment, all samples were still inert under long-wave and short-wave ultraviolet radiation. There was no change in the specific gravity and refractive index significantly. Fractures and healed fractures in the heated stones were more developed and resulted in a decrease in the sample transparency (Figure 3).

Table 1. Average chemical compositions of the studied yellow jadeite jade from Myanmar determined by WD-XRF.

Chemical composition (wt.%)	Yellow-Brown	yellowish-Brown	Light Yellow
Na_2O	15.873	15.771	14.714
Al_2O_3	22.661	21.302	21.652
SiO_2	60.281	61.870	63.181
Fe_2O_3	0.490	0.687	0.453
CaO	0.698	0.372	<<

Noted: << = below detection limit

Table 2. Representative of color changing of yellow jadeite jade samples from Myanmar before and after heat treatment at different temperatures.

Initial color	Unheated	400 °C	450 °C	500 °C	550 °C
Yellow-Brown					
yellowish-Brown					
Light yellow					

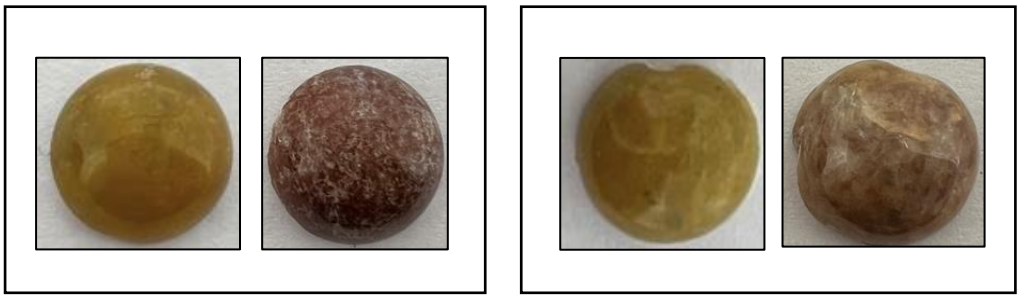

Figure 3. Comparison between the representative of yellow jadeite samples before (yellow samples) and after heat treating (red to reddish brown samples) showing plenty of fractures after heating and resulting in transparency decreasing.

The result from the X-ray diffractometer before heat treatment revealed that the studied samples consisted mainly of jadeite, hematite, and goethite. Although, jadeite, hematite, and goethite were still found in the heated samples after heating, hematite content was likely to increase after heat treatment (Figure 4). This probably implied that higher hematite content could cause the red color in the jadeite samples. The result from this study was consistent with the result of the study by previous work indicating that high goethite content was found in the yellowish-brown area of jadeite while in the red area, the amount of hematite is higher[6]. This was the result of a transformation of goethite into hematite after heat treatment as the following equation[7]: $Fe(OH)O \rightarrow Fe_2O_3 + H_2O$.

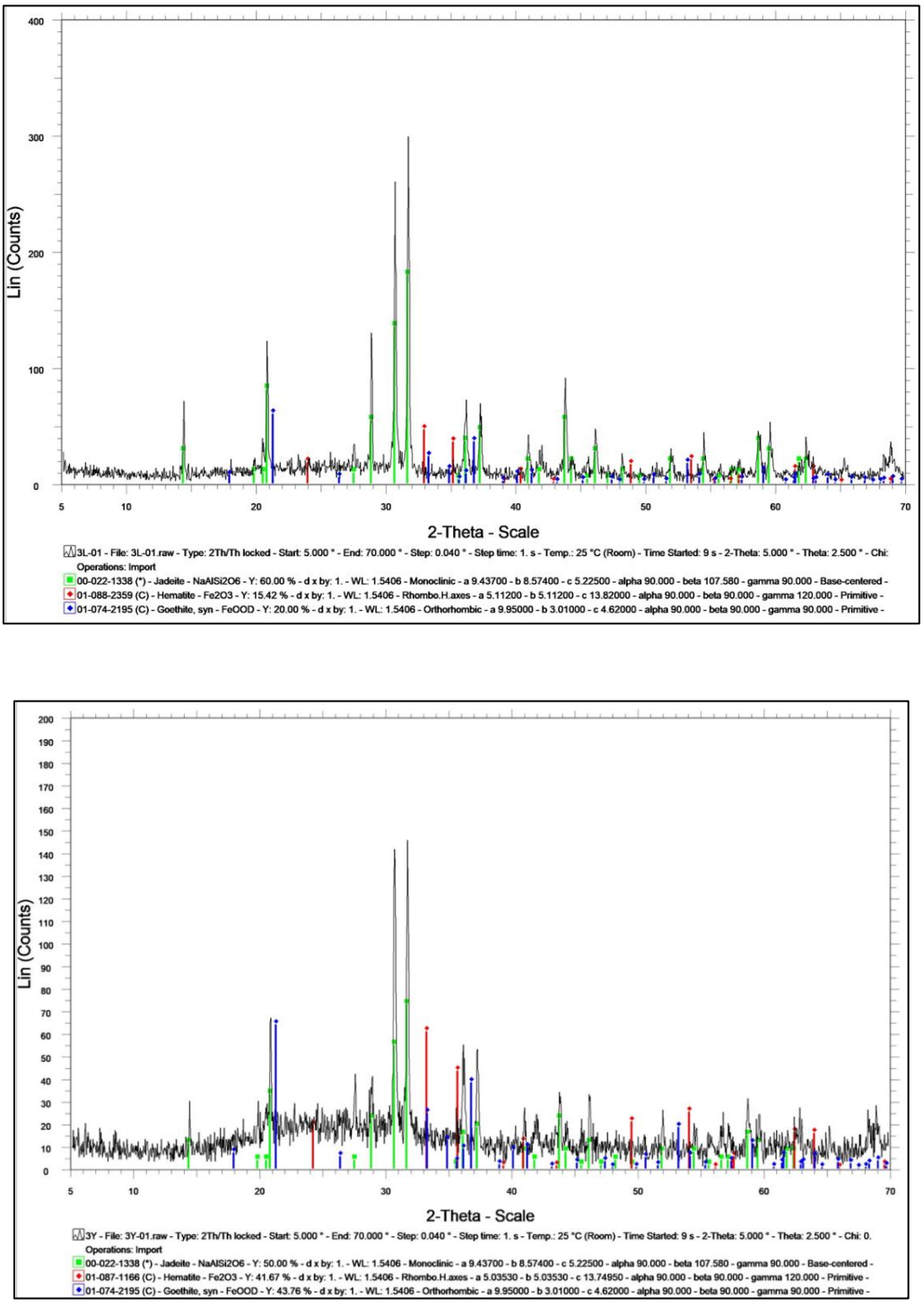

Figure 4. X-ray diffractometer before heat treatment (top) and hematite content (red line) was likely to increase after heat treatment (bottom).

The UV-Vis-NIR absorption spectra of the twenty unheated yellow jadeite samples showed a broad absorption between 410 - 490 nm[8] due to Fe^{3+} ions[9-10]. After heating under oxidizing conditions, the yellow color of the samples changed to red and the absorption band between 410 - 490 nm was intensified (Figure 5). This was consistent with the obtained absorption band which examined the cause of yellow color and hematite content in jadeite in the previous work[9-10].

FTIR absorption spectra of the twenty unheated yellow jadeite samples were dominated by the following features: the low absorption peaks in the range of 2800-3000 cm^{-1} due to some waxing substances used in the polishing process, and the absorption peaks between 3200-3600 cm^{-1} related to the mineral compositions of natural jadeite[7,11] (Figure 6).

Conclusion:

The studied yellow jadeite samples from Myanmar indicated that they were natural jadeite jade (A-type jade). Chemical composition data showed Na_2O, Al_2O_3 and SiO_2 as major elements, and CaO and total Fe_2O_3 as minor and trace elements. X-Ray Diffraction patterns confirmed the presence of goethite and hematite in the jadeite samples. The amount of goethite which probably caused yellow colors in the samples decreased while hematite contents which caused red color in jadeite increased after heat treatment. This mineral transformation after heating of the studied samples which were affected by Fe^{3+} resulted in the change of color from yellow to red. From this heating experiment, the optimum temperature to change yellow to red colors was 450-500 °C with minimal impact on the clarity of the samples. Heating at 550 °C could turn yellow to more red or reddish brown colors but it also made the samples nearly opaque with plenty of fractures.

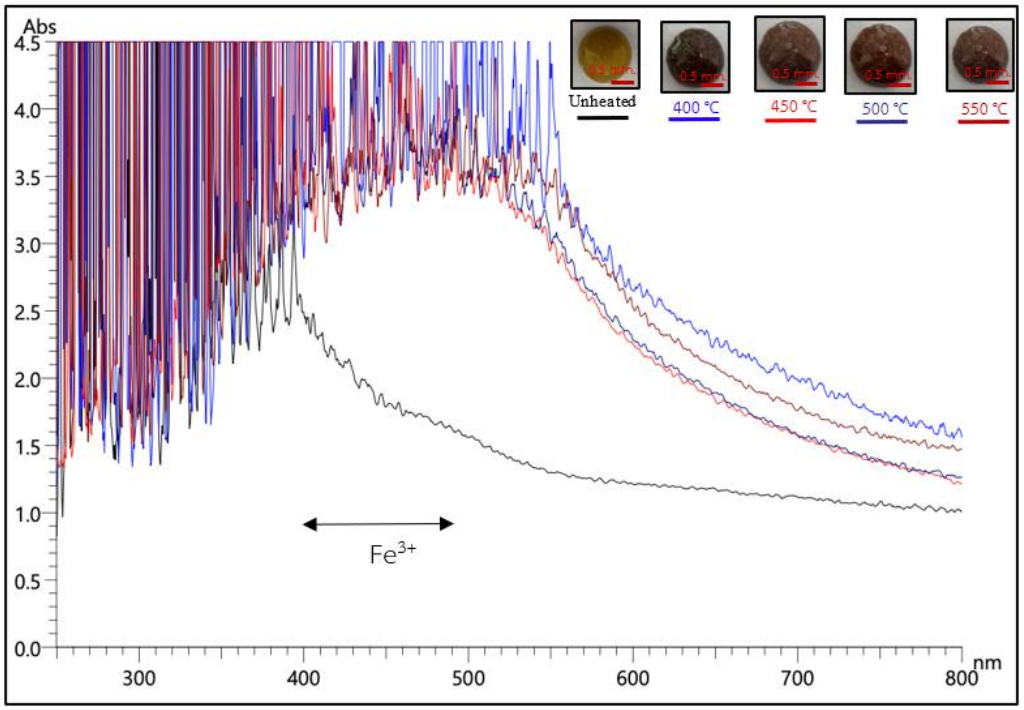

Figure 5. The UV-Vis-NIR absorption spectra of yellow jadeite samples from Myanmar before and after heat treatment under oxidizing conditions at different temperatures.

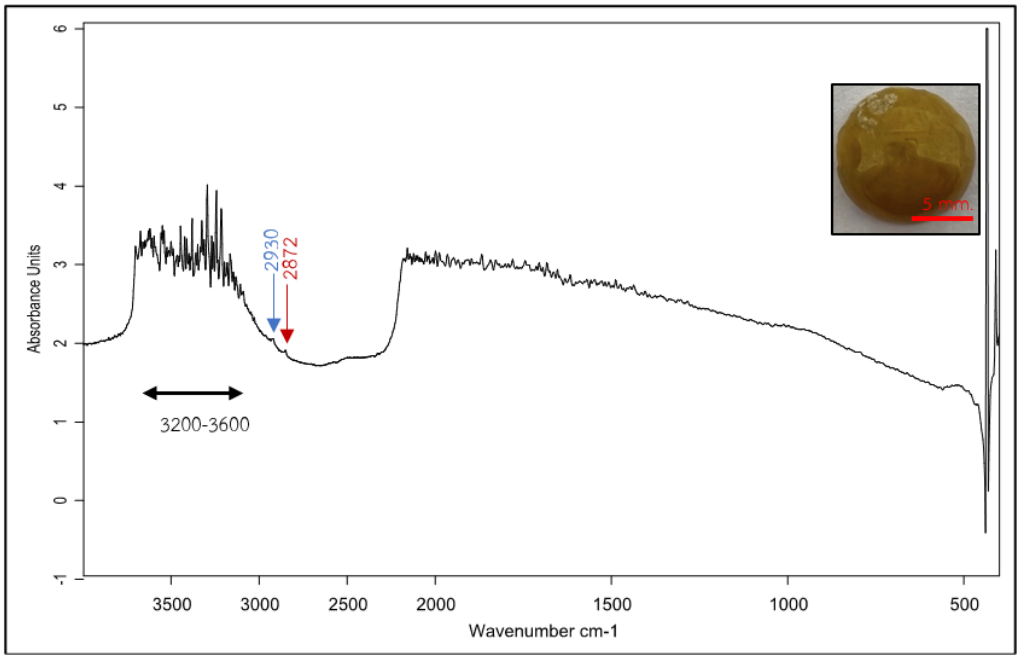

Figure 6. The FTIR absorption spectra of yellow jadeite samples from Myanmar before heat treatment.

Acknowledgements:
The authors would like to thank the 50th Geological Anniversary Chiang Mai University and Faculty of Science, Chiang Mai University for providing financial support for this research. Thanks are extended to Mr. Siwakon Chimnakphant, Dr. Boontarika Srithai, Ms. Opor Saidum, and staffs at the Department of Geological Sciences, Faculty of Science, Chiang Mai University for providing the facilities.

References:

1. Fritsch E, Wu STT, Moses T, M SF, Moon M. Gems Gemol. 1992;28(3):176-187
2. An M, Ye D, Xing Q, Zu E. **Key Eng. Mater**. 2013;544:178-182.
3. Avello LL, Zerpa CP, Ramos JAC, Delvasto P. Rev. Fac. Ing. 2017;26(45):33-45.
4. Wang Y, Nie S, Liu F, Shen A. Gems Gemol. 2016;52(4):436.
5. Pan X, Guo Y, Liu Z, Zhang Z, Shi Y. Earth Sci Res J. 2019;23(4):371-378.
6. Hobbs JM. Gems Gemol.1982;18(1):4.
7. Tan TL, NG LL, Lim LC. Cosmos. 2013;9(1):47-56.
8. Taran MN, Dyar MD, Matsyuk SS. Am Min. 2007;92(5-6):753-760.
9. Lui Z, Guo Y. Crystals. 2022;12(241):1-13.
10. Yuan X, Qi L, Du G, Chen X. J. Gems Gemol. 2003;5(4):11–16.
11. Cao SH, Qi LJ, Guo QH, Zhong ZQ, Qiu Zl, Li Zg. Spectrosc. Spectr. Anal. 2008;24(4):847-851.

MINERALOGY AND GEOCHEMISTRY OF CENOZOIC BASALTS ALONG NATIONAL HIGHWAY NO. 225, WICHIAN BURI DISTRICT, PHETCHABUN PROVINCE

Vimoltip Singtuen,* Piyakorn Preedeesanith

Department of Geotechnology, Faculty of Technology, Khon Kaen University, Khon Kaen, Thailand

*e-mail: vimoltipst@gmail.com

Abstract:

Phetchabun Basin is located in the lower northern part of Thailand and presents many interesting geological features, including Cenozoic columnar basalt, national geopark, petroleum, and other geological resources. Along national highway number 225 area, the outcrop appeared by new road cut. A distinctive point of the outcrop is the large porphyritic texture of basalt. This work aims to identify rock names and magma series as well as classify phenocrysts of basaltic rocks. The methodology comprises petrography, geochemistry analyzed by Handheld ED-XRF, and mineralogy of phenocrysts studied by SEM-EDS. Petrography classifies the rocks as porphyritic olivine tholeiite basalt, consisting of plagioclase (andesine), olivine, and clinopyroxene with a small amount of orthopyroxene opaque minerals. According to the geochemistry of phenocrysts, the plagioclases are classified as andesine-bytownite (An_{33-70}), and olivine is hyalosiderite (Fo_{57}). Major oxides and trace elements classify magma series as sub-alkali, including tholeiite and calc-alkali. So, the results show that these basaltic andesites were generated from transitional tholeiitic magma and erupted in continental rifting process of the Phetchabun Basin.

Introduction:

The collision of the Indian and Eurasian plates results in a separate displacement of the South China Ocean, and the buoyancy of the Hainan magma bulb caused the eruption of volcanic rocks in the late Cenozoic Era in Southeast Asia as well as the gulf of Thailand extension [1-5]. Therefore, it is assumed that such events also influenced volcanic rock eruptions in Thailand, which are controlled by complex tectonic processes [6]. Cenozoic basalts of Thailand erupted into small bulbs scattered in Chiang Rai, Lampang, Phrae, Lopburi, Phetchabun, Kanchanaburi, Surin, Ubon Ratchathani, Chanthaburi, Prachinburi, Trat Provinces, and the southern edge of the Korat Plateau, including Nakhon Ratchasima, Buriram, and Sisaket [2,7-13]. These basalts erupted as sheet flows, eruptions, conical hills, and bottlenecks (cones and plugs). Geological and metallurgical data of these basalt rocks are found to be alkaline basalt with some xenoliths[1,2,13] which has significance in the gemstone industry and tectonic evolution of Thailand during quaternary.

Mostly in Wichian Buri are shown basaltic, andesite, and basalt, they are generated in predominating in Magnesium Oxide and also have transitional composition between tholeiite calc-alkali series[14] and the age of basalt from Wichian Buri is 9.24 Ma[13]. The basaltic geosite of Wichian Buri is a part of the touristic destination (i.e., waterfall, column) of the Phetchabun Geopark, national geoparks symbolized the land of palaeo-sea and subduction of two microplates[15]. This geopark is located in Phetchabun province and has numerous geoheritage resources[16], especially basaltic columnar (i.e., waterfall[17], column), the most interesting volcanic geoheritages in the area.

This study's main points are studied mafic rocks in the new road cut outcrop for classifying the rock and mineral composition and identifying the magma series related to the

tectonic setting of eruption. However, research gaps are the analysis instrument and a lack of isotope techniques, which can be used for the age of eruption and source of magma.

Geologic Setting:

The study area is constituted by rock units from Permian to Quaternary shown in Figure 1. The Permian can be divided into four formations as Tak Fa, Pha Nok Khao, Hua Na Kham, and the Nam Duk formations[18]. The Quaternary is a colluvial deposit: sand, silt, and fine-grained gravel[18]. Igneous rock in the area is divided into two groups Permian to Triassic and Tertiary. The Permian to Triassic includes rhyolite, granite, and andesite porphyry. The Tertiary includes rhyolite mainly lava flow and basalt with phenocryst and megacrysts of olivine, pyroxene, and spinel.

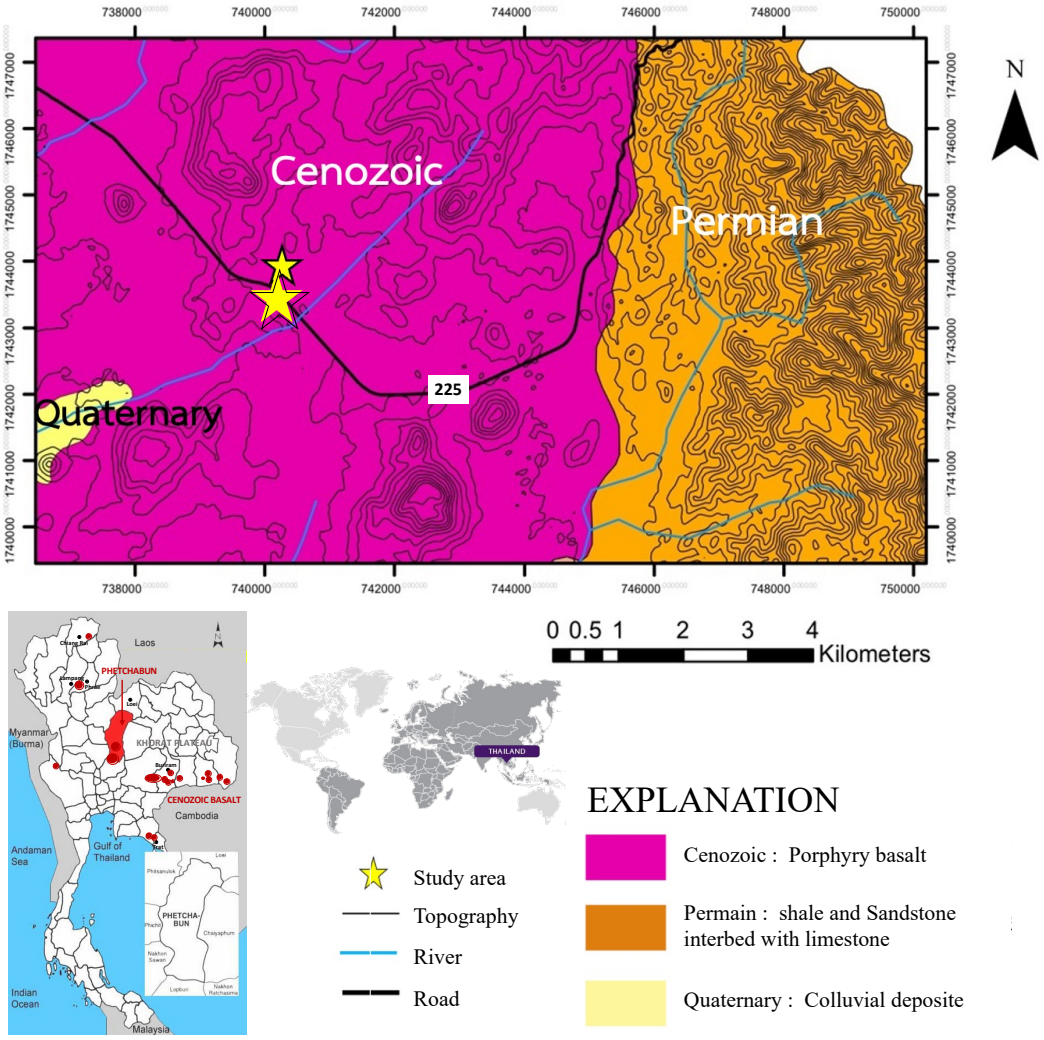

Figure 1. Geologic map of the studied area in Wichian Buri District, Phetchabun Province (modified from the geologic map of the department of mineral resources of Thailand, 2007).

Methodology:

This work studies Cenozoic mafic rocks along national highway number 225 in Phetchabun Province, Thailand. Field observation focuses on the distribution of mafic rocks, outcrop characterization, field investigation analysis, lithological characterization, and sample collection for the petrographic analysis and photomicrograph analysis by ZEN core Imaging Software, linking ZEISS imaging and microscope solutions at the Department of Geotechnology, Khon Kaen University.

The geochemistry of four selected samples (BS2-1, BS4-1, BS5-1, BS7-1) was studied by Olympus Vanta handheld XRF analyzers and analyzed their major and trace elements at the Department of Geotechnology, Khon Kaen University. The least-altered specimens with a flat face and without megacrysts and humidity were selected for analysis by Handheld ED-XRF about 3-5 times for each sample. Mg, Al, Si, P, S, Cl, K, Ca, Ti, V, Cr, Mn, Fe, Co, Ni, Cu, Zn, W, As, Pb, Bi, Zr, Mo, Ag, Cd, Sn, and Sb elements were customized on request in the 2 Beam Mining mode optimized for SDD-based systems to enhance SPEED and LOD for light elements. This mode is suitable for measuring percentage level analyte concentrations, ppm levels up to virtually 100% by weight, but cannot detect the elements with below 12 atomic numbers. The instrument was set up in a 4-watt X-ray tube with application-optimized anode material (RhW) 8–50 kV. Seven Certified Reference Materials (CRMs) NB-01, NB02, NB-03, and NB-04 by the New Brunswick Geological Survey Branch and TILL-2, TILL-3, and TILL4 by the Canadian Certified Reference Material Project were run to test the accuracy of the analysis as internal standards.

ongoing till geochemistry program Furthermore, the mineral geochemistry of phenocrysts used five polished samples (BS1-1, BS3-1, BS8-1) analyzed by Scanning Electron Microscope and Energy Dispersive X-ray Spectrometer (SEM-EDS) at the Faculty of Science, Khon Kaen University. Small cubic-like samples for SEM are mounted on gold stubs (12 mm or 25 mm diameter) using conductive sticky pads, and preparation may take only hours to a few days before analysis.

Field Observation:

The studied area is located along national highway number 225 at Wichian Buri District of Phetchabun Province, at coordinates approximately 14°38’26.51” N and 104°29’34.55” E. This area presents mafic igneous rocks that erupted cut through and were placed on top of Permian sedimentary rocks of Hua Na Kham Group. Outcrop exhibits as road-cut and in situ float rocks caused by road construction that covered approximately 2 km^2 with includes road building at that time leads to inconvenient to collect samples. This outcrop appeared with a new road cut and present joint and fracture as columnar based on Figure 2. The studied rock shows an aphanitic texture with mafic megacrysts. The weathered surface colors are brown and yellowish-brown or white-pale gray with plagioclase lath-shaped, altered equant olivine, black prismatic pyroxene, and (black) irregular-shaped of opaque minerals.

Figure 2. Outcrops of mafic igneous rocks along national highway number 225 at Wichian Buri District of Phetchabun Province.

Petrography and Mineralogy of Phenocrysts:

Twelve samples were collected from the studied use for petrographic analysis and classified as olivine basalt with olivine and plagioclase phenocrysts as shown in Figure 3.

The studied rock presents a porphyritic texture and the groundmass presents a trachytic texture that can be used to assume these rocks were formed from lava flow. Phenocrysts in rock samples found as plagioclase, olivine, and clinopyroxene formed cumulocrysts. The groundmass phase was mainly composed of plagioclase, olivine, clinopyroxene, orthopyroxene, and opaque minerals. An experimental study by petrological analysis divided the mafic igneous rocks along national highway no. 225 into 3 groups: (1) slightly altered phenocryst–phenocryst altered less than 37%, (2) moderately altered phenocryst–phenocryst altered 37-47%, and (3) highly altered phenocryst–phenocryst altered more than 47%. The criterion to divide rock samples is the alteration rate of phenocrysts by polarized light microscope by using sericite (altered from plagioclase), bowlingite-iddingsite (altered from olivine), and chlorite (altered from clinopyroxene).

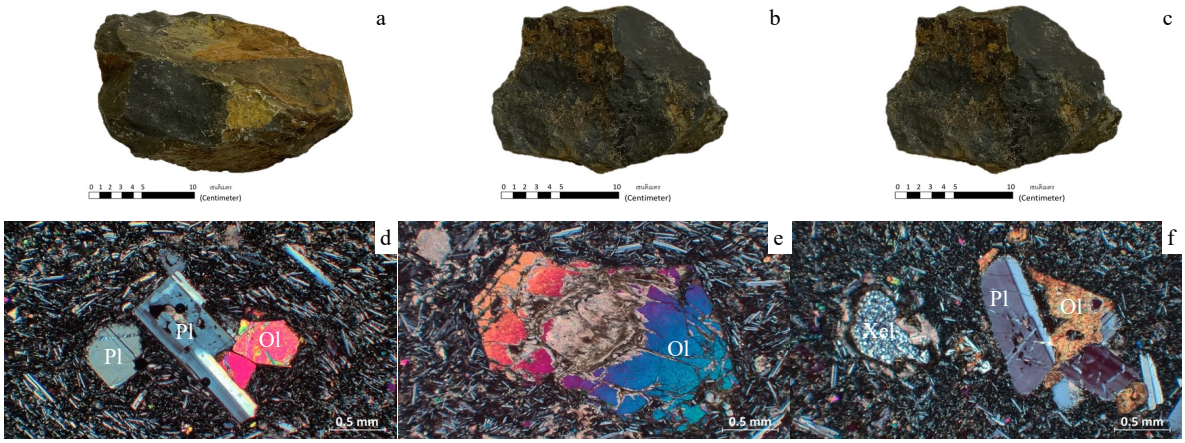

Figure 3. Hand specimens (a) unaltered basalt, (b) slightly altered basalt, and (c) moderately altered basalt. Photomicrographs of studied rocks in crossed polarized light (d) plagioclase-olivine cumulocrysts, (e) altered olivine, and (f) plagioclase-clinopyroxene cumulocrysts and xenolith. Pl: plagioclase, Ol: olivine, and Xel: xenolith.

Plagioclase subhedral-euhedral crystals present tabular shaped with approximately 2 to 0.25 mm. across. Their extinction angles are approximately 14.5-25 degrees, which can be classified as oligoclase-andesine series (An_{16-41}) and exhibits exsolution lamellae between andesine and bytownite according to SEM-EDS data. In addition, mafic minerals contain equant olivine and prismatic clinopyroxene, showing subhedral-euhedral crystals 0.10 to 0.25 mm. across.

Moreover, these basalts contain calcite amygdaloidal crystals, and quartz-rich xenolith size range from 0.5 to 1.5 mm. across. The xenolith may have been derived from the local sediments. The basalt contains a randomly oriented network of plagioclase grains with relatively slightly altered olivine crystals. However, some of the olivine grains may actually be fragments of the xenolith, which can be classified as xenocrysts similar to spinel megacrysts. A number of the olivine is fractured but not strongly altered (-to serpentine and talc), and fracturing is more pronounced towards the edge of the xenolith.

Some basaltic samples tend to be kindly weathered and to have their secondary openings filled by calcite and quartz (in vesicles/pores/fractures), which present secondary textures i.e., vesicular and amygdaloidal textures presented in Figure 3.

The SEM-EDS analysis in Table 1 presents the Mg and Fe ratio (Mg/Mg+Fe) that can be used to classify olivine as hyalosiderite (57Mg#, Fo_{57}). In addition, the ratio between Na and Ca (Ca/Na+Ca) of plagioclase classified them as andesine to bytownite (33-70 Ca#, An_{33-70}) that agreeable with euhedral prismatic and qualitative analysis in Figure 4.

Table 1. Mineral geochemistry of phenocrysts analyzed by SEM-ED

Sample		Elements							
		Mg	O	Na	Al	Si	K	Ca	Fe
BS1-1	wt%	-	06.68	01.73	07.55	17.57	0.78	06.81	02.26
	at%	-	17.53	03.16	11.75	26.28	0.84	07.14	01.70
BS3-1	wt%	-	07.29	01.73	08.26	16.20	00.70	05.69	01.68
	at%	-	19.17	03.26	13.24	24.95	00.78	06.14	01.30
BS8-1	wt%	11.37	07.48	11.37	01.17	10.96	01.49	00.30	08.42
	at%	20.87	20.86	20.87	01.94	17.41	01.66	00.28	06.73

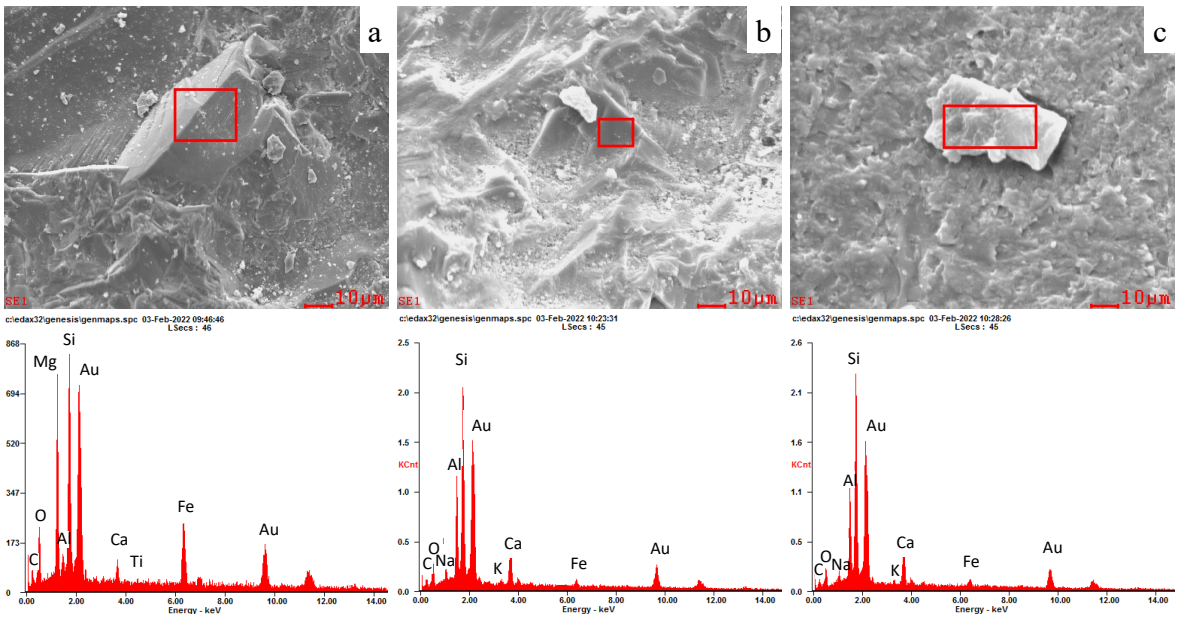

Figure 4. SEM images and EDS analysis of representative phenocrysts (a) orthorhombic olivine, (b) crystal face of plagioclase, and (c) prismatic plagioclase.

Whole-Rock Geochemistry:

Based on petrographic data, least-altered, least-phenocryst, and least-calcite replacement samples were selected for geochemical analysis including major oxides and trace elements that are shown in Table 2. The other major oxides of basalt along national highway number 225 Wichian Buri district, Phetchabun province include SiO_2 52.70-52.99 wt.%, TiO_2 1.52-1.63 wt.%, Al_2O_3, 20.20-20.37 wt.%, FeOt, 8.79–8.98 wt.%, MgO 4.48-5.63 wt.%, CaO 9.88-10.40 wt.%, K_2O, 0.45-0.63 wt.%, MnO 0.13-0.19, and P_2O_5, 0.54-0.62 wt%.

However, Na_2O cannot be detected by Handheld ED-XRF and LOI (loss on ignition) cannot be analyzed, so, the analysis results will be slightly inaccurate from fact. According to the previous works[7,13-14], Wichian Buri basalts present Na_2O between 1 wt.% to 5 wt.%, which presents a wide range because Na is a very lightweight element.

Based on K_2O and SiO_2 diagram[18], classified the studied rocks as basaltic andesite from the calc-alkali magma series (Figure 5a). Meanwhile, the ratio Nb/Y (0.226-0.367) and high Zr/Ti (0.019-0.021) classified these rocks as tholeiite tholeiitic andesite according to the classification of the Fe+Ti vs. Al and Mg ternary diagram[19] as shown in Figure 5b.

Table 2. Whole-rocks analysis of representative basalt by Handheld ED-XRF

Major oxides (wt%)	BS2-1	BS4-1	BS5-1	BS7-1	Elements (ppm)	BS2-1	BS4-1	BS5-1	BS7-1
SiO_2	52.70	52.72	52.99	52.96	Fe	66859	63413	66962	65216
TiO_2	1.52	1.56	1.63	1.56	Al	110492	102428	110502	107425
Al_2O_3	20.25	20.21	20.20	20.37	Ti	9681	9343	9384	9302
FeO_t	8.82	8.79	8.98	8.88	P	3100	3019	3238	2985
MgO	5.37	5.63	4.92	4.48	Sr	1542	1350	1122	1117
CaO	10.04	9.88	9.89	10.40	Mn	1109	1079	1340	1456
K_2O	0.52	0.45	0.63	0.58	Zr	183	186	194	187
MnO	0.17	0.13	0.15	0.19	V	151	212	161	203
P_2O_5	0.62	0.54	0.62	0.59	Cr	120	121	96	70
					Nb	10	7	10	11
					Y	29	31	32	30
					Rb	0	7	9	10
					Nb	10	7	10	11

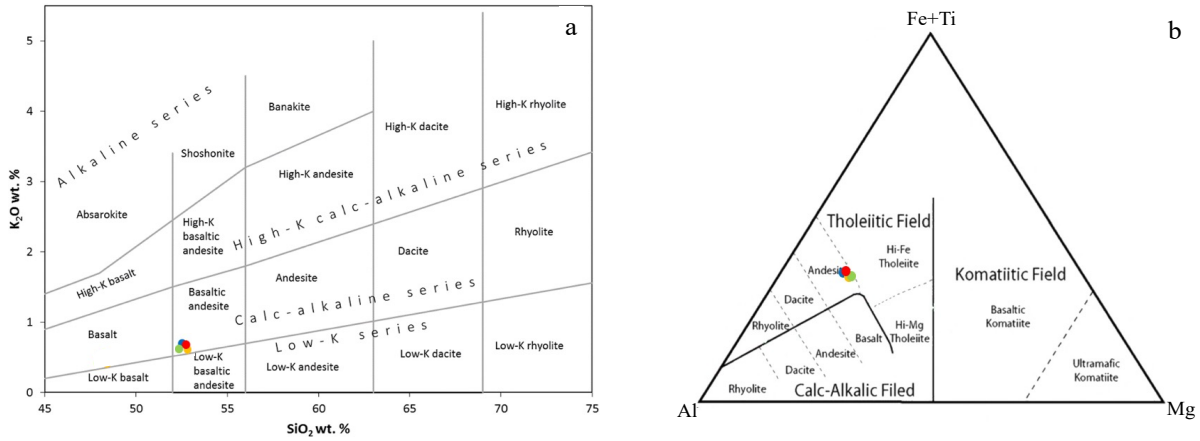

Figure 5. Geochemical classification of studied rocks (a) K_2O and SiO_2 diagram[18] and (b) Fe+Ti vs. Al and Mg diagram[19].

Additionally, the origin magma series by total tholeiite analysis plotted of FeOt/MgO and SiO_2[20] as shown in Figure 6a, while K_2O and SiO_2 determined the rock sample are calc-alkaline series[18]. Three ternary discrimination diagrams were used to interpret the tectonic eruption of the studied basalts (Figure 6). In addition, Ti–Zr–Sr[21] determined all samples are calc-alkaline basalt (Figure 6b). The trace elements "Nb–Zr–Y diagrams"[22] suggests that all samples are within-plate tholeiite (Figure 6c). Therefore, plotted within-plate tholeiite field supports the previous works[7] about petrochemistry and the origin of basalt breccia from Ban Sap Sawat area, Wichian Buri, Phetchabun (nearby area), and the results indicate that these basalts were generated from tholeiite magma and erupted in the within-plate.

Discussion:

To classify magma series, the K_2O-SiO_2 diagram[18] can indicate the calc-alkali basalt, while trace elements[19] suggest that these rocks are andesite. Whereas the samples are plotted to FeO/MgO versus SiO_2 diagram[20] present in the tholeiite field, which corresponds to the Fe_t+Ti-Al-Mg classification.

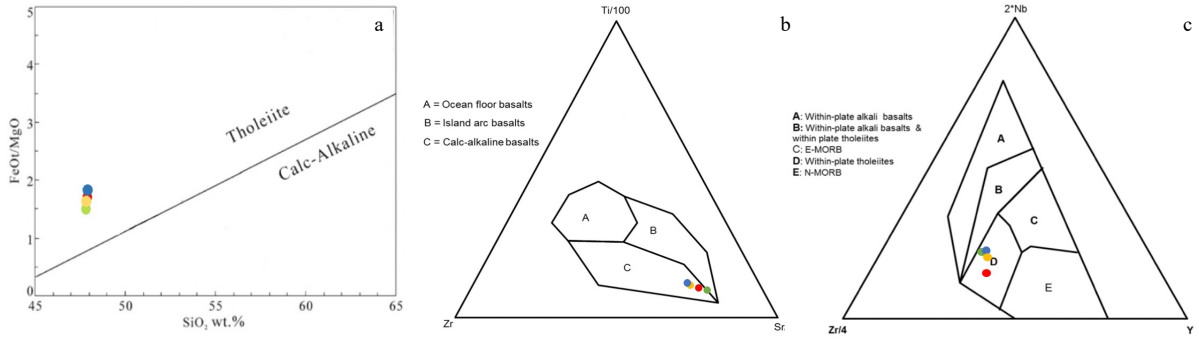

Figure 6. Discrimination diagram of studied rocks (a) FeOt/MgO and SiO_2 diagram[20], (b) Ti–Zr–Sr diagram[21], and (c) Nb–Zr–Y diagram[22].

From the geochemistry analysis, using trace elements and oxides to plot rock samples in tectonic discrimination diagrams. The Nb-Y-Zr diagram[22] classified them were formed by the within plate tholeiite. Moreover, the Ti-Zr-Sr diagram[21] suggests that the studied rocks are calc-alkaline basalts.

Although, the result of immobile elements is more plausible than major oxides that can be mobile, petrography and all geochemical data of this study are consistent in the same way. This study's result shows that Wichian Buri basalts magma has a composition between calc-alkaline to tholeiite (transitional tholeiite magma), which corresponds to previous research origin of basalt breccia, Ban Sap Sawat, Wichian Buri District, Phetchabun Province[7]. Thus, the mafic rocks in the studied area erupted from transitional tholeiite magma within the continental plate during the continental rifting process of the Phetchabun basin (Figure 7) and brought the phenocrysts (plagioclase and olivine), which firstly crystallized beneath the crust to the Earth's surface.

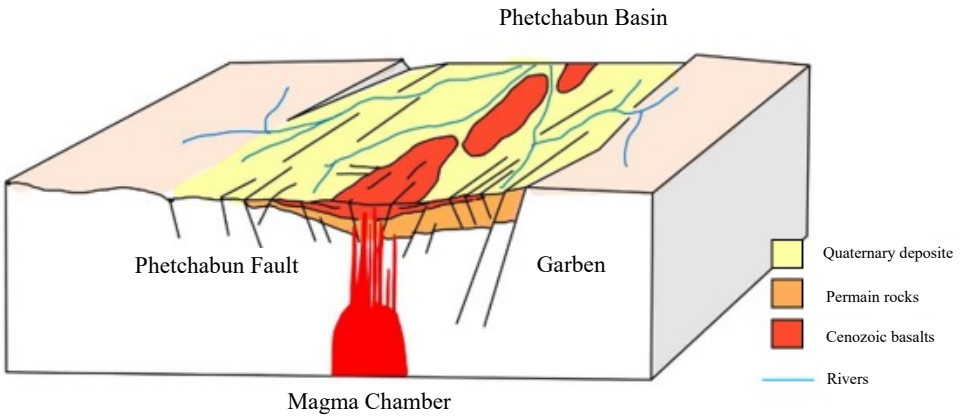

Figure 7. A schematic simple model of the Phetchabun Basin (basin evolution and basin style of the Petchabun Basin modified from previous works[23-24]).

The phenocryst minerals (olivine and plagioclase) intergrowth firstly together in the magma chamber, the ordering of crystallization is olivine, clinopyroxene, and plagioclase respectively following the Bowen's series. Meanwhile, mostly phenocryst was altered by the difference in temperature crystallization and stability when they come up near the surface. After that groundmass including plagioclase, olivine, orthopyroxene, clinopyroxene, and opaque minerals rapidly crystallized on the surface.

However, this study analyzed major and trace elements, which makes us limited discussion on the tectonic setting of volcanic rocks. For further research, we suggest that the analysis of rare earth elements and isotopes should be done to confirm their tectonic setting and magma series.

Conclusion:

The new road cut outcrops along national highway number 225, Wichian Buri, Phetchabun province is covered by Cenozoic Basalts, presenting columnar features and interesting phenocrysts. The studied rocks were classified as olivine basalts, presenting olivine and plagioclase (oligoclase to andesine) phenocrysts with trachytic texture. Olivine phenocrysts are slightly to moderately altered to bowlingite-iddingsite, while plagioclase phenocrysts are slightly altered to sericite. In addition, olivine phenocrysts were classified as hyalosiderite (57$Mg^{\#}$) and plagioclase range andesine to bytownite (33-70 $Ca^{\#}$). Major oxides (K_2O and SiO_2) identified the Wichian Buri mafic rocks as calc-alkaline basaltic andesite and trace elements (Fe-Ti-Al-Mg and Zr/Ti vs. Nb/Y) classified them as tholeiitic andesite. Trace elements classified these mafic rocks were generated from sub alkaline (calc-alkaline and tholeiite) or transitional tholeiite magma series erupted in the continental rifting process similar to previous reports. Moreover, olivine and plagioclase phenocrysts are the first order of crystallization of the rocks, then olivine, opaque mineral, orthopyroxene, clinopyroxene, and plagioclase rapidly together intergrowth as groundmass when the lava flows on the Earth's surface.

Acknowledgements:

The authors would like to thank the Department of Geotechnology, Faculty of Technology, Khon Kaen University for the valuable laboratories and facilities.

References:

1. Barr SM, Macdonald AS. Bull. Geol. Soc. Malays. 1978;10:25–52.
2. Barr SM, Macdonald AS. Geol. Soc. Am. Bull. 1981;92:1069–1142.
3. Morley CK. Tectonophysics. 2002;347:189-215.
4. Morley CK. Earth Sci Rev. 2012;115:37–75.
5. Yan Q, Shi X, Metcalfe I, Liu S, Xu T, Kornkaninan N, Sirichaiseth Th, Yuan L, Zhang Y, Zhang H. Nature. 2018;8(1):1-14.
6. Charusiri P, Daorerk V, Archibald D, Hisada K, Am-paiwan T. J. Geol. Soc. Thailand. 2002;1:1–20.
7. Limtrakun P, Panjasawatwong Y, Khanmanee J. Songklanakarin J. Sci. Technol. 2013;35(4):469-482.
8. Intasopa S, Dunn T. J. Southeast Asian Earth Sci. 1994;9(1/2):167–180.
9. Intasopa S, Dunn T, Lambert RSJ. Can. J. Earth Sci. 1995;32:393–409.
10. Fanka A, Kasiban Ch, Tsunogae T, Tsutsumi Y, Sutthirat Ch. J. Earth Sci. 2021;32(4):1035-1052.
11. Singtuen V, Phajan S. Data Br. 2021;39:107540.
12. Singtuen V, Phajan S, Anumart A, Phajuy B, Srijanta K, Promkotra S. Heliyon. 2021; 7(12):e08619.

13. Yuan L, Yan Q. Int. Geol. Rev. 2022;1-20.
14. Sriwichai M, Rachanark B, Assavapanuvat P, Wattanachareekul P, Makakum C, Watcharamai T, Ardkham P, Chaikam A, Phujareanchaiwon C, Srisunthon P, Leknettip S, Kaewpaluk S, Khamsiri S, Chawchai S. Bull. Earth. Sci. Thai. 2021;10(1): 44–54.
15. Singtuen V, Thitaree J. Geologos. 2022;28(1):39-50.
16. Paungya N, Singtuen V, Won-In K. Geoj. Tour. Geosites. 2020;31:1057–1067.
17. Singtuen V, Phajuy B, Gałka E. Geoj. Tour. Geosites. 2021;37(3):880–887.
18. Peccerillo A, Taylor SR. Contrib. to Mineral. Petrol. 1976. 1976;58:63-81.
19. Winchester JA, Floyd PA. Chem. Geol. 1977; 20:325-343.
20. Miyashiro A. Am. J. Sci. 1974;274:321-355.
21. Pearce JA, Cann JR. Earth Planet. Sci. Lett. 1973;19(2):290-300.
22. Meschede M. Chem. Geol. 1986;56:207-218.
23. Pongwapee S, Morley CK, Won-in K. J. Struct. Geol. 2019; 118, 340–361.
24. Pongwapee S, Won-in K, Morley CK, J. Geol. Soc. London. 2019; 177, 189–210.
25. Jitmahantakul S, Phetheet J, Kanjanapayont P. Front. Earth Sci. 2020; 8:578218.

DECARBOXYLATION OF FATTY ACID USING METAL/IONIC LIQUID CATALYST

Duangkamol Tiarpattaradilok,[1] Duangamol Tungasmita,[2] Tirayut Vilaivan[2,*]
[1] Program of Petrochemistry and Polymer Science, Faculty of Science, Chulalongkorn University, Bangkok, Thailand
[2] Department of Chemistry, Faculty of Science, Chulalongkorn University, Bangkok, Thailand
*e-mail: vtirayut@chula.ac.th

Abstract:

The decline of petroleum resources and concerns about environmental issues caused by excessive energy consumption have motivated the search for alternative energy sources. A potential solution for this problem is biomass, which can be found in plant and animal remains. Fatty acids are a component of biomass that is an attractive choice of renewable energy sources because they can be converted to long-chain hydrocarbons *via* the decarboxylation reaction. However, the process of fatty acid decarboxylation to alkanes is energy-intensive and suffers efficiency and selectivity issues. In this research, we aimed to develop new catalysts that can improve the fatty acid decarboxylation efficiency by using the combination of metal/ionic liquid as catalysts. The palladium-catalyzed thermal decarboxylation of stearic acid to heptadecane was used as a model reaction for this study. In the presence of a Pd catalyst in various forms, the decarboxylation proceeded poorly at 300 °C. Nuclear Magnetic Resonance (NMR) analysis demonstrated that the use of $Pd(OAc)_2$ catalyst alone at 2.86 mol% Pd loading gave only 8.8% conversion of stearic acid. Importantly, the addition of the ionic liquid $[BMIM]PF_6$ substantially improved the conversion to 95.0%. The improvement of conversion by ionic liquid and the formation of heptadecane was further confirmed by gas chromatographic analysis. Consequently, the Pd-ionic liquid combination is a promising new catalyst system for the decarboxylation of fatty acids with high conversion.

Introduction:

Petroleum has been the major energy source and raw material for chemical industries for several decades. However, the finite supply of petroleum makes it an unsustainable resource. Moreover, the production and use of petroleum also contribute to negative environmental impacts such as producing greenhouse gases and other pollution. Thus, modern research trends have paid a lot of attention to the development of alternative energy resources that are more sustainable and environmentally friendly. Biomass is an important class of renewable energy source that can be used in a sustainable fashion as it can be easily renewed. Furthermore, the renewal process involves the entrapment of carbon dioxide, leading to net zero carbon emission. Fatty acids are one of the most important constituents in biomass that is a potential source of renewable energy due to the high hydrocarbon contents that required little processing to get the compounds that are typically found in petroleum. This is a clear advantage over lignocellulosic-type biomass. In the last few decades, fatty acids have been used as starting materials for biodiesel synthesis by transesterification reaction with methanol. However, fatty acid methyl esters still contain too high oxygen content that leads to undesirable properties of the obtained products, such as high viscosity, low thermal stability, together with corrosive characteristics. Moreover, the use of methanol

as a raw material lacks the green aspect because its production caused a huge amount of waste.[1]

An alternative approach is the conversion of fats or fatty acids to long-chain hydrocarbons, which are useful as lubricants, vehicle fuels such as gasoline, diesel, and jet fuels, etc.[2-5] Two important processes for such conversion include hydrodeoxygenation, which gave hydrocarbon products together with water and carbon monoxide, and decarboxylation, which gave the hydrocarbon and carbon dioxide. Hydrogen gas is required for the hydrodeoxygenation reaction, and the formation of water as a byproduct also reduces the efficiency of the reaction.[6-8] Consequently, the decarboxylation process which produced the long-chain hydrocarbon products and carbon dioxide without water formation as the byproduct had attracted much attention in recent years.[3-4,9] Typically, metal catalysts such as nickel, palladium, or copper are usually required for the decarboxylation, where palladium was usually found to give the best activity.[3-4,10] However, the limitation of these catalysts include the requirement of extreme conditions,[11-13] long reaction time,[14-15] and the need for additives such as an acid.[16] It has been reported that ionic liquids can promote several reactions. There were reports on the stabilization and improvement of the activities of several metal catalysts including palladium for Suzuki cross-coupling by ionic liquids.[17] Therefore, in this work, we aim to develop the combined use of palladium and ionic liquids as a novel catalytic system for the decarboxylation of fatty acids[18] based on a hypothesis that the presence of ionic liquid might improve the catalyst efficiency (**Figure 1**).

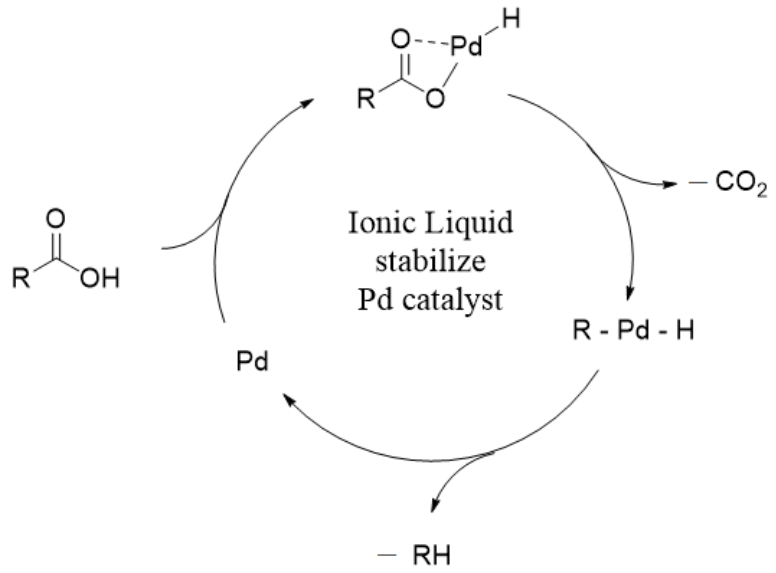

Figure 1. A proposed reaction pathway of decarboxylation of fatty acid using Pd/ionic liquid catalyst

Methodology:

Preparation of ionic liquids

Synthesis of 1-butyl-3-methylimidazolium chloride, [BMIM]Cl[19]

1-Butyl-3-methylimidazolium chloride was prepared by refluxing 1-methylimidazole (3.2 mL, 40 mmol) with 1-chlorobutane (5.4 mL, 52 mmol) in acetonitrile (4 mL) under nitrogen atmosphere at 80 °C for 48 h. The reaction mixture was cooled to room temperature. The resulting product was evaporated using a rotary evaporator, washed with ethyl acetate (5 mL × 3) and ether (5 mL × 3). Then, the prepared ionic liquid was dried under vacuum to give a light yellow liquid (6.2 g, 96% yield): ^{1}H NMR (500 MHz, DMSO-d_6) δ 9.20 (s, 1H), 7.78 (d

J = 1.4 Hz, 1H), 7.71 (d J = 1.1 Hz, 1H), 4.16 (t J = 7.2 Hz, 2H), 3.85 (s, 3H), 1.81 – 1.69 (m, 2H), 1.32 – 1.18 (m, 2H), 0.90 (t J = 7.4 Hz, 3H).; *m/z* (MALDI-TOF) 138.5 $[M\text{-}Cl]^+$.

Synthesis of 1-butyl-3-methylimidazolium hexafluorophosphate, $[BMIM]PF_6$[19]

A mixture of [BMIM]Cl (5.0 g, 28.7 mmol) and potassium hexafluorophosphate (5.3 g, 28.7 mmol) in water (40 mL) was stirred at room temperature (25 °C) for 12 h. The mixture was extracted with dichloromethane (5 mL). The dichloromethane extract was washed with water (5 mL × 3), dried over anhydrous $MgSO_4$, and concentrated using a rotary evaporator. The product was obtained as a yellow oil (7.7 g, 95% yield): ^{1}H NMR (500 MHz, DMSO-d_6) δ 9.07 (s, 1H), 7.73 (d J = 1.7 Hz, 1H), 7.66 (d J = 1.6 Hz, 1H), 4.15 (t J = 7.2 Hz, 2H), 3.84 (s, 3H), 1.82 – 1.70 (m, 2H), 1.33 – 1.19 (m, 2H), 0.90 (t J = 7.4 Hz, 3H); *m/z* (MALDI-TOF) 138.6 $[M\text{-}Cl]^+$.

Synthesis of 1-methylimidazolium-3-propylsulfonate, $MIMC_3SO_3$[20]

1-Methylimidazolium-3-propylsulfonate was synthesized using 1-methylimidazole (1.18 mL, 15 mmol) and 1,4-propane sultone (1.32 mL, 15 mmol). The mixture was sonicated at room temperature for 1 hour. Then, the mixture was wash with diethyl ether (5 mL × 3), dried under vacuum. The product was obtained as colorless liquid. (2.8 g, 91% yield): ^{1}H NMR (500 MHz, DMSO-d_6) δ 9.08 (s, 1H), 7.77 (t J = 1.8 Hz, 1H), 7.68 (t J = 1.7 Hz, 1H), 4.29 (t J = 6.9 Hz, 2H), 3.84 (s, 3H), 2.40 (t J = 7.2 Hz, 2H), 2.12 – 2.03 (m, 2H).

Synthesis of 1,1'-(ethane-1,2-diyl)bis(3-methyl-1*H*-imidazol-3-ium) dibromide, $[MIMC_2MIM]Br$

1-Methylimidazole (1.16 mL, 14.7 mmol) and 1,2-dibromoethane (0.60 mL, 7 mmol) were dissolved in acetonitrile (1.5 mL). The mixture was heated at 80 °C for 12 h under nitrogen atmosphere. After completing the reaction, the mixture was evaporated to dryness and washed with ethyl acetate (5 mL × 3) and ether (5 mL × 3). The mixture evaporated the solvent by using rotary evaporator to obtain a colorless liquid (2.52 g, 102% yield): ^{1}H NMR (500 MHz, DMSO-d_6) δ 9.03 (s, 2H), 7.72 (t J = 1.7 Hz, 2H), 7.60 (d J = 1.4 Hz, 2H), 4.67 (s, 4H), 3.84 (s, 6H).

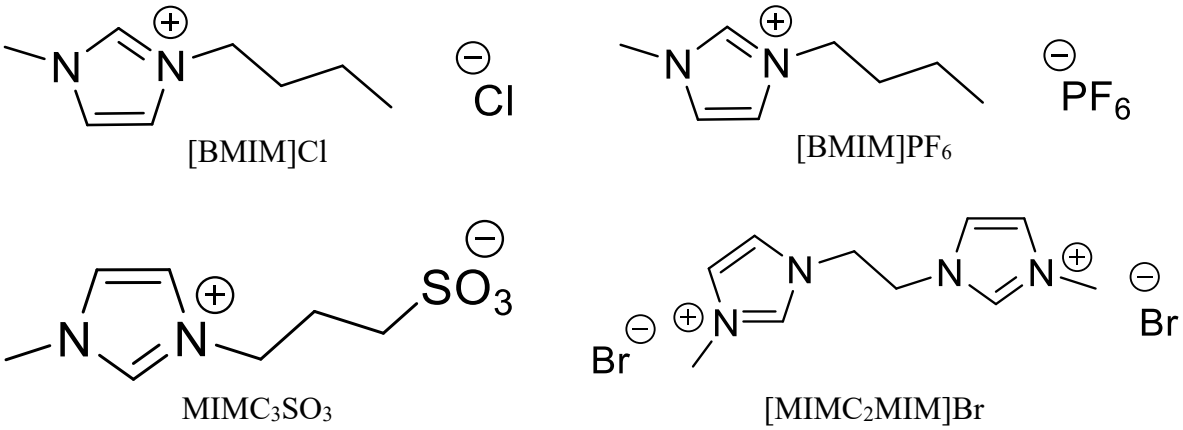

Figure 2. Structure of ionic liquids used in this study

Preparation of Pd-MCM-41[21]

Cetyltrimethylammonium bromide (CTAB) (2.4 g) was added to 120 g of deionized water, and then the mixture was stirred until a clear solution was obtained. Next, 25% NH_3 solution (10.24 mL) was added to the prepared CTAB solution with stirring for 5 min. When

the solution became homogenous, 10 mL of tetraethyloxysilane (TEOS) was dropped slowly, followed by stirring overnight at room temperature. The suspension was filtered and washed with deionized water:ethyl acetate (800:200 mL) until a neutral solution was obtained. The filtered precipitate was dried at 60 ºC for 24 h and then calcined at 550 ºC for 5 h to give the MCM-41 as a white powder.

Pd-MCM-41 was prepared by mixing 0.25 g of $Pd(NO_3)_2{\cdot}2H_2O$ and 1 g MCM-41. The mixture was stirred for 2 h at room temperature, dried at 80 ºC overnight, and calcined at 550 ºC for 3 h. The theoretical content of Pd is 9.1% (0.85 mmol/g).

Catalyst testing

Two experiments were conducted to compare the performance of the Pd catalysts for stearic acid decarboxylation in the absence and presence of ionic liquid. The experiments were performed in a sealed stainless-steel reactor under the specified conditions. In a typical reaction set up, 100 mg (0.35 mmol) stearic acid, a Pd catalyst (1% Pd loading by weight or 2.86 mol%) of Pd catalysts, and the ionic liquid ([BMIM]PF_6) (100 mg, 0.35 mmol) (optional) were added to the reactors. The reactor was placed in a pre-heated digital electric melting furnace at 300 ºC. When the optimal reaction time was reached, the reactors were cooled to room temperature and opened carefully. Next, the reactor content was transferred a vial by washing with n-pentane. The solid catalyst was filtered off using a syringe filter, washed with water, and dried under a stream of nitrogen gas.

The screening was performed with various Pd catalysts (10% Pd/C, Pd-MCM-41, $PdCl_2$, and $Pd(OAc)_2$ in the absence and presence of [BMIM]PF_6) and three ionic liquids ([BMIM]Cl, $MIMC_3SO_3$, and [$MIMC_2$MIM]Br) in the presence of $Pd(OAc)_2$.

Analysis of the decarboxylation product

The crude product was analyzed by nuclear magnetic resonance (NMR) spectroscopy on a JEOL JNM-ECZ500R/S1 NMR spectrometer operating at 500 MHz for ^{1}H NMR as will be further discussed in the Results and Discussion section.

For gas chromatographic analysis. The crude product from the decarboxylation reaction (20 mg) was derivatized to convert the stearic acid to methyl stearate by dissolving in a mixture of trimethylsilyldiazomethane (TMSD) (0.6 M in hexanes, 350 µL) and 20% MeOH-acetone (350 µL). The mixture was vortexed and left at room temperature for 20 min, then evaporated under a stream of N_2 gas. The resulting products were analyzed by a gas chromatograph with a flame ionization detector (GC-FID) (Varian CP 3800, equipped with a 29.13 m in length of CP-sil-8 capillary column with 0.25 mm outer diameter and 0.25 µm film thicknesses). The sample was prepared at 15 mg/mL of product with 2.5 mg/mL *n*-decane as internal standard in ethyl acetate (1 mL). The stearic acid (SA) conversion and product selectivity were calculated as follows:

$$\%SA\ Conversion = \frac{Mol\ of\ starting\ SA\ - Mol\ of\ SA\ after\ complete\ reaction}{Mol\ of\ starting\ SA} \times 100$$

Results and Discussion:

The prepared Pd-MCM-41 catalyst was characterized by X-ray diffraction (XRD) technique. **Figure 3.** shows the low angle XRD patterns of MCM-41 and Pd-MCM-41 catalyst. XRD pattern of the MCM-41 exhibits a very intense reflections at $2\theta = 2.3^\circ$ for d_{100} plane and two peaks with low intensity reflections at $2\theta = 3.98^\circ$ and 4.54° for d_{110} and d_{200} planes respectively, which are characteristic of MCM-41. The diffraction pattern of Pd-MCM-41 showed reflections at 2θ values of 2.4°, 4.1° and 4.72° for d_{100}, d_{110}, d_{200}

respectively. The intensity of the diffraction peaks decreased when the palladium was introduced into the pore of the MCM-41.

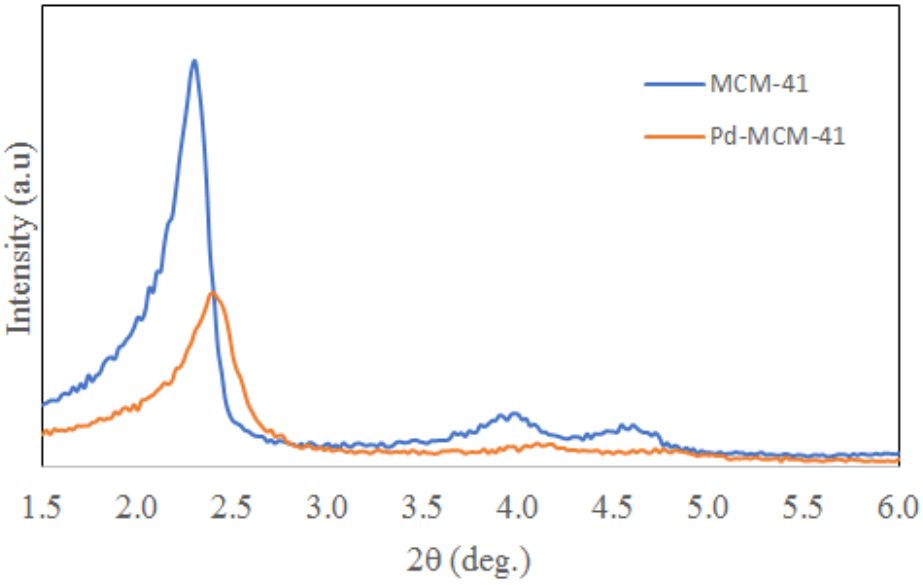

Figure 3. XRD pattern of MCM-41 and Pd-MCM-41

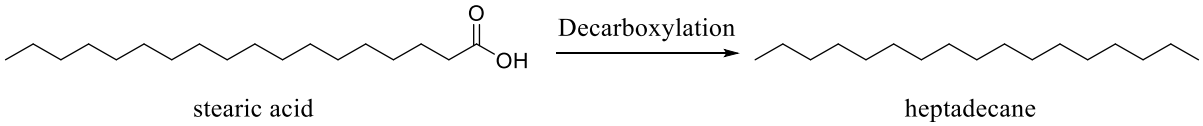

Figure 4. Decarboxylation of stearic acid

Stearic acid (SA) was used as a model to study the decarboxylation of fatty acid by ionic-liquid-modified Pd catalysts. The product from the decarboxylation of stearic acid is heptadecane (C17) (**Figure 4**). In preliminary experiments, ^{1}H NMR spectroscopy was used for a quick evaluation of the decarboxylation reaction by calculating the relative integration of the CH_2COOH signal of stearic acid at 2.33 ppm and the CH_3 signal of heptane and stearic acid at 0.86 ppm. Assuming quantitative conversion of heptadecane to stearic, the percent conversion was calculated using the following equation:

$$Percent\ Conversion = \frac{heptadecane}{heptadecane + SA} = \frac{0.167\ x\ (b - 1.5a)}{0.167\ x\ (b - 1.5a) + 0.5a}$$

Where a and b are referred to as the integrations of proton signals at 2.33 and around 0.86 ppm, which a is the proton signal of CH_2 (2H) that is the closest to the carboxyl functional group of stearic acid, and b is the proton signal of CH_3 from both the decarboxylated product (6H) and substrate (3H) as shown in **Figure 5**. Since the conversion of stearic acid will not give 100% to heptadecane in practice, the conversion based on this calculation should represent a lower limit of conversion. Nevertheless, it should be possible to use as a rough estimation for the decarboxylation efficiency.

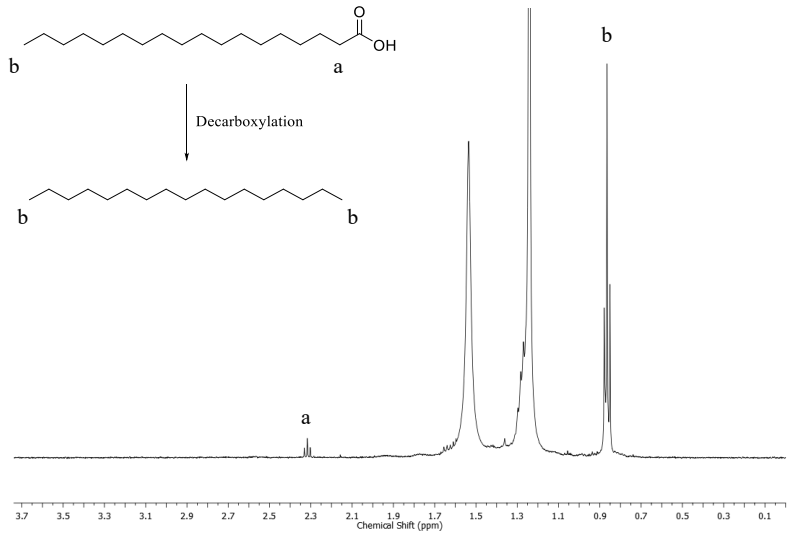

Figure 5. ^{1}H NMR spectrum of decarboxylation of stearic acid using $Pd(OAc)_2$ with $[BMIM]PF_6$ catalyst

For the optimization of catalysts, four Pd catalysts including 10% Pd/C, Pd-MCM-41, $PdCl_2$, and $Pd(OAc)_2$ were selected to examine the effect of the Pd catalyst under the same condition by controlling the Pd in the catalyst to be the same at 2.86 mol%. The reactions were conducted at 300 °C for 2 h in the absence and presence of the ionic liquid $[BMIM]PF_6$ (100 mg) without additional solvents. The percentage conversions based on NMR calculation are shown in **Table 1**. The low conversion values in the presence of the Pd catalysts alone (7 – 22%) were significantly improved in the presence of $[BMIM]PF_6$. The obtained results supported the beneficial role of the ionic liquid in the decarboxylation of stearic acid to heptadecane. The best Pd catalyst was found to be the combination of $Pd(OAc)_2$ and $[BMIM]PF_6$ which gave up to 95% conversion.

Table 1. Stearic acid conversion of decarboxylation reaction by using Pd catalysts

Metal catalyst	% SA conversion	
	without IL	with IL
Pd/C	21.6	90.4
Pd-MCM-41	6.9	89.0
$PdCl_2$	19.9	93.0
$Pd(OAc)_2$	8.8	95.0

Encouraged by the above results, other imidazolium-based ionic liquids were investigated next using $Pd(OAc)_2$ as the Pd catalyst at the same 2.86 mol% Pd loading. As shown in **Table 2**, the percentage conversion of stearic acid based on NMR analysis indicated that the ionic liquid $[BMIM]PF_6$ gave the highest conversion (95%) when combined with $Pd(OAc)_2$. Other ionic liquids gave lower conversion values in the range of 41 – 79%, but these values are still higher than the $Pd(OAc)_2$ catalyst alone (8.8%).

Table 2. Stearic acid conversion of decarboxylation reaction by $Pd(OAc)_2$ and different ionic liquids

Ionic liquid	% SA conversion
[BMIM]Cl	74.5
$MIMC_3SO_3$	40.7
$[MIMC_2MIM]Br$	78.8
$[BMIM]PF_6$	95.0

To confirm the decarboxylation of stearic acid to heptadecane by Pd-ionic liquid catalysts in both qualitative and quantitative senses, samples from model decarboxylation reactions using the $PdCl_2$ catalyst system with or without the ionic liquid $[BMIM]PF_6$ was selected to analyze by GC-FID. The GC chromatograms are shown in **Figure 6**. The decarboxylation of stearic acid in the presence of the Pd catalyst alone gave a poor conversion (32.6% conversion). The conversion was much improved in the presence of the ionic liquid (91.5% conversion). The values are slightly different from the results obtained from ^1H NMR analyses, but they are in good agreement overall. The retention time of the product corresponded to that of standard heptadecane. Moreover, the GC yield of heptadecane was estimated to be 4.9% and 27.5% in the absence and in the presence of $[BMIM]PF_6$ respectively as calculated by the use of the internal standard. This figure is somewhat low considering that no other significant peaks were observed in both ^1H NMR and GC-FID chromatograms. This could be attributed to the partial loss of the volatile heptadecane during the workup process. Nevertheless, the study clearly confirms that the presence of ionic liquid could indeed improve the performance of the Pd-catalyzed fatty acid decarboxylation to alkanes.

Compared with other studies, $PdCl_2$ has been used as a catalyst of decarboxylation of stearic acid. A poor conversion (7.21%) was obtained (reaction conditions: 1 g of stearic acid, 0.2 mmol $PdCl_2$ catalyst, 0.2 wt% acids, 2 MPa of H_2, 180 ^oC, 3 h).[22] Poor conversion was observed with Pd/C (stearic acid, 1MPa N_2 and H_2, 330 ^oC, 5 h, in water)[23] as well as Rh/C gave lower than 10% conversion. The Ru/C gave 60% conversion although the reaction required 5 h. On the contrary, the Pt/C and Ru/C gave relatively high conversion (>90%) of stearic acid but its required long reaction time (330 ^oC, 12.5 h)

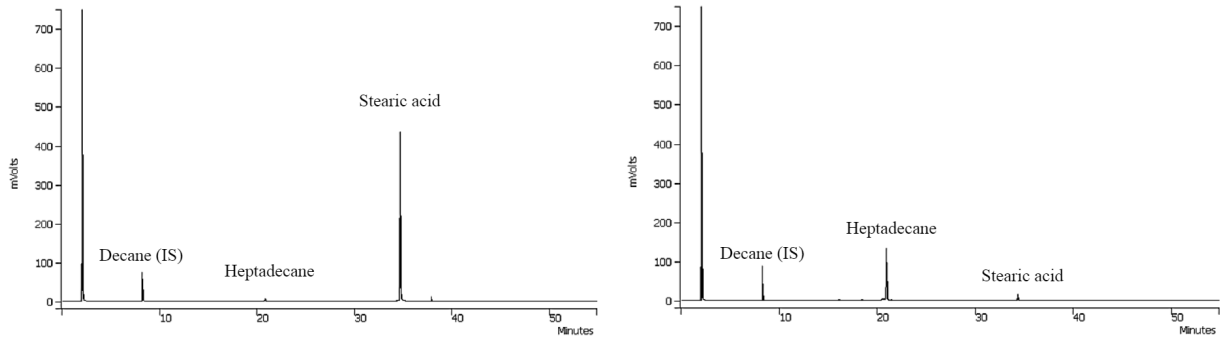

a b

Figure 6. GC-FID chromatogram of decarboxylation of stearic acid using $PdCl_2$ catalyst without ionic liquid (left) and with [BMIM]PF_6 ionic liquid (right)

Conclusion:

In summary, a new catalytic system for the decarboxylation of fatty acids to alkanes was developed by using the combination of Pd and ionic liquid additives. The decarboxylation of stearic acid to heptadecane at 300 ˚C for 2 h as a model reaction showed low conversion in the presence of the Pd catalyst alone. The conversion was greatly improved when the ionic liquid was added. The best catalyst combination was found to be $Pd(OAc)_2$/ [BMIM]PF_6 which gave up to 95% conversion based on ^{1}H NMR analyses. Preliminary analysis by GC-FID confirmed the improved conversion of stearic acid (up to 91.5%) and the formation of the heptadecane, albeit with a somewhat lower yield than expected (up to 27.5%) probably due to partial loss during the isolation. Nevertheless, the positive effect of ionic liquid in improving the catalytic system was clearly demonstrated.

Acknowledgements:

The financial support from the National Science, Research and Innovation Fund (NSRF) via the Program Management Unit for Human Resources & Institutional Development, Research and Innovation (B16F640101) is gratefully acknowledged.

References:

1. Bezergianni S, Dimitriadis A, Sfetsas T, Kalogianni A. Bioresour. Technol. 2010;101:7658–7660.
2. Kubičková I, Snåre M, Eränen K, Mäki-Arvela P, Murzin DY. Catal. Today. 2005;106: 197–200.
3. Snåre M, Kubičková I, Mäki-Arvela P, Eränen K, Murzin DY. Ind. Eng. Chem. Res. 2006;45:5708–5719.
4. Immer JG, Kelly MJ, Lamb HH. Appl. Catal. A. 2010;375:134–139.
5. Roberts WL, Lamb HH, Stikeleather LF, Turner TL. US Pat. US7816570;2010.
6. Gosselink RW, Hollak SA, Chang SW, Haveren J, de Jong KP, Bitter H, van Es DS. ChemSusChem. 2013;6:1576–1594.
7. Alwan BA, Salley SO, Ng KYS. Appl. Catal. A. 2015;498:32–40.
8. Roh HS, Eum IH, Jeong DW, Yi BE, Na JG, Ko CH. Catal. Today. 2011;164:457–460.
9. Na JG, Han JK, Oh YK, Park JH, Jung TS, Han SS, Yoon HC, Chung SH, Kim JN, Ko CH. Catal. Today. 2012;185:313–317.
10. Ford JP, Thapaliya N, Kelly MJ, Roberts WL, Lamb HH. Energy Fuels. 2013;27:7489–7496.
11. Aguiar E, Costa C, Couto M, Azevedo D, Filho J. Catalysts. 2021;11:995
12. Fu J, Lu X, Savage P. Energy Environ. Sci. 2010;3:311–317.
13. Fu J, Shi F, Thompson L, Lu X, Savage P. ACS Catal. 2011;1:227–231.

14. Doll K, Moser B, Knothe G. Int. J. Sustain. Eng. 2021;4:2018–2024.
15. Mao J, Jiang D, Fang Z, Wu X, Ni J, Li X. Catal. Commun. 2017;90:47–50.
16. Konwar L, Oliani B, Samikannu A, Canu P, Mikkola J. Biomass Convers. Biorefin. 2022;12:51–62.
17. Singh R, Sharma M, Mamgain R, Rawat D. J. Braz. Chem. Soc. 2008;19:357–379.
18. Han J, Sun H, Ding Y, Lou H, Zheng X. Green Chem. 2010;12:463–467.
19. Wei G, Yang Z, Chen C. Anal. Chim. Acta. 2003;488:183–192.
20. Liu X, Zhao J, Liu Q, Sun L, Tan Z, Biermann U. J. Chem. Eng. Data. 2010;55:4260–4266.
21. Yan K, Lafleur T, Jarvis C, Wu G. J. Clean. Prod. 2014;72:230–232.
22. Cai X, Zhang Z, Ye Y, Wang D, Li S. Biomass Bioenergy. 2022;156:106328.
23. Zhang J, Huo X, Li Y, Srathmann T. ACS Sustain. Chem. Eng. 2019;7:14400–14410.

Session F:
FOOD SCIENCE AND TECHNOLOGY/ AGRICULTURAL SCIENCE/ (SEA) FOOD INNOVATION/ FOOD SAFETY AND PACKAGING

EFFECT OF MILK ADDITION ON ANTIOXIDANTS AND QUALITY OF DURIAN DRINK DURING COLD STORAGE

Nantachaporn Chaichana[1], Supaart Sirikantaramas[2], Kitipong Assatarakul[1*]
[1]Department of Food Technology, Faculty of Science, Chulalongkorn University, Bangkok 10330, Thailand
[2]Dapartment of Biochemistry, Faculty of Science, Chulalongkorn University, Bangkok 10330, Thailand
*E-mail: Kitipong.A@chula.ac.th

Abstract:

Durian fruit, one of the most popular fruits in Thailand, is an excellent source of various nutrients such as minerals and vitamins and also rich in phenolic compound. In addition, development the new product from durian fruit is challenging to satisfy consumer's lifestyle. Functional beverage's trend is on the rise since consumer's demand includes improvement of overall health and availability in convenient formats. Therefore, the objectives of this research were to study effect of milk addition on stability of antioxidant properties (total phenolic compound, antioxidant activity by DPPH and FRAP assay), color value (L*, a*, b*) and microbial properties (total plate count and yeast and mold count) of durian drink during cold storage at 4°C for 15 days. Samples were pasteurized (90°C, 5 min) before stability experiment. The results showed that total phenolic compound and antioxidant activity of durian drink decreased with the increased storage time. However, addition of milk in sample provided an increase in antioxidant properties of durian drink compared to no milk addition. Furthermore, L*, and b* values tended to decrease while the increasing trend of a* value was found. According to microbial properties during storage, total plate count and yeast and mold count increased approximately 2 log CFU/mL at the end of storage. This study could be used as a fundamental information for the development of functional drink from durian. However, more studies should develop to increase the bioactivity and the shelf life these products.

Introduction:

Fruits are a vital food source that are loaded with healthy vitamins and minerals. Durian is referred to as the "King of the Fruits," and the Monthong durian (*Durian zibethius* Murray), one of the most widely cultivated durian varieties in Thailand, is the top export for sale abroad. As a result, many farmers are expanding their durian plantings and adding processing to raise the value of their harvests. According to reports, durian, which is well-liked in Asia and America, was the most popular fruit product exported in 2021. Due to its sweet flavor and distinctive aroma, durian pulp also has a high nutritional value and is very energizing. Monthong durian has been shown to be a rich source of vitamins, minerals, and various biologically active compounds, such as polyphenols and antioxidants, which protect against free radical damage and fight disease. An earlier investigation revealed that animals fed with Monthong durian showed higher antioxidant activity and lower cholesterol in their blood. (1). Currently, the functional drinks made from fruits has gained a lot of interest due to the increased awareness of benefits of products. Beverages that are made from fruits or contain milk as ingredient products are highly nutritional because fruits and milk are rich sources of bioactive compounds and antioxidant. This study evaluated the storage stability of durian drink (DD) and durian drink with milk (DM) after pasteurization (90°C, 5 min) by comparing bioactive compounds (total phenolic compound), antioxidant activity (by DPPH

and FRAP assay), color values and microbial analysis (total plate count, yeast and mold count) for 15 days at 4°C.

Methodology:

1.Preparation of durian drinks

The ripe freeze-dried Monthong durian pulp (*Durian zibethius* Murray) were obtained from Chanthaburi (Thailand) with size uniformity ground into a powder and sifted through a 50-mesh sieve. Weigh 15 g of durian powder mixed with 85 ml of distilled water (DD, 15% w/w) and 15 g of durian powder mixed with 35 mL of distilled water and 50 mL of milk (DM, 15% w/w) were blended with a blender for 1 min until getting homogenous. The pasteurization was accomplished using a water bath. Durian drink and durian drink with milk was poured into each sterile glass bottle, which were placed in a water bath had been prepared to 90°C for 5 min and chilled to room temperature (25 ± 2 °C) before stored at 4 °C and the results were analyzed every 3 days for 15 days.

2. *Analytical methods*

2.1 *Determination of antioxidant properties*

Total phenolic compounds (TPCs)

The total phenolic compound was measured using the Folin-Ciocalteau method at the absorbance of 765 nm with spectrophotometer (GENE-SYSTEM 20 Visible, Thermo Fisher Scientific, USA). The result was expressed as mg gallic acid equivalent (GAE)/100 mL (3).

Antioxidant activity by DPPH scavenging assay

Antioxidant activity was determined by the DPPH (2,2-diphenyl-1-picryhydrazyl) free radical scavenging method, according to (4). The absorbance was performed at the wavelength of 515 nm with spectrophotometer (GENE-SYSTEM 20 Visible, Thermo Fisher Scientific, USA) by using methanol as a blank. The results were expressed as %inhibition

Antioxidant activity by FRAP assay

FRAP determination, the absorbance of sample was determined at 593 nm with spectrophotometer (GENE-SYSTEM 20 Visible, Thermo Fisher Scientific, USA) by using distilled water as a blank. The result was expressed in mM Trolox/100 mL (2).

2.2 *Color values*

The color characteristics of durian drink and durian drink with milk were analyzed by using a chroma meter (Minolta, Model CR-300 series, Japan) and CIE LAB system (L*, a*, and b*) where L* represents lightness and darkness, a* redness and greenness and b* yellowness and blueness (2).

2.3 *Microbiological analyses*

Total plate count and yeast and mold count were performed. All media were prepared and autoclaved at 121°C for 15 min. After serial dilutions, samples were plated onto plate count ager in duplicate for total plate count, for yeasts and molds using a standard spread plate method in duplicate using potato dextrose agar. The plates were incubated at 37°C for 48 h for the total plate count and 30°C for 48h for yeast and mold count (5).

2.4 *Statistical analysis*

The experiment design was conducted using a completely randomized design (CRD) with analysis of variance (ANOVA) by SPSS software version 28.0.0.0 (SPSS Inc., Chicago, IL, USA) and the average was compared with Turkey's (HSD) multiple comparison test at the 95% of confidence level.

Results and Discussion:

Total phenolic content (TPCs) and Antioxidant activity by 2,2-diphenyl-1-picryhydrazyl (DPPH) and by ferric ion reducing antioxidant power (FRAP) assay of durian drink

The total phenolic content and antioxidant activity were determined using the Folin-Ciocalteau, DPPH and FRAP method, as shown in Table 1 and Figure 1. The total phenolic content of DD during the storage period between Day 0 to Day 15 were in the range 3.08±0.07 and 2.35±0.01 mg GAE/100 mL. Antioxidant activity, DPPH inhibition (%) were in the range 29.05±0.68 and 17.54±0.26, and FRAP were in the range 286.81±1.81 and 180.40±2.27 mM Trolox/100 mL. Futhermore, DM had total phenolic content in the range 3.62±0.46 and 2.46±0.02 mg GAE/100mL. Antioxidant activity, DPPH inhibition (%) were in the range 30.01±0.72 and 20.41±0.62, and FRAP were in the range 307.88±0.34 and 198.03±5.21 mM Trolox/100 mL. When comparing DD and DM, more total phenolic content and antioxidant activity were reported for DM. The result could be due to that fact that casein is the major protein of bovine milk that can inhibit lipoxygenase-catalyzed lipid oxidation, primary structure of casein molecules acts as a scavenger (6) and whey protein have antioxidant activity due to the chelation of transition metals and scavenging of free radical (7,8). In addition, there are also has ß-carotenoids are regarded as preventive antioxidants that act as scavengers of singlet oxygen and peroxyl radicals (9,10).

Table 1. Antioxidant properties (total phenolic compound, antioxidant activity by DPPH and FRAP) of durian drink during storage at 4 °C

Treatment	Storage day	Antioxidant properties		
		TPC (mg GAE/100 mL)	DPPH inhibition (%)	FRAP (mM Trolox equivalent/100 mL)
Durian drink (DD)	0	3.08±0.07[a]	29.05±0.68[a]	286.81±1.81[a]
	3	2.86±0.04[a]	28.10±0.24[a]	278.16±2.27[b]
	6	2.76±0.18[a]	26.24±0.90[a]	256.60±1.68[a]
	9	2.40±0.04[b]	22.91±0.79[a]	202.28±2.38[a]
	12	2.53±0.10[a]	19.78±0.95[a]	196.51±2.61[b]
	15	2.35±0.01[b]	17.54±0.26[b]	180.40±2.27[a]
Durian drink with milk (DM)	0	3.62±0.46[a]	30.01±0.72[a]	307.88±0.34[a]
	3	2.87±0.13[a]	29.79±0.72[a]	284.33±3.29[a]
	6	2.86±0.26[a]	27.98±1.02[a]	273.11±1.92[a]
	9	2.58±0.04[a]	24.22±1.94[a]	217.82±2.38[a]
	12	2.56±0.08[a]	21.85±0.35[a]	203.16±4.99[a]
	15	2.46±0.02[a]	20.41±0.62[a]	198.03±5.21[a]

*Remark: mean ± SD (from 3 replicates)
*Values in the column of each sample with different lowercase ([a,b]) were significantly different (P≤0.05).

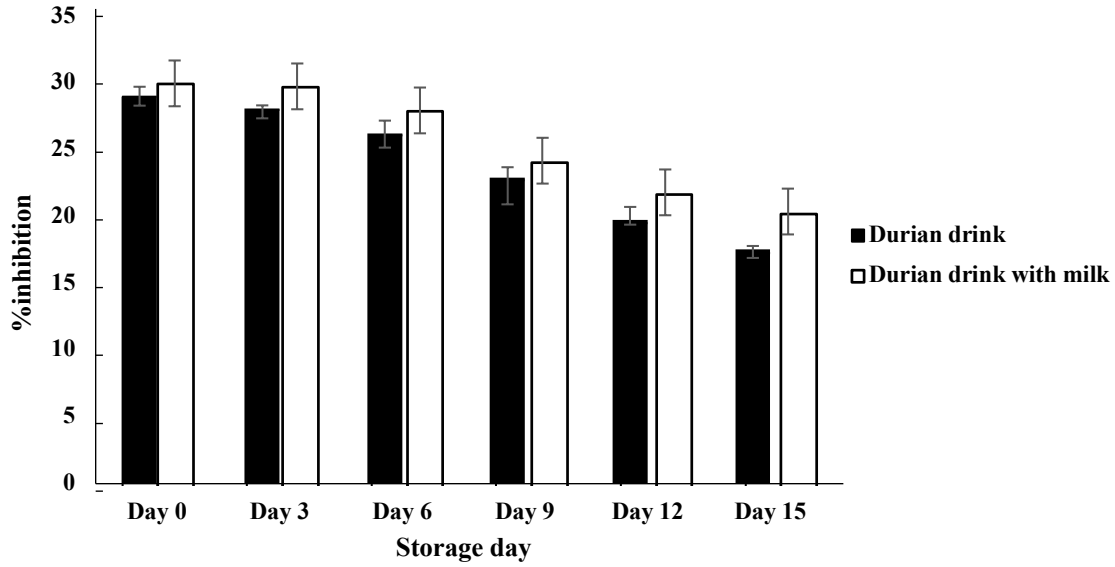

(a)

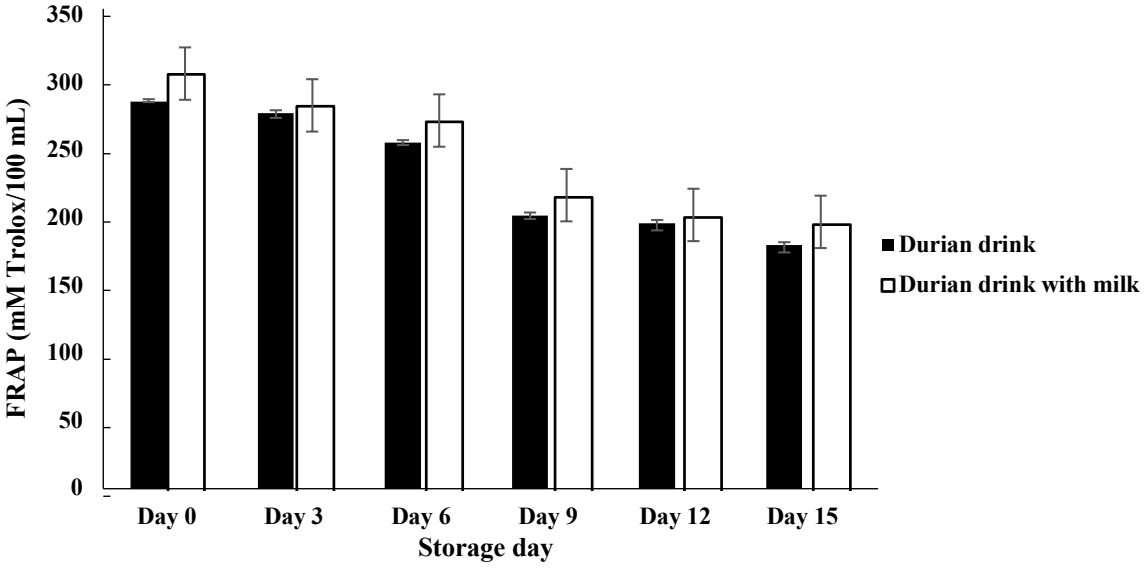

(b)

Figure 1. Varying antioxidant activity by DPPH assay (a), and FRAP assay (b) of durian drink (DD) and durian drink with milk (DM) during the storage period at 4°C.

Color values

The color of drinks is important food characteristic for consumer as an indicator of quality (11). Color values of durian drink and durian drink with milk were significantly different (P>0.05). When comparing the color values (L*, a* and b*) between DD and DM the results found that L* values of both samples were decreased by retention time because of the heat from pasteurization and non-enzymatic browning from Maillard reaction. The reaction between amino acids and reducing sugar in durian and milk darkened the color (12). In addition, a* values of both samples had a slightly increasing trend during storage. However, L*, a* and b* values of DM were higher than DD due to the mixture of milk and durian made the color lighter and brighter. According to color values, DD and DM had light yellow to greenish-yellow color.

Table 2. Color values of durian drink during storage period.

Treatment	Storage day	Color measuring		
		L*	a*	b*
Durian drink (DD)	0	43.36±0.17^{b}	-0.99±0.02^{a}	10.57±0.31^{b}
	3	43.99±0.32^{b}	-0.93±0.13^{a}	11.13±0.32^{b}
	6	42.90±0.35^{b}	-0.91±0.19^{a}	10.18±0.30^{b}
	9	42.26±0.33^{b}	-0.85±0.13^{a}	11.25±0.19^{b}
	12	41.56±0.38^{b}	-0.51±0.08^{a}	11.99±0.40^{a}
	15	40.49±0.60^{b}	-0.48±0.10^{a}	10.94±0.48^{b}
Durian drink with milk (DM)	0	50.18±0.54^{a}	-0.79±0.07^{a}	13.04±0.17^{a}
	3	49.61±0.53^{a}	-0.69±0.21^{a}	12.63±0.25^{a}
	6	49.04±0.38^{a}	-0.66±0.03^{a}	11.89±0.02^{a}
	9	48.58±0.37^{a}	-0.63±0.01^{a}	12.02±0.20^{a}
	12	48.49±0.43^{a}	-0.47±0.04^{a}	11.35±0.31^{a}
	15	47.74±0.43^{a}	-0.32±0.02^{b}	11.97±0.23^{a}

*Values in the column of each sample with different lowercase (^{a,b}) were significantly different (P>0.05).

Microbiological analyses

The presence of microorganisms can have a negative effect on beverage product in term of quality, color, odor and flavor which if eaten, may adversely affect the consumer's health. Total plate count (TPC) of DD and DM were increased from 1.48±0.01 to 3.34±0.02 and 1.30±0.03 to 3.58±0.05 log CFU/mL from days 0 to days 15. The yeast and mold (YMC) count was increased from 1.30±0.05 to 3.21±0.03 and 1.58±0.01 to 3.26±0.01 log CFU/mL which was more for DM than DD (Table 3) due to milk as a considered as a source of nutrients appropriate for growth of microorganisms that may cause product deterioration such as changes in color, taste, smell or texture that lead to coagulation or separation of drink.

Table 3. Microbiological changes of durian drink during storage period at 4°C.
(TPC: total plate count; YMC: yeast and mold count)

Treatment	Storage day	Microorganism's count	
		TPC (log CFU/mL)	YMC (CFU/mL)
Durian drink	0	1.48±0.01	1.30±0.05
	3	1.54±0.03	1.88±0.01
	6	2.16±0.02	2.24±0.04
	9	2.28±0.01	2.63±0.02
	12	3.01±0.02	3.14±0.03
	15	3.34±0.02	3.21±0.03
Durian drink with milk	0	1.30±0.03	1.58±0.01
	3	1.69±0.02	2.02±0.01
	6	2.25±0.01	2.27±0.04
	9	2.74±0.01	2.85±0.02
	12	3.11±0.04	3.20±0.03
	15	3.58±0.05	3.26±0.01

Conclusions:

The development of beverages to enhance nutritional values that are useful for consumption. In this experiment, the effect of milk addition on stability of bioactive compounds and antioxidants in durian drinks with different ingredients during cold storage at 4°C for 15 days were evaluated. The finding revealed substantial variations in total phenolic content, antioxidant activity, and color values (L*, a* and b*) between durian drink (DD) and durian drink with milk (DM). The addition of milk could enhance the antioxidant properties (total phenolic compound and antioxidant activity). However, the milk addition could support the growth of microorganisms during storage. Therefore, other technologies should be added into the production process to create highly-quality drink, such as sugar reduction technology, shelf-life extension technology and nutritional fortification technology that should be practical for customer's convenience and beneficial to health.

Acknowledgements:

This research was supported by the 90th Anniversary of Chulalongkorn University Fund (Ratchadaphiseksomphot Endowment Fund).

References:

1. Leontowicz H, Leontowicz M, Haruenkit R, Poovarodom S, Jastrzebski Z, Drzewiecki J, Ayala Al, Jession I, Trakhtenberg S, Gorinstein S. FCT. 2008;46:581-589.
2. Jafari S, Pongsarn K, Srestasupana C, Wetchasart N, Assatarakul KJL. LWT. 2021;152:112-309.
3. Silinkard K, Singleton VL. AJEV. 1997;28:49-55.
4. Brand-Williams W, Cuvelier ME, Berset C. FS&T. 1995;28:25-30.
5. AOAC Int. 2005;88:1269-1278.
6. Suetsuna K, Ukeda H, Ochi H. J Nutr Biochem. 2000;11:128–31.
7. Erel Ö. Clin Biochem. 2004;7:277–85.
8. Carthy TLM, Kerry JP, Kerry JF, Lynch PB, Buckley DJX, Meat Sci. 2015;1:45–52.
9. Kim HJ, Min DB. AOCS Press. 2003;1–30

10. Young AJ, Lowe GM, Arch Biochem Biophys. 2001;385:20–7.
11. Zhao Q, Yuan Q, Gao C, Wang X, Zhu B, Wang J, et al. F2021;10(8):1851.
12. Yu Y, Xu Y, Wu J, Xiao G, Wen J, Chen Y, Zhang Y. J Food Res. 2014;3(3):1-9.

DEVELOPMENT OF NAPIER GRASS SILAGE FORMULA FOR CATTLE FEED

Banthot Chomsawan*, Jinda Sirita, Piyada Yodsoontorn, Piyaporn Srisom, Waleepan Rakitikul
Faculty of Science and Technology, Chiang Rai Rajabhat University, Chiang Rai Province
*e-mail: banthod49@gmail.com

Abstract:

The purpose of this research was to study the Napier grass silage formula, and nutritional value of fermented Napier grass. The fresh Napier grass was fermented in 2 ways, fermented in bags and fermented in tank. In each form there are 3 formulas (Formula 1 100% pure fresh Napier grass ; Formula 2 Fresh Napier Grass 98% Molasses 2% ; Formula 3 Fresh Napier Grass 83% Molasses 2% Acacia 15%). After 21 days of fermentation, the acidity and alkalinity, color, odor, moisture and nutrient value of fermented Napier grass were examined. The results showed that acidity and alkalinity. After 21 days of fermentation, it had a pH in the range of 3.85 – 5.45, the fermentation in a bag was quite acidic with a pH in the range of 3.85-4.31. The physical characteristics of Napier grass fermented in bags have better fermentation conditions than fermented in tank, with yellowish green slightly damp Sour smell like fermented Miang. For recipes that add molasses, it will also have the aroma of sugarcane juice. The amount of Dry matter (DM), Crude fiber (CF), Ether extract (EE), Crude protein (CP), Nitrogen free extract (NFE) and Energy of the three formulas of Napier grass fermented in Bag and tank fermentation after 21 days of fermentation process were significantly different ($P< 0.05$). However, bag fermentation yields higher protein content than fermentation in tanks. By fermenting in bags for 21 days, Formula 3 had the highest crude protein content of 10.7%. The Napier silage formula with the highest dry matter content was Formula 3 fermented in a bag (20.08%). The highest ash content of Napier silage was Formula 2 silage in bags (11.35%). The Napier silage formula with the highest Crude fiber content was Formula 2 silage (33.91%). The highest fat content of the Napier fermented grass recipe is Formula 3 fermented in a bag (3.30%). The most Nitrogen free extract content of Napier grass is Formula 3 fermented in tank (47.7%). And the Napier silage formula with the highest energy content was Formula 3 fermented in a bag (4,078.50 cal/g). It can be seen that the Napier grass Formula 3 Silage in a bag is suitable for further use as a silage formula for raising cattle.

Introduction:

The fermentation process is one of the preservation of forage crops, with the purpose of preserving plants animal feed at the proper growth stage with high nutritional value and productivity for use in times of shortage. This fermented preservation has the advantage that it can be stored for a long time with little change in the nutritional value of the plant. In the fermentation of plants, the main principle is the plants used for fermentation must have proper humidity, and contains enough sugar to support the growth of lactic acid bacteria. In addition, as much air is removed from the fermentation container as possible, this can be done by shortening the plants. Then compress and then close the fermentation container as quickly as possible. For forage crops suitable for fermentation plants. It should be a plant that is easy to grow and manage, has a high yield, has a water soluble carbohydrate (WSC) content of not less than 6% of dry weight. For example, corn (Zea mays), which has a high yield per rai with high WSC content, resulting in a good quality silage crop with a high proportion of grains. This results in high palatability and highly digestible tops (67–70 %),

but the disadvantage is that it can be cut only once. Must be replanted every time, while forage crops such as Napier grass are multi-year crops therefore can be cut many times high yield per rai and is appetizing. But grass family plants have average WSC values in the range of 3-5%, especially in Para grass have water-soluble carbohydrate (WSC) contents ranging from 3.2-7.7% (Sath et al., 2013)[1]. Therefore, in the Make silage, so it is often recommended to add a supplement that is a food source for lactic acid-producing microorganisms, such as molasses, will complete the fermentation process.

The of good quality fermentation plants can be done in various types of fermentation containers, such as pits, floor type, fermentation pond, bales wrap, plastic tank and packaged in plastic bags, etc. Each type has its advantages, disadvantages, and suitability. For composting plants in plastic bags is an easy method and suitable for smallholders who have less working area or have less time to manage forage (Manjunath et al., 2019)[2]. Because it is a method of fermentation that does not require much investment. Materials are readily available locally can be done gradually and conveniently.

There are many farmers in Chiang Rai who make a career in raising cattle. There are both made as a supplementary occupation and making it the main occupation. Cow raising is both natural and domesticated and planting grass plots for raising cattle which farmers often encounter problems are, there is more grass than necessary in the rainy season. But when the dry season came, there was a shortage of grass for raising cattle. The researcher is interested in making Napier grass silage in various formulas to provide quality cattle feed to replace the shortage of fresh grass in the dry season.

Methodology:

Materials and chemicals

Materials used were about 30 days old fresh Napier grass (*Napier: Pennisetum Perpureum*) from Chiang Rai. All chemicals used were of an analytical grade or equivalent.

Development of Napier grass silage formula

Cut and cut fresh Napier grass to size 2-2.5 cm with a chopper. Fresh Napier grass is fermented in 2 ways, bag (60x100 cm) fermentation and tank (20L) fermentation, in each form there are 3 sample for 3 formulas;

F1, 100% pure fresh Napier grass

F2, Fresh Napier Grass 98% and Molasses 2%

F3, Fresh Napier Grass 83%, Molasses 2% and fresh Acacia 15%

Fermentation in bags is done by packing the mixed ingredients into 20 kg thick, opaque plastic bags and sucking out all the air. After that, tie the bag tightly and ferment for 21 days.

Tank fermentation is done by packing the mix well into a plastic tank, compacted to full tank no air gap. Then close the lid of the tank tightly and ferment for 21 days.

Napier grass silage physical properties measurement

A color of silage, after the fermentation period visual assessment was performed to identify the color of the silage in an open container in approximately 3 minutes.

Silage odor is classified into 3 levels, namely normal aroma, musty grass smell and the smell of rotten grass.

Measure moisture, acidity and alkalinity of silage by using the Soil-pH-Humidity tester.

Analysis of the composition and nutritional value of silage

Weigh the silage sample and annealed for dry matter (DM) at 105 °C for at least 24 h until the dry weight was stable. Take the second part of silage bake to dehumidify at 60°C for 72 hours. The sample was then grinded through a 1 mm sieve to be used for the determination of the chemical composition, such as Crude fiber (CF), Ether extract (EE), Crude protein

(CP), Nitrogen free extract (NFE) according to AOAC (1990), and measure the total energy with a bomb calorimeter.

Results and Discussion:

The acidity and alkalinity values (Table 1) after 21 days of fermentation were at a pH range of 3.85 – 5.45. The fermentation in a bag was quite acidic with a pH in the range of 3.85-4.31. The pH value of all fermented forages were below 4, which was an indicator of well-preserved napier grass silage. According to Nurjanaa et al. (2016)[3], pH value for silage should be below 4.5 to preserve the silage. It indicated all napier grass silage met these criteria as well-preserved quality, while fermentation in a tank had the mean pH was 5.10±0.31. This is quite high, probably because there is still a lot of air in the tank, affecting the fermentation process.

Table 1.
Napier grass silage acidity and alkalinity value in various recipes

Napier grass silage	pH
F1 before fermentation	6.75±0.12a
F2 before fermentation	6.64±0.15a
F3 before fermentation	6.70±0.11a
F1 in Bag	4.31±0.19bd
F2 in Bag	3.88±0.11b
F3 in Bag	3.85±0.19b
F1 in Tank	5.45±0.14c
F2 in Tank	5.01±0.33cd
F3 in Tank	4.85±0.18cd

a, b, c, d: Means bearing different within the same column are significantly different at $p<0.05$

Table 2.
Napier grass silage physical properties in various recipes

Napier grass silage	physical properties	odor
F1 before fermentation	fresh green	fresh grass smell
F2 before fermentation	fresh green	fresh grass smell
F3 before fermentation	fresh green	fresh grass smell
F1 in Bag	yellowish-green, quite dry	normal aroma
F2 in Bag	yellowish-green, slightly damp	normal aroma
F3 in Bag	yellowish-green, quite wet	normal aroma
F1 in Tank	green-brown, with mold on the front, wet	musty grass smell
F2 in Tank	green-brown, with mold on the front, wet	musty grass smell
F3 in Tank	green-brown, with mold on the front, wet	smell of rotten grass

From Table 2, the 21-day yield of Napier silage was found that silage Napier grass in both containers was yellowish-green in color, and has a typical fermented smell, that was similar to Randa, et al. (2017)[4], except for silage in tank is spoiled. This is caused by exposure to air on the surface under the lid of the tank, causing the fermentation process to be incomplete, especially when fermenting in tank the formula 3, there was a smell of rotten grass, probably because the fresh acacia put into it caused spoilage after being air exposed. And there is a little white fungus on the surface causing a loss of about 1.5 percent.

The results of Dry matter (DM), Crude fiber (CF), Ether extract (EE), Crude protein (CP), Nitrogen free extract (NFE) and Energy were displayed in table 3.

Table 3.
Napier grass silage nutritive value in various recipes

Napier grass silage	DM (%)	Ash (%)	CF (%)	EE (%)	CP (%)	NFE (%)	Energy (cal/g)
F1 before fermentation	20.88±0.10a	8.10±0.03a	31.58±0.14a	2.15±0.02a	5.70±0.06a	47.80±0.58a	3,961.19±3.46acd
F2 before fermentation	19.75±0.12b	8.13±0.02a	27.04±0.06c	1.83±0.03b	5.10±0.05b	52.70±1.15a	3,838.05±4.04f
F3 before fermentation	20.83±0.12ac	10.02±0.06b	22.22±0.05d	2.22±0.01ab	9.80±0.12c	50.40±0.75a	3,942.25±2.89ac
F1 in Bag	20.11±0.11bcd	10.60±0.03cf	33.68±0.13b	2.81±0.01cd	6.00±0.17abd	42.90±0.52b	3,999.10±3.46be
F2 in Bag	18.52±013e	11.35±0.12c	28.78±0.09e	3.02±0.05cde	6.50±0.12ade	46.40±0.81ab	3,939.20±5.20acd
F3 in Bag	20.08±0.09d	10.75±0.07cd	25.42±0.15f	3.30±0.04d	10.70±0.17cf	46.00±0.46a	4,078.50±4.62g
F1 in Tank	16.43±0.13f	9.81±0.05be	34.75±0.10g	1.55±0.02f	5.30±0.09abd	46.00±0.17ab	3,974.71±2.31cd
F2 in Tank	16.90±0.13f	9.49±0.08e	33.91±0.05b	1.93±0.02b	6.00±0.08ade	47.20±0.69ab	3,978.63±3.00bde
F3 in Tank	18.54±0.11e	10.45±0.14bdef	31.55±0.08a	2.51±0.01e	10.30±0.05cf	47.70±0.98ab	4,038.53±2.48h

a, b, c, d, e, f, g, h: Means bearing different within the same column are significantly different at $p<0.05$

The amount of Dry matter, Crude fiber, Ether extract, Crude protein, Nitrogen free extract and Energy of the three formulas of Napier grass fermented in bag and tank fermentation after 21 days of fermentation process were significantly different ($P< 0.05$). The Napier grass silage nutritive values were consistent with the reports of Suksatit, et al. (2005)[5]. However, bag fermentation yields higher protein content (CP) than fermentation in tanks. By fermenting in bags for 21 days, Formula 3 had the highest crude protein content of 10.7%, for Napier grass fermented formula 3 at high protein content, this may be due to the addition of 15% acacia that have high cp content (Mousa, 2011)[6] , which can be a nitrogen source for protein formation (Jones et al., 1992)[7] in the fermentation process by microorganisms. The Napier silage formula with the highest dry matter content was Formula 3 fermented in a bag (20.08%). The highest ash content of Napier silage was Formula 2 silage in bags (11.35%). The Napier silage formula with the highest Crude fiber content was Formula 2 silage (33.91%). The highest fat content of the Napier fermented grass recipe is Formula 3 fermented in a bag (3.30%). The most Nitrogen free extract content of Napier grass is Formula 3 fermented in tank (47.7%). And the Napier silage formula with the highest energy content was Formula 3 fermented in a bag (4,078.50 cal/g). It can be seen that the Napier Grass Formula 3 Silage in a bag is suitable for further use as a silage formula for raising cattle.

Conclusion:

The Napier Grass silage Formula 3, that consists of 83% fresh napier grass, 2% molasses, and 15% acacia fermented in bags. It is suitable for further use as a silage formula for raising cattle. The next study should be studied further in the case of cattle raising should consider the daily feeding rate and the rate of weight gain, etc.

Acknowledgements:

Researchers would like to thank the Research Fund of Chiang Rai Rajabhat University for the sponsorship and the support experimental devices and analysis tool provided by Chiang Rai Rajabhat University.

References:

1. Sath K., Khen K., Holtenius K. and Pauly T. Para grass (*Brachiaria mutica*), ensiled or supplemented with sugar palm syrup, improves growth and feed conversion in "Yellow" cattle fed rice straw. Livest. Res. Rural. Dev. 2013; 25(7):133.
2. Manjunath P., Anant R. D. and Raju G T. Ensilaging in Polyethylene Bags: A Low Cost Technology for Resource Poor Livestock Farmers. Int. J. Livest. Res. 2019; 9(1):166-173. [doi: 10.5455/ijlr.20180628051301]
3. Nurjanaa D. J., Suhartib S. and Suryahadib. Improvement of Napier Grass Silage Nutritive Value by Using Inoculant and Crude Enzymes from *Trichoderma reesei* and Its Effect on *in Vitro* Rumen Fermentation. Media Peternakan. 2016;39(1):46-52. [doi: 10.5398/medpet.2016.39.1.46]
4. Randa S. Y., Lekitoo M. N., Iyai D. A. and Pattiselanno F.. Nutritive Value and the Quality of Ensiled Napier Grass (*Pennisetum Purpureum* Schum.) and Banana (*Musa Acuminata*) Peelings. Animal Production. 2017;19(2):101-110.
5. Suksatit S., Wattanachant C., Sonssang A. and Suwanapugdee A.. A Study of Suitable Silage Packaging Material for Small Dairy Farms at Paphayom District, Phatthalung Province. Thaksin.J. 2005;8(1): 26-36.
6. Mousa, M.R.M. Effect of Feeding Acacia as Supplements on the Nutrient Digestion, Growth Performance, Carcass Traits and Some Blood Constituents of Awassi Lambs under the Conditions of North Sinai. Asian J. Anim. Sci. 2011;5: 102-117. [doi: 10.3923/ajas.2011.102.117]
7. Jones, B.A., R.D. Hatfield, and R.E. Muck. Effect of fermentation and bacterial inoculation on lucerne cell walls. J. Sci. Food Agric. 1992;60: 147-153.

UTILIZATION OF FOOD WASTE AND BIOMASS TO PRODUCE BIO-COMPOST

Pithan Theeropas,[1] Wipawee Srihanon[1,*], Sanchai Kuboon[2], Wanwitoo Wanmolee,[2,*]
[1]Princess Chulabhorn Science High School Lopburi,15120, Thailand
[2]National Nanotechnology Center (NANOTEC), National Science and Technology Development Agency, Khlong-Nueng, Khlong Luang, Pathumthani, 12120, Thailand
*Corresponding authors, email: wipawee@pccl.ac.th and wanwitoo.wan@nanotec.or.th

Abstract

The aim of this research is to study compost production in a nano-composter machine. By using food waste mixed with 2 types of biomass, corncob and rubber tree roots as raw materials, it took about 24 hours for compost production. The compost was crushed to a size of less than 2 mm using a Hammer mill. The results showed that the corncob compost had a C/N ratio of 17.49, moisture content of 9.38%, and pH of 4.34. where the C/N ratio and moisture content met the criteria for compost, but the pH did not. From the sunflower sprouts' seedling test, they germinated well on the obtained compost. However, it did not grow well in corncob compost mixed with soil. For rubber tree root compost, it has a C/N ratio of 31.49 ± 1.86 and a pH of 4.83, which did not meet the criteria of compost.

Introduction

64% of waste in Thailand is food waste which is managed incorrectly because of throwing litter away in the river, burning it or throwing it away on the side of the road causing effects to the environment such as global warming, climate variability etc.

Thailand is called an agricultural country. It has many significant goods that are economically beneficial to Thailand. There are unwanted or unsalable materials from agriculture that can be reused or recycled. In our research, corncob and rubber tree root are mentioned respectively since they are commercial plants that are the cause of the most agricultural waste. These problems that are mentioned above affect the environment and our health.

Therefore, we use waste hierarchy to be the guide for waste management. Composting is a process that changes organic waste to be a soil amendment. Compost can be produced by using microorganism activity to help the decomposition of organic waste. Composting is the method producing from natural materials. In addition, compost is friendly product of soil.

Compost is considered as an alternative product for reducing food waste and agriculture residues.

Methodology

1. Production of bio-compost

The bio-compost was obtained using nanocomposter. Different compositions of food waste consisting of cucumber (0.09 g), tomato (0.09 g), watermelon peel (0.09 g), pineapple peel (0.09 g), morning glory (0.15 g), onion (0.15 g), lentils (0.15 g), cabbage (0.15 g), soybean meal (0.62 g), edamame shell (0.07 g), rice (0.07 g), peanut shell (0.07 g), ginger (0.04 g), galangal (0.04 g), pandan leaf (0.04 g), potato (0.04 g), and eggshell (0.04 g) were mixed with biomass (*i.e.,* corncob and rubber tree root) in a ratio of 2:1. After that, they were put into the

nanocomposter and agitated at 80 rpm for 24 hours. The temperature profile of composting used in this work is shown in **Figure 1**. After finished the composting, a product (bio-compost) was kept in a plastic bag.

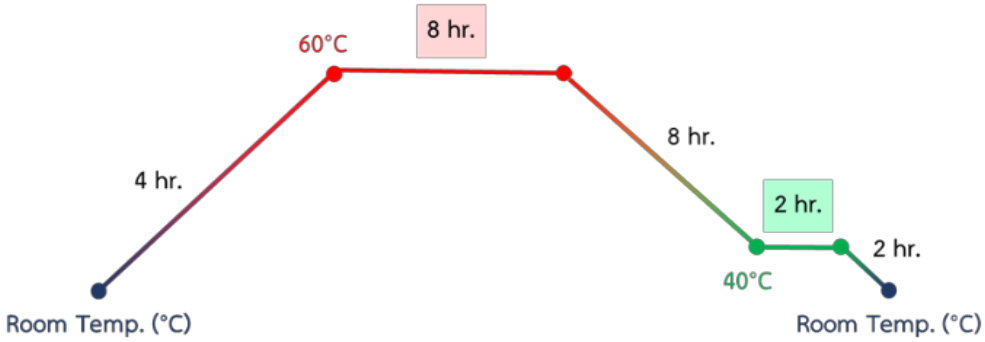

Figure 1. Temperature profile of composting.

Figure Error! Unknown switch argument.**.** Nanocomposter used in this study.

2. Analysis of bio-compost

The parameters consisted of compost yield, C/N ratio, pH, particle size, and moisture content were investigated.

2.1. Compost yield

All food waste and biomass, used for producing compost were weighed. When each compost was finished. It was weighted. The yield was calculated by

$$\%\text{yield} = \frac{\text{weight of raw materials}}{\text{weight of bio-compost}} \times 100$$

2.2. C/N ratio

Bio-composts were milled to approximately 2 mm, then the samples were weighed to be 100 mg, and incubated at 60 °C overnight to remove moisture. After that, the samples were analyzed by a CHN analyzer (LECO 628 series). The analyzer shows the proportion of carbon, nitrogen, and hydrogen. C/N ratio can be calculated by

$$\text{C:N} = \frac{\%\text{Carbon}}{\%\text{Nitrogen}}$$

2.3. pH

Bio-composts were mixed with distilled water in a ratio of 1:2 (w/v) and analyzed by pH meter

2.4. Particle size

Bio-composts were milled by Hammermill to be 2 mm diameter.

2.5. Moisture content

Each food waste and biomass were put into a crucible for 3 g. The crucibles with the sample were incubated at 105 °C for 4 hours and then weighed. The samples were incubated and weighed until the mass difference of the sampleswas 0.5 mg or lower. The moisture content was calculated by

$$\%\text{moisture content} = \frac{\text{weight of raw material} - \text{weight of material after drying}}{\text{weight of raw material}} \times 100$$

3. Planting test

3.1. Production of greenhouse

Greenhouse was made from plastic, joint, and PVC tube, according to **Figure 3**.

Figure 3. House for sunflower sprout germination.

3.2 Preparation of sunflower sprout seed

Sunflower sprout seeds from Railungtopfarmshop soaked in the water for 12 hours and wrapped with wet wipes for 12 hours before planting.

3.3 Planting

Sunflower sprout seeds were germinated in seeding tray (25 pits). Each pit contains five sunflower sprout seeds (**Figure 4**) and watered twice a day for 7 days. Different planting soil amendments including soil, corncob compost, rubber tree root compost, corncob compost mixed soil, rubber root tree compost mixed soil, and peat moss were investigated. After 7 days, various parameters including length of trunk and root, weight, and a number of leaves were recorded.

Figure 4. The position of sunflower sprout seeds in pit of seeding tray.

4. Pelletization of bio-compost

4.1 Preparation of binder

Tapioca flour was weighed to be 5 g and mixed with 95 g of water. After that, boiling at 80 °C for 15 minutes. Finally, 5% (w/v) Tapioca flour solution was obtained.

Figure 5. 5% (w/v) Tapioca flour solution.

4.2 Pelletization without binder

Bio-composts were weighed to be 0.5 g and then put into a molding. Samples were pressed at different pressures (1, 1.5 and 2 tons) and time (30, 60 and 90 sec).

4.3 Pelletization with binder

Bio-composts were weighed to be 0.5 g mixed with 0.05 g of 5% (w/v) Tapioca flour solution and put into molding. The samples were pressed at similar conditions in section 4.2 (Pelletization without binder).

5. Statistical analysis

In this study, two statistical analyses were evaluated consisting of average and standard deviation. For the average, it was calculated by $\bar{x}=\frac{\sum_{1=1}^{N} x_i}{N}$ and the standard deviation was calculated by $S.D.=\frac{\sqrt{(x-\bar{x})^2}}{N}$.

Results and Discussion

1. Moisture content

1.1 Material moisture

According to **Table 1**, cucumber has the highest moisture content of 97.38%. On the contrary, the lowest moisture content (17.18%) was obtained with eggshell. Typically, it is made up of 97% inorganic matters especially calcium carbonate [1].

Table 1. Moisture content of food waste and biomass

Materials	Moisture (%)
Cucumber	97.38 ± 0.28
Tomato	95.88 ± 0.18
Watermelon peel	93.89 ± 0.03
Pineapple peel	82.69 ± 0.39
Morning glory	93.81 ± 0.22
Onion	90.75 ± 0.76
Lentils	91.98 ± 0.06
Cabbage	92.78 ± 0.17
Soybean meal	80.92 ± 0.13
Edamame shell	79.81 ± 0.18
Rice	60.84 ± 0.11
Peanut shell	21.51 ± 2.05
Ginger	90.28 ± 0.61
Galangal	79.64 ± 0.49
Pandan leaf	87.75 ± 0.98
Potato	83.95 ± 0.89
Eggshell	17.18 ± 1.07
Corncob	55.74 ± 1.11
Rubber tree root	6.72 ± 1.04

1.2 Bio-compost and soil moisture content

The data in **Table 2** shows the moisture content of bio-compost and soil. The highest moisture content was peatmoss, as expressed by 47.26%, while rubber tree root compost is the least accounted for 1.99. In addition, the moistures of corncob compost and corncob compost mixed with soil are 9.38 and 27.13, respectively.

Table 2. The moisture content of planting materials (bio-compost and soil).

Planting materials	Moisture content (%)
Corncob compost	9.38 ± 0.11
Rubber tree root compost	1.99 ± 2.17
Soil	27.13 ± 0.47
Corncob compost mixed with soil (1:1)	14.56 ± 0.91
Rubber tree root compost mixed with soil (1:1)	18.25 ± 0.22
Peat moss	47.26 ± 1.77

2. Yield of compost

According to **Table 3**, the yield of rubber tree root compost is significantly higher than corncob compost which corresponds to the moisture content of biomass.

Table 3. The percentage of the compost yield.

Type of compost	Before (kg)	After (kg)	Yield (%)
Corncob compost	3.01	0.71 ± 0.04	23.64 ± 1.35
Rubber tree root compost	3.01	1.29 ± 0.00	42.84 ± 0.03

3. C/N ratio

As shown in **Table 4**, rubber tree root compost has a higher C/N ratio, accounted for 31.49, while corncob compost and corncob compost mixed with soil are 17.49 and 7.31, respectively. Interestingly, it is obvious that there are differences in the proportion of carbon and nitrogen in each planting material. The rubber tree root compost could not use directly because the C/N ratio was higher than the criteria (C/N ratio is 20 or lower) [2]. The C/N ratio plays many roles in plants such as causing mineralization and immobilization, controlling the decomposition rate in soil, etc.

Table 4. C/N ratio of planting material.

Planting material	C/N ratio
Soil	0.00
Peat moss	21.69 ± 0.67
Corncob compost	17.49 ± 0.41
Corncob compost mixed with soil	7.31 ± 1.94
Rubber tree root compost	31.49 ± 1.86
Rubber tree root compost mixed with soil	19.84 ± 0.75

From the result of C/N ratio as presented in **Table 5**, it was apparent that there are 31.08 and 45.35 in the proportion of carbon and nitrogen of corncob and rubber tree root, respectively which affected on the difference of C/N ratio of compost.

Table 5. C/N ratio of raw materials.

Materials	C/N ratio
Cucumber	9.19 ± 0.46
Tomato	14.40 ± 0.22
Watermelon peel	17.90 ± 0.50
Pineapple peel	40.04 ± 0.75
Morning glory	7.59 ± 0.10
Onion	16.29 ± 0.95
Lentils	7.71 ± 0.11
Cabbage	14.54 ± 0.77
Soybean meal	9.54 ± 0.14
Edamame shell	24.54 ± 1.06
Rice	26.17 ± 1.96
Peanut shell	26.73 ± 0.40
Ginger	24.04 ± 0.42
Galangal	47.29 ± 3.37
Pandan leaf	14.08 ± 0.38
Potato	14.63 ± 0.09
Eggshell	10.53 ± 0.36
Corncob	31.08 ± 3.46
Rubber tree root	45.35 ± 3.11

4. pH

From **Table 6**, products from the nanocomposter are acidic, affecting the growth of the plant. Sunflower sprouts can germinate in corncob compost mixed with soil as well as germinate in soil but the germination rate in the soil is better than in corncob compost mixed with soil as shown in **Table 6**.

Table 6. The pH of planting material.

Planting material	pH
Soil	6 - 7
Peat moss	5
Corncob compost	4
Corncob compost mixed with soil	4 - 5
Rubber tree root compost	4 - 5
Rubber tree root compost mixed with soil	-

5. Particle size

Compost was milled by Hammermill to be 2 mm in diameters, as illustrated in **Figures 6 – 7**.

Figure 6. Grinding of compost

Figure 7. 2mm bio-compost

6. Planting test

6.1. Germination test

According to **Table 7**, the most suitable planting is corncob compost mixed with soil, in which sunflower sprouts can germinate for 110 seeds. On the other hand, sunflower sprouts

cannot grow in corncob compost. However, sunflower sprouts cannot grow well in the compost when it was overhydration

Figure 8. Corncob compost mixed with soil after watering

Table 7. Germination of sunflower sprouts.

Planting material	The number of seeds						
	Day 1	Day 2	Day 3	Day 4	Day 5	Day 6	Day 7
1. Soil*	1	17	86	96	105	105	105
2. Peat moss*	3	25	49	53	55	55	55
3. Corncob compost	1	0	1	1	1	3	5
4. Corncob compost mixed with soil	0	11	74	96	102	107	110
5. Rubber tree root compost**	-	-	-	-	-	-	-
6. Rubber tree root compost mixed with soil**	-	-	-	-	-	-	-

*Some of the sunflower sprouts in soil and peat moss destroyed.
**Rubber root compost and rubber root mixed with soil were not tested.

6.2. Growing

From the **Table 8**, it is apparent that sunflower sprouts mostly grew in peat moss which observed from wet weight, length of trunk, and the number of leaves. The root's length shows that a sunflower sprout can absorb nutrients well. A more root length referred it is more absorbent.

Table 8. The average wet weight, length of trunk and root, and number of leaves.

Planting material	Wet weight (g)	Trunk length (cm)	Root length (cm)	Number of leaves
1.Soil	0.57 ± 0.17	5.00 ± 1.19	8.00 ± 2.65	4.00 ± 0.71
2.Peat moss	0.86 ± 0.30	6.60 ± 1.58	5.30 ± 2.43	4.00 ± 0.76
3.Corncob compost	0.29 ± 0.06	2.80 ± 0.30	0.80 ± 0.26	3.00 ± 1.10
4.Corncob compost mixed with soil	0.47 ± 0.18	3.70 ± 1.19	2.10 ± 1.11	3.00 ± 1.10
5.Rubber tree root compost*	-	-	-	-
6.Rubber tree root compost mixed with soil*	-	-	-	-

*Rubber root compost and rubber tree root compost mixed with soil were not tested.

Conclusion

Analysis of compost showed that C/N ratio, particle size, and moisture in corncob compost passed the criteria [2] but pH did not pass, while rubber root compost shows that particle size passed the criteria, but pH and C/N ratio was under-qualified. From the planting result, sunflower sprouts can germinate in the compost mixed with soil as well as in soil. On the other hand, the sunflower sprouts can grow well in peat moss, soil, corncob compost mixed with soil, and corncob compost, respectively.

Acknowledgements

I would like to thank the National Science and Technology Development Agency for supporting this research. I would also like to my teachers from Princess Chulabhorn Science High School who gave me knowledge and insight for my research.

I am grateful to Mrs.Wipawee Srihanon, Dr.Sanchai Kuboon and Dr.Wanwitoo Wanmolee for sharing their knowledge, checking this paper, and taking good care of mentally and physically.

I would like to thank Mrs.Srirana Kongtago for commenting on an earlier draft and reviewing this paper which actually enhanced the paper.

References

1. Hunton, P.J.B.J.o.P.S., Research on eggshell structure and quality: an historical overview. 2005. 7: p. 67-71.

2. Lovett, G.M., K.C. Weathers, and M.A.J.E. Arthur, Control of nitrogen loss from forested watersheds by soil carbon: Nitrogen ratio andtree species composition. 2002. 5(7): p. 0712-0718.

PROPERTIES OF SOY PROTEIN ISOLATE FILM INCORPORATED WITH EPIGALLOCATECHIN GALLATE AND GREEN TEA EXTRACT

Akiraya Phaikhleaw, Thanachan Mahawanich*
Department of Food Technology, Faculty of Science, Chulalongkorn University, Bangkok 10330, Thailand
*e-mail: thanachan.m@chula.ac.th

Abstract:

Epigallocatechin gallate (EGCG) and green tea extract (GTE) of different oxidation states (oxidized and non-oxidized) were used as safe cross-linking agents to improve the properties of soy protein isolate (SPI) film. It was found that SPI film containing 7.2% oxidized EGCG possessed the highest tensile strength while the highest elongation at break was demonstrated by that added with 1.8% oxidized EGCG. The addition of 3.6 and 7.2% EGCG in oxidized states into SPI film revealed significantly higher tensile strength than in non-oxidized states ($p \leq 0.05$). Different oxidation states of EGCG or GET significantly affected the elongation at break of SPI film ($p \leq 0.05$). Besides, SPI film containing 7.2% oxidized EGCG significantly exhibited the lowest %transmittance in both UV/visible light ($p \leq 0.05$). As compared to the control, SPI films added with EGCG or GTE, either in oxidized or non-oxidized state, exhibited significantly greater thickness, UV and visible light barrier, and water vapor barrier, with a decrease in water solubility, surface hydrophobicity, and hue angle ($p \leq 0.05$). SPI film incorporated with EGCG displayed significantly improved mechanical properties, UV and visible light barrier than that added with GTE ($p \leq 0.05$). In summary, EGCG and GTE could be used to modify properties of SPI film via covalent C-N cross-linking of protein as proven using SDS-PAGE and FTIR spectroscopic techniques.

Introduction:

Soy protein is a food protein with excellent film-forming ability. Therefore, it has a potential to be used as a polymeric base for edible as well as biodegradable films. The major fractions of soy protein are glycinin and beta-conglycinin. Both proteins are capable of forming protein lattice through various bondings and interactions, such as covalent bonds, hydrogen bond, and hydrophobic interaction[1]. Despite that, soy protein films generally exhibit moderate mechanical strength, which is still inferior when compared to those films made from synthetic polymers. This is one factor responsible for the limited application of soy protein films[1].

Mechanical properties of protein films can be improved by promoting protein cross-linking using various means. Naturally occurring phenolic compounds can induce covalent C-N and C-S bond formation among protein chains[2]. It was proposed that the ability of a phenolic compound to react with proteins depends on its propensity to undergo oxidation to its corresponding quinone[3]. The mechanism of phenolic-induced protein cross-linking was described elsewhere[4], in which the first and necessary step is the oxidation of a phenolic compound to its quinone derivative.

In earlier study, the effect of ferulic, caffeic, and gallic acid, in non-oxidized and oxidized states, on properties of soy protein film was investigated[2]. It was reported that the oxidized phenolic acid yielded a film with greater tensile strength compared to that added, at the same concentration, with the same phenolic acid in non-oxidized state. Protein cross-linking was confirmed by SDS-PAGE and FTIR spectroscopy, as well as the decrease in available lysine and free sulfhydryl contents[2]. Similar finding was also reported for turmeric-

gelatin film cross-linked with tannic acid, caffeic acid, and green tea extract[5]. Greater degree of protein cross-linking was found in those films added with oxidized phenolics than those added with non-oxidized ones. In another study, epigallocatechin gallate (EGCG) in its oxidized state was reported to demonstrate increasing binding capacity to serum albumin protein[6].

Catechins are the main phenolic compounds in green tea. The major catechin in green tea is EGCG which constitutes 7380 mg/100 g of dried tea leaves. EGCG and green tea extract (GTE) have found their uses in various biopolymer films[7-9]. Due to protein cross-linking ability of catechins[10], it is of high potential to utilize catechins, EGCG, or GTE to improve mechanical properties of protein films.

Protein cross-linking of whey protein isolate by EGCG was reported in previous study[11]. At basic condition (pH9.0), EGCG was shown to induce covalent cross-linking of whey protein as confirmed using an SDS-PAGE. In addition, fluorescence spectroscopy revealed that the cross-linked whey protein had a denser tertiary structure than the unmodified whey protein. Similar results were also reported for EGCG-modified beta-lactoglobulin[12]. The objective of this study was therefore to investigate the effect of EGCG and GTE in oxidized and non-oxidized states on mechanical, barrier, and optical properties of soy protein isolate (SPI) film.

Methodology:

Materials

SPI (90.2% protein) and glycerol were obtained from Krungthepchemi (Bangkok, Thailand). EGCG (98.0% purity) and GTE were purchased from Chanjao Longevity (Bangkok, Thailand).

Preparation of EGCG and GTE solution

For the current study, EGCG concentration was varied as 1.8, 3.6, and 7.2% by weight of SPI. GTE concentration was varied as 5, 10, and 20% by weight of SPI so that the films contain similar EGCG content to those films added with EGCG. EGCG and GTE in different oxidation states (oxidized and non-oxidized) were used.

To prepare the non-oxidized phenolic solution, EGCG or GTE was dissolved in phosphate buffer (pH8.0) at the designated concentrations. Meanwhile, the oxidized EGCG and GTE solutions were prepared by first dissolving EGCG or GTE in phosphate buffer (pH8.0) and pH of the solution was adjusted to 9.0 using 1 M NaOH[5]. Oxygen was continuously purged into the solution for 4 h at room temperature (25°C) to induce oxidation of the phenolics and subsequent formation of quinone intermediates.

Preparation of SPI films

SPI film without phenolic addition was used as a control. Film samples were prepared using the method described elsewhere[2] with some modifications. The film-forming solution was prepared by adding 5% SPI (w/w) to phosphate buffer (pH8.0) containing 50% glycerol by weight of SPI. The solution was homogenized using a homogenizer (model X10/25, Ystral, Ballrechten-Dottingen, Germany) at 22,000 rpm/min for 2 min. The film-forming solution was then heated at 70°C for 30 min to partly denature the protein. After that, air bubbles were removed using an ultrasonic technique. An aliquot (40 mL) of the film-forming solution was casted on an acrylic mold (15 cm ×15 cm) and dried at 40°C until 10% moisture content (wet basis) was reached. The dried film was removed from the mold and equilibrated at 50% RH at 25°C for 48 h before being determined for its properties.

For those films incorporated with EGCG or GTE, the preparation steps were similar to those of the control, except that an extra step of adding EGCG or GTE solution was done after the film-forming solution was heated at 70°C for 30 min and then cooled down to room

temperature. Then, the solution was homogenized at 22,000 rpm/min for 1 min before being subjected to ultrasonication and casting.

Determination of film properties

Film thickness

Film sample was trimmed to a 3 cm × 10 cm strip. Thickness was measured with a thickness gauge (model 7301, Mitutoyo, Tokyo, Japan) at ten random points on each stip. The average was calculated and counted as the thickness of one replication.

Mechanical properties

Tensile test of the film samples was done according to the ASTM D882 method[13] using a texture analyzer (model TA.XTplus, Stable Micro System, Godalming, UK) attached with tensile grips (A/TG) probe and equipped with 1 kg load cell. A film sample (3 cm × 10 cm) was fixed on both sides of the grip by clamping onto the 3 cm-wide sides. Grip distance and test speed were set at 50 mm and 8.33 mm/s, respectively. The film sample was pulled until failure. The maximum load needed for pulling the film sample and the distance at which the sample can be stretched before breaking apart were used to calculate tensile strength and elongation to break using Equations (1) and (2):

$$\text{Tensile strength (MPa)} = (F/W\,D) \times 10^{-6} \quad \ldots(1)$$

where F is the maximum load (N) needed to pull the film sample; W is the film width (m); and D is the film thickness (m)

$$\text{Elongation at break (\%)} = (L_f/L_i) \times 100 \quad \ldots(2)$$

where L_f is the film extension at the point of rupture (m); and L_i is the initial length of the film sample (m).

UV and visible light barrier

UV and visible light barrier properties of the film samples were evaluated according to the ASTM D1746 method[14] using an Evolution™ UV-visible spectrophotometer (model 260 Bio, Thermo Scientific, Waltham, MA, USA). %Transmittance was measured at the wavelengths of 275 and 500 nm, for UV and visible light, respectively. A film sample was cut to a size of 1 cm × 4 cm and then mounted onto the inside of a quartz cuvette with 1 cm-light path. An empty cuvette was used to set 100% transmittance.

Film color

Color of the film samples was measured in CIELAB system using a color spectrophotometer (model CM-600d, Konica Minolta Sensing, Osaka, Japan). Determinations were done using standard D65 daylight illuminant and and 10° observer angle. Color was assessed at five random locations on each film strip (3 cm × 10 cm) and then the data were averaged to obtain a measurement of one replicate. Color attributes were expressed in terms of L*, a*, b*, hue angle, and chroma[15].

Water vapor permeability (WVP)

WVP was analyzed according to ASTM E96-95 method[16]. A glass permeation cup was loaded with 20 g of dried silica gel (0% RH) and then silicone grease was sparingly applied onto its rim. A piece of film sample (6 cm × 6 cm) was firmly mounted onto the cup and secured with a rubber ring and Parafilm®. The cup was weighed to obtain an initial weight. The cup was then placed in a desiccator containing distilled water (100% RH) and stored at 25°C. Weight change over time was recorded until a constant weight was obtained. WVP was calculated using Equation (3):

$$\text{WVP (g m/ Pa m}^2\text{ h)} = w\,D/A\,t\,(P_2\text{-}P_1) \quad \ldots(3)$$

where w is the weight gain (g); D is the film thickness (m); A is the area of the film available for water vapor permeation (m^2); t is the time to reach equilibrium (h); P_2-P_1 is the vapor pressure difference across the film (Pa).

Contact angle

Contact angle between a water droplet and the film surface was determined using a contact angle meter (model DM-CE1, Kyowa Interface Science, Saitama, Japan). A film piece (1 cm × 5 cm) was installed on the sample stand, and then a droplet (1.5 µL) of distilled water was deposited on the film surface. Two measurements were done for each sample and averaged out to obtain the contact angle of the replicate.

Water solubility

Water solubility of the film samples was analyzed following the method described earlier[17]. A film sample (2 cm × 2 cm) and Whatman grade 4 filter paper were dried in hot air oven at 70°C for 24 h. The dried film and filter paper were weighed to obtain the initial weight. The film was then transferred to a test tube containing 20 mL of distilled water and the tube was shaken continuously using an Innova® laboratory shaker (model 2050, New Brunswick Scientific, Edison, NJ, USA) for 24 h at 25°C. The mixture obtained was filtered through the dried filter paper and rinsed with 10 mL of distilled water. The filter paper with the remaining film residue was dried in hot air oven at 70°C for 24 h and then weighed to obtain the final weight. The weight of the remaining film was calculated by subtracting the weight of the dried filter paper. Water solubility was calculated according to Equation (4):

$$\text{Water solubility (\%)} = [(W_i - W_f)/W_i] \times 100 \quad \ldots(4)$$

where W_i is initial weight of the dried film sample (g); and W_f is weight of the dried remaining film residue (g).

Microstructure

Cross-sectional microstructure of the film samples was investigated using a scanning electron microscope (SEM) (model JSM-IT300, JEOL, Tokyo, Japan). Sample preparation was carried out by storing the film sample in a desiccator containing dried silica gel for 7 days. The film sample was cut with a sharp razor blade to expose the cross-section, installed onto a brass rod, and sputtered with gold. Microstructure of the film samples was observed at 500× magnification.

SDS-PAGE

Protein pattern was analyzed using SDS-PAGE[18]. The film sample was first solubilized in 5% SDS solution. Then, it was mixed, at a ratio of 1:1 (v/v), with sample buffer (0.5 M Tris-HCl, pH6.8, containing 20% (w/v) SDS, 20% (v/v) glycerol and 1% (w/v) Bromophenol blue). The sample solution was then loaded into polyacrylamide gel made up of 10% running gel and 4% stacking gel. The gel was subjected to electrophoresis at a current of 120V using a Mini-PROTEAN® electrophoresis system (Bio-Rad Laboratories, Bangkok, Thailand). The gel was stained with Coomassie brilliant blue R-250 and then destained to reveal the protein bands.

Fourier transform infrared (FTIR) spectroscopy

C-N cross-linking was monitored using an FTIR spectrometer (model Spectrum One, Perkin Elmer, Waltham, MA, USA) equipped with an attenuated total reflectance (ATR) accessory. %Transmittance was measured in a wavenumber range of 4000-500 cm^{-1}, with a resolution of 4.00 cm^{-1}, and number of scans of 64.

Statistical analysis

The experiment was done in three replicates. A completely randomized design (CRD) was used. Data were analyzed using Analysis of Variance. Duncan's new multiple range

test[19] was used to determine the difference among sample means at p=0.05 using SPSS Statistics 22.0 (IBM, Armonk, NY, USA).

Results and Discussion:

Film thickness

Thickness of the film samples was in a range of 0.186-0.225 mm (**Table 1**). Film thickness was found to increase slightly with increasing EGCG and GTE concentration. Film thickness seemed to be minimally affected by type and oxidation state of the phenolic additive. Addition of 20% oxidized GTE resulted in a film with the greatest thickness (0.225 mm) which is significantly different from that of the control ($p \leq 0.05$). This finding agrees with earlier study which reported a thickness of 0.23 mm for epicatechin-added SPI film[20].

Table 1. Thickness and %transmittance of SPI films incorporated with oxidized and non-oxidized EGCG and GTE at different concentrations

Film samples	Thickness (mm)	%Transmittance	
		UV (275 nm)	Visible (500 nm)
Control	0.178 ± 0.01^{f}	23.77 ± 0.81^{a}	26.65 ± 1.50^{a}
EGCG 1.8%	0.186 ± 0.00^{ef}	14.89 ± 2.82^{b}	7.57 ± 1.22^{c}
EGCG 3.6%	0.187 ± 0.01^{ef}	13.97 ± 1.89^{bc}	6.55 ± 1.31^{cde}
EGCG 7.2%	0.189 ± 0.00^{def}	9.28 ± 0.73^{ef}	3.30 ± 0.62^{f}
Oxi-EGCG 1.8%	0.189 ± 0.01^{def}	13.04 ± 1.38^{bcd}	6.36 ± 2.17^{cde}
Oxi-EGCG 3.6%	0.198 ± 0.01^{cde}	10.86 ± 0.27^{cde}	4.00 ± 1.11^{ef}
Oxi-EGCG 7.2%	0.211 ± 0.01^{abc}	5.54 ± 0.90^{g}	0.69 ± 0.20^{g}
GTE 5%	0.189 ± 0.01^{def}	11.72 ± 3.02^{bcde}	11.89 ± 0.60^{b}
GTE 10%	0.203 ± 0.01^{bcd}	9.29 ± 0.17^{ef}	8.02 ± 1.10^{c}
GTE 20%	0.213 ± 0.01^{ab}	6.77 ± 0.57^{fg}	4.28 ± 0.34^{def}
Oxi-GTE 5%	0.191 ± 0.01^{def}	10.62 ± 3.91^{de}	13.64 ± 3.33^{b}
Oxi-GTE 10%	0.199 ± 0.01^{bcde}	9.98 ± 1.04^{def}	6.84 ± 1.09^{cd}
Oxi-GTE 20%	0.225 ± 0.01^{a}	7.02 ± 0.49^{fg}	2.35 ± 0.46^{fg}

Mean±SD of three replicates

Means in the same column with different superscript letters differ significantly at p=0.05.

Mechanical properties

Tensile strength and elongation at break of the film samples are shown in **Figure 1.** Addition of EGCG or GTE yielded a film with significantly greater tensile strength as compared to the control ($p \leq 0.05$). Tensile strength increased with increasing EGCG or GTE concentration. The film added with 7.2% oxidized EGCG possessed the greatest tensile strength. Tensile strength of the films containing 3.6 and 7.2% oxidized EGCG was greater than the corresponding films added with non-oxidized EGCG or GTE ($p \leq 0.05$). The films added with oxidized EGCG exhibited higher tensile strength than those added with oxidized GTE at the same concentration ($p \leq 0.05$). Similar results were reported earlier for soy protein films fortified with polyphenol extracts[21-22].

This improved tensile strength is attributed to protein cross-linking induced by EGCG and GTE which was monitored using SDS-PAGE (**Figure 2**). The fading protein bands, particularly for the film added with 7.2% EGCG and those added with oxidized EGCG of any concentration, indicated that soy proteins underwent cross-linking to form higher molecular weight species.

Phenolic cross-linking with amino group of proteins results in covalent C-N bond[4]. In this study, formation of C-N bond was monitored using FTIR spectroscopy (**Figure 3**). Changes in transmittance were observed in the C-N stretching region around a wavenumber of 1100 cm^{-1} [23]. A peak in the C-N stretching region became clearly visible in the FTIR spectra of the films added with EGCG or GTE, either non-oxidized or oxidized, as compared to control film. The reduction in transmittance was also observed upon increasing EGCG and GTE concentration in which transmittance of the film added with oxidized EGCG or GTE was lower than that added with the non-oxidized ones. This confirmed the formation of covalent C-N bond in the films incorporated with EGCG or GTE.

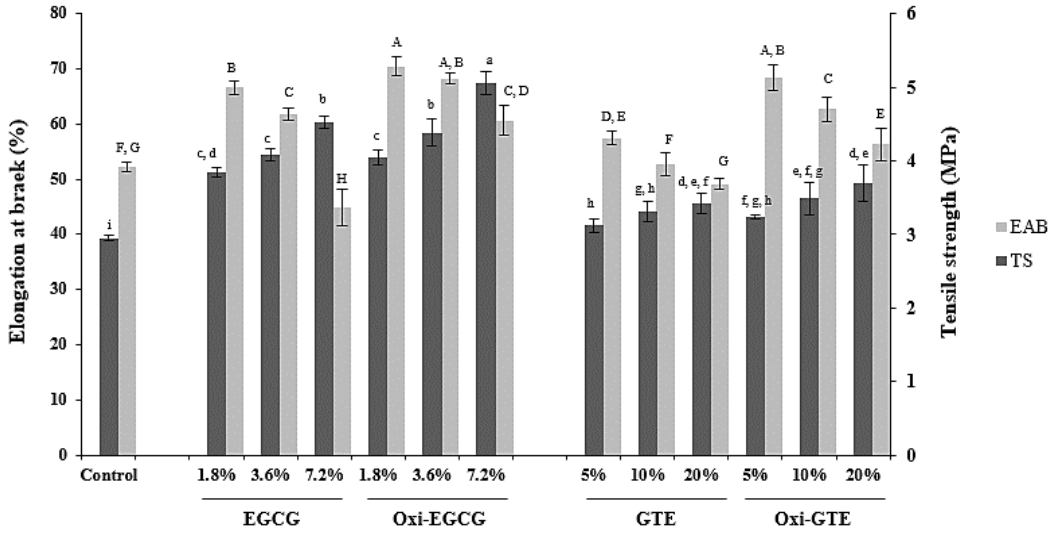

Figure 1. Tensile strength (TS) and elongation at break (EAB) of SPI films incorporated with oxidized and non-oxidized EGCG and GTE at different concentrations

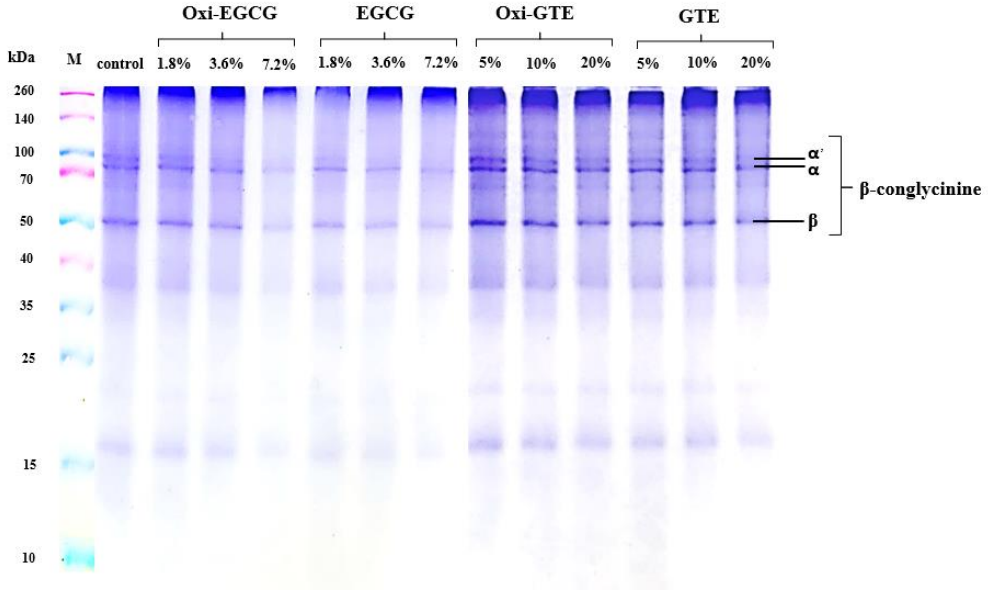

Figure 2. SDS-PAGE patterns of SPI films incorporated with oxidized and non-oxidized EGCG and GTE at different concentrations

In terms of elongation (**Figure 1**), addition of oxidized EGCG or GTE was found to increase elongation at break of the film as compared to the control ($p \leq 0.05$). The highest elongation at break was demonstrated by the film added with 1.8% oxidized EGCG. This may be due to that, besides covalent cross-links, addition of phenolics also promotes the formation of non-covalent interactions, e. g. hydrogen bonding and hydrophobic interaction, among the protein chains which are responsible for the greater flexibility of the film samples. For the decrease in elongation upon increasing EGCG and GTE concentration, this is possibly due to that the enhanced covalent cross-linking among protein chains led to reduced free volume of the polymeric matrix, resulting in a more rigid film structure[5,10]. The finding of this study is consistent with previous report[21] which revealed a decrease in elongation at break of soy protein film with increasing concentration of phenolic-containing licorice residue extract.

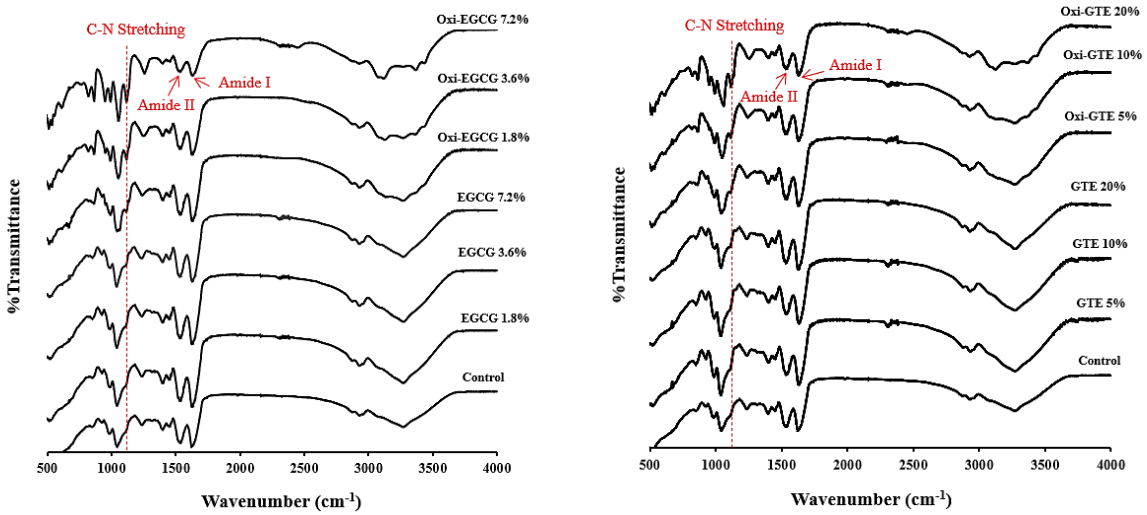

Figure 3. FTIR spectra of SPI films incorporated with oxidized and non-oxidized EGCG and GTE at different concentrations

UV and visible light barrier

UV and visible light barrier properties of the film samples were delineated in **Table 1**. Addition of non-oxidized and oxidized EGCG and GTE caused a significant decrease in UV and visible light transmittance as compared to the control ($p \leq 0.05$). This decrease in light transmission is a combined effect of several factors, namely, the increase in cross-linked protein induced by EGCG and GTE addition, the inherent color the EGCG and GTE, the color of the oxidized phenolics and the polymerized quinones, and the colored products of the reaction between phenolics and protein[2,21,24]. However, the effect of type and oxidation state of phenolic substrates on light transmittance was not different statistically ($p > 0.05$). A reduction in UV transmission of soy protein film incorporated with phenolic-containing chestnut bur extract was also reported earlier[25]. These results show that soy protein film incorporated with non-oxidized and oxidized EGCG and GTE could function as UV and visible light barrier.

Color

Color parameters of the film samples are shown in **Table 2.** Incorporation of non-oxidized and oxidized EGCG and GTE influenced the film color as evidenced by a significant decrease in L* and an increase a* and/or b* ($p \leq 0.05$). Similar changes in color parameters were reported for soy protein film added with phenolic-containing pinhão coat extract[26]. Hue angle of the control film was 92.65° which is close to the yellow hue angle

(90°). Upon adding EGCG and GTE, hue angle gradually changed towards the angle of red (0°). This was mainly due to the color of the oxidized phenolics and the polymerized quinones, as well as the colored products of the reaction between phenolics and protein[2,21,24]. For chroma, the EGCG and GTE-added films were greater in chroma than the control. In spite of that, increasing EGCG and GTE concentrations led to a reduction and chroma value ($p \leq 0.05$).

Table 2. Color parameters of SPI films incorporated with oxidized and non-oxidized EGCG and GTE at different concentrations

Film samples	L*	a*	b*	Hue angle (°)	Chroma
Control	83.64±0.6^{a}	-0.85±0.4^{i}	19.13±1.0^{g}	92.65±1.4^{a}	19.15±1.0^{i}
EGCG 1.8%	48.97±0.7^{d}	15.45±0.4^{f}	32.68±0.5^{c}	64.66±0.9^{c}	36.17±0.3^{e}
EGCG 3.6%	41.43±0.3^{f}	18.24±0.7^{e}	26.63±0.4^{e}	55.44±1.4^{e}	32.32±0.2^{f}
EGCG 7.2%	38.63±1.0^{g}	19.83±0.5^{d}	22.93±1.1^{f}	48.93±1.8^{f}	30.36±0.8^{g}
Oxi-EGCG 1.8%	47.63±1.5^{d}	18.15±0.6^{e}	33.12±0.9^{c}	61.25±0.9^{d}	37.79±1.0^{de}
Oxi-EGCG 3.6%	37.32±2.1^{g}	19.50±0.4^{d}	19.35±0.9^{g}	44.67±0.7^{g}	27.49±0.9^{h}
Oxi-EGCG 7.2%	30.07±2.4^{h}	13.95±0.7^{g}	7.51±0.6^{h}	27.33±2.2^{h}	15.91±0.8^{j}
GTE 5%	62.26±0.3^{b}	11.81±0.4^{h}	34.24±0.9^{bc}	71.00±0.6^{b}	36.23±0.9^{e}
GTE 10%	53.83±0.6^{c}	17.22±0.8^{e}	36.16±0.5^{b}	64.55±0.8^{c}	40.06±0.8^{c}
GTE 20%	44.89±3.0^{e}	21.01±1.0^{c}	29.99±3.0^{d}	54.70±3.9^{e}	36.73±1.9^{e}
Oxi-GTE 5%	63.15±2.1^{b}	14.73±1.1^{fg}	40.51±0.6^{a}	70.06±1.4^{b}	43.12±0.7^{b}
Oxi-GTE 10%	52.04±0.5^{c}	23.22±0.3^{b}	40.01±1.4^{a}	59.84±1.0^{d}	46.29±1.2^{a}
Oxi-GTE 20%	42.28±0.8^{f}	26.79±0.3^{a}	28.80±1.7^{d}	46.79±1.7^{fg}	39.42±1.3^{cd}

Mean±SD of three replicates
Means in the same column with different superscript letters differ significantly at p=0.05.

Water vapor permeability

Water vapor permeability (WVP) of the film samples was in a range of 7.5-9.24 $\times 10^{-7}$ g m/Pa h m^2 (**Table 3**). Addition of EGCG and GTE to SPI film induced a decrease in WVP as compared to the control ($p \leq 0.05$). However, different oxidation state of EGCG and GTE posed no significant effect on WVP of the films ($p > 0.05$). The reduction in WVP may be due to that the induced protein cross-linking resulted in a decrease in intermolecular spaces of the protein available for water vapor diffusion[21,27]. This implied that EGCG and GTE fortification improved water vapor barrier of the SPI film.

Water solubility

Water solubility of the film samples was tabulated in **Table 3.** Compared to the control, addition of EGCG and GTE, either oxidized or non-oxidized, rendered a decrease in water solubility of the film ($p \leq 0.05$). This was due to that phenolic-induced protein cross-linking brought about proteins with increasing molecular weight. Moreover, the cross-linking could also induce a change in the protein net charge thus affecting its solubility[28]. A decreasing trend in water solubility was observed upon increasing concentration of EGCG or GTE. The difference in oxidation state of EGCG and GTE did not pose an effect on water solubility ($p > 0.05$). These findings were in good agreement with the study of the effect of oxidized phenolic compounds on properties of turmeric-gelatin film[5].

Contact angle

Table 3 depicts the contact angle of a water droplet with the surface of the film samples. The films containing EGCG and GTE, either oxidized or non-oxidized, exhibited a lower contact angle than the control ($p \leq 0.05$), indicating that the surface of the modified

films became more hydrophilic upon adding EGCG or GTE. This may be due to the hydrophilic nature of EGCG and GTE[22]. Different oxidation state of EGCG and GTE did not pose an effect on the contact angle ($p>0.05$).

Table 3. Water vapor permeability, water solubility, and contact angle of SPI films incorporated with oxidized and non-oxidized EGCG and GTE at different concentrations

Film samples	WVP ($\times 10^{-7}$ g m/Pa h m^2)	Water solubility (%)	Contact angle (°)
Control	11.5 ±0.18^{a}	63.1 ± 1.22^{a}	52.0 ± 3.23^{a}
EGCG 1.8%	8.12 ±1.6^{b}	46.1 ± 3.26^{bcde}	38.9 ± 2.36^{bc}
EGCG 3.6%	8.04 ±1.79^{b}	43.4 ± 1.84^{cde}	34.7 ± 5.50^{cd}
EGCG 7.2%	7.98 ±1.82^{b}	41.8 ± 1.26^{e}	28.4 ± 0.64^{defg}
Oxi-EGCG 1.8%	7.50 ±1.56^{b}	49.2 ± 1.90^{b}	22.0 ± 0.21^{gh}
Oxi-EGCG 3.6%	7.83 ±1.66^{b}	45.5 ± 2.18^{bcde}	26.4 ± 3.45^{efgh}
Oxi-EGCG 7.2%	8.19 ±2.29^{b}	42.8 ± 21.6^{de}	32.9 ± 0.52^{cde}
GTE 5%	7.69 ±1.1^{b}	47.2 ± 2.34^{bcd}	23.4 ± 2.95^{fgh}
GTE 10%	7.88 ±1.91^{b}	45.6 ± 1.73^{bcde}	32.6 ± 1.11^{cde}
GTE 20%	7.98 ±1.87^{b}	43.4 ± 2.03^{cde}	41.6 ± 1.65^{b}
Oxi-GTE 5%	7.81 ±1.78^{b}	49.5 ± 4.32^{b}	21.3 ± 3.18^{h}
Oxi-GTE 10%	8.09 ±1.17^{b}	47.9 ± 3.94^{bc}	22.6 ± 2.75^{gh}
Oxi-GTE 20%	9.24 ±0.95^{ab}	45.8 ± 2.47^{bcde}	29.4 ± 3.75^{def}

Mean±SD of three replicates
Means in the same column with different superscript letters differ significantly at $p=0.05$.

Microstructure

SEM micrographs of cross-section of the film samples are shown in **Figure 4.** No major microstructural differences were noticed among the film samples. All samples were found to have homogeneous structure and were similar in density.

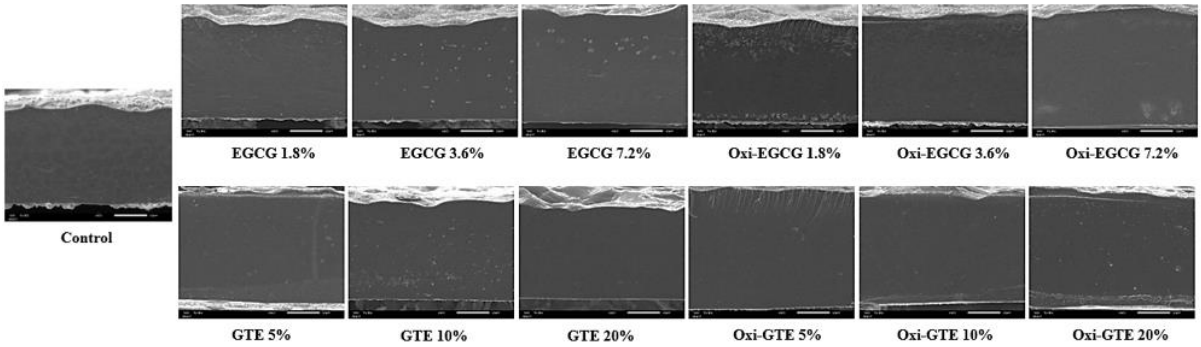

Figrue 4. SEM micrographs of cross-section of SPI films incorporated with oxidized and non-oxidized EGCG and GTE at different concentrations, taken at 500× magnification

Conclusion:

In the current study, EGCG and GTE were proven as efficient modifiers of soy protein film properties via inducing covalent C-N cross-linking of protein. SPI films incorporated with EGCG or GTE, either oxidized or non-oxidized, demonstrated increasing tensile strength and elongation at break, UV and visible light barrier, water vapor barrier,

while water solubility and surface hydrophobicity became decreasing as compared to the control film. Addition of EGCG resulted in a film with the higher tensile strength and elongation at break than those added with GTE.

References:

1. Cho SY, Rhee C. LWT - Food Sci. Technol. 2004;37:833-839.
2. Insaward A., Duangmal K, Mahawanich T. J. Agric. Food Chem. 2015;63:9421-9426.
3. Rawel HM, Czajka D, Rohn S, Kroll J. Int. J. Biol. Macromol. 2002;39:137-150.
4. Strauss G, Gibson SM. Food Hydrocolloids. 2004;16:81-89.
5. Choi IC, Lee SE, Chang Y, Lacroix M, Han J. LWT - Food Sci. Technol. 2018;93:427-433.
6. Peter B, Saftics A, Kovacs B, Kurunczi S, Horvath R. Analyst. 2020;145:588-595.
7. Jamróz E, Kulawik P, Krzyściak P, Talaga-Ćwiertnia K, Juszczak L. Int. J. Biol. Macromol. 2019;122:745-757.
8. Siripatrawan U, Noipha S. Food Hydrocolloids. 2012;27:102-108.
9. Yu S-H, Tsai ML, Lin B-X, Lin C-W, Mi F-L. Food Hydrocolloids. 2015;44:491-505.
10. Prodpran T, Benjakul S, Phatcharat S. Int. J. Biol. Macromol. 2012;51:774-782.
11. Jia Z, Zheng M, Tao F, Chen W, Huang G, Jiang J. LWT - Food Sci. Technol. 2016;66:305-310.
12. Tao F, Xiao C, Chen W, Zhang Y, Pan J, Jia Z. Int. J. Biol. Macromol. 2019;126, 1186-1191.
13. ASTM D882:2009. Standard test method for tensile properties of thin plastic sheeting.
14. ASTM D1746:2015. Standard test method for transparency of plastic sheeting.
15. Mclellan MR, Lind LR, Kime RW. Journal of Food Quality. 1994;18:235-240.
16. ASTM E96-95:1999. Standard test method for water vapor transmission of materials.
17. Perez-Gago MB, Krochta JM. Journal of Food Science. 2001;66:705-709.
18. Laemmli UK. Nature. 1970;227:680-685.
19. Cochran WG, Cox GM. Experimental Designs. Wiley, New York, 1957.
20. Friesen K, Chang C, Nickerson M. Food Chemistry. 2015;172:18-23.
21. Han Y, Yu M, Wang L. Food Hydrocolloids. 2018;75: 13-21.
22. Zhou X, Dai Q, Huang X, Qin Z. e-Polymers. 2021; 21: 575–589.
23. Sisson K, Zhang C, Farach-Carson MC, Chase DB, Rabolt JF. Biomacromolecules. 2009;10:1675-1680.
24. Dai Q, He Y, Ho CT, Wang J, Wang S, Yang Y, Gao L, Xia T. J Food Sci Technol. 2017;54(9):2919-2928.
25. Wang H, Hu D, Ma Q, Wang L. LWT - Food Sci. Technol. 2016;71:33-39.
26. de Souza KC et al. Food Bioprocess Technol. 2020;13:998-1008.
27. Munir S, Javed M, Hu Y, Liu Y, Xiong S. Polymers. 2020;12:2281.
28. Yan S, Xie F, Zhang S, Jiang L, Qi B, Li Y. Colloids and Surfaces A. 2021;609:125641.

ENZYMES-ASSISTED EXTRACTION OF BIOACTIVE COMPOUNDS FROM NONI LEAVES (*Morinda citrifolia*)

Waraporn Sorndech,[1*] Thongkorn Ploypetchara,[1] Siriporn Butseekhot,[1] Chiramet Auranwiwat,[2] Wiriyaporn Sumsakul[2] and Sinee Siricoon[1]
[1]Expert Center of Innovative Health Food, Thailand Institute of Scientific and Technological Research, 35, Mu.3, Klongha, Klongluang, Pathum Thani, 12120, Thailand
[2]Expert Center of Innovative Herbal Products, Thailand Institute of Scientific and Technological Research, 35, Mu.3, Klongha, Klongluang, Pathum Thani, 12120, Thailand
*e-mail: waraporn_s@tistr.or.th

Abstract:
Noni leaves provide several health benefits as food and traditional medicines due to their bioactive compounds. This study investigated the preliminary effects of cellulase and hemicellulase assisted extraction on bioactive compounds extraction from noni leaves compared to maceration technique. Cellulase and hemicellulase-assisted extraction formed small holes on the extracts surface and provided rough surface, angular and fragmentation structures indicated some breakdown of noni leaves cell wall after enzyme reaction. There was a significant difference of the extracts particle size between the samples from cellulase assisted extraction and hemicellulase assisted extraction while no significant difference was observed between the samples from maceration technique and cellulase assisted extraction. For antioxidant activity, cellulase assisted extraction provided the highest antioxidant activity (92.83 and 73.05 mg TEAC g of sample^{-1} which was determined by DPPH and FRAP method respectively). However, hemicellulase extraction exhibited the lowest antioxidant activity (36.38 and 33.33 mg TEAC g of sample^{-1} in DPPH and FRAP method respectively). This results can lead to the use of green technology for bioactive compounds extraction from plant sources for use as a medical and functional food ingredients.

Introduction:
Noni (*Morinda citrifolia*) leaves and fruits are recognized as a food source and traditional medicinal such as to heal the affected parts of the skin and reduce pain.[1] Many active ingredients were found in the leaves such as β-carotene, saponin, kaempferol, alkaloids, iridoid glycosides, quercetin, rutin, tannins, terpenoids, ursolic acid, and flavonoids.[(1,2)] Moreover, these phytoactive compounds were possessed as anticancer[3], antiviral activity anti-inflammatory, antidyslipidemic, and antioxidant activities.[2] Recent studies showed that Noni leaf extracts by maceration technique could protects against cerebral ischemia and osteoporosis in menopause.[4] Shalan et al. reported that the water extracts of noni leaves increased bone regeneration biomarker expressions indicating benefits for the aged and menopausal women.[5] The properties of Noni leaf crude extract have been reported by Thani et al. who suggested that the compounds from Noni leaf extract provided a beneficial as a treatment of cancer cell. The dried Noni leaves were extracted by dichloromethane and the results showed that the extract presented cytotoxicity against the human epidermoid carcinoma or KB cell line.[6] These results suggested that the utilization of crude noni leaves extract provided more safety as a treatment of cancer cell as compared to the pure compounds. In addition, noni leaves extract could provide the antimicrobial activity, Zhang et al. reported that the noni leaves extract by using n-butanol as a solvent provided the most effective extracts to destroy *Escherichia coli*, *Proteus vulgaris*, *Staphylococcus aureus*, and

Bacillus subtilis.[7] Hence, the preparation of noni leaves extract is the key factor to obtain high fraction of bioactive compounds.

Preparation or extraction of bioactive compound from plants for experimental purposes is the most important step to achieving the target compounds. The most common extraction technique is maceration which is the simplest extraction techniques. This method consist of the preparation of dried pieces plants materials, soaked the plant materials into the appropriate solvent, incubated and recovered the extracts. The maceration process has the purpose to soften and destroy the cell wall of plant to release the solvent soluble phytochemicals. However, the maceration technique may has some limitation such as take a long extraction time, low extraction efficiency, low extraction yield, and need large amount of extraction solvents which can lead to a high cost of waste management and health disadvantages.[8]

Enzymes are biological molecules defining structural organization that influence their catalytic function with great specificity and rate enhancements.[9] Enzyme technology could be seen the application to employ in industrial biotechnology for numerous purposes for the production of novel and sustainable products at a speedy rate. According to the bioactive compounds extraction from plant materials, the plant cell wall is normally consisted of carbohydrate-based polymers, such as cellulose, hemicelluloses and pectins, etc. Hence, the cell wall degrading enzymes are considered to utilize as an alternative way of bioactive compounds extraction from plant materials. Cellulases enzymes which are produced by cellulolytic microbes capable of hydrolizing β-1,4 glycoside bond in cellulose, were indicated a target for both academic as well as industrial research.[10] The cellulase enzyme system consists of three groups of hydrolytic enzymes; endo-(1,4)-β-D-glucanase (endoglucanases), exo-(1,4)-β-D-glucanase (exoglucanases), and β -glucosidase.[10] Hemicellulases, substance hydrolysis by commercial pectinases or cellulases yields hydrolytic products, are an enzyme of the major hemicellulolytic enzymatic components include endoxylanase (EC 3.2.1.8, 1,4-β-D xylan xylanohydrolase), which hydrolyzes β-D xylano pyranosyl linkages of xylan to form xylo-oligosaccharides.[11] Cellulases and hemicellulases have been played a crucial role as biocatalysts which a potential application in a large number of industries such as in food biotechnology as well textile, paper and pulp, laundry and detergent, agriculture, medicine, and feed industries.[12] Thus, the objectives of this preliminary experiment were to investigate the effect of cellulase or hemicellulase catalysis on the efficiency of bioactive compounds extraction from Noni leaf (*Morinda citrifolia*) as determined by antioxidant activity. The morphology of the extracts and particle size distribution were determined in order to observe the reaction of enzymes catalysis. All results from this preliminary experiment can be used as a fundamental data for the further investigation of functional food ingredients or novel medicine development.

Methodology:

Materials

Noni leaves (Morinda citrifolia) were obtained from Backyard Herbal Store (Chonburi, Thailand). Cellulase and hemicellulase were the gifts from Amano Enzyme Asia Pacific Co., Ltd. (Pathum Thani, Thailand). Enzyme activity units of cellulase and hemicellulase were given according to the supplier.

Bioactive polysaccharides extraction

Preparation of dry Noni powder. Fresh noni leaves were washed. Small pieces of Noni were prepared and dried at 60ºC for 24 h in tray dryer. The dried Noni leaves was pulverized to fine powder and sieved through a 100-μm filter. The obtained powder was kept in a zipped plastic bag for further extraction and analysis.

Maceration technique. Maceration of bioactive polysaccharides from noni leaves was performed according to the method of Minjares-Fuentes et al.[13] The dry powder (10% wv^{-1}) was prepared in an erlenmayer flask, dissolved in deionized water and incubated at 60oC, at 150 rpm for 3 h in a shaking incubator. The sample were centrifuged at 4°C, at 8,000 rpm for 30 min and supernatant was collected. The supernatant was precipitated using 2 volumes of absolute ethanol, for 16 h at 4°C and centrifuged at 4°C, 8,000 rpm for 30 min. The precipitate was collected and lyophilized to obtain the water extracted polysaccharides. The yield of each extract was calculated, and the sample was kept in a zipped plastic bag for further analysis.

Cellulase and hemicellulase assisted extraction. The extraction of bioactive polysaccharides from Noni was performed according to the modified method of Minjares-Fuentes et al.[13] The dry Noni leaves powder (10% wv^{-1}) was prepared in an erlenmayer flask with 0.05 M, pH 4.5 sodium acetate buffer. Cellulase (100 U g $powder^{-1}$) was added and incubated at 55°C while hemicallulase (100 U g $powder^{-1}$) was incubated at 50 °C at 150 rpm for 16 h in a shaking incubator. The reaction was stopped by heating at 100oC for 30 min. The sample was centrifuged, precipitated in 2 volumes of absolute ethanol and dried, following the water extraction method and the sample was kept for further analysis.

Microstructure of bioactive polysaccharides

The microstructure morphology of all extracts was observed according to Prompiputtanapon, et al.[14] with field emission scanning electron microscopy (FESEM) (JEOL JSM-7800F, Japan). The samples were coated by gold and stick into the stainless stub for SEM.

Particle size distribution

Particle size distribution (D50) of all samples was determined according to Prompiputtanapon, et al.[14] with slightly modification by using diffraction particle size analyzer (HORIBA LA-950, HORIBA Scientific, Japan). The sample (approximately 0.3–0.5 mg) was prepared in deionized water (200–250 mL) and analyzed using a He–Ne gas laser. The analysis were performed at room temperature using 1.33 as the refractive index of deionized water.

Total phenolic content

The total phenolic content of each extract was determined as described by Aryal, et al.[15] A 0.5 mL of sample extract was mixed with 0.5 mL Folin–Ciocalteu's reagent, followed by addition of 10 mL of 7% Na_2CO_3 solution. The mixture was incubated for 1 h at 25°C in the dark and then absorbance was measured at 765 nm. The gallic acid standard curve was drawn and the results were expressed as mg of gallic acid equivalents per g of extract (mg GAE g^{-1} dry weight).

Antioxidant activity

DPPH assay. The determination of antioxidant activity of bioactive polysaccharides was performed by using 1,1-diphenyl-2-picrylhydrazyl (DPPH).[16] DPPH (100 µL, 200 µM) was added to the samples (50 µL). The mixtures were placed in the dark condition for 30 min. The absorbance was measured at 517 nm using a microplate reader (DKSH (Thailand)., Ltd, Thailand). Antioxidant activity was calculated from a standard curve as milligrams trolox equivalent per 1 grams of sample (mg TEAC g of $sample^{-1}$).

FRAP assay. The ferric reducing antioxidant power (FRAP) assay of the extracts were measured according to the method of Benzie and Strain.[17] The FRAP reagent was freshly prepared by mixing of 10 mM of TPTZ (2,4,6- tripyridyl-s-triazine) in 40 mM HCl, 20 mM FeCl3 6H2O in distilled water and pH 3.6 of 300 mM acetate buffer. The polysaccharide extracted or trolox (30 µL) was added by 270 µL of FRAP reagent and incubated for 30 min

at room temperature. The absorbance was measured at 593 nm and the standard of trolox was plotted. Antioxidant activity was calculated from a standard curve as milligrams trolox equivalent per 1 grams of sample (mg TEAC g of sample^{-1}).

Results and Discussion:

Microstructure of noni leaves extracts with different procedures under field emission scanning electron microscope (original magnification 3,000x) was showed in Figure 1. The reachable surface area of cellulose by enzymes and substrate porosity are expected to change during cellulase or hemicellulase hydrolysis. Generally, cellulose contains crystalline and amorphous regions, they have strong hydrogen bonds among the glucose subunits to form strong tendency of inter and intra-glucose polymers which are occurred within and between cellulose chains. The single enzyme extractions of noni leave provided sponge-like erosion and roughened surface due to the exo-corrosion of enzymes reaction (Figure 1B, C). However, the noni leaves extracts from maceration technique showed flake structure and smoother surface as compared to the enzyme extraction. This result may be explained by the fact that these two enzymes mainly attacked cellulose cell-wall which are the major component of the plant cell wall and producing the porous surface. Moreover, the formation of the noni leaves surface pores were expected to occur within amorphous region which consisted of the less ordered structure as compared to crystalline region. In addition, noni leaves also consist of the other β-D-glucopyranosides derivatives such as quercetin-3-*O*-β-D-glucopyranoside and quercetin-3-*O*-α-L-rhamnopyranosyl-(1-6)-β-D-glucopyranoside, etc. which could be partially hydrolyzed by cellulase or hemicellulase.[18] This finding is consistent with that of Fan et al. who reported that the surface area of sulfite pulp were increased during cellulase hydrolysis within the first 6h of incubation which corresponded to the formation of surface pores.[19]

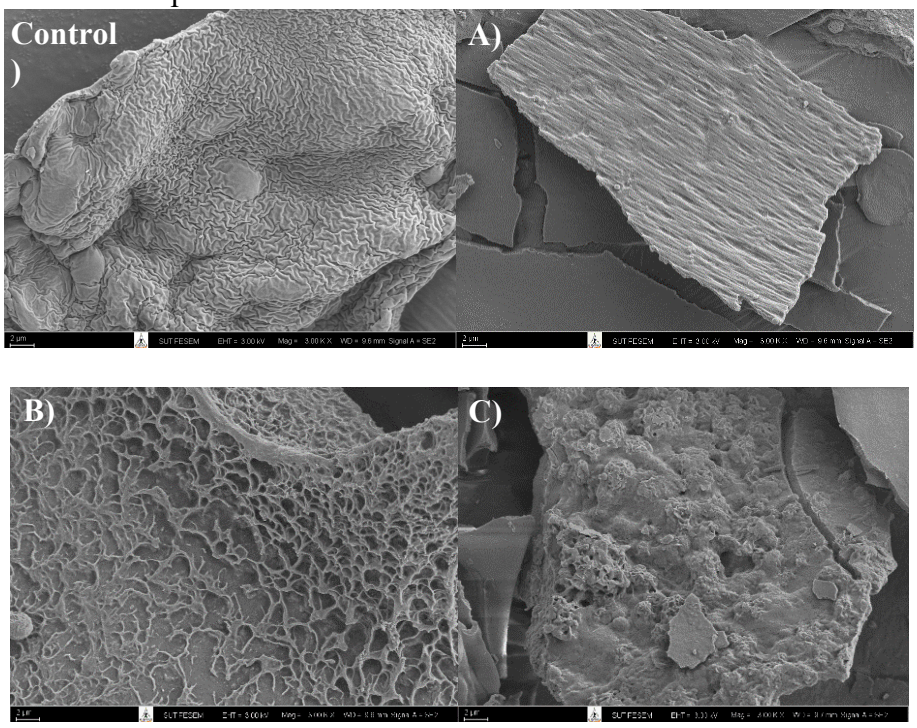

Figure 1.

Internal microstructures of raw noni leaves and noni leaves extracts. Control) raw noni leaves, A) maceration technique, B) cellulase and C) hemicellulase assisted extraction with a magnification of 3,000x.

In order to investigate the effect of enzymes assisted extraction of bioactive compounds from noni leaves on the particle size, the diffraction particle size analyzer was used in this study (Table 1). Generally, particle size is related to storage time and moisture absorption properties, which linked to the process of handling and transportation of powders.[20] The average particle sizes from maceration technique, cellulase assisted extraction and hemicellulase assisted extraction were 121.09, 122.95 and 136.91 μm, respectively which showed in Table 1. There was a significant difference ($p < 0.05$) between the samples from cellulase assisted extraction and hemicellulase assisted extraction while no significant difference ($p \geq 0.05$) was observed between the samples from maceration technique and cellulase assisted extraction. The results indicated that the larger particle size of extract was obtained when using hemicellulase assisted extraction. A possible explanation for this might be that there was some aggregation of bioactive compounds after hemicellulase hydrolysis. This finding is contrary to previous studies which have suggested that the increase of cellulose surface area may cause by the particle size reduction by cellulase accessibility of cell-wall structure.[21]

Table 1.
Particle size distribution of noni leaves extracts from maceration technique, cellulase and hemicellulase assisted extraction.

Sample	Particle size distribution (μm)
Maceration technique	121.09±1.85^{b}
Cellulase assisted extraction	122.95±0.17^{b}
Hemicellulase assisted extraction	136.91±3.44^{a}

Each value represents mean ± SD (n = 3). Different superscript letters in the same column indicate significant difference ($p \leq 0.05$).

The total phenolic compounds and antioxidant activity of noni leaves extracts which determined by 2,2-Diphenyl-1-picrylhydrazylradical scavenging activity (DPPH) and ferric reducing ability of plasma (FRAP) assay were showed in Table 2. All samples displayed very low content of total phenolic compound which ranging from 0.04-0.06 mg GAE g of sample-1. Cellulase assisted extraction provided the highest antioxidant activity (92.83 and 73.05 mg TEAC g of sample-1 which was determined by DPPH and FRAP method respectively). In contrast, hemicellulase extraction exhibited the lowest antioxidant activity (36.38 and 33.33 mg TEAC g of sample^{-1} in DPPH and FRAP method respectively). In the case of water extraction, the whole structure of leaves cell wall and some cell wall debris were obtained. Thus, some bioactive compounds was trapped inside the cell-wall and restrict the antioxidant activity. Generally, cellulase catalyze the degradation of cellulose yielding, mainly glucose, cellobiose, and higher Mw oligosaccharides while hemicellulase catalyze the degradation of cellulose and xylan yielding, mainly glucose, xylose and arabinose. Cellulase extraction can release abundant glucose content from noni leaves cell walls which opened the plant structure to release the bioactive compounds. This result is corresponded to the releasing of some iridoid glycosides compounds such as deacetylasperulosidic acid, asperulosidic acid and asperuloglycosides which has glucose in their chemical structure.[22] Moreover, the antioxidant activity data was related to Soonsit, et al. who reported that *Morinda citrifolia* (noni) leaves

extract by water extraction can significantly increase cell proliferation and alkaline phosphatase activity in human fetal osteoblast cell line (hFOB1.1.9).[23]

Table 2.
Phenolic compound and antioxidant activity of noni leaves extracts by using water, cellulase and hemicellulase-assisted extraction.

Sample	Phenolic compound (mg GAE g of sample^{-1})	Antioxidant activity (mg TEAC g of sample^{-1})	
		DPPH assay	FRAP assay
Raw noni leaves	15.70±0.7500^{a}	9.96 ± 2.10^{d}	35.27 ±1.23^{c}
Maceration technique	0.04±0.0004^{b}	72.30±2.91^{b}	70.38±1.92^{b}
Cellulase-assisted extraction	0.06±0.002^{b}	92.83±0.91^{a}	73.05±1.37^{a}
Hemicellulase-assisted extraction	0.05±0.001^{b}	36.38±3.43^{c}	33.33±1.03^{c}

Each value represents mean ± SD (n = 3). Different superscript letters in the same column indicate significant difference ($p \leq 0.05$).

Conclusion:

The bioactive compounds from noni leaves (*Morinda citrifolia*) was extracted by enzymes-assisted extraction technique. Cellulase and hemicellulase-assisted extraction showed small-hole, rough surface, angular and fragmentation structures. The larger particle size of extract was obtained when using hemicellulase assisted extraction which was 136.91 µm. Moreover, cellulase-assisted extraction provided the highest antioxidant activity (92.83 and 73.05 mg TEAC g of sample-1 which was determined by DPPH and FRAP method respectively). Hence, using cellulase-assisted extraction is the alternative clean technology to increase the bioactive compounds that has high antioxidant activity. Further research should be undertaken to explore how bioactive compounds target delivery and control bioactive compounds release which will be a pivotal role in the future of medicinal and functional food ingredients.

Acknowledgements:

This research was supported by The National Research Council of Thailand (project no. 109296) and Thailand Institute of Scientific and Technological Research (TISTR).

References:

1. Ananthanawat C, Vilaivan T, Hoven VP. Sens Actuators B. 2009;137:215–221.
1. Rezeki S, Sunnati, Vidirachmilla N. 2017;10(4):1735–1740.
2. Chong CLG., Othman F, Hussan F. 2018;6317434.
3. Torres M, de Fátima Braga Magalhães I, Mondêgo-Oliveira R, de Sá JC, Rocha AL, Abreu-Silva AL. 2017;31(7):971–979.
4. Wattanathorn J, Thipkaew C, Thukham-mee W, Muchimapura S, Wannanon P, Tong-un T. 2018;1039364.
5. Shalan NAAM, Mustapha NM, Mohamed S. 2017;33:42-51.
6. Thani W, Vallisuta O, Siripong P, Ruangwises N. 2010; 41(2): 482–489.
7. Zhang WM, Wang W, Zhang JJ, Wang ZR, Wang Y, Hao WJ, Huang WY. 2016;81(5):M1192–M1196.
8. Farooq S, Mir SA, Shah MA, Manickavasagan A. 2017:23-37.

9. van Beilen JB, Li Z. 2002;13(4):338–344.
10. Lokapirnasari WP, Nazar DS, Nurhajati T, Supranianondo K, Yulianto AB. 2015;8(3):367–371.
11. Meena M, Zehra A, Dubey MK, Aamir M, Upadhyay RS. 2018:167–186.
12. Jayasekara S, Ratnayake R. 2019:66517.
13. Minjares-Fuentes R, Rodríguez-González VM, González-Laredo RF, Eim V, González-Centeno MR, Femenia A. 2017;168:327-336.
14. Prompiputtanapon K, Sorndech W, Tongta S. 2020;72(3-4):1900133.
15. Aryal S, Baniya MK, Danekhu K, Kunwar P, Gurung R, Koirala N. 2019;8(4).
16. Olugbami JO, Gbadegesin MA, Odunola OA. 2015;7(1):49.
17. Benzie IFF, Strain JJ. 1996;239:70-76.
18. Abou Assi R. Darwis Y, Abdulbaqi IM, Khan AA, Vuanghao L, Laghari MH. 2017;10(5):691-707.
19. Fan LT, Lee Y-H, Beardmore DH. 1980;22:177-199.
20. Janiszewska-Turak E, Dellarosa N, Tylewicz U, Laghi L, Romani S, Dalla Rosa M, Witrowa-Rajchert D. 2017;236:134-141.
21. Ragauskas AJ, Meng X, Yoo CG, Li M. 2016;1(3):87-94.
22. Deng S, West BJ, Palu AK, Jensen CJ. 2011;22(1):26-30.
23. Soonsit O. Suksiriphattanapong B. Sorndech W. Kasekarn W. 2021;BMB 2021.

Corresponding Author Index (Proceeding Book)

สมาคมวิทยาศาสตร์แห่งประเทศไทยในพระบรมราชูปถัมภ์
http://www.scicoc.or.th/stt/